Proceedings of:

The Fourteenth Annual Meeting

The American Society for Precision Engineering

October 31 - November 5, 1999

Monterey Conference Center and Doubletree Hotel at Fisherman's Wharf

Monterey, California

The American Society for Precision Engineering (ASPE) is a multidisciplinary professional and technical society concerned with research and development, design, manufacture and measurement of high accuracy components and systems. ASPE activities encompass relevant aspects of mechanical, electronic, optical and production engineering, physics, chemistry, and computer and materials science. Membership is open to anyone interested in any aspect of precision engineering.

Founded in 1986, ASPE provides a new focus for a diverse but important community. Other professional organizations have covered aspects of precision engineering, always as a sideline to their principal goals. ASPE is based on the core of generic concepts necessary to achieve precision in any application; independent of discipline, ASPE intends to be the focus for precision technology — and to represent all facets from research to application.

ASPE — The American Society for Precision Engineering
301 Glenwood Avenue, Suite 205, Raleigh, NC 27603
P.O. Box 10826, Raleigh, NC 27605-0826
Phone (919) 839-8444 Fax (919) 839-8039

Preface

This book comprises the proceedings of the 1999 Annual Meeting. The contributions reflect the authors' opinions and are published as presented to ASPE, without change. Their inclusion in this publication does not necessarily constitute endorsement by the ASPE, or its editorial staff.

Individual readers of this book and nonprofit libraries acting for them are permitted to make fair use of the material contained in this book to be used in teaching or research; provided they copy said paper in total, as written by the author. Permission is granted to quote excerpts from the scientific or technical works in this book with proper acknowledgement of the source to include: the author's name, the book name, and the ASPE tag line. Reproduction of figures and tables is likewise permitted from the contents of this book, provided that the same acknowledgment of the same source and content is printed.

Any other type reproduction, systematic copying or multiple reproduction of any material in this book is expressly prohibited except with the written permission of the ASPE editorial staff, addressed to the Society's headquarters.

ISBN 1-887706-22-4

1999

American Society for Precision Engineering
301 Glenwood Avenue, Suite 205
Raleigh, NC 27603

Printed in the United States of America

Welcome Note

The American Society for Precision Engineering celebrates its Fourteenth Annual Meeting this year in Monterey, California. The remarkable growth and success of the Society is reflective of the increasing importance of precision engineering in a wide variety of fields of endeavor, from manufacturing to microelectronics to basic science. The Society serves as a focus for precision engineers across all of these fields. The Annual Meeting has evolved into a premier international forum for the exchange of ideas and presentation of research results relating to precision engineering problems involving mechanical parts, electronic components, materials and material processing, metrology, controls, and system integration. Precision engineers and scientists from private industry, government laboratories, and universities meet to learn about the latest developments and to exchange ideas about the future directions of these technologies.

This year's meeting continues the tradition of offering two full days of tutorials presented by some of the foremost precision engineers and scientists in the world. Many participants cite the tutorial program as one of the most valuable features of the meeting. The technical sessions and poster presentations offer the latest research results in the areas of ultraprecision machining, metrology, controls, precision grinding, micro-positioning, material processing, design, precision transducers, surface profilometry, machine tool metrology, and error compensation. The commercial exhibit will provide attendees with the opportunity to view and discuss the latest precision engineering equipment, products, and services that are commercially available. The open forum will give attendees the opportunity to express their opinions and pose questions for discussion by the group, enhancing the exchange of information.

The conference organizing committee is proud to present the program for the Fourteenth Annual Meeting of ASPE. We welcome your participation.

Welcome to Monterey.

1999 ASPE Meeting Organizing Committee

Irving F. Stowers – Chairman – Lawrence Livermore National Laboratory

Ekkard Brinksmeier – University of Bremen
John H. Bruning – Tropel Corporation
James B. Bryan – Bryan Associates
John Corbett – Cranfield University & euspen Director
Bradley N. Damazo – National Institute of Standards and Technology
David William Davis – Precitech, Inc.
Thomas A. Dow – North Carolina State University & ASPE Executive Director
W. Tyler Estler – National Institute of Standards and Technology
Chris J. Evans – National Institute of Standards and Technology
Steven C. Fawcett – MicroE, Inc.
Yuji Furukawa – Tokyo Metropolitan University & JSPE President
Anthony E. Gee – Cranfield University
Don Golini – QED Technologies
Andrew J. Hazelton – Nikon Research Corporation of America
Debra A. Krulewich Born– Lawrence Livermore National Laboratory
Erwin G. Loewen – Consultant
Don A. Lucca – Oklahoma State University
Dan E. Luttrell – Corning, Inc.
Don L. Martin – Lion Precision
E. Ray McClure – Tumax Engineering
Patrick McKeown – Pat McKeown & Assoc. & euspen President
Michele H. Miller – Michigan Technological University
Yoshiharu Namba – Chubu University
Dennis A. Swyt – National Institute of Standards and Technology
Hooman Tajbakhsh – Lawrence Livermore National Laboratory
E. Clayton Teague – National Institute of Standards and Technology
Hy D. Tran – University of New Mexico
David L. Trumper – Massachusetts Institute of Technology
Andrew D. Woodfin – University of North Carolina-Charlotte & ASPE Student Chapter President
Dave H. Youden – Eastman Kodak Company & ASPE President
Carl A. Zanoni – Zygo Corporation

1999 Annual Meeting
Contents

Preface . . . . . *ii*

Welcome Note . . . . . *iii*

Organizing Committee . . . . . *iv*

Sponsor Members . . . . . *vi*

Cooperating Sponsors—Technical Exhibitors . . . . . *vii*

Program . . . . . *viii*

Keynote Speaker . . . . . *ix*

1999 Scholarship Recipients . . . . . *ix*

1999 Lifetime Achievement Award . . . . . *x*

Executive Forum/Commercial Session/Open Forum *1*

Technical Paper Index *2-12*

Technical Papers *15-613*

Authors Index *615-618*

Sponsor Members of the ASPE

3M Company
St. Paul, MN 55144
Contact: William J. Bryan
(612) 575-1465

ADCOLE Corporation
Marlborough, MA 01752
Contact: Addison D. Cole
(508) 485-9100

ADE Corporation
Newton, MA 02466
(617) 831-8000
Contact: Jon Allen

Chardon Tool & Supply Company, Inc.
Chardon, OH 44024
Contact: Weldon Bennett
(216) 286-6440

Contour Fine Tooling, Inc.
Marlborough, NH 03455
Contact: Jeffrey Tomlin
(603) 876-4908

Corning Inc.
Science & Technology Division
Corning, NY 14831
Contact: Dan E. Luttrell
(607) 974-3393

Cranfield Precision, Div. of Landis Lund
A Western Atlas Corporation
Cranfield, Bedford MK43 OAL, England
Contact: Keith G. Dobson
011-44-1234-752789

D.A.C. Vision
Carpinteria, CA 93013
Contact: John R. Keller
(805) 684-8307

Dover Instrument Corporation
Westboro, MA 01581
Contact: Stephen L. Hero
(508) 366-1456

Fabreeka International, Inc.
Stoughton, MA 02072
Contact: Robert P. Haley
(781) 341-3655

Federal Products Company
Providence, RI 02940
Contact: Robert A. Frick
(401) 784-3313

Fisba Optik, L.L.C.
Rochester, NY 14620
Contact: John J. Nemechek
(716) 473-3990

Lawrence Livermore National Laboratory
Livermore, CA 94550
Contact: Robert Burleson
(925) 423-1967

Lion Precision
St. Paul, MN 55126
Contact: Don L. Martin
(612) 484-6544

MicroE, Inc.
Natick, MA 01760-1313
Contact: Robert W. Morgenroth
(508) 903-5000

Moore Special Tool Company
Bridgeport, CT 06607-0088
Contact: Kevin Uhlig
(203) 366-3224

New Way Machine Components
Aston, PA 19014
Contact: Andrew J. Devitt
(610) 494-6700

Precitech, Inc.
Keene, NH 03431
Contact: David Davis
(603) 357-2511

Professional Instruments Company
Minneapolis, MN 55416
Contact: James Arneson
(612) 933-1222

Reflexite-Precision Technology Center
West Henrietta, NY 14586
Contact: Steven M. Scott
(716) 272-0309

Seagate Technology
Scotts Valley, CA 95067
Contact: Bernd M. Seeger
(408) 439-3781

Tropel Corporation
Fairport, NY 14450
Contact: John H. Bruning
(716) 388-3400

Zygo Corporation
Middlefield, CT 06455-0448
Contact: Carl A. Zanoni
(860) 704-5102

Cooperating Sponsors

Elsevier Science, Inc.
euspen – European Society for Precision Engineering and Nanotechnology
Japan Society for Precision Engineering

Technical Exhibitors

ADE Phase Shift
ADE Technologies, Inc.
Advance Hivolt
Bal-tec
Burleigh Instruments, Inc.
Center for Optics Manufacturing—University of Rochester
Center for Precision Metrology—University of N.C. at Charlotte
Chardon Tool
Contour Fine Tooling, Inc.
Cranfield Precision, Division of Landis Lund
Digital Instruments, Veeco Metrology Group
Dover Instrument Corporation
euspen – European Society for Precision Engineering and Nanotechnology
Fabreeka International, Inc.
Heidenhain Corporation
K & Y Diamond Ltd.
Lawrence Livermore National Laboratory
Lion Precision
Machine Dynamics Research Lab.—Penn State University
Moore Nanotechnology Systems LLC
New Way Machine Components, Inc.
Precision Engineering Center—N.C. State University
Precitech, Inc.
Professional Instruments Company, Inc.
Queensgate Instruments, Inc.
SNU Precision Company, Ltd.
Techmetals, Inc.
Technodiamant U.S.A. Inc.
Tropel Corporation
Veeco Metrology Group
Zygo Corporation

Program

1999 ASPE Annual Meeting

Time	Sun., Oct. 31	Mon., Nov. 1	Tues., Nov. 2	Wed., Nov. 3		Thurs., Nov. 4	Fri., Nov. 5
8:00	Registration		Registration and Continental Breakfast				
9:00	Tutorials	Tutorials + Executive Forum	Technical Session 1	Technical Session 4	Technical Session 7	Technical Session 10	Technical Tours
10:00	Break	Break	Break	Break		Break	
11:00	Tutorials	Tutorials + Executive Forum	Technical Session 2	Technical Session 5	Technical Session 8	Technical Session 11	
12:00			Lunch and Committee Meetings	Awards Lunch and Business Meeting		Lunch and Invited Paper	
1:00							
2:00	Tutorials	Tutorials + Executive Forum	Technical Session 3	Technical Session 6	Technical Session 9	Technical Session 12	
3:00			Break	Break		Break	
4:00	Break	Break	Commercial Session Hospitality Hour	Poster Papers Session and Commercial Exhibits Hospitality Hour		Technical Session 13	
5:00	Tutorials	Tutorials + Executive Forum					
6:00			Poster Papers Session and Commercial Exhibits	"Horrobilia" Open Forum			
7:00	Student Reception	Keynote Address					
8:00		Welcome Reception	Dinner Banquet				
9:00							

Keynote Speaker

Graham J. Siddall

Monday, November 1, 6:30 p.m.

Session Chair: Irving F. Stowers, Lawrence Livermore National Laboratory

Graham Siddall has recently been named President and Chief Executive Officer of Credence Systems Corporation in Fremont, California. Credence Systems is a leading manufacturer of automatic test equipment that serves a broad spectrum of the worldwide semiconductor industry's testing needs. Prior to joining Credence, he was Executive Vice President of the Wafer Inspection Group of KLA-Tencor Corp. Dr. Siddall joined Tencor in 1988 as VP of Marketing and was named Executive Vice President and Chief Operating Officer in 1995. He became VP of the Wafer Inspection Group when Tencor Instruments merged with KLA Instruments in 1997. Before joining Tencor, Graham was employed by GCA Corp. and Hewlett Packard. He came to the U.S. in 1976 as a research fellow in physics at Stanford University.

Dr. Siddall was awarded the M.Sc. and Ph.D. degree in instrument design in 1971 and 1975 respectively from the University of Aberdeen in Scotland. He previously earned a BS degree in Production Engineering and Management from the University of Nottingham in England.

Dr. Siddall has extensive experience with precision instrument design and completed his thesis work under the 1990 ASPE keynote speaker, R. V. Jones. He has worked on gyro rotor measurement techniques, x-ray lithography, laser interferometry, precision microlithographic lenses and advanced metrology systems for the semiconductor industry.

1999 Scholarship Recipients

P. Douglas Knight, Jr., University of North Carolina at Charlotte
R. V. Jones Memorial Scholarship

Todd N. Hinnerichs, University of New Mexico
Guang Lu, University of California at Bekeley
Shane C. Woody, University of North Carolina at Charlotte

1999 Lifetime Achievement Award

George Tlusty

Professor George Tlusty has had a long and distinguished career as a metrologist and designer of machine tools. Beginning in Czechoslovakia in 1941, Professor Tlusty was actively involved in research on machine tool metrology. In 1959 he wrote a paper on machine tool testing that included a powerful new method for testing the Axes of Rotation errors of milling machine spindles. It uses an accurate ball attached eccentrically to the spindle with two electronic pick-ups indicating the movement of the ball in two perpendicular directions with respect to the table. When these signals are displayed on the X and Y axes of an oscilloscope, a circular pattern is created. The non-roundness of this pattern is a measure of the spindle rotational accuracy at any spindle speed. We now refer to this procedure as the Tlusty Method.

Professor Tlusty is credited with much of the research on the causes of machine tool chatter. His publications on chatter date from 1954. He was one of the first to realize the critical relationship between dynamic stiffness and chatter. This work has been pivotal to the recent development in high-speed machining. He is considered one of the pioneers in this field.

Professor Tlusty was director of research at VUOSO in Prague in 1963. He was the founder of the Laboratory for Machine Tools and Robots at McMaster University in Canada, and is presently the Director of the Machine Tool Research Center at the University of Florida. He is a founding member of the North American Manufacturing Research Institute of SME. He became a member of CIRP in 1957 and served as its President in 1968. He is a Fellow Member of ASME and SME. He is fluent in six languages. Many of George's students are now as famous as he.

His book, Structures of Machine Tools, *published in 1971, is widely regarded as a classic. His new book,* Manufacturing Processes and Equipment, *1999, will undoubtedly become a classic.*

In 1972, while at McMaster University, George acquired one of the new Hewlett-Packard laser interferometers and carried out innovative measurements on the accuracy of large numerically controlled machine tools. This work is very well documented in the Ph.D. Thesis of Dr. Gordon Mutch, "The Accuracy of Numerically Controlled Machine Tools," published at McMaster in 1975.

At the age of 74, George started his own machine tool company, Manufacturing Laboratories, Inc. MLI has recently designed and built a large, hydrostatic bearing, super stiff, one of a kind, customer proprietary, turning machine with a positioning accuracy of a few microinches.

Executive Forum

Monday, November 1, 8:00 a.m. – 5:00 p.m.

Session Chair: John H. Bruning, Tropel Corporation

The ASPE Executive Forum will be conducted again this year on Monday, November 1, 1999, just prior to the start of the formal ASPE meeting and overlapping one day with the Tutorial Program. The session will be organized and chaired by John H. Bruning of Tropel Corporation. As in previous years, the program combines business and technology issues of contemporary interest to leaders and executives in the precision engineering community. The program will consist of morning and afternoon talks, a lunch break and ample time to network with peers. The morning will be a highly interactive session devoted primarily to business issues with two highly qualified speakers. The first of the morning speakers will be Dr. Balamanian, the founder of several high-tech Silicon Valley companies and a member of the Organization of Silicon Valley Entrepreneurs. Dr. Balamanian will speak about the new role of the engineer in the rapidly changing and overlapping landscapes of semiconductors, optics and health-care. The second speaker will be Mr. Joe Gortych, formerly of IBM and now an independent intellectual property consultant and attorney. Joe will speak about intellectual property issues facing technology companies.

In the afternoon, we will have talks of a more technical nature. Professor Hiroshi Toshiyoshi, a visiting professor from the Institute of Industrial Technology in Japan, will provide an exciting update to the field of micro-electromechanical systems (MEMS). Chris J. Evans will give a review of next generation interferometry in use at NIST and elsewhere for large-scale programs such as LIGO and the emerging international efforts in EUV lithography. Several other technical talks are planned which, when finalized, will be posted on the ASPE web site.

Commercial Session

Tuesday, November 2, 3:30 p.m.

Steven C. Fawcett, MicroE, Inc.

The Commercial Session will take place early in the week on Tuesday afternoon. This is a special session where company representatives are invited to make brief presentations on new products associated with precision engineering. In this session, conference participants will have the opportunity to receive timely information on new technologies that have been commercialized into products and services. The presentations will contain details and technical specifications of current product offerings, as well as information on advances that can be expected in the near future.

Open Forum

"Horrobilia" Hour

Wednesday, November 3, 5:00 p.m.

Session Chair: Erwin G. Loewen

A new experimental session called "Horrobilia" is being organized this year. Dr. Erwin Loewen, an Honorary Member of ASPE, coined the word "Horrobilia" some years ago. The session will consist of a series of stories describing the great mistakes made by precision engineers in the past. Dr. Loewen has a marvelous collection of such stories, and he will open the session with some of his best examples. The audience will then be asked to tell even better tales.

A Horrobilia story generally covers some sort of problem that was totally unexpected, created significant program delays, caused great discouragement and embarrassment, and wasted a lot of money. Identification of the problem was difficult and often took days, weeks, and sometimes months. The solution, on the other hand, turned out to be relatively simple.

Those who would like to participate may need to do some thinking about the best way to bring their points across. In some cases, a viewgraph may be helpful. Nothing needs to be in writing.

Most conference participants have never experienced a Horrobilia Hour. It is hard to imagine that anyone would be willing to talk about his or her mistakes in public. Experience has shown, however, that people will be happy to do so, if the mood is properly established.

The benefits can be enormous. Everyone in our business has made or will make some big mistakes. Hearing about the great errors of the past can be more educational than hearing an endless series of successes.

One of the most important lessons to be learned is the extent of discouragement of the people involved, and the degree of patience and perseverance that was necessary to finally pin-point the problem. This should be an inspiration to young engineers who will inevitably find themselves in similar situations.

Technical and Poster Paper Index

The technical program for the 1999 ASPE Annual Meeting contains over 154 papers on precision engineering advances. Papers that lent themselves to significant verbal interaction, concise but important discoveries, or strongly visual or tactile subjects have been selected for the poster session. Authors will be present to discuss their work on Tuesday, November 2, from 5:00 to 6:30 p.m., and again on Wednesday, November 3, from 3:30 to 5:00 p.m.

Session I
Large Scale Metrology

Tuesday, November 2, 1999, 8:30 a.m. – 10:00 a.m.

Session Chair: W. T. Estler (National Institute of Standards and Technology)

Welcome Remarks
I. F. Stowers, Annual Meeting Chairman (Lawrence Livermore National Laboratory)

1. **Self-compensation of Atmospheric-refraction Errors in Optical Metrology (Invited Paper)**
   L. G. Shirley (MIT Lincoln Laboratory) . . . . . page 15
2. **Metrology System for the Green Bank Telescope**
   D. H. Parker, J. M. Payne (The National Radio Astronomy Observatory) . . . . . page 21
3. **Precision Surveying of the National Ignition Facility**
   W. S. Rorke, Jr. (Sandia National Laboratories) . . . . . page 25
4. **The Implementation of Simultaneous Trilateration to Measure Dynamic Three-dimensional Contours Using the Laser Ball Bar**
   T. L. Schmitz (National Institute of Standards and Technology) and J. C. Ziegert (University of Florida) . . . page 29

Session II
Mesoscale Manufacturing

Tuesday, November 2, 1999, 10:30 a.m. – 12:00 p.m.

Session Co-Chairs: E. C. Teague (National Institute of Standards and Technology), and P. A. McKeown (Pat McKeown Associates)

1. **Microsystems: Manufacturing and Packaging Challenges (Invited Paper)**
   R. M. Mehalso (Microtec Associates) . . . . . page 33
2. **An Overview of Design for Manufacturing at Mesoscopic Scale (Invited Paper)***
   B. Carlisle (Adept Robotics)
3. **Fabrication of In-pipe Mobile Micromachines Driven by Pneumatic and Vacuum Pressure**
   S. Kato, M. Shirakawa, M. Ohno, S. Fukumoto (Nippon Institute of Technology) . . . . . page 37
4. **DNA Extraction from Cell Nuclei and DNA Fishing Using a 3D Nano-probe**
   M. Nakao, K. Matsumoto, T. Ooi, H. Hirayama, M. Otsubo, S. Shirakata, Y. Hatamura (The University of Tokyo) . . . . . page 41

**Extended abstract not available at press time.*

Session III
Novel Processes and Techniques

Tuesday, November 2, 1999, 1:30 p.m. - 3:00 p.m.

Session Co-Chairs: T. A. Dow (North Carolina State University), and M. H. Miller (Michigan Technological University)

1. ***Manufacturing Feasibility of Continuous Relief, Gray-scale Diffractive Optical Elements***
   H. E. Fawcett, D. K. Mitchell, S. C. Fawcett, B. Thorburn (MicroE, Inc.) . . . . . page 45
2. ***Errors in Progressive Dies for Electronic Components***
   S. Kiani (Teradyne Connection Systems), R. R. Vallance (University of Kentucky), and A. H. Slocum (Massachusetts Institute of Technology) . . . . . page 49
3. ***Three-dimensional Microforming by Metal Jet***
   K. Yamaguchi, K. Sakai (Nagoya University) . . . . . page 53
4. ***Diamond Flycutting Machine for Producing Flat Surfaces on Half-meter Scale Diamond-turnable Optics***
   R. C. Montesanti, S. F. Locke, S. L. Thompson (Lawrence Livermore National Laboratory) . . . . . page 57

Poster Session

Tuesday, November 2, 1999, 5:00 p.m. – 6:30 p.m. and
Wednesday, November 3, 1999, 3:30 p.m. – 5:00 p.m.

Session Chair: M. H. Miller (Michigan Technological University)

PROCESSES

Machining

1. ***Ultraprecision Cutting for Gallium Arsenide***
   F. Z. Fang, Z. J. Yuan (Harbin Institute of Technology) . . . . . page 62
2. ***Investigations on the Wear Profile of Dicing Wheels***
   H. H. Gatzen, C. Morsbach (Hanover University), and G. M. Jones (Seagate Technology) . . . . . page 67
3. ***The Effects of High Feed Rate of Hardened Steel Milling Upon Tool Life***
   T. Miyaguchi, M. Masuda, H. Iwabe (Niigata University), E. Takeoka (Industrial Research Institute of Niigata Prefecture), and B. L. Wegener (Otto-von-Guericke University Magdeburg) . . . . . page 71
4. ***Measurement of Cutting Tool Wear with Shape-From-Focus (SFF) Method***
   K. S. Moon, Z. K. Ling (Michigan Technological University) . . . . . page 75
5. ***Surface Generation Mechanism in Flat End Milling***
   S. H. Ryu, C. N. Chu (Seoul National University), and D. K. Choi (Kangnung National University) . . . . . page 79

Grinding

1. ***Plate Topography Influence on the Nanogrinding Process***
   H. H. Gatzen, H. Siekmann (Hanover University) . . . . . page 83
2. ***Glass Grinding Using Structured Superabrasives***
   R. D. Grejda, E. R. Marsh (The Pennsylvania State University) . . . . . page 87
3. ***Studies on the Nature of Surface Quality in Precision Grinding of Carbon Steels***
   K. H. P. Reddy, P. K. Nair, B. Ramamoorthy (Indian Institute of Technology) . . . . . page 91
4. ***Water Jet In-process Dressing – First Report***
   M. Hirao, M. Izawa, K. Ootani, T. Yasui (Kanazawa University), N. Iguchi (Kuroda Seiko Co., Ltd.) and K. Shirase (Osaka University) . . . . . page 95
5. ***In-situ Characterization of Grinding Wheel Surface***
   A. Hosokawa, K. Sakuma, T. Ueda (Kanazawa University) . . . . . page 99

6. ***Truing and Dressing of Diamond Wheels for High Speed Grinding of Brittle Materials***
H. Huang (Gintic Institute of Manufacturing Technology) . . . . . page 103

7. ***The Study of Ductile-brittle Transition on Micro-cutting of Single Crystal Silicon***
S. Kaji, T. Goto (Mitsubishi Heavy Industries, Ltd.), and T. Sumomogi, M. Nakamura (Hiroshima Kokusai Gakuin University) . . . . . page 107

8. ***Cutting Performance of CVD Diamond Coated Tool in Machining of Green Body of Silicon Nitride Ceramics — Wear Mechanism of Diamond Coated Tool to the Milling Operation***
H. Kato, K. Shintani (Kanazawa Institute of Technology), and H. Hanyu (OSG Corporation) . . . . . page 111

9. ***Benefits of Variable Speed Grinding***
B. R. Knapp, E. R. Marsh (The Pennsylvania State University) . . . . . page 115

10. ***The Effect of Parallel Modulation on Subsurface Damage***
W. Qu, M. H. Miller, A. Chandra (Michigan Technological University) . . . . . page 119

11. ***The Mechanism of CBN Quill in Surface Grinding***
Q. Yan, (Shantou University), K. Tanaka, K. Syoji (Tohoku University), and T. Honoki (Mitsubishi Electric Corporation) . . . . . page 123

12. ***Ultra-smoothness Grinding of Fine Ceramics with #104-Mesh Grain Size Diamond Wheel***
H. Yasui, G. Yamazaki, Y. Hiraki, S. Sakamoto, M. Sakata, M. Saeki (Kumamoto University), and A. Hosokawa (Kanazawa University) . . . . . page 127

13. ***Precision Grinding Apparatus Specially Developed for Micro-cylindrical Components***
Yeo S. H., M. Zhou, Tan B. H., Balon S. A. P. (Nanyang Technological University) . . . . . page 131

Polishing, Lapping and ECM

1. ***Tribo-chemical Smoothing of Diamond Film***
K. Horio, M. Hyohdoh, T. Kasai (Saitama University) . . . . . page 135

2. ***CMP Interfacial Fluid Pressure and Modeling***
L. Shan, S. Danyluk (Georgia Institute of Technology) . . . . . page 139

Manufacturing (Precision Mass Production)

1. ***Modeling of Geometric Errors of Manufactured Parts for Manufacturing Process Control***
X. D. Zhang (Cummins Engine Company), and C. Zhang, B. Wang (Florida A&M University) . . . . . page 146

Non-Conventional Processes

1. ***Improvement of Micro-machining Accuracy by Two-dimensional Vibration Cutting***
J. H. Ahn, H-S. Lim, S-M. Son (Pusan National University) . . . . . page 150

2. ***Improvement of Characteristics of Aluminum Casting Using Ceramic Porous Mold***
S-I. Chung, D-S. Jeong, Y-G. Im, H-D. Jeong, K-K. Cho (Pusan National University) . . . . . page 154

3. ***Surface Modification by Electrical Discharge Machining with Titanium Powder Suspended in Working Fluid***
K. Furutani, A. Saneto, H. Takezawa, N. Mohri (Toyota Technological Institute), and H. Miyake (Mitsubishi Electric Corporation) . . . . . page 159

4. ***Elliptical Vibration Cutting of Steel with Diamond Tools***
E. Brinksmeier, R. Gläbe (University of Bremen) . . . . . page 163

5. ***Effects of Gamma Irradiation and Accelerated Aging on Wear Properties of UHMWPE Artificial Joint***
T. Kaneeda (Okayama University of Science), and M. Utsumi, E. Watanabe (Chiba University) . . . . . page 167

6. ***Study on Force Controlled Micro Grooving Using Burnishing Tools***
M. Masuda, Y. Waki, A. Inada, A. Mutoh (Niigata University), and Y. Maeda (Hitachi Ltd.) . . . . . page 171

7. ***Silicon Wafer Bonding Process for Preventing Intrinsic Bubbles After Low Temperature Thermal Treatment***
D-M. Moon, I-H. Cho, H-D. Jeong, W-S. Che (Pusan National University) . . . . . page 175

8. ***Development of Water-soluble Coolant for Multi-wire Saw Slicing of 400 mm Diameter Silicon***
H. Oishi, K. Asakawa, J. Matsuzaki (Super Silicon Crystal Research Institute Corp.), and A. Ashida (Ohtomo Chemical Industrial Corp.) . . . . . page 180

9. ***A Study on Thermal Strains in Plate Glass During Thermal Cutting Using Hot Air Jet***
E. S. Prakash, K. Sadashivappa (Bapuji Institute of Engineering and Technology), V. Joseph (University BDT College of Engineering), and M. Singaperumal (Indian Institute of Technology) . . . . . page 184

10. ***Micro Drilling of Non-conducting Materials Using Electro Chemical Spark Machining (ESCM)***
S. H. Somashekhar, K. Sadashivappa (Bapuji Institute of Engineering and Technology) . . . . . page 188

11. ***Influence of Redeposition Effect for Focused Ion Beam Three-dimensional Micromachining***
Y. Zhang, Y. Fu (Nanyang Technological University) . . . . . page 192

EQUIPMENT, MACHINES & INSTRUMENTS

Design and Testing

1. ***Design of Orientation Stages for Step and Flash Imprint Lithography***
B. J. Choi, S. Johnson, M. Colburn, S. V. Sreenivasan, C. G. Willson (University of Texas at Austin) . . . . page 196

2. ***Effects of Active Balancing on High-speed Milling Precision***
S. W. Dyer (BalaDyne Corporation), and E. I. Al-Regib (The University of Michigan) . . . . . page 200

3. ***Fabrication of a Microrobot Movable in the Small Intestine of a Pig***
S. Kato, M. Shirakawa, M. Ohno, M. Tabata (Nippon Institute of Technology) . . . . . page 204

4. ***Design Analysis of the National Ignition Facility Kinematic Pin (NIFKP) or Flexural Pivot***
K. K. Leung (Lawrence Livermore National Laboratory)[1] . . . . . page 208

5. ***System Modeling and Identification of a Precision Fast Tool Servo System***
G. Lu (University of California at Berkeley), J. F. Cuttino (University of North Carolina at Charlotte), D. Schinstock (The University of Tulsa), and T. Haskew (The University of Alabama) . . . . . page 212

6. ***Development of Pin-type Vacuum Chuck for High Precision Machining***
S. Matsui, F. Ohira, Y. Ishikawa, K. Koyabu (NTT Telecommunications Energy Laboratories), and A. Une (The National Defense Academy). . . . . page 216

7. ***Development of a New Palm-size and Clean Spherical Mirror-finish Surface Processing Machine for the Fabrication of Optical Fiber Connectors***
K. Ohno, M. Mitsuhashi (NEC Corporation) . . . . . page 221

8. ***Microfabrication of a Mold Insert Made of Hardened Steel and First Molding Results***
T. Schaller, M. Heckele, R. Ruprecht, K. Schubert (Forschungszentrum Karlsruhe GmbH) . . . . . page 225

9. ***Development of an Ultraprecise Positioning Stage Engaged with Gratings***
T. Wada, S. Honda (Tokyo Metropolitan Institute of Technology). . . . . page 229

Controls

1. ***Identification and Compensatory Control of Time-varying Volumetric Errors in Machining Centers***
J-Y. Ahn, S-C. Chung (Hanyang University). . . . . page 233

2. ***Laser-material-removal Process as a Subject of Automatic Control***
E. V. Bordatchev, S. K. Nikumb (National Research Council of Canada) . . . . . page 237

3. ***Micro-displacement/Capacitance Measurement and Control System with Phase-locked Loop***
S-B. Chang, B. C. S. Chou, J. J. Chang (National Science Council) . . . . . page 241

4. ***Implementing Geometric Error Compensation Software in a PC-based Controller***
V. Graves (Oak Ridge National Laboratory) . . . . . page 245

5. ***Robust Cutting Force Control Using Indirect Force and Disturbance Estimators in the End Milling Process***
S-C. Kim, S-C. Chung (Hanyang University) . . . . . page 249

6. ***A Discussion on Stability of Air Bearing Spindles***
Z. Shang, P. Greene, D. Bittner (Dover Instrument Corporation) . . . . . page 253

Analysis and Modeling

1. ***Basic Research on Development of Magnetostrictive Sensor for Detecting Cutting Force***
H. Aoyama, H. Murashita, T. Ishii (Keio University), and H. Ohzeki (Mitsubishi Materials Corporation) . . . page 257

2. ***Polygon-based Large Diameter Measurement with Modular Gauges***
B. Li (Southeast University) . . . . . page 261

3. ***Prediction of Temperature and Dimensional Changes During Soakout Using FEA***
B. Chakravarthy, H. P. Cherukuri, R. J. Hocken, R. G. Wilhelm (University of North Carolina at Charlotte) . . . . . *page 265*

4. ***CAD/CAM Integration of On-the-machine Measuring and Inspection System for Free-form Surfaces***
S-C. Chung (Hanyang University) . . . . . *page 268*

5. ***Magnetic Actuator Characterization for Nanometer-level Positioning***
T. N. Hinnerichs, H. D. Tran (University of New Mexico) . . . . . *page 272*

6. ***The Effects of Interstitial Media on Thermal Condition Monitoring***
Y. Huang (The University of Alabama), Z. Chen (Zhejiang University) and J. F. Cuttino (University of North Carolina at Charlotte) . . . . . *page 276*

7. ***The Calibration of Tilting and Refractive Index of Specimen in Confocal Scanning Microscopy***
J. W. Seo, S. L. Park, H. R. Oh, J. H. Lee, D-G. Gweon (Korea Advanced Institute of Science and Technology) . . . . . *page 280*

Micro-Electro-Mechanical Systems and Nanotechnology

1. ***Automatic Precise Micro-drilling System by Distributed Insect Robots***
H. Aoyama, S. Tadokoro, T. Shigeno, T. Ono (University of Electro-Communications) . . . . . *page 284*

2. ***Development of a Tweezers Robot Equipped with Bimorph Piezoelectric Actuators***
T. Fujishita, S. Honda (Tokyo Metropolitan Institute of Technology) . . . . . *page 288*

3. ***Linear Motion Microsystem Fabricated on a Silicon Wafer***
N. Moronuki, K. Uchiyama (Tokyo Metropolitan University) . . . . . *page 292*

4. ***Optimization Design of Micro-diffuser/Nozzle Elements and Development of Implanted Drug Delivery Micropump***
Y. H. Mu, X. D. Wang, B. K. A. Ngoi, J. G. K. Gan (Nanyang Technological University) . . . . . *page 296*

Novel Systems

1. ***The Design of a Capacitive Transducer for Operation with Non-grounded Targets***
B. Herndon, K. Lamppa, J. McCleskey, C. Fleddermann, H. D. Tran (University of New Mexico) . . . . . *page 300*

2. ***An Object Transport System Using Traveling Waves Generated by Ultrasonic Flexural Vibrations***
B-G. Loh, P. I. Ro (North Carolina State University) . . . . . *page 304*

METROLOGY

Instrumentation, Design and Testing

1. ***Tolerance Allocations for Automated Insertion of Optical Components in the National Ignition Facility***
S. M. Bahowick, W. R. Horton, T. G. Sheridan, W. S. Rorke, Jr., D. S. Bartel (Lawrence Livermore National Laboratory) . . . . . *page 309*

2. ***High-precision Dimension Measurement of Large Scale Workpiece by Laser***
Q. Feng (Northern Jiaotong University), and J. Liang, Q. Tian (Tsinghua University) . . . . . *page 313*

3. ***Direct Measurement of Spindle Error Using a Double 2-point Method***
Y. J. Gao, B. K. A. Ngoi, L. E. N. Lim (Nanyang Technological University) . . . . . *page 317*

4. ***Development of Three-dimensional profile Measuring Method for Microparts***
K. Mitsui (Keio University) . . . . . *page 321*

5. ***Development of Noncontact Coordinate Measuring Machine Implementing High Precision Optics and Precision Image Processing Algorithms of Subpixel Accuracy***
H-J. Pahk, I. H. Lee (Seoul National University) . . . . . *page 325*

6. ***Traceability of CMM Measurements***
B. W. J. J. A. van Dorp, F. L. M. Delbressine, H. Haitjema, P. H. J. Schellekens (Eindhoven University of Technology) . . . . . *page 329*

7. ***A New Photo-electronic Length Measuring Instrument with 0.1nm Resolution and 110 mm Range***
Z-Q. Zou, W-Y. Zou, L-D. Hu, J-T. Chen, Y-C. Zhu (Beijing Institute of Ultraprecision Engineering) . . . . . *page 333*

Surface and Subsurface

1. ***An Internet-based Surface Texture Analysis System***
   S. H. Bui, V. Gopalan, J. Raja, K. R. Subramanian (University of North Carolina at Charlotte) . . . . . *page 337*
2. ***Quantitative Stress-induced Birefringence Measurements of Large Optics by a Prototype Imaging Polarimeter***
   P. D. Knight, Jr. (University of North Carolina at Charlotte), P. R. Wilkins (Lawrence Livermore National Laboratory) . . . . . *page 341*
3. ***Optical Measurement of COP Defects on Silicon Wafer Surface by Laser Scattered Defect Pattern***
   S. Takahashi, T. Miyoshi, Y. Takaya (Osaka University), and K. Shirai (Nihon University) . . . . . *page 345*
4. ***A Scanning Phase-knife Technique for Quantitative Surface Slope Measurements and Defect Identification***
   P. R. Wilkins, D. C. Pigg (Lawrence Livermore National Laboratory), and P. D. Knight, Jr. (University of North Carolina at Charlotte) . . . . . *page 349*

Form and Geometry

1. ***The Three-dimensional Surface Topographic Characterization of Conventional and Superabrasive Grinding Wheels***
   D. L. Butler (Nanyang Technological University), J. A. Webster (Unicorn International), and L. A. Blunt, K. J. Stout (University of Huddersfield) . . . . . *page 353*
2. ***Surface Topography Assessment of Textured Mold and Aesthetic Quality of Injection Molded Plastic Surface***
   S. Hara, K. Yanagi, T. Endoh (Nagaoka University of Technology) . . . . . *page 357*
3. ***Optical Measurement for Flank Wear in Peripheral Cutting Edges in Endmills***
   H-S. Lee, T. Nagashima, H. Haga, T. Wakabayashi (Nihon University) . . . . . *page 361*
4. ***Volumetric Error Measurement and Compensation Using the Vector Method***
   C. Wang, R. Griffin (Optodyne, Inc.), and J. Janeczko (Giddings & Lewis Machine Tools) . . . . . *page 365*
5. ***Surface Roughness Limit for Super-machined Mirrors Measured with Scanning Probe Microscopy***
   J. Yu, Y. Namba (Chubu University), and B. K. A. Ngoi, Z. W. Zhong (Nanyang Technological University) . . . . . *page 369*

Analysis and Modeling

1. ***A Learning Quality Control Approach to Improve Manufacturing Quality in the Turning Process***
   C. Ament, G. Goch (Bremen University) . . . . . *page 373*
2. ***Anisotropic Artifacts Introduced by Horizontal Scanning Instruments in Surface Metrology***
   T. S. Bergstrom, C. A. Brown (Worcester Polytechnic Institute) . . . . . *page 377*
3. ***The Characterization of Engine Liner Wear Using Novel Bearing Area Curve Parameters***
   D. L. Butler (Nanyang Technological University), L. A. Blunt, X. Jiang, K. J. Stout (University of Huddersfield) . . . . . *page 381*
4. ***Geometric Error Analysis and Calibration of a Stewart Platform***
   J-S. Chen (National Chung-Cheng University) . . . . . *page 384*
5. ***Sampling and Measurement Uncertainty in Coordinate Metrology***
   R. M. Edgeworth, R. G. Wilhelm (University of North Carolina at Charlotte) . . . . . *page 389*
6. ***Thickness Correction for Edge Detection of Optical Coordinate Measuring Machines***
   J. Fu, R. J. Hocken (University of North Carolina at Charlotte) . . . . . *page 393*
7. ***Modeling of Low Order Temperature Dependant Errors of Machine Tools***
   J. J. Kroll, S. R. Patterson (University of North Carolina at Charlotte) . . . . . *page 397*
8. ***Improving Machine Tool Accuracy Through Auto Calibration***
   M. C. Lee, P. M. Ferreira (University of Illinois at Urbana-Champaign) . . . . . *page 401*
9. ***Experiences with the Master Axis Method for Measuring Spindle Error Motions***
   E. R. Marsh, R. Grejda (The Pennsylvania State University), and D. Martin (Lion Precision) . . . . . *page 405*

10. **Foundation for Dynamic Metrology of Machine Tools**
J. A. Miller, R. J. Hocken, V. Ramanan, Q. Feng (University of North Carolina at Charlotte) . . . . . page 409

11. **A New Method for Characterization for the 5-DOF Spindle Volumetric Error Motions i n Machine Tools**
H-J. Pahk, H-J. Shin (Seoul National University) . . . . . page 413

12. **Dynamic Error Characterization of a Scanning Coordinate Measuring Machine**
P. H. Pereira, R. J. Hocken (University of North Carolina at Charlotte) . . . . . page 417

13. **An Experimental Investigation into Spindle Error Motions Under Load**
A. K. Sharma (The Boeing Company), and S. R. Patterson (University of North Carolina at Charlotte) . . . page 421

14. **Study of Nano-tribology Using a Scanning Force Microscope**
T. Sumomogi, T. Endo, S. Matsuo (Hiroshima Kokusai Gakuin University) . . . . . page 425

Optics and Interferometry

1. **A Compact Industrial Distance Measuring Interferometer System**
M. L. Holmes, L. L. Deck, B. Shull, M. Samuels, S. Altieri, E. Ebert, J. Soobitsky, R. Gecewicz (Zygo Corporation) . . . . . page 429

2. **Arbitrary N-step Algorithm for Removal of Higher Order Test Optics Errors**
S-W. Kim, H-G. Rhee, B-C. Kim (Korea Advanced Institute of Science and Technology) . . . . . page 433

3. **Sensitivity Analysis of a Cylindrical Interferometer**
P. D. Knight, Jr., S. R. Patterson (University of North Carolina at Charlotte) . . . . . page 437

4. **Non-contact Acousto Optic Scanning Laser Doppler Vibrometer**
B. K. A. Ngoi, K. Venkatakrishnan (Nanyang Technological University) . . . . . page 441

5. **A Low Coherence Interferometer for Absolute Distance Measurement**
A. D. Woodfin, F. Farahi, R. J. Hocken (University of North Carolina at Charlotte) . . . . . page 445

6. **In-situ Absolute Calibration of Interference Microscopes**
S. Zhang, M. Kanai, W. Gao, S. Kiyono (Tohoku University), and T. Aramaki (Nikon Corporation) . . . . . page 449

Session IV
Machine Tool and CMM Metrology

Wednesday, November 3, 1999, 8:30 a.m. – 10:00 a.m.[1]

Session Co-Chairs: J. Corbett (Cranfield University), and B. A. Damazo (National Institute of Standard and Technology)

1. **Advanced CMM Design (Invited Paper) ***
G. N. Peggs (National Physical Laboratory)

2. **A Fully Elastically Guided Three-dimensional CMM with a Measuring Volume of 1 cm^3**
A. Jansen, N. Rosielle, P. H. J. Schellekens (Eindhoven University of Technology) . . . . . page 453

3. **Sequential Determination of Kinematic Parameters in Assembled Parallel Kinematic Mechanisms**
B. Jokiel, Jr. (Sandia National Laboratories), and J. C. Ziegert (University of Florida) . . . . . page 457

4. **Experimental Study on Dynamic Accuracy Behavior of a High Speed CNC Machine Tool with Semi-closed and Fully-closed Feedback Control**
K. Yamazaki, Y. Kawahara, J. Liu (University of California at Davis), J. Braasch (Johannes Heidenhain GmbH), and M. Fujishima (Mori Seiki Co., Ltd.) . . . . . page 462

**Extended abstract not available at press time.*
[1] *Steinbeck Auditorium*

Session V
Optical Metrology

Wednesday, November 3, 1999, 10:30 a.m. – 12:00 p.m.[1]

Session Chair: A. E. Gee (Cranfield University)

1. ***NIF Optical Specifications and Means to Quantify Mounting Stresses (Invited Paper)***
   P. R. Wilkins, R. E. English, D. M. Aikens (Lawrence Livermore National Laboratory), and P. D. Knight, Jr. (University of North Carolina at Charlotte) . . . . . *page 466*
2. ***A Portable Grazing Incidence Interferometer for Measuring the Flatness of Slideways and Surface Plates***
   A. W. Kulawiec, P. G. Dewa, R. S. Hordin, J. H. Bruning (Tropel Corporation) . . . . . *page 470*
3. ***Fringe Projection Method for Measuring Geometry and Wear of Cutting Tool Inserts***
   A. Weckenmann (University Erlangen-Nuremberg), V. P. Radhakrishnan (Indian Institute of Technology), and S. Schmitz (Robert Bosch GmbH) . . . . . *page 473*
4. ***Optical Frequency Stabilization of a Compact Heterodyne Source for an Industrial Distance Measuring Interferometer System***
   L. L. Deck, M. L. Holmes (Zygo Corporation) . . . . . *page 477*

Session VI
Grinding

Wednesday, November 3, 1999, 1:30 p.m. – 3:00 p.m.[1]

Session Chair: D. A. Lucca (Oklahoma State University)

1. ***Influences on Surface and Subsurface During Ultrasonic Assisted Grinding of Advanced Ceramics***
   G. Spur, E. Uhlmann, S.-E. Holl, N. A. Daus (Technical University Berlin) . . . . . *page 481*
2. ***In-situ Three-dimensional Observation of Active Grain Distribution on a Grinding Wheel and Introduction of Experimentally Evaluated Parameters to Grain Depth of Cut***
   A. Kanai, F. Inaba, A. Tajima (Ashikaga Institute of Technology), and M. Miyashita (Nano-Tec Associates) . . . . . *page 485*
3. ***Study on Vibration OD-Blade Slicing with Air-Mist Working Fluid for Environment — Effect of Applied Vibration Amplitude on Slicing Characteristics***
   K. Ishikawa, H. Suwabe, M. Uneda (Kanazawa Institute of Technology) . . . . . *page 489*
4. ***Wear and Self-dressing of Resin Bound Grinding Wheels***
   M. H. Miller, T. S. Kakumanu (Michigan Technological University) . . . . . *page 493*

Session VII
Optical Quality Finishing

Wednesday, November 3, 1999, 8:30 a.m. – 10:00 a.m.[2]

Session Co-Chairs: Y. Namba (Chubu University) and D. Golini (QED Technologies)

1. ***Fixed Abrasive Vertical Spindle™ Process to Generate Mirror Finishes on a Variety of Advanced Ceramic Components***
   T. Puthanangady, M. Tricard (Norton Company) . . . . . *page 497*
2. ***Single Point Contributions to Free Abrasive Polishing***
   A. E. Gee, D. F. Williams (Cranfield University) . . . . . *page 501*

[1] *Steinbeck Auditorium*
[2] *Serra II Ballroom*

3. **Nano-Abrasion Machining of Brittle Materials**
O. Horiuchi, F. Naruse, J. Ikeno (Toyohashi University of Technology) . . . . . page 505

4. **Finishing of Optical Materials Using Fluid Jet Polishing**
O. W. Fähnle (FISBA-Optik), and H. van Brug (Delft University of Technology) . . . . . page 509

Session VIII
Precision Engineering Methods

Wednesday, November 3, 1999, 10:30 a.m. – 12:00 p.m.[2]

Session Co-Chairs: Y. Furukawa (Tokyo Metropolitan University), and D. H. Youden (Eastman Kodak Company)

1. **Overview of a Second Generation Large Aperture Deformable Mirror for the National Ignition Facility**
S. E. Winters, T. J. Arnold, E. S. Bliss, M. J. Dailey, P. M. Danforth, J. A. Koch, R. A. Sacks, C. J. Stolz, W. T. Whistler, B. W. Woods, R. A. Zacharias (Lawrence Livermore National Laboratory). . . . page 513

2. **Dynamic Analysis of Porous Air Bearings and Balanced Force Bearing Concept ***
S. Nayfeh (Massachusetts Institute of Technology), and A. J. Devitt (New Way Machine Components, Inc.)

3. **New Micro-assembly Technique of Three-dimensional Micro-structure by YAG Laser Beam**
D. Sawaki, J. Ikeno, O. Horiuchi (Toyohashi University of Technology). . . . . page 517

4. **Nanoindentation by Using a Newly Developed Nanomachining Instrument**
W. Gao (Tohoku University), R. J. Hocken, J. Patten, J. Lovingood (University of North Carolina at Charlotte), and D. A. Lucca (Oklahoma State University) . . . . . page 521

Session IX
Coordinate Measuring Machines

Wednesday, November 3, 1999, 1:30 p.m. – 3:00 p.m.[2]

Session Chair: D. Krulewich Born (Lawrence Livermore National Laboratory)

1. **A General Quantitative Method to Validate Instrument Calibration Techniques**
S. D. Phillips (National Institute of Standards and Technology). . . . . page 525

2. **Performance Evaluation for Vision Coordinate Measuring Machines**
C.-C. Huang, X. D. Zhang (Cummins Engine Company, Inc.) . . . . . page 529

3. **Pixel Size Calibration for Video Probe Measuring Machines**
J. G. Salsbury (University of North Carolina at Charlotte) . . . . . page 533

4. **Vector Touch Sensor Probe**
S. C. Woody, S. T. Smith (University of North Carolina at Charlotte). . . . . page 538

Session X
Precision Tooling

Thursday, November 4, 1999, 8:30 a.m. – 10:00 a.m.

Session Co-Chairs: E. Loewen (Consultant), and S. C. Fawcett (MicroE, Inc.)

1. **Contour Mode Deteministic Microgrinding**
J. Ruckman, E. Fess, Y. Li (University of Rochester). . . . . page 542

2. **Compensation of Tool Forces in Small Diameter End Mills**
T. A. Dow, E. Miller, A. Sohn, K. P. Garrard (North Carolina State University), and T. Wright (Eastman Kodak Company) . . . . . page 546

**Extended abstract not available at press time.* [2]*Serra II Ballroom*

3. **Deterministic Design of "Engineered Tool" [A New Diamond Tool]**
T. Tatsumi, T. Ikeda (Komatsu Electronic Metals Co., Ltd.), K. Imai, H. Hashimoto (Kanagawa Institute of Technology), and T. Takeda, S. Hamada (Sumitomo Heavy Industries, Ltd.) . . . . . page 551

4. **An Empirical Survey on the Influence of Machining Parameters on Tool Wear in Diamond Turning of Large Single Crystal Silicon Optics**
D. K. Born, C. Syn, P. Davis, M. Zimmermann, K. Blaedel, J. Carr, J. Haack (Lawrence Livermore National Laboratory), and M. R. McClellan, W. A. Goodman (Schafer Corporation) . . . . . page 555

Session XI
Industrial Practice

Thursday, November 4, 10:30 a.m. – 12:00 p.m.

Session Co-Chairs: D. E. Luttrell (Corning Inc.), and E. Brinksmeier (Bremen University)

1. **Development of Ultraprecision Double-disk Grinding Machine for Silicon Wafer**
K. Hara, S. Isobe, H. Nagata, A. Iwase, Y. Tomita (Sumitomo Heavy Industries, Ltd.), A. Kanai (Ashikaga Institute of Technology), and M. Miyashita (Nano-Tec Associates) . . . . . page 559

2. **A Precise Track-following Control Using a Single-stage Tracking Mechanism for Magneto-optical Disk Drives**
I. Watanabe, T. Kawabe, H. Kobayashi, J. Ichihara (Fujitsu Laboratories, Ltd.), and T. Ikeda, S. Otsuka (Fujitsu Limited) . . . . . page 563

3. **Calibration and Control of a Rotary Fast Tool Servo**
S. J. Ludwick, D. A. Chargin, J. A. Calzaretta, D. L. Trumper (Massachusetts Institute of Technology) . . . page 567

4. **Quasi-kinematic Couplings: A Low-cost Method for Precision Coupling of Product Components and The-like in Manufacturing Processes**
M. L. Culpepper, A. H. Slocum (Massachusetts Institute of Technology), and F. Z. Shaikh (Ford Scientific Research Labs) . . . . . page 571

Special Lunchtime Session

Thursday, November 4, 1:00 p.m. – 1:30 p.m.

Re-encasing the "Charters of Freedom" – A Precision Engineering Project?*
C. J. Evans (National Institute of Standards and Technology)

Session XII
Lithography and Stage Design

Thursday, November 4, 1:30 p.m. – 3:00 p.m.

Session Chair: A. J. Hazelton (Nikon Research Corporation of America)

1. **Projection Optics Box Design for Extreme Ultraviolet Lithography ***
H. Tajbakhsh, L. Hale, S. Jensen, T. Malsbury (Lawrence Livermore National Laboratory)

2. **AFM Vibration Isolator with High Performance Using Eddy Current Damping**
G-H. Chung (Samsung Display Devices), and D-G. Gweon, H-W. Chung, J-Y. Shim (Korea Advanced Institute of Science and Technology) . . . . . page 575

3. **High Precision Systems Using Modern High Energy Permanent Magnet Materials**
H. Kube, E. Kallenbach (Technical University of Ilmenau), and B. Pawlowski, J. Toepfer (hitk e. V.) . . . . . page 579

4. **Magnetic Levitation Scanning Stage for Extreme Ultraviolet Lithography**
M. E. Williams, P. Faill (Equilibria, Inc.), S. P. Tracy, P. Bischoff (Ultratech Stepper), and J. Wronosky (Sandia National Laboratories) . . . . . page 583

**Extended abstract not available at press time.*

Session XIII
Advances in Metrology

Thursday, November 4, 3:30 p.m. – 5:00 p.m.

Session Chair: D. Martin (Lion Precision)

1. ***An Advance in Metrology and Manufacture – The Engineered Surface (Invited Paper)***
   K. J. Stout, L. A. Blunt (University of Huddersfield) . . . . . page 587
2. ***KGM-plus – Device for Simultaneous Measurement in Six Degrees of Freedom on Machine Tool Trajectories***
   S. Weikert, W. Knapp (Swiss Federal Institute of Technology) . . . . . page 602
3. ***Subsurface Damage Measurements as a Tool for Process Monitoring***
   R-J. M. van der Bijl (TNO Institute of Applied Physics), O. W. Fähnle (FISBA-Optik), and H. van Brug (Delft University of Technology) . . . . . page 606
4. ***In-process Measurement of Wear of Grinding Wheel by Hydrodynamic Pressure***
   K. Furutani, T. Katoh, N. Mohri (Toyota Technological Institute) . . . . . page 610

Technical Papers

A S P E

SELF-COMPENSATION OF ATMOSPHERIC-REFRACTION ERRORS IN OPTICAL METROLOGY*

Lyle G. Shirley
MIT Lincoln Laboratory, Lexington, MA

INTRODUCTION

Many measurements in precision engineering rely on the assumption that light travels in a straight line through air. Examples of these measurements include certain methods for determining errors of motion in precision machines, measuring straightness, and monitoring surface deformations of large structures. Land surveying is one application that relies heavily on this assumption. It is well-known, however, that temperature, pressure, or humidity variations acting perpendicular to the direction of propagation cause light rays to be refracted into a curved path [1]. This curvature can produce relatively large deviations between the expected and actual ray positions. For instance, a transverse temperature gradient of 10°C/m produces a beam deviation of approximately 0.5 mm after 10 m of propagation. Because the beam deviation is proportional to the square of the distance traveled, this deviation increases to 2 mm after 20 m of propagation through the same gradient. Clearly, atmospheric refraction is an important effect that must be accounted for in high-precision optical measurements.

In principle, one could monitor parameters affecting beam curvature along the beam path and calculate corrections based on these measurements [2]. Besides being cumbersome to implement and requiring access to the beam path, this approach fails to produce reliable results because of the difficulty of producing accurate closely spaced measurements of quantities such as temperature gradients along the propagation path. Another approach to compensation relies on dispersion, or wavelength dependence, in the index of refraction of air [3]. In this approach, a correction is estimated by observing the displacement between the endpoints of two rays of differing wavelength. The resulting displacement between rays, however, is only a small fraction of the total refractive error. In fact, there is less than a 2.5% variation in the magnitude of the refractive error over the visible spectrum. Consequently, this approach is prone to errors because it requires precise measurements of a second-order effect in order to calculate the correction. Although this approach has met with some success, its complexity and expense limit its applications.

The ideal measurement approach would compensate for atmospheric refraction automatically without the need for auxiliary measurements or calculations. A novel approach to atmospheric-refraction compensation is presented here that achieves this goal by automatically correcting for the dominant component of refractive error. This approach is based on optical interference and the concept of controlling the paths of interfering components such that phase errors produced by atmospheric refraction cancel. This approach represents a fundamental departure from more traditional measurement approaches such as sighting the position of a target with a theodolite or measuring deviations with respect to a laser beam.

The work reported here was motivated by the need to monitor deformations of the primary surface of the Large Millimeter Telescope (LMT) being constructed in Mexico [4]. The LMT represents a new class of radars and radio telescopes that actively maintain antenna shape against outside influences [4–6]. These influences include, for example, the variation of gravitational distortion with elevation angle, bending and vibration due to antenna motion or wind, and thermal distortions due to temperature variations of the surrounding air or radiative heating of the structure from the sun.

*This work was sponsored by the Defense Advanced Projects Agency and the Lincoln Laboratory Advanced Concepts Program under Air Force contract F19628-95-C-0002. Opinions, Interpretations, conclusions, and recommendations are those of the author and not necessarily endorsed by the U. S. Air Force.

DISPLACEMENT SENSING

Before describing the atmospheric-compensation technique, it is necessary to summarize the underlying concept for measuring surface displacement [5,7–8]. Figure 1 depicts two mutually coherent point sources obtained by splitting a laser beam of wavelength λ. Light from the two sources, which are separated by the distance a, expands slowly and produces a sinusoidal interference-fringe pattern in the area of overlap. A corner cube is attached to the surface whose out-of-plane displacement along the z-axis is to be measured. The corner cube reflects the light back towards the sources, where it strikes a beam splitter (BS) that directs the light to a detector or detector array. (Alternately, the detector is placed on the surface being monitored.) The interference-fringe period at the detector is $d = 2\lambda R/a$, where R is the distance between the source and the corner cube. (The factor of two accounts for round-trip propagation. This factor is absent if the detector is located on the surface.) A displacement z_0 along the z-axis of the surface being monitored produces a displacement of the fringe pattern at the detector of $2z_0$. Thus, if d is known, surface displacements can be monitored by observing motion of the fringe pattern at the detector.

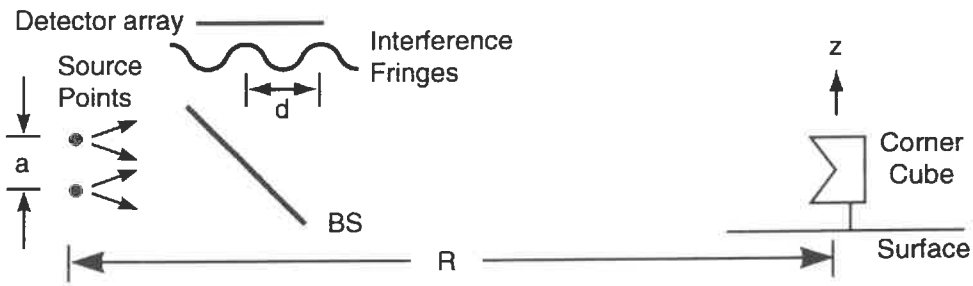

FIGURE 1. Physical basis of displacement-sensing technique.

In a system based on this concept, the fringe period d can be set such that expected surface displacements fall within one fringe period. For example, with a wavelength of $\lambda = 0.7$ µm and a point separation of $a = 2.8$ mm, the fringe period at a distance of $R = 20$ m is $d = 10$ mm. Alternately, motions exceeding the fringe period can be measured using, for example, fringe counting. It is possible in practice to determine fringe motion to better than one part in one thousand, providing micron-level displacement measurements at distances of tens of meters. The basic technique is readily extended to include many simultaneous displacement measurements distributed over a surface.

ATMOSPHERIC REFRACTION ERRORS

Although the above measurement concept has many positive features, including simplicity, robustness, speed, versatility, and minimal cost, it does suffer from the basic limitation described above—atmospheric refraction. It should be pointed out, however, that because the two beams that interfere to produce a fringe pattern travel, essentially, over a common path, the fringes are quite insensitive to other temperature-related effects. For instance, a bulk change in temperature of the air mass or temperature gradients parallel to the propagation path of the laser beam have minimal effect on the fringe pattern. As described above, the atmospheric effect that limits accuracy is the bending of light rays due to temperature gradients in the z direction—the direction in which displacement is to be measured.

Before describing the compensation technique, it is beneficial to calculate the degree of error introduced into a displacement measurement by atmospheric refraction. For simplicity, we assume there is no corner cube, and the detector is attached directly to the surface whose displacement is being monitored. In Figure 2, z_0 represents the displacement of the measurement point on the surface, and s_1 and s_2 are the optical path lengths of rays from each of the point sources to the measurement point. The objective of the analysis is to determine the motion (induced by atmospheric refraction) of the fringe

pattern at z_0. Fringe motion corresponds to variations in the optical phase difference between the interfering components from the two source points. These variations in optical phase are directly proportional to the optical path length difference (OPD), given by s_2-s_1. Thus, the refractive error can be analyzed by determining the effect of temperature gradients on the OPD.

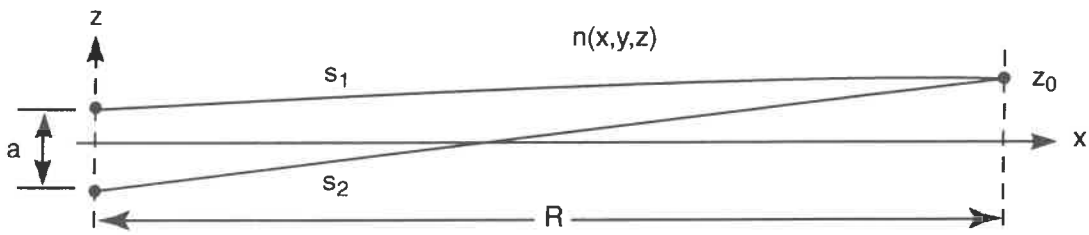

FIGURE 2. Coordinate system for calculating atmospheric-refraction errors.

To calculate the OPD, we first determine the curved ray trajectories that the two rays in Figure 2 take through the varying index of refraction n. Because deviations from the x-axis are small, the paraxial ray equations [9]

$$\frac{d^2z(x)}{dx^2} = \frac{1}{n_0}\frac{\partial n}{\partial z} \quad , \tag{1}$$

and

$$\frac{d^2y(x)}{dx^2} = \frac{1}{n_0}\frac{\partial n}{\partial y} \quad , \tag{2}$$

provide an excellent approximation to the ray trajectory. In these equations, n_0 is the average index of refraction and y points into the page in Figure 2. Once the ray paths have been determined, the optical path lengths s_1 and s_2 can be found by multiplying each length element along the ray trajectory by the value of the index of refraction at that location and integrating, yielding:

$$s = \int_0^R n(x, y(x), z(x))\sqrt{1 + \left(\frac{dy(x)}{dx}\right)^2 + \left(\frac{dz(x)}{dx}\right)^2}\, dx \quad . \tag{3}$$

The radical in Eq. (3) accounts for the slope with respect to the x-axis of the length element.

To proceed further with the calculation, it is necessary to specify the form of the index of refraction gradients $\partial n/\partial z$ and $\partial n/\partial y$ in Eqs. (1) and (2). The gradient $\partial n/\partial y$ does not produce an apparent motion of the fringe pattern because it displaces the fringes along their direction of orientation. Consequently, this gradient does not significantly affect the measurement of fringe displacement, and we set it to zero. For the purpose of illustration, we set the other gradient $\partial n/\partial z$ to a constant value P_0 that does not depend on the x position along the beam path. In a Fourier-series expansion of the x dependence of the general gradient $\partial n/\partial z$, we would refer to this uniform component as the DC component. In practice, the DC component is likely to be the leading source of refractive error because it acts along the entire path length with the same sign. By contrast, high-frequency Fourier components of the index-of-refraction gradient tend to produce a small error because these components vary sinusoidally in x and have zero mean.

Even if a uniform index-of-refraction gradient P_0 is assumed, the form of the OPD resulting from Eqs. (1)–(3) is complex and difficult to interpret. A simple and useful expression for the OPD, however, is obtained by noting that, in practice, the point-source separation a is small compared with the path length R. Thus, an accurate expression for the OPD can be obtained from the lowest-order terms of a power series expansion for small a. The resulting OPD expression for a uniform gradient P_0 is

$$\mathrm{OPD} = \frac{an_0}{R} z_0 - \frac{P_0 R}{2} a \quad . \tag{4}$$

The solution of Eq. (4) for z_0 is

$$z_0 = \mathrm{OPD}\frac{R}{an_0} + z_{\mathrm{error}} \quad , \tag{5}$$

where

$$z_{\mathrm{error}} = \frac{1}{2}\frac{P_0}{n_0} R^2 \quad . \tag{6}$$

The index of refraction gradient can be approximated in terms of the temperature gradient as [10]

$$P_0 \approx \frac{\partial T}{\partial z}\frac{\partial n}{\partial T} \approx -\frac{\partial T}{\partial z} 9.3\times 10^{-7}/^{\circ}\mathrm{C} \quad . \tag{7}$$

It should be pointed out that although Eq. (6) was derived for fringe motion, the same result is obtained for displacement. Thus, the numerical example given in the introductory paragraph applies equally well to fringe patterns and optical rays.

COMPENSATION

The objective of compensation is to eliminate the error term in Eq. (5). There is, however, no combination of experimental parameters that will achieve this objective and produce a measurement of z_0 (other than requiring P_0 to vanish). Obviously, a different approach to the problem is required. Suppose that instead of observing the fringe pattern associated with the interference of the rays depicted in Figure 2, we have a means of selecting the ray paths shown in Figure 3 and causing the two separated rays at the $x = R$ plane to overlap and interfere. A repetition of the above analysis of the OPD, but for the situation described by Figure 3, yields

$$\mathrm{OPD} = \frac{(a+b)n_0}{R} z_0 - \frac{P_0 R}{2}(a-b) \quad . \tag{8}$$

Thus, the refractive error associated with this measurement is

$$z_{\mathrm{error}} = \frac{1}{2}\frac{P_0}{n_0}\frac{a-b}{a+b} R^2 \quad . \tag{9}$$

Note that Eq. (9) reduces to Eq. (6) when $b = 0$. By inspection of Eq. (9), we see that the refractive error can be eliminated by requiring that $b = a$.

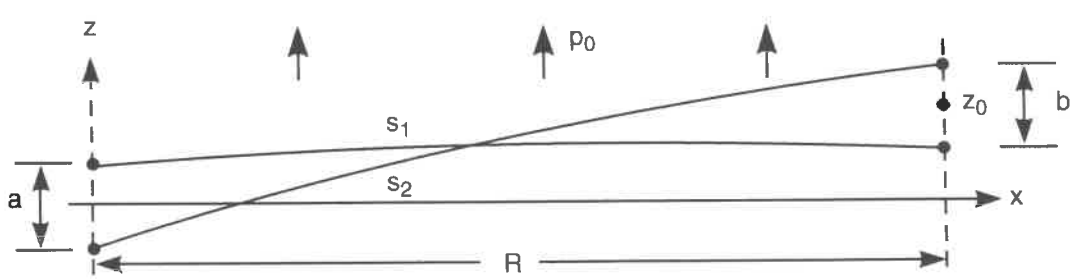

FIGURE 3. Physical basis for atmospheric-refraction compensation.

The above compensation technique has a simple intuitive explanation. Because the index-of-refraction gradient P_0 is uniform along the x-axis, the contribution to the OPD at a given value of x due to the refractive error is proportional to the vertical separation of the two rays at the point x. Thus, the rate

of buildup of refractive error gradually decreases as the rays propagate from the two sources to the crossing point. At the crossing point, the positions of the rays switch, causing the sign of the contribution to the refractive error to reverse. By the time the rays have propagated to the $x = R$ plane, the cumulative error has been completely canceled due to symmetry (assuming a uniform gradient P_0).

There are many possible methods of selecting the crossed ray paths shown in Figure 3 and causing them to interfere. One class of techniques relies on polarization coding—accomplished by cross polarizing the beams emanating from the source points. The rays coming from the desired source can then be selected for each endpoint by using an appropriate pair of crossed analyzers.

In practice, it is desirable to co-locate the sources and the detector, as is done in the original non-compensated system depicted in Figure 1. Compensation can be achieved with this constraint by causing the rays to follow nearly the same path on the return trip to the detector. Thus, the rays traveling in either direction cross in the middle, and both outgoing and incoming paths are compensated.

Figure 4 depicts an optical configuration for achieving compensation with a co-located source and receiver. Here, polarization coding is achieved with a birefringent crystal, such as calcite, which separates an incident laser beam into cross-polarized ordinary and extraordinary rays. (The ordinary ray obeys Snell's law of refraction at the crystal interface; the extraordinary ray does not.) In Figure 4, an ordinary and an extraordinary ray are selected such that they cross midway between the source/receiver and the target assembly. (In general, these two rays are not generated from a single ray coming from the point source.) The target assembly consists of a polarizing beam splitter (PBS) having offset corner cubes attached to two faces. The PBS reflects the ordinary ray and transmits the extraordinary ray, or vice versa, so that each ray strikes the vertex of the corresponding corner cube. The offset of the corner cubes is set such that the distance b between the two rays entering the PBS is equal to the distance a between the two rays leaving the calcite crystal. The return rays follow the same path back through the system and are reflected by the beam splitter (BS) onto a CCD array. Because the two rays are cross polarized, it is necessary to place an analyzer before the CCD array to select a common polarization component. Otherwise, the two contributions will not interfere.

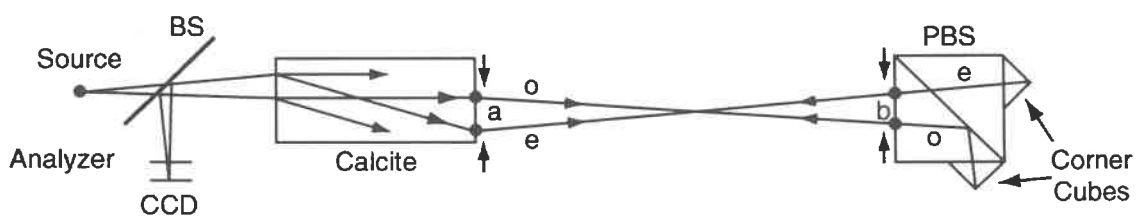

FIGURE 4. Apparatus for achieving atmospheric-refraction compensation.

The ability of the system depicted in Figure 4 to compensate for atmospheric refraction has been demonstrated experimentally [11]. This particular implementation has the advantage that the separation b can be varied by changing the offset between the corner cubes. Doing so varies the crossing point and may make it possible to optimize the system for index-of-refraction gradients whose magnitude varies along the x-axis. Research is currently under way to use the additional information obtained from additional crossing points to make higher-order refractive-error corrections.

CONCLUSIONS

A new technique has been introduced that automatically compensates for the dominant source of refractive errors in many precision optical measurements. This technique, which requires no auxiliary measurements or calculations, is simple to implement and requires no cabling or electrical communication with the target. The compensation technique can be incorporated into existing measurement techniques and provides a means for overcoming a fundamental source of measurement error that has long plagued optical metrology.

ACKNOWLEDGMENTS

This work was sponsored by the Defense Advanced Research Projects Agency and the Lincoln Laboratory Advanced Concepts Program. The author gratefully acknowledges the contributions and support of M.P. Kavalauskas, D.L. Feldkhun, L.B. Spence, J.C. Chow, and J.A. Tabaczynski.

REFERENCES

1. *Refractional influences in astronomy and geodesy*, International Astronomical Union Symposium. No. 89, E. Tengstrom and G. Teleki, eds., D. Reidel, Dordrecht, Netherlands, 1979.
2. O.A. Mozzhukhin, "Correction of leveling by refraction determined from meteorological measurements," Acta Geodaetica, Geophysica et Montanistica, **14**, 81-91 (1979).
3. L. Zeng and H. Matsumoto, "Compensation of the air turbulence by two-color method for straightness measurement," J. of the Japan. Society of Precision Engineering/Seimitsu Kogaku Kaishi **60**, 111–113 (1994).
4. G. Cortez-Medellin and P.F. Goldsmith, "Analysis of active surface reflector for a large millimeter wave radio telescope," IEEE Trans. on Antennas and Propagation, **42**, 176–183, (1994).
5. J.F. Cannon, J.A. Ball, J.E. Salah, L.G. Shirley, "A new high-efficiency surface for the Haystack antenna at millimeter-wavelengths," MIT Haystack Observatory Technical Report, February 15, 1996.
6. R.J. Lacasse, "Green Bank telescope active surface system," in *Telescope Control systems III*, H. Lewis, ed., Proc. SPIE **3351**, 310-319, (1998).
7. L.G. Shirley, "Optical sensor for active control of antenna surfaces," in Proceedings of the 1999 IEEE Radar Conference, pp. 32-35, Waltham, Massachusetts, April 20-22, 1999.
8. US Patent 5,900,936, L.G. Shirley and G.R. Hallerman, "Method and apparatus for detecting relative displacement using a light source," May 4, 1999.
9. *Handbook of Optics*, Vol. 1, p. 1.23, M. Bass, ed., McGraw-Hill, New York, (1995).
10. B. Edlen, "The refractive index of air," Metrologia **2**, 71-80 (1966).
11. L.G. Shirley and M.P. Kavalauskas, "Self-compensation of atmospheric-refraction errors: method and results," to be submitted to Appl. Opt.

METROLOGY SYSTEM FOR THE GREEN BANK TELESCOPE

David H. Parker*, John M. Payne†
The National Radio Astronomy Observatory‡

The National Radio Astronomy Observatory (NRAO) is constructing a 100-meter aperture, 60-meter focal length offset paraboloid, fully steerable, radio telescope in Green Bank, West Virginia. The Green Bank Telescope (GBT)[1] will be the world's largest fully steerable telescope when completed in late 1999. The GBT stands 150-meters at its peak and has a moving weight of 8000 tons suspended on 16 conical steel wheels on a 32-meter radius track. The goal is to obtain a reflector surface accuracy of 0.25 mm RMS and a pointing accuracy of 1 arcsecond, under benign weather conditions, in order to work up to a frequency of 100 GHz (3 mm wavelength). To accomplish this goal, a number of unique features are included in the design of the GBT. The surface is composed of 2004 reflector panels mounted on motor operated actuators to correct the surface for thermal and gravity deflections of the support structure. Custom designed and automated Electronic Distance Measurement (EDM) instrumentation[2 3] is included to provide closed-loop feedback of the surface shape at the 2209 actuator locations, and measurements from fixed ground-based instruments provide closed-loop measurements for pointing error corrections. Six instruments are mounted on the structure above the main reflector looking into 2209 retroreflectors mounted on the surface, to produce a complete survey of the reflector every 8 minutes. Twelve ground-based instruments, equally spaced on a 120-meter radius around the telescope, track retroreflectors mounted on cardinal points on the telescope structure[4]. The two systems are tied into a survey network referenced to the 12 ground-based instrument monuments. The instruments use a laser diode modulated at 1500.000 MHz and a digital phase measurement technique to produce a measurement modulo 100 mm. A servo-controlled mirror is used to switch between targets. The instrument accuracy is around 0.100 mm at 100 meters (1 ppm) with a measurement speed of 5 points per second for near neighbor retroreflector targets. All coordinates are calculated by trilateration, i.e., only distances are used in the reduction. The group refractive index, the major limit to accuracy, is corrected by a combination of refractometer paths between ground monuments; temperature, pressure, and humidity profile measurements; and possibly acoustic thermometry. For example, a 1°C change in temperature produces a 1 ppm change in the group refractive index—the entire error budget if uncorrected. The 18 instruments are interconnected via Ethernet to a central computer that orchestrates the required measurements and computes the coordinates. The central computer tracks the telescope motion from 24-bit encoders and a finite element analysis model of the structural deformations as a function of telescope elevation angle.

These measurements will be used in the early stages to study deflection of the structure[5] and refine the finite element analysis model.[6] In operation, the measurements will be used to correct the surface shape and absolute pointing.

Key Words: electronic distance measurement, retroreflector, Green Bank Telescope.

---

* Green Bank, WV, dparker@nrao.edu, (304)456-2121
† Tucson, AZ, jpayne@nrao.edu, (520)822-8250 X118
‡ The National Radio Astronomy Observatory is operated by Associated Universities, Inc., under cooperative agreement with the National Science Foundation.
[1] http:\\info@nrao.edu
[2] J. M. Payne, D.H. Parker, and R.F. Bradley, "Rangefinder with Fast Multiple Range Capability," *Rev. Sci Instrum.* 63 (6), June 1992.
[3] J. M. Payne, D.H. Parker, and R.F. Bradley, "Optical Electronic Distance Measuring Apparatus with Movable Mirror, US Pat 5,455,670, Oct. 3, 1995.
[4] D. Wells, "Visualizing the Geometry of the GBT Metrology Systems," NRAO GBT Memo #177, February 25, 1998; Figure 2.
[5] A.L. Petticrew, "Laser Rangefinder Deflection Measurements of the GBT Derrick," NRAO GBT Memo #160, November 18, 1996; Figure 5; D.H. Parker, "First Measurements of the GBT Feed Arm," GBT Archive #L0535, July 29, 1999.
[6] R. Hall, M.A. Goldman, D.H. Parker, J.M. Payne, "Measurement program for the Green Bank Telescope," *Proceedings of the Society of Photo-Optical Instrumentation Engineers*, V 3357, pp. 265-276, March 26-28, 1998.

INSTRUMENT SPECIFICATIONS

Model	PSH97
Absolute Accuracy	50 μ m + 1 ppm
Differential Accuracy	5 μ m + 0.2 ppm (no group refractive index correction)
Maximum range	≈1 km (3" retroreflector, fair conditions)
Phase Ambiguity	modulo λ\2 (≈100 mm)
Phase Accuracy	0.01° (3 μm)
Sampling	16 bit, 64 kHz, DMA, trigger synchronized to LO
Measurement Integration Time	1-1000 ms (128 ms typical)
Radiation Source	amplitude modulated laser diode
Power	10 mW
Wavelength	780 nm
Beam Size	3 x 3 mm
Beam Divergence	≈0.4 x 0.4 mrad (fwhp)
Detector	PIN diode
Signal Level Range	0.030-10.0 V
Frequency Reference	100.000 MHz rubidium
Amplitude Modulation (CW)	1500.000 MHz
LO Frequency	1500.001 MHz ϕ locked to modulation + IF
IF	1 kHz
Weight	150 lbs
Instrument Dimensions	43" x 16" x 16"
Mount	Kelvin clamp
Mirror	dual axis, closed loop servo
Panel Measurement Rate	5/s
Encoders	100 000 count, incremental

EMBEDDED CONTROL SYSTEMS SPECIFICATIONS

Bus architecture	ISA (PC/AT), 8 slots
Power	120 VAC, 3 A
Servo control	dual LM628 PID
Servo amplifier	pulse width modulated (20 kHz)
Control Panel Dimensions	42" x 24" x 8"
Embedded Computer	286 PC (minimum)
Operating System	DOS
Time Sync	IRIG
Interface	Ethernet

GBT OPTICAL METROLOGY ARCHITECTURE

Panel Retroreflectors	25 mm, BK7 glass corner cubes, total internal reflection
Spherical Retroreflectors	cat's eye, 35 mm entrance pupil, ± 60 degree acceptance angle
Panel Retroreflectors	2209
Spherical Retroreflectors	19
Cardinal Points	42
Ground Instruments	12 equally spaced on 120 m radius
Tipping Structure Instruments	6
Monument Baseline Accuracy	≈100 μm
Monument Construction	4 foot ϕ concrete, 15 feet long, undisturbed soil, cased below freeze line
Data Adjustment method	least squares trilateration (using distances only)
Refraction Correction	combination of ground based refractometers, weather stations, meteorological model, and possibly acoustic thermometry

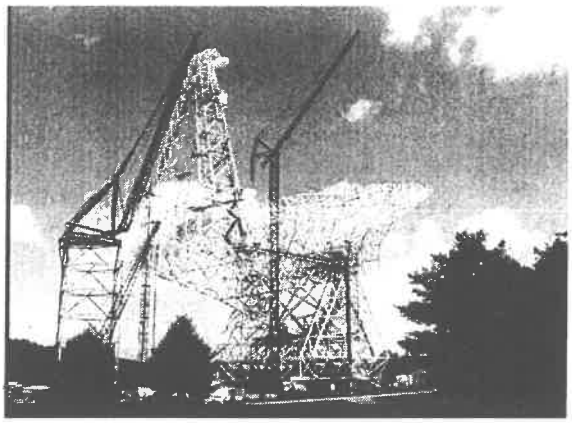

Figure 1
The GBT construction progress as of 7/28/99. All major structural steel has been erected. Estimated completion date is late 1999.

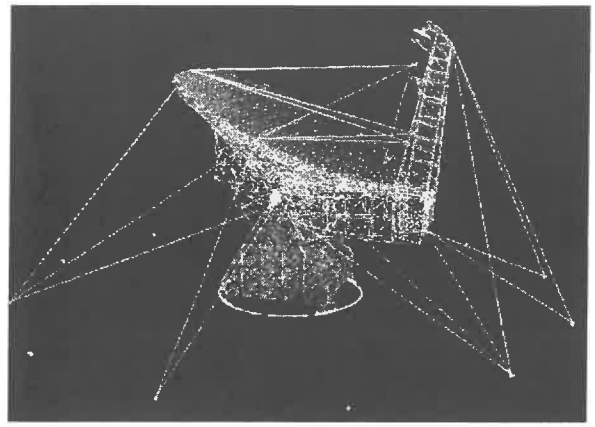

Figure 2
A schematic diagram of the metrology system with 12 fixed ground instruments, 6 instruments on the feed arm, retroreflectors at cardinal structural nodes and panel actuators.

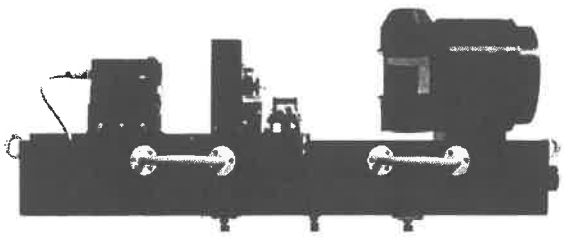

Figure 3
A PSH97 Instrument. Note the servo controlled mirror (on the right side) used to direct the beam to selected targets.

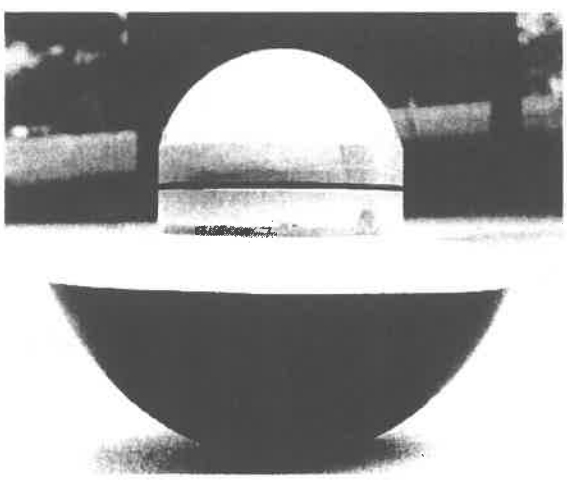

Figure 4
A Spherical Retroreflector built by the University of Arizona.

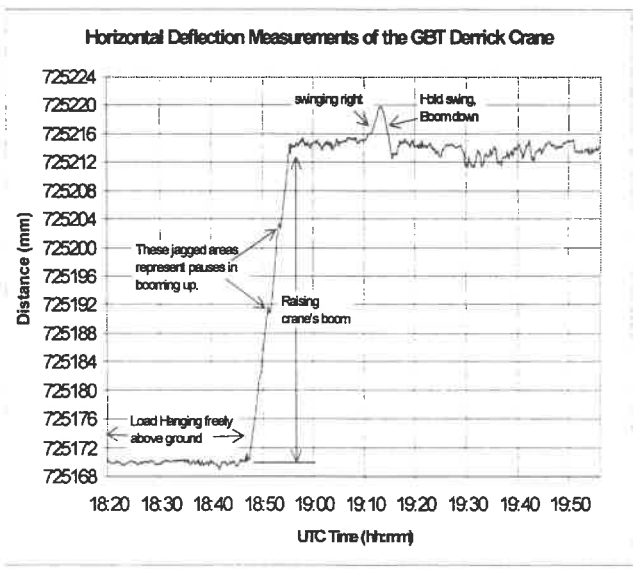

Figure 5
A plot showing deflection of the derrick tower while lifting a 45-ton load. Note this was at a distance of 725 meters from a test range.

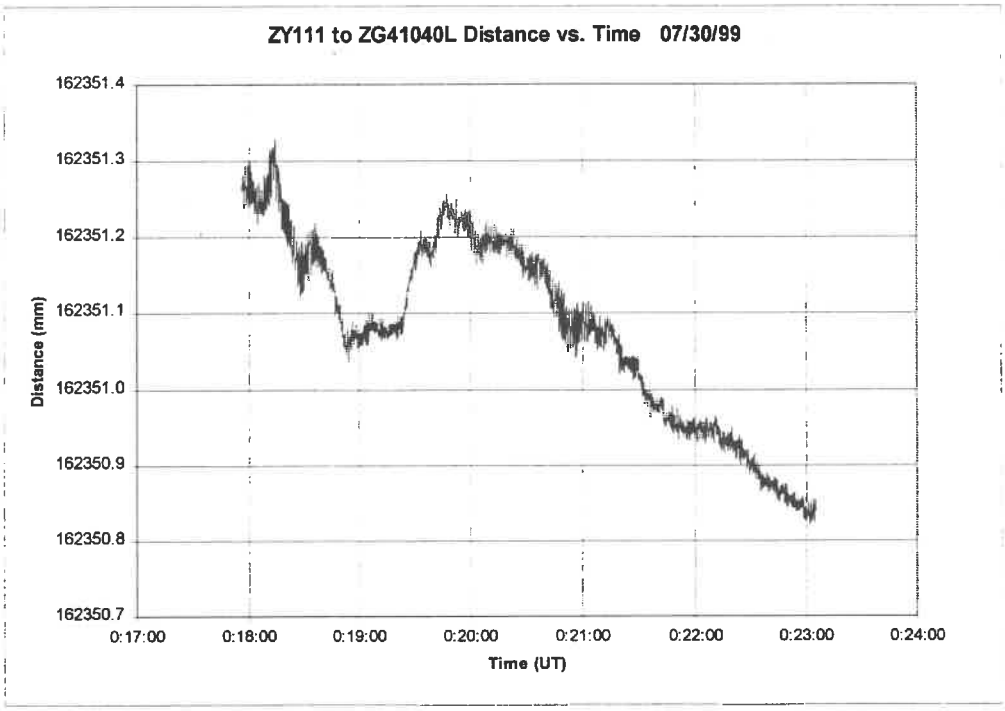

Figure 6
Data taken from a ground instrument to a target on the tip of the feed arm.
Note the oscillations riding on the gentle motion of the structure.

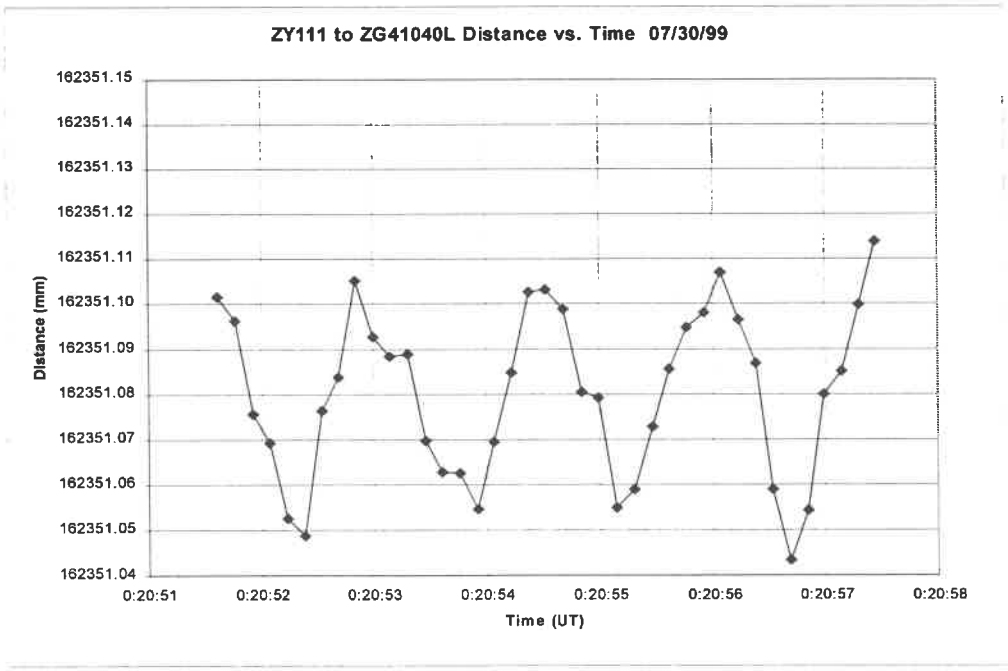

Figure 7
Expanded section of Figure 6 showing the oscillation of the feed arm at the natural frequency.

Precision Surveying of the National Ignition Facility

William S. Rorke, Jr.
Sandia National Laboratories, Livermore, CA

I. Overview of NIF

The world's largest laser, the National Ignition Facility (NIF), presently being constructed in Livermore, CA will contain 192 laser beamlines of 40cm-square aperture housed in a building 200 m long x 100 m wide x 30 m tall. Arrayed along each beamline are more than 40 optics that must be positioned to stringent tolerances. Precise positioning of the main beamline optical components is necessary to maintain the laser's clear aperture; sized to deliver the required power and energy. Non-optical components and structures also have ambitious alignment requirements. Achieving this requires the establishment of a very large virtual coordinate measurement machine.

The laser design severely constrains the solution. The laser optics must be kept very clean and the laser light is a hazard so all the beams and optics are enclosed for cleanliness and safety. To improve the cleanliness the optics are inserted into the enclosures from below which puts the bottom of the laser approximately 3m and in most places 5m above the floor. Many components must be surveyed looking nearly straight up. Provisions are required to survey into the opaque beam enclosure using high quality windows. The glass must be accurately fabricated and characterized and the refraction modeled and compensated.

The components are distributed throughout five building-sized rooms. Walls separating the rooms severely limit the lines of sight between the rooms. Two of the rooms are 30m cubes and have hardware on four different floors. One room is a 30m diameter cylinder 30m tall. It contains the target chamber and is where all the lasers converge. This room has equipment on seven floors. In these multi-story rooms, the control network must be run vertically to connect the various floor levels.

The target chamber is a 10m diameter sphere with 72 ports through which the lasers enter. The ports must be accurately placed on the sphere and their mounting flanges accurately oriented normal to the radial.

Presently the target chamber has been installed in the building where it will be completed and aligned. Installation of the other laser hardware begins this fall (1999) and will take until 2003 for completion. The first phase of hardware installation requires only rough alignment. Fine alignment to the specified tolerances begins next spring (2000).

II. Alignment Requirements

Many of the optics are sized to allow +/-3mm lateral (transverse to the laser axis) misalignment. Some optics such as lenses, pinholes at the lens' foci, and alignment light sources must be positioned to +/-1mm laterally. Some of the lenses must be positioned to +/-1mm longitudinally also.

In general the alignment tolerance is evenly allocated between the Line-replaceable Unit holding an optic and the kinematic mount that locates the LRU in the laser. For optics that have +/-1mm tolerance, their kinematic mounts are allocated +/-0.5mm. These are limit values and have been interpreted as 3-sigma values in the statistical analysis.

III. Alignment Strategy

Most of the laser was designed using a CAD system using a Cartesian coordinate system. Alignment merely requires an equivalent coordinate system be physically established in the building and the hardware put at the design coordinates. (The rest is left to the reader as an exercise.)

The decision to use a control network and align each component to its design coordinates was made after considering several other concepts. The concept we had the hardest time convincing the laser engineers would be a mistake was that of boresighting. This would involve some variation on sitting at one end of the laser and looking at crosshairs on each optic down the laser. In theory, superimposing the crosshairs would assure alignment. However, there are many reasons this would be unworkable. At best, boresighting provides only lateral alignment. Most of the NIF hardware has longitudinal requirements and much does not lie along the laser axis. Also boresighting is not very flexible. We do use boresighting in certain applications – primarily the alignment of rails and tracks.

For the method chosen, specific points (fiducials) are defined on each component and their "global" coordinates and tolerances specified. Relative coordinates and tolerances are also specified where appropriate. By placing each point at its defined coordinates within the allowable error bars it is assured that each component is properly

positioned and aligned (with some exceptions for pointing). This strategy requires the establishment of an accurate Cartesian coordinate system, and techniques to measure the location of fiducials within that coordinate system.

The thousands of different parts each have a few to tens of points producing a total of tens of thousands of discrete points (some physical and some theoretical) which must be tracked over the life of the facility.

Specification of the desired design coordinates cannot be done accurately by manual or spreadsheet calculations. To date more than 90% of all manually specified coordinates contain at least one error. Improper specification of coordinates would result in hardware being precisely positioned at the wrong location. A method has been developed to calculate the design coordinates using simplified CAD models containing laser points of interest (beam centerlines, etc.) and fiducials. The models are mated in CAD to a skeleton and the fiducial coordinates are output in electronic files that are downloaded into surveying instrument computers.

Generally measurement (including surveying) concentrates on determination of the best estimate of a value. For the NIF project we have devoted almost an equal amount of effort toward quantification of the error bars about the best estimate value. Uncertainty constitutes approximately half the job. Measurement geometries are analyzed in advance (pre-analysis) and the results are used to refine the design and measurement plan. Tests are run to validate the assumptions used in the predictions. Finally actual measurement data is thoroughly analyzed both for self-consistency (best-fit residuals) and against the predictions to detect improvements or degradations.

IV. Measurement Methodology

A. Planning

Planning this work began at the end of the conceptual design phase of the project. This was a fortunate decision. Even with the relatively advanced start we have played catch-up since. Unfortunately most of the engineers could not bring themselves to factor alignment concerns into their designs until the designs were far into detailed design. So far, our overall strategy has been sufficiently flexible to accommodate the late definition (and re-definition) of requirements.

While the majority of NIF engineers are focused on the near-term installation, the alignment strategy has been developed to support the long term needs of NIF. The alignment tolerances are very small compared to the anticipated building motion so realignment is highly probable. Measurements will be needed throughout the 30 year life of the facility probably starting just after the first laser becomes operational. The facility's scheduled and unscheduled maintenance downtime budget is very small. Measurements will need to be rapid and must not compromise the optic cleanliness.

B. Control Network

The backbone of the measurement system is a control network of thousands of survey targets. The positions of the monuments relative to each other is measured, then a Cartesian coordinate system is superimposed over the monuments and coordinates assigned to each monument. Because the measurements are imperfect the true position of any monument can only be estimated within error bands. Our goal is to assign coordinates to an accuracy of +/-0.300mm 3-sigma. With minor exceptions, this allows the measurement of the coordinates of a survey target anywhere in the building to a 3-sigma error of +/-0.500mm relative to the absolute Cartesian coordinate system.

Control networks gain accuracy much like trusses gain stiffness through "depth of section". Typically networks can be relatively stiff horizontally because targets and instruments can be placed throughout the area and interconnected. However the NIF network is weakest vertically since in the laser bays instruments are generally confined to zone no more than about 3m above the floor. It is difficult to stiffen this by triangulation or trilateration. The network is similar to a sheet of paper; stiff in plane (horizontally) and flexible out of plane (vertically).

1. The Role of Gravity and Uncertainty in the Geoid

One way to stiffen the network vertically is by referencing gravity. Over small areas a precision level can provide a very accurate horizontal reference plane. NIF is large enough that the curvature of the earth must be accounted for. An imaginary horizontal plane tangent to a perfect earth at the target would be more than 2 mm above the earth at the other end of the laser bay. Total stations and levels generate a reference surface parallel to the earth. To correct this to a pure Cartesian plane it is necessary to know the local curvature very precisely – whether the local curvature actually is known accurately enough remains unresolved.

Earth curvature also affects the networks on the various floor elevations. Vertical lines at each corner of the building diverge significantly over the height of the building when compared to the control network accuracy requirements.

2. Free Adjustment

The control network does not have a "golden" monument. Instead the network is measured and then a coordinate system superimposed over the network. The superimposition can have six degrees of freedom. After the network has evolved sufficiently and a significant amount of hardware installed, it is desirable to hold the coordinate system as stable as possible. If the coordinate system were tied to a fixed monument, any movement in that monument would change the values everywhere else. By leaving the network free the coordinate system stays fixed to the centroid of the network. Independent movement of any monument is detectable and quantifiable.

3. Free-centering

Unlike traditional surveying where instruments are force-centered (setup directly over monuments), we set-up away from monuments and then accurately determine the instrument location by measuring position relative to the monuments. This eliminates centering errors. Similarly the precision spherical targets nest into conical seats for good repeatability.

4. Network motion

Measurement of the network is made more difficult because the building moves. Monuments are installed in the concrete foundation slabs (1 – 2m thick) and walls (in some places 4m thick). No monuments are used on the massive steel columns framing the building because they have too much diurnal and seasonal motion. Over the course of the past year the 100m-long target building slab shrank 25mm in length. Vertical deformations are anticipated also.

5. Lines of sight

One reason survey planning needs to start early is to establish adequate lines of sight for the control network. The building design led the laser design by approximately a year and was nearly complete before the survey planning started. Very late in the building design changes were made to provide vital lines of sight. Originally the walls between the laser bay and switchyards had no holes or doorways – doorways were added solely for surveying. Similarly holes were added to the elevated floors in the target bay to provide vertical sight lines for connecting the network between floors.

C. Instrumentation

State of the art instruments are not a factor of 10x better than the NIF measurement accuracy requirements. Meeting the requirements necessitates high accuracy instruments combined with explicit attention to quantifying their achieved accuracy. We promise our measurements to be accurate in three orthogonal dimensions to +/-20ppm of range (3-sigma). By measuring multiple targets from multiple stations that accuracy can be further improved.

The primary measurement instruments are Leica Total Stations, SMX Model 4500 Laser Trackers, and a Leica Model NA3003 Digital Level. Other instruments such as a Hamar Laser Plane Reference and a Quest "Euclid" Laser Line Reference are also used.

Total stations report elevation (more properly "zenith") and azimuth (horizontal) angles and range to target. Total stations are gravity referenced – the zenith angle is measured from the local gravity vector. The best total stations have accuracies better than +/-0.5 arc second (+/-2.5 microrad) in both angles, and better than +/-1mm range (values are specified at 1-sigma). Testing of Leica's current high-end guns (TCA 2003 and 5000) with Automatic Target Recognition (by which the instrument self-aims at the center of the target) reveals the ATR does not work well at ranges on the order of 20m or less. Also, the optics necessary for ATR appear to degrade the range accuracy from better than +/-0.2mm (TC 2002) to +/-1.0mm. The +/-1.0mm range error is adequate for construction but cannot be tolerated for the final control network and alignment. The 2002 and 2003 have the same performance specifications but while the 2003 just barely meets its range accuracy spec, the 2002 performs almost an order of magnitude more accurately. We limit the use of our 2003s to jobs where their in-accuracy is acceptable. For critical measurements with total stations we rent 2002s. Leica has discontinued the 2002s and they are only available second-hand.

We prefer servo-driven total stations over the manual models because of their increased speed in rough centering onto known targets. Typically manually acquired shots are needed to a few targets to orient the instrument, then the computer can drive the gun to the remaining targets with the operator only needing to fine tune the aiming just prior to each shot. All shots are made at least twice (direct and reverse face) from each setup and the servo greatly speeds the work. The servo also helps prevent misnumbering the targets.

Laser trackers are similar to total stations in that they both measure two gimbal angles and range. It is neither necessary nor possible to sight through a laser tracker to a target. Trackers are slightly worse than total stations in angle (although also less than +/-1 arc-second) and much better in range – typically a few ppm (close to

interferometric accuracy). One significant advantage is their ability to measure in any attitude. They are not gravity referenced. They can measure targets directly up and down where total stations are limited to about 45 degrees above and below horizontal. Because the laser is overhead with access ports on the bottom side, most measurements must be made shooting nearly directly straight up. Another critical application for the tracker is measuring vertically up and down between floors in the switchyards and target bay to extend the control network to all levels. The tracker allows the establishment of a truly 3-dimensional network.

The primary targets are 1.5 inch diameter spherically mounted retroreflectors (SMRs). These are comprised of hollow hardened tooling balls with first-surface internal corner cubes set within less than 0.0005 inches of the ball center. The corner cubes must be very accurate – the incoming and outgoing beams must be parallel within 1-2 arc-seconds. In places where the standard SMR is too large to fit we use a 0.5 inch diameter SMR. Typically the balls are retained in conical seats with magnets on the axis of the cone. It can be very difficult to visually aim at the center of an SMR so total stations are aimed at 1.5 inch diameter hemispheres with bullseyes located at the center of the sphere. Once the gun is aimed, the bullseye is replaced with an SMR and the measurement taken. Aiming at the bullseye sets the two angles and the SMR allows accurate ranging. Laser trackers nearly always use SMRs although there are specialized targets for unique applications.

The Leica NA3003 digital level plays a key role. It must be rough leveled to get within the range of its compensator, then it is pointed at a vertical "rod" covered with bar code. The level can read the code to within a few microns. The level can be run down a course 100m and back and close to under 0.100mm. It is very fast and we rely on it to provide sufficient strength vertically for our network and as an efficient method to detect building motion (assumed to virtually always have a vertical component). The level is used also to orient a set of targets measured by a tracker, because the tracker has no gravity reference.

D. Software

Even the most basic construction surveying is computer-intensive. Software also plays a central role in designing the control network and measurement process, analyzing the measurements and archiving the data. For NIF we rely heavily on software developed at the Stanford Linear Accelerator Center for operation of the total stations, preanalysis (simulation) and analysis of the observation data. The SLAC software includes database capabilities. Our other primary program is the laser tracker software (which recently incorporated SLAC routines).

We have also developed custom software (mostly Microsoft Excel macros) to handle some of our unique needs. For example the target chamber center is defined as the center of the smallest sphere that intersects the centerlines of all the target chamber port flanges. We wrote a routine that accepts the survey data on the port flanges and calculates the location of the target chamber center and the size of the intersection sphere. Another area where our needs are apparently unique is in calculating best-fits from data. Typically best-fits try to minimize the root-mean-square error. If nine out of ten points are perfect and the tenth is off by 1.0, the best fit will adjust to move the nine points off by 0.1 and leave the tenth out by 0.9. For NIF the worst beam is the only one that matters. If the worst point is within specification, the others will be better. We frequently use custom best-fit routines that would leave all ten points in the previous example out by 0.5.

Our search for useable commercial software has not been fruitful. One good network analysis code (Star-Net) is limited by being constrained to a local gravity reference. It does not analyze arbitrarily oriented instrument axes (as for laser trackers). Brunson's Spatial Analyzer software can handle both total stations and laser trackers (and other instruments) and might be a good solution for anyone who cannot obtain the SLAC programs.

For nearly two years we have had one person working full time with the software (not writing it). We have just added a second data analyst to handle the surge of data that will occur as hardware starts being placed and aligned.

V. Closing

The measurement of NIF is a world-class challenge. There are thousands of items with stringent alignment specifications. The equipment is arrayed in ways that make accurate measurement difficult – spread over a large area, separated by walls and floors, enclosed in metal, placed overhead, etc. The control network accuracy requirements press at the limits of the most accurate gravity models available. The job could not have been done a few years ago – the technology is being developed simultaneously with our planning to use it.

The majority of our work to date has been preparation. Actual alignment work is now ramping up. The next several years will reveal the strengths and weaknesses of our preparation.

The Implementation of Simultaneous Trilateration to Measure Dynamic Three-Dimensional Contours Using the Laser Ball Bar

Tony L. Schmitz
National Institute of Standards and Technology, Gaithersburg, MD
John C. Ziegert
University of Florida, Gainesville, FL

Introduction

In computer numerical control (CNC) machining, the desired trajectory of the tool is defined by the part program. The purpose of the part program is to place the tool tip at specific coordinates relative to the part at every instant in time, leaving behind surfaces which form a workpiece of proper dimensions. Errors in the machined part dimensions are determined by the accuracy with which the commanded tool trajectory is followed, combined with any deflections of the tool, part, or machine caused by cutting forces. The accuracy of the tool trajectory is dependent on the static machine geometry, the machine's thermal state, and dynamic errors of the control system. Using current technology, it is possible to measure the quasi-static geometric errors of a machine tool and their thermally induced deviations. With this data, one can construct a thermal/geometric error model of the machine which predicts the static tool point positioning error anywhere in the workspace at any thermal state [1]. This machine error model can be used to predict tool position errors at discrete points along arbitrary CNC paths, and predict the dimensional errors of a machined part caused by the imperfect machine geometry. Comparisons of predicted and actual part dimensions show that the thermal/geometric error model obtained from static measurements is capable of predicting some, but not all, of the resulting part dimensional errors [1][2][3]. In order to improve the accuracy of models seeking to predict part dimensions, it is necessary to extend these models to include trajectory errors related to the controller, as well as errors induced by the cutting process.

The purpose of this text is to demonstrate the use of an instrument capable of measuring arbitrary, dynamic tool paths through three-dimensional space with ±1 μm accuracy. The results of these dynamic path measurements can ultimately be used in two ways. First, differences between the measured dynamic path and the path predicted by the static thermal/geometric error model must be due to dynamic effects in the machine's control system. The dynamic errors can then be separated from the thermal/geometric errors and used to evaluate, model, and optimize the contouring performance of NC systems. Second, differences between the dynamic path of the tool and the final part dimensions must be caused by cutting forces. These discrepancies between part dimensions and dynamic path errors may then be used to understand and model the cutting process dynamics.

The instrument described here for the measurement of dynamic spatial paths is based on the laser ball bar (LBB), developed by Ziegert and Mize [4]. The laser ball bar uses sequential trilateration to measure the static spatial coordinates of the tool at arbitrary points throughout the work volume of a CNC machine tool. This new sensor uses three LBBs simultaneously (i.e., Simultaneous Trilateration Laser Ball Bar or STLBB system) to allow for dynamic path measurements. The design and testing of this instrument have been described previously [5]. Therefore, we will concentrate on the 3-D contour measurement results. Machining verification has also been completed, but will not be included here due to space limitations.

Three-Dimensional Contour Measurement Results

To demonstrate the versatility of the STLBB system for 3D dynamic path measurements, several paths combining multi-axis linear and circular interpolation were chosen. Two will be discussed here.

Corkscrew Path

The STLBB measurement results for a corkscrew path are shown in Figure 1. For this path, a counter-clockwise half-circle was commanded in the XY plane, followed by a step in the -Z direction. Next, the half-circle was completed and followed by another step in the -Z direction, etc. In Figure 2, the transition from the first half-circle to the first -Z motion is shown. An elliptical distortion of the half-circle in the XY plane is evident as well as undershoot in both the X and Y directions for the start of the -Z motion. The elliptical distortion of the circular path suggests a gain mismatch between the X and Y axes, while the cornering undershoot suggests low axis gains.

Oblique Rectangle

Figure 3 shows a rectangle situated on a plane oblique to the three axes of the machine tool and two different measurement results at feed rates of 889 and 1778 mm/min. Figure 4 displays the section of the contour

which includes the transition from -X, +Z linear interpolation to +X, +Y, +Z linear interpolation. The figure shows a steady state contouring error in the XZ plane and velocity dependent undershoot at the interpolation direction transition.

Evaluation of CNC Contouring Accuracy

Two applications of STLBB contouring accuracy evaluation will now be demonstrated. The first is the diagnosis of controller gain mismatch between individual machine tool axes. The second is an examination of the source(s) of machine vibrations which modulate the spatial path of the cutting tool.

Diagnosis of Controller Gain Mismatch

The oblique rectangle path (Figure 3) showed steady state following errors in all three planes. The projection of the selected cornering portion of the motion (Figure 4) on the XY plane is given in Figure 5. This plane view may be used to determine the gain relationship between the X and Y axes of the machine tool.

Using Figure 5, the difference in gain between the X and Y axes (ΔK_{XY}) can be calculated. The expression for ΔK_{XY} is formulated in Equation 1. In order to solve this equation, a value for either the X or Y axis gain must be known because the measurement data only provides a difference between the X and Y positional lags (Δ_{XY}). The X axis velocity lag ($e_{ss,x}$) was found by measuring the following error during a constant velocity move in the X direction. This data was obtained by recording the commanded and actual encoder counts (using the machine tool's PMAC controller software), then determining the difference between the commanded and actual position under constant velocity motion. At a feed rate of 508 mm/min, this steady-state positional error was found to be 520 μm. The X axis gain was then calculated according to Equation 2.

$$\Delta K_{XY} = K_X - K_Y = K_X - \frac{F_Y}{e_{ss,Y}} = K_X - \frac{\frac{F_{com}}{\sqrt{2}}}{\frac{F_{com}}{\sqrt{2}}\frac{1}{K_X} + \Delta_{XY}} \tag{1}$$

$$K_X = \frac{F_X}{e_{ss,X}} = \frac{\frac{508}{60}}{0.520} = 16.28 s^{-1} \tag{2}$$

Referring again to Figure 5, it is seen that the Y axis lags 410 μm more than the X axis during the constant velocity section of the 1778 mm/min +X, +Y motion. Substitution of this steady-state error difference, the experimental value for the X axis gain, and the commanded path velocity into Equation 1 yields a gain difference (ΔK_{XY}) of 3.93 s^{-1}. This value is positive because the X gain is greater than the Y gain (i.e., the Y lag is greater than the X lag). The uncertainty of the calculated gain difference includes imperfect knowledge of the true feed rate and velocity lag. It is estimated at ±0.2 s^{-1}.

Similar calculations carried out for the X-Z and Y-Z projections of the cornering motion yielded gain differences of ΔK_{XZ} = -5.13 s^{-1} and ΔK_{YZ} = -8.84 s^{-1} between the X and Z axes and the Y and Z axes, respectively.

Path Modulation by Machine Noise

Early experimental results showed that single axis motions were modulated by some high frequency disturbance. In order to determine the source of this disturbance, the 3-D motions of the tool point were measured with the machine on (no commanded feed) and with the machine off (1 kHz sampling rate in both cases). The frequency content of the 'machine on' measurement is shown in Figure 6 (the 'machine off' measurement exhibited no significant frequency content above the noise floor). It can be seen in Figure 6 that significant frequency content exists at 60, 120 and 180 (±1) Hz in the X axis, 60 Hz in the Y axis and 60 and 120 Hz in the Z axis. The 60, 120 and 180 Hz frequency components in the machine noise were therefore attributed the three-phase power of the axis motor amplifiers.

The single axis path modulation is demonstrated in the Y and Z error motions during a commanded X axis travel in Figure 7. Figure 8 shows the corresponding frequency content. It can be seen in Figure 7 that the Y and Z motions (which are nominally zero) are modulated and contain a rapidly varying dynamic non-straightness of motion. In Figure 8, the expected frequency components (displayed in Figure 6) are identified in each axis (60 Hz in Y, 60 and 120 in Z).

Conclusions

We have developed an instrument capable of measuring arbitrary, dynamic CNC tool paths through three-dimensional space with micrometer-level accuracy. The utility of the 3D measurements in identifying controller gain mismatch errors and servo switching frequency errors was shown.

References

1. Donmez, M.A. "A General Methodology for Machine Tool Accuracy Enhancement: Theory Application and Implementation," Ph.D. Dissertation, Purdue University, West Lafayette, IN, 1985.
2. Srinivasa, N. "Modeling and Prediction of Thermally Induced Errors in Machine Tools Using a Laser Ball Bar and a Neural Network," Ph.D. Dissertation, University of Florida, Gainesville, FL, 1994.
3. Chen, J.S. and Ling, C. "Improving the Machine Accuracy through Machine Tool Metrology and Error Correction," *International Journal of Manufacturing Technology*, 11(3), 1996, pp. 198-205.
4. Ziegert, J.C. and Mize, C.D. "Laser Ball Bar: A New Instrument for Machine Tool Metrology," *Precision Engineering*, 16(4), October, 1994, pp. 259-267.
5. Schmitz, T. and Ziegert, J.C., "A New Sensor for the Micrometre-Level Measurement of Three-Dimensional, Dynamic Contours", *Measurement Science and Technology*, 10(2), 1999, pp. 51-62.

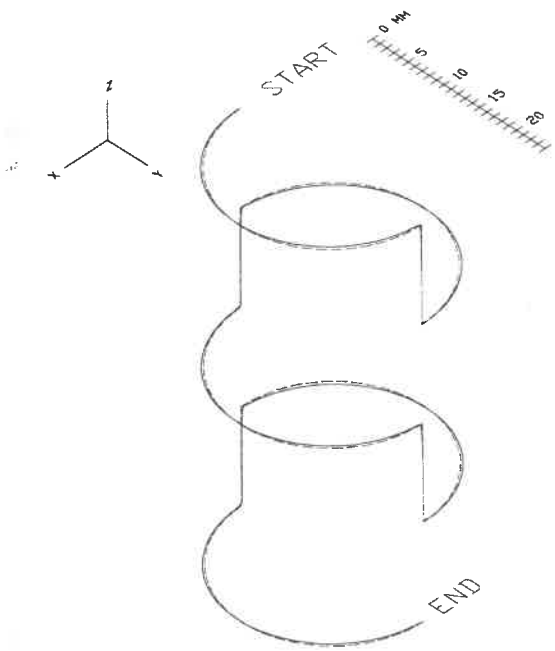

Figure 1: Corkscrew Path

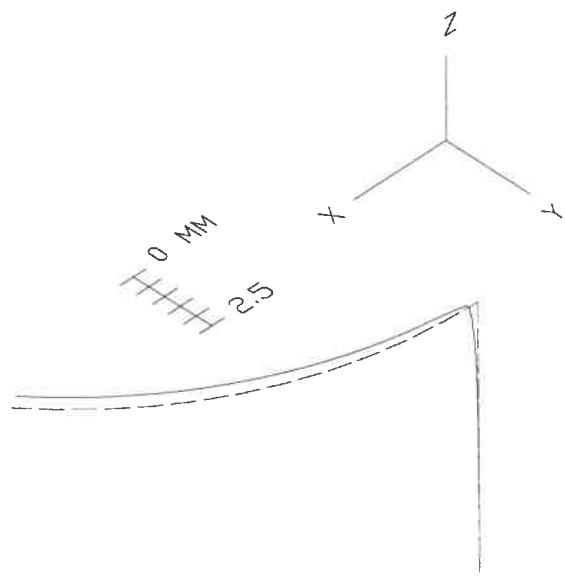

Figure 2: Corkscrew Path Section

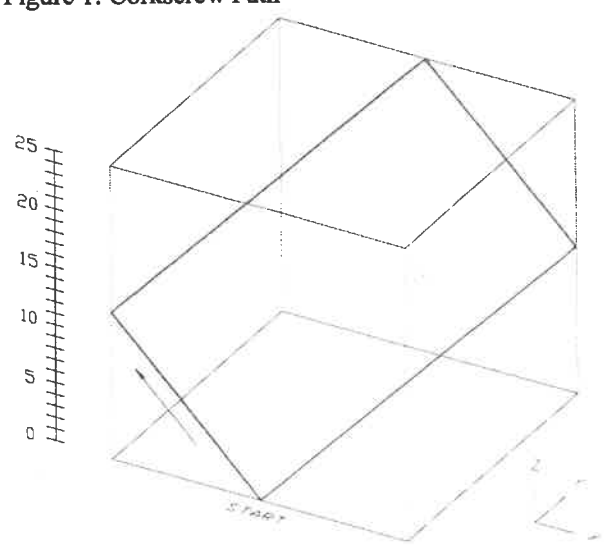

Figure 3: Oblique Rectangular Path

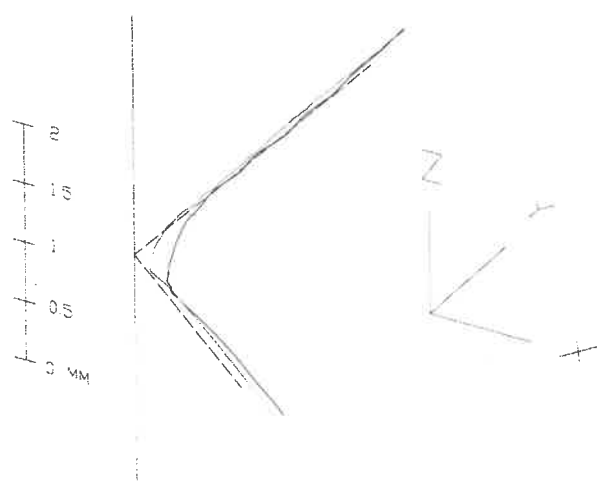

Figure 4: Oblique Rectangular Path Section

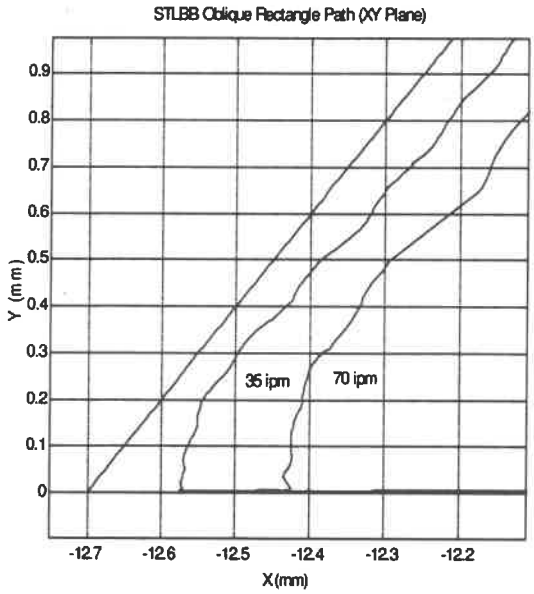

Figure 5: Oblique Rectangular Path (XY Plane)

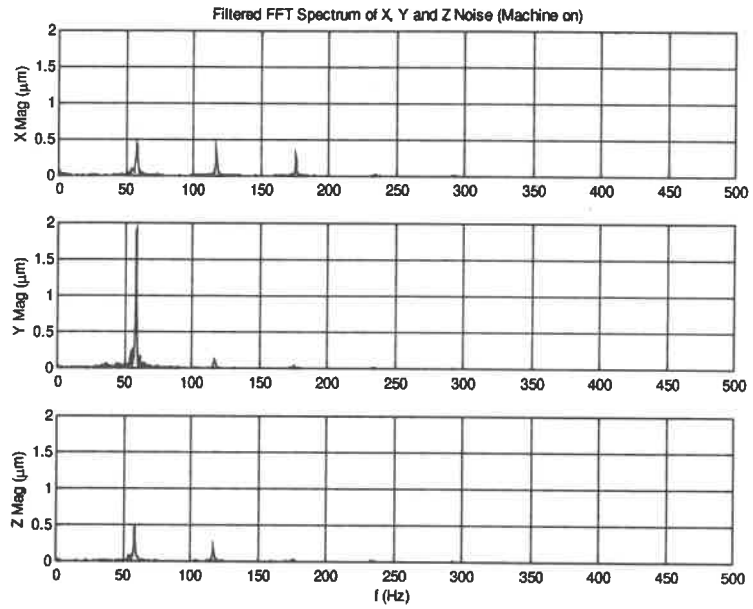

Figure 6: Machine Noise Frequency Content

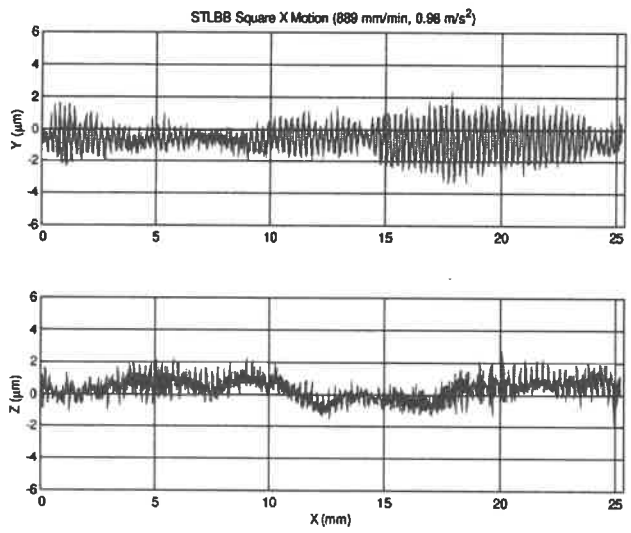

Figure 7: Y and Z Error Motions

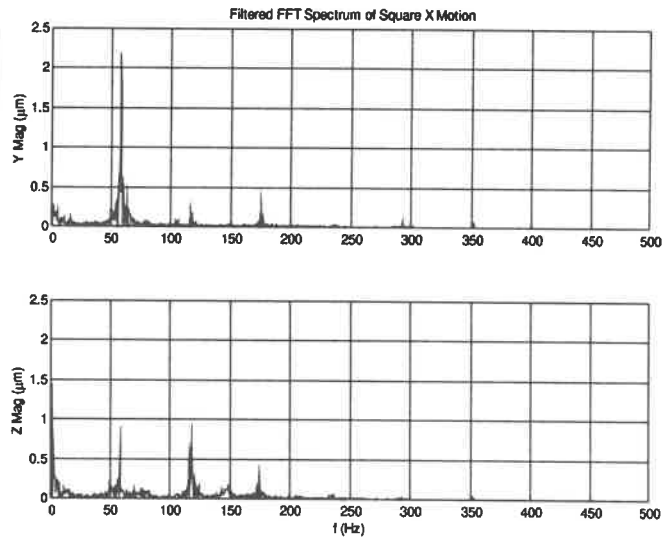

Figure 8: Y and Z Error Motions Frequency Content

MICROSYSTEMS: MANUFACTURING AND PACKAGING CHALLENGES

Dr. Robert M. Mehalso
Microtec Associates and Rensselaer Polytechnic Institute, Troy, NY
E-Mail: microteca@worldnet.att.net

INTRODUCTION

Microelectromechanical systems, or MEMS, is also referred to as Microsystems and as Mechatronics. These systems are manufactured by microfabrication or microassembly approaches. Initially, MEMS was associated with the integrated circuit industry where mechanical and electronic functions were integrated on a single silicon chip. Today the term MEMS tends to refer to a complete device with all the packaging requirements. Miniaturization technologies typically employ silicon-based electronics, but the miniature mechanical parts can be fabricated from silicon and from a variety of materials depending upon the application.

Over the last ten years, MEMS has matured from a laboratory curiosity and a favorite of science fiction writers, to a viable technology with potential widespread applications. Initially, MEMS was introduced to the public with a great deal of hype and visions of microrobots running through ones blood vessels, removing plaque and plugging holes. At the present time, the first MEMS devices are entering commercial production. In silicon based MEMS, integrated circuit fabrication techniques are used to reduce the size of mechanical devices to the miniature dimensions of microelectronics. Integration of these mechanical devices with electronic circuits on the same chip offers a wealth of new product opportunities not possible with conventional design and manufacturing approaches.

Simple MEMS devices have begun to appear in commercial applications, particularly in pressure sensors for medical and automotive applications and in automotive accelerometers for airbag sensors. Advanced MEMS devices have applications in the following industries:

- health care
- automotive
- aerospace
- information storage
- consumer electronics
- telecommunications
- scientific instruments
- environmental monitoring
- defense
- heavy equipment
- industrial machinery
- semiconductor manufacturing

More specifically, MEMS technology can be used to fabricate extremely sensitive sensors for a variety of applications including pressure, sound, mass, motion,

acceleration, rotation, flow, chemicals, vibration, and temperature. The technology can also be used to fabricate field-emission tips and probes for use in high-brightness specialized displays, electron-beam sources, information storage applications, and precision temperature sensing. Actuators can be fabricated for use in optical switching, flow control, micropositioning, adaptive optics, and displays. Finally, a variety of passive, three-dimensional, micromechanical structures can be fabricated with applications in telecommunications, electronic components, and sensors.

Various marketing studies have estimated the worldwide market for packaged functional MEMS systems will be approximately $100 billion in the year 2000. It is estimated that the MEMS device within the package is expected to have a market value of approximately $10 billion by the year 2000. Although still a topic of active academic research, in certain applications MEMS technology has reached a level of maturity where it is being commercialized and transferred into products. Products on the market today include accelerometers for airbags sensors, pressure sensors for automotive applications, micromotors for medical drug delivery systems, jetting systems for ink jet, and microvalves for consumer appliances.

PACKAGING OF MEMS DEVICES

The silicon MEMS chip is of little value to anyone unless it is put into a package. As stated above, the value of a packaged system is an order of magnitude higher than the chip. Once the silicon processing of the MEMS chip is complete, the challenges are just beginning. The chip cannot stand alone. It must be integrated with other components to make a functioning device. For example, a mechanical actuator on a chip does no work unless it can be "connected." Conventional connection and interconnection approaches do not play a role in the fabrication of a MEMS device or microsystem. In fact, conventional connection technology does not appear in MEMS devices. Connections and interconnections become integrated into the packaging and become a part of the process of making the MEMS package itself. One cannot define a distinct connection. Multi-disciplinary connections and interconnection approaches must be developed for MEMS devices that include electrical, fluid, thermal, optical, and motion transfer. In nearly all devices, a combination of two or more connection disciplines are integrated, with electrical generally being one of the disciplines. Miniature parts can also be fabricated in non-silicon based technologies. As in the silicon case, the connection is an integral part of the device. The work or function that any MEMS device performs must be delivered to the world outside of the device for mankind to benefit. The challenge is to develop technologies that can permit the connection, interconnections, and packaging of the MEMS chip into a MEMS system.

Customers do not want to purchase a chip; they want a completely packaged device. Suppliers who can 'build" the connections in place are very difficult to find. Finding a source with process capability to build a prototype is nearly impossible, and certainly the ability to design and build microassembly automation equipment to manufacture the microsystem is very limited. Within the United States, there is a lack of an infrastructure of MEMS packaging capability to produce a microsystem. There are limited developed metrics, specifications, experience bases, depositories for knowledge, and infrastructures from which to select microfabrication and microassembly packaging

and connection schemes. Each product that is conceived starts from ground zero in the development of the microfabrication and microassembly packaging and connection concepts.

Companies have not stepped up to integrated microfabrication technologies because of philosophical conflicts with current manufacturing methods, an existing large monetary investment in current assets and infrastructure, and lack of personnel who are skilled in this new approach. This difficulty starts at the very beginning of the product design cycle. The typical engineer at most companies, at best, has little capability and experience in a microfabrication approach to product design. Even if the engineer has the interest and sees the advantages of using microtechnology, he must work with an institution, a supplier, or a consultant who has an experience base to draw upon to create a design. Otherwise, his risk of failure is far too great. Those who develop the understanding for the metrics of microsystems design find that getting their design concepts built to test functionality can be a problem. The silicon-based MEMS technology has been more successful as compared to, for example, piezo materials, because the infrastructure exists to build a proof of concept /device and, to a lesser extent, to build prototypes and for scale-up. However, even with silicon, the established infrastructure does not fully support MEMS fabrication because of differences in the circuit fabrication process and the MEMS process. Additionally, silicon fabrication capabilities are geared to extremely high volume production beyond the requirements for MEMS devices. There is little interest by the silicon fab community in meeting the relatively low volume of MEMS devices.

The microfabrication approach requires the integration and development of various technologies, such as photolithigraphy, electroforming and electroplating, vacuum and chemical vapor deposition, injection molding, and hybrid electronic fabrication processes to "package" miniaturized MEMS devices. The devices must be packaged in such a way as to move from the micro world of the silicon chip, or other substrates which can contain electronic and mechanical functions, to the macro world of the human, for the communication of inputs and outputs. Table1 illustrates the various microfabrication technologies that are used to package MEMS devices. The packaging and "connections" use plastics, metals, and ceramics in combination with each other, and generally with silicon. Microfabrication by subtractive techniques, where material is removed, and by additive techniques, where material is added or grown in place, are used to form microparts. These microparts are assembled together or form connections with each other by a variety of bonding techniques such as diffusion and anodic bonding, as well as by using adhesives. Mechanical fasteners are not used because the surface areas that they require limit the ability to miniaturize. Also, stress concentrations result from features in the part and from the uneven forces when parts are mechanically fastened. Fasteners also limit the size reduction possible and the tolerances that can be held. Microfabrication technologies are generally used in such a manner that one process can build upon another. For example, photolithography creates a pattern, followed by the plating of a metal to form a metal structure of connections or fluid pathways. The part may be put into a molding machine and plastic micromolded around the part to insulate, seal, or protect the device, as well as to provide mechanical and fluid connection to the outside world.

The trend toward microsystem products is significantly hampered by the lack of microfabrication and microassembly engineering capability and infrastructure to design and package MEMS and microsystem-based products. Enabling technologies in the areas of micropositioning, imaging, and in attachment and packaging need to be developed further to support the development of microfabrication and microassembly equipment. This will aid in establishing a healthy industry infrastructure to support deployment of MEMS related technologies for commercial products.

Table 1: Microfabrication Processes

Material	Subtractive Process	Additive Process	Attachment Process
silicon	* wet etching * dry etching * dicing	* PVD * CVD * sol gel	* bonding * adhesives
plastics	* plasma etching * ion beam etching * LASER ablation	* LIGA * PVD * electroforming * micro molding	* welding * adhesives
metal	* wet etching * micro machining * LASER ablation * dicing * EDM	* LIGA * electroforming * PVD * LASER CVD	* adhesives * micro-welding * micro-soldering * LASER welding * sonic welding
ceramics	* LASER ablation * dicing * ion beam etching	* LIGA * sintering * LASER CVD	* plating * adhesives * soldering * bonding

Adapted from MicroParts - Dortmund Germany

FABRICATION OF IN-PIPE MOBILE MICROMACHINES DRIVEN BY PNEUMATIC AND VACUUM PRESSURE

Shigeo KATO, Mizuyuki SHIRAKAWA, Manabu OHNO and Seiichi FUKUMOTO

Nippon Institute of Technology
Miyashiro, Saitama 345-8501, JAPAN
E-mail: kato@nit.ac.jp

Abstract

This paper presents two in-pipe mobile micromachines which are driven by pneumatic and vacuum pressure. The one earthworm type micromachine is made by three flexible metal bellows which are 6.8 mm in diameter and total length of 48 mm. The another inchworm type micromachine is structured by only two parallel arrayed rubber bellows which are 5 mm in outer diameter and 20 mm long. The pneumatic pressure is used to stretch and the vacuum pressure is used to shrink the bellows. It is confirmed that the former micromachine is able to move with the maximum speed of 18.2 mm/s, and the latter micromachine can pass freely through the junction with the angle of 120 degree.

***Keywords*:** In-pipe, Mobile, Micromachine, Inchworm, Earthworm

1. Introduction

New micromachines to inspect or to repair thin pipes in the the human body or pipelines have been developed. Takahashi et al. have presented a flexible inching micromachine which is 20 mm in diameter and able to inch in pipes by imitating the creeping motion of an earthworm [1]. Kato et al. also have presented an earthworm type micromachine which is 16 mm in diameter and moves in a speed of 77 mm/s [2]. However, these micromachines are suitable for the pipes of diameter more than 20 mm but not suitable for the thin pipes less than 12.7 mm diameter.

Yoshida et al. a new micromachine which is made of a rubber tube and a spring of 3 mm in diameter and driven by water pressure [3]. However, moving speeds of this micromachine is not sufficient for the micromachines to inspect or to repair thin pipes in the the human body or pipelines, because the speed of the micromachine is 7 mm/s. Moreover, the blood vessel has many junctions. The former micromachines are not able to pass freely the junctions.

We fabricated new small size micromachines which are able to move in the pipes of 12.7 mm in diameter with the medium speed. The one micromachine is earthworm type and the another micromachine is inchworm type. These micromachines are made of metal and rubber bellows, respectively. The stroke of the micromachines are enlarged, because the pneumatic pressure is used to stretch and the vacuum pressure is used to shrink the bellows of the micromachines. Consequently, the earthworm type micromachine is able to move with the speed of 18 mm/s in the pipe of 9 mm in diameter and the inchworm type micromachine is able to move with the speed of 32 mm/s in the pipe of 11 mm in diameter and pass freely the junction of 120 degree.

2. Earthworm type micromachine

2.1 Structure of the fabricated micromachine

The section of the fabricated micromachine is shown in Fig. 1. The micromachine is able to move in pipes by imitating the motion of an earthworm. The micromachine is structured by three flexible Ni metal bellows. A bellows-cell is 6.8 mm in outer diameter and 15 mm (18 mm only front one) long. The total length of the micromachine is 48 mm. Three plastic air-tubes which feed

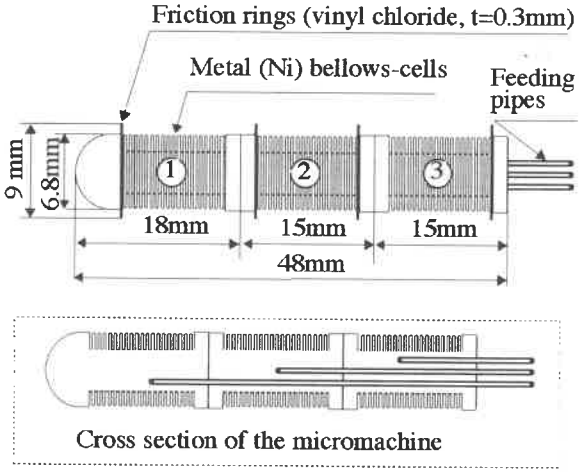

Fig. 1 Structure of the fabricated earthworm type micromachine

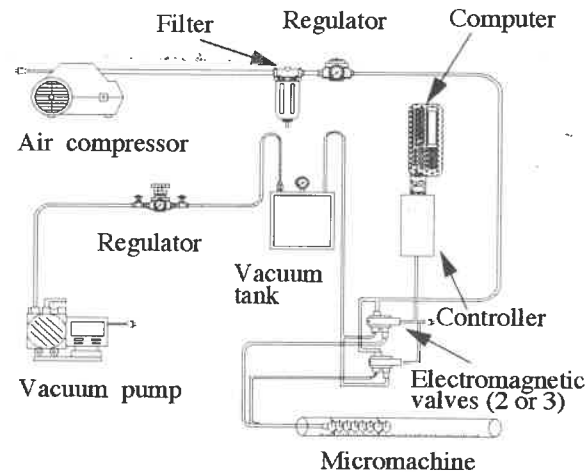

Fig. 2 Experimental apparatus for measuring speed of the micromachines

pneumatic pressure to the micromachine are 0.5 mm in inner diameter, 1 mm in outer diameter and 500 mm long. Four friction rings which are 9 mm in outer diameter, 3.5 mm in inner diameter and 0.3 thick are fixed at the ends of the three bellows. These rings make friction force between the pipe and the micromachine. The rings make cones, because the inner diameter of the rings is a little smaller than the diameter of the bellows. A ring makes the force of 0.03 N for the forward direction and 0.12 N for the backward direction.

An experimental apparatus for measuring the speed of the micromachine is shown in Fig. 2. In the figure two electromagnetic valves are shown, but in the earthworm type micromachine, a computer controls three electromagnetic valves through a valve controller. Three feeding air-tubes are connected from the electromagnetic valves to three bellows-cells and independently feed the pneumatic and the vacuum pressure to each bellows-cell.

The time-chart of the pneumatic pressure for the micromachine is shown in Fig. 3. First, the all bellows-cells are shrunk by the vacuum pressure. Then the pneumatic pressure pulses are sequentially supplied to the cell-1, the cell-2, and the cell-3. A tractile wave generated by the stretching and shrinking motion goes to the backward direction in the flexible bellows. Consequently, the in-pipe mobile micromachine is able to move to the forward direction.

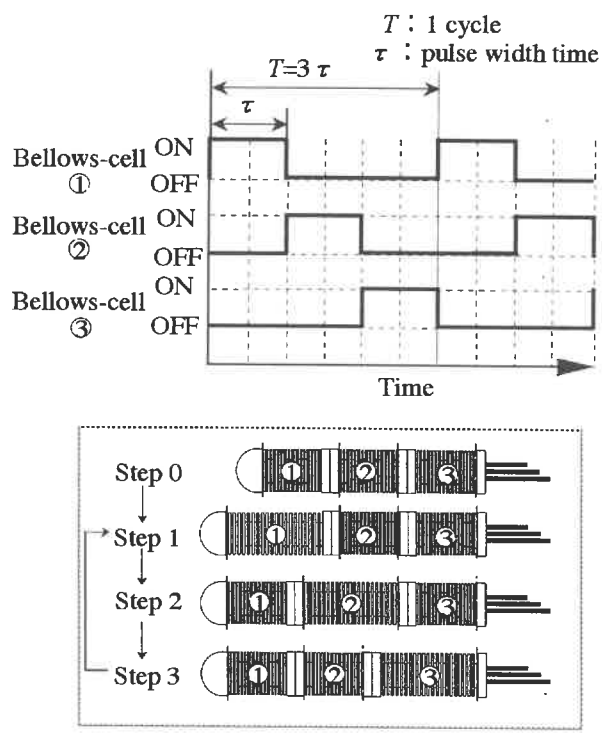

Fig. 3 Time chart of pneumatic pressure for the earthworm type micromachine

2.2 Moving characteristics of the fabricated micromachine

The moving speed is measured. The vacuum pressure is -0.095 MPa and the pneumatic pressure is +0.08 MPa. The pulse width time is changed from 0.02 seconds to 1 second. The relationship between moving speed of the micromachine in an acrylic pipe of 9 mm in diameter and the pulse width time is shown in Fig. 4. The maximum speed of 18.2 mm/s was obtained at the pulse width time of 0.07 seconds.

3. Inchworm type micromachine with a steering mechanism

3.1 Structure of the micromachine

The fabricated new in-pipe mobile micromachine with a very simple steering mechanism is shown in Fig. 5. The micromachine is structured by only two parallel arrayed rubber bellows which are 5 mm in outer diameter, 2 mm in inner diameter and 20 mm long. The two bellows are fixed at double ends by nylon-strings. The bellows are connected with a thin tube which is 1 mm in inner diameter, 500 mm long and feeds pneumatic and vacuum pressure to the bellows. Four friction rings which are 9 mm in diameter, 1.5 mm in inner diameter made of vinyl chloride are fixed at the ends of the two bellows. The rings make cones because the inner diameter of the rings is a little smaller than the diameter of the bellows. The rings make friction force of 0.14 N for forward direction and 0.35 N for the backward direction. The backward force is greater than than the forward force. Consequently the micromachine can move in the pipes.

3.2 Straight movement of the fabricated micromachine

First, the vacuum pressure is supplied to the two bellows, the bellows are shrunk. Then, the pneumatic and vacuum pressure are alternately supplied in the pulse width time of τ seconds. The two bellows reciprocally moves in parallel. The chart of the pressure and the movement is shown in Fig. 6. The moving speed is measured. The vacuum pressure is -0.08 MPa and the pneumatic pressure is +0.1 MPa. The pulse width time is changed from 0.03 seconds to 0.2 seconds. The maximum speed of 39 mm/s was obtained at the pulse width time

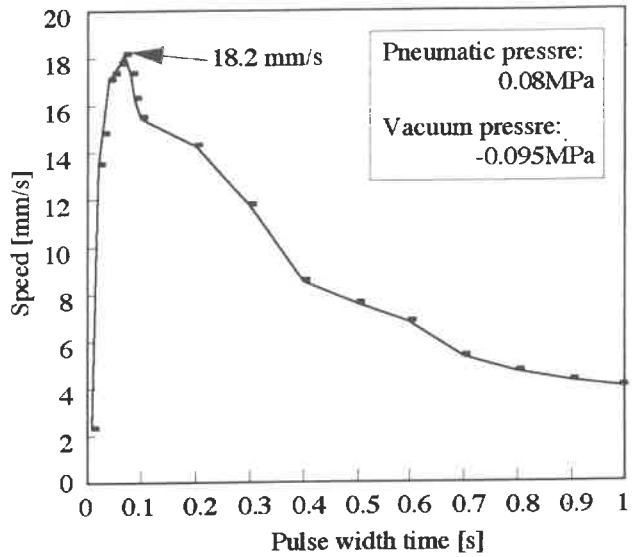

Fig. 4 Relationship between speed of the micromachine and the pulse width time

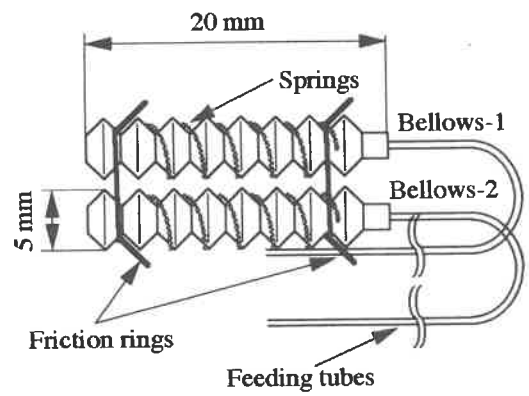

Fig. 5 A new in-pipe mobile micromachine with a very simple steering mechanism

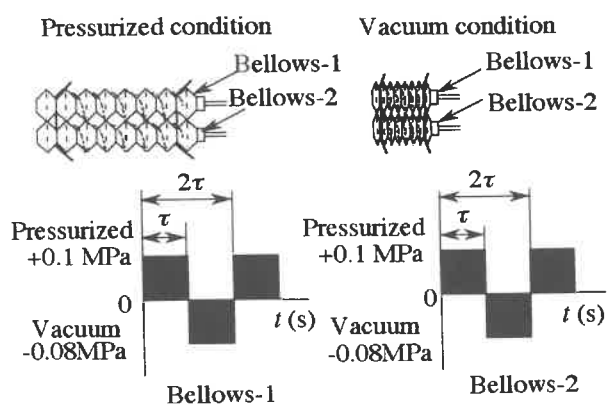

Fig. 6 The chart of the pressure and the movement of the bellows (at straight pipe)

of 0.08 seconds.

3.3 Steering movement of the fabricated micromachine

In order to steer, the micromachine must bend its head. Therefore, the pneumatic and vacuum pressure are supplied shown as Fig. 7. That is, bellows-2 is shrinking in all the time, because the pneumatic pressure is not supplied to the bellows-2. The other hand, the bellows-1 reciprocates by the alternate supply of the pneumatic and vacuum pressure. The double ends of the bellows-1 and bellows-2 are fixed. Consequently, the micromachine move to the forward bending its head and can pass the junction to the desired direction. The speed is good to be slow at the junction. When the micromachine moves at the slow speed of 29 mm/s, the micromachine is confirmed to pass easily the junction with the angle of 120 degrees to the desired direction. This movement is shown in Fig. 8.

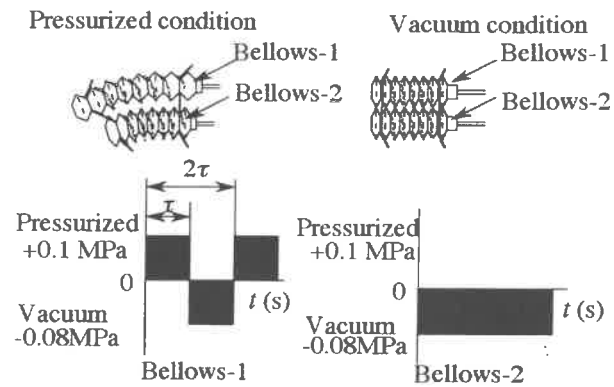

Fig. 7 The chart of the pressure and the movement of the bellows (at the junction)

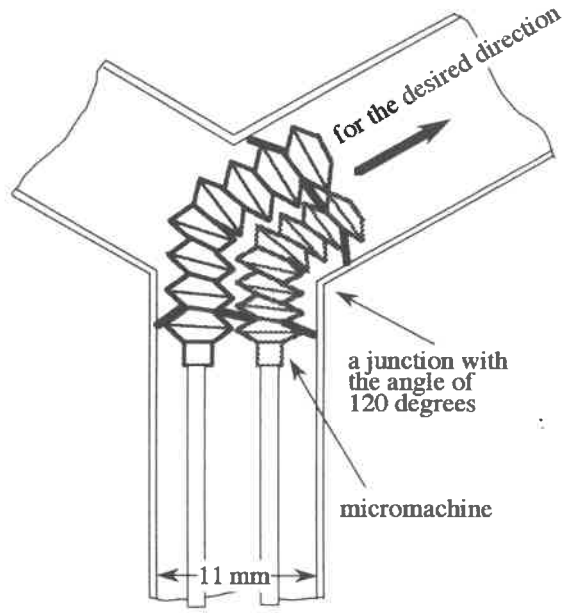

Fig. 8 The movement of the micromachine at the junction with the angle of 120 degrees

4. Conclusions

A fabrication of prototypes of new micromachines to inspect or to repair thin pipes in the the human body or pipelines was performed. The followings are the conclusions of the fabrication.

1) We fabricated a new earthworm type micromachine which is constructed by three flexible Ni metal bellows 6.8 mm in outer diameter and 48 mm long. The micromachine is able to move in an acrylic pipe of 9 mm in diameter. The maximum speed of 18.2 mm/s was obtained at the pulse width time of 0.07 seconds, the vacuum pressure is -0.095 MPa and the pneumatic pressure is 0.08 MPa.

2) We fabricated a new in-pipe mobile micromachine with a very simple steering mechanism. The micromachine is structured by only two parallel arrayed rubber bellows which are 5 mm in outer diameter and 20 mm long. The two bellows are fixed at double ends by nylon-strings. When the vacuum pressure is -0.08 MPa and the pneumatic pressure is 0.1 MPa, the maximum speed of 39 mm/s was obtained at the pulse width time of 0.08 seconds. The micromachine was confirmed to pass easily the junction with the angle of 120 degrees to the desired direction.

References:

[1] M. Takahashi, I. Hayashi, N. Iwatsuki, K. Suzumori and N. Ohki, *Journal of the Japan Society for Precision Engineering*, Vol. 61 No. 1 (1995), pp. 90-94.

[2] S. Kato and T. Hirayama, *Proceedings of 4th Japan-France Congress & 2nd Asia-Europe Congress on Mechatronics*, Vol. 2 (1998), pp. 429-432.

[3] K. Yoshida, K. Takahashi and S. Yokota, *Proceedings of IMPT-100, The Japan Society of Mechanical Engineers* (1997), pp. 667-670.

DNA extraction from cell nuclei and DNA fishing using a 3D nano-probe

Masayuki NAKAO, Kiyoshi MATSUMOTO, Takeshi OOI, Hiroshi HIRAYAMA,
Masato OTSUBO, Satoshi SHIRAKATA and Yotaro HATAMURA
Dep. of Eng. Synthesis, Faculty of Eng., The Univ. of Tokyo, 7-3-1 Hongo, Bunkyo-ku, Tokyo, Japan

1 Introduction

Now, rapid progress has been made in the research area of DNA, and new and efficient technique for DNA analysis is highly demanded.

In conventional methods of sequencing and recombination of DNA, many DNA fragments are cut from long DNA fibers on a nucleus with restriction nuclease; each fragments are sequenced by electrophoresis[1]. But with these methods, it is difficult to identify where a fragment was located in the long DNA fibers. We propose a new method to extract DNA fibers from a specific nucleus without cutting and to pick up a specific DNA fragment (we call it "DNA fishing"). This method simplifies the reconstruction process because the order of DNA fragments was known in fishing.

Fig. 1 illustrates the concept of our method. First, we extract DNA fibers from nuclei using a SAW(Surface Acoustic Wave) device. Next, we attempted DNA fishing with a nano probe made by a new EBD(Electron Beam Deposition) process.

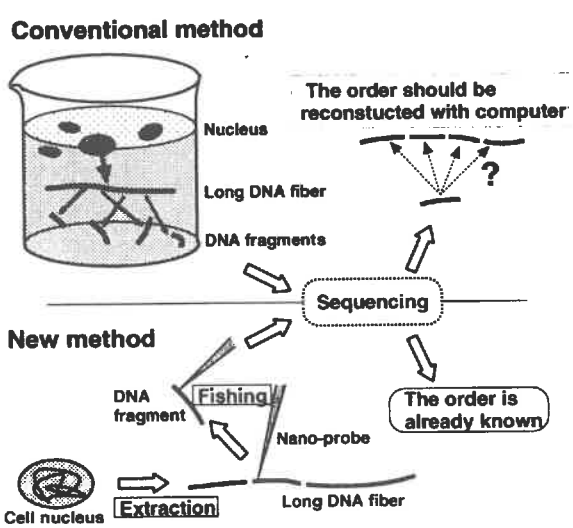

Fig. 1: Concept of the new method of sequencing DNA compared with conventional method.

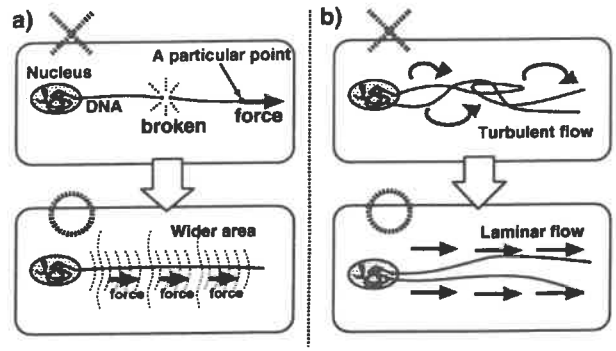

Fig. 2: Requirement for DNA extraction

2 DNA extraction

2.1 SAW device

The following two points are required for extraction and expansion of DNA fibers. 1) The force should affect not only at a particular point but also in wider area of the fiber, so as not to break the DNA fiber(Fig. 2a). It is suitable to apply a elastic-wave-like vibration to a long fiber. 2) The flow should be laminar so as not to entangle the fibers(Fig. 2b). The laminar flow can be generated by the method of dynamic molecular combing[2], but this method cannot identify the original nucleus where a DNA fiber was extracted. We employ SAW for DNA extraction.

SAW is high-frequency(10MHz–10GHz) vibration that travels only on the surface of a substrate. Vibration is generated by high-frequency electrical fields on a piezoelectric crystal.

We made an SAW device which has 16 pairs of $50\mu m$ wide electrodes on a $LiNbO_3$substrate. The electrodes were fabricated by vapor deposition of Cr and Cu, and lift-off process (Fig. 3).

Fig. 4 demonstrates that the SAW device can generate a laminar flow.

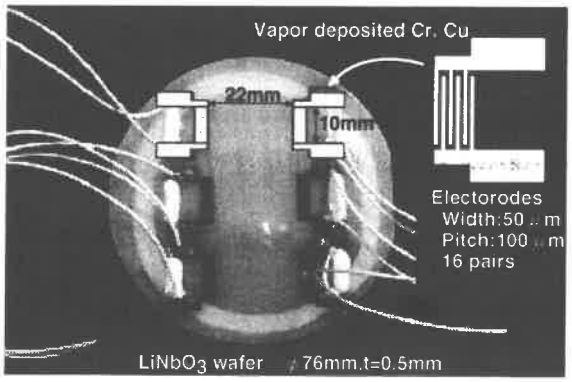

Fig. 3: SAW device; 6 electrodes made by vapor deposition of Cr, Cu on $LiNbO_3$

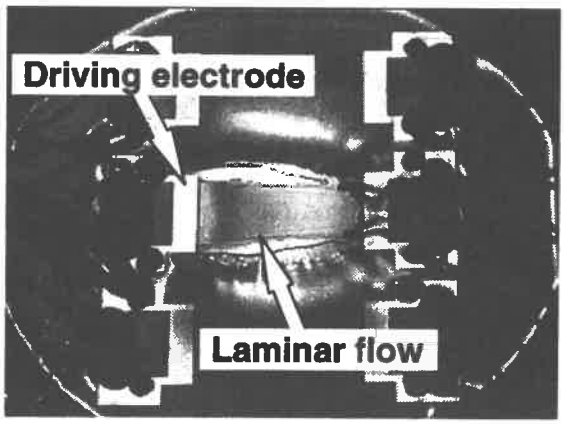

Fig. 4: Laminar flow generated by SAW device

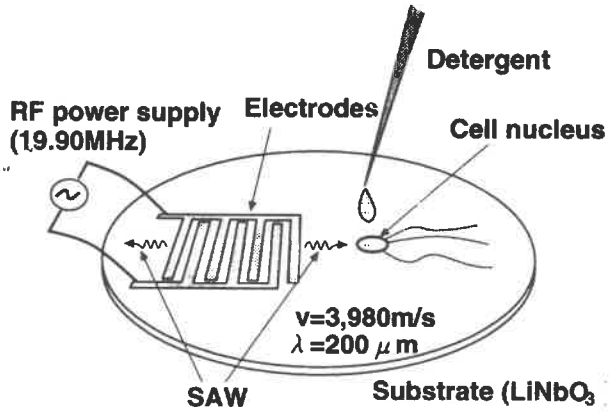

Fig. 5: Schematic of DNA extraction using SAW device

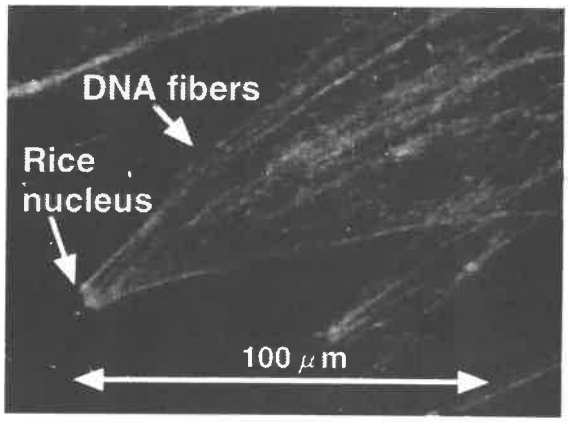

Fig. 6: Fluorescent microscopic view of the DNA fibers extracted and expanded from rice nuclei by SAW device. The fibers were not entangled.

2.2 Experiment of DNA extraction

We made the following experiment to extract DNA fibers from nuclei (Fig. 5) . The phosphate buffer including rice nuclei was dropped onto the substrate and dried to be fixed. Detergent(0.5% Sodium dodecyl sulfate) was pipetted to dissolve the nucleic membrane. High frequency electrical field (20MHz, 1W) was impressed to the electrodes to generate SAW, and the solution flew along with the wave. In this way, DNA fibers were extracted and expanded about 0.5mm long (Fig. 6). The fibers spread fan-wise without any entanglement because the applied flow was laminar.

These DNA fibers should be about 10mm, so they are not perfectly expanded because they may still be wound onto histones. An enzyme to dissolve histones(Proteinase K) will be effective.

3 DNA fishing

3.1 Nano-probe for DNA fishing

A nano-probe for DNA fishing requires two essential functions. First, its tip should be nanometer-sized because a DNA fiber is 2nm in diameter and a nucleotide is 0.3nm long. Next, it should cut and pick up a DNA fiber. Optical tweezers is usually used for manipulation of a DNA fiber[3], but its spatial resolution is restricted by the diameter of optical beads(typical size is about 1μm). We developed a new process, "3D-EBD", to form the tip

of the nano-probe in a nanometer resolution, and attempted to coat the tip of the nano-probe with a restriction enzyme and a chemical adhesive to cut and pick up a DNA fiber.

3.2 3D-EBD

In EBD process, high energy electrons induce to dissociate molecules and the dissociation is adsorbed on a surface. The dissociation mechanism is complex and is not well understood because of the huge number of excitation channels available even for small molecules. However, EBD has been demonstrated as a new technique of lithography for many applications, a scanning tunneling microscope tip[4] and a field emission tip[5].

In conventional methods, the dissociation of molecules grows only in the reverse direction of the beam. But the new method can make the 3D feature as the dissociation grows on a perpendicular plane to the beam(Fig. 7). A tens nanometers thick wire of carbon compound is formed just along the beam path. When the beam is controlled slowly from the edge of a base toward a space, a wire grows along the beam path in the space as designed(Fig. 8). Additionally, rotating the base, we can easily fabricate various wires with 3D structure(Fig. 8(c,d,e)). The 3D-EBD example were fabricated in vacuum of about 10^{-6} Pa using a FE-SEM of HITACHI S-4000 at 15kV.

3.3 Experiment of DNA fishing

We made a nano-probe of 20nm in diameter, 1μ long on the tip of a glass needle of 1μ in diameter and covered with aluminium(Fig. 9 a).

Then we coated the nano-probe with an amorphous teflon film, and strip it on the tip of the nano-probe with electron beam in an SEM. Avidin was fixed on the bald tip to fish a biotin labeled DNA fiber. In this case, avidin-biotin interaction was utilized because it is a very strong biological binding.

We made an experiment of DNA fishing; pipeted bacteriophage T4-DNA (54μm long) solution (0.2ng$/\mu\ell$) on a slide glass; pipeted YOYO-1 lodide; set the probe as to put its tip inside the solution; covered with a cover glass,; and observed with an inverted fluorescent microscope.

As a result, the tip of the probe hooked up a single DNA fiber flowing in the solution (Fig. 10). This figure shows that the probe can fish a single DNA fiber. We also plan to cut a long DNA fiber at

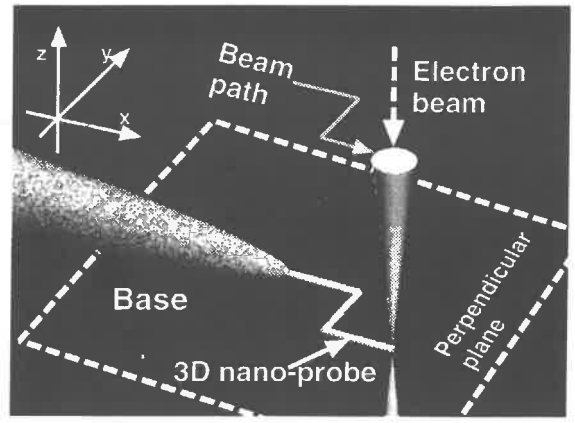

Fig. 7: Schematic of 3D-EBD method

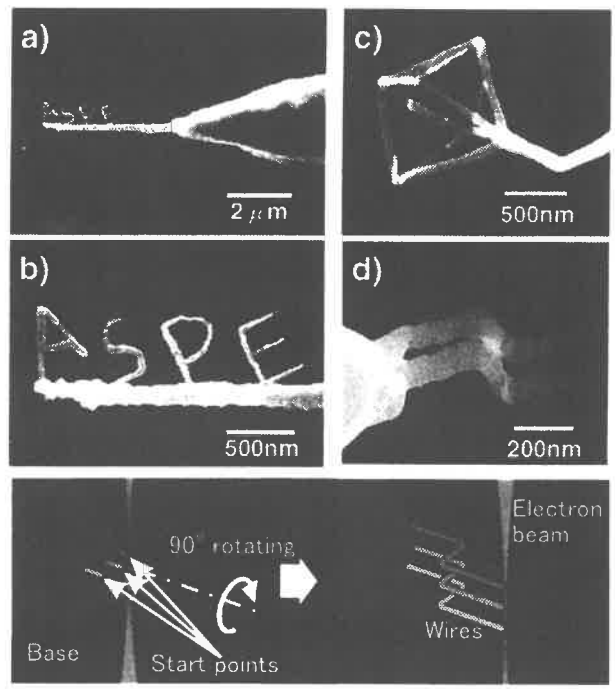

Fig. 8: Examples of 3D-EBD: a,b)Nano illuminations lettered *"ASPE"*. Dimension of one character is about 400nm, and the line width is about 40nm. c)A regular octahedron frame, each side is 1μm in length, consisting of 100nm thick wire. d)Three parallel wires. e)The process of fabricating parallel wires; making start points, 90° rotating the base, making the beam scan from the start points.

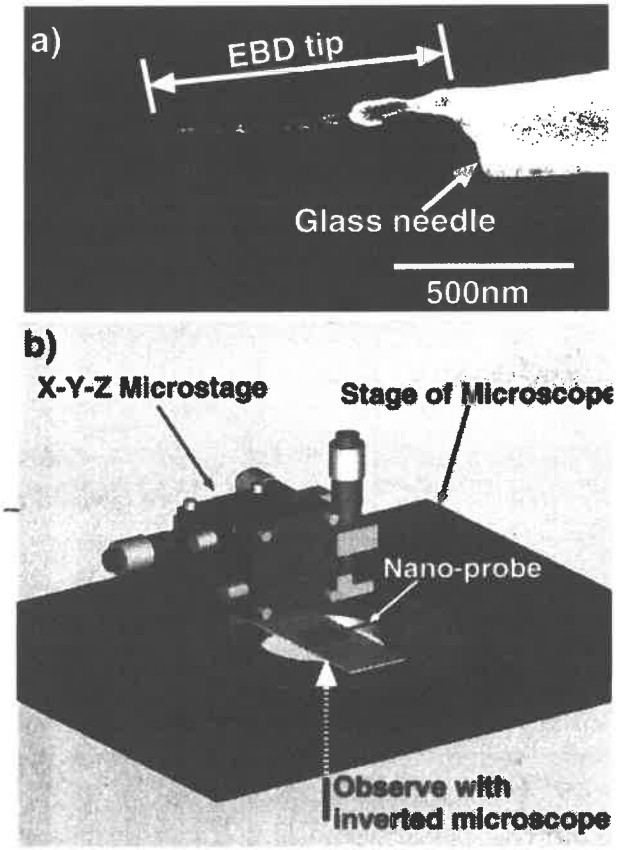

Fig. 9: a) SEM view of the tip of the nano-probe made by 3D-EBD method on the glass needle with hydrophobic coating . b) Schematic of DNA-fishing Experiment; we fixed the nano-probe on the X-Y-Z microstage moved its tip into the solution of the DNA fibers, pipetted on a slide-glass fixed on the stage of microscope, and observed from below with a inverted fluorescent microscope.

desired point using a probe coated with restriction enzyme.

4 Conclusion

To easily reconstruct the order of DNA fragments, a DNA extraction and DNA fishing is proposed.

DNA extraction was achieved on a $LiNbO_3$ substrate with a SAW(Surface Acoustic Wave) device, and DNA fibers of rice were expanded up to 0.5mm length.

Next, DNA fishing was achieved by a 3D nano-probe. We developed a 3D-EBD(Electron Beam Deposition) process. We applied chemical modification to the tip of a nano-probe and fished a specific DNA fiber by the probe.

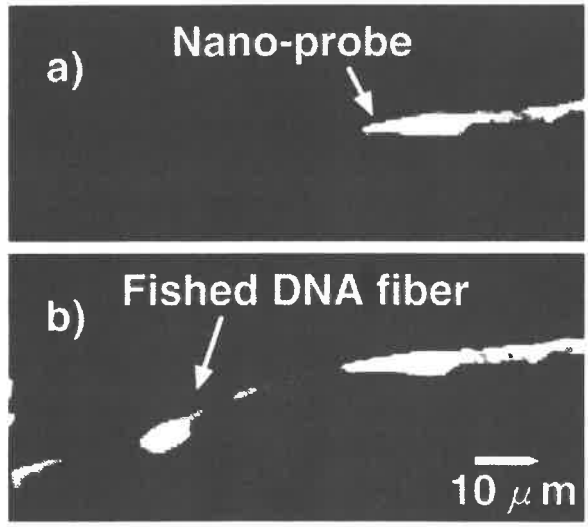

Fig. 10: Fluorescent microscopic view of the DNA fishing; a)Nano-probe before experiment b)Fished a T4 phage DNA fiber of 50μm long by the nano-probe

References

[1] Burce Alberts et. al., MOLECULAR BIOLOGY OF THE CELL, Newton Press,pp292-298, 1995

[2] Xavier Michalet et. al., Dynamic Molecular Combing: Stretching the whole Human Genome for High-Resolution Studies, Science Vol. 277, pp1518-1523, 1997

[3] Yasuharu Arai et. al., Tying a molecular knot with optical tweezers, Nature Vol. 399, pp446-451, 1999

[4] Y. Akama et. al., New scanning tunneling microscopy tip for measuring surface topography, J. Vac. Sci. Technol. A8(1), 1990, pp429-433.

[5] Hans W. P. Koops et. al., Characterization and Application of Materials Grown by Electron-Beam-Induced Depositing, Jpn. J. Appl. Phys. Vol. 33, pp7099-7107, 1994

Manufacturing Feasibility of Continuous Relief, Grayscale Diffractive Optical Elements

Helen E. Fawcett, Donald K. Mitchell, Steven C. Fawcett, and Bill Thorburn
MicroE, 8 Erie Drive, Natick, MA 01760

Abstract

We are investigating the possibility of replacing binary diffractive optical elements and molded aspheric lenses with a continuous relief optical element known as a kinoform. With continuous relief optical elements, diffraction efficiencies of over 90% have been reported [1,2]. Using a grayscale master and altered properties of a normally analog resist, continuous relief optical elements can be produced with repeatable results. Typical binary structures require multiple masters to be generated. These masters approximate a continuous slope through a binary staircase profile. Alignment of these masters from layer to layer is critical and time consuming. With a gray scale master, multiple mask alignments are eliminated. As a first approximation to determine the manufacturing feasibility of such continuous relief optical elements a calibration master was procured from Canyon Materials. The following atomic force microscope (AFM) scan shows one set of blazed gratings produced from the master.

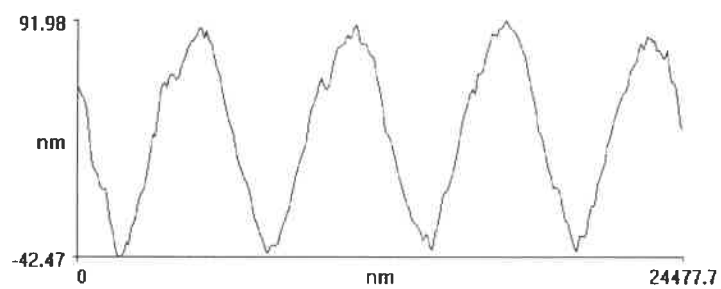

Figure 1. AFM scan of 8 μm blazed grating. Burleigh Instruments AFM was used.

These initial results led to an investigation into producing continuous relief optical elements from grayscale masters. This paper will present the fabrication issues associated with the kinoform elements and the resulting optical characteristics. Specific areas of interest include materials, diffraction efficiencies, wavefront quality, and manufacturing yields.

Introduction

We are investigating the manufacturing feasibility of using a gray-scale master in place of multiple binary masters to produce structures with a continuous profile. The grayscale masters for these experiments use a High Energy Beam Sensitive (HEBS) glass. HEBS glass turns dark when exposed to an e-beam with increasing optical density relative to the total electron exposure. The HEBS glass is a low expansion zinc-borosilicate glass that contains alkali to facilitate ion-exchange reactions that achieves the sensitivity of the glass toward high energy beams.[1] With the ability to control the darkening of the HEBS glass, Diffractive Optical Elements can be manufactured in a single photoprocessing procedure. Typical binary structures are manufactured using multiple masters and a mask aligner. The first layer is exposed and the substrate is processed to reproduce that level into the substrate. A second photoprocessing step is required where the next level mask is aligned to the first and the process repeats. The process of using binary masks results in a stepped approximation of a continuous profile. As the number of

[1] Chuck Wu. Canyon Materials, Inc. Products Overview HEBS-Glass Calibration Plates.

binary levels increases, this stepped profile will more closely approximate a continuous slope. The efficiency of such devices is directly related to the number of phase levels and also to the inherent manufacturing inaccuracies. This limited efficiency can be improved by using the grayscale technology [3]. The following schematic (Figure 2) exaggerates the difference in this processing.

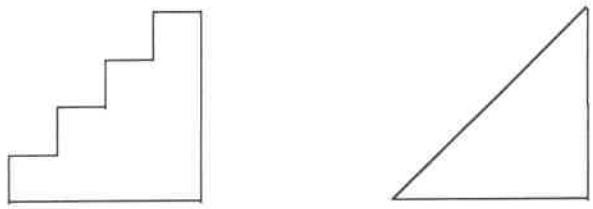

Figure 2. The staircase profile on the left is a binary approximation of the continuous profile on the right. The profile on the right is achievable using grayscale mastering. With binary masters, the steps on the staircase profile are reduced as the number of levels is increased; however the increased cost and the manufacturing inaccuracies can outweigh the efficiency improvements. For this reason, 4 to 8 level structures are typically used to approximate a blazed grating.

Experiment

Using the calibration mask from Canyon Materials, initial prints using a grayscale master were completed. This master contained grayscale images for producing blazed gratings with periods ranging from 8 to 400 μm. Figure 3 is a profilometer scan of the larger period structures (400 μm). These results showed significant potential with sharp edges and angled slopes.

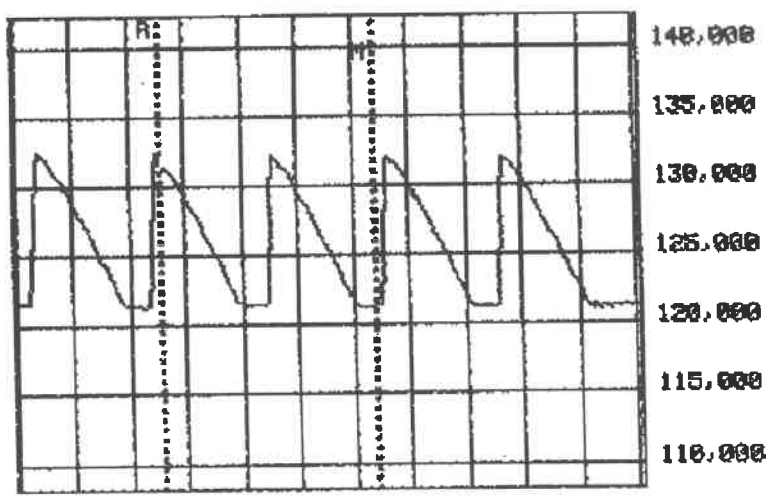

Figure 3. Dektak scan of a 400 μm blazed grating. The stylus used in this scan has a 12.5 μm radius and the vertical scale is in Angstroms.

Other areas on this sample with shorter periods were scanned using a Digital Instruments Atomic Force Microscope (AFM) to evaluate the surface morphology. Figure 4 shows the AFM scan of a 10 μm blazed grating.

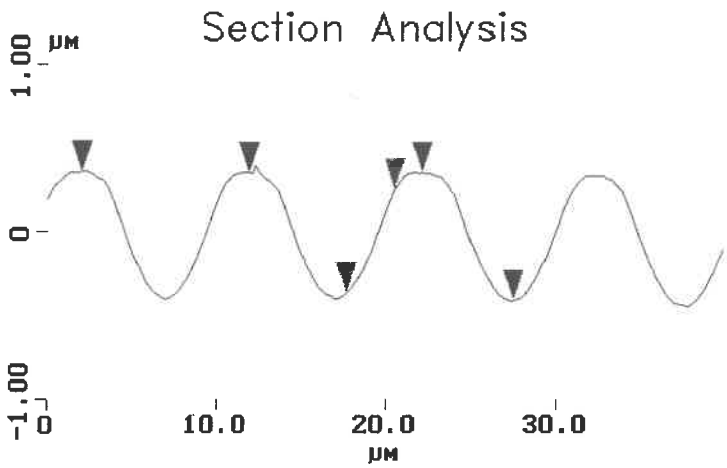

Figure 4. AFM scan of a 10 µm blazed grating.

These features appeared sinusoidal instead of the sharply angled blazed profile that was intended. This resulted from an inadequate match of the relative optical densities of the grating image in the master to our processing techniques. In this type of lithography, the modulation transfer function (MTF) of the contact printing process is a critical parameter. MTF is a measure of the reduction in contrast from the object to the image [4]. To correct for the MTF of our exposure tool, the peak optical density of the master image was reduced toward the bottom of the feature in order to obtain a sharp sidewall. The exposure dosage for the grayscale master was determined from the sharpest features in the larger blazed gratings, shown previously in Figure 3.

To continue with the experimental work, a new master was developed with 10 µm blazed gratings that are closer to the feature size of interest. Ten proximity corrections were included in this master to accurately determine the proper correction to obtain sharp, triangular features. The following AFM scans (Figure 5 and 6) display some early results from this master.

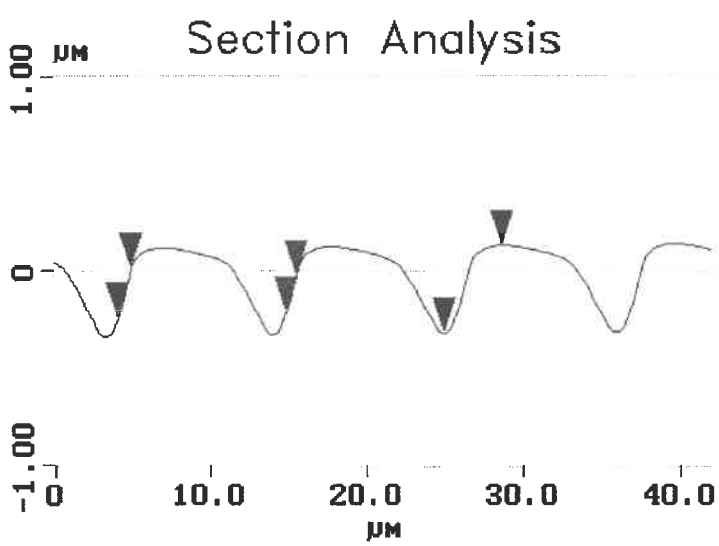

Figure 5. AFM scan of mask (10 µm blazed grating) printed from proximity correction master.

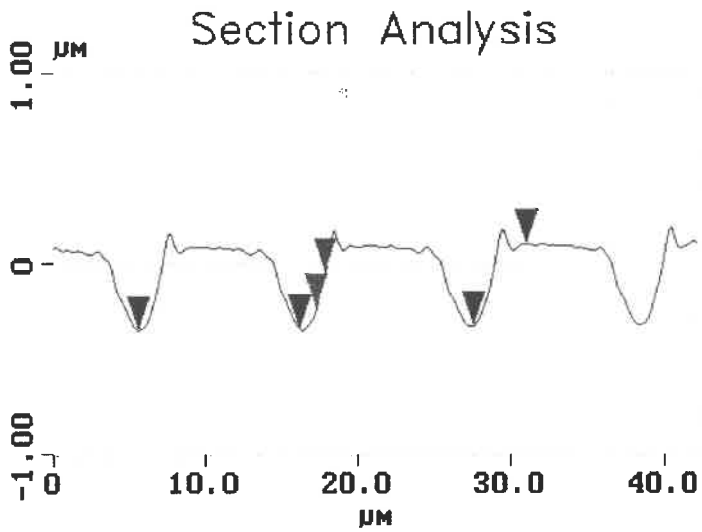

Figure 6. AFM scan of the resulting 10 µm blazed grating produced from mask.

These results show some promise toward achieving the desired triangular shape in the deeper areas of the grating. The degradation of the taller portions of the features resulted from photoprocessing issues not related to the master image. Adjusting these parameters should correct for the truncated shape of the blazed grating.

Further Work

Serious effort into correcting the blazed grating images in the master and projecting this corrected shape into different materials is required. Once the proper shape is achieved on the test structures, testing of the efficiency and wavefront quality will be performed. This information will allow the proper proximity correction for our exposure tool to be finalized and then optical devices can be created using the defined grayscale image levels. This investigation will continue through the process development and manufacturing issues for producing optical devices for solid state laser devices.

Acknowledgements

We would like to thank the following people for their help in this research: Anlee Krupp, Chuck Wu, and Eileen Sayers.

References:

[1] Peter Ehbets, Hans Peter Herzig, Philippe Nussbaum, Peter Blattner, and René Dändliker, "Interferometric fabrication of modulated submicrometer gratings in photoresist." Applied Optics, Vol. 34, No. 14, May 10, 1995. p. 2540-2547.

[2] Walter Däschner, Robert Stein, Pin Long, Chuck Wu, and Sing H. Lee, "One-step lithography for mass production of multilevel diffractive optical elements using High Energy Beam Sensitive (HEBS) gray-level mask", SPIE Vol. 2689, p. 153-155, 1996.

[3] Walter Däschner, Michael Larsson, and S. H. Lee, "Fabrication of monolithic diffractive optical elements by the use of e-beam direct write on an analog resist and a single chemically assisted ion-beam-etching step." Applied Optics, Vol. 34, No. 14, May 10, 1995. p. 2534 – 2539.

[4] Eugene Hecht and Alfred Zajac, Optics, Addison-Wesley Publishing Company. Massachusetts, 1974.

ERRORS IN PROGRESSIVE DIES FOR ELECTRONIC COMPONENTS

Sepehr Kiani*, R. Ryan Vallance†, and Alexander H. Slocum*†
*Teradyne Connection Systems, Nashua, NH
†University of Kentucky, Lexington, KY
*†Massachusetts Institute of Technology, Cambridge, MA

Introduction

Electronic systems contain a variety of small, metal components used for conducting electrical signals between subsystems. Examples of such parts include stamped signal contacts such as shown in Fig. 1 and package lead-frames. These components are manufactured in progressive diesets that stamp the components from a strip of stock material. Stamping operations and dieset elements contribute to the dimensional variation in the finished product and thus affect the quality, performance, and cost of electronic systems.

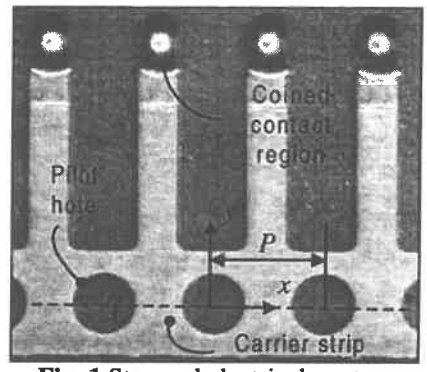

Fig. 1 Stamped electrical contact

Dimensional variation is attributable to the compound effect of manufacturing errors in dieset assemblies (Fig. 2) and components, design clearances, operational variability, tool wear, and variation in product material. Complex relationships between these factors make the design of progressive dies difficult to systemize. Prior research on designing progressive dies focused on CAD systems[1,2,3], expert systems[4,5], and simulation of the forming process[6,7]. Few investigations into precision aspects have been published[8,9]. Precision design methods[10] such as error modeling[11] and error budgeting[12] that are common for precision machines do not exist for progressive dies, so die design remains an area governed by rules of thumb and diverse opinions[13].

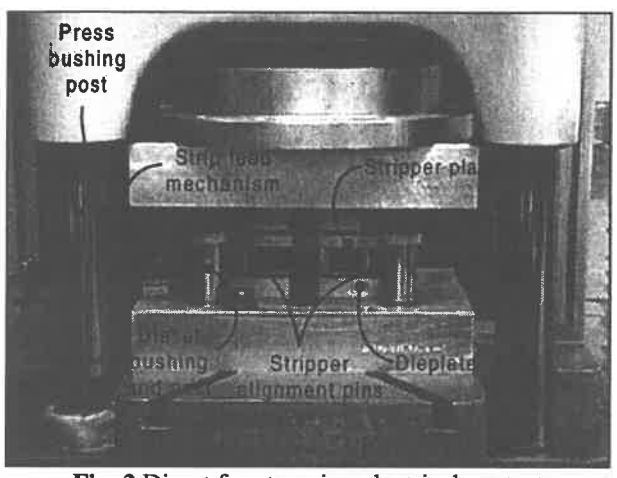

Fig. 2 Dieset for stamping electrical contact

The pilot holes within a carrier strip or lead-frame are crucial features in stamped products. The blanking operation that creates the pilot holes is generally the first operation within the dieset. Pilot pins at subsequent stations along the progression use the pilot holes to locate the metal strip. Furthermore, pilot holes are often used for locating the product strip in subsequent operations like assembly. Pilot holes therefore provide the fundamental datum for a stamped strip and hence constitute a natural place to begin developing precision design methods. In this paper, variation in pilot holes is characterized by pitch (distance between hole centers) and y-errors (distance normal to the pitch). This paper presents a measurement technique, an error model, and a simulation process to characterize and conservatively estimate these errors.

Measuring pilot hole errors

This section presents a technique for measuring errors in the position of pilot holes. The process involves four steps: measurement of the pilot hole locations with an optical gage, fitting the measured points to a circle, calculation of the errors from the best-fit circle, and characterizing the errors statistically.

This technique was used to measure samples from the stamped strip shown in Fig. 1. The x and y coordinates for the center of each hole were measured on a SmartScope™ FOV from Optical Gaging Products, Inc. of Rochester, NY. Stamped strips often exhibit camber, which is a permanent

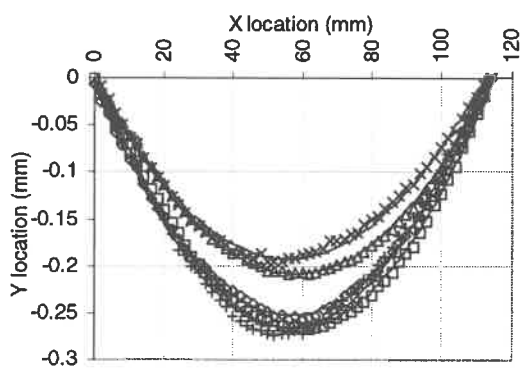

Fig. 3 Measurement of hole centers and fitted circles

strain induced by an imbalance between the residual stresses on opposite edges of the carrier strip. The fixture for the strips of contacts permitted camber but prevented additional strain. Therefore, the strips exhibit a constant radius of curvature (near 6 m).

Fig. 3 shows experimental data for the location of the pilot holes' centers along with circular curve-fits. The errors are measured with respect to the circle as shown in Fig. 4. The curve-fit effectively removes the camber to provide true pitch and y-error information. The y-error is the distance between the point and the curve, measured normal to the circle. The pitch is the arc length along the circle between the normals of two consecutive points. The mean and standard deviation for the pitch were 2.001 mm and 3.4 μm, respectively. The mean and standard deviation for the y-errors were 0.01 μm and 4.8 μm, respectively.

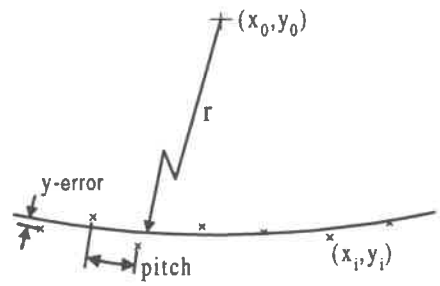

Fig. 4 Errors measured from circular fit

Error model for random variation

An error model that combines the principal error sources to estimate the variance in the pitch and y-errors of the pilot holes is presented. The model is derived by considering two independent operations: locating the carrier strip with several pilot pins and punching the pilot hole. Eq (1) and Eq (2), which express the expected values and variances of a linear combination of uniformly or normally distributed random variables[14], are applied in the model.

$$E(Y) = a_1 E(X_1) + a_2 E(X_2) + \ldots + a_m E(X_i) \tag{1}$$

$$\sigma_Y{}^2 = a_1{}^2\sigma_{X_1}{}^2 + a_2{}^2\sigma_{X_2}{}^2 + \ldots + a_m{}^2\sigma_{X_m}{}^2 + \sum_{i<j}\sum_{j=2}^{m} a_i a_j \sigma_{X_i}\sigma_{X_j} Cor(X_i, X_j) \tag{2}$$

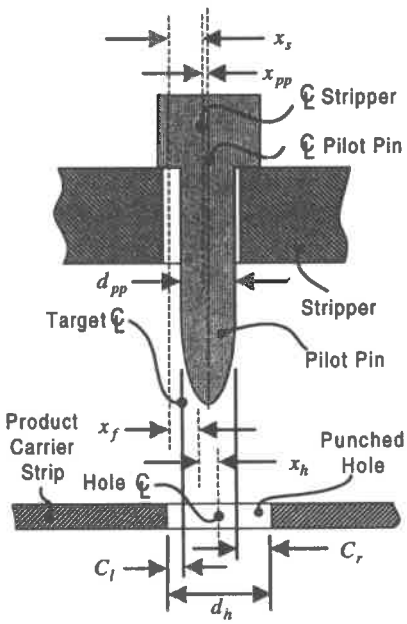

Fig. 5 Errors between a pin and hole

Fig. 5 shows a pilot pin randomly located inside a hole in the randomly located stripper. The position of the strip and the location of the hole in the strip are random due to feed errors and variation in punching operations. The clearances on the sides of the pin are given in Eq (3) and Eq (4).

$$C_l = \frac{1}{2}d_h - x_f - x_h - \frac{1}{2}d_{pp} + x_s + x_{pp} \tag{3}$$

$$C_r = \frac{1}{2}d_h + x_f + x_h - \frac{1}{2}d_{pp} - x_s - x_{pp} \tag{4}$$

The clearances are linear combinations of the errors, so applying Eq (1) and Eq (2) yields the expected values and the variances for the clearances:

$$\mu_C = \mu_{C_l} = \mu_{C_r} = \frac{1}{2}\left(\mu_{d_h} - d_{pp_{nom}}\right) \tag{5}$$

$$\sigma_C{}^2 = \sigma_{C_l}{}^2 = \sigma_{C_r}{}^2 = \frac{1}{4}\sigma_{d_h}{}^2 + \sigma_{x_f}{}^2 + \sigma_{x_h}{}^2 + \sigma_{x_s}{}^2 + \sigma_{x_{pp}}{}^2 \tag{6}$$

Locating the carrier strip with multiple pins is similar to selecting a set of values from the distributions for the clearances. The minimum value within each set represents the clearance between the carrier strip and the entire set of pins. The minimum value is random and called the first order statistic[14]. The expected value of the first order statistic, given in Eq (7), is used in Eq (8) to estimate the variance in the uniformly distributed location of the carrier strip with respect to ground.

$$\mu_{C_S} = \int_{-\infty}^{\infty} C_S\, n\left\{1 - \frac{1}{2}\left\{1 - erf\left[\frac{C_S - \mu_C}{\sqrt{2}\,\sigma_C}\right]\right\}\right\}\frac{1}{\sqrt{2\pi}\,\sigma_C}\exp\left[\frac{-(C_S - \mu_C)^2}{2\,\sigma_C{}^2}\right]dC_S \tag{7}$$

$$\sigma_{x_c}{}^2 = \frac{(2\mu_{C_S})^2}{12} \tag{8}$$

Fig. 6 illustrates the punch randomly located inside a hole in the randomly located stripper plate. The punch cuts a hole through the randomly located carrier strip. As shown in Eq (9), the position of the punched hole is a linear combination of the location of the stripper, punch, and carrier strip. The variance in the location of the punched hole is found by applying Eq (2), but correlation between the stripper and the carrier strip is expected.

$$x_h = x_s + x_p - x_c \tag{9}$$

$$\sigma_{x_h}{}^2 = \sigma_{x_s}{}^2 + \sigma_{x_p}{}^2 + \sigma_{x_c}{}^2 - \sigma_{x_s}\sigma_{x_c} Cor(x_s, x_c) \tag{10}$$

Eq (11) expresses the pitch between two consecutive holes in terms of the nominal pitch and the location of the two holes. From Eq (2), the variation in the pitch is twice the variation in the location of an individual hole.

$$P = P_{nom} + x_{h_2} - x_{h_1} \tag{11}$$

$$\sigma_P{}^2 = 2\,\sigma_{x_h}{}^2 \tag{12}$$

The variation in the stripper, punch, pilot pins, and feed are determined from design parameters such as bearing clearances and feed uncertainty. Eq (6), Eq (7), Eq (8), Eq (10), and Eq (11) form a (non-linear) system of equations that can be solved for the variance in the strip location, hole location, pitch, and probable hole clearances. Using conservative estimates for the design parameters, this error model predicts a standard deviation of 6.2 μm for the pitch errors.

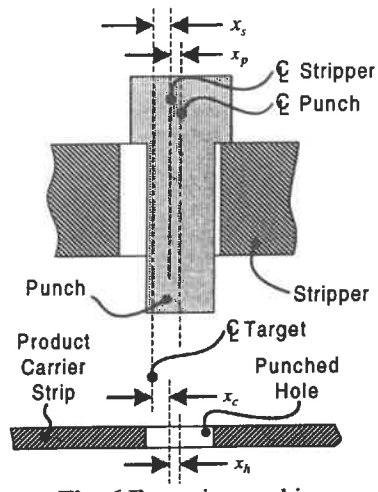

Fig. 6 Errors in punching operation

Error simulation

A simulation for the variation in pilot holes was developed within SciLab[15]. The simulation emulates the punching and piloting operations in a sequence similar to a real progressive die. A series of punched holes is indexed through the dieset, so piloting actually depends upon the variation in prior punch operations.

The simulation consists of three nested loops. The primary loop operates the stripper plate. Each time the die cycles, a random location for the stripper plate is generated. A simplification for the presence of multiple bearings in the plate provides a conservative estimate. The next loop randomly locates all the pilot pins in the stripper and then shifts them by the stripper position. This gives the locations for all pilot pins relative to the global coordinate system. The third loop recursively adjusts the position of the carrier strip until it fits within the range of clearance for the entire set of pilot pins. The punch is then randomly located within the stripper and offset by the stripper position to obtain its location relative to the global coordinate system. Finally, the hole is punched through the carrier strip. The entire process is repeated for the desired quantity of die strokes.

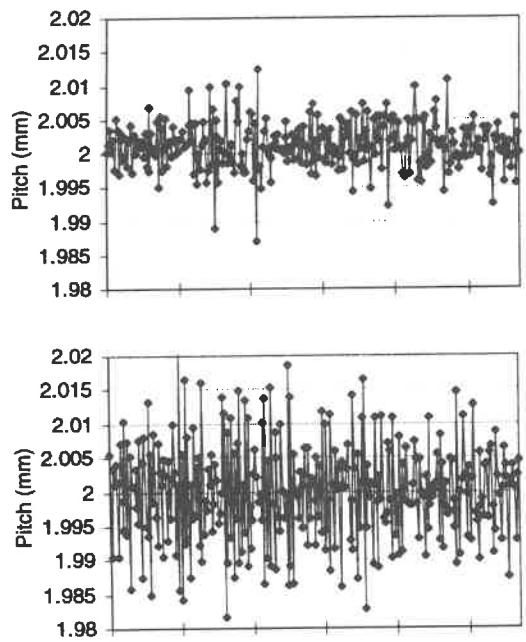

Fig. 7 Pitch per cycle, experimental (top), simulation (bottom)

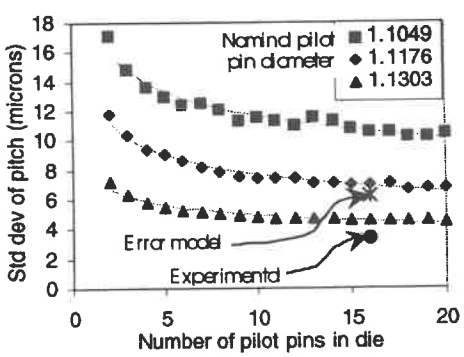

Fig. 8 Pitch error as a function of the number of pilot pins

Fig. 8 shows the results of the simulation for various numbers of pilot pins and three different pin diameters. Two additional points identify the value predicted by the analytical model and the measured value. The simulation was configured with the same geometry as the test die, and clearances and means matched those used in the analytical model (nominal manufactured values). Both the measurements and the simulation exhibit an alternating cycle of short and long pitches. Thus, the nature of the simulation follows closely with the real die. Like the error model, the simulation yielded larger errors, but this is expected due to the conservative nature of the stripper bearing assumptions.

The pitch errors in Fig. 8 decrease as the quantity of pilot pins in the die increases. The pitch error asymptotically approaches a minimum value set by the geometry and clearances in the dieset. A change in the diameter of the pilot pins (which changes the clearance between the pilot and pilot hole), therefore results in a different minimum limit in the pitch error.

Conclusions

This paper presents a technique for measuring pitch and y-errors in stamped pilot holes of carrier strips or leadframes. An error model is developed that considers design parameters of the progressive die such as punch clearance, stripper bearing clearances, pilot pin clearances, and the quantity of pilot pins in the progressive die. Solving a system of non-linear equations provides an estimate of the pilot hole pitch. In addition, the error model offers input in to a complete system simulation that reproduces the characteristic output of the experimental data. Using this approach to design the piloting system for a progressively stamped product provides knowledge of achievable pitch repeatability. These methods help the designer achieve the quality requirements at minimum cost, by minimizing wasted material in the carrier strip.

This exploration has shown that predictive error models and simulations can be created for stamping operations such as the blanking of pilot holes. Extending these models by providing design optimization and incorporating manufacturing tolerances, is the next step. This methodology may also be applicable to additional stamping operations such as trimming, coining, etc. This provides additional opportunities to develop more precision design tools that help reduce or eliminate the dependence on opinion and rules of thumb common to progressive die design.

Acknowledgements

The authors want to acknowledge Teradyne Connection Systems, Nashua, NH, and the College of Engineering at the University of Kentucky, Lexington, KY for funding this research. The research was conducted with the Precision Engineering Research Group at MIT's Laboratory for Manufacturing and Productivity, Cambridge, MA.

References

[1] Shirai, K and H. Murakami. "Development of a CAD/CAM System for Progressive Dies". *CIRP Annals*. Vol. 34, No. 1. 1985.

[2] Huang, K., H.S. Ismail, and K.K.B Hon. "Automated Design of Progressive Dies". *Proceedings of the Institution of Mechanical Engineers, Part B: Journal of Engineering Manufacture*. Vol. 20, No. 4 1996. p. 376-376.

[3] Cheok, B.T., and A.Y.C. Nee. "Configuration of Progressive Dies". Artificial Intelligence for Engineering Design, Analysis, and Manufacturing: AIEDAM. Vol. 12, No. 5. 1998.

[4] Cheok, B.T., K.Y. Foong, and A.Y.C. Nee. "Intelligent Planning Aid for the Design of Progressive Dies". *Proceedings of the Institution of Mechanical Engineers, Part B: Journal of Engineering Manufacture*. Vol. 210, nB1. 1996. p. 25-35.

[5] Ismail, H.S., K.K.B. Hon, and K. Huang. "Intelligent Object-Oriented Approach to the Design and Assembly of Press Tools". *CIRP Annals*. Vol. 44, No. 1. 1995. p. 91-96.

[6] Spisak, E. and F. Stachowicz. "Deformation Analysis of Large-Sized Autobody Panels". *Journal of Materials Processing Technology*. Vol. 53, No. 3-4. Sept. 1995. p. 817-826.

[7] Thomas, W. and T. Altan. "Application of Computer Modelling in Part, Die, and Process Design for Manufacturing of Automotive Stampings". *Steel Research*. Vol. 69, No. 4-5. Apr-May, 1998. p. 181-187.

[8] Jimma, T. and F. Sekine. "On High Speed Precision Blanking of IC Lead-frames Using a Progressive Die". *Journal of Materials Processing Technology*. Vol. 22, No. 3. Sept, 1990. p. 291-305.

[9] Breitling, J. B. Pfeiffer, T. Altan, and K. Siegert. "Process Control in Blanking". *Journal of Materials Processing Technology* Proceedings of the 1996 2nd International Conference on Sheet Forming Technology. Vol. 71, No. 1. Nov. 1997. p. 187-192.

[10] Slocum, A. H. *Precision Machine Design*. Society of Manufacturing Engineers. Dearborn, Michigan. 1992.

[11] Donmez, M. A., D. S. Blomquist, R.J. Hocken, C. R. Liu, and M.M. Barash. "A General Methodology for Machine Tool Accuracy Enhancement by Error Compensation". *Precision Engineering*. American Society of Precision Engineering. Vol. 8, No. 4. October 1986. p. 187-196.

[12] Donaldson, R. R. "Error Budgets". *Technology of Machine Tools, Vol. 5*. Machine Tool Task Force. Robert J. Hocken, Chairman. 1980.

[13] Keeler, S. P. "Sheet Metal Stamping Technology – Need for Fundamental Understanding". Mechanics of Sheet Metal Forming. Plenum Press. New York. 1978.

[14] Scheaffer, R. *Introduction to Probability and Its Applications*. Duxbury Press. New York. 1995.

[15] INRIA - Unit´e de recherche de Rocquencourt - Projet Meta2, Domaine de Voluceau - Rocquencourt - B.P. 105 - 78153 Le Chesnay Cedex (France), http://www-rocq.inria.fr/scilab.

THREE-DIMENSIONAL MICROFORMING BY METAL JET

Katsumi YAMAGUCHI
Katsuhiko SAKAI

Department of Mechanical Engineering, Nagoya University
Furo-cho, Chikusa-ku, Nagoya, 464-8603 Japan

1. Introduction

Various microprocesses have been developed to produce 3-dimensional micro models in recent years. Small sensors or micro parts can be produced by a silicon fabrication process. LIGA, a laser assisted etching and 3-dimensional photo fabrication processes have also been developed to produce various micro components. However, these processes are based on a patterning technique, so it is difficult to make 3-dimensional models. On the other hand, rapid prototyping techniques such as the sheet laminating method, laser sintering method and stereo lithography technique have been developed. These techniques, however, have serious limitations in forming micro 3-dimensional models i. e., the accuracy, quality and structure of products.

The authors have proposed a 3-dimensional microstructure generation process. In this technique, molten metal is jetted onto a plate to form an image. The most attractive feature of this method is its potential to form 3-D functional structures made of not only metals but also ceramics or plastics ejected out of multiple nozzles at the same time. In the first step, the basic principle and performance of this technique are described, and typical examples of 3-D models and structures are demonstrated.

2. Principle of forming and system

Figure 1 shows the forming principle, and the structure of the metal-jet head used in this research is shown in Fig. 2. The driving mechanism is similar to that in ink jet printing. The metal is melted in an electrically-heated tank mounted above the nozzle, and the molten metal is then supplied to the chamber by gravity. The chamber has a diaphragm which connects to the piezoelectric actuator. The volume of the chamber (filled with molten metal) is changed by applying voltage to this actuator, and the molten metal drops are then jetted out of the nozzle onto a plate. The temperature of molten metal is controlled by adjusting the electric current of the heater. The forming procedure is as follows. First, a 3-D CAD model is sliced into layers of 2-D images in the computer. Then, the 2-D image is formed on the base plate by scanning molten metal drops. Thin layers are piled up by repetition of this procedure so as to form 3-D models.

Figure 3 shows a flow chart of the forming system. This system consists of a CAD to make 3-D models and a CAM to control the X-Y-Z table and nozzle driving signal. In this study, Form Z is utilized as a 3-D rendering tool. This software has almost the same functions as in the software for a commercial rapid-prototyping system. The 3-D model is automatically divided into layers by a macro program as shown in Fig. 4 and 5. The layer thickness is determined the same as for a layer in metal printing. These layer data are then processed by image analyzer and the scanning data are prepared. Finally, nozzle actuating signal and X-Y-Z table are simultaneously controlled on the basis of the scanning data, and thus the 3-D model can be formed. Figure 6 is a photo of the experimental apparatus.

In this study, U alloy with a composition of Bi-44.7%, Pb-22.6%, In-19.1%, Sn-8.3% and Cd-5.3% was used. Melting point of this alloy is 46.7 ℃, density 8.8 g/cm^2, tensile strength 37 MPa. All experiments are performed in laboratory air. Other conditions are as follows. Diameter of nozzle: 200 μm ; temperature of molten metal in the nozzle: 55 ℃; distance between nozzle and base plate: 2 mm; speed of metal jet: 1 m/s; diameter of metal drop: ~300 μm; frequency of ejection: 4~20 Hz; and scanning speed: 0.8~4 mm/s.

3. Examples of the formed models

At first, 2-D images were printed on the base plate on the basis of the data from the image scanner. The scanned original images and the printed metal images are shown in Fig. 7(a) and (b) respectively. Fine metal printing can be done using any kind of black and white image. Moreover, 2.5-D forming can be performed easily

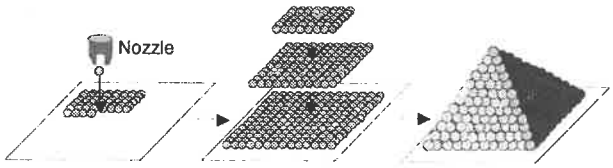

Fig. 1 Principle of metal-jet forming

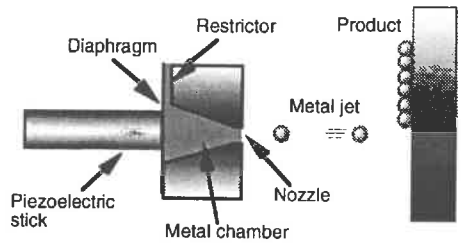

Fig. 2 Schematic illustration of metal-jet

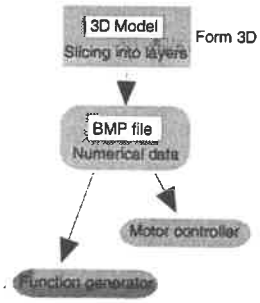

Fig. 3 Block diagram of 3-dimensional modeling

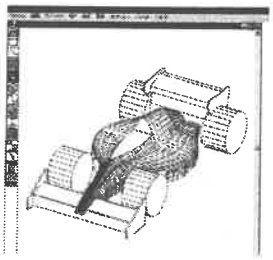

Fig. 4 Racing car designed by Form Z

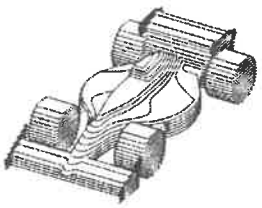

Fig. 5 3-D model sliced into layers

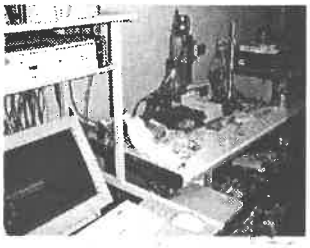

Fig. 6 Experimental apparatus

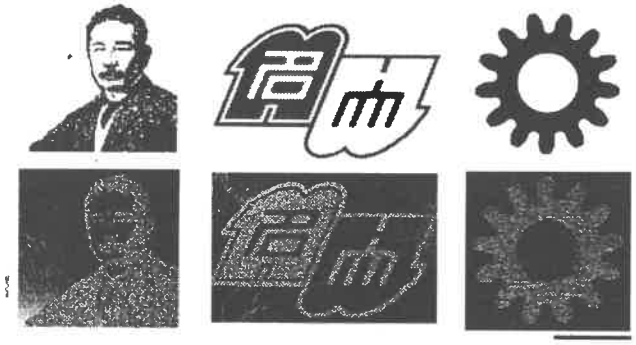

(a) Portrait (b) Logo of Nagoya University (c) Gear

Fig. 7 Some examples of metal printings

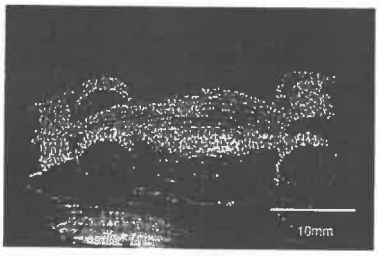

Fig. 8 3D model made of U alloy

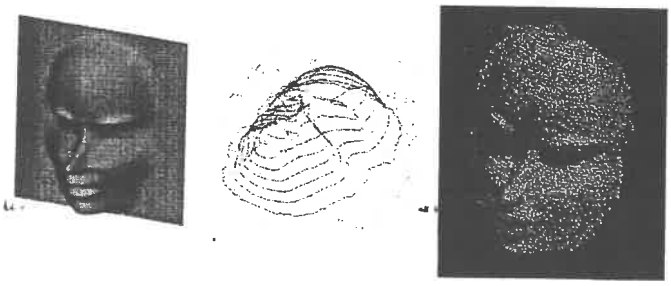

(a) CAD model (b) Sliced model (c) 3D model

Fig. 9 3D modeling of human face

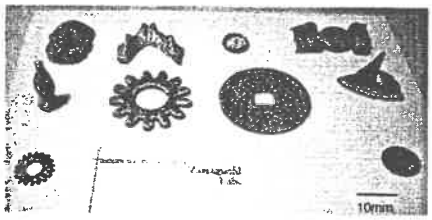

Fig. 10 3D models made of U alloy

by stacking on one another the same image layers. See gear wheel in Fig. 7(c).

Figure 8 shows a 3-D model formed using the data shown in Fig. 5. This is, as it were, a precisely prototyped model generated from 3-D data. 3-D data of human face and the formed model are presented in Fig. 9 (a), (b) and (c). Forming is successfully done although the shape of the human face model consists of intricate surfaces. Other examples formed using this system are shown in Fig. 10.

4. Bonding strength between metal drops

A metal drop has three kinds of bonding surfaces OX, OY and OZ which are shown in Fig. 11. The shearing test between two drops was conducted. The shearing strengthes are shown in Fig. 12 in comparison with those of bulk material. The differences of these shearing strength are due to the time intervals (duration of oxidation) and the directions of collisions with the pre-ejected drops.

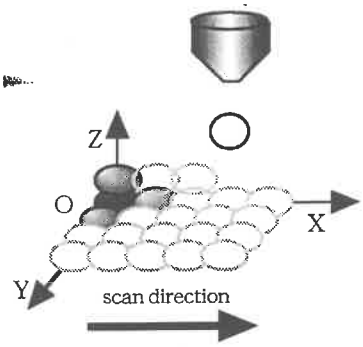

Fig. 11 Three kinds of bonding types

5. Forming by fine metal jet

In these experiments, the diameters of metal drops were relatively large. Thus, the structure is not fine, and the accuracy of forming is not sufficient. So, the forming was done using smaller drops. Drops of 80 μm in diameter were realized using the 50 μm nozzle. Some typical examples of micro parts made by these finer drops are shown Fig. 13, Fig. 14 and Fig. 15. Compared with the previously shown models, the surfaces are smoother and

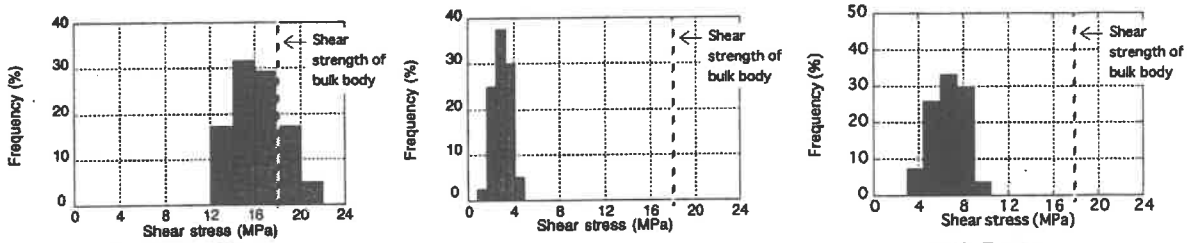

(a)O-X type
Time interval: 0.1 s

(b)O-Y type
Time interval: 100 s

(c)O-Z type
Time interval: 100 s

Fig. 12 Distribution of shear strength

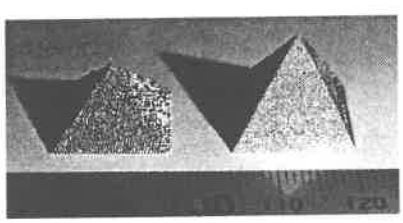

Fig. 13 Comparison between two pyramids made by 200 μm and 80 μm drops

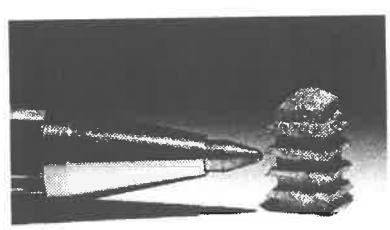

Fig. 14 Pagoda made of fine metal drops

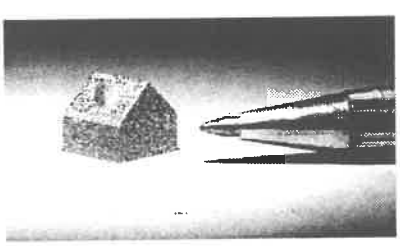

Fig. 15 Micro house made of fine metal drops

Fig. 16 Embossed printing

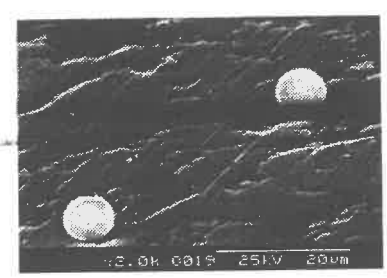

Fig. 17 Ultra fine metal drops ejected on base plate

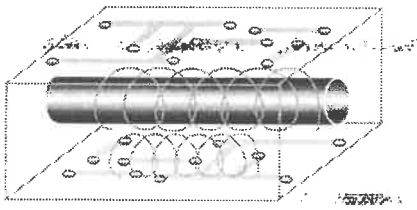

Fig. 18 Concept of 3-dimensional electro-magnetic structure

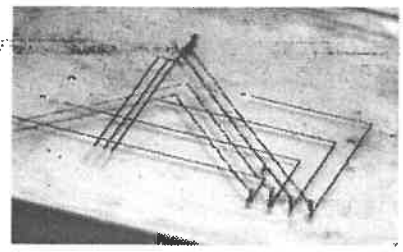

Fig. 19 3-dimensional electric circuit

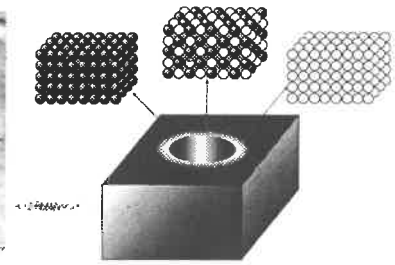

Fig. 20 Concept of 3-dimensional functional gradient material

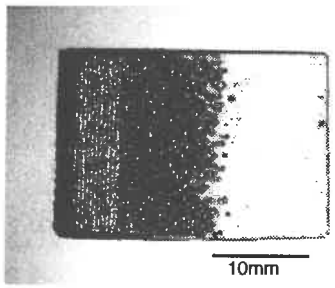

Fig. 21 Basic sample of 3-dimensional functional gradient material

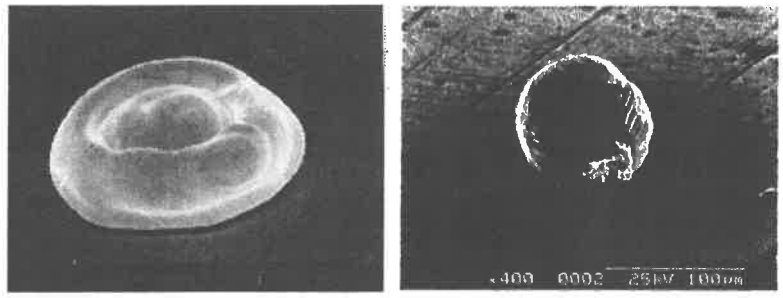

(a) gold drop (b) nickel drop

Fig. 22 Drops of high melting temperatures

the edges sharper. Further, the embossed-like printing was done as shown in Fig. 16. The fineness of this printing is almost the same as the conventional ink-jet printing because the diameter of the metal drop is almost the same as that of an ink-jet printer's dot.

To form a finer structure, it is necessary to use a finer jet nozzle. Figure 17 shows ultra-fine metal drops jetted out of another type of metal-jet nozzle. The diameter of the drops is only 8 μm. Fine structure can be formed using this nozzle, though it takes 40000 times as long in comparison with 300 μm drops to make the same model if the forming is done by a single jet nozzle.

6. Forming of functional structure

The key point in this study is the advantage of being able to form a 3-D functional structure. Virtually any kind of 3-D structure can be formed by jetting several kinds of materials through multi-nozzles.

If an electric conducting material and insulator are used, an electromagnetic structure with a 3-D electric circuit and coil can be realized as shown in Fig. 18. Figure 19 show an example of a 3-D electric circuit formed from metal and resin.

Further, by distributing different material jets of different functions, 3-D functionally gradient material can be generated as shown in Fig. 20. Figure 21 is a basic example of a functional gradient structure made of metal and resin.

These examples are all made of U alloy and resin. Recently, the author developed a new nozzle which can eject gold, silver and nickel. Fig. 22 shows the drops of gold and nickel. The author is attempting to form a 3-D micro structure using these metals of high melting temperatures.

7. Conclusion

1) A metal-jet nozzle was developed. This nozzle can eject drops of fusible alloy with a melting point of 47°C. 3-D models were formed using this nozzle.
2) Bonding strength between two drops are clarified.
3) Fine structure was formed by smaller metal drops.
4) Formation of a 3-D functional structure was shown along with some basic examples.

Diamond Flycutting Machine for Producing Flat Surfaces on Half-Meter Scale Diamond-Turnable Optics

Richard C. Montesanti, Stanley F. Locke, and Samuel L. Thompson

Lawrence Livermore National Laboratory (LLNL)
Livermore, CA 94551
August 30, 1999

Key Words: machine design, precision machine tool, ultra-precision machining, diamond flycutter, vertical stage, diamond turning, optics, KDP crystals, National Ignition Facility (NIF)

Overview

A diamond flycutting machine for producing flat surfaces on half-meter scale diamond-turnable optics was designed, built, and tested at LLNL. The machine can accommodate surfaces as large as 490 mm x 490 mm, and has a vertical positioning range of 100 mm. A new LLNL vertical stage supports the workpiece and provides elevation, orientation, and depth-of-cut control, allowing the use of a fixed-position vertical-axis flycutter. The vertical stage has 100 mm of travel, a depth-of-cut accuracy of ± 25 nm, and an average stiffness in all three directions of at least 13 N/μm (14 μin/lb compliance). It also provides tip and tilt angle adjustments of +/- 0.25° with 0.2 μrad accuracy. Designed to function as a stand-alone system, the LLNL vertical stage can be easily used on other precision machine tools.

Supporting an effort by the NIF project to use equipment already within the DOE complex, the diamond flycutting machine uses a surplus Moore #5 Jig Boring Machine. (See Figure 1) The #5 Machine was stripped down to the base and upright columns. The X-axis slideway (double-vee with roller bearings), servomotor, and Moore leadscrew were retained. The existing geometry of the X-axis slideway met our requirements (measured values of 0.33 μm vertical straightness of travel and 0.25 arcsec of roll in the workzone). New hardware for the machine includes the vertical stage and its metrology system, bridge, motorized air-bearing spindle, flycutter, spindle brake, machine controller, and user interface. (See Figure 2) This paper will describe the development of the machine, and the key elements of the design.

Referred to as the "Prototype Flatness Machine", it is a prototype for the production machines needed for fabricating the Potassium Di-hydrogen Phosphate (KDP) crystalline optics for the National Ignition Facility (NIF). The machines will be used to generate flat surfaces on 410 mm x 410 mm KDP plates, and orient those surfaces to the crystallographic axis. The specifications for the surfaces produced by the machine are 1.6 μm flatness with 0.3 μm repeatability, 12 nm rms roughness, and 5 μrad orientation accuracy. (12 nm rms is sufficient to allow optical testing of the surface. A different but related machine is used to produce a final surface finish of 3 nm rms.) The approximately 600 crystals will be used as Pockels cells (polarization rotating devices) and laser-light frequency doublers and triplers. The NIF is planned to be the world's most powerful laser system, with a design goal of achieving nuclear fusion ignition and moderate gain.

In June 1999 the Prototype Flatness Machine produced two 410 mm x 410 mm surfaces on a 100 mm thick aluminum part. The first surface had a flatness of 0.8 μm and a roughness of 10 nm rms. The part was then re-machined, producing a second surface with a flatness of 1.0 μm and an average roughness of 10 nm rms (8 – 13 nm rms range over nine locations). Approximately 50% of the flatness errors are due to room air temperature fluctuations during the final machining passes. (The prototype machine does not yet have a temperature-controlled oil shower, machine enclosure, or air isolators.) The vertical stage demonstrated angle adjustment accuracy within 0.2 μrad.

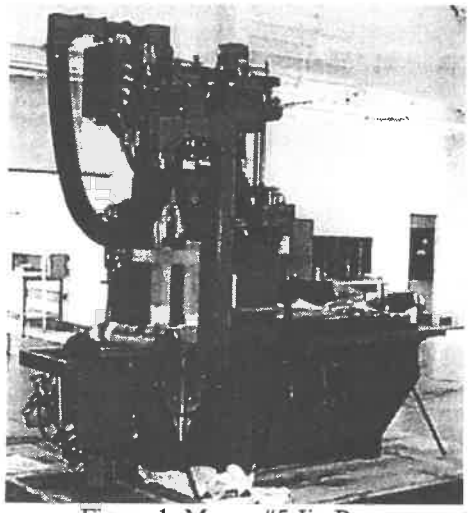

Figure 1: Moore #5 Jig Borer

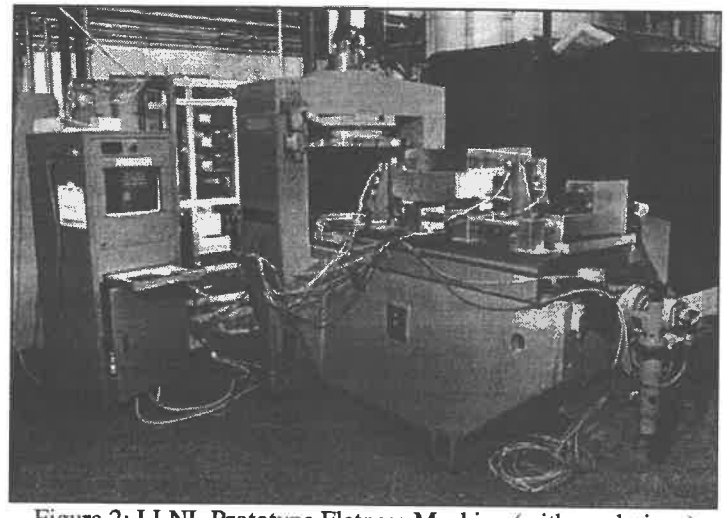

Figure 2: LLNL Prototype Flatness Machine (with workpiece)

Description of the Machine

A bridge supports a vertical-axis spindle and flycutter over a horizontal-axis slide. Mounted to the horizontal slide is a vertical stage that provides elevation and orientation control of the workpiece. The surface to be machined lays in a horizontal plane. The vertical stage is made up of a workpiece platform supported by a three-vee kinematic mount on three independent vertical-axis linear slideways. (See Figure 3) Three laser linear interferometers are used to measure the vertical position and orientation of the platform. The measurement beam for each interferometer is near and runs parallel to the vertical slide that predominantly depends on it. A laser-based metrology system was chosen because the tip and tilt rotations of the platform (and the associated in-plane rotation and translation motions) do not significantly effect its performance. Optical linear scales were considered, but they require special mounting hardware or master-slave slide systems. (Interferometers and optical scales both require sealing against debris and oil, and since the cost of the purchased components was comparable, the tip and tilt effects drove the decision towards the laser system.)

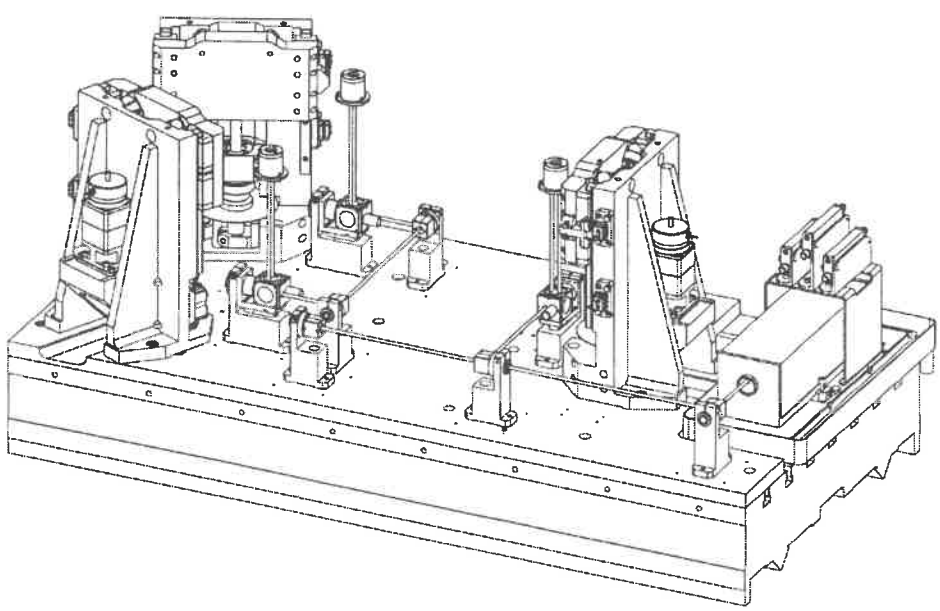

Figure 3: Vertical Stage (platform removed)

The accuracy requirement for spindle squareness drove the decision to fix the spindle to the bridge. A 1 arcsec squareness error between the spindle axis and the horizontal-slide travel produces a 0.7 μm flatness error in the workpiece, so a spindle slideway would need sub-arcsec angular motion accuracy. (In contrast, orientation errors of the workpiece do not create flatness errors.) Mounting the spindle to the bridge with front-to-back and left-to-right symmetry has a number of advantages over a more common arrangement of cantilevering it from the front of the bridge. Heat from the spindle bearing and motor create a symmetrical temperature profile in the bridge when the spindle is centered, reducing squareness errors caused by thermal distortion of the bridge. Centering the spindle in the bridge also provides a stiffer structural loop between the tool and workpiece, and a lower rotational inertia about the long axis of the bridge (the first leads to a better surface finish, both combine for a higher first natural frequency). Locating a sub-arcsec spindle slideway in the center of the bridge appeared formidable. Cantilevering it from the front of the bridge, and dealing with the stiffness, inertia, and thermal sensitivity issues appeared to be a brute-force approach. By fixing the spindle symmetrically within the bridge, we gained the advantages described above, and narrowed the critical design effort to one aspect of the machine, the vertical stage.

All of the other subsystems involve proven technology or straightforward machine design practices. The bridge is a steel weldment with a closed section and internal gussets to provide high torsional and bending stiffness. It sits on three adjusting screws that allow alignment of the spindle axis to the horizontal-slide travel. One of the screws has a differential thread for providing sub-arcsec roll adjustment of the bridge. The bridge is currently held down by eight bolts on each end, but has provisions to be grouted to the columns for increased stiffness and temporal stability of the alignment (if needed). The flycutter has a lightweighted conical-shaped aluminum body with a constrained-layer-damping back cover (similar to an earlier flycutter built by LLNL for an older related machine). An annular reservoir built into the top of the flycutter is provided for feeding workpiece coolant to the tools by centrifugal force though internal passages. The flycutter has provision for four tool holders that are staggered radially from each other to allow multiple-tool machining of a workpiece. The toolholders mount to the flycutter in a semi-kinematic fashion that provides both high stiffness and repeatability of depth-of-cut location (allowing off-machine tool setting). The spindle is a Professional Instruments motorized 10R air bearing. Similar spindles have being used on related machines at LLNL with great success (the LLNL "Small KDP Machine" routinely produces 1.5 – 2.0 nm rms surfaces on 50 mm x 50 mm KDP samples). The machine controller is based on an IBM PC platform using a Windows NT operating system and a Delta Tau PMAC2 controller card. The control software and user interface for coordinated motion of the vertical stage and X-axis slide were created at LLNL using the PMAC and Java programming languages.

The Vertical Stage (Patent Pending)

The vertical stage represents the enabling technology for this machine. It supports the workpiece and provides elevation, orientation, and depth-of-cut control. The underside of the workpiece platform has three vees that open down. Each of the three vertical slides functions as a "ball" that engages a vee. Together, the system behaves exactly as the well known three ball-and-vee coupling. (See Figure 4) Elevation and orientation is accomplished by providing each "ball" with an independent vertical translation. Consider the following evolution of a ball into one of the vertical slides. (See Figure 5) The normal contact forces (N) acting on a ball from its vee are directed through the center of the ball. Therefore it is desirable to support each ball at its center so that the normal contact forces do not generate an overturning moment (Figure 5a). Any tangential contact force will rotate the ball about its center, but not move the center. In Figure 5b, a hole through the ball allows it to be supported at its center by a vertical-axis ballnut (the centerline of the ballnut and its ballscrew lay in the same plane as the normal contact forces (N) on the ball). In Figure 5c, a vertical-axis linear guide is added to both sides of the ball (both guides lay in the same plane as the normal contact forces). In Figure 5d, the vertical slide is

completed by removing the portions of the ball that do not contact the vee or are not needed for other purposes.

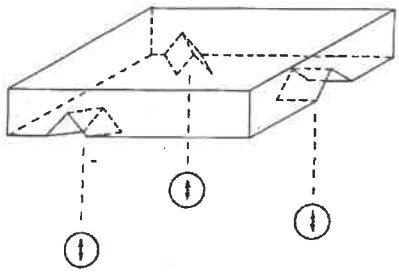

Figure 4: Three ball-and-vee coupling

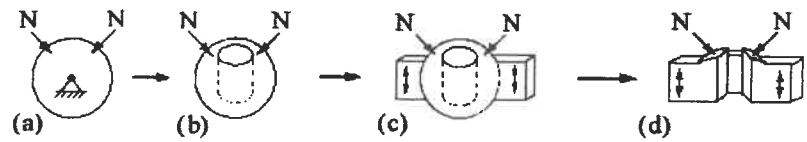

Figure 5: Evolution of a ball into a vertical slide

Figure 6 shows the critical load carrying elements of the three vertical slides (arranged to match the three vees in the underside of the workpiece platform). Consider the slide on the right. The normal contact forces (N) on this "ball" from its vee act upon two small sections of a sphere (having a common center with the ballnut), and develop a force at the center of the ballnut. The vertical component of the force at the center of the ballnut passes straight down the centerline of the ballscrew and is balanced by a vertical force (V1, shown in two pieces) on the thrust bearing that supports it. A piezoelectric actuator (PZT) that is described later also develops a vertical force on the end of the ballscrew (V2, shown as the force supporting the PZT). The horizontal component of the force at the center of the ballnut is balanced by forces (H) developed by two pairs of recirculating-ball linear bearings. For each vertical slideway the normal contact forces (N), ballnut, ballscrew, and linear bearings all lay in a common vertical plane, so there are no overturning moments in the system. (Tip and tilt motions of the workpiece platform cause the normal contact forces (N) to move slightly out of the plane of the load carrying hardware, but the effects are negligible for the small angles involved.)

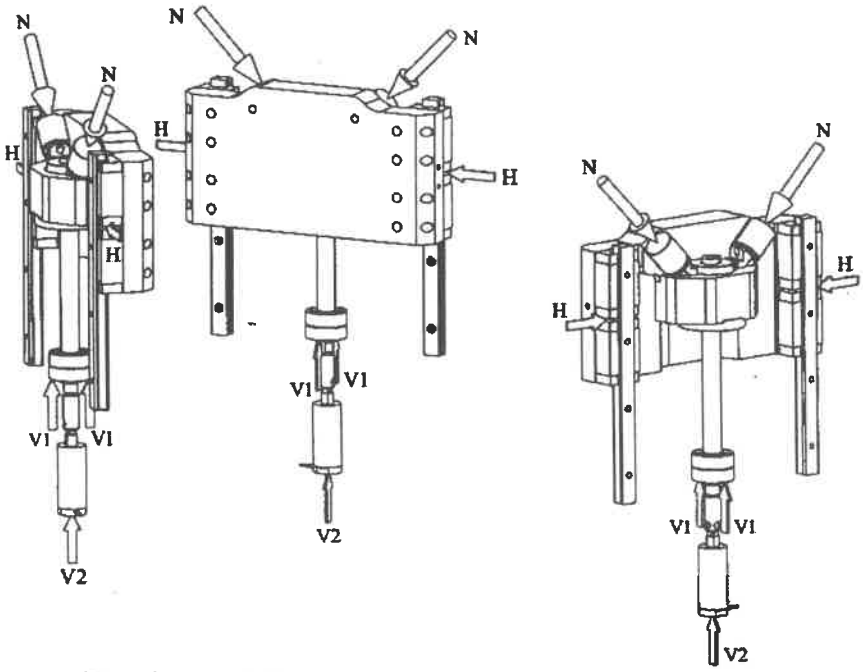

Figure 6: Load carrying elements of the three vertical slides

Note that as with the classic ball-and-vee coupling, horizontal forces along the vee are not restrained (towards the center of the platform). Tangential contact forces (not shown) on the spherical sections will tend to rotate the vertical slide around the center of the ballnut, and to first-order not effect the vertical position of the vee that it controls. To the extent that this center of rotation departs from the center of the

ballnut (as it does when slipping occurs between the vee and spherical surfaces), a second-order displacement of the platform occurs (which is negligible for the small angles involved). By avoiding overturning moments, standard off-the-shelf rolling-element hardware could be used. (What has been described utilizes a plane bearing at the contact points between each vertical slide and the platform. To avoid possible detrimental effects of sliding friction on the performance of the vertical stage during its first tests, the present hardware actually uses a rolling element connection. Each of the spherical contact surfaces was replaced with a ball supported by an array of ball bearings in a spherical cup.)

The vertical position and orientation of the workpiece platform is controlled by coarse and fine adjustment systems used to position each of the three vertical slides to a target position. Course adjustment is provided by a stepper motor that drives the ballscrew through a 105 to 1 gear and pulley reduction, and positions the slide with an accuracy of ± 0.5 μm. The coarse adjustment is commanded to position each vertical slide 6 μm below its target position. A disk brake on each ballscrew is then actuated and the stepper motor drives are disabled. (To reduce on-machine heat sources. Since the stepper motor is used in a microstepping mode, the brake prevents the magnetic poles of the motor from "cogging" and effecting the ballnut position). A piezoelectric actuator (PZT) located at the bottom end of the ballscrew provides fine adjustment. (See Figure 5) The PZT deflects the ballscrew upwards relative to the thrust bearing that supports it by partially unloading that bearing, raising the ballnut and the slide to the target position with a closed-loop accuracy of ± 25 nm. In addition to providing a tight depth-of-cut accuracy, the PZT's compensate for thermal drift of the workpiece platform position and orientation during a sequence of machining passes (which takes several hours). Also, by creating a second structural path between each ballscrew and the X-axis slide, the PZT's increase the overall vertical stiffness of the system.

Remaining Work

Hardware for the described plain bearing connections between the workpiece platform and the three vertical slides already exists (simple sections from a 174 mm diameter ball made of hardened 440C bearing steel). These need to be installed and tested to determine if the effects of sliding friction are acceptable (so that a simpler system can be realized). Tests should be conducted to determine if the ± 25 nm depth-of-cut accuracy and drift compensation afforded by the PZT system is needed for successfully machining the NIF KDP crystals. The present machine provides a benchmark. The performance of the stepper motor "coarse" adjustment system could be more fully optimized (not much effort was spent on tuning it), or a sufficiently more accurate primary drive for the ballscrew could be pursued. The vertical stage and the X-axis slide need covers to protect their components from machining debris. A design for the vertical stage cover that uses flexible bellows and a sheet metal skirt is nearly complete. Weights were added to the platform for the aluminum machining tests to suppress a low-level ~60 Hz rotational oscillation around its long axis. A more formal treatment of damping or preloading the platform needs to be considered (along with the protective covers for the vertical stage). The motorized spindle has a 70 mm thru-hole in it. Coupled with a thru-hole in the flycutter, air can flow into the workzone as the flycutter displaces the air radially (as a centrifugal fan). The effects of the flycutter airflow on the flatness of a finished workpiece need to be investigated to determine if the hole is required for this machine and its successors. The use of multiple tools in the flycutter needs to be tested, as does the centrifugal workpiece coolant system built into the flycutter. An emergency brake for the spindle was built, but not installed or tested. In addition to fitting into a confined space, the brake system acts as a passive mechanical restraint for the flycutter in case of a catastrophic spindle failure. (The brake was not needed for the machine tests performed to date, so a simple two-piece steel collar currently provides the passive axial and radial restraint for the flycutter.) A thorough evaluation of the emergency-stop requirements for the machine will indicate if the spindle brake is needed.

Acknowledgements

This work was performed under the auspices of the U.S. Department of Energy by the Lawrence Livermore National Laboratory under contract No. W-7405-ENG-48. The authors acknowledge the dedicated efforts of Richard Arney, Blaine Beith, Charlie Cass, Doris Denson, Mercedes Dickerson, Jim Dressler, Frank Gonzales, Dick Grayson, Keith Huffer, Dannie Johnson, Susan Locke, Gary Martin, Mary Pitta-Fry, Peggy Poggio, Doug Sweeney, George Weinert, and Timm Wulff, and the support of Jeff Atherton and the NIF Project.

ULTRA-PRECISION CUTTING FOR GALLIUM ARSENIDE

F. Z. Fang*, Z.. J. Yuan
Department of Mechanical Engineering, Harbin Institute of Technology, 150001, China

ABSTRACT Gallium Arsenide (GaAs) is widely used in semiconductor and optical industries because of its excellent performance, which is the most important of the III-V compound semiconductors today for fabricating high-speed field-effect and bipolar transistors, infrared-emitting diodes, solid-state lasers, and integrated circuits. With this material, there is an immense need to obtain nanometric surface finish owing to the advantage of improved performance of the components. Thus, the use of ultra-precision machining becomes critical for this case. However, the mere use of ultra-precision machining for this brittle material would not yield mirror surface finish. Therefore, experiments were conducted by using diamond cutting for machining GaAs. Based on the experimental work, a new strategy was proposed for obtaining nanometric surface finish and the cutting mechanism was studied in detail. Also, in this paper an alternative approach was recommended for the sharpness measurement of diamond cutters.
Keywords: Gallium arsenide, Brittle materials, Ultra-precision machining

INTRODUCTION

The gallium arsenide (GaAs) integrated circuit industry continues to mature and emerge from its position as an advanced laboratory activity. After several years of promoting the superiority of GaAs ICs over silicon ICs in speed, power, temperature range and radiation hardness, many people began to think of GaAs ICs as exotic devices in a world by themselves. Ironically, one of the principal goals of industries today is to minimize the differences between the two kinds of products. The unusual properties of GaAs are recognized by the users of high-speed digital and analog ICs although the higher cost and more limited availability of GaAs ICs must be considered in any plans to replace an existing silicon IC with a GaAs IC.

As a brittle material, it is hard to obtain the mirror surface finishing for GaAs because of its high hardness and low fracture toughness. Diamond turning as an ultra-precision machining technology is increasingly demanded in the area of the mirror surface finishing[1-4]. Its advantages are particularly recognized in the machining of spherical and aspheric surfaces. During the machining, the surface finishing is directly influenced by the cutting conditions and tool geometry. And also, the sharpness of cutting tools is very critical. In this paper, in addition to the above goal, a new approach for measuring the sharpness of cutting tools by using vertical scanning-interferometry is proposed. Subsequently, the mirror surface was obtained, and the integrity of the machined surface was analyzed by atomic force microscopy and scanning electron microscopy.

GALLIUM ARSENIDE

Gallium arsenide (see Table 1)[5,11] is the most important of the III-V compound semiconductors today for fabricating high-speed field-effect and bipolar transistors, infrared-emitting diodes, solid-state lasers, and integrated circuits.

Table 1: Material properties

Properties	GaAs	Si
Young's Modulus, GPa	83	168
Density, g/cm^3	5.37	2.34
Knoop Hardness, kg/mm^2	750	1020
Poisson's Ratio	0.31	0.27
Melting point, ^{0}C	1240	1420
Thermal Conductivity, w/cm/^{0}c	0.46	0.2

*Current address: Gintic Institute of Manufacturing Technology, 71 Nanyang Drive, Singapore 638075

Like silicon, GaAs belongs to the cubic class of crystals. The crystal structure of GaAs consists of two interpenetrating face-centered cubic sublattices, which are called the zinc blend structure[5]. In GaAs, each sublattice contains atoms of only one element type. When both sublattices contain identical atoms as in the case of silicon, the lattice is called the diamond cubic lattice. The energy gap of GaAs is 1.43 eV at room temperature.
Semi-insulating optical GaAs provides an alternative to ZnSe in medium and high power CW CO_2 laser systems for lenses and rear mirrors. GaAs is particularly useful in applications where toughness and durability are important. Its hardness and strength make GaAs a good choice where dust or abrasive particles tend to build up on, or bombard, the optical surface.

DIAMOND CUTTING

Brittle materials, as mentioned above, exhibit properties which are needed for today's and future advance applications. However, hardness and brittleness often renders them difficult to finish-machine using conventional turning and grinding machines without causing substantial brittle fracture[6-9].

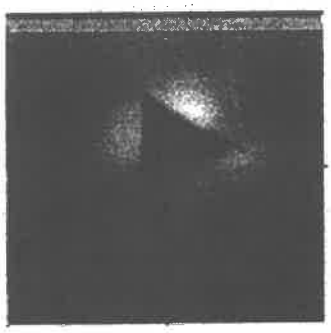

(a) Top view of nano-indentation

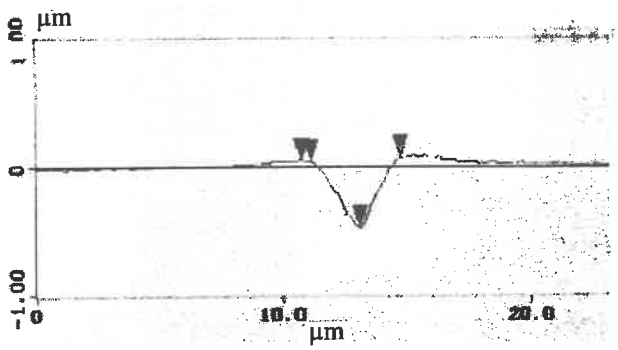

(b) Section analysis

Figure 1 Nano-indentation for the critical stress intensity of GaAs.

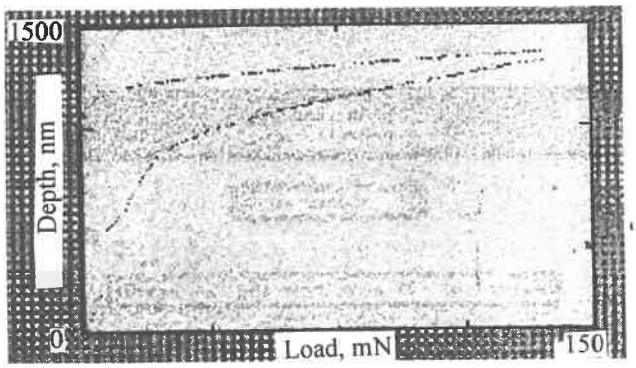

Figure 1 (c) Loading curve.

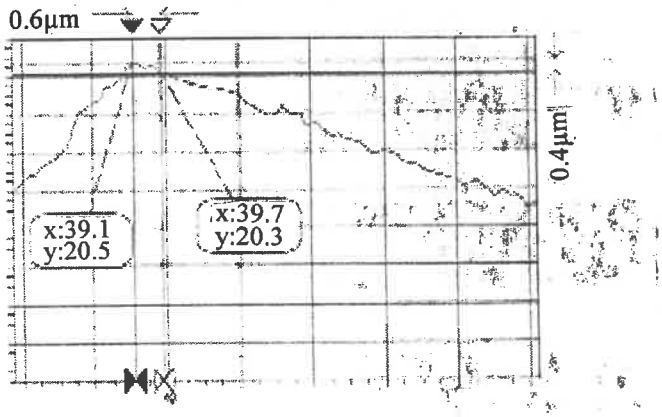

Figure 2 VSI for measuring the sharpness.

There is one hypothesis recently advanced involving "ductile" machining of brittle materials. According to this hypothesis, all materials, regardless of their hardness and brittleness, will undergo a transition from a brittle to a ductile machining region below a critical machining in feedrate. Below this threshold depth of cut, the energy required to propagate cracks is believed to be larger than the energy required for plastic deformation, so that plastic deformation is the predominant mechanism of material removal in machining these materials.
Ductile regime machining is necessary for obtaining mirror surfaces. In order to have a basic understanding of the ductile mode cutting, it is necessary to look into the indentation model which provides a criterion for the transition between the ductile and

brittle regimes. An indentation fracture mechanics approach attempts to describe chip formation via crack propagation. Fig. 1 shows the nano-indentation with different loads. A load P pushes the indentor into the surface to a depth of d. This induced a plastic zone to form in the high stress zone under the indentor tip. When the indentor (or the cutting tool moves away), residual stress remains at the plastic zone boundary which, if large enough, will result in median and lateral cracks.
According to fracture mechanics theory[8-10, 12], crack propagation occurs when the stress intensity K_I at the crack tip exceeds the critical stress intensity K_{IC} of the material.

$$K_I \leq K_{IC} \tag{1}$$

Where $K_{IC} \propto \sigma_0 \sqrt{a}$ is critical stress intensity, 2a is crack length (as shown in Figure 1) and σ_0 is stress normal to the crack. Subsequently,

$$d_C = \beta \left(\frac{E}{H}\right)\left(\frac{K_{IC}}{H}\right)^2 \tag{2}$$

Where E and H are the elastic modulus and the hardness of the material respectively. β is a factor that will depend upon geometry and process conditions, such as rake angle and coolant etc. From the results of the Fig. 1, the critical stress intensity of 1.22 $MNm^{-3/2}$ can be calculated.
After understanding the critical depth of cut dc, we can control the cutting in ductile regime.

TOOL SHARPNESS MEASUREMENT

Measurement of diamond tool edge geometry is essential for quantitative study of the ultra-precision machining process. Recently reported work has shown significantly differences in the surface finishing which results when machining with different tool sharpness of single diamond tools. In the present study, the tool sharpness was quantitatively measured by vertical scanning- interferometry, atomic force microscopy, and scanning electron microscopy.

(1) Vertical Scanning-Interferometry

Vertical scanning-interferometry (VSI) is a new technique for measuring surface profile. In principle, a white light beam passes through a microscope objective to the sample surface. A beam splitter reflects half of the incident beam to the reference surface. The beams reflected from the sample and the reference surface recombine at the beam splitter to form interference fringes. The system measures the degree of fringe modulation, or coherence, instead of the phase of the interference fringes unlike phase shifting-interferometry (PSI). That's why it is able to measure a wide range of surfaces. Figure 2 shows the sectional analysis of the diamond tool edge by using this technique. The edge sharpness measured for the cutter in the Fig. 2 is 400 nm.

(2) Atomic Force Microscopy

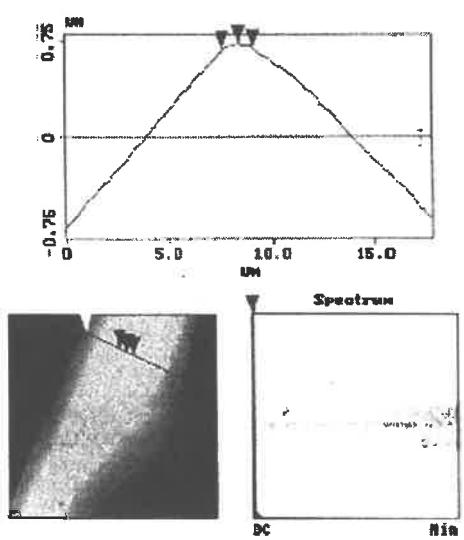

Figure 3 AFM for measuring the sharpness.

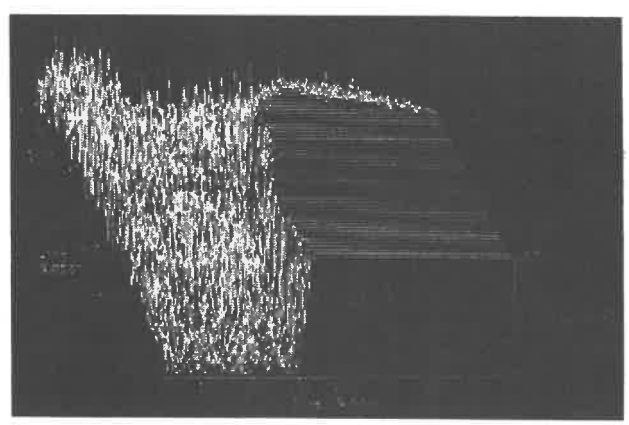

Figure 4 SEM for measuring the sharpness.

Scanning probe microscopy (SPM) offers researchers and technologists the capability to make images of many surfaces at near-atomic and even atomic resolution. The field of SPM has expanded enormously because of the subsequent proliferation of many types of high resolution imaging mechanisms. In many types of probe-based techniques used successfully in research on microscopic surface phenomena, the most important technique is the atomic force microscope (AFM), which measures surface topography in a straightforward way.
The use of atomic force microscopy, whereby a diamond tool is positioned directly under the scanning cantilever tip has also shown promise for characterization of single crystal diamond tools. Suppliers of commercially available Si_3N_4 cantilevers estimate tip radii to be in the range of 20-40 nm[4]. As a result, when using the force microscope to measure the edge of a diamond tool, there will be a convolution of cantilever tip and tool edge geometry which will become important when the tool edge radius is of the order of the cantilever tip radius (Figure 3). A number of cutters have been measured during the experiments. Figure 3 shows that the value calculated for the cutter edge sharpness is 210 nm.

(3) Scanning Electron Microscopy
The scanning electron microscope (SEM) is popular because it uniquely combines some of the simplicity and ease of specimen preparation of the optical microscope with much of the performance capability and flexibility of the more expensive and complex transmission electron microscope. By means of scanning electron microscopy, a graphical representation of the grey levels with the image of the cutter (Figure 4) can be obtained. According to the figure, the edge of the diamond tool can be analyzed. The sharpness value of the cutter is about 400 nm.

MIRROR SURFACE FINISHING

Diamond cutting experiments were performed on a diamond turning machine using single crystal diamond tool with a rake angle of 0 degree with a radius of 0.50 mm (waviness controlled, 0.25 μm). For turned gallium arsenide, mirror surfaces of 1.0 nm roughness are achieved, where a depth of cut of 1.0 μm, width of cut (feed rate) of 0.6 μm/rev, and a cutting speed of 90 m/min are used. It can be seen clearly that the ideal ductile cutting is substantiated through 3-D analysis and section analysis by using an atomic force microscope (Digital Instruments Inc.) as shown in Figure 5. The roughness values of the turned mirror surfaces are Ra=1.0 nm, Rmax=10.0 nm and Rms=1.3 nm in the area of 10 x 10 μm^2.
Originally, it was hypothesized that the maximum chip thickness, t_m, would be the dominant parameter in determining whether the surface suffered pitting damage or not. But the understanding of pitting along the tool shoulder eliminates that hypothesis. The pits created at the point of maximum chip thickness are not very deep (0.1-0.3 μm, compared to a depth of cut of 2-200 μm). Their creation would have little to do with the final surface.

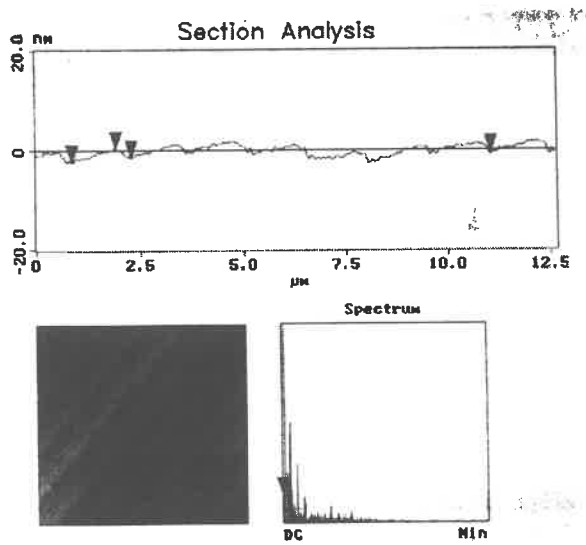

Figure 5 Mirror surface analysis.

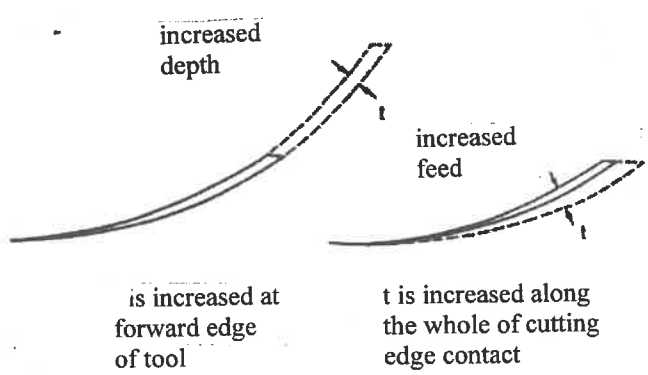

Figure 6 The effects on the undeformed chip cross-section of increased depth and increased feed.

More significant would be the chip thickness at the point along the tool shoulder where pits ceased to be created. It can be seen that the feed per revolution will have a dominant effect on the chip thickness. Figure 6 illustrates the effect of increasing depth of cut on the cross-sectional shape of the chip, and the effect of increased feed. Increased depth increases t_m, but merely by making the chip wider, leaving the relationship between chip thickness and distance along the chip width unchanged. However, increasing the feed increases the chip thickness along its whole width[8,10].

CONCLUSIONS

Gallium arsenide material is widely used in semiconductor and optical industries today. Its excellent electronic and optical performance makes itself obtain more and more attention. For the ultra-precision machining of gallium arsenide, the sharpness of diamond tools affects heavily the surface finishing. Different approaches were investigated in the experiments, and atomic force microscopy is alternatively selected to measure the edge of the tools since it has a high resolution and is easy to obtain the accurate coordinate values of the edge. As a kind of brittle material, gallium arsenide's mirror surface finishing was realized in ductile mode, and surface roughness of Ra=1.0 nm was achieved successfully. The surface integrity was analyzed by scanning electron microscopy and atomic force microscopy. It appears that a truly ductile cutting response can be achieved only when the effective cutting depth, or chip thickness, is less than a critical value. Factors such as tool rake angle are significant in that they will affect the actual value of the critical depth of cut for transition from brittle to ductile response.

REFERENCES

[1] Bifano, T. G., Dow, T. A., and Scattergood, R. O., 1991, Ductile Regime Grinding: a New Technology for Machining Brittle Materials, ASME J Eng Industry, Vol. 113, 118-114.

[2] Fang, F. Z., Venkatesh, V. C., 1998, Diamond Turning of Silicon with Nanometric Finish, Annals of the CIRP, 47/1: 45-49.

[3] Vorburger, T. V., Dagata, J. A., Wilkening, G., and Lizuka, K., 1997, Industrial Uses of STM and AFM, Annals of the CIRP, 46/2: 597-620.

[4] Lucca, D. A. and Seo, Y. W., 1994, Aspects of Surface Generation in Orthogonal Ultra-precision Machining, Annals of the CIRP, 43/1: 43-46.

[5] Scalter, N., 1988, Galium Arsenide IC Technology, TAB Books Inc., 1-25.

[6] Yuan, Y. J., Geng, L., Dong, S., 1993, Ultra-precision Machining of SiCw/Al Composites, Annals of the CIRP, 42/1: 107-109.

[7] Fang, F. Z., Zhang, Y. Q., Zhang, G. X., 1996, Study on a Novel Method for Refractive Index Compensation of Laser Measuring System on Ultra-precision Machine tools, ASPE, Vol. 14: 95-99.

[8] Blake, P. N., Scattergood, R. O., 1988, Ductile-regime Turning of Germanium and Silicon, Intersociety Symposium on Machining of Advanced Ceramic Materials and Components, Chicago, USA, 249-265.

[9] Komanduri, R., 1996, On Material Removal Mechanisms in Finishing of Advanced Ceramics and Glasses, Annals of the CIRP, 45/1: 509-514.

[10] Shaw, M. C., 1984, Metal Cutting Principles, Clarendon Press-Oxford, 487-543.

[11] Musikant, S., 1985, Optical Material, Marcel Dekken Inc., 116-121.

[12] Kapp, J. A., 1983, J –R Curve Determination Using Precracked Charpy Specimen and the Load-Drop Method for Crack Growth Measurements, Sixteenth National Symposium on Fracture Mechanics, USA, 281-292.

INVESTIGATIONS ON THE WEAR PROFILE OF DICING WHEELS

Hans H. Gatzen[1], Gordon M. Jones[2], Caspar Morsbach[1]
[1] Institute for Microtechnology, Hanover University, Germany
[2] Seagate Technology, Bloomington, MN, U.S.A.

ABSTRACT

During wafer separation through a dicing process the grinding wheel is subjected to wear. This wear not only changes the wheel's diameter but also its cross sectional profile by a rounding of the edges. The actual wear profile of a wheel substantially affects the kerf's geometry and surface finish. For many processes it is attempted to stay as close to a rectangular wheel profile as possible. This is accomplished by periodically interrupting the production process to square the wheel in a truing process. The disadvantage of this method is obvious: the wheel never reaches a stable wear profile, a condition highly undesirable in any production process.

This paper describes a different approach to wheel wear: allowing a wheel to approximate a wear profile and to keep this profile stable. It describes how to simply monitor the wear profile and how to find cutting parameters at which the profile stabilizes. By choosing an appropriate combination of pre-process and in-process dressing stick, grinding wheel, and process parameters a stable wear profile could be reached.

INTRODUCTION

For dicing or slicing ceramic wafers the cutting tool is a diamond wheel, with the abrasive diamond grit embedded in a resin or metal binder. Typically, the depth of cut is great compared to the cut width. Therefore, some unique process features evolve: the vast majority of the cutting action is executed by the wheel's circumference while the cutting conditions at the wheel's sidewall are very poorly defined. Radial wear will reduce the wheel diameter. Furthermore, if the wheel starts out with a rectangular profile, both edge areas of the wheel's circumference are subject to excessive wear which causes a rounding of the corners. All in all, due to wear, a dicing wheel not only changes its diameter, it will also change its shape.

The actual wear profile of a wheel substantially affects the kerf geometry and the surface finish. Furthermore, due to the wheel's edge rounding, the depth of cut has to exceed the workpiece thickness by more than the edge radius; else, the wheel will create a burr at the kerf's bottom.

For many processes it was felt to be desirable to stay close to a rectangular wheel profile. Whenever the inevitable rounding of the corners exceeds a given value, the wheel's profile has to be brought back to a square one in a truing process. The disadvantages of this approach are obvious: the wheel is constantly changing its profile, with the greatest changes right after truing. It is never reaching a stable wear profile. These are conditions, which are highly undesirable in any production process.

An alternative (and novel) approach is to allow the wheel's starting profile to change into a wear profile. Obviously, such a process will only be practical if a stable wear profile will be reached. However, if this is the case, such an approach seems to be vastly superior than maintaining a square profile through repeated truing.

WHEEL PROFILE MEASUREMENT

A precondition for developing a dicing process resulting in a stable wear profile is a simple way to determine the wheel profile. During the experiments, we came up with one to do so. It is based on the following idea: while direct measurements of the wheel contour are time consuming, it is rather easy to optically inspect the kerf's intersection with the workpiece's surface. This measurement not only provides us with the actual kerf width. By the wheel exiting the workpiece vertically before having cut all the way to the end, the contour at the kerf's end represents closely a stretched negative of the wheel's profile. Furthermore, the difference in length of two consecutively cut kerfs represents the reduction of the wheel diameter due to radial wear. A wheel moved up vertically at the same feed position will have cut a shorter kerf if its diameter is smaller, in our case smaller due to radial wear.

Besides establishing a simple way to determine the wheel profile, we also needed an equally simple approach to describe it. Figure 1 depicts the proposed approach. Pairs of lines parallel to the kerf's symmetry axis representing a distance of 95%, 80%, and 50% of the nominal (i.e. fully cut) kerf width are established. Next, the *y*-coordinates of the intersection of lines and kerf contour are determined. These three *y* dimensions are adequately describing the wear profile. In order to convert the measured values into the absolute kerf profile, a geometric correction factor had to be applied. This factor takes into account both the actual wheel diameter and the depth of cut.

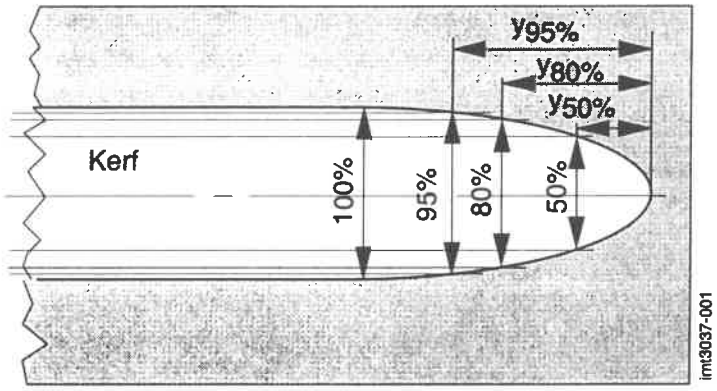

Fig. 1: Kerf end measurements to determine the wheel's wear profile

A combination of radial wear and wear profile measurement allowed to easily establish and describe all required wheel wear data. Such an easy method was a precondition for executing the following wear profile tests.

EXPERIMENTAL PROCEDURE AND RESULTS

Let us now move on to the actual wear experiments and first discuss the wheel break in procedure. At the beginning of each test run, a new wheel was mounted on the dicing machine. Both resin and metal wheels were hubless and were mounted between a pair of flanges on the dicing machine's air bearing spindle. To break them in, we followed industry practice: a wheel was first trued to establish both wheel concentricity and a square wheel profile and then dressed to expose the diamond by receding the binder. The processes for metal bonded wheels differ from the one for resin bonded wheels.

For resin wheels, truing was performed by executing a series of shallow cuts in a dresser board, e.g. made out of SiC. During the workpiece cutting process, resin bonded wheels are self dressing. This is due to the fact that the forces holding a diamond are small enough to allow diamonds to break out after becoming dull. To achieve a wear profile, the resin wheel simply had to be subjected to cutting tests. No further dressing was performed during the tests.

For metal wheels, truing is accomplished by means of a SiC cup wheel. Pre-process dressing is done by executing a couple of dozen cuts in a dressing stick. The stick material (e.g. SiC), as well as grit size, density, porosity, and hardness may be chosen to match the wheel parameters. When cutting the workpiece, metal bonded wheels contrary to resin bonded ones require in-process dressing. This is due to the fact that the forces holding a diamond are much greater than for resin bonded wheels (which also is the reason for their greater longevity). As a result, dull diamonds are not breaking loose during the regular cutting process. To remove dull diamonds and recede the binder in-process dressing is performed by mounting a dressing stick in front of the workpiece. For each feed the metal wheel first cuts the dressing stick before dicing the work piece.

For the investigations, one wheel with a hard resin bond and one with a soft metal bond was used. The material used for the experiments was Altic, a uniaxially hotpressed advanced ceramic consisting of appr. 70% Al_2O_3 and 30% TiC, and a Vickers hardness of 2000 HV. The data storage industry uses it extensively as a wafer material for thin film recording heads. The 1.25 mm thick wafer was cut in a single step, every pass ending within the workpiece in order to allow the inspection of the kerf's end. Figure 2 depicts the test setup. To be able to observe the rather quick change of the wheel profile during the early test phase, we started out with a short first cut. On the consecutive cuts,

the cut length is increasing in increments of 5 mm each. Table I depicts the experiment's dressing and cutting parameters.

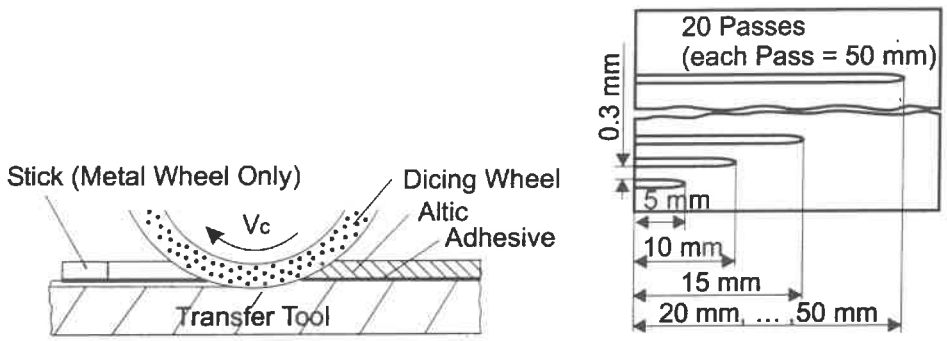

Fig. 2: Test setup

TABLE I
CONDITIONING AND DICING PARAMETERS

Binder	Diamond Grain Size d_g	Rotational Velocity	Cutting Speed v_c	Feed Rate v_f	Depth of Cut a_e	Cut length l_p
			Pre-Process Dressing Parameters			
Hard Resin	8 – 16 µm	30,000 RPM	86 m/s	-	0.15 mm	1,500 mm
Soft Metal	6 – 15 µm	20,000 RPM	55.5 m/s	3 mm/s	1.5 mm	625 mm
			Dicing Parameters			
Hard Resin	8 – 16 µm	20,000 RPM	55.5 m/s	2 mm/s	1.5 mm	300 mm
Soft Metal	6 – 15 µm	20,000 RPM	55.5 m/s	3 mm/s	1.5 mm	1,250 mm

As mentioned above, resin wheels were used without employing a stick during the cutting of the work piece. Any wear was strictly a result of cutting the Altic wafer. Figures 3 shows the development of the radial wear and the wear profile, respectively. The values $y_{50\%}$, and $y_{80\%}$ were becoming stable very quickly. However, this was not the case for $y_{95\%}$. The radial wear was stabilizing once a cut length of 50 mm has been reached.

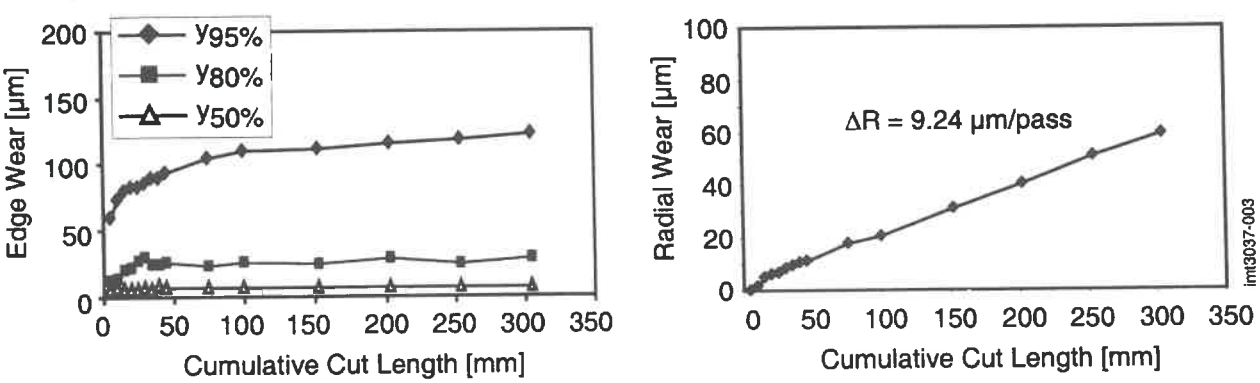

Fig. 3: Development of edge wear and radial wear of a hard resin bonded dicing wheel over cut length.

Of even greater interest was the wear behavior of the metal bonded wheel. Since it wears substantially less than a resin bonded one, in general it is the wheel of choice of production. Due to the mandatory use of a dressing stick during workpiece machining, there was also more potential for process variations dependent on what dressing stick was used. To find an optimal wear profile, four different dressing stick combinations for predressing and in-process dressing were used in combination. Table II demonstrates the wear profile and radial wear results. The minimal

length of cut to achieve a stable wear profile was 450 mm. The radial wear per pass was between 0.45 µm and 0.78 µm.

TABLE II
CHARACTERISTIC WEAR DATA

	Edge Wear			Radial Wear	Stable State
Dressing Stick Combination	$y_{95\%}$	$y_{80\%}$	$y_{50\%}$	ΔR	Above a Cut Length of
A	31 µm	13 µm	4 µm	0.45 µm/pass	500 mm
B	78 µm	30 µm	7 µm	0.50 µm/pass	450 mm
C	-	-	-	0.49 µm/pass	No stable state
D	117 µm	34 µm	7 µm	0.78 µm/pass	700 mm

Obviously it is desirable that a wheel not only reaches a stable wear profile, it also has to create a good kerf sidewall quality. Therefore the wear profile results were compared to kerf wall waviness and flatness. Figure 4 shows the respective average and mean root square waviness and roughness data, respectively. Of particular interest are the waviness results since they are directly related to the wheel's wear profile curvature. By far the best results were achieved by dressing stick combination B. Since it also yielded both wear results and a state of the art surface finish, it is the combination of choice.

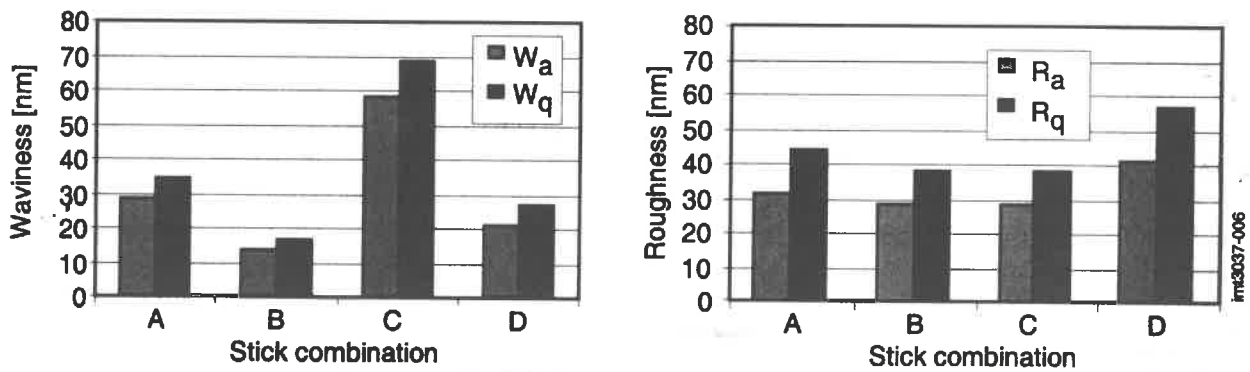

Fig. 4: Stick dependent waviness and roughness of the kerf sidewall using a soft metallic bonded wheel

CONCLUSION

By allowing the dicing wheel to change its profile into a wear profile, the dicing process is greatly simplified. It eliminates the need to squaring up the wheel regularly which in the case of a metal bonded wheel had to be done by cup wheel truing. A stable wear profile was accomplished by using an appropriate combination of dressing sticks for initial and inline dressing. A wheel with a stable wear profile achieved a state of the art flatness and surface roughness. Therefore, a substantially simplified production process was achieved without, in any way, compromising the parts' quality.

Furthermore, a simple method was devised how to measure a wheel's profile. It was accomplished by allowing the wheel to exiting the wafer vertically before having cut all the way through. By doing so, the contour at the kerf's end represents the wheel's profile.

Key words: Dicing, Slicing, Wheel wear, Wear profile, Wear profile measurement method

The Effects of High Feed Rate of Hardened Steel Milling upon Tool Life

Takashi Miyaguchi, Masami Masuda, Hiroyasu Iwabe
Graduate School of Science & Technology, Niigata University, Niigata 950-2181, Japan
Etsuo Takeoka
Industrial Research Institute of Niigata Prefecture, Niigata 950-0915, Japan
Björn L. Wegener
Otto-von-Guericke-University Magdeburg, Postfach 4120 D-39016 Magdeburg, Germany

1. Introduction

Hardened steel used for plastic mold dies or forging dies has started milling in trial, because it has the possibility of cost reduction and shortening delivery time.

It has been reported that the load worked on cutting edges could be reduced in the high cutting speed[1], and especially for milling hardened material. It results in realizing more efficient milling at a higher feed rate and a higher spindle speed using a small ball endmill.[2)3)4)]

In the meantime, it is known that tool life is drastically reduced by a rotating deviation of cutting edges on usual endmilling. Since the rotating deviation produces the imbalance in cutting force, it seems to result in excessive abrasion on some of cutting edges. However, in case of milling with a small ball endmill, it was reported that there was not any significance in the tool life in 20μm deviation or less[5]. Thus, the influence of the rotating deviation of cutting edges on the tool life has been unclear in the high spindle speed milling using a small ball endmill.

In this paper, the tool displacement and cutting force during milling are measured simultaneously for a small ball endmill with 2 cutting edges, and the correlation between abrasion and a rotating deviation of cutting edges is examined. Furthermore, the procedure to reduce the imbalance of tool wear is also proposed.

Table1 Experimenntal conditions

Specifications of ball endmill		Cutting conditions		
Tool radius	1mm	Spindle	Air bearing	
Shank diameter	4mm	Spindle speed	29000 min^{-1}	
Number of teeth	2	Feed rate S_z	0.1mm/tooth	
Material	WC+(Ti,Al)N clad	Coolant	Dry	
		Axial depth of cut	force & displacement measurement	0.2mm
			tool life test	0.5mm
		Radial depth of cut	force & displacement measurement	0.2mm
			tool life test	0.5mm

2. Experimental method and conditions

2.1 Measurement of tool displacement and cutting force

Tool displacement on cutting edges was calculated from the displacement at a tool shank bottom during free run or milling. The rotating deviation on the cutting edges in feed and transverse directions was calculated from the fluctuation of tool displacement and cutting force. The cutting force was measured on a measurement stage on the work table of a machining center (Fig.1). The frequency response of the dynamometer was even up to 10kHz in x and y directions using a capacitance type gap sensor. The signals from the dynamometer and the gap sensor were acquired in PC at the 10kHz sampling rate. Milling conditions are shown in Table 1.

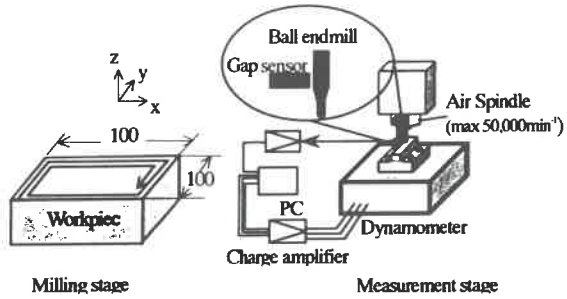

Fig.1 Experimental Setup

2.2 Evaluation of tool life

Tool life tests were carried out under the milling conditions shown in Table 1. The tool displacement and cutting force were measured in the initial state of a ball endmill. After 120m milling the maximum width of flank wear V_{Bmax} was measured using SEM, and cutting force was also measured.

Climb milling toward the inside from the outside was applied on the top surface of a workpiece (JIS SKD61, 40HRC), while it is paralleled for each side. Because, the arc of contact with a workpiece is considerably lengthened at the inside corners to bring abnormal abrasion on cutting edges, when it is milled toward the outside from the inside.

In usual tool life tests of the uni-directional milling, it becomes the intermittent milling which produces the steep and cyclic temperature gradient accelerates damage on cutting edges. Therefore, the spiral milling where a chisel on the ball endmill tip is always in contact with the workpiece surface, was applied to the following tool life tests.

3. Experimental results and discussion

3.1 Rotating deviation and tool life

At first, tool life tests were carried out at such high tool stiffness as the extrusion of the tool L is 11mm. Examples of x component F_x and y component F_y are shown in Fig.2. The maximum normal component of cutting force F_n can be estimated from F_x, F_y and rotating angle θ_{max} where true depth

of cut reaches maximum. In case of the figure, the ratio of maximum F_n on both cutting edges is given as 1.36, resulting in the true cutting depth of cut ratio 1.36.

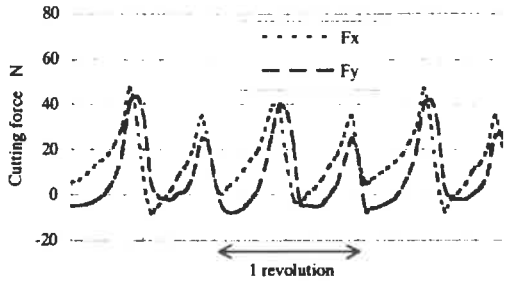

Fig.2 Cutting force of L=11mm

A photograph of the worn cutting edges is shown in Fig.3. Each V_{Bmax} on both cutting edges is 122±2.5μm, 66±2.5μm respectively, and the ratio of them has reached 1.85.

On the other hand, though Fig.4 is a photograph of the cutting edges, when both normal components of cutting force were almost equal to each other in the initial cutting state. According to the figure, each V_{Bmax} on both cutting edges is 90±2.0 and 96±1.4 μm respectively, resulting in the ratio between them as 1.07. One of both cutting edges is abraded rapidly by the rotating deviation between them in the former ball endmill (Fig.3) in comparison with the latter(Fig.4).

The relation of the abrasion and the rotating deviation of cutting edges can be also explained according to analyzing a locus of resultant force vector F_{xy} (F_x ,F_y) during 1 revolution, as shown in Fig.5, in the initial state of cutting edges in correspondence to Fig.3. The large continuous line locus and the small dotted line locus in a counter clockwise direction are respectively induced by the revolution of both cutting edges. Two loci are apparently different from each other.

Sampling points at 10kHz rate are also put on the loci. As the true cutting time from the time at a maximum force to the detaching time from the workpiece can be detected in the figure, the ratio of the true cutting time on both cutting edges is estimated almost 1.3. Thus the fretting distance differs on both cutting edges when the rotating deviation exists.

Therefore, it is verified that imbalanced abrasion depends on the different fretting distance and the different cutting force on both cutting edges.

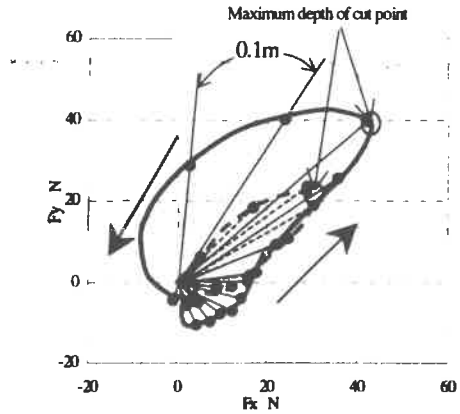

Fig.5 Cutting force vector locus through 1 tool rev. (L=11mm)

3.2 Reduction of effect of the rotating deviation

As shown in Fig.6, the milling model around a cutting edge at any rotating angle on xy plane is considered. From the equilibrium of the force applied on the cutting edge,

$$d_{tr} = \frac{k_m}{k+k_m} d_s, \quad \varepsilon = \frac{k}{k+k_m} d_s \qquad (1)$$

are lead. Where,

d_s ; setting depth of cut
k_m; relative stiffness between a ball endmill and a workpiece
ε ; relative elastic deformation at a cutting edge
d_{tr} ; true depth of cut
k ;cutting stiffness
$\varepsilon k_m = d_{tr} k_m$.

In case that $d_s = d_{s0} \pm \delta$,

$$d_{tr+} = d_{s0} + \frac{k_m/k}{2+k_m/k}\delta, \quad d_{tr-} = d_{s0} - \frac{k_m/k}{2+k_m/k}\delta \qquad (2)$$

$$\varepsilon_+ = \frac{k}{k_m} d_{s0} + \frac{1}{2+k_m/k}\delta, \quad \varepsilon_- = \frac{k}{k_m} d_{s0} - \frac{1}{2+k_m/k}\delta \qquad (3)$$

where

d_{s0} ; average setting depth of cut
δ ; rotating deviation of cutting edges.

True depth of cut and elastic deformation converge in several rotations of a end mill, because of $0 < k/(k+k_m) < 0.3$ in ordinary ball endmilling process. The fluctuation terms in eqs. (2),(3) seem to be a dominant factor in tool abrasion. Setting depth of cut d_{s0} at a rotating angle θ relative to the tool feed direction is

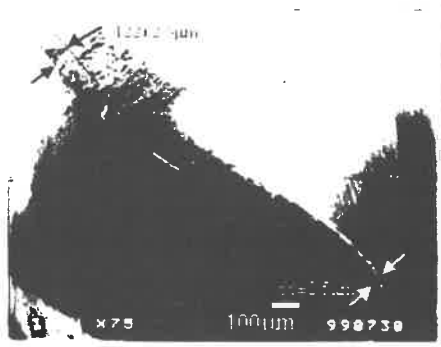

Fig.3 Worn cutting edges of L=11mm. "imbalanced endmill"

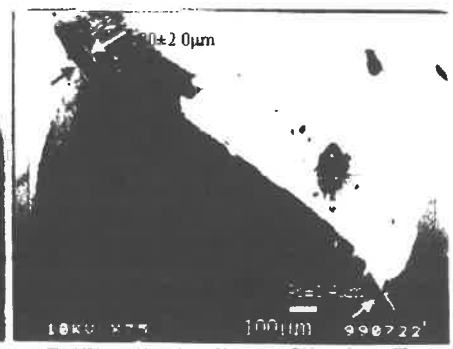

Fig.4 Worn cutting edges of L=11mm. "balanced endmill"

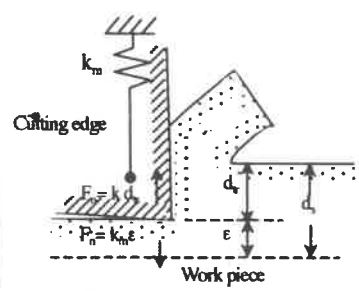

Fig.6 Milling model around cutting area

nearly equal to $S_z\cos\theta$, if $S_z \ll R$ (R; cutting radius). In the meantime, δ is constant. Tool stiffness can be representative of the relative tool stiffness k_m.

The true depth of cut ratio d_{tr+}/d_{tr-} is written as

$$\frac{d_{tr+}}{d_{tr-}} = \frac{d_{s0} + \dfrac{k_m/k}{2 + k_m/k}\delta}{d_{s0} - \dfrac{k_m/k}{2 + k_m/k}\delta} \qquad (4)$$

from eq. (2). As k_m/k is small, the true depth of cut ratio d_{tr+}/d_{tr-} is close to 1, and the disproportion of the cutting force decreases. The estimated results of d_{tr+}/d_{tr-} relative to stiffness ratio k_m/k are shown in Fig.7 in changing the parameter δ/d_{s0} in eq.(4) . It is clarified that the effect of δ on the true depth of cut diminishes to reduce the imbalanced abrasion of cutting edges, when the tool stiffness is low in this figure. The above-mentioned discussion is applied to the milling not only with small ball

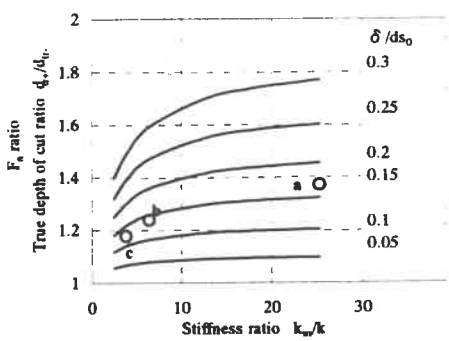

Fig.7 Influence of stiffness ratio on true depth of cut ratio

endmills but also with general endmills.

3.3 Effect of tool stiffness on tool life

The effect of the tool stiffness on the tool life is examined by changing extrusion length L as shown in Table 2, for confirming the predicted results. However, in case of tool **d**, the cutting edge was broken just after touching the endmill on a workpiece. So it was not possible to continue the tool life tests. V_{Bmax} was measured after 120m milling. The values except L in Table 2 are calculated in the following.

Table 2 Tool length and stiffness

		Tool a	Tool b	Tool c	Tool d
Length	L mm	11	18	22	26
Stiffness	k_m/k	25.	6.4	3.8	2.5
Force ratio	F_{max}/F_{min}	1.37	1.24	1.18	-
δ	μm	11	9.3	8.2	-

An example of the tool displacement in x direction is shown in Fig. 8 using tool **b**. A continuous line and a dotted line show the displacement during milling ε'_x and during free-run ε_{x0} .

In Fig.8, the followings are recognized;

1)The distance between the milling curve and the free-run curve means the elastic deformation on a cutting point in x direction.

2)2 spikes in one revolution on the milling curve mean the maximum tool displacement induced by milling at the maximum uncut chip area.

3)Cutting edges are always contact with a workpiece, because some elastic deformation always exists through the milling test.

The mean elastic deformation $\bar{\varepsilon}_{x\max}$ of the cutting edges at the rotating angles $\theta = \theta_m$ and $\theta_m+\pi$ is obtained 60.3μm in x direction. In the same way, $\bar{\varepsilon}_{y\max}$ in y direction at $\theta = \theta_m$ and $\theta_m+\pi$ is obtained as 39.1μm. Therefore, the mean normal deformation $\bar{\varepsilon}_{\max}$ of cutting edges at $\theta = \theta_m$ and $\theta_m+\pi$ is calculated as 10.59μm. k is obtained as 0.13N/μm by substituting $\bar{\varepsilon}_{\max}$=10.59μm, d_{s0}=66μm and experimented data k_m=0.81N/μm into in eq. (5).

$$\bar{\varepsilon} = \frac{\varepsilon_+ + \varepsilon_-}{2}, \quad k = \frac{\bar{\varepsilon}}{d_{s0}} k_m \qquad (5)$$

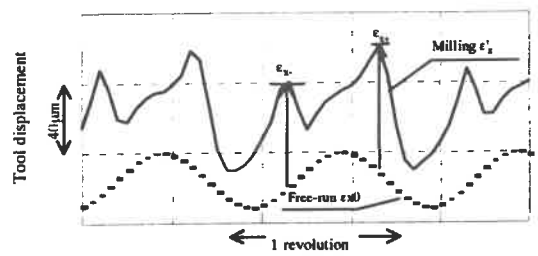

Fig8 An example of Tool displacement along x direction

The points **a-c** in Fig.7 show the milling results using tools **a-c** as δ/d_{s0} =0.15 at $\theta = \theta_m$.

A photograph of the worn cutting edges using tool **c** is shown in Fig.9. Each V_{Bmax} on 2 cutting edges is almost equal; 73±2.3, 74±3.5μm respectively, so V_{Bmax} ratio ≈ 1.01. The roughly uneven cutting stripes are observed on each flank of tool **c** and are smaller in the amplitude than that in the case of tool **a** in Fig.3. The amplitude on each flank in tool **b** indicates intermediate value between the other tools.

The relationship between k_m/k and V_{Bmax} ratio at δ =10μm is shown in Fig.10. It is verified that V_{Bmax} ratio rapidly decreases with the decrease of the tool stiffness. By lowering the tool stiffness, imbalanced abrasion of cutting edges can be suppressed to extend the tool life at the stiffness as low as a break-free ball endmill. In the range of present experiments, it is possible to achieve V_{Bmax} ratio <1.06, even if a rotating deviation δ of 10μm exists, when stiffness ratio is in

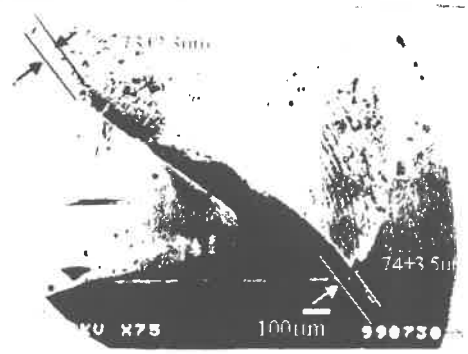

Fig.9 Worn cutting edges of tool c

$3.8<k_m/k<6.4$. V_{Bmax} was plotted in Fig.11. The error bar is the 95% confidence limit. A mean value of V_{Bmax} increases with the increase of k_m/k. This is because the uneven undulations on both flanks appear as shown in Fig.3. Especially, it tends to intensify distinctive wear on the boundary.

3.4 Effect of endmill stiffness on true cutting distance

In the reason why V_{Bmax} becomes unbalanced on both cutting edges, the true cutting distance ratio l_1/l_2 would increase, when the tool stiffness is high. Since both cutting edges are asymmetric, the lower cutting edge is detached from the workpiece in the wider rotating angle. However, the rotating angle during detaching decreases, when the tool stiffness is low, and the true cutting distance approaches to equality on both cutting edges.

Eq. (2) is lead to

$$l_1/l_2 = \frac{\cos^{-1}\left(-\frac{k_m/k}{2+k_m/k}\frac{\delta}{S_z}\right)-\theta_0}{\cos^{-1}\left(\frac{k_m/k}{2+k_m/k}\frac{\delta}{S_z}\right)-\theta_0}, \qquad (6)$$

where θ_0 is the rotating angle when a cutting edge comes into contact with a workpiece. The correlation of k_m/k with l_1/l_2, estimated with eq. (6) is shown in Fig.12, where δ is 8.2-11μm and S_z is 0.1mm. According to the figure, l_1/l_2 increases with the increase of k_m/k, and l_1/l_2 has reached 1.28 using tool **a**. This agrees with the ratio of the true cutting time on both cutting edges being 1.3, as the vector locus was analyzed in Fig.5. The increase of l_1/l_2 dominated by the tool stiffness seems to be another cause of the increase in V_{Bmax} ratio.

4. Conclusions

In high spindle speed and high feed rate milling of the hardened steel using a carbide ball endmill with 2 cutting edges, the relation between the tool life and the rotating deviation was investigated, and the followings were clarified.

1)The uneven cutting force on both cutting edges is enhanced by the rotating deviation and the tool life remarkably decreases, when the endmill tool stiffness is high.

2)The imbalance of the tool wear on both cutting edges can be suppressed to extend the tool life, when the tool stiffness is lowered as well as a break-free ball endmill.

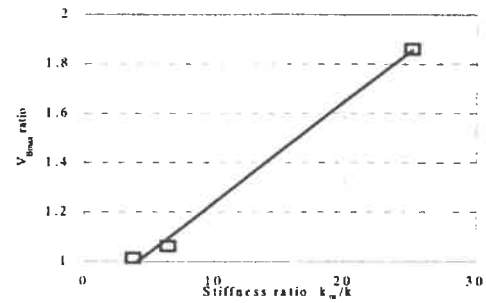

Fig.10 Influence of stiffness ratio on V_{Bmax} ratio

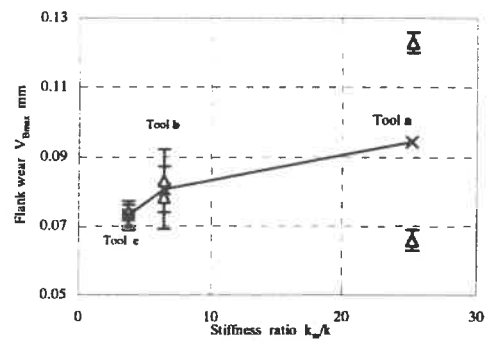

Fig.11 Influence of stiffness ratio on flank wear

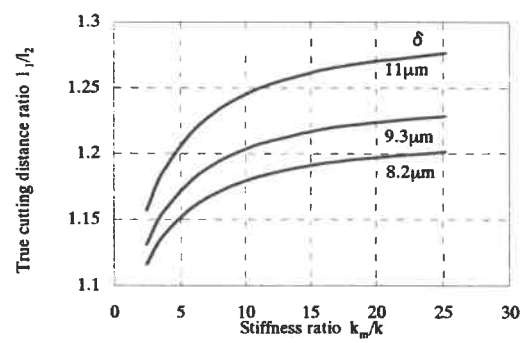

Fig.12 Influence of stiffness ratio on true cutting distance ratio

References

1) Takeoka E. "Study on End Milling of Hardened Steel by a High Speed Air Bearing Spindle, Doctoral dissertation (Univ. Tokyo) " (in Japanese) (1999).

2) Takeoka E., Saitoh H., Aida S., Miyaguchi H., Ishikawa A, Iwabe H., J. JSPE (in Japanese), 62,1(1996) 115.

3) Takeoka E., Miyaguchi T., Iwabe H., J. JSPE (in Japanese), 65,2(1999) 209.

4) Takahashi I., Anzai M., Nakagawa T., J. JSPE (in Japanese), 65,6(1999) 867.

5) Takahashi I., "Development of Ultra High Speed Milling Machine as Reciprocating Layer Machining, Doctoral dissertation (Univ. Tokyo)" (in Japanese) (1999)79.

Measurement of Cutting Tool Wear with Shape-From-Focus (SFF) Method

K. S. Moon and Z. K. Ling
Dept. of Mechanical Engineering and Engineering Mechanics
Michigan Technological University
Houghton, MI 49931

Abstract

This study presents a tool wear measuring method based on conventional tool microscope and image-processing technique. The image of a cutting edge formed by an optical system, such as a lens, contains geometric information about the shape of cutting edge. In Shape-From-Focus (SFF) methods a sequence of images is obtained by continuously varying the distance between the lens and the image detector. In this paper a tool wear measurement method based on the Shape-From-Focus (SFF) is presented. Using the technique, the accurate 3-D shape of a cutting edge can be recovered from image focus. The proposed method is verified by experiments.

Key words: Machining, Tool Wear, 3-D Measurement, Computer Vision, and Shape-From-Focus (SFF) Method

Introduction

Tool wear is one of the important problems in machining. Tool wear can cause poor quality in finish and dimensional accuracy. Research continues to predict, monitor, and prevent the tool wear (DeVies 1992, Stephenson and Agapiou 1996). Several of the common types of wear have been identified on a cutting edge. Flank wear develops where the cutting edge rubs the work piece surface. On the rake face where the chip flows over the cutting edge, a crater can develop, due to diffusion, abrasion and adhesion. This form of wear is referred as crater wear. Nose wear on the tip of the cutting edge is also caused mainly by abrasion. Depth of cut notching occurs along the cutting edge. Although the amount of these wear types can be defined three dimensionally, they are usually quantified two dimensionally because of the difficulty in measurement.

Measuring wear is a typical activity often done in machining processes. Because of the microscopic size of tool wear and the shape of the cutting edge, microscopy has been a popular means of the wear measurement. Most methods are based on measuring 2-D distance of wear land along the cutting edge using a microscope. Recently, some special computer-aided microscopes have been developed such as white-light interferometric microscopes. Although these microscopes are useful measuring very fine surfaces with micro (nano) -roughness or vertical step-like micro features, which can be found in MEMS, they may not be appropriate for measuring tool wear because of the roughness of tool wear.

In this paper a tool wear measuring method based on conventional tool microscope and image-processing technique is presented. The microscopic image of a cutting contains geometric information about the shape of cutting edge. Recovering the geometric information from a set of images sensed by a camera is an important problem in computer vision. Shape-From-Focus (SFF) methods provide one solution to the problem. In SFF methods a sequence of

images is obtained by continuously varying the distance between the lens and the image detector (Krotkov 1987, Subbarao and Choi 1995). For image in the sequence, a sharpness measure or focus measure is computed at each pixel using a small image neighborhood (e.g., high pass filter) around the pixel. At each pixel, that image frame among the image sequence, which gives a maximum sharpness measure, is determined. In this paper a tool wear is measured based on the SFF method. The method is capable of measuring 3-D shape of crater wear.

Shape-From-Focus (SFF) methods

In a microscopic image, as the magnification of a lens increase, the depth of focus decreases. As a result of this limitation it is not possible to focus on an entire detail if the height (or depth) of the specimen exceeds the depth of focus. The nature of such 3-D specimens, especially those that have a cavity or indentation in them, makes it impossible to obtain a useful understanding of their topography using conventional microscopes.

The limitation that is inherent with conventional microscopes and traditionally reduces the usefulness of microscopes in examining 3-D details proves to be advantageous in the SFF methods. In the methods, generation of a three dimensional surface can be accomplished by varying the height of the specimen and thus varying the location of the field of focus and the region of the specimen that is in focus. For each image in the sequence, a sharpness measure of focus measure can be determined. A simple measure of sharpness of an image is its gray level variance. A high pass digital filter can be used to calculate the focus measure. The digital filter can attenuate the low frequency components (blurred area) as well as enhance the high frequency components (focused area) of an image. Among the image frame sequence, a pixel which gives a maximum sharpness measure and the camera parameter values for the image frame are used to compute the distance of the object point in the specimen corresponding to the pixel.

Experimental Setup

Figure 1 shows the experimental setup. In order to employ the SFF method the height adjustments of the specimen must be accurate and repeatable. The figure shows the height adjustment assembly developed for this research. The assembly consists of a stepper motor, which has a torque rating of 35 oz-in, and a precision micrometer attached to the stepper motor with a coupling. This component controls the position of the focus plane on the specimen by adjusting the height of the microscope table that the specimen sits on with respect to the microscope lens. A PC controls the rotation motion of the stepper motor. The rotational motion is then translated to the barrel of the micrometer via a coupling. When the barrel of the micrometer rotates the spindle on the micrometer moves up or down depending on the direction of rotation. The assembly has a resolution of 0.001 mm and a range of 250 mm in the linear motion. A CCD camera was used in the acquisition of the 2-D parent images with a PC based PCPLUS image acquisition hardware and software. A PC was used to control the height adjustment assembly and run the software programs that are necessary for image acquisition and processing.

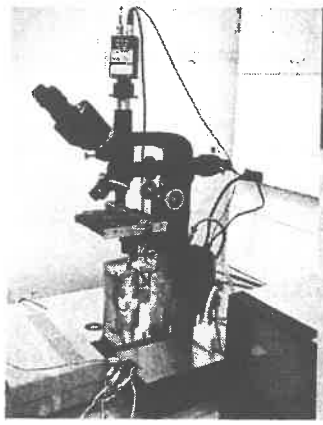

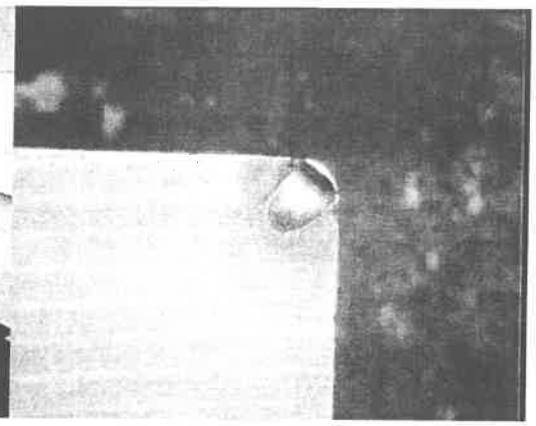

Figure 1. The Experimental Setup. Figure 2. The Carbide Insert Used for Crater Wear Measurement.

Results and Discussions

This section discusses the imaging of a portion of the crater wear on a carbide turning insert. Figure 2 shows the crater wear developed during the machining. The carbide insert was run at 400 rpm, with a feed rate of 0.0085 in/rev, at a cutting depth of :020 in on a Cincinnati – Milacron CNC lathe. The type of metal that was cut with the insert was 1040 steel. An area of the crater wear at nose that occurred during the metal cutting operation was used as the specimen for the 3-D image generation.

The 14 2-D parent images that were used to generate the 3-D image and 2 of them are shown in Figures 3. The images were taken with the 10X lens on the microscope. The height distance between the images was 10 microns (0.01 mm). From Figure 3, it is evident that the focused are of the images are not the same each other. Figure 4 shows the 3-D shapes of the crater wear constructed by the SFF method. It can be noted that the method can provide accurate 3-D shape of tool wear (crater wear). Note that the 3-D plot in Figure 4 has 10-micron height intervals, which were the height distances between the 2-D parent images. Smaller height intervals can provide more accurate 3-D image construction. However, it will cost more computation time.

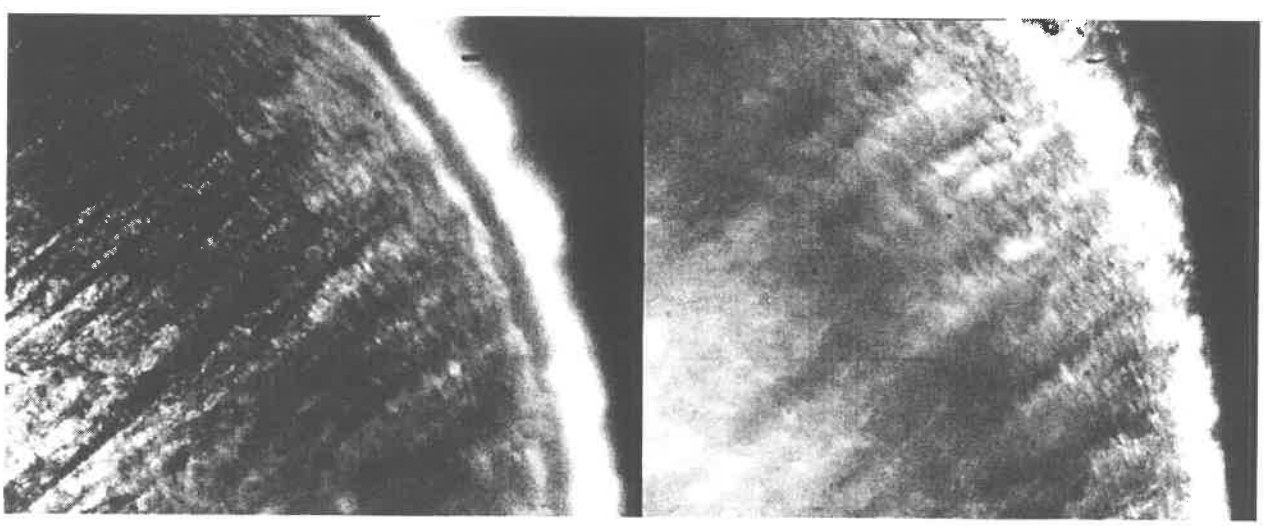

Figure 3. The 2-D Image Samples Obtained by the Experimental Setup (Image Frame 1 and 14)

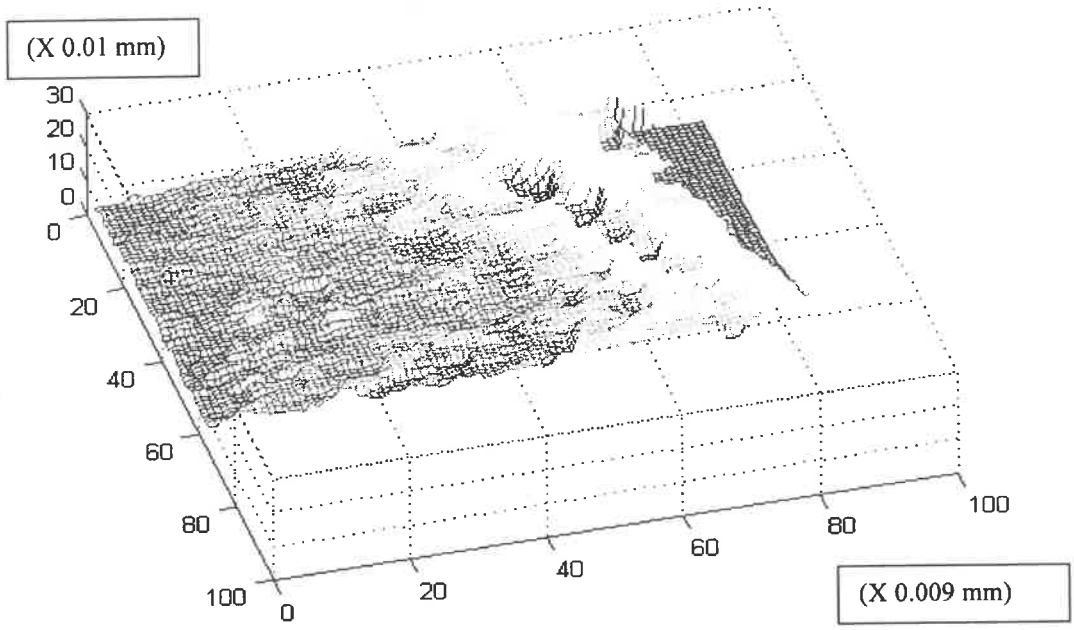

Figure 4. The 3-D Shape of Tool Wear (Crater Wear) Obtained by the SFF Method

Conclusions

The purpose of this research was to develop a 3-D imaging generation technique using a microscope and a personal computer to capture images and perform the necessary image processing for tool wear measurement. In this paper, first, the background and theory was briefly described. Next, the experimental setup was presented. The experimental setup included a computer-aided microscope for the image acquisition and 3-D image construction. The height adjustments were controlled by a micrometer barrel and spindle powered by a computer controlled stepper motor that allows very accurate height adjustment intervals. To generate the 3-D surface Matlab was used to manipulate the images so that each region in focus will correspond to the region of the 3-D plot at a specified height. The results section contained a 3-D image that were generated using the equipment and method discussed in the previous sections. It was shown that the proposed method could accurately measure crater wear three-dimensionally.

Acknowledgments

The authors are indebted to Mr. Eric Walsh at Michigan Tech. University for conducting experiments.

References

1. DeVries, W. R., *Analysis of Material Removal Processes*. New York: Springer, 1992.
2. Krotkov, E., "Focusing," *International Journal of Computer Vision*, Vol. 1, pp. 223-237, 1987.
3. Stephenson, D., and J. S. Agapiou, *Metal Cutting: Theory and Practice*. New York: Marcel Dekker, 1996.
4. Subbarao, M., and T. Choi, "Accurate Recovery of Three-Dimensional Shape from Image Focus," *IEEE Transctions of Pattern Analysis and Machine Intelligence*, Vol., 17, No. 3, 1995.

SURFACE GENERATION MECHANISM IN FLAT END MILLING

Shi H. Ryu*, Deok K. Choi and Chong N. Chu***

* School of Mechanical and Aerospace Engineering, Seoul National University, Seoul, Korea

** Dept. of Precision Mechanical Eng., Kangnung National University, Kangnung, Korea

1. Introduction

Recently, the demands for precision die and mold manufacturing technology are increasing. The quality of die and mold is determined by their surface roughness and form accuracy. In this regard, high speed machining is widely used for high productivity and high precision. In high speed machining, feed per tooth and pickfeed are very small compared to those in general machining. As a result, it is necessary to study surface texture characteristics precisely in microscopic view. End milling is an important machining process used extensively in the manufacturing industry to make flat surfaces of precision dies and molds. To date, considerable effort has been made to explain the surface generation mechanism of end milled surfaces. Recently, Sutherland[1] presented a two dimensional worst case analysis of the plane surface generated by the end cutting edges. Melkote[2] improved the surface texture model including the effects of radial rake and primary relief angles. In this study, an effective surface prediction model in plane end milling is developed. Considered in this study are back cutting by the trailing cutting edge, tool run-out, tool setting error, and tool deflection caused by cutting forces. For understanding the surface texture more efficiently, three dimensional surface topography parameters such as RMS deviation, skewness and kurtosis are used in expressing the surface texture characteristics. From a series of cutting tests, it is verified that the presented model predicts the surface texture accurately.

2. Surface Generation

Plane surface is generated by the end cutting edges of an end mill. The end cutting edge angle is necessary for avoidance of rubbing between the tool and the machined surface. The rotation of the bottom edge makes the machined surface shape as a part of a conical surface. Plane surface texture is constructed by the superposition of a series of surface generation process in feed direction. The machined surface is cut once again by the trailing cutting edge. The shape of back cutting is determined by the phase difference and tool deflection. The magnitude of phase difference is decided by the combinations of tool diameter and feed per tooth. Tool deflection reduces back cutting. Surface texture and roughness are affected by tool run-out and tool setting error. Tool run-out consists of radial run-out and axial run-out (Fig. 1). Radial run-out has a serious effect on chip load variation of each flute. Axial run-out has an important role in surface texture generation. Tool setting error also influences surface texture characteristics. Tool setting error can be decomposed as eccentricity and tilting between tool axis and spindle axis (Fig. 2).

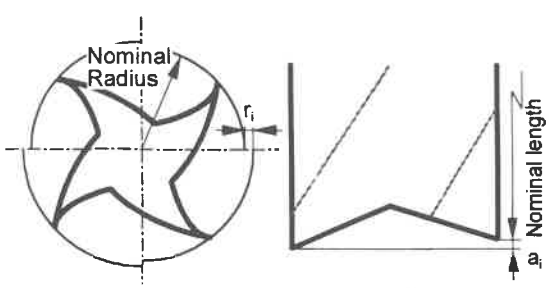

(a) radial run-out (b) axial run-out

Fig. 1 Tool run-out

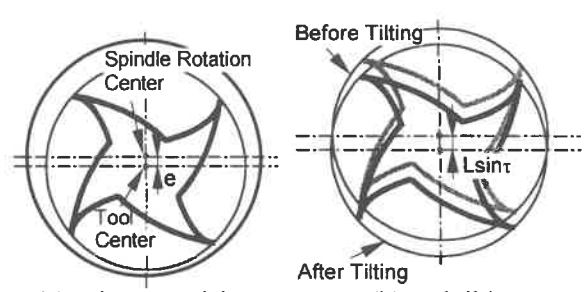

(a) axis eccentricity (b) tool tilting

Fig. 2 Tool setting error

The factors determining surface texture are shown in Fig. 3. Two coordinates are established to describe the surface generation vectors more efficiently. X axis is in the feed direction and X' axis is set in accordance with tool tilting direction. The position vectors, $\boldsymbol{P}$, $\boldsymbol{F}_i$, and $\boldsymbol{V}_i$ represent the peak point of bottom edge, cutting edge end point, and side cutting edge, respectively. The subscription i means the flute number. The vector origin, O, is the point of contact between the axis of spindle rotation center and the bottom surface of tool arbor. Surface texture is

constructed through the superposition of surface generation process with cutting edge vectors expressed by a series of vector transformations considering tool run-out and tool setting-error.

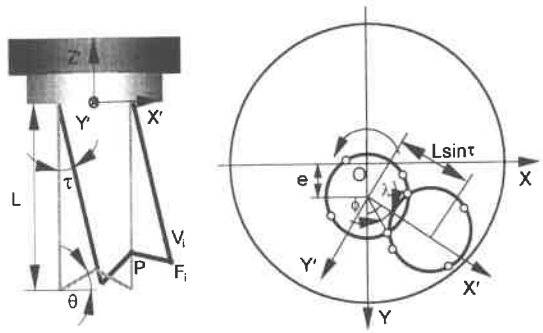

Fig. 3 Coordinate system

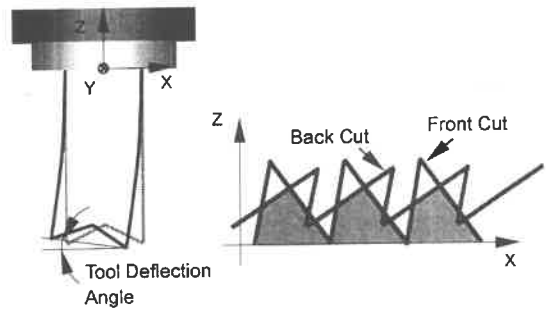

Fig. 4 Effect of tool deflection on surface generation

Tool deflection caused by cutting forces affects the surface texture and surface flatness. As shown in Fig. 4, the magnitude of back cutting is influenced by tool deflection. In this work, tool deflection angle is calculated using a cantilever beam theory under the assumption of quasi-static tool motion.[3] The area moment of inertia of flute part is assumed to be equivalent to that of a cylinder with 0.8 times tool diameter.[4]

In end milled surfaces, the R_a and R_{max} values are quite different according to measurement position and direction.[3] Hence three dimensional surface topography parameters are used for assessing the surface texture characteristics more precisely. In this paper, RMS deviation, skewness and kurtosis are used.[5] The RMS surface roughness is a widely used parameter. Skewness indicates the asymmetry of surface deviations about mean plane and kurtosis represents the peakness or sharpness of the surface height distribution. These three parameters are used to analyze surface characteristics.

3. Results and Discussion

A set of cutting experiments were carried out to verify the surface generation model. The work material, SUS 420J2 stainless mold steel, was milled by two-fluted WC end mill with 30° helix angle. Tool run-out was measured using a vision system by mounting the tool on a V-block. Tool setting error was measured by capacitance type proximity sensors in air cutting condition. Table 1 lists the measured cutter geometry parameters and setting errors. The end cutting edge angle was measured indirectly by a coordinate measuring machine from a cast NYLON MC901 workpiece machined by the tool without feed motion. Surface texture was measured using Rank Taylor Hobson Form Talysurf.

Table 1 Tool specification and setting error

Overhang (mm)	Axial run-out (um)	Radial run-out (um)	Tilting angle (degree)	Eccentricity (um)
86	1.8	23.9	0.0096	29.5

Figures 5 and 6 show the measured and the predicted surface textures in slot cutting with 0.05mm and 0.3mm axial depth of cut, respectively. In Fig. 5, back cutting occurred in all area because of small tool deflection. However, back cutting didn't occur in Fig. 6 because tool deflection is large. It can be shown that real surface textures agree well with those obtained from the simulations. Smearing of the cut surface in the middle area results from the interference between chip and sharp peaks.

Figure 7 shows the R_a and R_{max} variations according to measurement direction of end milled surface. Deflection, run-out and setting error are not considered in this simulation. Feed per tooth is 0.1mm and other tool geometry is equivalent to that used in cutting experiments. Surface roughness in the middle area is worse than that in the side area by about 2μm in R_{max} and 0.5μm in R_a. Figure 8 shows the difference of surface roughness according to the combinations of feedrate and pickfeed. In this simulation, cutting conditions are selected as having the same material removal rate and cutting time with the same tool. It can be seen that surface roughness is better at low feedrate with large pickfeed than that at the high feedrate with small pickfeed.

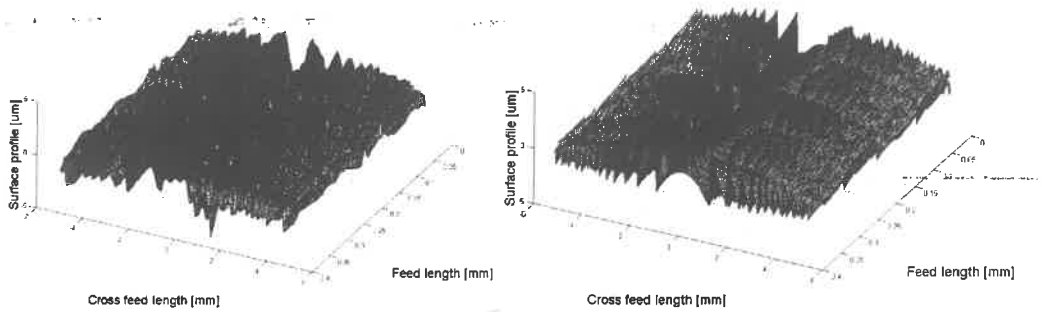

(a) measured (b) predicted

Fig. 5 Surface texture (depth of cut: 0.05mm, feed per tooth: 0.1mm)

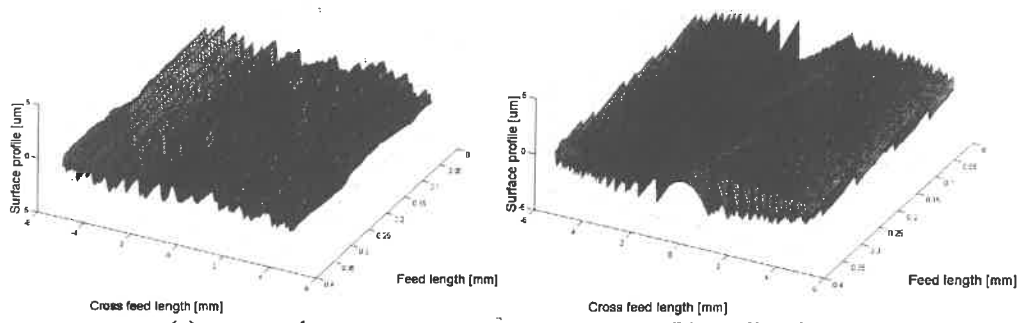

(a) measured (b) predicted

Fig. 6 Surface texture (depth of cut: 0.3mm, feed per tooth: 0.1mm)

The relationships between surface topography parameters and tool run-out and setting error are simulated in Figs. 9 and 10. As run-out increases, the RMS deviation increases and skewness and kurtosis decrease. Tool tilting increases RMS deviation but decreases skewness and kurtosis. The result means that tool tilting and run-out reduce the peaks of surface texture. But these factors are insensitive to eccentricity.

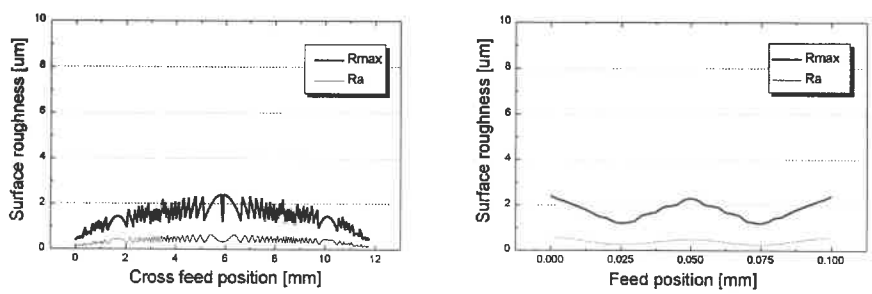

(a) surface roughness in feed direction (b) surface roughness in cross feed direction

Fig. 7 Surface roughness deviations with respect to measurement direction

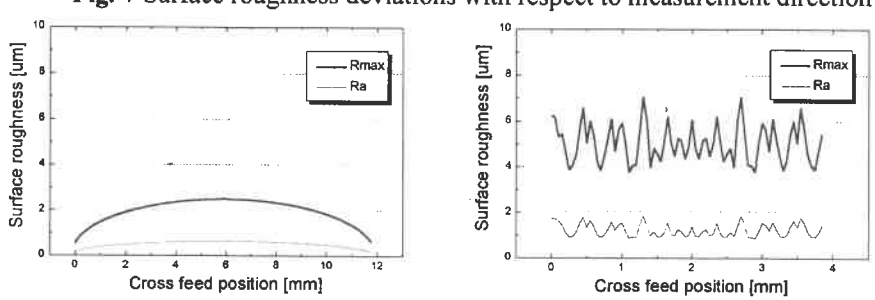

(a) feed per tooth: 0.1mm, pickfeed: 12mm (b) feed per tooth: 0.3mm, pickfeed: 4mm

Fig. 8 Effects of feed per tooth and pickfeed on surface roughness

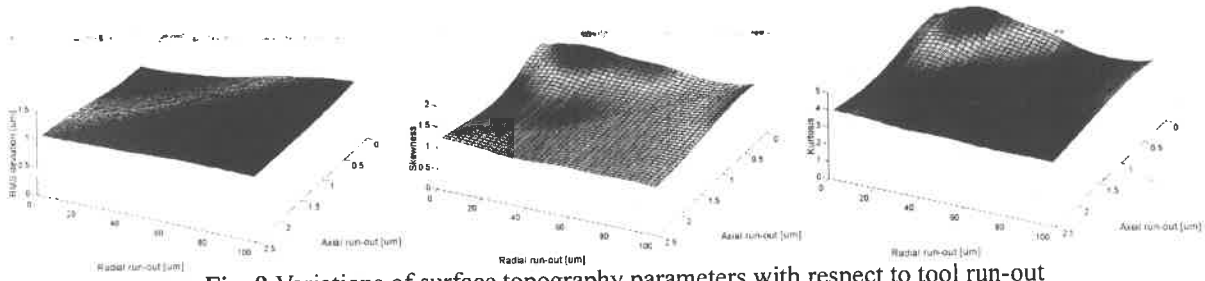

Fig. 9 Variations of surface topography parameters with respect to tool run-out

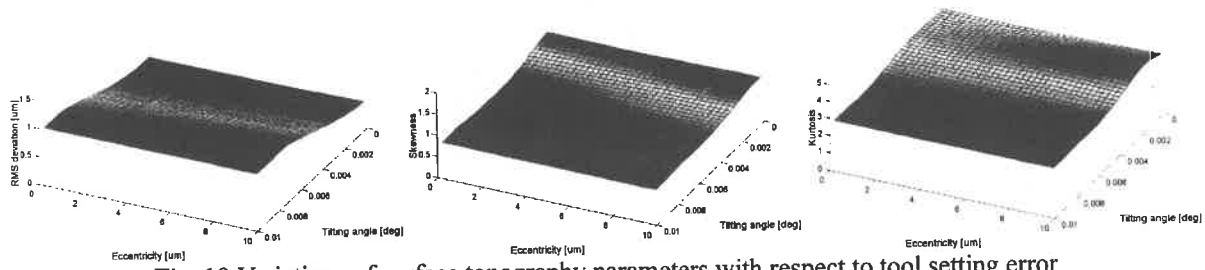

Fig. 10 Variations of surface topography parameters with respect to tool setting error

4. Conclusions

In this research, surface generation mechanism in plane machining with a flat end mill is studied. The cutting edges are expressed by the position vectors. Surface is generated through a series of vector transformations considering tool run-out and tool setting error. Developed model considers back cutting frequently observed in finishing process. Tool deflection is also included under the assumption of quasi-static tool motion using a cantilever beam theory. Surface topography parameters are introduced and used in expressing the surface texture characteristics. For a range of cutting conditions, it is confirmed that the presented model predicts the surface profile precisely. The following conclusions can be made based on the simulated and experimental work.

Surface roughness in the middle area is worse than that in the side area by about 2μm in R_{max} and 0.5μm in R_a under the test condition. Surface roughness is better at low feedrate with large pickfeed than that at the high feedrate with small pickfeed. The R_a and R_{max} values are not sufficient for representing the whole surface characteristics because these values are quite different according to measurement position and direction. So it is necessary to use three dimensional surface topography parameters. As tool run-out increases, the RMS deviation increases and skewness and kurtosis decrease. Tool tilting increases RMS deviation but decreases skewness and kurtosis. The results show that tool run-out and tool tilting reduce the peaks of surface texture. But surface topography parameters considered here are insensitive to eccentricity. This study contributes to effective cutter design, optimal cutting condition selection and tool path generation for the reduction of machining and manual finishing time especially in precision die and mold industry.

Acknowledgments

This work is financially supported by ERC/NSDM in Pusan National University.

References

1) J. W. Sutherland, T. S. Babin, "The Geometry of Surface Generated by the Bottom of an End Mill," Proc. 16th North Am. Manuf. Res. Conf., pp. 202-208, 1988.
2) S. N. Melkote, A. R. Thangaraj, "An Enhanced End Milling Surface Texture Model Including the Effects of Radial Rake and Primary Relief Angles," ASME J. of Eng. for Ind., Vol. 116, pp. 166-174, 1994.
3) S. H. Ryu, M. T. Kim, D. K. Choi, C. N. Chu, "Plane Surface Generation with a Flat End Mill," J. of. KSPE, in Korean, Vol. 16, No. 2, PP. 234-243, 1999.
4) L. Kops, D. T. Vo, "Determination of the Equivalent Diameter of an End Mill Based on Its Compliance," Annals of the CIRP, Vol. 39/1, pp. 93-96, 1990.
5) K. J. Stout, "Three Dimensional Surface Topography; Measurement, Interpretation and Applications," Penton Press, London, pp. 89-121, 1994.

Plate Topography Influence on the Nanogrinding Process

Hans H. Gatzen, Heiko Siekmann
Institute for Microtechnology, Hanover University, Germany

Key words: nanogrinding; surface machining; advanced ceramics; grinding plate conditioning; grinding plate topography.

Abstract --- Nanogrinding is an ultraprecision process capable of creating surfaces with an average roughness R_a in the subnanometer range. Since the nanogrinding process is very dependent on the grinding plate's topography, the creation of this topography has been investigated. An initial conditioning process creates an average plate roughness R_a in the order of 1 µm. A consecutive diamond impregnation process truncates the peaks by creating mesa surfaces. Differences in surface topography also influence the cutting rate of the nanogrinding process.

Introduction

Nanogrinding is an ultraprecision surface machining process similar to fixed abrasive lapping. It is applied to machining ultrasmooth surfaces on ceramic microparts [1]. The grinding tool is a soft metal plate in which diamond grit used for the nanogrinding cutting process is embedded. To accommodate a fluid film thickness necessary to support the workpiece, nanogrinding requires a considerable plate roughness. It is achieved by conditioning the plate with an abrasive medium. After the conditioning, diamond impregnation with a coplanar alignment of the diamonds' summits takes place. As in the case of other surface finishing techniques like polishing and lapping, for nanogrinding the plate conditioning process is one of the key factors for achieving an optimal workpiece surface finish.

Grinding Plate Creation and Nanogrinding Process

The nanogrinding plate has a diameter of 400 mm. For conditioning, the plate was first moistened with the conditioning slurry. The slurry consisted of a conditioning medium, dispersed in DI-water with a ratio of 250 g/ℓ. Next, a cast iron conditioning ring was positioned on the plate. Driving the plate resulted in its rotation and a revolving of the conditioning ring. The conditioning ring forced the plate's shape to conform to the negative of its envelope, thus controlling flatness. It also machined the plate by removing its top layer and roughen its surface. The surface roughness may be controlled by the appropriate choice of the conditioning medium's material and grain size.

The conditioning media used for this investigation were pumice (a mineral consisting of Al_2O_3 and SiO_2), pure alumina (Al_2O_3), and silicon carbide (SiC). Furthermore, not only the grain size of the three conditioning media was chosen differently but also the grain size of the same medium was varied (s. Tab. I).

The grinding material for nanogrinding is diamond grain which is impregnated in the nanogrinding plate. The diamond impregnation process was executed after the completion of plate conditioning. It was accomplished by running a conditioning ring with ceramic pellets on the plate surface while applying the diamond slurry. The slurry consisted by volume of 70% DI water, 20% ethylene glycol, and 10% ethanol, plus 0.3 g/ℓ of 0.5-1 micron size diamond powder. The same fluid sans diamond was later used for the nanogrinding process. After diamond impregnation, the nanogrinding plate is carefully decontaminated in an ultrasonic cleaner to remove all loose grit.

Following the reinstallation of the nanogrinding plate, 60 min. of nanogrinding experiments were conducted. The workpiece material was Altic, a material extensively used in data peripherals and consisting of 70% Al_2O_3 and 30% TiC.

Table I
Conditioning Media

Conditioning Medium	Grain Size [µm]
Pumice (Al_2O_3 / SiO_2)	0 – 50
Al_2O_3	5 - 7
Al_2O_3	9 - 12
Al_2O_3	15 - 18
SiC	4 - 6
SiC	8 - 11
SiC	15 - 18

Plate Topography

To determine the plate's topography, i.e. its flatness, roughness, and texture, various analysis methods may be applied [2]. Scanning electron microscopy (SEM) was used for gaining qualitative topography information. Plate topography measurements were conducted by white light interferometry in the vertical scanning mode (VSI). Atomic force microscopy (AFM) was applied whenever nanometer scale resolution was required.

Fig. 1 depicts the average roughness R_a of the grinding plate over the duration of the experiment for the various conditioning materials. The starting value for each curve is the roughness after conditioning, the value for t=0 min. after diamond impregnation. The following values are the respective plate roughness conditions during the consecutive nanogrinding process with the changes caused by plate wear.

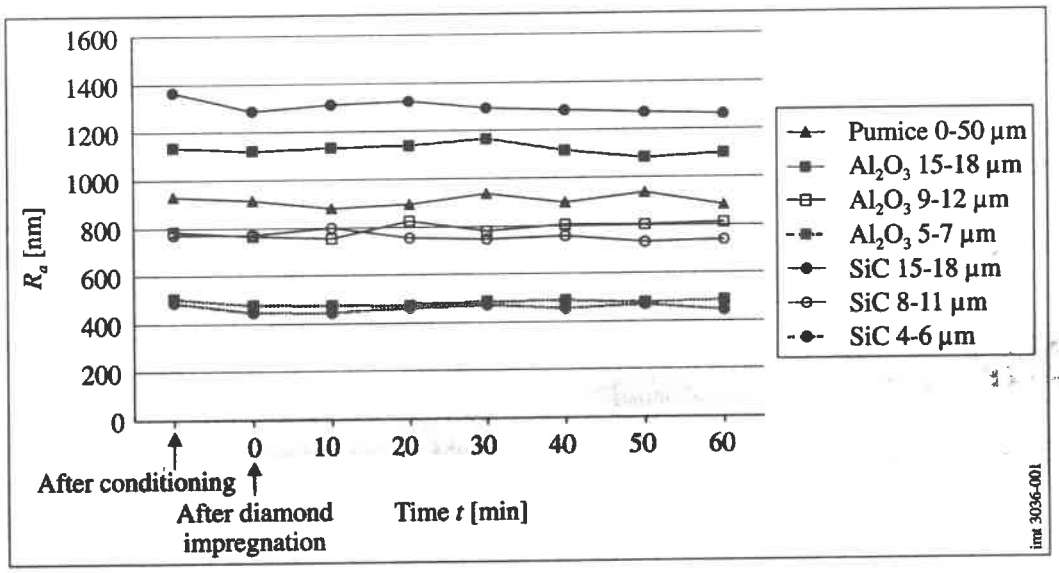

Fig. 1 Plate roughness R_a versus time as a function of the condition media (WLI measurements)

Fig. 2 sheds some light on the nature of surface topography change during the course of the experiment. It presents AFM micro topography graphs of exactly the same region of the plate surface at different states of the plate after conditioning. Left, it depicts the virgin plate after conditioning, at the center it shows the plate after diamond impregnation, and right it presents the plate at the end of the experiment after 60 min of nanogrinding. After conditioning, the plate started out with a random profile. However, the diamond impregnation process caused a very distinctive change to the topography: the conditioning ring apparently was truncating the peaks, creating some mesa type plateau surfaces in which the diamond grains are embedded. The consecutive machining process resulted in a further flattening of the peaks and thus in an increase of the mesa surface areas.

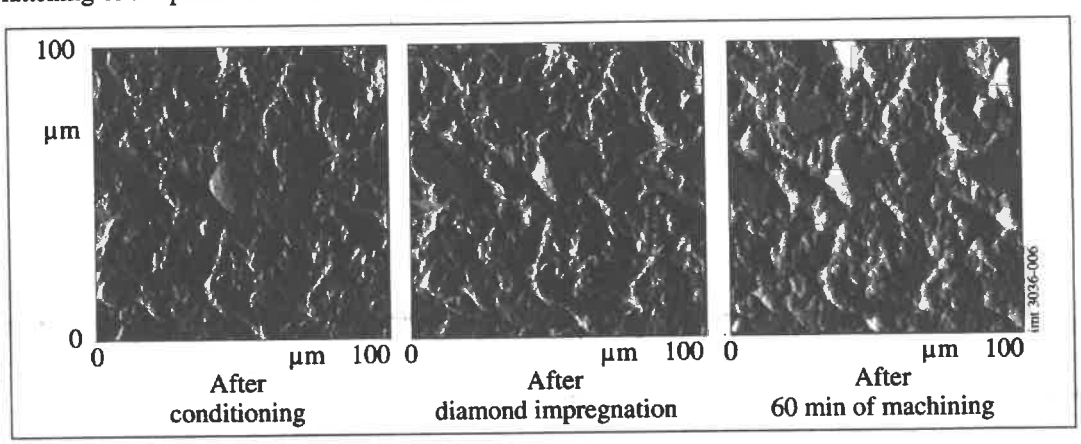

Fig. 2 Different states of the plate's surface topography (AFM measurements)

The distinctive formation of mesa surfaces provides us with a measurement challenge. The average roughness R_a is well suited to describe the plate's state after the conditioning. However, it does not lend itself to classify the changes the plate is exposed to during diamond impregnation and during the nanogrinding process. While the average roughness stays more or less constant over the machining time, the size of the mesa surfaces in which the diamond grain is embedded, does change. To describe the changes in the mesa areas the reduced peak height R_{pk} is chosen. Fig. 3 depicts the relationship between R_{pk} and the Abbott curve. The Abbott curve represents the density distribution of material M_r in the depth of the roughness profile and povides information on the shape of the profile [3, 4]. The Abbott curve was originally developed to describe tribological properties of surfaces.

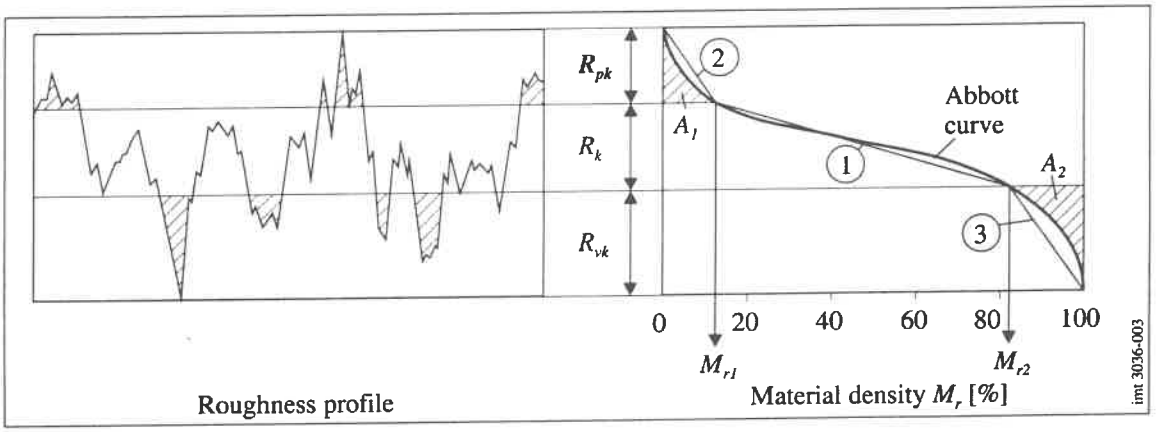

Fig. 3 Roughness profile and Abbott curve

Fig. 4 depicts the reduced peak height R_{pk} as a function of plate life. To describe the changes the plate is experiencing during the duration of the experiment the reduced peak height R_{pk}.

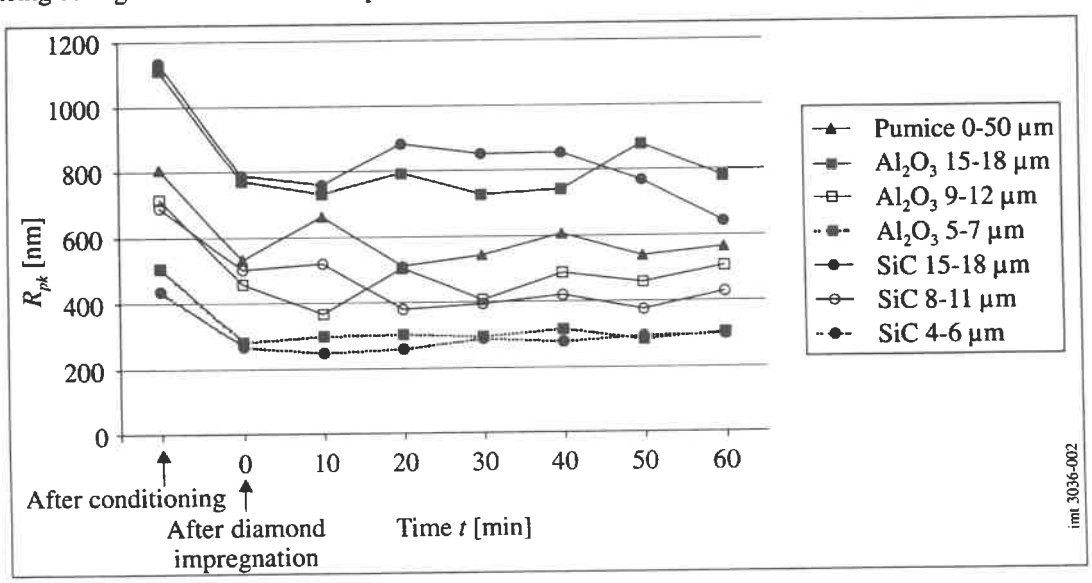

Fig. 4 Reduced peak hight R_{pk} versus time as a function of the applied conditioning media (WLI measurements)

The importance of plate conditioning apparently is to provide a plate topography with very distinctive features. First of all, the plate surface has to be rather rough. This roughness is both required to allow a peak truncation and to form mesa surfaces in which the embedded diamonds ultimately are doing the cutting. The height between mesa surface and valley has to match the thickness of the fluid film used for nanogrinding. During the nanogrinding process, the mesa surfaces are increasing their size, which means the distance "mesa to valley" is continually decreasing. Since the fluid film thickness is constant, this wear results in a lack of engagement of diamond grains at the workpiece.

Cutting Rates

To determine the cutting rates as a function of the conditioning process, nanogrinding tests were performed. Four samples of Altic with a size of 2.5 mm x 15 mm were mounted on a workpiece holder. By applying weights, a workpiece pressure of 420 kPa was achieved. The rotational velocity of the grinding plate and the workpiece holder were 45 RPM and 65 RPM, respectively. Fig. 5 shows the cutting rate results. Depending on the applied conditioning medium it differed by a factor of five between 0.2 and 1 µm/min. Apparently the variation in conditioning media result in surface topography differences causing a variance in diamond impregnation behavior.

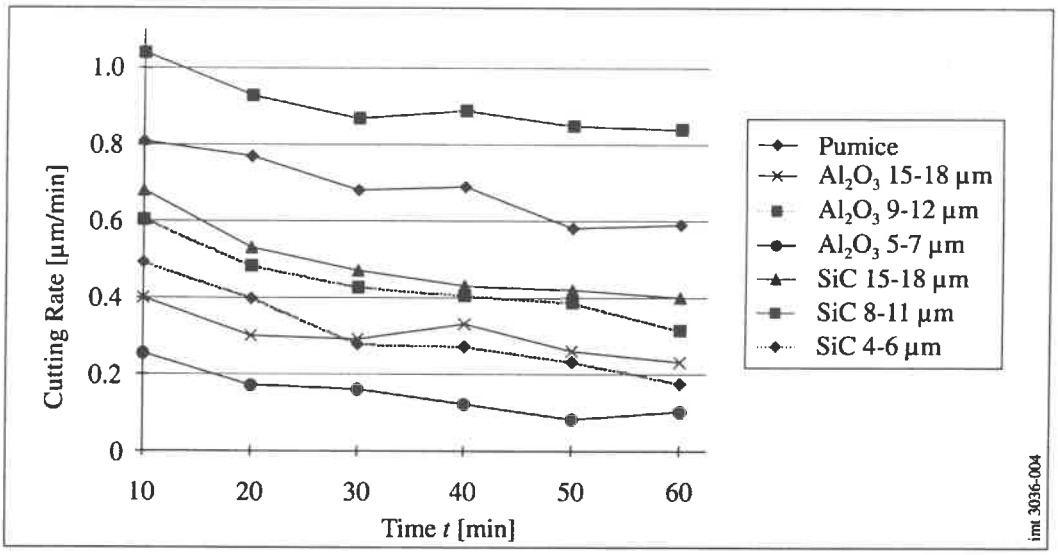

Fig. 5 Cutting rates for different conditioning media

Conclusion

By varying the conditioning media a range of plate average roughness between appr. 0.5 and 1.5 µm may be achieved. The differences in surface topography ultimately also result in different cutting rates during the nanogrinding process. While the average roughness R_a is a value appropriate to describe the plate surface topography after conditioning, this roughness value is not suited to specify the plate topography changes occurring after conditioning. A roughness value better suited to characterize the change of profile during diamond impregnation is the reduced peak height R_{pk}. This roughness value, originating from the Abbott curve, decreases during diamond impregnation and stays more or less constant during workpiece machining.

References

[1] Gatzen, H.H.; Maetzig, J.C.: Nanogrinding. Precision Engineering, Journal of the ASPE, Vol. 21, No. 2/3, pp. 134-139, 1997,

[2] Gatzen, H.H.; Maetzig, J.C.; Ruhbach, L.P.: Grinding Tool Topography Analysis by White Light Interferometry and Atomic Force Microscopy - A Comparison. Proceedings of the 9th IPES / 4th UME, Vol. 2, Braunschweig, pp. 245-248, 1997

[3] Bodschwinna, H.; Hillmann, W.: Oberflächenmeßtechnik mit Tastschnittgeräten in der industriellen Praxis. DIN Deutsches Institut für Normung e.V., Beuth Verlag, Berlin, Köln, 1992

[4] ISO 4287-1: Surface Roughness - Terminology - Part 1: Surface and its parameters
ISO 4287-2: Surface Roughness - Terminology - Part 2: Measurement of surface roughness parameters

GLASS GRINDING USING STRUCTURED SUPERABRASIVES

Robert Grejda, Eric Marsh
Machine Dynamics Research Laboratory
The Pennsylvania State University
University Park, PA 16802

ABSTRACT
In this paper, the feasibility of using microstructured (resin bond) and flexible, metal bond belts for glass grinding is explored. The results indicate that excellent surface finish can be achieved at high stock removal rate (up to 100 microns/minute infeed). Microstructured belts generate the best surface finishes, while the metal bond belts provide good surfaces with longer belt life. Grinding forces were measured and found to be typically less than 4 N.

INTRODUCTION
In this project, the performance of 3M diamond abrasive belts in glass grinding was studied. Two belt types are considered, including resin bond micro-replicated products. Previous work indicates that slow speed lapping can achieve a polished surface with minimal sub-surface damage. However, the material removal rate of the lapping process is slow and requires multiple lapping steps to achieve a finished product. Because of the relatively long processing time, this project explored the feasibility of belt grinding, which may offer substantially improved material removal rates.

Factors that influence the quality and rate at which glass parts may be ground include:
1. Coolant type, flow rate, orientation, and pressure
2. Abrasive type, concentration, bond material, geometry, and condition
3. Machine operation parameters such as grinding surface speed and infeed
4. Glass material type

In this study, special attention is given to the abrasive belt and the machine operating parameters; coolant and glass type are pre-selected based on the recommendation of 3M. In this study, four parameters were considered:

1. Abrasive belt type
   - metal flex
   - microstructured
2. Grinding speed:
   - 1000, 2000, & 3000 m/min
3. Abrasive grit size:
   - 20, 10, & 6 microns – metal bond
   - 15, 6, & 3 microns – resin bond
4. Infeed rate
   - 10, 30, and 100 microns/min

EXPERIMENTAL SETUP
The tests were carried out on a custom designed belt grinding machine designed and built by Professional Instruments. The belt grinding machine features two air bearing spindles that are used with 1 meter long, 25 mm wide diamond abrasive belts. The belt grinding spindles are capable of surface speeds of 3000 m/min (10,000 ft/min). The belts and coolant are completely enclosed by an acrylic and aluminum box. Figure 1 shows a schematic of the Professional Instruments belt grinding machine.

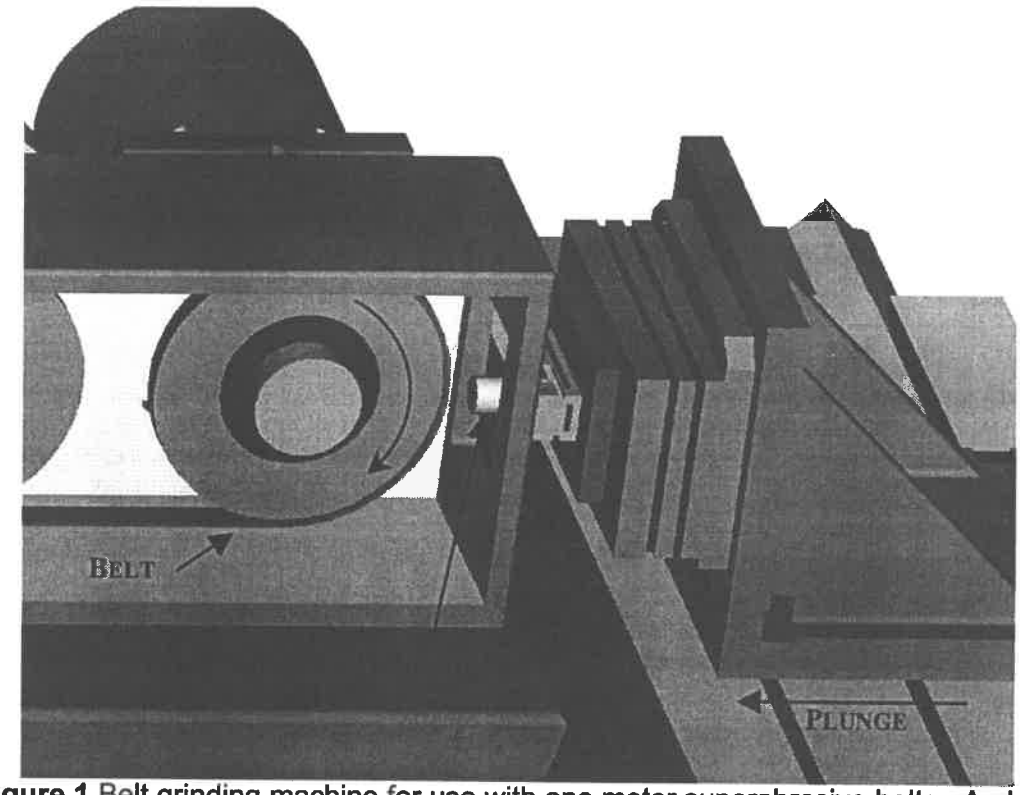

Figure 1 Belt grinding machine for use with one meter superabrasive belts. A glass workpiece is shown prior to being plunge ground against the rotating drive spindle.

Once the belt is installed in the machine, a 20 mm diameter by 4 cm long piece of soda lime glass is mounted onto a Kistler Force Dynamometer, which allows the cutting force to be monitored during grinding in three orthogonal directions.

Each plunge test is performed by first grinding enough glass to impart the concave shape of the round belt grinder drive wheel. An additional 0.25 mm of length is also removed at the infeed rate dictated by the particular grinding test. The grinding forces are recorded at high bandwidth for post processing using a Hewlett Packard 35670a Dynamic Signal Analyzer.

The surface roughness of each ground test piece is measured at 3M using a Mahr Corporation M4Pi Perthometer. The roughness is reported as the average of three measurements taken at various locations on the ground surface of the glass.

RESULTS: METAL BOND BELTS

Table 1 shows the results of the tests conducted with the metal flex belts. Visual and microscope inspections of the belts showed negligible belt wear. The grinding forces remained constant during individual grinding tests and any combination of material removal rate and belt speed yielded a low-force grind. The surface finish ranged from cloudy to slightly cloudy, depending on grinding parameters.

Table 1 Test results from metal flex belts.

Infeed (microns/min)	10			30			100			
Spindle speed (surface km/min)	1.0	2.0	3.0	1.0	2.0	3.0	1.0	2.0	3.0	
20 micron belt	1.0	1.0	1.0	1.5	2.0	NA	5.0	5.0	5.0	Normal Force (N)
Row #1	2.92	0.54	0.44	0.64	0.44	0.27	0.25	0.65	0.28	Ra (microns)
10 micron belt	1.0	1.0	1.0	3.0	3.0	1.5	5.0	6.0	4.0	Normal Force (N)
Row #2	0.23	0.42	0.45	0.19	0.25	0.23	0.63	0.35	0.21	Ra (microns)
6 micron belt	1.0	0.5	0.5	2.0	1.5	1.0	3.5	3.0	3.5	Normal Force (N)
Row #3	0.49	0.30	0.81	0.38	0.15	0.19	0.41	0.20	0.19	Ra (microns)

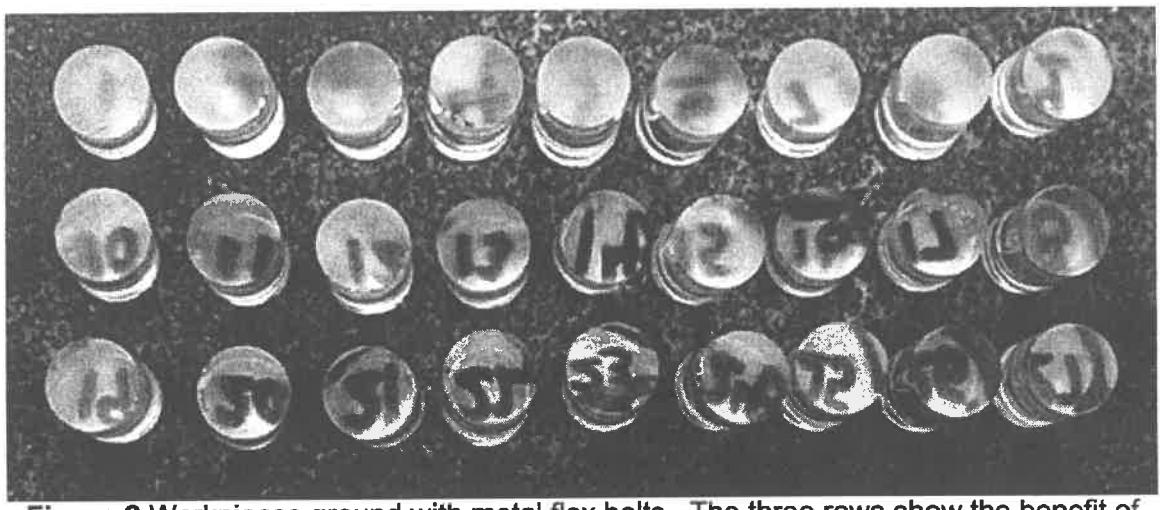

Figure 2 Workpieces ground with metal flex belts. The three rows show the benefit of decreasing the abrasive particle size, along with the benefit of *increasing* material removal rate.

Test Results: Microstructured (Resin Bond) Belts

Table 2 shows the results of the tests conducted with the microstructured belts. The high speed grinding at 3000 m/min (10,000 SFPM) was not possible because of breakdown of the belts from lack of adequate coolant exposure. Grinding forces remained constant during individual trials and variations in microstructure pattern were clearly visible in measured forces. Surface finish ranged from faintly cloudy to excellent, depending on grinding parameters.

Table 2 Test results from microstructured (resin bond) belts.

Infeed (microns/min)	10			30			100			
Spindle speed (surface km/min)	1.0	2.0	3.0	1.0	2.0	3.0	1.0	2.0	3.0	
15 micron belt	1.0	0.5	NA	2.5	1.5	NA	6.0	5.0	NA	Normal Force (N)
Row #1	0.19	0.35	NA	0.28	0.24	NA	0.19	0.53	NA	Ra (microns)
6 micron belt	3.5	3.0	NA	7.0	7.0	NA	45	17	NA	Normal Force (N)
Row #2	0.24	0.23	NA	0.17	0.32	NA	0.32	0.20	NA	Ra (microns)
3 micron belt	3.0	3.5	NA	11	NA	NA	30	15	NA	Normal Force (N)
Row #3	0.22	0.17	NA	0.20	0.37	NA	0.19	0.18	NA	Ra (microns)

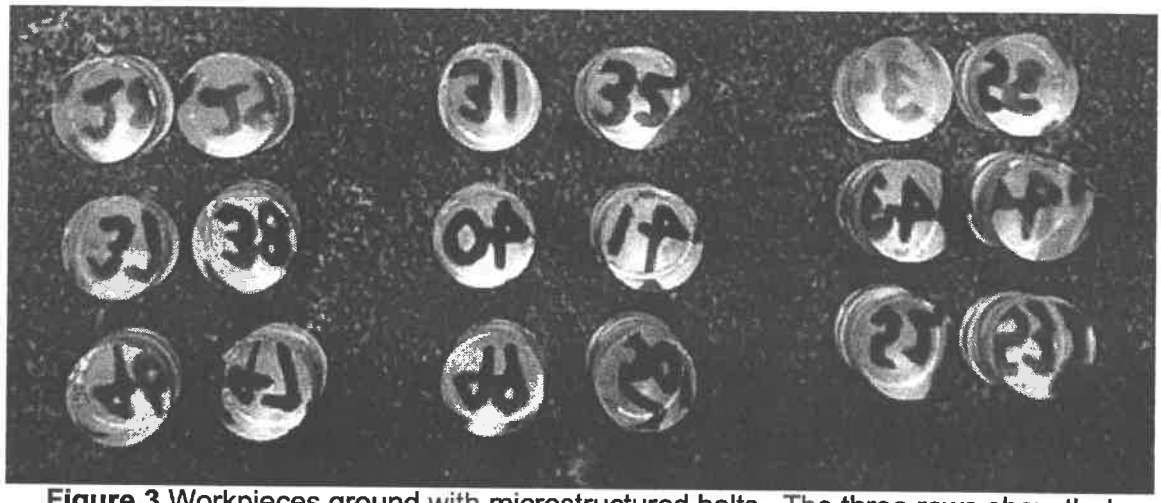

Figure 3 Workpieces ground with microstructured belts. The three rows show that excellent surface finish can be achieved with moderate abrasive particle size, moderate belt speed, and high material removal rate.

CONCLUSIONS

The current belt grinding test setup is capable of generating reasonable surface finishes on soda lime glass using the superabrasive belts with high material removal rates. For the microstructured belts, excellent results are observed for a relatively coarse (6 micron) abrasive size with a high material removal rate. Two additional observations are apparent.

1. The 30 and 100 microns/minute infeed give as good or better surface finish than the 10 micron/minute infeed.
2. Combinations of infeed (30 microns/min) and spindle speed (2000 surface m/min) exist where grinding force is very low (about 4 Newtons) and surface finish is excellent.

ACKNOWLEDGEMENTS

The authors wish to thank Dave Arneson and Steve Sanner of Professional Instruments and Karl McKeague, Mark Schwabel, and Robert Visser of 3M.

STUDIES ON THE NATURE OF SURFACE QUALITY IN PRECISION GRINDING OF CARBON STEELS

Reddy, K.H.Prasad, Nair, P.Kesavan, Ramamoorthy, B.
Indian Institute of Technology, Madras, INDIA.
E-mail: hariprasadreddy@hotmail.com

INTRODUCTION

Grinding is one of the most versatile methods of removing material from machine parts to provide precise geometry. In addition to dimensional control, the objectives in precision grinding of any component include satisfaction of surface quality or surface integrity requirements. In grinding operation, randomly distributed abrasive particles of various geometrical forms, varying in their cutting characteristics induce plastic deformation, thermal damage and consequent macro and micro residual stresses. The present work is a systematic study of the influence of grinding parameters on the surface quality (macro and micro residual stresses, phase transformations) of ground finished components.

EXPERIMENTAL DETAILS

For the present study, medium carbon steel (0.4%C) specimens of diameter 30mm and thickness of 8 mm were used. All the samples were normalized at 900^{0}C for 2 hours to maintain a uniform initial state. Horizontal spindle reciprocating table surface grinding machine was selected for the present study. Traverse grinding was carried out with different grinding conditions. Grinding conditions were selected as per Taguchi's L8 orthogonal array with different grinding parameters at different levels by considering the high and low practical limits as indicated in Table 1.

Trial No.	Depth of cut (μm)	Wheel Speed (m/sec)	Cross feed (mm)	Dressing speed (mm/min)	Coolant condition
1	5	15.4	0.01	200	Dry
2	5	30.9	0.1	700	Wet
3	10	15.4	0.01	700	Wet
4	10	30.9	0.1	200	Dry
5	20	15.4	0.1	200	Wet
6	20	30.9	0.01	700	Dry
7	40	15.4	0.1	700	Dry
8	40	30.9	0.01	200	Wet

Table 1: Orthogonal array of grinding parameters

During grinding, spark temperature at the wheel-workpiece contact zone was measured with the help of infrared radiation pyrometer by focussing very close tot he wheel-workpiece contact zone. Surface finish was measured using perthometer. Residual stresses were estimated using multiple exposure X-ray diffraction technique employing Rigaku stress analyzer in directions parallel and perpendicular to the lay. Micro strain values were determined using the X-ray line profile analysis by double line integral breadth method. Phase analysis was carried out with X-ray diffractometer using Fe-Kα radiation. Results are

analyzed and the most influencing parameter on the macro and micro residual stresses was determined with ANOVA analysis.

RESULTS AND DISCUSSION

As the depth of cut, wheel speed and cross feed increases more thermal damage will be induced on the workpiece due to increase in the wheel-workpiece contact zone temperature. In the case of fine dressing condition free cutting is not possible and it introduces more thermal damage on the surface of the work piece. In the case of dry grinding, the temperature that is developed in the grinding zone is very high compared to the wet grinding. The surface roughness and temperature values are indicted in Table 2.

Trial No.	1	2	3	4	5	6	7	8
Surface Roughness, R_a (μm)	0.43	0.62	0.66	0.95	0.73	0.44	1.49	0.35
Temperature (^{0}C)	< 400	500	400	850	500	700	750	500

Table 2. Surface Roughness and Temperature results as per Experimental Trials.

The temperature and Surface roughness values are high in the case of trial 4 and trial 7 compared to other trials. In the case of trial 4 this is due to the cumulative effect of high wheel speed, high cross feed, fine dressing condition and dry grinding. In the case of trial 7 due to high depth of cut, high cross feed and dry grinding the temperature and surface finish are having high values. From the ANOVA analysis of the observed temperature and surface finish values, cross feed, depth of cut and coolant have major influence on the temperature and surface finish. Dressing speed is the least significant factor, which has about 7% contribution on the observed values.

Figure 1 shows the variation of macro residual stress and micro strain with depth of cut estimated through Taguchi techniques. In the grinding process, the induced residual stresses arise due to three different mechanisms, viz. mechanical effects, thermal effects and transformational effects. During grinding, the contact zone can be considered as a strip heat source, that moving in the cutting direction which induces thermal damage. The residual stresses induced purely due to this thermal effect will be highly tensile in the direction of motion of the heat source (i.e. parallel to the lay) and somewhat less in the direction perpendicular to the lay. The purely mechanical effects on the other hand will introduce compressive residual stresses. The absolute magnitudes of these stresses depend up on the extent of plastic deformation. The transformational effect if present, on the other hand will introduce a highly compressive stress due to the volumetric expansion involved originating through crystallographic reasons. The resultant stresses will be an algebraic sum of the stresses due to these three effects. At low depth of cut (5μm), the influence of thermal effect is negligible as the observed temperature is very less and mechanical effect is the only factor, which introduces the residual stresses. This could be the reason for compressive nature of the residual stress at this condition. At 10μm depth of cut, the thermal effects are fairly high and the result is increase in the residual stress value. Further increase in depth of cut, increases the influence of mechanical effect. The observed temperature values showed that the influence of thermal effects is less than the previous one. Hence, the result is decrease in the residual stress. At 40μm depth of cut, due to increase in thermal effects the induced residual stresses also increased. As far as the micro residual stresses are concerned as the depth of cut increases, recovery/recrystallization effects bring down the micro strain values. The change in the peak position and breadth of the ferrite phase from the X-ray phase diffractograms provides the information for change in the microstrain values. Figure 2 shows the variation of residual stresses and micro strain as a function of cross feed. At low cross feed the contact zone temperature is less (~500^{0}C) compared to that of high cross feed (650^{0}C). Hence, at high cross feed the thermal effects influence is high and induces more tensile residual stresses. More over, the effect of

increasing the cross feed is to reduce the reheating effect of the already machined region. This implies that as the cross feed increases the thermal annealing effects become less, i.e. an increase in both macro and micro residual stresses could be expected. Figure 3 shows the variation of residual stresses and microstrain as a function of wheel speed. As the cutting speed increases, the specific grinding energy required to remove the material will increase. The thermal damage at high wheel speed is more than that of low wheel speed. These factors contribute to increase in the residual stress values as the wheel speed increases. Similar to the depth of cut condition, recovery/recrystallization effects bring down the micro strain values other wise microstrain has to increase with increase in wheel speed. Figure 4 indicates the variation of residual stresses and microstrain with coolant condition. Grinding with coolant reduces the thermal damage and reduces the forces that are developed during grinding. This could be the reason for the reduction in the residual stress values while grinding with coolant. In the fine dressed wheel condition (dressing speed: 200mm/min), the structure of the wheel will be closed grain structure and results in wheel surfaces that are not free cutting which leads to an increased thermal impact. This induces tensile residual stresses although the surface quality is improved in many cases. This can be the reason for the reduction in the residual stresses as the dressing speed increases. As the present study is based on the traverse grinding, the influence of dressing speed is very less. In the present analysis, the wheel-workpiece contact zone didn't cross the A3 line of the iron-ironcarbide diagram. Hence, the influence of transformational effects were not present The thermal damage and the plastic deformation which takes place during grinding has more influence in the direction parallel to the lay compared to that of perpendicular to the lay. This can be the reason for less residual stress values in the direction perpendicular to the lay in all the cases. The ANOVA analysis results showed that the major influencing parameter in controlling the macro residual stress is cross feed (~60%) and depth of cut (~30 %). Depth of cut (49%) and wheel speed (42%) has more influence on the microstrain than other grinding parameters.

CONCLUSIONS

During the grinding process, in the direction perpendicular to the lay high compressive residual stresses are induced when compared to that parallel to the lay. As the grinding conditions become severe (high depth of cut, wheel speed and cross feed, low dressing speed and dry grinding), the magnitude of residual stresses increases unless there is no transformational effect. The origin of induced microstrain and macro residual stresses is different from each other. The major influencing parameters on the induced macro residual stress is cross feed and depth of cut. The major influencing parameters on the induced microstrain is depth of cut and wheel speed. Dressing speed has very little influence on the induced macro residual stress and microstrain in traverse grinding. There is not much change in the existing phases due to grinding.

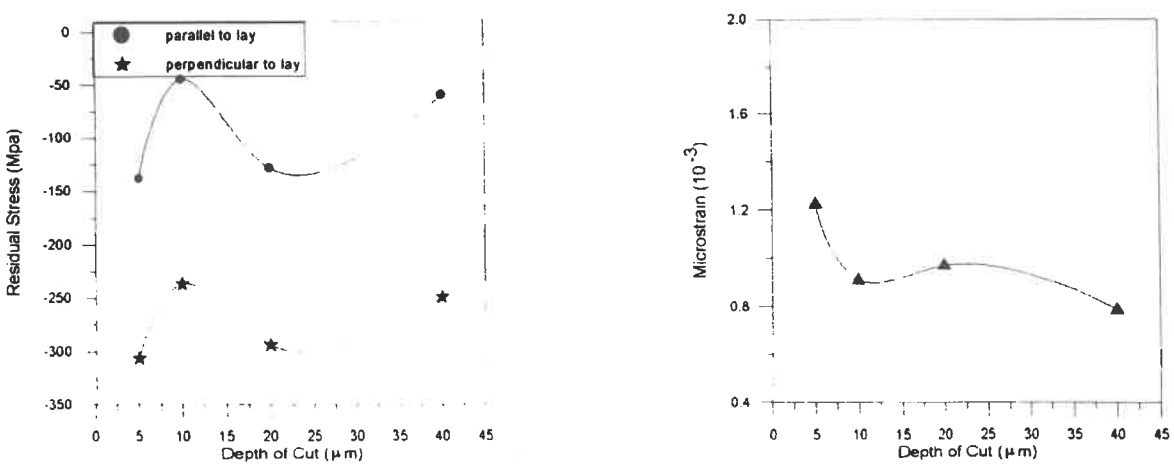

Fig. 1 Variation of macro residual stress and microstrain with depth of cut

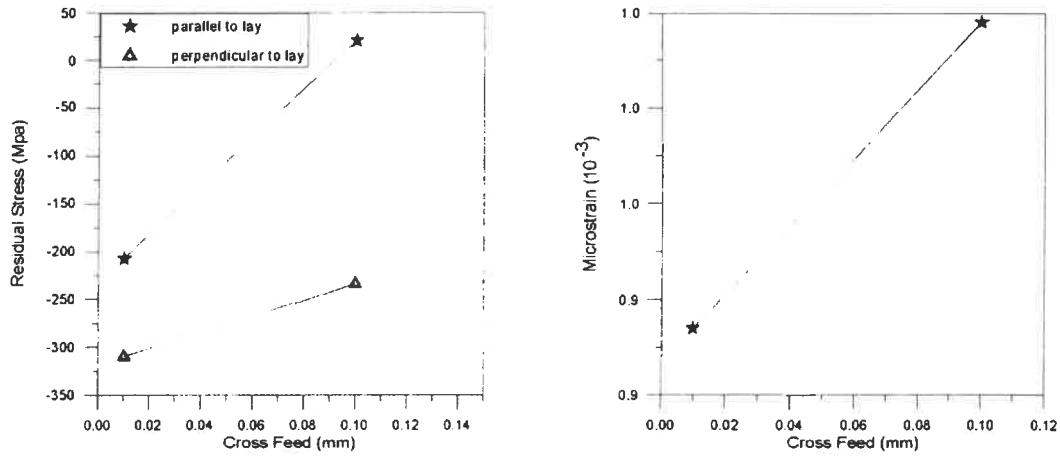

Fig:2 Variation of macro residual stress and microstrain with cross feed

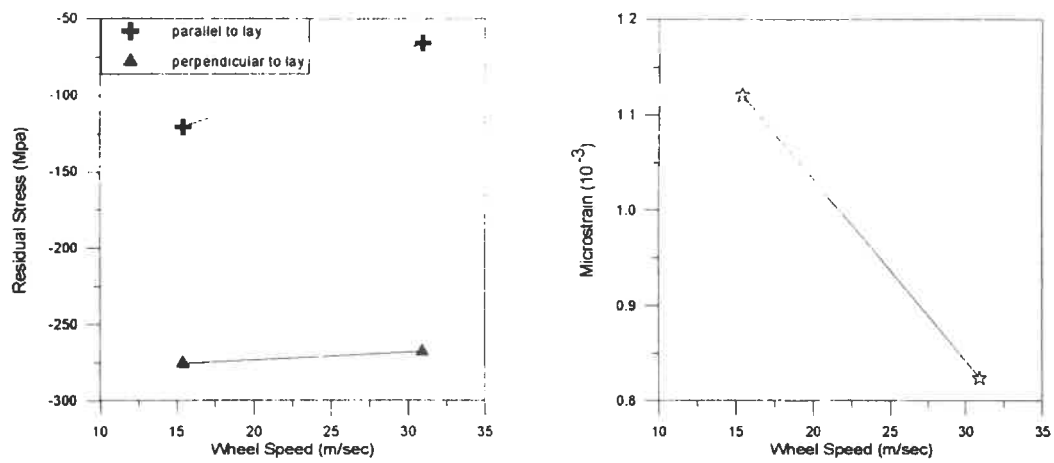

Fig:3 Variation of macro residual stress and microstrain with wheel speed

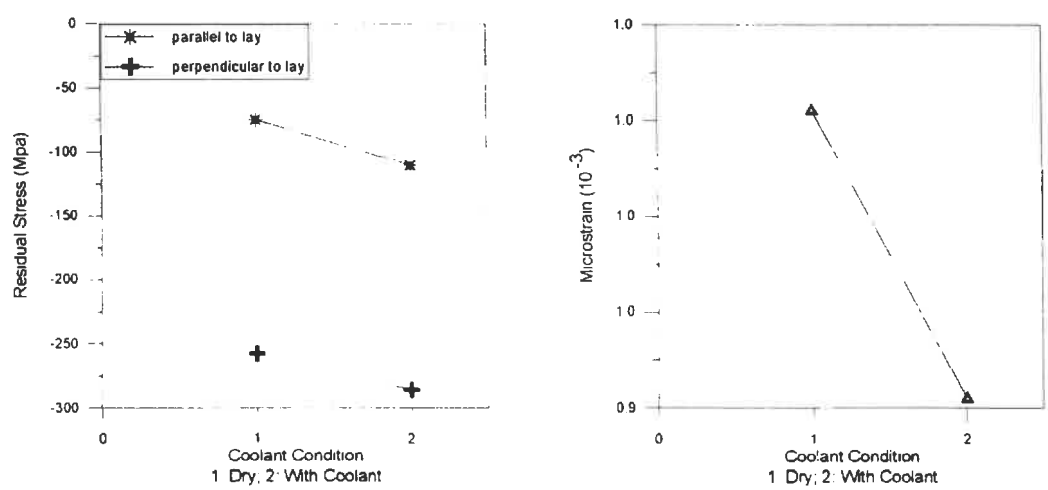

Fig. 4 Variation of macro residual stress and microstrain with coolant condition

WATERJET IN-PROCESS DRESSING (1ST REPORT)

Masatoshi HIRAO*, Masaki IZAWA*, Nobuaki IGUCHI**, Keiichi SHIRASE***,
Kunio OOTANI* and Takeshi YASUI*
* Department of Mechanical System Engineering, Kanazawa University, 2-40-20 Kodatsuno, Kanazawa 920, Japan
** Kuroda Seiko Co.,Ltd., 239 shimo-hirama, Saiwai-ku, Kawasaki, Japan
*** Department of Manufacturing Science, Osaka University, 2-1 Yamada-oka, Suita, Osaka

1. INTRODUCTION

Super abrasive grain wheels using diamond or CBN abrasive grains are increasingly applied to the state-of-the-art technology in various fields such as the vehicle, aerospace, electronics and communication industries. Super abrasive grain wheels are suitable for grinding of materials which are difficult to grind. However, they do not have self-sharpening characteristics and tend to cause loading.

Recently waterjets have been utilized in various types of processing, such as civil engineering and the mechanical, medical and food industries. it can eliminate weak parts of material by adjustment of the injection air pressure without causing damage to other parts.

This report offers a proposal of in-process dressing using a water jet. As shown in Figure 1, a water jet is injected to the surface of the grinding stone for machining material which is difficult to grind and chips are removed from the stone without damaging the stone.

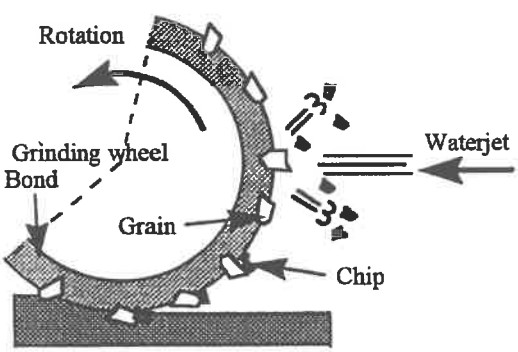

Fig.1 Principle of waterjet in-process dressing

2. MEASURING DEVICES

The configuration of the devices used in this study is shown in figure 2. A water jet device was installed on the grinder to inject water on the surface of the CBN wheel. The high pressure water was injected as water jet through the nozzle. Figure 3 shows the outline of our proposed system, an in-process dresser. A nozzle is the nozzle head,which revolves by compressed air. Since both the dresser nozzle head and the CBN wheel revolve, water jet is spread over the CBN wheel surface evenly.

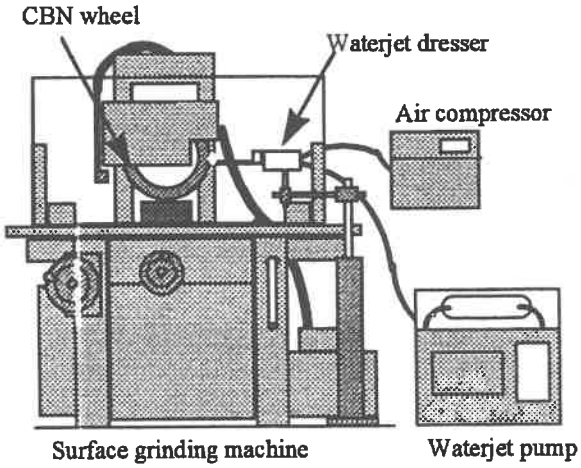

Fig.2 Constitution of experimental apparatus

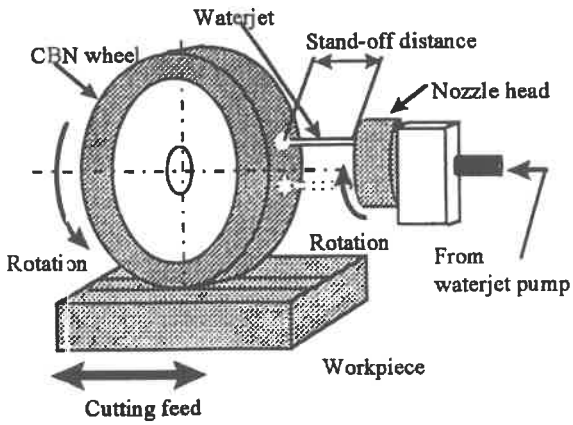

Fig.3 Outline of waterjet in-process dressing

3. METHOD

3.1 IN-PROCESS EROSION

Since water jet was used for in-process dressing in this study, it was suspected that if water jet pressure is too high, erosion may occur on the CBN wheel although chips attached to the abrasive grains can be removed. We examined the surface change and erosion of the CBN wheel along with dressing as the water jet pressure was changed when the CBN wheel was revolving with no grinding. Table 1 shows the conditions of the test.

Table1 Conditions of in-process erosion test

Grinding wheel	ϕ 180*10 mm, straight Metal bond, CBN #325
Wheel speed	33 m/s
Injection pressure of waterjet	77.2-124.5 MPa
Stand-off distance	20 mm
Nozzle diameter	0.2 mm
Nozzle revolution diameter	40 mm
Nozzle revolution number	1120 rpm

3.2 IN-PROCESS DRESSING

We examined the effectiveness of water jet in-process dressing We used a metal bond CBN wheel on the surface grinder and Ti6Al4V as a material and performed rectilinear motion grinding with water-misrable grinding fluid. At the same time, in-process dressing by water jet was conducted and the dressing effect under the different level of water jet pressure was examined. As grinding proceeded, we measured the surface roughness of CBN wheel and the surface roughness of the material. Table 2 shows the conditions of this test.

Table2 Conditions of in-process dressing test

Grinding wheel	ϕ 180*10 mm, straight Metal bond, CBN #325
Wheel speed	33 m/s
Feed speed	10 m/min.
Depth of cut	5 μm
Workpiece	Ti6Al4V
Injection pressure of waterjet	54.7-124.5 MPa
Stand-off distance	20 mm
Nozzle diameter	0.2 mm
Nozzle revolution diameter	40 mm
Nozzle revolution number	1120 rpm

4. RESULTS AND DISCUSSION

4.1 IN-PROCESS EROSION

Figure 4 shows magnified photographs of the CBN wheel surface when the injection time is approximately 300s. When the injection pressure was high, at levels such as 107.1 MPa and 124.5 MPa, there were releasing traces of CBN abrasive grains on the surface of the wheel. We suspected this was because the metal bond adjacent to the abrasive grains was eroded due to water jet impact.

Figure 5 shows the change of the CBN wheel surface roughness along with water jet injection.

when the injection pressure was 107.1 MPa and 124.5 MPa, the surface roughness increased as the injection proceeded. It was suspected that the metal bond on the CBN wheel was eroded due to water jet impact, the abrasive grains protruded and eventually

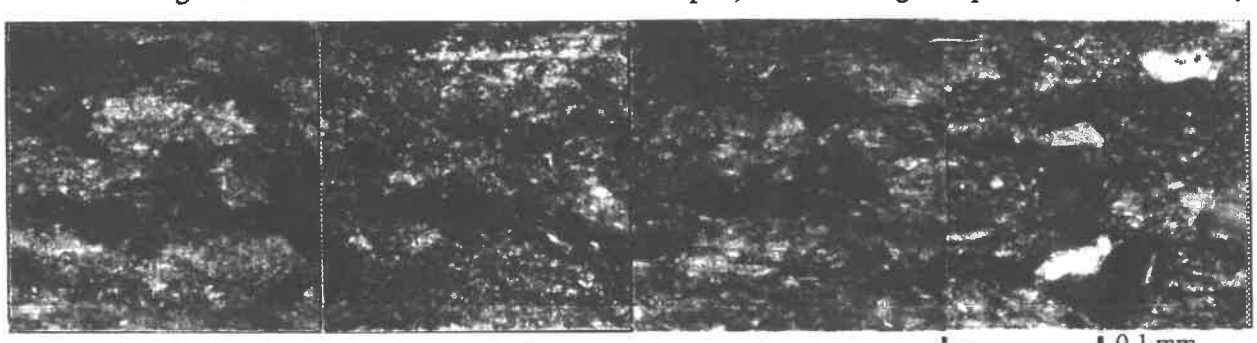

Rotation direction →

(a) Injection pressure : 72.2 Mpa Injection time : 301.0 s

(b) Injection pressure : 89.6 Mpa Injection time : 301.0 s

(c) Injection pressure : 107.1 Mpa Injection time : 301.5 s

(d) Injection pressure : 124.5 Mpa Injection time : 301.5 s

Fig.4 Photograph of wheel surface on in-process erosion test

came off the wheel, resulting in an increased *Rz* value.

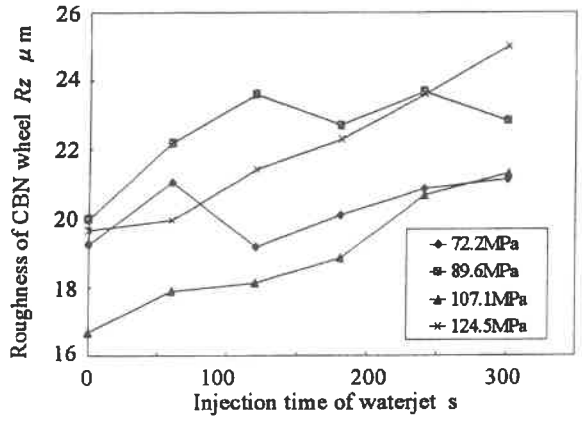

Fig5. Relationships between injection pressure of waterjet and roughness of CBN wheel

4.2 IN-PROCESS DRESSING

Figure 6 shows how the surface roughness of the material and the CBN wheel changes as grinding proceeds. The value (*z/b*) given by the volume *z* (mm^3) divided by CBN wheel width *b* (mm) is used as a parameter to indicate the degree of grinding.

When the injection pressure was 72.2 MPa, *Rz* showed low value as long as *z/b* was around 9 mm^3/mm. However, subsequently, the *Rz* value rose sharply. In light of these results, it is speculated that waterjet dressing allowed chips on the CBN wheel to be removed to some extent, but not completely and chips accumulated on the wheel and loading happened as grinding proceeded. Consequently, it was revealed that an injection pressure of 72.2 MPa was not sufficient to prevent loading in in-process dressing.

When the injection pressure was 80.9 MPa and 107.1 MPa, the surface condition was good from the beginning as long as *z/b* was 20 mm^3/mm. Subsquently, however the surface condition worsened. In the test of 80.9 MPa and 107.1 MPa, the point of z/b where the surface roughness drastically worsened was quite similar After that point, the cutting performance of the CBN abrasive grains also got worse sequentially in both cases, causing dulling and worse surface roughness. Accordingly, we predict that until *z/b* reaches 20 mm^3/mm, waterjet in-process dressing is effective and proper cutting performance was maintained without being affected by chips for the duration of the CBN wheel's lifetime.

When the injection pressure was 124.5 MPa, no loading or dulling happened at any time during the grinding process. The value *Rz* was low and a good surface condition was maintained. However, the results of the erosion test indicate that the

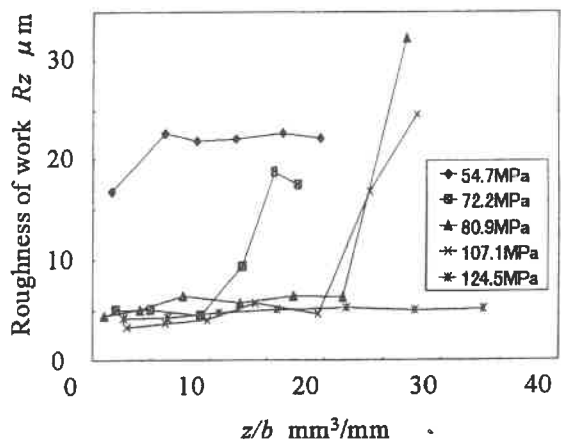

(a) Relationships between *z/b* and roughness of work

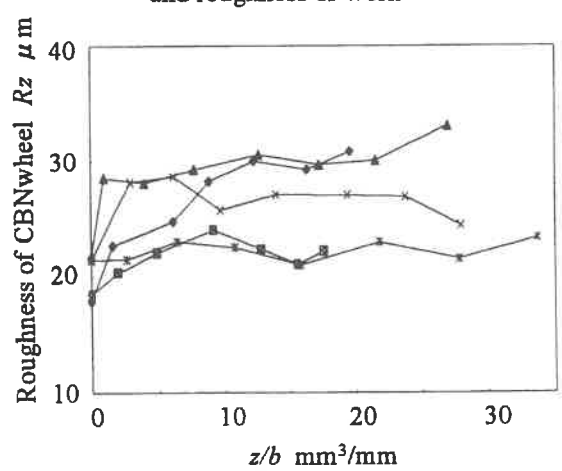

(b) Relationships between *z/b* and roughness of CBN wheel

Fig.6 Result of in-process dressing test

water jet pressure for dressing was too high so that the bond on the CBN wheel was eroded and grains came off the wheel before dulling, and that new abrasive grains protruted as cutting blades. The grinder did not lower its performance and maintained a constant surface condition without any effects caused by grinding. As such self-sharpening becomes active, grinding ratio as well as surface accuracy may decrease. Judging from the final surface condition

(a) Injection pressure: 54.7 Mpa z/b=19.6 mm^3/mm
(b) Injection pressure: 107.1 Mpa z/b=19.5 mm^3/mm
(c) Injection pressure: 124.5 Mpa z/b=33.6 mm^3/mm

Fig.7 Photograph of CBN wheel surface on in-process dressing test

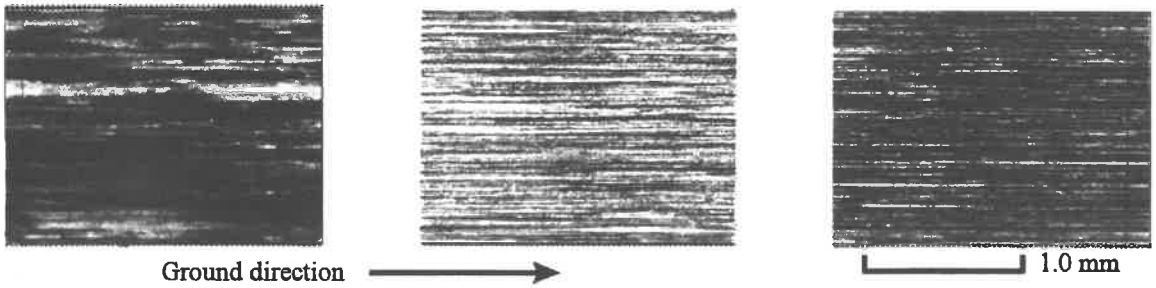

(a) Injection pressure: 54.7 Mpa z/b=19.6 mm^3/mm
(b) Injection pressure: 107.1 Mpa z/b=19.5 mm^3/mm
(c) Injection pressure: 124.5 Mpa z/b=33.6 mm^3/mm

Fig.8 Photograph of work surface on in-process dressing test

after this test, 107.1 MPa is the most suitable value for water jet pressure.

Figure 7 shows the photographs of the CBN wheel surface in this test. In the case of (a), the abrasive grains were embedded with melted chips. (b) shows that chips were removed from the wheel due to in-process dressing, while in (c), it is characteristic that the metal bond holding the CBN abrasive grains was eroded. Figure 8 shows the finished surface ground by the CBN wheel shown in figure 7. In (a), the surface was not flat because water jet in-process dressing was not effective, while in (b) and (c), a good surface condition was obtained.

5. CONCLUSION

We tested the effect of in-process dressing by means of water jet using this system. The following are the results obtained from the test.

(1) In-process dressing by means of water jet on a surface grinder with a CBN wheel in Ti6Al4V linear motion grinding was effective.

(2) Water jet removed only chips on the CBN wheel and the wheel lasted its full lifetime. A water jet pressure of 107.1 MPa was the most suitable to obtain good results.

(3) It was confirmed that if the water jet pressure is too low, in-process dressing is not effective and if it is too high, the CBN wheel becomes eroded.

REFERENCES

1) Kuniaki Unno: How to use a CBN diamond wheel, Industrial Survey Association (1991)

2) Suehisa Kawamura, Akinari yano, Masahiro Higuchi, Tadaaki Sugita: Grinding and abrasive grain processing, Kyoritu Press Co.,Ltd. (1984)

3) Kunio Takahashi: Present situation of diamond/ CBN wheel and problems to solve, Machinery and tools, What is demanded now to meet the needs, 59,1 (1992)

4) Water Jet Association: Water Jet Technical Dictioary, Maruzen (1993)

IN SITU CHARACTERIZATION OF GRINDING WHEEL SURFACE

Akira HOSOKAWA, Kunio SAKUMA and Takashi UEDA
Department of Mechanical Systems Engineering, Kanazawa University
2–40–20 Kodatsuno, Kanazawa 920–8667, Japan

1. INTRODUCTION

In grinding operation, machining accuracy and surface finish depend directly on the grinding wheel topography: shape and distribution of cutting grains on the wheel surface. Therefore, several techniques have been developed concerning the measurement of wheel topography such as profilometry, dynamometry, microscopy and others [1]. In-process measurement is actually desirable because the condition of a wheel surface is likely to change during grinding.

In this study, an in-process characterization of the wheel surface is proposed, where the grinding sound and/or vibration are analyzed by a neural network technique. The in-cycle measurements of the static wheel topography are also developed, in which a stylus profilometer and a digital image scope are equipped on the grinding machine [2, 3].

2. EXPERIMENTAL PROCEDURE

Parameters for characterizing grinding wheel surface are classified into two categories: *'static'* and *'dynamic'* parameters. In the static evaluation, the wheel surface is directly measured by means of the stylus method or the microscopic observation. In the dynamic measurement, on the other hand, the wheel condition is evaluated by analyzing the grinding sound and/or vibration, which are generated by the wheel-work interaction in the grinding zone. In this method, however, it is difficult to quantify the geometrical or morphological characteristics of the wheel surface from these signals in the present stage. Hence several conditions of the wheel surface —standard or reference condition— are formed by dressing and the grinding sound/vibration generated by these wheels are regarded as the standard signals. Then the sound/vibration during grinding are discriminated by a neural network technique.

2.1 Conventional Vitrified-Bond Alumina Wheel

2.1.1 Formation of wheel surface

In order to form a reference wheel surface, the wheel is dressed in some dressing conditions as shown in **Table 1**. The variations of tangential grinding force F_t and three-dimensional arithmetic average roughness

Table 1 Dressing conditions of A60K7V-wheel

Condition No. N_d	Dressing depth a_d μm	Dressing feed s_d μm/rev
(1)	5	20
(2)	20	20
(3)	5	100
(4)	20	100
(5)	5	200
(6)	20	200
Dresser : Single-point diamond dresser		

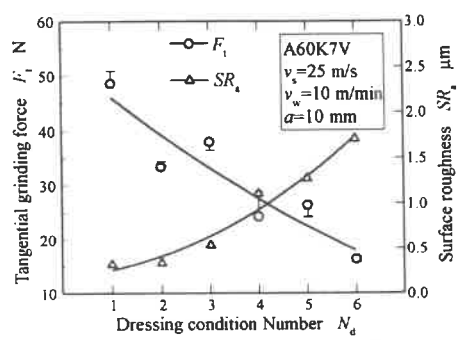

Fig.1 Variations of tangential grinding force and surface roughness with dressing conditions

SR_a with dressing conditions are shown in **Fig.1**. It is found from the figure that six different surface are generally formed although clear distinction does not appear between the condition-(2) and (3); and the condition-(4) and (5).

2.1.2 Experimental setup and conditions

Figure 2 shows the experimental arrangement. The plunge grinding of carbon steel at a constant depth of cut is carried out with six different wheel conditions presented in Table 1. The grinding sound, vibration and grinding forces are measured by the noise level meter, accelerometer and piezoelectric dynamometer, respectively. The acceleration pickups are fixed on the high-stiffness mount base as shown in Fig.2 in order to avoid the vibration effect of the dynamometer. Three one-pass plunge grinding tests are done in each wheel condition. The experimental conditions are summarized in **Table 2**.

2.2 Superabrasive Resinoid-Bonded Diamond Wheel

2.2.1 Formation of wheel surface

Because of the non-porous type grinding wheel, the resinoid-bonded diamond wheel is firstly trued by the metal-bonded diamond block truer and then the bond material is removed by dressing with WA-stick so as to make appropriate chip pocket. Here, four reference surface conditions are formed having the different depth of chip pocket. In this case, unlike the alumina wheel, there is little difference of cutting edge geometry in each wheel surface.

2.2.2 Characterization of wheel topography by stylus method and optical microscopy

A profile trace along the circumference of the wheel is measured by a stylus coupled to a displacement transducer mounted on the grinding machine, and the average depth of chip pocket h_p is calculated from the digitized profile data [2]. **Figure 3** shows the definition of h_p and examples of wheel profiles of four reference conditions. It is found that the depth of chip pocket changes in four steps within the rage of approximately 9~25 μm at about 5 μm intervals. The morphology of abrasive grains is observed by the digital image microscope and the distribution of cutting edges is calculated by means of an image processing method [3].

The grinding experiments are carried out in a similar way to that with the alumina wheel as described in §2.1.2. The truing and dressing conditions are listed in **Table 3**.

3. EVALUATION OF GRINDING WHEEL SURFACE BY MEANS OF NEURAL NETWORK TECHNIQUE

The frequency spectrum of grinding sound emitted from the standard wheel surface are discriminated by the neural network learning algorithm. The network program is constructed on the MATLAB® software. The

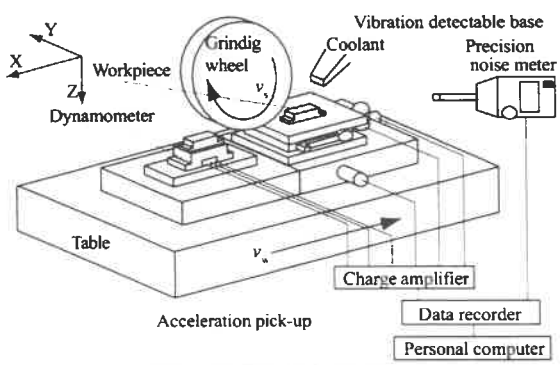

Fig.2 Experimental setup

Table 2 Experimental conditions

Grinding wheel	A60K7V	SDC140N75B
Workpiece	S55C(AISI 1055)	HIP-Si_3N_4
Wheel speed v_s m/s	25	25
Work speed v_w m/min	10	10
Depth of cut a μm	10	2
Grinding fluid	Water-based solution type	

Table 3 Truing and dressing conditions of SDC140N75B-wheel

Truing	Dressing
Truer : SD100Q100M-block	Dresser : WA180H7V-stick
Truing depth a_t 2 μm	Dressing depth a_d 50 μm
Table speed v_w 10 m/min	Table speed v_w 10 m/min
Truing feed s_t 50 μm/rev	

parameters of the neural the network used are listed in **Table 4**. The input signal is described [501×N] matrix which consists of N column vector with 501 elements of SPL (Sound Pressure Level) values within a range of 0 to 10 kHz at 20 Hz intervals. Here N is the number of reference conditions (N=6: alumina wheel, N=4: diamond wheel). The network produces [N×N] diagonal matrix. The grinding sound discrimination is judged by the position of the maximum value on the i-th row against the j-th column in the output matrix. In this experiment, the multiple layer networks are constructed and the learning algorithm is error-back-propagation (EBP) method.

It is necessary to determine the optimal learning rate and number of cells in hidden layer by learning experiments. In this study, the number of epochs required for network convergence is measured under various network configuration in which the number of cells in hidden layer and learning rate are changed in the range of 100~500 (alumina wheel) / 50~400 (diamond wheel) and 0.001~0.0005 (at 0.0003 intervals), respectively. Learning stops when either the number of epochs have attained a maximum value of 3000 or the network sum-squared error has dropped below the error goal of 0.1.

4. EXPERIMENTAL RESULTS

4.1 Conventional Vitrified-Bond Alumina Wheel

Figure 4 shows the typical frequency spectrum of the grinding sound for six reference conditions of the wheel surface. All spectrum curves have the similar pattern showing the almost flat response in the whole range although small peak appears at 2~3kHz. According to this figure, it is obvious that we can not distinguish these sounds aurally.

Figure 5 represents the learning result of the neural network as a mesh plot when the frequency spectrums of the grinding sound are discriminated. As the diagram indicates, learning begins to converge when the

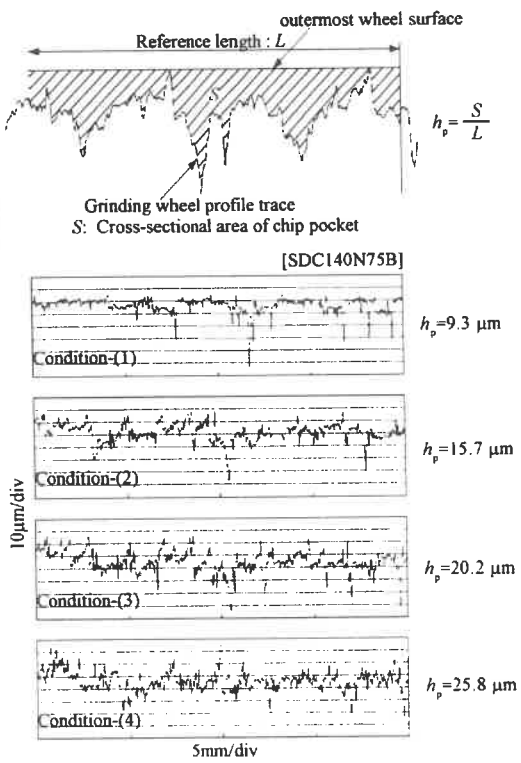

Fig.3 Definition of depth of chip pocket h_p and typical circumferential profiles of dressed wheel surface

Table 4 Parameters of neural network configuration

Structure	Multiple layer network
Hidden layer	1
Cell	Static analog model
Learning algorithm	EBP:Error Back Propagation
Transfer function	Log-sigmoid
Number of cells in input layer	501
Number of cells in hidden layer	100~500
Number of cells in output layer	6 or 4

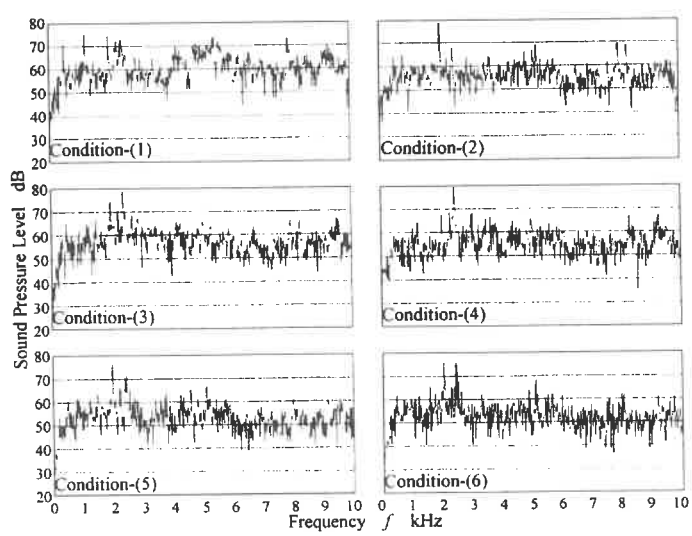

Fig.4 Frequency spectrum of grinding sound for six kinds of grinding wheel conditions

number of cells in hidden layer is more than about 100 and the number of epoch decreases as the number of cells increases. In addition, the larger a learning rate the less time a network needs to be trained. However, if the learning rate is too large learning becomes unstable, which is the general tendency of a neural network [4]. On the whole, the grinding sound can be identified under the optimum network configuration in such that the learning rate is set in the range of 0.002~0.0035 and the number of cells in hidden layer is not less than 300.

The output matrix for the discrimination of grinding sound is presented in **Fig.6**. In this matrix, the largest values are positioned diagonally, which means that the wheel surface is successfully recognized. From the above results, it can be said that the condition of the wheel surface is discriminated by the neural network technique in spite of acoustically indistinctive situation. After re-dressing, however, the network classifies into three categories: condition-(1), (2)~(5) and (6). One of the reasons for this result is that the equivalent wheel surface is not created by dressing. There is room for further investigation on the learning algorithms of the network.

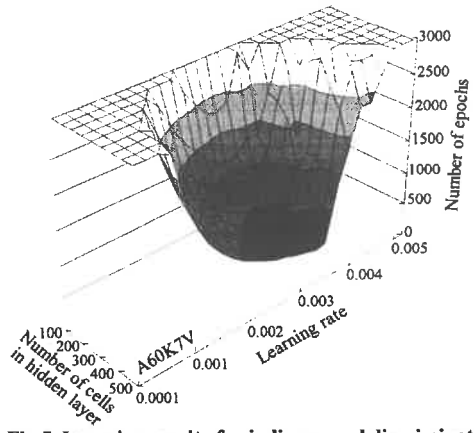

Fig.5 Learning result of grinding sound discrimination

Cond.-(1)	Cond.-(2)	Cond.-(3)	Cond.-(4)	Cond.-(5)	Cond.-(6)
0.6364	0.0577	0.0834	0.0482	0.0164	0.0287
0.1063	**0.2657**	0.0533	0.0605	0.1109	0.0591
0.0557	0.1949	**0.4043**	0.0432	0.0674	0.0993
0.0957	0.0434	0.0858	**0.4275**	0.0751	0.0533
0.0186	0.0615	0.0344	0.1550	**0.5972**	0.0513
0.0286	0.0411	0.0765	0.0355	0.0770	**0.7497**

Fig.6 Output matrix of grinding sound discrimination

4.2 Superabrasive Resinoid-Bonded Diamond Wheel

In the case of the resinoid-bonded diamond wheel, the number of cells in output layer is four because four kinds of standard wheel conditions are formed. The learning result of the neural network is shown in **Fig.7**, in which stable learning are obtained as in the case of the alumina wheel.

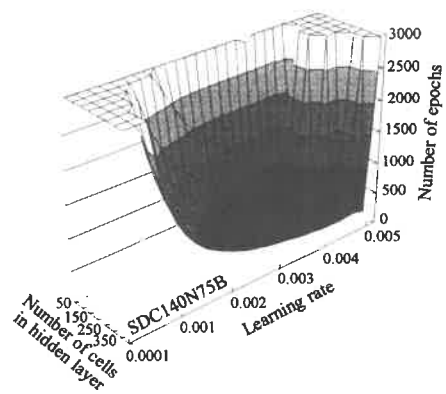

Fig.7 Learning result of neural network for SDC140N75B-wheel

5. CONCLUSIONS

The neural network technique is effective to recognize the difference of the grinding wheel surface for both conventional alumina wheel and superabrasive diamond wheel by analyzing the grinding sound insofar as the wheel topography is relatively widely changed by dressing procedure. This method is found to be useful for in-situ characterization of the wheel surface.

REFERENCES

[1] Verkerk, J., "Final Report Concerning CIRP Cooperative Work on the Characterization of Grinding Wheel Topography," Annals of the CIRP, Vol.26, No.2, 1977, pp.385–395.

[2] Nakazono, H., Yasui, H., Kurusu, M. and Hosokawa, A., "Studies on Dressing of the Resin-Bond CBN Grinding Wheel (1st Report)," Bull. JSPE, Vol.24, No.1, 1990, pp.51–56.

[3] Hosokawa, A., Yasui, H. and Nagae, Y., "Characterization of Grinding Wheel Surface by Means of Image processing," Proc. CESA'96 IMACS Multiconference, 1996, pp.428–32.

[4] Uesaka, Y., "Fundamental Mathematics for Neurocomputing," Kindaikagaku-sha, 1997.

Truing and Dressing of Diamond Wheels for High Speed Grinding of Brittle Materials

Han HUANG
Gintic Institute of Manufacturing Technology, Singapore 638075

1 Introduction

Wheel preparation generally includes truing and dressing. The truing and dressing efficiency strongly influences the grinding efficiency as it is often required during the course of a grinding process to keep the cutting grains sharp to maintain a consistent material removal rate [1-3]. To achieve an efficient and appropriate truing and dressing for diamond wheels, (i) the effect of truing and dressing conditions on the truing and dressing efficiency and wheel surface topography and (ii) the effect of truing and dressing conditions on the subsequent grinding process must be taken into accounted. This requires systematic investigations of various truing and dressing methodologies and their effects on the subsequent grinding process. In the present paper, we report a systematic study of two types of truing and dressing methods, motor driven mild steel and silicon carbide rollers, for preparing vitrified diamond wheels. After truing and dressing wheels were then used to grind ceramics at ultra high speeds to examine the corresponding grinding performance. The two types of rollers are compared in terms of truing or dressing efficiency and grinding performance.

2 Experimental Set-up

The truing and dressing system is illustrated in Fig. 1. During truing/dressing, a mild steel or silicon carbide (GC80M7V) roller was traversed across a grinding wheel at a feed rate with a down feed per pass. The vitrified diamond wheel (SD120J100C2) has a diameter of 200 mm and a width of 6 mm. Down-cut truing/dressing was adopted. The truing/dressing force was measured by a dynamometer. The run-out was measured by a capacitance sensor. The truing/dressing conditions for studying the truing/dressing efficiency are listed in Table 1. It should be noted that the truing/dressing was carried out using the same motor driven device for either steel or SiC rollers. The difference between them is only the values for each condition. In this experiment, a reasonably wide range for each condition was selected to cover both truing and dressing. Thus, unless particularly mentioned, 'dressing' is used to represent both truing and dressing to simplify the terminology. Grinding tests was conducted to examine the wheel performance after dressing. During grinding the creep rate was fixed at 320 mm/min. Various speeds from the conventional speed of 30 m/s to a high speed of 120 m/s were applied. The truing and dressing conditions for studying the wheel grinding performance are listed in Table 2.

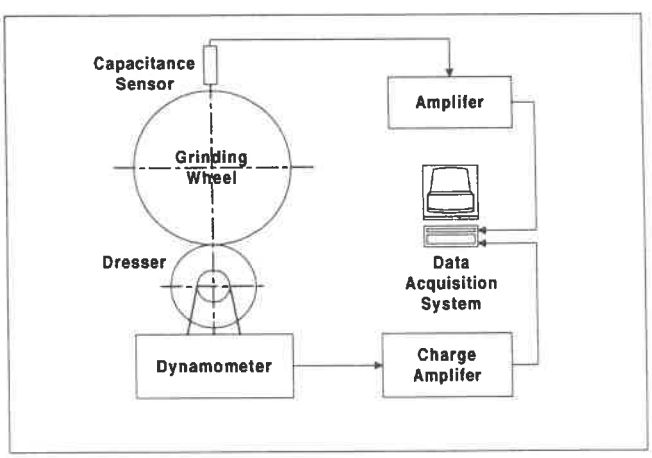

Figure 1: Schematic of the truing and dressing system.

Table 1: Truing/dressing conditions for studying truing/dressing efficiency.

Conditions	Sign	Unit	Variation Range	
			SiC	Steel
Wheel Speed	V_w	m/s	6.28	10-30
Roller Speed	V_r	m/s	2-4	5
Cross feed rate	f_d	mm/min	100-300	100-300
Down feed per pass	a_d	μm	0.2-30	0.2-3

Table 2: Truing/dressing conditions for grinding partially stabilized zirconia (PSZ).

Wheel preparation		Roller type	V_r/V_w (m/s/m/s)	f_d (mm/min.)	a_d (μm)	Dressing passes
Truing (dry)		Steel	5/10	200	2	40
Dressing (with dropping coolant)	1	SiC	3.8/15.2	100	2	200
	2	SiC	3.8/11.2	200	20	40
	3	Steel	5/30	100	2	80
	4	Steel	5/15	100	2	80

3 Results and Discussion

3.1 Effect of Truing/Dressing Conditions on Wheel Run-out and Topography

In Fig. 2, the run-out of the wheel is plotted as a function of the truing time for both SiC and steel rollers. It is seen that the run-out decreases more rapidly when using the steel roller than using the SiC roller, corresponding to a higher truing rate. The run-out reaches a saturated value for both rollers, with the SiC roller having a smaller run-out.

The wheel topography after dressing was examined using the Scanning Electron Microscope (SEM). The SEM examination revealed that there exist some differences between the wheel topographies dressed by the two rollers. On the wheel dressed by the SiC roller diamond grains with micro-cutting edges were more frequently observed than the wheel dressed by the steel roller. For the wheel dressed using the steel roller, larger and sharper cutting edges were easily observed.

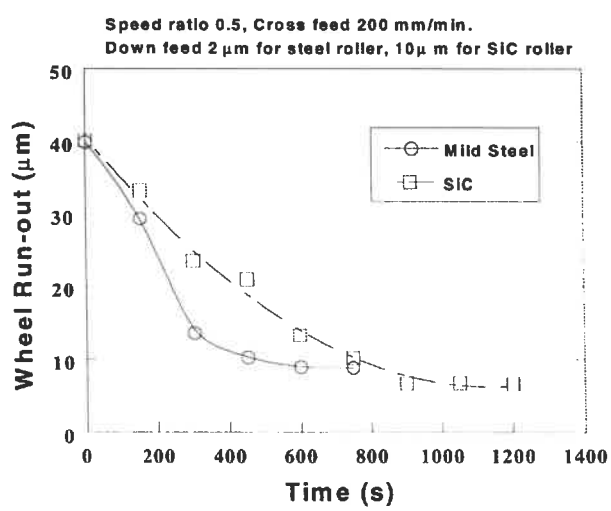

Figure 2: The run-out decreases with the progress of truing.

3.2 Effect of Dressing Intensity on Dressing Efficiency

Dressing ratio and rate are used to evaluate the dressing efficiency. The dressing ratio is the ratio of the material removal volume between the wheel and the roller. The rate equals to the material removal

volume of the wheel over the dressing time. The dressing intensity, which is defined as the resultant force acting on an individual grain, is used to characterize the dressing process. The dressing ratio and rate for various conditions listed in Table 1 are plotted as a function of the intensity in Fig. 2 and 3. It is seen that when using the SiC roller, all the data almost lie on a common curve for various dressing conditions, indicating that the intensity does give a good measure of the dressing efficiency. The data obtained using the mild steel roller are not dropping on one common curve. However, when classifying those data into two categories according to their speed ratios, both the ratio and rate exhibit good relationships with the intensity, regardless of the other dressing conditions. In summary, for 'truing' the speed ratio between the wheel and the roller should be larger than 0.5 for both mild steel and SiC rollers in order to achieve a sufficiently large removal rate. For 'dressing', the speed ratio should be decreased to reduce the removal volume of the wheel.

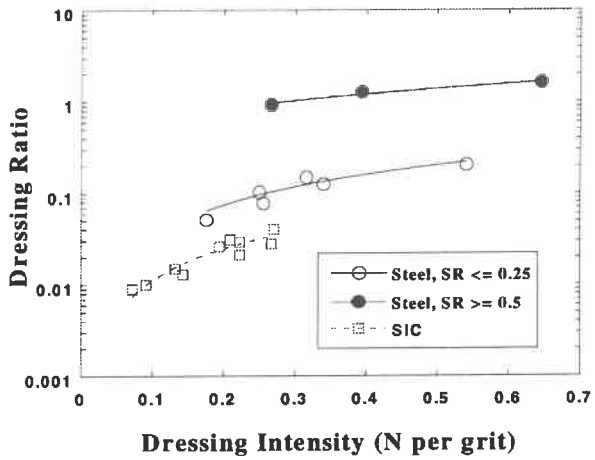

Figure 2: Dressing ratio against dressing intensity.

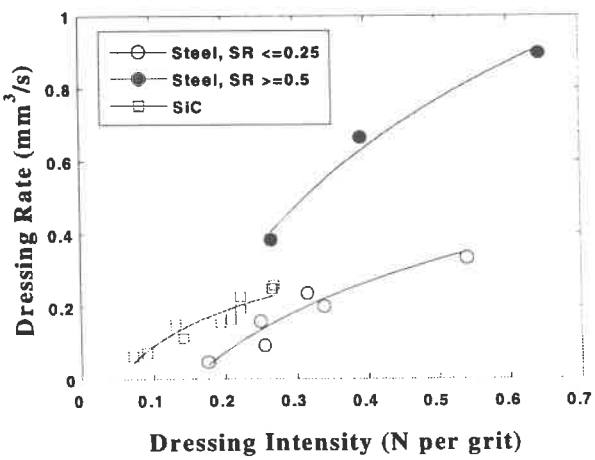

Figure 3: Dressing rate against dressing intensity.

3.3 Effect of Dressing Intensity on Grinding Performance

The normal force was measured during grinding and the surface roughness of the workpiece was measured as well. It was found that the grinding force decreases with the increasing dressing intensity for all the grinding speeds and the depths of cut, indicating that the dressing intensity also gives a measure of the wheel grinding performance. For high speed grinding, the influence of dressing intensity on the grinding force was not so significant as that for conventional grinding. Increasing the wheel speed also

reduced the grinding force. As a result, the effect of the dressing intensity was relieved. It was also found that the smaller the dressing intensity is, the better the surface quality is achieved. To measure the wheel life after each dressing the wheel was used to continuously grind the zirconia until the normal grinding force was significantly increased. The grinding time before next dressing was recorded to represent the wheel life. In Fig. 4, the wheel life is plotted as a function of the dressing intensity. It is seen that the wheel life generally increases with the increasing intensity for either SiC or steel roller. It is apparent that the effect of the dressing intensity on the wheel life at the higher speed is more significant than that at the conventional speed. Apparently, sharper cutting edges produced by the larger intensity dressing are more suitable for high speed grinding of zicornia. It is also found in Fig. 4 that the wheel dressed using the steel roller with the largest dressing intensity didn't possess the longest life. This could be because the wheel dressed by different rollers has different wear mechanisms during grinding. Raman Microscopy revealed that the graphitization on diamond grains was caused during dressing using the steel roller. It is thus inferred that the small amount of graphite-type carbon existing on some of the abrasive grains may lead to the excessive wheel wear during grinding.

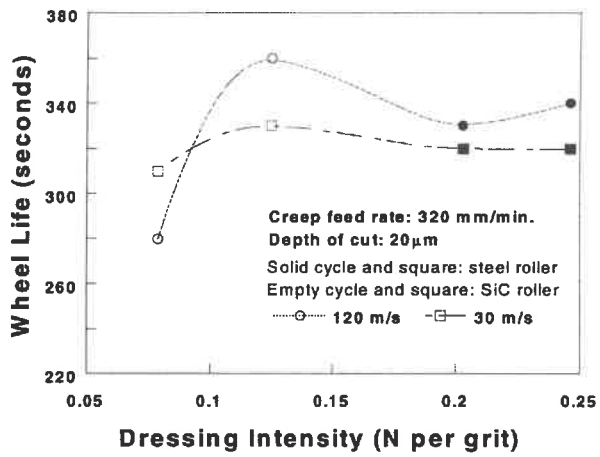

Figure 4: Wheel life as a function of dressing intensity.

4 Concluding Remarks

Truing/dressing intensity gives a good measure to evaluate the truing/dressing efficiency. A higher intensity can result in a higher efficiency. The steel roller generally gives a higher dressing intensity than the SiC roller. The surface topography is also influenced by the intensity. A higher intensity dressing produces more large cutting edges and a lower intensity dressing leads to more micro-cutting edges. Higher intensities should be used to dress the wheel for rough grinding as they can produce sharper cutting edges. This is of particular importance for high speed grinding of ceramics. On the other hand, lower intensities can be applied to achieve micro-cutting edges for fine grinding.

References:

[1] Inasaki, I., Dressing of resinoid bonded diamond grinding wheels, Annals of CIRP 38/1 (1989), 315-318.

[2] Klocke, F., O. Gerent & C. Schippers, High speed grinding of ceramics, Machining of Ceramics and Composites, Edited by Said Jahanmir, M. Ramulu and P. Koshy, Marcel Dekker, Inc. 1999, 119-137.

[3] Malkin, S., Grinding technology: theory and applications of machining with abrasives, John Wiley & Sons, 1982.

[4] Notter, A.T. & G.R. Shafto, A new truing and dressing technique for resin bond peripheral grinding wheels, Industrial Diamond Review, 6 (1979), 203-210.

The study of ductile-brittle transition on micro-cutting of single crystal silicon

Satoshi Kaji*, Takayuki Goto**, Tsunetaka Sumomogi***, Masayoshi Nakamura***

*Hiroshima Research & Development Center , Mitsubishi Heavy Industries, Ltd.
4-6-22 Kannonshinmachi Nishi-ku Hiroshima, 733-8553, Japan
**Advanced Technology Research Center , Mitsubishi Heavy Industries, Ltd.
1-8-1 Sachiura Kanazawa-ku Yokohama, 236-8515, Japan
***Faculty of Engineering, Hiroshima Kokusai Gakuin University
6-20-1 Nakano Aki-ku Hiroshima, 739-0321, Japan

INTRODUCTION

The studies of ultra precision machining of brittle materials, such as silicon, ceramics and so on, have been widely noticed recently. It has been made clear that material removal with plastic deformation was accomplished by a very small depth of cut. The presence or the absence of surface cracks occurred in cutting are generally applied as the criteria to decide machining mode brittle mode or ductile mode. On the other hand, it has been reported that various types of cracks are developed from the border between a plastic and an elastic deformation zone in indention tests for the brittle materials. These include internal cracks that progress inside the materials. These are invisible with the observation of material surface. The internal cracks influence the quality of semi-conductor. The observation of internal cracks plays important roles in the evaluation for the machining of brittle materials. On these backgrounds, the authors have investigated the ductile-brittle transition on micro-cutting of single crystal silicon.

EXPERIMENTAL METHODS

The workpiece material used in the experiment was polished single crystal silicon with (100) and (110) surface. A single crystal Vickers diamond penetrator with 148° apex angle was used as the cutting tool. Face-turning of the workpiece was done from the center to the outside with the fixed feed rate 30μm/rev. Cutting speed was 170 and 700m/min. The workpiece, single crystal silicon wafer, was mounted on a vacuum chuck. A partial inclination was given to the mounted workpiece by a partly inserted spacer between the workpiece and the chuck surface. Machining the inclined workpiece could generate various depth of grooves. Table 1 shows some machining conditions.

Table 1. Machining conditions

Cutting method	Face-turning
Workpiece	Single crystal silicon Crystallographic plane : (100), (110) Dimensions : ϕ100×0.7mm
Cutting tool	Vickers diamond penetrator Apex angle : 148°
Cutting speed	170, 700m/min
Feed rate	30μm /rev
Coolant	Dry

The investigation has been performed by observing not only the surface cracks but also the internal cracks grown inside the workpiece. An atomic force microscope (AFM) was used for observing the surface of the workpiece. This microscope was also used to measure the depth of grooves and surface crack ratio of each groove. It is the ratio between the total length of surface cracks generated along a groove and the length of the groove in the observing area on the AFM. Moreover a part of the workpiece was lapped obliquely to measure the depth of internal cracks on a laser scanning microscope. Furthermore the lapped workpiece was etched to manifest the internal cracks. The depth of internal cracks was evaluated as the depth form the deepest point of the groove to a pointed end of the internal crack progressed inside.

RESULT AND DISCUSSION

An AFM image of a cutting groove is shown in Fig.1 for example. The groove was generated on the (110) surface of single crystal silicon with cutting speed 170m/min. Surface cracks are observed in the right side of the groove.

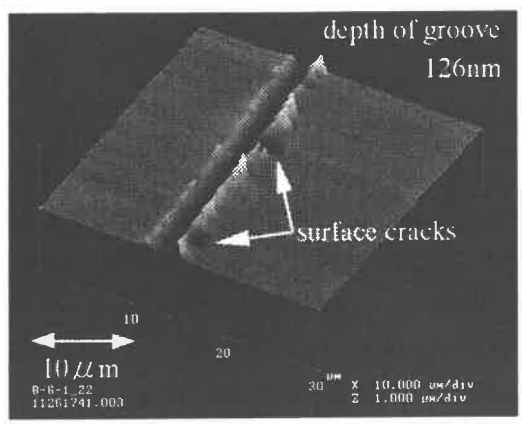

Fig.1 An AFM image

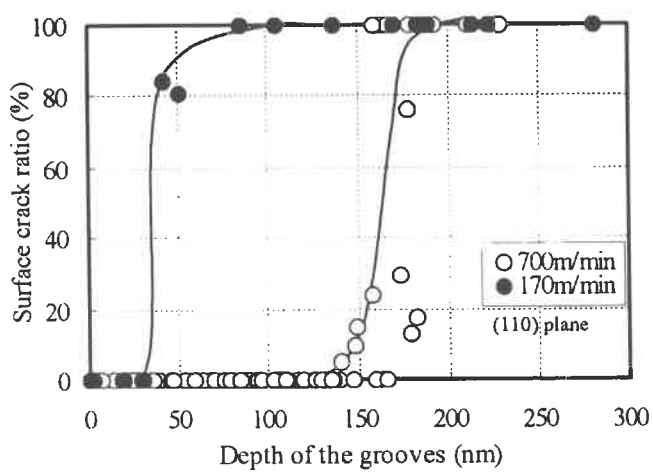

Fig.2 The relation between the depth of the grooves and the surface crack ratio

The relation between the depth of grooves and the surface crack ratio on the (110) surface is shown in Fig.2. The surface cracks are invisible around the depth less than approximately 30nm and 120nm at the cutting speed 170m/min and 700m/min, respectively. When the depth of grooves become more than 30nm and 120nm, respectively, the surface crack ratio increases rapidly. The ratio reaches 100% at the depth approximately 100nm and 170nm, respectively. The transition points evaluated by the surface cracks would be approximately 30nm at the cutting speed 170m/min and approximately 120nm at 700m/min on the (110) surface.
The surface crack ratio and the depth of internal cracks as a function of the depth of grooves on the (100) surface are shown in Fig.3. The surface cracks were not observed around the grooves which depth are less than approximately 50nm and 100nm at the cutting speed 170m/min and 700m/min, respectively. The transition points based on the surface cracks would be approximately 50nm and 100nm at each cutting speed on the (100) surface. Compared the (100) surface and the (110) surface, the transition points at each cutting speed would be nearly equal on both surface. The transition points would be dependent upon the cutting speed on the (100) and (110) surface.

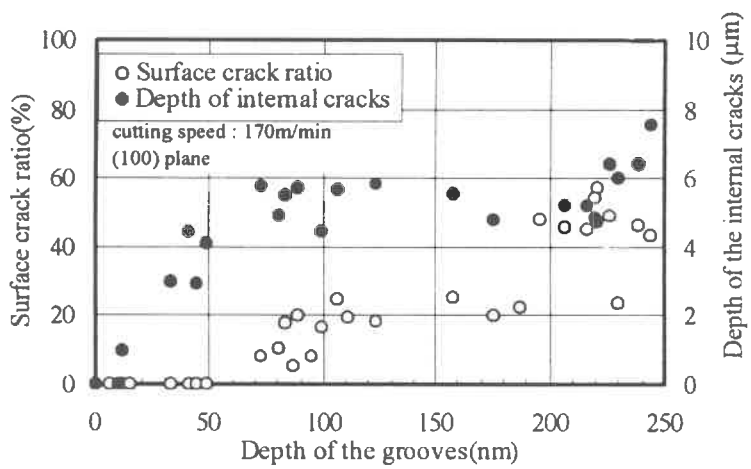

(a) Cutting speed 170m/min

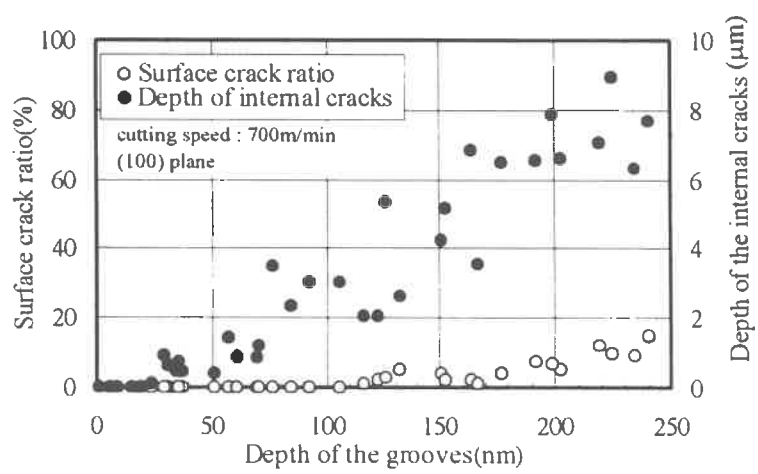

(b) Cutting speed 700m/min

Fig.3 The surface crack ratio and the depth of the internal cracks as a function of the depth of grooves

On the other hand, the internal cracks begin to be generated earlier than the surface cracks in the Fig.3. The internal cracks generated under the grooves which seem to be crack-free with the surface observation. The images of the (100) surface cut at the cutting speed 700m/min was observed by the laser scanning microscope, as shown in Fig.4. Fig.4(a) is the cut surface with a groove and Fig.4(b) is a obliquely lapped and etched surface with the internal cracks. Although crack-free cutting seems to be accomplished in Fig.4(a), the internal cracks progress under the grooves in Fig.4(b).

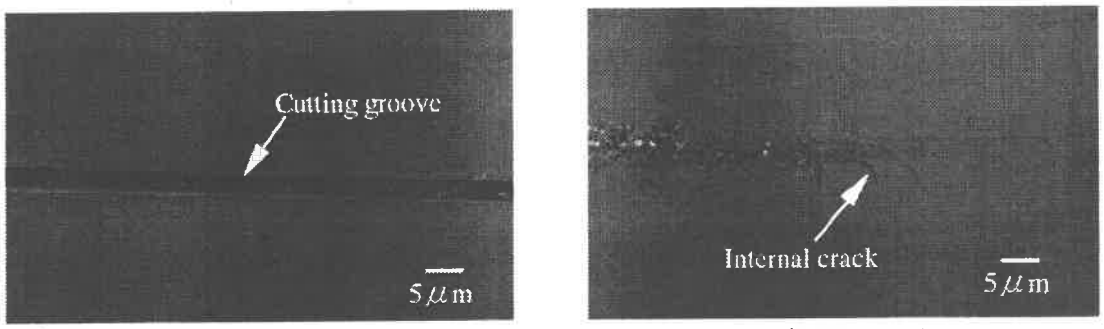

(a) Surface

(b)Cross section
(Obliquely lapped and etched)

Fig.4 The laser microscope images

CONCLUSION

The micro-cutting experiment using the Vickers penetrator was carried out on (110) and (100) surface of single crystal silicon with cutting speed 170m/min and 700m/min. The conclusions are as follows.

(1) The internal cracks are generated under the cutting grooves in some case, even if the depth is less than transition point. It is detected that the ductile-brittle transition point determined by the internal cracks is shallower than that determined by the surface cracks. Therefore to estimate these internal cracks would be important especially in finishing.

(2) Compared two different cutting speed, the relatively high speed cutting expands crack-free surface range and is unlikely to create the internal cracks.

Cutting Performance of CVD Diamond Coated Tool in Machining of Green Body of Silicon Nitride Ceramics - Wear Mechanism of Diamond Coated Tool to the Milling Operation -

Hideharu KATO*, Kazuhiro SHINTANI* and Hiroyuki HANYU**
* Department of Mechanical Engineering, Kanazawa Institute of Technology,
7-1 Ohgigaoka, Nonoichi, Ishikawa 921-8501 Japan
** OSG Corporation, 1-15 Honnogahara Toyokawa, Aichi, 442-8544 Japan

1.Introduction

Many attempts have been made to apply ceramic materials to machine parts used under high-temperature conditions, as these materials have excellent characteristics in terms of heat and wear resistance at elevated temperatures. The production process of this material consists of powder treatment, forming and sintering to make the finished products. Generally, a grinding process is used to finish the sintered parts to end products, as the material is extremely hard to machine[1, 2]. Especially, in case of large and complicated parts, the application of a cutting process may be effective, as a certain degree of volume elimination is required to shape the part. To arrange the shape of material, therefore, cutting process must be applied to the green body Si_3N_4 ceramics before sintering. Up to this moment, it has been clarified that diamond coated tool is effective in terms of tool life, since the green body Si_3N_4 ceramics is an aggregate of ceramics particles having high hardness characteristic[3]. However, the tool life using diamond coated tools varies depending on the difference in the thickness of the diamond coated film, and sufficient tool life cannot be obtained at present.

In this paper, the wear mechanism of a diamond coated tool and the effect of the deposit condition of diamond coated film on tool life were investigated in machining of green body Si_3N_4 ceramics.

2.Experimental procedure

The workpiece material was the green body of silicon nitride ceramics, which consists of an agglomeration of silicon nitride ceramic particles and an organic binder before the sintering process(**Fig. 1**). The silicon nitride ceramic particles are 1 μ m or less. The shape and geometry was a rectangular solid shape of 40×90×130 mm. The tools tested are shown in **Table 1**. As shown in this table, diamond coated film was generated under different deposit conditions by using the microwave plasma chemical vapor deposition (CVD) method[4-5]. The deposit condition were varied: deposit temperature:1123K, density of methane gas: 1 and 3% , density of carbon monoxide gas: 0 and 10%, and deposit time: 24, 32, 48 and 72 h. All of the diamond coated tools were used silicon nitride ceramics for the substrate material[6].

The type of tool was TPMN160304. This tool was attached to a milling holder with the specifications of 25mm, A.R. +7 degrees and R.R.-4 degrees. The cutting conditions were as follows: cutting speed (V): 2.0 m/s, feed rate (Sz): 0.10 mm/tooth, depth of cut (t): 2.0 mm, and dry condition. The tool life was determined by measuring the width of nose wear (VBc) or flaking on the flank face. The limited value of VBc to determine the life was set as VBc=0.2 mm.

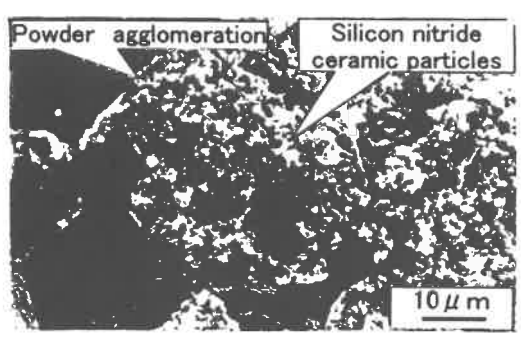

Fig.1 SEM micrograph of cross section for green body of Si_3N_4 ceramics

Table 1 Deposit condition of diamond film

Tool type	CH_4 Gas conc. (cc/min)	CO Gas conc. (cc/min)	H_2 Gas conc. (cc/min)	Deposit time (h)	Temperature of substrate (K)	Thickness of diamond film (μm)
SC100-L	1	0	99	72	1123	44.0
SC100-LP						40.0
SC100-S				24		14.1
SC110-M		10	89	32		7.5
SC310-S	3		87	24		13.6
SC310-M				48		30.4

Type of tool:TPMN160304 P:Polishing

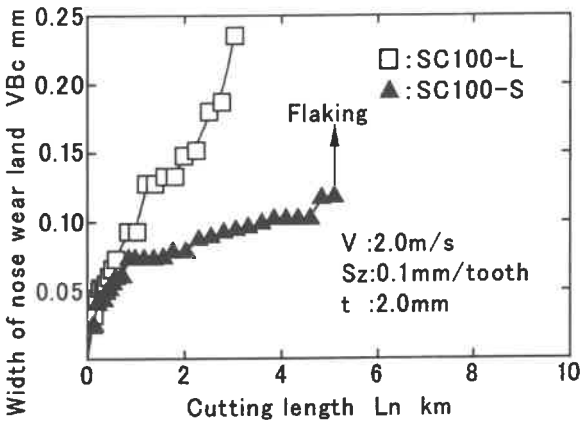

Fig.2 Comparison of VBc-Ln curves for diamond coated tools in different thickness

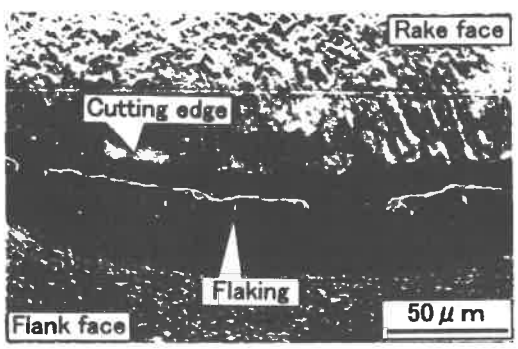

Fig.3 SEM micrographs of typical flaking pattern of the SC100-S tool

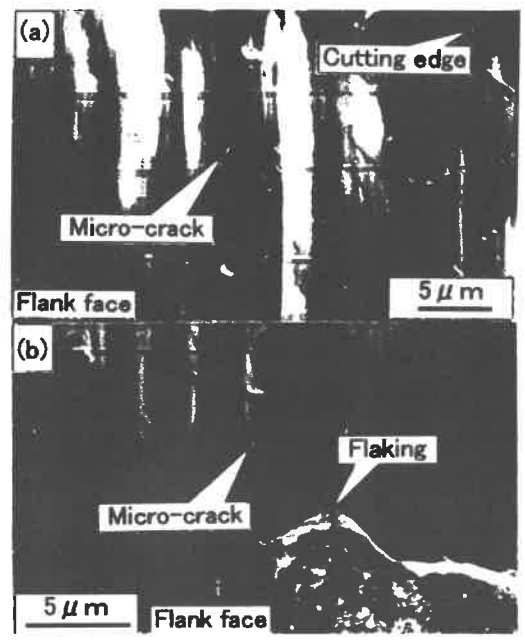

Fig.4 SEM micrographs of typical flank wear part with diamond coated tool; (a) before flaking and (b) after flaking

3. Results and discussion

3.1 Wear mechanism of diamond coated tool for difference in the thickness of coating film

Fig. 2 shows the test results regarding the effect of the thickness of diamond coated film on the tool life. As shown in this figure, the SC100-S tool performed better in terms of wear resistance than the SC100-L tool. However, the tool life of the SC100-S tool was determined by the flaking at cutting length of 5km(**Fig. 3**). And in the case of the SC100-L tool, the wear rate was remarkable, as the width of nose wear land exceeded 0.2mm with a short cutting length. **Fig. 4** shows SEM micrograph of comparison between the flank wear part before and after flaking in detail. As seen in **Fig. 4(a)**, many micro-cracks on the flank wear in parallel with the cutting edge were observed, and the occurrence position of these micro-cracks corresponds with the flaking position (**Fig. 4(b)**) . It is considered that the occurrence of flaking on the flank wear face is caused by residual stress.

On the other hand, the wear development rate of SC100-L tool is higher, but the occurrence of flaking on the flank face cannot be observed. A comparison of the cutting edges between the SC100-S tool and SC100-L tools is shown in **Fig. 5**. As seen in this figure, in the case of the SC100-S tool, small diamond particles with good crystallinity are uniformly distributed on the head surface of the diamond coated film (**Fig. 5 (a)**). In the case of the SC100-L tool, the diamond particles grow very big, and uniform diamond particles are also generated among these particles are observed(**Fig. 5 (b)**).
In addition, the convex portion of the diamond

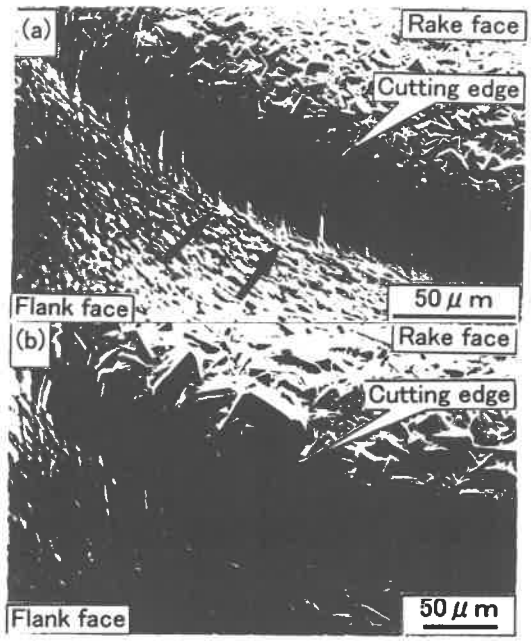

Fig.5 Comparison of the wear mode of cutting edge;(a) the SC100-S tool and (b) the SC100-L tool

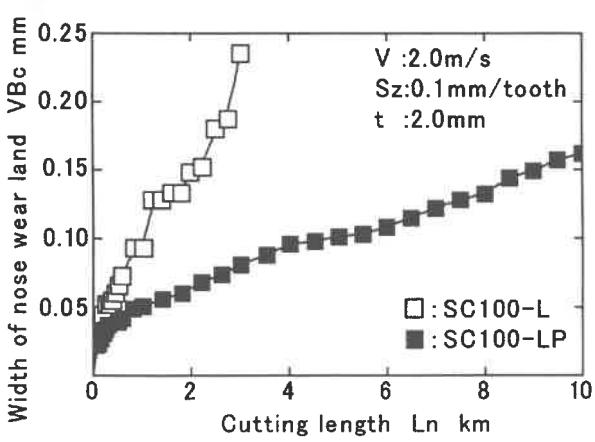

Fig.7 Increase of width of nose wear land (VBc) with cutting length(Ln) both as coating tool(SC100-L) and polishing tool(SC100-LP)

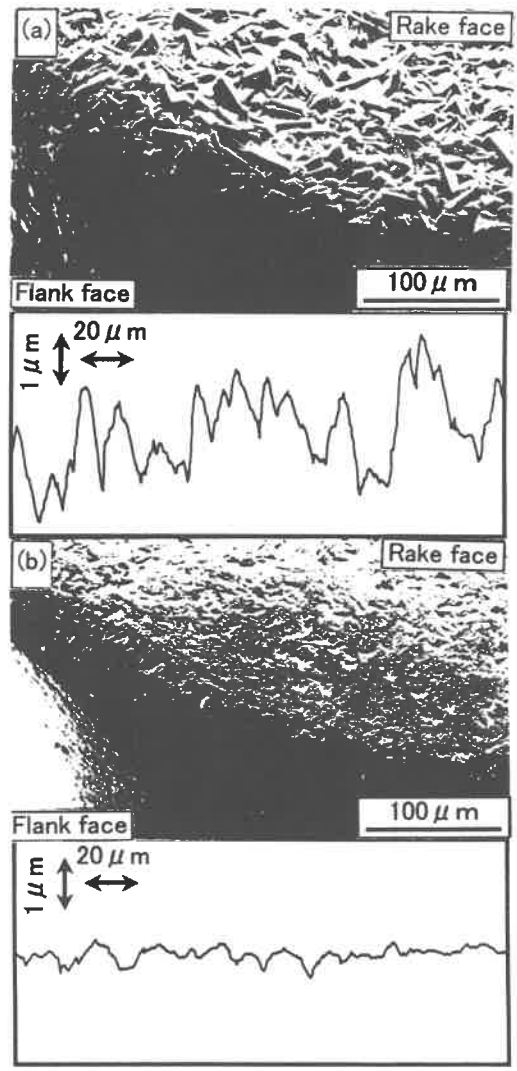

Fig.6 SEM micrographs of cutting edge and surface profile of the diamond coated tool comparison between before and after polishing; (a)the SC100-L tool and (b)the SC100-LP tool

particles wears at first, and then the width of the flank wear increases (portion indicated with arrow). In particular, the SC100-L tool is inferior in wear resistance, which is typical of tool that have larger diamond particles. In order to solve the cause of wear using diamond coated tool, the effect of difference in the ruggedness on the head surface of diamond film was investigated. **Fig. 6** shows SEM micrographs and surface profile of comparison between cutting edge of the SC100-L tool before and after polishing (the SC100-LP tool). The ruggedness of the SC100-LP tool is improved significantly, the tool life is approximately 4.5 times longer than that of the SC100-L tool (**Fig. 7**).

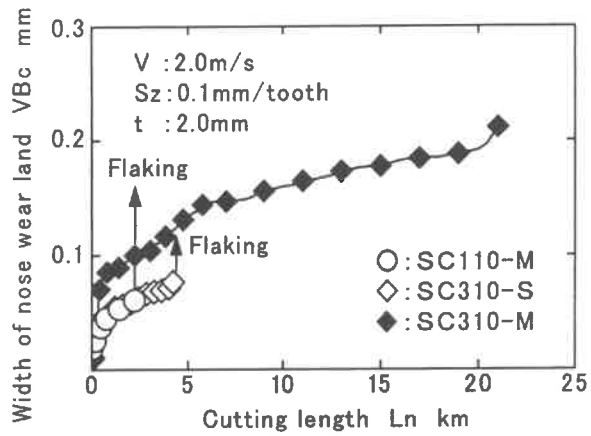

Fig.8 Increase of width of nose wear land (VBc) with cutting length(Ln) for the SC110-M tool, the SC310-S tool and the SC310-M tool

3.2 Effect of deposit condition of diamond film on tool life

As mentioned in a previous section, the wear mechanism of the diamond coated tools varies depending on the difference in the coating thickness and ruggedness on the head surface of diamond film. A study of the possibility of improving tool life by increasing the thickness and decreasing the ruggedness of diamond coated film was investigated.

The diamond coated film of the SC310-S tool and the SC310-M tool is generated by increasing the density of methane to 3% under the deposit conditions for the SC110-S tool. In three tools, carbon monoxide gas has been added to 10% in order to attempt that it tries growth suppression and equalizing of the particle[7]. As seen in **Fig. 8**, the SC310-M tool shows the long life without accompanying by the occurrence of flaking, though the initial wear is bigger than other tool. In this respect, the wear resistance and flaking resistance of the SC310-M tool is remarkably improved, the tool life was extended to 20km.

4.Conclution

In machining of the green body of silicon nitride ceramics using a diamond coated tool, the wear mechanism and effect of deposit condition of diamond film on tool life were investigated. The results obtained can be summarized as follows:

(1) The life of the SC100-S tool with the thin diamond film is determined by the occurrence of flaking on the flank wear face.

(2) The convex portion of the diamond particles wears first, and then the width of the flank wear increases

(3) The occurrence of flaking and the wear resistance in the SC310-M tool is improved significantly by the control of the formation speed and particle size of diamond coated film.

(4) The tool life of the SC310-M was extended to a cutting length of approximately 20km.

References

[1]N.Iijima,H.Takeyama and M.Kashiwase, J.S.P.E., 50, 7 (1984), 1110.(in Japanese)
[2]N.Narutaki, J.W.Lee, K.Noguchi and T.Mizutani, J.S.P.E., 52, 11 (1986), 1876.(in Japanese)
[3]H.Kato, K.Shintani, and Y.Shibuya, ICPCG-'98, Urumqi and Turpan, China (1998), 112.
[4]M.Kamo, Y.Sato, S.Matumoto, and N.Setaka, J.Cryst. Growth, 62 (1983), 642.
[5]K.Kanda, S.Takehara, S.Yoshida, R.Watanabe, S.Takano, H.Ando and F.Shimakura, Surface and Coatings Technology, 73 (1995), 115.
[6] Y.Shibuya, M.Takaya, Surface and Coatings Technology, 106 (1998), 66.
[7] R.Ramesham et al., Diamond Films Technology,5, 6 (1995), 307.

BENEFITS OF VARIABLE SPEED GRINDING

Byron R. Knapp, Eric R. Marsh
Machine Dynamics Research Lab
The Pennsylvania State University
University Park, PA 16802

Introduction

In the current state of technology, it is easy to overlook the complications involved in the manufacture of many of the products that are used on a daily basis. In order to convert raw materials into finished products, any number of machining processes can be used including boring, turning, drilling, milling, and grinding. Of these, grinding yields the highest degree of accuracy and surface quality, but is the most costly due to relatively low material removal rates. Despite the large costs involved, grinding still accounts for 20-25% of all machining in the United States [1]. To achieve lower grinding costs it is desired to minimize relative vibrations between the grinding wheel and workpiece in order to increase production rates.

During a grinding operation, forced vibrations from motors, hydraulic systems, bearings, belts, imbalance, and workpiece and wheel non-uniformity can cause an initial disturbance in the cutting process. This disturbance causes relative motion between the wheel and the workpiece that leaves a wave, or undulation, on the surface of the workpiece (and/or wheel). As the workpiece rotates and the wheel comes into contact with the wave from the previous revolution, the wheel is again deflected with respect to the workpiece forming another wave. If the second wave is larger than the first the instability is known as regenerative chatter and its onset is a major limitation of production grinding rates. Depending on the machining parameters, these regenerative waves will exist only on the workpiece, only on the grinding wheel, or on both (doubly regenerative).

Although regenerative chatter is well understood in most metal cutting processes, a model for grinding is complicated by geometric, thermal, and time scale issues. As a result, several different approaches to understanding grinding chatter have been proposed over the last 50 years that model workpiece, wheel, and doubly regenerative chatter [2-6]. The current research deals with the suppression of workpiece regeneration via workspeed variation.

Approach

The objective of this research is to demonstrate experimentally the benefits of variation of workspeed in order to reduce chatter in cylindrical plunge grinding. Several researchers have proposed models that show increased stability with variable wheel speed grinding but few have shown the effect of variable workspeed. Using a short grinding cycle and a compliant (low natural frequency) workpiece, only workpiece regeneration is considered.

Experiments are conducted on an external cylindrical grinder in which the equivalent grinding chip thickness, h_{eq} as defined by CIRP, is held constant over a range of workspeeds [7]. The equivalent grinding thickness is the volume of workpiece removed (Z') at a given grinding wheel speed (v_s). Equation 1 shows that h_{eq} can also be expressed as a function of workpiece diameter (d_w) and the infeed rate (v_f). Grinding data such as normal force and surface roughness have been shown to be logarithmic-linear functions of h_{eq}. [7]

$$h_{eq} = \frac{Z'}{v_s} = \frac{\pi d_w v_f}{v_s} \qquad 1)$$

Infeed rates of 340 and 510 nm/s (13 and 20 μin/s) are used to plunge grind for 200 seconds. The chatter growth is recorded and compared to chatter growth when grinding with a variable workspeed and the same equivalent chip thickness. The reduced chatter amplitude as compared to constant speed

grinding indicates that variable workspeed grinding may be an effective solution for increasing production rates.

Experimental Setup

The chatter experiments are performed on the Myford MG 12 manual cylindrical grinder shown in Figure 1a. A Professional Instruments 4B BLOCKHEAD® air bearing spindle is used in lieu of the original ball bearing workhead to eliminate spindle error. The reed style flexure shown in Figure 1b allows for small motions at a known frequency in the chatter sensitive direction. The workpiece is bolted directly to the BLOCKHEAD® air bearing spindle which is held in the flexure.

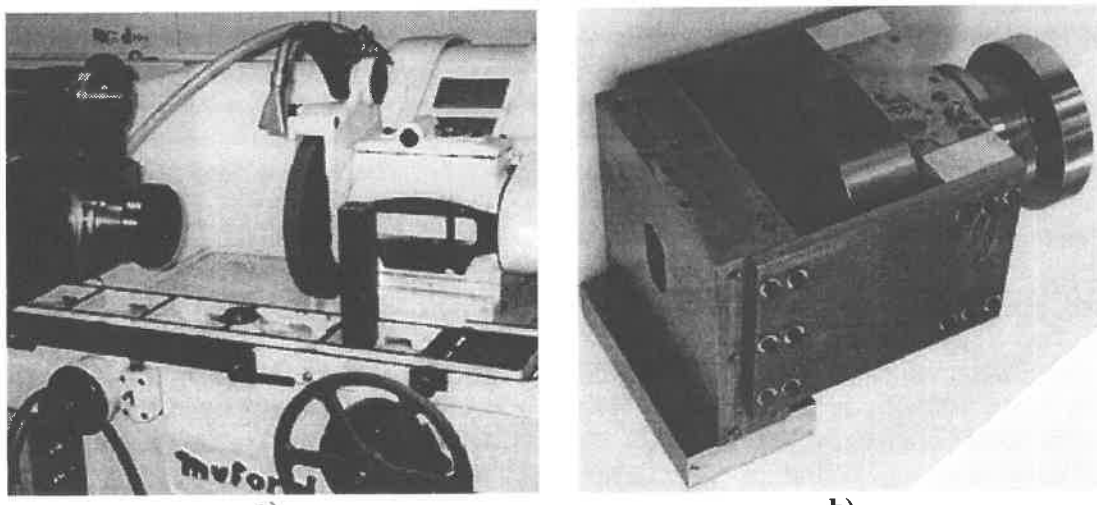

a) b)

Figure 1 a) Cylindrical grinding testbed, **b)** single degree of freedom workhead flexure.

Mild steel workpieces 115 mm in diameter by 23 mm wide are ground with a 250 mm (10 in) diameter vitrified aluminum oxide wheel (Norton 32A60-KVBE). The coolant is a 10% chemical emulsion (Master Chemical VHP 320). The wheel is dressed before each test using a single point diamond dressing tool traversing at 130 mm/min. Two passes are taken at dressing depths of cut of 25 μm. The tests are conducted using h_{eq} = 3.9 nm and h_{eq} = 5.8 nm for workspeeds of 200, 300, and 395 RPM with workspeed step variations of 0%, ± 5%, ± 10%, and ± 20% every 10 seconds. The vibration amplitude of the flexure and the workpiece roundness is recorded.

Results

The chatter amplitude results of four tests, each using h_{eq} = 3.8 nm, are shown in Figure 2. The vibration envelope illustrates that a variation of 20% of the workspeed suppresses the grinding chatter for nominal workspeeds of both 200 RPM and 400 RPM. The roundness polar plots for the same four tests are shown in Figure 3. A summary of the average roundness for all the tests is shown in Table 1. The chatter suppression obtained from workspeed variation results in improved roundness traces.

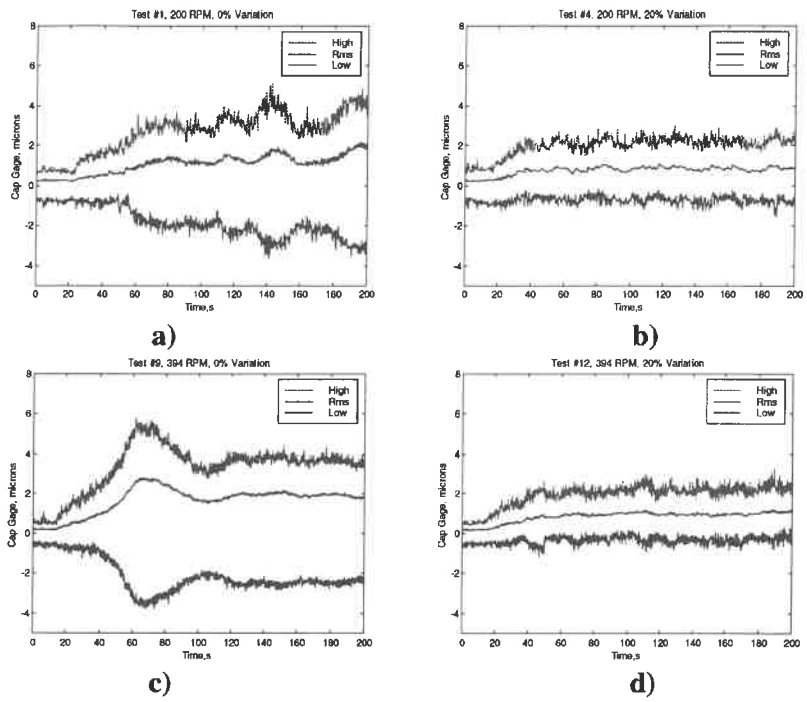

Figure 2 Grinding chatter envelope for **a)** constant 200 RPM grind, **b)** 200 RPM grind with 20% variation, **c)** constant 400 RPM grind, **b)** 400 RPM grind with 20% variation.

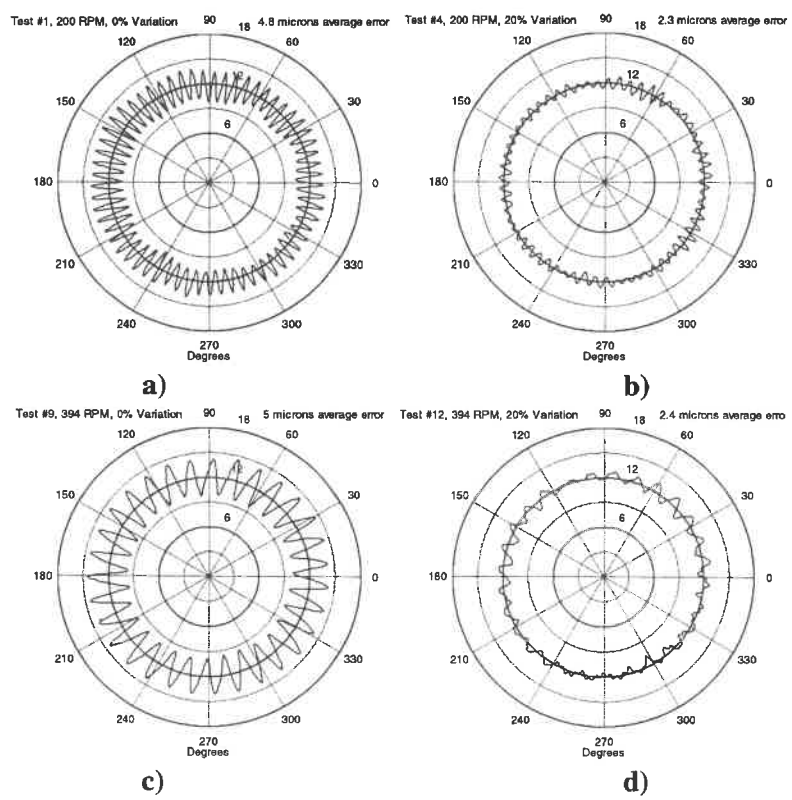

Figure 3 Roundness polar plots for **a)** constant 200 RPM grind, **b)** 200 RPM grind with 20% variation, **c)** constant 400 RPM grind, **b)** 400 RPM grind with 20% variation.

Table 1 Summary of average roundness results.

Roundness, microns		Workhead speed variation			
	RPM	-	5%	10%	20%
h_{eq} 3.9 nm	200	4.8	3.3	1.9	2.3
	300	4.3	4.3	1.9	4.1
	394	5.0	5.2	4.6	2.4
h_{eq} 5.8 nm	200	5.3	4.9	1.7	2.6
	300	7.0	5.7	5.2	4.2
	394	6.8	6.7	5.4	3.5

Conclusions

Grinding chatter experiments are performed in an effort to demonstrate the benefits of variable speed workhead grinding. Cylindrical plunge grinding experiments are conducted and the amplitude of vibration and the workpiece roundness are used to quantify chatter intensity. Increased stability is achieved by decreasing the equivalent grinding thickness and increasing the workhead speed variation.

The amount and period of workhead speed variation are critical parameters in realizing the optimal conditions for each grinding operation. Future work includes determining the optimal variation parameters in order to maximize the MRR. In addition, the tests will be repeated on a production size grinder to validate the testbed results. Finally, this method is beneficial only in operations in which work regenerative chatter exists, for example, operations in which the workpiece has a low natural frequency.

Acknowledgements

The research for this project was made possible through funding provided by the National Science Foundation, Weldon Machine Tool, and Professional Instruments Company. The authors are grateful for the many hours of discussion, consulting, and testing with David Arneson and Mel Liebers at Professional Instruments. Furthermore, the authors are indebted to Jim Flinchbaugh and George Sipe at Weldon Machine Tool for supporting and guiding the direction of the research.

References

[1] Malkin, S., *Grinding Technology*, John Wiley & Sons: New York, 1989.

[2] Hahn, R.S., "On the Theory of Regenerative Chatter in Precision Grinding Operation." *Transactions of the ASME*, v 76, n 1, 1954, p 593-597.

[3] Pahlitzsch, G. and Cuntze, E., "Reduction of Chatter Vibration During Cylindrical and Plunge Grinding Operation." *Proceedings of the 6th MTDR Conference*, 1965, p 507-523.

[4] Bartalucci, B. and Lisini, G., "Grinding Process Instability." *Journal of Engineering for Industry, Transactions of the ASME*, v 91, Series B, n 3, 1969, p 597-606.

[5] Snoeys, R. and Brown, D., "Dominating Parameters in Grinding Wheel and Workpiece Regenerative Chatter." *Proceedings of the 10th MTDR Conference*, 1969, p 325-348.

[6] Bartalucci, B., Lisini, G., and Pinotti, P., "Grinding at Variable Speed." *Proceedings of the 11th MTDR Conference*, 1970, p 633-652.

[7] Snoeys, R., Peters, J., and Decneut, A., "The Significance of Chip Thickness in Grinding." *Annals of the CIRP*, v 23, n 2, 1974, p 227-237.

THE EFFECT OF PARALLEL MODULATION ON SUB-SURFACE DAMAGE

W. Qu, M. H. Miller and A. Chandra

Department of ME-EM
Michigan Technological University
Houghton, MI 49931

1 Introduction

Precision ceramic components are being used today in an increasing variety of engineering applications. Compared to metals, however, ceramics are much harder and more susceptible to brittle fracture. Ceramic components, in most cases, require finishing operations to achieve surfaces of required geometry, tolerance, and finish. Grinding is an enabling technology in the manufacture of ceramic components because it produces accurate shapes deterministically. However, grinding generally induces surface and sub-surface damage in the finished part, which can severely degrade its strength and life under service conditions.

Several other researchers have introduced high frequency vibrations into the machining process. Compared to traditional machining, modulation assisted machining has several benefits. It can reduce the critical depth of cut (for ductile removal), reduce friction at the tool-chip interface and the cutting force, permit better coolant penetration, and inhibit the build up of debris [1-4]. Our previous work [5] focused on the effect of vertical modulation on sub-surface damage. In this paper, we focus on the effect of parallel modulation on sub-surface damage.

2 Theoretical Motivation

Crack shielding can reduce the depth of subsurface damage in brittle materials [5-6]. The shielding effect can be achieved by intermittant unloading. The intermittant unloading does the following:

1. Initiates the material removal mechanism of lateral damage early in the process, before normal damage is fully developed.
2. Utilizes the shielding effects of lateral damage to retard and potentially eliminate normal damage from the finished product.

Vertical modulation results [5] indicate that sub-surface damage may be reduced in single point scratch tests since the acting force between nib and workpiece is unloaded and reloaded intermittently. To further investigate this shielding effect, we considered scratch tests under parallel modulation.

With parallel modulation, the cutting grit moves relative to the workpiece in the form:

$$u(t) = Vt - a\cos(\omega t)$$

where

$u(t)$ is the displament of the cutting grit;

V is the nominal cutting velocity;

a and ω are the amplitude and the angular velocity of the vibration modulation.

Therefore, the relative cutting grit velocity is:

$$u'(t) = V + a\omega\sin(\omega t) = V + V_m\sin(\omega t)$$

where $V_m = a\omega$ is the maximum modulation velocity.

When $v \geq v_m$, $u'(t) \geq 0$, the cutting grit is always in contact with the workpiece. Therefore, the unloading and reloading phenomenon in this cutting situation doesn't occur, and the shielding effect is not expected.

When $v < v_m$, $u'(t)$, the velocity of the cutting grit relative to the workpiece, is not always positive. When $u'(t) > 0$, the cutting grit extends and tends to cut the workpiece; when $u'(t) < 0$, the cutting grit retracts and does not cut the workpiece. When $u'(t) > 0$ and the cutting grit begins to be in contact with the workpiece, the cutting force on the workpiece is loaded; when $u'(t) < 0$, the cutting grit retracts and the cutting force on the workpiece is unloaded. Therefore, the unloading and reloading phenomenon in this cutting situation does occur.

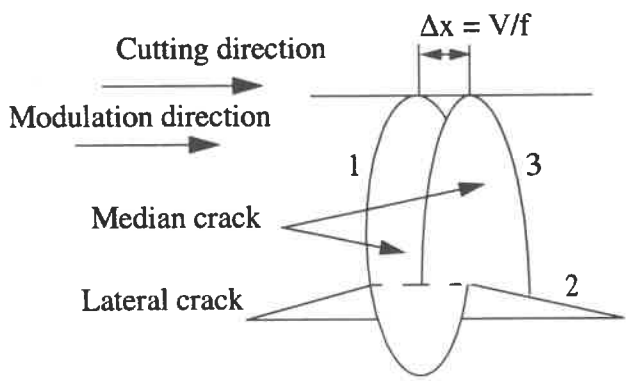

Figure 1: Shielding effect in single point modulation cutting

The unloading and reloading phenomenon in a cutting situation where cutting is modulated in the direction of the cutting is shown in Fig. 1. Loading produces the median crack 1. Subsequent unloading produces the lateral crack 2. Reloading then produces median crack 3. The distance $\Delta x = V/f$ is the displacement of the cutting grit in one cycle, where V is the cutting speed and f the modulation frequency. If Δx is small enough, the lateral crack 2 can act as an effective barrier against further depthwise penetration of the median crack 3. To see any beneficial effect, Δx must be smaller than the length of the lateral crack. Further reducing Δx (by decreasing V or

increasing *f*) should increase the shielding effect. The minimum damage depth that could be realized would be the depth at which the lateral crack is initiated upon unloading.

3 Experimental Investigation of the Effects of Intermittent Unloading on Single Point Scratches Under Vertical Modulation

Figure 2 shows a schematic representation of the experimental setup. Pyrex glass, because of its transparency, is chosen as the work material. As shown in Figure 2, the workpiece is vibrated in the Y direction by a magnetostrictive actuator. A diamond cutting nib is mounted on the spindle. The cutting and modulation are in the same direction (Y). A force sensor is placed underneath the cutting nib. To establish initial contact, the table is moved in the Z direction until the force sensor reads 0.1 N. To make a scratch with intermittent unloading, the workpiece extends and retracts within one spindle rotation in Z direction while the actuator is modulating.

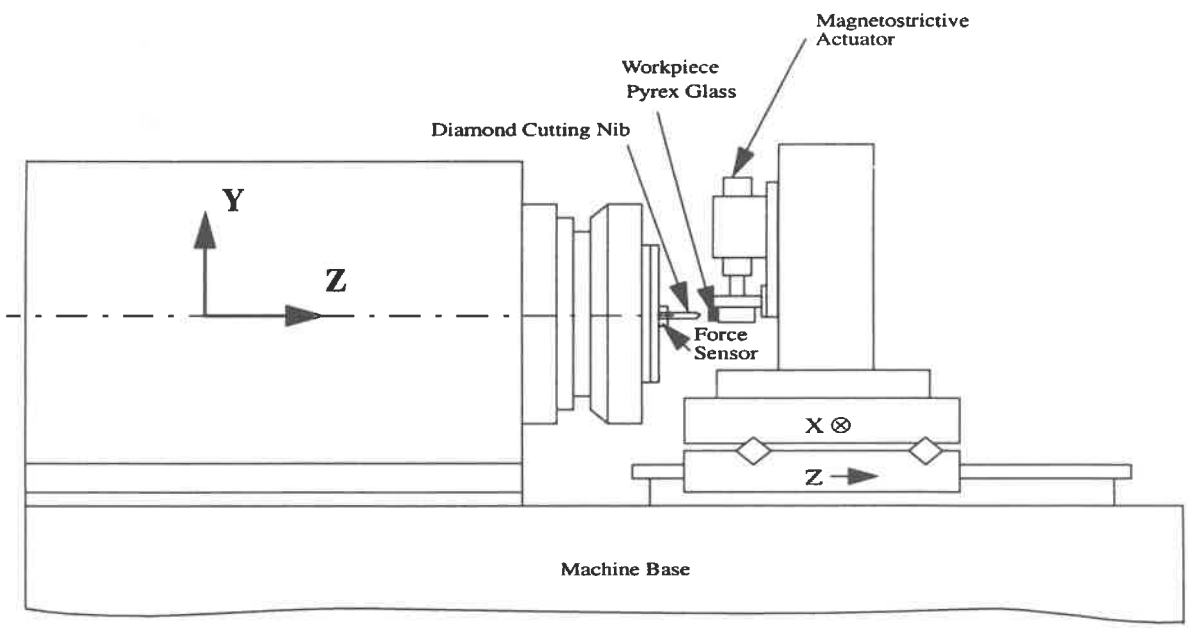

Figure 2: Experimental setup for scratch tests under parallel modulation

Single point scratch experiments were carried out with and without parallel modulation at two cutting speeds -- 40 and 120 mm/sec. Maximum modulation frequency attainable with reasonable amplitude for our magnetostrictive actuator was 4.5 kHz. Accordingly, modulation tests were carried out below this frequency at 3 kHz. The modulation amplitude is 20 μm (peak to valley). Because of the limitation in the maximum actuator frequency, the scratch tests described in this paper were performed at cutting speeds much lower than typical grinding speeds. Table 1 summarizes the results. The damage depth values represent the average of 5 tests. Modulation reduces the damage depth by 33% at 40 mm/s and by 20% at 120 mm/s. As expected, the modulation had less effect at higher cutting speed (higher Δx). When Δx increases relative to the lateral crack zone width, the shielding effect diminishes.

Table 1: Effect of V/f = Δx on damage depth for parallel modulation with depth of cut = 25 μm, peak-to-valley modulation amplitude = 10 μm

Velocity (mm/s)	Modulation Frequency (kHz)	Δx (μm)	Median Damage Depth (μm)
40	0	∞	125.5
120	0	∞	124.8
40	3	13.3	83.2
120	3	40	99.2

4 Conclusions

We performed scratch experiments in which the workpiece was modulated parallel to the cutting direction. The conclusions are as follows:

a. Parallel modulation can achieve the shielding effect. The smaller Δx is, the bigger the shielding effect is.
b. The reduction in subsurface damage for parallel modulation is comparable to the results for vertical modulation. For the same Δx = 40 μm, parallel modulation reduced damage depth by 20% while vertical modulation reduced damage depth by 21%.

References

[1] Moriwaki, T., E. Shamoto and K. Inoue, "Ultraprecision Ductile Cutting of Glass by Applying Ultrasonic Vibration," *Annals of the CIRP*, Vol. 41, No. 1, pp. 141-144, 1992.
[2] Markov, A. I., *Ultrasonic Machining of Intractable Materials*, Illife Books, London, 1966.
[3] Colwell, L. V., "The Effects of High-Frequency Vibrations in Grinding," *Trans. ASME*, May, 1956, pp. 837-846.
[4] Astashev, V. K., "Effect of Ultrasonic Vibration of a Single Point Tool on the Process of Cutting," *Journal of Machinery Manufacture and Reliability*, No. 3, pp. 65-70, 1992.
[5] Qu, W., M. H. Miller and A. Chandra, "Effect of Modulation on Single Grit Scratch Tests," *Proceedings of the Thirteenth ASPE Annual Meeting,* Vol. 18, pp. 618-621, 1998.
[6] Chandra, A., K. Wang, Y. Huang and G. Subhash, "Role of Unloading in Machining Brittle Materials," *Proceedings of ASME IMECE*, MED-Vol. 6-2, pp. 83-90, 1997.

THE MECHANISM OF CBN QUILL IN SURFACE GRINDING

Qiusheng Yan*, K. Tanaka**, K. Syoji**, T. Honoki***
*Department of Mechatronics Engineering
Shantou University, Shantou, Guangdong, 515063, P.R.China
**Department of Mechatronics and Precision Engineering
Tohoku University, Sendai, 980-8579, Japan
***Mitsubishi Electric Corp.
3-18-1 Oshika, Shizuoka, Japan

1. Introduction

Parts with deep-grooves and the grooves need be precisely machined are extensively used, nowadays, the grooves are generally machined by using end mill. But, with constructions of these parts are improved, materials of these parts become high strength and high hardness, machining process become simple and low cost, and machining precision requirements are risen and so on, in more and more situations the grooves need be ground. In this research, deep-grooves are ground precisely by using CBN wheel with shaft (quill), by which, the flanks and bottom of curved shape deep-grooves can be ground. For analyzing the characteristics of CBN quill in grinding process, it is divided into surface grinding and face grinding, then study is individually conducted. In the preceding paper [1,2], the experimental research of CBN quill in surface grinding process is stated, it is said that reason of CBN quill being bad in grinding performance is CBN grits early fall off. In this paper, by theoretically analyzing the characteristics of quill in surface grinding process, the reasons of CBN grit fall off are discussed, and the selections of CBN quill grinding parameters are experimentally researched by selecting grain cutting parameters.

2.Exprimental procedures

The equipment of experiment is refitted by a surface grinding machine, its spindle is re-equipped by air and oil-spray high-frequency spindle (the maximum rotational speed 8×10^4 rpm, output 2.8 kw). Figure 1 shows the shape of resinoid bonded CBN quill for trial this experiment. The width of grinding is taken as 5 mm, and the grinding is carried out by using the front end of CBN quill. The CBN quill was dressed by a cup type of GC wheel. Coolant is 5% aqueous emulsion and down-cut grinding are used. The workpiece material is cast iron and its dimensions are L105×H45×T5 mm. The grinding forces are measured by using a parallel plate dynamometer. The wearing values of wheel are got by means of copying the surfaces of CBN quill in carbon pieces.

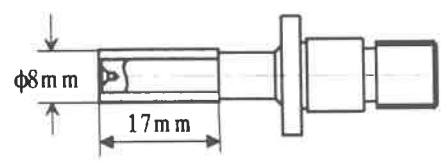

Fig.1 Shape of resinoid CBN quill

3.The characteristics of CBN quill in surface grinding

We can take the surface grinding process as a collective effect of individual grain cutting action, as shown in the Figure 2. The fundamental grinding parameters can be indicated by maximum grain depth of cut g_m, wheel-workpiece contact length l_c and the maximum grain cutting force f_g.

The grain cutting parameters of quill (ϕ8mm) and general diameter wheel (for example ϕ80mm) in

surface grinding are calculated, the specific values of their parameters $\lambda(y)=y(\phi 8)/\ y(\phi 80)$ are listed in Table 1.

Table 1. The specific values in surface grinding

y	V(m/s)	n(rpm)	g_m	l_c	f_g
$\lambda(y)$	1	10	3.17	0.31	3.17^t

As shown in Table 1, for CBN quill, the maximum grain depth of cut g_m is 3.17 times as large as one in general diameter wheel grinding, and the wheel-workpiece contact length l_c is decreased to be less than one third. That is, the cut layer shape of grain is changed to being short and thick, the maximum cutting force acted on grain f_g is 3.17^t ($0<t<1$) times as large as one in general grinding. The peak value of cutting force pulse is increased, the acting time is shortened and the cutting force is changed as one with impact. This is the essential reason why the fall off and break of the grits of CBN quill are brought out easily. On the other hand, the grain grinding frequences of CBN quill are ten times as large as one in general grinding in the same time. CBN grits are high frequently used for grinding, high frequently impacted by cutting force and cutting heat, which can result in the bond around CBN grits is fatigued and injured. It makes the bondability between CBN grits and bond be weakened, and becomes the reason why fall off of CBN grits of quill is brought out. It is thus clear that cutting environment of CBN grits in CBN quill surface grinding is seriously worsened as compared with general grinding. So, which result in the questions of CBN quill being excessively worn, machining precision being low, machining process being unstable and so on. The ways by which the grinding performance of CBN quill can be risen, on the one hand are to select the essential factors of CBN quill (for example, bond type, grain density) which can make the retentivity of CBN grits be risen, and on the other hand are to select the grinding parameters which can make the maximum grain depth of cut g_m be decreased and the wheel-workpiece contact length l_c be increased.

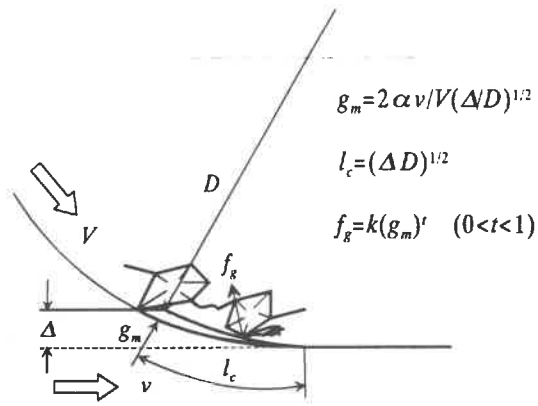

α : Length between successive cutting grain

Fig.2 Model of a grain in cutting

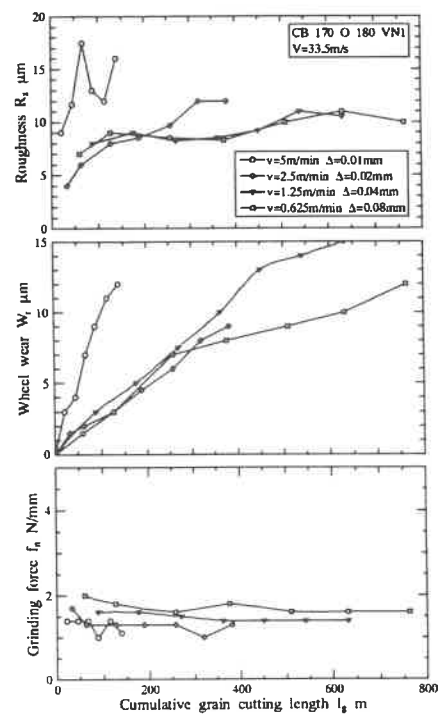

Fig.3 Experiment results in the differential g_m

4. Grinding experiments

The effect of various factors on grinding process is analysed by comparing the changes of ground surface roughness R_z, wheel worn value W_r and normal grinding force in unit grinding width f_n with cumulative grain cutting length l_g ($l_g = \Sigma l_c$).

4.1 The Effect of g_m in same grinding efficiency

When the volume of wheel removal in unit grinding width and unit grinding time ($Z = v \times \Delta$) is constant, but grinding feed speed v and depth of grinding Δ are changed, experiment results are shown in Figure 3.

It can be seen that grinding force tends to be decreased but wheel worn is steeply increased and ground surface roughness is increased and unstable when table is speedily fed and depth of grinding is small. It is shown the characteristics of grain fall off type of wheel worn. As grinding feed speed is decreased and depth of grinding is increased, grinding force value is increased but wheel worn is slowed down, ground surface roughness value tends to be stable and grinding of wheel is in a condition approaching to normal one. That is to say, when the maximum grain depth of cut g_m is decreased wheel worn is slowed down. But at same time the wheel-workpiece contact length l_c is increased, the number of grits which join the cutting is increased, it result in the grinding force of wheel is increased. From these experiment results, it can be known that using small grinding feed speed and large depth of grinding can make the cutting force acted on grains be decreased, so that fall off of CBN grits of wheel be decreased in CBN quill grinding.

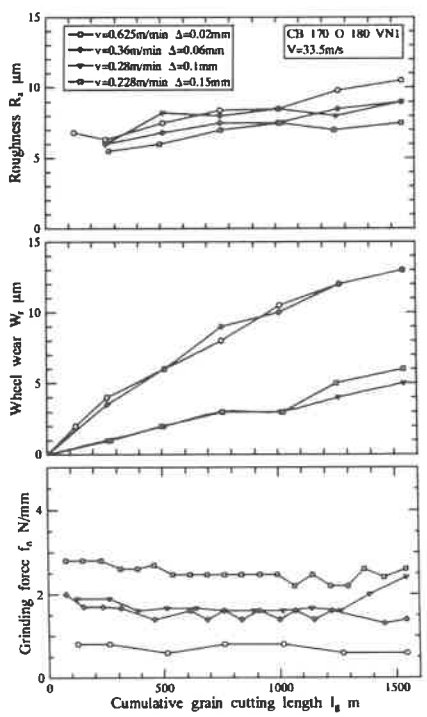

Fig.4 Experiment results in the differential l_c

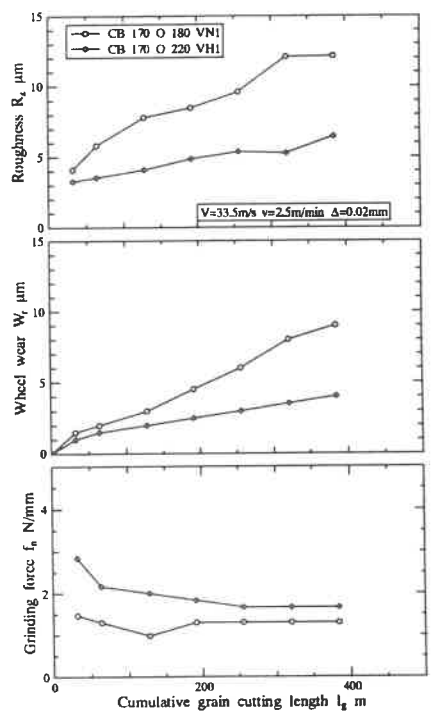

Fig.5 The effects of wheel grain density

4.2 The effect of l_c when g_m is fixed

Taking v =0.625 m/min, Δ=0.02mm as comparison, when the maximum grain depth of cut g_m is fixed, and wheel-workpiece contact length l_c is changed with grinding feed speed v and depth of grinding Δ being changed. Experiment results are shown in Figure 4.

As wheel-workpiece contact length l_c is increased, grinding force is increased in turn, but wheel worn

and ground surface roughness are decreased correspondingly. Particularly, in creep feed grinding (v<=0.28 m/min), wheel worn is steeply decreased and ground surface roughness is improved also. From the characteristics of experiment curves, it can be considered that grinding process of CBN quill in creep feed grinding is in normal grinding conditions. That is to say, wheel-workpiece contact length l_c increment can make the number of grain cutting edges which join the cutting at same time increment and the impact of cutting force on grains be decreased, they are beneficial to the grinding process being smoothly carried out.

4.3 The effect of α

It can be known from Figure 2, that another parameters which affects on maximum grain depth of cut g_m is the length between successive cutting grain of wheel α. When grain density of wheel is increased, α is decreased, g_m is also decreased in the meantime but wheel-workpiece contact length l_c is fixed. The experiments rising grain density of CBN quill in the same grinding parameters are carried out, which results are shown in Figure 5. It can be seen that grinding force is increased but wheel worn and ground surface roughness are all decreased, the grinding process is stable and grinding of CBN quill is in a condition approaching to normal one as grain density of wheel being risen. It is result brought by rising grain density of CBN quill, decreasing maximum grain depth of cut g_m and increasing grain cutting edges which join the cutting at the same time.

5. Conclusions

In this paper, by theoretically analyzing the characteristics of CBN quill in surface grinding process, the essential reason which affects on grinding performance of CBN quill is fully understood. It is the maximum grain depth of cut g_m is increased and the wheel-workpiece contact length l_c is decreased, then the grain cutting force is increased, which results in CBN grain early fall off easily. Using the grinding parameters which can make the maximum grain depth of cut g_m be decreased and the wheel-workpiece contact length l_c be increased, that is, grinding feed speed is small and depth of grinding is large, can make batter grinding performance of CBN quill, obtain good grinding results in surface grinding. Using the high grain density of wheel can also obtain the same results.

References

1) K. Tanaka, K. Syoji and T. Honoki: Grinding of Deep-Groove Flank with CBN Quill, Proceedings of 1995' Autumn Annual Meeting of JSPE, (1995)179.
2) Q. Yan, K. Tanaka, K. Syoji and T. Honoki: Grinding of Deep-Groove Flank with CBN Quill-Effects of bond and grain size-, Proceedings of Tohoku Meeting of JSPE, (1998)57.

Ultra-Smoothness Grinding of Fine Ceramics with #140-Mesh Grain Size Diamond Wheel

Heiji YASUI*, Go YAMAZAKI*, Yutaka HIRAKI*, Shigehiko SAKAMOTO*, Masato SAKATA*, Morihiko SAEKI*, Akira HOSOKAWA**

* Dept. of Mechanical Engineering & Materials Science, Kumamoto University, Kumamoto 860-8555, JAPAN
** Dept. of Mechanical System Engineering, Kanazawa University, Kanazawa 920-8667, JAPAN

1. Introduction

Grinding operation is one of the most effective manners for high smoothness machining of fine ceramics. It is difficult, however, to form crack-free high smoothness surface by ductile-mode grinding because of their mechanical properties of high brittleness [1]. Then it is necessary for ductile-mode grinding that the suitable grinding conditions are selected. Some reports [2], [3] concerning ductile-mode grinding have been done with the wheel of finer grain size than #1500-mesh. But the truing and dressing technics for the fine grain size wheel are difficult. In addition, the depth of cut and/or table speed are also limited to a certain small range because the active grain is thrown off easily from the wheel surface by small grinding force.

Therefore, in our previous researches [4]-[6], the adaptation of the coarse #140-mesh grain size wheel to the ductile-mode grinding of silicon carbide ceramic was investigated experimentally in the surface plunge grinding and found to be possible. The surface roughness in the surface plunge grinding, however, is limited to about 200nm(Rmax) because of the formation of the grinding grooves.

In this research, the effect of the newly devised ultra-smoothness grinding method, in which the grinding grooves can be removed and diminished, is examined experimentally by grinding fine ceramics with the coarse #140-mesh diamond wheel. From the result, it is found that the formed surface roughness is attainable below about 10nm(P-V) and 1nm(RMS) for the hot pressed silicon carbide.

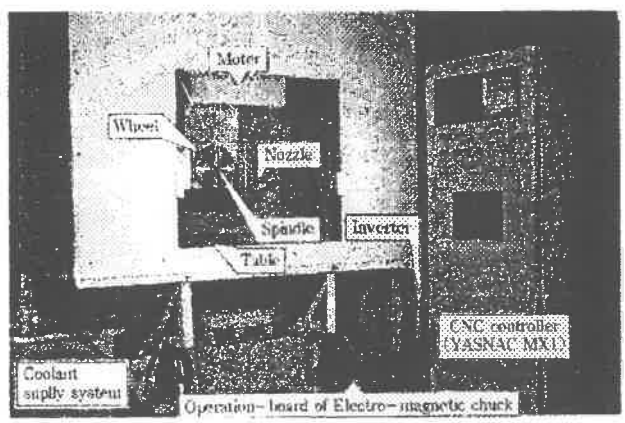

Fig.1 Appearance of NC grinding machine

2. Experimental procedure

The experiments are carried out with the NC grinding machine as shown photographically in Fig.1. The machine is reconstructed of a conventional NC equipment which has the accuracy of 1μm for each movement of the X, Y and Z direction. The newly devised ultra-smoothness grinding method is shown schematically in Fig.2. In the method, the workpiece is fed simultaneously toward the both directions normal and parallel to grinding direction. The method is different from the usual traverse surface grinding method in which the cross-feed normal to grinding direction is done after grinding the whole width of workpiece in a pass or stroke of table. However the cross-feed $(v_w)_n$ normal

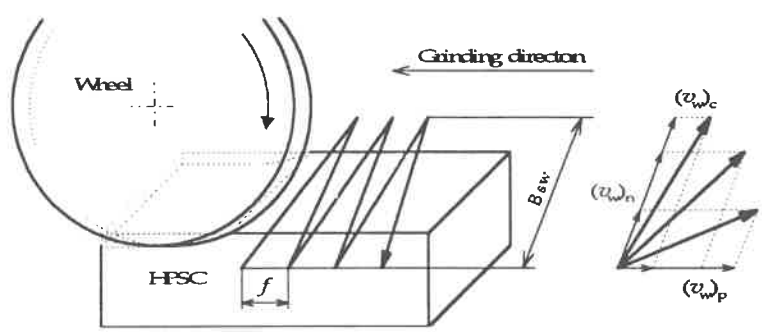

Fig.2 Ultra-smoothness grinding method

to grinding direction is faster than plunge-feed $(v_w)_p$ parallel to grinding direction. In the experiments, the $(v_w)_n$ and $(v_w)_p$ are set by determining the resultant feed $(v_w)_c = \{(v_w)_n + (v_w)_p\}^{1/2}$, the cross-feed width *B*sw and the feed width *f*.

The experimental conditions are summarized in Table 1. The grain size and concentration of the wheel used are #140-mesh and 50, respectively. The fine ceramics used are the hot pressed silicon carbide (HPSC), the hot isostatic pressed silicon nitride (HIPSN) and the alumina-titanium carbide (Al_2O_3-TiC). The observation and roughness measurement of the ground workpiece surface are done with Nomarski microscope and SEM, and with the surface interferometer (WYKO TOPO-3D) and AFM (NanoScope III), respectively.

Table 1 Experimental conditions

Grinding method	**Ultra smoothness**
Wheel	**SD140Q50M**
Workpiece	**Hot pressed silicon carbide, Hot isostatic pressed silicon nitride, Alumina-titanium carbide**
Wheel speed	v_g = 20 mm/s
Resultant feed	$(v_w)_c$ = 0.833 mm/s, 3.33 mm/s
Cross feed width	Bsw = 18 mm
Plunge feed	f = 20 μm/stroke
Depth of cut	t_t = 2 μm
Coolant	**Soluble (1/50) Flow rate : 12 L/min**

3. Results and discussions

3.1. Ductile-mode grinding of fine ceramics with #140-mesh diamond wheel

Figure 3 shows the microscope photographs of the Al_2O_3-TiC surfaces plunge-ground at $(v_w)_p$=0.05mm/s and $(v_w)_p$=0.005mm/s under the wheel speed of V_g=20m/s with the #140-mesh diamond wheel. From the figure, the grinding cracks along with the ductile-mode grinding area are observed on the workpiece surface ground at $(v_w)_p$=0.5mm/s. At the extremely slow table speed of $(v_w)_p$=0.005 mm/s, on the other hand, the ductile-mode ground surface without grinding cracks is obtained all over the whole observed workpiece area. However the whole ground workpiece area of 10mm square observed widely is also confirmed to consist of ductile-mode ground surface. Accordingly the grinding cracks are considered to decrease with the decrease of table speed.

A WYKO 3D image of 256μm square surface of Al_2O_3-TiC ceramic plunge-ground at v_w=0.005mm/s is shown in Fig.4. From the figure, it is found that the grinding grooves parallel to grinding direction are observed on the surface. The height and pitch of grinding groove are about 400nm(P-V) and below about 100μm, respectively. The height is closely related to the maximum surface roughness. The similar results are obtained for HPSC ceramic and HIPSN ceramic.

Accordingly the ductile-mode grinding of fine ceramics with the #140-mesh wheel of the low concentration of 50 is possible in the surface plunge grinding with a conventional surface grinder. It is considered that the problem for the formation of ultra-smoothness is the high grinding grooves.

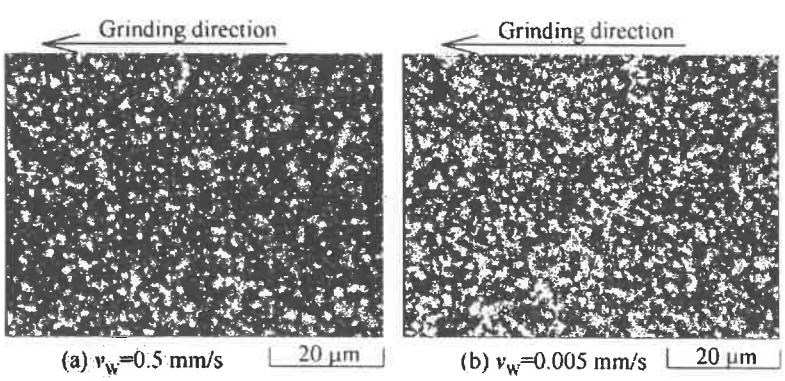

Fig.3 Microscopic photographs of the Al_2O_3-TiC ceramic surfaces plunge-ground at $(v_w)_p$=0.5mm/s and $(v_w)_p$ =0.005mm/s with the #140-mesh wheel
[SD140Q50M, Vg=20m/s, t_t=2μm, Soluble (1/50)]

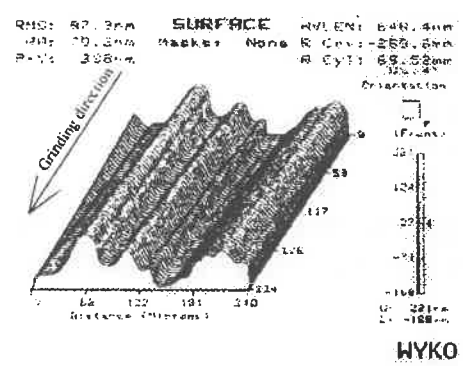

Fig.4 3D image of the Al_2O_3-TiC ceramic surface plunge-ground at $(v_w)_p$=0.005mm/s with the #140-mesh wheel
[SD140Q50M, *V*g=20m/s, t_t=2μm, Soluble (1/50)]

3.2. Ultra-smoothness grinding of fine ceramics with #140-mesh diamond wheel

Figure 5 shows the WYKO 3D image along with microscopic photograph of the Al_2O_3-TiC ceramic surface ground at $(v_w)_c$ =0.83mm/s by ultra-smoothness grinding method with the #140-mesh wheel. From the photograph, a few of grinding cracks can be found on the observed workpiece area. But it is obvious from the WYKO 3D image that the workpiece surface is not formed by continuous regular grinding grooves found in plunge-grinding as shown in Fig.4, but some discontinuous short grinding grooves. The 3D surface roughness of 256μm square surface, which is much better than that formed by plunge-grinding is about 28nm(P-V)s, 4.7nm(RMS)s and 3.8nm(Ra)s. Accordingly the grinding grooves are considered to be removed to large extent.

Figure 6 shows AFM 3D images and 2D profiles of 50μm square surface of HPSC, HIPSN and Al_2O_3-TiC ceramics ground at $(v_w)_c$=3.33mm/s. The upper and lower 2D profiles are measured for the direction parallel and normal to grinding direction, respectively. The obvious micro-hole can be hardly found on the 3D image of the HPSC ceramic surface. From the 2D profiles the surface roughness parallel to grinding direction is about 3.8nm(Rmax)p and 0.91nm(RMS)p for excluding micro-holes. The surface roughness normal to grinding direction is about 5.3nm(Rmax)n for excluding the micro-hole and 54nm(Rmax)p for including the deepest micro-hole.

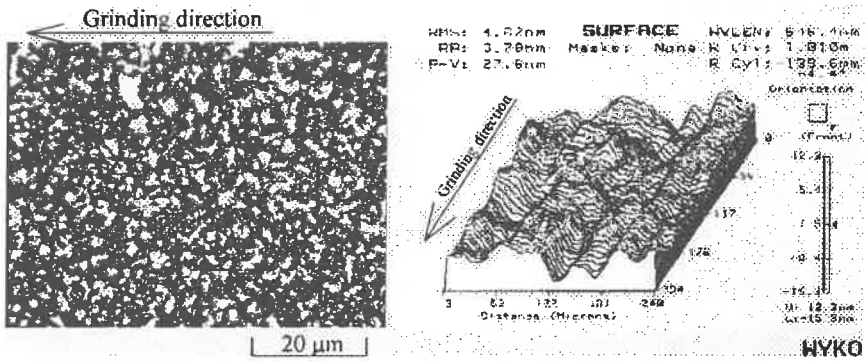

Fig.5 WYKO 3D image with microscopic photograph of the Al_2O_3-TiC ceramic surface ground at $(v_w)_c$=0.83mm/s by ultra-smoothness grinding method with the #140-mesh wheel
[SD140Q50M, Vg=2m/s, t_t=2μm, Soluble (1 /50)]

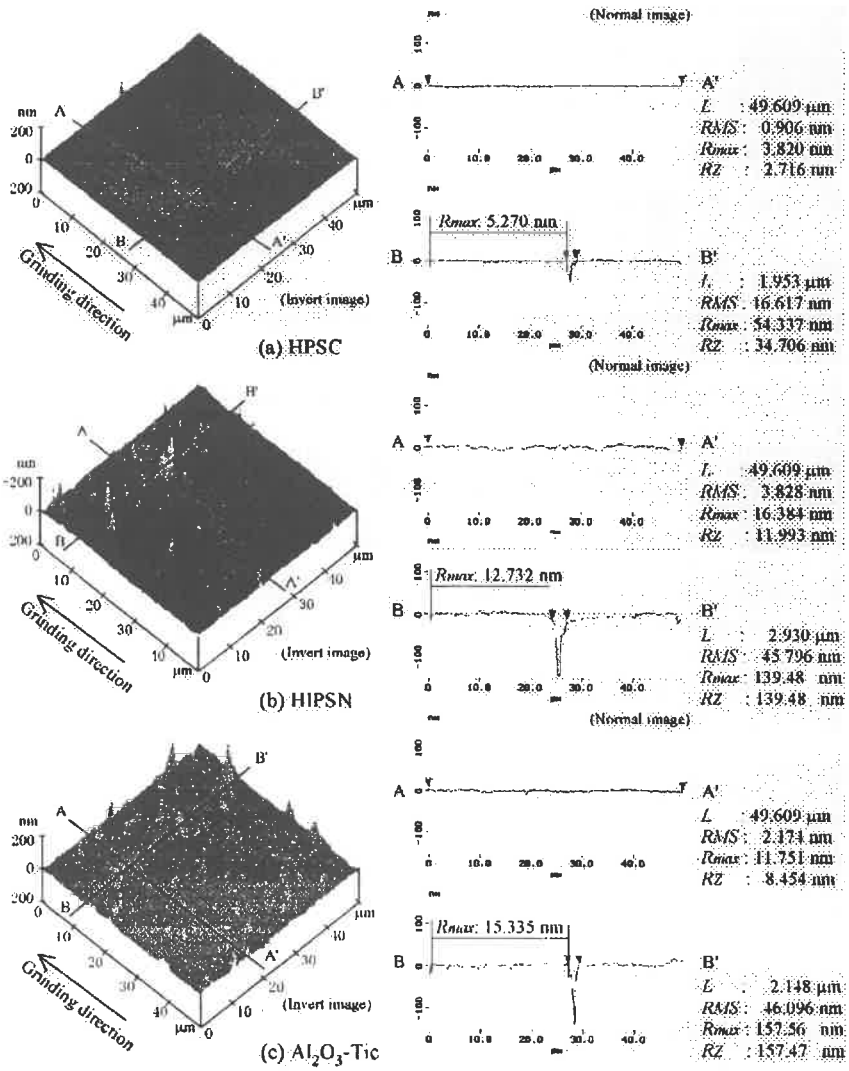

Fig.6 AFM images of fine ceramic surfaces ground at $(v_w)_c$=3.33mm/s by ultra-smoothness grinding method with the #140-mesh wheel
[SD140Q50M, Vg=20m/s, t_t=2μm, Soluble (1/50)]

For the HIPSN and Al_2O_3-TiC ceramics, on the other hand, a lot of micro-holes are found on the ground surface. The surface roughnesses parallel and normal to grinding direction for HIPSN ceramic are about 16.3nm(Rmax)p and 3.8nm(RMS)p for excluding micro-holes, and about 12.7nm(Rmax)n for excluding micro-holes and 140nm(Rmax)n for including a micro-hole, respectively. The surface roughnesses parallel and normal to grinding direction for Al_2O_3-TiC ceramic are about 11.8nm(Rmax)p and 2.1nm(RMS)p for excluding micro-holes, and about 15.3nm(Rmax)n for excluding micro-holes and 158nm(Rmax)n for including a micro-hole, respectively.

It is considered from these results that the suitable ultra-smoothness grinding conditions depend on the characteristics of fine ceramics. In this research, the suitable conditions are not found for ultra-smoothness grinding of various kinds of fine ceramics. However, it is reasonable to say that the newly devised ultra-smoothness grinding method is effective for the formation of ultra-smoothness surface by grinding fine ceramics with the coarse #140-mesh diamond wheel.

4. Summary

The ductile-mode grinding of fine ceramics of the hot pressed silicon carbide (HPSC), the hot isostatic pressed silicon nitride (HIPSN) and the alumina-titanium carbide (Al_2O_3-TiC) with the coarse #140-mesh metal-bonded diamond wheel is found to be possible in the surface plunge grinding. The surface roughness in the ductile-mode plunge grinding, however, is rough over 200nm(Rmax) because of the formation of the grinding grooves. The newly devised ultra-smoothness grinding method in which the grinding grooves can be removed and diminished is effective for the formation of ultra-smoothness surface on the fine ceramics. When using the new method, the surface roughness of the ground hot pressed silicon carbide ceramic area of 50μm square measured with AFM is attainable about 3.8nm(Rmax) and 0.91nm(RMS).

Acknowledgement

The authors would like to thank Okamoto Machine Tool Works Co. Ltd., Yasukawa Electric Co. Ltd., Noritake Diamond Industries Co. Ltd., Osaka Diamond Industries Co. Ltd. Yushiro Chemical Industry Co. Ltd., TOTO Co. Ltd. and Nihon Tungsten Co. Ltd. for providing surface grinder, NC equipment, grinding wheels, grinding fluids and workpiece materials.

References

[1] J. Yoshioka, F. Hashimoto, M. Miyashita, A. Kanai, A. Abo and M. Daito: Ultraprecision Grinding Technology for Brittle Materials, ASME M.C. Shaw Grinding Symposium, PED Vol. 16 (1985) 255.

[2] Y. Namba, Y. Yamada, A. Tsuboi, K. Unno and H. Nakao: Surface Structure of Mn-Zn Ferrite Single Crystals Ground by an Ultra-Precision Surface Grinder with Various Diamond Wheels, Annals of the CIRP, 41, 1 (1992) 347.

[3] Y. Ichida et al: Mirror Finish Grinding of Silicon Nitride Ceramics, Proc. 1st. Int. Conf. on New Manufacturing Technology (1990) 317.

[4] Heiji YASUI, Akira HOSOKAWA, Yoshihiro ARINO and Kunio MATSUNAGA: Influence of Sintering Method on High Smoothness Grinding of Fine Ceramics, Proc. 3th Int. Conf. on Progress Cutting and Grinding, Vol.III (1996) 530.

[5] Heiji YASUI, Yoshihiro ARINO and Kunio MATSUNAGA: Ductile-mode High Smoothness Grinding of Fine Ceramics by Diamond Wheel of Coarse Grain Size (1st Report), J. Japan Soc. Precision Eng., 63, 9 (1997) 1270.

[6] Akira HOSOKAWA, Heiji YASUI, Kunio MATSUNAGA, Go YAMAZAKI and Morihiko SAEKI: Ductile-mode High Smoothness Grinding of a Silicon Nitride Ceramic by #140-Diamond-Wheel, Proc. 6th Int. Symposium on Ceramic Materials and Components for Engines (1998) 475.

PRECISION GRINDING APPARATUS SPECIALLY DEVELOPED FOR MICRO-CYLINDRICAL COMPONENTS

Yeo, S.H., Zhou, M., Tan, B.H, Balon, S.A.P.
Precision Engineering Strategic Research Group
School of Mechanical and Production Engineering
Nanyang Technological University
Nanyang Avenue, Singapore 639798, Singapore
Tel: (65) 790 5539 Fax: (65) 7911859

Abstract
This research work presents the development of a precision grinding apparatus used to manufacture micro-cylindrical components. The different steps of this development from the conceptualisation to the prototyping have been reported. Finally, a test of the precision apparatus has demonstrated that micro-cylindrical components can be ground down to 45μm with an aspect ratio of 4.

Keywords
Precision machine design, micro-grinding, miniature part.

Introduction
The growing needs of micro-mechanical tools are increasing tremendously, for example the micro-milling tools, micro punch, wire bonding capillary, etc .All this micro-components are in common a cylindrical geometry, which is basically a micro-shaft. A micro-shaft has been defined by Friedrich et al.[1] as a cylindrical component with a major diameter of 200μm or less, which is also the border between micro to macro set by Masuzawa and Tönshoff [2].

Manufacturing Process Employed	Minimal Diameter Achieved	Material Used	Conductivity	Aspect Ratio	References
Micro-EDM	2.5μm	Tungsten	Yes	5	[3]
	12μm	HSS	Yes	20	[4]
	4.3μm	Tungsten Carbide	Yes	11	[5]
Turning	10μm	--	--	6	[6]
	25μm	Aluminium (4043-O)	Yes	3	[1] [7]
Grinding	8μm	Tungsten	Yes	8	[8]
	65μm	Ceramic Alumina	No	4	[9]

Table 1: Micro-shaft comparison

Table 1 illustrates some achievements from the fabrication of micro-cylindrical components, using different material removal technology and material. The aspect ratio is defined as the length of the micro-shaft divided by its diameter.

Some micro-cylindrical components have to be made in ceramic because of their specific properties such as the wear resistance, hardness, and non-electrical conductivity. On another hand ceramic micro-components combine two major problems which are the difficult to machine material and the production of miniature components. These two problems can lead to the breakage of the micro-cylindrical component during the machining process. Therefore to produce a ceramic micro-cylindrical components, a precision grinding apparatus has been specially developed to solve simultaneously the two problems reported previously. This paper is to present the different steps of the development (conceptualisation, prototyping) and conclude on the testing of the precision grinding apparatus.

Conceptualisation

The development of the precision grinding apparatus for micro-cylindrical components has started with a theoretical model reported by Balon [10]. This model compared the theoretical grinding force applied and the maximal strength of the micro-component derived from the material mechanical properties. The theoretical grinding force has been approximated using Equation 1 reported by Shaw [11].

$$F_c = \frac{E' v_w d B}{v_s} \qquad (1)$$

where F_c *is the cutting force (N),* E' *is the specific grinding energy (J/mm*^{3}*),* v_w *is the linear speed of the specimen (m/s),* v_s *is the linear speed of the grinding wheel (m/s), d is the depth of cut (mm), and B is the grinding wheel width (mm)*

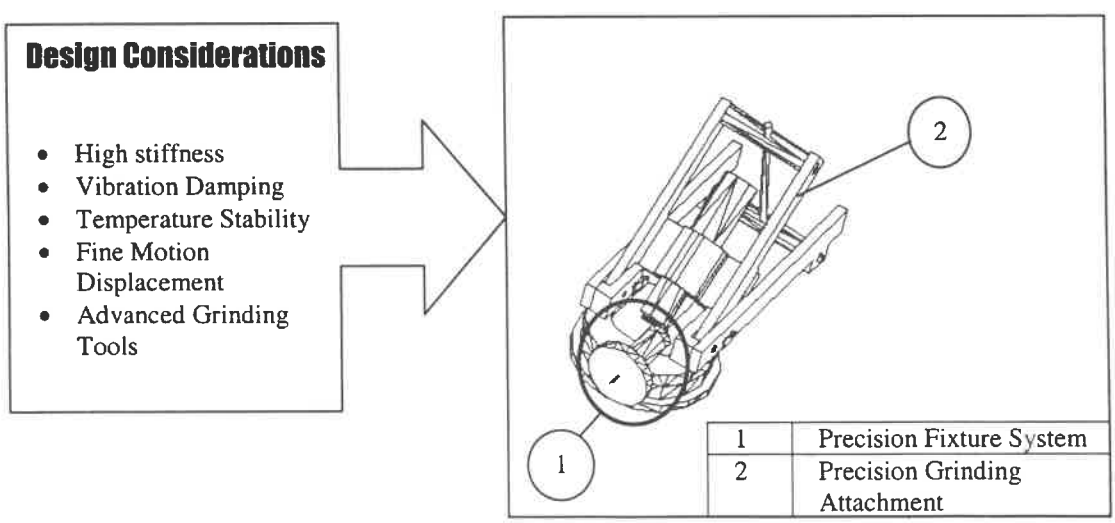

Figure 1: Design considerations and the technical drawing

Balon [10] reported that to reduce down the diameter of the micro-component the grinding force has to be extremely small, below 1mN. Therefore the solutions selected to reduce F_c were to adopt a high rotational speed for the grinding wheel (v_s) and to select a grinding wheel with the minimal width (B). The theoretical model and the design considerations reported by Yeo and Balon [12] has lead to the technical drawing (see Figure 1) of the precision grinding apparatus. The design of the precision grinding apparatus as seen in Figure 1 consists of two main elements namely the Precision Grinding Attachment and the Precision Fixture System.

Prototyping

Figure 2 shows the prototype of the precision grinding apparatus mounted on a commercially available high precision turning machine. A high-speed precision spindle mounted on the precision grinding attachment is used to drive the diamond wheel of few ten of micron width. The raw ceramic rod is clamped by the precision fixture system during the full grinding operation.

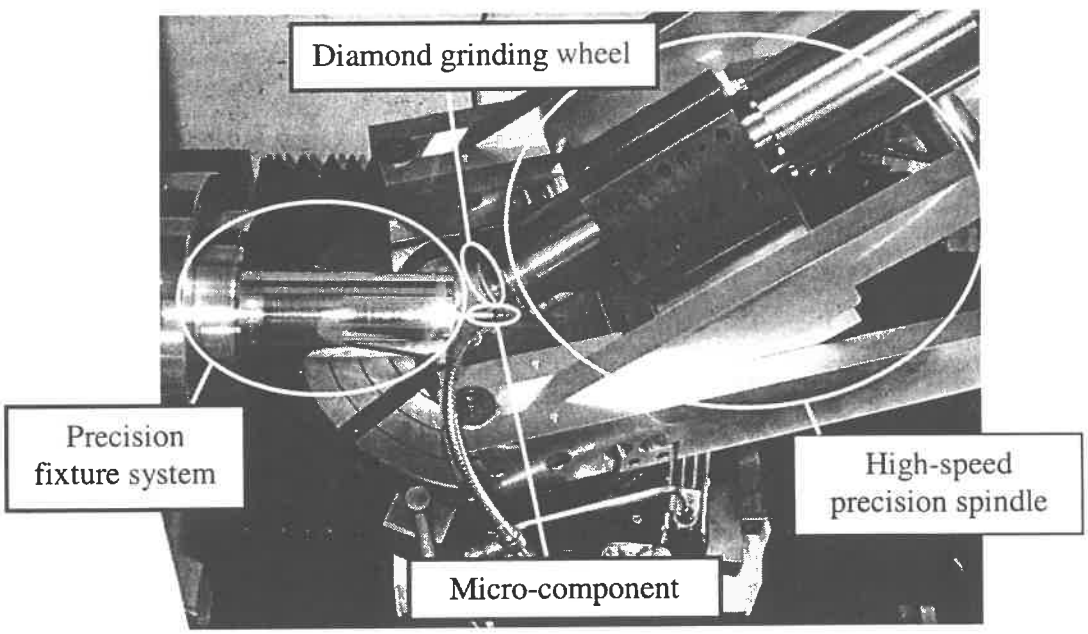

Figure 2: Overview of the precision grinding apparatus

Testing

The precision grinding apparatus has been tested by grinding a micro-cylindrical component made of polycrystal aluminium oxide (99.8%), with a grain size range varying from 2 to 50μm. Figure 3 shows the micro-cylindrical component obtained after grinding. The diameter obtained is 45μm with a length of 184μm. The aspect ratio is then around 4. Yeo and Balon [13] has shown that the material removal occurred in the ductile zone, which means that minimal crack is generated during the grinding process. Therefore the risk of cracks propagation which could lead to the breakage of the micro-cylindrical component is minimised, due to the ductile grinding.

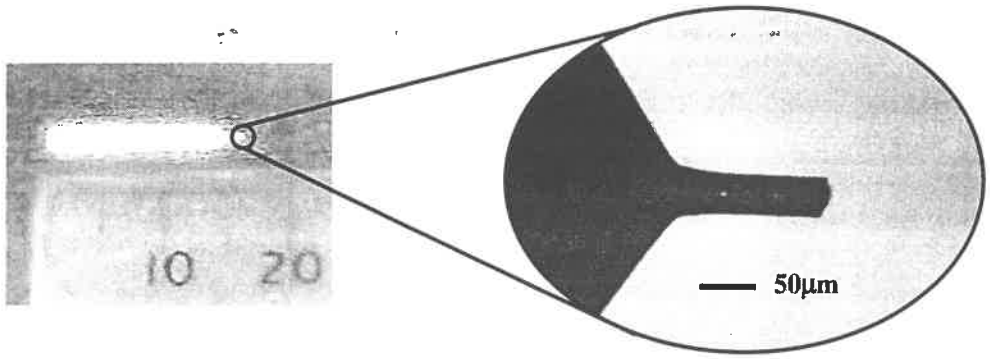

Figure 3: Micro-cylindrical component

Summary

This paper presents the evolution of the precision grinding apparatus from the conceptualisation to the final testing. The precision grinding apparatus has been designed to minimise the breakage of the micro-cylindrical components during the manufacturing process, and has proven experimentally good capability to get it. In the experiment conducted, a micro-cylindrical part made of alumina has been ground successfully to diameter 45μm with an aspect ratio of around 4.

References:

[1] Friedrich, C.R. and Kithiganahalli, B. (1994). *Deflexion compensation model for the machining of microshafts*. Processing of the American Society of Precision Engineering, Annual Meeting, pp. 461-464.

[2] Masuzawa, T. and Tönshoff, H.K. (1997). *Three- dimensional micromachining by machine tools*. Annals of the CIRP, Vol.46, No.2, pp.621-628.

[3] Masuzawa, T. and Fujino, M. (1990). *A process for manufacturing very fine pin tools*. Technical Paper, Internal Manufacturing Technology Conference'90, Chicago Illinois.

[4] Masuzawa, T., Fujino, M., Kobayashi, K. (1985). *Wire electro-discharge grinding for micro-machining*. Annals of the CIRP, Vol.34, No.1, pp.431-434.

[5] Li, H. and Masaki, T. (1991). *Micro-EDM*. Technical Paper, Electrical Discharge Machining Conference, Michigan US.

[6] Yamagata, Y. et al. (1996). *A new fabrication method for microactuators with piezoelectric thin film using precision cutting technique*. Proceeding of IEEE MEMS, San Diego, CA, pp. 307-311.

[7] Frazier, B., Friedrich, C., Warrington, R.O. (1994). *The miniaturisation technologies: Past, Present, and Future*. Proceeding of the 20th Annual Conference of the IEEE Industrial Electronics Society, Bologne Italy, pp.1460-1465.

[8] Kugler Gmbh (1998). Micro Mill Technical Brochure

[9] Mason,F. (1997). *Making Tiny Ceramic Tools*. Manufacturing Engineering, Vol.118, No.1, 3 pp.

[10] Balon, S.A.P. (1999). Development of a Novel Precision Grinding Technique for Micro-Parts. Master thesis, NTU, Singapore.

[11] Shaw, M.C. (1996). Principles of Abrasive Processing. Oxford University Press.

[12] Yeo, S.H. and Balon, S.A.P. (1999). *Development of a New Grinding Set-Up for Micro-cylindrical Parts Fabrication*. 1st International Conference of EUSPEN., Bremen Germany, pp.155-158.

[13] Yeo, S.H. and Balon, S.A.P. (1999). *Fabrication of micro-cylindrical parts based on a novel grinding technique*. Journal of Engineering Manufacture. Accepted for publication

Tribo-chemical Smoothing of Diamond Film

Ken'ichiro HORIO, Makoto HYOHDOH, Toshio KASAI
Mechanical Engineering Department, Saitama University
255 Shimo-ohkubo, Urawa, 3388570, JAPAN

1. Introduction

For last twenty years much effort for depositing diamond film has being conducted. Chemical Vapor Deposition (CVD) technique that uses combination of carbon contented gas (for example methane, ethane and so on) and hydrogen has developed successfully. The diamond film is good material from the point of high hardness, high heat conductivity, high electrical insulation, chemical resisting, high transparency and high index of refraction. So the film is expected to apply (1)coating where wear resistance is needed, (2)a new material candidate of semiconductors for severe environment, (3)optical window material for severe environment for example ultraviolet or X-ray irradiation, or other fields.

In order to apply the diamond film for those particular areas, it can be necessary to smooth the surface of the deposited diamond. Generally speaking, smoothing is conducted by removing only the peak area of the surface. If you intend to wear the diamond peak mechanically, strong friction is needed. The strong friction may cause exfoliation (peeling off) because bond strength between the diamond and the substrate is not so high. Thus our developing polishing technique for tools for diamond turning may be hard to be applied.

As the CVD diamond film is an accumulation of minute crystal growth, the film is polycrystalline and has small peak and valley. Another problem caused by the polycrystalline is that the wear rate by mechanical friction along the different crystal axis varies very much at the diamond, which makes hard to remove all the peaks uniformly. In this study our object is to smooth rather thin, a few micrometer, film for optical or semi-conductor application. Therefore to avoid exfoliation (peeling off) is the biggest issue.

2. Comparison among three method

We tried three kinds of polishing technique. The first one was using iron lap and fine diamond powders with rather high speed rotation that is the way to be used for sharpening the diamond tools or brightening jewelry which is single crystal.

The second one was using resinoid bond diamond wheel that is widely used in machining sintered polycrystalline diamond tools. However in this study, constant pressure type grinding like lapping was adopted to avoid strong force to the film. The experimental setup was almost same as drawn in Fig.1 except using diamond wheel instead of quartz glass.

The last one was ordinary conditioning ring type plain polishing with unique combination of glass disc tool with very fine silicone dioxide (SiO_2) powders. Fig.1 shows a setup of the method. The reason of using glass disc or SiO_2 is expectation of oxidization.

Table1 shows features of the three methods.

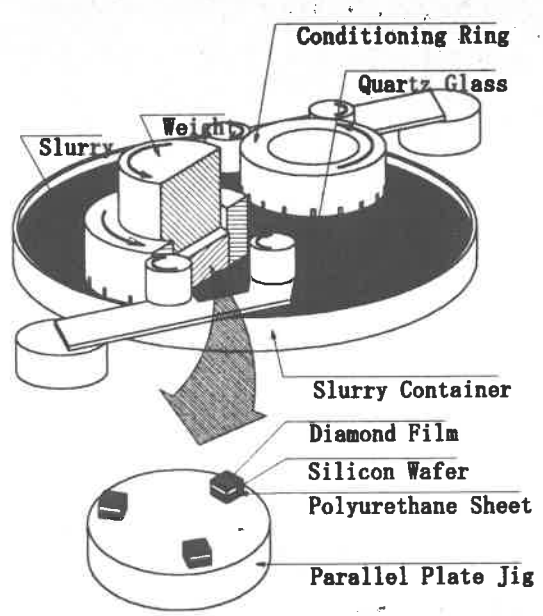

Fig.1 Setup of polishing machine (Conditioning ring type)

Table 1 Features of three smoothing method for CVD diamond film

*Type**	*Tool*	*Abrasive*	*Depth of cut*	*Tool rotating speed*	*Machining loci*
A	Steel	Diamond	Constant pressure	High	One direction
B	Diamond wheel (resinoid bond)	SiO_2	Constant pressure	Low	Multi direction
C	Quartz glass	SiO_2	Constant pressure	Low	Multi direction

* *A: Polishing method for single crystalline diamond*
B: Grinding under constant pressure
C: Conditioning ring type plain polishing

Polishing experiments by three ways were performed. The specimens were CVD diamond films deposited upon silicon wafers.

The first (A) and the second (B) attempts did not succeed. The exfoliation occurred in these processes and it was not able to get good surfaces.

In the last process (C), the exfoliation never occurred and better surface was obtained. In the process the oxidization generated by mechanical friction (tribo-chemical reaction) was expected. The reaction could aid the smoothing without peeling off. Fig.2 shows a SEM photograph of the diamond film polished by the last way (C). You can see that some wear was happened and only the peak was removed.

Fig.2 SEM photograph of polished diamond

3.Process parameters in glass disc polishing

To clarify the effect of each process parameter or to search an optimum polishing conditions in the glass disc polishing, some experiments were conducted. Table 2 shows the experimental conditions. Standard polishing condition was the combination of the glass disc tool and the SiO_2 abrasive. Zygo New View 100 measured surface roughness of the polished diamond film. We investigated the effect of tool material, abrasive material, slurry density, machining load and size of abrasive.

3.1.Tool material

Fig.3 shows the experimental results for the tool material. The horizontal axis is machining duration, and the vertical axis is the surface roughness of the diamond film at each time. We tried both polyurethane and cast iron disc as a tool in comparison with quartz glass. SiO_2 was used as abrasive at each experiment. In the case of the cast iron disc, exfoliation occurred during polishing. Between two other materials the glass disc showed better surface roughness.

Table 2 Experimental conditions

Machine	Conditioning ring type plain polishing machine
Tool	Quartz glass Polyurethane Cast iron
Abrasive	9, 14, 55nm SiO_2 30nm TiO_2
Slurry density	0(pure water), 2, 4, 10wt%
Polishing pressure	100, 300, 500kPa
Polishing speed	14m/min
Polishing duration	Up to 3.5hr
Surface roughness measurement apparatus	New View 100 (Zygo)

3.2.Abrasive material

To comparison with SiO_2 powder, we tried using TiO_2 powder and no powder condition where polishing was done with pure water only. Fig.4 shows the result.

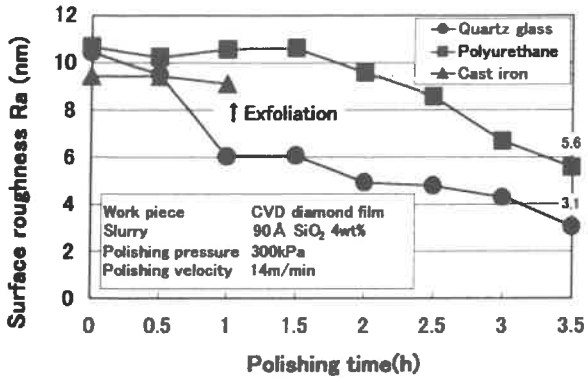

Fig.3 Effect of polishing tool

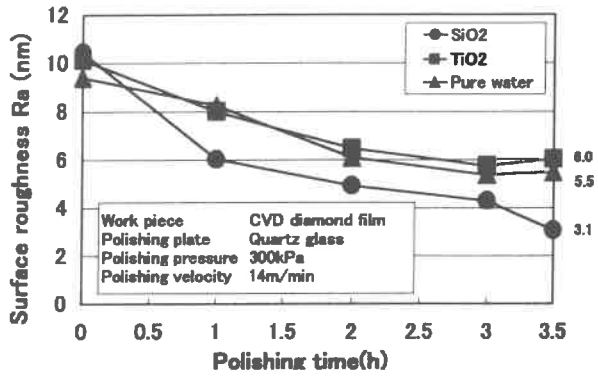

Fig.4 Effect of abrasive material

Using the SiO_2 powders shows the best result and there is almost no difference between the other two conditions. The SiO_2 abrasive works the best for smoothing the diamond film.

As even glass disc with pure water only (without any powders) can smooth the diamond film of 10nmRa surface to less than 6nmRa, it is clarified that the glass disc itself acts some effect to smooth the diamond. The main component of the glass is SiO_2 as well. Some action between SiO_2 in the glass disc or from the abrasive and carbon atoms in the diamond takes a great role to remove the diamond from only the summit area.

3.3.Slurry density

Fig.5 shows the experimental results to investigate the influence of slurry density at the combination of quartz glass disc and SiO_2 abrasive. Higher the density is, better the surface becomes. In the case of density of 10%, 2.4nmRa surface could be realized. We think viscosity of the slurry may affect some extent as higher density slurry shows more viscosity.

3.4.Machining load

Fig.6 shows the effect of polishing pressure at glass disc and SiO_2 abrasive combination. Higher pressure condition can get better surface roughness. We think that contact ratio between SiO_2 abrasive and diamond surface becomes higher when more loads are supplied and the rate can accelerate the chemical action on the surface.

3.5.Size of abrasive

Fig.7 shows the influence of the abrasive size. It shows there is almost no effect of the size. If the smoothing action is thought to be mechanical, the diameters of the abrasive affect more. However as

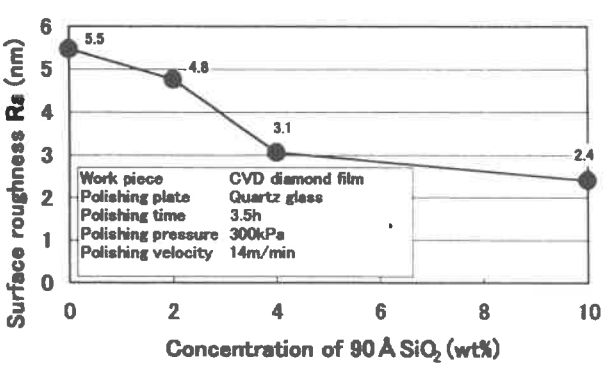

Fig.5 Effect of slurry density

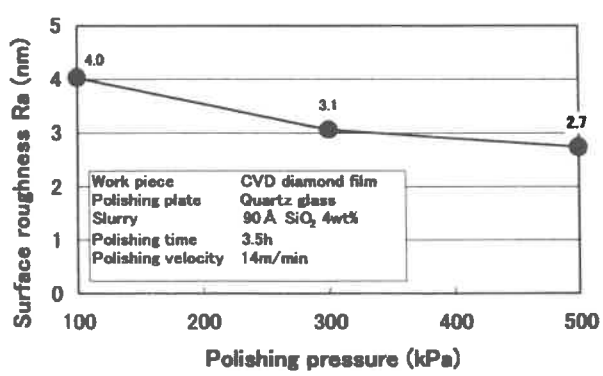

Fig.6 Effect of polishing load

the action is thought to be some chemical action, it can be convinced that the powder size has no effect.

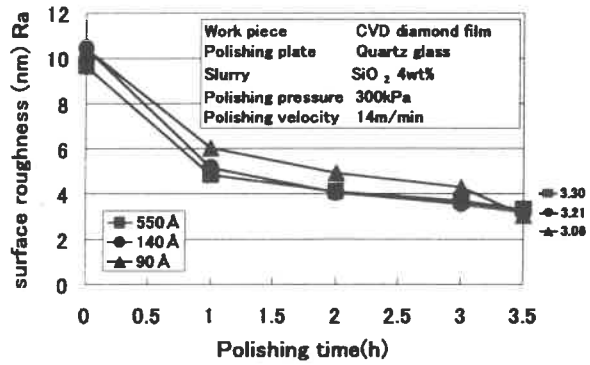

Fig.7 Effect of abrasive size

4.Conclusion

1) The combination of glass disc and SiO_2 powder on ordinary conditioning-ring-type plain polishing machine is a good choice to smooth the diamond film surface.
2) Under the condition any exfoliation cannot be occurred.
3) Both the glass disc and the SiO_2 powder contribute to smooth the surface.
4) High slurry density and high machining pressure is preferable.
5) The size of SiO_2 powder has no effect to smooth the diamond. (within our experimental conditions)
6) Under the best combination, surface roughness of 2.4nmRa can be obtained.

CMP Interfacial Fluid Pressure and Modeling

Lei Shan and Steven Danyluk

The George W. Woodruff School of Mechanical Engineering
Georgia Institute of Technology, Atlanta, GA 30332-0405

Abstract

This work represents our research of the interfacial fluid pressure measurement and modeling during CMP (chemical mechanical polishing), which includes pad surface profile and compression analysis, measurement of the interfacial fluid pressure and shear force during sliding, and modeling. For most CMP applications, the interfacial fluid pressure exhibits a sub-ambient value at the leading two-thirds of the contact and a positive value at the trailing third, and the resulting (suction) force of the average interfacial fluid pressure can be of the order of up to 50~100% of the applied normal load [1]. The effects of process variables on this interfacial fluid pressure were studied, including fluid viscosity, pad structure and modulus, velocity, normal load, pad surface roughness, and wafer surface curvature. A model, based on contact stress analysis, interfacial fluid film estimation, and the fluid mechanics, can explain the pressure dependence of those process variables and predict the fluid pressure reasonably well.

Introduction

Chemical Mechanical Polishing (CMP) is an emerging technique specially used in the preparation of silicon substrates (wafers) and the planarization of partially processed silicon wafers for integrated circuit fabrication. Conventionally, the planarization of partially processed silicon wafers can be done with processes such as reflow, spin-on, or etchback. However, CMP becomes the only planarization method that can give the required global planarity (planarity on scale larger than 10μm) for multilevel interconnection in ULSI devices [2]. CMP causes material removal by rubbing a polishing pad against the wafer in the presence of a chemically active, abrasive containing liquid slurry. In practice, The silicon wafer is held facing down and a normal load is applied while the polishing pad, mounted to a rigid turntable, rotates beneath the wafer.

The mechanisms of material removal in CMP are related to both chemical and mechanical effects. For different target surface materials, the contribution of chemical or mechanical interactions to the material removal and planarity may vary greatly. However, regardless of what material is to be polished, the mechanical interaction contributes more to the planarization of the polished surface (because chemical effect is generally conformal), which is in turn affected by the contact stress and fluid transport and pressure at the silicon/pad interface. There are mainly two trends of CMP interface mechanics. One suggested that the silicon wafer is separated from the polishing pad by a hydrodynamic film of slurry and polishing is done by abrasive collision, the so-called fluid base wear. The other said that the hydrodynamic effect is not strong enough to separate the wafer from pad and pad/abrasive abrasion dominates the polishing process. Both of them assumed the existence of a positive fluid pressure at the interface. Unexpectedly, in our experiments of interfacial fluid pressure measurements, large area of sub-ambient pressure was measured, and the overall effect was a suction force in addition to the applied normal load, which indicates a potential effect on the polishing rate and uniformity. To understand the physical mechanism of the suction and model the CMP process to address the need of precise production prediction, the effects of process variables on this interfacial fluid pressure were studied, including fluid viscosity, pad structure and modulus, velocity, normal load, pad surface roughness, and wafer surface curvature.

Experiments

The apparatus shown in Figure 1, was a commercial bench top polishing machine (Logitech model PM4 built in 1994) with custom-built additions. The polishing machine had a 305 mm (12 inch) diameter stainless steel turntable driven by a 1/3 horsepower speed controlled DC drive. Speed was controllable to within 1 rpm from 5 to 70 rpm and the turntable could withstand 450 N vertical loads as well as 450 N horizontal (frictional drag) loads. Polishing pads were bonded onto the turntable with sheets of double sided pressure sensitive adhesive. A custom-built overhead structure was added to support samples and to mount instrumentation. The pressure of the slurry trapped at the 'wafer/pad' interface was measured with the data acquisition system as shown in Figure 2. This the pressure sampling fixture is a 100 mm diameter, 25 mm thick, stainless steel disk with 16 – 0.4 mm diameter holes drilled through to the 'pad/wafer' interface. The array of holes of the pressure fixture can be aligned at any desired direction during CMP. Interfacial pressure was measured by connecting the holes to 16 pressure sensors that have a resolution of 0.1 kPa. The typical polishing pad used in the experiments was a commercially available (Rodel IC1000), impermeable, void filled, cast polyurethane sheet approximately 1.34 mm thick. After conditioned with 80μm grit tool, it has an average surface roughness of about 5μm. For comparison, a sheet of mylar tape was attached on the top of the pad which has an average surface roughness of about 0.5μm and decreases the friction coefficient from 0.4 to 0.1. During most of the pressure measurements, the pad was flooded with water, and the fixture was held stationary. To determine the effect of wafer surface curvature, a different fixture shown in figure 5 was designed with the capability of surface curvature adjustment. There are 12 holes in each orthogonal direction.

Results

The typical magnitude and distribution of the interfacial fluid pressure is shown at the left bottom in figure 2, i.e. the leading two-thirds of the wafer exhibits a negative pressure, and the trailing third a positive pressure. The overall average pressure at the interface is "negative" and act as a suction force of the order of 50–100% of the normal load applied during polishing.

Figure 3 shows an example of the transition of friction and fluid pressure at the interface, for the IC1000 perforated pad conditioned with 150μm grit tool, 20kPa normal load, 10μm flatness of the fixture surface, and 0.3m/sec relative velocity. The magnitude of the friction within the stable region refers to an appearance of the friction coefficient of 0.3. The fluid pressure shown in the graph is the average value of the overall pressure at the interface. The 16-hole fixture and the first friction measurement configuration were used for these results. The friction at the interface increased in the first minute and then kept decreasing until stabilized. The average fluid pressure similarly increased in magnitude and then decreased after one and half minutes, which coincides with the transition of the friction. This indicates there exists a relationship between the friction and overall fluid pressure at the interface.

Figure 4 is an example that shows the effects of relative velocity and pad surface roughness. With the increase of the relative velocity, the magnitude of the sub-ambient pressure increases and the zero point shift backward. The magnitude of the sub-ambient pressure increases with the increase of pad surface roughness, and the effect is significant. Figure 5 shows the effects of surface profile on the interfacial fluid pressure, for IC1000 non-perforated pad, 20kPa normal load, and 0.3m/sec relative velocity. The result obtained from the measurement on new fixture, whose center deflection of the surface was set at 100μm (convex) by the setting screw, was compared with the data of the 16-hole fixture. The effect of the surface profile on the fluid pressure is significant, i.e. with the surface changed from flat to convex, the fluid pressure at the leading half of the interface changed from sub-ambient to positive, and that at the trailing half almost flatted out to zero.

Analytical Model

The contact stress between a rigid wafer and a compliant pad is not constant but has a bowl shape, i.e. high stress at the edge and low stress at the center [3]. And with the motion of one part, due to the shear stress caused by the friction force, the contact stress distribution shifts backwards, behind the leading edge of the moving surface. The applied load between the two surfaces is supported by asperities and there exists a liquid film at the interface [4], which varies with the contact stress, i.e. thicker film at the center and thinner film at the edge (Figure 6). From lubrication theory, we know that a divergent gap always leads to negative pressure and a convergent gap always leads to positive pressure [5]. This is the reason for the negative pressure at the leading edge and positive pressure at the trailing edge. By using the above physical model, the pressure distribution along the tangential central line can be calculated by solving the following differential equation:

$$\frac{d}{dx}\left(\phi_x h^3 \frac{dp}{dx}\right) = 6\mu V \frac{dh}{dx}$$

where, ϕ_x is the flow factor for correction of isotropic rough surfaces [6]:

$$\phi_x = 1 - 0.9\exp\left(-0.56\frac{h}{s}\right)$$

h is the liquid film thickness:

$$h(x) = s\ln\left(\frac{\sqrt{\pi}\,\eta E R^{1/2} s^{3/2}}{(1-\nu^2)\sigma(x)}\right)$$

and s is the contact stress:

$$\sigma(x) = \frac{P\cos\pi\gamma}{\pi(a^2 - x^2)^{1/2}}\left(\frac{a+x}{a-x}\right)^{\gamma}, \qquad \cot\pi\gamma = -\frac{2(1-\nu)}{f(1-2\nu)}$$

Figure 7 shows an example of the magnitude and distribution of the calculated fluid pressure vs. measured curve. The two curves fit each other reasonably well.

Conclusion

The results show that the leading two-thirds of the wafer/pad interface exhibits a negative pressure, and the trailing third a positive pressure during CMP process. The magnitude of this pressure can be of the order of the applied load, and thus it could result in a non-uniform polished surface.

References

[1] L. Shan, J. Tichy, and S. Danyluk, *"Interfacial Fluid Mechanics and Pressure Prediction in Chemical Mechanical Polishing"*, to be published on Journal of Tribology, 1999

[2] K. Holland and T. Bibby, *"Planarization by CMP for ULSI Applications"*, Process Information by IPEC, Process Technology

[3] K. L. Johnson, "*Contact Mechanics*", P41, Cambridge University Press, Cambridge, UK, 1985

[4] J. A. Greenwood and J. B. P. Williamson, 1966, *"Contact of Nominally Flat Rough Surfaces"*, Proc Roy Soc London, A295, p300-319.

[5] B. J. Hamrock, 1994, "*Fundamentals of Fluid Film Lubrication*", McGraw-Hill, p141.

[6] N. Patir and H. Cheng, 1978, *"An Average Flow Model for Determining Effects of Three Dimensional Roughness on Partial Hydrodynamic Lubrication"*, ASME Journal of Lubrication Technology, Vol. 100, No. 1, p12-17.

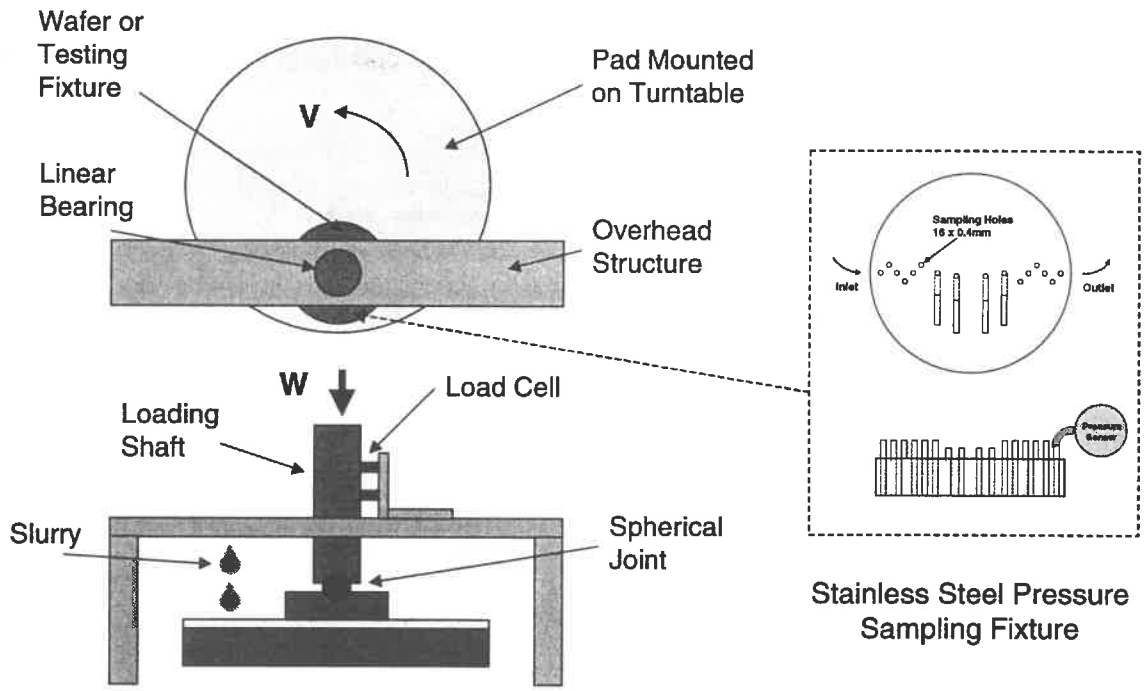

Figure 1. Schematic of the polishing platen and overhead structure

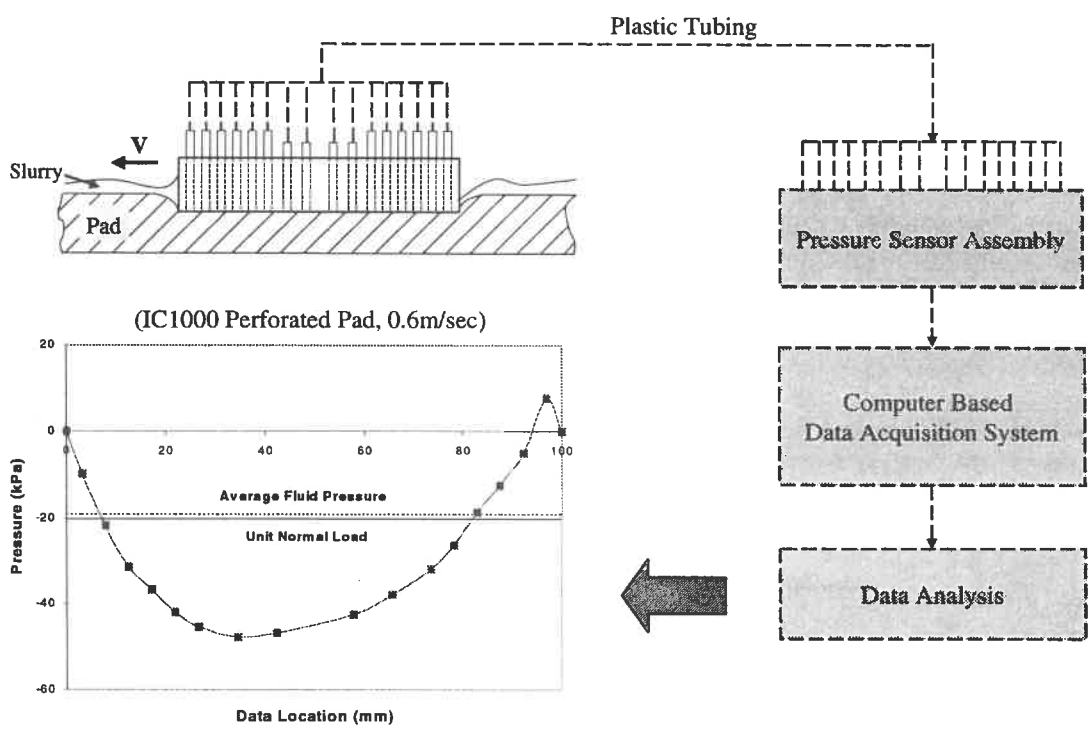

Figure 2. Data acquisition system

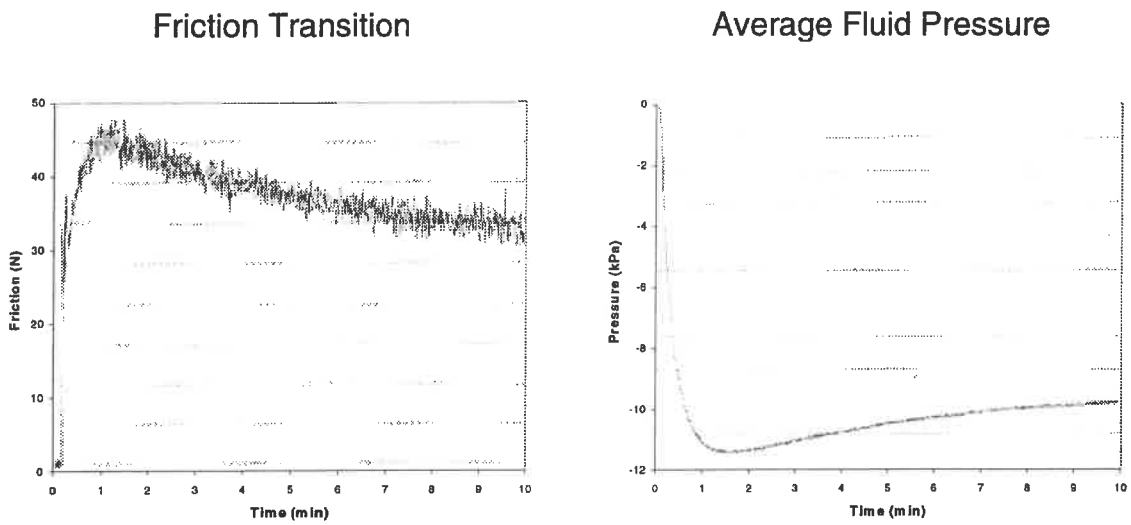

Figure 3. The transition of friction and fluid pressure at the interface.
IC1000 perforated pad, 20kPa normal load, and 0.3m/sec relative velocity.

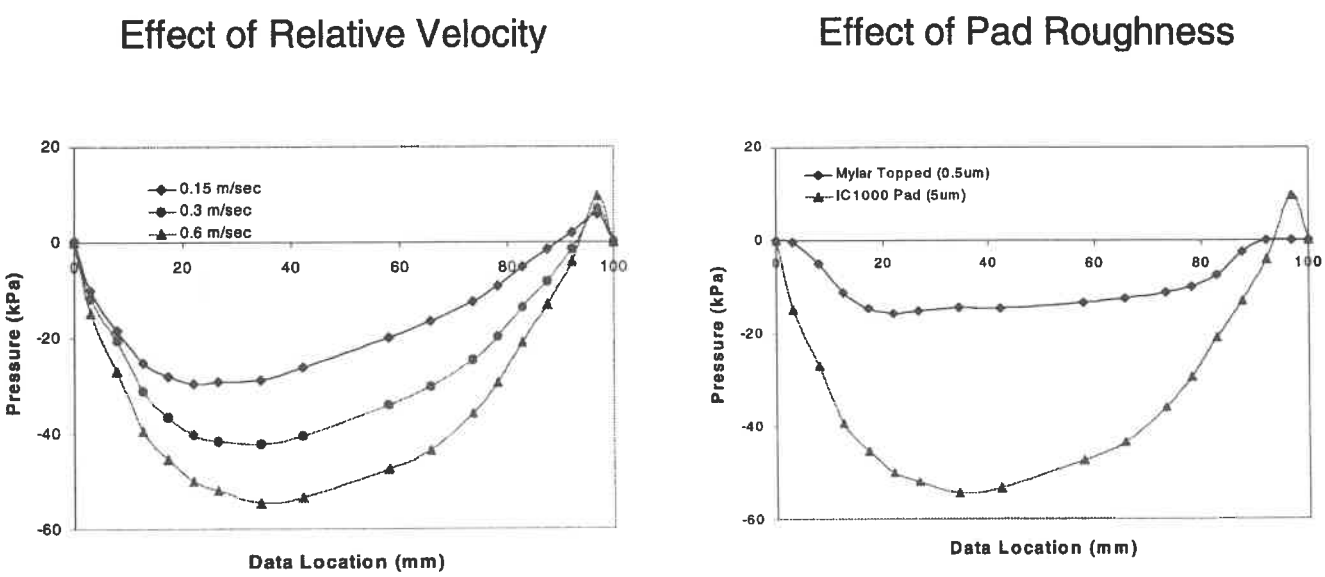

Figure 4. The effects of relative velocity and pad surface roughness.
IC1000 perforated pad, 20kPa normal load

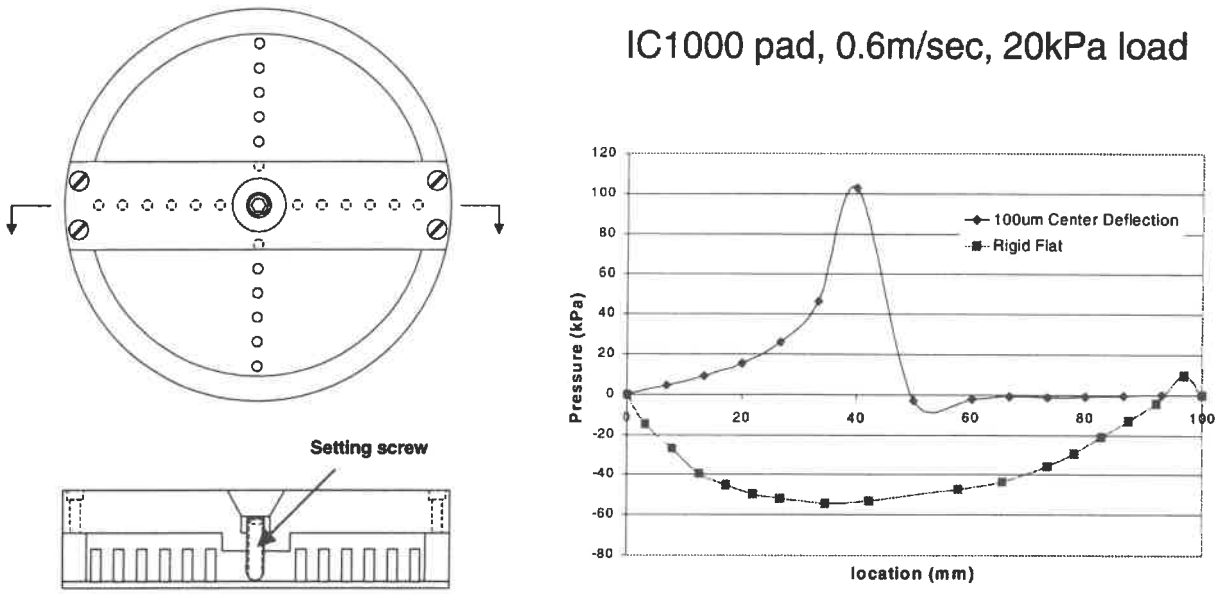

Figure 5. The effects of surface curvature on the interfacial fluid pressure. IC1000 perforated pad, 20kPa normal load, and 0.3m/sec relative velocity

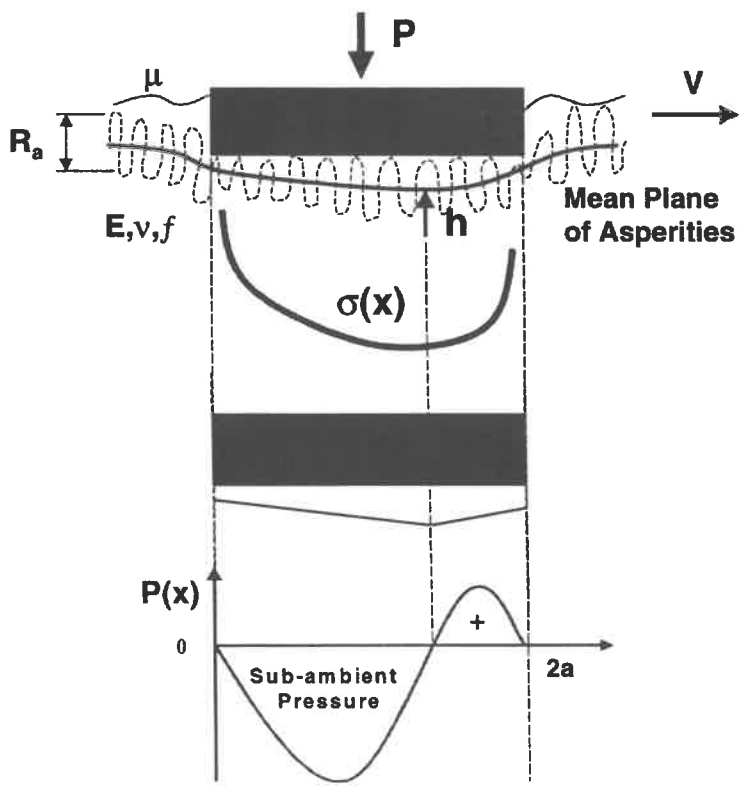

Figure 6. Schematic of the physical system (with compressed asperities), contact stress, and predicted pressure distribution.

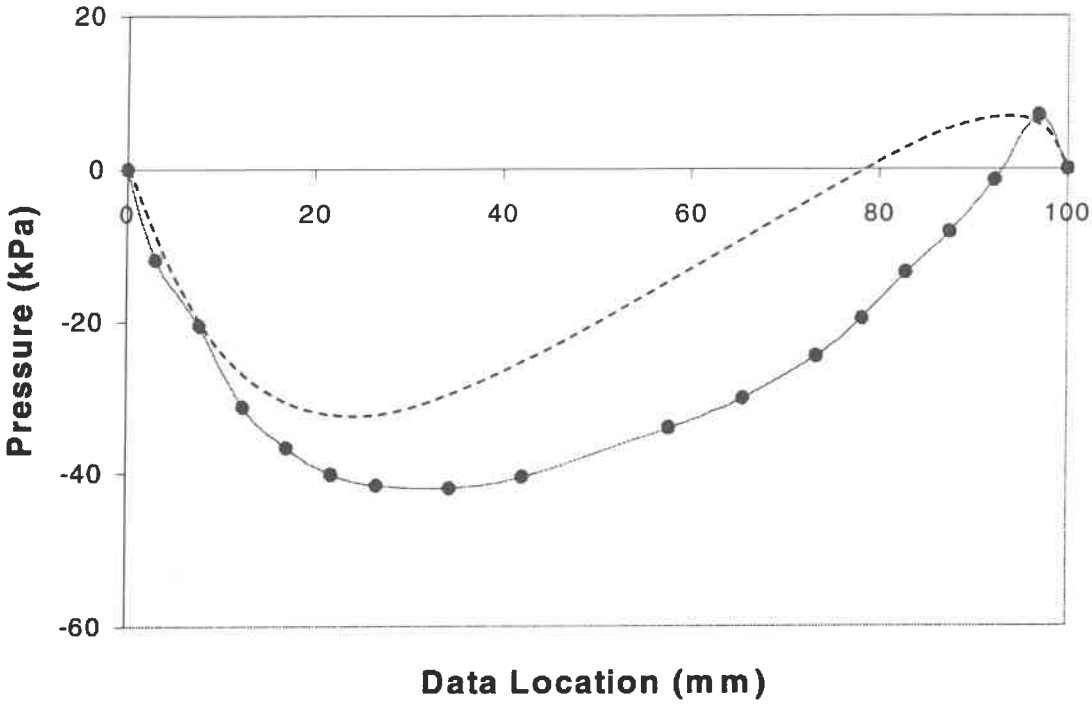

Figure 7. The calculated fluid pressure vs. measured curve.
IC1000 perforated pad, 20kPa normal load, 0.3m/sec velocity

Modeling of Geometric Errors of Manufactured Parts for Manufacturing Process Control

X. David Zhang[1], Chuck Zhang[2], and Ben Wang[2]

[1] *Fuel Systems, Cummins Engine Company*
[2] *College of Engineering, Florida A&M University – Florida State University*

Introduction

Imperfections in manufacturing processes (such as spindle errors of machine tools, thermal expansion of workpiece, and tool wear) cause machined workpieces to deviate from their ideal designed geometry. The manufactured geometric errors are usually measured with coordinate metrology devices in terms of standard geometric errors such as straightness errors, roundness errors, etc. Although these errors may have some links to product performance, they often do not have direct correlation with the imperfections (or errors) of manufacturing processes and thus they are not suitable for manufacturing process control. In the last decades, attempts have been made to manipulate or decompose the measured geometric errors into various frequency components: a high frequency component as *roughness error*, an intermediate frequency component as *waviness errors*, and a low frequency component as *form errors*. Although the manipulated error information is helpful in manufacturing process control, its effectiveness for identifying error sources of a manufacturing process has been unsatisfactory.

In this research, a new method based on *Legendre and Fourier (L-F) polynomials* is introduced for modeling geometric errors of machined cylindrical parts. The method is demonstrated through the modeling of manufactured errors in precision cylindrical turning and grinding processes. These errors and their sources are studied in three independent categories, cross-section form errors, axial form errors, and cross-section size errors. In each category, modeling of typical manufactured errors is discussed. The intention of this research is to use the novel method to better understand the root causes of the errors and provide an effective diagnosis tool for manufacturing process control.

Cross-Section Form Errors

Cross-section error of a manufactured cylindrical part is the error out of roundness in a cross section perpendicular to the axis of a manufactured part. Modeling of the errors produced by spindle defects of a machine tool and fixturing distortion is discussed.

The spindle of a lathe or a chucking-type spindle grinder is supported by a series of bearings in headstock of a machine tool. Some imperfections on bearing components make the spindle unstable in the radial direction as the spindle rotates. The radial variation of spindle causes geometric errors on the manufactured workpiece. Typical imperfections on bearing components are form errors and size errors of a bearing component such as a bearing ball, roller, or groove. The imperfections often produce sine and cosine shape errors on a machined workpiece. In an example of a ball bearing with the oversized ball by ΔD in a lathe spindle, it is not difficult to mathematically derive a geometric error function, $\Delta r(\theta)$, on the workpiece as shown in Equation (1).

$$\Delta r(\theta) \approx -\Delta D \cos[\frac{1}{2}\frac{R_1}{R_1+R_2}\theta] \qquad (1)$$

$\Delta r(\theta)$: radial error;
ΔD: diameter error of the oversized ball;
R_1: radius of the inner groove of the bearing;
R_2: nominal radius of the oversized ball;

As in the above example, many other defects on a ball or inner groove of a journal bearing can lead to sine and cosine form errors on a machined cylindrical workpiece. If there is a dominant defect in the bearing components, a machined surface error may appear in an obvious sine or cosine pattern, such as a two-lobing shape, three-lobing shape, and so forth. In general, the geometric error function, $\Delta r(\theta)$, by the spindle bearing components on the machined surface is a sum of sine and cosine functions as Equation 2.

$$\begin{aligned} r(\theta) &= r_0 + \Delta r(\theta) \\ &= r_0 + \sum A_i \cos(i\theta) + \sum B_i \sin(i\theta) \end{aligned} \qquad (2)$$

θ:	angle in cross-section;
$r(\theta)$:	radius of a workpiece at θ;
r_0:	average radius of a workpiece;
$\Delta r(\theta)$:	radius error of a workpiece at θ;
A_i and B_i:	constants.

For workpieces with low rigidity, fixturing force may cause a geometric error on the workpieces, and the error normally appears as a sine or cosine function. In turning and grinding a diameter of sleeve, for example, the geometric error caused by the force of a three-jaw chuck on the workpiece can be modeled as Equation 3.

$$\begin{aligned} r(\theta) &= r_0 + \Delta r(\theta) \\ &= r_0 + A\cos(3\theta) \end{aligned} \qquad (3)$$

Axial Form Errors

Axial error of a manufactured cylindrical part is the error out of cylindricity along a section plan passing the axis of a manufactured part. Modeling of some typical errors in cylindrical turning and grinding processes are discussed here, including errors by fixturing misalignment, workpiece deflection, and heat expansion.

When work centers on a lathe or grinder are not aligned to the feeding direction of the cutting tool or traverse direction of the grinding wheel, the misalignment will lead to cylindricity errors along the axis. If the misalignment between the axes of two work centers is offset by Δr in a horizontal plane, a taper error of Δr will be produced. It is approximately the difference of the maximum and minimum radii (see Figure 3). The taper error by the misalignment is modeled in Equation 4.

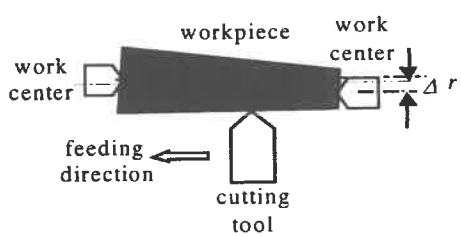

Figure 3: Taper Error by the Horizontal Misalignment

$$\begin{aligned} r(z) &= r_0 + \Delta r(z) \\ &= r_0 + Az \end{aligned} \qquad (4)$$

z:	axial coordinate of the workpiece;
r_0:	average radius;
A:	constant.

When a shaft is turned or ground in a chuck or between work centers, cutting force causes deflection of the workpiece (see Figures 4 and 5). The deflection makes the workpiece away from the cutting tool. The degree of the deflection at cutting location (point) varies and depends on how far the cutting tool is from supporters of the chuck or work centers. The deflection at cutting location is a function of the distance of the tool from the supporters. The error function can be determined by the deflection function from the materials mechanics [3].

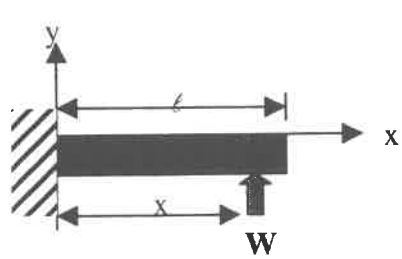

Figure 4: Workpiece in a Chuck as Beam Fixed at One End

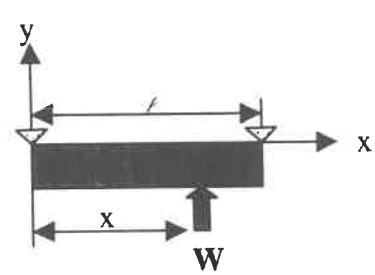

Figure 5: Workpiece Between Work Centers as Beam Supported by Both Ends

When a shaft is held in a chuck, it is viewed as a beam fixed at one end and under an intermediate load (see Figure 4). The deflection at cutting position, y, is calculated by Equation 5. The form error caused by the deflection

can be rewritten in a form of polynomial functions as Equation 6. If the form error is modeled in Legendre functions, Equation 6 can be approximately replaced by Equation 7.

$$y = \frac{Wx^3}{6EI} \qquad (5)\,[3]$$

$$\begin{aligned} r(z) &= r_0 + \Delta r(z) \\ &= r_0 + Az^3 \end{aligned} \qquad (6)$$

E:	modulus of elasticity of the material;	z:	coordinate of workpiece axis;
I:	moment of inertial of cross-section of beam;	$r(z)$:	radius of a workpiece at z;
W:	load on beam;	r_0:	average radius of a workpiece;
y:	deflection at cutting location.	Δr:	radius error of a workpiece at z.

$$\begin{aligned} r(z) &= r_0 + \Delta r(z) \\ &= r_0 + Bz + C(3z^2 - 1)/2 \end{aligned} \qquad (7)$$

In the case of a shaft hold between work centers, it is a problem where a beam is supported at both ends under an intermediate load (see Figure 5). The deflection, y, at cutting position is calculated by Equation 8. The error by the deflection in a form of polynomial functions is rewritten as Equation 9. The approximate model in Legendre functions is shown in Equation 10.

$$y = \frac{W}{3EI\ell}\left(\ell^2 x^2 - 2\ell x^3 + x^4\right) \qquad (8)[3]$$

$$\begin{aligned} r(z) &= r_0 + \Delta r(z) \\ &= r_0 + Az^2 + Bz^3 + Cz^4 \end{aligned} \qquad (9)$$

$$\begin{aligned} r(z) &= r_0 + \Delta r(z) \\ &= r_0 + D(3z^2 - 1)/2 \end{aligned} \qquad (10)$$

In turning and grinding operations, energy dissipated in cutting operations is converted into heat, which, in turn, raises the temperature in the cutting zone. The temperature results in expansion in size of the workpiece. During a cutting operation, the graduate change of temperature causes a geometric form error on the workpiece. Thermal expansion in diameter of the workpiece is calculated by Equation 11. Since the temperature rising is a linear function of time [1], the form error caused by the heat will be a taper as expressed in Equation 12.

$$\Delta D = CD\,(T - T_0) \qquad (11)[3]$$

$$\begin{aligned} r(z) &= r_0 + \Delta r(z) \\ &= r_0 + Az \end{aligned} \qquad (12)$$

ΔD:	change in diameter;	z:	coordinate of the workpiece axis;
D:	diameter;	$r(z)$:	radius of the workpiece at z;
C:	thermal conductivity;	r_0:	average radius of the workpiece;
T_0:	initial temperature of the workpiece;	$\Delta r(z)$:	radius error of the workpiece at z;
T:	final temperature of the workpiece.	A:	constant.

Cross-Section Size Errors

In this study, size of a cylindrical workpiece refers to the diameter of the workpiece. Diameter of a manufactured cylinder is defined as an average diameter of the workpiece. Size (diameter or radius) error of a manufactured cylindrical part is equal to the difference between an actual size and the expected size of the manufactured part. In precision turning and grinding, many factors affect the size. The most common factors in manufacturing are the setup error and tool wear. The diameter error by the two factors can be expressed in Equation 13.

$$\begin{aligned} r(z) &= r_0 + \Delta r(z) \\ &= r_0 + A \end{aligned} \qquad (13)$$

z:	coordinate of the workpiece axis;
r:	radius of the workpiece at z;
r_0:	average radius of the workpiece;
Δr:	radius error of the workpiece at z;
A:	constant.

L-F Polynomials Modeling

From the above discussion, a cross-section form or size error from typical manufacturing error sources can be expressed by a Fourier function, and an axial form error can be modeled by a Legendre function. The combined geometry and size error of a manufactured cylindrical part can be represented in a form of Legendre- Fourier (L-F) polynomials as Equation 14.

$$\begin{aligned} r(\theta, z) &= r_0 + \Delta r(\theta, z) \\ &= \sum A_{0j} P_j(z) + \sum \sum [A_{ij} P_j(z)\cos(i\theta) + B_{ij} P_j(z)\sin(i\theta)] \end{aligned} \qquad (14)$$

P: Legendre functions;
A and B: constants.

Conclusions

The following conclusions can be drawn from this study:

1. A geometric error of a manufactured part caused by an individual manufacturing source normally appears in a shape of one or two functions of the L-F polynomials.
2. The combined geometric error on a manufactured part is resulted from several error sources in a manufacturing system. The combined error of a manufactured cylindrical part can be decomposed into a series of L-F functions. Each L-F function normally corresponds to an error source of a manufacturing system.
3. Dominant manufactured error components can be identified by a comparison of coefficients of L-F functions. Thus, major error sources for the manufactured errors can be identified or estimated from all the error sources in the manufacturing system. The L-F polynomials modeling of manufactured errors of cylindrical parts can provide an effective tool for diagnosing and correcting errors for manufacturing process control.
4. Since dominant components of a manufactured error can be modeled by limited lower order F-L functions, computational complexity of the modeling process is relatively low.
5. The method has a good potential to be applied in an automatic system for diagnosing error sources of a manufacturing system as shown in Figure 6.

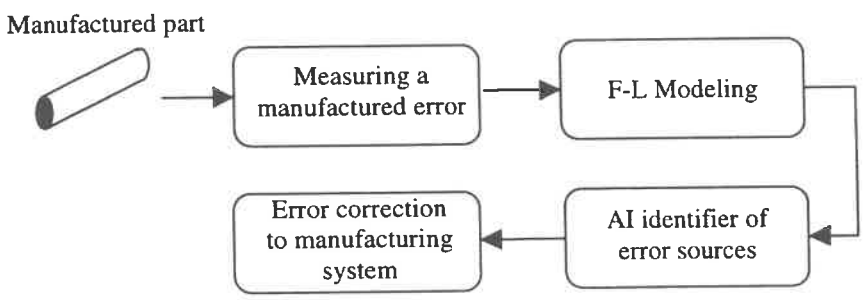

Figure 6: Error Source Diagnosis System of a Manufacturing System

References

1. Boresi, A. P., Schmidt, R. J., and Sidebottom, O. M., "Advanced mechanics of materials," *John Wiley & Sons, Inc.*, 1993.
2. Kalpakjian, S., "Manufacturing processes for engineering materials," *Addison-Wesley Publishing Company Inc.*, 1991.
3. Green, B. E., "Machinery's handbook, 24th Edition," *Industrial Press Inc.*, 1992.
4. ASME Y14.5M-1994, "Geometric dimensioning and tolerancing," *the American Society of Mechanical Engineers*, New York, NY.
5. Whitehouse, D. J., "Handbook of surface metrology," *Institute of Physics Publishing, Bristol*, UK, 1994.
6. Zhang, X. D., "A unified functional tolerancing approach for integrated design, manufacturing, and inspection," Ph.D. Dissertation Proposal, *FAMU-FSU College of Engineering*, Tallahassee, FL, 1998.

Improvement of Micro-machining Accuracy by 2-Dimensional Vibration Cutting

Jung-Hwan Ahn, Han-Seok Lim, Seong-Min Son
School of Mechanical Engineering, Pusan National University, Pusan, 609-735, Korea

1. Introduction

High-precision micro-machining technology has been progressing in order to manufacture optics such as non-spherical mirror and flat lens. In accordance with the needs for the audio/video products to be compact and comfortable, especially, optical core parts are continuing to be miniaturized multi-functioned like fresnel lens and diffraction grating. However, these lenses get complicated in profile and need higher form accuracy. This is why high-precision micro-machining is getting more important than ever.

In general, in micro-machining, the size effect increases cutting forces due to causes such undesired problems as form deformation, chatter and burr. These troubles deteriorate the quality of optical parts both in form accuracy and surface roughness. A lot of studies have been done developing new methods to overcome. Those are on stiff and low thermal structures of machine tool, micro-feeding mechanism to be controlled down to sub micron, and micro-machining process itself.

Vibration cutting is one of the attempts to increase micro-machinability. This research aim at investigating the two-dimensional vibration cutting and its effect on surface roughness, burr and so on. Elliptical vibration cutting mechanism is analyzed and experiments are carried out using a tool-vibrator composed of two PZT actuators.

2. Model of two-dimensional vibration cutting

One-axis vibration mechanism, in which a horn was used to achieve the vibration of high frequency and quite large amplitude, was proved very effective in decreasing cutting forces. But it has been mainly applied to turning. On the other hand the two-dimensional vibration mechanism has an additional advantage to be able to generate a variety of tool path by combining two-axis vibratory movements.

Assuming amplitude A, frequency f, phase Φ and workpiece feedrate v in the two-dimensional vibration cutting, the tool locus is expressed by equation (1). Fig. 1 shows a model of the two-dimensional vibration cutting. While the tool is engaged in down-cutting, during the period C_I, it cuts the workpiece upward during the period C_{II}. Therefore the thrust cutting force changes from positive to negative.

$$X = A\sin(ft + \Phi) + vt \qquad (1)$$
$$Y = A\sin(ft)$$

In the model, theoretical maximum surface roughness (R_{max}) can be calculated and it depends on the tool locus parameters as described in equation (1).

Assuming their relationship Φ constant is expressed as equation (2). Because phase Φ effects the pattern of tool locus, it would be desirable to select Φ for an appropriate tool locus once depth of cut and feedrate are given.

$$R_{max} \propto F\left(\frac{1}{A}, \frac{1}{f}, v\right) \qquad (2)$$

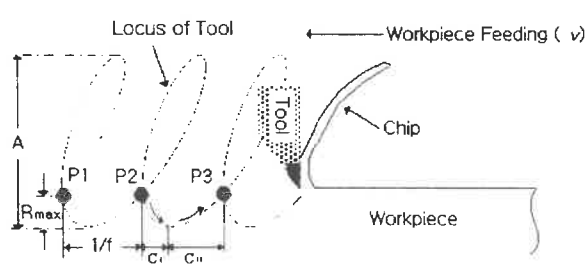

Fig. 1 2D Vibration Cutting

Theoretically, the larger amplitude, the higher frequency and the slower feedrate make the better surface. However, too slow feedrate lowers the cutting efficiency and a vibration mechanism limited dynamic characteristics, Therefore, amplitude, frequency and feedtate must be decided based on the actual system.

3. Experimental Apparatus

Fig. 2 shows the schematic diagram of the experimental apparatus. A micro-drilling machine tool composed of a xy table and a z-axis column is equipped with a tool two PZT actuators are located perpendicularly each other in the tool vibrator so that two-dimensional vibrational tool path is created. In order to remove cross-interference of each axis vibration, cross-shaped voids are devised in the tool vibrator. If a sine wave generated from a function generator is input to a two-phase signal generator, two sinusoidal signals with phase difference Φ corresponding to a required tool pattern are output. The two-phase signals are amplified enough to actuate PZT actuators by a two-channel signal amplifier. A current booster is needed to make PZT actuators respond quickly well to a rapid input. Table 2 summarizes the vibration cutting conditions in this study.

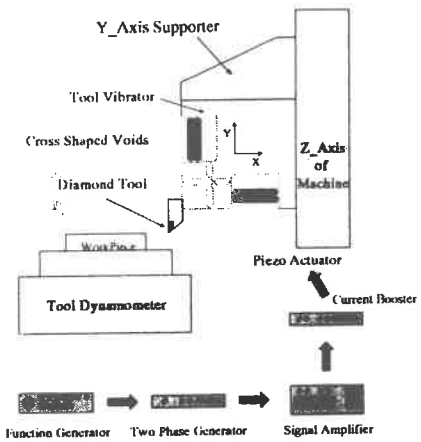

Fig. 2 Schematic Diagram of Experimental Apparatus for 2-D Vibration Cutting

Table 1 Conditions in 2D Vibration Cutting

Tool	Diamond Tool		Arc 180° Arc 90°
Workpiece	Brass(7-3)		
Cutting Condition	Depth of Cut	(tc)	1, 1.5, 2, 3, 4, 5 [μm]
	Feed Rate	(v)	0.5, 1, 2, 3, 4 [mm/sec]
Vibration Condition	Vibration Type		Elliptical Vibration
	Frequency	(f)	1 kHz
	Amplitude	(A)	5 μm

4. Experimental Results

4.1 Cutting Force

With a diamond tool of arc 180° and workpiece feedrate of 1 mm/sec and depth of cut 1～5 μm, the behavior of cutting forces is investigated during cutting both in the mode of two-dimensional vibration and non-vibration.

Fig. 3(a), 3(b) shows cutting forces -principle, thrust- in the non-vibration cutting and in the 2-D vibration cutting respectively. While the cutting forces for non-vibration cutting are constant with a some fluctuation, those for vibration cutting change periodically in sinusoidal way. The cutting forces increase in the period of C_I and decrease in C_{II} and the whole cycle repeats. This face justifies the model described in Fig. 1, in which in the period of C_I, the tool cuts down gradually to the deepest point, whereas in C_{II} the depth of cut decreases to zero. Around the end of C_{II} there is even a region where the thrust force gets negative.

Fig 4. shows the comparison of the average cutting forces over 1 μm to 5 μm of depth of cut. Principal forces for vibration cutting ranges from 0.7N to 2.2N depending on the depth of cut, which is almost half as much as those for non-vibration cutting. While thrust force for non-vibration ranges from 0.3N to 0.7N, that for vibration cutting is nearly zero. Much smaller cutting force increase of vibration cutting is thought mainly due to the air lubrication between tool and chip intermittently provided by tool vibration.

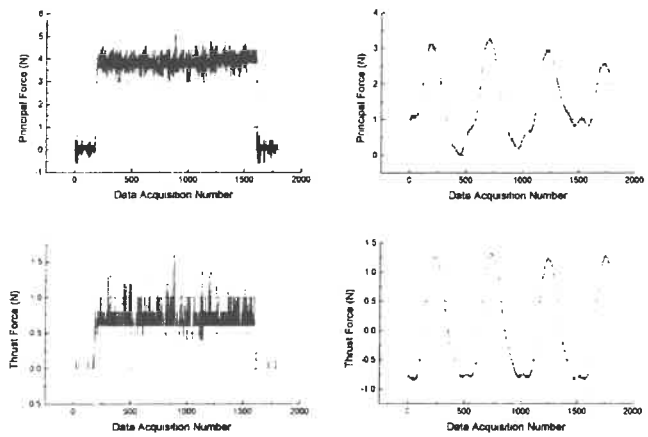

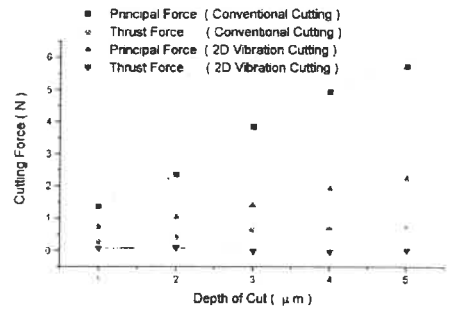

(a) Conventional Cutting **(b) 2D Vibration Cutting**

Fig. 3 Measured Cutting Forces ; Principal, Thrust Force

Fig. 4 Comparison of Cutting Forces Between Non-vibration Cutting and Vibration Cutting

4.2 Surface Roughness

The effects of vibration cutting on surface roughness are investigated varying depth of cut or cutting speed with a diamond tool of arc 180° . Fig. 5 shows the comparison of surface roughness between vibration and non-vibration cutting versus depth of cut with a cutting speed of 1㎜/sec. Surface roughness for non-vibration cutting fluctuates a little under a depth of cut of 2㎛. This might be because of unstable cutting such as ploughing due to too small depth of cut compared to the tool edge radius. However, that for vibration cutting is stable even in the depth of cut less than 2㎛ and so better than that for non-vibration cutting. The comparison according to cutting speed with a critical depth of cut of 2㎛ is shown in Fig. 6. Surface roughness for non-vibration cutting gets worse as cutting speed increases, whereas that for vibration cutting is much better and almost independent of cutting speed. Moreover, it gets closer to the theoretical value over a cutting speed of 2㎜/sec.

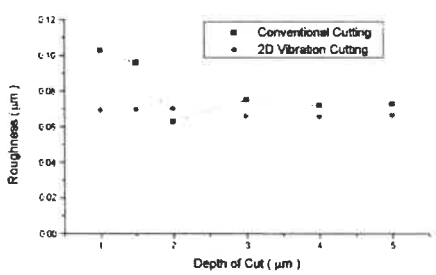

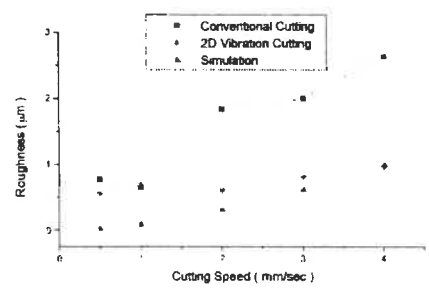

Fig. 5 Surface Roughness Versus Depth of Cut

Fig. 6 Surface Roughness(Rmax) Comparison between Simulation and Experiment

4.3 Burr

The effect of vibration cutting on burr is investigated cutting brass plate 1㎜ thick with one edge of a 90° diamond tool. Since burr generation is known to be closely related to depth of cut rather than cutting speed, depth of cut is varied and cutting speed remains constant, or 1㎜/sec. Fig. 7 shows the comparison of side burr, which generated in the edge of machined surfaces. In non-vibration cutting thick burr is formed even in a depth of cut as small as 1㎛, whereas burr, in vibration-cutting, is hardly found even after 20passes with a depth of cut of 5㎛.

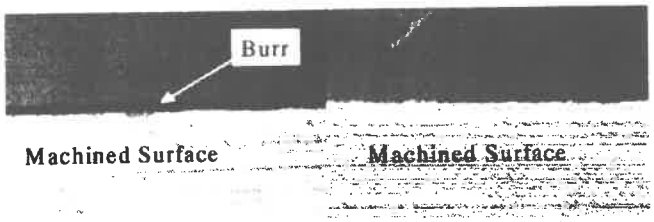

(a) Non-vibration Cutting (tc=1 ㎛) (b) Vibration Cutting (tc=5 ㎛)

Fig. 7 Comparison of Side Burr

4.4 Chip

Fig. 8 shows the comparison of chips by two cutting modes. With depth of cut constant, or 1 ㎛, the type of chip by non-vibration cutting changes in such a way as from continuous to shear as cutting speed increases. That for vibration cutting is the continuous one over the entire range of speed. In addition, it is composed of many small lamellas which differentiates continuous chips of vibration cutting from that of non-vibration cutting. Lamellas are considered to be formed due to the periodical tool vibration. In general, continuous chips bring the high quality surface.

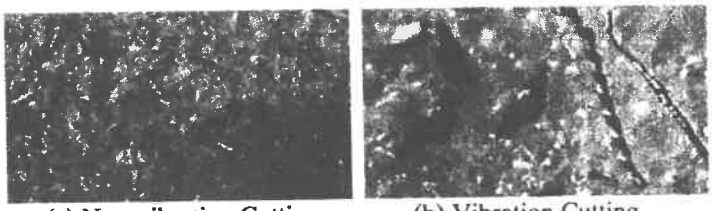

(a) Non-vibration Cutting (b) Vibration Cutting

Fig. 8 Comparison of Chips

5. Conclusion

Two-dimensional vibration mechanism using two PZT actuators is devised and its performance for micro-machining is investigated in comparison with the conventional, or non-vibration cutting. The conclusion is that two-vibration cutting has many advantages over the non-vibration cutting. They are as follows:

1) Cutting force level is reduced;
   (a) About half to one third for principal force
   (b) Nearly zero for thrust force
2) Surface roughness is improved up to three and half times
3) Burr is largely reduced
4) Smooth and continuous chip is formed over the wide cutting conditions.

Acknowledgment : This work was supported in part by the Korea Science and Engineering Foundation(KOSEF) through the Engineering Research Center for Net Shape and Die Manufacturing at Pusan National University.

Reference

[1] Yamagata, Y., Higuchi, T., " Three-Dimensional Micro Fabrication by Precision Cutting Technique", JSPE, Vol.61, No.10, pp.1361-1364, 1995. (in Japanese)
[2] D.A. Lucca, R.L.Rhorer, R.Komanduri, "Energy Dissipation in the Ultra precision Machining of Copper", CIRP, Vol. 1, NO 1, pp.69-72, 1991.
[3] Kumabe, J., Precision Machining using Vibration Cutting – the fundamentals and applications -, 34-49, 1979. (in Japanese)
[4] Shamoto. E, Moriwaki, T "Study on Elliptical Vibration Cutting", Annals of the CIRP Vol. 43/1, pp.35-38, 1994.
[5] Shamoto, E., Moriwaki, T., Morimoto, Y., "Elliptical Vibration Cutting (1st Report)", JSPE, Vol62, No.8, pp.1127-1131, 1996. (in Japanese)

Improvement of Characteristics of Aluminum Casting Using Ceramic Porous Mold

S.I. Chung*, D.S. Jeong, Y.G. Im***
H.D. Jeong*, K.K. Cho**

* School of Mechanical Engineering Pusan national University San 30, Changjeon-Dong, Kumjeong-ku, Pusan, 609-735, Korea
** Department of Industrial Engineering Pusan national University

1. Introduction

The RP&M[1] (Rapid prototyping and Manufacturing) is the most appropriate technology for the small-lot production system, in which the production cycle is getting shorter owing to various needs from consumers[2]. In this paper, RP&M is applied to a casting process. A casting process has a merit of being able to reflect complicated shapes at one time. But it has not been applied to the precision industry because of bad quality on surface. So we will improve characteristics of aluminum casting process using porous ceramic mold.

2. Fabrication of porous ceramic mold

Fig.1 shows the fabricating process of porous ceramic mold. First, the temporary mold, which is made from silicon rubber, has to be prepared to fabricate porous ceramic mold. In the second place, the slurry should be prepared, which consists of powder and binder.

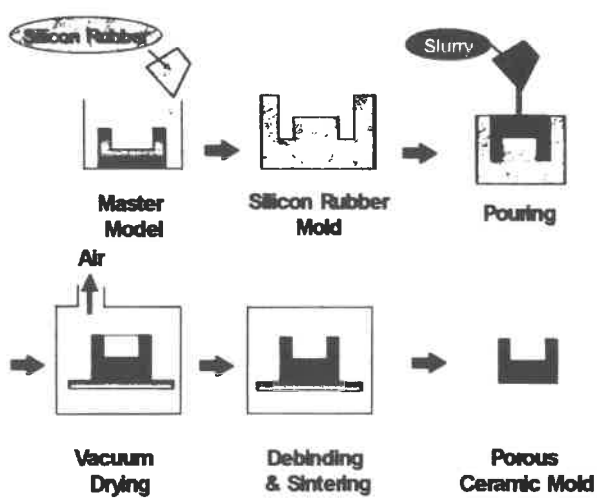

Fig. 1 The Fabricating Process of Porous Ceramic Mold [3]

The mixing process of powder and binder is very important because the powder's uniform dispersion has a great effect on the strength of porous ceramic mold. Slurry is poured into the silicon rubber mold. Once slurry hardens enough to, it is separated from the silicon rubber mold. Then the green part which means hardened slurry in non-sintering, has to be removed water at 100℃ with vacuum condition. Micropores are caused by getting rid the green part out of water during vacuum drying, have an effect of preventing cracks throughout the debinding and sintering process. At last process, the debinding and sintering convert the green part to the sintered part. Because the porous mold is made from ceramic, the process of rising and decreasing temperature should be done slowly. Otherwise cracks are taken place on the surface of porous ceramic mold.

3. Evaluating of porous ceramic mold

In this study, we adopt the porous ceramic mold as a casting mold for aluminum casting. Therefore it doesn't need to have the strength like as conventional ceramic products do. The air permeability, dimensional accuracy, and transferability are more important than the strength to be adopted as the casting mold for the vacuum sealed casting. As the size of mean diameter is larger, the air permeability of porous ceramic mold will be higher, whereas the porous mold has the limit in expression of delicate shapes. So we prepare two types of specimen to evaluate the air permeability, dimensional change and transferability. A-type specimen is made from 45㎛ zirconia and 55㎛ alumina powder and B-type specimen from 45㎛ zirconia and 4.5㎛ alumina powder.

3.1 Air permeability and dimensional change

Tab. 1 shows the result of the air permeability and dimensional change evaluated by specimens in cylindrical shape of 50㎜ diameter and 50㎜ height. It is found that the size of powder's mean diameter has a great effect on the air permeability and dimensional change. As the size of mean diameter is larger, air permeability and dimensional accuracy is higher.

Tab. 1 *Result of Air-permeability and Shrinkage*

	A-type Specimen	B-type Specimen
Air permeability ($cm^2 \cdot cm$ / $cmH_2O \cdot cm^2 \cdot min$)	17.6	7.7
Shrinkage (%)	0.5	1.2

Fig. 2 which shows microstructure of A, B-type specimen's surface, is quite self-explanation. The vacancies between 45㎛ zirconia and 55㎛ alumina powder in the A-type specimen are broader than the vacancies between 45㎛ zirconia and 4.5㎛ alumina powder in the B-type specimen because the vacancies of B-type specimen are filled

up partly during the debinding and sintering process. As the result, the air permeability and dimensional accuracy of A-type specimen are higher than that of B-type specimen.

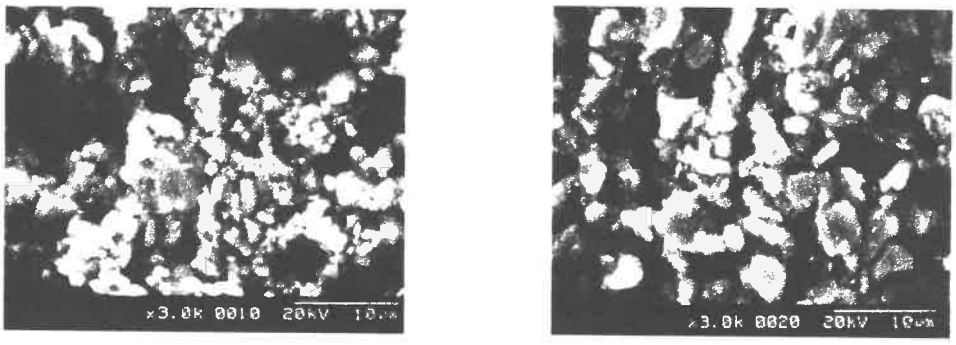

(a) A-Type Specimen *(b) B-Type Specimen*

***Fig. 2** Microstructure of Porous Mold*

3.2 Transferability

Next, the standard specimen of surface roughness (R_{max}=12.5μm) is adopted to evaluate transferability, which is measured by comparing V-slot of standard specimen and A, B-type specimen respectively. Fig. 3 shows the results of the transferability. A-type specimen can't transfer exactly the shape of standard specimen. B-type specimen, however, is able to transfer with nearly the same shape because 4.5μm alumina powder among 45μm zirconia powder enables one to fabricate the porous casting mold with a delicate surface.

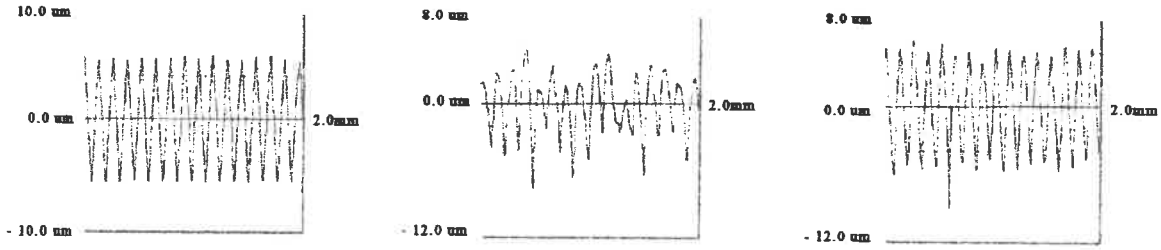

(a) Standard Specimen *(b) A-type Specimen* *(c) B-type Specimen*

***Fig. 3** The results of transferability*

4. Vacuum sealed casting

The vacuum sealed casting is a process of removing air bubbles between the porous casting mold and the liquid metal under vacuum condition. It has advantages of the microstructure of casting product being fine and its delicate pattern being able to be transferred. Fig. 4(a), (b) compare the surface of conventional casting product with that of vacuum sealed casting. Because the suction force of vacuum sealed casting reduces the tension force on surface of liquid aluminum during solidification of liquid aluminum, the surface of vacuum sealed casting is finer than that of conventional casting, resulting in transferring

the delicate and sharp parts. Fig. 4(a'), (b') show the microstructures of conventional casting product and vacuum sealed casting product respectively after polishing. The vacuum sealed casting has a small amount of the dendrite, compared with that of conventional casting. Since ceramics has a tendency of slow cooling, the size of grain is coarser in vacuum sealed casting. However, it is not a serious problem because water or oil cooling can make the size of grain fine.

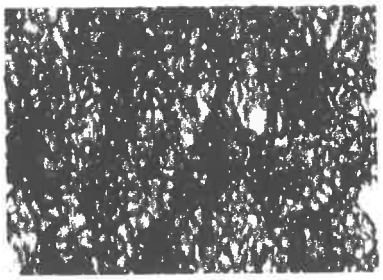

(a) Conventional casting (before polishing)

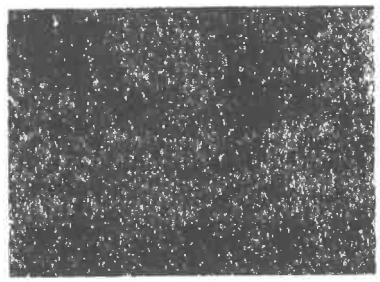

(b) Vacuum sealed casting (before polishing)

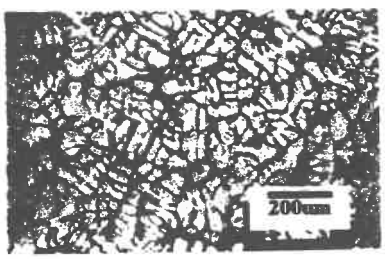

(a') Conventional casting (after polishing)[4]

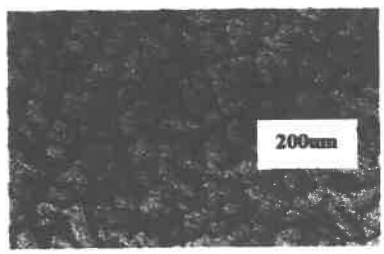

(b') Vacuum sealed casting (after polishing)

Fig.4 *Surface of conventional casting and vacuum sealed casting*

5. Application to investment casting

The investment casting is classified into solid mold and shell mold method. The gypsum has been widely used in the solid mold method because it can be easily broken into pieces. However, it has its limitation to transfer complicate and sharp parts due to the poor air permeability. The porous ceramic mold is designed to overcome this limitation by obtaining attributes of both good air permeability and fragility. Fig. 5 (a), (b), (c) show master model, wax pattern, and casting product of impeller respectively.

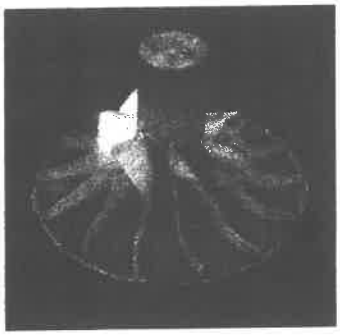

(a) Master Model

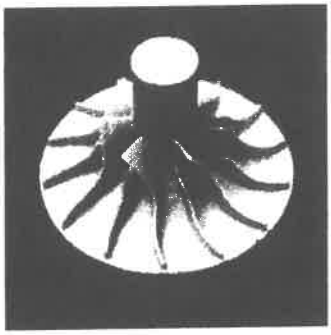

b) Wax Pattern

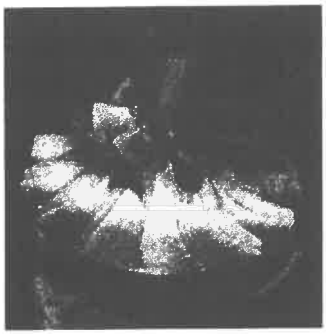

c) Casting Product

Fig. 5 *The example for investment casting : impeller*

The master model is made by stereo lithography apparatus, and the wax pattern is made by vacuum casting with silicon rubber mold. Finally the casting product is made by vacuum sealed casting with aluminum alloys (A356). The vacuum sealed casting has a advantage of being able to transfer the complicate and sharp parts as blades of impeller in a lower temperature

6. Conclusion

1. As mean diameter of ceramic powder is larger, the air permeability and dimensional accuracy are getting higher, whereas the transferability is getting lower.
2. It is possible to accomplish rapid fabrication of porous ceramic casting mold, which is indispensable to improve the characteristic of aluminum casting.
3. The investment casting product of aluminum, which is manufactured using the porous mold and vacuum sealed casting process in solid mold method, has a merit of being able to transfer delicate and sharp parts with higher quality than the conventional casting product.

7. Reference

1) Paul F. Jacobs, PhD : Stereolithography and other RP&M Technologies, Society of Manufacturing Engineers, 1996, pp.4 ~ 15
2) Nakagawa, T. & Imamura, M. & Xu, Y.: Overview of rapid prototyping research and development in Japan, Proceedings of the 8th International Conference on Production Engineering, 1997, pp.3 ~ 16.
3) S.I. Chung & D.S. Jeong & Y.G. Im & H.D. Jeong & K.K. Cho : Rapid Tooling of Porous Ceramic Mold Using Slip Casting, Journal of the Korean Society of Precision Engineering Vol.16 No.5, 1999, pp.98 ~ 104)
4) Y.S. Lee : A study on the Manufacturing Motor Cycle Connecting rod Using Casting/Forging Process of Aluminum Alloy, Graduated school of Pusan national university, 1999, pp.38

Surface modification by electrical discharge machining with titanium powder suspended in working fluid

Katsushi Furutani *, Akinori Saneto **, Hideki Takezawa *,
Naotake Mohri * and Hidetaka Miyake ***
* Toyota Technological Institute
12-1, Hisakata 2-chome, Tempaku-ku, Nagoya 468-8511 Japan, e-mail: furutani@toyota-ti.ac.jp
** Toyota Technological Institute (Yazaki Corp. at present)
*** Industrial Electronics & Systems Lab., Mitsubishi Electric Corp.
1-1, Tsukaguchi-Honmachi 8-chome, Amagasaki, Hyogo, 661-8661 Japan

Key words: electrical discharge machining, surface modification, titanium carbide

1. Introduction

Electrical discharge machining (EDM) has been widely used as a removal process to produce parts, dies and molds for several decade. In these years, a surface modification and an accretion methods by EDM with a green compact or a semi-sintered electrode have been studied [1][2]. Fig. 1 shows examples of a green compact electrode and a result of the accretion. A thick and hard layer can be obtained. Titanium alloy powder or tungsten powder is always supplied from the green compact electrode and adheres on a workpiece after powder reacts on cracked carbon that comes from working oil by the heat caused by discharge. As results, thick TiC or WC layer can be obtained. However, production of an electrode takes much labor. An accretion process with a wire brush or bundled wire electrodes has been proposed [3]-[5]. Because a thin wire electrode wears heavily and melted electrode material adheres on a workpiece, the electrodes must be changed frequently.

On the other hand, EDM with conductive powder suspended in working oil has been studied to finish a surface [6]. In the conventional powder suspended EDM which mainly works as a removal process, powder material is dispersed into a workpiece with a several micrometers beneath its surface [7]. This phenomenon is observed also in EDM removal process with solid tungsten or silicon electrode.

In this paper, a material accretion method by EDM with powder suspended in working fluid is proposed to skip the production process of the green compact electrode. An appropriate shape of an electrode is considered after considering flow of the working fluid. Then performance of an EDM process with titanium powder suspended in working oil is discussed.

2. How to keep powder density thick

Fig. 2 illustrates flow of working fluid during EDM. A gap between an electrode and a workpiece soaked in working fluid is several micrometers up to several tens micrometers. The electrode moves reciprocally to stabilize a machining process. When the electrode moves upward as shown in Fig. 2(a), the powder flows into the gap together with the working fluid so that a powder density becomes thick. However, discharge seldom occurs because of a long gap. When

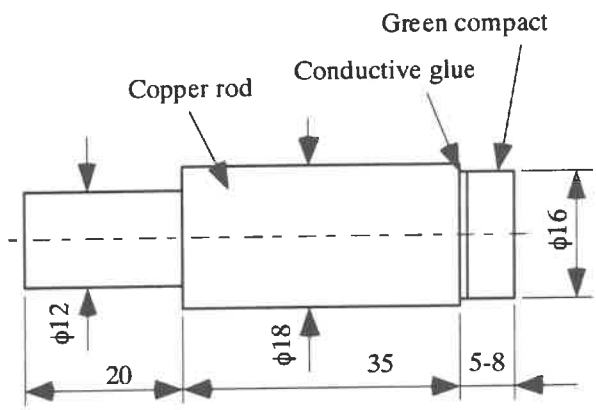

(a) Green compact electrode

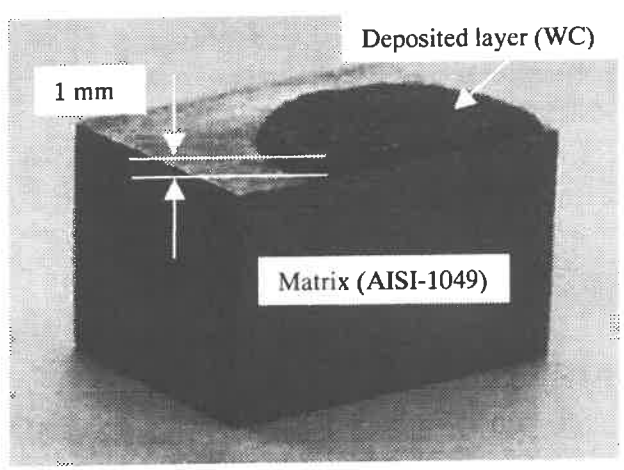

(b) Accretion with WC-Co green compact

Fig. 1 Accretion with green compact electrode

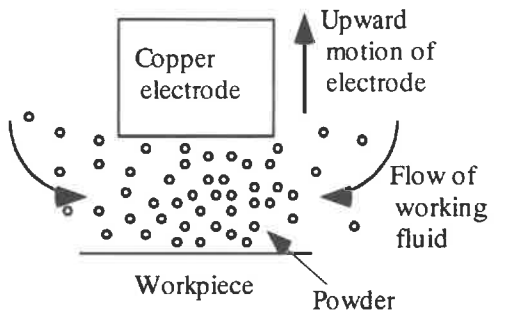

(a) Upward motion of electrode

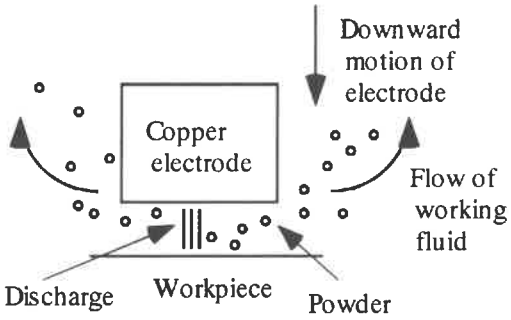

(b) Downward motion

Fig. 2 Flow of working fluid during EDM

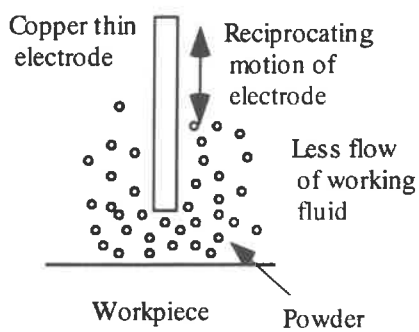

(a) Thin electrode

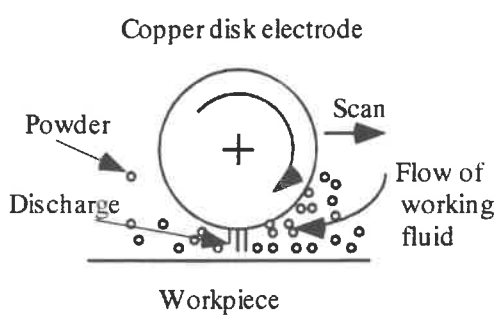

(b) Rotating electrode

Fig. 3 Two types of electrode

the electrode moves downward as shown in Fig. 2(b), the powder is flushed with the working fluid from the gap. Though discharge often occurs, the powder density is thin. Therefore, the powder hardly adhere on

Table 1 Machining conditions

Powder	Titanium (< 36 μm)
Working fluid	Oil (EDF-K by Mitsubishi)
Electrode	Copper rod ϕ1 mm
Density	50 g/l
Polarity of electrode	+,-
Peak current	1-20 A
Pulse duration	2-2046 μs
Pulse interval	2-2046 μs
Duty factor	0.04-50 %
Gap voltage	80-320 V

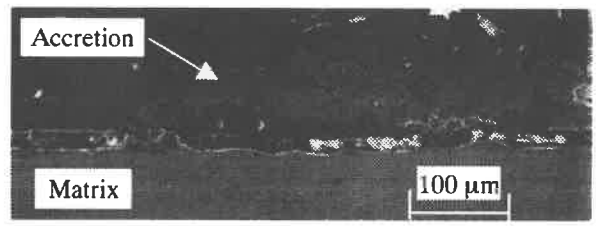

Fig. 4 Example of accretion machining by powder suspended EDM

the workpiece in the conventional powder suspended EDM. The powder should be provided into the small gap to keep the powder density thick.

There are two ways to keep the powder density thick: the use of a thin electrode and a rotating disk electrode. A thin electrode seldom thrusts the working fluid as shown in Fig. 3(a). A rotation of a disk electrode drags the powder into the gap with the working fluid because of the viscosity of the working fluid as shown in Fig. 3(b).

The use of a thin electrode and a disk electrode is investigated in Sections 3 and 4, respectively.

3. Accretion process with thin electrode

Titanium powder with a diameter of 36 μm is suspended in working oil like kerosene. A density of the Ti powder is 50 g/l. A carbon steel plate (AISI-1049) is used for a workpiece. The working fluid is circulated manually. Table 1 shows electrical conditions for accretion machining. In the case of negative as a electrode polarity, 3 A as a peak current, 2 μs as a pulse duration and 1024 μs as a pulse interval, the thickest layer is obtained. Fig. 4 shows an example of accretion. After EDM for 2 minutes with a copper electrode of 1 mm in diameter, a layer grows a thickness of 150 μm. Fig. 5 shows an analysis result by EPMA. A bright area contains a certain element. Both tungsten and carbon exist from the matrix surface up to 20 μm. The accretion is porous from 20 μm above the

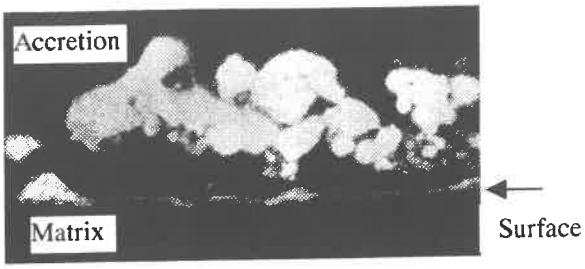

(a) Ti-Kα image

100 μm

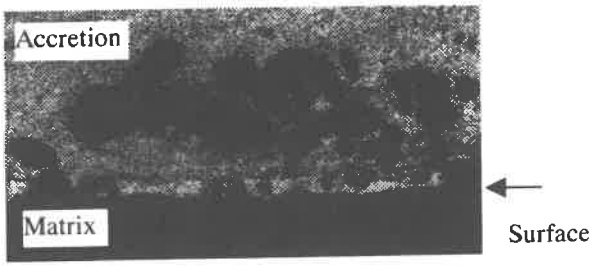

(b) C-Kα image

Fig. 5 Analysis result by EPMA

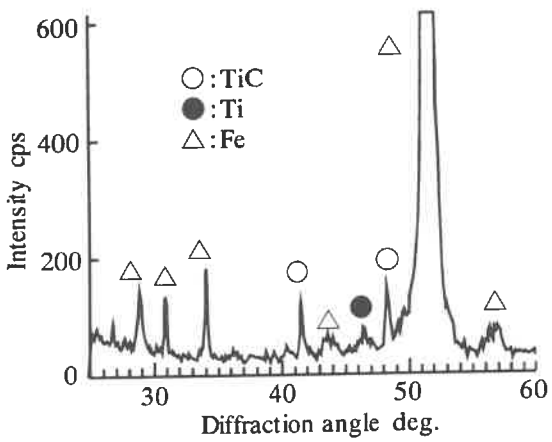

Fig. 6 Analysis result by X-ray diffraction

surface. A hardness of the accretion layer near matrix surface is 1600 Hv which is much harder than a matrix hardness of 240 Hv. Fig. 6 shows an analysis result by X-ray diffraction. Some peak angles with respect to Ti and TiC are observed on the matrix. Therefore, a material with a thickness of 20 μm on the matrix surface is TiC. Carbon in TiC comes from cracked carbon in the working fluid. By combining a planetary motion of the electrode, a wider area of the accretion can be obtained.

ASTM-D2 powder with a diameter of 3.4 μm is mixed with the Ti powder to improve adhesion of the TiC layer with the matrix. A ratio of the D2 powder to the Ti powder is 9:1. Although the adhesion is improved, a hardness of an accretion layer is decreased.

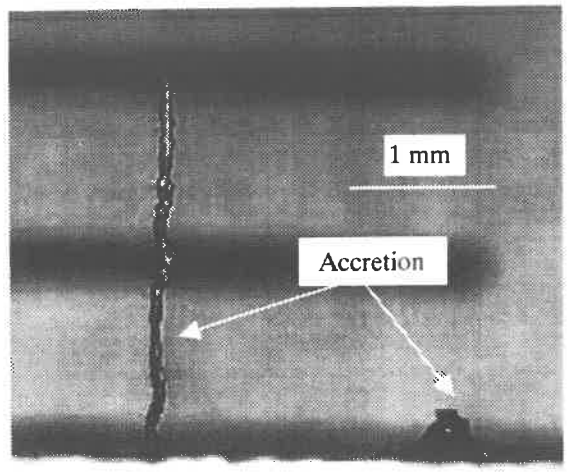

Fig. 7 Example of column-like accretion

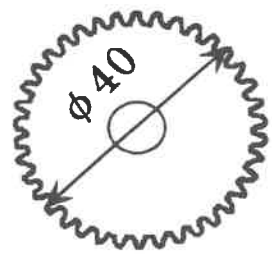

Fig. 8 Gear shaped electrode

A column with 2 mm-height and 50 μm-diameter can be fabricated without scanning in the xy-plane as shown in Fig. 7.

4. Accretion process with rotating electrode

Fig. 8 shows a shape of a disk electrode. The electrode shapes like a gear with a tip diameter of 40 mm, a whole depth of 2 mm, 38 teeth and a width of 1 mm. A circular disk with a diameter of 40 mm and a thickness of 1 mm is also used. Each of them rotates from 0.63 to 6.3 m/s as a peripheral velocity. A thick layer is obtained with the gear shaped electrode rotating at 6.3 m/s.

Fig. 9 shows a comparison between accretion areas with the thin electrode and with the gear shaped electrode. Conditions for the rotating electrode are the same as the conditions for the thin electrode. A wider area of the accretion layer with uniform thickness can be obtained by using the rotational electrode with the gearlike shape. A rotation of the electrode promotes dragging the powder to the gap between the electrode and a workpiece.

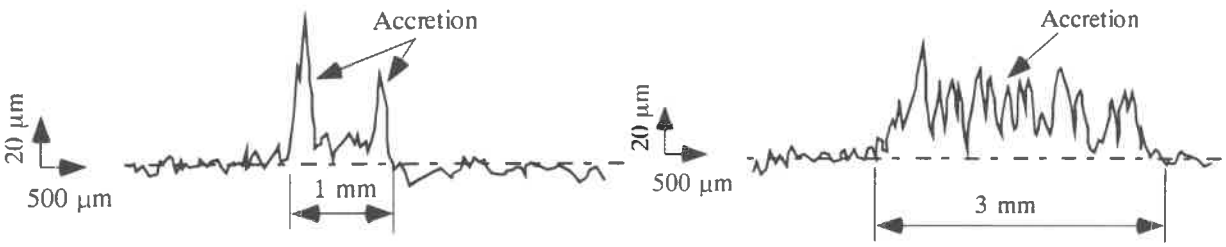

(a) Thin electrode (b) Rotating electrode

Fig. 9 Comparison of accretion

5. Use of other powders

Some other powders are also tried. Accretion of TiC layer is obtained with TiO_2 powder which is an insulator. Accretion of a hard layer can not obtained with TiC, TiN or W powder suspended in working oil though a surface of a workpiece is modified and becomes smooth and lustrous. These are the same phenomena as the conventional powder suspended EDM [6].

Accretion of TiNi layers are also obtained with a blend of Ti and Ni powder mix suspended in pure water. A diameter of Ni powder is 30 μm. TiNi alloy works as a shape memory alloy. This will lead new technical feasibility of fabrication of miniature sensors and actuators.

6. Conclusions

In this paper, a material accretion method by EDM with powder suspended in working fluid is proposed. Conclusions can be drawn as follows:

(1) Accretion of TiC layer can be obtained by using a thin electrode or a rotating disk electrode to keep the powder density thick.
(2) A wide area with uniform thickness can be deposited with the gear shaped rotating electrode.
(3) Ti-Ni layer is also fabricated.

The authors will measure properties of accretion in detail, will try to fabricate miniature structures and other functional layer for the shape feedback machining method [9].

Acknowledgement

The authors wish to thank Mr. Masaru Ohta and Mr. Motoya Furuichi of Toyota Technological Institute for their helpful cooperation. This study is financially supported by Research Foundation for OSG (Osawa Scientific Grant) Fund, the Electrotechnology of Chubu and Grant-in-Aid for Encouragement of Young Scientists (A) (11750110) of the Ministry of Education, Science, Sports and Culture, Japan.

References

[1] N. Mohri, N. Saito and Y. Tsunekawa: Metal Surface Modification by Electrical Discharge Machining with Composite Electrode, Ann. CIRP, 42, 1, pp. 219-222 (1993).
[2] A. Goto, T. Magara, T. Moro, H. Miyake, N. Saito and N. Mohri: Formation of Hard Layer on Metallic Material by EDM, Proc. Int. Sympo. Electro-Machining XII, Aachen, Germany, pp. 271-278 (1998).
[3] B. Nowicki, R. Pierzynowski and S. Spadlo: The Electrodischarge-Based Surface Alloying Process Using Brush Electrode, Proc. Int. Sympo. Electro-Machining XII, Aachen, Germany, pp. 289-298 (1998).
[4] K. Furutani, T. Enami and N. Mohri: Dot-Matrix Electrical Discharge Machining for Shaping Fine Structure, Proc. IEEE Int. Workshop Micro Electro-Mechanical Syst., Nagoya, Japan, pp. 180-185 (1997).
[5] N. Mohri, K. Fujii, K. Furutani, H. Takezawa and T. Sata: Materials Accretion by Electrical Discharge Machining with Thin Electrodes, Proc. Int. Seminar Improving Machine Tool Performance, San Sebastián, Spain, 2, pp. 829-837 (1998).
[6] H. Narumiya, N. Mohri, N. Saito, H. Ootake, Y. Tsunekawa, T. Takawashi and K. Kobayashi: EDM by Powder Suspended Working Fluid, Proc. Int. Sympo. Electro-Machining IX, Nagoya, Japan, pp. 5-8 (1989).
[7] K. Masui, K. Demizu, Y. Sato and T. Sone: Surface Modification of Tool Steels by Alloying Method Using EDM Process, Proc. Int. Sympo. Electro-Machining XI, Lauzanne, Switzerland, pp. 419-426 (1995).
[8] J. D. Madden and I. W. Hunter: Three-dimensional Microfabrication by Localized Electrochemical Deposition, J. Microelectro-mechanical Syst., 5, 1, pp. 24-32 (1996).
[9] H. Takezawa, K. Furutani and N. Mohri: Precision Machining by Feedback of Shape Data, Proc. Jpn.-Frn. Cong. Mechatronics, Kitakyushu, Japan, pp. 732-736 (1998)

Elliptical Vibration Cutting of Steel with Diamond Tools

E. Brinksmeier, R. Gläbe

LFM Laboratory for Precision Machining, University of Bremen, Germany

Abstract

Diamond turning of steel alloys is impractical due to catastrophic tool wear caused by a combination of chemical and abrasive wear. In the literature, several modifications of the cutting process have been proposed, e.g. cutting in an inert gas atmosphere, cryogenic cutting and vibration assisted cutting, e.g. elliptical vibration cutting (EVC) [1-5]. In this work, the EVC method was investigated, because of best results due to wear reducing effect [3]. By carefully monitoring and adjusting the tool oscillation, tool wear could be reduced by a factor of 10 and surface roughness could be improved.

Introduction

Several discussions regarding the wear mechanisms of diamond tools have been presented in the literature [1-5]. The observed wear has been divided into mechanical-abrasive wear (abrasion, micro-cracking) and chemical-reactive wear (diffusion, oxidation, catalytic graphitization and carbide-formation) or a combination of both. Correlation between tool wear and workpiece hardness or the melting point of the workpiece material do not seem to help predicting the wear behaviour. An interesting correlation was published by Evans [3] who compared the diamond machinability of the elements with the electron configuration of the atoms. He presumes that unpaired d-electrons are responsible for breaking up the carbon bonds in the diamond lattice and therefore should be responsible for chemically activated wear.

Experimental setup

The experiments were carried out on a precision lathe Hembrug Super-Mikroturn CNC. The diamond tools used in the face turning experiments had a tool nose radius of 3 mm, rake angle of 0° and a clearance angle of 5°. The radius of the unused cutting edge was less than 40 nm. Mineral oil was used as lubricant. The outer diameter of the workpiece was 60 mm and the inner diameter 15 mm. The workpiece material was Ck45N (0.45 % C) carbon steel. Surface roughness of the turned samples, cutting edge radius and wear characteristics were determined with a Perthen roughness-profiler, a scanning electron microscope (SEM), a Phase Shift Technology MicroXAM white-light interferometer (WLI) and a Nanoscope III atomic force microscope (AFM).

In Figure 1 the experimental set-up is shown. A 40 kHz, 700W ultrasonic generator (BRANSON) and an air-cooled piezoelectric converter was used to stimulate the tool. A 'booster' enlarges the amplitude up to 6 µm and was coupled to a non amplifying resonator (length $5 \cdot \lambda/2$). The diamond tool was fixed 'off axis' to the face side of the transducer. Due to the displacement of the tool mass the tool vibrates elliptically. Using a counterweight, the elliptical motion could be controlled within a certain range.

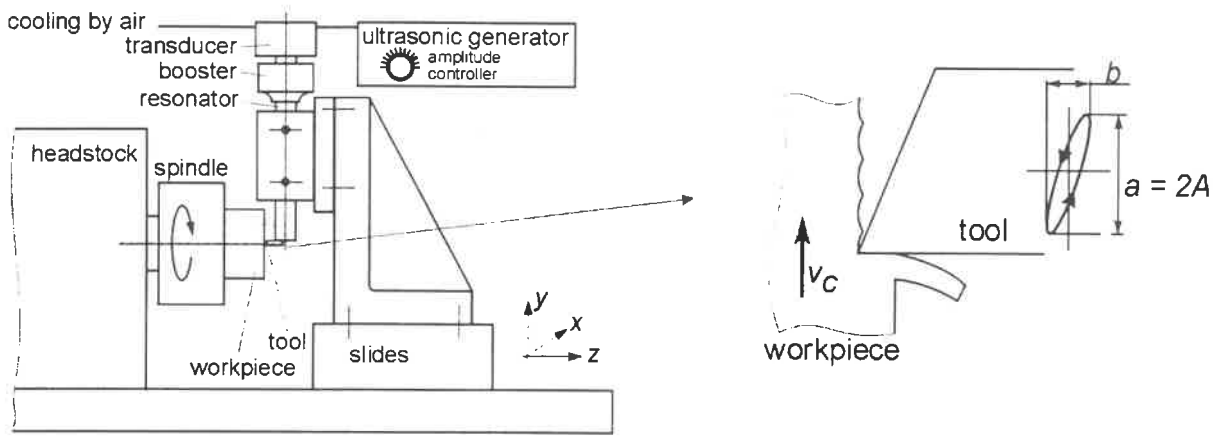

Figure 1: Experimental set-up for EVC (elliptical vibration cutting) of steel with monocrystalline diamond tools

In order to understand chip-forming, surface-structure and the process-stability it is necessary to record the full motion of the diamond tool. Therefore, two eddy-current sensors were used to record the main oscillating direction parallel to the resonator (y) and normal to the face turned surface (z) (Figure 1). A MICRO-EPSILON Series 500 displacement measuring system and a LE-CROY Series 9310A digital oscilloscope were used to record the tool motion. The accuracy of the system was better than 0.2 µm. In-situ measurement is possible due to the insensitiveness to oil-contamination. The recorded signal was analyzed with a personal computer. The amplitudes in y and z direction, the phase lag between the two axes and the tool path were documented.

If $b/a \approx 0$, the effective contact time only depends on vibration frequency, vibration amplitude and cutting speed, since in this case the depth of cut is unimportant. Figure 2 shows the theoretical effective contact times for different amplitudes and cutting speeds for a fixed vibration frequency of 40kHz. If tool and workpiece are in permanent contact, the effective contact time reaches 100%.

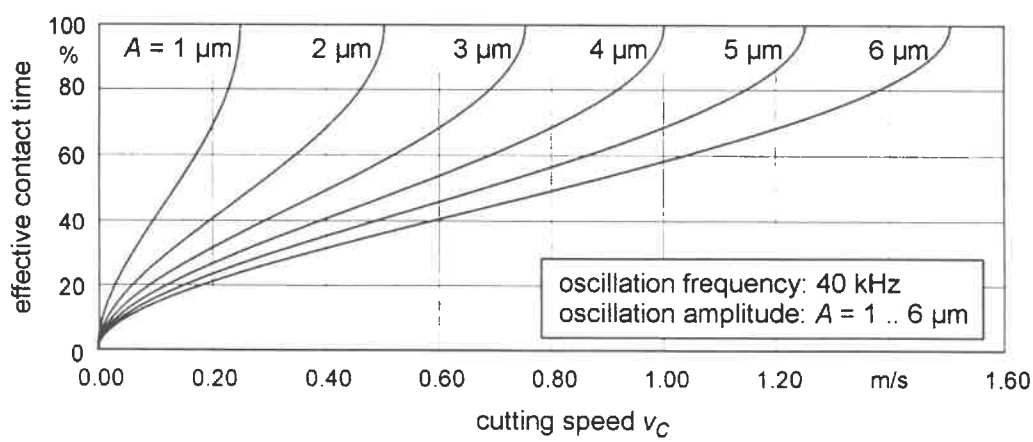

Figure 2: Calculated effective contact time in EVC

›sults

face generation

› roughness of EVC surfaces depends on several factors, e.g. cutting parameters, shape of the cutting ge shape, tool motion and the plastic and elastic properties of the workpiece material. In Figure 3 the chined surfaces of aluminum and steel are compared which were machined under identical conditions. › aluminum surface exhibits regular chatter marks across the whole measured area. Apparently, grain ›ndaries have no influence on the formation of chatter marks.

› the other hand, two effects are observed when cutting carbon steel:

Height variation from one feed mark to the next, caused by an increasing cutting edge radius due to progressive tool wear.

Height variation from one chatter mark to the next, caused by irregularly oriented ferrite and pearlite grains with different elastic and plastic properties. Metallographic investigations including SEM of taper sections did reveal a plastically deformed surface layer in the range of the PV-roughness.

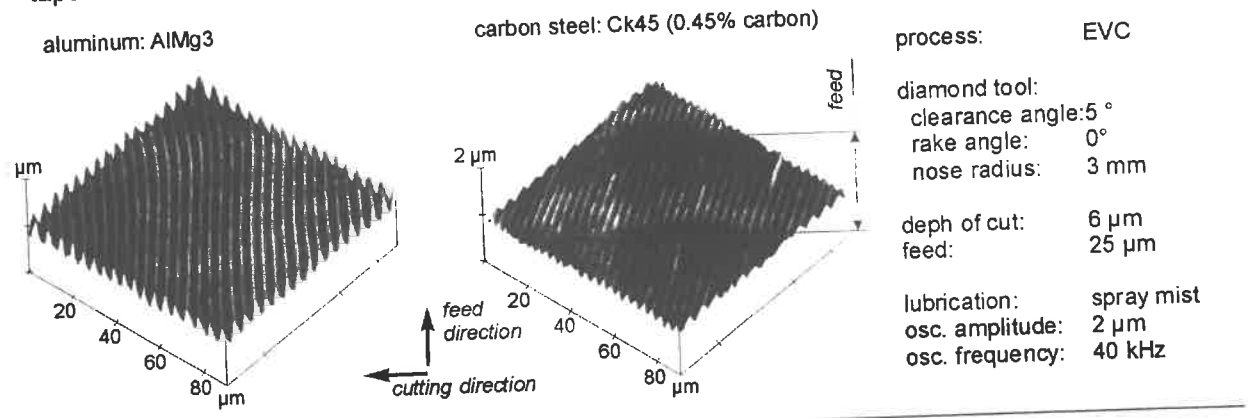

Figure 3: Comparison of EVC machined surfaces of aluminum and steel

Tool wear and effective contact time

The effective contact time has a large influence on diamond tool wear, since the rate of chemical reactions and the temperature in the cutting zone both depend on the effective contact time. Figure 4 shows the measured cutting distance as a function of the effective contact time. A cutting distance of 20 m could be achieved with an effective contact time of 22%. The end of the useful tool life was defined as the cutting distance with a roughness of the machined surface of RMS > 40 nm.

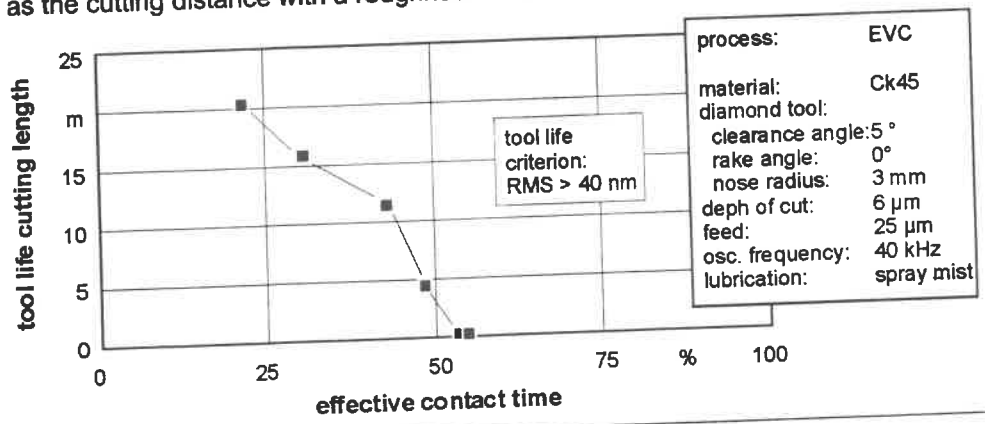

Figure 4: Relation between cutting length and time of contact

No wear reduction was detected for effective contact times >54 %. Probably, elastic response of the workpiece material and of the resonator lead to a longer effective contact time than calculated.

Optimized cutting conditions

In further experiments the ratio of *b/a* was varied between 0 and 0.1. Tool wear and surface roughness were investigated as a function of the cutting distance. It was found that tool wear decreases significantly with increasing ratio *b/a*. Strong abrasive wear (chipping) is observed, if *b/a* is close to 0. If *b/a* approaches 0.1, wear characteristics change into chemical rounding of the cutting edge (Figure 5b). Using optimized conditions the cutting edge radius was only 105 nm after a cutting distance of 1500 m (Figure 5a).

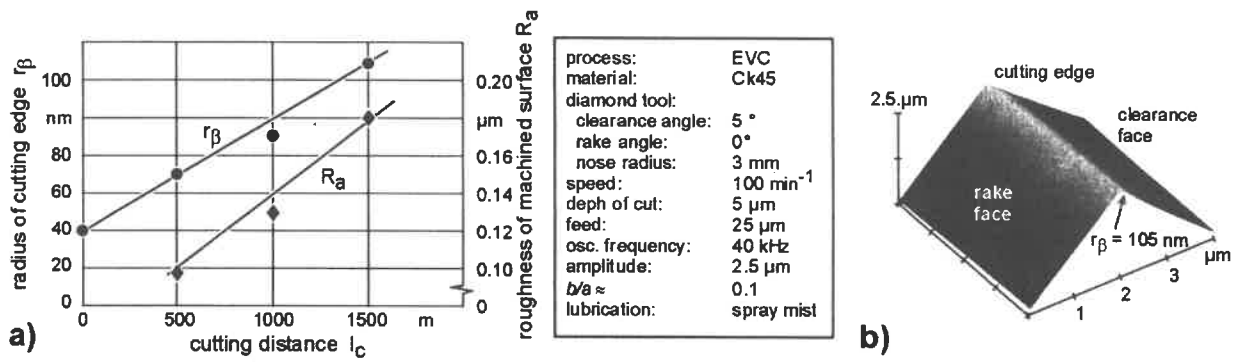

Figure 5: EVC cutting of Ck45N steel with diamond tools:
a) Dependence of cutting edge radius and roughness of machined surface on cutting distance
b) AFM-image of a tool edge after a cutting distance of 1500 m with optimized conditions

Conclusions

Several cutting experiments of aluminum and carbon steel using elliptical vibration cutting (EVC) were performed in order to determine diamond tool wear when cutting steel. A strong correlation between diamond tool wear, effective contact time between tool and workpiece and tool motion could was found. Using optimized cutting conditions, the cutting distance on steel could be increases up to 1500 m while the roughness of the machined surface was still acceptable.

References

[1] Evans, C.: "Cryogenic Diamond Turning of Stainless Steel", Annals of the CIRP, Vol. 40, 1 (1991), p. 571-575.

[2] Evans, C.J.; Paul, E.; Mangamelli, A.; Mc Glauflin, M.L.: "Chemical aspects of tool wear in single point diamond turning", Prec. Eng. 18(1996)1, p. 4-19.

[3] Brinksmeier, E.; Preuss, W.; Glaebe, R.: "Single Point Diamond turning of Steel ", Proc. of the 1st international euspen conference 1999, p. 446-449.

[4] Moriwaki, T.; Shamoto, E.: "Ultraprecision Diamond Turning of Stainless Steel by Applying Ultrasonic Vibration", Annals of the CIRP, 40(1991)1, p. 559-562.

[5] Moriwaki, T.; Shamoto, E.: "Ultraprecision Diamond Cutting of Hardened Steel by Applying Elliptical Vibration Cutting", Annals of the CIRP, 48(1999)1, p. 441-444.

Effects of Gamma Irradiation and Accelerated Aging on Wear Properties of UHMWPE Artificial Joint

Toshiaki Kaneeda*, Masahiro Utsumi** and Eiichiro Watanabe**

* : Department of Mechanical Engineering, Okayama University of Science
**: Department of Orthopedic Surgery, School of Medicine, Chiba University

Abstract

Oxidative degradation of ultra-high molecular weight polyethylene (UHMWPE; PE), due to gamma irradiation sterilization in air, increases wear rate in artificial joint. Not only adhesive and abrasive wear but also delamination (flaking), a typical wear of the PE component in artificial knee joint, and fracture could be observed. This paper deals with gamma-irradiation effects on severe wear mechanism of PE components. Scanning electron microscope (SEM) observation provided that the freeze-fractured surface of the both of components had a double-layer structure, bordered below 300-700 μm depth from the surface, and at closer observation of subsurface layer below the border, we could find an extremely rough and porous structure. Fourier Transform Infrared (FT-IR) analysis presented that the rough region had the highest extent of oxidation. Wear test result by pin-on-disc machine also demonstrated that this rough region provided the maximum wear volume.

Keywords: UHMWPE, total knee arthroplasty, polyethylene wear, gamma-irradiation

1. Introduction

Wear of UHMWPE tibial insert is a major cause of failure of total knee arthroplasty (TKA). Gamma irradiation in air, the method generally used to sterilize the polyethylene components, has been cited as a major factor affecting in vivo destructive wear such as delamination and fracture, which could be observed in retrieved PE tibial inserts. (1)(2) (Fig. 1)

We have performed revision surgeries owing to some kinds of PE problems, e.g. delaminations, fractures or a number of forms of wear out, which were clinically presented as pain, joint effusion or joint instability. Those were all sterilized by gamma irradiation in air before implantation. On the other hand, although we have also used that of ethylene oxide sterilization for a number of TKAs, we have never performed any revision surgery on them. A number of reports have focused on the subsurface white band seen on the cross-sections of PE components as oxidative degradation due to gamma sterilization in air.(1)(2)(Fig.2)

This study demonstrated the microstructural features of oxidative degradation of PE. We could determine the main reason for the frequent occurrence of delaminations and fractures with additional result from pin-on-disc wear test.

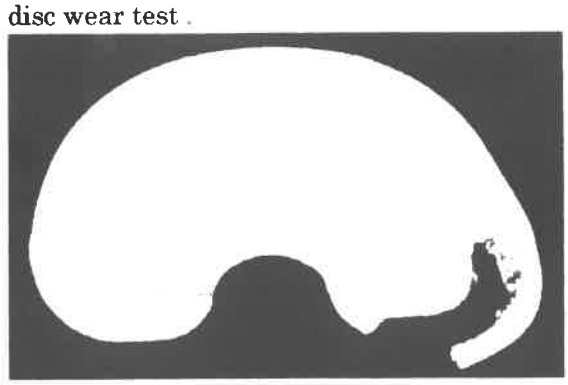

Fig. 1. Destructive wear of PE tibial insert

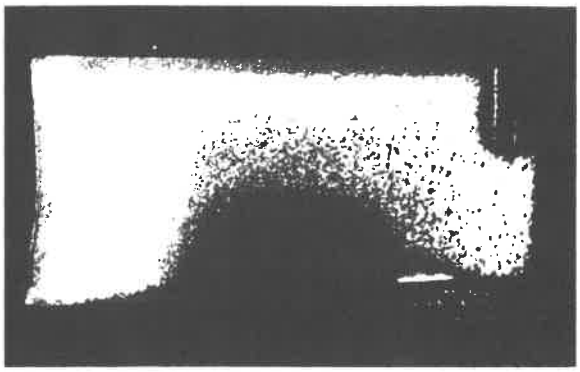

Fig.2. subsurface white band of PE component

2. Experiment

2.1; Materials

2.1.1 Retrieved or stored PE tibial inserts

Retrieved PE tibial inserts (n=29) from five different products, with an average duration after TKA of 5.5 years, and a range of 1-8.1 years (total time from sterilization range 4-12 years), and various kinds of 14 shelf-aged components from four products which were stored for some years after sterilization (range 2-10 years) were prepared for analysis. These components had all been sterilized by gamma irradiation in air.

2.1.2 Accelerated aging of PE discs

As oxidation rate is significantly slow, accelerated aging protocols have already been proposed by earlier reports.(3) Disk specimens which were directly compression-molded from Hoechst GUR1120 by the manufacturer, and sterilized by gamma irradiation at a nominal 25KGy in air. Then those were placed in an oven at a constant temperature of 80°C for 23 days adopting one of these protocols.(3) An oxygen environment of 1 atm was maintained. Test specimens without acceleration controls from the same manufacturing method were used throughout the testing.

2.2 Techniques

2.2.1; SEM

We divided these components into smaller specimens and fractured them at high strain rates in liquid nitrogen in order to analyze the vertical cross sections. SEM observation at 3.0kV accelerating voltage was then performed on these specimens.

2.2.2; FT-IR spectroscopy

Using a Poly Cuts Microtome (Reichert-Jung), we cut the specimens into approximately 50 μm-thickness horizontal sections from the articulating surface to a depth of 3 mm at 20 mm s^{-1} in air at room temperature. The extent of oxidation in each PE components were determined by Fourier Transform Infrared spectroscopy (Perkin Elmer Model 2000 FT-IR). All the spectral resolution were 4 cm^{-1}.

2.2.3; Pin on disk wear test

A pin-on-disc wear testing machine (JT-TOHSI INC., Japan) was used to investigate the tribological behavior of the PE discs against Co-Cr-Mo pins with distilled water as a lubricant. A contact stress 10MPa, a constant sliding velocity of 60mm s^{-1} and test durations up to 382166 revolutions (138.9h) were chosen. To determine the friction coefficient (μ=f/F), the friction force f was measured with a load cell.

3. Results

3.1; SEM findings

SEM observation showed that the freeze-fractured surface of the components had a double-layer structure, the border of which was 300-700μm below the surface (Fig. 3). At closer observation, the layer below the border exhibited an extremely rough structure with numerous spikes and cavities (Fig. 4-B), while the upper layer just below the articulating surface showed a relatively smooth and homogeneous structure (Fig. 4-A).

This structure had a tendency to become prominent and expanded broadly in proportion to the total aging time from sterilization. These findings were observed in both retrieved and stored PE components.

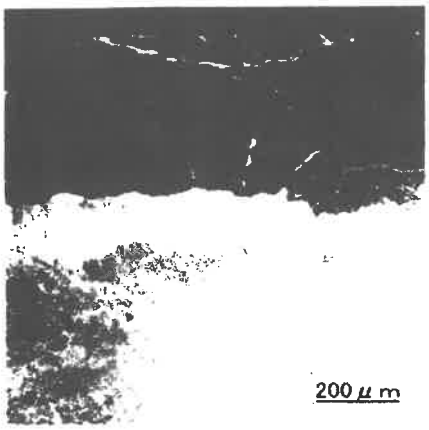

Fig.3. Freeze-fractured surface of PE tibial insert which was sterilized 10 years ago by gamma irradiation in air.

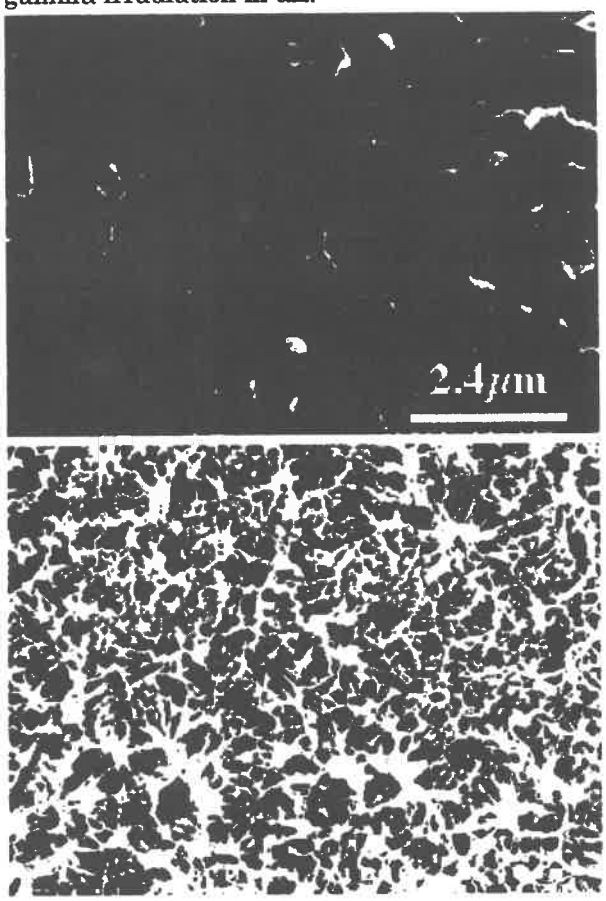

Fig. 4-A and 4-B: closer observation of each layer in Fig.3. Both are same magnification.

3.2; FT-IR analysis and oxidation index

The IR peak at 1716cm^{-1} corresponds to carbonyl functional groups, which is seen for the oxidized sample, but not for the virgin UHMWPE sample. Carbon-oxygen functional groups can exist in various forms (ketone, ester or hydroxylic acid); in general, the IR oxidation peaks appear in the range of 1660cm^{-1} to 1800cm^{-1}. The integrated peak area in this range can be used to quantify the extent of oxidation. To have a valid comparison from sample to sample, the oxidized peak area is divided by the 1464cm^{-1} (CH_2 group) peak area, using the range of 1400cm^{-1} to 1560cm^{-1}, to give an oxidation index. The highest oxidation peak according to FT-IR was found to take place at the subsurface region showing the rough structure by SEM. We could find the greatest degree of crystallization and the highest density in that region.

3.3; Pin on disk wear test

Figure 5 shows, after 382166 cycles, oxidatively accelerated discs had the maximum average total wear volume (0.0823g) followed by the control discs having the average total wear volume(0.0413g). The gamma irradiated samples without acceleration had the minimum total wear (0.0249g). There were no significant volume loss or remarkable wear marks in the pins, except for slight polyethylene transfer which was evidently confirmed by optical microscopy. After the start of the test, there was a immediate increasing trend of the friction coefficient in each sample. While the average friction coefficient in control discs gradually increased during the testing, that of oxidatively accelerated discs had a tendency to decrease.

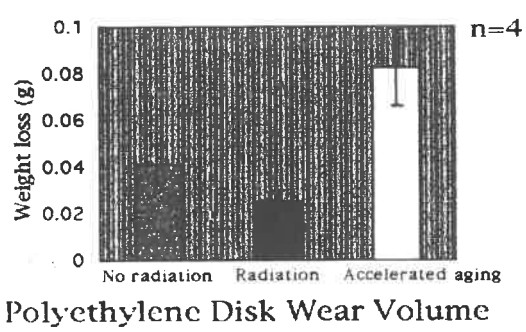

Fig 5 Wear volume comparison of UHMWPE

4. Discussion

Examination of the morphology of freeze-fractured surfaces by a SEM offered a new approach for assessing the nature and characteristics of the internal structure of PE components, especially when they contain oxidatively degraded areas in which delaminations or other manifestations of wear are present. Some researchers already revealed that the visible subsurface white band is a zone of highly oxidized, embrittled material with reduced ultimate tensile strength and elongation, resulting from gamma irradiation in air. (1)(2)

The oxidation index by FT-IR techniques in both the retrieved PE and stored one for years after gamma irradiation showed a subsurface maximum. The SEM findings showed that the subsurface highly-oxidized region which has been generally called the white band, has an extremely rough structure with many spikes and cavities. Togethering with the results of IR and the results of other papers (4)(5), high extent of oxidation, increased crystallization and high density at the region, we could comprehend the dynamic morphological changes by the oxidative effect after gamma sterilization in air. It seems reasonable to suppose that the main cause of delaminations and fractures is due to that subsurface structural weakness by shrinkage of material. The results of our pin-on-disk wear test indicated not only the weakness at the rough structure, considering its high wear rate despite its low friction coefficient, but also the possibility that such a structural change might has a correlation with delaminations. It was shown by Bartel (6) that the repeated stresses by weight bearing result in increased maximum shear stresses occurring 1 to 2 mm below the surface. If there are such increased stress concentrations to the brittle region of subsurface rough structure, the delamination and the fracture easily occur.

5. Conclusion

This study demonstrated the microstructural features of oxidative degradation after gamma irradiation in PE components.

The mechanisms of destructive wear could be elucidated by observing freeze-fractured surfaces using a SEM.

Acknowledgments

We gratefully thank Koichi Kuramoto Ph.D., Akiko Mori M.S., The Medical Division, Nakashima Propeller Co., 688-1 Jodo-kitagata, Okayama-city, 700-8691 JAPAN for their support this work.

References

1. Sutula LC. et al., Impact of Gamma Sterilization on Clinical Performance of Polyethylene in the Hip, Clin Orthop 319: 28-40, 1995
2. Collier JP. et al., Impact of Gamma Sterilization on Clinical Performance of Polyethylene in the Knee, J. Arthroplasty 11. 4 (1996): 377-389
3. Sun DC. et al., A Simple Accelerated Aging Method for Simulations of Long-Term Oxidative Effects in UHMWPE Implants, Proceedings of the OrthopaedicResearch Society, 42nd Annual Meeting, Atlanta, Geogia, USA, 1996:493.
4. Streicher RM. UHMW Polyethylene Used as a Material for the Articulating Components of Endoprosthesis, Biomed Technik 1993, 38: 303
5. Duus LC, Real Time Aging of UHMWPE Sterilized at Different Gamma Dosages, Proceedings of the OrthopaedicResearch Society, 44th Annual Meeting, New Orleans, Louisiana, USA, 1998:785.
6. Bartel DL. Et al., The effect of conformity, thickness and material on stresses in ultra-high molecular weight components for total joint replacement. J Bone Joint Surg 68A: 1041, 1986

Study on Force Controlled Micro Grooving Using Burnishing Tools

Masami Masuda, Yoshiharu Waki, Akihiro Inada, Atsushi Mutoh
Grad. Sch. of Sci. & Tech., Niigata University, 8050 Ikarashi 2-no-cho, Niigata 950-2181, Japan
Yukio Maeda
Prod. Eng. Res. Lab., Hitachi Ltd., 292 Yoshida-cho, Totsuka-ku, Yokohama 244-0817, Japan

1. Introduction

Functions of components are decided by a micro texture formed on their surfaces, which are characterized statistically and are difficult to understand the correlation with the surface functions, because the surfaces have a random micro texture produced by grinding or polishing process in general. This brings about a try and error iteration in R&D process of new products, or becomes occasionally a serious accident in the market. Therefore, it is essential that surfaces are characterized quantitatively in order to optimize surface functions in the field of optics, tribology, chemical action and so on. Therefore, normalized surfaces covered with such a uniform texture as the aggregate of a well-defined micro groove are useful for analyzing quantitatively the effect of a texture surface upon surface functions instead of a random micro texture surface.

In this paper, effects of grooving conditions upon groove geometry are discussed for the purpose of producing arbitrary micro grooves and their aggregate. Surfaces with micron or sub-micron grooves and textures covered with them are expected to use not only in the above-mentioned tentative texture but also in many other applications. Therefore, various kinds of grooves with sharp-edged shoulders, with large burrs on the shoulders or with an accurate bottom radius are required on specialized surfaces as shown in Table 1.

Table 1 Groove geometry and its feature

	Schema of groove	Feature & application
① Burr-free shoulders	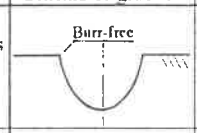	* Most popular application * Unnecessity of burr removal process ・Micro dynamic bearing
② Large burr on both shoulders	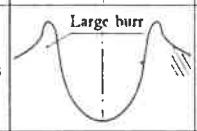	* Large surface area ・Heat transfer ・Anchor effect for adhesion * Small contact area ・Preventing from sticking
③ Accurate bottom radius	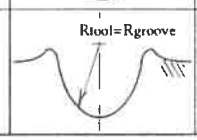	* Normal design & appl. ・Lenticular sheet ・Riblet ・Micro guide way ・Oriented reflecter

2. Experimental procedure and conditions

2.1 Grooving machine

A grooving machine used for the experiments has a rotary table for chucking a circular workpiece and a sliding table for traversing a burnishing tool in a radial direction[1)2)]. The features of the machine are as follows;

1) The normal component of burnishing force can be controlled constant at accuracy of ± 0.1mN, since preventing from chucking errors or parallel errors of workpieces.
2) The machine can produce a texture pattern with the aggregate of a straight line, a circle line and /or sinusoidal line.

2.2 Grooving conditions

Grooving conditions are shown in Table 2. Coni-

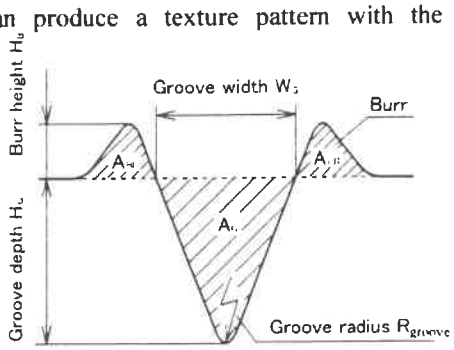

Fig.1 Definition of groove geometry

Table 2 Grooving conditions

Forming equipment	Micro texturing machine
Tool	① Conical tool Single crystal diamond Top angle θ=143°, 170° Radius of sphere SR=7.5um, 43um
	② Keel-shaped tool Single crystal diamond Trans. radius R=0.2um,Top angle θ=150° Longitudinal radius R'=10mm
	③ Spherical tool Spphire Radius of sphere SR=10um
Workpiece	cf. Table 3
Normal load	W = 0.5-500mN
Rubbing speed	v = 3-120mm/min
Lubricant	① Dry
	② Wet (Nisseki, Spinox S4) Viscosity : 3.96cst/313K

Table 3 Mechanical properties of work material

Work material	Vickers hardness	Density [mN/mm³]	Young's modulus [N/mm²]
Pure Al	60	25,100	70,600
Ni-P	500		119,600
Sodalime glass	680	24,400	71,500
Glass ceramics	610	23,500	96,800

cal, spherical and keel-shaped tools made of either single crystal diamond or sapphire are used for grooving. The keel-shaped tools have 10mm radius in a rubbing direction and 0.2μm radius in a transverse direction. Workpieces are made of pure Al, Ni-P, sodalime glass and glass ceramics, whose mechanical properties are shown in Table 3.

2.3 Measurement of groove geometry

It is significantly interested in the grooving process and grooving conditions if tool geometry would be copied on work surfaces with any accuracy. The parameters of grooving geometry as shown in Fig.1 are measured with SPM (TopoMetrix TMX-2000).

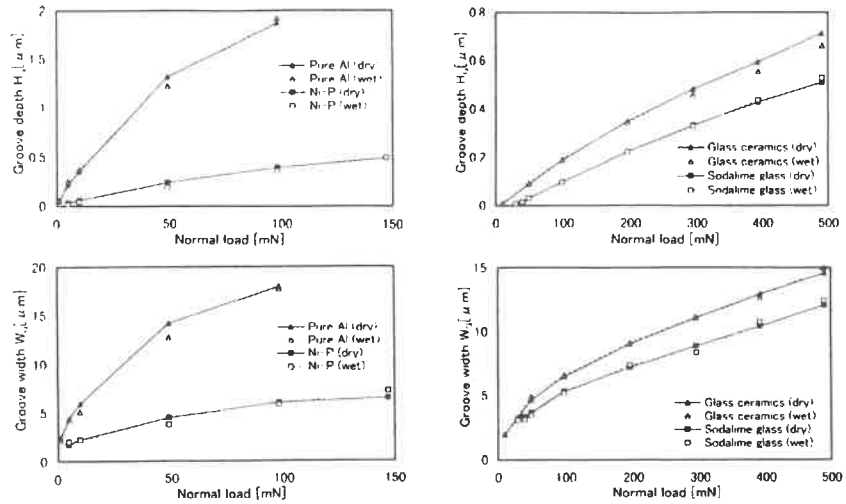

(a) Pure Al and Ni-P (b) Glass

Fig.2 Effect of normal load on groove depth and groove width

3. Grooving results and discussion

3.1 Groove geometry

Grooving tests on four kinds of work materials were carried out using a conical tool (θ =143° , SR=7.5μm). Fig.2 shows the effect of normal load on groove depth and groove width. The groove depth and groove width are approximately proportional to the square root of normal load. This behavior is similar to the fact in indenting tests. On the other hand, the groove depth and groove width except tool life seems to be not so sensitive to the lubricant.

3.2 Relation between groove depth and groove width

Fig.3 shows the correlation between groove depth and groove width. The groove width on sodalime glass and glass ceramics is 1.6 - 2.2 times larger than that on pure Al. Any cracks or chippings did not appear around grooves even at a maximum normal load of 490mN, according to SEM observation. As a result, sub-micron forming is possible on such brittle material as glass.

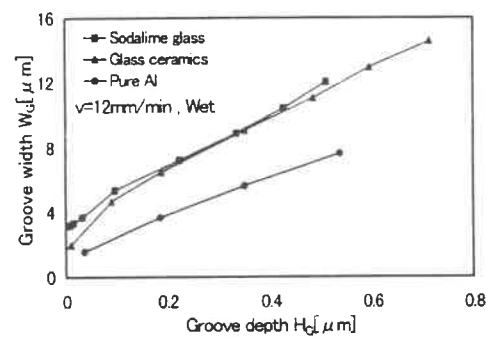

Fig.3 Relation between groove depth and groove width

3.3 Effect of Rubbing speed

Groove depth on sodalime glass grooving increases 60% with the decrease of a rubbing speed from 120 mm/min to 3 mm/min, although groove depth and groove width on pure Al fluctuate approx.± 10% in the same range of the rubbing speed as well as groove width on sodalime glass.

Forming accuracy can be investigated by "radial ratio" of a groove radius relative to a tool radius. Fig. 4 shows the correlation between groove depth and the radial ratio. In this figure, the radial ratio increases with the decrease of groove depth for sodalime glass or glass ceramics grooving, especially on wet grooving of glass.

On the other hand, tool geometry is copied more accurate on pure Al, because radial ratio indicates 1.1 - 1.8 at a groove depth less than 0.6um.

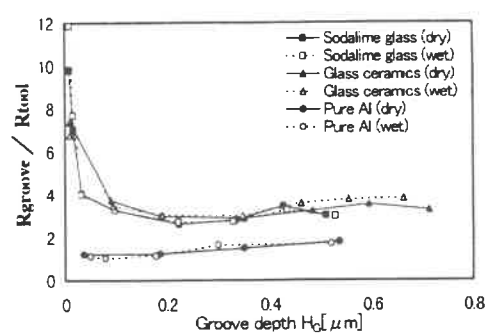

Fig.4 Relation between groove depth and radial ratio

3.4 Burr height and burr width

Fig.5 shows the influence of normal load on burr height and burr width in pure Al and Ni-P grooving. According to the figure, groove depth and burr height in Ni-P grooving are relatively smaller and groove width and burr width are relatively larger in comparison with pure Al grooving. A

good texture is achieved by pure Al grooving at a low normal load, when relatively large surface area, small contact area or large burr height is required. Although larger burr width and smaller burr height are obtained in wet Ni-P grooving than those in dry Ni-P grooving. The lubricant seems to affect delicately the burr width and burr height. The effect of lubricant has to be continued investigating.

3.5 Adjacent grooving

Only a micro groove is scarcely applied to actual products, but some aggregate of micro grooves is more useful in industry. Therefore, the interference between adjacent grooves has been investigated in the grooving process, using parameters as shown in Fig. 6.

The first and the second grooves were made in the similar way, except a rubbing direction in the second groove across the first groove at a small angle. Thus, the interference between adjacent groves can be made clear by profiles in a transverse direction at any groove pitch.

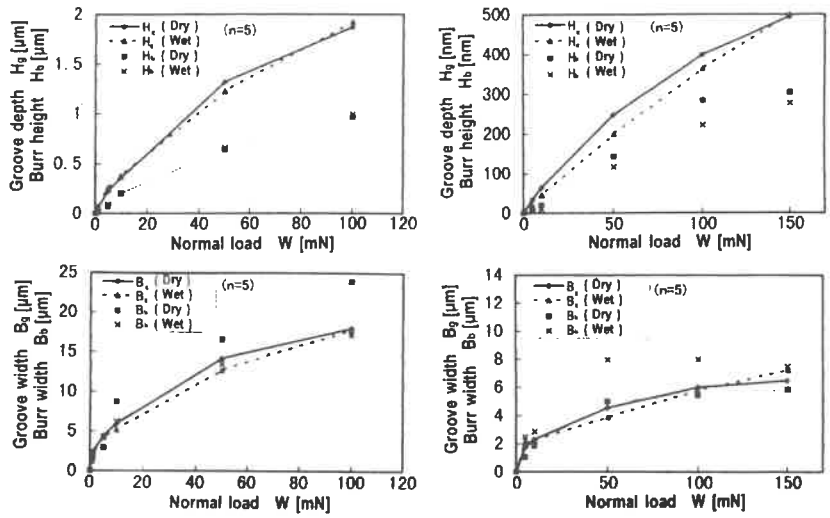

(a) Pure Al (b) Ni-P

Fig.5 Influence of normal load on groove geometry

Fig. 7 shows the symmetricity between adjacent grooves in wet grooving of pure Al. SR7.5μm conical tool and SR100μm sapphire tool are used in (a) and (b) respectively. A tool makes two grooves in the same rubbing direction in (a) and (b), but in the inverse rubbing direction each other in (c). Although the symmetricity between adjacent grooves seems to fluctuate considerably in this figure, some regularity is observed .

1) Maximum values of out-of-symmetry indicates at a larger groove pitch when the groove depth is larger.
2) This is because that the groove depth at the second grooving becomes smaller when a tool rubs on the burr formed further from the center of the first groove in the case of a large groove depth.
3) At an extremely large groove pitch, good symmetricity is obtained substantially, without any interference each other.
4) Symmetricity in opposite direction grooving (c) is analogous to that in same direction grooving (a), but the former has not so strong correlation with the latter. This means the burr indicates any orientation induced by the grooving.

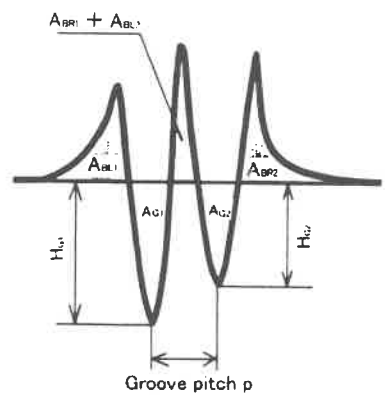

Fig.6 Definition of groove geometry in adjacent grooves

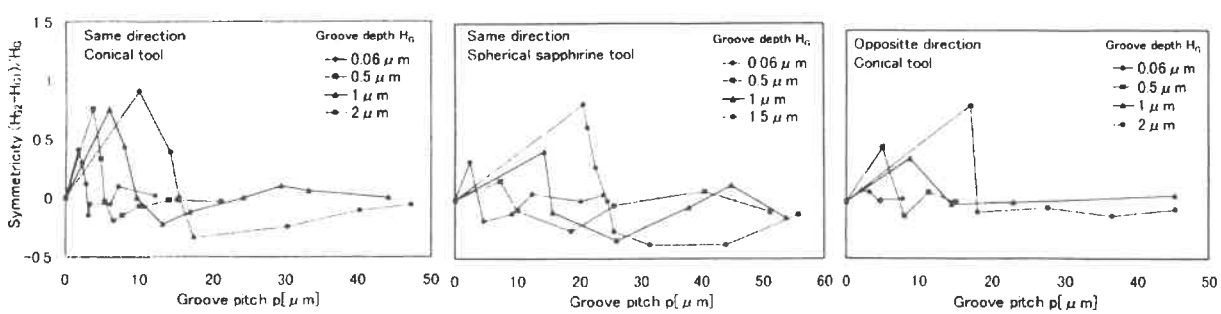

(a) Same direction with conical tool (b) Same direction with spherical sapphire tool (c) Opposite direction with conical tool

Fig.7 Influence of groove pitch on symmetricity

3.6 Examples of texture pattern with micro grooves

Various kinds of textures were made tentatively using the developed grooving process. Some examples are shown in the following ;

ex.1) Fig. 8 shows a texture covered with numerous short grooves. The work material is Al alloy, so the burrs are piled up at the ends of all grooves.

ex.2) Fig. 9 shows an example of a texture covered with cross grooves, pitches of which are 50μm and 18μm respectively. The workpiece was diamond turned to an undulation surface with 2um amplitude prior to micro grooving.

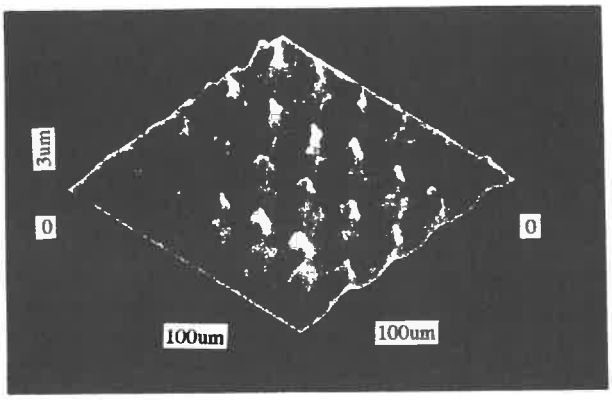

Fig.8 Texture with short grooves

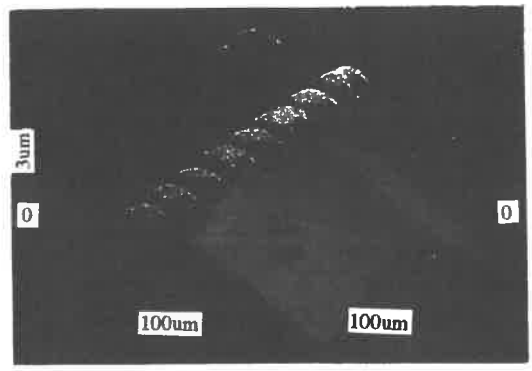

Fig.9 Texture with cross grooves

4. Conclusions

The groove geometry is discussed in sub-micron grooving processes for non-ferrous metals and brittle materials on a force controlled micro grooving machine with a burnishing tool made either of single crystal diamond or of sapphire.

1) For pure Al, the burr on the groove shoulders is inevitably large because of plastic flow from grooves, although the groove radius is copied relatively precise from the tool geometry.
2) The groove width on glass is 1.6 - 2.2 times larger and bottom radius of grooves is almost twice larger than those on pure Al, when grooves on glass are formed as deep as those on pure Al.
3) The burrs on groove shoulders force to decrease the groove depth at a closer pitch between adjacent grooves, because the actual volume to be removed in the following grooving pass increases on the burrs.

Acknowledgement

The authors would like to express their sincere appreciation to the Science and Research Foundation of the Education Ministry for financial supporting of this research.

References

1) Yukio Maeda, et al : Study on ultra micro grooving (1) ---Development of grooving machine, Proc. of JSPE (1992/9) p339
2) Yukio Maeda, et al : Study on ultra micro grooving (2) ---Grooving characteristics for Ni-P plated substrate, Proc. of JSPE (1993/9) p373

Silicon Wafer Bonding Process for Preventing Intrinsic Bubbles after Low Temperature Thermal Treatment

Do Min Moon, In Ho Cho, Hae Do Jeong, Woo Seong Che
School of Mechanical engineering, Pusan National Univ, Pusan, Korea

The interface bubble in SDB(silicon wafer direct bonding) was investigated, for the development of SDB-based SOI(silicon on insulator) wafer and MEMS(micro-electromechanical system) fabrication process. In this study, we have prepared the bonded surfaces with thermally oxidized and bare silicon wafers by the successive processes such as physical and chemical pretreatment, mating and annealing at 600～1000℃.

The bonding interface is investigated by an infrared(IR) topography system which uses the permeability of infrared through silicon wafer. Using this procedure, we observed intrinsic bubbles at elevated temperatures. And so, the bonded wafers was fabricated which didn't appear intrinsic bubbles in the atmospheric pressure annealing. Those bonded wafers without intrinsic bubbles were employed to verify that the generation of intrinsic bubble was related to the outside pressure using annealing process at low temperature in 1×10^{-6} torr. The result of this study will be helpful in the development of low temperature annealing process and the prevention of interface bubbles.

1. Introduction

SDB(silicon wafer direct bonding) technology allows two silicon wafers to stick together without any adhesives and thus has been applied to various fields, such as SOI and MEMS1) 2). The success of SDB technology can be established by bonding on the bonded interface with no defects. The defects on the bonded interface can be generated, critically depending on silicon wafer surface conditions before bonding. They are called voids or bubbles, and observed by transmitting X-ray and infrared light.

According to the generation point of time, the bubbles are divided into extrinsic bubbles and intrinsic bubbles: the extrinsic are generated during the mating process at the normal temperature, whereas the intrinsic during the annealing process at 200～800℃. The causes that the bubbles are generated are supposed to be insufficient flat surfaces, trapped air in mating, particles on the silicon surfaces, contamination by hydrocarbon, and the moisture on the wafer surface3) 4). And, according to the size of bubbles, the bubbles are also divided into group X and IR: the bubbles of the group X are observed by transmitting X-ray with the diameter of smaller than 500㎛ and those of the group IR by transmitting infrared light with bigger than 1mm. The bubbles of the group X disappear during the annealing at 200℃～800℃, while those of the group IR are generated5).

This study was focused on the thermodynamic model, which shows how the bubbles are generated. This model was verified by experiments through annealing under the atmospheric pressure after annealing

at the low temperature (around 200℃) in vacuum of 1 ×10-6 torr.

2. Experiment

The two types of wafers are used in this experiment: one is (100) oriented p-type bare silicon wafer and the other has the thermal oxidation layer of 1200Å. First, the silicon wafer is dipped and cleaned for 10 minutes in mixtures of sulfuric acid and hydrogen-peroxide in the volume ratio of 3:1. The mixtures is removed from silicon surfaces by DI (deionized) water rinsing and then dipped in the weak HF solution in the dilution ratio, 1:100 in order to strip the native oxide layers and impurity-containing oxide film. Part of the thermal oxide layer is etched, and so a activated and fresh surface is created. After the HF cleaning, the silicon wafer was rinsed by the DI water again and dried by nitrogen gas blowing. Again the wafer surface is dried by a spin dryer. The wafer spines at 600 rpm with the DI water jetted. And, the wafer is spin-dried with 1200 rpm to 2400 rpm and the heated nitrogen gas blown. After cleaning and drying, the bare wafer and the wafer with the thermal oxidation layer are put together and bonded in the clean-room of class 10 and 20℃. After mating at the normal temperature, part of the wafer is annealed at around 200℃ in the vacuum of 1×10-6 torr by heated tungsten filament. Later, the annealing for all the bonded wafers are carried out in a tube furnace at 600℃~1000℃. After bonding and annealing, the bonded interface is analyzed by an infrared topography system. It makes use of the permeability of infrared light for the silicon and detects particles and bubbles on the bonded interface.

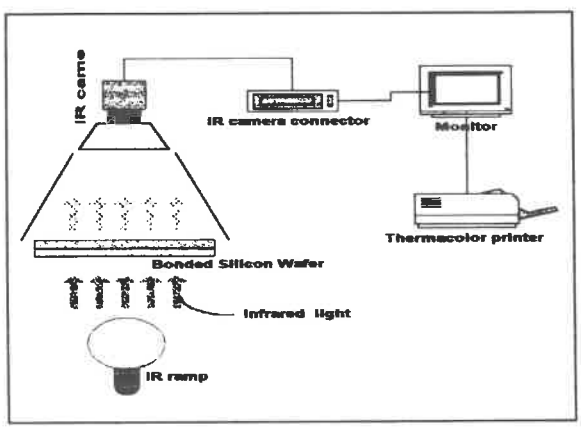

Fig. 1. IR (infrared) topography system

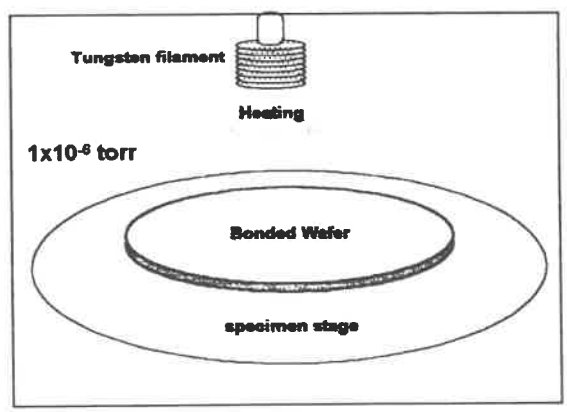

Fig 2. Annealing in Vacuum Chamber

3. Result and Analysis

In order to research the behavior of intrinsic bubbles on the bonded silicon wafer, depending on outside pressure, the two annealing experiments were carried out. Bonded silicon wafers were annealed at around 200℃ in the vacuum of 1×10-6 torr and at 600~1000℃ in atmospheric pressure. The desired bonded interface was obtained by hand under the cleaning and drying conditions as above mentioned.

As shown in Fig. 3, Si-Si bonded wafer with two bare silicon wafers was made and annealed at 600℃ in

atmospheric pressure. As a result, the number of dark fringe in the extrinsic bubble was considerably increased. Also, a number of small intrinsic bubbles were generated during the annealing. In case of SiO2-SiO2 bonded wafer with two wafers which has the thermal oxide layer of 1200Å, as in Fig. 4, some of the extrinsic bubbles were detected after mating and no intrinsic bubbles were generated after annealing at 600℃.

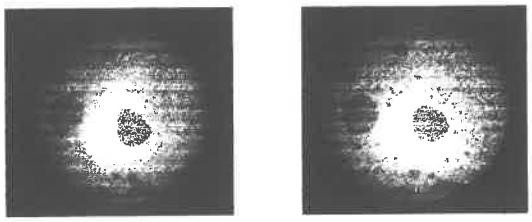

(a) Room temperature bonding (b) Annealed at 600°C for 1 hr

Fig 3. IR Topographs of bubbles : Si-Si bonding

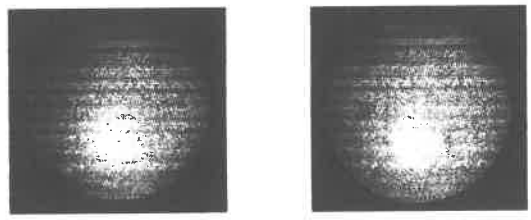

(a) Room temperature bonding (b) Annealed at 600°C for 1 hr

Fig 4. IR Topographs of bubbles : SiO2-SiO2 bonding

As shown in Fig. 5, in the Si-Si bonding, the size of extrinsic bubbles was increased and the irregular shapes turned into the circular ones after the annealing in the vacuum. Also, a relatively large and circular intrinsic bubble was generated in the center. The number of dark fringes of extrinsic and intrinsic bubbles was increased after the annealing at 600℃. In the SiO2-SiO2 bonding, however, any intrinsic bubbles were not generated after mating and annealing in the vacuum. Instead, tiny intrinsic bubbles were generated when annealed once more in atmospheric pressure after annealing in the vacuum.

Si-Si and SiO2-SiO2 bonded wafers turned out to have similar results after annealing at 1000℃. In Si-Si bonding, intrinsic bubbles were generated during the annealing and then large bubbles out of them contracted. Those contracted bubbles persisted even after annealing at 1000℃. In SiO2-SiO2 bonding, the perfectly bonded interface was obtained aside from a few extrinsic bubbles.

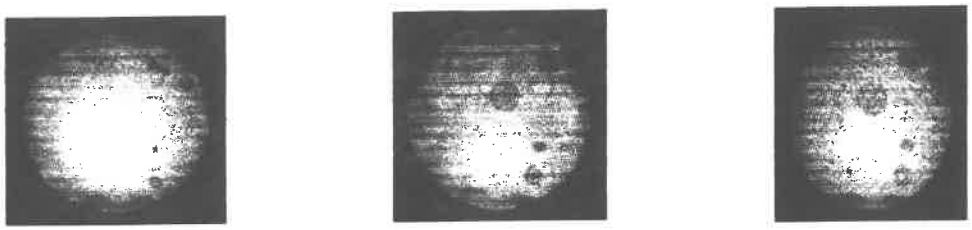

(a) Room temperature bonding (b) Annealed in vacuum for 10 min (c) Annealed at 600°C for 1 hr

Fig 5. IR Topographs of bubbles : Si-Si bonding

According to the generation condition and the behavior, intrinsic bubbles are divided into two types. One is relatively large bubbles with more than two dark fringes and the other is small ones with 1 to 1.5 dark fringe. The former was generated at the low temperature in the vacuum of Si-Si bonding and the number of fringe was increased in the additional annealing. The latter was generated in the annealing at 600～900℃, but

disappeared at higher than 900℃. In case of SiO2-SiO2 bonding, It was generated exclusively when annealed once more in atmospheric pressure after annealing in the vacuum.

K. Mitani suggested the relation between critical radius of bubbles and pressure. The relation among bubble height(h), radius (r), and the difference of inside and outside pressure is as follows:

$$\Delta p = \frac{64hD}{r^4} \qquad (1)$$

$$D = \frac{Ept^4}{12(1-v^4)} \qquad (2)$$ (E: Young's modulus , v: Poisson's ratio)

$\Delta p = p_i - p_{outside}$ (p_i : a pressure in the bubbles , $p_{outside}$: usually equal to 1atm)

The relation between Δp and critical radius, R_{crit} is shown in (3).

$$R_{crit} \propto \left(\frac{1}{\Delta p^2}\right)^{\frac{1}{4}} \qquad (3)$$

As the temperature gets higher, desorbed free molecules come to assemble, have critical pressure above and separate the bonded interface. Then, the two types of bubbles are generated. The increase of the fringe number according to the annealing temperature means that the radius of curvature of the bubble is reduced through the annealing. It also shows that the inside pressure increases as the annealing temperature gets higher. The increase of the inside pressure also causes the irregular-shaped bubble to turn into the circular shape. It is assumed that the increase of the intrinsic bubble pressure takes place from the start. As the temperature in the bonded area gets high, the adsorbed gas molecules on the surface are desorbed. If the pressure on the bonded interface is more than the bonding strength and the bubbles are generated on the interface, the gas molecules get together around the bubble and then the pressure turns high.

The large bubbles with more than two fringes are generated at the low temperature and they have a relatively big radius of curvature. They also destroy the wide bonded interface with the low pressure. It is assumed that these bubbles separates the bonded interface with weak bonding strength.

The small bubbles with 1 to 1.5 fringes can be explained by the Thermodynamic Model of K. Mitani etc. They are generated in the annealing at the relatively high temperature. They also have circular shapes and relatively high pressure when generated. In the SiO2-SiO2 bonding, bubbles were not created in the annealing at 600℃~900℃, but generated when annealed at 600℃ in atmospheric pressure after annealing in the vacuum. It is assumed that the boned interface was not destroyed, because of the gas absorption effect of the oxide layer. But, intrinsic bubbles are nucleated easily in annealing in the vacuum, as the critical radius in the vacuum is smaller than it is under atmospheric pressure, as shown in (3).Yet the

size of the bubble is a bit bigger than the critical radius. It is not recognized in the infrared light after annealing in the vacuum. It grows to be found by the infrared topography system in the atmospheric annealing at 600℃.

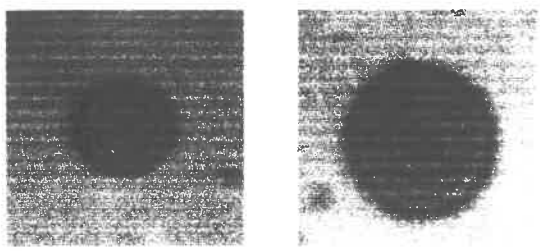

Fig 6. The increase of fringe number after annealing

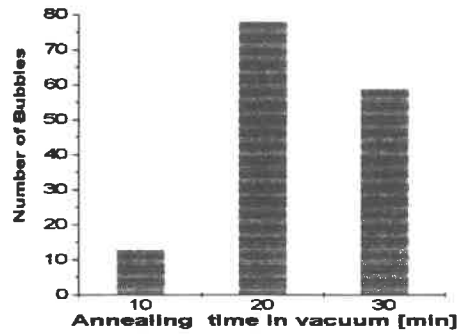

Fig 7. Histogram of small bubbles : SiO2-SiO2 bonding

(annealed at 600℃ in atmospheric pressure after annealing in the vacuum.)

5. Conclusion

In the silicon wafer direct bonding, the behavior of the intrinsic bubbles on the bonded interface were observed by transmitting the infrared light and the increase of the bubble pressure was found. The bonded wafers were achieved in the SiO2-SiO2 bonding, which generated no intrinsic bubbles in the annealing under the atmospheric pressure. The intrinsic bubbles were generated in the annealing at around 200℃ in the vacuum of 1×10^{-6} torr. The experiment result proves the relation between the bubble nucleation and the pressure in the thermodynamic model. It will provide the basis for the annealing process at the low temperature and the control of the intrinsic bubbles in the direct bonding of silicon wafers.

Reference

1) S. M. Sze, *Semiconductor Sensor*, (John Wiley & Sons, New York, 1994) Chap. 2.

2) Sorin Cristoloveanu, Sheng S. Si, Electrical Characterization of Silicon On Insulator Materials and Device, (Kluwer Academic, Boston, 1995) Chap. 2.

3) M. Shimbo, K. Furukawa, K. Fukuda, T. Tanzawa , J. Appl. Phys. 60, 2987 (1986)

4) R. Stengl, T.Y. Tan, U. Gosele, Jpn. J. Appl. Phys. 28, 1735 (1989)

5) K. Mitani, U. Gosele, Appl. Phys. A 54, 543 (1992)

DEVELOPMENT OF WATER-SOLUBLE COOLANT FOR MULTI-WIRE SAW SLICING OF 400mm-DIAMETER SILICON

Hiroshi Oishi★, Keiichiro Asakawa★, Junichi Matsuzaki★, Akio Ashida★★
★Super Silicon Crystal Research Institute Corp., 555-1, Nakanoya,
Annaka, Gumma, 379-0125, Japan
★★Ohtomo Chemical Industrial Corp., 2-17-10, Yashiro,
Sumida, Tokyo, 131-0041, Japan

ABSTRACT

This paper presents the constituent features of the newly developed water-soluble coolant for multi-wire saw slicing of 400mm-diameter silicon, together with its characteristic requirements from a rheological viewpoint.

1. Introduction

In the shaping process of silicon substrate wafers, a major raw material for device chips, ID saw had exclusively been used to slice them for about 30 years and had caught up with wafer diameter growths by increasing its machine dimensions. However, the slicing method is changing to the multi-wire saw at 200mm-diameter as a turning point. And the wire saw seems the most realistic option for 400mm-diameter silicon slicing, too.[1] In developing the slicing technology for 400mm silicon, the authors are pursuing an optimization of quality, productivity, and cost from the following 3 developmental points; (1) wire saw machine, (2) water-soluble coolant (slurry), and (3) slicing conditions (SOC). Among them, this paper presents the current developmental status of the water-soluble coolant.

2. Objective of a development of water-soluble coolant

For the wire saw slicing, a slurry with the mineral oil-based coolant is the most commonly used now for its stable slicing performance. On the other hand, a development of slurry with the water-soluble coolant will largely contribute to a realization of a safe and kind-to-environment operation of the wire saw slicing for its intrinsic merits such as; ① Non-flammable and suitable for a laborsaving or an automatic operation, ② Easy post-slice cleaning of a wire saw machine and wafers only with tap water, ③ Good bio-degradability for the used slurry. However, the water-soluble coolant has the following issues to be solved; ④ Difficult to secure a good abrasives suspension in the slurry, ⑤ Need to control water evaporation, ⑥ Some coolants have peculiar odor.

Due to the above issues, although the water-soluble coolant is used for 200mm slicing by some limited wafer manufacturers, it has proved to be insufficient to 300mm slicing which takes longer slicing time. And there was no water-soluble coolant available for 400mm slicing because of heavy segregation and settlement of abrasives from the slurry during the slicing.

3. Improvement of odor, bio-degradability, and water evaporation

(1) The new water-soluble coolant adopted Polypropyleneglycol as a base (approx. 75wt%). This chemical has no peculiar odor unlike mineral oils or fatty acids. And polypropyleneglycol is more bio-degradable than polyethyleneglycol which is also commonly used for other water-soluble coolants as a

base.

(2) Approx. 15wt% of water is added to the new coolant in order to give the non-flammability characteristic. The new coolant contains hydrophilic bentonite particulates to improve the abrasives suspension in the slurry. Being contained in these bentonite particulates as thier crystal water, the added water has non-evaporative characteristic and the slurry has got rid of water supply to control its viscosity during the slicing operation.

4. Improvement of abrasives suspension

Approx. 0.5wt% of bentonite, clay mineral, is added to improve the abrasives suspension in the slurry. Fig.1 shows chemical structures of bentonite. It has a layered chemical structure as shown in Fig.1(b) which is composed of unit structures shown in Fig.1(a). A layered structure swells by taking in the water between the unit structures. This layered bentonite structure forms a cardhouse or a cross-linkage structure (a kind of shelves) and prevents abrasives from segregating and settling in the slurry as shown schematically in Fig.2.

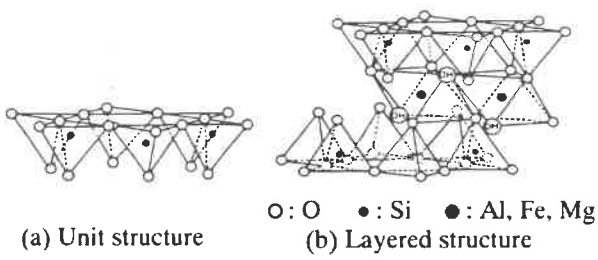

Fig.1 Chemical structure of bentonite.

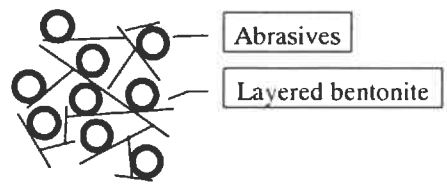

Fig.2 Schematic diagram of cardhouse or cross-linkage structure of bentonite.

5. Measurement of slurry rheology with respect to shearing speed

Wire saw slicing performance is largely affected by the slurry rheology. Among the rheological factors, a slurry viscosity is the most important as it governs the adhesion of slurry onto a wire and the supply of abrasives to grinding points. When a viscosity is too low, the slurry does not adhere to the running wire well. When it is too high, the slurry dose not go into narrow wire grooves on the other hand. Both cases give poor wafer qualities and also become a cause of abrasives settlement where the slurry flow becomes stagnant in the machine or between wafers.

As slurries have non-Newtonian characteristic in which a viscosity changes largely with the slurry flow speed (shearing velocity), it is necessary to measure the viscosity at various velocities in order to correlate the viscosity with the slicing performances. Although the slurry viscosity measurement has been conducted at a certain shearing velocity using an axial cylinder viscometer in general, the authors has introduced the cone & plate viscometer (Fig.3) which can measure a viscosity at various velocities,

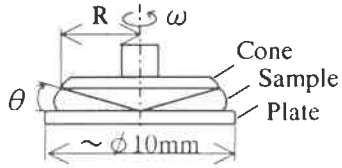

Fig.3 Schematic drawing of the cone & plate viscometer.

and quantified non-Newtonian characteristic of the slurries.

Fig.4 shows examples of the viscosity-shearing velocity characteristics of various slurries (including the oil-based slurry). The characteristics show various types such as the water-soluble slurry B, C which are close to Newtonian fluid, or as the slurry A and the oil-based slurry which are close to non-Bingham fluid. Comparing these measurement results with actual slicing performances experienced so far, it has proved that the most desirable non-Newtonian characteristic as a wire saw slurry lies roughly in a region shown in Fig.5, and has a low viscosity at a high shearing velocity and a high viscosity at a low speed. This characteristic becomes one of goals for new coolant developments. The following test coolants are prepared to have "Slurry A" characteristic.

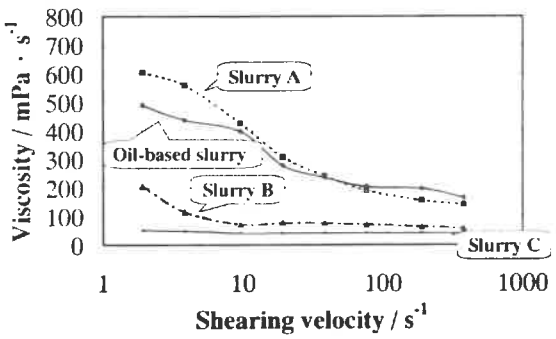

Fig.4 Viscosity characteristics of various slurries with respect to shearing velocities.

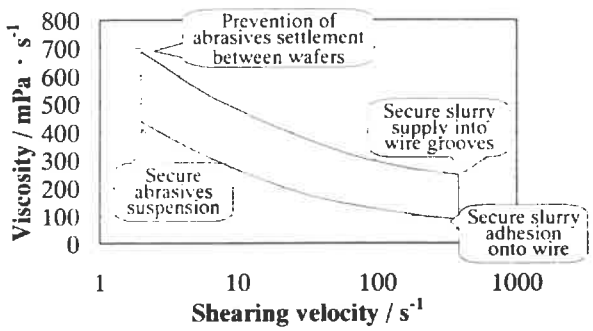

Fig.5 The most desirable non-Newtonian characteristic as a wire saw slurry.

6. Viscosity change of the water-soluble coolant

Fig.6(a) shows an example of viscosity changes of the water-soluble slurry developed in a first stage of the test. Viscosity which had been approx. 200mPa s before the test dropped to 60～100mPa s in a depth of 0～100mm work feed. Causes of a viscosity decrease and a deterioration of abrasives suspension are supposed as follows;

① Crushing of bentonite by shearing stress caused by a slurry stirring or an ingot slicing.

② Metasilicate ions generated from the silicon sludge adhere to the layered bentonite and decompose it chemically to unit structures, and thus loses the cardhouse structure.

$$Si + 2OH^- + H_2O \rightarrow SiO_3^{2-}\text{(metasilicate ion)} + 2H_2$$

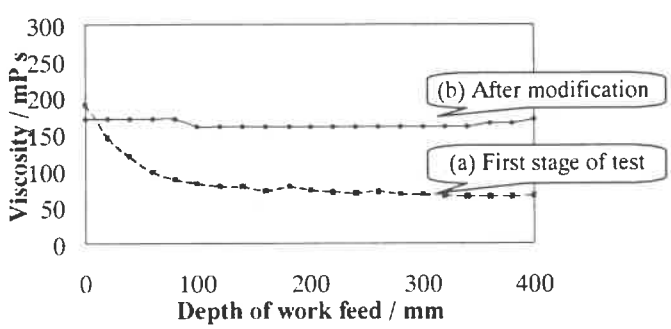

Fig.6 Example of slurry viscosity changes (measured with an axial cylinder viscometer).

7. Improvement of viscosity change

Slurry viscosity in the first stage of developmental test showed a thixotropy as shown in Fig.6(a) in which the viscosity decreased with a slicing duration. Therefore, in order to compensate it, crystalline cellulose was added which had a rheopectic nature and increased a viscosity with a slicing duration. Futhermore, synthetic mica which had constant viscosity was added to adjust a total viscosity level. Fig.7 shows viscosity changes of these 3 additives. They are added, respectively, to polypropylene base and stirred by the homogenizer (high speed) stirrer to simulate the slicing condition. Fig.6(b) shows a viscosity change of the modified slurry. By this modification, a practical wire saw slicing for 400mm-diameter silicon has become achieved through an improved abrasives suspension and an eased wire withdrawal from an ingot following slicing. However, amounts of these 3 additives are so sensitive to the coolant characteristics that a fine adjustment of these additions is needed.

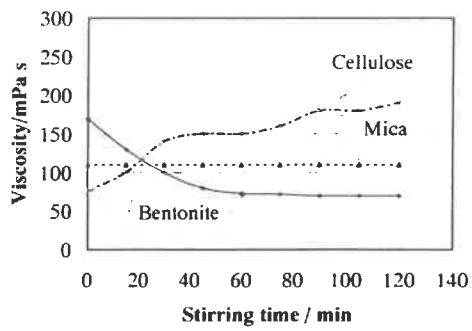

Fig.7 Viscosity characteristics of 3 additives (bentonite 0.5wt%, cellulose 0.25wt%, mica 2wt%).

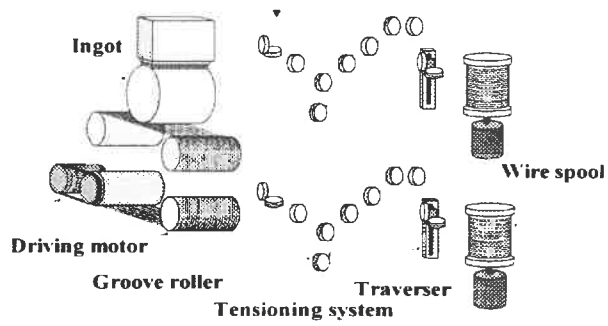

Fig.8 Schematic drawing of the wire saw.

Fig.8 shows a schematic diagram of the wire saw [1] and Table 1 indicates major slicing conditions for 400mm silicon. Table 2 shows, in rough figures, 400mm as-sliced wafer qualities.

Table 1 Major slicing conditions for 400mm.

Ingot feed rate	Ave. 0.26mm/min
Wire (high tension steel) Wire tension Wire speed Reversing cycle	0.18mm in diameter 2.5kg (25N) Ave. 500 (Max. 750) m/min 30s
Slurry tank capacity Slurry flow rate, temperature	400L 110L/min, 23.5±0.1°C
Abrasive	GC#600 (50wt% in slurry)

Table 2 400mm as-sliced wafer qualities

Item	Quality level	
Center thickness variation (TH)	x-bar σ	1,020μm, 4μm
Tatal thickness variation (TTV)	x-bar σ	40μm, 5μm
Surface roughness (Pt)	x-bar σ	15μm, 2μm

8. Summary

A new water-soluble coolant for multi-wire saw slicing of 400mm-diameter silicon was developed. It has non-Bingham rheology, and consists of polypropylene base and 3 additives; hydrophilic bentonite to improve abrasives suspension, crystalline cellulose to compensate a thixotropy of bentonite, and synthetic mica to adjust total viscosity level.

Reference

[1] H. Oishi, et al : Proc. 1998 ASPE Spring Topical Meeting, (1998) 109.

A STUDY ON THERMAL STRAINS IN PLATE GLASS DURING THERMAL CUTTING USING HOT AIR JET

E.S. Prakash[1] K. Sadashivappa[1] Vince Joseph[2] M. Singaperumal[3]
[1]Bapuji Institute of Engineering and Technology, Davangere-577004.
[2]University BDT College of Engineering, Davangere-577004.
[3]Indian Institute of Technology, Chennai-600036, India.
[1]Fax: (08192) 31261, E-mail: biet@dvgbiet.kar.nic.in

Keywords: Thermal strains, plate glass cutting, thermal cutting, strain measurement, crack propagation.

1. Introduction

Glass is widely used in both domestic and industrial applications. Fabrication of glass blanks is very important in the case of optical lens, opthalmic lens and orthodental photographic mirrors. Cutting of glass is invariably the first step in any of the glass fabrication methods. Profile generation without internal flaws and obtaining smoother profiles is difficult by conventional diamond cutting.

A new method of glass cutting by the above authors has been reported earlier[1]. This method makes use of a hot air jet for cutting plate glass. Plate glass is kept on the X-Y table which can be moved at required speed under a stationary hot air jet issuing from the hot air gun. The cutting speed depends upon the thickness of the plate glass and the air temperature at the nozzle tip. Complex profile cutting by the above method on plate glasses is easier and economical. Profiles generated by the new method are smoother as compared to that by diamond cutting.

A compact portable hot air jet gun was designed and fabricated to study the parameters which influence the crack propagation. Experimental studies have shown that the thermal cutting time increases with the plate glass thickness[2].

2. Experimental details

Thermal stresses are setup in glass due to heating. Thermal strains are required to be measured for computing these thermal stresses. Experimental setups were fabricated for measuring temperature distribution and thermal strains on the plate glass surface during thermal cutting using hot air jet.

2.1 Temperature measurement

Fig. 1 shows photograph of experimental setup for temperature measurement. It consists of a hot air blower with 2 mm diameter nozzle, X-Y table to move the plate glass under the stationary hot air jet, a plate glass with thermocouples mounted on it, a millivoltmeter to indicate the thermocouple output.

Four iron-constantan thermocouples, keeping a distance of 10 mm apart, were mounted on the glass surface for measuring temperature during cutting. Mountings were at a distance of 20 mm away from the cutting path. Thermocouple outputs were measured using a millivoltmeter and then the readings were converted into temperature in °C. Fig. 2 shows thermocouple mountings on plate glass surface. The glass plate (2 mm thick) was moved under a stationary hot air jet and the thermocouple outputs were measured and recorded during cutting.

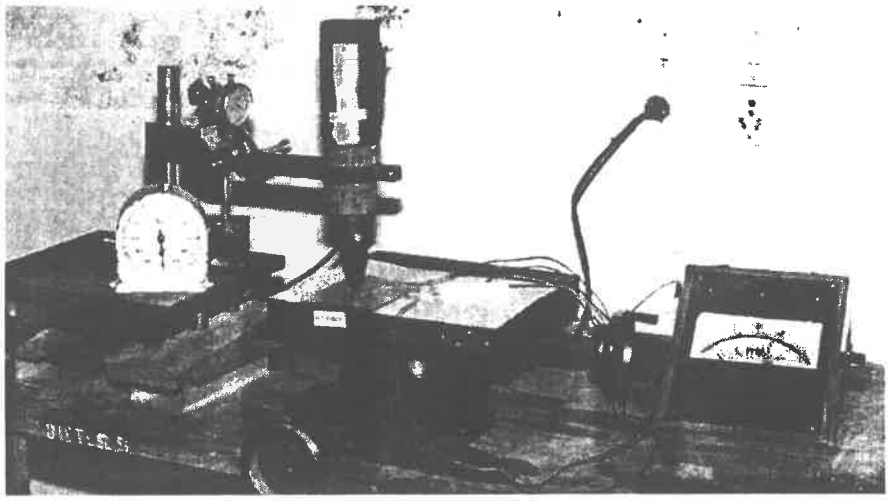

Fig.1 Experimental setup for temperature measurement

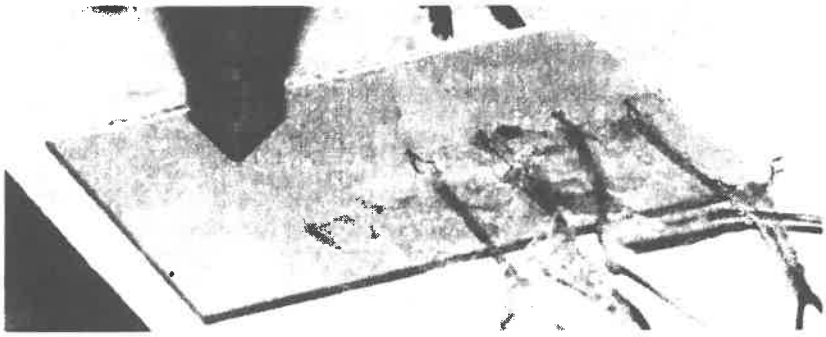

Fig. 2 Thermocouple mountings on plate glass

2.2 Strain measurement

An electrical strain gage was mounted on the plate glass surface, at 45° with respect to the cutting path, using suitable adhesive. Fig.3 shows photograph of the strain gage mounting. The strain gage leads were connected to the digital microstrain indicator. The plate glass (2 mm thick) with strain gage mounting was placed on the X-Y table. The table was moved under a stationary hot air jet and the plate glass was cut. The cutting path was at 20 mm away from the strain gage location. Thermal strain variations at the gage location were measured and recorded.

Fig. 3 Photograph of the strain gage mounting on glass surface at 45°

3. Results and Discussion

Temperature variations on the plate glass surface during cutting as the jet advances is shown in Fig. 4. It is observed from the figure that glass surface temperatures are higher nearer to the jet positions. Temperatures on glass surface at 20 mm away from the cutting path vary from 39°C to 55°C as the jet advances from position J1 to J4.

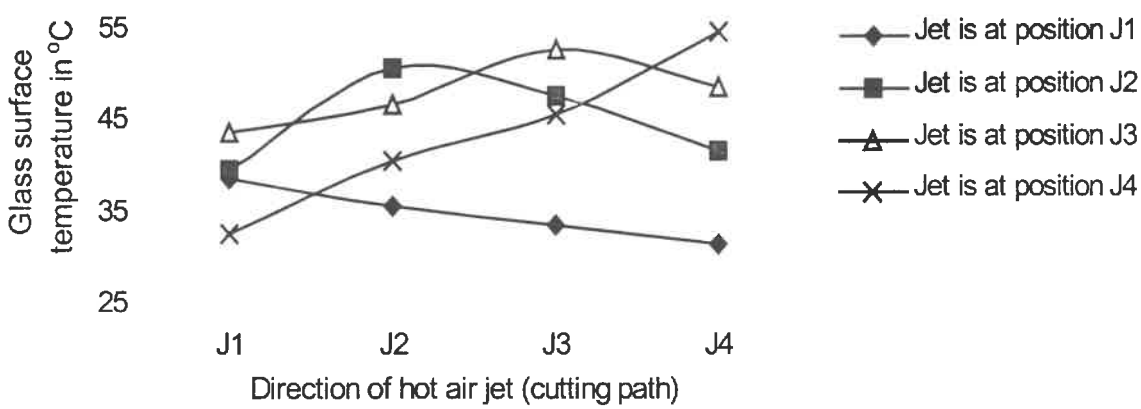

Fig. 4 Temperature variations on glass surface during thermal cutting of glass as jet advances.
J1 to J4 – Successive jet positions during cutting, Stand off distance = 1.6 mm

Fig. 5 shows thermal strain variations at the gage location during cutting. It is observed from the figure that the thermal strains gradually increase as the hot air jet passes nearer to the gage and then starts decreasing as the nozzle moves past the strain gage location. Maximum strains (647 microstrains) were observed when the jet was nearest to the strain gage.

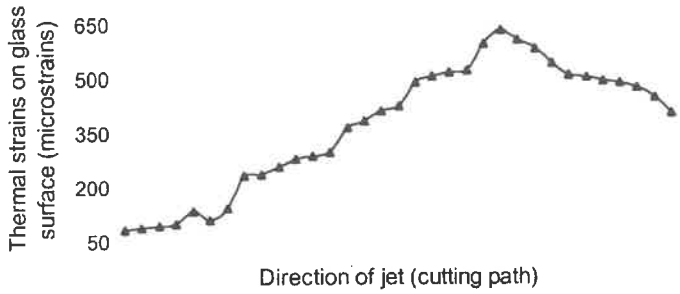

Fig. 5 Strain variations at the gage location (45°) during cutting.
Stand off distance = 2 mm, Nozzle diameter = 2 mm

Strain measurements at 0° and 90° orientations of strain gage are under progress and will be reported. A photograph of sinusoidal cut on a plate glass of 3 mm thick is shown in Fig. 6.

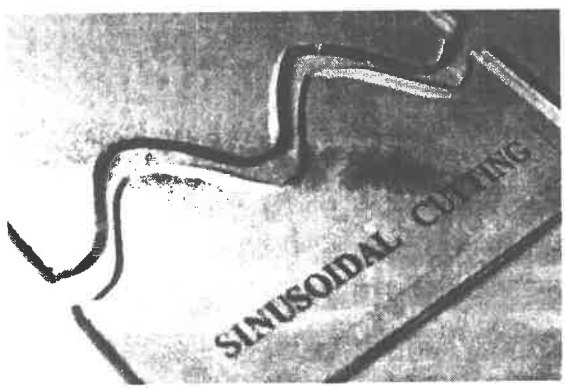

Fig. 6 Photograph showing sinusoidal cut on plate glass

4. Conclusions

Experimental setups for the temperature measurement and thermal strain measurement on plate glass surface during thermal cutting were fabricated. Experiments were conducted and results are reported. It is observed that temperature and thermal strains are highest nearest to the jet positions and increase along the cutting path as the jet advances.

Acknowledgement

The authors wish to thank the AICTE New Delhi for sponsoring this research work.

References

1. K.Sadashivappa, C. S.Bhaskar Dixit, M. Singaperumal, Thermal cutting of plate glass, Proc. 11th Annual Meeting, ASPE, Vol. 14, Monterey, USA, 1996, 551-556.
2. K. Sadashivappa, E.S.Prakash, M. Singaperumal, Compact portable air jet gun for thermal cutting of plate glass, Proc. 13th Annual Meeting, ASPE, St. Louis, Missouri, USA, 1998.
3. R.S.Sirohi, H.C. Radhakrishna, Mechanical Measurements, III Edn., New age Int.(P) Ltd., New Delhi, 1996.

* * *

MICRO DRILLING OF NON CONDUCTING MATERIALS USING ELECTRO CHEMTCAL SPARK MACHINE (ECSM)

SOMASHEKHAR. S.H. **K.SADASHIVAPPA**

DEPARTMENT OF MECHANICAL ENGINEERING
BAPUJI INSTITUTE OF ENGINEERING AND TECHNOLOGY,
DAVANGERE – 577004, INDIA

TELEPHONE: 08192 – 31461 FAX: 08192 – 31261 Email : biet@dvgbiet.kar.nic.in

1.0 INTRODUCTION

So far the research was centered towards the developement of new materials such as chlorides, nitrides, wasp alloy, fiber reinforced plastics etc., but at last the attention is also being paid towards the industrial manufacture of products of these new materials. Traditional cutting methods are not able to machine these materials accurately and precisely, which is the prerequirement of different industrial factories like aerospace, missiles, automobiles, nuclear reactors etc. They give rise to low tool life, fuzzing, delamination, poor quality of innovative etc. Only a few non-conventional method of machining are applicable for electrically non-conductive composites and ceramics viz; water jet machining, abrasive jet machining, laser beam machining and hybrid processes such as abrasive water jet machining, electro chemical spark machining. ECSM is a new and potential process. Sparks are generated across hydrogen bubbles evolved at cathode. Thermal energy of spark is utilised to drill the microholes in the non-conducting materials[1].

A simple electro chemical cell consists of two electrodes dipped in the electrolyte. When an external potential is applied between the electrodes, electric current flows through the cell resulting in electrochemical reactions such as anodic dissolution, cathode deposition, electrolysis[3].

If a suitable electrolyte is choosen and electrodes are of grossly different sizes, then beyond a certain value of the applied potential, electric spark appears at the smaller electrode and the cell current drops. This is known as electro chemical spark phenomenon. The electric discharge involves two stages:

1. Bubble generation during electro chemical reactions as well as water vaporisation , and
2. Dielectric breakdown of the medium when the applied potential difference between the electrodes, separated by gaseous medium is greater than the breakdown voltage of the gas.

2.0 EXPERIMENTAL DETAILS

The experimenal setup of electrochemical spark machining consists of the following components (Fig.1)

- Wooden platform (size 900mm x 600 mm x 75 mm)
- Wooden frame: for guiding and holding the tool electrode.
- Adjustable worktable: consisting of three glass rods (for guiding and driving purpose) and circular acrylic plates of 200 mm diameter for holding workpiece.
- Anode : a zinc plate of approximately 100 x 150 x 10 mm was used as anode
- Cathode: a stainless steel wire of 600 μm diameter was used as cathode. The tool electrode vertical feed was achieved by a friction drive mechanism provided in wooden frame.
- Ammeter

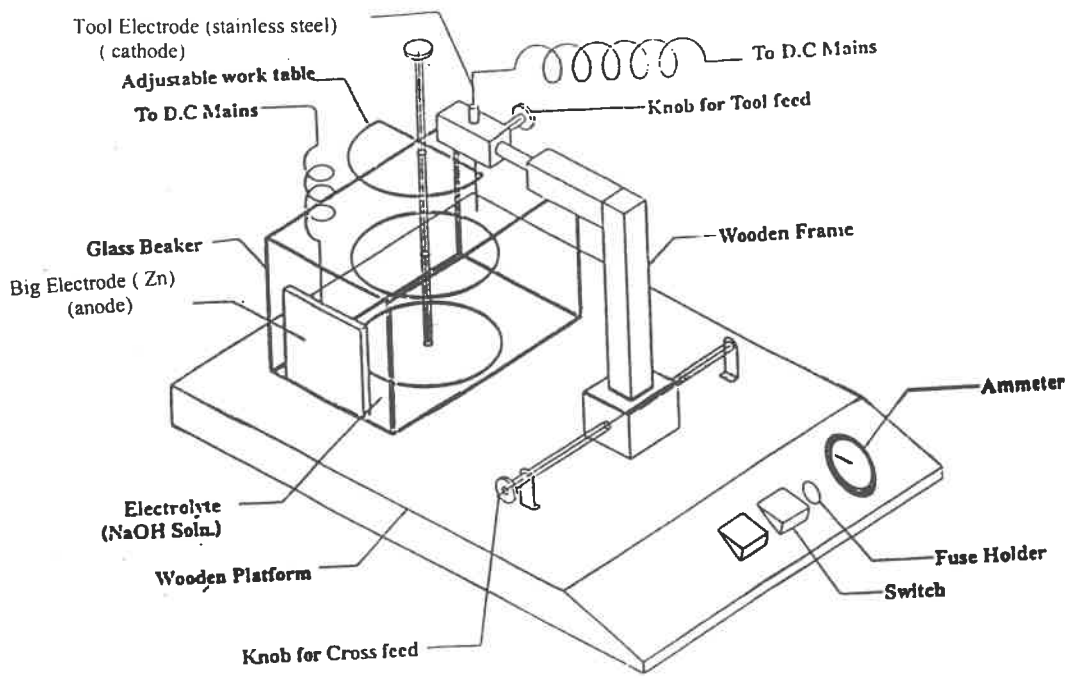

Fig.1 Schematic view of ECSM experimental set up.

3.0 EXPERIMENTAL PROCEDURE

Following procedure was adopted for micro drilling. Electrolyte of known concentration was taken in a glass beaker. Workpiece in which micro hole is required was placed in the worktable and gap between the workpiece and cathode was adjusted. Then, DC supply was given. Spark between tool and workpiece was observed. Tool was fed at controlled rate until through hole was obtained. Diameter of the drilled micro hole was measured using a profile projectorwith a magnification of 50x.

It was noticed that when the voltage reaches 30-40 volts, sparking starts at tool -electrolyte interface and it was quite visible. The spark became increasingly vigorous as the voltage was increased. Workpiece material evoparates due to high temperature of spark (8000 – 10000 °C).

The height of electrolyte above the workpiece was maintained between 2 to 3 mm.

4.0 RESULTS AND DISCUSSION

It was tried to drill holes in glass plate using Nacl. However, the attempt was not successful. Then it was tried successfully to make holes using NaOH. The results are given below. Due to side sparks, heat affected and micro crack zones were observed and holes drilled were out-of-round.

Fig.2 shows a micro hole drilled in a glass plate .The diameter of the hole measured along the X-axis is 680 μm.

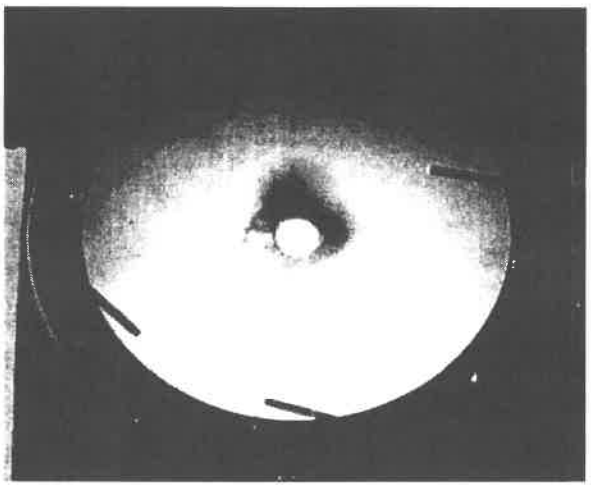

Fig.2 Magnified view of the hole No. 1.

Hole no –1
Work material- Glass (2 mm thick)
Electrolyte used- NaOH
Concentration- 30% NaOH
Voltage- 50 – 55 volts
Current – 0.7 amps
Time taken- 30 minutes
Diameter of tool - 600 μm.
Tool material – Stainless steel

Fig. 3 shows the heat affected and micro crack zones for the hole No.1.The size of the micro crack zone measured along the Y-axis are 2.65 mm.

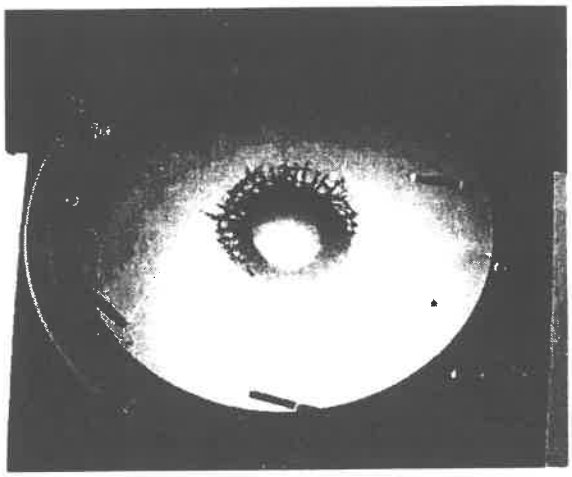

Fig.3 Heat affected and micro-crack zone.

The microdrilling was also tried successfully in asbestos sheet of 4 mm thickness [3].

5.0 CONCLUSION

An experimental set up for ECSM was fabricated and experiments were conducted using different electrolytes and work materials. The results and discussions are presented in this paper. It is observed that side sparks affects the roundness of hole and micro crack and heat affected zones are formed around the hole.

6.0 REFERENCES

1) Some investigation in to the sparkking machining of non conducting materials- K. Allesu and A.Ghosh,Proc of 12th AIMTDR conf.,IIT Delhi,1996, Tata Mc Graw Hill Pub. Co. Ltd., New Delhi, pp 521-524.

2) Electro chemical discharge machining: Principle and possibilities – Amitab Ghosh, invited lecture delivered at the Int. Conf. on advances in Mech.Engg.(ICAME),Dec.20-22,1995, Bangalore. pp 62-66.

3) Qualitative analysis of microdrilled non conducting materials, drilled by electrochemical spark machine- Somashekhar.S.H and Dr. K.Sadashivappa, communicated to National Conference on Quality Control In Metallurgical Industries, PSG College of Technology Coimbatore, Sept. 1999.

* * *

Influence of redeposition effect for focused ion beam 3D micromachining

Yong Zhang Yongqi Fu
Precision Engineering Laboratory, School of Mechanical and Production Engineering
Nanyang Technological University, Singapore 639798

Around the redeposition effect, its influence on FIB 3D micromachining process is discussed. Experimental results are analyzed combining with theoretical model. It can be drawn from the analysis that recycle milling orders are very important for 3D microfabrication due to redeposition during the process. On the other hand, A groove will be formed at the root of sidewall for the sake of ion sputtering yield variation and sidewall redeposition. Finally, avoiding methods are come up with in terms of the analysis outcome.

INTRODUCTION

3D nano-scale manufacturing is one important aspect of advanced manufacturing technology. Such advanced manufacturing technology is dependent on the nanometer accuracy in manufacturing. The FIB technology is one of the most widely used in the semiconductor industry for failure analysis, device modifications and micro-component fabrication.

Using a finely focused gallium ion beam, the FIB head can precisely remove and deposit materials in nano-scale. The production of high contrast images also assist in the removal and deposition process. Even materials like insulators and conductors can be deposited on any surface with nanometer resolution. With the FIB, depositing materials in very fine lines can be realised. It is especially very useful in manufacturing semiconductors, sensors and actuators. Therefore, it's a challenging technology facing to 21 century in the area of nanometer.

Combining with experimental 3D micro manufacturing by FIB, influencing factors are analyzed for milling process. It includes ion dose, beam limiting aperture size, beam current, etc. In addition, influence of redeposition effect for focused ion beam 3D micromachining was analyzed individually.

THEORETICAL MODEL

Redeposition is a serious negative complication to milling. As material is sputtered away, some of it becomes redeposited in the volume that is being sputtered. In normal mechanical machining, buildup of machined material is avoided by the use of liquid or air streams that carry the swarf away. Redeposition is critically dependent upon how the milling is done. It has been shown that for the same total dose, scans that are repeated many times to mill a rectangular area cause less redeposition to occur than a single slow pass to mill the rectangle. For the slow scan, redeposited material is not removed, whereas for the fast repeated scans, some fraction of the primary beam is used to sputter away redeposited material, so that the sputter yield is less for the fast scans.

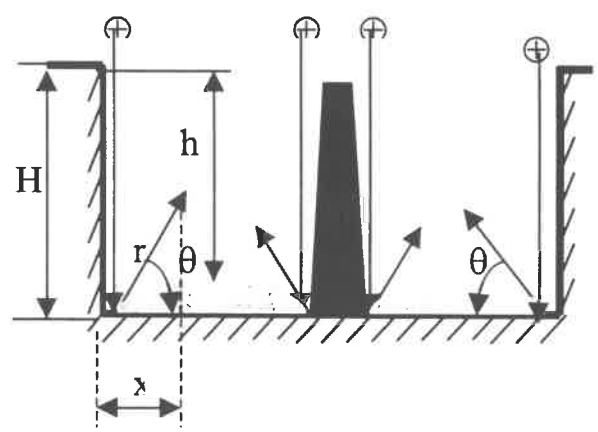

Fig.1 schematic of redeposition effect at root of sidewall

A simple geometric two-dimensional analysis of redeposition shown as Fig.1. The flux density of sputtered atoms, which escape without striking the sidewalls, is given by

$$F(x) = \frac{F_0}{2}\int_0^R \frac{\sin^2\theta dx}{r} \qquad (1)$$

F_0— total number of atoms emitted per unit length

R — outer circle diameter

R — sputtering path

θ— sputtering angle

F_0 is determined by ion dose and aperture size. The more large ion dose and aperture size, the more F_0 will be. At an aspect ratio<1, more than half of the sputtered atoms from the bottom surface redeposit. Therefore, the actual milling depth is smaller than designed value for the sake of accumulated material at the bottom.

The etch depth $z(x,y)$ can be expresses as following[1]. It describes the relationship among depth and other parameters. As can be seen, etch depth is proportional to ion dose and sputtering yield. The sputtering yield is varied for different milling position of structure that will be shown by the post experimental results.

$$z(x,y) = D(x,y)\frac{Y(F,J,T_s,E,t_d,t_f)}{\rho} \qquad (2)$$

Here

$Y(F,J,T_s,E,t_d,t_f)$ —ion sputtering yield

$D(x,y)$ — ion dose,

F — chlorine flux,

J — ion flux,

T_s— substrate temperature,

E— beam energy,

t_d— dwell time,

t_f— and frame time,

ρ— atomic density.

EXPERIMENTAL RESULTS ANALYSIS

Bowl-like 3D structure milling

Experiments have been done by Micrion 9500EX FIB machine with SEM column and EDX. Fig.2 is the experimental results of milling bowl-like 3D structure with shown parameters, milling area 10μm ×10μm, Default_Mill mode. The following phenomena and rule can be drawn based on the above experiments.

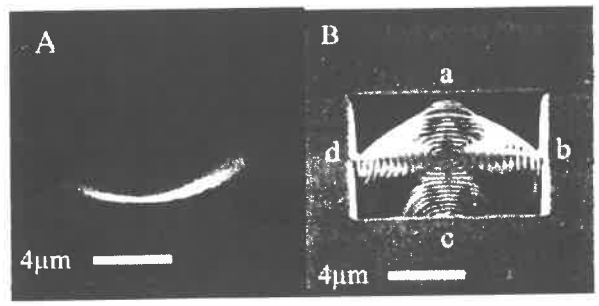

Fig.2 curve profile 3D milling

A: FIB image	B: SEM image
Program controlled milling from outside to center .	manual operated milling from center to outside.
Aperture size 250μm	aperture size 150μm

The 3D structure manufacturing can be realized only by the way of spelling many discrete 2D pattern together step by step because there is no 3D continuously moving workplate which moves along x_i, y_i, z_i, 3D points and the corresponding servo control system for the sake of design. For the case A, the bowl-like 3D structure was milled automatically by programming operation mode. Used aperture size is 250μm, it corresponds to larger spot size. The redeposition material is removed away every time by the next milling. The sidewall is smooth by virtue of overlapping each other for neighboring 2D periphery edges. But the depth is smaller than the designed value. For the case B, convex curve profile designed, the milling procedure is from center to outside edge by manual operating in a defined modifying box step by step. As can be seen, the redeposition remark is obvious along cross direction due to narrow space at the parts of *a, b, c*, and *d*. The more high aspect ratio, the more redepositing material accumulated on the convex surface. Because the near the ion beam is to the edge, the higher the sputtering yield from the sidewalls. High sputtering yield leads to milling depth increasing and produces more material removed away from root of sidewall that was

accumulated along ion sputtering direction to form the shape shown as Fig.2 case B.

Annulus with tip structure milling

Milling annulus pattern structure on silicon wafer by FIB with parameters of aperture size 250μm, ion dose 15 nC/μm^2, beam current 8.66nA, Default_mill mode. A tip was formed during milling process due to the act of wing of Gaussian distribution profile. The more large aperture size selected, the more big cone angle of the tip because large aperture size corresponds to large spot size and beam current that shown as Fig.3. A phenomenon was found that a deep groove has been formed at the root of sidewall and tip for the sake of redeposition.

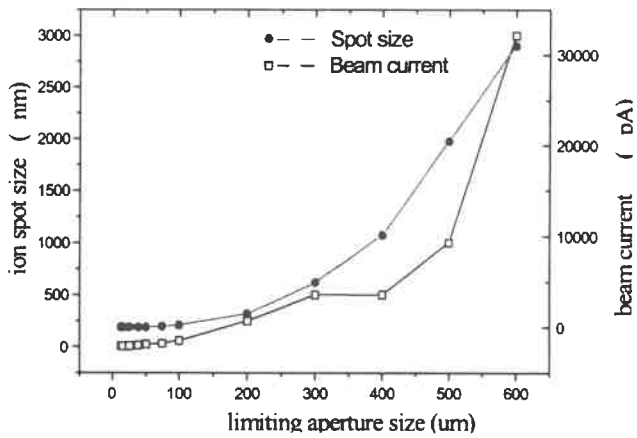

Fig.3 relationship among aperture size, beam current and spot size for 5nm ion column

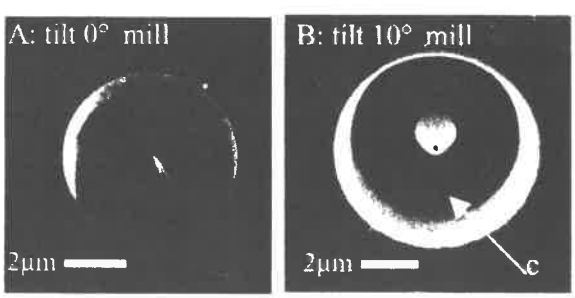

Fig.4 milled tip under different tilting angle of workpiece

When the workpiece was tilted in angle α, the down side of the redeposited groove will be milled more in the direction of ion sputtering angle θ (as shown in Fig.1). It can be seen from Fig.4 that the width of the groove is getting large. It's largest at the lowest point *c*. The more big tilt angle α, the more large width of cut groove is at the down sidewall. The thickness of redeposited material is difference in the tilt case. The upper part is thicker than the lower part. In the case of A, the thickness of redeposition is uniform.

What we wanted depth is H, but the actual depth we obtained is *h* due to the redeposition. The difference $\Delta=H-h$ will be increased with the increasing of ion dose and limiting aperture size. In order to look for the changing rule between the groove depth and limiting aperture size. A series of milling experiment have been done under the conditions of constant ion dose 15nC/μm^2 , X space 0.01002μm, Y space 0.01003μm, dwell time 3μs, retrace time 10μs. The milling results were measured by AFM and shown as Fig.5.

It's shown from Fig.5 that the more large aperture size, the more deep groove and large sputtering angle θ. The bottom depth *h* (shown

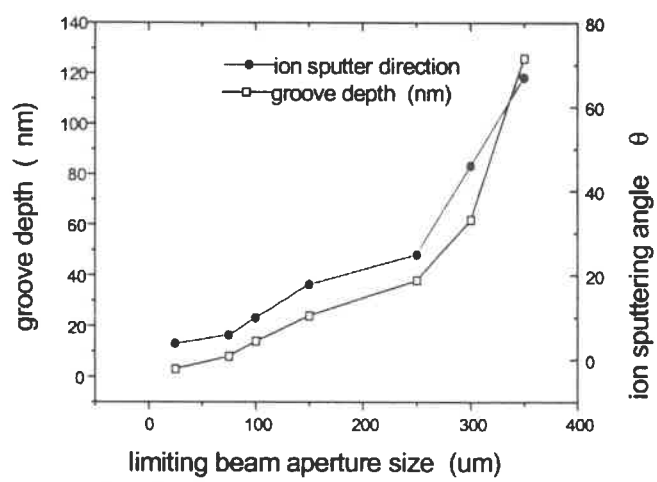

Fig.5 aperture size vs groove depth and sputtering angle θ

as Fig.1) will be increased consequently. But their relationship is nonlinear. The sputtering yield near the sidewall is high. It leads to depth for the sidewall is deeper than the other area. This rule is coincide well with the theoretical relationship describes by formula (2).

CONCLUSION

Combining with experimental milling and theory model, influence of redeposition effect for focused ion beam 3D micromachining has been analyzed. On the base of above analysis, the following conclusions can be drawn:

- The sidewall causes the variation of ion sputtering yield that leads to redeposition at the bottom and groove forming.
- The more large aperture size used, the more serious redeposition phenomenon is.
- The redeposited material will adhere on the sidewall for milling 3D structure with aspect ratio>1, and land on the bottom causing variation of milling depth for the structure with low aspect ratio (normally <1).
- In order to avoid redeposition for 3D milling, the recycle milling orders should be from outside edge to center. On the other hand, GAE mode can be used to refrain from redeposition. Reaction of the irradiated surface species with absorbed halogen produces volatile species which is advantageous because redeposition of surface material is essentially quenched[2].

Reference

1. A. Kalburge, A. Konkar, T. R. Ramachandran, P. Chen, and A. Madhukar. Focused ion beam assisted chemically etched mesas on GaAs(001) and the nature of subsequent molecular beam epitaxial growth. J. Appl. Phys. 82 (2), 15 July 1997, 859~864.
2. J.M. Lindquist, R.J. Young and M.C. Jaehnig. Recent advances in application of focused ion beam technology. Microelectronic Engineering 21 (1993) 179-186.
3. Craig Friedrich and Bharath Kikkeri, Rapid fabrication of molds by mechanical micromilling : process development. SPIE, Vol.2640/161.
4. . Jon Orloff edited, Handbook of Charged Particle Optics. Boca Raton, Fla. : CRC Press. 1997.
5. L. Bischoff, J. Teichert and E. Hesse, Interconnection lines following the surface topography fabricated by writing focused ion beam implantation. Microelectronic Engineering 27 (1995) 351~354.
6. Zheng Chui, Philip D Prewett, John Watson and Brain Martin, FIB repair of defects in rim and attenuated phase shift masks. Microelectronic Engineering 27 (1995) 331-334.
7. J. F. Walker, D. F. Moore and J. T. Whitney, Focused ion beam processing for microscale fabrication. Microelectronic Engineering 30 (1996) 517~522.

Design of Orientation Stages for Step and Flash Imprint Lithography

B. J. Choi, S. Johnson, M. Colburn, S.V. Sreenivasan, C.G. Willson
University of Texas at Austin
Austin, TX 78712

Key Words : Template-wafer alignment, template stage, flexure mechanism, imprint lithography

1. Introduction

Step & Flash Imprint Lithography (SFIL) has been introduced as a high throughput novel approach that can potentially generate circuit patterns with sub $0.1\mu m$ line width without projection optics [Co99]. To achieve these goals, SFIL uses no projection optics and operates at room temperature and low template pressures. The process largely relies on chemical and mechanical processes to transfer patterns. One could probably best describe SFIL as a micro-molding process (See [Ch96], [Ha96], [Wa97], [Wi96] and [XW98] for other imprint processes under development). SFIL and other imprint lithography techniques are similar in the fact that they use the topography of a template to define the pattern created on the substrate. The key difference between SFIL and other imprint lithography techniques is the use of a liquid etch barrier. This low viscosity solution eliminates the need for high temperatures and pressures. High temperatures and pressure can cause major technical problems in accurate overlaying of multiple layers of a circuit and is hence undesirable. Figure 1 illustrates the SFIL process.

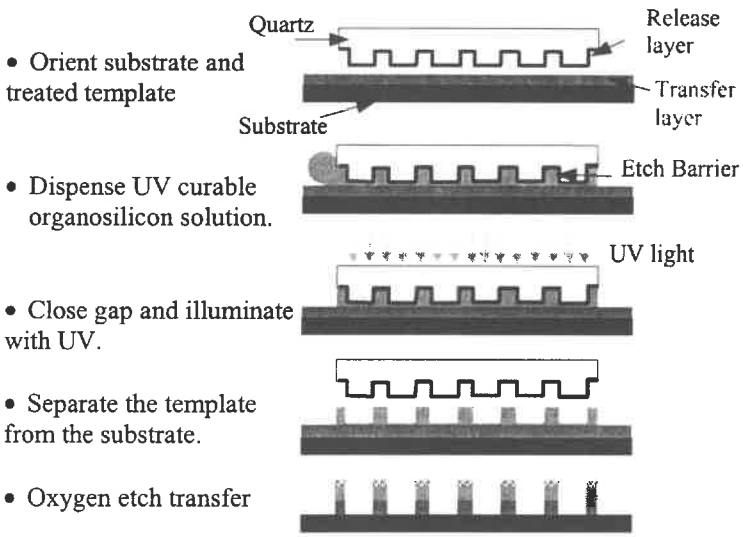

Fig. 1 Step and flash imprint lithography process on a flat substrate

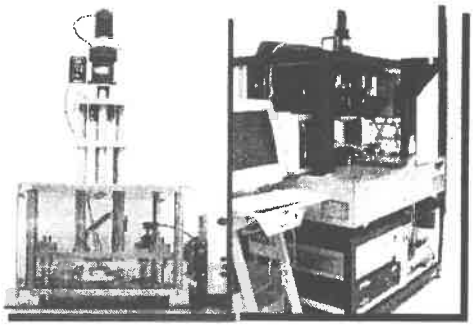

Fig. 2 Single- and Multi-Imprint machines

2. Mechanical Issues of SFIL

Figure 2 shows two imprint machines for the feasibility study of SFIL process. Their subsystems include sensing, stage actuation, light source, etch barrier dispense, and others. One of challenging mechanical issues for these machines is the fine orientation between template and wafer where orientation stages must bring template and wafer into contact while minimizing relative lateral motions. Orientation motions with passive stages are generated via pushing the template against wafer. Another mechanical issue is the need to minimize the particle generation

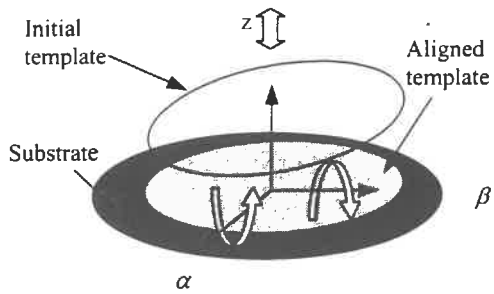

Fig. 3 Two flats representing template and wafer

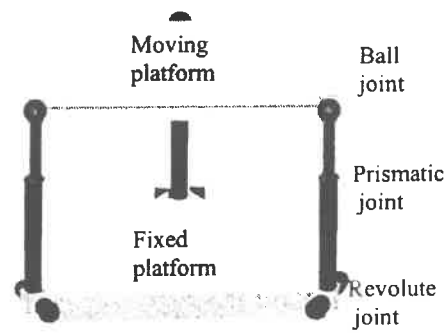

Fig. 4 Three-degree-of-freedom in-parallel mechanism schematic

from orientation stages and other moving bodies. Particle contamination is expected to be a major source of defect propagation for the repeated imprint process. The single-imprint machine was developed as an imprint tool for the feature resolution test and material development. The multi-imprint machine is under development to investigate defect propagation. In this research, first, kinematic requirements of template stages are studied. Based on the analytical results, passive stages satisfying the kinematic requirements are developed using flexure mechanisms i) to eliminate wearable parts affecting precision and, ii) to minimize particle contamination due to frictional contacts.

3. Orientation Stages for Imprint Machines

Figure 3 shows two flat surfaces representing a template and substrate respectively. A proper alignment between these two flats ideally leads to a perfectly uniform surface contact between them. Such an alignment can be accomplished with one translation motion (z displacement) and two tilting motions (α and β) between two flats.

Figure 4 shows an ideal stage composed of perfect rigid bodies and joints. Non-ideal behavior including distributed structural compliance, backlash and stiction in joints, etc., are neglected. Ideal kinematic stages provide insight into the geometry and force transmission at the template-substrate interface. This insight is then extended to the design of distributed flexure stages with selectively compliant and stiff directions. The connection from the base platform to the moving platform is via a combination of a revolute (R) joint, a prismatic (P) joint and a ball (B) joint. The ideal kinematic stage has several practical limitations with respect to SFIL process. Presence of sliding contacts in joints can cause wear, generate undesirable particles and lead to stiction that makes precision motion control difficult. Particles on the template and substrate generate major defects in the SFIL process. Presence of clearances in joints can lead to reduced repeatability in the motion of the mechanism.

Flexures generate motion by elastic deformation and can avoid all the problems associated with joints. Also, provided elastic and fatigue limits are not exceeded, flexures can provide extremely repeatable motion and long life for the stage. Flexure stages are becoming quite common in the precision engineering industry [SC92].

3.1 Side motion error due to coupled tilting motions

Three necessary orientation motions were identified above. In ideal situations, the translation motions of template in x and y should be eliminated. Figure 5 shows a coupled effect between tilting and translation motions. Coupled motions arise when a tilting axis does not exist on the surface of the template. A side drift, d_s, of template is given by $d_s = l_{off} \sin\theta \cong l_{off}\,\theta$, where, l_{off} is the offset of the tilting axis from the surface and θ is the tilting angle in radian.

As an example, when l_{off} = 3 *mm* and θ= 0.0001 rad, d_s is 300 nm. Such an excessive template side motion must be avoided because during a separation process in which the etch barrier has already been UV exposed, excessive side motions may destroy transferred images.

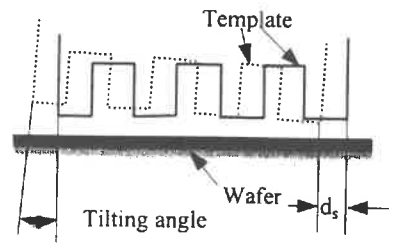

Fig. 5 Side motion of template due to off-set

3.2 Orientation Stage for Single Imprint Machine

For the single-imprint machine, a wafer orientation stage has been developed [Jo99]. The basic element of the flexure is derived from the work presented by Badami *et al.* [Ba96]. They presented a ring that is comprised of three fixed-fixed beams. The mid-point of each of these beams provide a vertical deflection due to an applied vertical load. This vertical spring can be considered to be equivalent to a leg of the R-P-B stage where the P joint is a passive linear spring. A modified version of this design yields the distributed flexure stage of Figure 6.

The three mid-points of the fixed-fixed beams are connected to the vacuum chuck. The parameters of the ring (material and geometry) can be arrived at by using the desired motion range for the z-translation and the two tilting motions. A finite element model is used to compute the non-ideal compliance matrix of the distributed flexure stage. FEM results are then used to examine the stage's principal motion capabilities. To minimize the side motion between template and wafer, the flexure ring is installed where its height is aligned with the template-wafer interface.

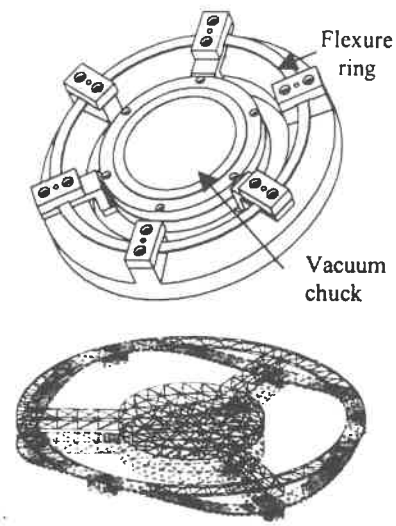

Fig. 6 Wafer orientation stage and a FEM analysis showing the deformed ring structure

3.3 Template Orientation Stage for Multi-Imprint Machine

Multi-imprint is can be performed via moving a 8" wafer to various positions while holding a template stationary in x and y directions. For the multi-imprint process, it is necessary to have the compliant flexure move the template since a rigid template and compliant wafer stage can lead to unstable configuration for multiple x-y position of the wafer. Hence a new orientation stage design that can tilt about "remote axis" was developed (Fig. 7). These remote axes allow tilting about axes that ideally lie on the interface plane of the template and wafer. Two four-bar flexures are mounted orthogonal to each other in order to generate two tilting motions. The geometry of the notch is designed so that under 5*N* load applied at a 0.4in off from the center, the stage can rotate 0.0005radian. FEM analysis of these flexure structures showed less than 5*nm* side motions for 0.00038radian tilting of the template surface.

4. Imprint Results and Conclusions

All results shown in this section were processed using the single imprint machine with a passive stage. Fig. 8 shows 60*nm* features on template and wafer. It has been observed that SFIL process can duplicate not only such small features but also much smaller defects on the template due to stitching errors in the electron beam process. Hence, it is expected that the limit of feasible line width that SFIL can process is significantly smaller than 60*nm*. A SEM image of 150*nm* features on the wafer surface indicates that features have clearly defined side walls.

Passive selectively compliant flexure stages have been designed for single- and multi-imprint lithography machines. It is assured that the kinematics of the stages are consistent with the requirements of aligning two flats into intimate contact. Further, tilting axes are placed at the template-wafer interface to ideally eliminate x-y motion due to change in tilting angles. FEM analyses have been used to ensure the functionality of the flexure stages.

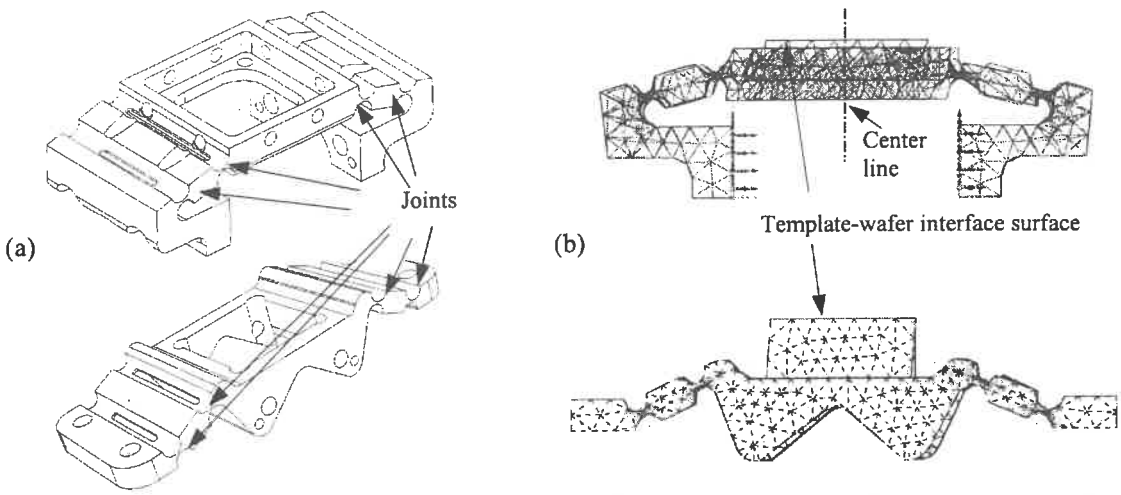

Fig. 7 (a) Flexure stages and (b) Side deformations; deformations are magnified for the visualization

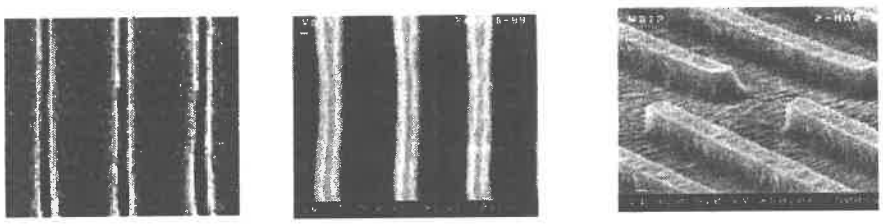

Fig. 8 60*nm* features on template and wafer side and 150*nm* features transferred to the etch barrier

Acknowledgement We gratefully acknowledge the financial support of SRC (contract 96-LC-460) and DARPA (grant N66001-98-1-8914).

Reference

[Ba96] Badami, V.G., *et al.*, 1996, "A Metrological Three-Axis Translator and Its Application for Constant Force Profilometry", Proceedings of ASPE 1996 Annual Meeting, p. 391-395.

[Co99] Colburn, M., *et al.*, 1999, "Step and Flash Imprint Lithography: A Novel Approach to Imprint Lithography", SPIE's 24th Annual International Symposium on Microlithography, Santa Clara, CA.

[Jo99] Johnson, S., 1999, "Selectively Compliant Orientation Stages for Imprint Lithography", MS thesis, The University of Texas at Austin.

[SC92] Smith, S., and Chetwynd, D.G., 1992, "Foundations of Ultraprecision Mechanism Design," *Gordon and Breach Science Publishers*, Philadelphia,

[Ta98] Tajbakhsh, H., *et al.*, 1998, "Three-Degree-of-Freedom Optic Mount for Extreme Ultraviolet Lithography", Proceedings of ASPE 1998 Annual Meeting, p. 359-362.

[Ha96] Haisma, J., *et al.* "Template-assisted nanolithography: A process for reliable pattern replication," *J. Vac. Sci. Technol. B* 1996, *14*(6), 4124-29.

[Ch96] Chou, S.Y., *et al.*. "Nanoimprint lithography," *J. Vac. Sci. Technol. B* 1996, *14*(6), 4129-33.

[Wi96] Widden, T.K., *et al.*, 1996, "Pattern Transfer to Silicon by microcontact printing and RIE," *Nanotechnology*, *7*, 447-451.

[XW98] Xia, Y.; Whitesides, G.M., 1998, "Soft Lithography," *Angew. Chem. Int.*, *37*, 550-575.

[Wa97] Wang, D., *et al.*, 1997, "Nanometer scale patterning and pattern transfer on amorphous Si, crystalline Si, and SiO2 surface using self-assembled monomlayers," *Appl. Phys. Lett.*, *70* (12).

EFFECTS OF ACTIVE BALANCING ON HIGH-SPEED MILLING PRECISION

Stephen W. Dyer
BalaDyne Corporation
Ann Arbor, Michigan 48108-2200

Emad I. Al-Regib
Department of Mechanical Engineering and Applied Mechanics
The University of Michigan
Ann Arbor, Michigan 48109-2136

ABSTRACT

High-speed machining processes can be very sensitive to variables not necessarily important at lower cutting speeds. Unbalanced toolholders and spindles, for example can generate forces at high-speed that cause significant dynamic error motion of the cutting tool.

Experimental results are presented here that show how spindle-housing vibration can be minimized at each operating speed using active mass balancing. The relationship between unbalance and dynamic tool runout is quantified for a common type of machining center. Unbalance-induced runout is shown to contribute to dimensional errors and cutting instability in end milling by increasing the effective radial depth of cut. Theoretical analyses of milling cutter kinematics show that eliminating unbalance-induced runout through active balancing can improve surface finish for cases in which static runout is very small.

INTRODUCTION

Because unbalance forces are proportional to the square of the rotational speed, these forces can be the same order of magnitude as high-speed cutting loads. Since ball bearing fatigue life is known to be inversely proportional to the cube of the effective bearing load (Harris, 1991), the presence of even moderate unbalance loads can potentially reduce spindle life. Unbalance forces also excite the spindle and support structure, leading to tool error motion.

To minimize unbalance forces, tool/toolholder combinations for high-speed machining are often balanced "off-line" prior to insertion into the spindle. Even using balanced tools, however, the spindle/toolholder rotating assembly can still exhibit significant unbalance variation after each tool change due to the combination of residual unbalance in the spindle itself, toolholder clamping tolerances and clearances in the clamping and drawbar assembly.

To balance the tool/spindle assembly after each tool change would significantly increase cycle-time and not typically be cost-effective. Furthermore, a single-plane balance at the toolholder at one speed may not be suitable at another speed because of the potential for unbalance located in the drawbar or toward the rear of the spindle. To thoroughly compensate for such a situation one would need to perform multiple-plane balancing. Another approach is to utilize single-plane active balancing to minimize unbalance-induced vibration at the desired spindle operating speed.

To eliminate the potential harmful effects of increased spindle loads and error motion, an active balancing device was developed (Dyer et al., 1998) that can adjust toolholder balance while the spindle rotates at operating speed. Mass balance compensation can, therefore, take place rapidly after each tool change prior to metal cutting. The effect of such on-line balancing was quantified using several measures of machining precision.

ACTIVE BALANCING TO MINIMIZE HOUSING SPINDLE MOTION

Tests were performed on a horizontal machining center to measure the vibration induced by residual spindle/toolholder assembly unbalance after inserting a balanced toolholder. The vibration was then minimized at each spindle speed up to the maximum 14,000 rpm operating speed. The resulting spindle housing vibration before and after active balancing is shown in Figure 1.

Figure 1 shows that active balancing was successful at maintaining low vibration levels regardless of the spindle speed. However, the balance correction magnitude and phase angle required to minimize vibration varied dramatically with spindle speed. Figure 2 shows the optimal balance correction phasor (magnitude and phase angle) to minimize dynamic spindle motion at different speeds through the operating speed range.

At 10,000 rpm about 200 g-mm at 340° was required. At top speed of 14,000 rpm, 30 g-mm at 120° was the best correction. If one were to manually fix the balance at one speed, therefore, the

unbalance and resulting vibration at another speed may in some cases actually be worse than with no balance correction at all. Active balancing in this case allowed rapid balance corrections to minimize spindle motion at the exact cutting speed.

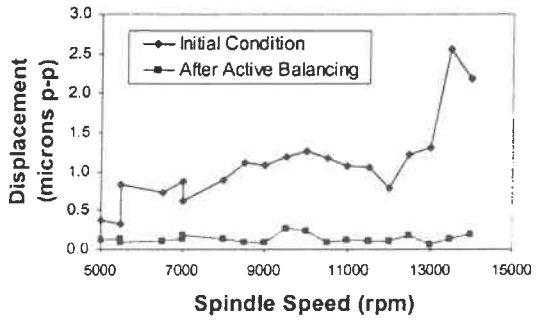

Figure 1. Horizontal Machining Center Spindle Housing Vibration Before and After Balancing With Balanced Toolholder

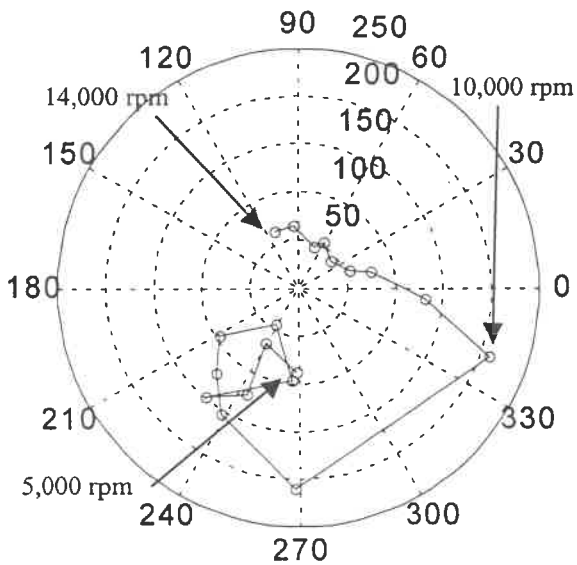

Figure 2. Horizontal Machining Center Effective Single Plane Unbalance (g-mm) for Various Spindle Speeds

EFFECT OF UNBALANCE ON DYNAMIC TOOL RUNOUT

As seen from the above results, unbalance forces cause dynamic error motion in the machining spindle that can vary after each tool change. The dynamic tool runout combines with the static runout to make the tool diameter effectively larger (or smaller) depending on how the two runout vectors add together.

The effect of unbalance on tool runout was measured for a vertical machining center with a 40 taper toolholder. An active balancing device mounted on the toolholder was used to adjust balance at various speeds to minimize spindle housing motion (measured using accelerometers in two axes at the spindle nose). The motion of a gage tool was measured using capacitance probes in two orthogonal radial directions. The active balancing device was then used to adjust the unbalance to a known amount and the tool motion again measured. Figure 3 shows the magnitude of the change of spindle-synchronous runout caused by a 210 g-mm unbalance at the toolholder.

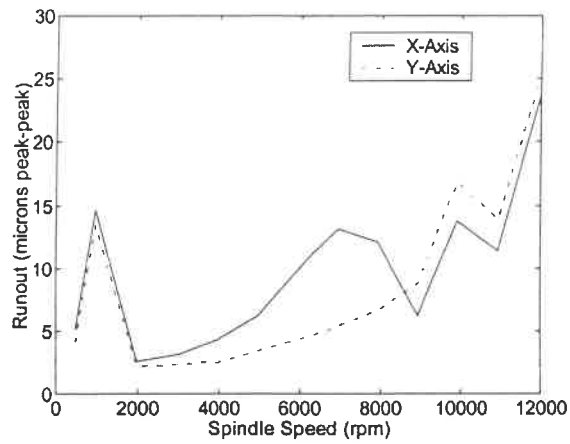

Figure 3. Measured Change in Spindle-Synchronous Tool Runout Caused by 210 g-mm Unbalance at Various Spindle Speeds

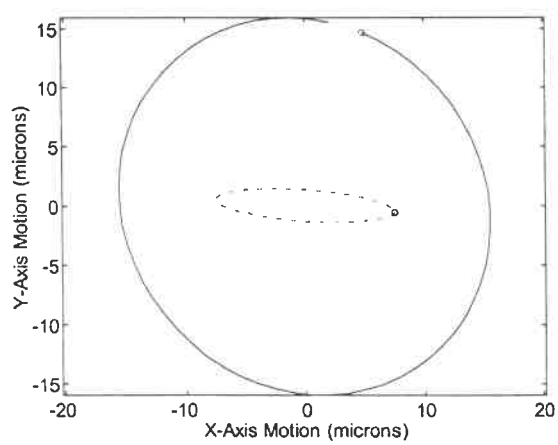

Figure 4. Measured Tool Motion With Toolholder/Spindle Assembly Balanced and Unbalanced 210 g-mm at 12,000 rpm

Capacitance probe system sampling rate limitations did not allow measurements above 12,000 rpm even though the spindle was capable of

operating up to 15,000 rpm. The greatest change in runout in the measurement range was effected at 12,000 rpm. Figure 4 shows the spindle-synchronous tool orbits in the balanced and unbalanced condition at 12,000 rpm.

EFFECT OF UNBALANCE-INDUCED DYNAMIC TOOL RUNOUT ON END MILLING DIMENSIONAL ACCURACY

As shown by the results above, unbalance can cause tool runout. Researchers have in the past shown that runout causes one flute to do more cutting than the rest, leading to larger variation in cutting loads from one flute to the next (Kline and DeVor, 1983). Thus unbalance-induced runout could, therefore, contribute to premature wear of a single cutter flute. Another effect of this runout is to increase the radial depth of cut unintentionally. This can lead to dimensional errors in the workpiece.

This effect was measured for a representative process. Slots were milled in extruded aluminum using a two-flute, 19 mm diameter cutter at 16,000 rpm. Each slot was milled under conditions of different amounts of unbalance-induced spindle housing vibration. A machine will exhibit different sensitivities to unbalance at various speeds for various tools. Therefore, the critical parameter for predicting machining inaccuracies is not necessarily unbalance, but rather the error motion caused by unbalance at a given speed. Figure 5 shows the effect of such unbalance-induced spindle-housing vibration on slot width accuracy. The maximum vibration of about 11 microns corresponds to about 300 g-mm unbalance for the spindle at the given speed.

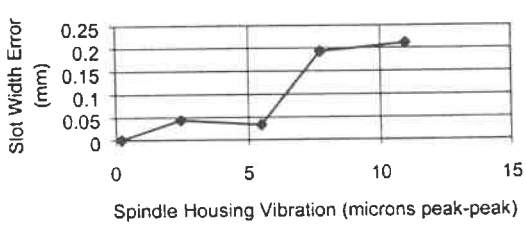

Figure 5. Milled Slot Width Error vs. Unbalance-Induced Spindle Housing Vibration (16,000 rpm, 19 mm, 2-flute cutter, 0.1524 mm feed/rev)

EFFECT OF UNBALANCE-INDUCED RUNOUT ON MACHINING STABLILITY

As discussed above, unbalance can induce significant tool runout that effectively increases the cutter diameter and radial depth of cut. Increasing the radial depth of cut in this way can have a detrimental effect on milling stability margin. Figure 6 shows the spindle housing vibration during an unstable cut (on the left) compared to the stable cut (on the right) achieved by balancing the spindle at the same operating conditions.

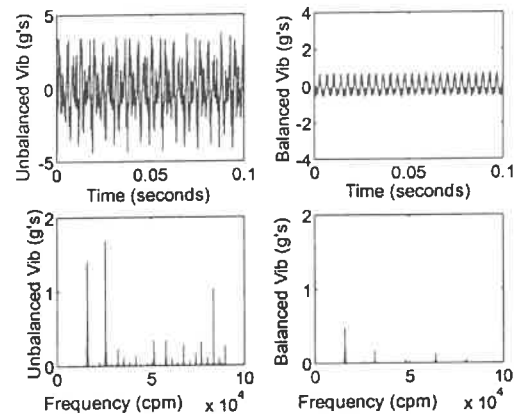

Figure 6. Measured Spindle Housing Vibration During Unbalanced and Balanced Slotting Cut (19 mm 2-flute cutter, 1.4 mm axial depth of cut, 0.1524 mm feed/rev, 16,000 rpm)

The vibration spectrum on the left of Figure 6 from the unbalanced cut displays not only higher spindle-frequency vibration at 16,000 cpm, but also vibration at a chatter frequency at 25,200 cpm. Such unbalance-induced machining instability would only be expected to occur if one were operating very close to the stability limit and, therefore, is not in itself a tremendously significant issue. However, it is another indication of the significant dynamic runout caused by unbalance.

EFFECT OF UNBALANCE ON MACHINING SURFACE FINISH

As other researchers have noted, tool runout can effect the surface waviness generated during end-milling (Liang et al., 1993). In the best scenario of no tool runout, all the flutes contribute equally to generating the surface profile. If enough runout is present, only one flute will act to generate the surface and the other flutes do not contact the generated surface. The amount of tool runout present will determine whether something approaching the best surface profile is achieved (generated by all flutes in the cutter) or the worst surface profile is achieved (generated by only one cutter flute). An example of surfaces generated using a four-flute cutter with and without runout is shown in Figure 7. The idealized surfaces shown were predicted using simple kinematic simulation, assuming perfectly sharp cutting edges and neglecting tool flexibility.

As runout increases, the idealized generated machined surface would change from the solid lower

surface to become more like the upper dashed surface. When the runout reached a certain level only one cutting point would be effective and the machined surface will correspond to that of a single-point cutting process.

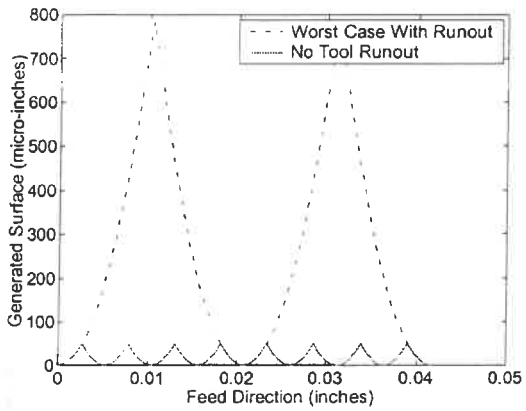

Figure 7. Predicted End-Milled Surfaces: 0.125 Inch, 4 Flute Cutter, 0.0052 Inch Feed/tooth

Interestingly, if the runout increases beyond this level, the surface will not change because the effective number of cutting flutes is still one. (Although the location of the surface will exhibit dimensional error as noted previously). Thus the "worst case" surface generated will correspond to that of a single-point cutter of the same diameter. Figure 8 shows, for a fixed feed-per-tooth, the best-case (no tool runout) and worst-case surface waviness for two and four flute cutters of varying diameters. The surface profiles predicted in Figure 8 were based on the same kinematic assumptions as for Figure 7.

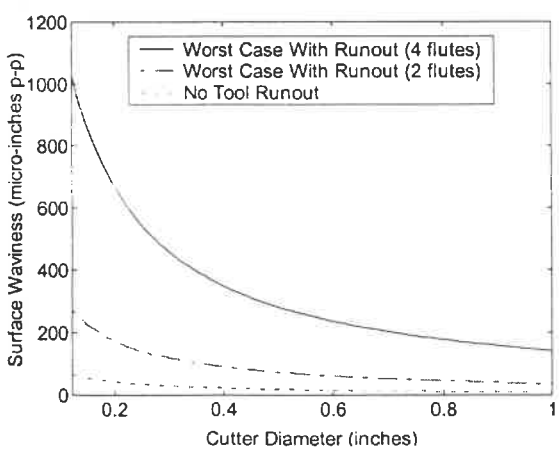

Figure 8. Predicted Surface Waviness on Upcut (0.006 Inch Feed/tooth)

It can be noted from Figure 8 that the difference between the worst- and best-case surface waviness increases as the number of flutes increases and as the cutter diameter decreases (for a fixed feed).

If static tool runout is very small, eliminating the unbalance-induced runout will enhance surface profile by ensuring that all cutter flutes participate in generating the milled surface instead of just one. If the static tool runout exceeds a given value, however, eliminating unbalance will not effect surface waviness because the surface will still be generated by only one cutting point.

SUMMARY AND CONCLUSIONS

Unbalance forces can be significant contributors to overall spindle loads for high-speed milling. Aside from potentially limiting spindle bearing life, unbalance loads also cause dynamic tool runout. The amount of runout for a given unbalance depends on the machine sensitivity to unbalance at the specific spindle speed. Because runout increases the effective cutter diameter and radial depth of cut, unbalance can lead to significant milling dimensional inaccuracies. Balancing can also theoretically extend tool life and improve surface waviness by helping to ensure that all cutter flutes engage equally in the cut. Balancing the tool/spindle assembly on the machine helps ensure optimal processes even with tool clamping misalignment and unbalanced spindles. Active balancing provides the potential to cost-effectively perform such on-machine balancing. Active balancing is thus a means for eliminating a significant process variable, resulting in enhanced precision, reliability and productivity.

REFERENCES

Dyer, S. W., Hackett, B. K., and Kerlin, J., 1998, "Electromagnetically Actuated Rotating Machine Unbalance Compensator", *U.S. Patent No. 5,757,662*, May 26.

Harris, T. A., 1991, *Rolling Bearing Analysis*, Third Edition, John Wiley and Sons, New York, p. 683.

Kline, W. A., DeVor, R. E., 1983, "The Effect of Runout on Cutting Geometry and Forces in End Milling", *International Journal of Machine Tool Design and Research*, Vol. 23, No. 2/3, pp. 123-140.

Liang, S. Y., Wang, J. J. J., Herman, P. A.., 1993, "Surface Finish Enhancement in End Milling Via Inverse Runout Trajectory Following", *Transactions of NAMRI/SME*, Vol. XXI, pp. 103-109.

FABRICATION OF A MICROROBOT MOVABLE IN THE SMALL INTESTINE OF A PIG

Shigeo KATO, Mizuyuki SHIRAKAWA, Manabu OHNO and Masako TABATA

Nippon Institute of Technology
Miyashiro, Saitama 345-8501, JAPAN
E-mail: kato@nit.ac.jp

Abstract

This paper describes the fabrication of an in-pipe mobile microrobot which is able to move in the small intestine of a pig. The microrobot is inchworm type and is structured by a flexible plastic bellows which is 17.3 mm in outer diameter and 50 mm long. The microrobot is driven by the pneumatic pressure and the vacuum pressure. It is confirmed that the microrobot is able to move with the maximum speed of 65 mm/s in the small intestine of a pig.

***Keywords*:** In-pipe, Inchworm, Microrobot, Pig's small intestine

1. Introduction

New in-pipe mobile microrobots to inspect or to repair the intestine or blood vessel in the the human body have been investigated. Kato et al. have presented in-pipe mobile robots which are driven by only pneumatic pressure [1], [2]. However, these in-pipe mobile microrobots were not yet able to move in the the large intestine or the blood vessel.

We fabricated a prototype of a new mobile inchworm type microrobot which is able to move in the small intestine of a pig. The microrobot is driven by pneumatic and vacuum pressure. The pneumatic pressure is used to stretch and the vacuum pressure is used to shrink the microrobot. The microrobot is made by a flexible plastic bellows which is 17.3 mm in diameter and 50 mm long. The microrobot is equipped two thin friction-rings which are located at the front and the rear of the microrobot. The rings are 25 mm in outer diameter and 0.3 mm thin made of vinyl chloride with the cutting lines. The friction for inching motion of the microrobot comes from these friction rings.

The pneumatic pressure of +0.02 MPa and the vacuum pressure of -0.095 MPa are used to drive the microrobot. These two pressures are switched by an electromagnetic valve. The maximum speed in a pig's small intestine was confirmed to be 65 mm/s. The length of the large intestine of the man is less than 1000 mm. If this microrobot can move in the large intestine of the man, the microrobot is able to move in the large intestine in the time of 16 seconds.

2. Structure of the fabricated microrobot

The section of the fabricated microrobot is shown in Fig. 1. The microrobot is able to move in pipes by imitating the motion of an inchworm. The microrobot is structured by a flexible plastic bellows. The bellows is 17.3 mm in outer diameter and 50 mm long. A plastic air feeding tube which feeds pneumatic and vacuum pressure to the microrobot is 2 mm in inner diameter, 3 mm in outer diameter and 1000 mm long. Two friction rings 25 mm in outer diameter, 10 mm in inner diameter are fixed at the double ends of the bellows. Materials of the friction rings are vinyl

chloride and rubber. The friction rings of vinyl chloride are 0.4 mm thick and the friction rings of rubber are 0.5 mm thick. These friction rings make friction force between the pipe and the microrobot. The friction rings make cones, because the inner diameter of the friction rings is smaller than the diameter of the bellows. The friction rings are slitted for the direction of radius. The friction forces made by the friction rings are shown in Table 1. The friction force of the vinyl chloride is smaller than that of the rubber. The friction forces between the vinyl chloride pipe and the vinyl chloride rings are 0.09 N for the forward direction and 0.48 N for the backward direction. However, the friction forces between the small intestine of a pig and the vinyl chloride rings are as large as 0.9 N for the forward direction and 1.21 N for the backward direction. The large forces come from the transforming of the small intestine by the friction rings, because the small intestine is very flexible. This matter is shown by the small difference between the friction force for the forward direction and the friction force for the backward direction.

An experimental apparatus for measuring the speed of the microrobot is shown in Fig. 2. A computer controls a electromagnetic valve through a valve controller. The feeding air-tube is connected from the electromagnetic valve to the bellows. A air-compressor is connected to the entrance port of the electromagnetic valve and a vacuum pump is connected to the exit port of the electromagnetic valve. When the pneumatic pressure is supplied to the bellows in the time of τ seconds, the bellows is stretched. The front friction ring slips, because its friction force is smaller than that of the rear friction ring. The other hand, the rear friction ring holds the pipe, because its friction force is larger than that of the front friction ring. Consequently in this period, the front

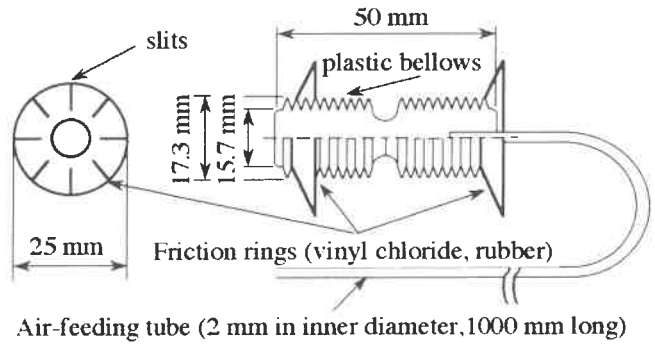

Fig. 1 The section of the inchworm type microrobot

Table 1 The friction forces made by the friction rings

	Friction ring	Forward direction (N)	Backward direction (N)	Difference (N)
Vinyl chloride hard pipe	Vinyl chloride	0.09	0.48	0.39
	Rubber	0.55	1.47	0.92
Pig's small intestine	Vinyl chloride	0.90	1.21	0.31
	Rubber	1.71	2.48	0.77

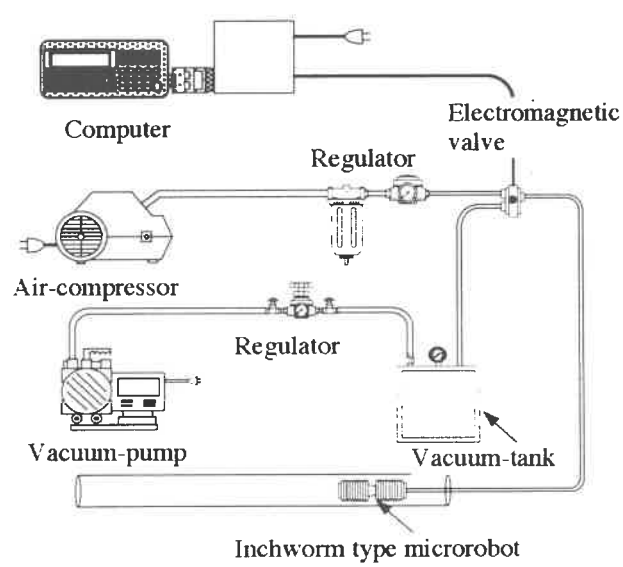

Fig. 2 The experimental apparatus for measuring the speed of the inchworm type microrobot

part of the microrobot goes forward. When the vacuum pressure is supplied to the bellows in the time of τ seconds, the bellows is shrunk. At this time, the front friction ring holds the pipe, because its friction force is larger than that of the rear friction ring. The other hand, the rear friction ring slips, because its friction force is smaller than that of the front friction ring. Consequently in this period, the rear part of the microrobot goes forward. Consequently the microrobot goes forward about the displacement of the bellows in the cycle time of 2τ.

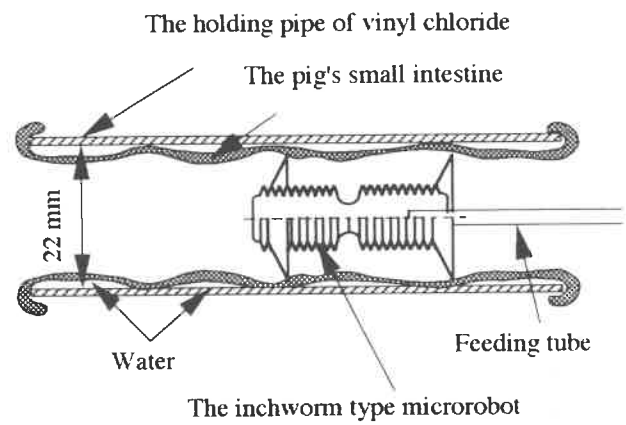

Fig. 3 The inchworm type microrobot in the pig's small intestine

3. Moving characteristics of the fabricated microrobot

The moving speed of the microrobot is measured. The fabricated microrobot in the pig's small intestine is shown in Fig. 3. The small intestine is that used to make the sausage. The small intestine is held in the vinyl chloride hard pipe which is 22 mm in the inner diameter. The outer diameter of the small intestine is a little smaller than 22 mm, because small quantity of water exists between the intestine an the pipe. The vacuum pressure for the shrinking of the bellows is -0.095 MPa and the pneumatic pressure for the stretching is +0.02 MPa. The cycle time 2τ is changed from 0.04 seconds to 0.6 seconds.

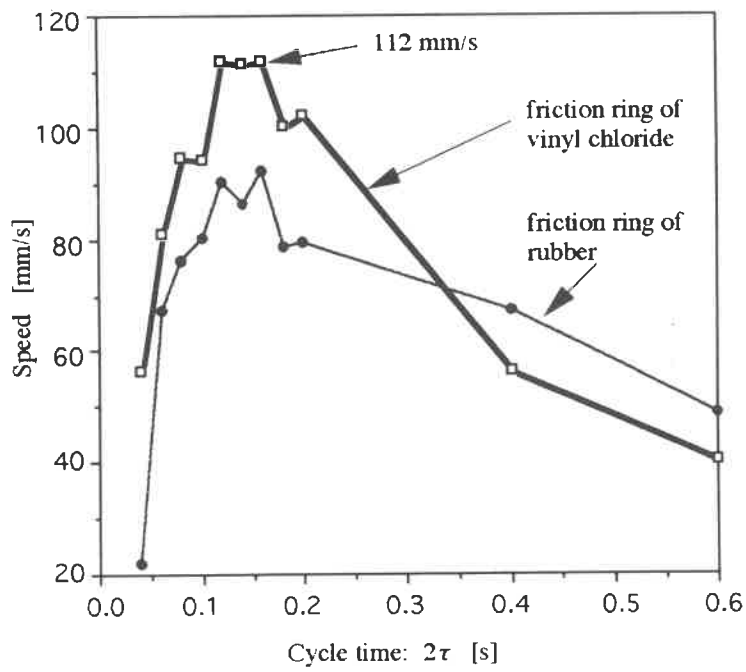

Fig. 4 The speed of the inchworm type microrobot in the hard straight pipe

3.1 Moving characteristics in the hard straight pipe

First, the moving speed of the microrobot in the hard straight pipe made of vinyl chloride is measured. The speed of the microrobot in the hard straight pipe is shown in Fig. 4. The speed of the microrobot using the friction rings of vinyl chloride is higher than that of the microrobot using the friction rings of rubber. The one side of friction rings must slip. The speed of the microrobot may be small when the rubber, which is large in the friction force, is used. The maximum speed of 112 mm/s was obtained at the cycle time of 0.16 seconds, when the friction rings of vinyl chloride was used. This speed is 1.5 times of the former maximum speed of

our microrobot.

3.2 Moving characteristics in the pig's small intestine

The speed of the microrobot in the pig's small intestine is shown in Fig. 5. The speed of the microrobot in the pig's intestine using the friction rings of vinyl chloride is also higher than that of the microrobot using the friction rings of rubber. The maximum speed of 65 mm/s in the pig's small intestine was obtained at the cycle time of 0.18 seconds, when the friction rings of vinyl chloride was used. This speed is about 1/2 times of the speed in the hard straight pipe. The reasons of small maximum speed in the small intestine are that the friction force is large and the intestine is movable against the microrobot.

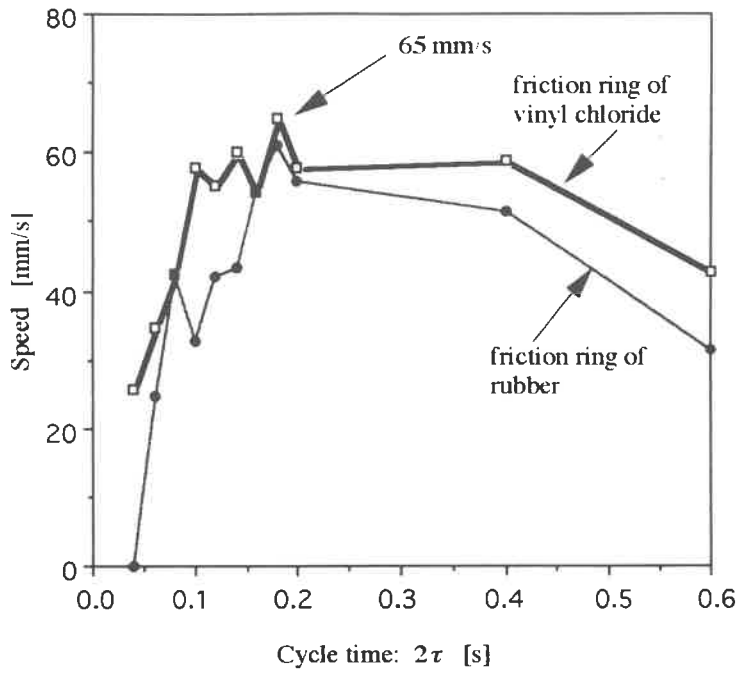

Fig. 5 The speed of the inchworm type microrobot in the pig's small intestine

4. Conclusions

Fabrication of a prototype of a new microrobot to inspect or to repair thin pipes in the the human body or pipelines was performed. The followings are the conclusions of the fabrication.

(1) We fabricated a new inchworm type microrobot which is constructed by a plastic bellows which is 17.3 mm in outer diameter and 50 mm long. A plastic air feeding tube which feeds pneumatic and vacuum pressure to the microrobot is 2 mm in inner diameter and 1000 mm long.

(2) Two friction rings of vinyl chloride 25 mm in outer diameter are fixed at the double ends of the bellows. These friction rings make friction force between the pipe and the microrobot. The friction forces between the vinyl chloride pipe and the vinyl chloride rings are 0.09 N for the forward direction and 0.48 N for the backward direction.

(3) The microrobot is able to move in a vinyl chloride hard pipe of 22 mm in diameter. The maximum speed of 112 mm/s was obtained at the cycle time of 0.16 seconds, the vacuum pressure is -0.095 MPa and the pneumatic pressure is +0.02 MPa.

(4) The microrobot can move in pig's small intestine. The maximum speed of 65 mm/s was obtained at the cycle time of 0.18 seconds, the vacuum pressure is -0.095 MPa and the pneumatic pressure is +0.02 MPa. This speed is about 1/2 times of the speed in the vinyl chloride hard pipe.

References:

[1] S. Kato and K. Ohtsuki, *Proceedings of the ASPE 1998 Annual Meeting*, Vol. 18 (1998), pp. 248-251.

[2] S. Kato and T. Hirayama, *Proceedings of the 4th Japan-France Congress & 2nd Asia-Europe Congress on Mechatronics*, Vol. 2 (1998), pp. 429 - 432

DESIGN ANALYSIS OF THE NATIONAL IGNITION FACILITY KINEMATIC PIN (NIFKP) OR FLEXURAL PIVOT

Kent K. Leung

National Ignition Facility, NIF Operations Engineering,
University of California, Lawrence Livermore National Laboratory
Email: kkleung@llnl.gov

ABSTRACT

A kinematic pin is a flexural pivot used for precision positioning. Many NASA contractors have successfully applied flexural pivots in space programs [1]. Some space program in optical communication system requires high precision design considering micro-yield stress [2] and dimensional stability of the material [3]. Kinematic pins designed for maintaining sub-micron position of focusing magnets in a particle accelerator have been successful designed [4]. Flexural pivots are also used as seismic isolators for earthquake safety design in seismic industries [5, 6]. The NIFKP is designed for precision performance and earthquake safety. It is used to register a system as a reference position in a laser beam line. The reference position is maintained by three NIFKPs on balancing of forces of these pins [7].

INTRODUCTION

The National Ignition Facility (NIF) is a high power laser facility for fusion research and development. The project's design philosophy modularizes the laser's optical subsystem components into Line Replaceable Units (LRU) for ease in maintenance over its expected 30-year life. The LRUs are transported between the Optics Assembly Building (OAB) and the laser structure by a robotic material handling system. A major component of this handling system is a portable clean room, or canister, which seals the optics of the LRU during transport between the OAB and the laser from ambient air. The canister itself contains robotic systems that move the LRU into a position inside the clean laser cavity, once the canister is docked to the laser's enclosure. The bottom-loading canister carries a variety of different LRUs for placement in different portions of the laser with a permanent carriage platform, which elevates the LRU from underneath the laser enclosure to the laser system. Guiding a set of NIFKP into a precise position are the receptacles mounted on the bottom of the LRU elevating system. Once docked, the canister becomes the reference from which the robotic insertion mechanisms inside the canister load the LRUs into the laser beam-line. The NIFKP is shown in Figure 1 without the seismic support. The LRU and the elevating system used in the demonstrated design sample weigh over 2000 pounds. Each NIFKP is subjected to 750 pounds vertical load for normal operation. Horizontal force developed from the vertical load is limited to 300-lb maximum depending on the surface contact resistance. Load limiting stops transfer excessive seismic load to a seismic pin jointed at the bottom of the NIFKP assembly. Finite element method (FEA) is employed to solve the complex stress and deflection with microyield limit. The NIF seismic pin that supports the NIFKP uses post-elastic stiffness and energy dissipation to controlling the seismic response.

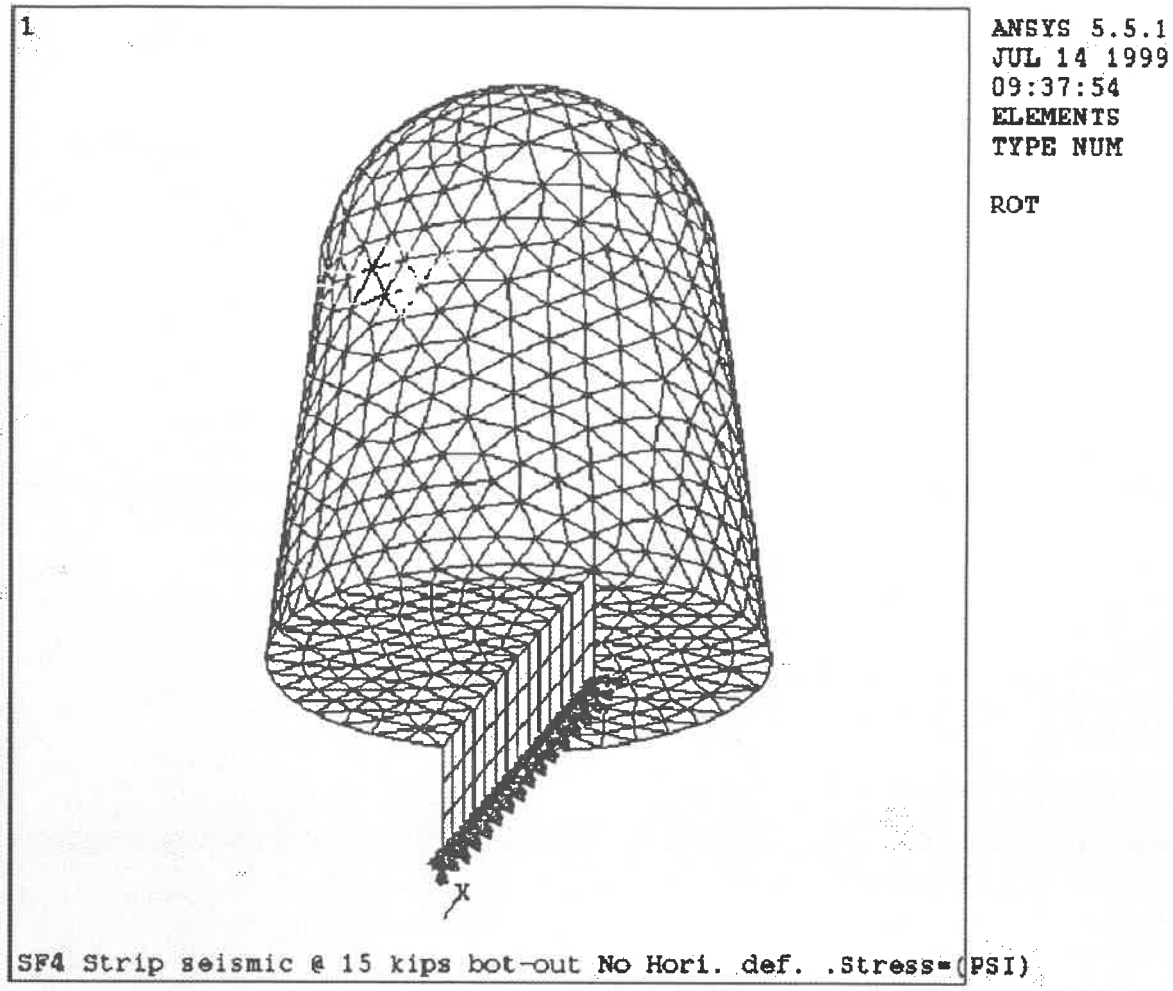

Figure 1. Finite Element Model of the NIFKP with A Conical Head for Docking.

The seismic analysis of the NIF component and receptacle [8, 9, 10] have been reported. To support the LRU in a level position with stability, the ball end must in full contact to the conical cavity of the receptacle (Fig. 2 line B-B). Optimizing the NIFTKP strip height and cross section is necessary for repeatability in precision positioning by observing the micro yield limit.

The NIFKP as shown in Figure 1 is designed to support a 2250-lb LRU with positioning accuracy within 0.025 in. The NIFKP machined from 440C stainless steel to form a ball end integrated with a flexural strip in dimensions as follows: 1.25"(height), 0.28"(width) and 0.03"(thickness).

A Seismic support designed to joint to the NIFKP, is served as an isolator to modify the system frequencies. The method for such design and analysis to avoid the system frequency within the critical range of the NIF site earthquake spectra has been reported [8]. The paper predicts that the NIFKP design has met all the requirements. (1) 0.0250 inch in horizontal deflection. (2) 750-lb vertical load. (3) Under the capacity of the horizontal force generated by the dead weight of the LRU. (4) To have the maximum combined stress, 145 ksi (Figure 3) within the micro stress limit. (190 ksi Stainless Steel.)

The NIFKP as reported in the present paper can support a 2250-lb weight LRU for docking to a specified position within a 0.025 inches. Owing to the maximum strain developed in the flexural strip is less than one part per million of the material elastic limit, we are confident that the requirement of 30 years high precision positioning performance of the NIFKP has been met.

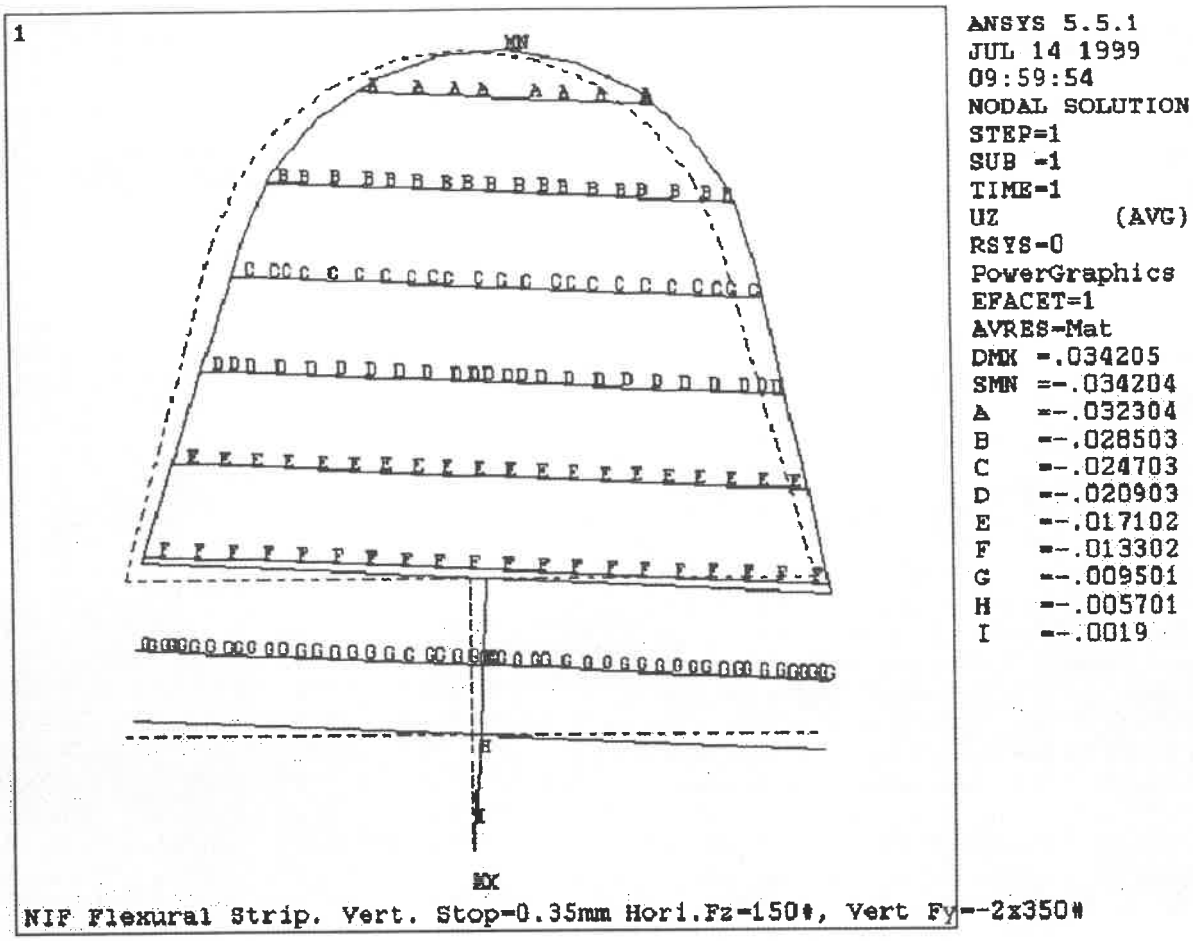

Figure 2. NIFKP under 2250 operational load and specified maximum horizontal movement of 0.0285", and vertical bottom out movement of 0.35 mm.

REFERENCES

[1] F. A. Seelig, "Flexural Pivots for Space Applications." Third Aerospace Mechanisms Symposium. JPL. Pasadena. CA. October 1968.

[2] W. D. Weinstein, "Microperformance of Metals." Machine Design. December 1969.

[3] K. K. Leung, "Design Analysis of Flexural Pivots for The Talon Gold Marker Base Plate for Optical Communication System" Report 8742-83-BED-049UR, GTE Government Systems, Electro-Optics Division, 1987.

[4] K. K. Leung, " Dynamic Analysis of a Six-Strut Supporting System for Accelerator," Fifth Annual International Industrial Symposium on the SuperCollider, San Francisco, CA. May 1993.

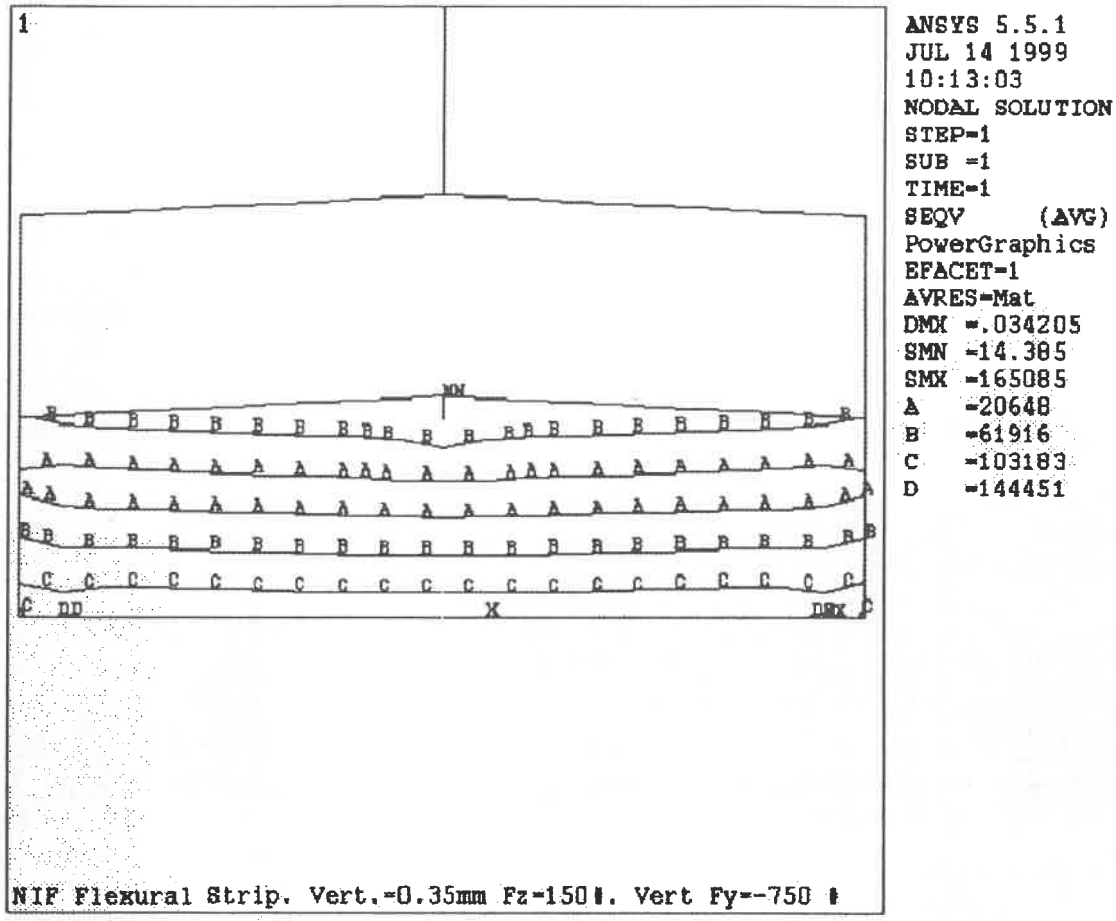

Figure 3. Maximum von Mises stress on the strip of the NIFKP under 2250 operational load and specified maximum horizontal movement of 0.0285", and vertical bottom out movement of 0.35 mm. The 156 ksi is less the micro yield stress limit for the material SS 440C.

[5] Report No. EERCL/94-02, "Testing of FIP Proprietary Seismic isolation Hardware." Earthquake Engineering Research Center, University of California at Berkeley, December 1994.

[6] Report to Missouri Highway Depart, " Testing of Sesimic Isolation Device for 3rd street Viaduct, St. Louis, Missouri. April 1997. Construction Technology Laboratories, Inc. Skokie, IL.

[7] K. K. Leung, " BL Kinematic Pin Design and Analysis." NIF-WBS1.9 Report. NIF-19674. March 1999.

[8] K. K. Leung, "Three-Dimensional Simulation of Rotary Latch Assembly in Seismic Response and Interactions," ASME/JSME Pressure Vessels & Piping Conference July26, 1998, San Diego, CA.

[9] K. K. Leung, "Seismic Stress Analysis for NIF Mechanical Components." 1999 ASME Pressure Vessels and Piping Conference, Boston, 1999.

[10] K. K. Leung, "Automatic Registering Receptacle Safety Design for Bottom Loading System Used in National Ignition Facility." American Nuclear Society and American Robotic Society 8 Annual Tropical Meeting, Pittsburgh. 1999.

System Modeling and Identification of a Precision Fast Tool Servo System

Guang Lu[1], James Cuttino[2], Dale Schinstock[3], and Tim Haskew[4]
[1]University of California at Berkeley, [2]University of North Carolina at Charlotte
[3]University of Tulsa, [4]The University of Alabama

I. INTRODUCTION

Conventional Diamond Turning Machines (DTMs) are limited to rotationally symmetric surfaces due to the low bandwidth of their slide systems. By adding Fast Tool Servo (FTS) systems, DTMs can produce rotationally non-symmetric surfaces without lowering the turning speed. This improves their machining capabilities, and gives engineers many more choices of design. Most of previous fast tool servos used piezoelectric (PZT) actuators, which have high stiffness and relatively low moving mass. The drawbacks to using piezoelectric actuators include the limited range of motion, heat problems, and hysteresis.

At The University of Alabama, a long-range fast tool servo using a voice coil actuator has been developed. Voice coil actuators have a low armature mass and can produce high accelerations while operating at high frequencies. They generate a long range of motion with high resolution and bandwidth. The problems associated with voice coil actuators include considerable heat loss and low structural stiffness.

The system components of this fast tool servo were designed concurrently. Principal system parameters were defined at the beginning of the research. In order to verify the system parameters for the real system, system identification and modeling techniques were conducted to ensure the system would perform as it was predicted. These techniques were significant for the successful development of the FTS system.

II. SYSTEM CONFIGURATION

For precision PID control considerations, the bandwidth of the control loop was designed to be over 3 kHz. In order to separate the dynamics of the current loop from the control loop, the bandwidth of the current loop was designed to be over 30 kHz. Similarly, the bandwidth of each of the components in the current loop must be over 300 kHz in order not to have significant effects on the current loop. The mechanical system was expected to be a second-order system with its mode at 50 Hz. These defined the principal system parameters of the fast tool servo. Successful implement of these parameters was significant to the development of the system.

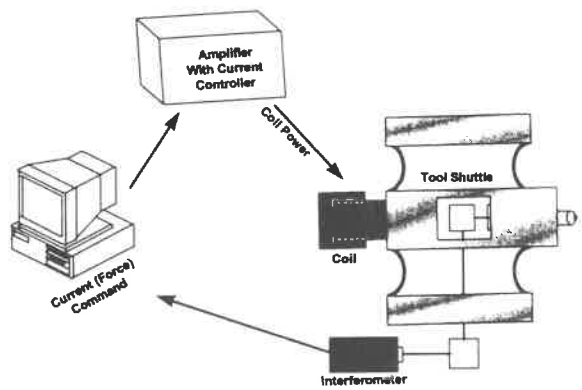

Fig.1 The FTS built at University of Alabama

The FTS system is shown in Fig.1. A flexure system was built as the principal part of the mechanical system. The controller built in the PC sends out current commands to an amplifier, and the amplifier drives the voice coil actuator to move the diamond tool on the shuttle that is suspended by the flexure bearings. A laser interferometer sensor detects the actual position of the shuttle and feeds it back to the controller.

III. SYSTEM COMPONENTS

The dynamic performance of each of system components has been individually verified in system identification and analyzed

in system modeling to ensure that each of them satisfies the system requirements.

A. Flexure System

The flexure system in the FTS, is a monolithic structure fabricated from one piece of 316 stainless steel. Four curved flexures connect the moving part in the middle, the shuttle, to the fixed part that is attached to the base. The shuttle is used to hold the diamond tool and is fixed to the coil in the actuator. The monolithic design helps to ensure alignment and material uniformity, and it also makes the stiffness in all flexures the same to reduce the error motions caused by unbalanced stiffness. Compared to conventional flexures that are usually flat, curved flexures provide higher stiffness, lower stress, and occupy more compact space.

The mechanical system was designed and modeled to be a second-order system. The transfer function of this system is $\frac{z(s)}{F(s)} = \frac{1}{ms^2 + bs + k}$. This model was verified using finite element analysis method.

Dynamic testing using impact method was conducted to verify this model and identify the dynamic parameters of the flexure system, which were important to the controller design. The resonance frequency was found to be 66.8 Hz. The frequency response of the flexure system is shown in Fig.2 and Fig.3. However, after the coil in the actuator was attached to the flexure system, the resonance of the system was later verified to be at 48.5 Hz.

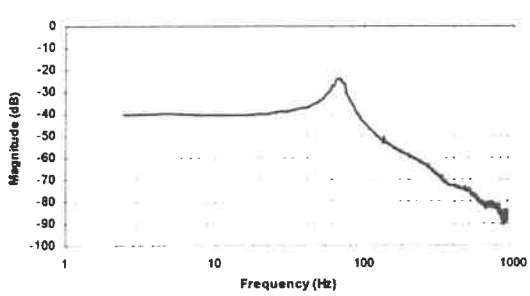

Fig.2 The magnitude plot of the frequency response of the flexure system

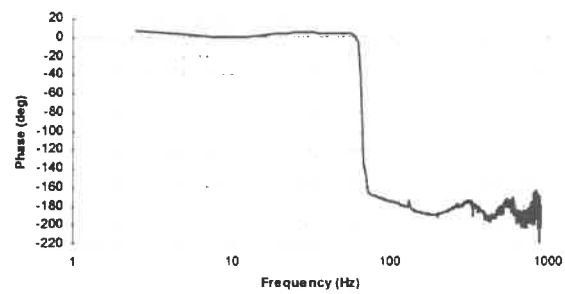

Fig.3 The phase plot of the frequency response of the flexure system

B. Voice Coil Actuator

The voice coil actuator is composed of a coil assembly and a permanent magnet. The coil assembly is suspended in the magnetic field by the flexure system. The displacement of the coil in the fixed magnetic field is proportional to the current through the coil in a limited range of motion. Voice coil actuators have high bandwidth and resolution. The linear actuator used in FTS is a BEI linear voice coil actuator, model number LA25-42-000A.

In system design, the electrical circuit in the voice coil actuator was modeled as a first-order dynamic system. Its transfer function is $\frac{1}{Ls+R}$.

C. Amplifier

Until recently, linear operational amplifiers were the only considerations for high bandwidth amplifiers. However, they were limited in current and power at high frequencies. Compared to the linear amplifiers, PWM (Pulse-Width Modulation) types are much more efficient, typically more than 95% efficiency. But one of the major disadvantages of PWM amplifiers is that their bandwidths are restricted by the switching frequencies. However, recently developed PWM amplifiers switch at much higher frequencies, which makes PWM amplifiers with broad bandwidths available.

A closed loop PWM amplifier was built with an APEX SA02 PWM amplifier chip. The SA02 is an 80 volt, 250 kHz switching PWM amplifier. The full bridge output circuit can provide 10 Amps of continuous drive current. The pole in the voice coil, $Z = R/L$, is detrimental to the system performance since it results in a phase lag. Therefore, a PI controller is used to cancel it by placing a zero at R/L. It increased the system bandwidth and improved dynamics of the current loop. Two power resistors were used to measure the currents in two opposite directions in the H bridge in the PWM as the feedback. The frequency response of the system is shown in Fig.4 and Fig.5. These figures show that the bandwidth of the amplifier is over 30 kHz.

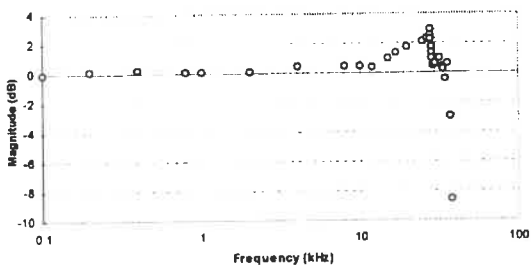

Fig.4 Magnitude plot of the frequency response of the PWM amplifier

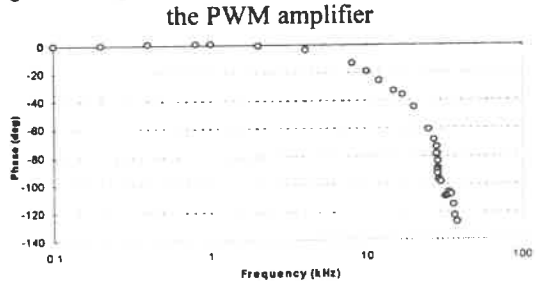

Fig.5 Phase plot of the frequency response of the PWM amplifier

D. Controller

The mechanical system of the FTS, including the tool shuttle and the coil assembly, was assumed to be a spring-mass-damper model. Its transfer function is $\frac{z}{F} = \frac{1}{ms^2+bs+k}$. Note that the mass includes the mass of the shuttle in the flexure system and the mass of the coil assembly. Using the identified parameters m, b, and k, the theoretical frequency response was characterized and computed. It shows that the system (including mass of the shuttle and coil) has a resonance at 48.5 Hz, while the resonance in the flexure system alone was verified during dynamic testing to be at 66.8 Hz. The additional mass from the coil assembly lowered the resonance frequency in the mechanical system.

A PID controller using a pole-zero cancellation method was developed to provide an initial benchmark with which other controllers could be compared. The system bandwidth was chosen to be 4 kHz, and the zeroes were used to cancel the poles in the mechanical system. The theoretical error of this controller design is 1.25% at 50 Hz. The PID controller was implemented using an MC8-DSP-ISA board made by Precision MicroDynamics Inc. This board contains an Analog Devices 2106X family DSP processor. The standard configuration is a 40MHz ADSP-21061. The ADSP-21060 SHARC (Super Harvard Architecture Computer) is a single-chip, 32-bit computer optimized for signal computing applications. A DSP program has been built to run the control loop with the sampling frequency of 40 kHz.

IV. SIMULATION

Simulation was used to facilitate the concurrent design process of the system. It indicated the predicted adequacy of the controller, the amplifier, and the other system components and pointed out potential problems and sources of errors. Corresponding to the system identification and modeling process of the system components, the simulation models and parameters were made close to the real system, and further simulation was conducted to predict the system performance based on the identified system components.

The simulation of the FTS system was conducted in SIMULINK. The inputs

provided to the system were sinusoidal signals to represent the position commands. The commanded position was a 50 Hz sinusoid with the amplitude of 0.5 mm. Fig.6 shows the error between the simulated position command and the actual position. The peak-valley amplitude of the position error is 11.6 micrometers, representing a 1.16 % error. This error is close to what was predicted in the controller design.

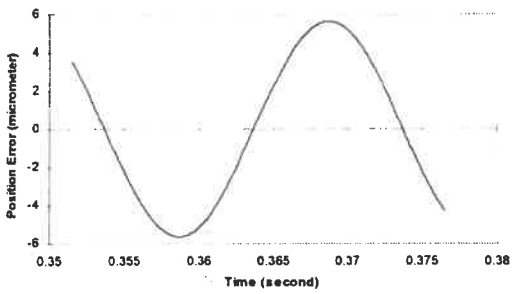

Fig.6 Simulated position error

V. TESTING

The DSP program generates sinusoidal commands at a sampling frequency of 40 kHz. In this GUI program, users can easily change the frequencies and magnitudes of the position commands. Users can also change the PID gains (K_p, K_i, K_d). The DSP program generates current commands and outputs them to the amplifier through a DAC port of the board. When the amplifier drives the voice coil actuator to move the flexure, the DSP program reads the measured position from the laser interferometer through a digital input port. The measured current in the voice coil is input into the DSP board through an ADC port. Data was stored into the external memory of the DSP.

The position commands were sinusoidal signals with the magnitude of 0.5 mm at different frequencies to test the system's ability to operate in the desired frequency region. The position error is shown in Fig.7. In this figure, a 680 Hz component is superimposed on top of a 50 Hz component. The 50 Hz component was caused by the natural resonance of the mechanical system and its appearance was normal. However, the 680 Hz component was undesirable. It could be caused by the compliance in the fixture used to hold the flexure system or compliance in the flexures whose natural frequency was close to or higher than the bandwidth of the impact signal and thus was not identified in the system identification tests of the flexure system.

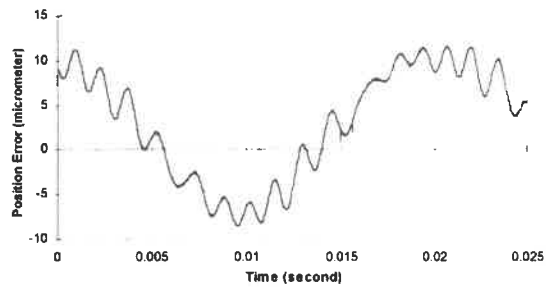

Fig.7 Position error for sinusoidal signal testing with magnitude of 0.5 mm at 50 Hz

VI. CONCLUSIONS

The developed fast tool servo can be controlled to move across ± 0.5 mm motion range with 10 μm position error at 50 Hz. The amplifier provides over 30 kHz bandwidth required by the system. The monolithic flexure system was designed and verified to be a second-order system with the resonance at 50 Hz. An unusual laser interferometer setup has been applied to this fast tool servo. The resolution of this interferometer is ± 5 nm. Only 5-10 nm noise is generated from the interferometer. These parameters satisfy the system requirements, and the real system performs close to the theoretical model. Research is still being conducted on the amplifier to reduce the noise and to solve the other problems that limit the system performance. A new flexure system is going to be designed to be able to move across a longer range of motion safely. Other control algorithms are going to be implemented to the FTS system to improve the system performance.

Development of Pin-type Vacuum Chuck for High-Precision Machining

Shinsuke Matsui, Fumikazu Ohira, Yoshiyuki Ishikawa, Kunio Koyabu,
and Atsunobu Une*
NTT Telecommunications Energy Laboratories,
The National Defense Academy*

1. Introduction

The wafer machining that enables sophisticated higher-performance electrical and optical devices needs to be improved to handle larger and more complex wafers[1), 2)]. An important aspect of advanced machining is the chucking method. The vacuum chuck provides easy operation, high precision, and high reproducibility. However, dust such as abrasives decreases machining precision by intruding between the wafer workpiece and chuck plane. We have developed a pin-type vacuum chuck to solve this problem[3)]. In this presentation, we study the influence of pin-suspension for a wafer theoretically and experimentally in order to determine the optimum chuck design.

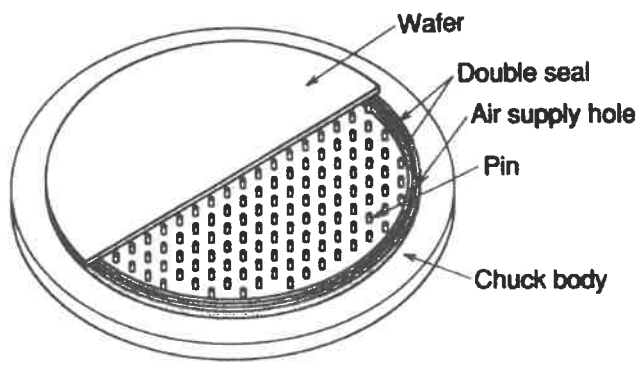

Fig.1 Schematic diagram of pin chuck.

2. Pin-type vacuum chuck

The chucking plane that supports a wafer is made up of an array of many tiny pins that are 0.22 mm in diameter and 0.25 mm high. The chucking plane, which is made of alumina, is finished to a flatness of less than 0.2 μm. A very small contact-area ratio of 0.4% reduces the probability of dust existing between the wafer and the pin-heads. Even if there is some dust, it can be removed from the pin-heads by slightly sifting the wafer. This small ratio also enhances the clamping power available for flattening. In addition, the chuck includes a slurry invasion prevention mechanism.

However, if the wafer has low rigidity, for example because it is thin or the pins are too far apart, the wafer will deform between the pins. Such deformation leaves dimples on the b wafer after machining. Thus, we have studied wafer deformation between the pins and how it

afer after machining. Thus, we have studied wafer deformation between the pins and how it affected the flatness of the machined wafer. We calculated the Si wafers deformation using the finite element method and experimentally measured the deformation with a Fizeau-interferometer. We found that deformation of more than 0.02 μm occurred for wafers thinner than 100, 300 and 1100 μm when the pin pitches were 1, 2, and 5 mm, respectively, under a 1 a.t.m. clamping vacuum pressure. Our experimental results agreed with our calculated results.

3. Influence of pin suspension in wafer polishing

Next, we studied this dimpling in practical Si-wafer polishing. We used wafers having low rigidity because of their thinness and from being clamped with a wide-span pin-chuck. All wafers were finished to a thickness of 300 μm using a 5-mm-pitch pin chuck. The relative work speed was 45 m/min. Colloidal-silica-abrasive polishing was done with polishers having a rubber hardness of 61, 82, or 95 (ASKER-C). The 82- and 95-hardness polishers were cross-grooved with 2-mm-wide grooves and 15-mm spacing. We believe the dimpling-formation process was as follows. When we use an extreme soft polisher on a deformed wafer surface, the removal rate was the same throughout the plane and almost uniform machining pressure was applied. On the other hand, when polishers had certain hardness, convex regions of the wafer were polished faster, apparently because of a high polishing pressure. This caused dimpling. The dimples became larger ad polishing continued and the polishing rate difference became smaller. Eventually, the wafer surface being polished became flat, and then the polishing pressure on the wafer surface became uniform. However, the opposite surface of the wafer was deformed by the vacuum and polishing pressure. After polishing, when the wafer was removed form the chuck, this deformation caused dimpling of the polished surface. The dimpling depth was determined by the deformation that resulted from these two pressures. In other words, the dimpling depth changed with polishing pressure at a uniform vacuum chuck pressure.

Figure 2 shows the typical cross-sectional shape of dimpling on the polished surface of a Si wafer. The profile valleys corresponded to the pin positions. It revealed that the profile represents reversed suspended lines between two pins. Similar profiles were obt ained from other parts of the polished wafer.

Fig. 2. Typical dimpling shape

Figure 3 shows the dimpling depth and stock removal as a function of polishing time for polisher hardness of 61, 82, and 95, and polishing pressure of 9.8 and 29.8 kPa. The calculated deformation is indicated by the dashed lines in Fig. 3. We took the grooves on the polisher into

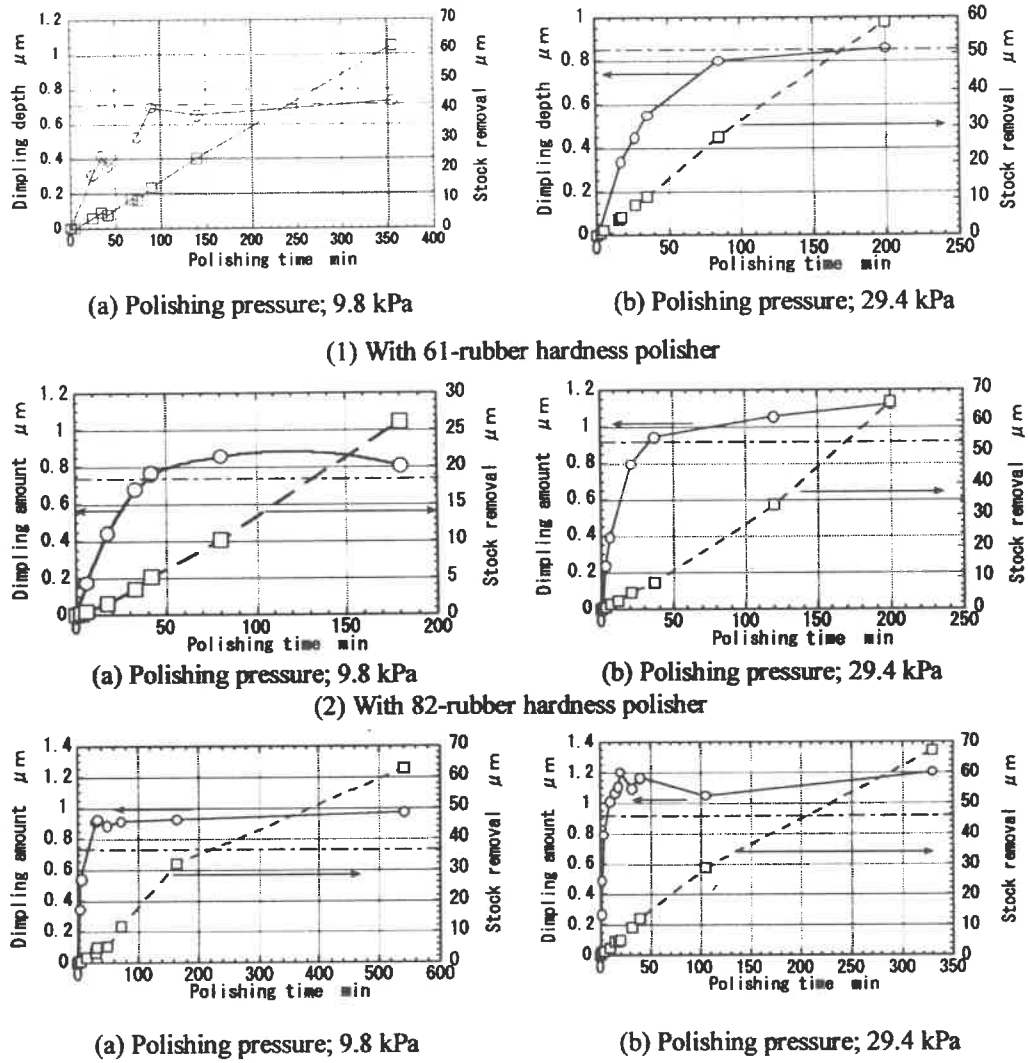

(a) Polishing pressure; 9.8 kPa (b) Polishing pressure; 29.4 kPa

(1) With 61-rubber hardness polisher

(a) Polishing pressure; 9.8 kPa (b) Polishing pressure; 29.4 kPa

(2) With 82-rubber hardness polisher

(a) Polishing pressure; 9.8 kPa (b) Polishing pressure; 29.4 kPa

(3) With 95-rubber hardness polisher

Fig. 3. Dimpling amount and stock removal as a function of polishing time

consideration when calculating the nominal contact area. We defined the force divided by this area the nominal pressure. The dimpling depths initially increased with polishing time, then saturated. This saturation occurred earlier for harder polishers and higher polishing pressures. The faster saturation seems to have been due to a larger removal-rate difference with unflatness of the wafer surface under these conditions. We also found that the saturated values were

higher than the calculated deformation when the polisher hardness was 82 or 95. It will be caused by the inhomogeneity of polisher surface. The polisher surface inhomogeneity such as the surface roughness and the grooves causes force distribution among pin spans. It is considered that the largest force of this distribution, which is larger than the force calculated by the nominal polishing pressure, decides the dimpling depth. Figure 4 shows the relationship between the dimpling depth and the nominal polishing pressure. The dimpling for all polishers increased at almost the same rate as the calculated value. This means the dimpling increased with an increase in wafer deformation caused by higher machining pressure. In our experiments, the dimpling depth was less than twice the calculated value, so we believe the dimpling depth with a 1-mm-pitch pin-chuck can be suppressed to less than 0.02 μm for Si wafers more than 200 μm thick.

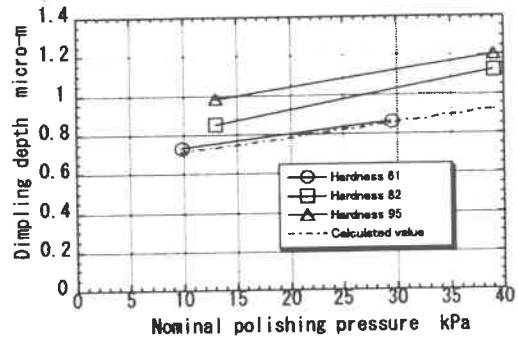

Fig. 4. Relationship between dimpling depth and nominal polishing pressure.

4. Conclusion

We investigated the pin influence for practical wafer polishing in order to optimize the structure of the pin-type vacuum chuck that we developed for precision wafer machining. As a result, the dimpling depths caused by pins were less than One and half of the calculated values. Thus the dimpling depth with a 1-mm-pitch pin-chuck can be suppressed to less than 0.02 μm for Si wafers more than 200 μm thick for less than 50 kPa polishing pressure. The difference between experimentally results and calculated values were believed to be due to the inhomogeneity of polisher surface.

Reference:

1) F. B. Kaufman et al.: Chemical-Mechanical Polishing for Patterned W Metal Features as Chip Interconnects, J. Electrochem. Soc., 138,11, (1991) 3460.bb

2) Y. Yamada, A. Takagi, I. Ogawa, M. Kawachi and M. Kobayashi: Silica-based Optical Waveguide on Terraced Silicon Substrate as Hybrid Integration Platform, Electron. Lett., 29,5, (1993) 444.

3) Shinsuke Matsui, Fumikazu Ohira, Yoshiyuki Ishikawa, Atsunobu Une, and Akira Shimizu: J. of JSPE, 63, 12 (1997) 1705 (in Japanese)

DEVELOPMENT OF A NEW PALM-SIZE AND CLEAN SPHERICAL MIRROR-FINISH SURFACE PROCESSING MACHINE FOR THE FABRICATION OF OPTICAL FIBER CONNECTORS

Kenichi Ohno and Masashige Mitsuhashi

Functional Devices Research Laboratories, NEC Corporation,

1-1 Miyazaki 4-chome, Miyamae-ku, Kawasaki, Kanagawa, 216-8555 JAPAN

1.Introduction

With the increasing use of optical fiber networks has come an increasing demand for on-the-spot mirror-finish processing of optical fiber connector surfaces in order to respond to network design changes or new construction needs. For such purposes, a small, light-weight, portable processor is needed. Table 1 shows an example of optical fiber connector specifications. In general, PC(Physical Contact) connectors, used with single mode optical fibers are used in optical fiber networks. Figure 1 illustrates a typical PC connector and shows fiber-to-fiber contact. In this type of connector, convex spherical mirror-finish endfaces of 10~25mm radius curvature are needed to avoid optical loss and reflection. This paper describes a new palm-sized processing machine(processor) that employs lapping tape to fabricate spherical mirror-finish surfaces on PC connectors for optical fiber communications networks.

Table 1 Optical fiber connector specifications

Item	Specification
Sphered radius	10—25mm
Sphered symmetry degree	≦50μm
Sphered shape	Undistorted, smooth sphere
Insertion loss	≦0.3dB
Return loss	≧40dB

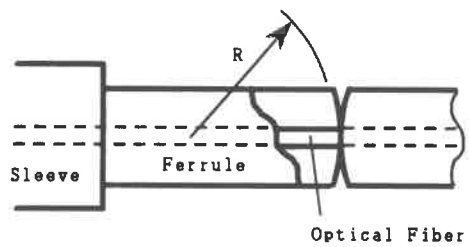

Fig.1 PC connectors in contact

2. Development of a New Processing Machine for the Fabrication of Optical Fiber Connectors

Figure 2 shows the principle of operation and an external view of the newly developed processor. The processor is, 89mm in width, 90mm in depth, 102mm in height, and about 0.5kg in weight.

The head of the processor has on its surface a spherical depression, into which the connector end is pressed, with lapping tape between the head and the connector end. The lapping tape is moved at a slow speed, and the connector is rotated at the same time, which produces a spherically convex surface on the connector end.

Space savings with this processor are significant: the tape is rolled, so that a long length of tape can be contained within a compact cartridge, and the need for a large polishing pad is eliminated. Further, the tape cartridge is secured with only a single screw, making cartridge replacement fast and simple.

A sponge is used to supply moisture to the lapping tape.

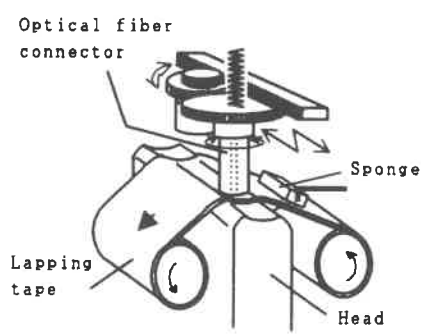

Fig.2 A new palm-size spherical mirror-finish surface processor

3.Experimental Method and Results

3-1 Experimental method

Table 2 shows the main experimental conditions. There are two stages to actual processing: spherical shaping and mirror-finishing. Since the sphered radius of the connector end depends on that of the head, we set the latter at 17.5mm, which is the middle value of the sphered radius specification for optical fiber connectors. The workpieces are a glass ferrule optical fiber connector and a zirconia ferrule optical fiber connector of 2.5mm in diameter.

Table 2 Experimental Conditions

	Spherical shaping process	Mirror-finishing process
Sphered radius of stage	17.5mm	
Connector feed mean speed	2600mm/min	
Lapping tape mean speed	75mm/min	
Load	220—900gf	
Processing time	30sec—50min	
Lapping tapes (Grain size)	Alumina(8μm) SiC(8μm) Diamond(8μm) Diamond(5μm)	Diamond(1μm) Diamond(0.3μm) CeO_2(0.3μm) Alumina(0.1μm) SiO_2

3-2 Results and discussion

3-2-1 Spherical shaping of glass ferrule optical fiber connectors

First of all, optical fiber connectors (with a flat connector end) were shaped into a spherical configuration, using three kinds of lapping tapes(alumina, diamond, and Silicon Carbide(SiC)), all of which are 8 μm in grain size, and the surface conditions on the processing side of the optical fiber connectors were compared and evaluated after the shaping was finished. Figure 3 compares the profiles of the processing sides processed with alumina tape, diamond tape, and SiC tape. When using alumina tape and diamond tape, surface roughness was 0.2 μmRmax and 0.15 μmRmax respectively, and scratches remained on the fiber core part of the connectors. On the other hand, when using SiC tape, the surface roughness was only 0.07 μmRmax, and no scratches on the fiber core part were observed.

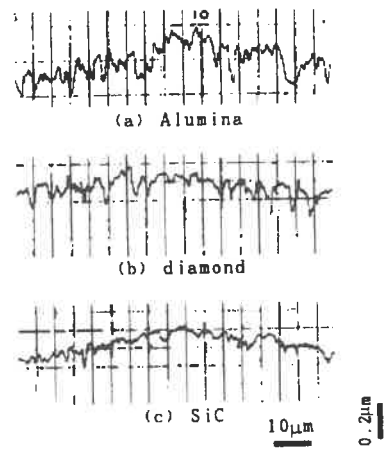

Fig.3 Profile of endface after spherical shaping process

In observing the surface conditions of the lapping tape by SEM, it was found that the angles of the alumina grains had been rounded, and that the diamond grains were completely covered by the binder. In contrast, the angles of the SiC grains were sharp and the grain blades were not covered by the binder. This appears to be the reason for the excellent performance obtained in using SiC tape for the spherical shaping

Diamond tape removes 2~2.5 times as much material as SiC tape; however, as previously described, scratches remained on the fiber core part. It appears that SiC tape is most suitable for use as the lapping tape for the spherical shaping process, because it is desirable for the surface roughness to be as low as possible at the end of the spherical shaping process.

3-2-2 Mirror-finishing of glass ferrule optical fiber connectors

The glass ferrule optical fiber connectors were mirror-finishing processed with three kinds of lapping tapes, and the mirror-finishing processing sides were evaluated. The three kinds of tape were cerium oxide(CeO_2,0.3 μm grain size), alumina(0.1 μm grain size) and diamond(0.3 μm grain size). Generally, CeO_2 is used for the surface-finishing of glass systems. It is expected that using alumina or diamond can improve

processing efficiency because of their high hardness. For the workpieces, we used glass ferrule optical fiber connectors, and SiC tape, with which the excellent results described in the previous section were obtained was used for the spherical processing. The three kinds of lapping tapes all achieved a surface roughness of less than 0.01 μmRmax, and no scratches on the fiber core part were observed.

We evaluated whether these lapping tapes could be applied to the mirror-finishing process of an optical fiber connector by measuring the insertion loss and return loss. Figure 4 and Figure 5 show distributions of insertion loss and return loss against a master connector. For insertion loss, 0.3dB or less was obtained with all optical fiber connectors, and the specifications were satisfied. An average return loss of 34.1dB was obtained in the optical fiber connectors mirror-finishing processed by alumina tape, and 36.3dB on the average was obtained for those processed by diamond tape. In comparison, the average obtained for those processed by CeO_2 tape was 50.2dB.

It appears that alumina tape and diamond tape damage the fiber endface considerably more than CeO_2 tape, and that this is the cause of the thin damaged layer produced by the mirror-finishing process on the fiber endface processed by alumina tape or diamond tape.

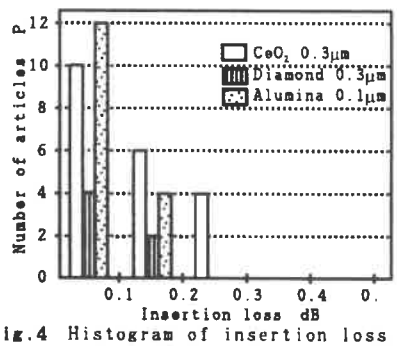

Fig.4 Histogram of insertion loss According to abrasive type

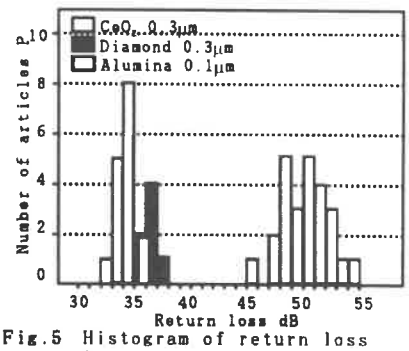

Fig.5 Histogram of return loss According to abrasive type

From these examinations, it became clear that, in the mirror-finishing process, CeO_2 tape, because it only lightly damages the processing side, even though processing efficiency is higher with the other two tapes.

3-2-3 Spherical shaping of zirconia ferrule optical fiber connectors

This section describes the results obtained in examining spherical shaping of zirconia ferrule optical fiber connectors. When zirconia ferrule optical fiber connectors are processed, the fiber withdraws because zirconia ferrule is harder than the fiber(consisting of the fused silica). Therefore, zirconia ferrule and the fiber are removed at the same time and it is necessary to control the withdrawing of the fiber when the endface is processed. Optical fiber connectors were processed by using diamond tape with high removing power and cheap SiC tape, and the processing sides were observed. The examined processes were the following:

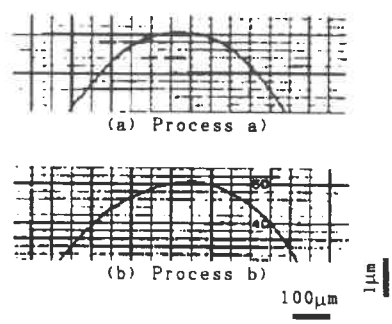

Fig.6 Profile of endface after spherical shaping process

a) diamond tape(8 μm grain size) - diamond tape(5 μm grain size) - diamond tape(1 μm grain size)

b) SiC tape(8 μm grain size) - diamond tape(5 μm grain size) - diamond tape(1 μm grain size)

Figure 6(a) and (b) show respectively, the profiles on the processing side to which the a) and b) spherical shaping processes were applied. No fiber withdrawing occurs and excellent spherical shaping is obtained for both processes. In terms of processing cost, process b) appears to be more suitable because it uses SiC tape instead of diamond tape in the 1st step of the process.

3-2-4 Mirror-finishing of zirconia ferrule optical fiber connectors

We next continued our study of mirror-finishing of zirconia ferrule optical fiber connectors. To control the fiber withdrawing in the mirror-finishing process, we used lapping tape made of silicon dioxide(SiO_2) which is the same material as that used in fused silica fibers, because the processing rate of the fused silica to zirconia is decreased.

Figure 7 shows the result of changing processing pressure in four stages(220gf, 500gf, 700gf, 900gf) mirror-finishing, and measuring return loss. It can be seen that the return loss performance is excellent, and that the processing is steadiest under processing load of 700gf(14kgf/cm^2).

Mirror-finishing of 10P was processed under these conditions. Figure 8 shows the result of measuring the return loss; an average of 51.7dB was obtained and thus it was concluded that the connectors had sufficient reliability for practical use.

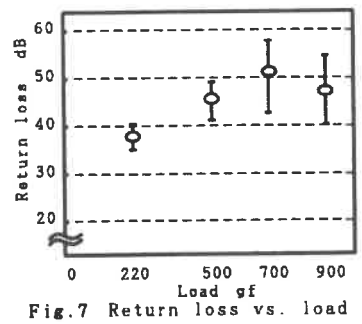

Fig.7 Return loss vs. load

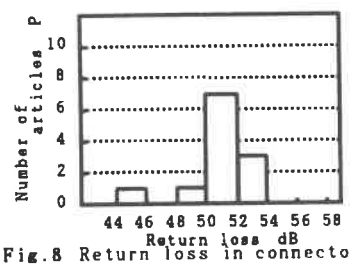

Fig.8 Return loss in connectors

4.Conclusion

A new palm-sized processing machine that employs lapping tape to fabricate spherical mirror-finish surfaces on PC(Physical Contact) connectors has been developed. The experimental results obtained with this machine are as follows:

(1) In tests on glass ferrule optical fiber connectors, silicon carbide tape(8 μm grain size) was used for the spherical processing and achieved a surface roughness of only 0.07 μmRmax. Cerium oxide tape(0.3 μm grain size) was used for the mirror-finishing, and achieved a surface roughness of only 0.01 μmRmax, and an average optical return loss of 50.2dB.

(2) In tests on zirconia ferrules, the finest spherical shaping was attained with a SiC tape(8 μm)→diamond tape(5 μm)→diamond tape(1 μm) process. This use of SiC tape for initial shaping reduces the need for diamond tape, thus helping to hold down costs. Silicon dioxide tape was used for the mirror-finishing. With a processing load of 700gf(14kgf/cm^2), average return loss was 51.7dB.

Acknowledgments

The authors wish to thank Dr. Setsuo Kaneko for his helpful guidance and encouragement. We also thank Messrs. Etsuo Ikeda, Kazunori Suzuki, Kazuhiro Hanaue, Nobuyuki Fujino and Torahiko Kanda for their valuable advice.

References

[1] T. Kanda, et al., "A New Spherical Mirror-Finish Surface Machining Technology for Optical Fiber Connector," *NEC Res. & Develop.*, **36**, 2, pp. 271-279,1995.

[2] Y. Ando, et al., "Advanced Optical Connector for Single-Mode Fibers," *NTT Rev.*, **3**, 3, pp. 110-121,1991.

MICROFABRICATION OF A MOLD INSERT MADE OF HARDENED STEEL AND FIRST MOLDING RESULTS

Th. Schaller[1], M. Heckele[2], R. Ruprecht[3] and K. Schubert[1]

Forschungszentrum Karlsruhe GmbH / Karlsruhe Research Center
[1] Hauptabteilung Versuchstechnik / Central Experimental Department
[2] Institut für Mikrostrukturtechnik / Institute for Microstructure Technology
[3] Institut für Materialforschung III / Institute for Materials Research III
P.O. Box 3640, D-76021 Karlsruhe
Deutschland / Germany

Introduction

For the production of plastic, metallic and ceramic microparts, microstructured mold inserts are used in replication techniques, such as injection molding and hot embossing. Replication was developed as part of the LIGA process, and considerable experience has been gained by the Karlsruhe Research Center in the fabrication of molded microstructures /1/. The factor limiting the number of replications is the mold insert material, currently electroplated nickel and nickel alloys (made by LIGA), and brass, copper, aluminum and other non-ferrous materials (made by mechanical micromachining using diamond tools). As known from the conventional mass production of macroscopic structures, masters made of steel are desired for microstructures as well, in order to ensure a long mold insert lifetime.

Steel can be cut by using micro end-mills made of hard metal (tungsten carbide) with a minimum cutter diameter of less than 50 µm available /2/. The burrs occurring during the cutting process have to be removed to ensure a secure molding process, namely, an easy mold release. It was shown that the burr removal can be done by electrochemical polishing /3/.

So far, electrochemical polishing has been performed on a structured area of some 100 mm^2, due to the limited currents of the power supplies available /4/. The structured area of the mold inserts usually used at the Karlsruhe Research Center, and as required for many technical applications, has a maximum size of 26 x 66 mm^2. In this work, we present a microstructured mold insert of that size, the burr removal by electrochemical polishing, and the replication of the hardened mold insert.

Results

Micromachining

The microstructuring work of mold insert fabrication is done by mechanical micromachining, using hard metal tools for cutting of trenches with approx. 100 µm minimum width. The martensite steel 1.2709 (X 3 NiCoMo18 9 5) is chosen as the workpiece material. The material is structured in the unhardened state and hardened after structuring by maraging at 490°C for 3 to 5 hours, with an overall shrinkage of 0.09%. One of the main advantages of the steel 1.2709 besides easy structuring is the low warp after hardening.

For the burr removal tests and the molding experiments, mold inserts were prepared with a trench structure in a 300 µm and 500 µm pitch. The actual trench widths were approx. 220 µm and 420 µm, respectively, and the depth ranged from 200 µm to 330 µm. Burrs occurred at the upper edges of the freestanding wall structures between the trenches, with a height of approx. 15 µm (Figures 1 and 2).

Electrochemical Polishing

In the experimental setup a 1.5 liter thermostated etching vessel, an electrically insulating housing for the mold insert with a window for the structured 26 x 66 mm^2 area and a metallic cathode plate with 78 x 70 x 3 mm^3 in outer dimension were used. The distance between the anode and the cathode was 40 mm. For etching, a stirred standard solution /5/ of 70%(vol.) concentrated phosphoric acid, 10%(vol.) of concentrated sulfuric acid and 20%(vol.) water was used at an etching temperature of 40°C.

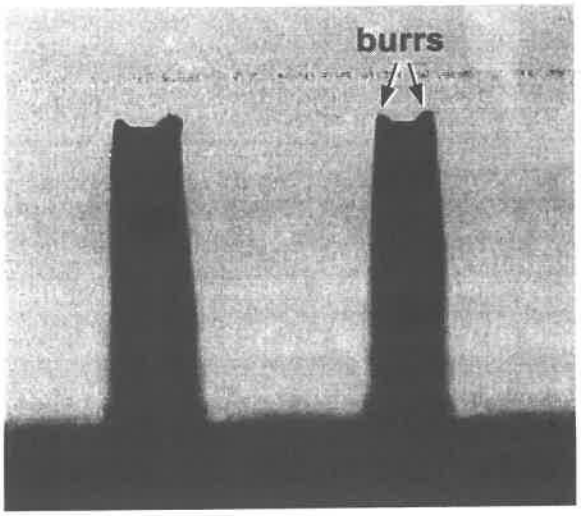

Figure 1: **100 µm**
Light-microscopic side view of trenches (light) and walls (dark) with burrs on top of the walls.

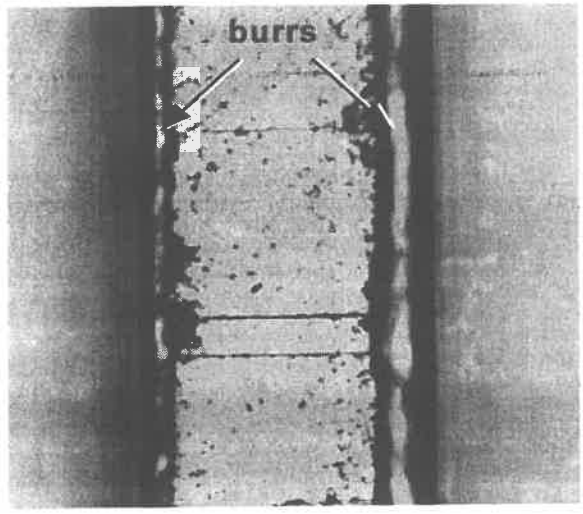

Figure 2: **25 µm**
Light-microscopic top view of burrs at the upper edges of a wall structure.

The power supply used was a "Knuerr Heinzinger Type PTN 65 - 60 2P" with 65 Volts maximum voltage and 60 Amps maximum current. The voltage and current were varied from 5 Volts / 6 Amps to 16.7 Volts / 35 Amps. Good etching results were achieved with duty cycles of 10 seconds etching time and 10 seconds current-free time. For the given structures, the burrs could be removed completely after 4 to 6 high current cycles. After electropolishing of the surface, grain boundaries were clearly visible.
As to be expected, the material removal was not uniform for all height levels of the microstructures. In particular we observed that for high currents most material was removed from the burrs and the upper surface of the wall structures, whereas at the bottom of the trenches almost no etching was observed. For low currents, a planarization of the complete surface (both wall top and trench bottom) took place. By combination of low and high current cycles (e.g. 4 x 10 seconds 35 Amps and 6 x 10 seconds 6 Amps) we achieved burr removal and overall planarization of the surface with a structure height loss of 5 to 9 µm (Figures 3 and 4).

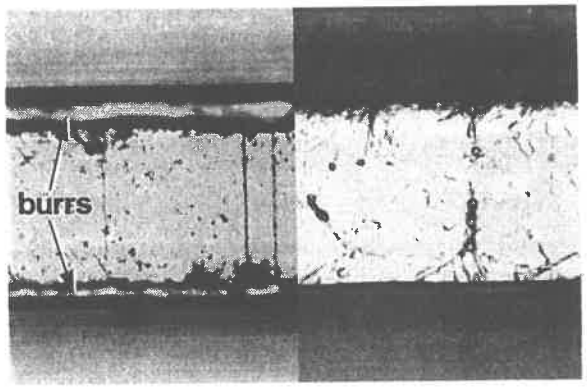

Figure 3: **25 µm**
Light-microscopic top view of a wall structure before (left) and after (right) electrochemical polishing. The burrs were completely removed. The width of the wall is reduced from 92 µm to 76 µm. The lateral material removal of 8 µm is of the same order as the reduction of the structure height.

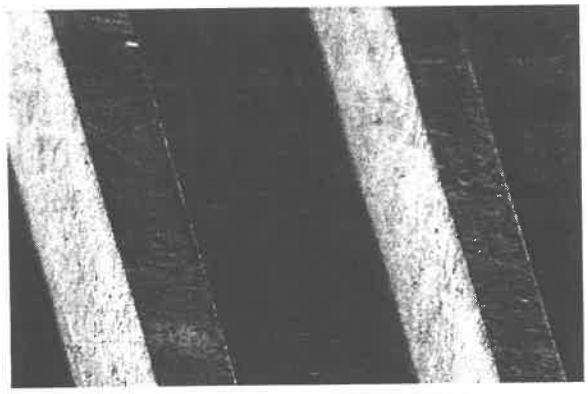

Figure 4: **100 µm**
SEM detail view of an electrochemically polished mold insert. Please note that there is no burr visible and that all surfaces (dark bottom, light sidewalls, gray top) show a similar smoothness. The radius of curvature of the upper wall edges is estimated to be less than 2 µm.

Hardening
The deburred mold insert was hardened to a Rockwell hardness of 55 to 57 HRC by maraging at 490°C for 4 hours. Vacuum was applied to prevent any oxidation.

Molding Tests by Using Hot Embossing
Hot embossing is starting to be a production technology for sophisticated plastic components with delicate microstructures, such as microspectrometers or microvalve housings. Due to the versatility of the hot embossing machines, this technique allows a quick exchange of the microstructured mold insert. The experimental setup and molding parameters can be varied easily, which is important for the valuation of the molding tool quality during the experimental phase as well as for an inexpensive small-scale production of microparts.
The molding experiments were run on a hot embossing machine type WUM 1, a prototype built by the Karlsruhe Research Center, which is the base for the commercially available HEX02 machine from Jenoptik Mikrotechnik (Jena, Germany).
Previously used mold inserts cut into brass very often showed a significant burring. The burrs are forming undercuts which increase the demolding force when separating the microstructured polymer part from the mold insert. Because of the low mechanical stability of the burrs, a repeated replication process leads to a progressive deformation of the burrs or even to a complete tear-off of these burrs and a reduction of the undercuts. Thus, a multiple repetition of this hot embossing step can be used as a cleaning procedure. Unfortunately, this is no exactly defined procedure and damaging of the structures is also possible. In contrast to this, working with deburred mold inserts from steel is free from this inconvenience. From the first replication on, the demolding forces which are measured to be inferior to those known for brass-made mold inserts indicate that the microstructure surface of the steel mold inserts is smooth and that there is no need of a cleaning procedure due to the lack of burrs. The polymer used for the first tests was PMMA. The quality of the molded microstructures is good and reproduces the surface quality of the mold insert (Figures 5 and 6), so other thermoplastic polymers used in hot embossing will also be applicable. The advantage of using steel is the greater temperature range which can be covered in the hot embossing technology, resulting in an extended material choice from the high-temperature polymers, such as polyetheretherketone (PEEK).

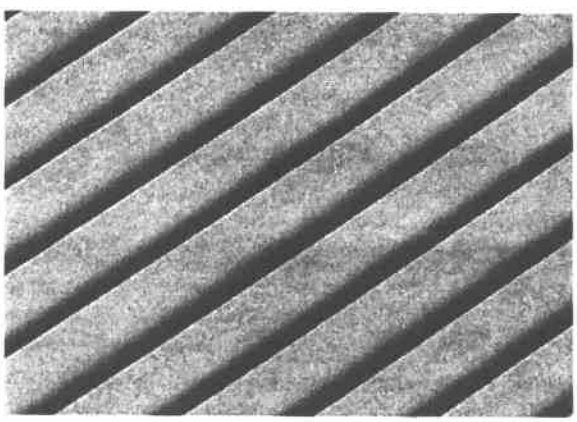

Figure 5: **200 µm**
SEM of a PMMA structure, replicated from an electrochemically polished mold insert made of hardened steel. The trenches of the mold insert were transformed into broad walls (light), whereas the walls of the mold insert appear as narrow trenches (dark).

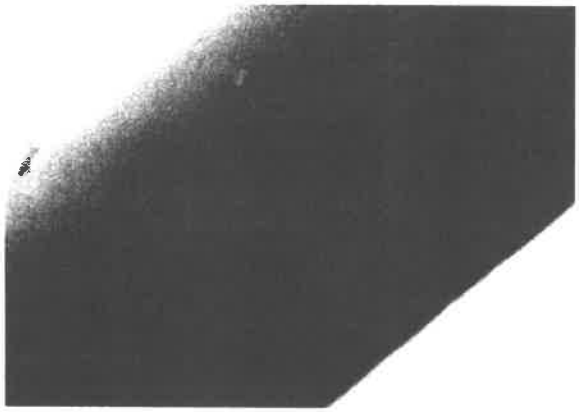

Figure 6: **20 µm**
SEM detail view of a trench wall showing the surface smoothness of a replicated PMMA structure. The trench bottom appears dark (middle), the sidewall gray (left). The light areas at the upper left and lower right are the top of the walls (out of focus).

Discussion and Outlook

Steel mold inserts have been tested successfully for the replication of microstructures by hot embossing. For the first time, burr-free mechanically microstructured mold inserts made of hardenable steel are now available for microparts production. The material properties will ensure a long lifetime of the mold insert compared to the brass and nickel mold inserts available so far. Even abrasive filled polymers will be accessible for molding.

Further molding experiments will be performed using injection molding. Injection molding of plastic microparts using microstructured mold inserts has been performed at the Karlsruhe Research Center for more than ten years. The mold inserts were made mechanically by cutting into brass and aluminum alloys or by replication of nickel structures from a master structure by means of electroforming. All these mold materials restricted the economic use of the mold inserts to unfilled plastics. For PMMA (polymethylmethacrylate), PSU (polysulfone), PA (polyamide), PE (polyethylene), POM (poly-oxymethylene) and PEEK (polyetheretherketone) small-scale production processes are available. Without any chemical corrosion a mold insert lifetime of more than 10,000 cycles can be achieved /6/. The lifetime is reduced to less than 5,000 cycles when using filled plastics because of tool wear. The newly available microstructured mold inserts made of hardenable steel are the key to a higher wear resistance, resulting in cost reduction for molding of particle-filled plastics (POM, PA, liquid crystal polymers). Due to their hardness and better wear resistance, the steel mold inserts are expected to be well fit to the metal and ceramic injection molding processes and will be tested in the replication using metal or ceramic powders mixed with polymer.

Acknowledgments

Although the structures being "micro", the contributions to this paper have been "macro". We would like to thank the staff of the Mechanical Microengineering Labs, namely, D. Scherhaufer for the microtool fabrication, F. Messerschmidt for the mold insert preparation, L. Eichhorn for the steel hardening experiments. Special thanks go to H. Jackisch for building the electrochemical polishing facility and P. Abaffy for the SEM investigations.

References

/1/ Schaller Th, Heckele M, Ruprecht R:
Mechanical Micromachining for Mold Insert Fabrication and Replication.
ASPE 1999 Spring Topical Meeting, Proceedings (in press)

/2/ Schaller Th, Bohn L, Scherhaufer D, Schubert K:
Microstructure Grooves less than 50 µm Wide Cut with Ground Hard Metal Micro End Mills.
ASPE 13th Annual Meeting, Proceedings Vol. 18 (1998) 108-111

/3/ Schaller Th, Bohn L, Mayer J, Scherhaufer D, Schubert K:
Microstructure Grooves less than 50 µm Wide with Reduced Burr.
Micro System Technologies 98, Reichl H and Heuberger A (Eds.),
VDE-Verlag GmbH, Berlin (1998) 664-666

/4/ Schaller Th. Mayer J, Schubert K: Approach to a Microstructured Mold Made of Steel.
Precision engineering - nanotechnology: Proceedings of the 1st International euspen Conference,
McKeown P et al. (Eds.), Shaker Verlag, Aachen, Vol. 1 (1999) 238-241

/5/ Tegart W J McG: The Electrolytic and Chemical Polishing of Metals in Research and Industry.
Pergamon Press, London (1956) 86

/6/ Nöker F, microParts GmbH, Hauert 7, D-44227 Dortmund, Germany: Personal Information (1997)

DEVELOPMENT OF AN ULTARA-PRECISE POSITIONING STAGE ENGAGED WITH GRATINGS

Takashi Wada and Satoshi Honda
Tokyo Metropolitan Institute of Technology, Japan

1. Introduction

Nowadays, an ultra-precise positioning stage is an indispensable component of a precise machine tool, a measuring instrument or a semiconductor manufacturing equipment. The ultra-precise positioning stages requires not only mechanical performance of high stiffness, accurate guidance, and the minimum lost motion but also control performance of precise positioning, minute resolution, dependable repeatability, and smooth driving. Some integrated ultra-precise stages with a devised mechanism and an intelligent control system have been developed.[1)2)3)4)] One integrated stage consists of a ball screw, an air slider and a laser interferometer.[1)] Another stage is formed into a linear electric motor with a precise linear encoder.[2)] Other stage composes an inchworm mechanism moving on a guide rail.[3)] The last stage composes an inchworm mechanism travelling on a micro-pitch rack which pitch is 120 micrometer. However, the first stage is bulky because individual instruments are assembled without merging. If stiffness of the ball screw and the air slider should be more rigid and if measurement accuracy of the laser interferometer should be higher, those elements become bigger and heavier. The second stage is compact; yet a control system is complicated because the linear motor can not control the position without regulating of electric current accurately. Control system of the third stage is constructed easily because inchworm motion is accomplished by using an open-loop control system; still, the stage can not position every step without slipping even if driving plates grip on a guide rail tightly. The last stage has some advantages for the compact feature, the open-loop control system and the positioning without slipping; nevertheless, the minimum resolution of positioning is larger than 30 micrometer.

In this paper, we present a novel ultra-precise positioning stage in which two gratings engage with a ruler grating in an inchworm motion. The stage is accurately positioned every one pitch of a grating without feedback control system composed of a laser interferometer and a complicated control algorithm. The structure becomes compact and its table is positioned by the open-loop control system.

2. Structure of the ultra-precise positioning stage

The ultra-precise positioning stage is consists of a linear guide, a ruler rail, a linear slider and a drive

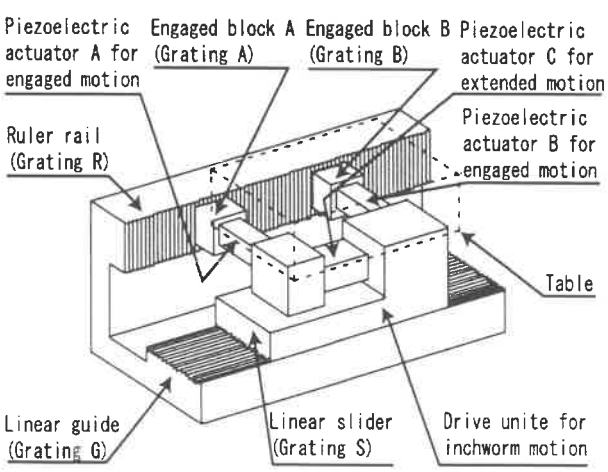

Figure 1. Structure of the ultra-precise stage

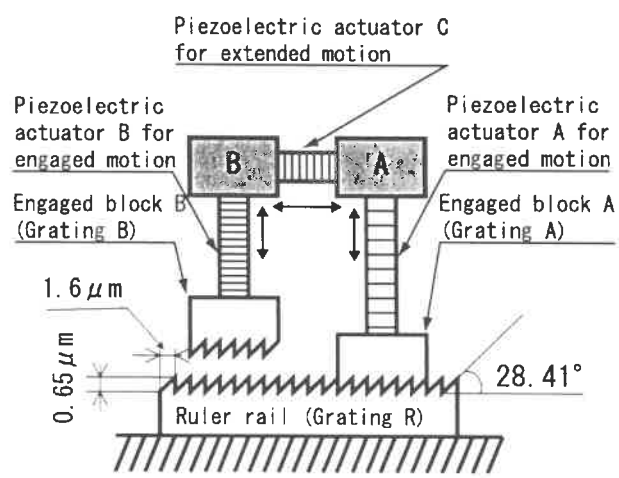

Figure 2. Inchworm mechanism

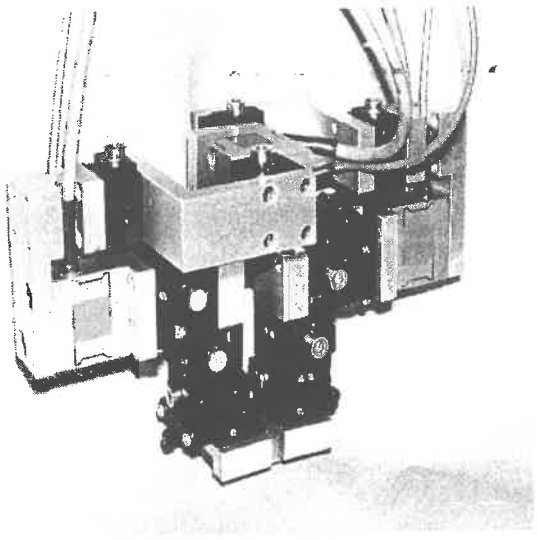

Figure 3. The drive units for inchworm motion

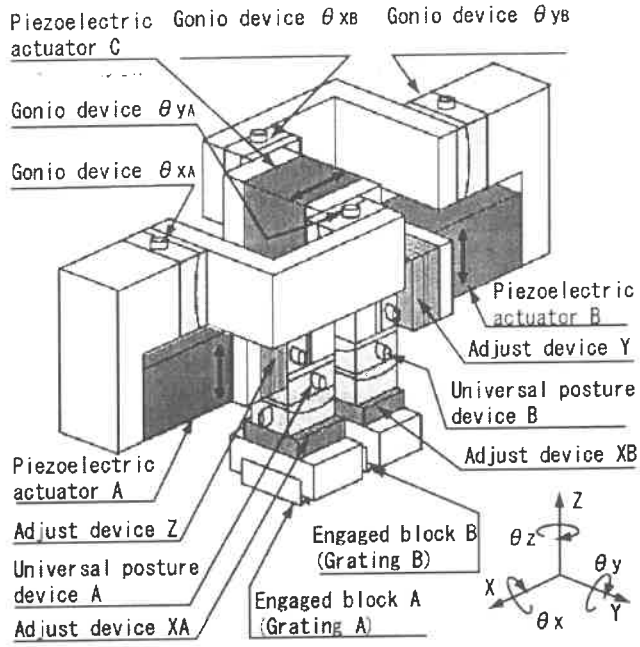

Figure 4. Structure of the drive units

unit for inchworm motion as shown in figure 1. The linear guide and the linear slider are gratings, and they compose an ultra-precise slide guide. The drive unit is consists of two engaged blocks and three piezoelectric actuators on the linear slider as shown figure 2. Two engaged blocks and the ruler rail are gratings, and both engaged blocks are meshed on the ruler rail step by step as shown in figure 2. The inchworm motion of the engaged block are generated by the piezoelectric actuators. As the pitch of gratings is usually about 1 micrometer, and depth of the grating is less than 1 micrometer, inchworm motion does not need any expander for displacement of the piezoelectric actuator. Thus the table is positioned at every one pitch of the grating.

The driving unit is shown in figure 3 and figure 4. The drive unite is consists of three piezoelectric actuator attached four gonio devices and two engaged blocks attached two universal posture devices and some adjust devices for x and z directions. The moved directions of those piezoelectric actuators are ultra-precisely adjusted by using four gonio devices, so two pairs of the piezoelectric actuator (C) for extend motion and the piezoelectric actuators (A or B) for engaged motion are perpendicularly moved each other. Both surfaces of the gratings are ultra-precisely adjusted into the same plane and both grooves of the gratings are adjusted in parallel by using the adjust device (Z) for z direction and two universal posture devices composed of three miniature gonio devices. The adjust devices (XA and XB) for x direction is used to adjust interval between both gratings into the distance multiplied pitch distance of grating by a certain integer. The adjust method for theses adjustment is appeared in the experimental result.

3. Experimental results

In the experiments, capacity of the gratings as a mechanical part was qualitatively measured, and an adjust method for the gratings of the engaged blocks was confirmed. Figure 5 showed the relationship between vertical cramping force and the maximum resisting force which acted into parallel direction against the grating grooves or acted into perpendicular direction against the grating grooves when the gratings were meshed with a certain vertical cramping force. In this figure, the maximum resisting force which acted into the parallel direction was proportional to the cramping force, and coefficient of static friction between the gratings was 0.31. The maximum resisting force which acted into the perpendicular direction without breaking the meshing was proportional to the vertical cramping force, and the maximum resisting force was approximately one and half of the minimum slide force.

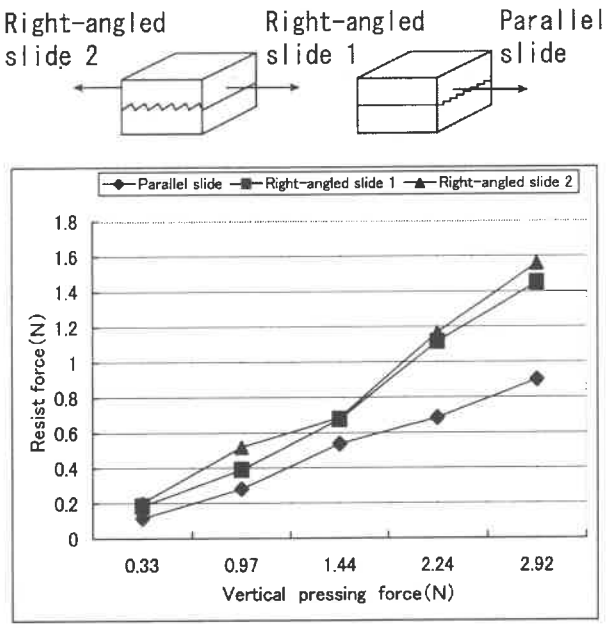

Figure 5. Experimental Result

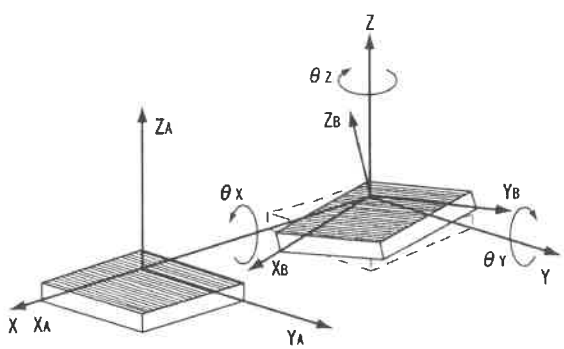

Figure 6. Coordinate frame of the gratings

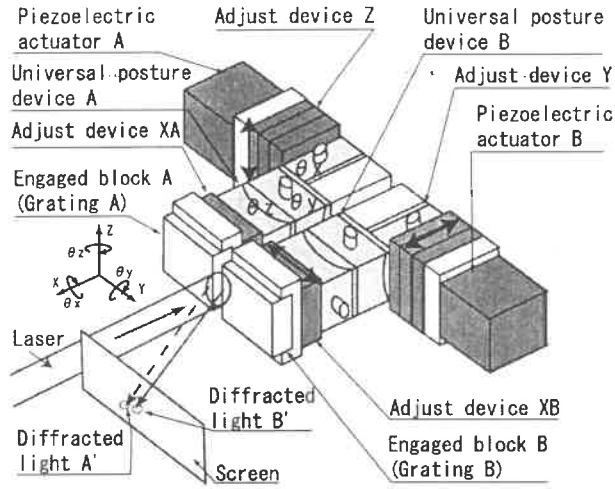

Figure 7. Experimental Equipment

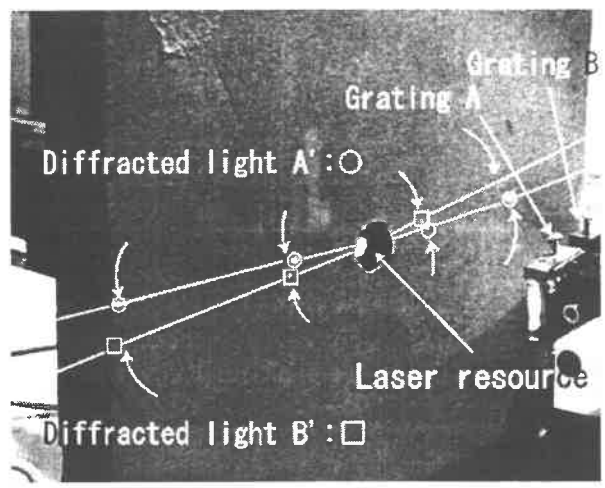

Figure 8. Adjustment result of θ z

Figure 6 showed the coordinate frame of drive units for the inchworm motion and the engaged blocks (A and B). When the piezoelectric actuators for engaged motion move into the z direction and the piezoelectric actuator for extend motion move into the x direction, the grating of the engaged block (A) must be adjusted as its surface becomes parallel against x-y coordinate plain and its grating grooves become parallel against y coodinates axis. Moreover, the grating of the engaged block (B) must be adjusted as its surface is in the same plane in which anther grating (a) is adjusted and its grating grooves become parallel against another grating grooves and also interval between both gratings becomes the distance multiplied pitch of grating by a certain integer. The grating of the engaged block has five degree of freedom in the adjustment. For this adjustment, diffracted lights is used as shown in figure 7. If the angle of θ z is not regulated, a series of spots of the diffracted light B' crosses to a series of spots of diffracted light A' as shown in figure 8; therefore, an adjust screw of θ z is regulated as both series of spots of the diffracted lights become parallel. If the angle of θ x is not regulated, both series of spots of diffracted lights (B' and A') are separated in parallel as shown in figure 9; therefore, an adjust screw of θ x is regulated as both series of spots of diffracted lights become the same line. If the position of z is not regulated, interval between each spot is not same as shown in figure 10; therefore, position z is regulated. If the angle of θ y is not regulated, both spots of the diffracted lights dose not corresponded as shown in

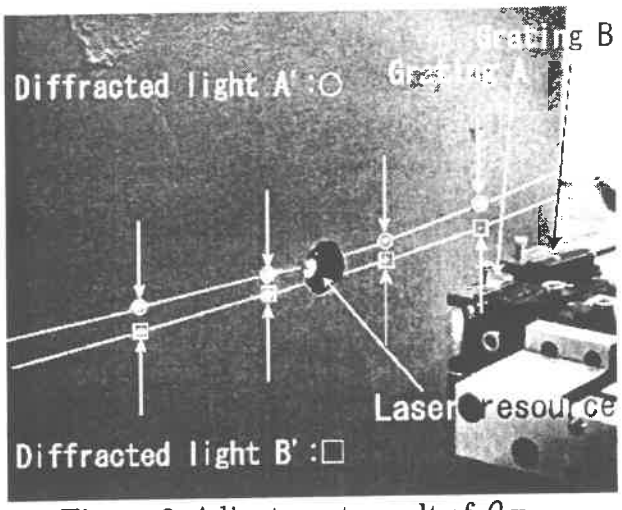

Figure 9. Adjustment result of θ x

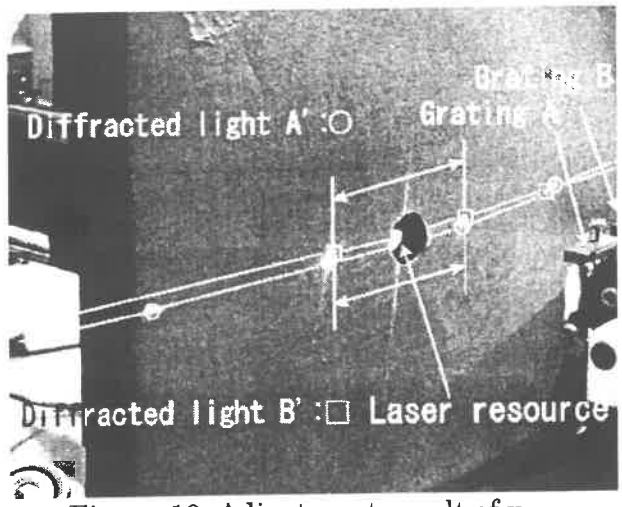

Figure 10. Adjustment result of x

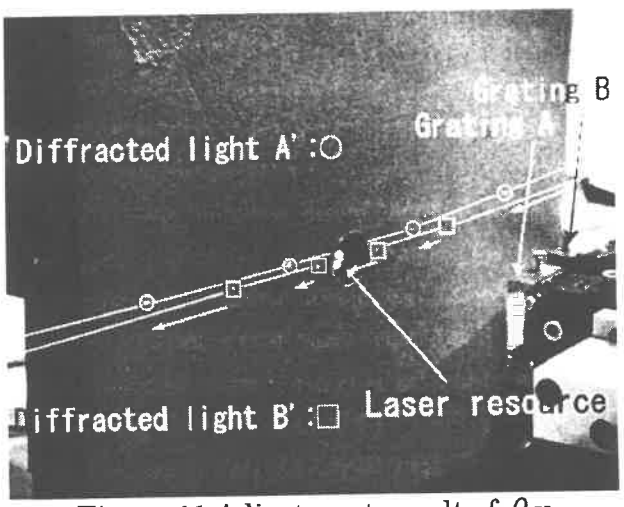

Figure 11 Adjustment result of θ y

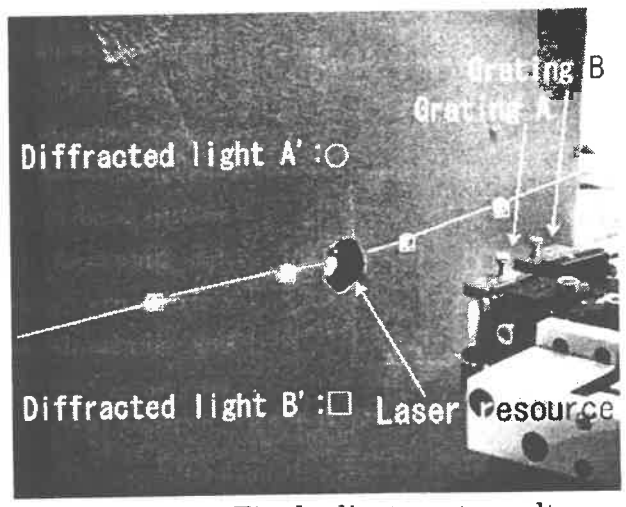

Figure 12. Final adjustment result

figure 11; therefore, an adjust screw of θ y is regulated as both spots become same point. Figure 11 showed the final regulated spots.

4.Conclusions

Novel ultra-precise positioning stage engaged with gratings was developed. The stage can position at every one pitch of the grating by meshing the engaged blocks to the ruler rail of the grating. The pair of grating is meshed tightly as the mechanical parts and the upper gratings side into parallel direction against grating grooves. The engaged blocks of gratings are ultra-precisely adjusted into the same plain and into parallel grooves by using diffracted lights.

References

[1] Jiro Otsuka, et al.: "Ultra-precision Positioning Using Lead Screw Drive", JSPE, 59, 10, (1993) 1655.
[2] Shigeru Futami, et al.: "Nanometric Positioning Using AC Linear Motor and Rolling Guide", JSPE, 57, 10, (1991) 1808.
[3] Tetsuro Sakano et al.: "Study on a Micro Piezoelectric Linear Actuator with Friction Drive Method", JSPE, 63, 9, (1997) 1246
[4] Satoshi Honda: "Development of a Precise Positioning Stage Traveling on Micro-Pitch Racks", Proceedings of 13th ASPE annual meeting, pp376-370(1998).

Identification and Compensatory Control of Time-varying Volumetric Errors in Machining Centers

Joong-Yong Ahn and Sung-Chong Chung

MAnufacturing Systems & Control LABoratory
Department of Mechanical Design & Production Engineering
Hanyang University, SungdongGu, Seoul 133-791, KOREA

Abstract : A real time error compensation system which can compensate for the time-varying volumetric errors due to thermal errors is studied by monitoring the machine temperatures. Volumetric errors due to squareness errors and linear thermal expansions of slides are formulated through the HTM (homogeneous transformation matrix). Measuring and identification methods for principal components of 21 geometric errors and thermal errors are proposed. The time-varying volumetric errors are modeled as functions of position and temperature variation by using the least square method and the GMDH (group method of data handling) algorithm. The experimental results showed that the positioning accuracy along the diagonal axes was better than ±5μm, while the accuracy without compensation was greater than ±100μm. It is confirmed that the volumetric error model proposed in this study is effective for precision manufacturing using this RTVEC (real time volumetric error compensation) system under no-load conditions.

Keywords : GMDH algorithm, Least square method, Real time volumetric error compensation system , Time-varying volumetric error

1. Introduction

The performance of machine tools in terms of accuracy is defined by the error of the relative movement between the cutting tool and the ideal cutting point on a workpiece. For a 3-axis machine tool, this relative error is called the volumetric error and can vary widely over the workpiece due to geometric errors and time varying thermal changes of machine tools. Peklenik remarked that thermal errors could comprise 40-70 percent of the workpiece error in precision machining.[1] Therefore, there have been extensive researches on formulation and compensation for the thermal error of machine tools. In this paper, identification of principal components of the time-varying volumetric errors due to thermal errors and an error compensation system which can compensate for them by monitoring the machine temperatures are studied.

2. Identification of thermal deformation

2.1 Thermal error model

In general, machine tools are built by the combination of fixed links and prismatic joints. These components comprise a closed chain between the tool contact point and the workpiece. The HTM method [2] offers an effective approach to the ideal thermal error model. Let's consider the case of a solid link. With a translational vector $\{a, b, c, 1\}^T$, the shape error matrix across the ideal link is given by

$$\mathbf{T}_{ideal} = \begin{bmatrix} 1 & 0 & 0 & a \\ 0 & 1 & 0 & b \\ 0 & 0 & 1 & c \\ 0 & 0 & 0 & 1 \end{bmatrix} \tag{1}$$

where, a, b and c are dimensions along each axis

In practice, a rigid body may have three rotational $\{\gamma^s, \beta^s, \alpha^s\}$ and three translational $\{\delta a, \delta b, \delta c\}$ error components along the reference coordinate axes. Under the assumption of small errors, the resultant HTM across the actual link with respect to its ideal position is given by

$$\mathbf{T}_{actual} = \begin{bmatrix} 1 & -\alpha^s(t) & \beta^s(t) & a+\delta a(t) \\ \alpha^s(t) & 1 & -\gamma^s(t) & b+\delta b(t) \\ -\beta^s(t) & \gamma^s(t) & 1 & c+\delta c(t) \\ 0 & 0 & 0 & 1 \end{bmatrix} \tag{2}$$

For a linear slide, errors are generated as functions of position along the joint axis. Angular errors along the moving axis cause straightness errors in perpendicular directions. Under the assumption of small errors, the resultant joint error matrix of the joint of X axis is

$$\Phi_{actual} = \begin{bmatrix} 1 & -\alpha(x,t) & \beta(x,t) & x+P(x,t) \\ \alpha(x,t) & 1 & -\gamma(x,t) & Q(x,t) \\ -\beta(x,t) & \gamma(x,t) & 1 & R(x,t) \\ 0 & 0 & 0 & 1 \end{bmatrix} \tag{3}$$

where, $\gamma(x,t), \beta(x,t)$ and $\alpha(x,t)$ are angular errors, $P(x,t)$ is the positioning error, and $Q(x,t)$ and $R(x,t)$ are straightness errors in Y and Z directions, respectively.

Fig. 1 shows the machining center with three axes. 8 coordinate frames are defined to derive a position vector representing a cutting point by using the HTM. The whole machine tool can be modeled as a kinematic chain with several links connected in series by prismatic joints as shown in Fig. 2.

For shape error matrices, it is assumed as follows: 1) only the thermal expansion along Z axis occurs in the spindle system because it has been designed with the consideration of thermal symmetry, 2) all of error components are neglected in the column because distance between CS3 and CS4 is very short, 3) only the thermal expansion along X axis occurs in the saddle, and 4) all of error components are neglected in the workpiece.

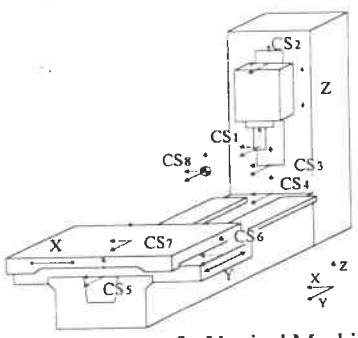

Fig. 1 Coordinate Systems of a Vertical Machining Center

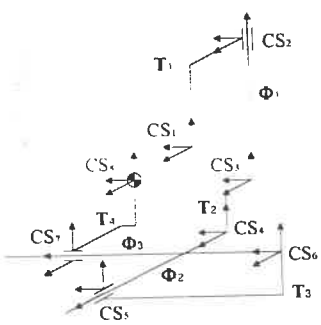

Fig. 2 Kinematic chains for a Vertical Machining Center

According to the previous studies, magnitudes of straightness and angular errors are smaller than those of positioning errors and squareness errors.[3] So, for the joint error matrices, only the latter are considered. A positioning error can be divided into a static positioning error and a thermal expansion along a axis. It is assumed that the former has been calibrated by a pitch error compensation and that the latter is linear along the axis.

To obtain an expression for the complete error matrix, a point in the workpiece coordinate system is expressed in the spindle coordinate system as follows:

$$\mathbf{r}_{s,actual} = \mathbf{r}_{s,ideal} = \mathbf{0} \tag{4}$$

$$\mathbf{r}_{s,actual} = \mathbf{H}_{actual}\{\mathbf{r}_t + \mathbf{e}\} \tag{5}$$

$$\mathbf{r}_{s,ideal} = \mathbf{H}_{ideal}\mathbf{r}_t \tag{6}$$

$$\mathbf{H} = {}^1\mathbf{T}_2\,{}^2\mathbf{\Phi}_3\,{}^3\mathbf{T}_4\,{}^4\mathbf{\Phi}_5\,{}^5\mathbf{T}_6\,{}^6\mathbf{\Phi}_7\,{}^7\mathbf{T}_8 \tag{7}$$

The relative error representing positioning errors between the tool and the workpiece becomes Eq. (9). The relative errors in 3 axes are given as Eq. (10)-(12).

$$\mathbf{r}_t = \mathbf{H}_{ideal}^{-1}\mathbf{0} \tag{8}$$

$$\mathbf{e} = \mathbf{H}_{actual}^{-1}\mathbf{0} - \mathbf{r}_t \tag{9}$$

$$e_x = -P_x x - \delta a_3 - S_{zx} z \tag{10}$$

$$e_y = -P_y y - S_{xy} x + S_{yz} z \tag{11}$$

$$e_z = -P_z z - \delta c_1 \tag{12}$$

2.2 Identification of error coefficients

In the previous error synthesis approaches, the distortion of individual machine elements is measured separately and the resultant error of the cutting edge is calculated by analyzing these error sources.[4] Because many thermal errors have to be measured separately in the previous complicated error model, the previous method not only repeats the tedious and sophisticated thermal testing tasks but also neglects the thermal interaction between error sources.

The workspace-measurement approach, on the other hand, is to measure the resultant thermal errors of the cutting edge directly at different slide positions.[4] Its disadvantage is that it is difficult to analyze machine error sources form the measured data.

In this paper, a simple and economic method, which combines the advantages of two approaches, is proposed from the simple error model derived above.

2.2.1 Identification by least square method

Positions are measured periodically from 5 gap sensors fixed on the table with the spindle rotating and the feed drive moving. The 5 DOF errors are acquired from the measured data by using geometric relations of the position of gap sensors. Therefore, 3 translational errors {ex, ey, ez} and 2 squarenesses {Szx, Syz} of Eq. (10) and (11) are directly identified on a position. This process is applied on the other positions and then the 5 DOF errors are acquired in the same way. By using least square method with the measurement data and error components acquired above, the rest error components, e.g., in case of error in X direction, can be identified through following equations.

$$e_x + S_{zx} z = \begin{bmatrix} -P_x & 0 & 0 & -\delta a_3 \end{bmatrix} \begin{bmatrix} x & y & z & 1 \end{bmatrix}^T \quad (13)$$

$$e_x = \Theta_x^T \mathbf{p} \quad (14)$$

$$\hat{\Theta}_x = \left(\mathbf{P}^T \mathbf{P}\right)^{-1} \mathbf{P}^T \mathbf{e}_x \quad (15)$$

where, $\mathbf{p}$ is the homogeneous position vector and matrix $\mathbf{P}$ is $\begin{bmatrix} \mathbf{p}_1^T & \mathbf{p}_2^T & \cdots & \mathbf{p}_n^T \end{bmatrix}^T$.

2.2.2 Identification by GMDH

Since the error coefficients which were identified by the least square method are varying with time according to the thermal environments, the dynamic modeling of error components is required. In this paper, the error coefficients are modeled as functions of temperature variations which are synchronized with the displacement data measured through 5 gap sensors. A GMDH algorithm is used for the modeling. The GMDH algorithm can describe nonlinear relations between temperatures and error components with a few input numbers and carry out automatically the selections of optimal input variables and structures of a model.[5] Through the least square method and the GMDH algorithm, the relative errors are modeled as time-varying volumetric errors which are the functions of temperature variations and positions as given in Eq. (16).

$$\mathbf{E}(\mathbf{p},\Delta T) = \begin{bmatrix} -P_x(\Delta T) & 0 & -S_{zx}(\Delta T) & -\delta a_3(\Delta T) \\ -S_{xy}(\Delta T) & -P_y(\Delta T) & S_{yz}(\Delta T) & 0 \\ 0 & 0 & -P_z(\Delta T) & -\delta c_1(\Delta T) \end{bmatrix} \begin{bmatrix} x \\ y \\ z \\ 1 \end{bmatrix} \quad (16)$$

3. Experiment and results

A vertical machining center, whose stroke is 760×430×500mm, is used for experiments. The experimental setup to measure the thermal displacement and temperature is shown in Fig. 3. The measurement is done on a position and then on the other positions by turns under the same operating conditions. The rotation speed of spindle is 3000rpm and the feed rates are equally 3000mm/min in 3 axes.

The results of the identification of thermal error components are shown in Fig. 4 and the error maps, which are acquired by substituting the results to equations (10)-(12), in Fig. 5.

4. Compensatory control of volumetric errors

Because the magnitude of squareness errors are as much as that of thermal drifts of the machine origin and positioning errors from linear expansions, the compensation is not complete with just the origin shift and the pitch error compensation. Therefore, the RTVEC system is to be developed.

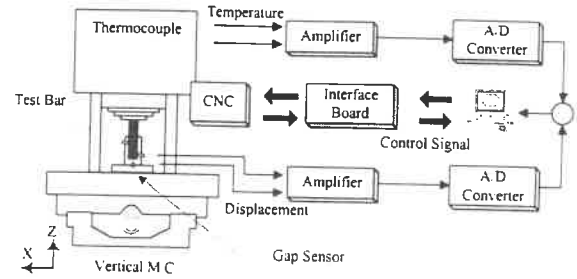

Fig. 3 Schematic diagram of experimental setup

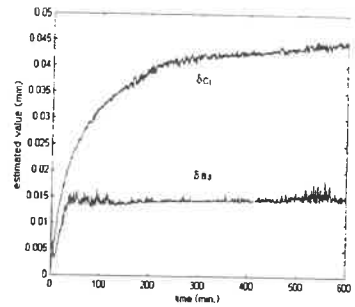

(a) Thermal expansions of links

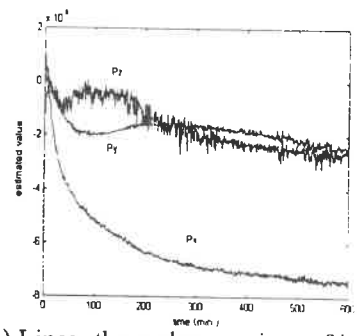

(b) Linear thermal expansions of joint

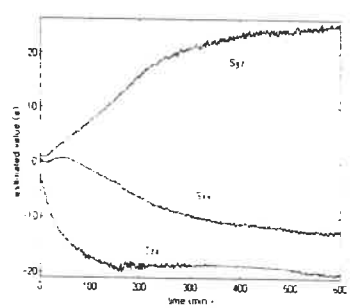

(c) Squareness

Fig. 4 The estimated error components

Fig. 6 shows configuration of the RTVEC system which consists of a real time position measuring module and a error calculator and compensator. The positions of feed drive systems are acquired from encoder signals and the temperatures are measured from thermocouples. The compensation signals are produced from the model with the measurement data

and sent to the CNC through the function of MPG interrupt which is the basic function of CNC. Therefore, the RTVEC system can be applied to the commercial machine tools without a large-scale modification.

The compensation results can be inferred by measuring six degrees of freedom errors for each axis and squareness of X, Y, and Z to each other. This is a time-consuming process. Thus, a quick assessment of volumetric errors has to be verified to confirm compensation results. In this paper, the HP 10768A diagonal measurement kit is used for the verification. It enables implementation of ANSI/ASME standards B.5 for machine tools. Fig. 7 shows the raw data without compensation and Fig. 8 shows the diagonal measurement with compensation. From the results, the diagonal errors reduced from 100μm to ±5μm.

5. Conclusion

In this paper, a real time volumetric error compensation system has been developed. Identification of principal components of the time-varying volumetric errors were measured and identified. From the results, the time-varying volumetric errors were modeled as functions of position and temperature variation by using the least square method and the GMDH algorithm. Experimental results show that the positioning accuracy along the diagonal axis is better than ±5μm, while the accuracy without compensation is about ±100μm. The test shows that the volumetric error model proposed in this study was effective for precision manufacturing using this RTVEC system under no-load conditions.

References

1. J. Bryan, 1990, "International Status of Thermal Error Research(1990)", Annals of the CIRP, Vol. 39, No. 2, pp. 645-656.
2. P. M. Ferreria and C. R. Liu, 1986, "An Analytical Quadratic Model for the Geometric Error of a Machine Tool", Journal of Manufacturing Systems, Vol. 5, No. 1, pp. 51-62.
3. E. S. Lee, S. H. Suh and J. W. Shon, 1998, "A Comprehensive Method for Calibration of Volumetric Positioning Accuracy of CNC-Machines", Journal of Advanced Manufacturing Technology, Vol. 14, pp. 43-49.
4. J. S. Chen and G. Chiou, 1995, "Quick Testing and Modeling of Thermally-induced Errors of CNC Machine Tools", Journal of Machine Tools and Manufacture, Vol. 35, No. 7, pp. 1063-1074.
5. J. Y. Ahn and S. C. Chung, 1998, "Estimation of Thermal Deformation for the Machine Origin of Machining Centers using GMDH Algorithm", Transactions of the Korean Society of Mechanical Engineers(A), Vol. 22, No. 12, pp. 2126-2135. (in Korean)

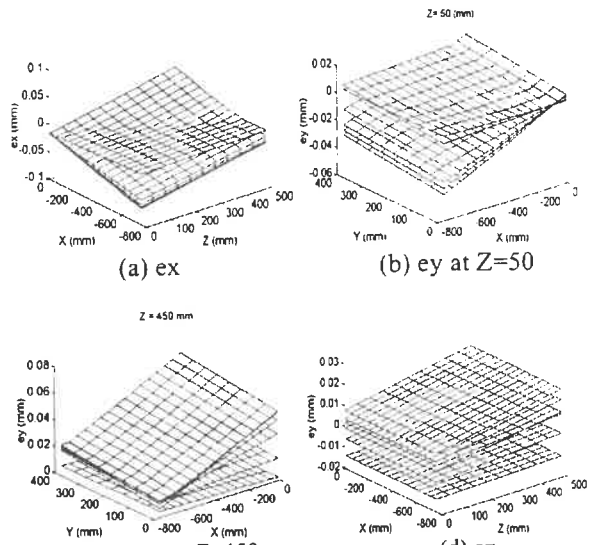

(a) ex (b) ey at Z=50

(c) ey at Z=450 (d) ez

Fig. 5 Error maps calculated by identified error components

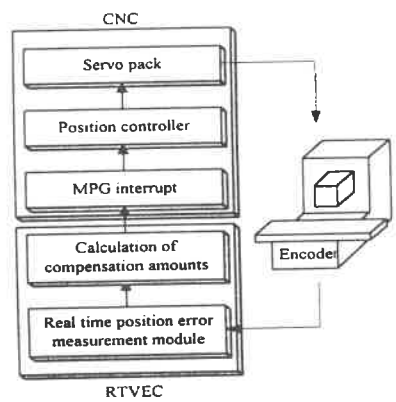

Fig. 6 Block diagram of RTVEC system

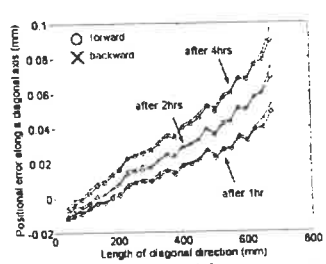

Fig. 7 Diagonal errors without compensation

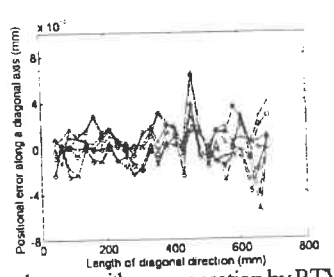

Fig. 8 Diagonal errors with compensation by RTVEC system

Laser Material-Removal Process as a Subject of Automatic Control

Evgueni V. Bordatchev, Suwas K. Nikumb
Integrated Manufacturing Technologies Institute, National Research Council of Canada
800 Collip Circle, London, Ontario, Canada N6G 4X8

Introduction

CNC-controlled laser machining of precision components is being used increasingly in modern industry. However, the laser machining system operator has to make a host of complex decisions, usually based on trial-and-error methods to set process control parameters. The laser-related parameters are laser power, focal position, frequency of the laser impulses, beam polarization and its mode structure, etc. Workpiece material and machine-related parameters are feed rate, focal spot overlap, etc. In addition to this, existing factors such as power fluctuations, intensity distribution, and thermal effects on optical components normally not controlled by the operator, also influence the machining process. In order to improve the reliability, tolerances and precision of laser machining, a closed-loop process control is required and utilized to compensate for the external and internal process disturbances, which essentially affect the final quality of the machined workpiece.

This paper deals with one of the important tasks in the analysis and the design of a control system by means of mathematical modelling of the laser material-removal process - a subject of automatic control. If we consider the process dynamics, the machining phenomena is a space-time interaction of the laser beam with workpiece material which results in the removal of a small quantity of material with each incident laser pulse. The quality of the machined workpiece depends on the control of fluctuations within the process parameters. The overall system approach ties together four main factors associated with the dynamic processes that play an important role during laser machining and influence the quality of the machined workpiece. These factors are (a) the kinematic and dynamic disturbances within the workpiece motion system, (b) the space-time fluctuations of the laser beam, (c) the laser-material interaction as a dynamic process, and (d) the forming of the workpiece surface as a dynamic process. The novel approach presented herein performs the dynamic analysis of a laser machining system for diagnostics, control and process optimization purposes.

Laser material-removal process - a "black box" approach

The general structure of a closed-loop control system can be represented as shown in Fig. 1, which consists of:

a) the controlled process, whose mathematical model describes a transformation of controlled variables into output variables
b) the controller, represented by a hardware/software system whose mathematical model is a control algorithm in view of transformation of input variables into controlled variables including the feedback variables
c) sensors, whose mathematical model represents a transformation of measured into feedback variables.

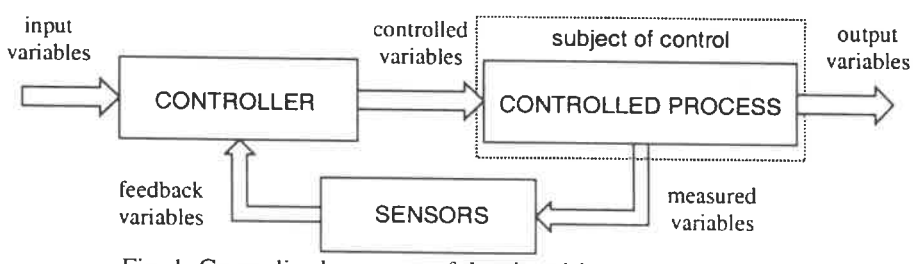

Fig. 1. Generalized structure of the closed-loop control system.

In view of the laser machining process, the controller represents the laser and CNC motion subsystems and provides the controlled variables. The controlled process box represents the laser material-removal process as a subject of automatic control. Based on this statement, the task of dynamic modelling of the controlled process consists of a mathematical description of the "black box" of the laser material-removal process as shown in Fig. 2. Here, the mathematical description represents the transformation of the controlled variables, such as parameters and characteristics associated with the laser beam and feed motions into output variables such as the geometrical features of the machined workpiece and its profile. A mathematical model can represent the transformation of these variables and predict or estimate the machined workpiece surface profile based on the dynamic behavior of the laser beam and the feed motions, and physical/mechanical/thermal properties of the machined material.

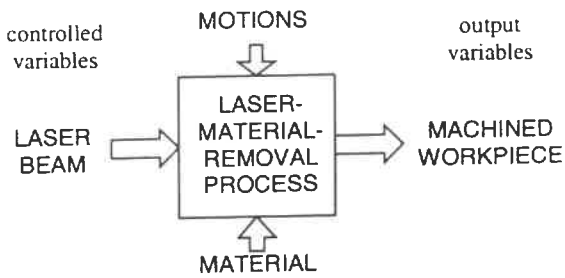

Fig. 2. "Black box" of the laser material-removal process.

Dynamic representation of the laser machining system

The laser machining system is a complex electro-optical-mechanical system consisting of:

- the laser/optics as a subsystem, which delivers the laser beam into the processing zone
- the workpiece motion subsystem which includes a base, electro-drives and translation stages to provide the feed motions.

The ideal laser machining system must provide adequate conformance of the laser beam focal spot into the workpiece surface in accordance with the predetermined tool path. However, laser machining experiments indicate that the geometric feature qualities of the machined workpiece are not only defined by the predetermined tool path but also influenced by the dynamic processes within the processing zone. Mainly, the following four dynamic processes must be considered.

The first process consists of kinematic (e.g., geometrical errors) and dynamic (e.g., frictional process) disturbances associated with the workpiece motion subsystem. A combination of these disturbances produce uneven feed motions and affects the synchronization with the individual laser beam impulses. These variations can be as high as 35% in the feed rate even for motion tables with air bearings.

The second process within the laser/optics subsystem is associated with the space-time fluctuations in the laser beam parameters and its characteristics, such as focal spot diameter, power density, mode structure, intensity distribution, frequency, polarization, etc. These inherent variations are due to imperfections within the laser, its control system, and the thermal gradients in the optical beam delivery system.

Laser-material interactions play an important role in the material removal process. Therefore, the formation of the workpiece profile must be considered as the ultimate result of the combined effect of all the dynamic processes involved in the interaction, including the laser/optics and feed motion subsystems, and the thermodynamic actions/changes in the processing zone. Based on this discussion, the dynamics of the laser-material interaction and the formation of the workpiece profile are respectively the third and the forth dynamic processes that influence the machined surface quality.

The laser-material interactions form a non-linear dynamic link between the laser beam and the machined workpiece. As a first approximation, this non-linear link can be described as a combination of two components. The first component that represents the linear properties of the laser-material interaction process is a dynamic operator. This operator mathematically describes the transformation of the laser beam into corresponding volume of material removal. We call this component the dynamic characteristic of the laser-material interaction process. The second component corresponds to the process noise in view of space-time random process, which symbolizes non-linear singularities of the laser-material interaction process and forms an additional component.

The final source is the dynamics of the workpiece profile formation. In reality the dimensional profile of the laser beam focal spot does not conform to the workpiece profile due to the space-time non-stationary thermodynamic process disturbances in the processing zone. These thermodynamic disturbances modify the physical/chemical properties of the workpiece material that leads to changes in the machined area.

Generalized dynamic modelling

A schematic representation of the laser machining system is shown in Fig. 3 and the laser material-removal process dynamics is illustrated in Fig. 4. The generalized mathematical model can be expressed as follows:

$$\begin{cases} \dfrac{d\mathbf{r}(t)}{dt} = \Phi\left(\mathbf{r}(t), \mathbf{v}(t), \mathbf{f}(t), \mathbf{v}^*(t), \mathbf{f}^*(t)\right) \\ \mathbf{R}(t) = \Psi\left(\mathbf{r}(t), \mathbf{v}(t), \mathbf{u}(t), \mathbf{f}(t), \mathbf{v}^*(t), \mathbf{u}^*(t), \mathbf{f}^*(t), \mathbf{q}^*(t)\right) \end{cases} \tag{1}$$

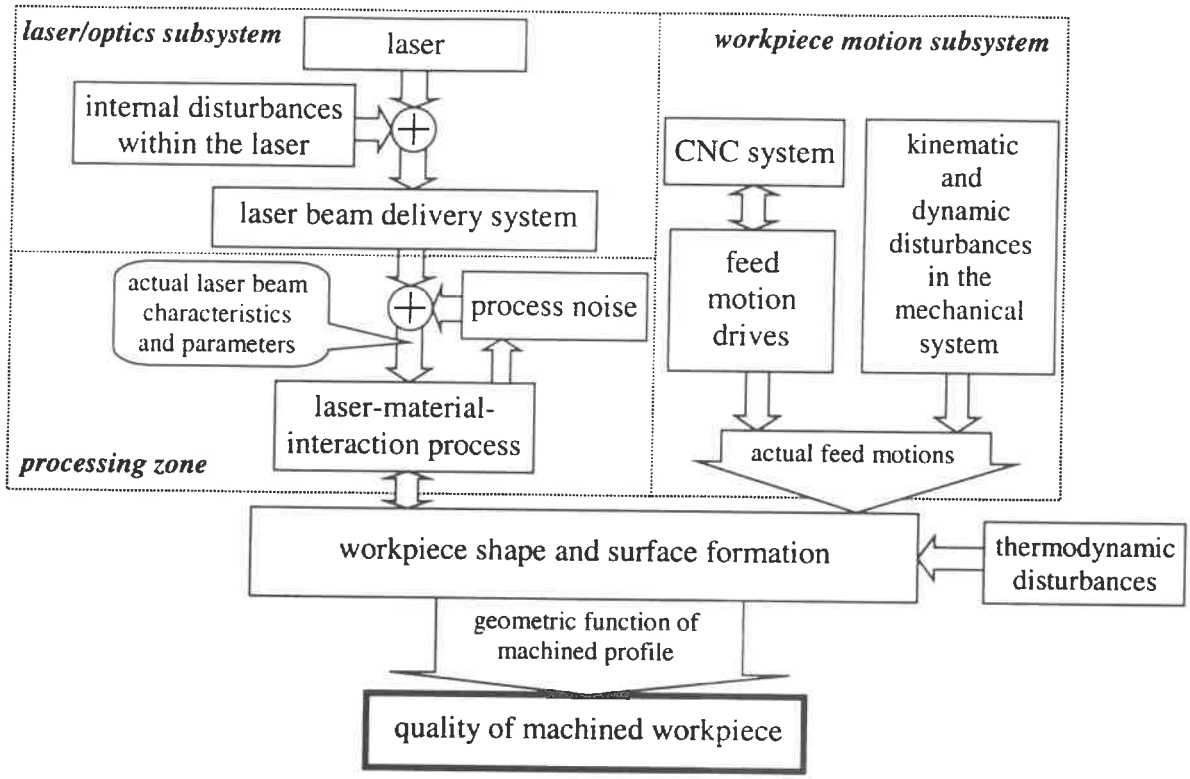

Fig. 3. Schematic representation of the laser machining system.

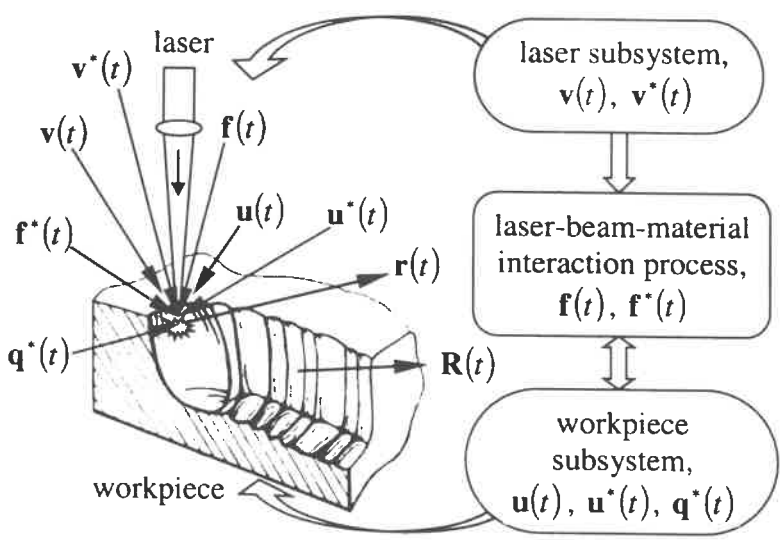

Fig. 4. Schematic representation of the laser material-removal process dynamics.

where $\mathbf{r}(t)$ is the vector for the volume of material removed and is defined in terms of the standard machine-tool coordinate system (X, Y, Z). The components of this vector $\mathbf{r}(t)$ describe material removal in time and space during simultaneous interaction of laser beam impulses and feed motions. $\mathbf{R}(t)$ is the vector for the final quality of the machined workpiece, which includes the dimensional features, surface roughness, hardness, etc. $\mathbf{v}(t)$ is the control vector for the laser/optics subsystem having several variables as its components, viz. focal spot diameter, power density, intensity distribution, mode structure, pulse width, frequency, etc. $\mathbf{v}^*(t)$ is the vector for the

internal disturbances in the laser/optics subsystem and represents the random components of $\mathbf{v}(t)$ elements. $\mathbf{u}(t)$ is the control vector for the workpiece motion system having its own variables as its components, viz. machining tool path, feed rate, spot overlap, etc. $\mathbf{u}^*(t)$ is the vector for kinematic and dynamic disturbances within the workpiece motion subsystem and represents random components of $\mathbf{u}(t)$ elements. $\mathbf{f}(t)$ is the vector for parameters and characteristics associated with the beam in the laser-material interaction zone and can not be measured in reality. $\mathbf{f}^*(t)$ is the vector for process noise, which represents an additional component for $\mathbf{v}^*(t)$ affecting the laser beam characteristics inside the processing zone. $\mathbf{q}^*(t)$ is the vector for thermodynamic disturbances in the interaction zone and finally influences the machined surface quality. $\Phi(\cdot)$ and $\Psi(\cdot)$ are functions of the vector variables.

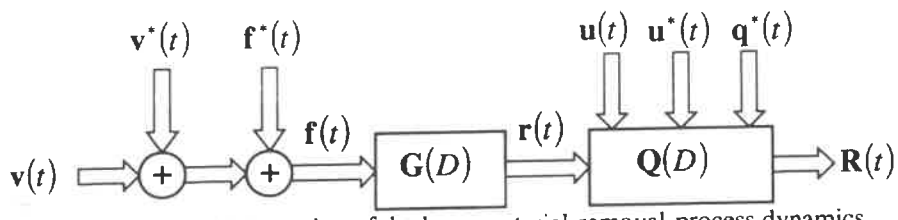

Fig. 5. System representation of the laser-material-removal-process dynamics.

The generalized mathematical model (1) of the laser machining system's dynamic structure is shown in Fig. 5 and is expressed in terms of linear approximation as follows:

$$\begin{cases} \mathbf{f}(t) = \mathbf{v}(t) + \mathbf{v}^*(t) + \mathbf{f}^*(t) \\ \mathbf{r}(t) = \mathbf{G}(D)\mathbf{f}(t) \\ \mathbf{R}(t) = \mathbf{Q}(D, \mathbf{u}(t), \mathbf{u}^*(t), \mathbf{q}^*(t))\mathbf{r}(t) \end{cases} \tag{2}$$

where $\mathbf{G}(D)$ is the transfer-function matrix of the laser-material interaction process which transforms the vector of the actual laser beam $\mathbf{f}(t)$ into corresponding volume of the material removal $\mathbf{r}(t)$; $\mathbf{Q}(D)$ is the transfer-function matrix of the workpiece profile formation as a dynamic process, which transforms the actual material removal volume $\mathbf{r}(t)$ into the final quality of the machined workpiece $\mathbf{R}(t)$ taking into account the control vector of the motion system $\mathbf{u}(t)$, kinematic and dynamic disturbances $\mathbf{u}^*(t)$, and thermodynamic disturbances $\mathbf{q}^*(t)$; $D = d/dt$ is the differential operator.

Conclusions

A systematic approach for the dynamic modelling of the laser material-removal process has been presented. The concept is based on the laser-material interaction as a dynamic process. The in-process disturbances within the laser/optics and workpiece-motion subsystems, the fluctuations associated with the process parameters and the thermodynamic disturbances have been included.

Introduced analysis lays a foundation for performing the following tasks:

- dynamic modelling and parametric identification of the transfer function matrix of the laser-material interaction process $\mathbf{G}(D)$
- dynamic modelling and parametric identification of the transfer function matrix of the workpiece profile and surface formation $\mathbf{Q}(D)$
- modelling/estimation of the statistical characteristics of the disturbances within the laser/optics $\mathbf{v}^*(t)$ and the workpiece-motion $\mathbf{u}^*(t)$ subsystems, the process noise $\mathbf{f}^*(t)$ and thermodynamic disturbances $\mathbf{q}^*(t)$

Acknowledgement

The authors greatly appreciate the support of Mr. Gavin McGregor, Director of Research, IMTI, in this work.

Micro-Displacement/Capacitance Measurement and Control System with Phase-Locked Loop

S. B. Chang, Bruce C. S. Chou and J. J. Chang

Precision Instrument Development Center, National Science Council,
20 R&D Road VI, Science Based Industrial Park, Hsinchu 300, Taiwan, R.O.C.

Keywords: capacitance measurement, micro-displacement servo control, MEMS, phase-locked loop

1. Introduction

Phase-locked loop□PLL□is a very popular and cheap tool for pulse generation with almost constant frequency. On the other hand, a user-friendly and cheap tool for micro-displacement/capacitance servo control system still lacks in the market, although it is increasing the need in MEMS (micro-electro-mechanical system) industries. In this article, a cheap□for a micro capacitance/displacement scan movement, without the need of A/D and D/A converters □and stable micro-displacement/capacitance measurement and control system is proposed. Due to the low cost, the high sensitivity between the capacitance of varactor diode and the output pulse frequency [1] and the fast and stable frequency servo capability, PLL is very suitable for us to use its property as controlling micro capacitance/displacement in MEMS or micro-positioning system. In the meantime, as the progress in the microfabrication and micromachining technology, micro capacitance/displacement detection and control system is, more than often, used in many MEMS such as in the micro accelemeter [2], micro pressure sensor [3], and micro flow sensor [4]. In this article, a PLL based micro displacement/capacitance measurement and control system is proposed. For use in a simple scan movement, no A/D and D/A converters are needed and it still can provide capacitance/displacement scan movement with high resolution. And if the properties of the electronic components in the PLL remain close to their nominal values, the scan movement can be achieved with good accuracy. Therefore, this overall system can be made cheaper than a common one. As shown in the simulations and experimental results, the fast and stable servo capability of the proposed system means that it has great potential in MEMS industries.

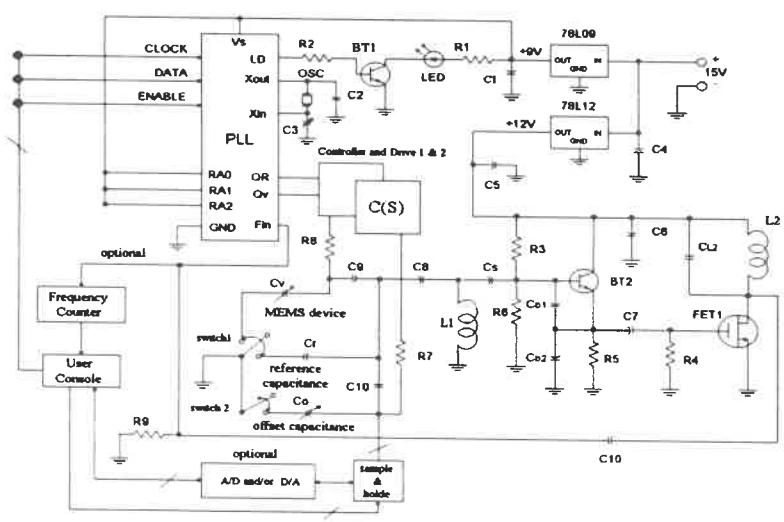

Fig.1 PLL based micro displacement/capacitance measurement and control system.

2. System Configuration

The proposed PLL based micro capacitance/displacement control system is shown in Fig.1. A NPC PLL0305A [5] is adopted as the main PLL IC Chip, and it can be operated blow 50 MHz under a normal condition. In the PLL frequency servo loop shown in Fig.1, the Clapp voltage controlled oscillator (VCO [6]) is adopted for its good stability against temperature variation. With the proper setting of peripheral electronic components, the oscillation frequency of the Clapp VCO (when the switch1 is closed to the side of the MEMS and the switch2 is open) is obtained as follows by neglecting the influences of the other coupling resistors, inductors and capacitors.

$$f = \frac{1}{2\pi}\left[L_1\left(C_v + \frac{1}{1/C_s + 1/C_{b1} + 1/C_{b2}}\right)\right]^{-1/2} \quad \dots (1)$$

where f is the oscillation frequency, L_1 is the inductance value of the coil, C_v is the capacitance value of the MEMS device such as a comb structure [2] or a diaphragm [3-4] in MEMS, and C_s , C_{b1} and C_{b2} are the capacitance values of the matching capacitors.

3. Frequency Servo Control of PLL for MEMS

As revealed in [2]~[4], the mechanisms in MEMS such as a comb drive or a diaphragm have the same property as a varactor diode that the capacitance value between the electrodes varies with the voltage difference of the electrodes. Therefore, a MEMS with the same property as the varactor diode can be used in a frequency servo PLL instead of a varactor diode. That is, as shown in equation (1), the frequency servo capability of a PLL can be regarded as the capacitance servo capability of a MEMS device if the electrical properties of all the electronic components used in the PLL remain constant. Therefore, by changing the reference frequency of the PLL, the capacitance/displacement of a MEMS device can be controlled near to its destination value. However, the controller used in the proposed PLL with a MEMS device as the capacitance tuning component is not the same as the controller for the PLL with a varactor diode inside [7], because the dynamics in a MEMS device is different from a varactor diode. As shown in Fig.2, we use a common electrostatic force driven diaphragm structure as an example of the MEMS device in the PLL based servo system. Because for the electrostatic force driven devices the capacitance value between electrodes varies as the voltage difference as a varactor diode as depicted in [8-9].

The linearized frequency servo system with PLL for MEMS device deflection control at its equilibrium point□ X, V □=□ $0, V_o$ □is as shown in Fig. 3. To avoid noise excitation due to on-off nonlinearity of PLL, we adopt an PI (proportional and integral) controller with negative gain as in C(S), i.e.,

$$C(S) = -\frac{k_p S + k_i}{S} \quad \dots (2)$$

And we denote k_1 as

$$k_1 = k_o \cdot \varepsilon_a \, A \, X_o^{-2} \cdot \frac{L_1}{4\pi}\left[L_1\left(C_{vo} + \frac{1}{1/C_s + 1/C_{b1} + 1/C_{b2}}\right)\right]^{-3/2} \quad \dots (3)$$

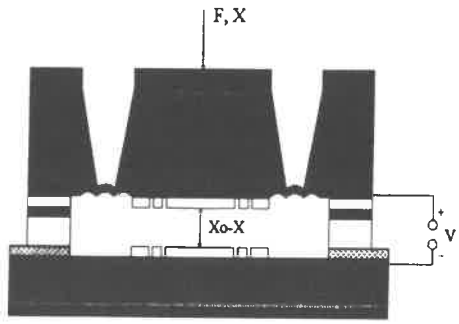

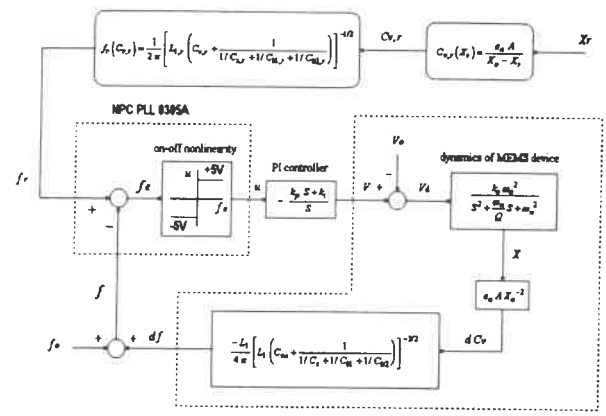

Clapp voltage controlled oscillator with a MEMS device instead of the varactor diode

Fig. 2 A diaphragm structure used as a MEMS device.

Fig.3 Block diagram of a capacitance control system for a MEMS device with PPL.

The describing function of the on-off element [10] is

$$N = \frac{4\,V_M}{\pi\,F_e} \quad \ldots (4)$$

where F_e is the amplitude of input sinusoidal signal □ in our case it is the amplitude of frequency error f_e □and V_M is the on-off output signal level and V_M is 5 Volt for PLL0305A.

Thus, this will cause a steady state error as

$$f_{e,\,ss} \le f_{e,\max} \quad \ldots (5)$$

$$\text{where } f_{e,\max} = \frac{4\,V_M\,k_1\,k_i\,Q}{\pi\,\omega_n}$$

4. Experiments and Simulations

The electric components with their default values as L_1=0.8μH, C_s=5pF, C_{b1}=47pF, and C_{b2}=68pF are used in our experiments. And when we use reference capacitor C_{r1}=8pF, the reference frequency f_{r1} measured by the frequency counter is 45.721MHz. Similarly, with the reference capacitor C_{r2}=16pF, the reference frequency f_{r2} measured by the frequency counter is 37.009MHz. Therefore, the value of $1/(1/C_s + 1/C_{b1} + 1/C_{b2})$ is 7.2028pF and the inductance of L_1 is about 0.7971μH. The default value of $1/(1/C_s + 1/C_{b1} + 1/C_{b2})$ is about 4.2376pF. Therefore, the frequency to capacitance sensitivity of the Clapp VCO is about 1.5037MHz/pF. And then when a varactor diode is used in the PLL instead of the reference capacitor and close the PLL with reference frequency set as around 45 MHz, the output frequency servos at steady state error within 1 kHz. That is 1fF measurement and control resolution is achieved if the properties of the electric components remain constant during operation. And thus we measure many reference capacitors with capacitive value as 5~20pF and tolerances within 5 %, the measurement error remains within 1pF. It shows good measurement accuracy is achieved when the capacitive value of the measured element is very small. The simulation results with reference displacement as 100 nm of the PLL based micro displacement servo control of MEMS device as a diaphragm structure shown in Fig.3 are shown in the following figures Fig.4a~d.

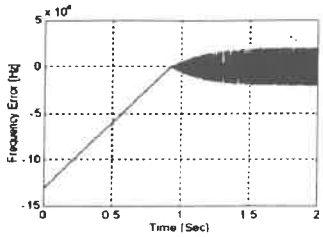

Fig.4a Frequency error v.s. time

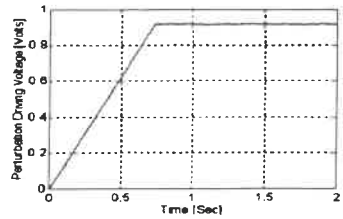

Fig.4b Perturbation driving voltage v.s. time

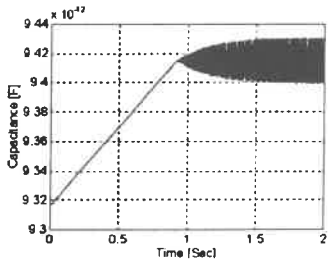

Fig.4c Capacitance between electrodes v.s.time

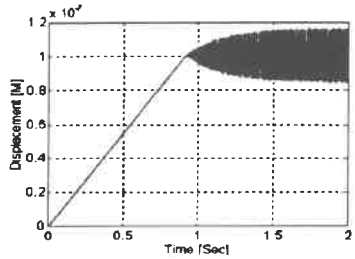

Fig.4d Displacement v.s. time

5. Application and Conclusions

The proposed PLL based micro capacitance/displacement measurement and control system can be used in many MEMS device such as in micro pressure sensor, micro flow sensor, micro accelerometer and micro spectrometer system. Due to its low cost nature □no any A/D and D/A converters are needed for a simple scan movement □, it has great potential in MEMS industries for batch production. And the measurement resolution can be raised with more higher oscillation frequency of VCO. In our experiments the oscillation frequency of around 45MHz is used and capacitance measurement resolution of 1fF can be achieved if properties of all the electric components used in Clapp VCO remains constant. And the simulation results of displacement servo control for a diaphragm structure shows the proposed PLL can provide 20 nm positioning accuracy. It shows a cheap and accurate displacement servo control system can be made with the proposed PLL based system. However, to assure the electric components used in the PLL have almost constant properties, environment conditions such as temperature should be controlled near constant during operation. Based on the proposed servo system, we are now developing low cost MEMS devices such as micro pressure sensors and micro spectrometers.

References

1. N. U. Ahmed and M. Aboud, "Optimum Design of a Feedback Controller for a Phase-Locked Loop," *IEEE Trans. on Communications*, Vol.23, No.12, pp.1521-1524, 1975.
2. A. Selvakumar and K. Najafi, "A High-Sensitivity Z-Axis Capacitive Silicon Microaccelerometer with a Torsional Suspension," *IEEE Jour. of MicroElectromechanical Systems*, Vol.7, No.2, pp.192-200, 1998.
3. D. C. Catling, "High-Sensitivity Silicon Capacitive Sensors for Measuring Medium-Vacuum Gas Pressures," *Sensors and Actuators*, A64, pp.157-164, 1998.
4. O. Berberig, K. Nottmeyer, J. Mizuno, Y. Kanai, and T. Kobayashi, "The Plandtl Micro Flow Sensor (PMFS) : A Novel Silicon Diaphragm Capacitive Sensor for Flow Velocity Measurement," International Conference on Solid-State Sensors and Actuators, Digest of Technical Papers, Vol.2, pp.155-158, 1997.
5. NPC Frequency Synthesizer PLL ICs, User's Manual, 1997.
6. R. R. Cordel, W.G. Garrett, "A High Stable VCO for Application in Monolithic Phase Locked Loop," *IEEE Jour. on Solid State Circuits*, Vol.10, No.6, pp.480-485, 1975.
7. Motorola Inc., "Phase Locked Loop Systems," 1973.
8. R. Legtenberg, A. W. Groeneveld, and M. Elwenspoek, "Comb-drive actuators for large displacements," *Jour. Micromech. Microeng.* Vol.6, pp.320-329, 1996.
9. D. A. Horsley, R. Horowitz, and A. P. Pisano, "Microfabricated Electrostatic Actuators for Hard Disk Drives," *IEEE/ASME Trans. on Mechatronics*, Vol.3, No.3, pp.175-183, 1998.
10. K. Ogata, *Modern Control Engineering*, Englewood Cliffs NJ : Prentice-Hall, 1990.

Implementing Geometric Error Compensation Software in a PC-Based Controller

Van B. Graves
Oak Ridge National Laboratory, Oak Ridge, TN

Introduction

In an effort to modernize its production manufacturing equipment, the Department of Energy's Y-12 Plant in Oak Ridge, TN is investigating replacing the existing proprietary CNC machine tool controllers with new controllers based on personal computer (PC) technologies. It is now possible to buy machine tool controllers that utilize PC hardware with common plug-in motion control cards that offer functionality equivalent to the 1980s-vintage controllers currently being used.

One of the controllers being considered is developed by Manufacturing Data Systems, Inc.® (MDSI) of Ann Arbor, Michigan. A characteristic that sets it apart from other PC-based controllers is that it utilizes no motion control cards. It is a software-based controller, which means that the motion control servo loop is closed by the PC's central processing unit. The controller software is called OpenCNC®, and it currently runs under two operating systems: Windows NT® from Microsoft® Corporation and QNX® from QNX Software Systems Ltd®.

Project Description

An area of particular interest to the Y-12 Plant is OpenCNC's ability to support software compensation of machine tool errors other than the lead-screw compensation currently implemented. A joint project was initiated between Y-12 and MDSI to implement within the OpenCNC controller a software architecture capable of compensating for geometric errors in two- and three-axis machine tools. The software was named the Geometric Error Compensation System (GECS), and the initial implementation was on an Excello 921 two-axis T-base lathe. These lathes were designed and built specifically for Y-12 in the 1960s. A computer model of this lathe is shown in Figure 1.

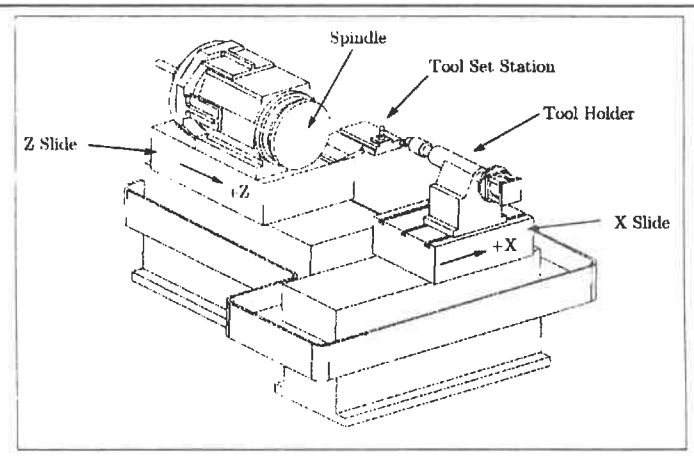

Figure 1. Excello 921 computer model

Based on a literature review of previous work in the area of geometric error compensation, examples of which are given by Hocken [1] and Donmez [2], previous implementations either utilized prototype controllers, or they required the use of external computers to perform the compensation calculations and special hardware to intercept the axis position feedback signals and to interject the compensation signal. This project may be the first in which the compensation system was totally implemented in software.

Geometric Error Model

As detailed by Slocum [3], an element of a machine tool (slide, tool, workpiece, base, turret, etc.) can be represented by a homogeneous transformation matrix (HTM). The HTM gives the position and orientation of that element relative to another element of the machine that has its own HTM assigned. Starting from the HTM of the machine base, one can create a series of HTMs that traverse the elements of the machine tool to either the cutting tool or to the workpiece. This gives the location of both the workpiece and the tool in the same base reference system, as shown in Figure 2.

In the ideal case the HTM of the workpiece relative to some reference frame R, ${}^{R}T_{work}$, and the HTM of the tool, ${}^{R}T_{tool}$, would coincide. However, in the actual cutting case, due to the inaccuracies of the system, the two HTMs are not identical. To make ${}^{R}T_{tool}$ coincide with ${}^{R}T_{work}$ one can use another HTM, referred to as E_{rel}, which quantifies the relative error between the tool and workpiece, as shown by the following formula:

$$ {}^{R}\mathbf{T}_{tool} = {}^{R}\mathbf{T}_{work}\mathbf{E}_{rel} \qquad (1) $$

The homogeneous transformation matrix E_{rel}, is thus given by

$$ \mathbf{E}_{rel} = {}^{R}\mathbf{T}_{work}^{-1}\,{}^{R}\mathbf{T}_{tool} \qquad (2) $$

where ${}^{R}\mathbf{T}_{work}^{-1}$ represents the inverse of the homogeneous transformation matrix.

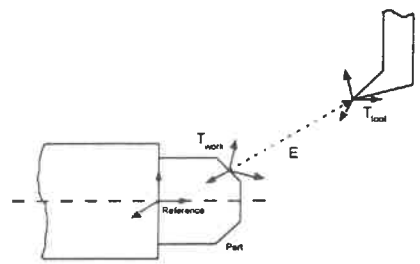

Figure 2. Relationship between cutting tool and workpiece

The relative error HTM E_{rel} quantifies the changes in position and orientation required to cause ${}^{R}T_{tool}$ to coincide with ${}^{R}T_{work}$. Because the contact between the tool and the workpiece is assumed to be point contact, the orientation of the tool, represented by the rotation matrix in E_{rel}, is of no concern. The position vector **P** in E_{rel} represents the translations relative to the tool's coordinate frame that must be made to the tool so that it is properly located on the workpiece.

Excello Error Model

The machine model used in the development of the error equations for the Excello lathe is shown in Figure 3, which depicts a plan view of the lathe. All the coordinate systems (HTMs) shown are at spindle center height. The HTMs are aligned so that the positive direction of the coordinate axes corresponds to positive displacement of the machine slides. The direction of positive rotation is also shown and is needed for compensation of angular errors. In Figure 3 and in the error equation development, uppercase Roman letters represent constant terms while lowercase Roman letters represent position variables, and Greek letters represent geometric errors.

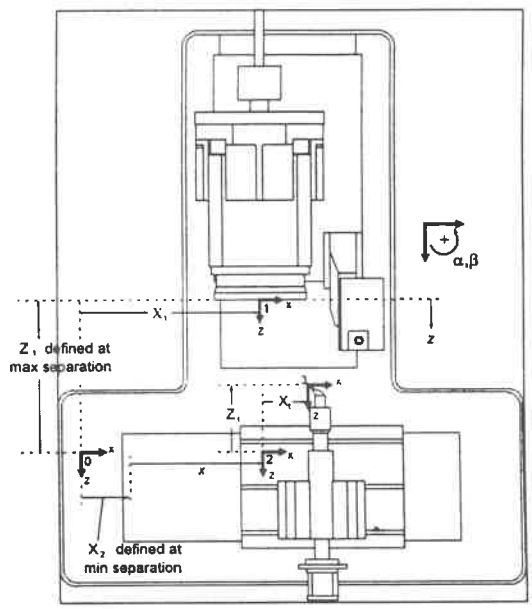

Figure 3. Excello error model diagram

HTM 0 is the base reference system used in the model, and its location does not change. HTM 1 is attached to the spindle face and moves with the Z-slide. HTM 2 is attached to the table of the X-slide and moves with it. The X-axes of HTM 0 and HTM 2 are aligned, so there is no Z offset between them. HTM 3 is defined at the tip of the cutting tool with constant offsets from HTM 2 of X_t and Z_t.

The error equations for a given machine tool are created using Equation (2). Before applying this equation to the Excello lathe, the HTMs for ${}^{R}T_{work}$ and ${}^{R}T_{tool}$ were developed as follows.

$$ {}^{R}\mathbf{T}_{work} = {}^{0}\mathbf{T}_{1} = \left[\begin{array}{ccc|c} 1 & 0 & \varepsilon_y(z) & X_1 + \delta_x(z) + \beta \cdot z \\ 0 & 1 & 0 & 0 \\ -\varepsilon_y(z) & 0 & 1 & Z_1 + z + \delta_z(z) \\ \hline 0 & 0 & 0 & 1 \end{array}\right] \qquad (3) $$

$$
{}^{R}T_{tool} = {}^{0}T_{2}\,{}^{2}T_{3} = \left[\begin{array}{ccc|c} 1 & 0 & \varepsilon_y(x) & X_2 + x + \delta_x(x) \\ 0 & 1 & 0 & 0 \\ -\varepsilon_y(x) & 0 & 1 & \delta_z(x) - \alpha \cdot x \\ \hline 0 & 0 & 0 & 1 \end{array}\right] \left[\begin{array}{ccc|c} 1 & 0 & 0 & X_t \\ 0 & 1 & 0 & 0 \\ 0 & 0 & 1 & Z_t \\ \hline 0 & 0 & 0 & 1 \end{array}\right] \tag{4}
$$

Term	Description	Term	Description
x, z	nominal positions of X- and Z-slides	$\delta_z(x)$, $\delta_x(z)$	straightness errors as functions of position
$\delta_x(x)$, $\delta_z(z)$	X- and Z-scale errors	α	perpendicularity error between X-slide and spindle
$\varepsilon_y(x)$, $\varepsilon_y(z)$	yaw errors as functions of position	β	parallelism error between Z-slide and spindle
X_1, Z_1, X_2, X_t, Z_t	offset constants		

Performing the mathematical operations given by Equation (2) produced expressions in *x* and *z* that described the position of the tool tip relative to the workpiece and included the positioning errors of all moving components between them. The equations were comprised of several terms, but these terms could be grouped as Nominal Positions, Offsets, or ΔP terms. When implementing a software compensation system, the terms of interest are those pertaining to the error motions of the slides, which are the ΔP terms. With this in mind, the error equations used to compute the actual axis compensations are given as

$$
\Delta P_x = \delta_x(x) - \delta_x(z) + Z_t \cdot \varepsilon_y(x) + (z + Z_1 - Z_t) \cdot \varepsilon_y(z) - \beta \cdot z \tag{5}
$$

$$
\Delta P_z = -\delta_z(z) + \delta_z(x) - X_t \cdot \varepsilon_y(x) + (x - X_1 + X_2 + X_t) \cdot \varepsilon_y(z) - \alpha \cdot x \tag{6}
$$

Error Characterization

Y-12 has procured a new laser system called the 5-D Laser Measuring System that significantly reduces the time required for error measurement. Automated Precision, Inc., in Gaithersburg, Maryland produces the system. By combining several sets of optics into one sensor head, the 5-D system allows the acquisition of five error measurements (scale, horizontal straightness, vertical straightness, pitch, and yaw) with a single setup of the laser. An available add-on module allows horizontal roll measurements to be made, creating a 6-D system, but that is currently not part of the Y-12 system. The 5-D laser system was used to provide the axis error data for the lathe as functions of axis position and direction of motion. Three error data files are produced by the 5-D system for each measured axis. Squareness and parallelism errors of the lathe were obtained using an electronic indicator.

System Implementation

In developing the system architecture of the GECS, an effort was made to make the system flexible enough to support machines of different configurations and numbers of axes. Another design goal was to seamlessly interface the software with OpenCNC. To accomplish this, variables and arrays were patterned after those used in the lead-screw error compensation system provided within OpenCNC.

One of the steps involved in implementing the GECS was creating an Error File that contained the measured error data. This file was read at system startup to load the internal error arrays. These arrays contained the error data needed by the error equations developed earlier. Software was written to combine the data from the multiple 5-D laser system files into a single file.

To facilitate the incorporation of the GECS functionality into OpenCNC, MDSI provided a software template for an external compensation system. This general-purpose template will allow any type of compensation system to be implemented within OpenCNC. Compensation of thermal errors and tool-wear are two examples of systems that could be supported with this template in addition to GECS. The template provided the interface code that communicated with OpenCNC. It obtained controller parameters needed by the compensation system and passed compensation values back to the controller. New code developed during the project included functionality to initialize the GECS, read the Error File data, and actually perform the compensation calculations. Given the machine

positions of the axes and their directions of motion, the GECS first converted the machine positions into the model space coordinates as depicted in Figure 3. The components of the error equation components were then computed, using data from the appropriate positive or negative data arrays, depending on the slides' directions of motion. Finally, the error terms were combined using Equations (5) and (6) to give the tool's total position errors.

System Evaluation

A Renishaw® ballbar was used to evaluate the effects of the compensation system. Shown in Figure 4, the ballbar was used to conduct static positioning tests on the lathe. The ballbar consists of a high accuracy displacement sensor housed inside a telescopic bar. The ends of the bar are held in strong magnetic cups, one held fixed on the spindle faceplate, and one held by the moving tool holder.

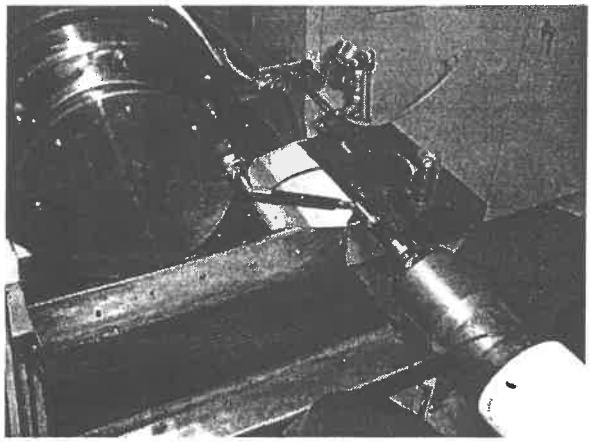

Figure 4. Ballbar setup

Three runs were performed with GECS disabled, and three were performed with it enabled. After the data was collected, the ballbar control software calculated a positioning error it referred to as circularity error. This error was calculated by combining the maximum and minimum deviations from the best-fit arc through the measurement data. For the case in which the GECS was disabled, a typical test resulted in a circularity error of 14 microns, which was considered to be very high for that machine. The uncompensated errors were on the order of the positioning compensations being applied to the axes, which would mask their effects. Tests with the GECS enabled sometimes showed positioning accuracy improvements, but not consistently. It was felt that the machine had some mechanical problems that prevented it from providing repeatable measurements, but project resources were not sufficient to allow machine maintenance operations to be performed or for further investigation.

Conclusions

While the desired result of showing definite positioning improvements due to axis compensation was not realized during this project, several other goals were achieved. Knowledge was obtained on application of geometric error compensation techniques, and the experience gained in performing the actual implementation details will be invaluable in future work. OpenCNC may be the first commercially-available machine tool controller to provide a software interface for external compensation processes, and the external compensation template will provide a unique platform for developing other types of compensation systems.

[1] R. Hocken et al, "Three Dimensional Metrology," in *Annals of the CIRP*, Vol. 26/2, pp. 403–408, 1977.

[2] M.A. Donmez, C.R. Liu, M.M. Barash, "A Generalized Mathematical Model for Machine Tool Errors," presented at The Winter Annual Meeting of the American Society of Mechanical Engineers, Anaheim, California, December 7–12, 1986.

[3] A.H. Slocum, *Precision Machine Design*, Society of Manufacturing Engineers, Dearborn, MI, 1992.

Robust Cutting Force Control Using Indirect Force and Disturbance Estimators in the End Milling Process

Seung-Cheol Kim and Sung-Chong Chung

MAnufacturing Systems & Control LABoratory
Department of Mechanical Design & Production Engineeering
Hanyang University, SungdongGu, Seoul 133-791, KOREA

Abstract : In this paper, a robust cutting force control system using an indirect cutting force estimator and disturbance observer is studied in the end milling process. The indirect cutting force estimator is derived from the geometric cutting force model and the feed and spindle motor currents. In order to regulate the cutting force at a desired level during wide range of machining conditions, a robust control system with a disturbance observer is developed using a feedrate override function.

Keywords : Cutting force regulation, Cutting geometry, Disturbance observer, End milling force model, Indirect force sensor, Motor current, Robust real-time control, Unmodelled dynamics

1. Introduction

In modern manufacturing processes, there is an ever-increasing demand for higher productivity by reducing machining time with the increase of cutting force and material removal rate.[1] However, the excessive increase of cutting force results in tool breakage, poor machined quality, and bad effects on the machine tool. Variation in cutting force may result in a variation of spindle or workpiece deflection, thus deteriorating resultant geometric accuracy. Nevertheless, variation of cutting force is often unavoidable due to factors such as a change in the depth of cut or workpiece geometry, hardness variation, and tool wear. One of the most straight-forward methods of improving productivity and quality in machining processes is real-time estimation and control of cutting forces during the machining process.[2] The purpose of such control is to maintain the cutting force at a prescribed level by adjusting cutting parameters. The adaptive cutting force control results in an increased metal removal rate while the machining system is protected against sudden failure due to overload. The part quality may be also improved.[3]

In this study, the robust cutting force control using indirect cutting force measurement is developed in the end milling process. This paper consists of two parts. One is an indirect cutting force estimator during the end milling process. The other is a robust adaptive cutting force controller. Cutting forces and torque models are derived from the cutting geometry in end milling processes. Relationships between motor currents and cutting forces are also developed from the proposed force models. Cutting forces are measured indirectly from the sensing currents of feed drive servo motors and the spindle motor through the estimator with the cutting geometry analyzer. Since the suggested method does not need an expensive sensor like a dynamometer, the method is expected to be used practically. In order to maintain the cutting force at a desired level during the cutting process in spite of variation of machining conditions, a feedrate override robust adaptive control system is studied using the disturbance observer. Nominal models of the feed drive system and the cutting process are identified by experiments. To account for any unmodelled dynamics and parameter uncertainty of a time varying end milling process, a robust controller with an adaptive PI scheme based on real time process gain estimation is designed with the disturbance observer. By reducing the machining time resulting from making the actual cutting forces follow the reference force, the increase of productivity are also expected, and the quality of cutting surface has been improved due to the adjusted feedrate. The validity of the developed system is verified on a horizontal machining center through the experiments.

2. Indirect Normal Cutting Force Estimator

2.1 Force Modeling of End Milling

Cutting forces are described as functions of cutting pressures acting on the instantaneous chip load area [4-6]

$$dF_t = K_s\, dz\, h(\phi), \quad dF_r = r_1 dF_t \tag{1}$$

where $dz = [R/\tan(\beta)]d\phi$ is thickness of the axial element of the cutting edge, $h(\phi) = l_f \sin(\phi)$ is instantaneous chip thickness, l_f is feed per tooth. The cutting pressure K_s can be expressed as a function of the average chip thickness. In the peripheral down-milling process instantaneous forces in the X and Y directions along the chip load of a single flute are given by

$$\begin{aligned} dF_x(\phi) &= \quad dF_t \cos\phi + dF_r \sin\phi \\ dF_y(\phi) &= -dF_t \sin\phi + dF_r \cos\phi \end{aligned} \tag{2}$$

Integrating Eq. (2) within the contact range of a single tooth as shown in Fig. 1,

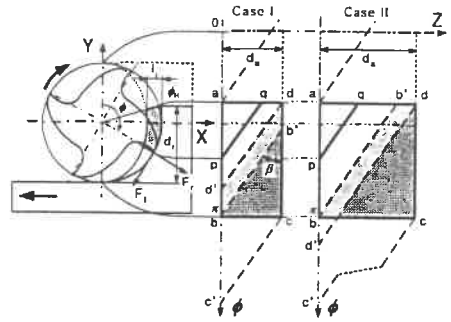

Fig. 1 Cutting mechanism of end milling process

$$F_x^i(\phi^i) = K\int_{\phi_q}^{\phi_p}(\sin\tau\cos\tau + r_1\sin^2\tau)d\tau$$

$$F_y^i(\phi^i) = K\int_{\phi_q}^{\phi_p}(-\sin^2\tau + r_1\sin\tau\cos\tau)d\tau \qquad (3)$$

$$F_t^i(\phi^i) = K\int_{\phi_q}^{\phi_p}\sin\tau d\tau$$

For several teeth cutting,

$$F_x(\phi) = K\sum_{i=1}^{N}\left(A^i(\phi^i) + r_1B^i(\phi^i)\right)$$

$$F_y(\phi) = K\sum_{i=1}^{N}\left(-B^i(\phi^i) + r_1A^i(\phi^i)\right) \qquad (4)$$

$$F_t(\phi) = K\sum_{i=1}^{N}C^i(\phi^i)$$

where, $A(\phi) = 0.25\left(\cos(2\phi_q) - \cos(2\phi_p)\right)$,

$B(\phi) = 0.5\left\{\phi_p - \phi_q - 0.5\left(\cos(2\phi_p) - \cos(2\phi_q)\right)\right\}$,

$C(\phi) = \left(\cos\phi_q - \cos\phi_p\right)$, $K = K_s R l_f / \tan\beta$

Fig. 2 shows average cutting forces according to various axial and radial depth of cuts. Simulated average forces are compared to measured forces for various radial DOCs as shown in Fig. 3.

2.2 Cutting Force Estimation Using Motor Currents

Dynamics of feed drive and spindle systems are given by

$$K_t I_M = J\frac{d\omega}{dt} + B\omega + T_f + T_d \qquad (5)$$

where, ω is the speed, I_M is the motor current, T_d is the disturbance torque due to cutting forces, and T_f is the coulomb friction torque.[2,3,6]

By using motor currents and identification procedures of [6], parameters of Eq. (5) can be extracted from a machining center. Fig. 4 shows measured and estimated results of average cutting forces through a dynamometer and motor currents, respectively.

2.3 Identification of Radial and Axial DOC

From cutting force models of section 2.1, radial and axial depth of cuts are able to be identified as shown in Fig. 5. The radial immersion ratio $R_r = d_r/R$ can be expressed by the force ratio of average feed force to average tangential force. And the axial immersion ratio $R_a = d_a/R$ can be derived from linear interpolation with the average force change for a radial immersion. The estimated cutting forces using motor currents in Fig. 4 are applied to the estimator of radial and axial depth of cuts in Fig. 5. From these results, radial and axial DOCs and the normal force and measured motor currents, can be estimated as shown in Fig. 6.

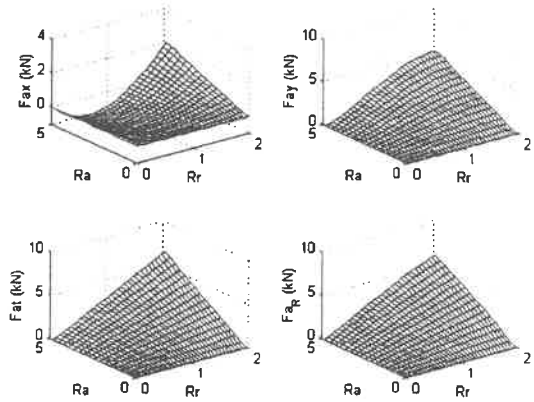

Fig. 2 Relationships between cutting forces and DOC

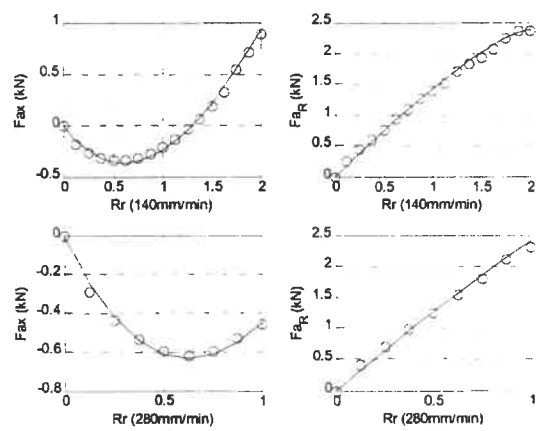

Fig. 3 Measured and simulated cutting forces (feedrate 140, 280 mm/min)

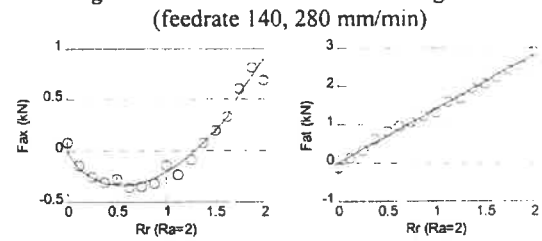

(a) Feed current (b) Spindle current

Fig. 4 Measured and estimated cutting forces

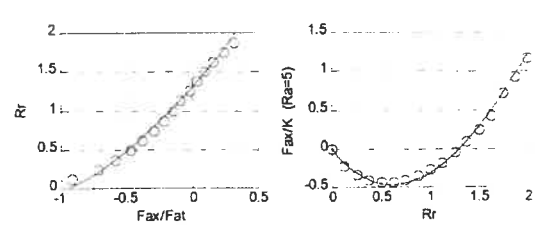

(a) Force ratio and Rr (b) Rr and force change for Ra

Fig. 5 Relationships between Rr, Ra and cutting forces

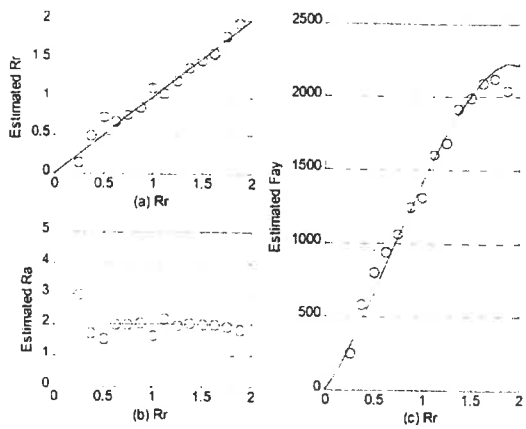

Fig. 6 Estimated radial and axial DOC, and normal force

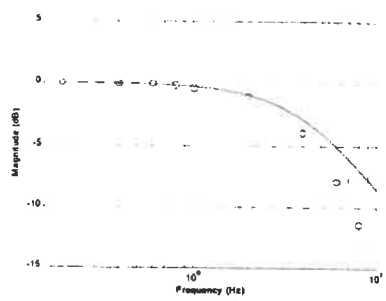

Fig. 7 Frequency response of the X-axis feed drive

Table 1 Cutting models for end milling processes (600rpm, 16mm dia., 4 teeth flat end milling)

Radial DOC (mm)	Gain (K_2)	Pole Location (p_2)
2	10.05	-2.35
3	12.57	-3.75
4	20.11	-5.35

3. Robust Cutting Force Control

3.1 Modeling of End Milling Process

To obtain a dynamic model of the end milling process, following identification procedures of the feed drive system are required. Sinusoidal inputs between 0.2Hz to 8Hz are used as excitation signals of feedrates. Feed velocities come from the encoder are measured as output signals. Fig. 7 shows the frequency response function between the input and the output signals of feedrates. From this frequency response function, a dynamic model of the feed drive is given by [7]

$$\frac{v(s)}{u(s)} = \frac{29.33e^{-0.1s}}{s+29.33} \tag{6}$$

The cutting force can be derived as follows [7]

$$\frac{f(s)}{v(s)} = \frac{K_2}{s-p_2} \tag{7}$$

Combining Eq. (6) and (7), the end milling process model becomes

$$\frac{f(s)}{u(s)} = \frac{29.33K_2e^{-0.1s}}{(s+29.33)(s-p_2)} \tag{8}$$

To account for any unmodeled dynamics and parameter uncertainty of the time varying end milling process, end milling experiments were conducted according to several values of cutting conditions. Table 1 shows cutting models obtained from some of end milling experiments. From this we can conclude that dynamics are varied during cutting. To follow up varying dynamics and design a cutting force controller, a robust controller is designed with the disturbance observer. In this case, the nominal model P_n of the plant P is chosen to be

$$P_n(s) = \frac{f(s)}{u(s)} = \frac{368.68e^{-0.1s}}{(s+29.33)(s+3.75)} \tag{9}$$

This model is based on 3mm radial depth of cut.

3.2 Design of Robust Controller

Fig. 8 shows a block diagram of the robust control system. The robust controller compensates for mechanical nonlinearities, parameter variation, and disturbances and lets the dynamic behavior of the actual feedback loop system stay close to the nominal plant. [8]

The disturbance observer is designed in the continuous time domain. The actual plant dynamics is $P(s) = P_n(s)[1+\Delta(s)]$, where $\Delta(s)$ represents the variation of the plant from the nominal dynamics. $F(s)$ is derived as

$$F(s) = \frac{P_n(s)[1+\Delta(s)]}{1+\Delta(s)Q(s)}E'(s) + \frac{[1-Q(s)]P_n(s)[1+\Delta(s)]}{1+\Delta(s)Q(s)}D(s) \tag{10}$$

Notice that $F(s) = P_n(s)[E'(s)+D(s)]$ for $Q(s)=0$ and $F(s) = P_n(s)E'(s)$ for $Q(s)=1$. By proper selection of $Q(s)$, we can let the actual plant behave like the nominal plant over a specified frequency region.

For internal stability $Q(s) \in RH_\infty$, and realizability $Q(s)/P_n \in RH_\infty$, $Q(s)$ is selected as the following form.

$$Q(s) = \frac{1}{(\tau s)^3 + 3(\tau s)^2 + 3(\tau s) + 1} \tag{11}$$

where τ is the response time.

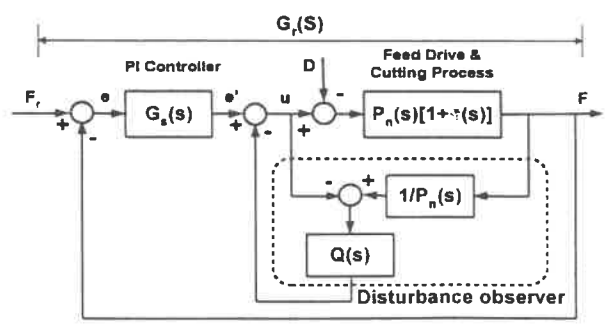

Fig. 8 Block diagram of a robust control system

4. Experiments

Combining the indirect force sensor and the robust adaptive controller, a robust adaptive cutting force control system is finally developed in the end milling process through the feedrate manipulation. An experimental setup was constructed for the commercial CNC machining center without major changes of the structure as shown in Fig. 9. The feedrate override function and PC/NC interface were accomplished by the programmable machine controller interface technique on a Fanuc 15MA NC controller.

Experiments are performed on-line to verify the robustness of the cutting force estimator and controller. Experimental results for 2 to 4 mm of DOC are shown in Fig. 10: (a) measured and estimated feed forces from feed current, (b) measured and estimated tangential forces from spindle current, (c) command feedrates, (d) estimated radial DOCs, (e) estimated axial DOCs, (f) measured and estimated normal forces.

5. Conclusion

The robust cutting force control using indirect cutting force estimators and the disturbance observer has been developed in the end milling process. Cutting force models are derived from the cutting geometry in end milling processes. Relationships between depth of cuts and cutting forces are also developed from the proposed force models. Cutting forces are measured indirectly from the observed currents of feed drive servo motors and the spindle motor through the mathematical estimator. In order to maintain the cutting force at a desired level during the cutting process in spite of variation of machining conditions, a feedrate override robust adaptive control system has been studied using the disturbance observer. Nominal models of the feed drive system and the cutting process were identified by experiments. The validity of the developed estimator and controller has been verified on a horizontal machining center through the experiments.

References

(1) Spence, A. and Altintas, Y., 1991, "CAD Assisted Adaptive Control for Milling," ASME Journal of Dynamic Systems Measurement and Control, Vol.113, pp.444-450.

(2) Stein, J. L. and Park, Y., 1988, "Measurement Signal Selection and a Simultaneous State and Input Observer," ASME Journal of Dynamic Systems Measurement and Control, Vol.110, No.2, pp.151-159.

(3) Altintas, Y., 1992, "Prediction of Cutting Force and Tool Breakage in Milling from Feed Drive Current Measurement," ASME Journal of Engineering for Industry, Vol.114, pp.386-392.

(4) Tlusty, J. and Macneil, P., 1975, "Dynamics of Cutting Forces in End Milling," Annals of the CIRP, Vol.24, pp.248-252.

(5) Sutherland, J. W. and Devor, R. E., 1986, "An Improved Method for Cutting Force and Surface Error Prediction in Flexible End Milling Systems," ASME Journal of Engineering for Industry, Vol.108, pp.269-279.

(6) S.C. Kim and S.C. Chung, 1998, "Cutting Force Estimation Using Feeddrive and Spindle Motor Currents in Milling Processes", Transactions of the Korean Society of Mechanical Engineers (A), Vol.22, No.11, pp.2029-2038. (in Korean)

(7) S.C. Chung, 1996, "A Pole-Assignment ACC System in the Peripheral End Milling Process", Journal of the Korean Society of Machine Tool Engineers, Vol.5, No. 2, pp.63-72. (in Korean)

(8) S. Endo, M. Tomizuka and Y. Hori, 1993, "Robust Digital Tracking Controller Design for High-speed Positioning systems", Proceedings of the American Control Conference, pp.2494-2498.

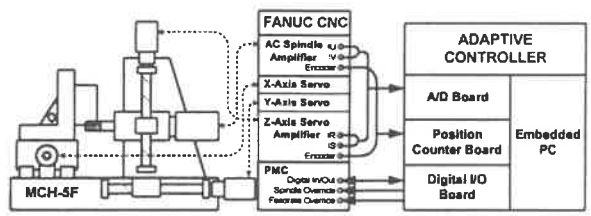

Fig. 9 Schematic diagram of experimental setup

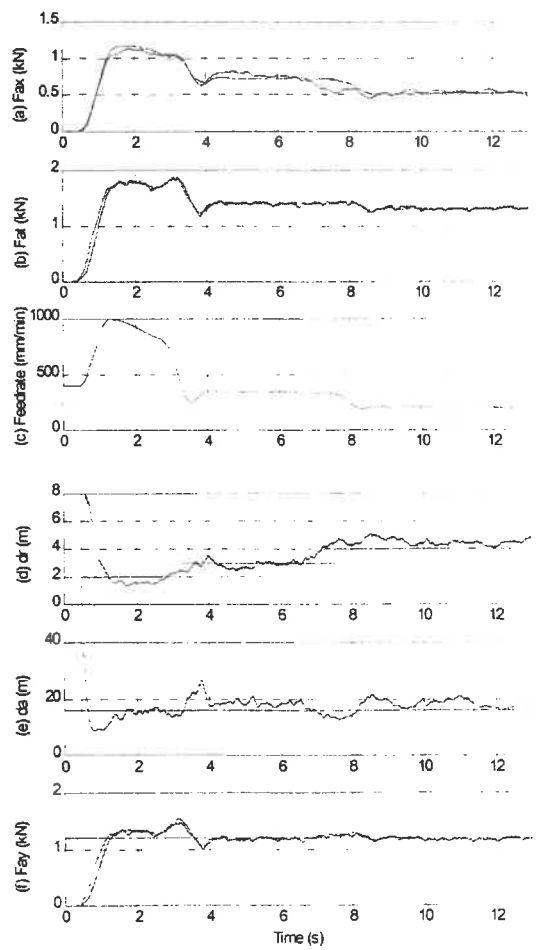

Fig. 10 Experiment results of robust control

A Discussion on Stability of Air Bearing Spindles

Zongren Shang, Philip Greene, Doug Bittner
Dover Instrument Corporation

Stability is a very common but difficult to solve problem in an air bearing system. The most cases that instability occurred were due to the lower damping in air bearings. It has been experimentally and theoretically verified that the stability of an air bearing will be increased by applying an increased external pressurized air into bearings [1], [2]. However, in our studies, instability appeared at lower speed with higher external supply pressure, and the speed at which instability appeared was increased with a decrease of external supply pressure. This phenomenon is contrary to normal analysis on stability issue. This paper will discuss this issue.

1. Introduction

Air bearings possess lower damping than other fluid lubricated bearings. Because of this characteristic, the high speed stability becomes a very important topic in the design of air bearings.

Firstly, our design goal was to develop a spindle that was able to handle twelve (12) computer disks and run 20,000 r.p.m. with eccentricity rate < 0.65 at 90 psi supply pressure. Even though the spindles can be balanced up to grade g0.5, because of test procedure operated by customers, the reality of imbalance after randomly adding the twelve disks on clamp was much worse than grade g0.5, which caused a large centrifugal force at 20,000 r.p.m. It is obvious that, the most focus should be on how to increase the bearing stiffness and load capacity on a dimension-limited air bearing to achieve the eccentricity ratio of less than 0.5.

Because of the dimensional limitation, even though the supply pressure was 90 psi, the static stiffness was still low, relatively. One important factor that can be used to increase the load capacity and stiffness was the aerodynamic property. In our regular Total Indicator Runout (TIR) tests, the TIR started to increase much more rapidly once the speed was over 15,000 rpm. Therefore, we needed to design an air bearing in which the aerodynamic performance should gradually play more important role on stiffness and load capacity at speed over 15,000 rpm. Based on this consideration, an air bearing spindle was designed with high pressure ratio and tighter air gap to provide higher dynamic performance. However, with heavier clamp made of steel instead of the one made of aluminum, the air bearing spindle exhibited a speed stability problem. The speed at which instability appeared decreased with the increase of supply pressure. This phenomenon led us to investigate the reasons.

2. Experiments and Analysis

Two types of clamps were used - aluminum clamp and steel clamp. The test setup was showed on Fig. 1.

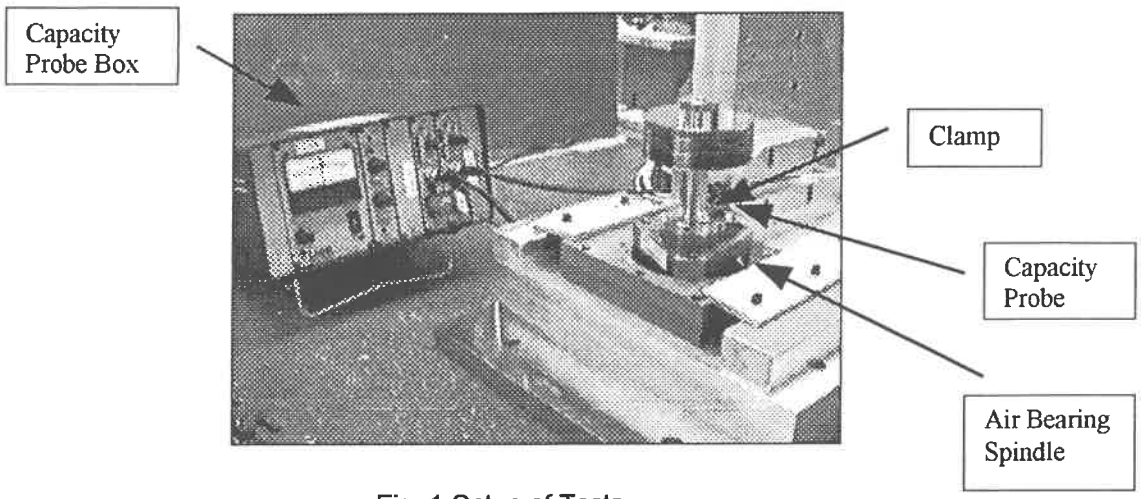

Fig. 1 Setup of Tests

2.1 Tests with light clamp made of aluminum

TIR test results of air bearing spindles showed on Fig. 2.

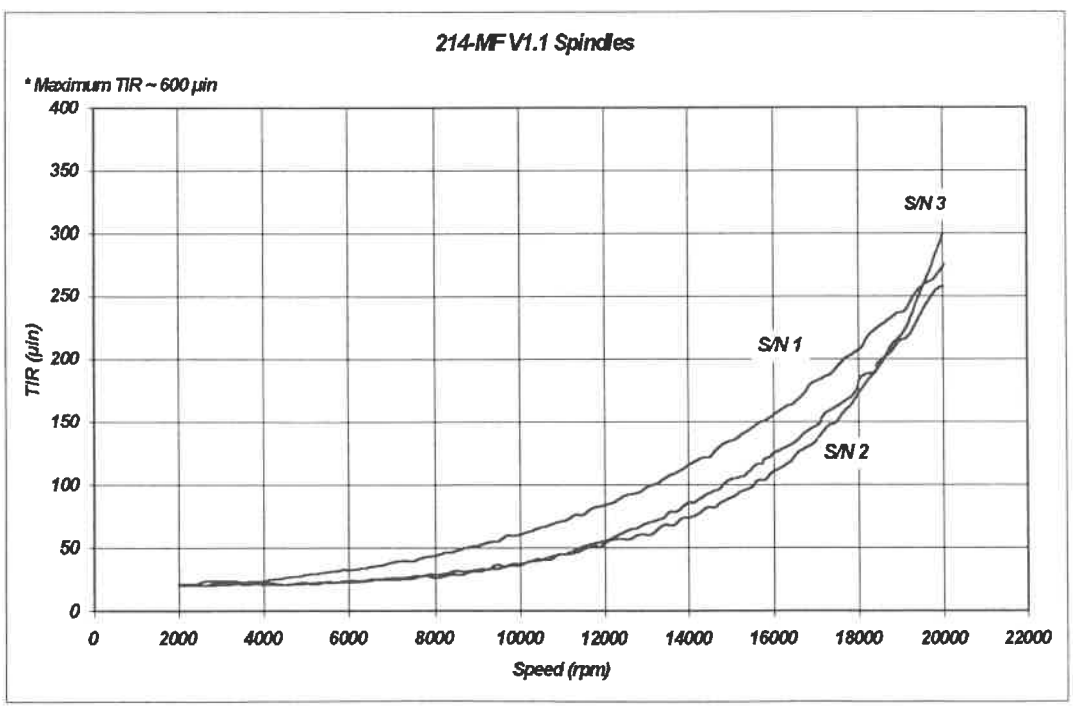

Fig. 2 TIR vs. Speed at 90 psi supply pressure with 10 disks by using Aluminum Clamp

From Fig. 2, we can see that the eccentricity ratios for the three spindles were between 0.4 to 0.5 up to 20,000 rpm with randomly added twelve (12) disks. After 15,000 rpm the TIR did not increase rapidly, which meant that the design of the air bearings succeed. The aerodynamic property had played sufficient function in the air bearing spindles over 15,000 rpm. The applications of high pressure ratio and step effect commonly used in oil lubricated bearings into air bearings were of importance for enhancing the dynamic performance.

Because of the application of high pressure ratio in the air bearing, the pneumatic hammer was also effectively eliminated, even though there were step pockets in the air bearings.

2.2 Tests with heavier clamps

After the clamp was changed to steel clamp, the instability occurred, Fig. 3.

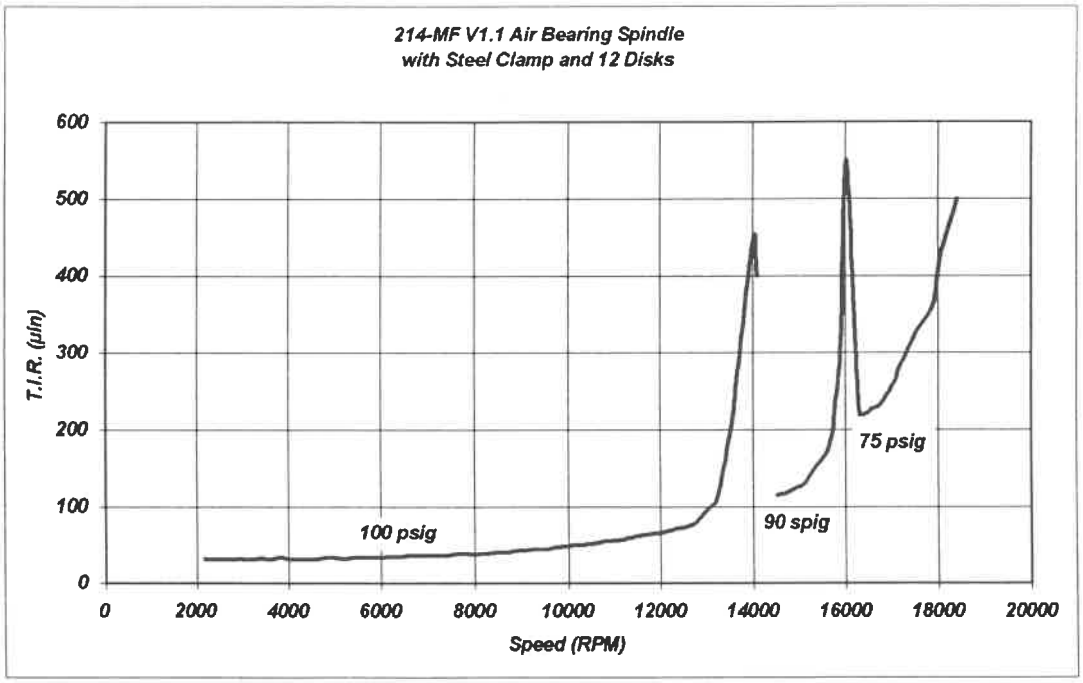

Fig. 3 TIR vs. speed at different supply pressures

When external supply pressure was 100 psi, the speed that instability occurred was ~14,000 rpm. At 90 psi, the speeds of instability were ~16,000 rpm. However, along with the decrease of supply pressure, the TIR increased more quickly because the load capacity was decreased (load capacity is proportional to supply pressure).

Generally speaking, an increase on external supply pressure will increase the stability, because the direction of static force points to the center of bearings to reduce the potential of whirl.

Firstly, we consider the effect of changing clamps. For example, at 90 psi supply pressure, there was not instability by aluminum clamp. But the instability did occur when steel clamp was used. Because of the use of steel clamp, the natural frequency was decreased, and the centrifugal force was increased (because the clamp was not balanced with spindle but centered only). The increased centrifugal force further offsets the center of the shaft from the center of housing. For this bearing with tighter air gap and the larger eccentricity ratio, the aerodynamic force and position angle was increased. The increase on both aerodynamic force and position angle was the major contribution to lead to instability of half speed whirl or resonant whip.

Secondly, we consider the effect of supply pressure on instability. In the studies with the steel clamp, if the pressure was decreased, the speed at which the instability occurred was increased. Based on this analysis, the major reason for this phenomenon was the variation of compensation among the orifices. To understand this phenomenon, consider the effect of orifices at static situation. Due to possible difference of compensation types, each orifice was actually functioning differently along circumferential direction. At higher pressure, shaft was pushed off center. The higher the pressure, the stronger the pushing force was. The shaft position was farther away from the center of bearing housing. The aerodynamic force generated due to the increased eccentricity ratio was increased, which resulted in a larger component force at 90^0 out of phase to the vector of eccentricity. This was the major force to push the shaft to whirl. When the pressure was decreased, i.e. 70 psi, the effect of static force that offset the center of shaft became smaller, thereby increasing the stability.

3. Conclusions

3.1 A design of air bearings with high pressure ratio improved the dynamic performance, leading to higher load capacity and stiffness at high speed. Step effect could be applied into air bearing designs for increasing dynamic performance. The air bearing design with high pressure ratio eliminated the pneumatic hammer.

3.2 The uniformity of compensation is important for air bearing stability.

3.3 Control on imbalance force is a valuable and easy method to control instability.

4. References

[1] Oscar Pinkus, Beno Sternlicht, "Theory of Hydrodynamic Lubrication", McGraw-Hill Book Campany, Inc., 1961

[2] Dudley D. Fuller, " Theory and Practice of Lubrication for Engineers", 2nd Edition, John & Sons, Inc., 1984.

[3] William T. Thomson, "Theory of Vibration with Applications", Prentice-Hall, Inc., 1972

[4] N.S.Grassam, J.W.Powell, " Gas Lubricated Bearings", Butterworths, 1964

Basic Research on Development of Magnetostrictive Sensor for Detecting Cutting Force

Hideki Aoyama*, Hiroki Murashita*, Tomoya Ishii*, and Hiro Ohzeki**

*: Keio University, Yokohama. Japan

**: Mitsubishi Materials Corporation, Ohmiya, Japan

1. Introduction

Monitoring of cutting processes is indispensable and important technology to realize a flexible and autonomous manufacturing system. A lot of works on monitoring technology have been done so far. However, most of the works were only effective for restrictive the cutting conditions, the restrictive machine tool, and so on. Then it is still desired to develop sensors and data processing methods for establishing a practical monitoring system.

The main targets of identification of cutting processes are tool wear, tool chipping, tool failure, and chatter. These items directly influence cutting force so that it is one of the most effective methods for monitoring them to detect cutting force. Cutting force can be traditionally detected by the table type sensor or the spindle attaching type sensor. The table type sensor is not suitable for practical use under considering viewpoints of the measurement range and fixing operation for each workpiece. The spindle attaching type sensor has the problem on rigidity in practical application. Cutting torque can also be estimated from the electric current of the main spindle. However, in this case, detection sensitivity of the cutting torque is not enough. Thus, authors have developed the magnetostrictive torque sensor [1] which is installed in the tool holder and has very high detection sensitivity.

In order to make more advanced actions according to the monitored information, it is desired to detect not only cutting torque but also x, y, and z components of cutting force. The final objective of this study is to develop a magnetostrictive force sensor which can detect x, y, and z components of cutting force, cutting torque, and deflection of the cutting tool with high detection sensitivity. To achieve this objective, in this paper, a coil-sensor to detect magnetostrictive effect and the force sensor using the coil-sensors are proposed and the characteristics of the coil-sensor and the force sensor are made clear by the experiments.

2. Coil-Sensor to Detect Magnetostrictive Effect

2.1 Magetostrictive Effect

A magnetic material has two kinds of magnetostrictive effect; one is the Joule effect and the other is the Villari effect. When a magnetic field with the intensity and the direction is given to a magnetic material, the magnetic material extends in the direction of the magnetic field in the case of positive magnetostriction and shrinks in the case of negative magnetostriction. This phenomenon is called as the Joule effect. On the other hand, as shown in Fig. 1, when tensile strain is given to a magnetic material

with positive magnetostriction, the material has a magnetic filed *H* with the magnetic direction and the magnetic intensity. The magnetic direction is the same with the tensile direction and the magnetic intensity depends on the given strain. When compressive strain is given to a magnetic material with negative magnetostriction, the magnetic direction and intensity according to the strain arises in the perpendicular direction for the compressive direction. This phenomenon is called as the Villari effect.

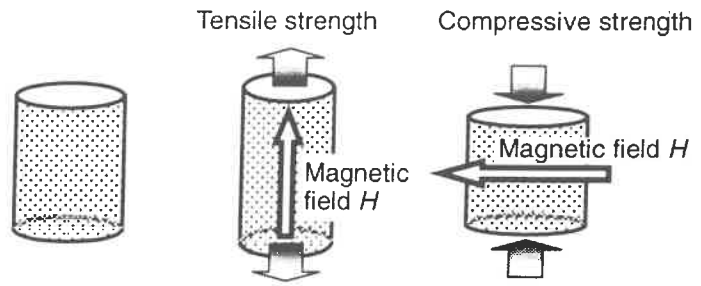

(a) No strain (b) Tensile strain (c) Compressive strain

Fig. 1 Villari effect (in the case of positive magnetostriction)

2.2 Coil-Sensor to Detect the Magnetostriction

As Mentioned above, the magnitude and the direction of applied force on a magnetic material can be identified from the intensity and the direction of the magnetic field generated in the magnetic material by the Villari effect. The intensity of the magnetic field in a direction can be detected as the impedance change of a coil. In this paper, a coil-sensor which detects the intensity of the magnetic field in the two perpendicular directions is proposed.

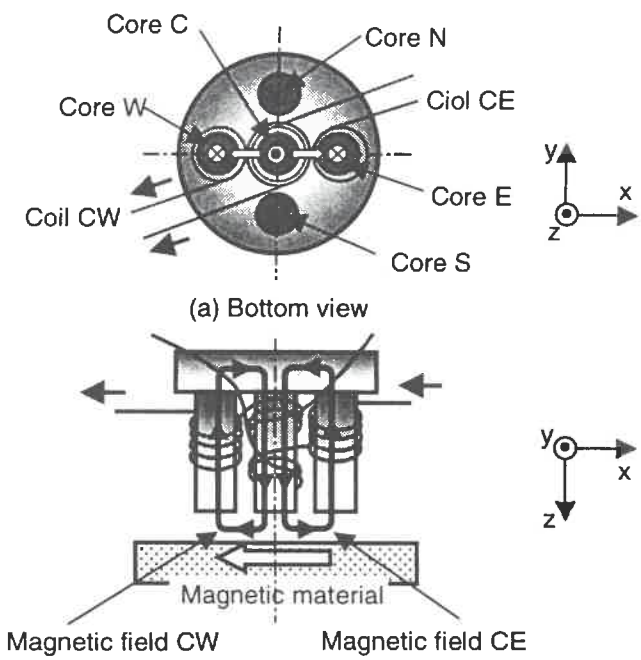

Fig. 2 Structure of the coil-sensor

Figure 2 shows the structure of the proposed coil-sensor. The coil-sensor is composed of the five cores C, N, S, E, and W and the four coils CN, CS, CE, and CW. As shown in Fig. 2, the coil CE is made by winding Nichrome wire around the cores C and E and the coil CW is formed by winding Nichrome wire around the cores C and W. In the same manner as the coils CE and CW, the coils CN and CS are made by winding Nichrome wire around the cores C and N and the cores C and S. The winding directions of the coils are determined to make the magnetic field from the center core C to the outside cores N, S, E, and W or the reverse magnetic field under alternation current flow.

As shown in Fig. 2, when the magnetic material has the magnetic field of the magnetic direction from +x to −x and the coils makes the magnetic field from the center core C to the cores E and W, the impedance of the coil CE will be increased and the impedance of the coil CW will be decreased. In the

case that the electric current flows in reverse, the impedance change will be opposite. The coil-sensor shown in Fig. 2 detects the intensity of the magnetic filed in the x direction by the coils CE and CW. Also, the intensity of magnetic filed in the y direction is detected by the coils CN and CS. As a result, the proposed coil-sensor can detect the intensity of the magnetic field in x and y directions.

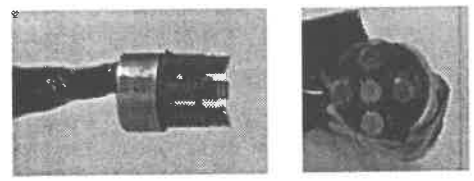

Fig. 3 Coil-sensor

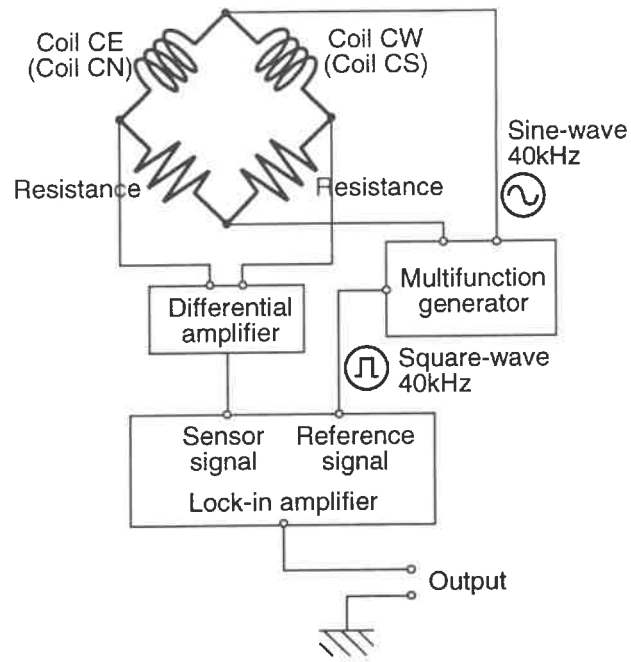

Fig. 4 Signal detecting system

3. Basic Characteristics of the Coil-Sensor and the Signal Detection System

Figure 3 shows the developed coil-sensor. Since the impedance change of the coil-sensor by the magnetic field change is extremely small, the signal form the coil-sensor is detected by using a lock-in amplifier and a direct current amplifier with a bridge circuit as shown in Fig. 4.

A film of magnetic material Fe-Ni-Mo-B was deposited on a test piece with the size of 110*20*10 mm by thermal spraying. The magnetic field change of the film surface was detected by the coil-sensor under different tensile strain for the test piece. Figure 5 shows the characteristic of directionality of the coil-sensor. In Fig. 5, the abscissa means the angle between the force direction applied on the test piece and the detecting direction of the coil-sensor. Thus it became cleat that the output depends on the detecting direction and the force applied on the test piece. And it is understandable that the output is also influenced by the gap between the coil-sensor and the magnetic film.

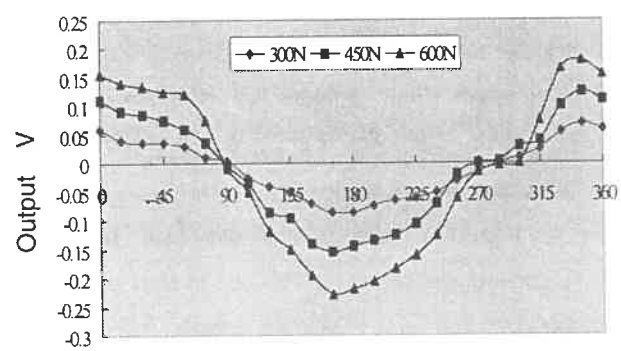

Fig. 5 Directionality of the coil-sensor

4. Magnetostrictive Sensor to Detect Cutting Force and Cutting Tool Deformation

The structure of the proposed magetostrictive force sensor is shown in Fig. 6. The sensor can detect x, y, and z components of cutting force, cutting torque, and the deformation of the cutting tool. The four coil-sensors N, S, E, and W are arranged with the directionality shown in Fig. 6 around the magnetic film of Fe-Ni-Mo-B which is deposited on the tool shank surface by thermal spraying.

Each coil-sensor has the two output signals corresponding to the magnetic field. When the output

signals from the coil-sensors N, S, E, and W are V_{n1}, V_{n2}, V_{s1}, V_{s2}, V_{e1}, V_{e2}, V_{w1}, and V_{w2}, respectively, x, y, and z components Fx, Fy, and Fz, cutting torque T, deformation in x and y directions Dx, and Dy are derived from the following equations.

$$Fx = \frac{V_{n1} + V_{n2} + \sqrt{2}V_{s1} + (2-\sqrt{2})V_{s2}}{2} \quad (1)$$

$$Fy = \frac{\sqrt{2}V_{w1} - (\sqrt{2}+2)V_{w2} - V_{w1} - V_{w2}}{2} \quad (2)$$

$$Fz = \frac{V_{n1} + V_{n2} + (2+\sqrt{2})V_{s1} - \sqrt{2}V_{s2}}{2} = \frac{V_{e1} + V_{e2} + (2-\sqrt{2})V_{w1} + \sqrt{2}V_{w2}}{2} \quad (3)$$

$$T = \frac{V_{n1} - V_{n2}}{2} = \frac{V_{e1} - V_{e2}}{2} \quad (4)$$

$$Dx = \frac{V_{n1} + V_{n2} + \sqrt{2}V_{s1} - \sqrt{2}V_{s2}}{2} \quad (5)$$

$$Dy = \frac{\sqrt{2}V_{w1} - \sqrt{2}V_{w2} - V_{e1} - V_{e2}}{2} \quad (6)$$

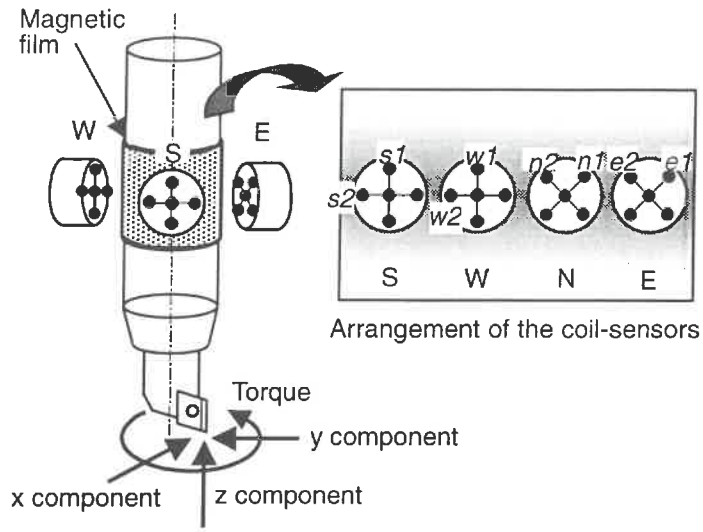

Fig. 6 Structure of the magnetostrictive force sensor

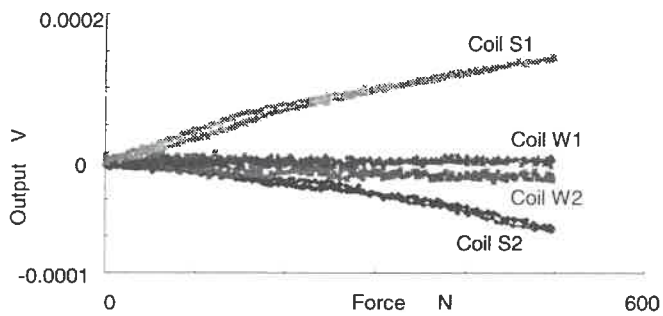

Fig. 7 Relationship between force and sensor output

Figure 7 shows the output signals $s1$, $s2$, $w1$, and $w2$ of the coil-sensors S and W when the horizontal force is statically applied on the cutting edge against the coil-sensor S.

5. Conclusions

(1) Strain can be measured by detecting the magnetic field change generated by magnetostrictive effect.

(2) The coil-sensor to detect the magnetic field change with directionality was proposed and developed.

(3) The measuring system to amplify the extremely weak signal from the coil-sensor was constructed by using a lock-in amplifier and a direct current amplifier with a bridge circuit

(4) The characteristics of the coil-sensor were made clear by basic experiments.

(5) The force sensor based on the magnetostrictive effect was proposed to detect x, y, and z components of cutting force, cutting torque, and deformation of the cutting tool.

(6) The detecting principle of the force sensor was theoretically explained with equations and its basic characteristics were made clear by the experiments.

References

[1] Hideki AOYAMA, et al.: Prediction of Tool Wear and Tool Failure in Milling by Utilizing Magnetostrictive Torque Sensor, Technical Papers of the North American Manufacturing Research Institution of SME (1998), pp125-130.

POLYGON-BASED LARGE DIAMETER MEASUREMENT WITH MODULAR GAUGES

Li Bin

Department of Mechanical Engineering, Southeast University, Nanjing 210018, China

1. INTRODUCTION

Measurement of large diameters (≥500mm) may encounter some difficult problems. It is due to the large dimension of the workpiece to be measured, which leads to the in-step increase of the volume and weight of the measuring apparatus. Thus, a series of problems occur to that apparatus: much difficulty of operation, large deformation of self-weight and temperature, high cost and poor versatility and so on[1]. The typical instances are large external and internal micrometers. On the other hand, those apparatus that employ the indirect methods such as height-chord gauge, saddle-shaped gauge and π-tape, although relative small, usually suffer the problem of limited accuracy[1-3]. Recently, grating, laser and some other advanced techniques have been used to this application; however, many problems remain unresolved[4-8]. Finally, although heavy coordinate measuring machine is a good tool to measure large diameters, it is too expensive, and the workpiece is sometimes too large to be taken into the working space of it.

In this extended abstract, a new method of measuring large diameters is described. By assembling in *situ* the measuring units around the circumference of the workpiece with magnets, any large size of external or internal diameters can be measured. In addition, the measuring apparatus has the advantages of compactness, simple structure and low cost and so on. More important, the precision of the method is very high.

2. PRINCIPLE

As shown in Fig.1, several identical but independent measuring units (large diameter gauges) are placed and, with magnets, fixed around the circumference of the workpiece to be measured. Each gauge has a ball and a roller at its two ends as the positioning elements. The gauges are arranged in such a way that the contacting elements between the adjacent gauges are one ball and one roller, so that the contacting area is always a point in theory. The diameters of the ball d_1 and the roller d_2 and the central distance l of each gauge are known. If the centers of all balls and rollers of each gauge are linked, such a polygon will be formed that all of their side lengths are known except for the last one. Therefore, if the closing size lc is determined by some other method, for example, with internal micrometer, the diameter of the workpiece D can be solved from the following equation according to the Cosine law:

$$\sum_{i=1}^{n}\cos^{-1}\left[\frac{(D+d1_i)^2+(D+d2_i)^2-4l_i^2}{2(D+d1_i)(D+d2_i)}\right]+\sum_{i=1}^{n-1}\cos^{-1}\left[\frac{(D+d2_i)^2+(D+d1_{i+1})^2-(d2_i+d1_{i+1})^2}{2(D+d2_i)(D+d1_{i+1})}\right]$$
$$+\cos^{-1}\left[\frac{(D+d2_n)^2+(D+d1_1)^2-4lc^2}{2(D+d2_n)(D+d1_1)}\right]=2\pi \qquad (1)$$

where n is the total number of the gauges that surround the workpiece. It can be seen that Eq.(1) is an implicit function, so the diameter D should be solved by numerical methods such as the iterative method.

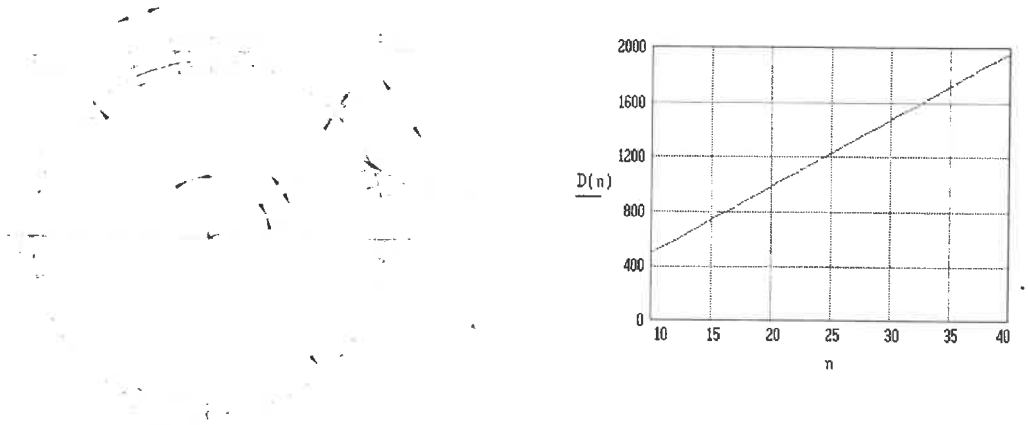

(a) (b)

Fig.1 (a) Principle of the method; (b) Relation of measured diameter versus the total number of the gauges that surround the workpiece, where $d=27mm$, $l=127mm$ for all gauges and $lc=100mm$.

There are two basic ways to place (assemble) the gauges upon the circumference of the workpiece. The first way, named the circling way, is to put the gauges one by one until the space between the first and the last gauges is not large enough to be put into another one gauge. This way usually needs many gauges especially when the diameter of the workpiece is very large, while the second way (alternating way) just employs a few of the gauges. If there are only three gauges available, it works like this: put the three gauges upon the circumference of the workpiece firstly. Then while keeping the first and the third gauges being unmoved, take the second gauge off slowly and place it again upon the workpiece but behind the third gauge. Afterwards, while holding the second gauge being unmoved, take the third gauge off slowly and put it again upon the workpiece but behind the second gauge. It is not stopped until the space between the first and the last gauges (the second or the third gauge) is not large enough to be placed into another one gauge.

3. EXPERIMENTAL RESULTS

Two kind of the experiments have been carried out. The first is the repeatability experiments. The aim is to evaluate the uncertainty introduced by the random factors such as the contacting deformations between the positioning elements of the adjacent gauges, the deviations of each gauge from the cross section of the workpiece and so on. The second is the comparison experiments, in which the results obtained by the method of this paper were compared with those obtained by some other methods. The uncertainty contributed by those factors of systematic ones can be found by the comparison experiments. Those factors include the calibrated diameter uncertainties of the balls and rollers of each gauge, the non-circularity of the workpiece and so on.

Table 1 Results of the repeatability experiments* Unit: mm

No.	lc	D	No.	lc	D
1	97.679	1279.988	6	97.678	1279.988
2	97.680	1279.989	7	97.690	1279.990
3	97.684	1279.990	8	97.684	1279.990
4	97.682	1279.989	9	97.677	1279.987
5	97.679	1279.988	10	97.674	1279.987
Standard deviation of D: 0.0011					

* Measured object: outside diameter of a bearing

Measuring parameters: d=27mm, l=127mm, n=26, m=7

Table 2 Results of the repeatability experiments* Unit: mm

No.	lc	D
1	99.958	2553.926
2	99.960	2553.927
3	99.955	2553.925
4	99.955	2553.925
5	99.957	2553.926
Standard deviation of D: 0.0008		

* Measured object: outside diameter of a disk

Measuring parameters: d=27mm, l=127mm, n=52, m=7

3.1 Repeatability experiments

Table 1 and 2 give two results of the repeatability experiments. It shows that the standard deviation of the measured diameter is very small. This means also that the contact deformation between the positioning elements of the adjacent gauges is very small and stable. It is an important conclusion, because it is the precondition and basis of the method of this paper.

It is worth mentioning that the repeatability experiment (Table 1) was done in a workshop without air-conditioner and lasted for several hours. The recorded temperature change of the workpiece was over 4°C during the measurement process, which means that the diameter change of the workpiece (steel) was close to 0.05mm. However, the experimental data did not respond to this change. It indicates that the expansion of the gauges (steel also) matched correspondingly to that of the workpiece. The reason lies in that the gauges and the workpiece are always holding contacted by the magnets during the measurement process, accelerating the heat exchange. Besides, the gauge is small, so the temperatures of them are easy to keep same.

Table 3 Results of the comparison experiments* Unit: mm

D1	D2	
First measurement: 1220.598	0° direction	1220.599
	45° direction	1220.600
Second measurement: 1220.598	90° direction	1220.590
	135° direction	1220.587
Mean: 1220.598	Mean	1220.594

*Measured object: outside diameter of a bearing

Comparison instrument: the caliper gauge with a dial at its end zeroed with blocks

Measuring parameters: l=127 mm, d=27mm, n=25, m=7

D1: obtained diameter with the large diameter gauge

D2: obtained diameter with the comparison instrument

Table 4 Results of the comparison experiments* Unit: mm

D1	D2
First Measurement: 978.872	0° Direction: 978.889
Second Measurement: 978.874	90° Direction: 978.870
Third Measurement: 978.874	Mean: 978.880
Mean: 978.8733	

* Measured object: outside diameter of a turbine rotor

Comparison instrument: large external micrometer zeroed With the length bar

Measuring parameters: l=127mm, d=27mm, n=20,m=7

D1: obtained diameter with the large diameter gauge

D2: obtained diameter with the comparison instrument

3.2 Comparison experiments

Table 3 and Table 4 show two results of the comparison experiments. The differences between the results obtained by the large diameter gauge and those obtained by the comparison instruments are 4μm and 6.3μm, respectively. In other words, the corresponding relative differences are 3.3×10^{-6} and 6.4×10^{-6}, respectively.

4. CONCLUSIONS

A new method of measuring large diameters has been presented. It has many valuable properties, such as that both external and internal diameters can be measured and there is no upper limitation of measuring range in theory. In addition, the measuring apparatus is compact and portable. Its structure is simple and cost is low. The theoretical estimation of uncertainty (omitted in this extended abstract) pointed out that, without considering the non-circularity of the workpiece, the extended uncertainty (3σ) will be ($0.002+1\times10^{-5}D$) mm or less. The results of the repeatability and comparison experiments proved this conclusion.

ACKNOWLEDGEMENTS

The author wish to thank Shanghai Measuring & Cutting Tool Works, Shanghai United Bearing Co., Ltd. and Shanghai Turbine Company Ltd. for their assistance in the making of the experimental setup and the accomplishing of the experiments.

The author is also indebted to Hwa-Ying Culture and Education Foundation for its support to attend this meeting.

REFERENCES

[1] Рубинов,А.Д, Контроль Больших Размеров в Машиностроении Справочник(*in Chinese*). Chinese Press of Machinery Industry, Beijing, 1987, pp.10-181.

[2] Currie, J.R., Kissel, R.R., Oliver, C.E., Smith, E.C., Redmon, J.W., Wallace, C.C. and Swanson, C.P., Cylindrical Surface Profile and Diameter Measuring Tool and Method. G01B/28, USA, No.:4821425, 18/04,1989

[3] Bar-Shay, A., Measuring Cylindrical Concave Surfaces with Large Central Angle by Means of a Portable Device. *Precision Engineering*, 1990, **12**(3), 172-178.

[4] Bahr, T., Blener, P. and Krattenmacher, G., Device for the Measurement of the Diameter of Cylinders. G01B3/12; G01B7/28, USA, No.: 5197200, 30/03, 1993.

[5] Ионак,В.Ф,Фидимонов, В А и Борисов, В.В., УСТРОЙСТВО ДЛЯ ИЗМЕРЕ-НИЯ ДЕТАЛЕЙ БОЛЬШИХ ДИАМЕТРОВ. G01B7/12, SU, No.: 1238504A, 15/06, 1980.

[6] Yin, Z.L., On Line New Method of Large Diameter Measurement with High Precision. *Chinese Journal of Scientific Instrument*, 1994, **15**(3), 276-280.

[7] Feng, Q., Tian, Q. and Liang, J.W., Development of a High Precision Measurement System for a Large Scale Workpiece Diameter by Using a Dual Frequency Laser Interferometer. *Chinese Journal of Scientific Instrument*, 1995, **16**(2), 145-150.

[8] Li, B. and Liang, J.W., Measurement of Large Internal Diameters with a Compact Apparatus Based on DHI. *Precision Engineering*, 1997, **21**(1), 36-42.

PREDICTION OF TEMPERATURE AND DIMENSIONAL CHANGES DURING SOAKOUT USING FEA

Chakravarthy B., Cherukuri H.P., Hocken R.J., Wilhelm R.G.
Dept. of Mechanical Engineering and Engineering Science,
Univ. of North Carolina at Charlotte, Charlotte, NC 28223.

In many manufacturing operations, parts are manufactured in a typical machine shop environment and then brought into a temperature-controlled metrology room for measurement purposes since dimensional measurements need to be referenced to the standard reference temperature of $20^{o}C$. Hence the parts are "soaked" to the standard temperature or to within a specified tolerance of the standard temperature prior to measurements. The time taken by the part to come to equilibrium with the ambient environment following a change in environment is called the soakout time and is a characteristic of the soakout process. Lack of proper understanding of the issues governing the soakout process may result in size errors and geometrical errors in the part. In certain cases, parts are measured while they are in the process of changing temperature or allowed to soakout for an extensive period of time. The purpose of this paper is to predict the temperature and dimensional changes during soakout using finite element analysis (FEA) on CAD models of parts of various shapes and identify parameters that affect the accurate prediction of soakout times.

This work employs a combination of experiments and finite element analyses. Parts of various shapes such as solid rectangular blocks, blocks with holes and a gear-pump housing are considered for soakout analysis. The rectangular blocks made of aluminum alloy are illustrated in Figure 1 and the plan view of the gear-pump housing is shown in Figure 2.

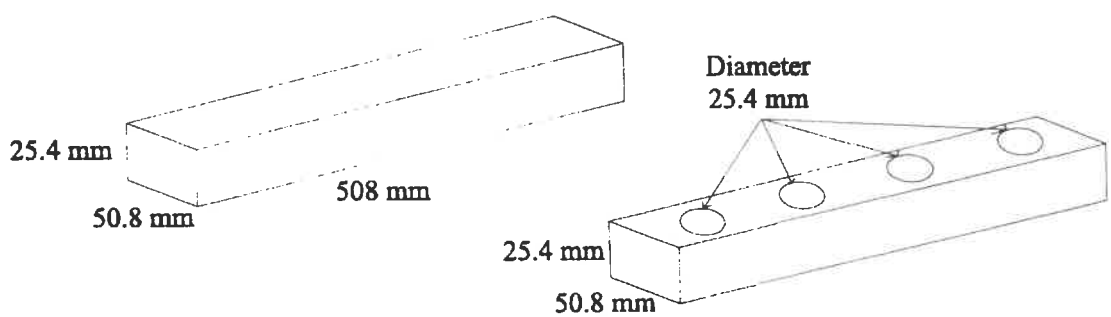

Figure 1: Aluminum blocks considered for experimental determination of soakout

The parts are heated in an oven to a predetermined temperature and then transferred to the metrology laboratory where surface temperature, dimensional changes and form error of the part surfaces are measured at various times as the part soaks. A coordinate measuring machine is used to measure the dimensional changes and indicate the form error of surfaces while surface temperatures are recorded by means of thermistors attached to the part. Different boundary conditions are considered for different soakout runs involving the blocks. The

blocks are placed either on the granite base of the CMM or given an elevation by placing them on steel roller supports.

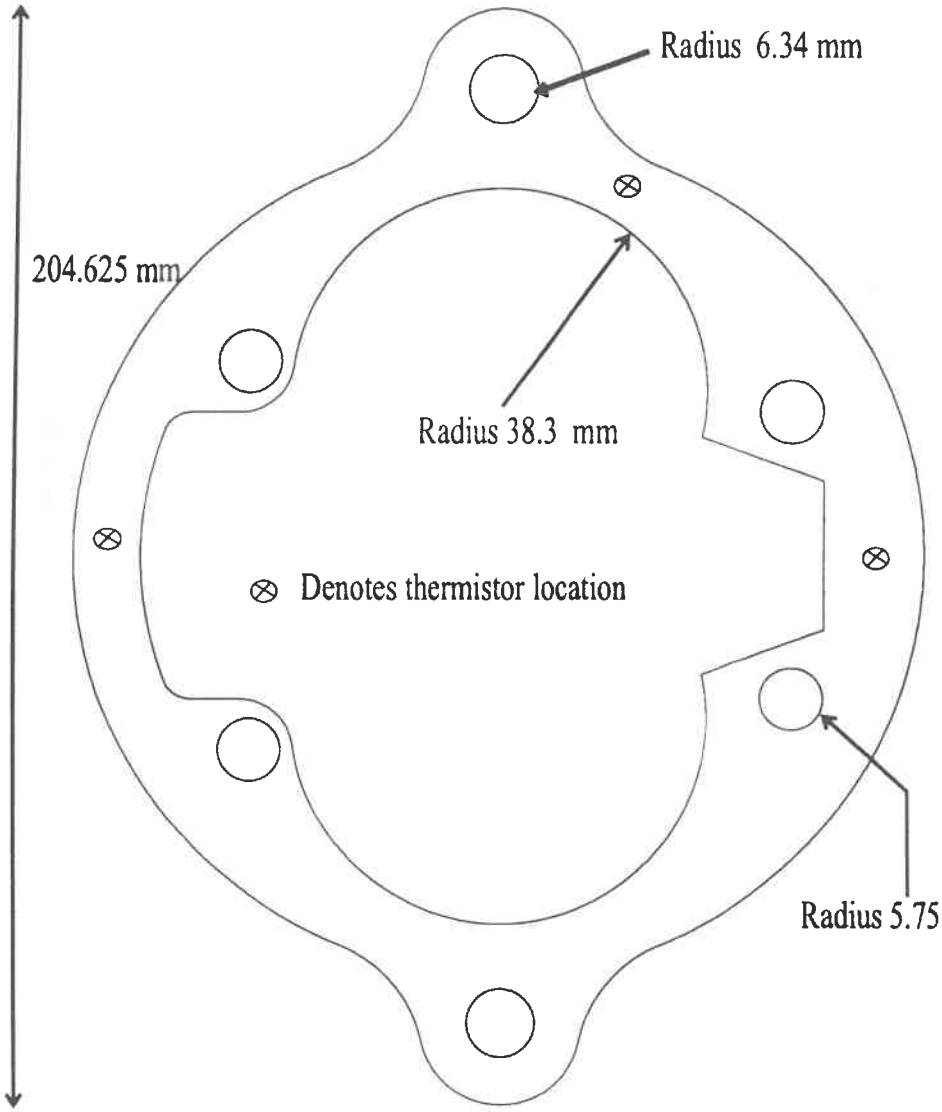

Figure 2: Gear-pump housing considered for experimental work

In the FEA modeling of the experiments, the boundary conditions were approximated by applying convective heat transfer on all surfaces except the bottom face which was considered to be insulated while convective heat transfer was applied on all surfaces in the latter case. However, the gear-pump housing is placed on an aluminum base with an appropriate fixture for all cases of soakout. The transition of the part from the oven to the metrology room introduced some complexities which had to be resolved in the FEA model since the ambient temperature and the magnitude of convection in the transition phase is different from those prevailing inside the lab. Suitable approximations are made in the FEA models regarding the actual existing conditions. Values of the heat transfer coeficient specified in the FEA model are inferred from

the experimental temperature data and an inverse approach. Two different values of the heat transfer coefficient are used in the FEA model for different time periods of soakout i.e. a high initial valule for the duration the part is in transition (around 2 minutes) and a lesser average value for the remaining part of soakout in the lab. This method is justified by the observed convection pattern for each case. Finite element analyses involved using uncoupled thermolasticity theory to determine the nodal temperature and displacements as functions of time.

Comparison of FEA results with experimental temperature data in each case shows good agreement for all times except the initial few seconds where there is some discrepancy due to uncertainties in predicting the heat transfer coefficient accurately. The error in predicting the temperature in the initial times varies from 8-15% in cases involving the aluminum block while it is 9-13% for cases involving the gear-pump housing. However the error is negligible near soakout times. Also, the FEA models are accurate in predicting the soakout times (appropriately defined) obtained experimentally. Similarly the dimensional variations predicted by the FEA model show a reasonable agreement with experimental measurements. In view of the observed results, FEA can be effectively used in CAD systems of manufacturing operations to characterize the soakout process effetively.

CAD/CAM Integration of On-The-Machine Measuring and Inspection System for Free-form Surfaces

Sung-Chong Chung

MAnufacturing Systems & Control LABoratory
Department of Mechanical Design & Production Engineeering
Hanyang University, SungdongGu, Seoul 133-791, KOREA

Abstract : Measurement and inspection of freeform surfaces are required in reverse engineering processes. In the conventional quality control system, a sculptured surface, after being machined in a machining center, requires to be moved to a coordinate measuring machine (CMM) for checking its surface accuracy. It needs a great deal of time and investment cost for transportation of the object, special jigs and fixtures, and programming of the CMM. The objective of this research is to minimize this time concerning job and capital investment by developing a measurement and error compensation system usable on the machining center itself, which is called on-the-machine measuring and inspection system. In order to build an automatic quality assurance process linked with precision FMS or CIM systems, information sharing between manufacturing processes have to be studied. In this paper, an on-the-machine measuring and inspection system with error compensation capability is interfaced with a CAD/CAM system through the neutral data format, IGES (Initial Graphics Exchange Specification). The IGES translator is designed for feature-based freeform surfaces represented by NURBS (Non-Uniform Rational B-Spline) surfaces. Measuring codes are obtained through the proper coordinate transformation and the uniform sampling software linked with the IGES translator. The normal vector estimation to compensate for probing error is also proposed via surface modeling. Usefulness and reliability of the developed system is verified by on-the-machine experiments.

Keywords : CAD/CAM interface, error compensation, IGES, machine tool errors, NURBS surface, on-the-machine, probing errors, reverse engineering

1. Introduction

CMMs are highly applicable to those parts normally produced by CNC machining centers and flexible manufacturing systems for prismatic parts. In recent years, CMMs have become critical equipment for quality control in modern manufacturing processes and industries, and play increasingly important roles as measuring stations for precise and complicated workpiece shapes such as free-form surfaces. However, in order to relieve bottlenecks of inspection processes on CMMs due to measuring time, difficulty of capital investment and time delay of material flow between CMMs and machine tools in the factory, on-the-machine measuring methodology are required.[1-4]

After developing touch trigger probes, probing on-the-machine has found a broad range of applications on machine tools where it is vital to automated production processes. Probing allows manufacturers in many industries to deliver precise components, minimize scraps, and maximize productivity. Many branches of the industry, particularly the automotive, the aerospace, the ship-building, the appliance, and the mold and die making facilities are involved in the manufacture of components comprising free-form surfaces. Those surfaces are designed according to aesthetic and functional requirements through CAD/CAM systems or reverse engineering processes.[5-6] In order to satisfy design specifications of the surfaces, measurement and inspection of free-form surfaces are required on some of strategic points during the production processes.[1,2,4]

In this paper, an on-the-machine measuring and inspection system equipped with a touch trigger probe is studied for free-form surfaces. Using probes on machine tools for process-intermittent and post-process measurements is complex procedures that require careful thought. Because machine tools and probing processes are fraught with error sources, many of which are intrinsic to the probing system themselves. Algorithms for calibration and compensation of measuring errors have to be proposed. To make a rapid measuring system and to build precision FMS systems, an automatic quality assurance process has to be integrated with the production process.[1,5,6] But that has not been active due to the difficulty of information sharing in manufacturing processes. In this paper, the measurement system is also interfaced with a CAD/CAM system through the IGES translator. That is designed for feature-based free-form surfaces represented by NURBS surfaces and is studied to automate measuring code generation according to the coordinate transformation.

The procedure of error analysis first starts with reading through pre-processed point-data of a CAD file. After measuring point-data of a machined surface by means of the on-the-machine system, a NURBS surface can be constructed on the basis of the acquired point-data. By comparing examined points between the CAD and the interpolated data, error analysis of free-from surfaces can be done. The usefulness and reliability of the developed system is confirmed through on-the-machine experiments.

2. Compensation of Measuring Errors

In case of surface measurements using a touch probe on a machine tool, geometric errors of the machine tool, probing and fixing errors of a probe assembly and the probe radius affect the measuring accuracy.[1-4] To ensure measuring accuracy of the on-the-machine measuring system, calibration and compensation

methods of measuring errors have been proposed by using a laser interferometer, ring gauges, a true sphere and a reference artifact.[3-4]

Calibration of pitch errors of feed drives is done by a laser interferometry. Modification of pitch error parameters of a CNC compensates for pitch errors.[3] Probing errors are identified through a small size of a precision sphere shown in [4]. Calibration of squareness and thermal expansion errors of the machine tool is performed by a large size of ring gages and a reference artifact. Fig. 1 shows the artifact developed for rapid calibration of volumetric errors of a machine tool.[3-4]

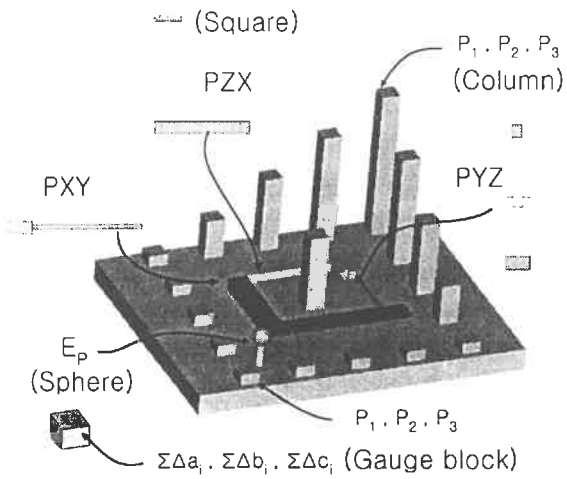

Fig. 1 Designed reference artifact

3. Design of IGES Translator

3.1 IGES Free-form Surfaces

Nowadays, many people use CAD softwares to generate surface patches. Most of CAD/CAM systems support NURBS curves and surfaces represented by

$$P(u) = \frac{\sum_{i=0}^{n} h_i \, P_i \, N_{i,k}(u)}{\sum_{i=0}^{n} h_i \, N_{i,k}(u)}; \quad 0 \le u \le n-k+2 \qquad (1)$$

$$P(u,v) = \frac{\sum_{i=0}^{n}\sum_{j=0}^{m} h_{i,j} \, P_{i,j} \, N_{i,k}(u) \, N_{j,l}(v)}{\sum_{i=0}^{n}\sum_{j=0}^{m} h_{i,j} \, N_{i,k}(u) \, N_{j,l}(v)} \qquad (2)$$

$$0 \le u \le n-k+2, \; 0 \le v \le m-l+2$$

To communicate with between different CAD files a neutral data translator is required. IGES is a widely used neutral electronic data file structure supported by all major commercial CAD/CAM systems.[7] IGES gives all information used to define the free-form parametric spline surfaces. Trimmed surfaces in CAD/CAM systems can be represented by 102, 126, 128, 142 and 144 IGES entity. The 126 and 128 entities support NURBS curves and surfaces, respectively. Fig. 2 shows a construction procedure of a trimmed surface.

3.2 Analysis and Transformation of IGES file

IGES files consist of the start, the global, the directory entry, the parameter data and the terminate section. In order to extract a trimmed NURBS surface analysis procedures of the IGES file are required. Fig. 3 shows analysis procedures of the directory entry section. After extracting pointers of parameter data, parameters of the specific geometry are recognized through the analysis procedure of parameter data.

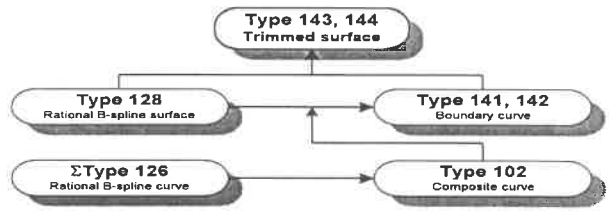

Fig. 2 Trimmed surface representation of commercial CAD/CAM

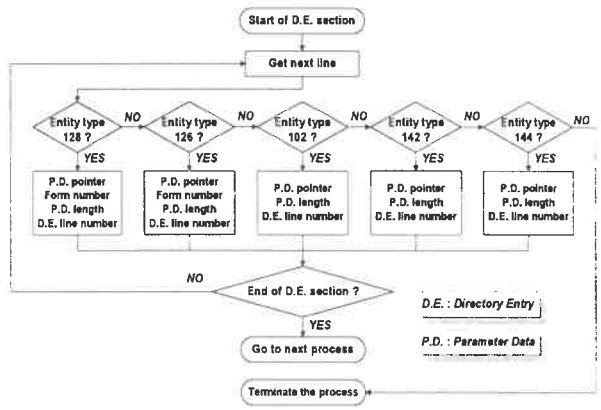

Fig. 3 Analysis procedure of directory entry section

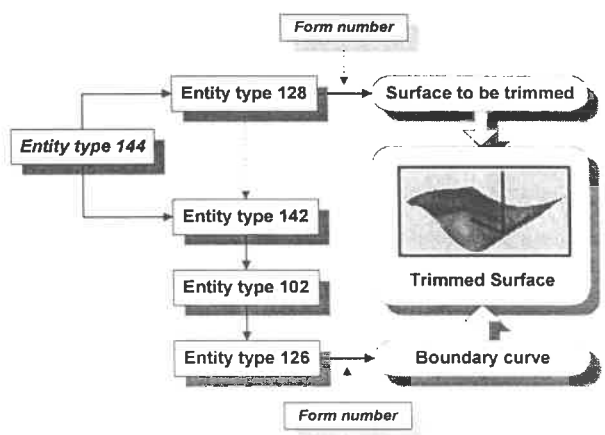

Fig. 4 Construction procedure of trimmed surfaces

3.3 Construction of Trimmed Surface

Through the analysis of geometries included in free-from surfaces and hierarchical relationships between entities, trimmed surfaces are derived as shown in Fig. 4.

4. Generation of Measuring Codes

In order to generate measuring codes of the identified trimmed surface, confirmation procedure of the free-form surface produced by the IGES translator is required on the screen. To display a 3 dimensional geometry on a 2 dimensional screen a coordinate transformation is performed. Fig.5 shows the result of the IGES free-form surface displayed on the screen.

Selection of the NURBS patch corresponding to the surface region of interest is performed on a screen by clicking the region. Generation of the measurement probe path is conducted according to the uniform sampling method.[2,4]

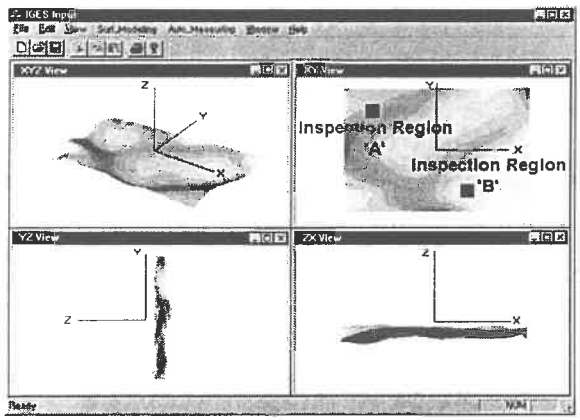

Fig. 5 IGES free-form surface generated through coordinate transformation on OpenGL

5. Probe Radius Compensation

After uniform sampling of 16 points from the selected region as shown in Fig. 5, compensation of measuring errors due to probing errors and geometric errors of the machine tool is performed according to the methods given in section 2. By using and interpolating the compensated sample points via Eq.(2), unit normal vectors at the sampled points are obtained as follows

$$N_{i,j} = \left. \frac{\dfrac{\partial \boldsymbol{P}^0(u_i,v_j)}{\partial u} \times \dfrac{\partial \boldsymbol{P}^0(u_i,v_j)}{\partial v}}{\left| \dfrac{\partial \boldsymbol{P}^0(u_i,v_j)}{\partial u} \times \dfrac{\partial \boldsymbol{P}^0(u_i,v_j)}{\partial v} \right|} \right|_{i,j=0,1,2,3} \tag{3}$$

where $\boldsymbol{P}^0(u,v)$ is the interpolated NURBS patch obtained from the compensated sample points. Probe radius compensation at a measuring point, $Q_{i,j}$ is performed as follows

$$Q^*_{i,j} = Q_{i,j} - R \cdot N_{i,j} \tag{4}$$

where $Q^*_{i,j}$ becomes the corresponding point of the sample point on the true inspection surface. Finally, the true NURBS model of the surface patch on the selected region is derived from $Q^*_{i,j}$ and Eq. (2).[2,4]

6. On-the-Machine Measurement

The IGES translator is connected to the on-the-machine measuring and inspection system[2,4] with 5μm accuracy capability in a 95% confidence interval. Fig. 6 shows the structure of the developed system.

To verify radius compensation capability of the system, a half cylinder surface shown in Fig. 7 is used. To minimize machining errors of the workpiece to be probed, a piece of engineering plastic is used for a workpiece material, and tool paths with 5μm of cusp height is applied. Twenty inspection regions are selected every 2 degrees along the curve AA' between regions of 0 to 38 degrees on the workpiece. Accuracy of the probe radius compensation is evaluated according to the accuracy of the NURBS surface modeling. Eq. (5) is applied for the accuracy evaluation.

$$E_{ave} = \frac{1}{n_p n_q} \sum_{p=1}^{n_p} \sum_{q=1}^{n_q} \left| \boldsymbol{P}(x_p, y_q) - \boldsymbol{P}^*(x_p, y_q) \right| \tag{5}$$

where n_p and n_q are number of sampling points in x and y direction, respectively. p, q mean measuring point numbers, $\boldsymbol{P}$ and $\boldsymbol{P}^*$ are the designed and the modeled surface, respectively. Fig. 8 shows measurement and inspection results. From the results, it can be concluded that the radius compensation and the on-the-machine measurement and inspection functions perform well.

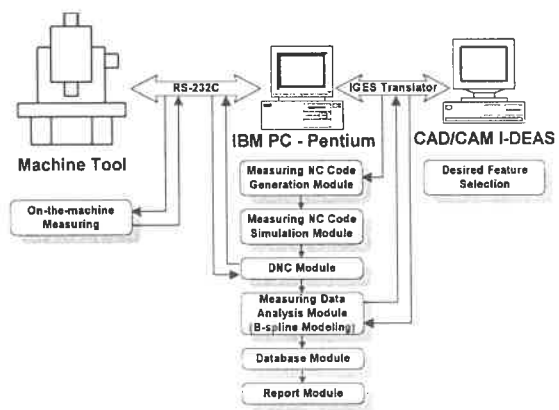

Fig. 6 Schematic diagram of on-the-machine measuring and inspection system

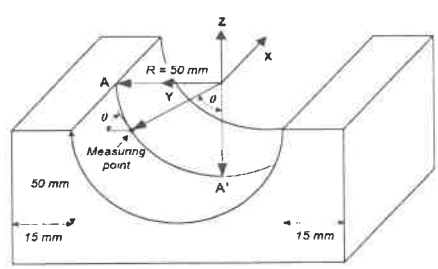

Fig. 7 A surface for on-the-machine measurement I : Contact angle test

To verify performance of the IGES translator and the on-the-machine measuring and inspection system for free-form surfaces, region A and B of Fig. 5 are selected for evaluation. Through the IGES translation and the NURBS surface fitting, error distributions of the inspection regions were obtained as shown in Fig. 9. Average errors of 7.2 and 8.8 ㎛ were inspected on the selected regions. Regardless of machining errors of the workpiece, accurate measuring results were obtained by the developed system. Usefulness of the IGES translator which integrates CAD/CAM systems and the on-the-machine measuring and inspection system was also verified through this experiment.

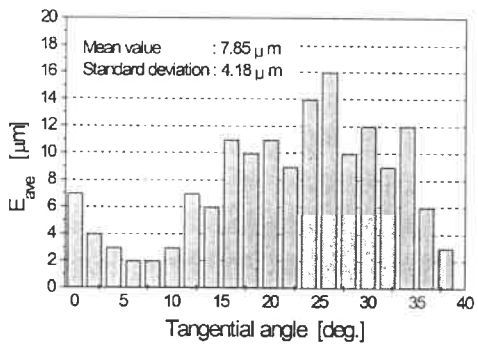

Fig. 8 On-the-machine measurement Ⅰ : E_{ave} vs. tangential angle at contact point

7. Conclusions

The on-the-machine measuring and inspection system and commercial CAD/CAM systems have been integrated using a IGES translator. Trimmed NURBS surfaces are extracted through the IGES translator. Measuring codes are automatically generated by means of coordinate transformation and uniform sampling method. To minimize measuring errors, measuring error compensation methods have been derived by the development of an artifact. Inspection accuracy of free-form surfaces confirms the usefulness and reliability of the developed system.

References

1. S.B. Lee and S. C. Chung, "On-the-machine measuring and inspection system for freeform surfaces based on IGES format", Transactions of the Korean Society of Mechanical Engineers (A), Vol. 23, pp. 590-607, 1999. (in Korean)
2. W.S. Nam and S. C. Chung, "A study on high speed and accurate on-the-machine measuring and inspection system for freeform surfaces", Transactions of the Korean Society of Mechanical Engineers (A), Vol. 22, pp. 2114-2125, 1998. (in Korean)
3. K. D. Kim and S. C. Chung, "Design and analysis of 2½ dimensional measurement and inspection system on the machine tool", Transactions of the North American Manufacturing Research Institution of SME, Vol. 27, pp. 281-286, 1999.
4. W.S. Nam and S. C. Chung, "System synthesis for on-the-machine measuring and inspection of freeform surfaces", Journal of the Korean Society of Precision Engineering, Vol. 15, No. 12, pp. 81- 88, 1998.
5. J. A. Bosch (Ed.), *Coordinate measuring machines and systems*, Marcel Dekker, Inc., 1995.
6. O. P. Bojanic, D. V. Majstorovic and R. V. Milacic, "CAD/CAI Integration with Special Focus on Complex Surfaces", Annals of CIRP, Vol. 41, pp. 535-538, 1992.
7. U. S. Department of Commerce, *The initial graphics exchanger (IGES) specification*, Version 5.0, NISTIR 4412, 1990.

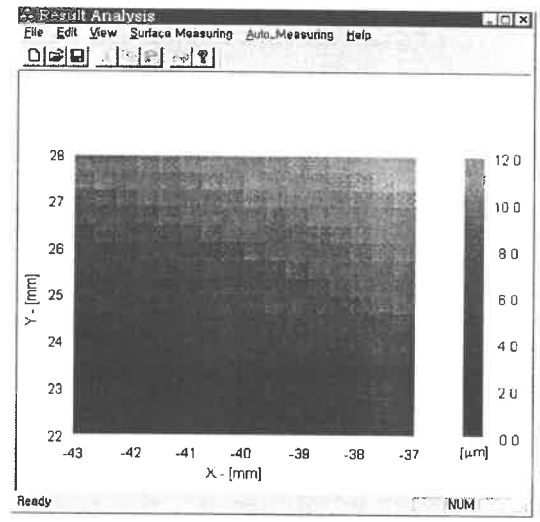

(a) Error distribution for inspection region 'A': E_{ave} = 7.2㎛

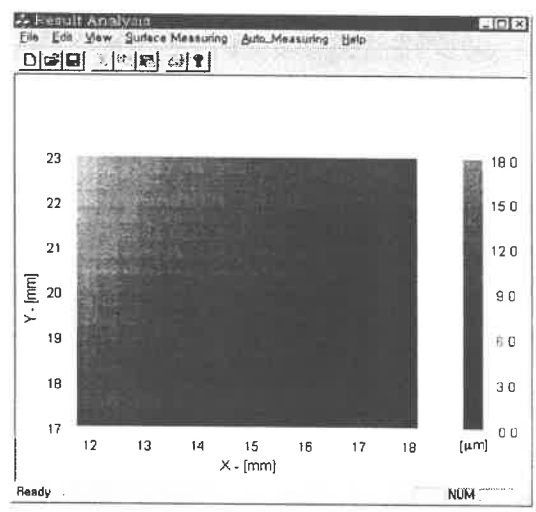

(b) error distribution for inspection region 'B': E_{ave} = 7.2㎛

Fig. 9 On-the-machine measurement Ⅱ : Error distributions of inspection regions

Magnetic Actuator Characterization for Nanometer-level Positioning

Todd N. Hinnerichs and Hy D. Tran*
Department of Mechanical Engineering
University of New Mexico
Albuquerque, NM 87131

Abstract

A kinematically coupled magnetic-bearing calibration fixture was designed based on the previous work of Poovey[1] and Groom[2], which provides the ability to experimentally explore some of the issues of concern in magnetic bearing technology. Since magnetic levitation requires the controlled production of force from an electrical signal and the dynamics of the magnetic bearing are inherently nonlinear, force characteristics (i.e., force as a function of coil current and air gap) are often developed to linearize the response of the bearing for typical precision positioning applications. The magnetic actuator characterization curves are most often implemented in a 2-D or 3-D type lookup table and can greatly enhance the bandwidth of the levitation system. Often, these curves are developed using classical magnetic circuit theory, which is accurate only at low flux densities. This linearization technique works quite well until ferromagnetic core saturation, which results in force hysteresis.

To properly understand the resulting force hysteresis, a reluctance type magnetic actuator was analyzed using the kinematically coupled calibration fixture. The maximum force of this actuator was designed to be approximately 150 N at saturation. The nominal air gap for this experimental analysis was 300 micrometers with a range of the nominal gap plus or minus 200 micrometers. To minimize the mechanical hysteresis in the system, the kinematic coupling was designed to have both high stiffness through high preload and minimal contact surface interaction. Experimental results using this calibration fixture are compared to a linear magnetic circuit model. In addition, effects of actuator/target angular misalignments on force production are presented.

Future research will include experimental testing of hysteresis force production after core saturation. The end goal of this analysis is to expand on the current understanding of reluctance based magnetic actuators and to present a more thorough model of reluctance magnetic actuators, which will aid in the future development of control systems for magnetic levitation.

Introduction

As today's semiconductor technologies demand smaller and smaller feature sizes, an attractive bearing mechanism for semiconductor lithography applications is magnetic bearings, which provide essentially frictionless, lubrication-free motion in up to six degrees of freedom with resolution limited only by the sensors and control system. Although magnetic bearings are attractive for these reasons, their inherent dynamic instability, nonlinearity (hysteresis and ferromagnetic core saturation), and damping characteristics make it necessary to fully characterize this type of bearing. However, if a complete understanding of magnetic bearings can be developed, nanometer-level positioning with high throughput is possible with a properly designed bearing.

To get a more thorough understanding of magnetic bearings, experiments were carried out using a reluctance-type magnetic actuator. The first phase of the analysis was to compare experimental data obtained from testing to a linear magnetic circuit model at the exact conditions (i.e., gap and current). From this comparison, a direct understanding of the limitations of linear magnetic circuit theory was found and will be described. In addition, experiments were run to compare target/actuator angular misalignments

* Address inquiries to Hy D. Tran; tran@me.unm.edu

Theory

Linear magnetic circuits were developed to model the magnetic actuator at small air gaps and low flux densities[3]. The models allow for the variation of current input, angular misalignments between the actuator and target, and number of incremental area units of the pole faces. The last parameter allows for very accurate calculation of iron core saturation (if the number of incremental areas is large), which in turn lets the user of the model know the bounds of the linear model (mainly useful for angular misalignment calculations).

In the first model, shown in Figure 1, the reluctance of the actuator and target's iron core is ignored. This simplification greatly reduces the complexity of the calculation by removing the necessity to find the permeability of the iron core, which varies as a function of the operating flux density. Using the electrical analogy on the magnetic circuit shown in Figure 1, the following two equations describe the magnetic circuit:

$$\Phi_{left} \cdot R_{air,left} + \Phi_{left} \cdot R_{air,mid} - MMF = 0 \tag{1}$$

$$\Phi_{right} \cdot R_{air,right} + \Phi_{right} \cdot R_{air,mid} + MMF = 0 \tag{2}$$

where Φ_{left} is the magnetic flux through the left air gap

Φ_{right} is the magnetic flux through the right air gap

$R_{air,left}$ is the reluctance of the left air gap

$R_{air,right}$ is the reluctance of the right air gap

$R_{air,mid}$ is the reluctance of the middle air gap

MMF is the magnetomotive force

We solve for the magnetic flux through each area gap. The force developed at each pole face can then be found using:

$$F_{poleface,X} = \frac{\Phi^2}{2 \cdot \mu_0 \cdot A} \tag{3}$$

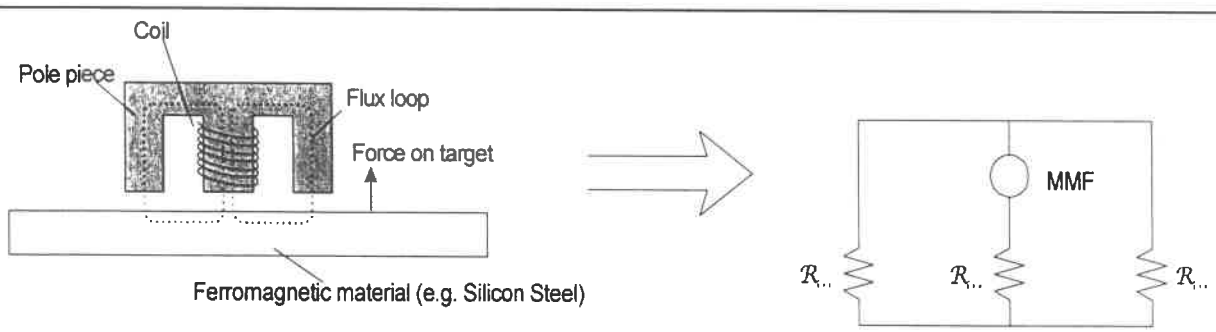

Figure 1. A typical "E-core" actuator, and its simplified magnetic circuit model for Equations (1-3).

The reluctance R of a gap is generally approximated by $R \approx \frac{l}{A \cdot \mu_R \cdot \mu_0}$, where l is the distance across the

gap; A is the area of the gap, μ_R is the relative permeability of the material, and μ_0 is the permeability of free space ($4\pi\times10^{-7}$ H/m).

This simplified linear analysis can be extended; first, by including the reluctance of the E-core and of the target in the magnetic circuit model; next, by modeling the effects of geometric misalignments, as shown in Figure 2.

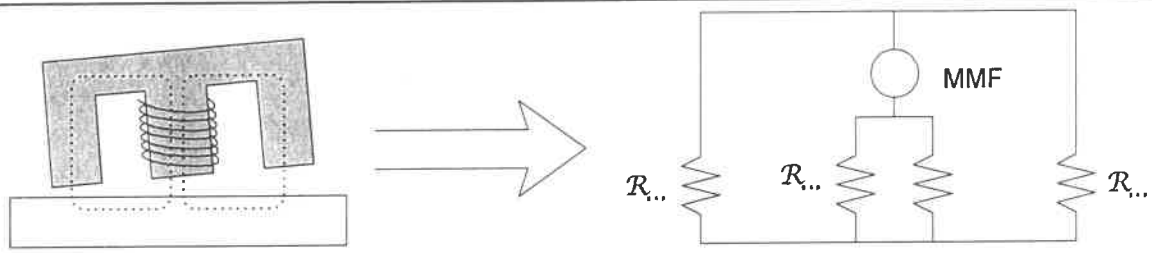

Figure 2. Effect of misalignment of the actuator on the magnetic circuit model.

We subdivide the actuator into individual area increments, and calculate the reluctance across the gap for each increment; then, we apply the magnetomotive force to obtain flux across each gap element. Force can then be calculated from Equation (3). A MATLAB program has been written to perform these calculations. The MATLAB model predicts the force at each pole face of the E-core actuator, based on current, gap, and misalignment. Furthermore, it is easy to incorporate the permeability of the core and target into this MATLAB model.

Experiments

We designed and built a calibration fixture based on the designs of Trumper and his students[1]. A solid model of this fixture is shown in Figure 3. The kinematic coupling between base and top plate is based

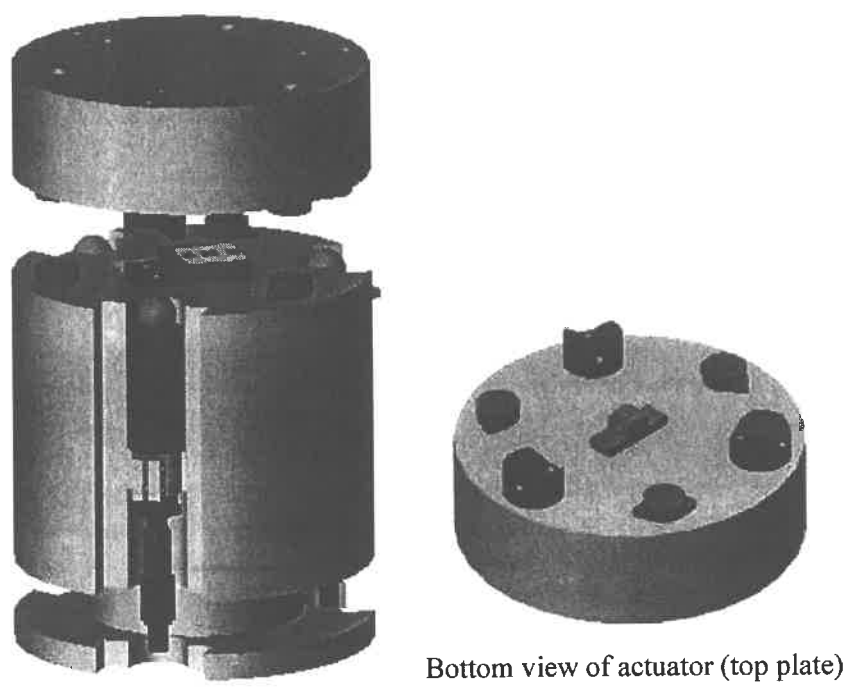

Figure 3. Solid model of kinematic actuator calibration fixture.

on the 3 balls/3 vees configuration (see, for instance, [4,5]). Micrometers are used to adjust the height of the balls (based on 3 balls/3 vees coupling between the base and the top plate). The actual spacing between the base and top plate are measured with capacitive gauges, and the forces are measured with load cells placed between the micrometer adjusters and the balls. Data from the capacitive gauges, the actuator current amplifier, and the load cells is collected via a National Instruments PCMIO-16 16-bit resolution A/D board. The system is calibrated by placing dead weights on the top plate and removing the deadweights.

Results and models will be presented at the conference.

References

1. Poovey, T., Holmes, M., and D. Trumper, "A kinematically-coupled magnetic bearing calibration fixture," *Precision Engineering*, Vol. 16, No. 2, pp. 99-108.
2. Groom, N., and W. Poole, "Description of a magnetic bearing test fixture," NASA TM-89081 [N87-20478].
3. Slemon, G., *Electric Machines and Drives*, Addison-Wesley, 1992.
4. Slocum, A., "Design of three-groove kinematic couplings," *Precision Engineering*, Vol 14, No. 2, pp.67-76.
5. Slocum, A., and A. Donmez, "Kinematic couplings for precision fixturing – Part 2: Experimental determination of repeatability and stiffness," *Precision Engineering*, Vol. 10, No. 3, pp. 115-122.

Acknowledgments

This work was supported in part by Sandia National Laboratory University Research Program grant BE-0226, and by the NASA PURSUE undergraduate research support program grant NCC5-350 from NASA MURED.

The Effects of Interstitial Media on Thermal Condition Monitoring

Yong Huang*, Zichen Chen** and James F. Cuttino***
*Dept. of Mechanical Engineering, The University of Alabama, Tuscaloosa, AL 35487-0276
**Dept. of Mechanical Engineering, Zhejiang University, Hangzhou 310027, P.R.China
***Dept. of Mechanical Engineering and Engineering Science, University of North Carolina, Charlotte, NC 28223

Abstract

The effects of interstitial media on thermal condition monitoring are studied in this paper. Conclusions are drawn from an experimental setup where thermal energy is introduced to the system and results are deduced using the t-hypothesis statistical approach. The statistical result can be used in practical monitoring and controlling processes.

1. Introduction

Precise machine condition monitoring systems often monitor temperature to determine the health of a machine. However, due to physical or practical limitations, the temperature of interest cannot be measured directly and must be inferred from temperature measured in another location. An example of this problem is illustrated in Figure 1& 2, where the temperature of a rotating component (rotor) of the mechanical seal face rig was of interest.

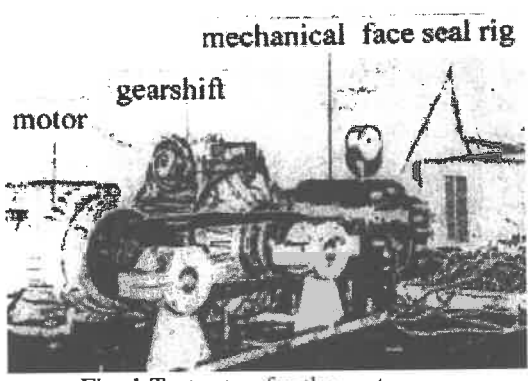

Fig. 1 Test setup for the system

In order to measure the temperature of the rotating member, the thermal information of a stationary ring (stator) which contacted the rotor, was used to reflect the condition of the rotor. However, the mechanics of contact greatly affect the heat flux and temperature distribution and must be investigated to provide accurate health monitoring. This problem is discussed in detail in this paper.

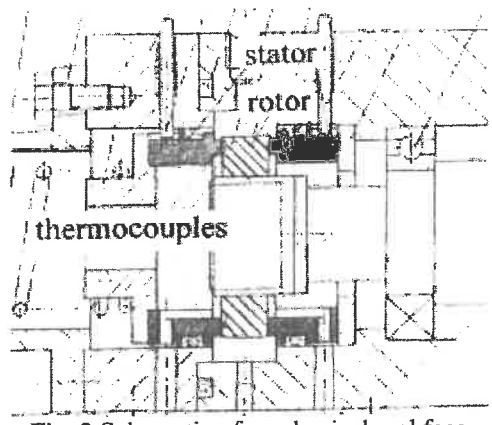

Fig. 2 Schematic of mechanical seal face

2. Effects of Interstitial Media on Thermal Condition Monitoring

The stator and the rotor of the mechanical face seal assembly were modeled in order to study the effects of the interstitial media on the nonlinearity of the temperature rise distribution through the contact face. An experimental setup was developed to verify the results. The rotor shown in Figure 2 was heated to different heat excitation power levels to simulate failure operation modes in the machine. The tests were conducted at 26.8°C and the heat excitation power ranged from 8W to 12W. The rings were made of steel and had a surface roughness of 0.8 μm. Three different interstitial media were examined, including air, No. 32 mechanical oil, and water. The thermal conductivities were 46.5w/m.k for the steel ring, 0.023w/m.k for air, 0.14w/m.k for the mechanical oil, and 0.58w/m.k for water.

For each medium, the temperature rise of the stator and the rotor were monitored, and the degree of nonlinearity in the temperature rise was determined using the *t-hypothesis* test. The hypothesis tested was as follows. The ratio of the

temperature rise of the stator, K_A, and the rotor, K_B, at a fixed time interval, was first estimated by the parameters μ_1 and μ_2 respectively. These parameters were determined from the temperature measurements of the rotor and the stator. Two conditions were then examined, the first being to accept a null hypothesis, H_0, where $\mu_1 = \mu_2$, and the second to accept an alternative hypothesis, H_1, where $\mu_1 \neq \mu_2$. The hypothesis test was conducted at a significance level, α.

2.1 *t-Hypothesis* Test

Hypothesis testing is a procedure where a sample of data is used to choose between two descriptions of the sample population represented by the null hypothesis, H_0, and the alternative hypothesis, H_1. The data are examined to see if they are consistent with the null hypothesis, or if they are inconsistent with the null and conform more closely to the alternative hypothesis.

The *t-hypothesis* test was used to test the mean of the normal distribution using samples that are normal. This method is used to determine the nonlinearity of the temperature rise since the normal distribution is a common phenomenon of the physical system. Assuming two independent samples, X_1 and X_2, with normal distributions $N(\mu_1, \sigma_1^2)$ and $N(\mu_2, \sigma_2^2)$, the means of samples are $\overline{K_A}$ and $\overline{K_B}$, respectively. Similarly, the mean-squares of the sample are s_1^2 and s_2^2 respectively. When σ_1 and σ_2 are unknown, we assume that $\sigma_1 = \sigma_2$ at a significance level α, and that the null hypothesis is $\mu_1 = \mu_2$ and the alternative hypothesis is $\mu_1 \neq \mu_2$. the region of the rejection is:

$$\left|\overline{K}_A - \overline{K}_B\right| \geq t_{\frac{\alpha}{2}}(n_1 + n_2 - 2) \times S_\omega \sqrt{\left(\frac{1}{n_1} + \frac{1}{n_2}\right)} \quad (1)$$

where

$$S_\omega^2 = \frac{(n_1 - 1)s_1^2 + (n_2 - 1)s_2^2}{n_1 + n_2 - 2} \quad (2)$$

Assuming the upper limit of the probability of P{accept $H_0 \mid H_0$ not true} is 0.2, that is β =0.2, when $\frac{|\mu_1 - \mu_2|}{\sigma} \geq 0.5$, the sample size of 24 is decided based on the table. So letting $n_1 = n_2 = 24$, we know that

$$\overline{K}_A = \sum_{i=1}^{24} K_A / 24 \quad (3)$$

$$\overline{K}_B = \sum_{i=1}^{24} K_B / 24 \quad (4)$$

$$S_1^2 = \frac{1}{n_1 - 1} \sum_{i=1}^{24} \left(K_{Ai} - \overline{K}_A\right)^2 \quad (5)$$

$$S_2^2 = \frac{1}{n_2 - 1} \sum_{i=1}^{24} \left(K_{Bi} - \overline{K}_B\right)^2 \quad (6)$$

$$S_w^2 = \frac{s_1^2 + s_2^2}{2} \quad (7)$$

and the region of the rejection is

$$\left|\overline{K}_A - \overline{K}_B\right| \geq t_{\frac{\alpha}{2}(2n-2)} \times S_\omega \sqrt{\frac{2}{n}} \quad (8)$$

When the significance level, α, is 0.05, the region of rejection is given by

$$\left|\overline{K}_A - \overline{K}_B\right| \geq t_{0.025(2n-2)} \times S_\omega \sqrt{\frac{2}{n}}. \quad (9)$$

2.2 Experimental Setup

Heat power was applied to the machine at two different levels, 8 Watts and 12 Watts. The interstitial media was changed and the temperatures of the two sides of the contacting rings were measured at 1 minute time intervals. The experimental data are shown in Tables 1 – 3 for air, No. 32 mechanical oil, and water, respectively. Among those tables, the first column represents the index of sampling points, the second column is the temperature rise of the stator when the heat power was 8 Watts, the third column is the temperature rise of the stator when the heat power is 12 Watts, the and the fourth column is the ratio of temperature rise, $K_A = \Delta T_{A12} / \Delta T_{A8}$, in which we were particularly interested. The fifth column contains the temperature rise of the rotor when the heat power was 8 Watts, the sixth column was the temperature rise of the rotor when the heat power

was 12 Watts, and the seventh column is the ratio of temperature rise $K_B = \Delta T_{B12} / \Delta T_{B8}$.

	T_A			T_B		
	8W	12W		8W	12W	
i	ΔT_{A8}	ΔT_{A12}	K_A	ΔT_{B8}	ΔT_{B12}	K_B
1	4.47	4.55	1.0179	6.11	6.49	1.0622
2	5.17	5.30	1.0251	7.72	8.65	1.1205
3	6.20	6.73	1.0855	9.28	10.46	1.1272
4	7.60	7.88	1.0368	11.03	12.05	1.0925
5	8.80	9.08	1.0318	12.49	13.99	1.1201
6	10.37	10.70	1.0318	13.98	14.86	1.0629
7	11.81	12.21	1.0339	14.68	16.27	1.1083
8	13.24	13.63	1.0295	16.12	17.97	1.1148
9	14.51	14.67	1.0110	17.27	19.55	1.1320
10	15.28	16.14	1.0563	18.79	20.94	1.1144
11	16.54	17.68	1.0689	19.99	22.60	1.1306
12	17.74	19.06	1.0744	21.12	23.95	1.1340
13	19.22	20.78	1.0812	22.56	25.23	1.1184
14	20.40	22.10	1.0833	23.65	26.70	1.1290
15	21.67	23.10	1.0660	24.86	28.08	1.1295
16	22.98	24.02	1.0453	26.10	29.37	1.1253
17	24.06	25.39	1.0553	27.18	30.77	1.1321
18	25.27	26.99	1.0681	28.27	31.97	1.1309
19	26.49	28.72	1.0842	29.37	33.10	1.1270
20	27.56	30.14	1.0936	30.35	34.42	1.1341
21	28.66	31.58	1.1019	31.37	35.51	1.1320
22	29.82	32.31	1.0835	32.39	37.72	1.1646
23	30.90	34.51	1.1168	33.46	38.79	1.1593
24	31.86	35.95	1.1171	34.34	39.60	1.1532

Table 1 The temperature rise where the interstitial media was air

	T_A			T_B		
	8W	12w		8w	12w	
i	ΔT_{A8}	ΔT_{A12}	K_A	ΔT_{B8}	ΔT_{B12}	K_B
1	1.79	2.96	1.6536	3.06	4.37	1.4281
2	2.77	3.47	1.2527	3.70	5.30	1.4324
3	3.41	4.71	1.3812	5.07	7.22	1.4241
4	3.89	6.26	1.6093	5.82	8.77	1.5069
5	5.98	8.41	1.4064	7.92	10.91	1.3775
6	6.04	10.22	1.6921	11.12	12.62	1.1349
7	9.36	11.81	1.2618	11.28	14.10	1.2500
8	10.33	13.77	1.3330	12.06	15.32	1.2703
9	13.61	14.74	1.0830	14.87	16.91	1.1372
10	13.10	16.16	1.2336	14.23	18.21	1.2797
11	14.14	18.02	1.2744	15.09	19.90	1.3188
12	14.89	19.57	1.3143	16.32	21.30	1.3051
13	16.03	20.72	1.2926	17.31	22.57	1.3039
14	16.65	22.25	1.3363	18.72	24.05	1.2847
15	18.68	24.02	1.2859	20.46	25.52	12473
16	20.26	24.99	1.2335	20.86	26.69	1.2795
17	20.45	26.60	1.3007	22.86	28.12	1.2301
18	22.21	27.81	1.2521	23.83	29.41	1.2342
19	22.97	29.06	1.2651	24.93	30.74	1.2331
20	24.20	30.53	1.2616	26.23	32.23	1.2287
21	25.12	31.76	1.2643	27.13	33.58	1.2377
22	26.18	33.05	1.2624	28.30	34.59	1.2223
23	27.36	34.53	1.2621	28.81	36.40	1.2635
24	28.26	35.62	1.2604	29.89	37.95	1.2697

Table 2 The temperature rise where the interstitial media was mechanical oil

	T_A			T_B		
	8W	12W		8W	12W	
i	ΔT_{A8}	ΔT_{A12}	K_A	ΔT_{B8}	ΔT_{B12}	K_B
1	4.40	4.20	0.9545	5.74	6.29	1.0958
2	5.56	6.32	1.1367	7.08	8.25	1.1653
3	6.86	8.21	1.1968	8.36	10.07	1.2045
4	8.13	9.92	1.2202	9.58	11.72	1.2234
5	9.47	12.05	1.2724	10.76	13.57	1.2612
6	10.59	13.75	1.2984	12.20	14.58	1.1951
7	11.88	14.58	1.2273	13.26	15.78	1.1900
8	12.91	16.28	1.2610	14.15	17.45	1.2332
9	14.03	17.91	1.2766	14.41	19.05	1.3220
10	14.47	19.21	1.3276	15.46	20.46	1.3234
11	15.18	20.67	1.3617	16.66	21.79	1.3079
12	16.16	22.10	1.3676	17.56	23.09	1.3149
13	16.99	23.33	1.3732	18.23	24.20	1.3275
14	18.12	24.76	1.3664	19.25	25.28	1.3132
15	18.85	26.01	1.3798	20.06	26.72	1.3320
16	19.57	27.47	1.4037	20.80	27.83	1.3380
17	20.31	28.78	1.4170	21.47	29.06	1.3535
18	21.16	30.07	1.4211	22.21	30.20	1.3597
19	21.88	30.60	1.3985	22.78	30.94	1.3582
20	22.56	32.03	1.4198	23.51	32.33	1.3752
21	23.02	33.25	1.4444	23.92	33.25	1.3901
22	23.64	33.68	1.4247	24.53	33.88	1.3812
23	24.37	34.83	1.4292	25.16	35.01	1.3915
24	24.74	36.74	1.4850	25.57	35.92	1.4048

Table 3 The temperature rise where the interstitial media was water

2.3 The Linearity Research on the Temperature Rise of the Contact Face

The goal of the project was to use the *t-hypothesis* test to determine whether the estimations of K_{Aair} and K_{Bair}, K_{Aoil} and

K_{Boil}, and K_{Awater} and K_{Bwater} were equal. The hypothesis to be tested was, at the signficance level, α, whether to accept the null hypothesis $H_0 : \mu_1 = \mu_2$, or the alternative hypothesis, $H_1 : \mu_1 \neq \mu_2$. In both cases, μ_1 and μ_2 were the estimations of K_A and K_B, respectively.

From table 1, we knew $\overline{K_{Aair}}$ =1.0625, $\overline{K_{Bair}}$ =1.1231, S^2_{Aair} =0.0006, S^2_{Bair} =0.0198 and S^2_{ω} =0.85, so the region of rejection was

$$|\overline{K_{Aair}} - \overline{K_{Bair}}| \geq 0.01694 \qquad (10)$$

But $|\overline{K_{Aair}} - \overline{K_{Bair}}|$=0.0606>0.01694, so it was in the region of rejection. Therefore, when α =0.05, we rejected the null hypothesis, indicating that there was a thermal nonlinear relationship of the temperature rise between the contact face when the interstitial media was air.

From table 2, $\overline{K}_{Aoil}$ =1.3238, $\overline{K}_{Boil}$ =1.2875, S^2_{Aoil} =0.0198, S^2_{Boil} =0.0081 and S^2_{ω} =0.01395, so the region of rejection was

$$|\overline{K}_{Aoil} - \overline{K}_{Boil}| \geq 0.06864 \qquad (11)$$

This time, $|\overline{K}_{Aoil} - \overline{K}_{Boil}|$=0.0363<0.06864, so it was out of the region of rejection. It was therefore concluded that, when α =0.05, the null hypothesis was valid and the thermal relationship of the temperature rise was linear when the interstitial media was mechanical oil.

Finally, Table 3 shows that $\overline{K}_{AWater}$ =1.3277, $\overline{K}_{BWater}$ =1.2984, S^2_{Awater} =0.0154, S^2_{Bwater} =0.0074 and S^2_{ω} =0.0114, so the region of rejection was

$$|\overline{K}_{AWater} - \overline{K}_{BWater}| \geq 0.06205 \qquad (12)$$

Again, $|\overline{K}_{AWater} - \overline{K}_{BWater}|$=0.0293<0.06205, so it was out of the region of rejection. It was therefore concluded that for α =0.05, the null hypothesis was valid and that the temperature rise was linear between the contact face when the interstitial media was water.

The thermal conduction of the contact face was related to the thermal conductivity of the interstitial media and the thickness of the interstitial media. The thickness of the media was dependent on the roughness, geometrical accuracy, and contact pressure of the contact face. In our experiments, the thermal conductivity of the steel ring was K =46.5w/m.k, of the air 0.023w/m.k, of the mechanical oil 0.14w/m.k, and of the water 0.58w/m.k. The thermal conductivities of the oil and water were much smaller than that of the steel ring, although still an order of magnitude greater than that of air.

3. Conclusions:

Several conclusions have been reached and are listed below.

(1) The thermal conduction of the contact face is dependent on the thermal conductivity of the interstitial media and the thickness of the interstitial media. The interstitial media thickness is in turn dependent on the ring roughness, geometric accuracy, and the contact pressure of the contact face.

(2) At the specified roughness and normal working conditions, the heat transfer is nonlinear when the interstitial media is air, but it is linear when the interstitial media is mechanical oil or water.

(3) When the interstitial media is mechanical oil or water, we can monitor the temperature rise of one side of the contact face and accurately predict the thermal condition of the other side.

(4) When the interstitial media is mechanical oil or water, thermal excitation can be applied on one side of the contact face to predictably control the temperature distribution of the other side.

References:

Anderson, T.W. Finn, J.D., *The new statistical analysis of data*, New York : Springer-Verlag, Inc., 1996

Huang, Y., *The research of the mechanical status monitoring technology based on thermal information*, M.S thesis, Zhejiang Univ., China, 1996 (in Chinese)

Sheng, Z., *Probability and statistical methods*, Beijing: High Education Press, 1990 (in Chinese)

The calibration of tilting and refractive index of specimen in confocal scanning microscopy

Jung Woo Seo, Sung Lim Park, Hyung Ryol Oh, Jun Hee Lee, Dae Gab Gweon
Department of Mechanical Engineering, Korea Advanced Institute of Science & Tech.
373-1 Kusung-Dong, Yusong-Gu, ME3265, Taejon, 305-701, Korea

Abstract

Confocal scanning microscopy(CSM) has been reported as an excellent method using the optical probe i scanning probe microscopy. However, it has the problems as formerly which make allowance for several off-axis effects from the deflection of beam or high numerical aperture, the lateral shift of primary focal point an the conditions of spcimen. These give rise to the poor resolution as the low spatial frequency and the obstacle of design the unitary lens and the other optical components. The axial distortion is resulted from the increase of th nonlinearity of optical transfer function. This article shows these primary problems in the image reconstruction. This paper shows the response experimently when the error sources such as the spatial offset of the element change and the parasitic condition of specimen, and the mathematical expression of the light in the optical fields of system. And we propose the progressive bounds of the geometry of optical components.

Keywords : confocal scanning microscopy(CSM), the lateral shift of primary focal point, optical transfer function, the parasitic condition of specimen , optical fields

1. Introduction

CSM(confocal scanning microscopy) has been used in biomedical application, materials science, semiconductor quality control and forensic application[1]. A confocal scanning microscope consists of a light projection device with which a small spot of a light beam is shaped on a specimen, a light detector device with a pinhole or single mode fibre[2], and a mechanism for two-dimensional beam scanning. An image profile can be regenerated in confocal scanning microscopy with many advantages of non-contact, high speed, high resolution of thick specimen comparatively. But it is an important matter for high resolution to align pinhole and other optical components.

Generally, the conditions of specimen give rise to the fatal distortion of an image profile, for instance, the tilting on the automated z-axis stage to section optical image[3] and variable refractive index. In a practical case, the peak intensity of detecting signal in the confocal point spread function diminishes by a factor of two or more when the beam spot is focused with less than 10 micron meter onto the specimen according to variation of refraction index[4].

In addition to the axial movement of the primary focal point having the information of specimen, the lateral movement of it gives a necessity of the unitary lens to the scanning system. Using the scanning mirror, the pupil of beam should be fixed at the nominal position. Further more, the use of a scanning mirror may result in a reduced numerical aperture of the objective lens and the loss of a great proportion of the radiation[5].

2. System description

In addition to conventional confocal microscope, two-dimensional scanner is used as shown at fig.1. Acousto optical deflector has advantages as variableness, speed and position controllability but disadvantages as dispersiveness, poor efficiency deflection dependent and complication optical set-up[5]. Most important fact is that the scanning speed of the object scanning type depends on the dynamic of automated XY stage almost. Technical progresses in the past have led to scanners with greater accuracy and higher frequencies of operation at larger scan angles with wider apertures. This system is used with the bulk acousto-optic deflector, which has the center drive frequency of 100 MHz and the active aperture of 2.5 mm for itself. In the separation of deflector and dichroic mirror, the unitary lens is used for the reduction of loss of energy.

3. Wave form through optical path

The source of beam is HeNe laser suffered from the uncertainty of wavelength. Neglecting it, through the filtering

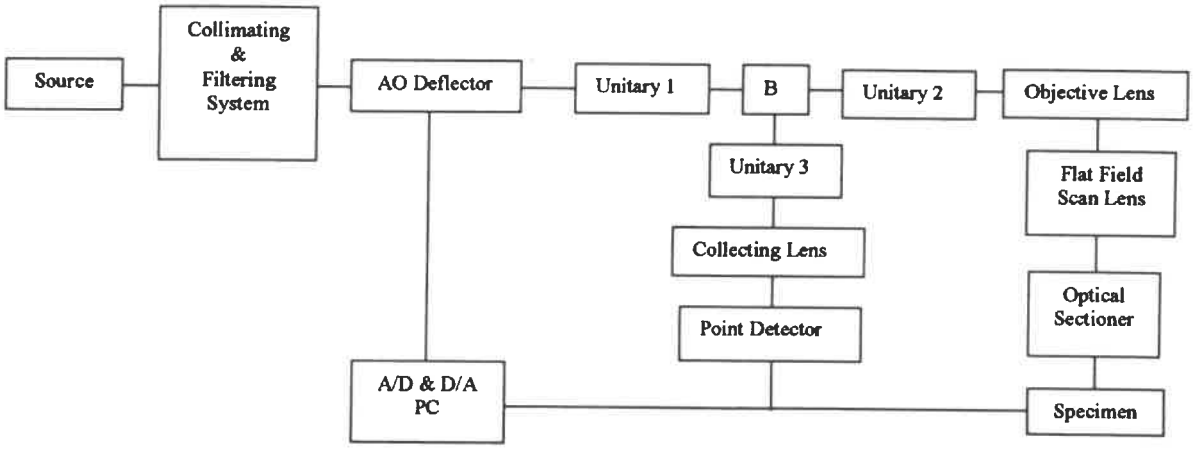

fig.1 Function scheme of confocal scanning microsopy using AO

and collimating system including lenses and pinhole, the wave leads to the diffractive light because of the finite size. And at the AO deflector, Fresnel diffraction[8] appears. After the AO deflector, the deflection angle of the diffracted beam can be expressed as,

$$\theta = \sin^{-1}\frac{\lambda_{of}}{2n_d\lambda}[1-(\frac{\lambda}{\lambda_{of}})^2(n_i^2-n_d^2)] \qquad (1)$$

where λ_{of} is the free space wavelength of the incident light, n_i and n_d are the indices for the incident and diffracted wave respectively[6].

In conventional confocal microscopy, the predominant approximations are used, if the lens of high numerical aperture is not involved. They are such conditions in which we have thin lenses and first order theory is sufficient for their analysis. Fourier analysis leads to a marvelous way of treating optical processes in terms of spatial frequency [6].

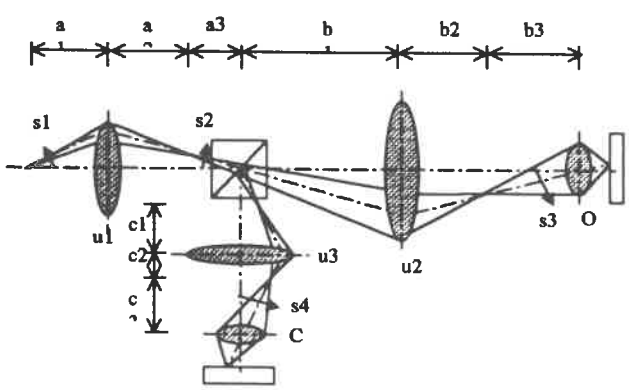

fig.2 The primary optical system in scanning microscopy

The optical component including common objects, pinhole, lenses, film, scanner and other detector has a finite pupil function in practice. From Maxwell's equations[7], a vectorial form of the wave equation for the propagation of light can be obtained. The Kirchhoff diffraction formula is a solution to the Helmholz equation that is derived a scalar form of the wave equation neglecting the polarization properties of light. The diffracted light in the condition can be expressed as

$$\Psi_2 = \frac{i}{\lambda}\cos(n,r)\iint \Psi_1(x_1,y_1)\frac{\exp(-ikr)}{r}dx_1dy_1 \qquad (2)$$

where Ψ_1 is the light field before the diffraction element, Ψ_2 after the element, r is the distance between the two diffraction plane, k is the wave number and $\cos(n,r)$ denotes the cosine of the angle between the wave vectors. The angle factor can be an important one in the scanning condition. The spherical wavelet propagator is usually expressed as the series including the coupling coordinates, which leads to Fourier transform of the combining wavelet.

The geometry of the optical system can be expressed as fig.2. Beam Scanning suffer from serious problem if the microscope is to operate at highest resolution [5]. If light is deflected by a deflector and is incident on an objective then either the full aperture of the lens will not be properly filled at all times during the scan, resulting in the objective having a reduced numerical aperture and a consequent loss of resolution or alternatively a great proportion of the radiation will be lost. In addition to primary lens, some lens system may be needed in order to minimize the loss of energy of

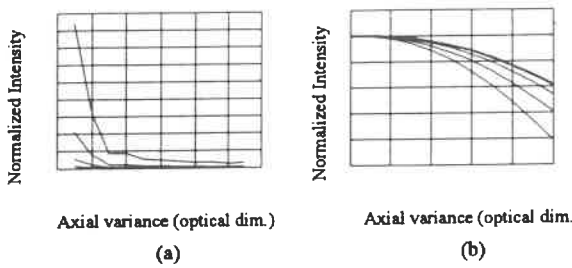

fig.3. The axial variance of the focal plane vs intensity of detection signal at zero deflection (a) when NA of Objective lens increases from 0.1 to 0.4, (b) when the finite size of pinhole increases from 20 to 60 micron meter.

light. In fig.2, the entrance pupil of beam can be fixed at the beam splitter, objective lens and collecting lens where the incident lights may be crossed twice.

Fig.3 (a) denotes that the high numerical aperture of the objective or collecting lens leads to the good sensitivity and the large nonlinearity as aberration. That means that the intensity profile for the open loop scanning method should be matched with its response to a perfect mirror as specimen, which can be minimized with the optical sectioning or the optical probe of the closed loop control. fig.3 (b) show that the axial response is a function of the finite size of detector. For a point detector, in which case imaging is coherent, the axial response becomes independent of the defocus distance in the limiting case of an infinitely large detector. The sensitivity of response increases greatly when the detector size decreases. The alignment of optical components becomes, however, a critical issue.

4. Ray path & design parameters

When the beam is scanned, the off-axis effects distort the waveform at each plane. In practice, it is important to know how seriously lens aberrations or defocus affect the optical performance of the microscope. At first, the optical axis should be traced as shown at the dashed line of fig.2. The incident angle at the beam splitter can be expressed as,

$$\theta_2 \approx \tan^{-1}\frac{a_1 \tan\theta_1}{a_2 + a_3} \tag{3}$$

at the objective lens as,

$$\theta_3 \approx \tan^{-1}\frac{b_1 \tan\theta_2}{b_2 + b_3} \tag{4}$$

and the collecting lens as,

$$\theta_4 \approx \tan^{-1}\frac{(a_3 + c_1)\tan\theta_2}{c_2 + c_3} \tag{5}$$

Three-dimensional transfer functions are based on the paraxial approximation. As this assumption may not hold for an objective of a numerical aperture higher than $1/\sqrt{2}$ we use the lenses of 0.25 NA. In the second place, the lateral shift of light should be defined at the specimen and point detector. When the collimated light shows the deflected path at each elements, the remain parameters can be expressed as,

$$a_3 = \frac{f_{u1}^2}{a_1 - f_{u1}} \tag{6}$$

$$b_3 = \frac{\{(a_3 + b_1) f_{u3}\}^2}{a_1(a_3 + b_1 - f_{u2})^2 + (a_3 + b_1 - f_{u2})(a_3 + b_1) f_{u2}} \tag{7}$$

$$c_3 = \frac{(c_1 f_{u3})^2}{(c_1 + a_3)(c_1 - f_{u3})^2 - (c_1 f_{u3})^2 (c_1 - f_{u3})} \tag{8}$$

where f_{ui} is the focal length of each unitary lens. Then the lateral shift of light at ΔL_s the specimen is,

$$\Delta L_s = \frac{f_o b_3}{b_3 - f_o}\tan\theta_3 \tag{9}$$

and the lateral shift of light at the ΔL_d detector is,

$$\Delta L_d = \frac{f_c c_3}{c_3 - f_c}\tan\theta_4 \tag{10}$$

where fo, fc is the focal length of objective, collecting lens respectively. The important facts can be explained with the results. All parameters must be positive number in the reasonable limits and three parameters for the design should be chosen in order to minimize the cost function which can be expressed as,

$$M_{\Delta L} = W_s S_s \Delta L_s + \frac{W_d}{S_d \Delta L_d} \tag{11}$$

where W_s, W_d is the weights and Ss, Sd is the scale factor of beam shift at the specimen and detector respectively. Of course, ΔL_d is a function of a1, b1 and ΔL_s of a1, c1. If the design parameters and weights are chosen properly in order to minimize the cost function M, the optimal condition can be acquired. When a1, b1 is changed in the reasonable bound, the lateral shift at the specimen (the scanning range) can be shown as fig.4 (a). At the same time, the lateral shift of light at the detector like as pinhole changes for the variance of c1. At the results, we can find the design variables of the optical system.

5. The condition of specimen

AO deflector has n-th order ray as multi-beam. Further more, the multi-beam is a symmetric form about optical

axis. This fact is the method of not only twice-stroke scanning, but also compensation for the condition of specimen. The signals of 1st and -1st order may have the low frequency distortion, the waviness of detection, because of the tilt of specimen or curvature of field. These problems can be removed by concerning the signals, for instance, the summing or extraction of normalized mean values.

6. Experiments

After choosing the design parameters for the cost function of other variables, the tolerance of set-up is a dominant problem. At fig.5, 'H' shape height sample with 80nm height and 2 micron meter pitch is scanned. If the amount of lateral beam shift at the detector is large comparing the size of pinhole, the waviness of signal possessing the information of specimen is evident, fig.5 (a)(b). In this case, the effect of beam shift at the pinhole is more fatal than the curvature of field. However, if the design parameters is given properly in order to minimize the later shift of light at the detector, the waviness can be eliminated dramatically, fig.5(c).

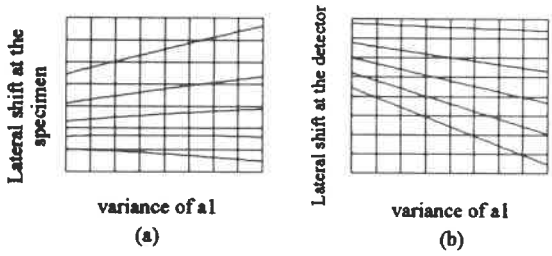

fig.4. The lateral shift of light with the variance of a1 (a) at the specimen when b1 increases from 45 to 60mm, (b) at the point detector when c1 increases from 135 to 150 mm.

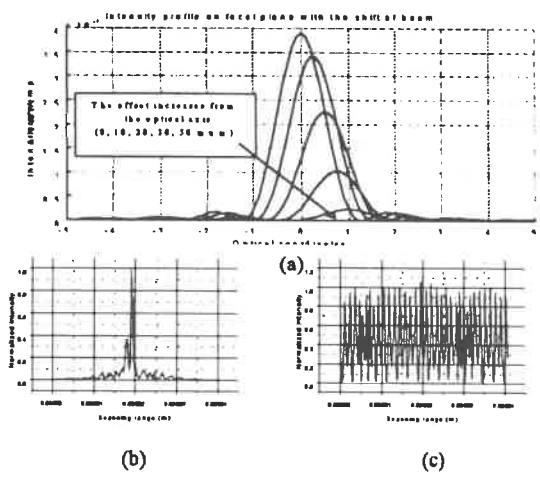

fig.5. 'H' shape height sample with 80nm heigh and 2 mu meter pitch, (a) the effect of beam shift at thepinhole, (b) the scanning result having the waviness, (c) with the design parameters using minimization of beam shift and compensation for the condition of specimen.

6. Conclusion

Confocal scanning microscopy (CSM) has the problems as which make allowance for the lateral shift of primary focal point. These give rise to the poor resolution as the low spatial frequency and the obstacles of design the unitary lens and the other optical components. We propose the progressive bounds of the geometry of optical components with the cost function having the scanning range and lateral shift of beam at the detector.

7. Acknowledgement

This work was supported by IITA on Korea under grant C1-98-0110-00. The author thanks IITA for their financial support.

References

[1] A. E. Dixon, S. Damaskinos, A. Rives & K. M. Beesley, J Microscopy Vol. 178. pt 3. June 1995. pp. 261-266

[2] P. Higdon, R. Juskaitis & T. Wilson, J Microscopy Vol. 187. Pt 1. July 1997. pp. 8-11

[3] F. R. Boddeke, L. J. Van Vliet & I. T. Young, J Microscopy Vol. 186. Pt 3. June 1997. pp. 270-274

[4] C. J. R. Sheppard & P. Torok, J Microscopy Vol. 185. Pt 3. March 1997. pp. 366-374

[5] T. Wilson, "Theory and practice of scanning optical microscopy", 1984

[6] H. Stark, "Applications of optical Fourier transforms", 1982

[7] M. Born and E. Wolf, "Principles of optics", 1980

[8] Min Gu, "Principles of 3-dim. imaging in confocal microopes", 1996

Automatic Precise Micro-Drilling System by Distributed Insect Robots

Hisayuki Aoyama, Shigeru Tadokoro, Tomohiro Shigeno and Takayuki Ono

Applied Micro Systems Group
Dept. of Mechanical Engineering & Intelligent Systems
University of Electro-Communications
Chofu, Tokyo 182-8585
Japan

1. Introduction

The demand for machine tools with much higher accuracy causes the development of ultra-precision mechanisms associated by accurate metrology system which can cover the wide working range with the sophisticated control properties. However this traditional approaches need much of cost to construct and energy consumption to maintain indeed. As an alternative approach to this problem, many unique insect size robots with precise tools workable in microscopic range have been developed by our group for these years[1]. These small robots are composed of piezo elements for micro locomotion and electromagnets for clamping as an platform mechanism. This simple arrangement can allow them to move on any inclined planes with submicron positioning resolution and good design modularity of optional micro facilities such as micro hammer, micro grating and dust capturing capillary probe[2],[3],[4]. These small robots with low production and maintenance costs have a great potential ability in the application of precision engineering.

In order to open up to the application fields, many small robots with the single tool on the desktop have to work simultaneously for more complicated tasks. In this report, we show the micro drilling system where many small insect size robots with micro tools are controlled to drive the thin drill shaft and transport the sample materials automatically.

2. Small Robots with Tools for Micro Drilling

As an useful application of the multiple insect size robots with a fine positioning and a high flexibility, the automatic micro drilling system for small parts are proposed as shown in Fig.1. Since the small size robots can facilitate just a small and simple actuator, it is required that multiple robots have to cooperate to perform

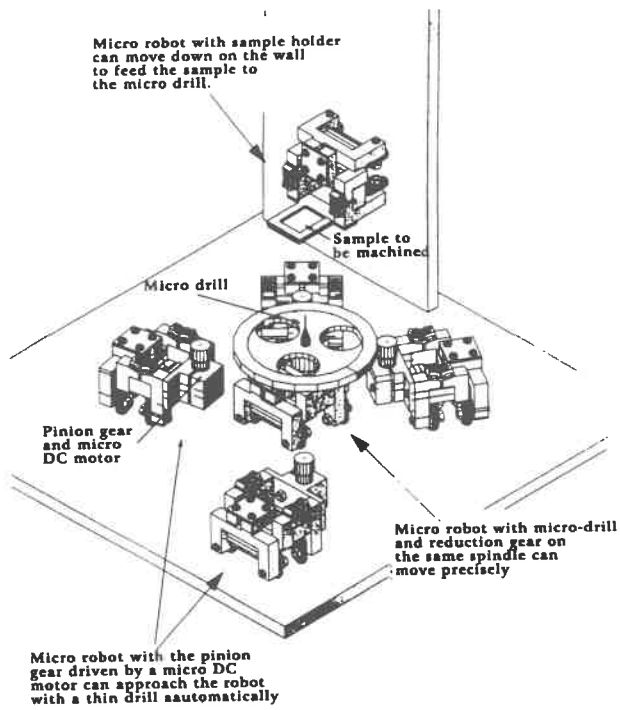

Fig.1 System concept; several insect robots can cooperate to rotate the thin drill tool and transport the small material automatically on the desktoop

the specified precise tasks. Each small robot is composed of piezo elements for micro locomotion and electromagnets for clamping on the steel surface. One small robot with the thin drill shaft is surrounded by the many tiny robots with the pinion gear driven by the micro DC motor. So they can rotate the thin drill together if they are controlled to move on the specified path. Then the other small robot which has the passive sample holder can transport the material to be machined on the vertical wall to fix it onto the drill top. Finally

(a) Thin drill shaft and reduction gear mounted on the small robots

(b) Micro DC motor with a pinion gear equipped on the tiny robot with oval outer frame

(c) Passive sample holder set on the robot to transport the material precisely

Fig.2 Developed insect size robots with unipe simple tools for automatic micro drilling systm on desktop

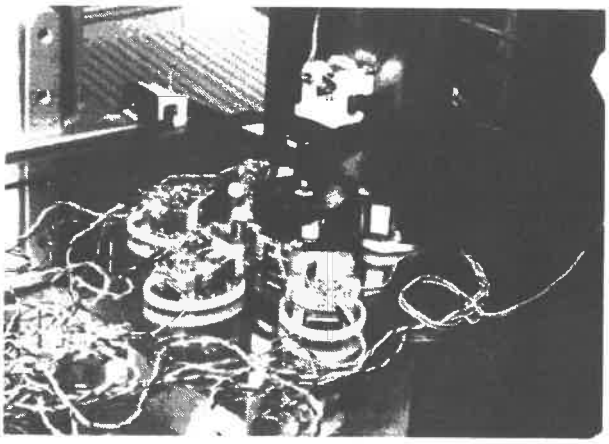

Fig.3 Experimental set-up established on the desktop to carry out the micro drilling operation

the sample can be pushed down so that the through-hole is accomplished .

Fig.2 shows the photographs of the insect size robots with micro tools. The robot in Fig.2(a) has a thin drill shaft of 0.4mm diameter with the large reduction gear on the axis. This small drill is supported by the brass bearing and magnetic thrust levitation to provide smooth rotation. The other small robot with the pinion gear and the micro motor is shown in Fig.2(b). The simple micro pager motor with the diameter of 6mm is mounted on the robot and the pinion gear is set on the motor axis. And the plastic oval outer frame is attached on its body to prevent the robots from unexpected dead locking. The remaining one in Fig.2(c) has the mechanical frame with the adhesive tape to fix the sample material although this holder should be improved to be an active device such as magnetic clamping mechanism. The experimental setup is shown in Fig.3,

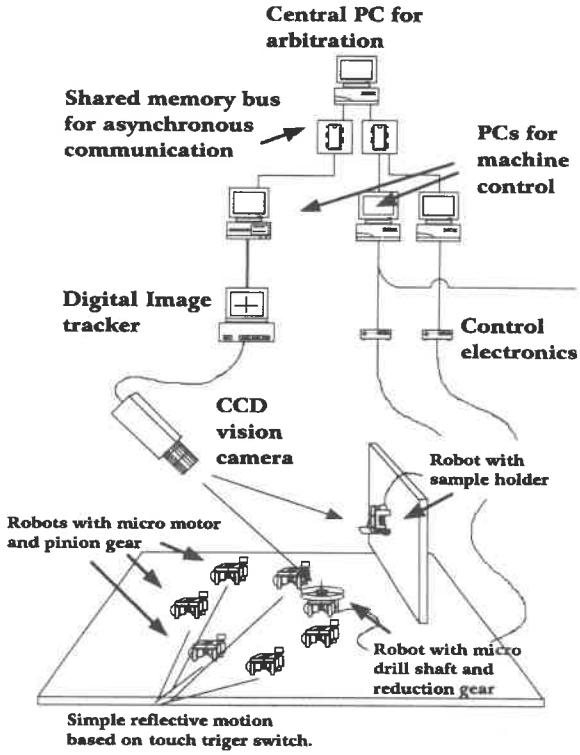

Fig.4 Control system; small robots can be monitored by the CCD camera and those coordinate positions can be analized by the image tracker to be passed onto the central computer. Finally the machine computers which are linked together can provide the commands for path control and operation signal.

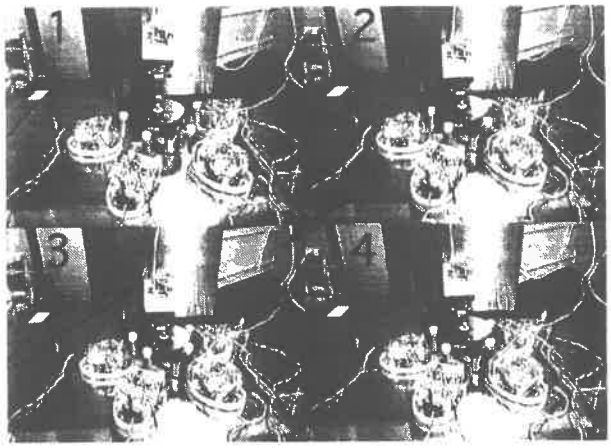

Fig.5 Sequencial pictures show that the simple process is performed by many small robots automatically. Each position and orientaion can be controlled by the vision based feedback system and parallel comutational facilities.

where many small robots stand by for precise task.

3. Control System for Distributed Insect Size Robots

In order to realize the high reliability to the distributed robots system, it is required to maneuver them into cooperating each other with the help of the visual monitoring system and the multiple computer controls. A part of our control system on going development is shown in Fig.4. In the beginning stage, a single CCD camera is mounted on the inclined frame of 45 degrees and it can monitor the position of the small robots on the horizontal and the vertical plane simultaneously to avoid the system to be complicated. The target of the optical reflector on each robot can be monitored and the coordinate position is acquired by using the special real-time image processing system which can provide the numerical data (x, y) of the center points of the brightening target with the resolution of 5000 x 5000 over the monitoring area with the sampling rate of 60Hz. These information are transmitted to the central computer to calculate the relative 3D positions and then passed on to the sub computers which are responsible to control remotely the robot motions. So the position and the orientation of each robot can be controlled easily by the visual camera based feedback loop. These computers can exchange such coordinate data, commands as well as robot's status with the shared memory bus interfaces. This parallel

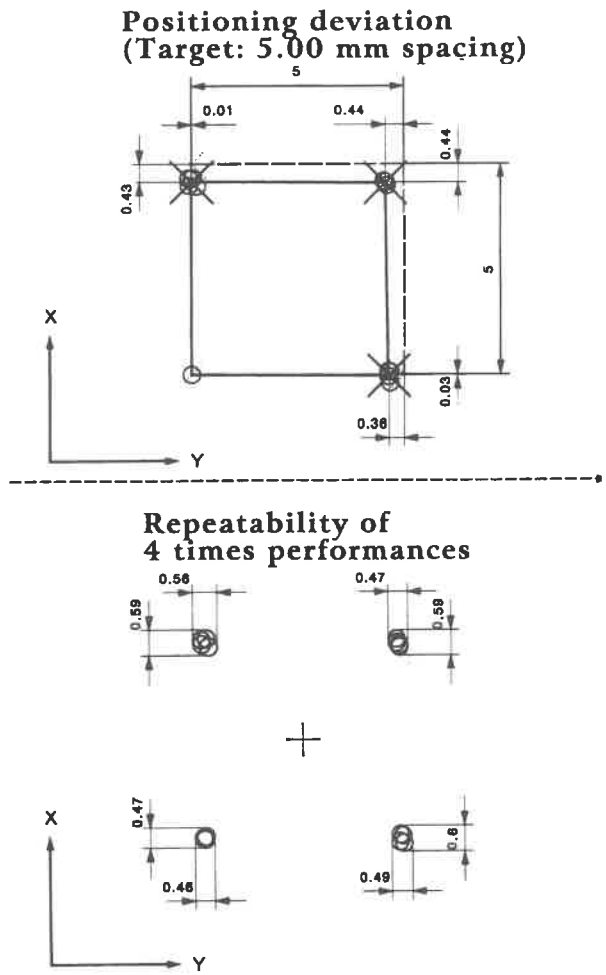

Fig.6 Experimental results show that four through -holes were drilled succesfully at the corner of 5mm square. The absolute accuracy and the repeatability are depend on the performance of coordinate measuring instruments.

control system can make it possible to provide the appropriate sequences for small robots with much of flexibility.

4. Performance

The control sequence for the small robots become so simple because the drilling task by multiple small robots can be performed almost by the path control as mentioned above. In the primary experiment, the positions of two small robots, one of which has a sample on the vertical plane and the other one has the thin drill on the horizontal plane are monitored and controlled. At first, the 2D position data of

the through-hole location to be machined are given by the operator to the central computer and then the robot with the thin drill is controlled to move and fix at the specified position. The command signals to activate the robots with a micro DC motor are give to the machine controllers and then they can approach to the robot with the drill. When all of the pinion gear come in contact with the reduction gear, the mechanical micro switch can turn on the motor drive electronics and the drill can be rotate. This means that a part of the system such as simple repeatable action is designed by the local reactive loop to eliminate the complex properties. The small robot with the sample plate on the wall can be governed to move down and fix the sample on the drill top, and push down to be machined as shown in Fig.5. The next through-hole can be also produced by repeating this simple sequence. In the actual experiment, the unique task that four through-holes of 0.4 mm diameter were given at the corner of square with the separation of 5mm were achieved on the aluminum plate shown in Fig.6. It seems that the absolute accuracy and the repeatability are not enough yet due to some error sources from such as visual camera measuring system and its alignment although they should be improved.

5. Conclusions

As a practical application of multiple insect size robots, the automatic micro drilling system was proposed. In this system, small robots which consist of piezo elements and electromagnets have a micro thin drill, a micro motor with a pinion gear and a passive sample holder. With the help of camera vision coordinate measuring system and parallel computers system, they can be controlled to perform the cooperative action to get the through-hole on the specified point of the sample. We succeeded in conducting the automatic micro drilling system by multiple insect size robots although the accuracy of coordinate metrology system should be improved.

References

[1] H.Aoyama and A.Hayashi; Multiple Micro Robots for Desktop Precise Production, Proc. of 1st Conf. of EUSPEN, (Bremenn, 1999) pp.60-63

[2]H.Kato, H.Aoyama, F.Iwata and A.Sasaki: Micro Hammer Forming Performed by Miniature Robot, Proc. of 2nd Int. Conf. on Prec. Engg., pp.680-683 (Singapore,1995).

[3]H.Aoyama, H.Nakano, A.Sasaki, J.Fukaya and T.Kubo: Collaborative Precise Operation by Two Miniature Robots-Single Diamond Cutting with Local Position Feedback, Proc. of 9th Annual Meeting of A.S.P.E., pp.238- 241 (Cincinnati,1994).

[4]H.Aoyama, F.Iwata, J.Fukaya and A.Sasaki: Miniature Robot with Micro Capillary Capturing Probe for Surface Clearing Operation, Journal of Robotics & Mechatronics,.Vol.7, No.6, pp.488-492 (1995).

DEVELOPMENT OF A TWEEZERS ROBOT EQUIPPED WITH BIMORPH PIEZOELECTRIC ACTUATORS

Toru Fujishita and Satoshi Honda
Tokyo Metropolitan Institute of Technology, Japan

1. Introduction

When we pick up a small soft capsule of unknown weight and unknown surface condition by using a tweezers, we must estimate the appropriate grasping force. If estimated value of grasping force is too weak or too strong, the capsule slips down or is distorted. If the picking robot picks up the soft capsule of unknown weight and unknown surface condition, the robot has to have an intelligent method to estimate the most suitable grasping force or has to have a huge date base for referring the value of the most suitable grasping force against all of capsules. However, to have the huge data base is not possible in fact because the value of the most suitable grasping force for individual capsule is different and there are many capsules that the picking robot might be required to grasp. Some tweezers robots have been developed with an intelligent method.[1)2)] This tweezers robot can automatically grasp the small soft capsule of unknown weight and unknown surface condition with its most suitable grasping force. The tweezers robot can estimate the most suitable grasping force by using active vibrating. This paper describes the structure of the tweezers robot, the grasping algorithm and theoretical analysis.

2. Structure of the tweezers robot

The tweezers robot has two parallel fingers. Each finger consists of the front slender beam attached

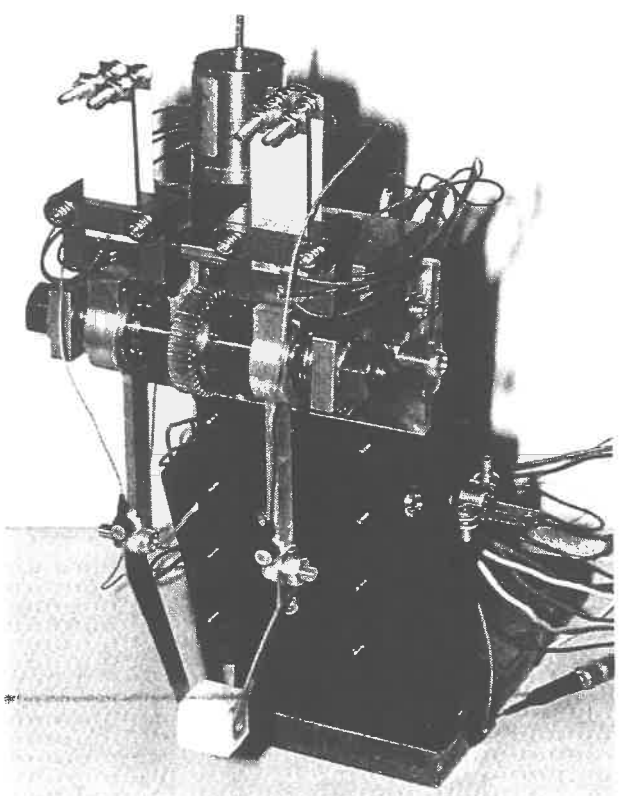

Figure 1. The tweezers robots equipped with bimorph piezoelectric actuators

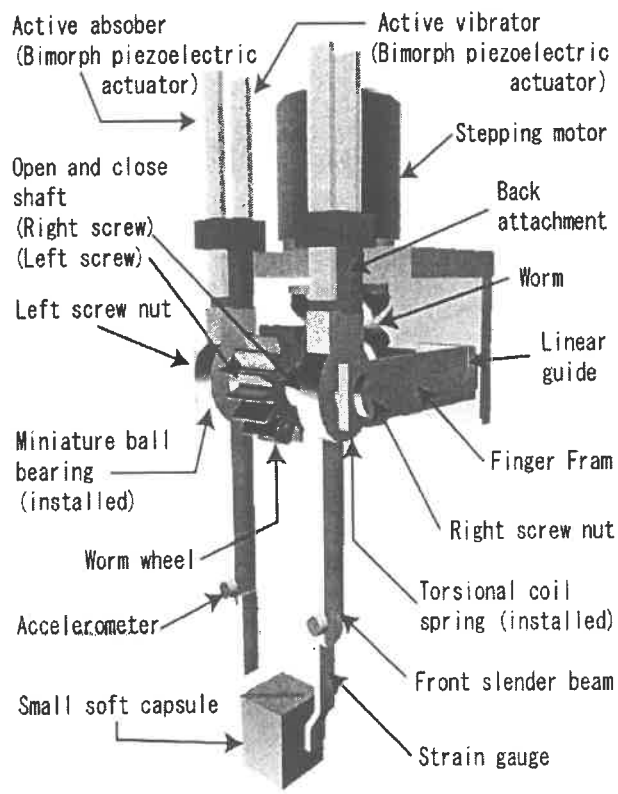

Figure 2. Structure of the tweezers robot

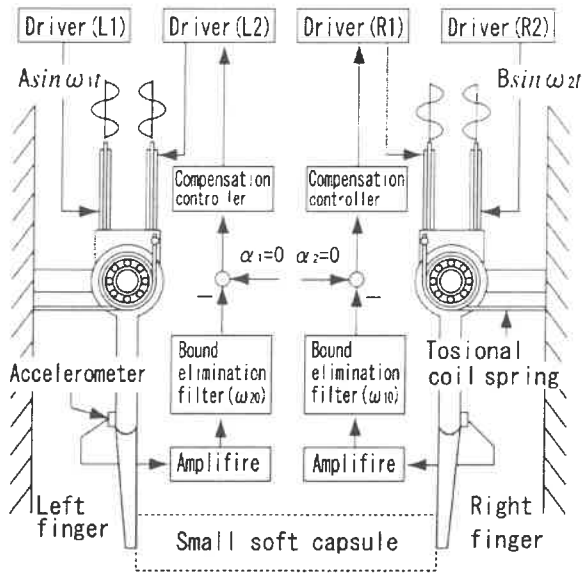

Figure 3. Control circuit for the active absorber and the active absorbers

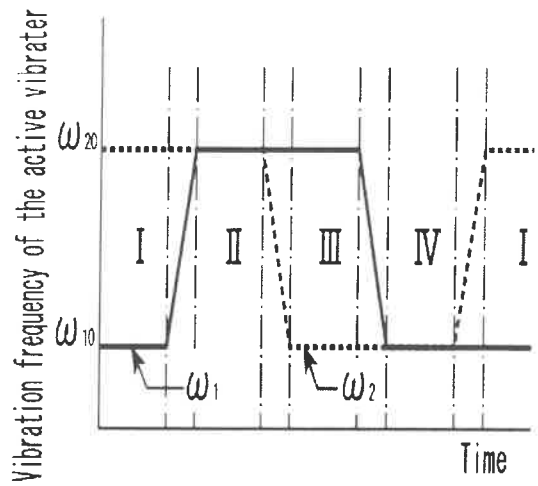

Figure 4. Control sequence of the vibrators

an accelerometer and a vibration unit composed of the active vibrator and the active absorber. The miniature ball bearing is installed between the front slender beam and the vibration unit. Each finger is supported on an open and close shaft as like a balancing toy. The torsional coil spring couples on the finger to a finger frame supporting the bearing shaft, so the finger composes a rotational vibration system. The active vibrator and the active absorber are composed of bimorph piezoelectric actuators. When the active vibrator shakes with a certain amplitude and a certain frequency, the tip of the front slender beam vibrates with relative amplitude and the same frequency. In the tweezers robot, the active absorbers are driven, so the rotational acceleration of the front slender beam reduces to zero and the tips of the front slender beams keep in a stationary condition. The small soft capsule is grasped between both tips of the front slender beams.

3. Grasping Method

3-1 Initial grasping process

Before the tweezers robot grasps the small soft capsule, vibration frequency of the active vibrators are set to the value of w1 (omega 1) and w2 (omega 2) individually. The tips of both fingers are controlled in the stationary condition by using control circuits as shown in figure 3. In this figure, acceleration of the tip is detected by the accelerometer. Each acceleration signal filters through a bound elimination filter which eliminatory frequency is w20 (omega 20) or w10 (omega 10). Error signal between reference acceleration which value is zero and detected acceleration is inputted to a compensation controller. The active absorbers are driven as the tips of the fingers are in the stationary condition.

In the tweezers robot, vibration frequency for the active vibrators changes in the sequence shown in figure 4. When the left active vibrator vibrates with frequency of w10 and the right active vibrators vibrates with frequency of w20, both tips of the fingers keep stationary as shown figure 5-A1. When the vibration frequency of the left active vibrator changes to frequency of w20, the tip of the left finger vibrates with frequency of w20 and the tip of the right finger remains stationary (See figure 5-A2). When the vibration frequency of the right active vibrator changes to frequency of w10, the tip of the left finger vibrates with frequency of w20 and the tip of the right finger vibrates with frequency of w10 (See figure 5-A3). When the vibration frequency of the left active vibrator returns to frequency of w10, the tip of the left finger become stationary and the tip of the right finger continues to vibrate (See figure 5-A4). When the vibration frequency of the active vibrators individually return to the initial frequency, both tips of the

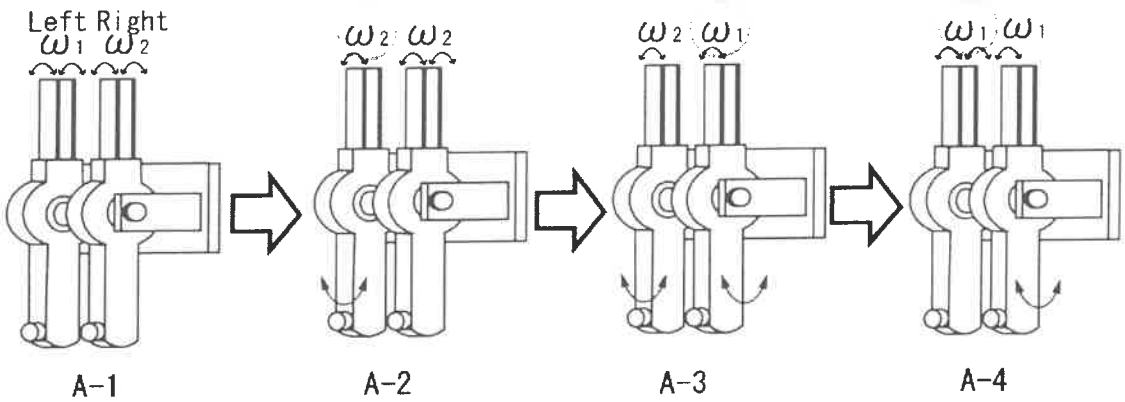

Condition of vibration at the tips of the fingers

Left	Stationary	Vibrate with ω_{20}	Vibrate with ω_{20}	Stationary
Right	Stationary	Stationary	Vibrate with ω_{10}	Vibrate with ω_{10}

Figure 5. Initial grasping process

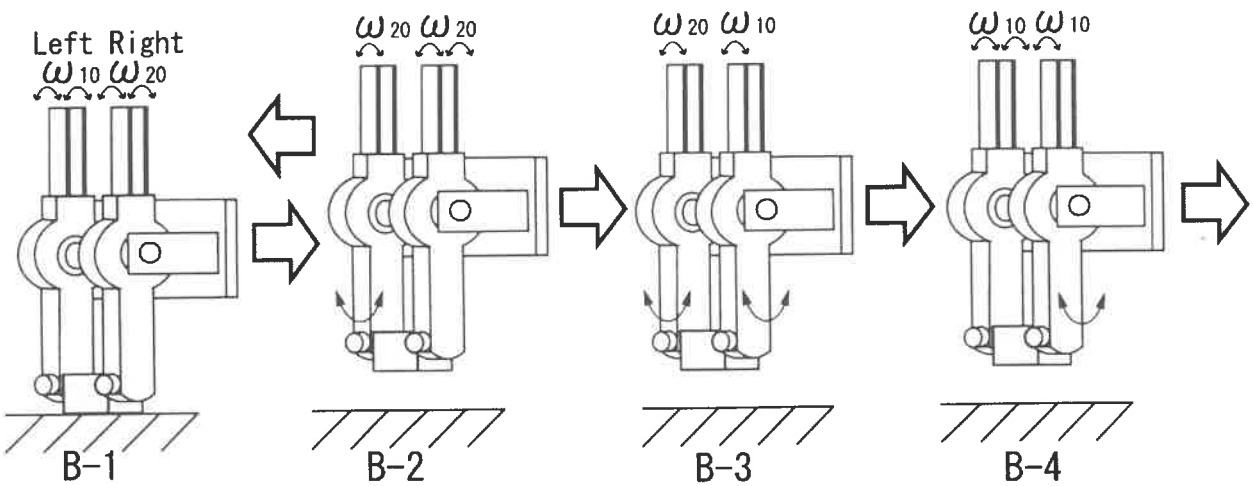

Condition of vibration at the tips of the fingers

Left	Stationary	Vibrate with ω_{20}	Vibrate with ω_{20}	Stationary
Right	Stationary	Stationary	Vibrate with ω_{10}	Vibrate with ω_{10}
		Grasping force is increased to the value in which the amplitude of left finger becomes smaller than the amplitude in process A-2	Grasping force is decreased to the value in which the amplitude of both finger becomes the same amplitude in process A-3	Grasping force is increased to the value in which the amplitude of right finger becomes smaller than the amplitude in process A-4

Figure 6. Holding process and the most suitable grasping condition

active vibrators become stationary.

3-2 Holding process and the most suitable grasping condition

When the tips of the fingers contact the small soft capsule with weak grasping force, both tips of the fingers remain stationary (See figure 6-B1). When the tweezers robot is slowly raised to lower height and

frequency of the active vibrator attached on the left finger changes to the frequency of w20, if the grasping force is smaller than the most suitable grasping force, the capsule slips down and tip of the left finger vibrates with the same amplitude explained process A2. (See figure 5-A2). The tweezers robot increases grasping force step by step, and the grasping trial is repeated. When the grasping force becomes to the most suitable value, amplitude at the tip of the left finger becomes smaller than the amplitude of process A2, for vibration at the tip of the left finger transmits to the right finger through the capsule and transmitted vibration is absorbed by the active absorber of the right finger (See figure 6-B2). In this process, the capsule is grasped with the most suitable grasping force. When frequency of the active vibrator attached on the right finger changes to the frequency of w10, if amplitude at the tips of both fingers remain in small amplitude, the capsule is grasped with excessive force (See figure 6-B3). The tweezers robot decreases grasping force. If amplitude at tips of both fingers become bigger, amplitude at tips of both fingers become bigger, frequency of both active vibrators change to the initial frequency of w10 and w20. The tweezers robot repeats the sequence and grasps the small capsule with the most suitable grasping force.

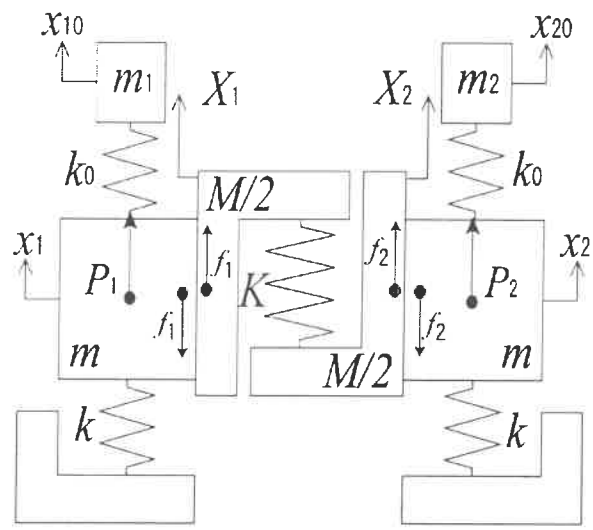

$$P_1 = m_p r \omega_1^2 \sin \omega_1 t \qquad P_2 = m_p r \omega_2^2 \sin \omega_2 t$$

$$\omega_{10} = \sqrt{\frac{k_0}{m_1}} \qquad \omega_{20} = \sqrt{\frac{k_0}{m_2}}$$

Figure 7. Analytical model

4. The most suitable grasping force

Figure 7 showed a theoretical analysis model which represent components of the tweezers robot by mass blocks and springs. Mass of the finger is m. Spring constant of torsional spring is k. The vibration forces generated by both active vibrators composed of bimorph piezoelectric actuators are P_1 and P_2. Passive absorbers composed of mass blocks (m_1, m_2) and spring (k_0) are substituted for the active absorbers composed of the other bimorph piezoelectric actuators. The capsule is consisted of two mass blocks (M/2) and a spring (K). To grasp the capsule with the most suitable grasping force in the process B-2 means to hold the mass block of (M/2) in which the mass block of the left hand is vibrating and the mass block of the right finger is stationary without slipping. The most suitable grasping force F_0 becomes as follows;

$F_0 = m_p r(Mm_1k_0^2 - Mm_2k_0^2 - 2mm_1Kk_0 + 2m_2^2Kk_0)/us(mm_1m_2k_0 + Mm_2^2k_0 + 2mm_2^2k_0 + 2mm_2^2k_0 - 2m_1m_2^2k_0 - 2m_1m_2^2K - 4m_2^3K)$, where us is coefficient of friction between the capsule block and finger block.

5.Conclusions

The newly developed tweezers robot can automatically grasp the small soft capsule of unknown weight and unknown surface condition with its most suitable grasping force. The grasping algorithm is designed and the tweezers robot is produced.

References

[1] Satoshi Honda: "Development of an Intelligent Gripper with a Dynamic Vibration Absorber", International Journal of The Japan Society for Precision Engineering, Vol.31, No.1, March (1997).

[2] Satoshi Honda: "Development of a Tweezers Robot Equipped with Active Vibrations and Active Absorbers", Proceedings of 1st international conference and general meeting of EuSPEN, Bremen, Germany, Vol.1, pp112-115 (1999).

Linear Motion Microsystem Fabricated on a Silicon Wafer

Nobuyuki MORONUKI and Kenji UCHIYAMA
Tokyo Metropolitan University, 1-1 Minami-Ohsawa, Hachioji, Tokyo 192-0397, JAPAN

1. Introduction

Anisotropic etching can produce regular shapes that consist of specific crystal planes. The shape-generating principle is different from the conventional copying rule of machine tools, in which the accuracy of relative motion between the tool and the workpiece is copied to the workpiece geometry. Thus, the accuracy by anisotropic etching is expected to be higher than that of the conventional machining processes. However, this etching has been used mainly for micromachining technique for MEMS[1,2] and its geometrical accuracy have not been extensively discussed.

This paper introduces the development of a precise linear motion microsystem fabricated on a silicon wafer that is produced by anisotropic etching to utilize the crystal regularity. Position control by applying vertical and horizontal vibrations simultaneously to the guide is also undertaken.

2. Linear Motion Microsystem

2.1 Fabrication process[3]

Figure 1 shows an example of regular shapes that consist of {111} crystal planes of silicon. When the (100) substrate with rectangular mask oriented to [110] direction is etched, V-grooves can be obtained. Its opening angle is determined as 70.5 degrees by crystallography, because the etching rate of {111} plane is much slower than that of the others and these planes form the groove face. As a result, high geometrical accuracy such as parallelism of grooves as well as good repeatability is expected.

In this study, silicon substrates with oxide layer of 1 μm thickness, which serves as an etch-mask, were used. An electron-beam pattern generator produced the mask pattern. The etchant was KOH solution (35 wt%, 333 K).

Figure 2 shows the process to fabricate the linear motion system. Two rectangular patterns produce two V-grooves. This groove is used as the guide. Also, three rectangular patterns produce two V shapes and this part is used as the slider. After etching, the necessary part is cut by a dicer. Assembling these V's completes the linear motion system. Table 1 shows typical dimension range. The longest dimension 3.7 mm is limited by the capacity of the electron-beam pattern generator

Once an accurate mask pattern is exposed aligning with the crystal orientation, precise process control is not necessary. Since etching rate is as slow as 0.3 μm/min against the (100) plane, the control of etching time is not critical.

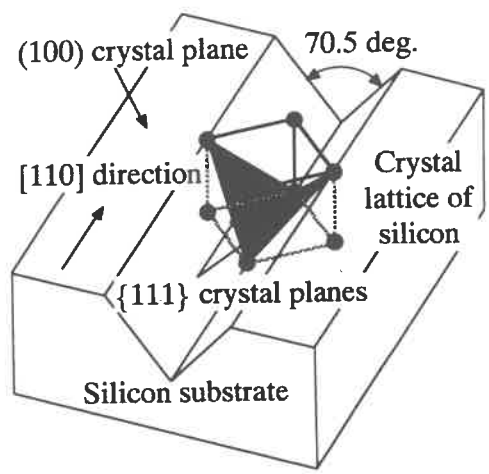

Fig.1 V-groove that consists of {111} crystal planes

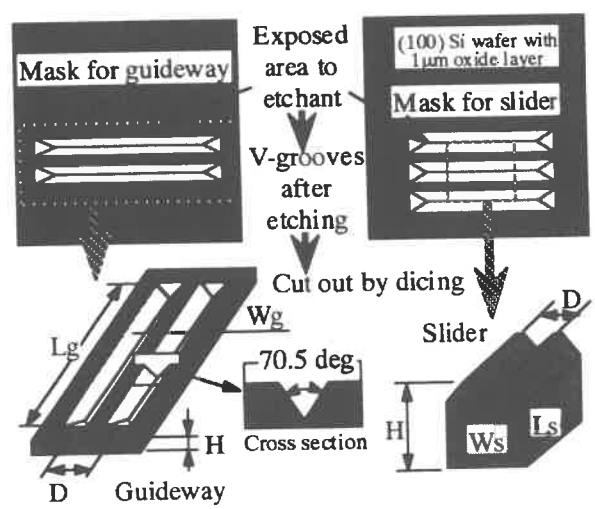

Fig.2 Process for linear motion system

2.2 Evaluation of accuracy

Figure 3 shows the results of SEM observation of the developed system. Figure 3(left) shows a close-up of the sliding face. As can be seen, V-shapes are accurately machined though the slider's width is small as 327 μm. Figure 3(right) shows the assembled view. The V-shapes of the slider fit well with the V-guide, because both faces are made of {111} planes and the opening angle is same.

In the conventional slideway system design, a double-V configuration is preferred to achieve good motion accuracy. However, the machining accuracy is crucial and the desired accuracy is difficult to obtain. Therefore, other configurations such as V-flat, are often adopted. By making use of crystal regularity described above, the geometrical error of the V's can be minimized.

Figure 4 shows the edge profile of the grooves measured by a profilometer. It can be seen that the groove width is constant over the full length and the parallelism between grooves is good. However, the grooves are not straight but curved. The maximum deviation from the ideal straight line is about 4 μm over 3.7 mm length. The reason is considered as intrinsic error of the pattern generator during the lithography.

The groove width and depth are evaluated using a confocal-type laser microscope. The nominal resolution in vertical direction is 1 nm. Table 2 shows the results. The groove width and depth are measured at five points per one groove, and the opening angle was calculated, which coincide with the theoretical one, 70.5 degrees.

3. Drive and Control

3.1 Effect of adhesion force at the interface

The sliding motion of such a microscopic object is affected by the adhesion force F_a between the slider and the guide much more than by the inertial force. This effect was indirectly measured as shown in Fig.5. The motion system was set on an inclined stage and only vertical vibration with various amplitudes and frequencies was applied. The critical acceleration when the slider begins to slide down was measured.

Figure 6 shows the results. The lines in the figure show the calculated results assuming arbitrary adhesion force F_a. Fitting the experimental results, the F_a is estimated as large as 16 μN, though its own weight is just 4 μN.

Table 1 Range of dimensions of the system

Element	Items	Minimum Size (μm)	Maximum Size (μm)
Guideway	Length Lg	3700	3700
	Width Wg	90	280
	Thickness H	450	450
	V-groove depth	64	198
Slider	Length Ls	187	360
	Width Ws	250	420
	Pitch of V's D	30	80

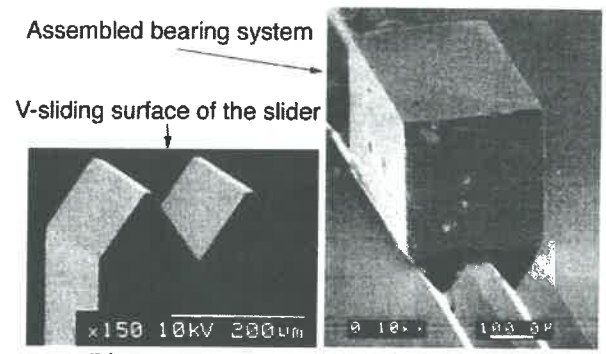

Fig.3 SEM photos of the microslider

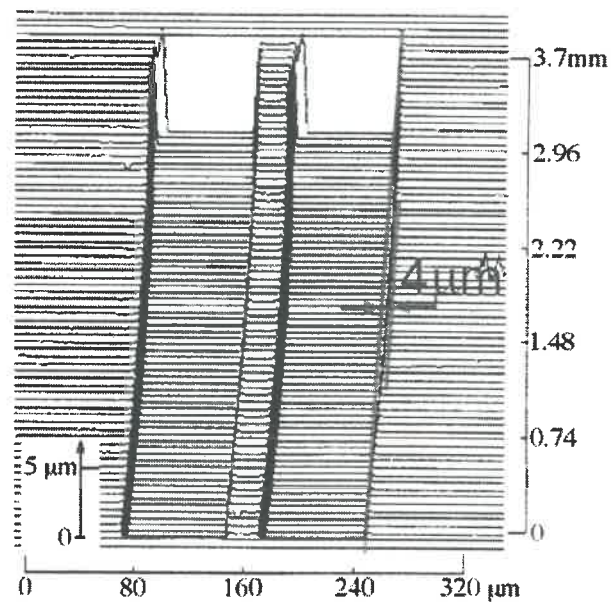

Fig.4 Profile of groove edge

Table 2 Evaluation of geometrical accuracy (Average of five points measurement)

Item	Groove width [μm]	Groove depth [μm]	Opening angle [deg]
Left groove(Fig.4)	77.43	54.52	70.7
Right groove(Fig.4)	76.80	54.45	70.5

3.2 Drive method

Vibrations in two directions, vertical and horizontal, are applied simultaneously to the guide to drive the microslider as shown in Fig.7. If the downward acceleration is sufficiently high, the slider jumps slightly due to inertia and moves intermittently along the guide. By adjusting the amplitude ratio and phase difference between the two vibrations, the motion speed and direction can be controlled.

Figure 7 also shows the experimental setup. Two voice coil motors apply vibrations in two directions, and a two-channel function generator, which is interfaced with a PC, controls their signals. In the following experiments, the generated signals are 1.4 kHz sinusoidal waves, and the burst mode is adopted due to the limitations of the equipment. A laser micrometer with a resolution of 0.02 μm monitors the feed. This signal is used for feedback control.

3.3 Driving properties and position control

It was found from other experiments that the feed rate of the slider is almost proportional to the amplitude of the horizontal vibration. On the other hand, the relationship between the number of burst pulses and the feed per burst shows a nonlinear property. The feed rate is almost proportional to the pulse number when the burst number is larger than four, at which a constant and stable feed rate, in other word good controllability, is expected. However, when the number is less than four, the feed rate becomes larger and has greater scatter. This may result from the elastic deformation of the structural members. In the following experiments, the number of burst was kept at four.

Figure 8 shows the block diagram for closed-loop position control. The current slider position is measured using a laser micrometer and used for feedback. The vibration amplitude in the horizontal direction is changed according to the position error magnitude. On the other hand, the vertical amplitude is kept constant at 1μm. This amplitude is critical to achieve smooth motion, while overcoming large adhesion force at the interface. It was determined from the experience in this study. The phase shift between these two is set to zero or 180 degrees, depending on the positioning error sign, that is, the control of feed direction.

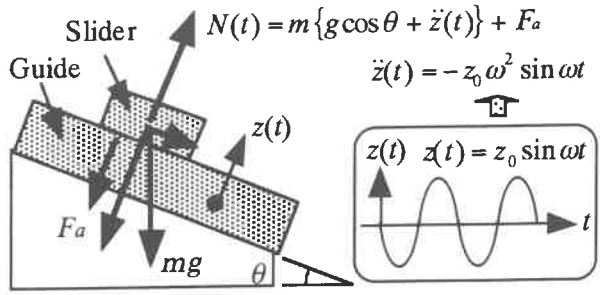

Fig.5 Measurement of adhesion force

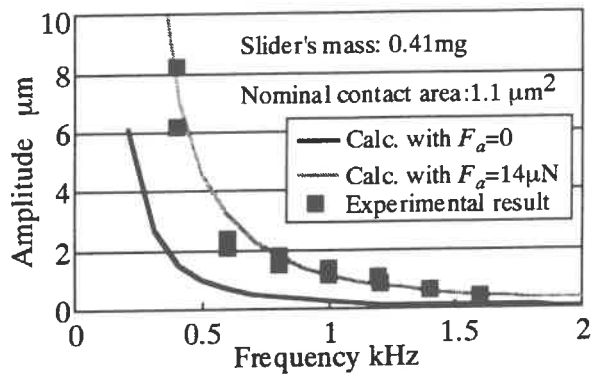

Fig.6 Effect of adhesion force at the interface

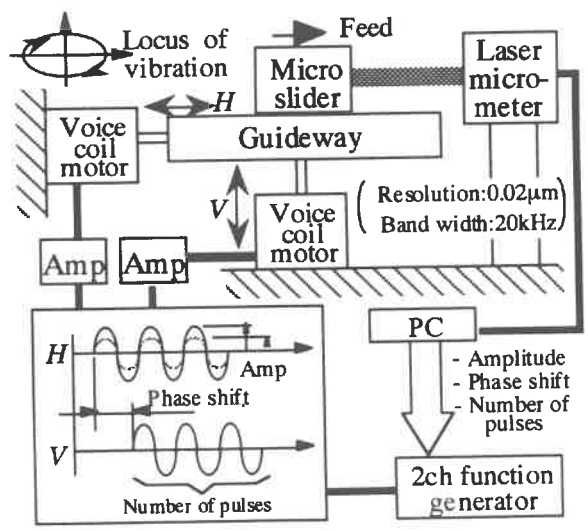

Fig.7 Experimental setup for vibration drive

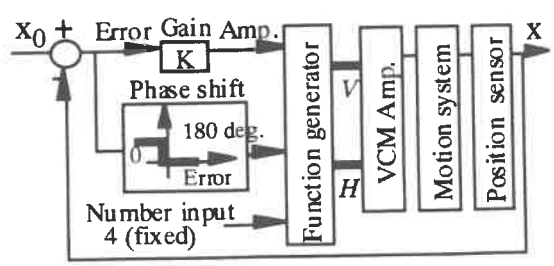

Fig.8 Position control system

The slider dimension is 330 μm in width, 625 μm in length, and 350 μm in height. The experiments were done in a clean room (class 10000) with the temperature control of 293±1 K.

Figure 9 shows the time history of the positioning process. The vertical axis shows the position of feed, where the starting point is zero and the destination is 160 μm, respectively. The slider position converged after repeating several stepwise motion cycles. The residual position error was 2 μm, where the slider position was no longer controlled, although the control was kept on. The adhesion force and friction at the interface may govern this limitation. The cycle time of control loop was long as 0.3 seconds due to the slow transmission rate of the interface between PC and function generator. By refining the apparatus, the response, as well as the positioning accuracy, will be improved.

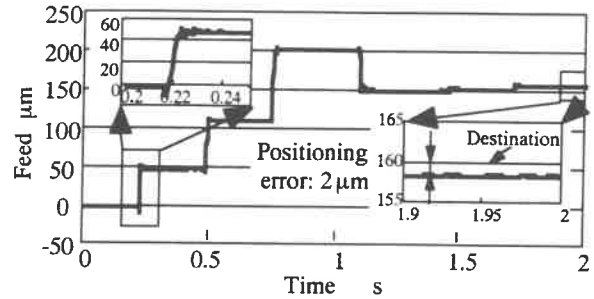

Fig.9 Result of feedback position control

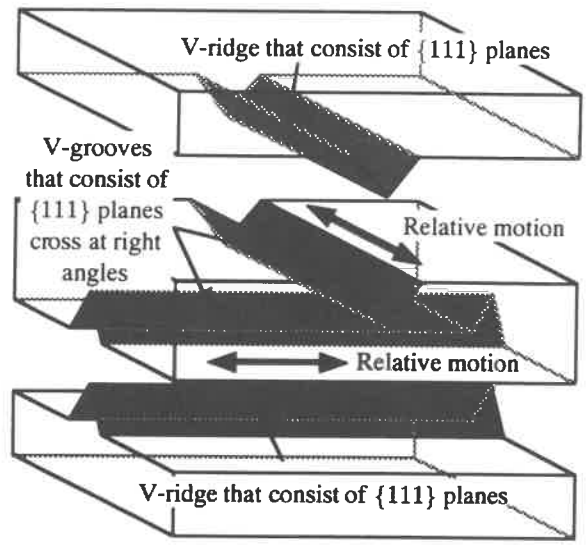

Fig.10 XY-stage utilizing crystal regularity

4. Further development

Utilizing the characteristic of cubic crystal system of silicon, an accurate XY table system can be achieved as shown in Fig.10. V-grooves that cross in right angles can be made on opposite side of a wafer by anisotropic etching from both sides. By mating V-ridge structures with these grooves, XY motion guide mechanism is completed.

The squareness of X- and Y-axis is determined crystallography again, because all of the groove faces are {111} crystal planes and high squareness is expected. However, the experimental result shows the error of 0.5 degrees in the squareness between the grooves. The reason of this error is considered as the off-angle of the substrate. That is, the top surfaces of ordinary (100) substrates are not exactly the (100) plane and often have certain angular error. It should be less than ±0.5 degrees, according to the specifications of the vendors. This error should cause a geometrical error, though this does not cause any problems in the semiconductor industries.

5. Conclusions

An application of an accurate anisotropic etching due to the use of crystal regularity has been demonstrated. The results are summarized as follows.

- A linear motion microsystem was developed, in which both the slider and the guide are produced by the anisotropic etching of silicon. The geometrical accuracy was examined.
- The developed system was driven and positioned with an accuracy of 2 μm by applying vibrations in horizontal and vertical directions.

References

(1) K. E. Peterson: Silicon as a Mechanical Material, Trans IEEE, 70, (1982), pp.420-457.
(2) M. Madou: Fundamentals of Microfabrication, CRC Press, (1997), p.449.
(3) N. Moronuki and Y. Furukawa: Microlinear Motion Bearing Produced by Anisotropic Etching of Silicon, Annals of CIRP, 46, 1, (1997), pp.151-154.

OPTIMIZATION DESIGN OF MICRO-DIFFUSER/NOZZLE ELEMENTS AND DEVELOPMENT OF IMPLANTED DRUG DELIVERY MICROPUMP

Yuhai Mu, Xiaodong Wang, Bryan Ngoi Kok Ann, and Jacob Gan Gah Kok
Metrology Lab, Department of Mechanical and Production Engineering,
Nanyang Technological University, Singapore, 639798

Abstract

A new valveless micro piezoelectric pump has been designed and fabricated. The pump consists of diffuser/nozzle elements connecting to a chamber with an oscillating diaphragm. The vibrating diaphragm produces an oscillating chamber volume, which together with the diffuser/nozzle elements creates a one-way fluid flow. ANSYS-CFD simulations of different diffuser/nozzle elements used in dynamic micropumps are presented. A micropump prototype with a chamber in diameter of 25 mm with conical diffuser/nozzle elements has fabricated and tested. A piezoelectric stack is used as the actuating element. The maximum liquid flow rate is 40 ml/min and the maximum pump pressure is 2.5 mH_2O.

Keywords: Micropump; Nozzle/Diffuser; Simulation; ANSYS; Micro Machining.

1. Introduction

A conventional diaphragm pump consists of two passive check valves connected to an oscillating diaphragm [Shoji,S.,1994] [Smits,J.G.,1990], which creates an oscillating chamber volume. Pumps with movable valves may suffer from problems such as a high-pressure drop across the valves, wear and fatigue of the movable parts. This may result in reduced lifetimes and reliability. There is a need for pumps with no movable parts.

The micro pump presented here is based on a new valveless pump principle using the different flow properties of diffuser/nozzle. ANSYS-CFD simulation method is used to optimize the design of the diffuser/nozzle elements. The valveless pump prototype is fabricated by micro machining methods, such as laser machining, EDM machining. The micropump prototype described here has properties such as simplicity and comparatively high pump volume, which makes it suitable for the applications, where high reliability and small size are required.

2. The Micropump Principle

The pump operation is based on the fluid flow rectifying properties of two diffuser/nozzle elements connected to a fluid cavity with an oscillating diaphragm. The nozzle/diffuser elements are shown schematically as Fig.1.

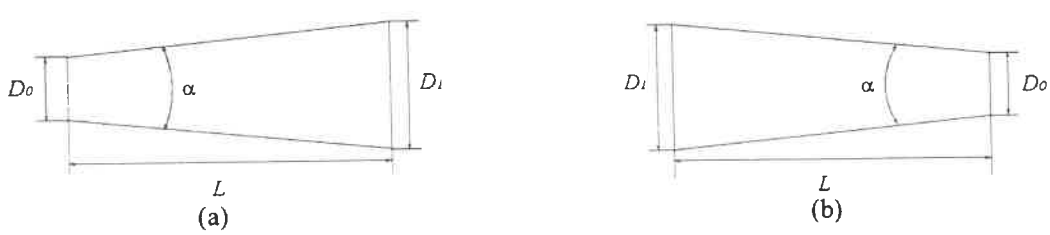

Figure 1. Schematic cross-sectional views of (a) a diffuser and (b) a nozzle

A diffuser is defined as a conduit with an expanding cross-sectional area, and a nozzle is a conduit with decreasing cross-sectional area in the flow direction. The flow direction in the pump is based on the fact that a diffuser/nozzle element can be geometrically designed to have a lower pressure loss in the diffuser direction than in the nozzle direction for the same flow velocity [White, F. M., 1986]. For a complete pump cycle, a net volume is transported from the input of the pump despite the fact that the diffuser/nozzle conveys fluid in both directions.

Generally, the flow resistance coefficient ξ of the diffuser/nozzle flow shown in Fig.1 can be written as:

$$\xi = \frac{2\Delta p}{\rho v^2} \tag{1}$$

Where, Δp is the pressure drops along diffuser/nozzle, ρ the fluid density, v the mean flow velocity at the narrowest part of the diffuser/nozzle.

The diffuser/nozzle elements in the valveless pump are considered completely the same. The actuation membrane is actuated by the harmonic distributed force. During one period T, the mean volume output flow rate of the pump is:

$$Q = \frac{A}{T}\int_0^T |V_d - V_n|\, dt \tag{2}$$

Where A is the cross-sectional area, V_d, V_n represent the mean flow velocities at the narrowest parts of the diffuser/nozzle respectively.

On the other hand, the maximum volume variability of the pump ΔV_m induced by deformation of the actuation membrane is:

$$\Delta V_m = \frac{A}{2}\int_0^T (V_d + V_n)\, dt \tag{3}$$

The mean output flow rate is then calculated by:

$$Q = \frac{2\Delta V_m}{T}\,\frac{\sqrt{\xi_n/\xi_d} - 1}{\sqrt{\xi_n/\xi_d} + 1} \tag{4}$$

From equation (4), if $\xi_n/\xi_d > 1$, the fluid will enter the pump chamber from diffuser and flow out from nozzle part.

3. Simulation and Optimization of the Diffuser/nozzle Structure

According to F. M. White's fluid mechanism theory [White, F. M., 1986] for micro channels, for a diffuser flow at very low Reynolds number (at least within 1<Re<30), the resistance coefficient of the diffuser is described as:

$$\xi_d = \frac{A_d}{\mathrm{Re}} \tag{5}$$

A_d is the function of both the angle α and the D_1/D_0, when α<40°:

$$A_d = \frac{20}{(\tan\alpha)^{0.75}}\left(\frac{D_1}{D_0}\right)^{0.66} \tag{6}$$

For a nozzle flow at very small Reynolds numbers (Re<30), the resistance coefficient of the nozzles is:

$$\xi_n = \frac{A_n}{\mathrm{Re}} \tag{7}$$

Within the limits α < 40°, A_n is:

$$A_n = \frac{19}{n_0^{0.5}\tan\alpha^{0.75}} \tag{8}$$

Where $n_0 = D_1^2 / D_0^2$

The above formulas can give theoretical guidance for selecting suitable nozzle/diffuser structure.

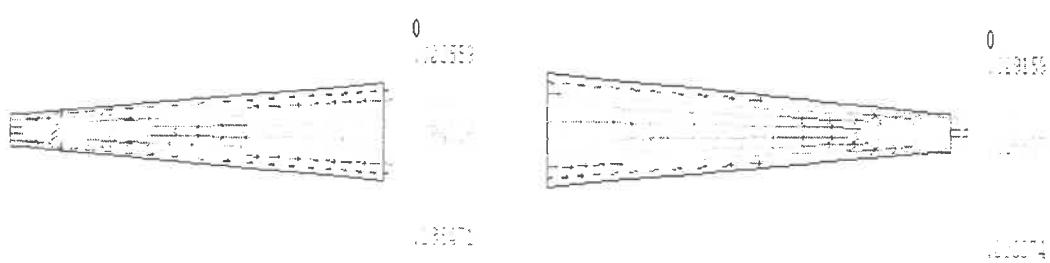

Figure 2. Flow patterns simulation for 2-dimensional model of a diffuser and a nozzle

The numerical simulations are done by using ANSYS-CFD software [ANSYS Inc., 1986]. Laminar flow situations is simulated using two-dimensional models, the D_0 is selected as 100 μm and the length L of the nozzle/diffuser elements as 2 mm. The conical angles varied from 1° to 40°. The flow model calculates the velocity in inlet and outlet of the nozzle/diffuser at various pressures and various angles. The model is meshed with quadrilateral element using higher densities near the inlet and the outlet.

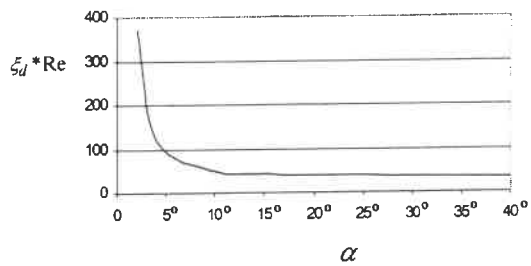

Figure 3. The relationship between ξ_d*Re and α

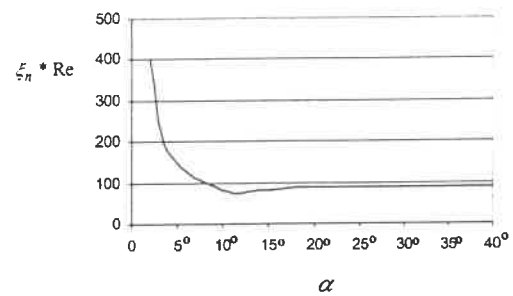

Figure 4. The relationship between ξ_n*Re and α

Fig.2. typically shows the simulated velocity change states of a typical nozzle/diffuser elements, the diverging and converging angles are 6°. By selecting the different conical angle (from 1° to 40°) and various pressures, the changing states of the resistances of ξ_d, ξ_n and ξ_n/ξ_d varying differently with α can be obtained as Fig. 3, Fig. 4 and Fig. 5 respectively. For a single nozzle or diffuser element, it shows the flow resistance coefficient is very large in the conical angle range of <10°, this is necessary for one direction flow function. From Fig.5, it shows, for achieving one direction flow function, α must be >5°, so that the ξ_n/ξ_d can be >1.5. The simulated diffuser/nozzle coefficient ratio has the similar changing trend as White's theory. From the simulation results, it shows that the conical angle of the nozzle/diffuser elements should be in the range of 5°-10°. Then the one direction flow function can be obtained.

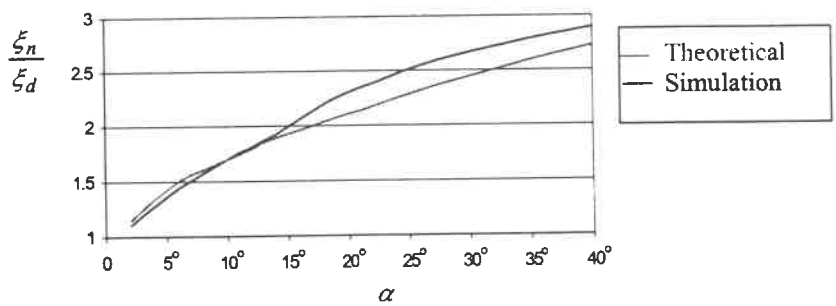

Figure 5. The relationship between ξ_n/ξ_d and α

4. Development of Valveless Micropump Prototype

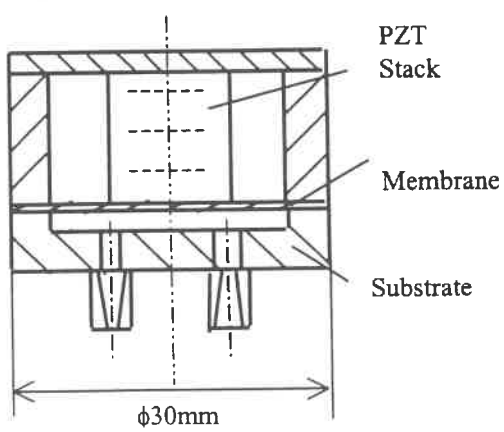

Figure 6. The diagram of the piezoelectric micro pump

Many micro pumps [Y.H. Mu, 1998, Lintel, H.T.G.V., 1988, Schoot, B.H.V.D., 1992] are developed by using piezoelectric disks as actuating elements, they need to bond the piezoelectric disks to the membranes by epoxy, the thickness of the epoxy should be as thin as possible, but it is difficult to achieve, this will greatly affect the actuating results. So these structures can not obtain high oscillating amplitude for the limited deformation of a single layer piezoelectric disk. One efficient way is to use piezoelectric stacks, which can produce tens of times deformation amplitude, this method can ignore the effect of the epoxy bonding. The prototype of micropump is shown in Fig. 6. It contains a chamber substrate, which is made of medical polymer and the nozzle/diffuser elements that are bonded to the chamber.

The nozzle/diffuser elements are fabricated by microelectro-discharge machine (EDM) system; its model is M-ED72W, a new product of Matsushita Electric Industrial Corporation Ltd. The fabricated microelectrode and corresponding nozzle hole are shown as Fig.7 and Fig.8 respectively, its structure parameters are selected according to the above simulation results.

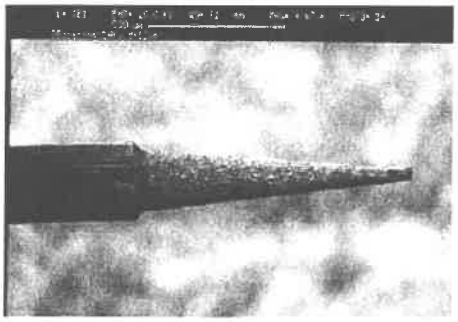

Figure 7. The SEM picture of the electrode fabricated by micro-EDM

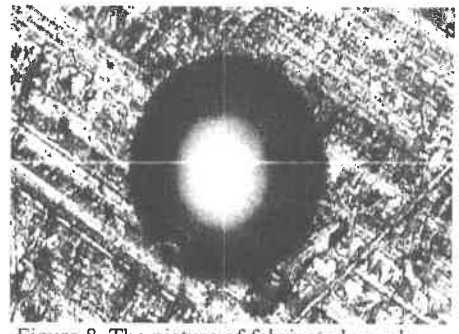

Figure 8. The picture of fabricated nozzle under optical microscope(×200)

5. Measurement Results

Deformation measurements at the center of the membrane are taken with a laser interferometer. The resolution of this type of interferometer is nominally a quarter of a wavelength or 158 nm for a helium neon laser with a wavelength of 633 nm. The deformation of an $11\times11\times18$ mm^3 sized PZT stack is approximately 15 μm for a voltage of 100 V and frequencies of 100 Hz to 5 kHz. The micro pump is tested with water. The pump rate is tested by measuring time and the output volume. A maximum pump rate of 40 *ml/min* is achieved at frequency of 200 Hz. The maximum backpressure of 2.5 mH_2O is achieved.

6. Discussions and Conclusions

This new pump has many advantages: simplicity, and high reliability; capability of pumping fluids with solid particle contents; miniaturizeability. With the diaphragm diameter of 25 mm, it demonstrated the pumping rate of about 40 ml/min and maximum pump pressures of about 2.5 mH_2O. We are planning to make a micropump to a miniaturized scale (3-5 mm), so that it can be used as an implanted component for the medical application.

References:

Shoji, S., and Esashi, M., 1994, Micro flow Devices and Systems", Int. J. of Micromech. Microeng., 4, 157-171.

Smits, J.G., 1990, Piezoelectric Micropump with Three Valves Working Peristaltically", Sensor and Actuators, A21-A23, 203-206.

White, F. M., 1986, Fluid Mechanics", McGraw-Hill, New York, 332-371.

ANSYS Inc., 1996, ANSYS_CFD FLOTRAN Analysis Guide Release 5.3, Houston, Pennsylvania.

Y. H. Mu, N. P. Hung, K. A. Ngoi, 1998, Simulation and Optimization of a Piezoelectric Micropump, Int. Conf. of ASME, California, USA, Nov. 15-20.

Lintel, H.T.G. V., De Pol, F.C.M. V., 1988, A piezoelectric Micropump based on Micro Machining of Silicon, Sensors and Actuators, 15, 153-167.

Schoot, B.H. V. D., Jeanneret, s., 1992, A Silicon Integrated Miniature Chemical Analysis System, Sensors and Actuators, B, 6, 57-60.

The Design of a Capacitive Transducer for Operation with Non-Grounded Targets

Brian Herndon*, Kerry Lamppa*, Justin McCleskey*,
Charles Fleddermann*, and Hy D. Tran†
Department of Mechanical Engineering
University of New Mexico
Albuquerque, NM 87131

Abstract
Capacitive gauges are a well-established commercial technology for non-contact displacement (or proximity) measurements; they work by measuring the capacitance of a gap between the probe and its target. Commercially available capacitive gauges are capable of nanometer-level resolution, and are used in spindle analysis, machine tool metrology, and other precision engineering applications. The drawback with current capacitive gauges is that the target must be connected to the instrument electrically, either with a grounding wire or through a low impedance capacitive coupling path. This makes capacitive gauges more difficult to use in applications that cannot permit any physical contact between target and instrument or that have an electrically noisy ground return path.

A capacitive transducer and associated signal conditioning which allows the target to "float" electrically have been designed and built. This not only eliminates the need for a ground return path from the measured target, but also reduces the potential for inadvertent ground loops during measurement setups. The design of the transducer is based on returning the probe excitation signal to the transducer, thereby virtually eliminating the measured target from the electrical signal loop. This new transducer design, and variations of the design that are capable of measuring three degrees of freedom (distance, tip, and tilt) with one transducer have been prototyped.

Introduction
Capacitive displacement gauges are a popular non-contact technology for proximity and displacement sensing. Commercial instruments are available with resolutions on the order of 16 bits (1 part in 64,000), but typical industrial usage uses lower resolutions. The resolution of capacitive transducers can reach the sub-nanometer level, exceeding the resolution of standard heterodyne laser interferometers. Capacitive gauges, which were initially developed in 1910 and refined by the research of R.V. Jones and J. C. S. Richards [1,2] in the fifties to the early seventies, are widely used by research and industry today.

Commercial applications have become widespread since Jones' work was published. The capacitive gauge is a fairly popular proximity transducer; a very popular application is as a fast, high resolution transducer. One of the applications is measuring thickness and flatness of raw silicon wafers prior to lithography in the semiconductor industry. Other applications are in the disk drive industry and in the machine tool industry in spindle dynamics analysis. The limitation with capacitive transducers has always been the need to electrically ground the target. This is a fundamental limitation of the transducer: even though it is non-contact at the point of the measurement, some form of "contact" is necessary elsewhere. Recent research in magnetic bearings and magnetically levitated stages for semiconductor fabrication has run into these limitations of capacitive gauges.

The development of a capacitive gauge that does not require a grounded target is reported here. This solves the problem of measurements of magnetically levitated stages, magnetic bearings, or other industrial applications.

* Department of Electrical and Computer Engineering, University of New Mexico.
† Address correspondence to Hy D. Tran; tran@me.unm.edu

Operating Principle

Capacitive gauges work by measuring the capacitance of a gap between the probe and its target. For a parallel plate capacitor, the capacitance C by can be approximated by

$$C = \varepsilon \frac{A}{x} \tag{1}$$

where ε is the permittivity ($8.854\ldots\times10^{-12}$ F/m in vacuum) of the gap, A is the area of the plate, and x is the distance separating the plates. Fringing of the fields can be ignored since in this application the gap distance is very small compared to the area of the plates so that fringing of the fields can be ignored. Typically, commercial capacitive gauges excite the probe using a constant frequency (typically 16 kHz to 1 MHz). The impedance of a capacitor is given by

$$Z = \frac{1}{j\omega \cdot C} \tag{2}$$

where ω is the applied frequency. So, the impedance of the probe is directly proportional to the distance from the target:

$$Z = \frac{x}{\varepsilon \cdot A \cdot j\omega} \tag{3}$$

Common methods for measuring the distance actually measure the impedance; not the capacitance.

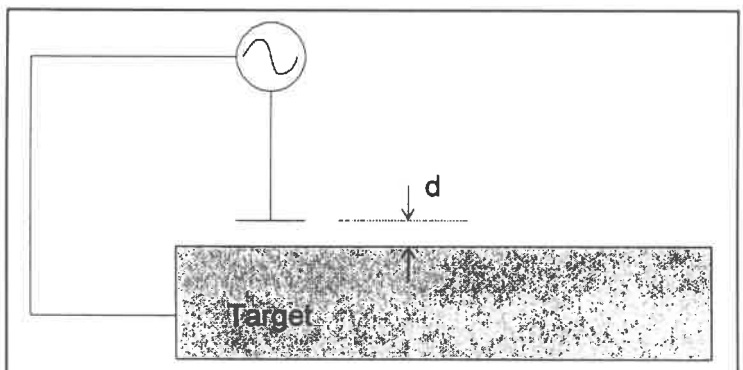

Figure 1. In a typical capacitive gauge, the distance "d" is measured by measuring the electrical impedance of the gap. This requires connecting the target to the instrument with either a grounding wire, or through a low impedance capacitively coupled return path.

In a typical commercially available gauge, the target must be grounded. This is accomplished either by physically grounding the target, or by providing a low impedance (e.g. large capacitance) return path to the instrument as shown in Figure 1. This limits the performance of commercial instruments. The gauge reported here permits the target to be at a floating potential. To accomplish this, the probe itself contains two electrodes (Figure 2a). The equivalent circuit of this probe is two capacitors in series(Figure 2b). As the target is displaced, the equivalent capacitance of each electrode is changed by an equal amount. The target no longer needs to be electrically connected to the instrument. The actual implementation of these devices makes extensive use of guard electrodes to linearize the fringing fields, and is shown in Figure 3.

In addition, by using symmetry in the design of the capacitive probe, one probe can measure multiple degrees-of-freedom: Not only the distance d, but also the tip and the tilt orientation of the target. This is achieved by segmenting the probe; the sum of the impedances gives the distance d, while the differences would give the tip and tilt. Using a four-quadrant probe, a single probe can measure distance, tip, and tilt of the target.

Interestingly, this probe can be manufactured using printed circuit board fabrication techniques; this has the potential to greatly reduce the cost of manufacturing these transducers. A photograph of the probe is shown in Figure 4.

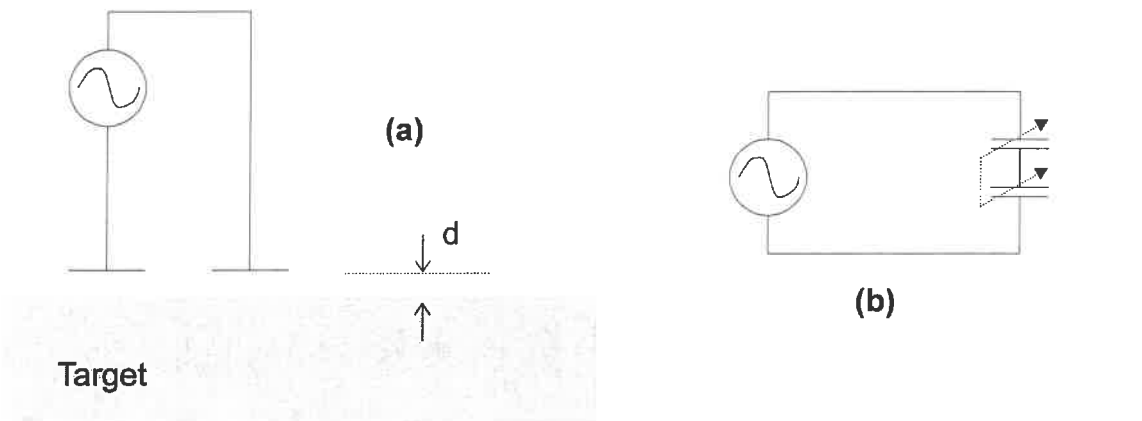

Figure 2. Schematic of the basic setup for capacitive displacement measurements with a floating target (a), and the equivalent circuit (b). In this configuration, the potential of the target is no longer an issue in measuring capacitance, since the signal return to the instrument is through the probe itself.

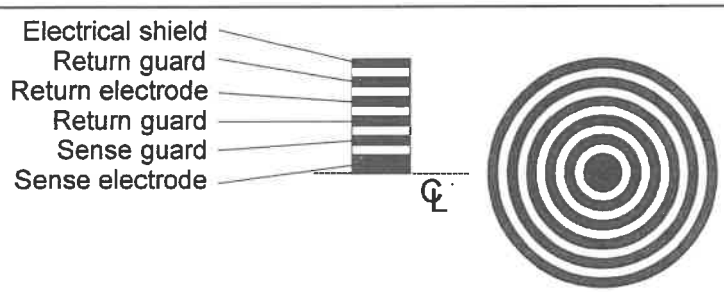

Figure 3. The actual gauge design includes guard electrodes, which are energized in-phase with sense or return electrode, in order to linearize the electric fields and minimize fringe field nonlinearities.

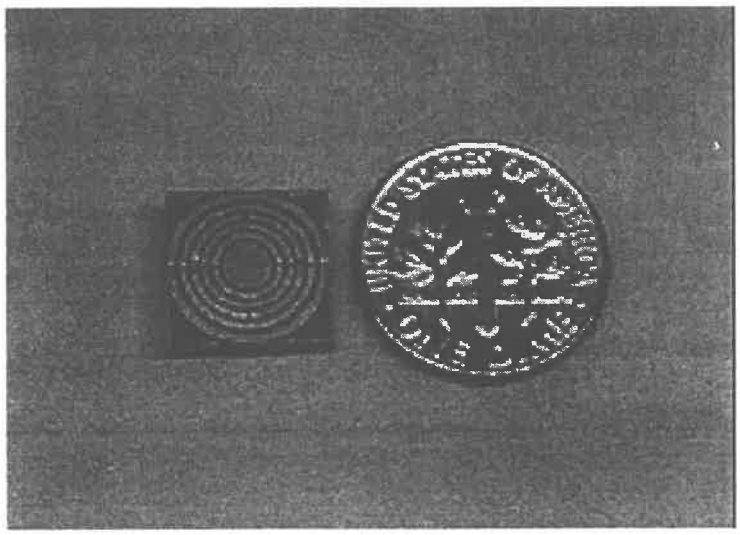

Figure 4. Photo of a circuit board probe. A dime is shown on the right for size comparison. This is a segmented probe design.

Circuit Design

The circuit for the prototype experiments is designed to drive the probe with a constant amplitude, constant frequency signal. The impedance is measured by comparing the voltage drop across the probe versus the voltage drop across a resistor. A block diagram of the circuit to drive this probe is shown in Figure 5; $\sin(\omega t)$ is sent to the sense and sense guard electrodes while $-\sin(\omega t)$ is sent to the return electrodes. Because this is an AC coupled system, the DC potential of the target no longer affects the impedance measurement (and therefore, the gap distance).

Experimental Results

Preliminary results comparing the amplitude of the sense signal with the amplitude of the oscillator drive indicate decreased amplitude with increased gap, as expected. We are adding synchronous demodulation to the circuit prior to reporting the final experimental results.

Conclusions

A unique capacitive displacement probe that does not require grounding of the target has been

described. Preliminary test results indicate that this probe performs as well as more traditional grounded probe designs.

This design should provide a viable alternative to grounded probes in applications where physical connections to the target are impractical or impossible.

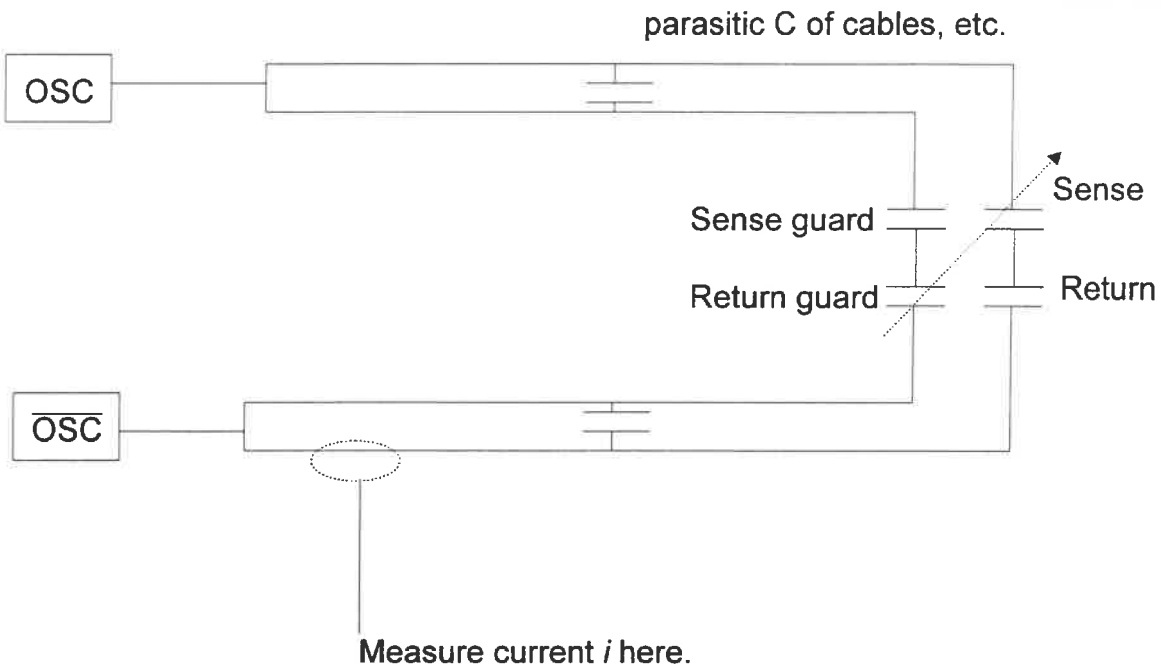

Figure 5. The circuit design uses a constant frequency and amplitude excitation; the "plus" side of the oscillator drives the sense electrode (and associated guard electrode) and the "minus" side drives the return electrode (and associated guard electrodes). The current measured through the sense or return electrode yields the impedance (and therefore, distance) to the target.

References

1. R.V. Jones and J. C. S. Richards, "The Design and Some Applications of Sensitive Capacitance Micrometers", *Journal of Physics E: Scientific Instruments,* Volume 6, Great Britain, 1973.
2. R. V. Jones and J. C. S. Richards, "The Measurement and Control of Small Displacements", *Bulletin of the Institute of Physics*, pp. 325-336, 1967.
3. US Patent #5793176: *Spatial Feature Tracking Impedence Sensor using Multiple Electronic Fields,* Inventor: James L. Novak, Assignee: Sandia Corporation, Albuquerque, NM, August 11, 1998.
4. D. Halliday, R. Resnick, and J. Walker, *Fundamentals of Physics, Fourth Edition*, John Wiley & Sons Inc., New York, 1993.
5. J. A. Nilsson and Susan A. Riedel, *Electronic Circuits, Fifth Edition*, Addison-Wesley, Reading, MA, 1996.
6. B. S. Guru and H. R. Hiziroglu, *Electromagnetic Field Theory Fundamentals*, PWS, Boston, MA, 1998.

Acknowledgments

Stefan Liming built the final circuit and conducted the experiments, whose results will be reported at the conference.

AN OBJECT TRANSPORT SYSTEM USING TRAVELING WAVES GENERATED BY ULTRASONIC FLEXURAL VIBRATIONS

Byoung-Gook Loh, Paul I. Ro
Precision Engineering Center, North Carolina State University, Raleigh, NC, USA

Abstract

An object transport system using low amplitude and high frequency traveling waves generated through the use of ultrasonic flexural vibrations is presented. A prototype was constructed to experimentally investigate transporting materials along a beam surface using ultrasonic traveling flexural waves. The prototype consists of a beam that is supported at either end by modules that contain piezoelectric actuators and horns. Two methods of generating traveling waves are investigated: impedance matching and excitation of two natural modes of vibration of the beam. In impedance matching method, one module produces flexural vibrations on one end of the beam while the other module absorbs the vibrations through impedance matching. This enables the propagation of traveling waves along the length of the beam. In the method using the excitation of two mode shapes, two modules are supplied with sinusoidal voltage signals having the same frequency but a phase difference of 90°. Then, two mode shapes that have natural frequencies closest to the supplied voltage play dominant roles in the total vibration. Excitation of these two mode with 90° out of phase signals results in generating traveling waves. Experimental results show that steel blocks weighing up to 0.5 kg can be transported with an average velocity of 5 cm/s through the frictional force. An integrated circuit chip weighing 1.4 g can be also transported with a velocity of 30 cm/s through acoustic levitation. For actual factory application, a simple stop-go and tracking control are implemented. Tests indicate that the stop-go control is accomplished with moderate accuracy but for the tracking, the closed-loop control is required.

1. Introduction

Many industrial environments are sensitive to the presence of magnetic fields generated by electromagnetic motors. An object transport system that does not produce magnetic fields would be quite useful in these environments, especially in the semi-conductor industry. Also, silent operation achieved through the use of actuators resonating at ultrasonic frequencies would not add to the already noise-polluted industrial environment. Due to the absence of conveyor belts, gears, and bearings, maintenance issues would also be significantly reduced. Transport of object is accomplished using the traveling waves produced on an elastic beam [1]. When the traveling waves propagates, the particles on the elastic beam traverse elliptic locus [2, 3]. Then, objects on the beam are forced to move due to frictional forces if the object has non-flat surface or its ratio of mass to area is greater than a certain threshold value. Otherwise, objects are transported by fluid coupled acoustic levitation. The main concern from a material handling perspective is achieving a consistently high transport velocity of an object on the beam. The factors that might affect this speed are weight of the transported object, the excitation frequency and the phase relationship between excitation forces. In this paper, the transport characteristics of the proposed system were investigated.

2. Prototype

The prototype shown in Figure 1 consists of a beam and modules that contain-piezoelectric actuators and horns. The modules are designed to be used in either an active or passive manner. The active module produces flexural vibrations on one end of the beam while the passive module absorbs the vibrations through impedance matching. As a result, traveling waves are generated.

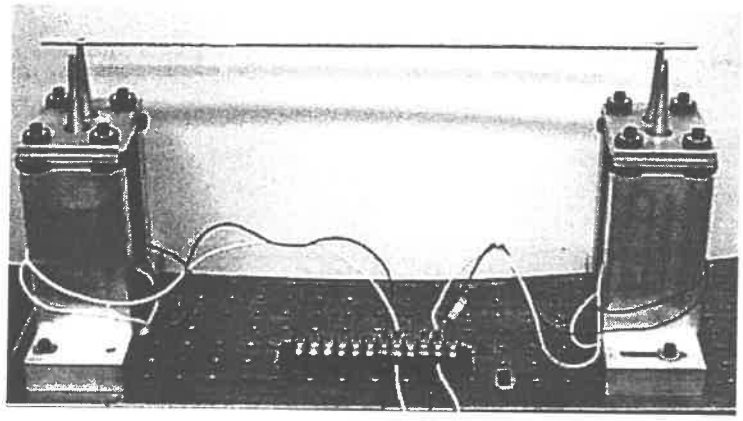

Figure 1: Prototype

Without the passive module, standing waves with fixed nodes along the length of beam would result. A beam and horns are made of aluminum (6061-T6) because of the excellent acoustical characteristics of this material. The size of the beam is 11 mm wide, 3.1 mm thick and 500mm long. The piezoelectric actuators are bolted Langevin type transducers manufactured by NGK Spark Plug Co. Ltd. (model no. DA2228). Their resonant frequency is 28 kHz. The conical horns were used to increase the amplitude of vibration provided by the actuators and thus maximize the displacement of the beam for a given power supply. A control box was constructed to connect either the excitation sine wave voltage or absorptive circuitry to either active or passive modules thereby allowing manual switching of the direction of the traveling waves during the experiment.

3. Traveling Wave Generation

There have been two ways of generating progressive waves on the finite length of an elastic beam. One is through impedance matching using transmission theory [2, 9, 11] and the other is through two mode excitation [4, 10] where two neighboring natural mode shapes are excited by forces with same frequency but a phase difference of 90°. Traveling waves can be generated through the use of a passive absorbing module connected to one end of the beam. The impedance of the absorptive module should be equal to the characteristic impedance of the transmission beam and the piezoelectric actuator. This is achieved by connecting an electrical circuit in which a resistor and an inductor are connected in parallel to the actuator on the passive end. The resistance and inductance values were determined using transmission line theory [3, 4]. When the two modules are supplied with sinusoidal voltages of the same frequency but a phase difference of 90°, the vibration of the beam can be represented by the linear superposition of infinite number of natural mode shapes of vibration [6-8]. Of particular interest are the two natural modes of vibration that have the natural frequencies closest to the excitation frequency. The vibration amplitudes of these two modes are large, compared to other mode shapes. The vibration can be approximated as superposition of these two mode shapes. Accordingly, the dimensions of the beam were chosen such that two natural frequencies of the two modes of interest are located in the vicinity of the excitation frequency. Excitation of these two modes with same frequency but a phase difference of 90° generates progressive waves [4].

4. Experimental results

4.1 Frictional Drive

Various sliders were built to test the object transporting capabilities of the vibrating beam system. The sliders were constructed using aluminum and steel of varying lengths, thereby varying the contact area between the slider and beam. The contact surface presented to the beam was made flat and relatively

smooth. Various other objects including coins, integrated circuit (IC) chips were also used to experimentally determine the optimum characteristics that would achieve maximum transportation speed. Test conditions were input voltage of 330 V, excitation frequency of 27.15 kHz, and peak beam vibration amplitude of 2 μm. The displacements of various sliders obtained from frictional drive were measured using an infrared sensor. The average velocities were calculated from the slope of the displacement versus time plot. The results are shown in Figures 2 and 3. The sliders with a contact area of 132 mm^2, 240 mm^2, 504 mm^2 and 693 mm^2 were constructed of steel with a mass of 18 g, 40 g, 85 g, and 96 g, respectively. Results of the slider tests indicate an increased velocity with a decrease in contact area and mass. Other objects were used to explore the effect of changing size, shape, surface finish, coefficient of friction, and mass on the speed of the object along the beam. Results are shown in Figure 4. Measured velocity of a nickel was 7.9 cm/s, a capacitor 8.2 cm/s, and a large steel block 5.2 cm/s.

4.2 Acoustic Levitation

Acoustic waves radiate from a flexurally vibrating. If a relatively light planar object is placed on the vibrating beam, the object acts as a reflector of the propagating acoustic waves. The object is levitated and transported due to the acoustic radiation pressure. The transport speeds of objects supported by an air film and driven through acoustic levitation were also measured using three different IC chips. Applying a load to the beam caused the beam to undergo flexure. The maximum flexure at the center of the beam was approximately 1 mm. Since there was no contact between the vibrating beam and the IC chips, the slope of the beam had an effect on the transport velocity. To gage the effect of the beam slope on the chip velocity testing was performed. An IC chip was placed in the center of the beam (at the point of maximum deflection) and allowed to levitate. The IC chip went up the slope and reached the end of beam with mild decrease in velocity. The test shown in Figure 5 was initiated from the end of the beam.

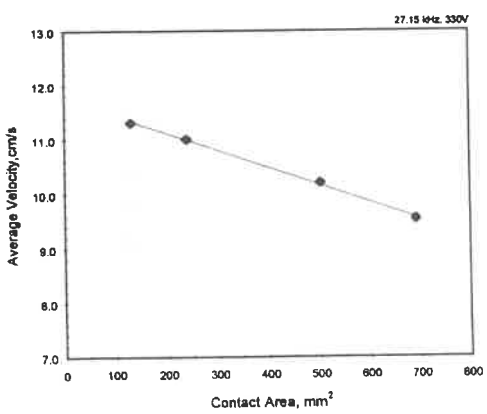

Figure 2: Contact Area vs. Average Velocity

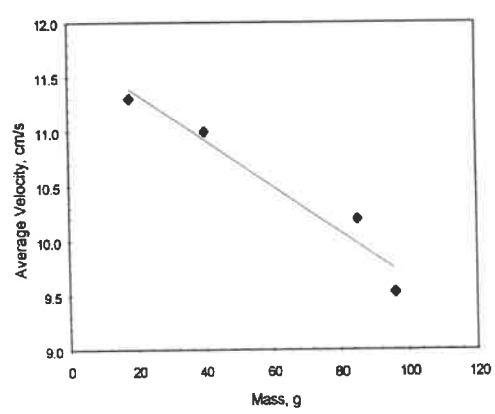

Figure 3: Mass vs. Average Velocity - Frictional Drive

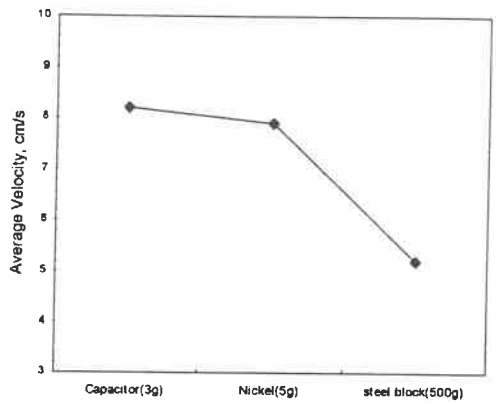

Figure 4: Average Velocity of Objects of Different Shape

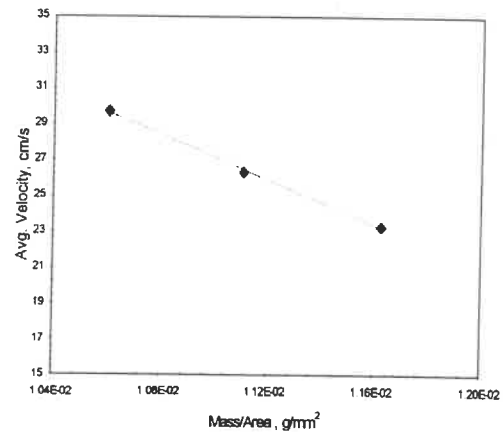

Figure 5: Mass/Area vs. Average Velocity - Acoustic Levitation

5. Open-Loop Control

In a typical factory environment, multiple speed settings, abilities to change transport direction, and simple stop-go control are required, which should be automatically handled through a computer. To achieve this, a function synthesizer having computer interface capabilities through General Purpose Interface Bus (GPIB) is used. It can independently generate two sinusoidal voltages through two output channels and modulate the phase relationships between two output channels. A simple stop-go control was implemented and the result is shown in Figure 6. 400V of sinusoidal voltage was supplied to the BLTs for 2 seconds and cut off for 2 seconds and supplied again for 2 seconds. The process was repeated until the slider reached the end of the beam.

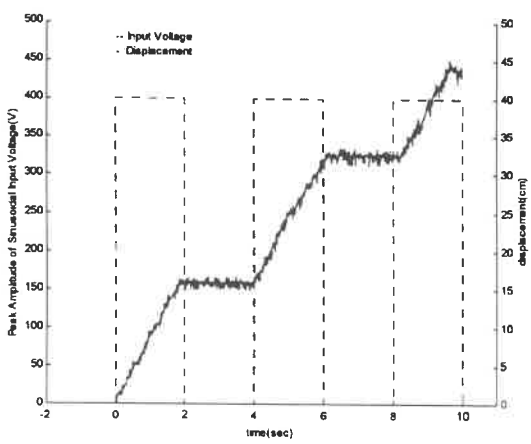

Figure 6: Stop-Go Control

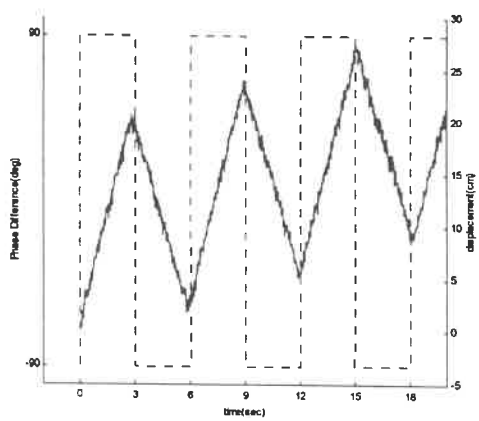

Figure 7: Tracking Control

The dotted line in Figure 6 represents the ideal voltage supply with a 2-second period. The timing function used to control the period has a resolution of 50 ms. The delayed motion of the slider shown at 8 seconds is due to the resolution of the timing function. The slider began to move right after the voltage was supplied and instantly stopped when the voltage was cut off. Therefore, using stop-go control, the

objects on the beam can be transported to a certain location, can be assembled or inspected, and can then be moved to the next position with moderate accuracy. A simple tracking control was also tested and shown in Figure 7. The phase difference between the two output channels of function synthesizer was kept at 90° for the first 3 seconds and changed to -90° for the next 3 seconds to change the transport direction. The process was repeated until the slider reached the end of the beam. The slider would return to the starting position after each period of the motion. However, the slider appears to move along the length of the beam because of the slight differences in the resonant frequencies of two BLTs and the input/output ratio of two channels of Trek power amplifier. For precise tracking, a closed-loop control should be considered.

6. Conclusions

An object transport system using progressive waves is presented. Object transport speeds of 11 cm/s using friction and 30 cm/s using acoustic levitation with a power input of 20 W were obtained for a wave propagation velocity of 800(m/s). With these transport speeds, the demands of clean room and semi-conductor manufacturing industries are effectively matched. For actual factory application, a simple stop-go and tracking control were implemented using a GPIB interface. The result of stop-go control revealed the proposed system can be used for assembly and inspection. For tracking tests, because of non-homogeneous characteristics of the BLTs and the two channels of power amplifier, feedback control is required for precise tracking.

References

1. William C. Elmore, " Physics of Waves", McGrow-Hill Book Company, 1991 pp.5-13
2. M. Kuribayashi, S. Ueha, E. Mori, "Excitation Conditions for Flexural Traveling Waves for a Reversible Ultrasonic Linear Motor," Journal of Acoustical Society of America, Vol 77(4), pp. 1431-1435, 1989
3. M. Kuroasawa, S. Ueha, "High Speed Ultrasonic Linear Motor with High Transmission Efficiency", Ultrasonics, Vol. 27, pp. 39-44, January 1989
4. Yoshiro Tomikawa, Kazunari Adachi, Hiroshi Hirata, Takanori Suzuki, and Takehiro Takano, "Excitation of Progressive Wave in a Flexurally Vibrating Transmission Medium", Proceedings of 10th Symposium on Ultrasonic Electronics, Vol. 29-1, pp. 179-181, 1989
5. Merkulov, L.G. "Design of Ultrasonic Concentrators", Sov. Phy.-Acoust. , Vol. 3, pp. 246-255, 1957
6. M.P. Norton, " Fundamentals of Noise and Vibration Analysis for Engineers", Cambridge University Press, 1989, pp. 94
7. Singiresu S. Rao, " Mechanical Vibrations", Addison-Wesley, 1995, pp. 527
8. Karl F. Graff, " Wave Motion in Elastic Solids", Dover Publication, Inc., 1991, pp. 163-167, 180-187
9. Paul I. Ro, Byoung-Gook Loh, and Javier Santiago "Feasibility of Contact and Non-contact Material Handling Using Traveling Waves and Transition Characteristics", IEEE Transactions on Industrial Electronics, submitted on April 1999
10. Byoung-Gook Loh and Paul I. Ro, "An Object Transport System Using Flexural Ultrasonic Progressive Waves Generated by Two-Mode Excitation", IEEE Transactions on Ultrasonic, Ferroelectrics, and Frequency Control, submitted on April 1999
11. Precision Engineering Center 1998 Annual Report, North Carolina State University, Vol.16, pp. 121-133, Jan. 1999

Tolerance Allocations for Automated Insertion of Optical Components in the National Ignition Facility

Sally M. Bahowick, William R. Horton, Terence G. Sheridan, William S. Rorke, Donald S. Bartel

Lawrence Livermore National Laboratory
P.O. Box 808, L-447, Livermore, CA 94551

Overview of the NIF

The National Ignition Facility (NIF) will achieve fusion ignition in a controlled laboratory environment early in the next century. In this facility, the size of a football stadium, 192 high power laser beams are directed toward a small fusion target after propagating through a series of optical amplification and image relaying systems. Each laser beam contains 44 optical assemblies that must be removed and replaced. There are thousands of these optical assemblies through out the facility that must be removed and replaced and these operations are, for the most part, automatic (see Figure 1). This paper address one typical optical assembly called the Spatial Filter 4 (SF4) and describes how the tolerance allocations for this automatic operation were developed, allocated, and documented.

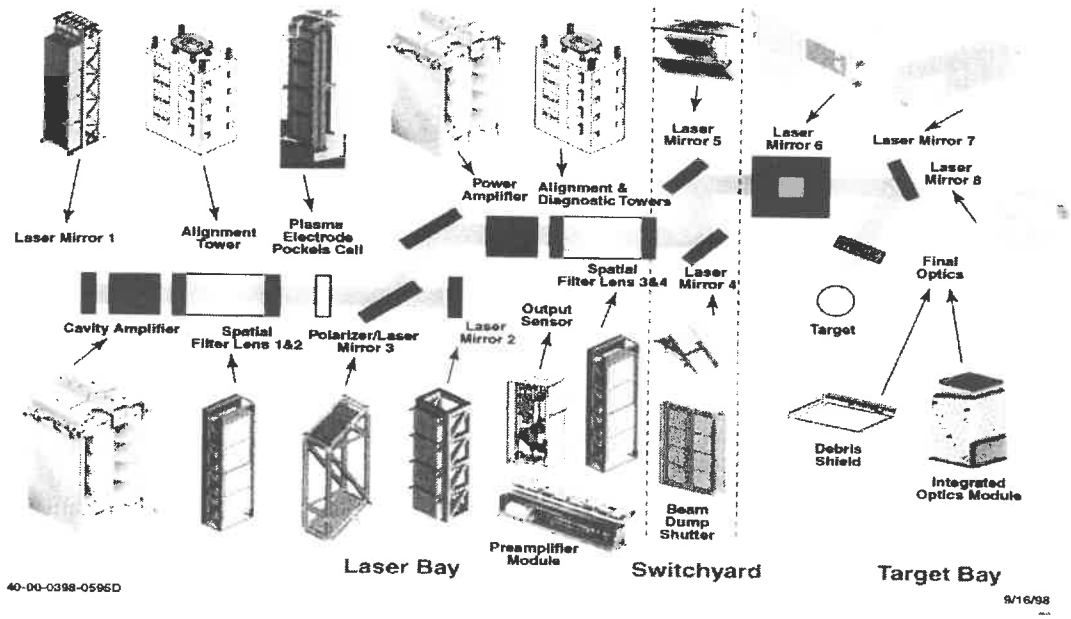

Figure 1. Pictorial of the optical assemblies in the NIF. A global coordinate system is used to precisely locate each optical assembly.

The SF4 optical assembly is inserted and removed by a bottom loading delivery system requiring the use of three sets of kinematic couplings. One set locates and secures the SF4 optical assembly in the laser beam, one set locates the bottom loading delivery system to the SF4 optical assembly, and one set locates the bottom loading delivery system to the docking structure. Four design teams were involved in developing these features: the SF4 optical assembly, the support structure, the bottom loading delivery system, and the survey team. The bottom loading delivery system is shown in Figure 2 docking to the support structure. The bottom loading delivery system consists of a canister with mechanisms for moving and placing the SF4 in the structure, and an automatically guided vehicle for delivering the canister with the SF4 to the target location.

This work was performed under the auspices of the U.S. Department of Energy at LLNL under contract no. W-7405-Eng-48.Document No.- UCRL-JC-133747-Extended Abstract DISCLAIMER: This document was prepared as an account of work sponsored by an agency of the United States Government. Neither the United States Government nor the University of California nor any of their employees, makes any warranty, express or implied, or assumes any legal liability or responsibility for the accuracy, completeness, or usefulness of any information, apparatus, product of process disclosed, or represents that its use would infringe privately owned rights. Reference herein to any specific commercial product, process, or service by trade name, trademark, manufacturer, or otherwise, does not necessarily constitute or imply its endorsement, recommendation, or favoring by the United States Government of the University of California, and shall not be used for advertising or product endorsement purposes.

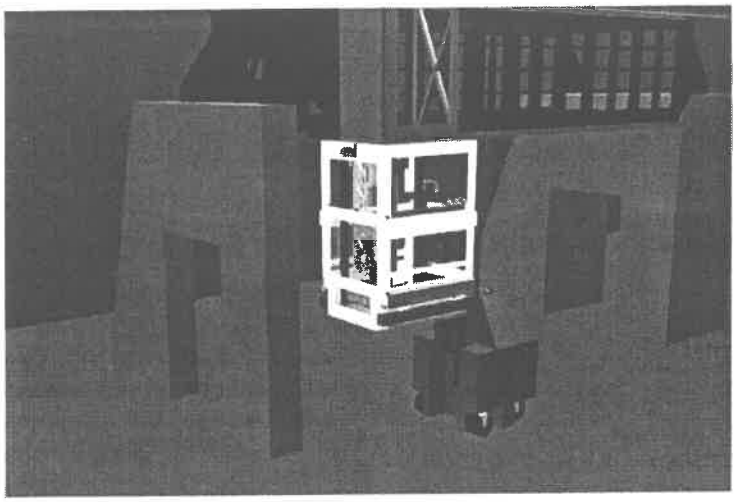

Figure 2. Bottom Loading Delivery System docking to the SF4 support structure.

Application of tolerance allocations

The success of automatically inserting and removing a SF4 optical assembly is directly dependent on the ability to place the SF4 inside the structure kinematic coupling capture zone. The SF4 capture zone is +/- 10mm and has been divided into tolerance allocations between the four design teams. The tolerance allocations are shown in Table 1. If all teams design, build, and install their systems to the agreed-to tolerances, the SF4 can be automatically installed and removed. For these tolerance allocations, the agreed-to tolerances placed on fabrication and installation are as stringent as that of aligning the laser optics themselves.

Table 1. Top-down tolerance allocation as determined by needs of the SF4 Optic

Capture zone of structure-mounted SF4 kinematic couplings:	+/- 10.0 mm
Survey (SF4, kinematic couplings for docking)	- +/- 1.0 mm
SF4 optical assembly (fab, assembly, and alignment)	- +/- 1.0 mm
SF4 structure (fab, assembly, and alignment)	- +/- 3.0 mm
SF4 structure (setting in the building)	- +/- 1.0 mm
Net tolerance left for the delivery system (fab, assembly, alignment, repeatability in operation)	*+/- 4.0 mm*

The capture zone for the structure mounted kinematic couplings for SF4 is +/- 10 mm. Starting with +/- 10 mm, and adjusting for tolerances in fabrication and assembly, setting, and survey error for both the SF4 and the structure, the net capture zone left for the delivery system canister is +/- 4 mm.

Interrelationships between the elements

Each team was using their own local datums to measure and locate the respective features. The tolerance stackup between the local datums was more than the tolerance allocation. To eliminate this additional tolerance stackup, a local global coordinate system based upon the local optical location was defined and tied to the global coordinate system. This local coordinate system was identified as an Assembly Coordinate System Origin (ACSO). Figure 3 illustrates how the ACSO provides a single point reference for each design team.

Now the features provided by each design team are located relative to the ACSO, and the survey team measures the location of all features relative to the ACSO and relates the measurements to the global coordinate system.

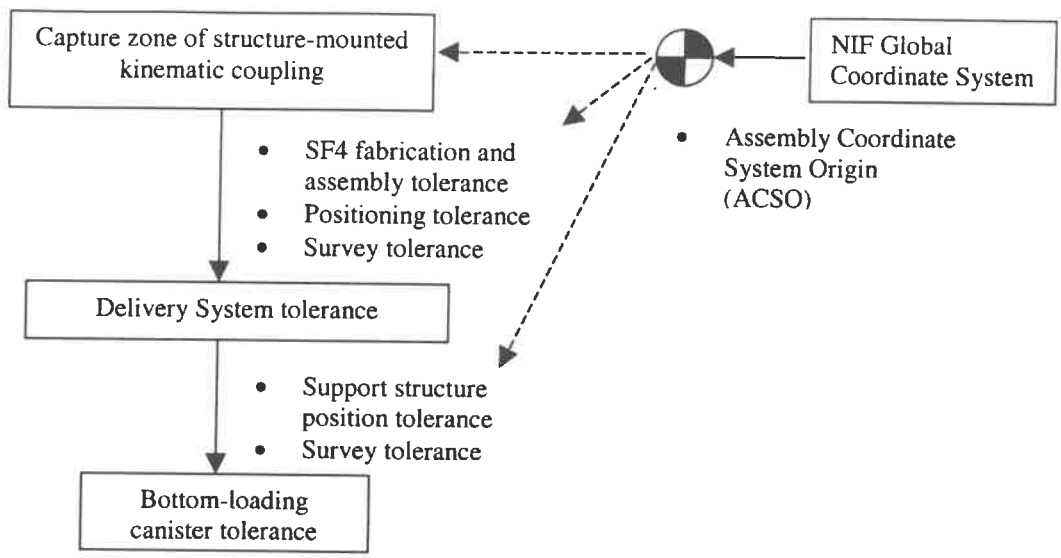

Figure 3. Flow-down requirements for tolerance for inserting an SF4

Details of the kinematic couplings and the structure tolerance allocation

The SF4 optical assembly package is the size of a refrigerator and houses the optics inside a support frame. Two sets of kinematic couplings are designed into the support frame. They position the SF4 to the support structure and the SF4 on the Delivery System.

The kinematic couplings to the support structure are two tapered pins in two slots. The lower pin constrains the SF4 laterally, while the upper pin fixes the vertical position. Four bolts at the corners of the SF4 hold it to the support structure, completing the 6-degree-of-freedom constraint.

The kinematic couplings at the interface between the delivery system and the SF4 are a form of the traditional tetrahedron-vee-flat, with the pins on the SF4 and the tetrahetron-vee-flat on the Delivery system. Other optical assemblies have different designs of kinematic couplings.

The bottom loading delivery system team must consider two tolerances: the accuracy and repeatability of the canister insertion mechanisms used to insert SF4, and the accuracy and repeatability of the docking structure where the delivery system docks. The docking accuracy and repeatability involves the amount, the accuracy, and the repeatability that the structure fabrication and placement can be controlled.

The delivery system docks to a three-point ball-vee kinematic coupling. Three counter bores are milled into the structure, into which machined cones are placed. In the structure, the positional tolerance specified for the three locations of each pattern is +/- 1.5 mm in the lateral directions, a vertical tolerance of +/- 5 mm, and a co-planarity tolerance between the bases of the three pockets of +/- 1 mm (Figure 4). Given that the distance between pockets is 750 mm, the co-planarity tolerance of +/- 1 mm results in a tilt of 2.67 mrad. When the cones are inserted into the support structure, they will be surveyed and shimmed to a co-planarity not to exceed +/- 0.22 mm. This results in a much smaller tilt angle of 0.59 mrad. For a 2500 mm tall SF4, a tilt of 0.59 mrad at the support structure will transmit throughout the delivery system to a net lateral misalignment at the top of the LRU of +/- 1.47 mm. The total lateral tolerance allotment for the support structure is then 1.5 + 1.47 = +/- 2.97 mm. The fabrication tolerance for the structure need to be tighter than the positional tolerances. Given that the structure is 30 feet long with 6 patterns of features to control, the fabrication tolerance of +/- 1.5 mm on position and +/- 1 mm on co-planarity provides a challenging fabrication. (See Figure 4).

Figure 5 illustrates the tolerance allocations for SF4. The figure also depicts the vertical and horizontal motions over which the tolerances must be held.

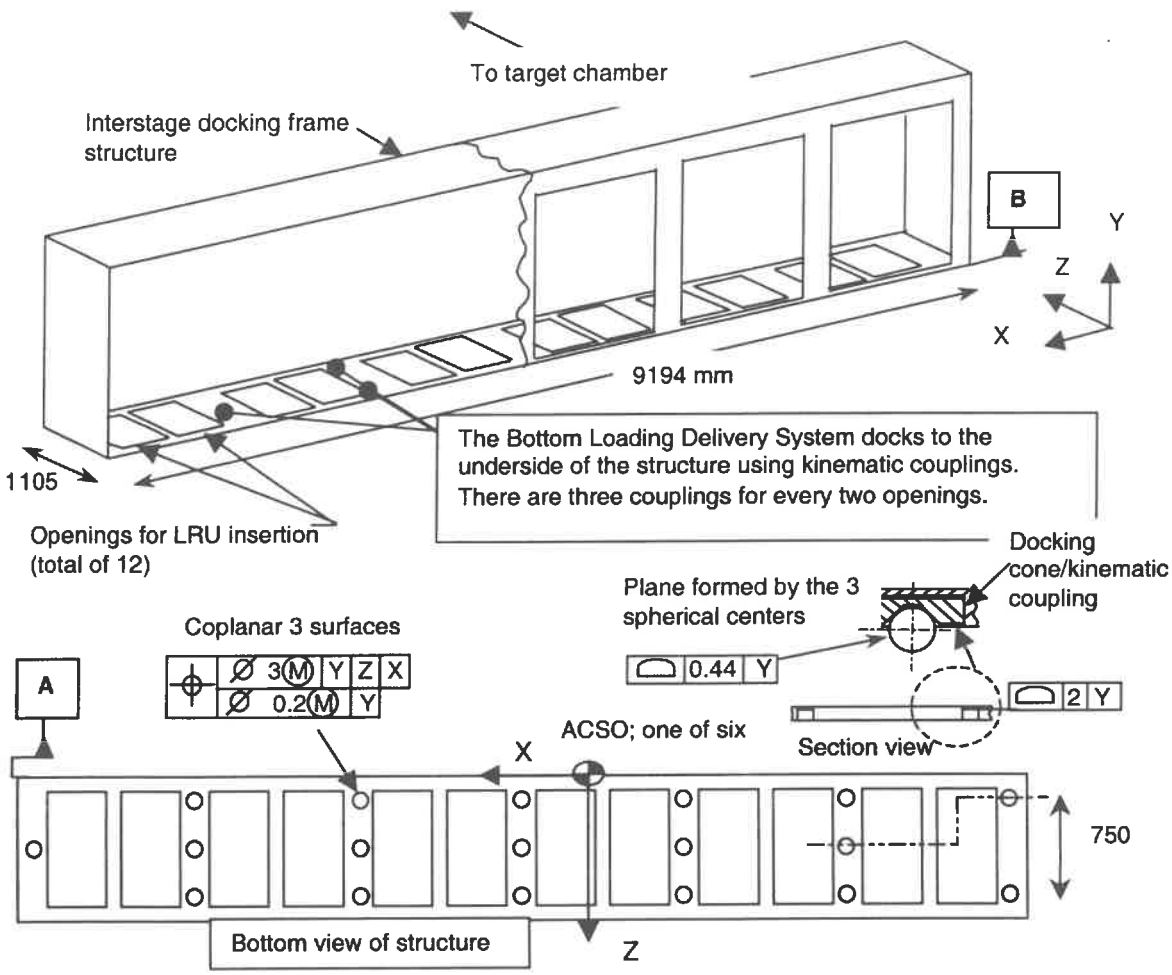

Figure 4. Positional tolerance imposed on the Interstage Docking Structure. To meet the positional tolerance allocation, the fabrication tolerance must be tighter still.

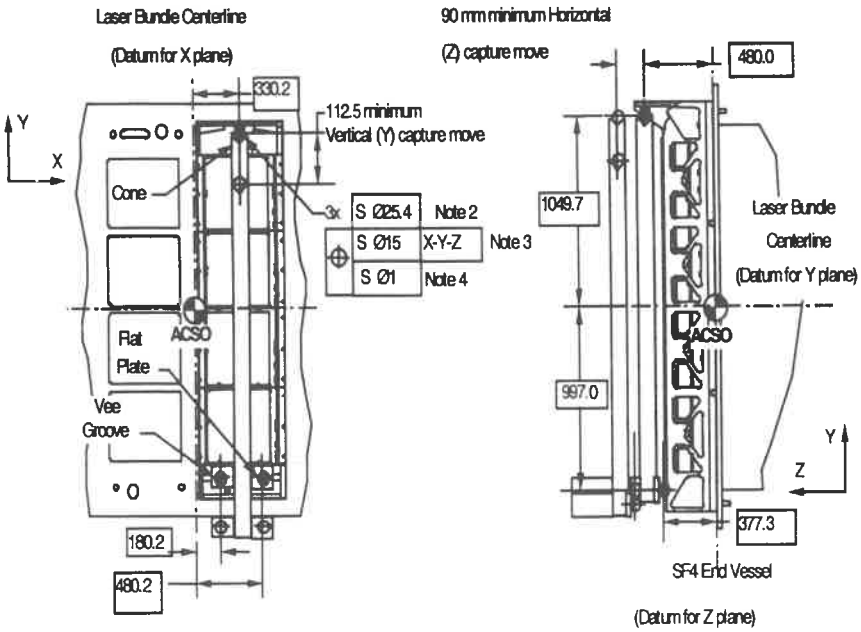

Figure 5. Interface Control Drawing showing location of kinematic couplings to the ACSO for the SF4.

High-Precision Dimension Measurement of Large Scale Workpiece by Laser

Qibo Feng

(Dept. of Physics, Northern Jiaotong University, Beijing 100044,P.R. of China)

Jinwen Liang, Qian Tian

(Dept. of Precision Instrument, Tsinghua University, Beijing 100084, P. R. of China)

Introduction

The dimension accuracy of a large scale workpiece is one of the most important parameters to assure the quality of heavy machines such as 60MW steam turbine rotors and fixers, however, there are not available methods to meet the needs of high-precision measurements for such machines. The most difficult problem with large dimension measurement is how to aim at and position to the measured points in a large-scale workpiece. This problem has not been solved properly up to now.

A new method of aiming at the points of a large workpiece is developed by using a laser beam from a host-built mono-mode fiber laser collimator, which is a Chinese Invent Patent[1]. The high-precision dimension measurement of large workpieces is realized by using a heterodyne interferometer such as a Hewlett-Packard laser interferometer. The experiment results on a 1000mm block gage and on a 500mm diameter workpiece show that uncertainty (three sigma) within 5 micrometers is obtained.

Principle of Aiming and Positioning

It is well known that a heterodyne laser interferometer is one of the most accurate length measurement methods. Typically, such a laser interferometer has a resolution of several nanometers with the relative measurement accuracy of about 10^{-7} within a measurement range of up to 60 meters. So, how to directly use a heterodyne laser interferometer for large dimension measurements, especially large diameter measurement is a target to be pursued. Unfortunately, this problem has not been solved up to now due to the fact that aiming at and positioning the measured points of a large diameter is very difficulty. A novel method of aiming at and positioning the measured points of a large diameter is put forward in this paper and high precise measurement of large workipeice is realized by using a laser interferometer.

There are some current optical methods to aim at and to position the measured points of a diameter. A light gauging method[2] by which a laser beam is used to aim at the two diametrically opposite points of a diameter is one of examples. In this measurement principle, the point of the measured workpiece diameter to be considered is aimed at correctly when 50 percent of laser energy is blocked by the edge of the workpicec. The dimension of the diameter can be measured by comparing it with a known size diameter, which makes it very inconvenient for this method to be used for large diameter in site. In addition, the positioning by a long mechanical arm limits greatly the measurement range of diameter.

Fig.1 shows a method of aiming at and positioning the measured points of a large diameter by a laser beam. The laser beam from a single-mode fiber laser collimator is divided into two parts by a beam splitter when it passes through a pentagonal prism in the measurement head. One part of the laser beam, which is reflected by the pentagonal prism at an angle of 90 degrees with respect to the incident ray, forms a datum line for aiming at the workpiece. When the measurement head is moved along a slideway,

the reflected ray successively aims at centers of two quadrant silicon photodiodes on the magnetic positioning chocks attached on the two end points of the measured workpiece. With the coincidence of the incident ray into the chock and the ray reflected from it, the correct positions of two chocks are ensured. In this way, the two diametrically opposite points are correctly aimed at. The another part of the laser beam, which passes through directly the pentagonal prism and is received by another quadrant photodiode fixed with the pentagonal prism, forms a datum line for adjusting the position of the measurement head. With this datum line as a reference for adjusting, the positions of the measurement head can be kept to be fixed when the reflected laser beam successively aims at two points of the measured workpiece, thus eliminating influences of the straightness error and the position error of the sildeway on the measurement results.

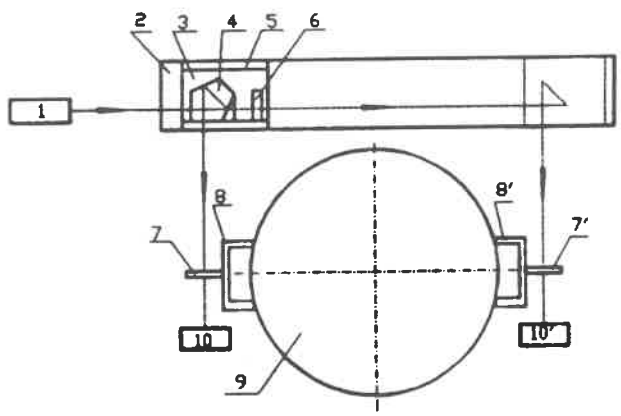

1 Single-mode fiber laser collimator, 2 Slideway, 3 Measurement head, 4 Pentagonal prism, 5 Carriage, 6.7.7' Quadrant photodiode, 8.8' Positioning Chock, 9 Workipece, 10.10' Signal processor.

Fig.1 Schematic Diagram of Aiming and Positioning

The theoretical analyses and experiments show that the Abbe error is greatly decreased even though there exists a large Abbe offset in the case of measurement of large outer diameters. The only source for Abbe error is from laser beam direction drift, but it decreases largely as the laser beam from a single-mode fiber laser collimator is very stable.

Measurement Principles

A schematic block diagram for high-precision measurement of large workpieces is shown in Fig.2. A Hewlett-Packard laser interferometer is used as a high accurate length measurement instrument. Before the measurement, it is necessary to make the measurement direction be perpendicular to the axis of the measured workpiece in order to reduce the Cosine error. It is also necessary to adjust the positions of the positioning chocks on the workpiece in order to ensure the correct measurement position of the chocks. When all these adjustments are correctly done, the distance between centers of two quadrant silicon photodiodes on the chocks can be measured directly by a laser interferometer when the measurement head is moved along the guideway to make the reflected laser beam from the single mode laser collimator aims at the two centers successively.

If the system is used to measure dimension between two parallel planes of a large scale workpiece, its size or dimension can be easily obtained by

$$L_0 = L - C \tag{1}$$

where L_0 is the length of the measured workpiece, L the distance between centers of the two quadrant photodiodes, C the distances between two centers when the two chocks are put together. All these parameters are shown in Fig.2.

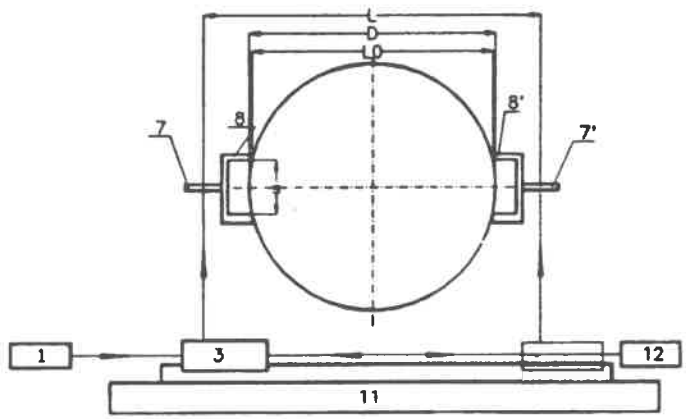

1 Single-mode fiber laser collimator, 3 Measurement head, 7.7' Quadrant photodiode,8.8' Positioning chock, 11 Chassis of a lathe, 12 Hewlett-Packard laser interferometer

Fig.2 Schematic diagram of measurement of large diameters

If the system is used for measuring both external and internal diameters, the equation for getting the dimension becomes

$$D = \sqrt{(L \mp C)^2 + S^2} \tag{2}$$

where S is the slot width of the chock. The signs of negative "-" and positive "+" are used when the sytem is used to measure external and internal diameters respectively.

Other high precise length measurement systems such as grating length measurement system etc. can be used as a substitute for a laser interferometer. In addition, a dual frequency wavelength beat wave interferometer can be used to measure absolutely diameters of extremely large workpieces without a guide[3], as in this case, uses of a guide can be very difficult or inconvenient in practice.

When the measurement chocks are positioned correctly, the whole measurement is completed automatically as there are several step motors and a computer installed on this system and it is now used in a steam turbine factory to measure large diameters of rotors.

Experiments

The experiments on a 1000mm gauge and on a 500mm diameter were made by the system on a laboratory not temperature-controlled with the correction of temperature errors for both the material and laser wavelength. A HP5528 laser interferometer is used in the measurement system. The two chocks are placed on the two end planes of the gauge, its dimension can be measured by using Equation (1). Table 1

shows four groups of experiment data with each group of resulting taken from 11 times of measurements. The gauge size measured by a 1000mm measurement machine is 1000.0035mm.

Table 1 The Experiment Results on a 1000mm Gauge (in mm)

Group Number	Results(with three sigma)
1	1000.0025±0.0019
2	1000.0025±0.0033
3	1000.0037±0.0050
4	1000.0041±0.0020

Table 2 shows the experiment results on a 500mm external diameter obtained by the system using the Equation (2). The result taken from a model MERLIN II coordinate measuring machine is 499.8775±0.004mm.

Table 2 The Experiment Results on a 500mm Diameter (in mm)

Group Number	Results(with three sigma)
1	499.8748±0.0028
2	499.8749±0.0021
3	499.8753±0.0018

The major error resources include: the error produced by the system, the fluctuation of the temperature and the temperature gradient existing in the measurement direction etc. as the experiments were conducted in a not-temperature-controlled laboratory. The uncertainty(three sigma) within 5 micrometers in measuring a 1000 diameter can be ensured if the temperature error can be corrected.

Conclusions

In this system, the application of a single-mode fiber laser collimation technology decreases greatly the Abbe error caused by the laser drift. The use of one pentagonal prism instead of two pentagonal prisms[2] to aim at two points of the diameters eliminates the Abbe error produced by angle manufacturing errors of the prisms and reduces the influences of the straightness error and position error of the carriage on the measurement results. The use of magnetic positioning chocks extends greatly the measurement ranges and makes it convenient to be used in practice. By using this aiming system together with a heterodyne interferometer, high-precision dimension measurements of large inner, outer diameters and lengths up to 10 meters can be realized. The experiment results on a 1000mm gage block and on a 500mm outer diameter show the three sigma uncertainty to be within 5 micrometers.

References

1. Qibo Feng, Qinwen Liang, Qian Tian, *A new apparatus and method to measure diameters of large scale workpiece by laser*. A Chinese invent patent No. 92103740.6.
2. A. Novak, *Sensing of Workpiece Diameter, Vibration and Out-Off-Roundness by Laser Way to Automate Quality Control*. CIRP, 1981, 30(1).
3. Qibo Feng, Qinwen Liang, *Study on absolute measurement method of a large diameter by a 3.39 μm dual frequency wavelength beat wave interferometer*, Chinese Journal of Lasers, 1994, A15 (11).

Direct Measurement of Spindle Error using a double 2-point Method

Y.J. Gao , B.K.A. Ngoi, L.E.N. Lim
School of Mechanical & Production Engineering
Nanyang Technological University
Nanyang Avenue, Singapore 639798

Abstract

This paper presents a new double 2-point method for an in-situ spindle error measurement. It overcomes the intrinsic difficulty of the typical 3-point method, i.e., the spindle error can be obtained only after the work-piece roundness error is determined; and the spindle error measurement precision is not so high. A standard bar was tested with the new developed system. The test result is compared with that measured with the Taylor Hobson Roundness Gauge's precise rotating table and both the results agreed well with each other.

Key words: Spindle error, roundness, eccentric error, displacement probes, Fourier series.

1. Introduction

Spindle error measurement and evaluation are critical for cylindrical work-pieces. The roundness measurement can be significantly influenced by the spindle error and eccentric error especially with the case of in-process roundness measurement. The rotating accuracy of a machine tool spindle directly affects the roundness of machined parts. Numerous papers [1,2,3,4,5] dealing with this problem were published. Commonly, the spindle axis error measurement consists of: a precision arbor (a precision sphere or cylinder), reversal method, Donaldson method and typical three-point method. The accuracy of the standard arbor is poor, as the measuring signal includes both the rotational error and the shape error, which are difficult to separate. For the reversal method, it is difficult to reverse the rotation axle by 180° precisely, so the accuracy is still problematic. As to the typical three-point method, it can precisely measure the workpiece roundness without the influence of the spindle axis error, but it cannot measure the spindle axis error accurately. In this paper, a new method, called the double 2-point method, is proposed which can precisely determine the spindle error without the influence of roundness error and eccentric error.

2. The Principle of Radial Rotation Error Measurement

The proposed double two-point method is actually an extension of the typical 3-point method. The three sensors are still used and located at points A, B and C which are aligned with angles of 0°, ϕ, and τ, as shown in **Fig.1**. The measurement setup should satisfy:

1) Small error principle: The form error of precisely machined workpiece and spindle axis error of the rotating device are small enough compared with the size of the workpiece;
2) Periodicity and repetitiveness of the spindle axis error motion and constant rotating speed;
3) Mounting condition: Three sensors are fixed at the same circumference of the axis to be measured, in order to ensure that the workpiece shape error at the assigned point could be measured by the three probes in turn.

S1, S2, S3 in Fig.1 indicate the three displacement probes. O is the intersection of the three probes' measuring direction. O_0, O_1, O_2, ..., O_n are the points on the spindle axis error motion trace. Supposing that the axis rotates in a clockwise direction, at the position of trigger 1, O_1 is the circle center, A_1 is a certain point in the measured circumference. After rotating through angle θ, the circle center moves to O_2, and the A_1 moves to A_2. If R(t) represents the roundness of the workpiece, and r(t) , the spindle error, under the above conditions, and the roundness of the workpiece should have the same and stable period for each probe, it can therefore be shown as:

$$R(t) = R(t+T), \quad T = 2\pi/\omega \tag{1}$$

The Fourier series of periodic function $R(t)$ can be expressed as:

$$R(\theta) = R_0 + \sum_{k=1}^{\infty} R_k \sin(k\theta + \varphi_k) \quad \theta = wt \tag{2}$$

where amplitude R_k and phase φ_k are constants. The first harmonic (k=1) is caused by the mounting error, and the high harmonics $k \geq 2$ represents the roundness. The roundness of the case $k \geq 2$ is the intrinsic characteristics of workpiece itself. It depends only on the machining accuracy and is independent of the used measurement method, the distribution and the number of the probes.

On the condition that the rotational angle speed ω is constant and the three probes are mounted around the same circumference, all roundness measured by the three probes have only some constant phase difference which are determined by the distribution of the probes. With the double two-point method, this shape error of the workpiece and the eccentric error from the measured signal can be eliminated and the spindle error can be got.

Supposing that the motion of the spindle axis error r(θ) is quasi-periodic, it can be expanded as the following Fourier series:

$$r(\theta) = r_0 + \sum r_k \sin(k\theta + \rho_k) \tag{3}$$

Where $X(\theta)$, $Y(\theta)$ are components of $r(\theta)$ in the direction of X and Y axes. The principle of the typical three-point method can be described by:

$$\begin{cases} S_1(\theta) = R_1 - R(\theta) - Y(\theta) \\ S_2(\theta) = R_2 - R(\theta - \phi) - Y(\theta)\cos\phi + X(\theta)\sin\phi \\ S_3(\theta) = R_3 - R(\theta - \tau) - Y(\theta)\cos\tau + X(\theta)\sin\tau \end{cases} \tag{4}$$

Where R_1, R_2, R_3 are defined as the initial radial distances of each probe at the position while the roundness $R(\theta)$ and error motion $X(\theta), Y(\theta)$ equal to zero; ϕ and τ represent the angles of probe S_1 to S_2 and probe S_1 to S_3 respectively. After choosing the proper coefficients a and b to satisfy

$$\begin{cases} a\sin\phi - b\sin\tau = 0 \\ 1 + a\cos\phi + b\cos\tau = 0 \end{cases} \tag{5}$$

The resultant signal $S(\theta)$ is obtained :

$$\begin{aligned} S(\theta) &= S_1(\theta) + aS_2(\theta) + bS_3(\theta) \\ &= (R_1 + aR_2 + bR_3) - R_0(1 + a + b) \\ &\quad + X(\theta)(a\sin\phi - b\sin\tau) - Y(\theta)(1 + a\cos\phi + b\cos\tau) \\ &\quad + \sum_{k=1}^{\infty}\{[A_k(1 + a\cos k\phi + b\cos k\tau) + B_k(b\sin k\tau - a\sin k\phi)]\cos k\theta \\ &\quad + [B_k(1 + a\cos k\phi + b\cos k\tau) - A_k(b\sin k\tau - a\sin k\phi)]\sin k\theta\} \\ &= (R_1 + aR_2 + bR_3) - R_0(1 + a + b) \\ &\quad + \sum_{k=2}^{\infty}[(A_k\alpha_k + B_k\beta_k)\cos k\theta + (B_k\alpha_k - A_k\beta_k)\sin k\theta] \end{aligned} \tag{6}$$

where:

$$\begin{cases} \alpha_k = 1 + a\cos k\phi + b\cos k\tau \\ \beta_k = b\sin k\tau - a\sin k\phi \end{cases} \tag{7}$$

By expanding $S(\theta)$ into the Fourier series, we get:

$$S(\theta) = S_0 + \sum(F_k\cos k\theta + G_k\sin k\theta) \tag{8}$$

and

$$\begin{cases} A_k = \dfrac{F_k\alpha_k - G_k\beta_k}{\alpha_k^2 + \beta_k^2} \\ B_k = \dfrac{F_k\beta_k + G_k\alpha_k}{\alpha_k^2 + \beta_k^2} \end{cases} \tag{9}$$

the result of equation (9) shows that:

1) If, $\alpha_k^2 + \beta_k^2 \neq 0$ roundness can be measured precisely without the effect of the spindle error and the mounting error of the workpiece;
2) Roundness does not include the eccentric error of the workpiece in case k=1, so that the typical three-point method can not remove this eccentric error caused by the workpiece mounting;

So, from equation (5):

$$\begin{cases} \overline{X}(\theta) = \left\{\left[S_2(\theta) - \overline{R}(\theta-\phi)\right]\cos\tau - \left[S_3(\theta) - \overline{R}(\theta-\tau)\right]\cos\phi\right\} / \sin(\phi-\tau) \\ \overline{Y}(\theta) = \overline{R}(\theta) - S_1(\theta) \end{cases} \tag{10}$$

The first harmonic representing eccentric error is incorrectly added to $\overline{X}(\theta)$, $\overline{Y}(\theta)$, and it damages the precision of the measured spindle axis error, especially for checking high accurate spindle.

The double 2-point method makes use of the phase differential of the three probes S_1, S_2, S_3, e.g., S_1-S_2 and S_1-S_3. By doing the differential, the spindle axis error can be obtained directly with the removal of the effect of workpiece roundness as well as eccentric error. The principle can be described with the following equations:

$$\begin{aligned} S_1(\theta) &= [R(\theta)]_1 + [r(\theta)]_1 \\ &= R_1 - [R(\theta+\beta) + r(\theta+\beta)\cos(\theta+\beta)] \\ &= [R_1 - R_0 - r_0\cos(\theta+\beta)] - \sum_{k=1}^{\infty} R_k \sin[k(\theta+\beta)+\psi_k] \\ &\quad - \sum_{k=1}^{\infty}(r_k/2)\{\sin[(k+1)(\theta+\beta)+\varphi_k] - \sin[(k-1)(\theta+\beta)+\varphi_k]\} \end{aligned} \tag{11}$$

$$\begin{aligned} S_2(\theta-\phi) &= [R(\theta)]_2 + [r(\theta)]_2 \\ &= [R_2 - R_0 - r_0\cos(\theta+\beta)] - \sum_{k=1}^{\infty} R_k \sin[k(\theta+\beta)+\psi_k] \\ &\quad \sum_{k=1}^{\infty}(r_k/2)\{\sin[(k+1)(\theta+\beta)+\varphi_k - k\phi] - \sin[(k-1)(\theta+\beta)+\varphi_k - k\phi]\} \end{aligned} \tag{12}$$

$$\begin{aligned} S_2(\theta-\phi) - S_1(\theta) &= (R_2 - R_1) \\ &\quad + \sum_{k=1}^{\infty}(r_k/2)\{\sin[(k+1)(\theta+\beta)+\varphi_k] - \sin[(k-1)(\theta+\beta)+\varphi_k]\} \\ &\quad - \sum_{k=1}^{\infty}(r_k/2)\{\sin[(k+1)(\theta+\beta)+\varphi_k - k\phi] - \sin[(k-1)(\theta+\beta)+\varphi_k - k\phi]\} \end{aligned} \tag{13}$$

So, the difference between the two signals of probes S_1 *and* S_2 is the function of the phase angle ϕ, and the angle can be precisely determined previously. With this result, the effects of the roundness and the eccentric error of the workpiece can be eliminated, and the spindle axis error can be directly obtained by using following expression:

$$\begin{aligned} S_2(\theta-\phi) - S_1(\theta) &= (R_2 - R_1) \\ &\quad + \sum_{n=1}^{\infty} A_n(n/2)\{\sin[(n+1)(\theta+\beta)+P_n+\varphi_n] + \sin[(n-1)(\theta+\beta)+P_n+\varphi_n]\} \end{aligned}$$

$$\begin{aligned} A_n &= \sqrt{2[1-\cos(n\phi/2]} \\ P_n &= Atg\{\sin(n\phi/2)/[1-\cos(n\phi/2]\} \end{aligned} \tag{14}$$

If angle ϕ is chosen properly, the calculation of $[S(\theta - \phi)]_2 - [S(\theta)]_1$ will be easier. Similarly, $[S(\theta - \tau)]_3 - [S(\theta)]_1$ can be obtained. An inherent problem with the typical 3-point method is that it is "blind" to the components at certain frequencies. By using these two phase differentials $[S(\theta - \phi)]_2 - [S(\theta)]_1$ and $[S(\theta - \tau)]_3 - [S(\theta)]_1$, this blind problem can be solved, and therefore the spindle axis error can be precisely determined.

3.Experimental Result

A specially designed frame was adopted to fix the three capacitance micrometer probes. The resolution of the capacitance micrometer is 0.02μm. The experiment was carried out for a standard bar, and the test result was verified by comparing the experimental result with that obtained from the Taylor Hobson Roundness Gauge's precise rotating table. The radial error of the spindle was evaluated by the least square method. The accuracy of the Taylor Hobson Roundness Gauge is 0.1μm+0.0005μm/mm, and the result obtained with the double 2-point method is r_{max}=0.1030098, r_{min}=0.000460, radial error of the spindle = r_{max} - r_{min} = 0.102638. These results verify the accuracy and reliability of the double two-point method.

4. Summary and Conclusion

A new method called the double 2-point method for spindle error measurement is proposed in this paper. It is able to separate the radial error of the spindle from the roundness error of the workpiece;

During the separation of the spindle error from the roundness error, eccentric error of the workpiece was accurately eliminated and high accuracy of the spindle error measurement was obtained;

Spindle error estimation has been experimentally realized, and the effectiveness of the double 2-point method was verified by the experimental results.

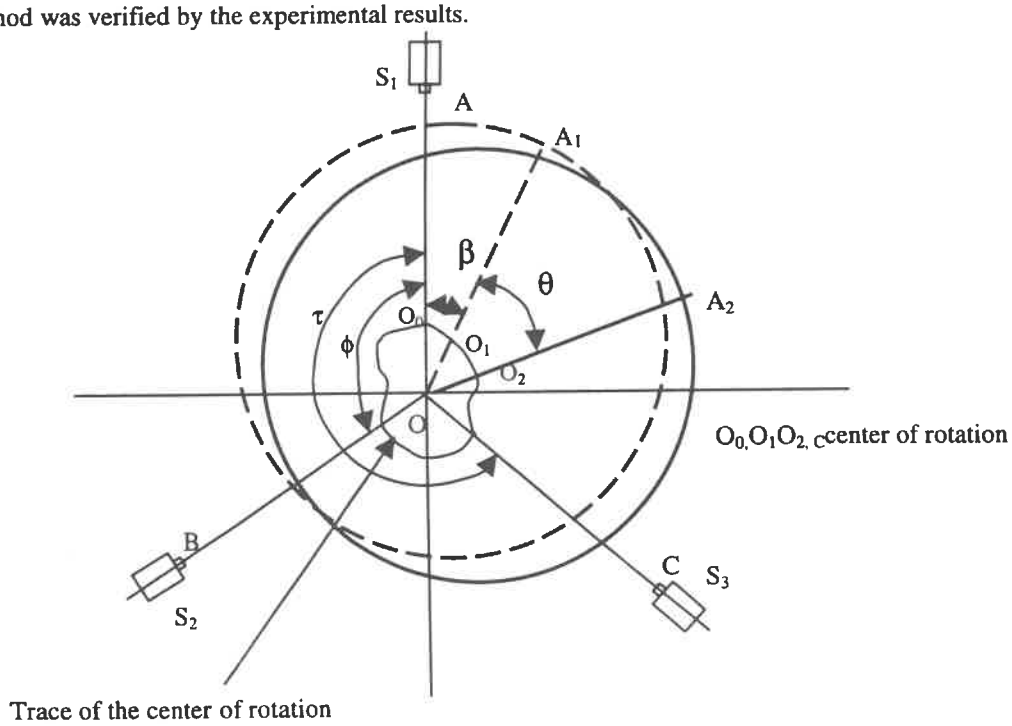

Fig. 1 The Schematic Diagram of Rotaion

REFERENCE

1. Muthy, T.S.R., Mallanna, C and Visveswaran, M.E. "New methods of evaluating axis of rotation error, " Ann CIRP, 1978, 27, 365-369
2. Noguchi, S., Tsukada, T. and Sakamoto, A. "Evaluation method of radial accuracy fro ultrahigh precision air spindle, " J Japan Soc Pre Eng, 1992, 58, 1053-1058
3. Figatner, A., Avdulov, A. and Tabenkin, A. " Evaluation of rotational accuracy in precision spindle bearings," Stanki i Instrument, 1974,1, 7-10
4. Figatner, A.M., Levin, A. and Fiskin, E. A. " Assessing spindle rotation error of precision machine tools, " Stanki i Instrument, 1990,61,19-21
5. Gao,W., Kiyono, S. and Nomura, T. New multiprobe method of roundness measurements, Prec Eng, 1996, 19, 37-45

Development of Three-Dimensional Profile Measuring Method for Microparts

Kimiyuki MITSUI
Department of Mechanical Engineering, Keio University
3-14-1 Hiyoshi, Kohoku-ku, Yokohama 223-8522, JAPAN

1. Introduction

Micromachine technology has considerable potential as a leading area of industry in future. For the progress of micromachine technology and microfabrication technology, it is necessary to devise a technique to measure both profile and dimension of microparts. Researches on measurement methods and instruments for microstructures have been reported[1-6].

For the inspection and measurement of micro parts, measuring methods for the profile and dimension including geometrical deviations such as straightness, circularity and perpendicularity are needed. It is thought that a small three-dimensional profile measuring apparatus with microprobe can be utilized as the measuring method for this purpose. In this paper a new three-dimensional profile measuring apparatus which has non-contact probe detecting proximity to measuring object through tunneling effect is described in detail. Then the validity of the measuring apparatus is shown through several specimens like roughness standard, micro hole and groove.

Tunnel effect is observed when gap between surface and probe is less than 1nm. In this research the tunnel effect is used to detect the contact of prove and surface, because no complicated devices are needed and measurement on the sloping surface is possible. The drawback of optical methods is the shadow effect of light beam against steep slope.

The trial apparatus is composed of X-Y-Z precision stages with linear encoders resolution of 0.1 μ m, θ (rotating) stage with rotary encoder and a personal computer controlling these stages through GP-IB interface. The probe is mounted to Z stage through piezo electric actuators so that it must be precisely controlled. The probes are most important components of this measuring method. Probes suitable for each microparts are fabricated by micro die-sinking electro discharge machining.

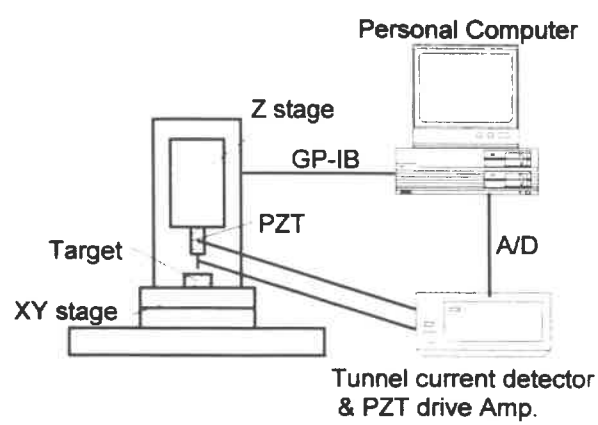

Fig. 1 Measuring principle

2. Measuring principle

Experimental apparatus for the three dimensional profile measurement for microparts was developed. A first generation apparatus shown in figure 1 consists of X-Y micro mechanical stages and a probe tip mounted on a Z micro mechanical stage through a PZT ceramic actuator. Proximity of the microprobe to object surface is detected by principle of STM (scanning tunneling microscopy). X-Y-Z stages are controlled by a personal computer through GP-IB interface and the position of stages are obtained by internal linear encoders (resolution of 0.1 μ m). Micropobes are fabricated by micro die-sinking electrical discharge machining.

When the probe approaches the object, the PZT actuator that holds the probe is fully expanded. The PZT actuator is shrieked when tunnel current is detected to avoid collision of the probe and the object before Z stage stops. The position of Z stage measured by internal linear encoder gives Z coordinate value. A personal computer is monitoring the applied voltage to the PZT actuator through A/D converter. When PZT voltage becomes zero, the computer stops Z stage. The error produced is depend on the linear encoder of the micro mechanical stages. The result obtained from the standard deviation value of 100 measurements was 0.2 μ m.

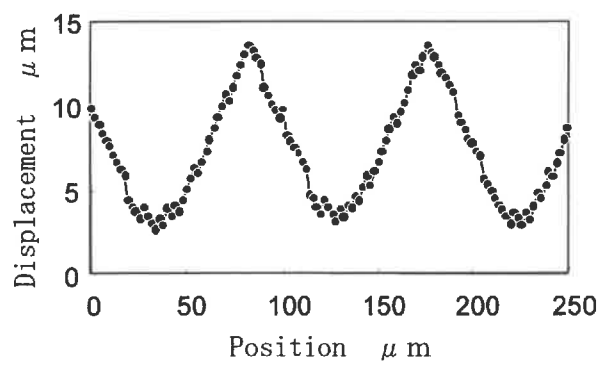

Fig.2 Measuring result from standard surface roughness test piece

Figure 2 shows measured result for a standard surface roughness test piece. The test piece has wavelength of 100 μ m and height of 11 μ m. The data was obtained while probe tip is moved every 2 μ m in X direction. Accurate values for both wavelength and height were obtained.

3. Configuration of measuring system and experimental results

Probe tip approach direction in the first generation apparatus is restricted only to Z direction. Therefore, form of measured objects is very limited, for example, measurement of inside hole and side of step are not possible. The second generation apparatus has θ rotating stage on

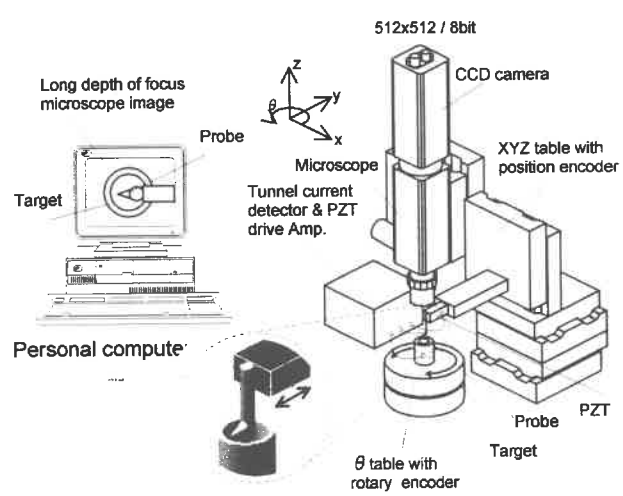

Fig.3 Configuration of experimental apparatus

X-Y stages. The rotating stage has internal rotary encoder (resolution of 3.48"). The apparatus has PZT actuator control system similar to the first generation apparatus, but expansion and contraction direction is optional. Figure 3 shows the second generation apparatus with PZT actuator control direction is set to X axis and installing X type probe that has probe projection in X direction. Figure 4 shows measured cross section of micro holes. Inside of micro holes of diameter about 300 μ m by drilling and electro discharge machining on aluminum plate are measured. Data are obtained at every 5 degrees of θ rotary stage positioning. Since the left side figures in Fig. 4 are showing measured data super positioned on base circle of 300 μ m diameter, they do not show inside diameter of the hole properly. Right side figures show the results after magnification; one scale unit is equivalent to 10 μ m. Because the measuring results are including rotational error of the θ stage, evaluation and compensation of the rotational error is needed for more accurate roundness measurement of the hole.

We have also developed probe tip fabrication method using micro die-sinking electro discharge machining. Figure 5 shows a photo micrograph of X-Z type probes. X-Z type probe has projections in both X and Z direction. By the X-Z type probe, continuous measurement of step shape object can

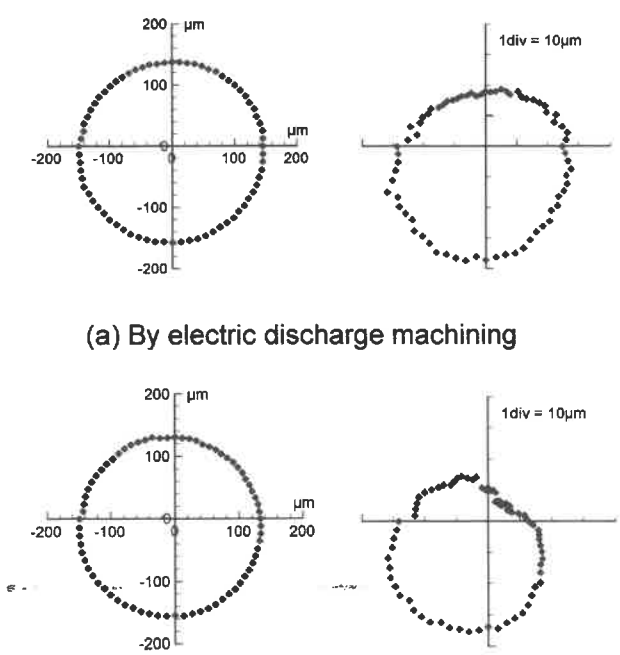

(a) By electric discharge machining

(b) By drilling

Fig. 4 Cross section of microholes

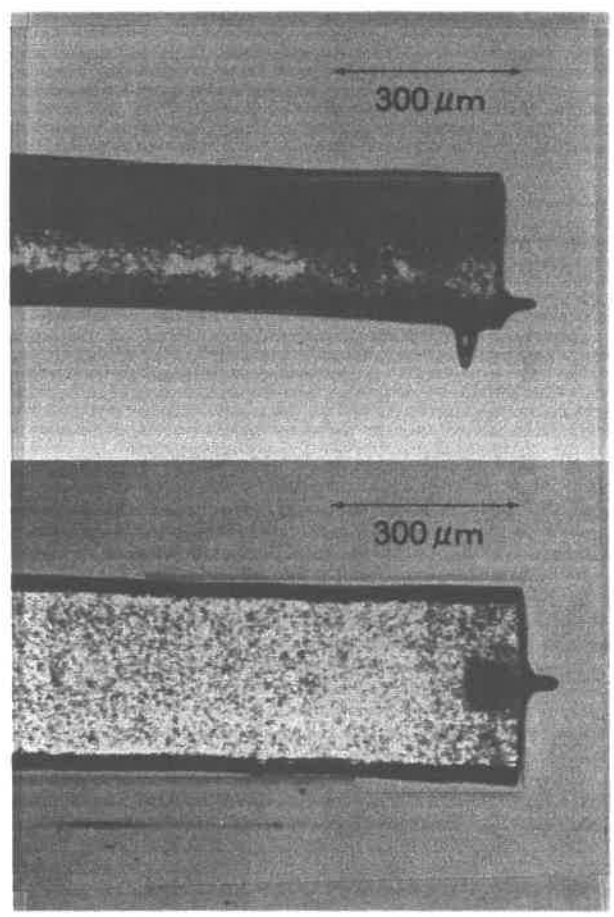

Fig. 5 Fabricated X-Z probe

be possible. Also perpendicularity of bottom and lateral surfaces, angular parallelism of bottom and upper surfaces can be evaluated.

4. Conclusion

The main conclusions obtained from this report are summarized as follows:

1) The measuring principle of three-dimensional profile measuring method for micro-parts and configuration of the apparatus were presented.

2) Metal surface with grooves can be measured continuously by X-Z type probe fabricated by micro die-sinking electro discharge machining.

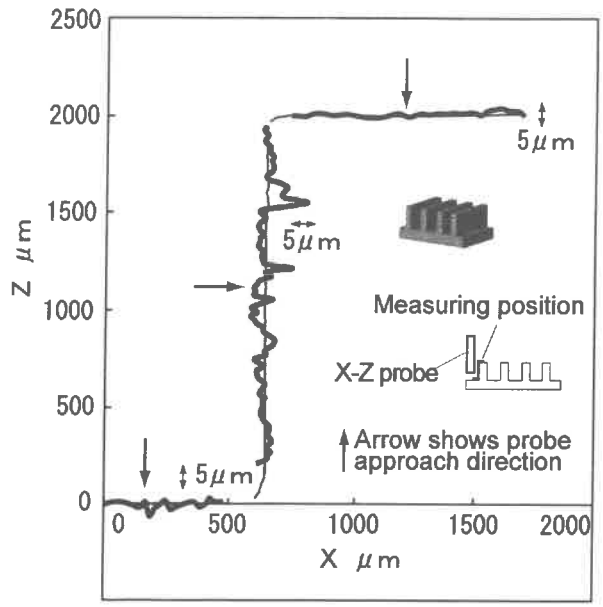

Fig. 6 Measuring results from metal surface with grooves

References

1) R. Kokawa and H. Sato: Profile Measurement of Aspheric Lenses Using a Scanning Electron Microscope, Trans. of the JSME, 55-515 (1989)1777. (in Japanese)
2) T. Masuzawa, Y. Hamasaki and M. Fujino: Vibroscanning Method for Nondestructive Measurement of Small Holes, Ann. CIRP,42/1 (1993)589.
3) K. Mitsui and T.Goto: Development of Dual Servo STM, Proc. of ASPE Annual Meeting (1996)146.
4) T.Masuzawa et al.:Twin-Probe Vibroscanning Method for Dimensional Measurement of Microholes, Ann. CIRP, 46/1(1997) 437.
5) T. Shiraishi and K. Mitsui: Development of Three Dimensional Profile Measuring Apparatus for Microparts -Measuring Principle and Measuring Results-, J. of the JSPE, 64-9 (1998)1395. (in Japanese)
6) Ji Guijun, H. Schwenke and E. Trapet: Opto-Tactile Sensor for Measuring Small Structures on Coordinate Measuring Machines, Proc. of ASPE Anual Meeting (1998)25.

Development of Noncontact Coordinate Measuring Machine implementing High Precision Optics and Precision Image Processing Algorithms of Subpixel Accuracy

Heui Jae Pahk, Il Hwan Lee
School of Mechanical and Aerospace Eng. Seoul National University, Seoul, Korea

1. Introduction

The noncontact coordinate measurement technology has been considered as one of very important tools for the automation of inspection of the parts and products in industry. As the size of the parts and products becomes smaller and more precise, such as semiconductor, the needs for precision dimensional measurement with high accuracy and high precision has been increased.

In this paper, a noncontact coordinate measuring machine has been developed; high precision optics head, precision motion stage, and the software of image processing algorithm. The optics head consists of high magnification optics units and illumination units, and the precision motion stage has been designed such that accurate scanning is obtained for the measurement objects. Auto focus imaging principle is implemented such as optimum focused image is captured by the proposed image focus measurement function, where optimum focusing distance is calculated and the optimally focused image is captured at the displaced capturing location. One of the key feature of the developed system is the precise and intelligent image processing algorithm for analysis of the measurement data. A new and precise image processing algorithm has been developed with subpixel accuracy. The developed image processing technique includes: various fine edge detection techniques, several feature scanning techniques. The developed system can be applied to various measurement/inspection processes in many practical application.

2. Precision Image Processing Algorithms

2.1. Auto Focusing

In vision inspection system, the focused image is required for precise detection. The defocused image inherently have distorted information of object, and aggravate the efficiency of edge detector. Thus the focus position providing the sharpest image must be calculated in advance. The optimum focusing position can be calculated by the image focus measurement function(IFMF), which is defined as in eq(1)

$$F(i,j) = \sum_{x=i-N}^{i+N} \sum_{y=j-N}^{j+N} ML(x,y) \qquad \text{for} \quad ML(x,y) \geq T_1 \tag{1}$$

where ML(Modified Laplacian) has the form as

$$ML(x,y) = | 2I(x,y) - I(x-step,y) - I(x+step,y) |$$
$$+ | 2I(x,y) - I(x,y-step) - I(x,y+step) |$$
$$T_1 = Threshold$$

$I(x,y)$ is the gray value at x,y in image

In the developed system, sequential images are captured at the displaced capturing locations, and the IFMF finds the focused image. Fig.1 shows the sequential images and IFMF evaluation.

2.2 Edge Detection with Subpixel Accurcy

In an Area of Interest(AOI), edge detection is usually performed in the normal direction to the edge, where the AOI can be defined by the user. Fig.2 shows an AOI and edge search direction for line and circle feature scanning. After setting the AOI and the search direction, edge detection is performed with the Laplacian-Gaussian operator, funding the Zero Crossing. The Laplacian-Gaussian operator is

defined as in eq(2)

$$\nabla^2 G(x,y) = \frac{1}{\pi\sigma^4}(1 - \frac{x^2+y^2}{2\sigma^2})\exp(-\frac{x^2+y^2}{2\sigma^2}) \quad (2)$$

where σ is space constant.

At the zero-crossing location, the intensity can be modeled as the polynomial form as in eq(3)

$$F(r) = k_0 + k_1 r + k_2 r^2 + k_3 r^3 \quad (3)$$

where r is the coordinates of edge search direction

With the polynomial equation F(r), we can divide the pixel into 5~10. With the divided pixels, the edge detection is performed again and we can find the edge point with subpixel accuracy.
In this paper, various edge detectors with subpixel accuracy have been developed such as common edge detector ,closest edge detector and first edge detector. Common edge detector determines the best or strongest edge in the AOI; the first edge detector find the first edge of a given strength and direction that lies within the search region; and the closest edge detector locates the peak point on a curved edge in a given direction.

2.3 Feature scanning techniques

Developed system includes several feature scanning techniques such as line feature scanning, arc/circle feature scanning, and ellipse feature scanning. Feature scanning is composed of edge detection, feature analysis by Least Squares Technique for removal of noise or corrupted data. Fig.3 shows the procedure of circle feature scanning technique. When there exists noise in object, the result of feature scanning can be used to remove that noise or corrupted data. Fig. 4 shows the removal of noise or corrupted data and the result of re-analysis.
The measured Items such as point, line, circle and ellipse can be saved in the list type and the relationship between items can be calculated by the developed operation software. Fig.5 shows the developed operation software, which includes image I/O, motion control, auto focusing algorithm, etc.

3. Measurement System

The developed measuring machine consists of the optical part with CCD camera, camera controller, illumination, motion part for motorized wide range scanning, and software part for operating measurement system.
The image frame grabber is implemented for capturing CCD camera image, and a light controller is also used for the illumination control. The whole optical image processing are performed under Windows based image analysis and light control software developed.
For scanning wide range, a precision X-Y stage has been designed using linear scale, AC servo motor,. Z axis motion part also has been designed for the focus adjustment. The motion control is operated by the Windows based motion control software developed. Fig.6 shows the noncontact coordinate measuring machine developed.

4. Results and conclusion

The developed coordinate measuring machine has been applied to various features such as distance of lines and radius of circle of precise grid. The measurement process has repeated 10 times, and the result is shown in Fig. 7, demonstrating the performance.

The conclusion is as follows.

(1) A noncontact coordinate measuring machine has been developed, giving measurement feature with subpixel accuracy upto a few micrometer resolution.
(2) For scanning wide range of object, precision XY stage, Z axis motion part have been designed, and

the measurement region can be easily selected by user-interactive software developed
(3) An auto focus technique has been implemented. The optimal focus position of CCD camera has been found very much effective in practical measurement application..
(4) Various edge detectors and several feature scanning techniques have been developed. These tools can be used in many inspection applications with high efficiency.

Reference

1. Andres Huertas, Gerard Medioni, "Detection of Intensity Changes with Subpixel Accuracy using Laplacian-Gaussian Masks", IEEE Trans. On Pattern Analysis and Machine Intelligence, Vol. Pami-8, No. 5, September 1986.
2. Eric Krotkov, "Focusing", International Journal of Computer Vision, 1, 223-237, 1987

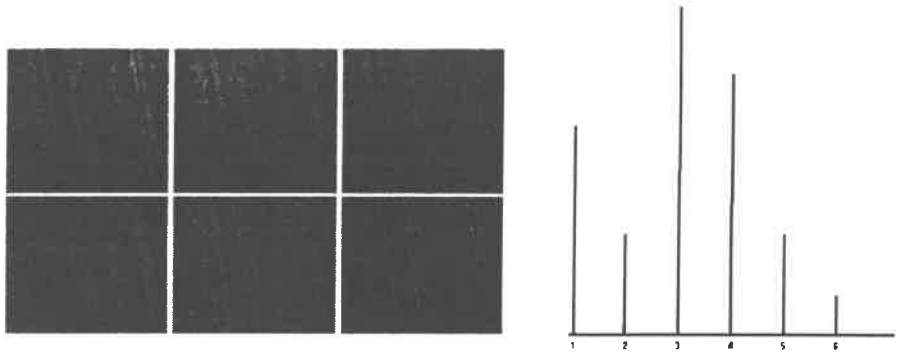

Fig.1 Sequential images with 100um step and result of IFMF

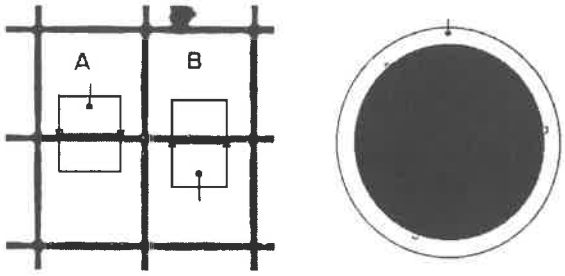

Fig.2 AOI and edge search direction for line and scanning technique

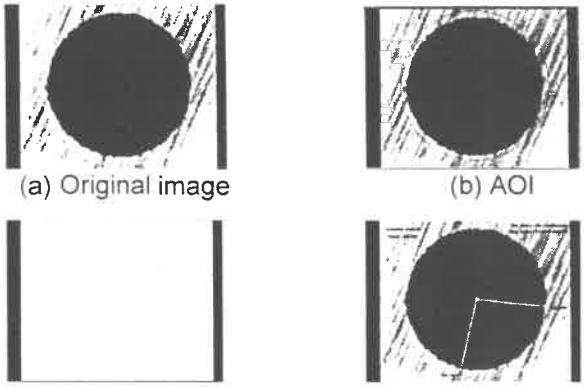

(a) Original image (b) AOI

(c) Edge detection (d) Result of analysis

Fig.3 Procedure of circle feature scanning technique

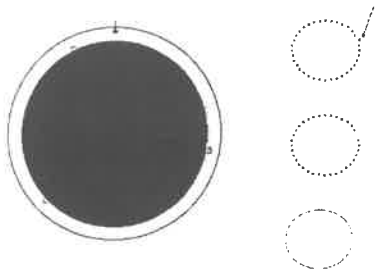

Fig.4 Removal of noise or corrupted data

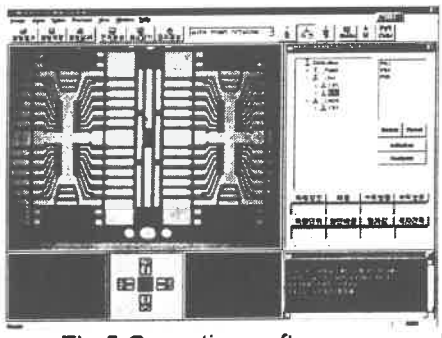

Fig.5 Operation software

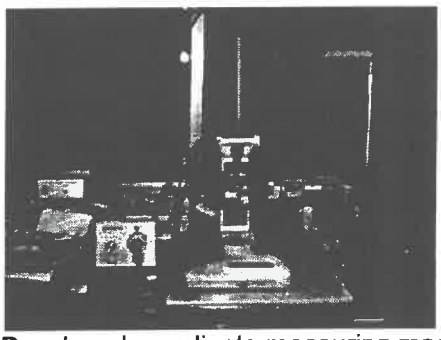

Fig.6 Developed coordinate measuring machine

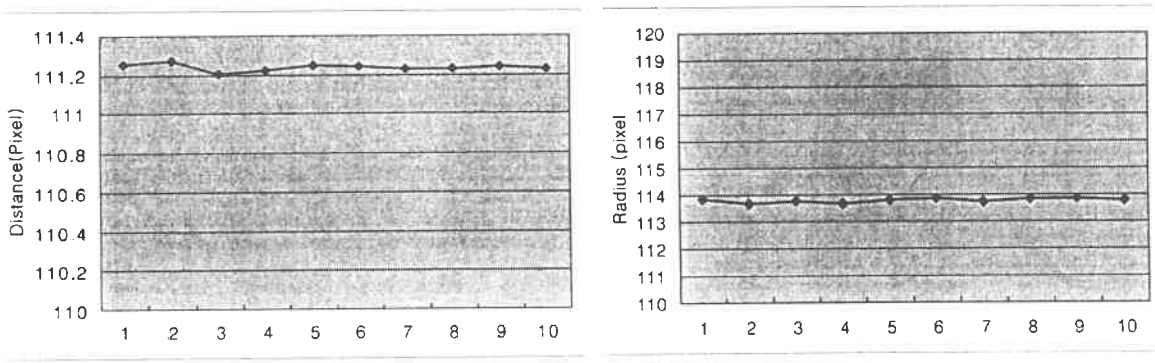

Fig.7 The result of line and circle analysis

Traceability of CMM Measurements

Bas.W. van Dorp, Frank.L. Delbressine, Han Haitjema, Piet.H. Schellekens
Eindhoven University of Technology, Precision Engineering Section

The need for traceability

In current measurement technology, traceability is of great importance. It can be required by a purchaser in a contract, or by standards such as ISO 9000-9004 and the relatively new standard ISO 14253. These standards are made to guarantee measurement quality and to protect the purchaser. The demand for traceability strongly influences measurement practice. Traceability of a measurement requires that the measurement uncertainty is stated.

Traceability of a measurement on a Coordinate Measurement Machine, CMM, is very difficult to obtain for most measurements, because the measurement uncertainty can't always be established. This is due to the complex error structure of the CMM.

How to obtain traceability?

In general, there are two approaches to obtain traceability on a CMM:

- Comparator Approach:

The CMM is used to compare the product with reference artifacts that have known uncertainties.

- Error Synthesis Approach:

The separate error sources are combined to an uncertainty on a specific measurement.

The comparator approach requires a reference artifact with approximately the same dimensions and shapes as the product to be measured. This is a great reduction in the versatility of a CMM.

With the error synthesis approach one should be able to achieve traceability for an arbitrary measurement. An important tool for this method is the Virtual CMM (VCMM).

This paper deals with the measurement uncertainty induced by geometrical errors, probing errors and measurement strategies. We combined these errors using a VCMM, which we developed ourselves. This is a model of a CMM that simulates the errors of a CMM and combines them using a Monte Carlo method.

In this paper, first we will show some possibilities of the method of the virtual CMM, next we will point out the existence of some gaps in current methods. These gaps have to be filled to make sure we can apply the method of the virtual CMM without the risk of faulty results.

Modelling Error Sources

The guideway of the carriage is not perfect, i.e. the path of the carriage deviates from its nominal movement. This causes errors in the determination of the coordinates of a measured point. At first, we assumed that we could model these errors as if they were "random". This means that the error plotted against the position of the carriage is modelled as a white noise signal. If a systematic error of the guideway is measured, one may or may not correct for this error and assume the remaining error "random". In this case the error of the

CMM is modelled as this systematic error, with a white noise added. Thus, there is no essential difference in the applied method for corrected or uncorrected machines.

Effect of Measurement strategy

Using the method of a virtual CMM, it's quite easy to evaluate the effect of measurement strategy on the measurement uncertainty. We did this for different measurement task, some of which we will demonstrate here. The first example is measurement of angles on an object. In figure 1, three different measurement strategies are shown. Each measurement involves twelve measurement points, six on each side. These points are arranged in a rectangle. The stars in the picture show a simulated measurement point, simulated with a 1000-fold magnification of the random error. The plane is an estimated least-squares plane through six simulated points. From left to right, the horizontal dimension of the rectangle is made larger. The pictures give an idea of the effect of the variation of this measurement strategy parameter. For the machine we investigated, a Zeiss UMC 550, the measurement uncertainty was calculated. The dimension of the long side of the rectangle proved to be the relevant parameter. For instance, with a length of 50 mm, the measurement uncertainty was 12 seconds of arch, for a length of 100 mm, it was 6 seconds of arch.

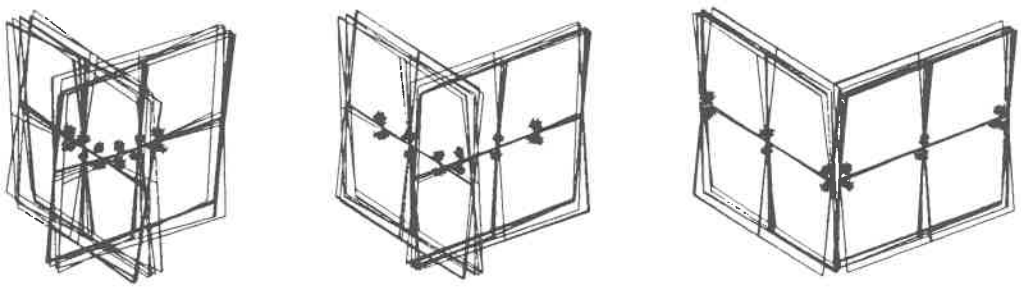

Figure 1: calculated LSQ-planes for angle measurements, 3 diferent measurement strategies

A similar exercise was done to investigate the influence of the measurement strategy on the measurement uncertainty of the diameter and position of a circle. In figure 2, some results are shown. The stars are simulated measurement points, again with 1000-fold magnified random error. The circles are estimated least-squares circles, the dots are the centers of these circles. This picture makes clear that the position of the measurement points on the circle is an important parameter in evaluating the measurement uncertainty

Figure 2: calculated LSQ-circles for diameter measurements, 2 different measurement strategies

Effects to be investigated in the future

So far, proposed and implemented methods for describing and simulating these errors assume that errors can be described as if they were "random". If we look closer, we see that these errors are not indeed random, but we call them random because we have no accurate way to describe them. If one wants to apply software correction, this approach can give satisfactory results. In software correction, we describe errors, and we correct for them. Errors that we cannot describe, can't be corrected for. Errors that are random by nature, can't be corrected for, but errors that are not random but unknown, can't be corrected for either. If we presume unknown errors "random", the correction for the known errors still works fine.

If we want to evaluate the measurement uncertainty according to the GUM [1], correct statistical representation of the errors is needed. Therefore, it is important that we develop a method that can describe all errors, known systematic errors, unknown systematic errors as well as "random" errors.

It may not be necessary to describe in detail all error sources, but it is sufficient to describe all statistical properties of these errors. If we want to use a Monte Carlo method, we must generate simulations that have the same statistical properties as possible real measurements. These statistical properties are not only standard error of a certain point, but also auto correlation of one error, and cross correlation between different errors.

In [2], the method of the virtual CMM is used to evaluate the measurement uncertainty of different measurement strategies when measuring a circle. Here, the measurement uncertainty is calculated for different numbers of measurement points, varying from 4 to 1000. In the case of 1000 measurement points, a very small measurement uncertainty is found (0.13 micrometer). This would only be true if all assumptions that were made would be true. One of the assumptions is that all errors are random and normal distributed. In fact, this is not true, this will be demonstrated below.

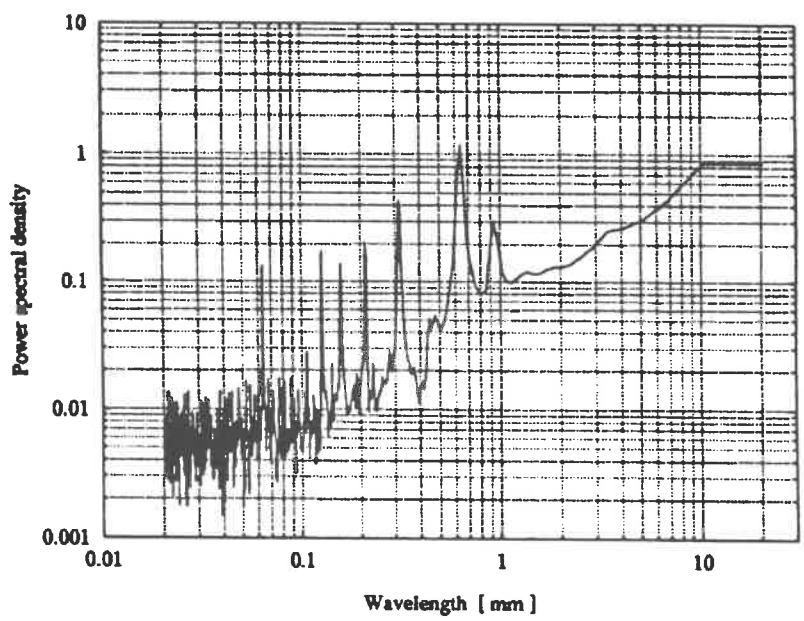

Figure 3: esitmated power spectral density of xTx error of a multi-axis machine (MAHO 700)

In [3], measurements of the error of a multi-axis machine are made, and the power spectral density of this error is estimated, see figure 3. This estimated power spectral density shows clearly that this signal can not be considered as white noise, this means that a series of measurement points can not be considered "random". If we simulate measurements points, using a random number generator, that generates points that are governed by a normal distribution, faulty results will occur. In particular, the expected "cancelling out" of errors when measuring many points will not occur. This means that the measurement uncertainty in the example with 1000 measurement points on a circle is probably not correct, and will in fact be larger.

The generation of simulated measurement points should be done in such a way that the preservation of relevant statistical quantities is assured. The method of surrogate data, as described in for instance [4], may be a good way to do this. This method is not yet implemented in current VCMM implementations, but the principle of this approach is a an essential step in the direction of a satisfying solution of the problem.

Conclusions

The VCMM method is a powerful tool to investigate the effect of measurement strategy on the measurement uncertainty. Current VCMM methods don't use correct assumptions, which may result in faulty results. Further research regarding the use of methods that preserve power spectrum and auto correlation behavior, like the method of surrogate data, is needed.

References

[1] International Organization for Standardization. *GUM – Guide to the Expression of Uncertainty in Measurement*, 1993

[2] H.-J. Neumann, *Vielpunktmessung kontra Einzelpunktmessung mit Koordinatenmessgeräten – Funktionsgerechte und stabiele Messergebnisse mit verringerte Messunsicherheid (=Multi-point measurement versus one-point measurement with Coordinate Measurement Machines – Functional based and stable measurement results with decreased measurement uncertainty),* In: Referatensammlung der DIN Tagung: 'GPS 99 Geometrische Produktspezifikation und –pruefung, 1999, (in German)

[3] H. Soons, *Accuracy of Multi-Axis Machines*, PhD-thesis, Eindhoven University of Technology, 1993

[4] James Theiler, et. al., *Testing for nonlinearity in time series: the method of surrogate data,* Physica D, vol. 58, pages 77 – 94, 1992, Elsiever Science Publishers B.V.

A New Photo-Electronic Length Measuring Instrument with 0.1 nm Resolution and 110 mm Range

Zi-qiang Zou, Wei-yu Zou, Li-dong Hu, Jing-tai Chen, Yu-cheng Zhu
Beijing Institute of Ultra-Precision Engineering (BIUPE), Beijing, P. R. China 100083

Instruction

Authors and their colleagues have been working on the field of manufacturing metrological gratings for more than forty years. We have developed kinds of dividing machines based on photo-electronic control principle to produce metrological gratings [1, 2, 3, 4, 5]. These metrological grating can have up to 1,000~2,000 lines per millimeter. The position accuracy of such grating lines is about ± (20~100) nm [6]. We also developed several series of photo-electronic length gauges with resolution of up to one nanometer and measuring range of 10~100mm [7, 8]. For the calibration of these series of length gauges, we built the instrument described by this paper.

Instrument

The exterior view of the instrument is shown in Fig.1 and the working principle is illustrated in Figure 2. There is a very big and steady iron base filled with special oil. On top of it, there fixed a special ultra-precision guide mechanism developed by us, what we call "optical guide". The straightness of the slideway is less than one sixth of wavelength within 310mm, and the uncertainty of this motion guide mechanism is 30nm within 110mm stroke. Moving resistance is about 0.02N when slideway is moved forward. Torque motor driven by control circuit rotates the leadscrew to push the working table forward continuously by passing through a special coupling mechanism. The nano-grating is supported upon the working table according to the principle of "Bessel point", and the reading system fixed on the base acquires four signals with phase-difference 90° to one another. The signals are passed through differential amplifier, flip-flop, direction distinguishing circuit, counter and are sent to computer to count the total number of moiré fringes. The signals are also passed through A/D converters and are sent to computer to get interpolation number of moiré fringe [9]. In order to get ultra-high accuracy, the photo-electronic signal is not formed by a few lines of nano-grating but by four thousand of lines of grating. Thus the random error and local error of grating are greatly reduced. However, careful mechanical construction and signal processing are important as well.

Environment

The temperature around the instrument must be highly controlled. We built the laboratory in three "layers", one enveloped inside another. The temperature is controlled better and better from outer room to inner ones. The smallest room is actually a glass room. It consists of two layers of glass plates. The instrument described by the paper is put in it. The temperature around the instrument is controlled to 20±0.005°C. All operations must be done outside the glass room. The instrument must be free from various vibrations. So the instrument and its base weigh about twelve tons altogether and are supported on a special vibration-free system developed by us.

Experiments

Because there is no higher accurate length standard available in China, we use a laser interferometer HP 5529A to make a relative comparison with our instrument temporarily. Although our instrument can work while continuously moving, the resolution of 5529A is 10nm when it moves continuously. Thus we have to make stationary comparison since the resolution of 5529A is 1nm only when it is stationary. We chose 10mm reading intervals to avoid spending too much time for each measurement. Fig. 3 shows the connection of our instrument and HP 5529A. Our instrument is not sensitive to air refraction index, air pressure, humidity and flow of air, and so that 0.1 nanometer steady reading can be got. But laser interferometers are different. Especially, when we tried to get steady reading data of magnitude order of nanometer, the laser interferometer is extremely sensitive to the flow of air. For this purpose, when the adjustment and alignment of these two kinds of instrument shown in Fig. 3 had been done, we still have to wait at least 24 hours for steady mechanism and steady air.

Fig. 4 shows the difference of reading data between our instrument and HP5529A. Fine solid line shows the first set of comparison, and fine dotted line shows the second set of comparison. Coarse solid line shows the average value of these two sets. The above-mentioned repeatability of measurement is obviously better when we use our nano-grating sensor instead of laser interferometer, and in this case, the repeatability of measurement, is $\sigma \leq 0.4$nm. Because the random error is comparatively small, if there is an enough accurate length standard, the systematic error of the instrument is easy to be corrected by computer technology.

References

[1] Zi-qiang Zou, "Development on Precision Ruling and Line Metrology", *Optics and Machinery*, pp51-54, March 1982;

[2] Zi-qiang Zou, "On the Principle of Multi-head Reading", *Symposium of AIM Conference on Instrumentation and Measurement*, pp185-192, 1992, Auckland, New Zealand;

[3] Zi-qiang Zou etc, "Photo-electronic Lithography of Radial Gratings with 162,000 Chromium-lines", *Chinese Journal of Scientific Instruments*, pp133-139, May 1985;

[4] Zi-qiang Zou, "On the Phenomenon of Double-period Run-out", *Acta Metrologica Sinica*, pp267-279, April 1982;

[5] Zi-qiang Zou etc, "A Calibration Instrument for High-precision Coded Discs", *Symposium of international Metrology Conference*, NELEX82, Glasgow, England;

[6] Zi-qiang Zou, "Recent Developments on Nanometer Measuring Technology", *Symposium of the conference on Nanometer Technology*, pp168-172, October, 1996;

[7] Zi-qiang Zou, "Precision Instruments Research in the People's Republic of China", *Proceedings of AIM Conference on Instrumentation and Measurement*, Adelaide, Australia, 1989;

[8] Zi-qiang Zou, "Nanometer Length Measuring Instruments and Its Applications", *Symposium of the National Conference on Micro-electronics*, December 1997;

[9] Wei-yu Zou, "Signal Processing of Nano-grating Measurement Techniques", *Symposium of the Conference On Nanometer Techniques*, pp202-205, October 1996.

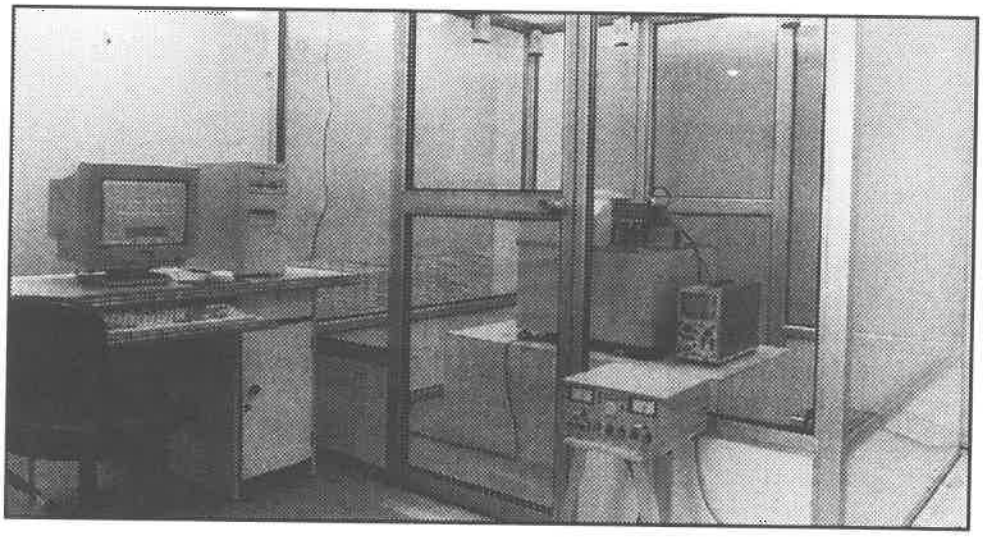

Figure 1. Exterior View

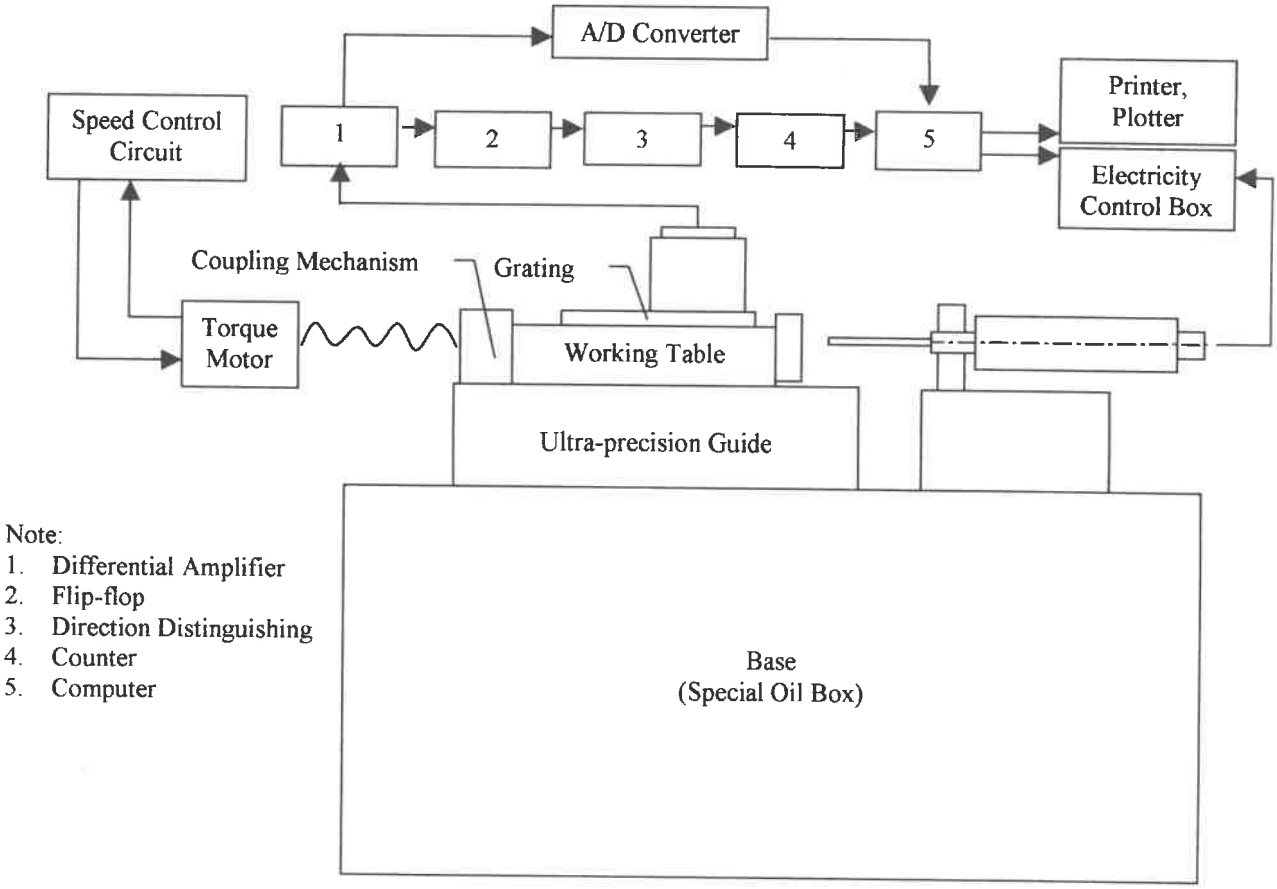

Figure 2. Working Principle Draft

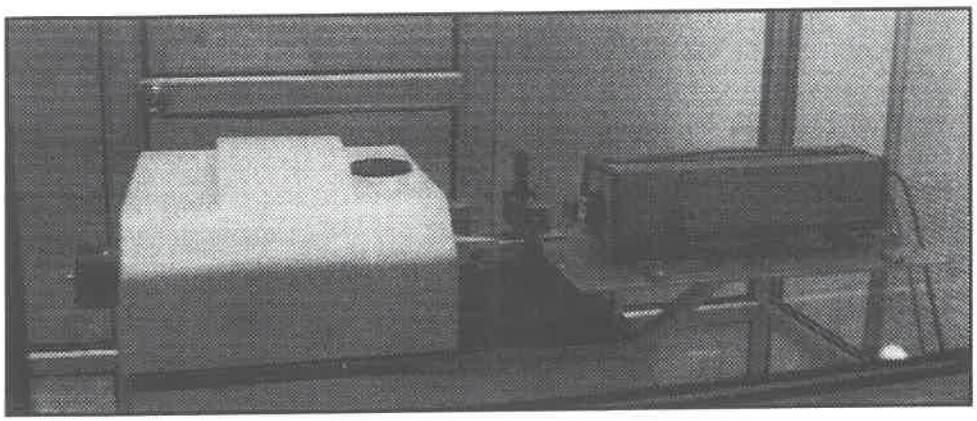

Figure 3. Comparison with HP5529A

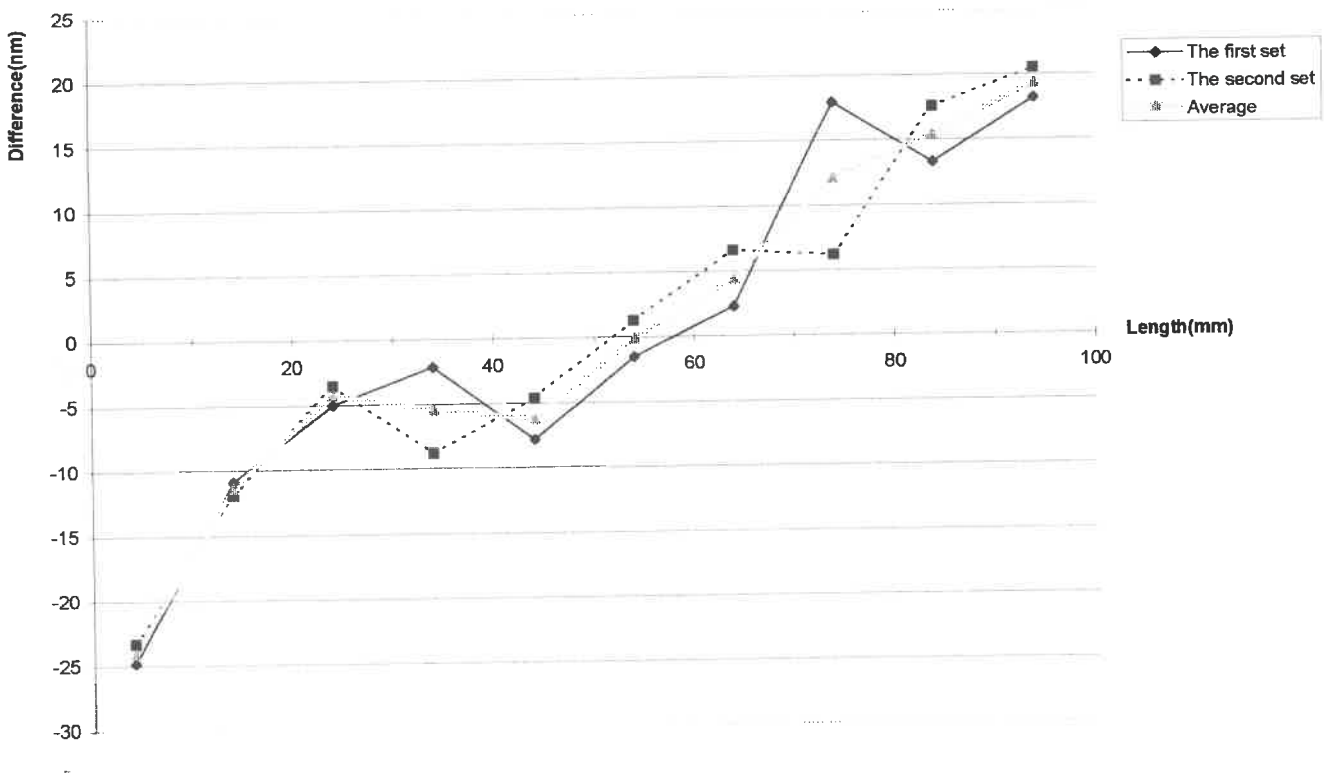

Figure 4. Comparison Result

An Internet based Surface Texture Analysis System

Son H. Bui and Vijoy Gopalan, Jay Raja, and K.R. Subramanian[+]
Center for Precision Metrology
[+]Department of Computer Science
UNC Charlotte, Charlotte 28223

1.0 Introduction

In recent years, large companies have moved away from manufacturing all the parts that are needed for the product they market. Instead of in house manufacturing, they are resorting to outsourcing of parts. The companies that manufacture the parts tend to be small and in many cases lack the metrology and process expertise needed to trouble shoot problems related to part quality and part variability. The large companies that design and build the products are still responsible for the quality and performance of the parts and therefore work with their vendors to ensure process capability and reduce part variability. Since the manufacturing processes are geographically separated from the large companies there is a need for remote access of data and ability to analyze and trouble shoot processes. This project addresses this need by developing an Internet based surface texture analysis system with database support. This paper deals with the development of the basic infrastructure to undertake remote process studies to reduce process variability and to accumulate process knowledge.

2.0 Internet Based Surface Texture Analysis

This project offers a unique way to analyze surface texture. It provides a repository for surfaces through a database, a set of tools for surface texture analysis, remote access to both data and analysis tools. The analysis program and the database program are accessible through a web browser with an Internet connection.

The analysis system is designed using object oriented programming technique. The main components of the system are the user interface classes and the background processing classes. All the classes of the system has been developed using Java (JDK 1.1) which is the de facto language of the web. Since this is an infrastructure project that will evolve in different directions, care has been taken to make the design to be robust and reusable. In developing the software an incremental approach towards gathering requirements, designing the software, and implementing and testing it was taken. This approach was taken so that the requirements could be modified to increase the scope after an iteration of the development cycle. This approach was also essential due to the lack of precedents in similar number crunching applications on the web.

2.1 Surface Characterization

The main features of the software include a database into which a user can insert measured data, query for specific datasets, and/or select specific datasets for analysis [1]. The software provides analysis tools that are available on the measuring instruments and then goes beyond by providing flexibility. It also provides advanced tools such as power spectral analysis, correlation, and wavelet analysis that are not available in current analysis systems. The ability to access data from a database of profiles is an important function of the software. This provides a way to understand

the parameters involved in the process. Two surfaces can have the same R_a but one might perform better than the other one. This is a common problem that is encountered. The "Compare Two Profiles" function of the software addresses this issue. The "Generating turned profiles" function gives the user a way to compare a theoretically generated profile with the actually produced surface. The "Asperity removal" [3] function removes asperities from the surface and gives statistics on them. This saves time, as the user need not measure the part again when the asperity is caused due to debris. This function also allows the user to analyze porous surfaces. Analyzing multiple files at the same time is a unique tool that is not offered by current analysis systems. This allows the user to analyze surfaces that have been generated at different times by the same tool. This is useful in monitoring for tool wear. Analyzing a surface at multiple cutoffs is another function that is provided by the software. Figure 1.0 shows the compare two surfaces function of the software. The figure shows the comparison of two plateau-honed surfaces.

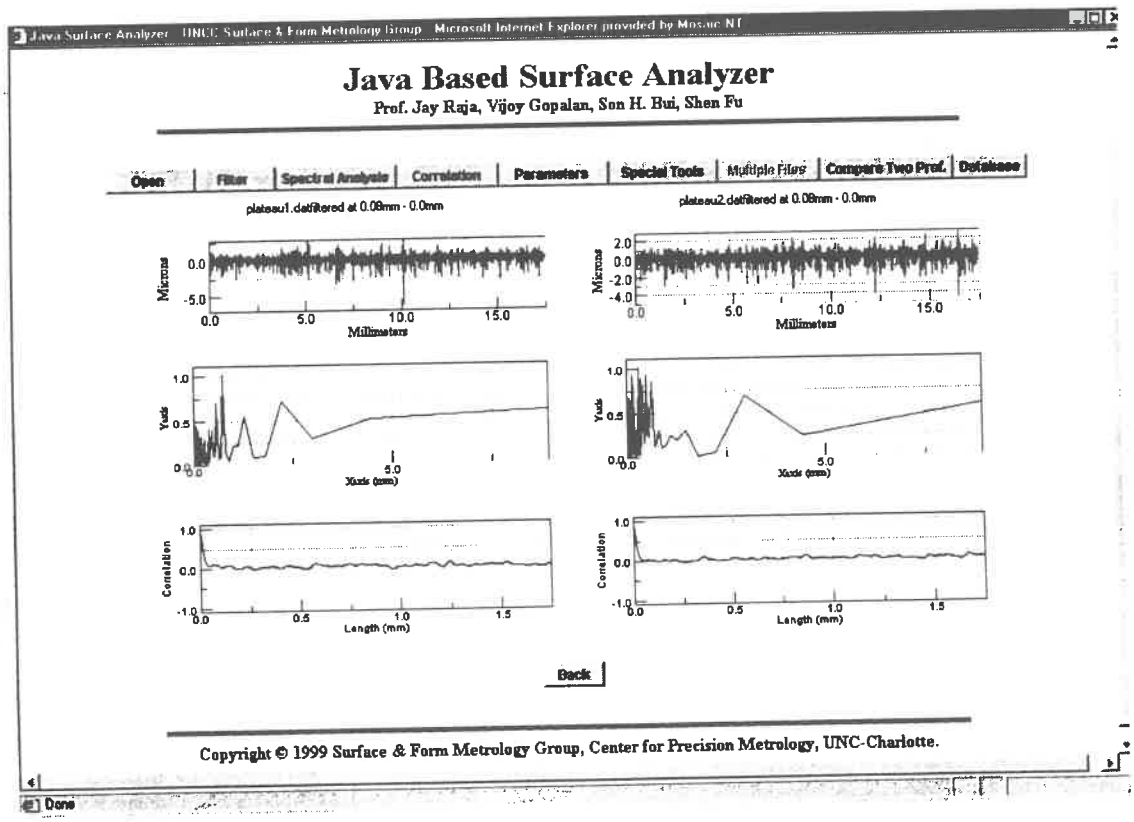

Figure 1.0 Comparison of two plateau-honed surfaces

2.2 Database

The database is used to organize the information of how the surfaces are produced [2]. Parameters of machine condition, cutting condition and other process parameters can be stored

along with the part information. In addition, the database is used to store data generated from surface finish instruments. With this database, a metrologist can quickly query information through the Web and use it to develop process knowledge and find the trends that cause process variability. The database provides features for querying information based on parameters, instrument name, process, filename, part name, time and date. It also provides tools for visualizing the information after doing the query. Tools for loading the data sets for analysis are also provided.

Each user is provided with separate account. The user can login to his account and can insert data into the database from his local disk or any other remote location. The user can also delete data sets that he had previously inserted. Figure 1.2 shows the output of a query for all data that have P_a less than 0.5 μm.

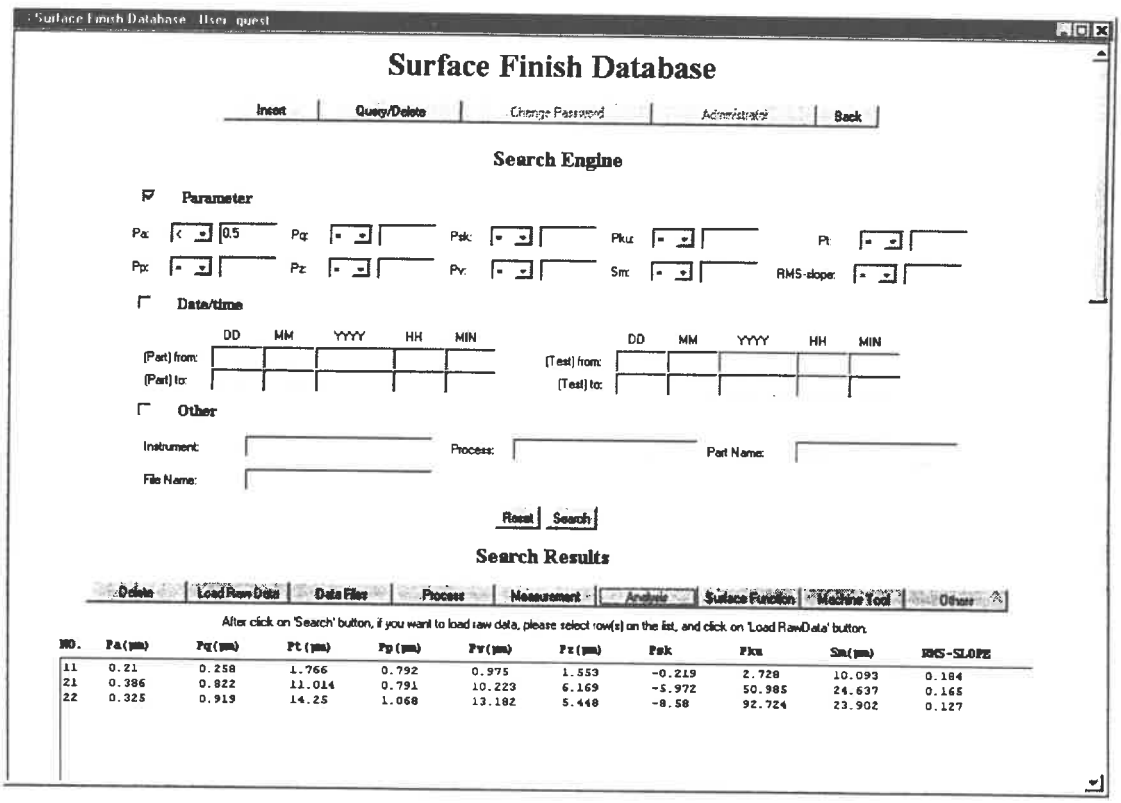

Figure 1.2 The result of a query from the database (P_a<0.5μm)

3.0 Conclusion

Internet based surface texture analysis offers a new way of analyzing surfaces. It offers advanced tools, along with a repository for surface metrology data and process information through a database. This harnesses the power of the computer to collect and store large datasets over a

sufficient time to make a cause and effect analysis between surface finish and function on the one hand and surface finish and the manufacturing process on the other. Using the work done so far as a foundation, a method for remote measurement can be visualized. An instrument in a laboratory/remote factory (location B) can be made as a server, and using web casting techniques, and the available tools on the web a person in location A can *measure and analyze* surfaces in location B and discuss the results with a person in location C. This type of system permits large companies to trouble shoot processes remotely by assembling the appropriate experts. The field testing of the software tools is currently being initiated and the results will be reported in the future.

3.0 References

1. Vijoy Gopalan, "An Internet based surface texture analysis system", Masters thesis, UNC, Charlotte, December 1999.

2. Son H. Bui, "Surface texture information system", Masters thesis, UNC, Charlotte, December 1999.

3. M.C. Malburg, D.G. Chetwynd, J. Raja, "The robust detection and removal of unwanted asperities in applied surface metrology", Intl. J. of machine tools and manufacture, March 01, 1998.

Quantitative Stress-Induced Birefringence Measurements of Large Optics by a Prototype Imaging Polarimeter

P. Douglas Knight[1], Paul R. Wilkins[2]

[1]Department of Mechanical Engineering and Engineering Science
The University of North Carolina at Charlotte
Charlotte, NC 28223

[2]Lawrence Livermore Nat. Laboratory
Livermore, CA 94550

This work was performed under the auspices of the U.S. Department of Energy by Lawrence Livermore National Laboratory under Contract No. W-7405-ENG-48.

UCRL-JC-133700-Abs

1. Introduction

The National Ignition Facility is a next generation inertial confinement laser with approximately 7,000 large optics (0.5 m x 0.5 m) in 192 separate lasers with each beam needing minimal wavefront aberrations to maintain the desired spot size upon the target. Since the laser cavity design uses polarization switches and phase-matched frequency conversion crystals, it is sensitive to polarization aberrations distributed among the 250 large optics in each beam. As the majority of the elements are transmissive elements, (such as amplifier glass slabs, vacuum windows, spatial filters and focal lenses); it is imperative to qualify that each transmissive element does not modify the polarization state of the incident linearly polarized beam. The primary aberration error of a transmissive optical element due to optomechanical mounting is stress induced birefringence, which interacts with the linear polarization state of the laser to create a spatially varying optical path difference (OPD) across the beam. The spatial variance in OPD caused by the stress induced birefringence is seen by a traditional interferometer as wavefront aberration (assuming linearly polarized light), and the small amount of birefringent retardance can also be directly measured using a large aperture imaging polarimeter. It has been proposed to replace the interferometric testing of all transmission elements with polarimetric measurements to both reduce environmental sensitivity and to quantitatively measure the stress-induced birefringent retardance. This paper discusses preliminary results from a prototype imaging polarimeter that can measure the spatially varying retardance of an element placed in a beam of linearly polarized light to less than 1 nm RMS.

2. System Concept

Imaging polarimeters have been developed by various groups for single point and area measurements of polarization states and birefringence in the last few years.[1,2,3] The imaging polarimeter developed to measure NIF optics incorporated a rotating retarder and simulated the linearly polarized input polarization state expected for the laser while detecting spatially varying retardance due to stress induced birefringence. Because the expectation is that the birefringence approaches zero, a Taylor series approximation was made to reduce the involved Mueller matrix intensity solution of the system to a simple sinusoidal phase dependence where retardance was measured using tradition synchronous detection techniques. Taking two measurements with the

initial linear polarization state rotated 45 degrees for the second, the system sensitivity to the fast axis angle of the sample can be determined and eliminated.

The optical layout of the system is shown in Figure 1. Combining quartz halogen and fluorescent tubes inside a light box created a spatially incoherent extended light source. The light passes through a vertical oriented polarizing sheet of Polaroid HN38S before reaching the sample. Following the sample are two converging lens used in a Newtonian telescope configuration to reduce the size of the light beam for one-inch aperture optics. Light baffles are employed between the imaging optics and the large collimation lens to reduce scattered light into the detector. A computer controlled rotation stage rotates a quarter-wave plate placed directly after the small converging lens in the collimated optical path. A final linear analyzer is crossed with respect to the initial polarizer followed by a 10-nm bandwidth interference filter centered at 632.8 nm with a simple lens imaging the sample under test onto a Cohu CCD camera array.

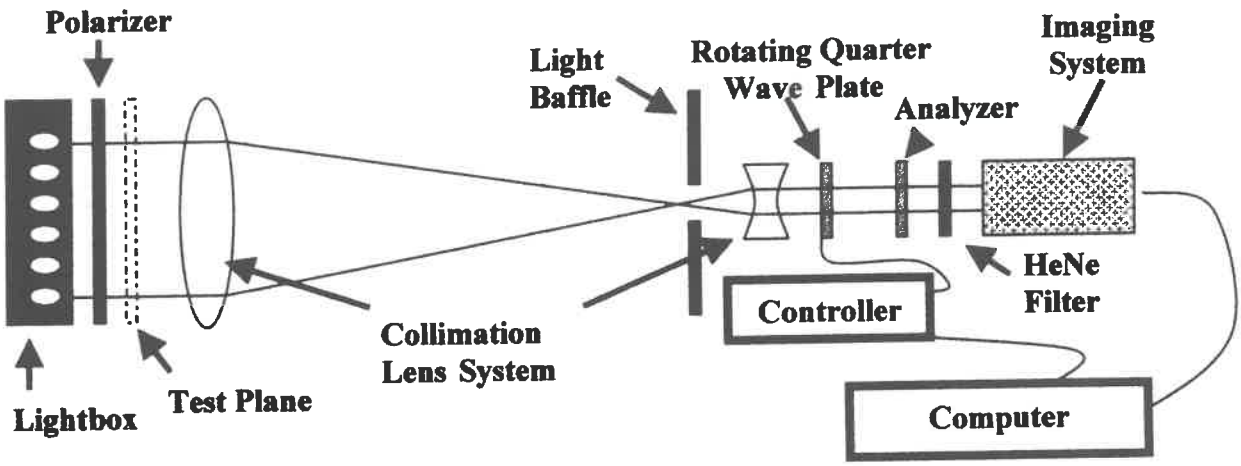

Figure 1: Schematic layout of prototype imaging polarimeter for measuring large optics

The spatial intensity of this polarimeter oscillated as a sinusoidal function repeating with every 90° of revolution of the quarter wave plate. (Equation 4) This angular functional dependence allowed synchronous detection techniques[4,5] to calculate sample retardance very accurately. For this instrument, a simple 4, 12 or 24 step algorithm evenly spaced over one complete period, 90 degrees, of the output intensity is employed. Multiple image frames or integration buckets (15, 30 or 60) are taken to reduce the noise in the measured retardance.

With only a single input polarization state, there is a cosine law sensitivity to fast axis angle for this type of imaging polarimeter. For an input polarization state perpendicular or parallel to the sample fast axis, the sensitivity of the instrument to retardance drops to zero. Likewise, when the sample fast axis angle is ± 45 degrees with respect to the input polarization state, the instrument has a maximum sensitivity. To effectively map sample retardance at all fast axis angles, two measurements are made; one at an initial polarization angle and the second with an input polarization state rotated 45° with respect to the first measurement. The two measurements are then root sum squared for a fast axis insensitive magnitude.

3. Theory

The imaging polarimeter can be represented as a transfer function of the light exiting the lightbox to the light detected by the CCD camera. A Mueller matrix[6] is assigned to each polarization element of the optical system. Upon multiplication, a system transfer function is

obtained as a function of the angle of the quarter wave plate and the angle of the fast axis angle of the sample. From this analysis, the normalized instrument output light intensity is represented as

$$I = 1 - C^2 * (c^2 + s^2 * \beta) - C * S * c * s * (1 - \beta) + S * s * \mu \tag{1}$$

where $C = \cos(2\theta)$ and $S = \sin(2\theta)$ for the quarter-wave plate, $c = \cos(2\varphi)$ and $s = \sin(2\varphi)$ for the sample, $\beta = \cos(\delta)$ and $\mu = \sin(\delta)$ for retardance of the sample, θ is the angle of the quarter wave plate with respect to the polarizer, φ is the fast axis angle of the sample, δ is the sample retardance, and unit input intensity was assumed. For small retardance, using a Taylor series expansion, setting $\sin(2\varphi)=1$, and grouping like terms, Equation 1 reduces to

$$I = (\frac{1}{2})\cos(4\theta + \delta) \tag{2}$$

which is the basic form for using synchronous detection phase-shifting techniques to find δ.

4. Experimental Results

Retardance images from the prototype imaging polarimeter are shown in Figures 2 and 3. Referring to Figure 2, plastic safety glasses were placed in the object plane of the instrument and the phase retardance due to internal stress in the plastic is illustrated. Figure 3 shows a NIF sized vacuum window optic approximately one-inch thick demonstrating stress induced birefringence due to a compressive point stress field. This image reflects a single measurement using linearly polarized light and demonstrates the variable sensitivity of the instrument due to fast axis angle of the test sample. The magnitude of the retardance due to stress induced birefringence matches that found using interferometric techniques to measured this same effect.[7] The noise floor of the full aperture empty cavity is measured as 0.33 nm RMS retardance. Circular streaks in this image indicate the noise floor may be limited to the tolerance of the quarter wave plate, quoted as $\lambda/350$ by the vendor. Difference measurements were taken between two successive retardance maps using differing numbers of phase steps and integration buckets to estimate its effect on repeatability of the imaging polarimeter. A standard of 12 steps, 60 integrating buckets was chosen with the RMS retardance across the full aperture was measured as 1.0 nm. The retardance phase maps were analyzed within Wyko image processing software.

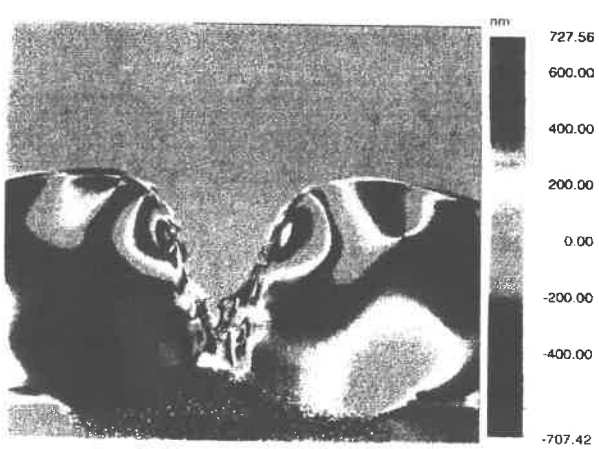

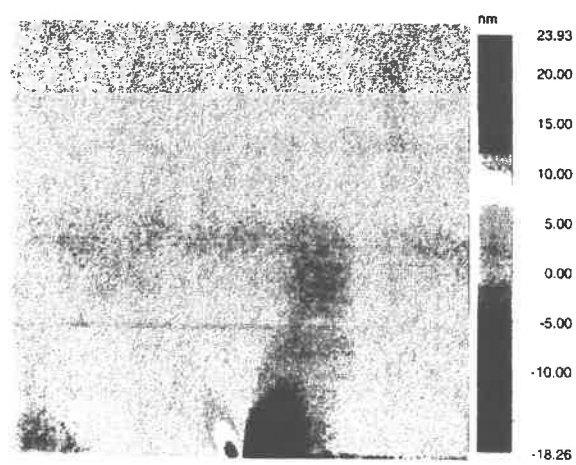

Figure 2: Retardance map of plastic safety glasses measured by imaging polarimeter
Figure 3: Retardance map of test window resulting from a point stress field

Error sources for this imaging polarimeter draw from both classical polarimeters and phase shifting interferometry algorithms. Systematic polarization dependent errors include those associated with a finite extinction of orthogonal polarization states for the polarizer and analyzer, spatially varying retardance of the quarter wave plate and mean retardance of the quarter wave plate varying from 90 degrees. Other sources of error are sample retardance so large that the small angle approximation resulted in analysis errors of the retardance phase maps and use of a finite bandwidth instead of monochromatic light for illumination. Possible element alignment errors happen when the transmitted light may not have been normal to the quarter wave plate. At very low stress backgrounds in the current system, there is some residually birefringent retardance of each system optical element that interacts with the sample polarization state. Errors associated with phase shifting interferometry algorithms include quantization effects due to sampling the retardance phase map with a digital CCD camera array, phase shifting errors from inexact rotation of the rotary stage and electronic and photon shot noise. Other error sources include time varying intensity fluctuations of the extended polarization source, residual scatter from individual optics, and thermal effects that contributed asynchronous errors into the system.

V. Conclusions

A prototype imaging polarimeter is developed that measured retardance due to stress induced birefringence of large optics. A synchronous detection scheme is utilized in the measurement of retardance. The instrument has a variable sensitivity due to fast axis angle of the sample being tested which is remedied by making two measurements with a linear input polarization state that rotated 45 degrees. This polarimetric technique is inherently less sensitive to environmental noise than interferometric techniques to measure stress induced birefringence and is able to measure residual retardance of assembled large optics within the tolerance required by the National Ignition Facility project

References

1. D. H. Goldstein, " Mueller Matrix Dual Rotating Retarder Polarimeter," *Appl. Opt.*, **31**, 6676-6683 (1992).
2. J. L. Pezzaniti and R. A. Chipman, "Mueller Matrix Imaging Polarimetry," *Opt. Eng.*, **34**, 1558-1568 (1995).
3. P. A. Williams, A. H. Rose, and C. M. Wang, "Rotating –Polarizer Polarimeter for Accurate Retardance Measurement," *Appl. Opt.*, **36**, 6466-6472 (1997).
4. J. H. Bruning, D. R. Herriott, J. E. Gallagher, D. P. Rosenfeld, A. D. White, and D. J. Brangaccio, "Digital Wavefront Measuring Interferometer for Testing Optical Surfaces and Lenses," *Appl. Opt.* **13**, 2693 (1974).
5. C. J. Morgan, "Least-Squares Estimation in Phase-Measurement Interferometry," *Opt. Lett.*, **7**, 368-370 (1982).
6. A Gerrard and J. Burch, *Matrix Methods in Optics*, Dover Publications, New York, New York (1975).
7. C. Ai and J. C. Wyant, "Testing Stress Birefringence of an Optical Window," *Proc SPIE* **1531**, 165-172 (1991).

OPTICAL MEASUREMENT OF COP DEFECTS ON SILICON WAFER SURFACE BY LASER SCATTERED DEFECT PATTERN

Satoru Takahashi[1], Takashi Miyoshi[1], Yasuhiro Takaya[1], and Kenji Shirai[2]
1 Department of Mechanical Engineering and Systems, Osaka University
2-1, Yamadaoka, Suita, Osaka 565-0871, Japan
2 Department of Computer Science, Nihon University
1, Nakagawara, Tokusada, Tamura-machi, Koriyama 963, Japan

Abstract: This paper presents new optical measurement method for evaluating the defects on a silicon wafer surface quantitatively by detecting the intensity distribution, " laser scattered defect pattern (LSDP)[1]", corresponding to the superposition of scattered light from a defect and reflected light from a surface. In order to verify a feasibility to detect "crystal originated particles (COPs)[2]" and to discriminate them from particulate contaminations, the basic experiments were carried out for the silicon wafer surface with COPs identified by making the use of Atomic Force Microscope (AFM). Then, it was found that COPs with the size of sub-micro meter scale were able to be detected as LSDPs and suggested that our proposed method had a feasibility of discrimination between COPs and particulate contaminations by measuring the contrast of LSDP.

Key words: laser applied measurement, surface inspection, silicon wafer, surface defects, COP

1. INTRODUCTION

In modern semiconductor technology, the reduction of the density of silicon wafer surface defects that may decrease device yield has become an important issue. And in order to fabricate the semiconductor device with high reliability, it is necessary to measure directly them during processing and control the fabrication process.

"Crystal originated particle (COP)" is one of the various silicon wafer surface defects. COPs have not been recognized as a kind of particulate contaminations but as a kind of pits caused by the etching effect of the Standard Cleaning 1 (SC1) solution of the RCA cleaning process. Their basic micro structure is thought to be octahedral shape with the size of sub-micro meter scale as shown in Fig. 1. It is very important to detect COPs and to discriminate them from particulate contaminations, because COPs have a different characteristics from particulate contaminations and will extensively decrease device yield for next ULSI generation. So far light scattering method[3)~5)] has been conventionally used to inspect the silicon wafer surface defects in the fabrication process. But this method gives only a few information on the intensity of light scattered by the defects, so it is difficult to discriminate between COPs and particulate contaminations. Therefore, the purpose of this study is to develop a new optical measurement method which can not only detect but discriminate the COP defects with the size of sub-micrometer scale. Fig. 2 shows a schematic diagram of the principle of our proposed method. A converged beam by an objective has a beam waist in the focal length of the objective. Then the beam is incident on a polished silicon wafer surface, which is placed at some distance (defocal length) away from the focal point of the objective. If there is a defect like a COP, scattered light by the defect as well as reflected light from the silicon wafer surface occurs. By detecting the intensity distribution, " laser scattered defect pattern (LSDP) ", corresponding to the superposition of the scattered light and the reflected light, we evaluate the defect quantitatively. LSDP is the scattered light intensity pattern which has much information about the defects, so this method has the possibility of discrimination between defects

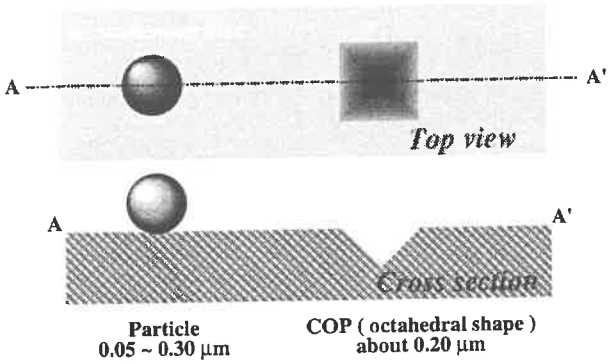

Fig. 1 Comparison of COPs with particulate contaminations

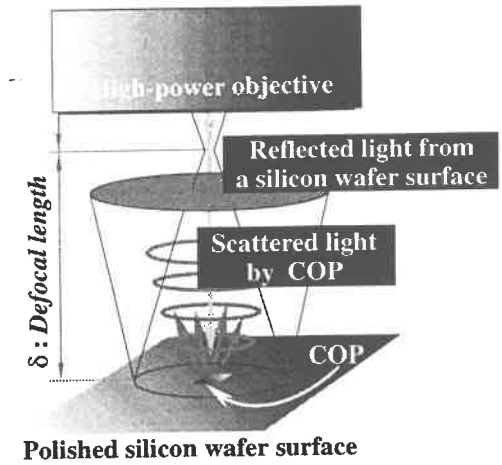

Fig. 2 Principle of measurement

as well as defects detection.

2. EXPERIMENTAL TECHNIQUES

The apparatus developed for this purpose, which is based on the principle of measurement mentioned above, is shown schematically in Fig. 3. To avoid particulate contamination of the test surfaces, the optical system is housed inside a clean enclosure of class 10. An Ar^+ laser of wavelength 488.0nm is used as the light source. After passing through the single-mode optical fiber (mode field diameter = 4.0μm), the beam is collimated and polarized. Using a high-power objective (with the numerical aperture of 0.95), the incident beam is converged on the surface of silicon wafer. The silicon wafer is fixed to a computer controlled XY-fine positioning unit with stepping motor for moving and scanning the silicon wafer relative to the laser beam. The smallest possible step is given by 0.5μm in both directions. The objective is mounted on the piezo actuator and can be moved over a range of 100μm with a resolution of 0.1μm in axial direction. The beam power was monitored with a power meter at the position shown in Fig. 3, to which all detected data were normalized. A pair of lenses is used to observe the LSDP corresponding to a Fourier transform image of reflected light from the silicon wafer surface in the exit pupil of the objective. The irradiance distribution detected by the CCD area sensor consisting of 510 (H) × 492 (V) pixels and 12.9μm

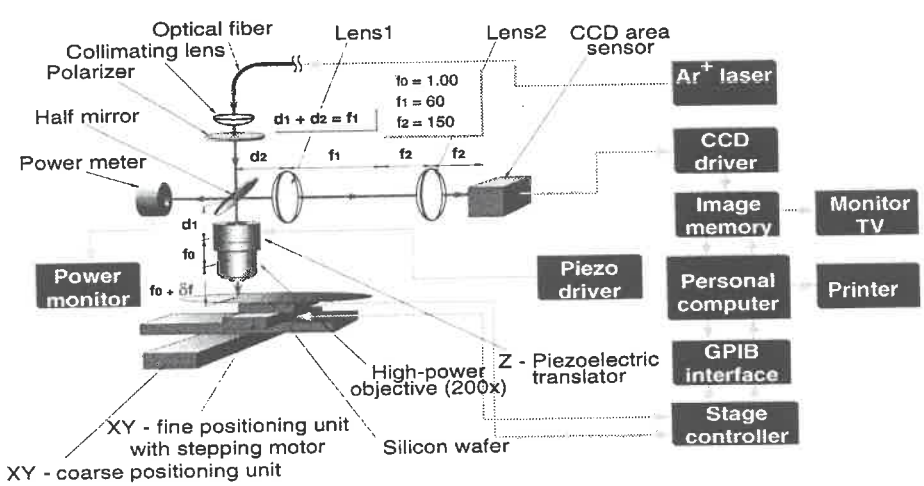

Fig. 3 Schematic diagram of silicon wafer surface defects measurement system

(H) × 17.9μm (V) pixels size is converged to 8bit digital image data and stored in the image memory. These data are dealt with by a personal computer with auxiliary memory.

3. EXPERIMENTAL RESULTS

3.1 Basic experiment for detecting COPs as LSDPs

First, the basic experiments for detecting COPs as LSDPs were carried out. In order to identify the COPs, the anodic oxide layer was made as a maker in the contact mode of the AFM[6]. By means of transforming the coordinate system between AFM and proposed optical system, the beam can easily illuminate the position of the COPs. The defocal length was adjusted to 5μm. The spot diameter on the surface of silicon wafer was about 15μm. Fig. 4 shows the procedure for getting LSDPs. A pattern (a) is an irradiance distribution obtained from the identical COP observed by AFM, a pattern (b) is an irradiance distribution obtained from a surface without any defects, and a pattern (c) is obtained by subtracting the irradiance distribution (b) form the irradiance distribution (a). We call pattern(a) "LSDP before subtracting process" and pattern(c) "LSDP after subtracting process", respectively. Fig. 5 shows the typical results obtained by detecting a COP. Figure (a) is an AFM image of a COPs (the right hand side means the schematic AFM image) and pattern (b) is the LSDP after subtracting process of the identical COP (a)(the right hand side means 3-D display of the irradiance distribution of LSDP). From this result, it is clear that COPs with the size of sub-micro meter scale were able to be detected as LSDPs.

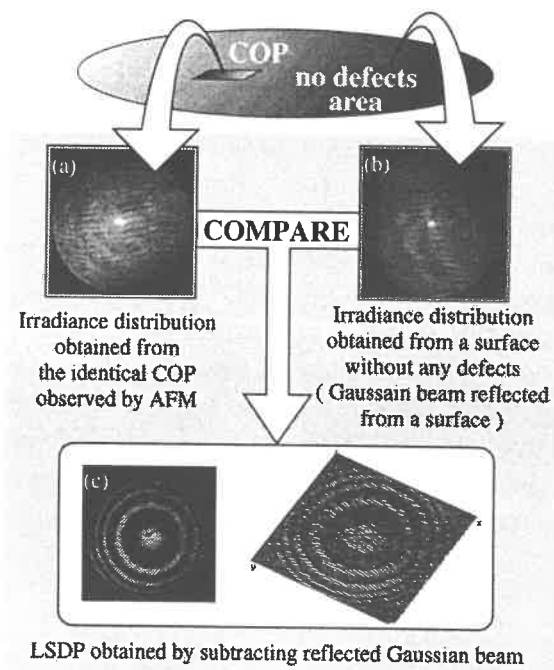

Fig. 4 Procedure for getting LSDPs after subtracting process

3.2 Discrimination between COPs and particles

Second, for the purpose of discriminating COPs from particulate contaminations, the characteristics of LSDPs were analyzed by comparing LSDPs of COPs with ones of the standard polystyrene particles. In this experiment, 0.21μm particles were employed, whose size is similar to the typical COPs. Fig. 6 shows the typical results obtained by detecting the 0.21μm particles. Figure (a) is a SEM photograph and pattern (b) is the LSDP after subtracting process of the identical particle (a) (the right hand side means 3-D display of the irradiance distribution of LSDP).

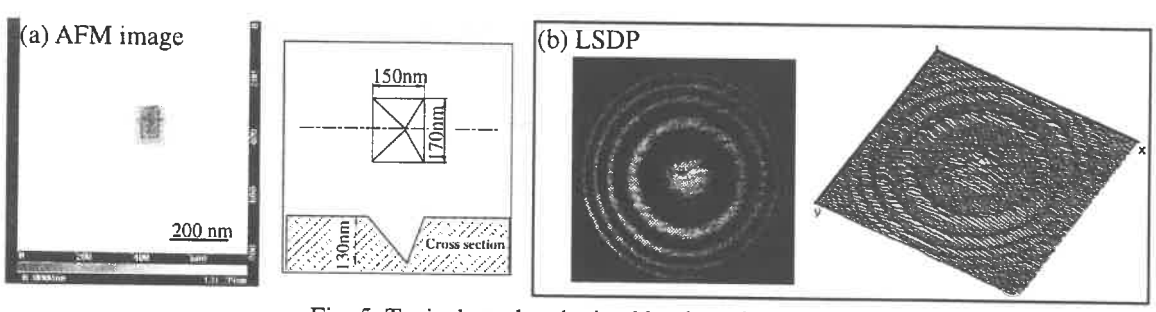

Fig. 5 Typical results obtained by detecting COPs

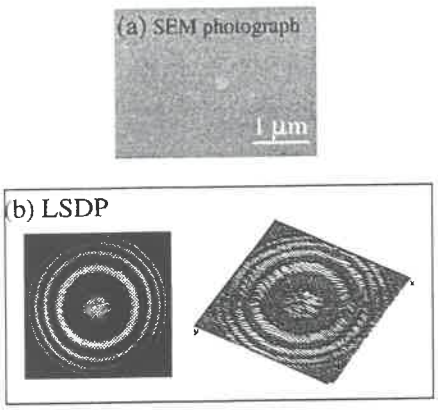

Fig. 6 Typical results obtained by detecting standard particles (0.21μm)

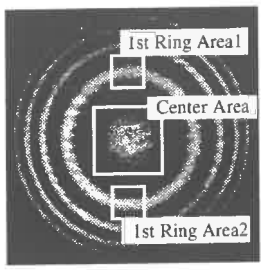

B_{ca} : average brightness at Center Area
B_{ra1} : average brightness at 1st Ring Area1
B_{ra2} : average brightness at 1st Ring Area2
Pattern contrast C is defined as

$$C = \frac{B_{ca}}{\left(B_{ra1} + B_{ra2}\right)/2}$$

Fig. 7 Definition of pattern contrast C

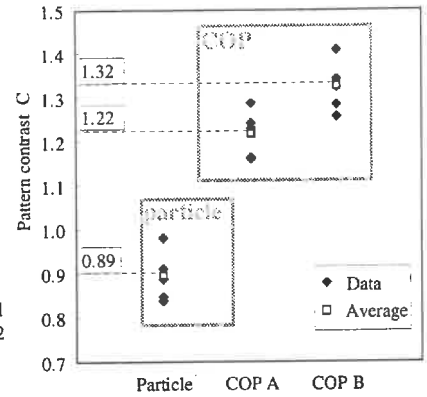

Fig. 8 Pattern contrast C of standard particles (0.21μm) and COPs

By comparing the Fig. 6 with Fig. 5, LSDPs are seen to form concentric circles like Airy disk in both cases. Next, the characteristics of LSDPs were analyzed, that is, the pattern contrast C is defined as

$$C = \frac{B_{ca}}{\left(B_{ra1} + B_{ra2}\right)/2} \tag{1}$$

in which B_{ca} , B_{ra1}, and B_{ra2} are average brightness at the center area, the 1st ring area1, and the 1st ring area2 as shown in Fig. 7, respectively. Fig. 8 shows the pattern contrast C of 0.21μm particles and COPs. From this figure, it is found that COPs were clearly distinguished from 0.21μm particles by measuring the pattern contrast C of LSDPs.

4. CONCLUSIONS

In order to verify a feasibility to detect COPs and to discriminate them from particulate contaminations, the basic experiments were carried. The results obtained in this paper are summarized as follows;

1. It can be seen that COPs with the size of sub-micro meter scale were able to be detected clearly as the laser scattered defect pattern.
2. It was suggested that our proposed method had a feasibility of discrimination between COPs and particulate contaminations by measuring the contrast of LSDPs.

ACKNOWLEDGMENTS

The authors gratefully acknowledge the support of Sumitomo Metal Industries, Ltd., especially in supplying the silicon wafer and the AFM data required for identification of COPs.

REFERENCES

1) S. Takahashi, T. Miyoshi, Y. Takaya, and K. Saito: Annals of the CIRP, **47**/1(1998)459.
2) J. Ryuta, E. Morita, T. Tanaka, and Y. Shimanuki: Jpn. J. Appl. Phys., **29**/11(1990)1947.
3) B. R. Locke and R. P. Donovan: J. Electronchem. Soc., **134**/7(1987)1763.
4) Thomas A. Germer: Appl. Opt., **36**/33(1997)8798.
5) Yu. Eremin and N. Orlov: Appl. Opt., **35**/33(1996)6599.
6) Y. Yanase, T. Ono, T. Kitamura, H. Horie, T. Ochiai, S. Okamoto, and H. Tsuya: Jpn. J. Appl. Phys., **36**/10(1997)6200.

A Scanning Phase-Knife Technique for Quantitative Surface Slope Measurements and Defect Identification

Paul R. Wilkins[1], P. Douglas Knight[2], David C. Pigg[1]

[1]Lawrence Livermore National Laboratory, Livermore, CA

[2]Department of Mechanical Engineering and Engineering Science
University of North Carolina at Charlotte, Charlotte, NC

1. Introduction

One of the earliest techniques for evaluating the quality of an optical surface is the Focault knife-edge test, a qualitative means to map the local slope of an optical surface along a particular axis[1]. A Focault knife-edge involves projecting a point source onto or through an optic, translating a one dimensional opaque edge across a returning convergent ray bundle that expands past focus and is imaged onto a detector array or film plane. Light ray bundles obscured by the translation of the knife edge exhibit a smooth change in intensity from maximum light levels to minimum light levels across the optic pupil as a function of local surface slope. The smooth decrease is controlled by the diffraction of light, depending on the aperture and the test wavelength. More recently, the advent of digital imaging arrays has allowed the extension of this technique to quantify the specific surface slope of an optic or optical system[2,3]. In the digital versions of the Focault test, the 50 percent decrease point in the illumination curve was selected to denote surfaces with the transverse slope deviation that match the position of the knife-edge. Limitations in the classic Focault test arise from the point source, which is usually an extended source larger than the diffraction limit of the collimator or optic and the use of an asymmetric signal such as the falling intensity edge to denote the transverse ray aberrations. The advantage of slope measurement systems is that they directly measure surface slope and are less sensitive to changes in the overall path length and vibration than an interferometer. Disadvantages include the requirement of calibration and numerical integration of the slope measurement to calculate the surface profile. Recent work concerning numerically integrated surface slopes has been found to closely match results obtained with an interferometer in previous work on the classic knife-edge[3]. Investigation of alternate wavefront measurement techniques as applied to Inertial Confinement Fusion laser mirror assemblies prompted revisiting this concept with two improvements: a 'quasi-perfect' spherical point source from a single-mode fiber and a switch to a half-wave phase-knife to provide a symmetric fringe function for improved signal processing. The encouraging results from this concept found even greater relevance in the inspection of magnetic media substrates or platters.

2. Application

Magnetic media platters are precision, polished disks produced at a rate measured in the tens of millions per month. The magnetic platters used in the highest density disk drives manufactured today require extremely flat and smooth surfaces for the air-bearing read/write heads to fly at the proper uniform height to maintain data integrity. In the last two years, the flying heights of these heads have dropped from above 1 microinch down to a current height of 0.7 microinches (18 nm). The crucial height requirement is the head distance above the sputtered magnetic layer, which has an additional overcoat layer of diamond-like carbon 8 nm thick. This leaves a total flying height spacing of 26 nm above the magnetic layer that must be maintained to within ± 6 nm for reliable data storage/retrieval. The integral air-bearing built into the read/write head surface allows the head to follow the surface for moderate departures from flatness. No longer is absolute flatness of the disk as critical, but instead both the tangential curvature and radial curvature have close tolerances; curvature measurement being well suited for the scanning phase knife.

The most commonly used substrate is a high tensile strength aluminum alloy that is polished and then nickel plated prior to sputtering the magnetic layer. The flatness of the media substrate is controlled in the polishing of the aluminum disk on large double-sided polishing tools that polish many parts in parallel. A common defect that now prevents certain substrates from being utilized at these high storage densities is the substrate polishing process. Small nodules of different alloy phases are present in the aluminum substrate, and this material polishes at a slightly differential rate from the bulk material. This differential removal rate results in the creation of small diameter (grain size < 1 mm), very shallow pits ranging from 3 to 12 nm deep. These pits are only a few hundred microns across and the air-bearing head will not track over any defect smaller than 1 mm while maintaining proper height. The read/write signal drops below threshold where the head glides over the small

diameter pits. Defects deep enough to cause a problem (> 5 nm) cannot be easily seen on commercial interferometers that are marketed to this industry. These pits are at the extreme limits of height resolution for the interferometers and the pit diameters are at the spatial resolution limit of these systems. However, the small diameters of the critical defect pits are such that the slope of the pit surface has a mean distribution of 10 to 20 microradians, well within reasonable detection by digital slope measurement. There is a need in this industry to simultaneously measure the disk curvatures that determine head tracking performance as well as identify defects that disqualify platter substrates. Currently, because of the sensitivity, vendors use old schlieren systems to inspect for these defects in a qualitative evaluation in place of an interferometer.

3. System Concept

The optical layout of the system is shown in Figure 1. The point source used for this prototype is a single mode fiber coupled to a 635 nm laser diode with an exit aperture of 3.5 microns from the fiber, well below the diffraction limit of the collimation lens. The diffraction of the light from this small aperture will theoretically describe almost a perfect spherical wave (within half a nanometer), and this has been shown by phase shifting interferometry[4]. The numerical aperture of the spherical light exiting the fiber overfills the 100 mm input aperture of the 780 mm focal length lens, providing uniform illumination of the media platter. The light expanding from the fiber passes through a 50 percent reflecting nitrocellulose pellicle oriented at 45 degrees prior to reaching the aplanatic doublet lens and disk. After reflecting from the 95 mm diameter disk surface, the return beam reflects off the pellicle and is transmitted through a phase knife at the conjugate focal plane. The phase knife is designed with two orthogonal edges, each at 45 degrees to the direction of travel to allow both X and Y axis cuts with a single translation stage. After the beam expands beyond the phase knife, the disk surface is relay imaged by a lens onto a Sony CCD camera array and digitized for each phase knife position. The phase knife is translated at the Fourier plane of the disk image and transverse ray aberrations calculated from the position of the symmetric signal peak in the same manner as described in reference 2 and 3. No vibration isolation or thermal control was used on the system.

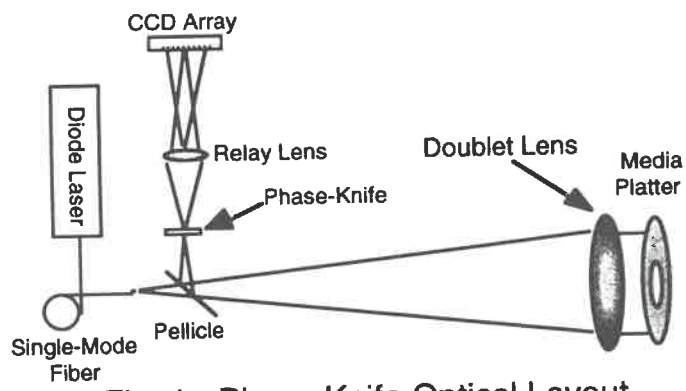

Fig. 1 - Phase Knife Optical Layout

4. Theory

The point source provided by the single-mode fiber expands to fill a 100 mm aperture of an aplanatic doublet to create a collimated wavefront at 635 nm. The plane wavefront then reflects from the surface of the media platter with twice the surface slope errors and is back collimated through the doublet to a conjugate point source in the plane of the half-wave phase step for $\lambda = 635$ nm. The interaction of the half-wave phase step with the surface slope of the disk is a simple convolution in the Fourier plane that is governed by diffraction theory. The distance of the conjugate image formed from the phase-knife and the numerical apertures involved allow for the quadratic Fresnel diffraction approximation to be used. A traditional knife edge yields an intensity decrease as a function of knife-edge position in the classic Fresnel edge diffraction equation. Prior digital knife-edge instruments selected the 50% intensity reduction point as the transverse ray aberration threshold where the relative position of the knife-edge for each point in the pupil provided a map of the corresponding slope of the surface[3].

For this prototype system, the knife-edge is replaced by a phase-knife that is mathematically represented as a coherent superposition of two Fresnel edge diffraction functions in reverse directions with a phase shift of 180 degrees between the two patterns[5]. The resulting intensity pattern is the magnitude of these two Fresnel functions and the interference at the phase step creates a symmetric oscillatory function with a central 'dark' fringe. Figure 2a and Figure 2b compare intensity patterns for both the classic opaque-knife edge and the phase-knife with the central null fringe. The intensity pattern for the phase-knife function is represented below in terms of the Fresnel sine and cosine integrals' as[6]:

$$I(\xi) = I_0\left\{[C(\beta\xi) - C(-\beta\xi)]^2 + [S(\beta\xi) - S(-\beta\xi)]^2\right\} \therefore \beta = \frac{\pi D}{\lambda f} \therefore S(x) = \int_0^x \sin\frac{\pi}{2}t^2 dt \therefore C(x) = \int_0^x \cos\frac{\pi}{2}t^2 dt$$

with D the system aperture (100 mm) and f the doublet lens focal length. The phase-knife intensity pattern is quite similar to an enveloped cosine function similar to a 'coherence envelope' with the difference that slope is measured instead of OPD. The symmetric central null 'dark' fringe provides a negative peak whose exact center is determined using a least-likelihood estimator algorithm. For a 100:1 signal-to-noise obtained on the camera array, the 1-sigma tolerance of the peak locations is approximately 1/250th the full width half maximum (FWHM) of the null fringe. Calculating the aperture diameter and wavelength into the Fourier plane the FWHM of the dark fringe angular width is approximated as an airy disk around 6 microradians wide. The tolerance in determining the peak of this fringe is about 1/250th this value and in practice is limited by the thermal turbulence of the air and vibration.

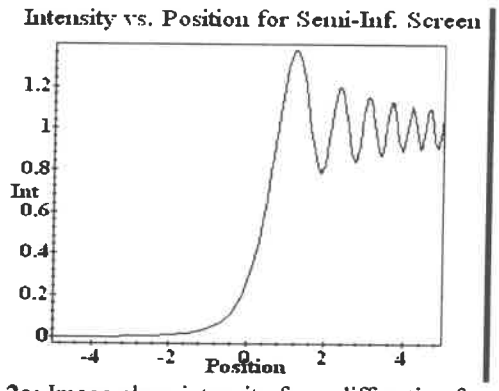

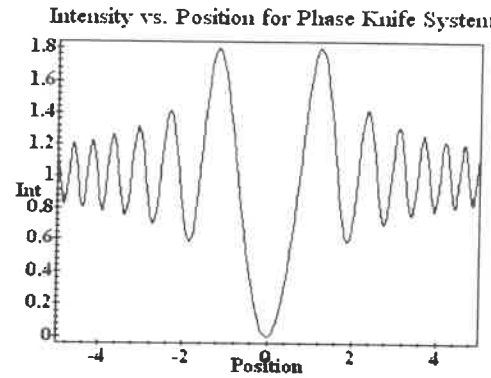

Figure 2a: Image plane intensity from diffraction from an opaque knife edge
Figure 2b: Image plane intensity from diffraction replacing opaque knife edge with 180° retardance phase knife

5. Experimental Results

Figure 3 is a measurement of an aberrated, reflective optic that possessed 0.3 waves P-V (0.078 waves RMS) of astigmatism to demonstrate the slope resolution of the instrument. The phase knife was scanned for a total excursion of 12 microns and the null fringe data converted to surface slope. This small change in flatness is quite evident in the graph and matches the slope data measurements by a Zygo Mark IV. The fine resolution of the slope data plotted at a contour interval of 50 nanoradians shows minimal noise. A repeatability measurement is also included to demonstrate the slope noise floor of the instrument with a λ/20 flat placed into the sample plane. Figures 4 and 5 show two empty cavity data sets taken at separate slope resolutions; the first plotted at 10 nanoradians per contour and the second at 5 nanoradians per contour line. A small amount of coma is visible in the slope data image indicating that the alignment of the lens axis to the fiber is not optimized for the flattest instrument background slope. In use, a flat is used to calibrate this background slope for later subtraction.

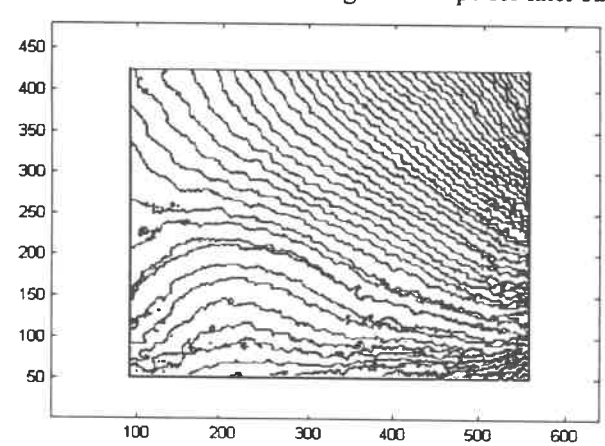

Figure 3 - Slope Data of Astigmatic Optic (Contour interval ~ 50 nanoradians)

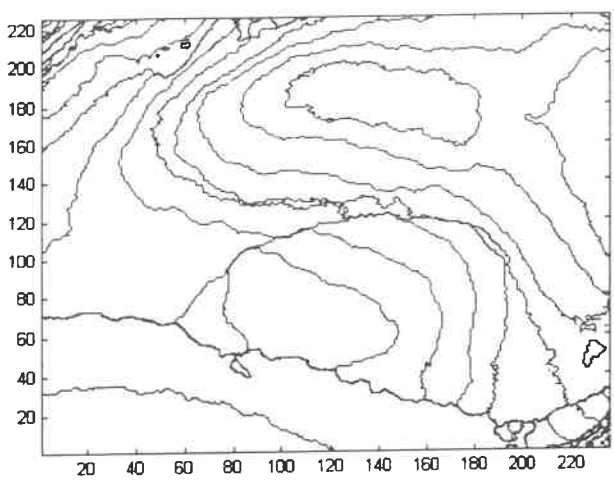

Figure 4 - First empty cavity data set
(Contour interval ~ 10 nanoradians)

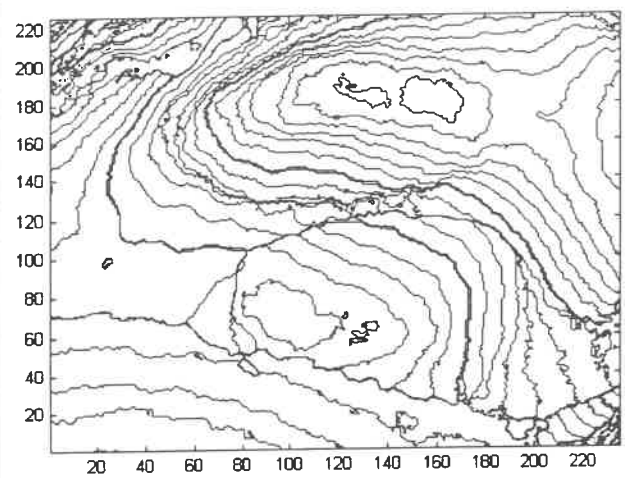

Figure 5 - Second empty cavity data set
(Contour interval ~ 5 nanoradians)

6. Conclusions

A prototype scanning phase knife measures surface slope of deformed optics or magnetic media substrates by digitally analyzing the recorded image of a surface as a 180 degree retardance phase step is scanned across the Fourier plane of the surface image. The high sensitivity of the scanning phase knife to local surface slope identified extremely shallow pits of limited extent not normally visible in an interferometer. The instrument is ideally suited for critical disk curvature metrology for head tracking performance along with determining overall surface flatness. The phase-knife slope measurement technique is less sensitive to environmental vibration and thermal issues than interferometry and can also identify detects not detected with conventional phase shifting interferometry. Additional data will be presented showing measurements of magnetic media disk flatness and defects along with a discussion of specific slope measurement applications.

7. References

1. D. Malacara, *Optical Shop Testing*, Wiley, pp. 231-246, New York (1978).
2. E. Granger, "Wavefront Measurements From a Knife Edge Test," *Proc. SPIE* **429**, 174-177 (1983).
3. D. E. Vandenberg, W. D. Humbel, and A. Wertheimer, "Quantitative Evaluation of optical surfaces by means of an improved Focault test approach," *Opt. Eng.*, **32**, 1951-1954 (1993).
4. G.E. Sommargren, "Phase Shifting Diffraction Interferometry for Measuring Extreme Ultraviolet Optics," *OSA Topics on Extreme Ultraviolet Lithography*, G. Kubiak and D. Kaniam eds., **4**, p. 108, OSA Washington, DC, (1996).
5. A. Kastler, "Un Systeme de Franges de Diffraction a Grand Constraste," *Revue D'Optique.*, **26(6)** , 306-314 (1950).
6. H. D. Betz, "Interferenzen von Laserlicht und ihre Anwendung bei Präzisionsjustierungen", Institut Für Angewandte Physik, UNILAC Report No. 2-67, Universität Heidelberg, Heidelberg, Germany (1967).

This work was performed under the auspices of the U.S. Department of Energy by Lawrence Livermore National Laboratory under Contract No. W-7405-ENG-48.

UCRL-JC-133726 Abs

THE THREE-DIMENSIONAL SURFACE TOPOGRAPHIC CHARACTERISATION OF CONVENTIONAL AND SUPERABRASIVE GRINDING WHEELS

David L. Butler[1], John A. Webster[2], Liam A. Blunt[3], and Ken J. Stout[3]

[1] School of Mechanical and Production Engineering, Nanyang Technology University, Singapore

[2] Unicorn International, United Kingdom (formerly University of Connecticut, Storrs, CT, USA)

[3] Faculty of Engineering, University of Huddersfield, United Kingdom

Introduction

The final surface topography of a grinding wheel is determined by the particular trueing and dressing conditions it is subjected to; although it is the dressing operation which imparts the fine scale surface features to the grinding wheel. The actual topography arises from the process of grit fracture and/ or bond fracture. The wheel topography and the grinding parameters affect the kinematic interactions between the abrasive grains and the workpiece. The wheel topography and the conditions under which it is prepared have a profound influence upon the grinding performance as evidenced by the grinding forces, power consumption, cutting zone temperatures and surface finish of the components. Clearly a detailed understanding of the nature of the surface of the grinding wheel would enable improved control of the grinding process in general.

The work presented in this paper is part of ongoing research aimed at comprehensively characterising the grinding wheel topography. Parametric analysis is provided by the three-dimensional characterisation suite developed at the University of Birmingham and by additional bearing area parameters more recently developed at the University of Huddersfield.

For the purpose of this paper only the density of summits parameter S_{ds}, which is analogous to G_{Astat} (the number of active static cutting grains), will be presented and discussed. A number of conventional and super abrasive wheels were subjected to different machining conditions after dressing. The wheel topography was measured using a 3-D contact instrument both after dressing and at the end of the test.

Wheel Characterisation

The cutting edges of a grinding wheel are geometrically undefined in location and shape. As a result, generalisations or estimations are difficult to make with any degree of accuracy. Thus it has been necessary to develop a number of techniques for examining the wheel topography in order to ascertain quantitative measurements of cutting edges. The techniques employed have included scanning electron microscopy, acoustic emission, thermocouples, and thin blade coupons, a review of the different methods has been carried out by CIRP [1].

In order to differentiate between the total number of cutting edges (static) and those that actually do the work (dynamic), Verkerk *et al* [1] proposed a number of parameters. In addition, it was

suggested that on one grain there is often more than one cutting edge so it is necessary to differentiate between the grains and cutting edges. Finally, in order to separate the 2-D measurement (linear) from the aerial (3D) the report recommended the use of subscripts *L* and *A* for linear and aerial respectively. *Table 1* lists the complete parameter set.

	Cutting Edges			Cutting Grains		
Linear (1/mm)	C_{Lstat}	C_{Ldvn}	C_{Lkin}	G_{Lstat}	G_{Ldvn}	G_{Lkin}
Aerial (1/mm^2)	C_{Astat}	C_{Advn}	C_{Akin}	G_{Astat}	G_{Advn}	G_{Akin}

Table 1. Parameters for designation of grinding wheel topography

Machining Conditions

A number of machining tests were carried out on a surface grinding machine using conventional aluminium oxide wheels, *table 2* summarises the conditions.

Wheel	Code	Dresser feed rate (s_d) mm/rev	Nominal downfeed (a) microns	Number of passes
1	A60I8V	0.05	25	200
2	A60K5V	0.05	25	200
3	A60H8V	0.05	25	125

Table 2. Summary of machining conditions

In addition, an electroplated CBN wheel was also used which had been subjected to extensive grinding tests on Inconel 718 (the actual machining conditions are not relevant to this research) was also analysed.

Measurement Strategy

A three-dimensional profilometry technique first proposed for grinding wheel measurement by Blunt and Ebdon [2] was employed. The measurement sampling strategy was based on the need to pass over each grain at least three times in order for the algorithm to register a summit. For conventional wheels the average grain size (d_g) is obtained by employing the formula suggested by Malkin [3].

$$d_g(mm) = 28 * M^{-1.1} \qquad \textit{Equation 1}$$

where *M* is the grit number of the wheel.

The optimum sample spacing (SS_{opt}) is achieved by employing the constraints given in *equation 2*.

$$\frac{d_g}{4} \leq SS_{opt} \leq \frac{d_g}{3} \qquad \textit{Equation 2}$$

By employing *equations 1* and *2* an optimum sample spacing for the conventional wheels of approximately 78 microns was chosen with a measurement area of 2mm by 2mm. For the superabrasive wheels a grit size of approximately 60 microns was used which resulted in an optimum sample spacing of 20 microns and a measurement area of 2mm by 2mm.

Analysis

Using the measurement conditions previously stated, each wheel was measured a number of times and analysed in terms of cutting grain density (c.g.d). For this analysis a cutting grain was defined as a peak on the three-dimensional map which protruded above a specified penetration level. The number of cutting grains was then analysed in terms of radial depth of penetration. This was achieved by truncating the surface map and counting the number of peaks intersecting the plane of truncation. A peak is defined, by convention, as a point in the data array which is higher than its eight nearest neighbours. The three-dimensional parameter S_{ds} [4] is indicative of the number of such peaks per mm^2 and can be used as a cumulative peak count. The values of G_{Astat} are related to the density of summits in such a way that G_{Astat} indicates the number of grains with the optimal sample spacing and therefore it can be assumed that $G_{Astat} = S_{ds}$.

Results

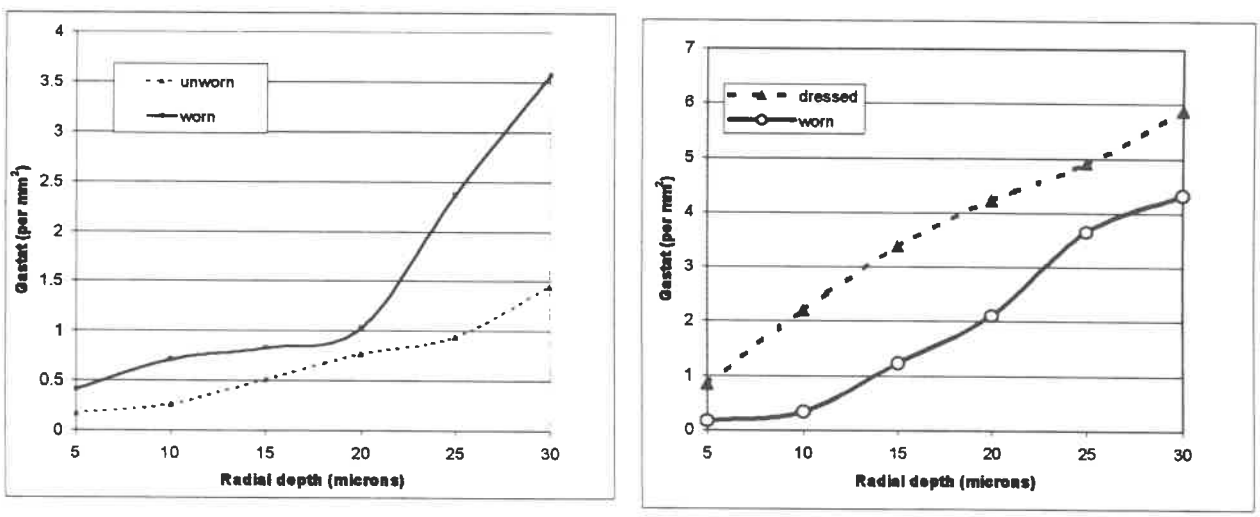

a) b)

Figure 1. Graphs showing the variation in G_{Astat} against the radial depth of penetration for a) CBN and b) conventional wheels

Discussion

Both graphs (*figures 1a* and *1b*) show a general trend of the c.g.d increasing as the radial depth of truncation increases. This is because as the truncation depth increases, more grains are exposed, thus the c.g.d increases. For the CBN wheels the G_{Astat} (*figure 1a*) is much lower for the unworn conditions (as would be expected) than for the worn wheel due to the reasons discussed in the following paragraph and illustrated in *figure 2a* and *2b*. For conventional wheels the results show (*figure 1b*) that the dressed wheels have a higher c.g.d than the worn wheels. This can be attributed to the wheel becoming dull with wear flats forming on the grains, furthermore, the gap between the grains may become filled with debris from the workpiece (a loading mechanism).

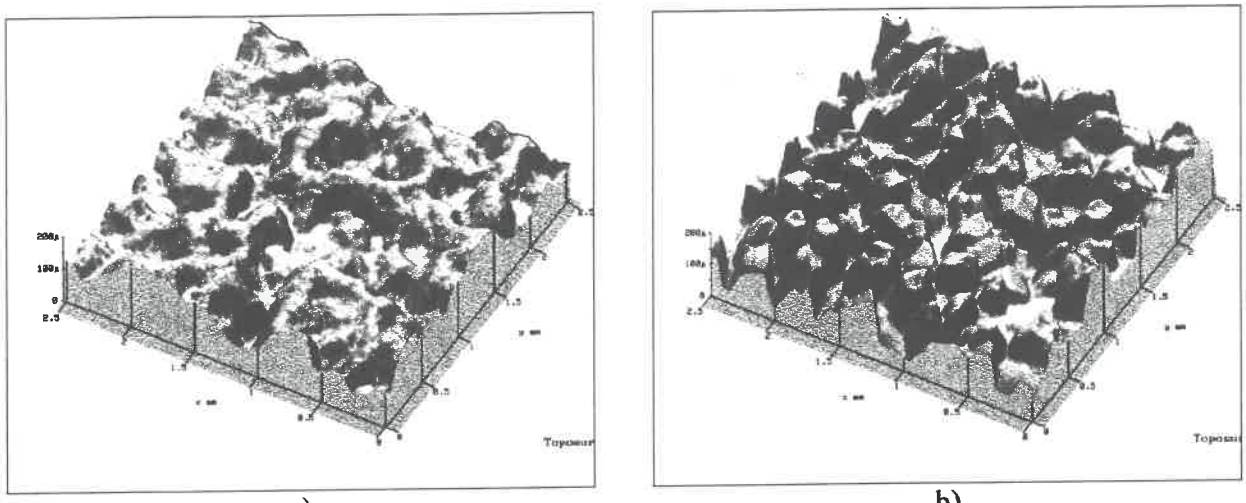

a) b)

Figure 2. Axionometric plots of the electroplated CBN wheel a) unworn and b) after the removal of material from the workpiece

The unworn CBN wheel gives a lower G_{Astat} for the original (untruncated) surface (S_{ds} =16.5) than after material removal has occurred (S_{ds}= 22.1). *Figure 2a* is an axionometric plot of the unworn wheel with very few grains clearly visible due to overplating. The G_{Astat} values for the untruncated wheel increase as the workpiece is ground. This could be attributed to the erosion of the bond material thereby exposing additional grains [3]. *Figure 2b* is a plot of the wheel after the wheel had been worn - it can be clearly seen that more cutting grains are now available and that some wear flats have developed due to attritious wear mechanisms.

Conclusion

- Three-dimensional stylus profilometry has been demonstrated to be a useful tool in evaluating the topographic characteristics of the grinding wheel to provide both a qualitative and quantitative meaning.
- The recently developed 3-D parameter S_{ds} has been shown to be analogous to G_{Astat} and is able to quantify the number of cutting grains per unit cm^2.
- For the electroplated CBN wheel, more cutting grains become available after the wheel is worn – this has been demonstrated both visually and quantitatively while for conventional wheels the opposite is true as grains break off, wear flats develop, and debris makes grain identification more difficult.

References

[1] J. Verkerk *et al*, *Final report concerning CIRP cooperative work on grinding wheel topography*. Ann. CIRP 26/2, 1975

[2] L.Blunt and S.Ebdon, *The application of three-dimensional surface measurement technique to characterising grinding wheel topography*. Int. J. Mach Tools Manufact., Vol 36, no 11, pp 1207-1226, 1996

[3] S.Malkin, *Grinding Technology; Theory and Applications of Machining with Abrasives*, Ellis Horwood, 1989

[4] K.J. Stout *et al*, *The development of methods for the characterisation of roughness in three dimensions*, European Commission, ISBN 0-7044-13132 (1993)

Surface topography assessment of textured mold and aesthetic quality of injection molded plastic surface

S. Hara, K. Yanagi and T. Endoh
Nagaoka University of Technology
Nagaoka, Niigata, 940-2188, Japan

Introduction

Visual appearance or aesthetic quality of the surface has come to be significantly important in most industrial products. In order to improve the visual appearance of the plastic products, texturing to the surface of injection mold is often used. From the recent consideration for the environment, texturing on the plastic surface is increasing its importance more and more in contrast to the painting process. However, the design of the texture relies on experience of the engineers. The aim of this paper is to disclose the relationship between the surface topography of the textured mold and the aesthetic appearance of injection molded plastic surface.

Geometrical Transfer

Geometrical transfer of the mold surface texture to the molded plastic surfaces has been investigated using the 3-D surface parameters[1, 2]. In this report, the geometrical transfer was examined using the representative 3-D surface parameters such as amplitude parameter S_q, spacing parameter S_{ds} and hybrid parameter $S_{\Delta q}$. In addition, angular distribution of the reflected light on the plastic surface is also examined.

Fig.1 shows the employed injection mold that has nominal depth of 8μm. Plastic samples were made using this mold in 4 different temperatures. Areal surface profile of the mold and injected samples were measured using surface profilometer with diamond stylus. Calculated roughness parameters were shown in table 1. It is clear that the surface topography of the injection mold is transferred to the molded plastic surface more truly with the mold temperature.

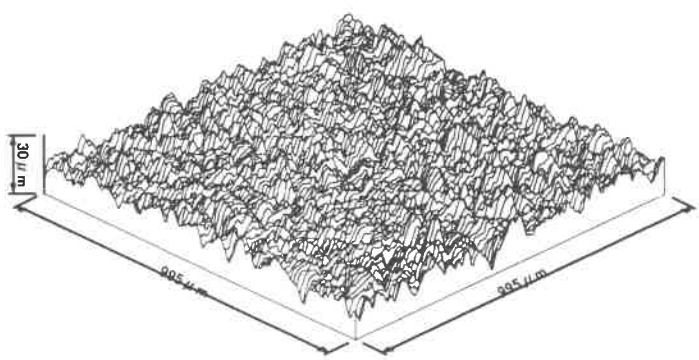

Fig. 1 3D plots of measured mold profile

Table 1 Surface Roughness Parameters of the Mold and Injected Plastic

	Mold temp. [°C]	S_q [μm]	S_{ds} [10^{-4}/μm^2]	$S_{\Delta q}$ [rad.]
Injected plastic	50	1.04	3.63	0.089
	60	1.21	4.26	0.109
	70	1.22	4.99	0.112
	80	1.54	5.99	0.148
Mold	-	1.74	7.96	0.166

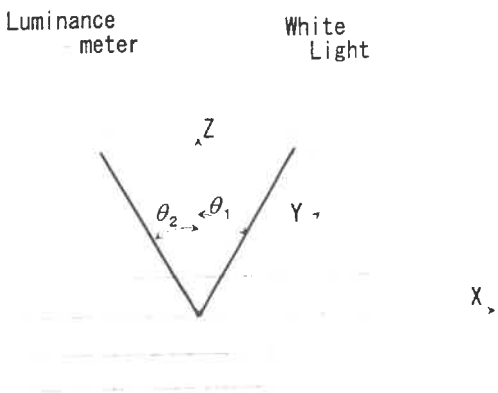

Light source	COLD SPOT PICS-NLX-150 (NIHON P·I Ltd.)
Incidence angle θ_1 [deg]	30
Measurement angle θ_2 [deg]	0~60

Fig. 2 Setup of the luminance meter

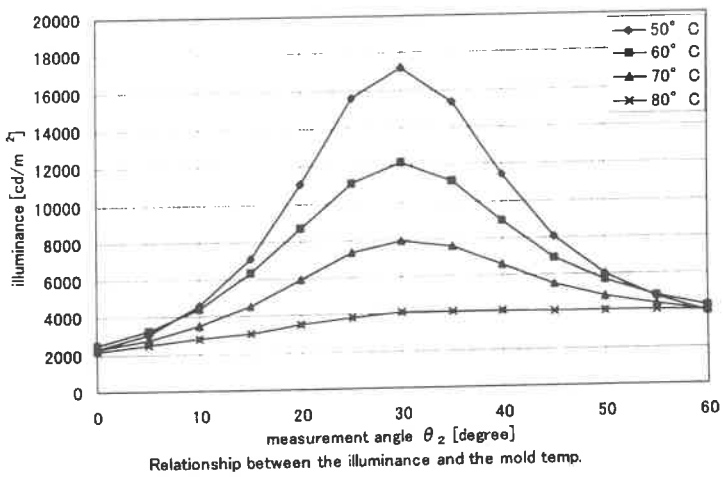

Nominal depth 8μm, Flat

Fig. 3 Luminance of the reflected light (Mold temperature)

Visual appearance of most engineering surfaces can be determined by the characteristics of the reflected light from the surface. The light reflection depends on the topographic features of the surface as well as optical properties of the material. An instrument to measure the intensity distribution of the reflected light is prepared. The schema of the instrument is shown in fig.2. The measured results shown in fig.3 show that the reflected light distributes widely when the mold temperature is higher. It is because the slope of the surface is steeper when the temperature of the mold is higher as shown in table 1.

Sensory Test

Four injection molds that have different spherical radius, 50mm, 100mm, 200mm and ∞(flat), were prepared. The molds were textured with certain nominal depth. Then, the plastic samples were made using the mold in 4 different temperatures. This procedure was repeated twice after removing the texture from the mold. The nominal depths of the texture were 8μm, 16μm and 25μm.

To examine the human impression of the plastic samples, Bradley's method[3] was employed. The inquired characteristics were "softness", "gloss" and "smoothness". Angular distribution of the reflected light on the target sample is also examined

1. Spherical radius of the surface

The result of the Bradley's test for the spherical radius is shown in table 2. It was made clear that the larger spherical radius gives the impression that the surface to be soft and smooth.

The angular distribution of the reflected light is shown in fig.4. The results show that reflected light distributes widely when the spherical radius of the surface is small.

2. Nominal Depth of the Texture

The result of the Bradley's test for the nominal depth of the texture is shown in table 3. The order of the judgments is different from that of the nominal depth. The angular distribution of the reflected light is shown in fig.5. The order of the width of the distribution is in good agreement with the result shown in table 3. It was made clear that those characteristics are not determined only by the nominal depth of the texture. Further investigation using various roughness parameters is needed to relate the sensory characteristic and the surface topographic characteristics.

Light Reflection Image

In addition, software is developed to simulate the intensity distribution of reflected light from the textured plastic surface under the condition that the topography data is given. Example of the generated images are shown in fig.6. The 80°C image is darker than that of the 50°C. This agrees with the result of fig.3. This intensity distribution could be used to presume the visual appearance of the plastic surface in the future.

Table 2 Result of the Sensory Test for Spherical Radius

Characteristic	Judgments
Softness	D>C>B>A
Gloss	A>B>C>D
Smoothness	D>C>B>A

Spherical radius A: 50mm, B: 100mm, C: 200mm, D: ∞(flat),
Nominal depth of the texture: 8μm, Mold temp. 50°C

Table 3 Result of the Sensory Test for Nominal Depth of the Texture

Characteristic	Judgments
Softness	C>A>B
Gloss	B>A>C
Smoothness	C>A>B

Nominal depth of the texture A: 8μm, B: 16μm, C: 25μm,
Spherical radius: ∞(flat), Mold temp. 50°C

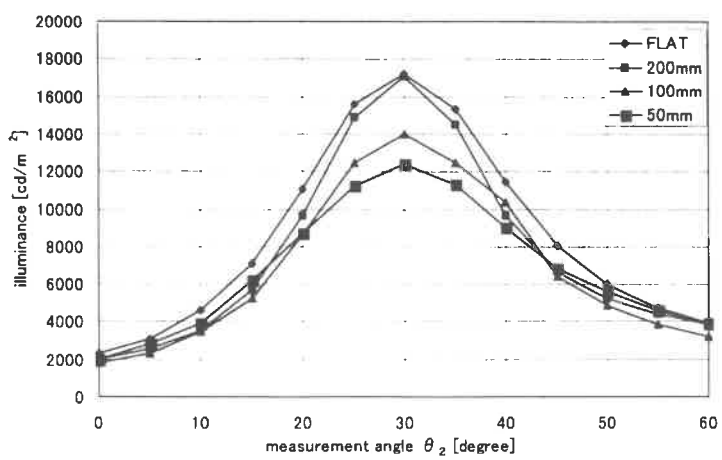

Relationship between the illuminance and the radius of curvature

Nominal depth 8μm, Mold temp. 50°C

Fig. 4 Luminance of the reflected light (Spherical radius)

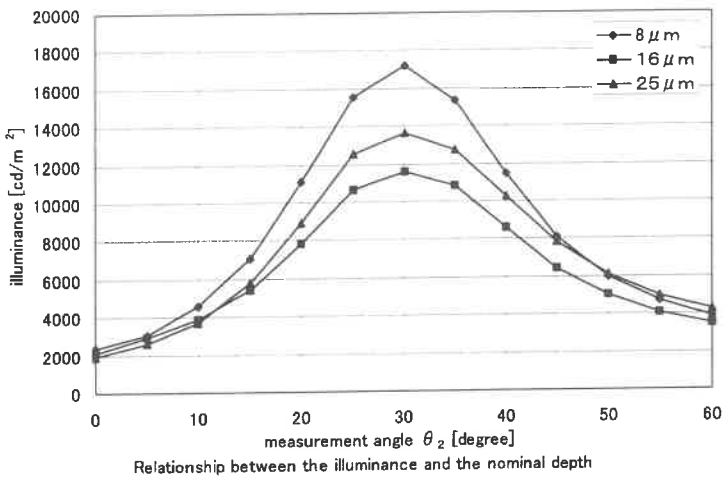

Mold temp. 50°C, Flat

Fig. 5 Luminance of the reflected light (Depth of texture)

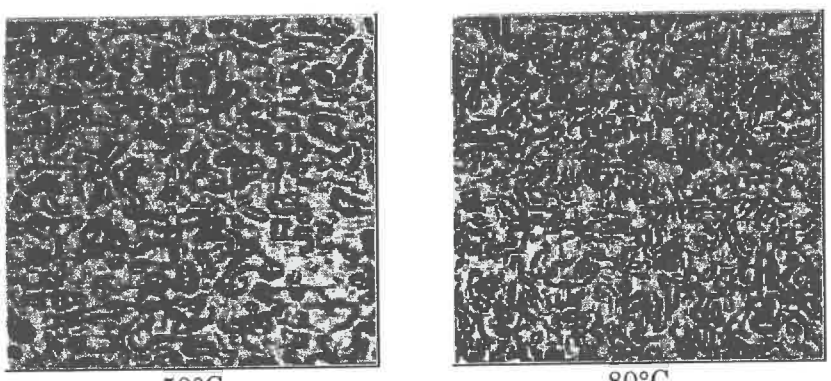

50°C 80°C

Nominal depth 8μm, Flat

Fig. 6 Simulation results of the surface appearance

Conclusion

1) The reflected light from the textured plastic surface distributes widely when the mold temperature is higher. It agrees the fact that the surface topography of the injection mold is transferred to the molded plastic surface more truly with the mold temperature.
2) Based on the sensory test, a certain relationship between the aesthetic quality of the plastic surface and its topographic characteristics was obtained.
3) The intensity distribution of the reflected light from the textured surface has good agreement with the result of the geometrical transfer and sensory test.

References

[1] U. Skands, P. Wahlberg, L. H. Christensen, B. Palfelt, L. Borregaard, N. B. Alexandersen, T. Johansen, A. Rønning, and J. C. Russ : Surface Analysis of Injection Molded TV Components, 7th Int. Conf. on Metrology and Properties of Engineering Surfaces, 1997, pp.55-62

[2] K. Yanagi and Y. Kumeda : An Evaluation of Injection Process by the Three-Dimensional Characterization of the Mold and Product Surfaces, 7th Int. Conf. on Metrology and Properties of Engineering Surfaces, 1997, pp.390-395

[3] R. A. Bradley and M. E. Terry : Rank Analysis of Incomplete Block Designs. I The Method of Paired Comparisons, Biometrika, 39(1952), pp.324-345

Optical Measurement for Flank Wear in Peripheral Cutting Edges in Endmills

Hwa-Soo LEE, Tsutomu NAGASHIMA, Hiroyuki HAGA
and Tadashi WAKABAYASHI

Department of Mechanical Engineering, College of Science & Technology,
Nihon University
1-8-14, Kanda-Surugadai, Chiyoda-ku, Tokyo, 101-8308, Japan

1. Introduction

In order to evaluate tool wear of peripheral cutting edges in endmills precisely, whole length of cutting edges have to be monitored. As well known, since the peripheral cutting edges of endmills have spiral geometry, conventional tool measuring method for turning tools cannot be applied as it is [1], [2]. This study aims to evaluate the flank wear in peripheral cutting edges quantitatively, a new optical measuring method of flank wear is proposed.

2. Measuring Principle of Wear Measurement

Since the geometrical shape of peripheral cutting edge is spiral in three dimension, flank wear taking place in whole cutting edge cannot be measured simultaneously. Therefore, in this study, flank wear occurred in whole edge is measured by repeating measurement of minute cutting edge part. That is, clamping an endmill to a rotating axis, a CCD camera is located on a slider fed in axis parallel to the rotating axis. Since this CCD camera is located with an incline as same as the edge twist angle, in this case 30 degree, cutting edge can be monitored horizontally. After positioning rotary axis to the measured part, camera is positioned to the measuring part and a video data is acquired. Repeating this procedure, whole image data in peripheral cutting edge can be monitored. Arranging these video data straight as shown in figure 1, flank wear in whole cutting edge can be evaluated.

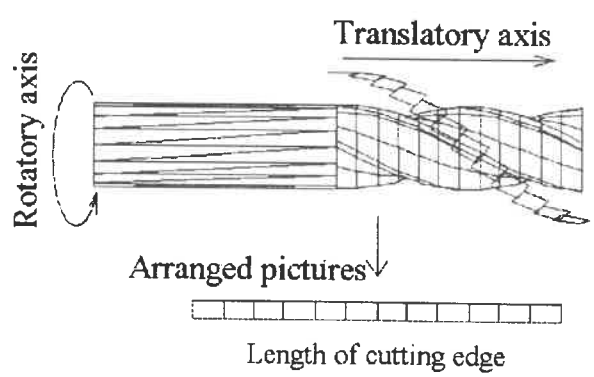

Fig.1 Repetitive measuring method

3. Design of Measuring Equipment

Figure 2 shows the schematic diagram of this measuring system. An endmill is clamped to a collet chuck located on a rotatory axis. While, a CCA camera and a halogen lump are located on a linear stage. Rotatory and translatory axes are controlled by two servo motors which have

least input increments 1/3 degree and 0.1 mm respectively.

Horizontal and vertical length of one video data is 512 pixel, 2.304 mm. In this measuring method, horizontal 200 pixel data, 0.9 mm, are acquired in a video data, and then data acquisition number is needed 23 times for the measuring 20 mm length of cutting edge. It takes about 2 minutes to measure 20 mm length edge.

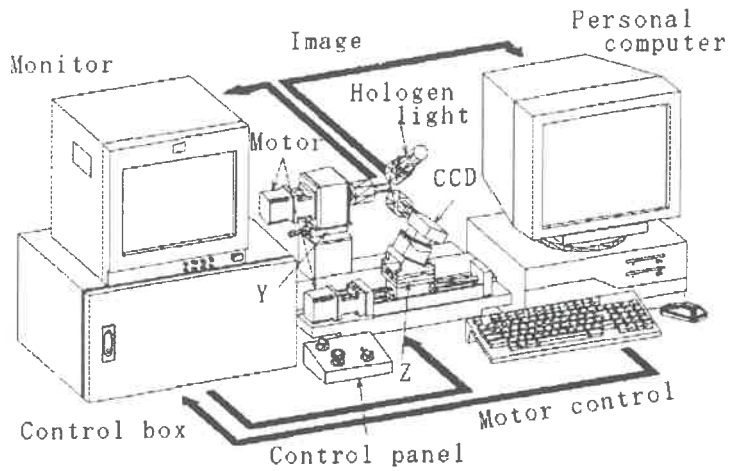

Fig.2 Schematic diagram of measuring equipment

4. Wear Measurement by Designed Equipment

4.1. A Measured Example of Flank Wear

Figure 3 shows a measured example of cutting edge after up-cutting. Figure 3(a) shows the cutting edge before cutting operation. In this figure, plots are concentrated linearly near the cutting edge. Figure 3(b) shows the same cutting edge after cutting operation, cutting length is 10,800 mm, removed metal volume per unit width is 4,320mm^3/mm. In this figure, the number of plots are increasing in the area from 2.5 to 15.0 mm from the right end which means the top of cutting edge. This area corresponding to the part used in cutting, 3.0 ~ 13.0 mm from the top of cutting edge.

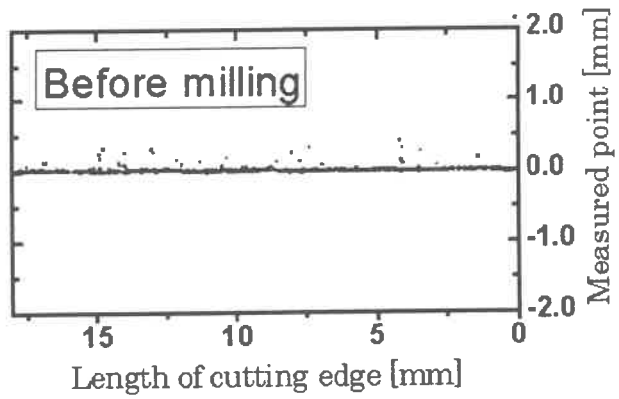

Area of flank wear : 0.1 [mm^2]

(a)

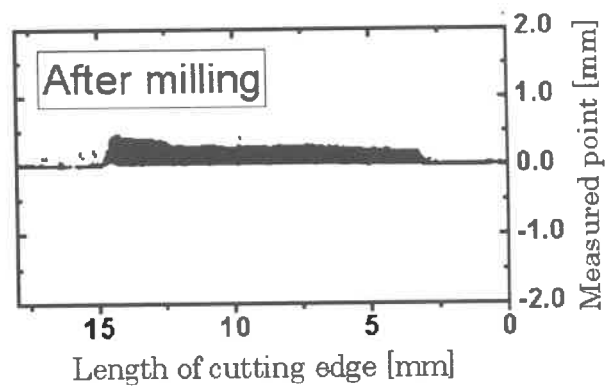

Area of flank wear : 1.65 [mm^2]

Max. width of flank wear : 0.24 [mm]

(b)

Fig.3 Measured example of flank wear

4.2. Flank Wear in Cutting Process

Figure 4 shows the variation of measured flank wear in cutting

process. This figure shows that the flank wear increases with the increase of cutting length. Figure 5 shows the variation of the area of flank wear in cutting process. This figure shows that the areas of flank wear in both cutting methods are increasing with the increase of cutting length.

4.3. Measurement of Retreat of Cutting Edge

Figure 6 shows a schematic diagram of cutting edge. As well known, width of flank wear shown a in this diagram increases in cutting process, and cutting edges also retreats as shown b simultaneously. In conventional optical measurement, it is very difficult to identify the retreat of cutting edge shown b in this diagram. In this study, a quantitative measuring method of this retreat is also proposed. Figure 7 shows a schematic diagram of the flank wear in cutting edge. In this figure, white part shows the flank wear as same as shown in figure 3. However, the bottom line does not coincide with the cutting edge before cutting operation. And then, superimposing the data before cutting to the data after cutting and carrying out their subtracting operation, retreat of cutting edge can be identified quantitatively. A measured example is shown in figure 8. The area a in this figure shows the flank

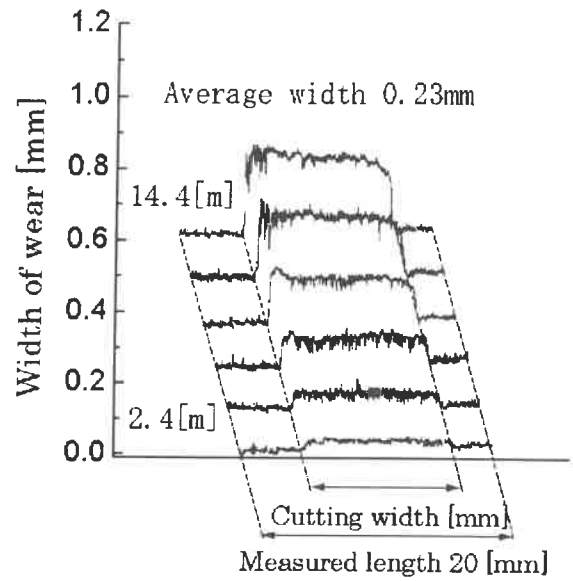

Fig.4 Measured flank wear in cutting process

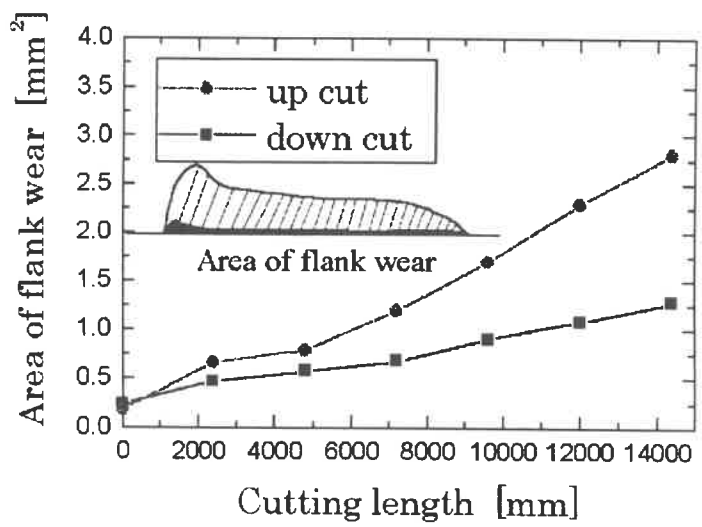

Fig.5 Area of flank wear in cutting process

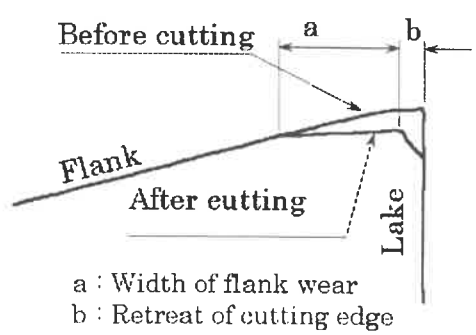

Fig.6 Flank wear and tool retreat

wear, and the area b shows the retreat of cutting edge. In this case, it is known that the amount of retreat is about 0.05 mm.

5. Conclusions

In this study, an optical measuring method of flank wear of peripheral cutting edge in endmill is proposed. As the result of this trial, flank wear and retreat of cutting edge can be measured quantitatively.

Acknowledgment

We are much grateful to Dr. Masumi IZUMI for having discussed with us on the present study.

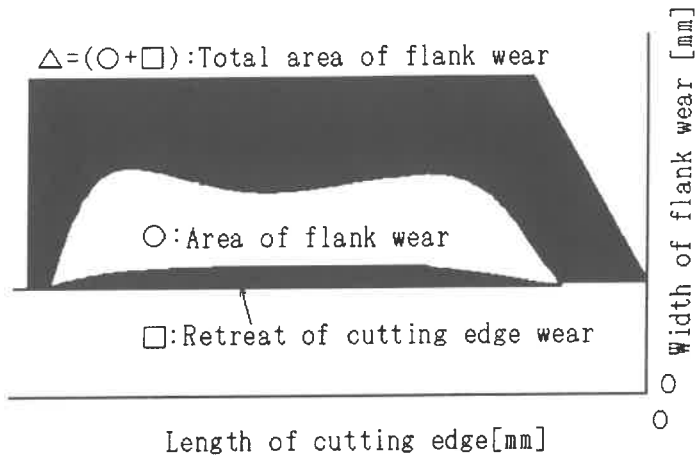

Fig.7 Measuring method of cutting edge retreat

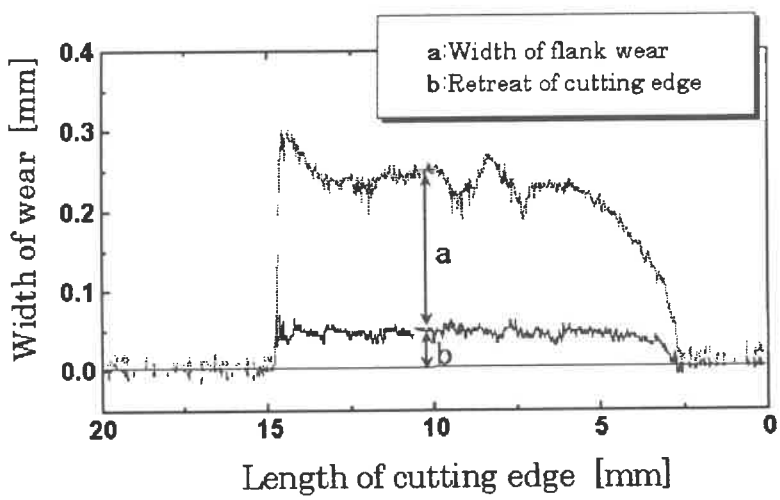

Fig. 8 Measured example of flank wear and edge retreat

References

[1] Hiroyuki OKAMOTO and Yoh YONEZAWA, "Atutomatic Measurement system for Crater Wear Depth of a Throwaway Chip by the Optical Cut Method", Journal of JSPE, Vol.59 No.10(1993-10),P.1643

[2] Nobushige SAWAI, Joonyeob SONG and Hwayoung PARK, "Automated Measurement of Tool Wear Using an Image Processing System", Journal of JSPE. Vol.61 No.3(1995-3), P.368.

Volumetric Error Measurement and Compensation Using the Vector Method

Charles Wang, Bob Griffin
Optodyne, Inc. Compton, CA
And
John Janeczko
Giddings & Lewis Machine Tools, Fond du Lac, WI

To achieve higher position accuracy of a machine tool, it is important to measure the volumetric errors and to compensate the volumetric errors provided that the machine tool is repeatable. Described here is a vector method developed by Optodyne. Using the vector method, the volumetric errors of a Giddings & Lewis machine, model, RAM 630 machining center have been measured. The measured volumetric errors were used to compensate the machine errors and achieved higher volumetric accuracy. The time required to compensate the machine using the vector method is significantly less than that using conventional measurement procedures.

Volumetric Compensation in a CNC Machine Tool

Competition in the global manufacturing market today requires improving the CNC machine tool performance to achieve higher productivity, better quality and less downtime. With the latest generation of CNC controls it is now possible to achieve higher quality even on a lower cost machine. To do this it is important to measure the volumetric errors of the machine tool and to compensate these errors. Many of the controls available today have this capability but very few take advantage of this technology.

For many years, the machine tool linear errors were measured and compensated by using laser interferometers. However, the linear error is only one of the many volumetric errors. The straightness errors, squareness errors, and the pitch, yaw, and roll angles may all cause poor overall volumetric accuracy, by compensating for just linear errors the overall volumetric accuracy of the machine is not significantly improved.

Most CNC machine controls today have the capacity to compensate the volumetric errors, for example on a typical three axes machine it is possible to compensate, three linear errors (or pitch error), six straightness errors (or cross errors or sag errors) and three squareness errors. The machine accuracy can be improved by measuring all these errors and then to compensate these errors, providing that the machine is repeatable. The key is how to measure all these errors accurately and quickly. There are many methods to measure these errors. However, all of these methods are very complex and the cost is normally prohibitive for smaller companies. This is one of the major reasons these errors are not compensated. The other reason is time, with the cost of machine time most companies are not willing to invest the 16 to 20 hours required to measure all these errors.

Described here is a vector method, it can measure all these errors, using a simple and portable laser interferometer or a Laser Doppler Displacement Meter (LDDM™) with 4 setups and within a few hours unlike possibly days required using conventional interferometer systems.

Basic Concept of Vector Measurement Technique

For years standards such as the ASME B5.54 and ISO 230-2 have recommended checking the volumetric accuracy of a machine by measuring the body diagonals, this is because the measured linear errors in the diagonal direction are sensitive to all 21 errors on the machine. More precisely, the measured linear errors, are the vector sum of errors, namely, the linear displacement errors (parallel to the linear axis), the vertical straightness errors (perpendicular to the linear axis), and horizontal straightness errors (perpendicular to the linear axis and the vertical straightness error direction). Furthermore, by pointing the laser beam in 3 different directions, all 3 components of the error vector can be determined. Since the errors of each axis of motion are the vector sum of the 3 perpendicular error components, we call this measurement a "vector" method.

In practice, first point the laser beam in one of the body diagonal directions, same as the standard diagonal measurement. For a standard laser diagonal the machine is programmed to move x, y, and z axes simultaneously to the next increment dR, stop and take a measurement. The problem with this method is that once the data is collected there is no way to determine what caused the errors. With the "vector" method, the machine is programmed to move the X-axis to dX, stop and take a measurement, then move the Y-axis to dY, stop and take a measurement, then move the Z-axis to dZ, stop and take a measurement. Here $dX*dX + dY*dY + dZ*dZ = dR*dR$.

As compared to the conventional body diagonal measurement where only one data point is collected at each increment dR, the vector measurement collects 3 data points, one at dX, one at dY and one at dZ, hence 3 times more data is collected. Furthermore, the data collected after dX is due to the x-axis movement only, and data collected after dY and dZ are due to the y-axis and z-axis movement respectively. Hence the error sources due to the x-axis motion, the y-axis motion and the z-axis motion can be separated.

After the first diagonal is completed point the laser beam in another body diagonal direction and repeat the same process until all 4-body diagonals are measured. Since each body diagonal measurement collects 3 sets of data, there are 12 sets of data when all 4 diagonals are measured. Hence, there is enough data to solve the 3 displacement errors, 6 straightness errors, and 3 squareness errors.

For conventional body diagonal measurement, the displacement is a straight line along the body diagonal; hence a standard laser interferometer can be used to do the measurement. However, for the vector measurement described here, the displacements are along the x-axis, then along the y-axis and then along the z-axis. The trajectory of the target or the retroreflector is not a straight line. The maximum deviation from the body diagonal is proportional to the size of the increment. A conventional laser interferometer would be way out of alignment even with an increment of a few mm.

To tolerate such large lateral deviation, a Laser Doppler Displacement Meter using a single aperture laser head and a flat-mirror as the target can be used. This is because any lateral

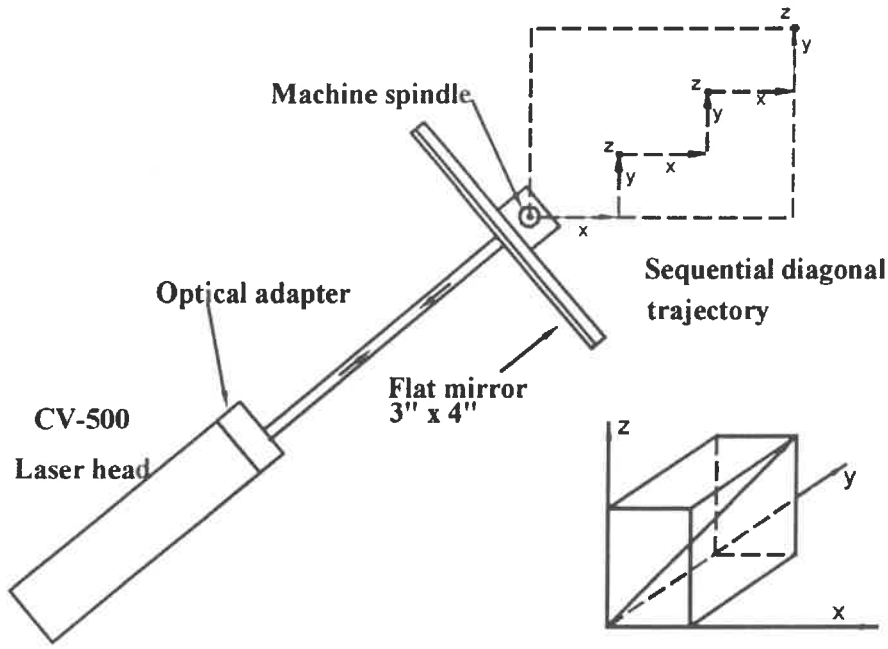

Fig. 1 Schematic of Sequential Diagonal Measurement

movement or movement perpendicular to the normal direction of the flat-mirror will not displace the laser beam, hence the alignment is maintained. After 3 movements, the flat-mirror target will move back to the center of the diagonal again, hence the size of the flat-mirror has only to be larger than the largest increment. A schematic showing the vector measurement setup is shown in Fig.1. Here the flat-mirror target is mounted in the machine spindle and it is perpendicular to the laser beam direction.

Measurement Data and Results

Using an Optodyne MCV-500 laser calibration system and a volumetric calibration package, the volumetric errors of a Giddings & Lewis, model RAM 630 horizontal machining center were measured.

The measured volumetric errors, linear errors, vertical straightness, and horizontal straightness of X-axis, Y-axis, and Z-axis respectively will be presented and discussed. It is noted that for the X-axis, the largest error is the linear positioning error and for the Y-axis the largest error is the vertical straightness which may be caused by the non-squareness, and for the Z-axis the largest error is the horizontal straightness. Hence, if the machine is compensated for the linear positioning errors only, the large straightness errors in the Y-axis and in the Z-axis will not be compensated.

The measured volumetric errors were used to generate the compensation files. The compensation files were loaded into the controller of the machine. The volumetric accuracy of the machine was checked by the conventional body diagonal measurement (ASME B5.54 standard). The body diagonal errors measured without compensation were about 60 um and the same measurements with compensation were about 14 um. Hence an improvement of diagonal accuracy of a factor of 4 is achieved.

Summary and Conclusions

To achieve higher position accuracy of a machine tool, it is important to measure the volumetric errors and to compensate the volumetric errors provided that the machine tool is repeatable. Using the Optodyne MCV-500 laser calibration system and the vector method, the volumetric errors of a machining center have been measured. These errors were then used to compensate the machine errors resulting in higher volumetric accuracy. The time required to compensate the machine using the vector method is significantly less than that using conventional measurement procedures.

In summary, we have shown that the volumetric errors of a machine tool can easily be measured by the vector measurement technique developed by Optodyne. The measured volumetric errors can be used to compensate the machine errors and achieve higher volumetric accuracy. Furthermore, the time required to compensate the machine using the vector method is significantly less than that using conventional measurement procedures making it easier for manufactures to take advantage to the advancements in CNC control technology.

Surface Roughness Limit for Super-Machined Mirrors Measured with Scanning Probe Microscopy

J. Yu[#, *], *Y. Namba*[*], *Bryan K. A. Ngoi*[#] *and Z. W. Zhong*[#]

 # Precision Engineering Strategic Research Programme, Nanyang Technological University, Singapore 639798

** Department of Mechanical Engineering, Chubu University, Kasugai, Aichi 487-8501, Japan*

Atomic surface roughness[1] is known as the roughness limit of a surface in the field of precision engineering, which is a target for ultra-precision machining or optical film fabrication. For example, atomic layer epitaxy (ALE) for various single crystals has been extensively studied[2-4] and applied to the fabrication of X-ray multilayer structures[5] in order to realize atomic interfacial roughness (the roughness limit) as well as high reflectance. Surface roughness is an important parameter in assessing the quality of high performance X-ray imaging optics, as a measure of topographic relief. Scanning probe microscope techniques have been desirable to perform experiments on surface roughness measurements, which had shown to correlate with the roughness affecting the X-ray reflectance and X-ray scattering.[6] Further, these methods offer the possibility of direct real-space determination of the atomic structure in three dimensions.

Fig. 1 shows the inter-atomic interaction for AFM, where λ is inter-atomic and inter-ionic spacing and r is the radius of the surface atom or ion. Based on the geometric model of atomic topography, we calculated a series of atomic surface roughness for pure metal crystals, shown in Fig. 2. The three-dimensional rms atomic surface roughnesses for pure metal crystals are between 0.28 Å and 0.68 Å. Table 1 shows the calculated surface roughness limits of the materials often used in X-ray multilayer fabrication.

The present work focuses on not only in above theoretical calculation but also in experimental measurements with scanning probe microscopy. We experimentally measured a muscovite at the atomic scale with the scanning probe microscope techniques as shown in Fig. 3. The nearly hexagonal array of light spots in the image corresponds to holes in the center of hexagonal rings of K^+ ions in the muscovite cleavage planes. The light spot rings are separated by approximately ~ 5.2 Å that is characteristic of cleaved muscovite in which the K^+ ions are left on lower hexagonal sheet. The three-dimensional root-mean-square (rms) roughness σ and

arithmetical mean deviation roughness R_a are 0.25 Å and 0.20 Å, respectively, while the theoretical σ is 0.35 Å and R_a is 0.28 Å.

Furthermore, we also measured the mirror surfaces generated by polishing, grinding and diamond turning techniques. The scaling surface roughness was measured on selected super-machined mirrors with scanning probe microscopy, shown in Fig. 4. The AFM maps of precision ground BK-7 glass and diamond turned nickel are shown in Figs. 5 and 6, respectively. From Figs. 3, 5 and 6, we can understand well the gap between the atomic level surface and the current super-machined mirror surfaces.

The authors would like to thank Mr. Y. G. Lu, Nanyang Technological University (NTU), for preparing this presentation. Most of the experiments were done in the Chubu University, Japan. This work was supported in part by a Grant-in-Aid for Scientific Research (B) No.11450063, a Grant-in-Aid Specially Promoted Research, No. 07102007 and Grant-in-Aid for JSPS (Japan Society for the Promotion of Science) Fellows, No. 95043 and No. 97316, from the Ministry of Education, Science, Sports and Culture, Japan. J. Yu was supported by grants from the JSPS. This work was also supported in part by the Funding for Strategic Research Programme on Ultra-Precision Engineering from the NSTB (National Science & Technology Board, Singapore) and Applied Research Fund ARC 9/96 from the Nanyang Technological University.

References

1. J. Yu and Y. Namba, "Atomic Surface Roughness," *Appl. Phys. Lett.* **73** (24), 3607-3609 (1998).
2. J. Nishizawa, "Molecular Layer Epitaxy," *J. Electrochem. Soc.* **132**, 1197-1200(1985).
3. Y. Aoyagi, "Atomic-Layer Growth of GaAs by Modulated-Continuous-Wave Laser Metal-Organic Vapor-Phase Epitaxy," *J. Vac. Sci. Technol.* **B5**, 1460-1464(1987).
4. T. Suntola, "Atomic Layer Epitaxy," *Thin Solid Films* **216**, 84-89(1992).
5. M. Ishii, S. Iwai, T. Ueki, and Y. Aoyagi, "Reflection-Wavelength Control Method for Layer-by-Layer Controlled X-Ray Multilayer Mirrors," *Appl. Opt.* **36**(10), 2152-2156(1997); M. Ishii, S. Iwai, H. Kawata, T. Ueki, and Y. Aoyagi, "Atomic Layer Epitaxy of Aluminum Phosphide and Its Application to X-Ray Multilayer Mirrors," *J. Cryst. Growth* **180**, 15-21(1997).
6. G. S. Lodha, K. Yamashita, H. Kunieda, Y. Tawara, J. Yu, Y. Namba and J. M. Bennett, "Effect of Surface Roughness and Subsurface Damage on Grazing-Incidence X-Ray Scattering and Specular Reflectance," *Appl. Opt.* **37**(22), 5239-5252 (1998).

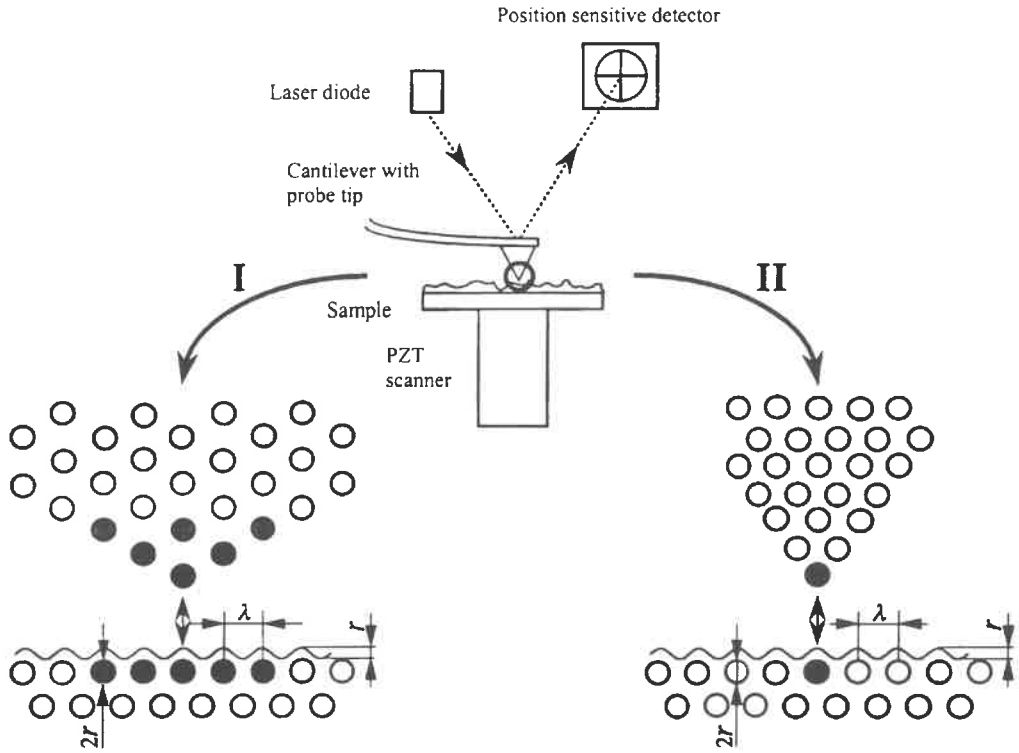

Fig. 1 Schematic illustration of inter-atomic interaction for AFM.

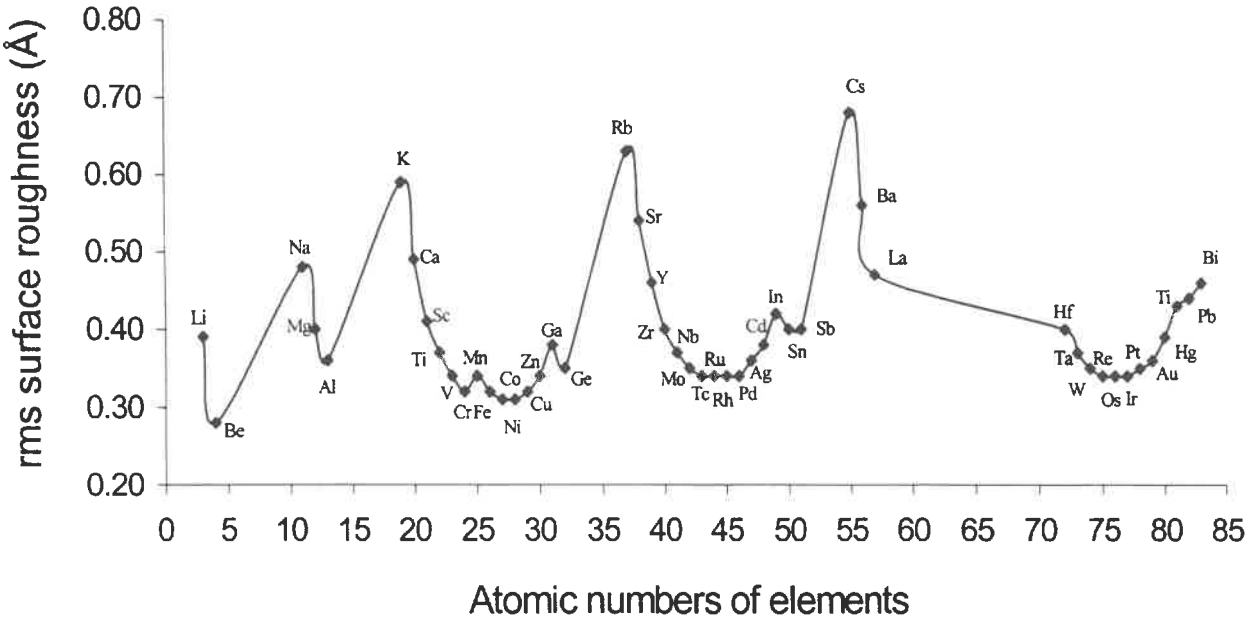

Fig. 2 Three-dimensional rms atomic surface roughness for pure metal crystals.

Table 1 Three-dimensional rms atomic surface roughness (in Å) for materials commonly used in X-ray multilayer fabrication.

Be (4) [a]	Fe (26)	Co (27)	Ni (28)	Mo (42)	Ru (44)	Rh (45)	Pd (46)	W (74)	Re (75)	Pt (78)	Au (79)
0.28	0.32	0.31	0.31	0.35	0.34	0.34	0.34	0.35	0.34	0.35	0.36
Be^{2+}	B^{3+}	C^{4+}	Si^{4+}	Fe^{2+}	Co^{2+}	Ni^{2+}	Mo^{4+}	Pd^{2+}	W^{6+}	Re^{4+}	
0.04 (3) [b]	0.03 (4)	0.02 (3)	0.07 (4)	0.16 (4)	0.19 (6)	0.14 (4)	0.16 (6)	0.16 (4)	0.11 (4)	0.16 (6)	
0.07 (4)	0.07 (6)	0.04 (4)	0.10 (6)	0.20 (6)	0.23 (8)	0.17 (6)		0.22 (6)	0.13 (5)		
0.11 (6)		0.04 (6)		0.23 (8)					0.15 (6)		
				Fe^{3+}			Mo^{6+}			Re^{7+}	
				0.16 (6)			0.10 (4)			0.10 (4)	
				0.20 (8)			0.15 (6)			0.13 (6)	

[a] Numbers in parentheses are the atomic numbers of elements.
[b] Numbers in parentheses are coordination numbers of ions.

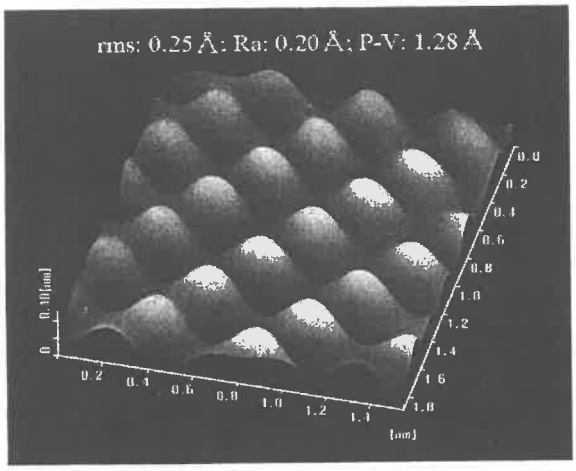

Fig. 3 AFM image of muscovite.

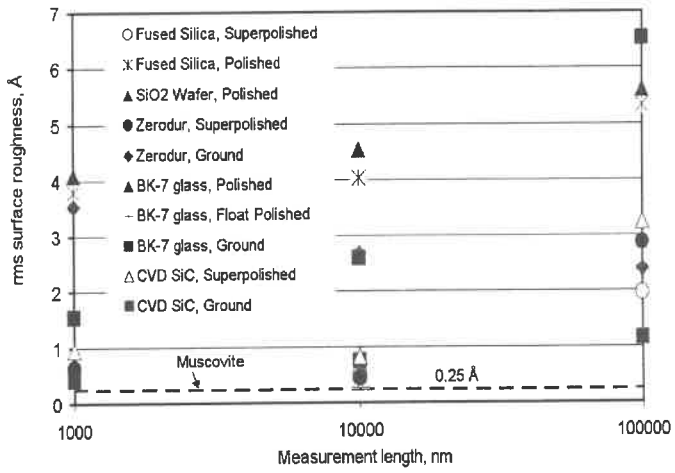

Fig. 4 Roughness of super-machined surfaces.

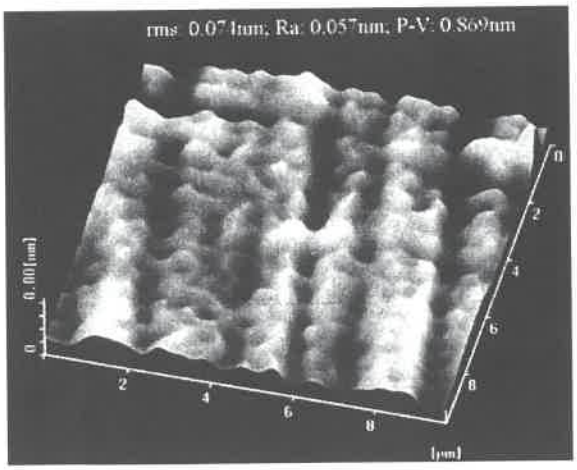

Fig. 5 AFM image of ground BK7 glass.

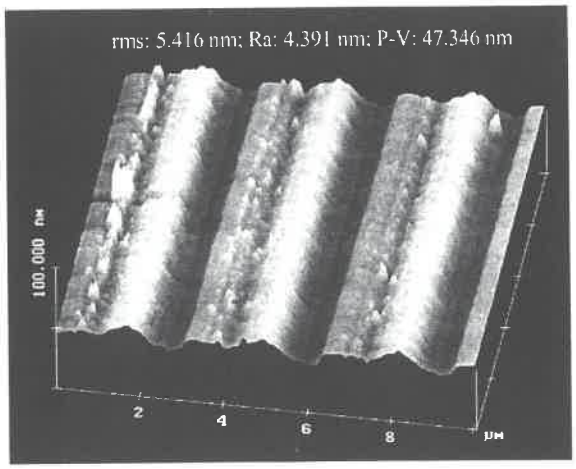

Fig. 6 AFM image of diamond-turned nickel.

A Learning Quality Control Approach to Improve Manufacturing Quality in the Turning Process

Christoph Ament, Gert Goch
Department of Measurement and Control, University of Bremen, Germany
Hochschulring 20, D-28359 Bremen, {am,gg}@biba.uni-bremen.de

1. Introduction

In general, a complete manufacturing process can be modelled as a sequence of local manufacturing subprocesses numbered by $i=1,...,n$ in Fig. 1. Starting with the non machined stage, the workpieces are processed in the subprocesses in ascending order until the final product is obtained.

In each subprocess the quality of the product is threatened by systematic and random errors. For that reason, the workpiece quality must be measured and a strategy has to be found, to use the measured data in order to compensate at least the systematic errors. In most cases the relation between the process observation and its control is highly non-linear and classical methods of linear control theory cannot be applied. At the moment, it usually depends on the process knowledge and experience of the process operator to adjust the parameters of the machine manually.

In the recent years methods of process control have been developed. If errors are observed at the end of a subprocess, the failure mode and effects analysis (FMEA) is able to list up possible reasons of the failure and makes suggestions for an improvement [2]. The statistic process control (SPC) investigates the measured data with statistic methods in order to predict developments in the subprocess in the near future [3].

But, both methods are not able to define an appropriate control action to optimize the workpiece quality immediately and automatically in a closed loop. It is the idea of the model based quality control to use a mathematical model of the process plant for the interpretation of the measured data [5]. The control unit has to determine its output such that in the model the measured failure is compensated as good as possible.

The problem remains that the model has to be developed, which is a time consuming and difficult task in most cases. E.g., in the turning process the passive force of the cutting tool leads to a bending of the workpiece during the process and finally to an undesired increase of the diameter. Modelling is not easy, since the equations of elasticity have to be solved to determine the workpiece bending. A similar example is the milling process without coolant, where the thermal extend of the workpiece and the tool results in an divergence in geometry which is difficult to model.

In this paper a simple learning algorithm is presented that is able to obtain a process model from measured data samples. It shows a fast convergence within a sequence of a few workpieces in the application of a simulated turning process. Especially in case when a sequence of identical workpieces has to be manufactured, the method seems to be advantageous to reach an optimized workpiece quality.

2. Quality Control Approach

2.1 Concept for One Subprocess

Since an in-process measurement is impossible or too expensive in most cases, we will restrict ourselves to a post-process measurement at the end of each subprocess. Therefore, the measurement is received only in the pace of the workpieces that are passing through and the control output is determined only once for each workpiece. The process can be characterized as a sequence (numbered by k) of measurements $y(k)$ and control actions $u(k)$. It will be called time discrete in pace of the process.

For the automation of the manual quality control

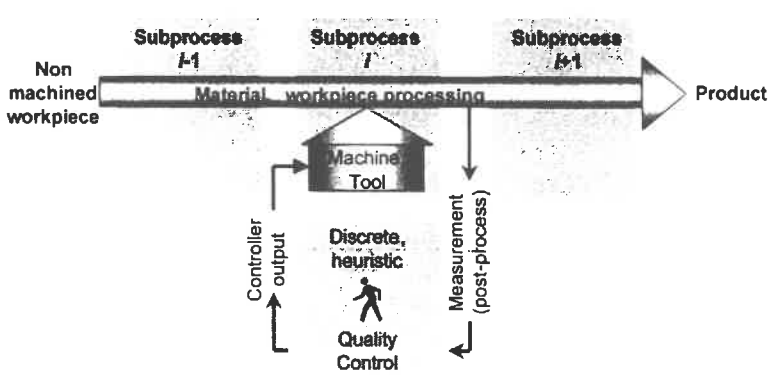

Figure 1: Subprocesses and heuristic quality control

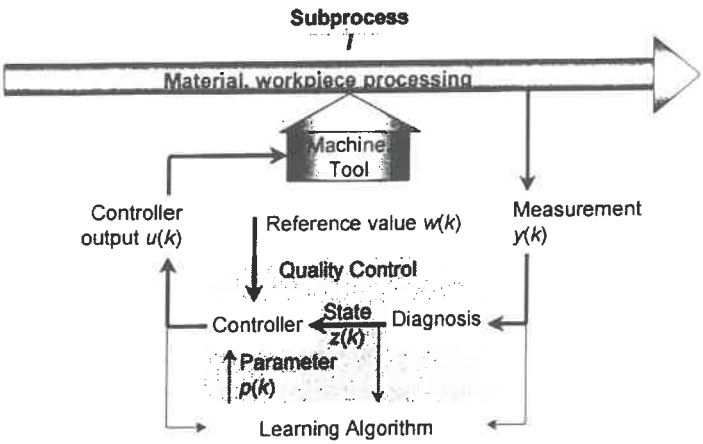

Figure 2: Structure of a automatic quality control feedback

shown in Fig. 1, an appropriate controller structure has to be developed. In order to supply the controller itself with the complete information about the current process state, a diagnosis unit is introduced which receives the measurement $y(k)$ and passes the state information $z(k)$ to the controller (see Fig. 2).

The control problem is now to find a controller output $u(k)$ such that the current measurement $y(k)$ is changed into the reference value $w(k)$. In general, this may need a sequence of steps k until $w(k)$ can finally be reached. But, in the present case of quality control we receive a new workpiece in every step and have to find the controller output leading to an optimal processing within this step. Hence, the given process meets the following definition: A process is called controllable in one step for any given state $z(k)$, if the measurement $y(k)$ can reach the reference value $w(k)$ within one step using an appropriate controller output $u(k)$:

$$y(k) = w(k) \tag{1}$$

Next, for this class of system a learning algorithm is proposed that uses the data $[u(k), z(k), y(k)]$ to adjust the parameters $p(k)$ of the control law (see Fig. 2).

2.2 Learning Algorithm

At the end of each process step the control output $u(k)$, the measurement $y(k)$ and the state information $z(k)$ are inquired. The question arises, how this sample can be used to improve the control law. Assuming for a moment that the obtained measurement $y(k)$ would just be the expected reference value $w(k)$, the corresponding optimal control output would exactly be $u(k)$. Using this interpretation a training set for the control law is obtained.

Next, a functional representation which maps the input $[w(k), z(k)]$ into the output $u(k)$ is needed. Comparing the sample and the training set, the input and the output are just exchanged. So, the demanded control law can be seen as the inverse function of the process plant.

As a representation of the control law a linear superposition of radial basis functions $\theta_j(k)$ is used to map the controller input $x(k) = [w(k), z(k)]$ to the output $u(k)$ (see [1], [6]):

$$u(k) = p'(k) \cdot \theta(k) \tag{2}$$

The components of the vector $\theta(k)$ are the radial basis functions $\theta_j(k)$. The total number of radial basis functions used for approximation is denoted with J. The weights $p_j(k)$ are the parameters of the controller and are summarized in the parameter vector $p(k)$ of the length J. A bell-shaped radial basis function is used:

$$\theta_j(k) = \exp(-\xi_j'(k) \cdot \xi_j(k)/2) \tag{3}$$

The component i of the vector $\xi_j(k)$ belonging to the radial basis function j is determined by the following transformation:

$$\xi_{j,i}(k) = \frac{x_i(k) - x_{0,j,i}}{\sigma_i} \tag{4}$$

In Eq. (4) the constant $x_{0,j,i}$ denotes the component i of the center point of the radial basis function j, and the constant σ_i characterizes the width of the radial basis functions referring to the dimension i. By introducing a grid of these bell-shaped functions in the vector space of x, this vector space is decomposed into local areas corresponding to the radial basis functions. The functions are overlapping which leads to a smooth approximation. Moreover, an interpretation of the control law in the scope of fuzzy sets is also possible. This point of view can be used to turn a linguistic formulation of an expert into an initial control law which is improved by learning later on.

Although non-linear functions can be approximated, the relation of the parameter vector in Eq. (2) is linear. For that reason, linear least square methods can be applied to obtain the parameter vector $p(k)$. The recursive Kalman filtering is used, in order to update $p(k)$ after each step [4].

2.3 Sequence of Subprocesses

The introduced method has focussed on one subprocess and is able to optimize the manufacturing process there for subsequent workpieces. Moreover,

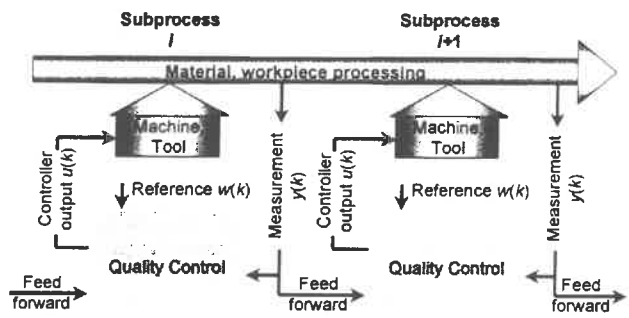

Figure 3: Feed forward to the next subprocess

the measurement $y^{(i)}(k)$ at the end of the step i can be used to compensate failures in quality of the measured workpiece in the next step. For that purpose, a feed forward can be added to the state vector $z^{(i+1)}(k)$ of the next step, see Fig. 3.

3. Example: Quality Control of the Turning Process

In order to rate the quality of a workpiece after turning, two parameters will be discussed in the following. As already mentioned in the introduction, the passive force F_P of the cutting tool results in an undesired increase ΔR of the workpiece radius R_0. Fig. 4a shows the workpiece geometry.
Furthermore, the quality of the workpiece surface is determined by the roughness R_Z which depends mainly on the feed f and the state of the cutting tool (see Fig. 4b). In the next section, a quantitative model for both values ΔR and R_Z is given.

3.1 Model of the Turning Process

The passive force is modelled in agreement with [5] as function of the feed f and the depth of cut a. Two cases must be distinguished:

$$F_P = \frac{1}{2-m_d} \cdot k_d \cdot r_\varepsilon \cdot f^{1-m_d} \cdot \left(\sqrt{\frac{a}{r_\varepsilon} \cdot \left(2 - \frac{a}{r_\varepsilon}\right)} \right)^{2-m_d} \quad \text{if} \quad a \le a_1 \tag{5}$$

and

$$F_P = k_d \cdot f^{1-m_d} \cdot \left(\frac{1}{2-m_d} \cdot r_\varepsilon \cdot (\sin\kappa)^{2-m_d} + \frac{\cos\kappa}{\sin^{m_d}\kappa} \cdot \left(a - r_\varepsilon(1-\cos\kappa)\right) \right) \quad \text{if} \quad a \ge a_1 \tag{6}$$

with the constant

$$a_1 = r_\varepsilon \cdot (1 - \cos\kappa) \tag{7}$$

The meaning and the numerical values of the parameters in Eq. (5) to (6) are summarized in Tab.1.

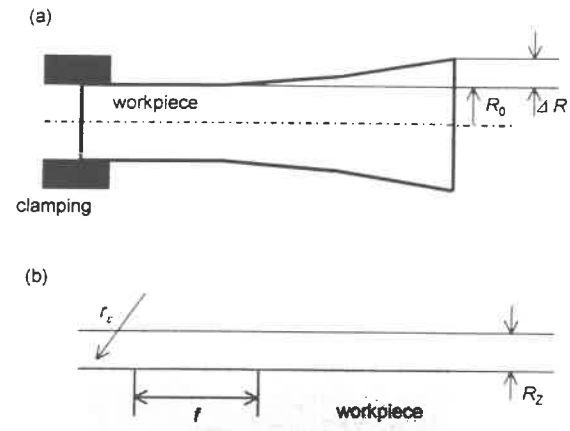

Figure 4: Radius increasement ΔR and surface roughness R_Z of the turned workpiece

Parameter	Meaning
$r_\varepsilon = 0.8$ mm	radius of the cutting tool
$\kappa = 95°$	rake angle of the cutting tool
$k_d = 506$ N/mm^2	machine constant
$m_d = 0.52$	machine constant
$E = 200$ kN/mm^2	Modulus of elasticity of the workpiece
$c = 3.5$	Relation of measured to theoretical roughness

Table 1: Model parameters

To obtain the bending of the workpiece caused by the passive force F_P that is applied at the location Z_0 the differential equation of bending

$$\frac{\partial^2 \Delta R(Z)}{\partial Z^2} = -\frac{F_P \cdot (Z_0 - Z)}{E \cdot I(Z)} \quad \text{with} \quad I(Z) = \frac{\pi}{4} \cdot R^4(Z) \tag{8}$$

is solved for $\Delta R(Z)$ numerically. The depth of cut a is actually reduced by $\Delta R(Z)$ and the effective depth of cut

$$a_{\text{eff}}(Z) = a - \Delta R(Z) \tag{9}$$

is obtained and introduced as model output.
Next, the surface roughness R_Z is modelled as a function of the feed f (see Fig. 4b and [5]):

$$R_z = \frac{c \cdot f^2}{8 r_\varepsilon} \tag{10}$$

The surface roughness R_Z is the second output of the turning model.

3.2 Application of the Learning Algorithm

For the application of the learning algorithm the reference workpiece displayed in Fig. 5 is used. In order to apply the learning algorithm the 3-dimensional vector space x of the measurement (a_{eff} and R_Z) and the state (location Z) must be approximated by a grid of membership functions. Their centers are set in the following points:

$$Z_0 = [-10\text{mm} \quad 30\text{mm} \quad 50\text{mm} \quad 80\text{mm} \quad 110\text{mm}]$$
$$R_{Z0} = [0\mu\text{m} \quad 20\mu\text{m} \quad 40\mu\text{m} \quad 60\mu\text{m}] \qquad (11)$$
$$a_{\text{eff}\,0} = [0\text{mm} \quad 0.8\text{mm} \quad 1.6\text{mm} \quad 2.4\text{mm}]$$

Hence, the total number of radial basis functions is $J = 4 \cdot 4 \cdot 5 = 80$. The two controller outputs (f and a) are handled separately. For each of them an approximation is recursively obtained by Kalman filtering.

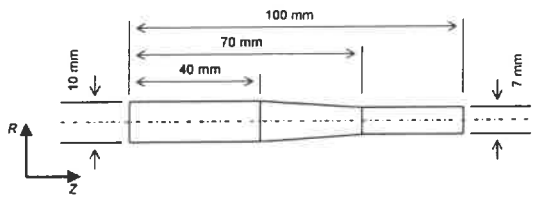

Figure 5: Reference workpiece (clamped at the left end)

3.3 Results

Simulation results are shown after a training sequence of 100 workpieces is completed. Each workpiece is measured from Z=0mm to Z=100mm in steps of 10mm, so, the total number of samples is 1100. During the training, the depth of cut a and the feed f is chosen by random equally distributed in [0mm 2.5mm] and [0mm 0.3mm], respectively. In Fig. 6 the obtained controller is compared to the optimal control law at the setpoint a = 1mm. It shows that a good approximation of the control law can be achieved. In Fig. 7 the control law of f is plotted as a function of the desired roughness R_Z. Also in this case, a sufficient approximation has been obtained.

In the presented simulation, the control law of the feed f is assumed to be a general function of the 3-dimensional vector $[a_{\text{eff}}\, R_Z\, Z]$ at the controller input.

If f would be modelled only as a function of R_Z, the number of membership functions can be reduced drastically and the convergence in the learning process will be improved.

4. Conclusions

In this paper, a model based quality control for the turning process has been presented. To overcome the difficulty that a process model must be obtained, a simple learning approach using radial basis functions for the approximation of the control law has been developed. It has been shown for the turning process, that a control law can be found within a few steps, even if there is no prior control knowledge.

This method can also be applied in the field of other modern cutting processes, in order to compensate undesirable failures like the thermal extend of the workpiece and the tool during milling without coolant or the bending of machine axes with reduced weight.

References

[1] Bertsekas, D.P., Tsitsiklis, J.N., "Neuro-Dynamic Programming", Athena Scientific, Belmont, 1998

[2] Bläsing J.P., "FMEA – Failure Mode and Effects Analysis", QZ 33, 1988, pp. 119-120

[3] Dutschke, W., "Qualitätssicherung mit SPC", VDI-Z, Vol. 131, 1989, pp. 62-66

[4] Mendel, J.M., "Lessons in Digital Estimation Theory", Prentice-Hall, New Jersey, 1987

[5] Sawodny, O., "Modellbasierte Qualitätsregelung in der Fertigung am Beispiel der Drehbearbeitung", VDI Fortschrittsberichte 2, Nr. 403, Düsseldorf, 1996

[6] Sutton, R.S.; Barto, A.G., „Reinforcement Learning: An Introduction (Adaptive Computation and Machine Learning)", MIT Press, 1998

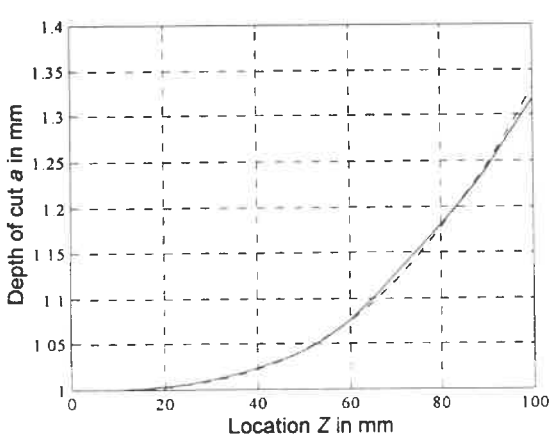

Figure 6: Control law for the depth of cut $a(Z)$ to obtain R_Z=10μm and a_{eff}=1mm: Trained controller (solid line) and optimal function (dashed line)

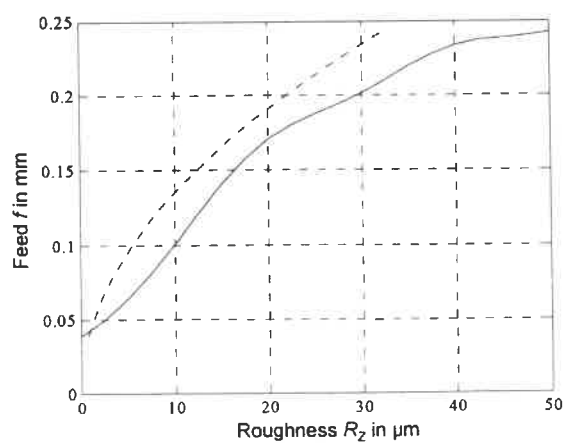

Figure 7: Control law for the feed f for different values of R_Z at z=0mm and a=1mm: Trained controller (solid line) and optimal function (dashed line)

Anisotropic Artifacts Introduced by Horizontal Scanning Instruments in Surface Metrology

Torbjorn S. Bergstrom and Christopher A. Brown
Surface Metrology Laboratory <www.wpi.edu/~tral>,
Worcester Polytechnic Institute, Worcester, MA 01609-2280

Introduction

The objective of this work is to study the extent and nature of artifacts that appear as differences in the tracing and scanning directions of surfaces measured by horizontal scanning instruments. These differences can impart, masque, or distort anisotropic characteristics in measured surface textures, which can confuse the assessment of anisotropy. A better understanding of these measurement artifacts can improve the quality of metrology systems for assessing anisotropy in surface textures.

Horizontal scanning instruments include atomic probe (e.g., AFM, STM), scanning laser and scanning stylus microscopes. These kinds of instruments repeatedly trace a sequence of profiles and scan a surface to build a data set of surface heights as a function of position in the tracing and scanning directions. Because of the similarity of the horizontal scanning we should suspect that these instruments might be subject to the same sorts of artifacts influencing the assessment of anisotropy.

Methods

In this work we use length-scale fractal analysis (Brown and Savary 1991) to analyze several measurements, made by a scanning laser microscope (SLM). The SLM was built in the Surface Metrology Laboratory at WPI for measuring runway surface textures in a project with NASA Langley Research center. In this work the SLM was used to measure a roughly finished sample of a concrete based pavement surface. A region 10mm x 10mm was measured with a sampling interval of 25μm in each direction.

Length-scale analysis is a type of fractal analysis based on the Richardson, coastline or compass method. The method analyzes the changes in the relative length (ratio of the measured length to the straight-line length) of a profile, which increases as the scale of measurement decreases (Fig. 1). Two parameters are derived from the analysis. The length-scale fractal complexity, Lsfc, is negative 1000 times the slope of a regression line fit to a portion of the log-log, length-scale plot (Fig. 2). The Lsfc is related to the fractal dimension (Fd = 1 + (Lsfc/1000)). The smooth-rough crossover, SRC, is the scale that delineates the coarse scale regions where the profile appears smooth, or Euclidean, from the fine scale regions where it appears rough, or fractal. At scales below the SRC the relative lengths are significantly greater than one. These parameters, unlike average roughness, depend on the order of the measured heights in the profiles. The complexity and crossover are orthogonal measurements, in that one can change without influencing the other.

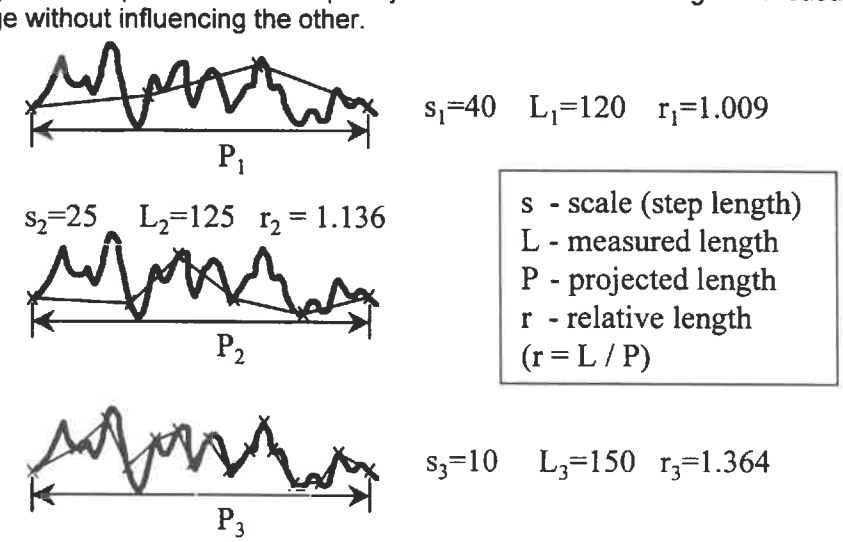

Fig. 1. Length-scale analysis

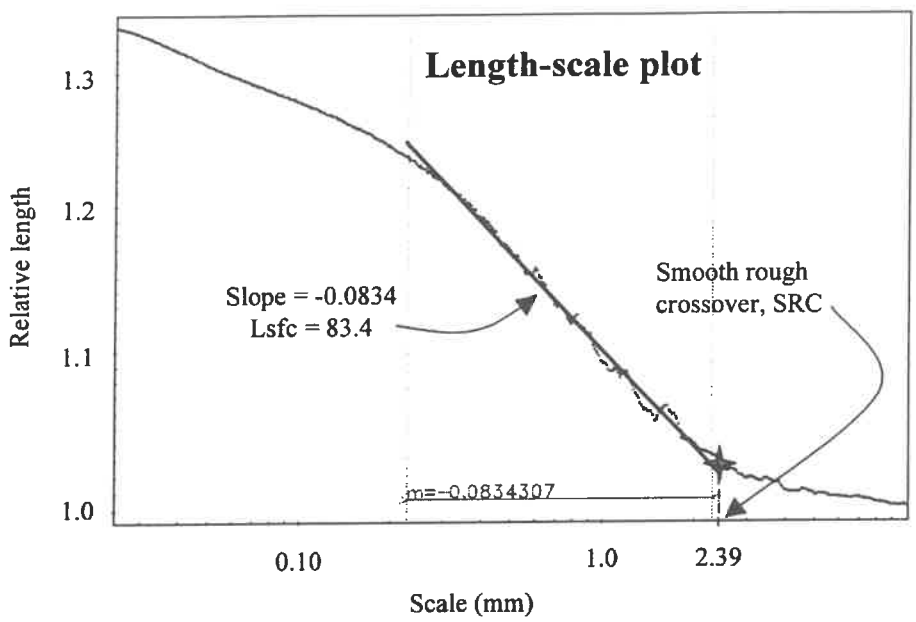

Fig. 2. Annotated length-scale plot.

More common profile characterization parameters, such as Ra, are not capable of detecting anisotropy without careful individual filtering of each profile from the data set. No filtering is used prior to the length-scale analysis.

There are two sources of potential artifacts to consider. First, the height sensors on the scanning instruments can have some directionality inherent in their design. The SLM uses a triangulation laser to measure the heights. Surface features with slopes approaching or exceeding the triangulation angle on the triangulation cannot be measured from at least one direction by conventional triangulation laser devices. Other kinds of sensors are also subject to directionality, e.g., the shape and stiffness of cantilevers on AFMs may not have the symmetry required for measuring features in the same way parallel and perpendicular to the axis of the cantilever. Second, non-random noise can be imparted on the measurements differently parallel and perpendicular to the tracing direction. One manifestation of this is the streaks frequently found on images of measured surfaces that indicate the tracing direction.

To be able to address both of these potential sources of artifacts, and assuming that the surface is anisotropic, 8 different cases are examined, perpendicular analyses each on 4 different measurement configuration at the same location. Twelve repetitions of each measurement are used so that it will be possible to separate systematic artifacts and random noise. One region on the surface was measured 12 times, after which the tracing and scanning directions were exchanged. The same region then was measured 12 more times. Following these measurements the surface was rotated 90° and the operation was repeated producing a total of 48 measurements. On each measured surface, the length-scale analysis was performed in both the tracing and scanning directions, for a total of 96 analyses.

Results and Discussion

The plot of complexity (Lsfc) versus smooth-rough crossover (SRC) shows seven distinct different groups of results (Fig. 3). There are only two cases where the scatter from the 12 measurements overlaps. This overlapping of the two cases is supposed to be a random event and is not considered to be consequential. The measurements within one case appear to be highly reproducible, yet when viewed in the complexity-SRC plane it appears that the results are sensitive to all the measurement variables, sensor orientation, tracing direction, and analysis direction. If the surface is isotropic and there is no influence of the orientation of the measurement then all the parameters for all eight cases would have the same values, which is not observed. If the surface is anisotropic and the complexity-SRC combination is not sensitive to the measurement variables, there would be two groups of four cases each, according to the direction of the analysis relative to the surface. This was not observed either.

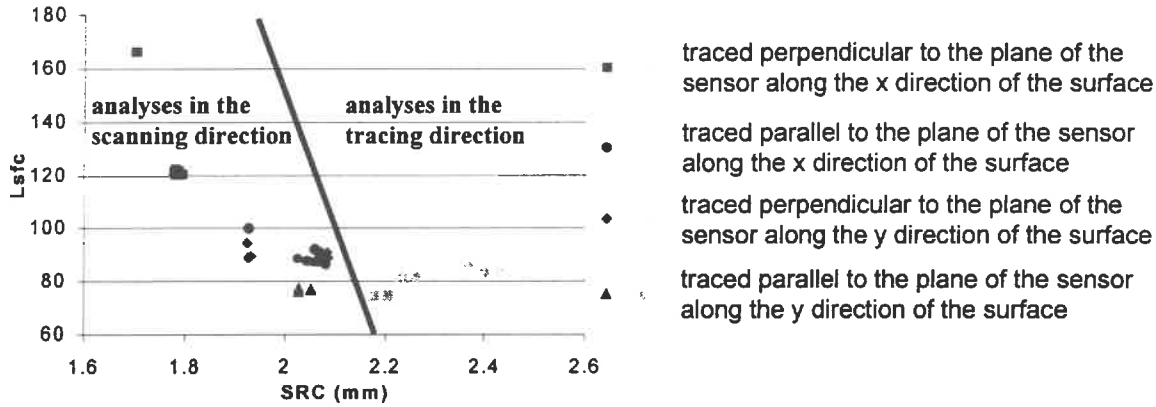

Fig. 3 Complexity (Lsfc) versus smooth-rough crossover (SRC) for all measurements and analyses. The gray symbols indicate analysis in the tracing direction.

If we consider the rotation of the surface relative to the SLM, to be essentially changing the orientation of the sensor relative to the surface then the anisotropic nature of the surface is apparent. For analyses made in the same direction on the surface, regardless of the measurement direction, the complexity is consistently greater when the analysis is made in the plane of the sensor triangulation, as shown in Fig. 4. This indicates that the surface is anisotropic, with respect to complexity. In other words, when the orientation of the sensor is controlled for then the anisotropy of the surface with respect to complexity is evident. The sensor orientation is able to masque the anisotropy.

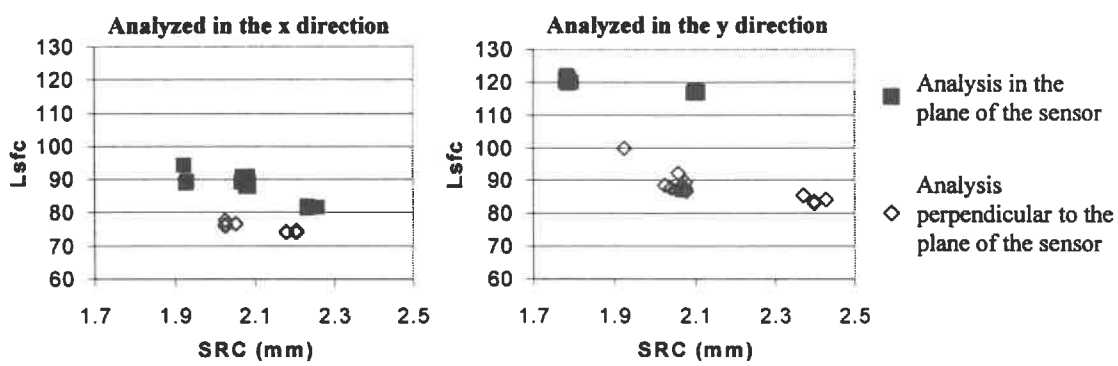

Fig. 4 Complexity (Lsfc) versus smooth-rough crossover (SRC), controlling for the analysis direction relative to the surface.

The influence of the tracing and scanning directions is apparent as the complexity of the analyses made in perpendicular to the tracing direction has greater scatter than parallel to the tracing direction. The standard deviation of each measurement analyzed in the scanning direction is greater than the standard deviation for the same measurement analyzed in the tracing direction. The influence of the tracing and scanning directions is also evident, as shown in Fig. 1, as the analyses in the tracing directions tend to have higher SRCs that those in the scanning direction. It may be that the noise is registered in the measured surface in the scanning direction in a way that tends to blur the features that contribute to the SRC, smoothing of the surface with respect to SRC.

Conclusions

- The complexity - SRC space can be used to differentiate sensor orientation, tracing direction and analysis direction on the same surface.
- Anisotropic characteristics with respect to complexity are apparent, only when the orientation of the sensor is controlled.
- Analyses perpendicular to the tracing direction results in a greater scatter in the complexity of the measurements.
- Analysis in the tracing direction results in a greater smooth-rough crossover.
- Artifacts are imparted both by the orientation of the triangulation laser sensor and by the scanning and tracing tables or some noise which varies with time.

Acknowledgements

We gratefully acknowledge the support of NASA Langley Research Center for their support in building the scanning laser microscope. We also acknowledge the excellent work of Dr.W.A.Johnsen, in building the microscope during his graduate studies in at WPI. Our thanks also go to Drs. Thomas and Buccellato of 3M for bringing the issue of these kinds of artifacts to our attention.

References

1. C.A.Brown, G. Savary, "Describing Ground Surface Texture using Contact Profilometry and Fractal Analysis" Wear 141 (1991) 211-226.

THE CHARACTERISATION OF ENGINE LINER WEAR USING NOVEL BEARING AREA CURVE PARAMETERS

David L. Butler[1], Liam A. Blunt[2], X. Jiang[2], and Ken J. Stout[2]

[1] School of Mechanical and Production Engineering, Nanyang Technology University, Singapore
[2] School of Engineering, University of Huddersfield, W.Yorks, United Kingdom

Introduction

The problems of increased oil consumption, blow-by, and scuffing have frequently been encountered and reported in heavy duty turbo-charged diesel engines [1]. One cause, first reported in the 1960s [2], is a wear phenomenon known as bore polishing which entails the generation of a bright mirror-like appearance on the cylinder liner surface along with full or partial loss of the honing pattern. Bore polishing has been attributed to either hard carbonaceous deposits, formed on the top land, or contaminants in the lubricating oil (or even both) [3].

Since the lubricating oil plays a major role in controlling these factors, bore polishing can be suppressed or even controlled by suitable oil formation. A number of engine tests have been developed for evaluation of the bore polishing tendency of lubricating oils. However, problems exist in the standardisation of testing due to design changes in test engines and models being withdrawn from production or becoming obsolete. Quantifying the amount of bore polish area present on a liner has involved manual inspection of the engine. This can be either destructive with removal and splitting of the liner or non-destructive with the inspector peering inside the engine block. The subjective nature of human inspection coupled with an obstructed view of the lower part of the liner has led to variations between inspectors' results of as high as 20%.

In order to minimise the variation between inspectors and to provide a more rapid, automated and repeatable polish detection system, the University of Birmingham, in conjunction, with a UK engine testing company embarked on the development of a 2nd generation laser bore scanner. As part of this research it was necessary to comprehensively characterise the topographic change occurring as the surface began to wear. This paper presents an attempt at characterising bore polish using surface parameters derived from the bearing area curve.

Bore polishing

Bore polish involves the removal of the honed topography, by two- or three-body abrasive wear, to generate a mirror-like surface finish. There are varying levels of polish depending on how much of the original honed topography is remaining. The Co-ordinating European Council (CEC)[4] defined bore polish as being "... *evidenced by clearly defined areas of bright mirror finish. It is caused by local mechanical wear of the surface.*" It went on further to categorise the visual rating of bore polishing as either light/low, medium, or heavy/high, the definitions are given in *table 1* and illustrated in the surface axionometric plots in *figure 1*.

CATEGORY	DESCRIPTION
Low Polish	A mirror finish overlaid on the original honing pattern
Medium Polish	A mirror finish showing faint traces of the original honing pattern.
Heavy Polish	A mirror finish showing no traces of the original honing pattern.

Table 1. Definitions of bore polish

As the bore polish progresses through these classified conditions, a very smooth surface is produced which leads to lubrication starvation. With insufficient boundary lubrication solid contact is made between the surfaces which can lead to welding and material transfer between the piston rings and liner, ultimately, complete engine failure can occur.

Experimentation

For this analysis a number of engine liners which had been subjected to a standardised 400 hour bore polish test were used. Areas of polish were detected using the laser bore scanner and these regions were then categorised using the classifications defined in *table 1*. Surface measurements were carried out using a number of 3-D stylus

instruments. sample spacing was 12 microns (both x- and y-direction) and an assessment area of 2mm by 2mm was employed. Over 150 measurements were undertaken.

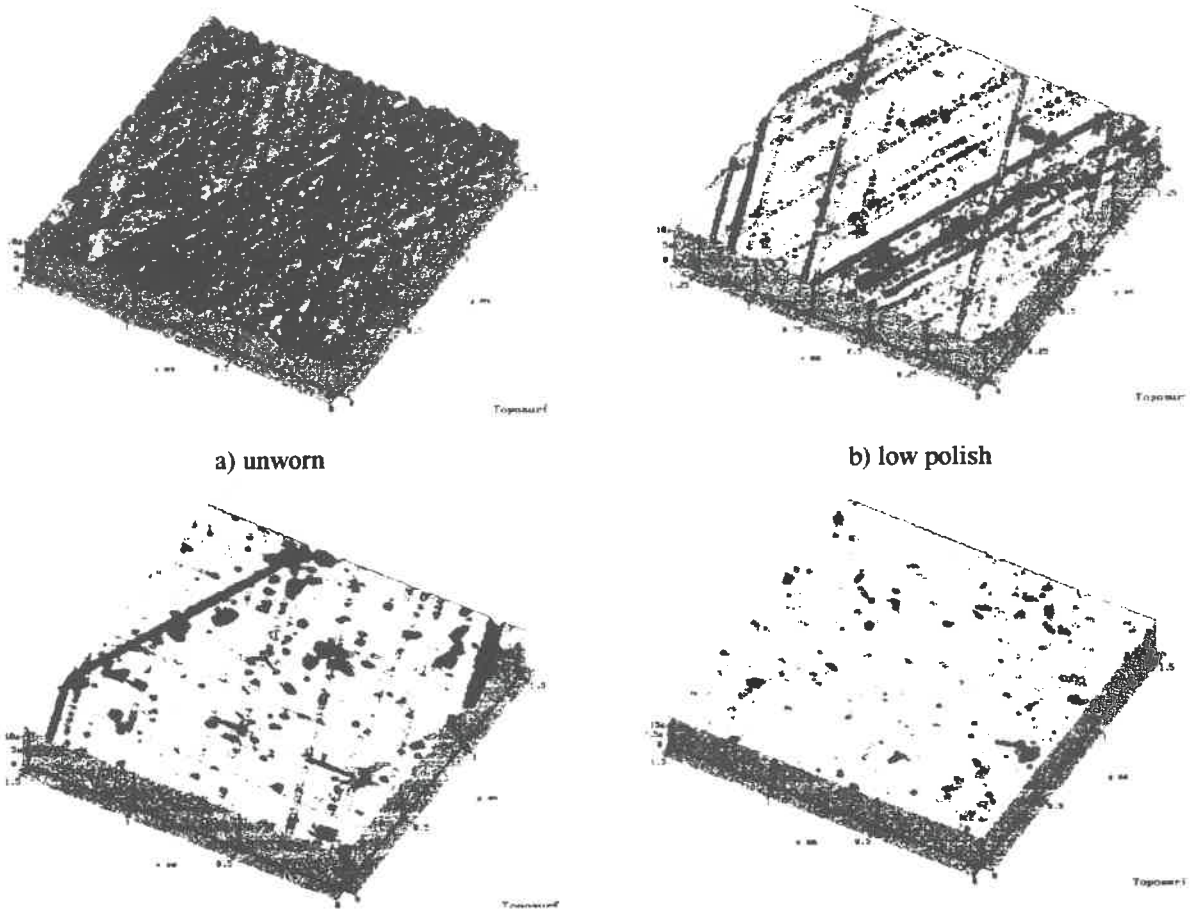

a) unworn

b) low polish

c) medium polish

d) heavy polish

Figure 1. Axionometric plots of bore polish

Parameters

Originally, an analysis was performed on the surface data employing a number of suites of parameters derived from the bearing area curve. The common theme throughout each suite is the classification of the surface and bearing area curve into peak, core, and valley regions. Unfortunately, although the parameters followed the expected pattern as the surface approaches a smooth valley-sparse topography the actual statistical analysis were not so promising. Both at the 90% and 95% level of confidence no set of parameters were significant. A method was required which could better characterise the subtle topographic changes occurring in the plateau region.

The Normal Probability Scale

A further development to the bearing area curve. first discussed over 30 years ago by both Williamson [5] and Eberle [6] was the plotting of the curve on normal probability paper. On normal probability (NP) paper any Gaussian distribution should fall in a straight line due to the unique horizontal scale. More recently, this technique has been formalised for 2-D profiles in a new ISO standard [7]. The surface of a cylinder liner is normally generated by a number of honing stages (usually two), each which leaves its unique 'fingerprint' on the surface. By plotting the cumulative amplitude distribution on a NP scale it is possible to identify two distinct lines (using the best fit criteria) corresponding to the plateau and base honing processes (*figure 2*). The gradient of each line corresponds to the rms. roughness (R_q for 2-D and S_q for 3-D) for that process. In this analysis the roughness of the plateau region is denoted as $S_{q(upper)}$ and the base-honed region as $S_{q(lower)}$.

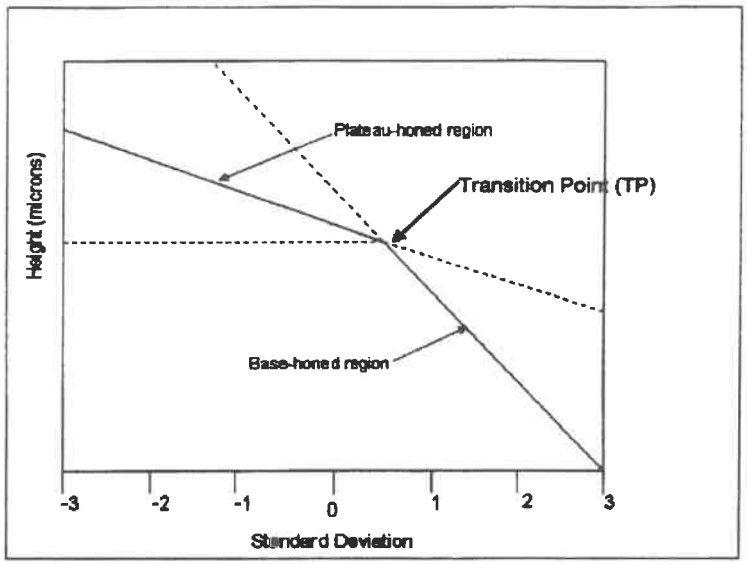

Figure 2. The Bearing area curve plotted on a normal probability scale

Results

Table 2 summarises the average parametric values for each degree of bore polishing while *figure 3(a-d)* illustrates the change in bearing area from an unworn to a heavy polished surface.

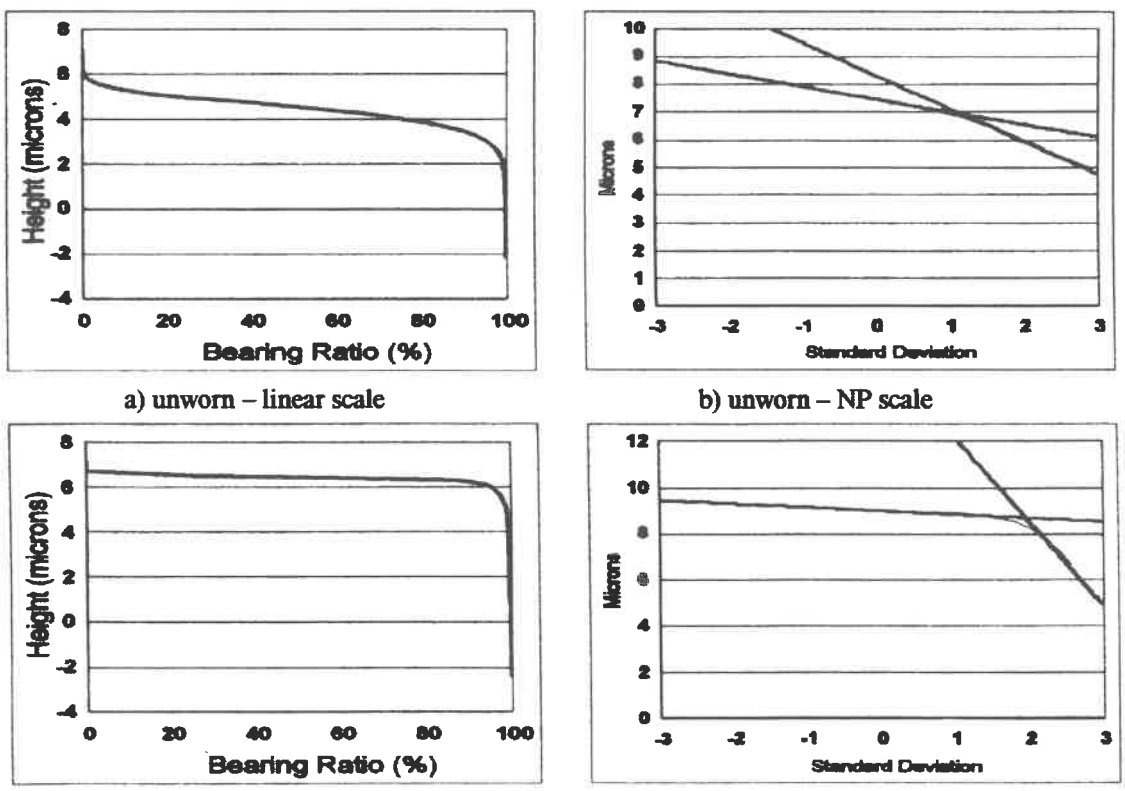

a) unworn – linear scale

b) unworn – NP scale

c) heavy – linear scale

d) heavy – NP scale

Figure 3. Dual plotting of the bearing area curve

CATEGORY OF WEAR	RMS ROUGHNESS (S_q)		
	OVERALL	UPPER	LOWER
Unworn	0.81	0.64	1.71
Low Polish	0.68	0.37	3.67
Medium Polish	0.41	0.25	1.89
Heavy Polish	0.26	0.14	1.95

Table 2. Comparison of average S_q values for overall and separate surface components

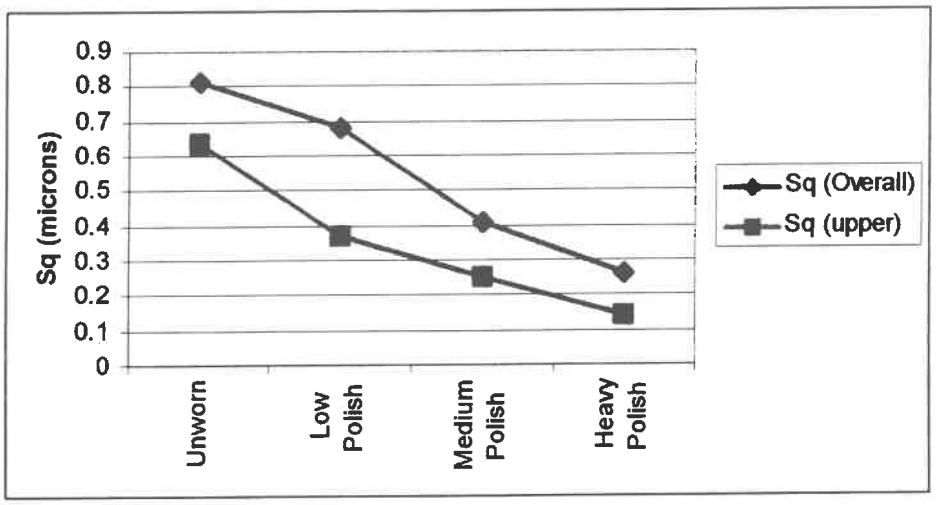

Figure 4. Variation of S_q with respect to degrees of polish

Discussion

From *table 2* and *figure 4* it can be clearly seen that the trend for the areal rms. roughness of the plateau region ($S_{q(upper)}$)is one of decreasing values (as is the trend for the overall roughness). The increase in $S_{q(lower)}$ could be attributed to pitting or possible scoring in the base-honed region. At the 95% confidence level the $S_{q(upper)}$ values were significant suggesting that this method could detect subtle topographic changes (attributable to bore polishing) in the plateau zone.

Conclusions

The plotting and subsequent analysis of the bearing area curve using the normal probability plotting has yielded a technique better adapted to detecting and measuring subtle topographic changes. The next stage of this research is to correlate these parameters with the output obtained from the laser bore scanner so as to provide a rapid, non-subjective, and validated method of polish detection.

References

[1] B. Haggh and E. Holmer, "*Experience and development of turbo-charged diesel engines: causes and proposed remedies*", SAE paper no 690746, 1969

[2] D.M. Hesling, "*A study of typical bore finishes and their effect on engine performance*", Lubrication Engineering, p 414, Oct 1963

[3] K.C. Ludema, "*A review of scuffing and running-in of lubricated surfaces with asperities and oxides in perspective*", Wear 100, p 315, 1984

[4] J.V.D Wilson and J.R.B Calow, "*Cylinder bore polishing in automotive diesel engines – A progress report on the European study*", SAE paper no 760722, 1976

[5] J.B.P Williamson, "*Microtopography of surfaces*", Proc. I.MechE, Vol 182, part 3k, pp21-30, 1967-68

[6] O.A. Eberle, "*Graphical method for statistical assessment of surface roughness comparison standards*", Proc. I.MechE, Vol 182, part 3k, pp 368-396, 1967-68

[7] ISO 13565-3 :*Geometrical Product Specifications (GPS) – Surface Texture; Profile method; surfaces having stratified functional properties – Part 3; Height characterisation using the material probability curve*, ISO, 1998

Geometric error analysis and calibration of a Stewart platform

Jenq-Shyong Chen
National Chung-Cheng University · Department of Mechanical Engineering
160, San-Hsing, Ming-Hsiung · Chia-Yi, 621, Taiwan, R.O.C.
Tel: 886-5-2428113, Fax: 886-5-2721522 · E-mail: imejsc@ccunix.ccu.edu.tw

INTRDOCUTION

A conventional Cartesian series-linking machine tool is known to have 21 geometric errors. Because its series-linking and stacked mechanism produce large Abbe offset length, angular errors of machine axes are considered to be the largest contributors to the volumetric errors of conventional machine tools. Another feature of a conventional machine tool is that the errors of the absolute link lengths and joint coordinates of each axis have not effect on the positioning accuracy of a machine. For a Stewart platform type machine, its parallel-linking mechanism not only reduces the Abbe error to minimum but also owns the advantage of averaging effect. The straightness and angular errors of each link has little effect on the positioning accuracy. However, a new class of errors from the universal joints or ball joints is introduced. Kinemater parameters including absolute link lengths and joint coordinates are absolutely required to determine the machine positioning accuracy. Our goal is to develop a calibration method for determining the link lengths and joint coordinates of a Steward platform.

Because the series-linking machine is an open loop mechanism, the geometric errors of a series-linking machine must be determined by external calibration instrument such as laser interferometers, artifacts or ball-bars. For a parallel-linking mechanism, the geometric errors can be calibrated by implicit method or self-calibration[1, 2] where additional motion information of the machine joints can be measured using redundant sensors. In this paper, we will present a self-calibration technique in which the rotations of some universal joints of the Stewart platform are measured using laser rotary encoders. Self-calibration principle and parameter estimation algorithm will be discussed.

PRINCIPLE OF SELF-CALIBRATION

The principle of self-calibration of a closed-loop four-bar linkage described by reference [2] is depicted in Fig. 1. b, and c represent the length of links AC and AB which are fixed length. Δa is the initial length of link BC and a_k is displacement of the actuator in link BC. $\Delta\alpha$ and α_k are the initial value and incremental value of angle $\angle$CAB. β_k is the value of the angle $\angle$CBA. If α_k can measured using redundant sensor and a_k is the known control-input, we are able to solve the kinemate parameters of $b, c, \Delta a, \Delta\alpha, \beta_k$ through the kinematic constraints and the following two equations:

$$c - b\cos(\alpha_k + \Delta\alpha) - (a_k + \Delta a)\cos\beta_k = 0 \tag{1}$$

$$b\sin(\alpha_k + \Delta\alpha) - (a_k + \Delta a)\sin\beta_k = 0 \tag{2}$$

In theory, all the kinematic parameters can be determined by giving four control-inputs, ie. k=1~4. Thus, we need to solve eight equations.

SELF-CALIBRATION ON A STEWART PLATFORM

The principle of self-calibration on a Stewart platform is depicted in Fig. 2. We separate the mechanism of a Stewart platform into six closed-loops. As shown in Fig. 2, each closed-loop involves a joint at the base, a joint at the platform, and a link. We name this loop as the ith loop. Using the inverse kinamtic analysis and the self-calibration principle, we will be able to derive the following equations of this loop:

$$\cos\gamma_i[x_k + r_{11k}P_{ix} + r_{12k}P_{iy} + r_{13k}P_{iz} - B_{ix}] + \sin\gamma_i[y_k + r_{21k}P_{ix} + r_{22k}P_{iy} + r_{23k}P_{iz} - B_{iy}] - (\bar{l}_{ik} + \Delta l_i)\sin\beta_{ik} = 0 \quad (3)$$

$$-\sin\gamma_i[x_k + r_{11k}P_{ix} + r_{12k}P_{iy} + r_{13k}P_{iz} - B_{ix}] + \cos\gamma_i[y_k + r_{21k}P_{ix} + r_{22k}P_{iy} + r_{23k}P_{iz} - B_{iy}] + (\bar{l}_{ik} + \Delta l_i)\sin(\bar{\alpha}_{ik} + \Delta\alpha_i)\cos\beta_{ik} = 0 \quad (4)$$

$$z_k + r_{31k}P_{ix} + r_{32k}P_{iy} + r_{33k}P_{iz} - B_{iz} - (\bar{l}_{ik} + \Delta l_i)\cos(\bar{\alpha}_{ik} + \Delta\alpha_i)\cos\beta_{ik} = 0 \quad (5)$$

where

$\Delta\alpha_i$:the initial value of the universal joint at the base as shown in Fig. 3;

$\bar{\alpha}_i$: the incremental value of the universal joint;

Δl_i: the initial length of the ith link;

$\bar{l}_i$: the incremental value of the ith link.

In theory, all the kinematic parameters can be determined by giving four control-inputs, ie. k=1~4. Thus, we need to solve twelve equations. The solution of the twelve equations can be obtained using Levenberg-Margqurdt numerical method.

EXPERIMENTAL VERIFICATION

A Stewart platform(shown in Fig. 4) was built for experimental verification. CANON's laser rotary encoders were designed at the universal joint on base (shown in Fig. 5). The laser rotary encoder has a resolution of 1.28millions of pulse/revolution. Table 1 shows the calibrated kinematic paramters of the loop 1. Table 2 shows the angular errors of the universal joints before and after calibration measured by the CANON laser rotary encoders. The result shows some accuracy improvement after calibration. However, the improvement was not good as expected. Noise of the sensor and backlash on the mechanism are considered to be the major reason. Table 3 shows the backlash values measured on the universal joints. Therefore, the backlash must be improved if better calibration accuracy is demaned.

CONCLUSIONS

In this work, self-calibration method of a Stewart platform using redundant sensors has been developed. From the computer simulation and experimental result, the feasibility of this approach has been proved. We found the backlash of universal joints and ball joints will be the major problem of our testing platform. This problem can be solved by adding proper preloads on the joints. However, backlash and sensor noise cannot be totally eliminated. To obtain high accuracy Stewart platform, kinematic parameter estimation algorithm must be improved. In this prelimary work, the kinematic parameters of each loop are directly solved from twelve equations obtained from four calibration positions. In the future work, kinematic parameter estimation algorithm based on least square method will be developed.

ACKNOLEDGMENT

This work was supported by the National Science Council grant No. NSC86-2212-E-194-006.

REFERENCES

[1] Charles W.Wampler"An implicit loop method for kinematic calibration and its application to closed-chain mechanisms" IEEE,1995.

[2] Hanqi Zhuang "Self-calibration of parallel mechanisms with a case study on stewart platforms" IEEE,1997.

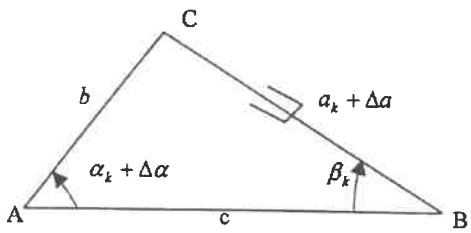

Fig. 1: Principle of self-calibration

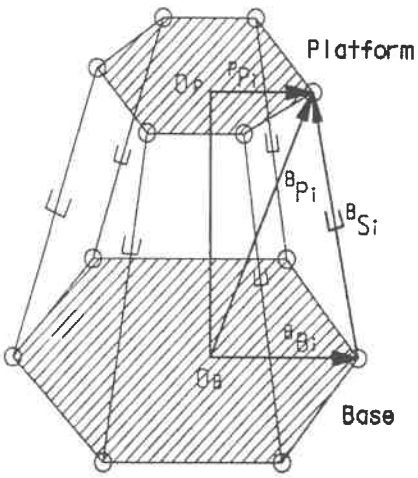

Fig. 2: Principle of self-calibration on a Stewart Platform

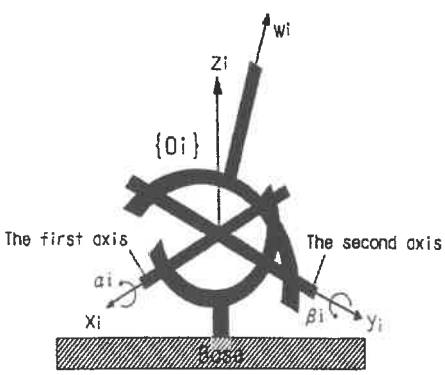

Fig. 3: The coordinate system of a univeral joint at the base

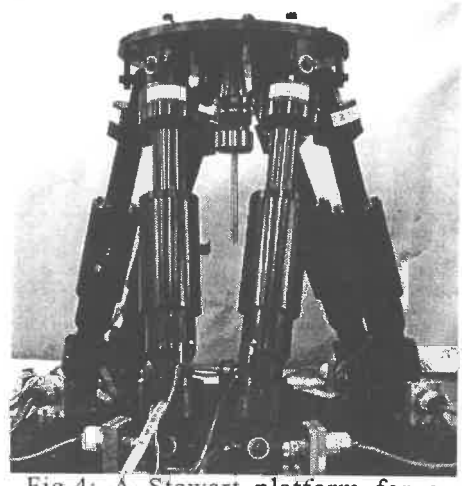

Fig.4: A Stewart platform for experimental verification

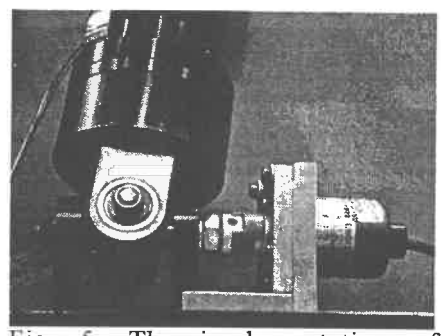

Fig. 5: The implementation of redundant sensor.

		Nominal value (mm)	Calibration (mm)
1	B_{ix}	50.3580	50.4264
	B_{iy}	285.5952	285.3575
	B_{iz}	38.0000	38.8386
	P_{ix}	89.3575	89.2791
	P_{iy}	106.5802	106.7169
	P_{iz}	-38.0000	-38.8386
	Δl_i	547.9565	546.2297

(B_{ix}, B_{iy}, B_{iz}): the coordinates of the joint on the base

(P_{ix}, P_{iy}, P_{iz}): the coordinates of the joint on the platform

Δl_i: the initial length of the ith link

Table 1: Kinematic parameters of loop 1

	Before calibration (degree)	After calibration (degree)
Loop 1	0.0771	0.0817
Loop 2	0.0974	0.0790
Loop 3	0.0736	0.0254
Loop 4	0.0760	0.0264
Loop 5	0.0886	0.0715
Loop 6	0.1448	0.0273

Table 2: Mean angular errors of the universal joints on base

Loop no.	1	2	3	4	5	6
Backlash (degreee)	0.0849	0.0599	0.0054	0.0069	0.0408	0.0592

Table 3: The backlash of the universal joint of each loop

Sampling and Measurement Uncertainty in Coordinate Metrology

Robert Edgeworth and Robert G. Wilhelm
Center for Precision Metrology
Department of Mechanical Engineering and Engineering Science
The University of North Carolina at Charlotte
9201 University City Blvd., Charlotte, NC 28223-0001

Introduction

In order for a measurement to be complete, it is necessary to know both the value of the measurand and the uncertainty of the result. Measurement process plans generally involve a compromise between the cost of inspection and the reliability of the measurement result. Since the cost of a failed inspection is usually orders of magnitude larger than the cost of the inspection itself, the critical issue is establishing that the measurement uncertainty is sufficiently small. In the case of coordinate measurement, the sources of uncertainty can be broadly divided into the categories of machine, environment, computation and workpiece.

Uncertainties attributable to the machine are the result of errors in the point coordinates reported by the measurement system over the course of the measuring process. Methods to quantify and minimize the magnitude of these errors are well known [1-4].

Environmental uncertainty is the result of deviations in temperature, pressure, humidity and vibration which affect the measurement system. Measurement and correction for these parameters is sometimes performed but nonuniformity throughout the work volume makes the practice difficult. The most common practice is isolation of the measurement system to minimize environmental uncertainties.

Computational uncertainties are measurement errors that appear after the point data has been processed by numerical algorithms to evaluate the measurement results. They may be the result of numerical representation errors, errors in the implementation of algorithms [4], or the result of interaction between fitting software and measured deviations [6, 7].

Workpiece uncertainty is the result of the nature of the coordinate measurement process. Discrete points are collected from a continuous surface and subsequently used to represent the complete surface. If the regions between sample points contain surface defects that are not represented by the sample points, the result will be an inaccurate evaluation of the surface [8,9]. Workpiece effects are **skewed**; The reported value is always less than the true form error.

This paper presents a model for the maximum error that can result from workpiece-sampling interaction in the case of uniformly distributed samples on a 2d section. The maximum error is a function of the wavelength of the workpiece form errors, the sampling spacing and the number of sample points collected. Extension of the method to evaluate the measurement of 3d surfaces is discussed..

Problem Formulation

To quantify the influence of sampling upon measurement uncertainty, numerical tests were applied to determine the maximum measuring error that could result from uniform sampling of an arbitrary surface with systematic form deviation. Sine waves of arbitrary frequency and phase are used to simulate deterministic errors. Figure 1 shows the parameters of interest for a uniform sampling pattern on a 2D profile. The nominal shape of the surface has been removed; Thus, perfect form is represented by a line through the zero point. It is assumed for the purpose of this work that there is no error involved with removal of the nominal surface.

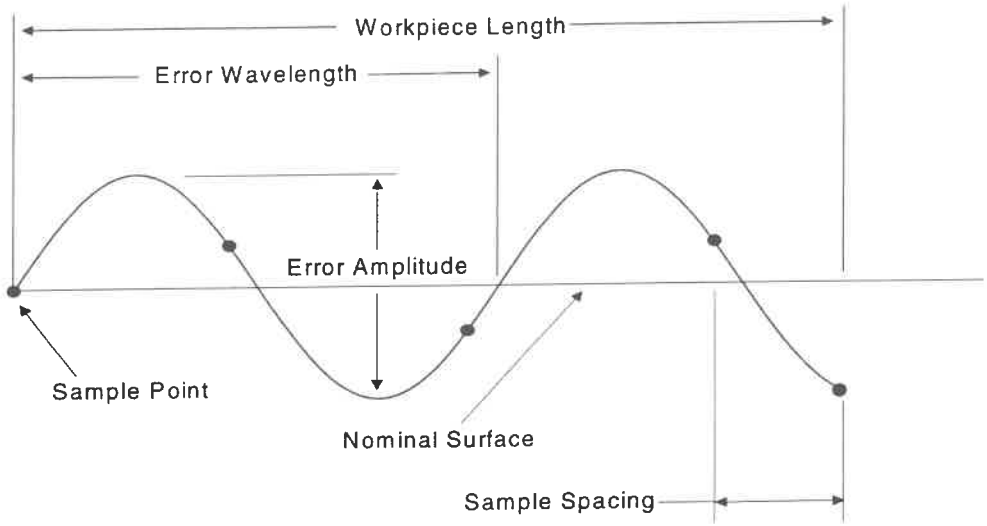

Figure 1: Sampling parameters

The principal parameters of the measurement are the sample spacing (ϕ), the number of samples (N), the error wavelength (T) and the amplitude of the error (A). Table 1 is a list of symbols used in this paper. Each measurement can be represented as a set (M) of values representing the deviation from the nominal surface. The measured deviation of the surface is the difference between the maximum and minimum values of the set M. Since the sampling pattern and the phase of the surface error are independent, the measured deviation will vary depending upon the phase relation (θ).

Table 1: List of Symbols

PARAMETER	SYMBOL
Sample Spacing	ϕ
Error Wavelength	T
Error Amplitude	A
Number of Samples	N
Set of Measurements	M
Phase Relation	θ
Sampling Ratio	T/θ, T_N
Measured Deviation	D
Measurement Error	ε

To simplify analysis of the problem, the parameters are non-dimensionalized by defining the amplitude of the error to be 1 and defining the ratio between the error wavelength and the sample spacing to be the sampling ratio (T_N). The sampling ratio is the number of samples per wave of the error signal and a sampling ratio of 2 corresponds to the Nyquist interval. The measurement error due to workpiece form can then be found from:

$$M = \{\theta, \theta+\phi, .., \theta+N\phi\} \quad (1)$$

$$D = \text{Max}\,[M] - \text{Min}\,[M] \quad (2)$$

$$\varepsilon = 1 - D \quad (3)$$

The maximum error due to workpiece form can be found by numerically searching for the value of θ which results in the largest value of ε for a given sampling ratio and number of sample points.

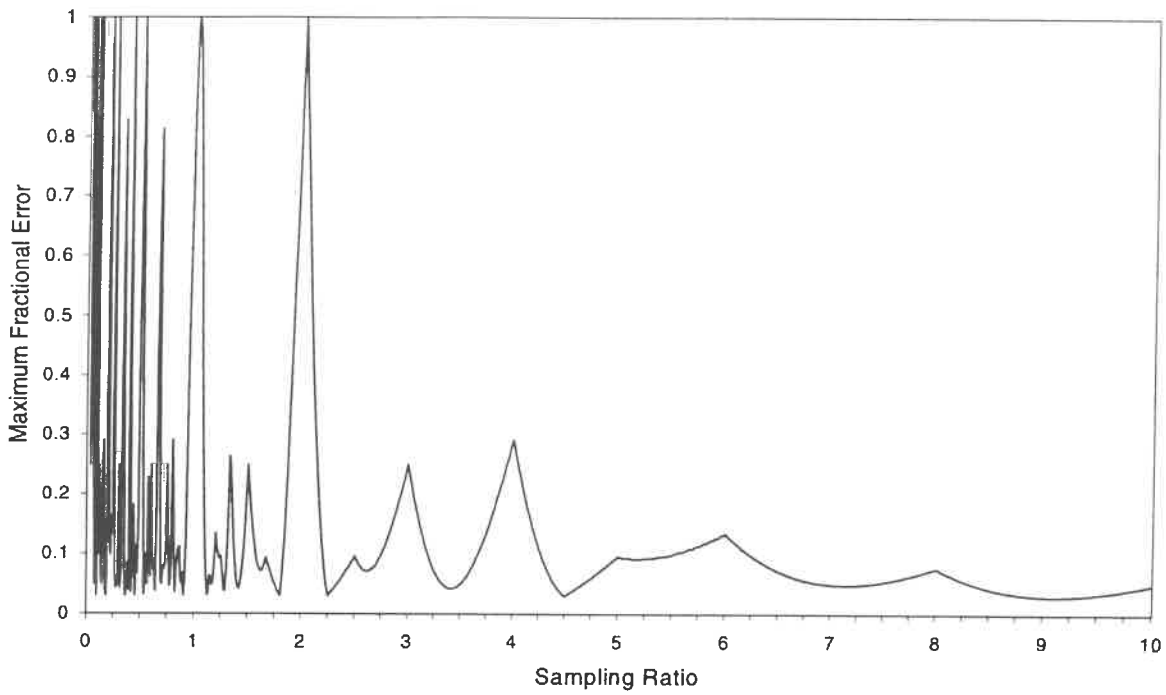

Figure 2: Maximum fraction error due to workpiece form error as a function of sampling ratio for 10 sample points.

Results

Figure 2 shows the influence of sampling ratio upon the maximum measuring error. The vertical axis indicates the maximum sampling error expressed as the fraction of signal amplitude that is unmeasured. The figure clearly shows that the amount of measurement error due to workpiece form decreases as the number of samples per wave grows beyond the Nyquist interval. Error wavelengths of greater than 8 times the sample spacing would be assured of being identified with less than 5% error due to workpiece form. The figure shows clear patterns between successive odd, even and fractional sampling ratios. Each error peak has a finite width; The error drops rapidly at values other than the integer ratios. The rate that the maximum error decreases as the sampling ratio changes is a function of sample size.

From the results of the numerical studies we can describe the following characteristics of maximum amplitude detection error due to workpiece form:

1. Sampling patterns that maintain a constant phase relationship with the error signal will have a nonzero maximum measurement error, regardless of sample size; Sampling ratios that can be expressed as integer fractions will have a maximum error peak.
2. The magnitude of the error peaks is dependent upon the odd or even number of samples per wave or set of waves and the sampling ratio.
3. As the sampling ratio changes from a peak value, the maximum error decreases at a rate proportional to the number of sample points and the sampling ratio.

The figure can be applied to specific measurement cases (with suitable sample sizes) by multiplying the sampling ratio by the spacing between sample points. The sampling ratio axis is then the form error wavelength in the same units as the sample spacing. Reading the maximum fractional error axis indicates the proportion of amplitude at the given wavelength that could be overlooked by the measurement process.

This method can be extended to 3d surface measurements trivially by the assumption that the surface errors can be represented by 2 sets of Fourier series in orthogonal basis directions. Such an assumption is most appropriate for parts manufactured with Cartesian coordinate systems. Surfaces that contain errors better represented by different basis functions such as suggested in the case of cylindrical holes by Henke et. Al. [11] would require the evaluation of maximum measuring error for the new basis functions. However, the variation in estimated maximum measuring error due to different basis sets is likely to be less than the variation due to the uncertainty in estimating the error frequencies that will be present.

Conclusions

A model for the maximum measurement error due to workpiece form error has been developed for uniform sampling patterns. The measurement error is a function of the ratio between the sampling interval and the form error wavelength, and the total number of samples collected

Acknowledgements

This work has benefited greatly from the exceptional research environment provided by the Center for Precision Metrology at UNC Charlotte and the Cameron Center for Applied Research. We would particularly like to thank Osborne Martin for implementing the numerical calculations in C code.
This material is based upon work supported by the National Science Foundation under Grant No. DMI-9457168, the UNC Charlotte Center for Precision Metrology Research Affiliates and the National Science and Engineering Research Council of Canada.

References

1. Knapp, W., Matthias, E., 1983, Test of the three-dimensional uncertainty of machine tools and measuring machines and its relation to the machine errors, Annals of the CIRP, 32/1:459-462
2. Phillips, S. D., 1995, Performance Evaluations, in *Coordinate Measuring Machines and Systems*, Bosch, J. A. *ed.*, Marcel Dekker, New York.
3. Balsamo, A., Di Ciommo, M., Mugno, R., Sartori, S., 1996, Towards instrument-oriented calibration of CMMs, Annals of the CIRP, 45/1:479-482.
4. Pfeifer, T., Spur, G., 1994, Task-specific guage for Inspection of coordinate measuring machines, Annals of the CIRP, 43/1:465-468.
5. Anthony, G. T., Anthony, H. M., Bittner, B., Butler, B. P., Cox, M. G., Drieschner, R., Elligsen, R., Forbes, A. B., Gross, H., Hannaby, S. A., Harris, P. M., Kok, J., 1996, Reference software for finding chebyshev best fit geometric elements, Precision Engineering, 19/1:28-36.
6. Shen, Y. L., Duffie, N. A., 1991, Uncertainties in the acquisition and utilization of coordinate frames in manufacturing systems, Annals of the CIRP, 40/1:527-531.
7. Phillips, S. D., Borchardt, B., Estler, W. T., Buttress, J., 1998, The estimation of measurement uncertainty of small circular features measured by coordinate measuring machines, Precision Engineering, 22:87-97.
8. Weckenmann, A., Knauer, M., 1998, The Influence of Measuring Stategy on the Uncertainty of CMM Measurements, Annals of the CIRP, 47/1:451-453.
9. Choi, W., Kurfess, T., Cagan, J., 1998, Sampling Uncertainty in coordinate measurement data analysis, Precision Engineering, 22:153-163.
10. Weckenmann, A., Eitzert, H., Garmer, H., Weber, H., 1995, Functionality-oriented evaluation and sampling strategy in coordinate metrology, Precision Engineering, 17:244-252.
11. Henke, R.P., Cassou, R. M., Summerhays, K.D., Baldwin, J. M., Brown, C. W., 1996, Methodologies for the evaluation of systematic form deviations for inside diameter cylindrical features and their relationship to process variables, Proceedings of the ASPE, 14/1:654-659

Thickness Correction for Edge Detection of Optical Coordinate Measuring Machines

Jiyou Fu and Robert Hocken
Precision Metrology Lab, University of North Carolina at Charlotte, Charlotte, NC 28223

Abstract: Edge detection is essential to ensure the accuracy of geometrical measurement in optical CMMs. In this paper, an edge model of a thick part is introduced and the approach to calculate the edge shift due to the thickness of the part is explained. In the end, the experimental data show that the bi-directional measurement error for parts with thicknesses larger than 3mm and measured at lens magnification 6.6 times is always near 3μm.

Key words: Optical CMM, OTF, edge shift, bi-directional measurement

1. Introduction

As the dimensions of microchip features shrink, the demand for high accuracy measurement in lithography grows rapidly. Optical coordinate measuring machines (CMM), also called video-based CMMs, are becoming widely used tools due to their non-contact and fast two-dimensional measurement [1]. In spite of many advantages, their measurement accuracy is degraded by improper illumination and characteristics of the part [2].

All measurements using optical CMMs are based on the coordinates of the measured points, specifically the edge position in the image. In bi-directional measurement, the variations in edge definition are added together when the two edges are taken from different sides, so the errors in bi-directional measurements are much larger than that from uni-directional measurement. This study focuses on bi-directional measurement, such as diameter measurement of ring gauges, width measurement of gauge blocks, etc.

Our test results have shown that the measurement variance due to different lighting conditions, such as top lighting and backlighting, is about 1μm for the same part. If the lighting intensity is controlled properly, the variance is less than 1μm. Surprisingly, we also found those the measurement error of a part is always about 4μm, no matter if its thickness is 5mm or 30mm. To explain why the same optical CMM, which can measure a thin part with error less than 1μm, produces such a constant bias error, an image acquisition model of an optical CMM will be introduced.

2. Image acquisition model of optical CMM [3]

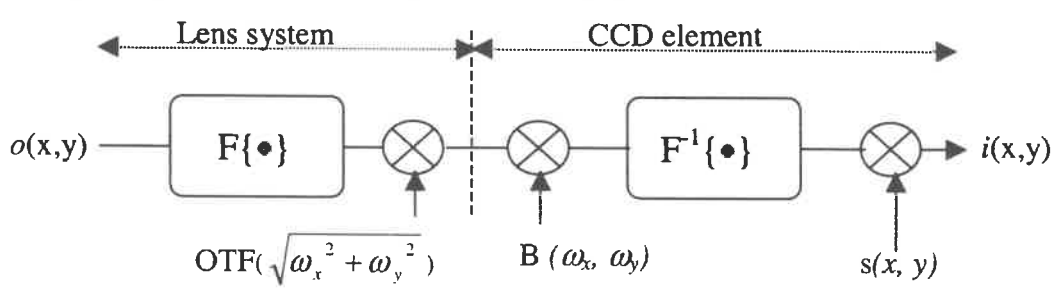

Fig.1 An image acquisition model of optical CMM

In this model, $o(x,y)$ represents an incoherently illuminated object. The diffraction-limited lens system acts as a low-pass filter, and its filtering effect can be described by the Optical Transfer Function OTF[4]. The OTF depends on the numerical aperture of the objective lens divided by the wavelength of light (NA/λ) and on the degree of defocusing. F{•} denotes the Fourier transform. The image intensity after the lens system can be obtained by multiplying the object intensity in the Fourier domain by the OTF.

The input $o(x,y)$ filtered by the OTF is then sampled by the pixels of the CCD elements. This can be expressed by first a convolution with a block function representing the size ($P_{size_}x \times P_{size_}y$) and shape of the pixels followed by a multiplication with the rectangular grid of unit impulse function P (ω_x, ω_y) (spaced by $P_{spacing_}x \times P_{spacing_}y$) representing the position of the pixels. The convolution with a block function in the spatial domain equals to a multiplication with $B(\omega_x, \omega_y)$ in the Fourier domain, where $B(\omega_x, \omega_y)$ is the Fourier transform of the block function b(x,y). The result is then sampled by multiplication by s(x,y), a rectangular grid of the unit impulse function δ(•), which is the same as a convolution with $S(\omega_x, \omega_y)$ in the Fourier domain. The block and sample functions in the both spatial and Fourier representation are listed in Table 1.

Table 1 the block function of a CCD pixel and the sampling function of CCD surface both in spatial and Fourier representation

Spatial domain	Fourier domain
$b(x,y)=\begin{cases}1 & \lvert x\rvert<\frac{P_{size_x}}{2}, \lvert y\rvert<\frac{P_{size_y}}{2}\\ 0 & else\end{cases}$	$B(\omega_x,\omega_y)=\sin c(P_{size_x}\cdot\omega_x)\sin c(P_{size_y}\cdot\omega_y)$ here, sinc(x)=sin(π·x)/x
$s(x,y)=\sum_{m,n}\delta(x-m\cdot P_{size_x})\cdot\delta(y-n\cdot P_{size_y})$	$S(\omega_x,\omega_y)=\sum_{m,n}\delta(\omega_x-m\cdot P_{size_x})\cdot\delta(\omega_y-n\cdot P_{size_y})$

m, n are pixel number along horizontal and vertical direction of CCD chip respectively.

Assuming the object is thin with respect to the depth of the focus of the optical system and treated it as two-dimensional (2D), the Fourier representation of the given model is:

$$I(\omega)=\{O(\omega)\bullet OTF(\omega)\bullet B(\omega)\}\otimes S(\omega) \qquad (1)$$

here $\omega = (\omega_x, \omega_y)$, indicating continuous spatial frequency in reciprocal meters. And ⊗ denotes a convolution.

3. Edge formation model for a thick part

Once the part becomes thicker than the depth of the field of the objective, the effect of finite thickness will change the intensity distribution in the edge transition area and therefore introduce measurement error using current edge detection methods, such as derivative and threshold methods. A thick part can be modeled as a stack of 2D object planes separated along the z axis by small intervals, Δz. The image of each object plane at the CCD surface is degraded by the OTF at varying degrees of focus. Thus the image is a sum of information from in focus as well as out of focus object planes[5]. This relation can be modeled with the equation

$$I_{thick}(\omega) = \sum_{j=0}^{j=d/\Delta z} \{O(\omega, j\Delta z) \bullet OTF(\omega, j\Delta z) \bullet B(\omega)\} \otimes S(\omega) \qquad (2)$$

here we assume the part has the thickness d and the object plane at j = 0 is where the CCD camera is focused.

In order to compensate for the error due to the thickness of part, the relation between edge shift and part's thickness is required. To avoid calculating the complex $OTF(\omega, j\Delta z)$ and Fourier transformation, we built up the new $I_{thick}(x,y)$ by adding all the intensity distributions of edge transition area at consecutive $j\Delta z$ positions. Clearly, the width of edge-transition area W_j increases as the out of focus $j\Delta z$ increases. Also, W_0, the width of edge transition area at the focus plane, is the smallest one. Knowing that the intensity decreases at the squared ratio of W_j/W_0, $(W_j/W_0)^2$ should be used as the weight coefficient when adding the intensity. Supposing the edge position at $j\Delta z$ plane as P_j, we define the edge shift at $j\Delta z$ plane is $E_j = P_j - P_0$. Thus the relation between edge shift and part's thickness $T(d)$ could be calculated by

$$T(d) = \frac{\sum_{j=0}^{j=d/\Delta z} \left(\frac{W_j}{W_0}\right)^2 \cdot E_j}{\sum_{j=0}^{j=d/\Delta z} \left(\frac{W_j}{W_0}\right)^2} \qquad (3)$$

4. Experiment and result

By using an *Voyager* 12×12 optical CMM [6] with lens magnification 6.6, NA=0.185, and CCD size 11μm, we took 200 images of a very thin edge pattern (thickness around 0.1μm) at consecutive z positions with the interval Δz = 0.01mm and backlight intensity 70 units. Starting from the focus position, the total z travel range is 2mm. For each image, the edge position P_j was found by the derivative method and its edge shift E_j equals to(P_j - P_0). The width of edge transition area W_j can be found by counting the pixel number in the edge transition area. To simplify W_j's calculation, we treated W_j as a arithmetic series due to the equal z interval. By fitting the previous W_j series, we obtained the new W_j series with the common difference about 0.6 pixel. Then the edge shift $T(d)$ could be calculated by formula (3). All data at each z position were the average results from 10 measurement of the same image(Table 2).

Table 2 Edge shift data

$j\Delta z$ (mm)	E_j (pixel)	W_j (pixel)	$T(d)$ (pixel)
0	0	2	0
0.01	0.03951	2.6	0.014688
0.02	0.080085	3.2	0.027574
0.03	0.141876	3.8	0.041588
0.04	0.16683	4.4	0.052082
...	...	...	...
1	11.99884	62	0.56989
1.01	11.05717	62.6	0.572724
...	...	...	...
1.9	18.33217	116	0.77231
1.91	20.02384	116.6	0.773791
...	...	...	...

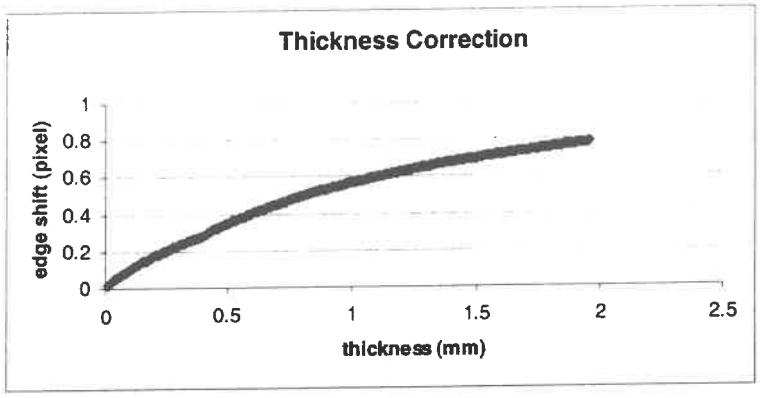

Fig.2 Relation between the edge shift and the thickness of a part

Figure 2 shows the thickness correction curve for this lens. By further extending the curve with geometrical progression the edge shift will converge to around 0.83 pixel, which means the maximum thickness compensation is about 2.8μm for this specific measurement configuration.

5. Conclusion

Depending on the illumination conditions and characteristics of the part, measured edge position can shift. The thickness of a part may also introduce larger measurement errors than the illumination. Based on the edge formation model of a diffraction-limited optical system, thickness correction plot which describes the relation between the edge shift and the thickness can be obtained by summing the edge shifts at varying degrees of defocusing. For the lens magnification 6.6 and NA=0.185 under backlighting 70 unit, the edge shift increases from zero to 3μm as the thickness grows from zero to larger than 3mm.

Acknowledgment: Help from Warren Lin at GSI Lumonics Inc. is gratefully acknowledged.

Reference:

[1] Garces A. et al, "Performance Test Procedures for Optical Coordinate Measuring Probes", Final Project Report, Part I, European Communities Brussels Contract No. 3319/1/0/159/89/8-BGR-D (30), July 1993
[2] Thakkar H.E, "Characterization of Hybrid Coordinate Measuring Machines", Master Thesis, UNC Charlotte, 1998
[3] Frank R Boddeke, Lucas J van Vliet, "Autofocusing in microscopy based on the OTF and sampling", Bioimaging, 2 (1994) 193-203
[4] Goodman, Joseph W., "Introduction to Fourier optics", McGraw-Hill Inc., 1988
[5] Michael A. Oliva, Miguel Bravo-Zanoguera, Jeffrey H. Price, "Filtering out contrast for microscopy autofocus", Applied Optics, Vol.38, No.4, p638-646, February 1999
[6] "Software manual: Voyager software version 5.0", GSI Lumonics Inc., 1997

Modeling the Low Order Temperature Dependant Errors of Machine Tools

Jeremy J. Kroll, Steven R. Patterson

Center for Precision Metrology
Department of Mechanical Engineering and Engineering Science
University of North Carolina at Charlotte, Charlotte, NC 28223

Introduction

Many machine tools are used in less than optimal environments. Certain errors of machine tools change with the ambient temperature. The temperature dependence of the quasistatic errors of machine tools is a contributor to volumetric error. We propose the use of low order models to correct temperature dependant errors. The use of such models could improve the accuracy of machine tools used in uncontrolled environments. By low order, we mean the errors can be modeled by polynomials of less than third order with respect to temperature.

The effect of geometric errors on part accuracy has been established in industry. Calibration tools[1] to map the geometric errors of machine tools are frequently used. This paper discusses the effect changes in temperature have on the quasistatic errors of a machine tool. Quasistatic thermal errors occur when the environment changes and the machine reaches equilibrium in its new surroundings. Experimental effective coefficients of expansion have been calculated for the scales of a Monarch VMC-45 machine tool. The effects of temperature changes on squareness errors have also been measured. . McClure[2] shows that thermal effects are linear dynamic processes. These results show that quasistatic thermal effects are also linear and can be modeled as low order errors.

Data was acquired for a Monarch VMC-45 machine tool which is located within a temperature-controlled room. Measurements were made using a Hewlett Packard 5528A Laser and Optics and a Federal 432P-58 Electronic Level.[4] Machine temperature was measured using 20 strategically placed thermistors. Three axis quasistatic error models[3] were created at three distinct temperatures. The machine was allowed to reach equilibrium before error measurements were taken. The temperature stability of the room was typically better than 1°C over the duration of the data acquisition. Once the room temperature reached a given value, the machine was allowed to soak out for more than 12 hours before error measurement.

Experimental Results

In machining, the expansion of the position feedback device will affect the overall accuracy of the machine. To account for this affect, the temperature dependence of linear displacement should be modeled and corrected. The Monarch VMC-45 is equipped with glass scales for position feedback. The manufacturer's value for expansion of these scales is 8.5 ppm/°C. Temperatures of the scales were measured using thermistors. Linear displacement accuracy data, which was not corrected for scale material expansion, was fitted with linear least squares method. The slopes of the fits were plotted versus the temperature of the scales. The slopes of these plots are the measured expansion coefficients of the scales. Values for the effective expansion coefficients are shown in table 1. The X and Y axes measured coefficients match the manufacturer's value well. The measured Z axis coefficient differs by more than 20 percent. The effective expansion coefficient calculated here is a lumped coefficient for the particular

machine axis. It does not give information for the expansion of the scales alone, since it is effected by thermally induced variations in any part of the overall metrology loop (e.g. scale mounting hardware).

Table 1: Experimental linear scale expansion coefficients

Axis of Motion	Expansion Coefficient (ppm/°C)
X	8.7
Y	8.2
Z	6.7

Upon reaching machine equilibrium, the machine error mapping was performed, including face diagonal displacement measurements. A full machine error model was created for each temperature using homogeneous transformation matrices.[3] Figure 1 and 2 show typical error plots for all errors except squareness. Figure 1 shows straightness error for three equilibrium temperatures. The straightness errors of the Monarch vary less than 2 microns over the 10°C temperature change. Figure 2 shows the average linear displacement accuracy for three temperatures after the application of the effective expansion coefficient. When the effective expansion coefficient is applied, x-axis average linear error shown in figure 2 varies less than 2 microns with a 10°C change in temperature. Without the expansion correction each average plot has a slope that increases linearly with temperature. The spread of the average error for the angular errors across the three temperatures was 2 arcseconds.

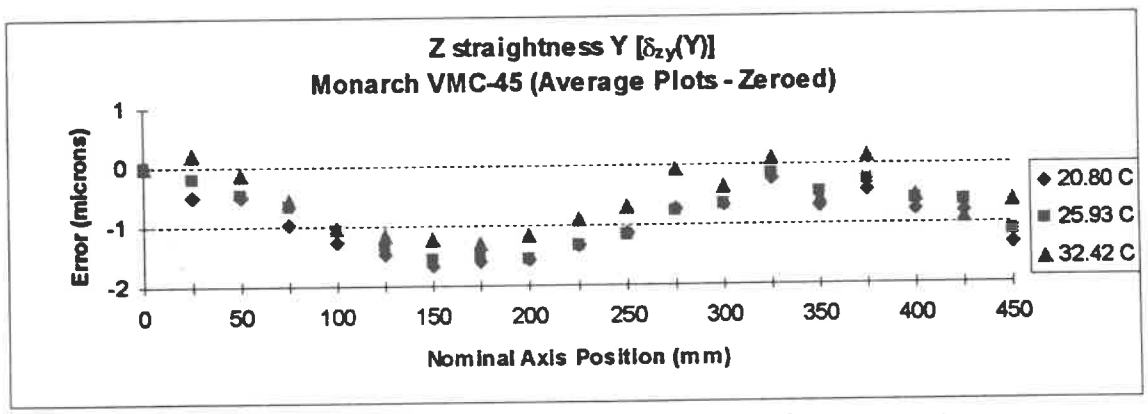

Figure 1: Typical average error plot showing error at three temperatures

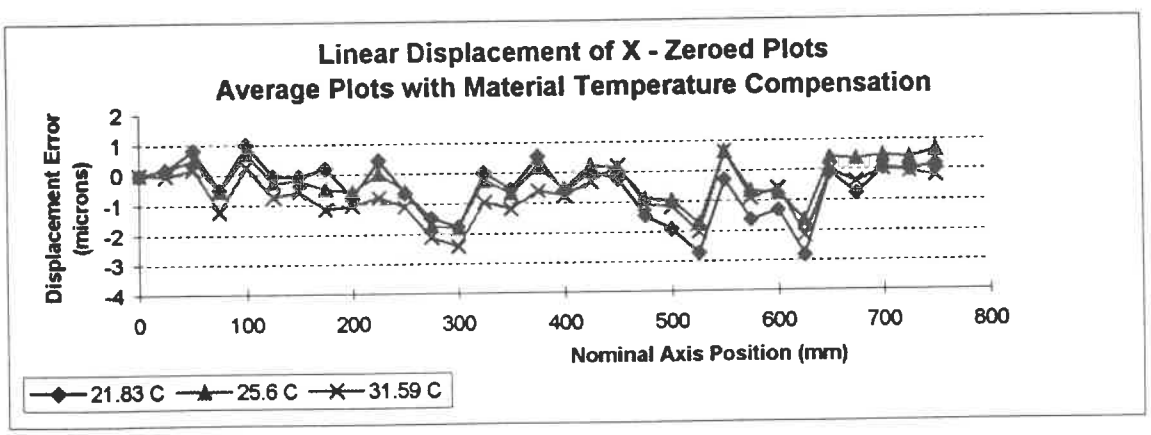

Figure 2: Linear displacement accuracy of x-axis shown for 3 temperatures.

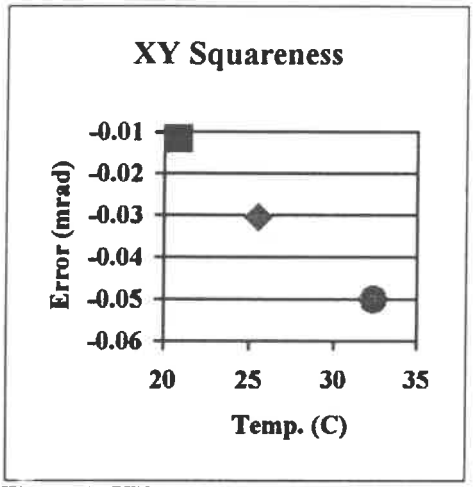

Figure 3: XY squareness vs. temperature

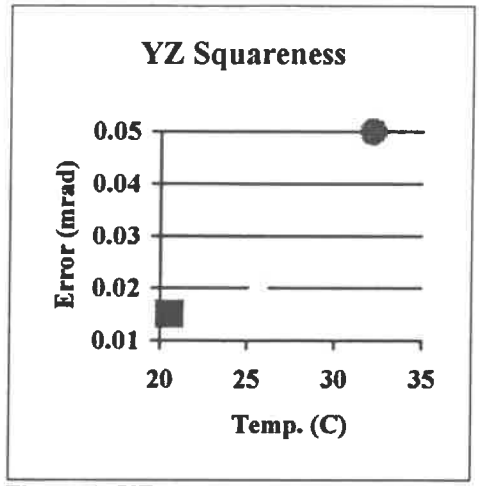

Figure 4: YZ squareness vs. temperature

Squareness errors were calculated using face diagonal measurements.[5,6] Using all errors except squareness, the homogeneous transformation matrices model[3] was created and the diagonal displacement measurements were corrected. From geometry, the deviation from 90° of one axis to the other in the plane of the diagonal was calculated. Figure 3 shows that the XY squareness of the Monarch changes linearly with temperature. The two measurements at 25°C, in figure 3, were separated by 23 months, indicating the stability of the machines thermal rèsponse. The YZ squareness, in Figure 4, could be non-linear, but is still low order in nature.

Conclusion

All quasistatic machine tool errors, except linear displacement accuracy and squareness, of the Monarch VMC-45 are stable with temperature as described in the results. This means that the spread of the average data for each temperature was on the order of the measurement uncertainty. This result allows the use of the same errors in the machine model at any temperature, within the testing temperature range.

The linear displacement accuracy can be used in the general model if the correct coefficient of thermal expansion is known. It has been shown that the thermal expansion of positioning accuracy, may not always follow the direct thermal expansion of the feedback device.

Squareness has been shown to vary with temperature. Although the variations are low order, the model should include a temperature portion. More study needs to be done to better quantify the quasistatic thermal squareness error.

References

[1] Precision Engineering Laboratory UNC Charlotte, *Software Correction of Precision Machines*, National Institute of Standards and Technology Report NIST-60NANB2D1214, 1993.
[2] McClure, E. R., *Manufacturing Accuracy Through the Control of Thermal Effects*, Lawrence Livermore National Laboratory Report UCRL-50636, 1969.
[3] Sethupathi, R. B., *Reduced Polynomial Representation for Machine Error Data*, Master's Thesis, UNCC, 1996.

[4] *Methods for Performance Evaluation of Computer Numerically Controlled Machining Centers,* ASME B5.54-1992, The American Society of Mechanical Engineers.
[5] Estler, W. Tyler, Magrab, Edward B., *Validation Metrology of the Large Optics Diamond Turning Machine*, U.S. Department of Commerce, NBSIR 85-3182®, Final Report, 1985.
[6] Zhang, G., Veale, R., Charlton, T., Borchardt, B., Hocken, R., "Error Compensation of Coordinate Measuring Machines," *CIRP Annals*, 1988.

IMPROVING MACHINE TOOL ACCURACY THROUGH AUTO CALIBRATION

Michael C Lee, Placid M Ferreira
Department of Mechanical and Industrial Engineering
University of Illinois at Urbana-Champaign, Urbana, IL

Key words: machine tool accuracy, self calibration, repeatability, coordinate system transformation, linear optimization techniques, transitivity, least square approximation, Chebyshev approximation, metrology

INTRODUCTION

Auto calibration (also known as self calibration) is a technique of calibrating a machine tool based on the repeatability and the metrological capability of the machine tool itself. Whereas a conventional calibration scheme requires an artifact with precisely positioned grid points to which a machine visits and reads the coordinate values, the auto calibration does not require such an accurate artifact. Therefore, the returned coordinate values from the machine are combined effect of the errors of the machine tool and the errors at each grid position on the artifact. However, by translating and rotating the artifact in a proper manner, these errors can be decomposed into two different sources. One of the advantages of this technique over a conventional one is that the accuracy of auto calibration algorithm does not depend on the accuracy of the artifact. Therefore, the use of an inaccurate artifact eliminates the difficulties, typically faced in a conventional calibration scheme, of fabricating an exact artifact and maintaining it. The use of an inaccurate artifact in auto calibration significantly reduces the cost of fabrication of an artifact as well as the maintenance cost.

A number of researchers have worked on auto calibration in the past, and this research work has its foundation in some of the major discoveries in auto calibration including Raugh's theory[1], Takac's transitivity[3], and Ye's results[3,4]. This research work investigates possible improvements on these earlier works and tries to remedy some of the difficulties faced by former researchers. These difficulties include[4]: (1) algorithm computationally expensive due to nonlinear formulation, (2) solution inexact due to oversimplified formulation, and (3) algorithm unstable in the presence of random noise. Further, this work evaluates the possibility of using the L_∞ norm in addition to the L_2 norm.

AUTO CALIBRATION FORMULATION

The auto calibration equations are derived based on the series of homogeneous coordinate system transformations. A possible non-exact positioning (both translational and rotational) of the artifact for each successive placement is also considered, and these misalignment errors are solved simultaneously with the errors on the artifact and of the machine tool. A linearized system of equations is derived and used for computational efficiency.

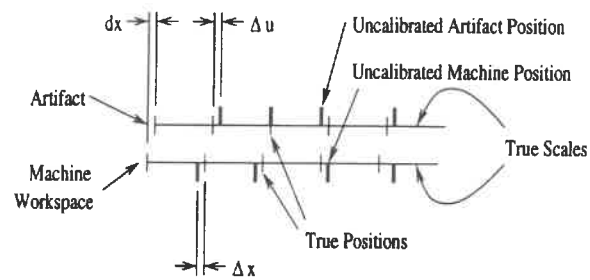

Figure 1 One-Dimensional Auto Calibration

Figure 1 illustrates the auto calibration in one-dimensional space. In this figure, the artifact and the machine workspace are misaligned by d_x at the origin. At each position i, the artifact and the workspace have errors Δu_i and Δx_i, respectively. Assuming the machine is reset at its origin, when the machine visits the mark position i on the artifact, the machine will return a value

$$r_i = i + \Delta u_i - \Delta x_i + d_x$$

If the artifact is translated one unit in positive x-direction relative to the machine workspace, the returned value from the machine at mark position i on the artifact becomes:

$$r'_i = (i + 1) + \Delta u_i - \Delta x_{i+1} + d'_x$$

These are the one-dimensional auto calibration equations that can be simultaneously solved for the errors, Δu_i and Δx_i.

In two-dimensional space, there are two such equations at each grid position, one each in x- and y-directions, as well as the translational misalignment errors, d_x and d_y, and the rotational misalignment error, θ. Based on Raugh's theory, in two-dimensional space, at least three different artifact placements are needed[1], and Ye has concluded that there are only four possible sets of three artifact placements when the rotation of artifacts are restricted to 90°[3,4]. The three placements (scenes) used here are (refer to figure 2 below):

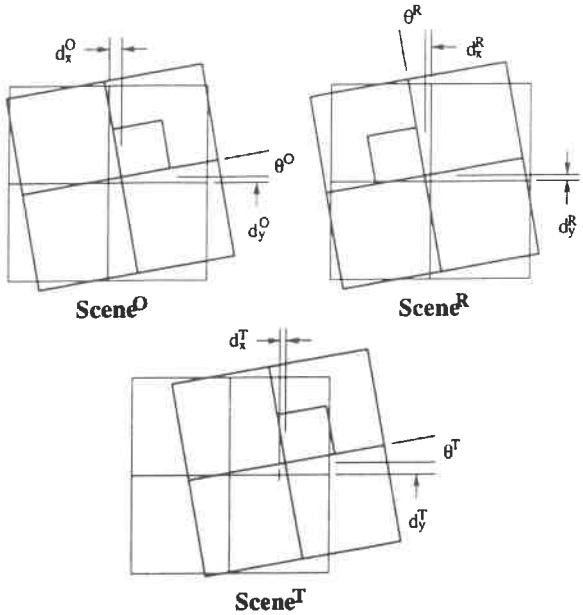

Figure 2 Three Artifact Placements in Two-Dimensional Auto Calibration

1. *Scene*^{O} when the origin of the **u-v** system (artifact) is placed over the origin of the **x-y** system (workspace) without rotation, 2. *Scene*^{R} when the artifact is rotated 90° counter-clockwise from *Scene*^{O} about the origin of **x-y** system, and 3. *Scene*^{T} when the artifact is translated one unit in the positive x-direction in the workspace from *Scene*^{O}. For simplicity, the grid positions are assumed to be unit distance away in both principle directions with the origin at the center on both the artifact and the machine workspace such that each grid position can be subscripted with $[i, j]$ pair.

Using homogeneous coordinate system transformation from the **u-v** system to the **x-y** system, the coordinate descriptions of the mark positions on the **u-v** system can be transformed to coordinate descriptions on the **x-y** system. For example, for *Scene*^{O}, the true coordinate description of the $[i, j]$ mark position of the artifact on the **x-y** Cartesian system is:

$$\begin{bmatrix} x \\ y \\ 1 \end{bmatrix} = \begin{bmatrix} 1 & 0 & d_x^O \\ 0 & 1 & d_y^O \\ 0 & 0 & 1 \end{bmatrix} \cdot \begin{bmatrix} Cos\,\theta^O & -Sin\,\theta^O & 0 \\ Sin\,\theta^O & Cos\,\theta^O & 0 \\ 0 & 0 & 1 \end{bmatrix} \cdot \begin{bmatrix} u_{i,j} \\ v_{i,j} \\ 1 \end{bmatrix}$$

Further, the pair of values returned by the machine is:

$$\begin{bmatrix} r_{x,i,j}^O \\ r_{y,i,j}^O \\ 1 \end{bmatrix} = \begin{bmatrix} x \\ y \\ 1 \end{bmatrix} - \begin{bmatrix} \Delta x_{i,j} \\ \Delta y_{i,j} \\ 1 \end{bmatrix}$$

Substituting the expressions for $[x\ y\ 1]^T$, $u_{i,j} = i + \Delta u_{i,j}$, and $v_{i,j} = j + \Delta v_{i,j}$ yields

$$\begin{bmatrix} r_{x,i,j}^O \\ r_{y,i,j}^O \\ 1 \end{bmatrix} = \begin{bmatrix} (i+\Delta u_{i,j})Cos\theta^O - (j+\Delta v_{i,j})Sin\theta^O + d_x^O - \Delta x_{i,j} \\ (i+\Delta u_{i,j})Sin\theta^O + (j+\Delta v_{i,j})Cos\theta^O + d_y^O - \Delta y_{i,j} \\ 1 \end{bmatrix}$$

after concatenation. With the small θ^O and negligible second order terms, the above nonlinear equations can be linearized as follow:

$$\begin{bmatrix} r_{x,i,j}^O \\ r_{y,i,j}^O \\ 1 \end{bmatrix} = \begin{bmatrix} i + \Delta u_{i,j} - j\theta^O + d_x^O - \Delta x_{i,j} \\ i\theta^O + j + \Delta v_{i,j} + d_y^O - \Delta y_{i,j} \\ 1 \end{bmatrix}$$

where $-(N\text{-}1)/2 \le i, j \le (N\text{-}1)/2$ for N by N grid. Similarly, for *Scene*^{R},

$$\begin{bmatrix} r_{x,i,j}^R \\ r_{y,i,j}^R \\ 1 \end{bmatrix} = \begin{bmatrix} -i\theta^R - j - \Delta v_{i,j} + d_x^R - \Delta x_{-j,i} \\ i + \Delta u_{i,j} - j\theta^R + d_y^R - \Delta y_{-j,i} \\ 1 \end{bmatrix}$$

where $-(N\text{-}1)/2 \le i, j \le (N\text{-}1)/2$.

For *Scene*^{T},

$$\begin{bmatrix} r_{x,i,j}^T \\ r_{y,i,j}^T \\ 1 \end{bmatrix} = \begin{bmatrix} i + \Delta u_{i,j} - j\theta^T + 1 + d_x^T - \Delta x_{i+1,j} \\ i\theta^T + j + \Delta v_{i,j} + d_y^T - \Delta y_{i+1,j} \\ 1 \end{bmatrix}$$

where $-(N\text{-}1)/2 \le i \le (N\text{-}1)/2 - 1$ and $-(N\text{-}1)/2 \le j \le (N\text{-}1)/2$. Note that for *Scene*^{T}, because of the one unit translation in positive x-direction of the artifact, there are no such values, $\Delta x_{i+1,j}$ and $\Delta y_{i+1,j}$ for $i = (N\text{-}1)/2$.

ASSUMPTIONS

This research work addresses some useful assumptions that can simplify the final system of equations and thus speed up the estimation processes while maintaining the accuracy of the error estimation. Some of the assumptions also relax the constraints that are typically imposed at the data observation stage and thus discourage frequent calibrations. These assumptions are:

- The origin of the superimposed Cartesian coordinate system on the artifact (**u-v** system) is placed exactly on [0,0] mark position such that this mark position does not have an error component. This translationally fixes the coordinate system on the artifact.
  - **Assumption 1.** $\Delta u_{0,0} = 0$
  - **Assumption 2.** $\Delta v_{0,0} = 0$
- The first principle axis (u-axis) of the superimposed Cartesian coordinate system on the artifact passes through $[(N\text{-}1)/2,0]$ such that this mark position does not have v-component error. This rotationally fixes the coordinate system on the artifact.
  - **Assumption 3.** $\Delta v_{(N\text{-}1)/2,0} = 0$
- The origin of the superimposed Cartesian coordinate system on the workspace (**x-y** system) is located at the origin of the artifact once the

artifact is placed in the workspace for the first scene ($Scene^O$). This translationally fixes the origin of the Cartesian coordinate system in the machine workspace. Further, the origin of **x-y** system does not have error components.

- **Assumption 4.** $d_x^O = 0$
- **Assumption 5.** $d_y^O = 0$
- **Assumption 6.** $\Delta x_{0,0} = 0$
- **Assumption 7.** $\Delta y_{0,0} = 0$

- The first principle axis (x-axis) of the superimposed Cartesian coordinate system on the workspace passes through $[(N\text{-}1)/2,0]$ such that this location does not have y-component error. This rotationally fixes the coordinate system in the workspace.
  - **Assumption 8.** $\Delta y_{(N\text{-}1)/2,0} = 0$
- The $[(N\text{-}1)/2,0]$ on the artifact does not have u-component error.
  - **Assumption 9.** $\Delta u_{(N\text{-}1)/2,0} = 0$

The assumption 9 is to provide the standard length information to the algorithm. The standard scale is a function of consensus[2]. Since auto calibration does not assume accurate grid positions on neither the artifact nor the machine tool, one fundamental requirement in auto calibration is to provide the information about the standard length to the algorithm. Auto calibration can be performed with an assumption that a distance between any two points on either the artifact or the workspace is the true distance. Which distance to choose is rather an arbitrary choice, but once the actual distance between the chosen points is identified, the dislocation errors of the positions on both the artifact and the workspace can be updated by the following:

$$\begin{bmatrix} \Delta u_{new,i,j} \\ \Delta v_{new,i,j} \\ 1 \end{bmatrix} = \begin{bmatrix} 1 & 0 & -i \\ 0 & 1 & -j \\ 0 & 0 & 1 \end{bmatrix} \cdot \begin{bmatrix} k & 0 & 0 \\ 0 & k & 0 \\ 0 & 0 & 1 \end{bmatrix} \cdot \begin{bmatrix} 1 & 0 & i \\ 0 & 1 & j \\ 0 & 0 & 1 \end{bmatrix} \cdot \begin{bmatrix} \Delta u_{old,i,j} \\ \Delta v_{old,i,j} \\ 1 \end{bmatrix}$$

$$\begin{bmatrix} \Delta x_{new,i,j} \\ \Delta y_{new,i,j} \\ 1 \end{bmatrix} = \begin{bmatrix} 1 & 0 & -i \\ 0 & 1 & -j \\ 0 & 0 & 1 \end{bmatrix} \cdot \begin{bmatrix} k & 0 & 0 \\ 0 & k & 0 \\ 0 & 0 & 1 \end{bmatrix} \cdot \begin{bmatrix} 1 & 0 & i \\ 0 & 1 & j \\ 0 & 0 & 1 \end{bmatrix} \cdot \begin{bmatrix} \Delta x_{old,i,j} \\ \Delta y_{old,i,j} \\ 1 \end{bmatrix}$$

respectively for the artifact and the workspace where

$$k = [\text{identified true length}]/[(N\text{-}1)/2].$$

CALIBRATION PROCEDURE

The assumptions addressed in the last section result in a rather simple calibration procedure. The calibration procedure for the auto calibration scheme discussed here is shown below:

1. Locate the artifact on the machine workspace such that the center of the artifact is located approximately at the center of the workspace to be calibrated.
2. Jog the machine to bring the machine end-effector to touch the mark position at the center of the artifact, and reset the machine such that this is the [0,0] position of the machine workspace. This is the $Scene^O$.
3. Jog the machine to visit all the mark positions on the artifact while recording the coordinate values returned by the machine.
4. To minimize the measurement noise, repeat step 3 multiple times.
5. Rotate the artifact 90° counter-clockwise. This is the $Scene^R$.
6. Perform steps 3 and 4.
7. Rotate the artifact 90° clockwise (to the original scene, $Scene^O$) and translate by one unit in positive x-direction. This is the $Scene^T$.
8. Perform steps 3 and 4.
9. Run the optimization algorithms (L_2 and L_∞ norm, described below) to identify the errors on the artifact and in the workspace.
10. Measure and identify the standard length of the choice, and update the errors obtained in step 9.

SOLUTION TECHNIQUES

In solving the system of calibration equations, two linear optimization techniques are employed; namely, the least square approximation (L_2 norm) and the Chebyshev approximation (L_∞ norm). The set of linear auto calibration equations derived for $Scene^O$, $Scene^R$, and $Scene^T$, together with the constraint equations obtained from 9 assumptions, can be summarized as:

$$\Sigma^n_{j=1}\, c_{i,j}\delta_j = r_i \qquad (i = 1, 2, \ldots, m)$$

where m = number of equations and n = number of variables, δ's. δ's consist of d_x's, d_y's, θ's, Δu's, Δv's, Δx's, and Δy's; and c's are the coefficients of these variables. r's are the values returned by the machine tool.

The optimization process is a process of identifying the error components (Δu, Δv) and (Δx, Δy) while minimizing the model prediction errors,

$$e_{model,i} = r_i - \Sigma^n_{j=1}\, c_{i,j}\delta_j^* \qquad (i = 1, 2, \ldots, m)$$

based on a given minimization criterion. Two minimization criteria can be formulated as follow[5]:

- **L_2 norm** minimize $\Sigma^m_{i=1}\,(r_i - \Sigma^n_{j=1}\, c_{i,j}\delta_j)^2$
- **L_∞ norm** minimize $max_i\, |\, r_i - \Sigma^n_{j=1}\, c_{i,j}\delta_j\, |$

COMPUTER SIMULATIONS

The auto calibration scheme discussed here has been computer simulated with an artifact with 7 by 7 matrix of points for two cases: with and without random measurement noise. The error components at each position on the artifact and in the workspace are randomly drawn from a normal distribution with

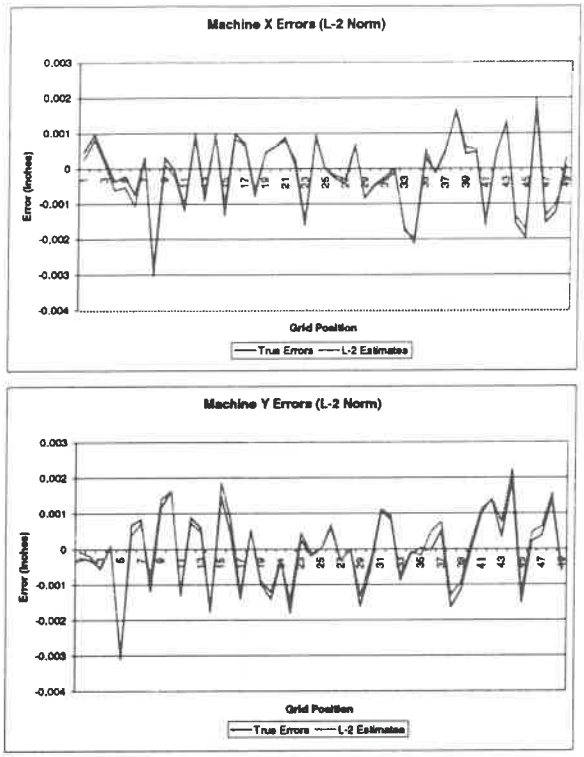

Figure 3 Estimation of Machine Errors with L_2 norm: random measurement noise with $\sigma_n = 0.0001$

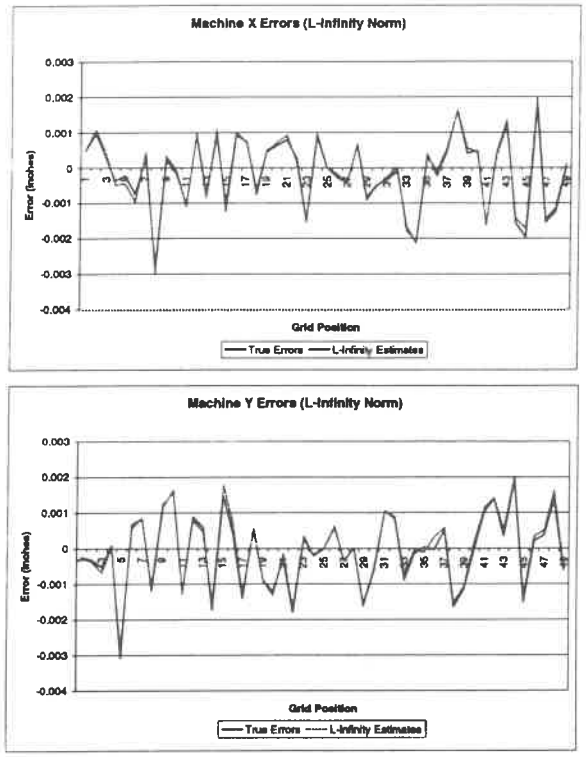

Figure 4 Estimation of Machine Errors with L_∞ norm: random measurement noise with $\sigma_n = 0.0001$

$\mu_e = 0$ and $\sigma_e = 0.001$ (inches). For the case when random measurement noise exists, the noises are randomly drawn from a normal distribution with $\mu_n = 0$ and $\sigma_n = 0.0001$ (inches).

The computer simulation results show the good performances both in accuracy and speed. Without random measurement noise, both estimation criteria returned the exact solution set. Other simulation results show that both estimation criteria closely approximate the errors in the presence of random measurement noise. Figures 3 and 4 show the estimation results using L_2 norm and L_∞ norm when there exists a random measurement noise. The estimation errors (differences between the true errors and the estimated errors) have $\sigma = 0.00018$ for the L_2 norm and $\sigma = 0.00012$ for the L_∞ norm. Note that the estimation errors for the L_∞ norm are about the same size as the random measurement noise.

For a 7 by 7 grid, the Chebyshev criterion returned the results almost instantly in all cases (with and without random noise). For the least square criterion, the coefficient matrix of the system of equations is constant for any N by N grid, and the pseudo-inverse of this matrix can be preprocessed and saved. This again allows an almost instant error estimation for the least square criterion.

CONCLUSION

The computer simulation results showed that the proposed scheme is accurate, computationally efficient, and stable in the presence of random measurement noise. In particular, the Chebyshev criterion showed performance of estimating the errors within the size of the random measurement noise.

References:

[1] Raugh M. R. Absolute Two-Dimensional Sub-Micron Metrology for Electron Beam Lithography: A Calibration Theory with Applications. *Precision Engineering*, 3-13, January 1985.

[2] Takac M. Self-Calibration in One Dimension. *SPIE*, 2087:80-86, September 1993.

[3] Ye J. et al. An Exact Algorithm for Self-Calibration of Two-Dimensional Precision Metrology Stages. *Precision Engineering*, 20(1):16-32, January 1997.

[4] Ye J. *Errors in High-Precision Mask Making and Metrology. Ph.D. Thesis.* Stanford University, Pasadena, California, 1996.

[5] Chvatal V. *Linear Programming*. W. H. Freeman and Company, New York, New York, 1983.

EXPERIENCES WITH THE MASTER AXIS METHOD FOR MEASURING SPINDLE ERROR MOTIONS

Eric Marsh[1], Robert Grejda[1], Don Martin[2]
[1] Penn State University, [2] Lion Precision, St. Paul, MN

ABSTRACT

In this paper, a new approach to machine tool spindle measurement is described. This approach, called the Master Axis Method, combines the benefits of traditional spindle testing with an artifact (e.g., synchronous and asynchronous error motions) with the ability to perform the same tests under load while at speed. For example, a load representing the cutting force in a turning operation can be conveniently applied during the characterization of a lathe spindle. The resulting error motions have been observed to vary in both magnitude and character under different loading conditions.

The Master Axis Method provides more appropriate test conditions than traditional artifact-based spindle measurements that are performed without load and traditional compliance tests that are performed at zero speed.

INTRODUCTION

Traditional spindle testing includes the measurement of error motions, compliance, and thermal drift to characterize an axis of rotation. The most familiar result of a spindle analysis is the rotating sensitive direction polar plot of synchronous error motion (in this case a combination of tilt and radial motion). The error motions are measured with capacitance gages targeting an artifact such as a steel ball.

An obvious shortcoming of the error motion tests is that the measurements are made without any load on the spindle. Presumably, the cutting forces will affect the spindle dynamics, and in fact, some milling spindles take cuts large enough to overcome the bearing preload. Bryan proposes a method of measuring spindle error motions with capacitance probes while machining which may be suitable for some classes of machine tools. Clearly, a next step in the characterization of machine tool spindles is the development of a general purpose method to measure error motions as a function of spindle load (cutting forces) and as a function of spindle speed.

In response to this need for a more suitable method of testing spindles, a team of engineers at Professional Instruments, Lion Precision, and Lorien have proposed the Master Axis Method of characterizing axes of rotation. The benefits of the method result from the elimination of artifacts such as the master ball that is used in traditional spindle error measurements. Instead, the method is based on the use of a precision air bearing spindle referred to as the master axis. The master axis typically has smaller error motion than an artifact because of the averaging effect of the high pressure air film, resulting in sub-nanometer error motions. The master axis also provides for the repeatable application of loads during spindle testing. Figure 1 shows a spindle under test with a master axis.

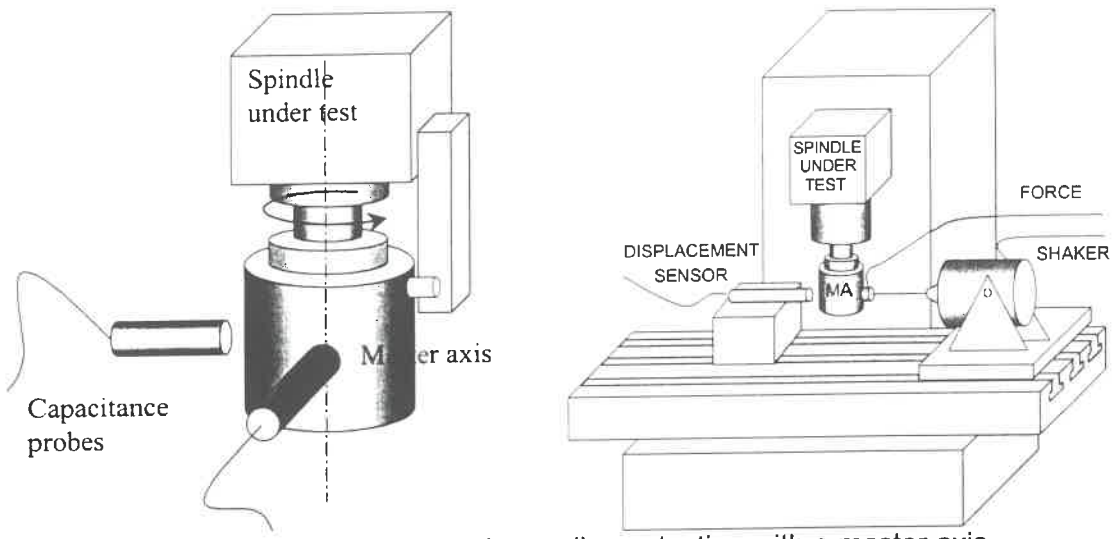

Figure 1: Error motion and compliance testing with a master axis.

The Master Axis Method offers several advantages to spindle measurement and characterization. First, the method is potentially more accurate than the best artifacts (e.g., polygons, balls, flats). For example, the roundness of a high quality ball is on the order of 25 nanometers, many times the error of a precision air bearing spindle. Second, the method allows both compliance testing and error motion measurement at speed and under load. For example, the compliance of a hydrodynamic spindle bearing may now be properly tested at speed and with very high accuracy. Third, the precision capacitance gages are targeting a stationary surface resulting in sub-nanometer resolution. Finally, the method is self-checking and reversal and multi-step techniques may be used to separate errors in high accuracy spindles from the master axis itself.

The Master Axis Method has led to the design and construction of several prototypes by Professional Instruments Co. The first prototype master axis spindle is embedded in a large granite fixture and features a rigidly mounted structure for holding the capacitance gages used in the testing. A high accuracy rotary encoder and high sensitivity Lion Precision capacitance gages are used along with dedicated software to measure the error motions of the spindle under test. Using this master axis, dubbed the Ultimate Spindle Calibrator, ultra-high precision air bearing spindles can be tested and characterized.

Other prototypes have been built by Professional Instruments to characterize lathe, milling machine, and grinder spindles. These prototypes feature built-in rotary encoders and may be set up on a given machine with one, two, or more capacitance gages depending on the desired information. These portable master axes have been used in the tests described in the rest of this paper.

EXPERIMENTAL SETUP

A series of experiments will be described to demonstrate the use of a portable master axis (PMA). The experiments are performed on a Bridgeport milling machine equipped with a ball bearing spindle. The spindle error motions were measured under a variety of speeds and loads to explore the spindle's behavior under a range of conditions. As expected, the spindle error motions vary with both speed and load. Not surprisingly, the error motions are not necessarily the worst at the highest operating speeds, although the vibrations generated by the spindle

drive do worsen with spindle speed. Table 1 outlines the parameters used in the spindle error motion measurements.

Table 1 Milling machine test parameters.

Spindle speeds:	
Low range	60, 140, 220, 300, 380, and 500 RPM
High range	500, 1400, 2300, and 3200 RPM
Capacitance probes	40 mV/micron
Spindle load	0, 20, 40, 60, 80, and 100 Newtons
Data capture rate	5000 points/rev
Capture period	50 revolutions

The PMA is fixtured in the milling machine using a rigid adapter. The static loop stiffness of the machine tool was measured independently to be only 3.5 N/micron. The loads were applied statically in the x-direction in a rough approximation of an average side milling force.

The three-dimensional plots shown in Figure 2 display the rotating sensitive direction error motions of the milling spindle at four different speeds. No attempt was made in this work to separate out radial, tilt, and axial error motion; the plots show a combination of radial and tilt measured 10 cm from the spindle nose. The spindle is observed to rotate at nearly constant speed through the individual tests (less than 0.5% variation in speed). The vertical axis shows the change that occurs with varying static loading in the x-direction of the machine. The severity of the effect of the radial force varies with spindle speed. For example, the data collected at 3200 RPM show the same general three lobed shape for each load case. However, the three lobes become much more pronounced as the load is increased. In fact, at 100 N radial load, the third lobe (bulge) is quite distinct.

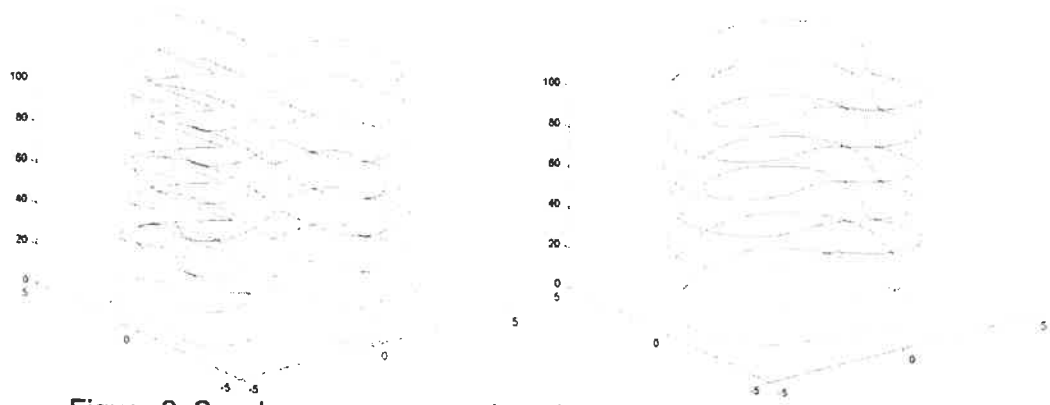

Figure 2: Synchronous error motions (microns) at 1400 and 3200 RPM.

Also seen in the figures is the dramatic difference in overall synchronous error motion at different spindle speeds. The data collected at 1400 RPM indicate error motions that are of substantially higher amplitude than even the error motions measured at higher speed. It is interesting to note that the first structural mode of vibration of this milling machine is around 100 Hz, which corresponds to roughly twice the 3200 RPM driving frequency.

Dynamic Stiffness Testing

The changes in dynamic behavior of high speed rotary systems are well known. The literature contains theoretical analyses of high speed machine tool spindles with angular contact bearings. Previously, experimental verification of these models was complicated by the difficulty of applying a time-varying load to a rotating spindle rotor. A special set of experiments was carried out using the portable master axis to investigate changes in dynamic stiffness of a rotating spindle.

Figure 3 shows the frequency response functions for two load levels, 20 N RMS and 40 N RMS. As expected, the nonlinear stiffness of the spindle bearings yields a slight difference in the apparent modal frequency of the third mode of vibration. Note that the other modes of vibration (structural) are unaffected.

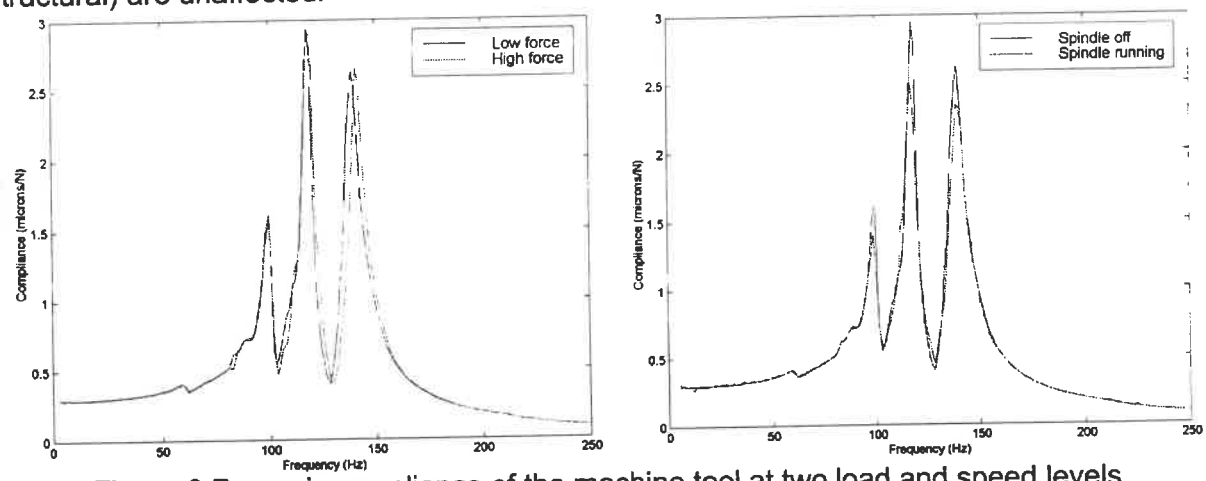

Figure 3 Dynamic compliance of the machine tool at two load and speed levels.

The spindle is then operated at moderate speed and the dynamic compliance again measured. Figure 3 shows two measurements of compliance, one with the spindle idle and the other with the spindle running. The RMS force level is 40 N in both cases. The modal frequencies are the same for both tests, however, the amplitude of the peaks is clearly affected by the spindle running.

Conclusion

The portable master axis holds great promise as a tool for axes of rotation metrology. Although it has not been explored in this paper, there is strong evidence to suggest that the uncertainty associated with the Master Axis Method of spindle calibration may be lower than the uncertainty of spindle calibrations performed with traditional artifacts.

As shown in the examples, the portable master axis can be used to measure spindle error motions not only as a function of speed, but also of load. The characteristics of the synchronous error motions were seen to vary with load on a low speed milling spindle. It is expected that further research with higher speed spindles will show even greater dependence with load.

Acknowledgements

The authors wish to thank Dave Arneson, Mel Liebers, and Dan Oss of Professional Instruments for their work in conceiving, designing, and building the master axis used in this testing.

Foundation for Dynamic Metrology of Machine Tools

Jimmie A. Miller, Robert Hocken, Vignesh Ramanan, Qibo Feng
Center for Precision Metrology (CPM)
University of North Carolina at Charlotte, Charlotte NC 28223

1. Introduction

The surge in demand for tighter tolerance machined parts has led to an increasing requirement that machining centers be specified with close accuracies measured according to accepted standards[1] and subsequently certified at regular time intervals. These standards typically specify measuring the positioning accuracy in the static state. As the tolerances are squeezed and machining techniques are developed for eliminating finishing processes, required machine performance will necessitate more detailed specifications for machines including the dynamic state.

Some data presented was acquired using a CPM designed and built, high speed (300 kHz) metrology acquisition system. Certain geometric error terms of two different machines were investigated both statically and dynamically. This presentation focuses on the observed dynamic errors with a brief description of the acquisition system mentioned later. Additionally, further dynamic error consideration is given which should affect non-axial machining along with some recommendations which should be included in any standard that includes dynamic measurement.

2. Dynamic Errors Observed

The inherent forces and moments of dynamic systems affect the characteristic positioning errors of a machine tool. The extent of these effects determines the necessity of measuring and/or compensating for them. Consider a table that is moving along a way. The orientation of this table may change by several arcseconds as it shifts from a static to dynamic state. Similarly, straightness errors have been observed to offset by many micrometers during the static to dynamic transition. Additionally, velocity errors along an axial direction may result in positioning errors as the machine contours along paths that are not along an axial direction.

2.1 Dynamic Observations with Commercial Instruments[2]

Dynamic measurement methods [interferometer based dynamic calibrators and telescoping ball bars (1 dimensional) and grid plates (2 dimensional)] are sensitive to motion induced errors. **Figures 1-3** show dynamic errors observed with a commercially available grid plate and ball bar on a machine having linear scale encoders which provide positional feedback information. **Figure 1** reveals one dimensional normal (perpendicular) error data taken with an telescopic ball bar while contouring along a circle at 1000 mm/min. Notice the error pattern along the circle. As the contour changes direction from an axial direction an oscillating error appears which increases in amplitude and spatial frequency as you approach a 45 degree contouring angle with respect to the axial directions. These errors are also visible when using a grid plate (two dimensional instrument), as shown in **Figure 2** for circular contouring at two different feedrates. The same pattern is observed along with a reduction in radial dimension. Using a grid plate to measure while contouring along a linear diagonal also reveals errors that have a definite spatial frequency as shown in **Figure 3** which also shows two sets of data taken using different machining parameters. One shows higher amplitudes at a specific frequency while the other shows a greater deviation from the commanded

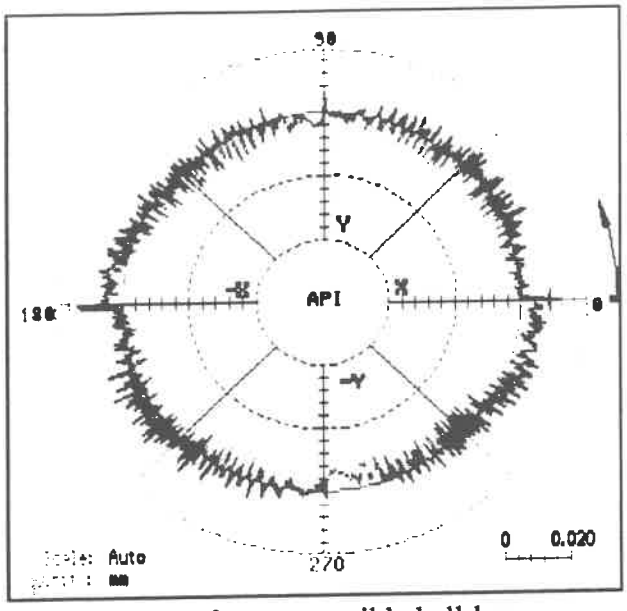

Figure 1. Data from extensible ball-bar revealing dynamic errors for 1.0 m/min feedrate.

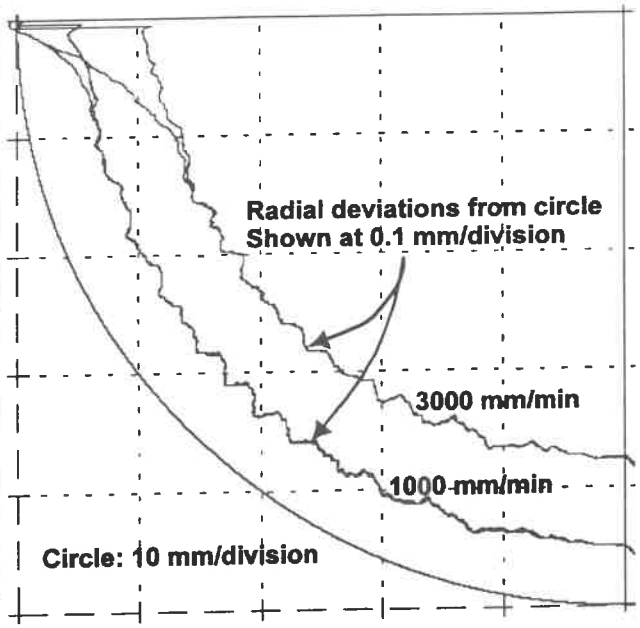

Figure 2. Grid plate measurement of circular contours with varied parameters.

path. Thus, the machining parameters of choice may be related to form and finish tolerances. The source of this error will be discussed later.

2.2 CPM Metrology Acquisition System Description

The present configuration of the acquisition system interfaces the digital servo port of a Zygo Axiom 2/20 laser system with two quadrature counters which employ the signals taken from either linear or rotary encoders which provide the reference to machine coordinates. The laser interface provided the capability of measuring either dynamic displacement accuracy, straightness error or angular error. The timing capabilities of the system provide for simultaneous (< 1μsec) triggering of individual components. Also capable of burst collection modes and FFT time analysis, the system provided comparison of the three input data types as a function of each other or time.

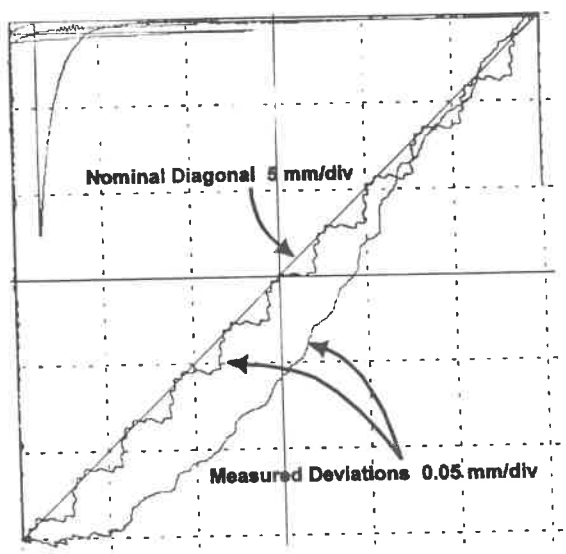

Figure 3. Grid plate measurement along a linear diagonal with varied parameters.

2.2 Dynamic Observations using CPM Metrology Acquisition System

Measurements utilized two vertical spindle machines, one with rotary encoders on the ballscrews and the other with linear scales. **Figure 4** is derived from data taken using the direct x and y

encoder readings as a function of time while contouring a circle at two different feedrates. The machine used has linear scale based encoders. Similar errors revealed by the ball bar and grid plate are shown with a component that changes in amplitude and spatial frequency while contouring in a non-axial mode. This is enough evidence to state that this error component is not a result of geometrical way errors. This is not enough evidence, however, to totally attribute this error to the control system. Since the spatial frequency does not seem to be dependent on the feedrate (and thus time related), other sources must be considered which may produce the error. This error component may be due to the linear displacement accuracy of the ball screw. Even if the motor turns the ballscrew at a constant velocity, the minute pitch changes in the ballscrew will cause velocity and acceleration errors in the associated carriage. Since the velocity (and thus position) changes, the vector sum of two independent carriages can produce an error component that is perpendicular to the direction of the contour. For a linear multi-axis operation, such as contouring along a diagonal, this effect can have minima and maxima amplitudes depending on the phase of the errors of the associated ballscrews. It has also been suggested by others[3] that the recirculation of the balls in the nuts may produce the same effect.

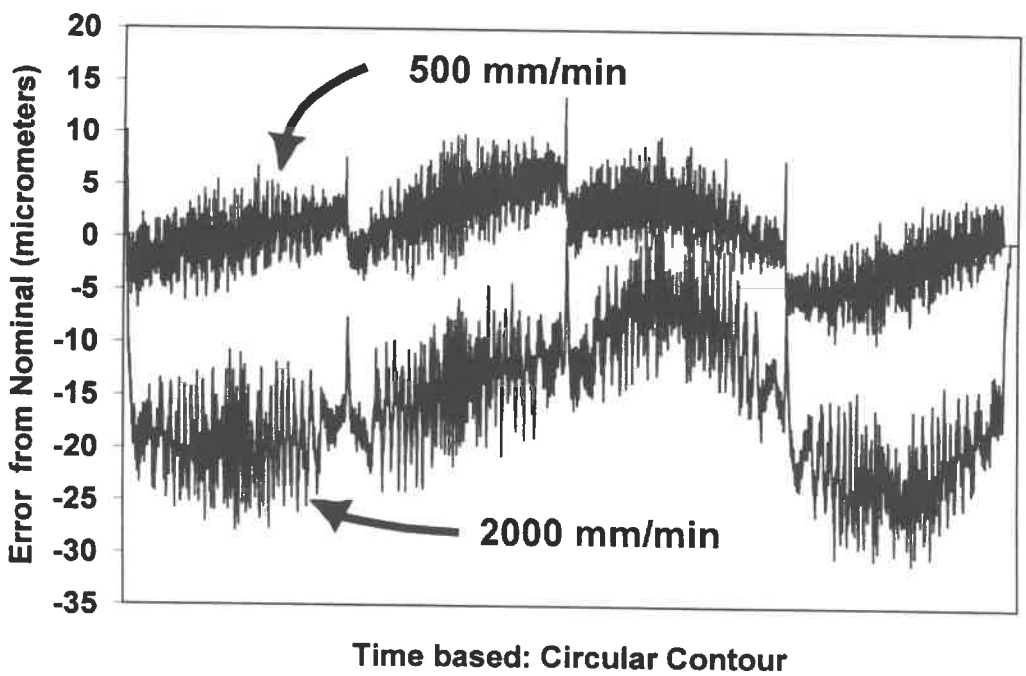

Figure 4. Time based data of encoder radial error from circular contour for two feedrates.

Additional analysis of data taken from a machine with angular encoders attached to the ballscrews revealed an offset between dynamic and static measurements such as those of **Figure 5** which shows an angular orientation jump of 2 arcseconds as the stage begins to move. This type of error has also been observed for straightness measurement where the effect has been observed to be as great as 25 micrometers. The question arises as to whether these errors are related to the

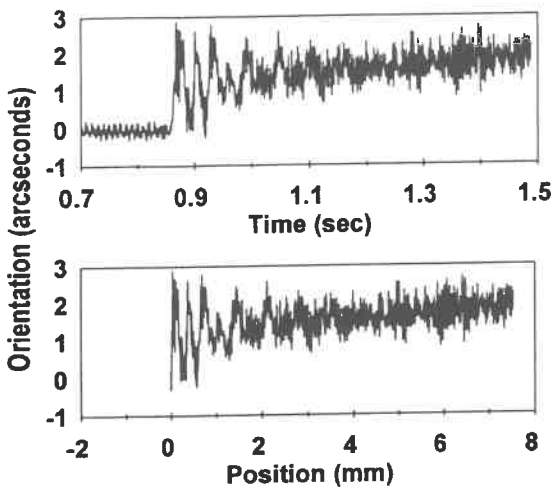

Figure 5. Angular reorientation of a table as it shifts from a static to a dynamic state.

carriage-way rigidity or the differences in servo control for each individual axis. An analysis was made of axis positions taken from direct encoder readings as the carriage began a diagonal displacement[4]. Although the position of the axes should be the same, comparison revealed a difference in encoder readings corresponding to a positioning error of about 24 micrometers between the axes. The particular error (believed to be servo driven) could result in a 17 micrometer form error in a production part within 1 mm of the beginning of a diagonal cut and an error in edge placement of about 9 micrometers.

4. Recommendations.

The following are recommended for precision manufacturing machines.

1. In addition to grid plate and telescoping ballbar techniques, additional dynamic specifications should be developed to ascertain contouring errors and static to dynamic transitions. This should be done along axes as well as along a diagonal to determine contouring capabilities.

2. Instruments should be built which allow for capturing machine encoder information in addition to other measurements. From this information, contouring correction of machines may be possible.

3. Machine tool builders should include an interface to each of their machine axes to facilitate dynamic measurements with commercial instruments that could relate external data with internal position and control. Machines could also be built which compare their desired positions with actual positions and update the process to account for current machine errors.

References

1. Such as: ANSI/ASME B5.54-1992 "Methods for performance evaluation of computer numerically controlled machining centers", ASME 1992.

2. Instruments used and similar ones available from the following suppliers:
Automated Precision, Renishaw, Heidenhain, and Hewlett-Packard.

3. Private communication with Dr. Steve Patterson, UNC-Charlotte.

4. Ramanan, Vignesh, "High Speed Machine Tool Error Measurements", Masters Thesis, University of North Carolina at Charlotte, 1998.

A New Method for Characterisation for the 5 DOF Spindle Volumetric Error Motions in Machine Tools

Heui Jae Pahk, Hyun Jang Shin

School of Mechanical and Aerospace Eng. Seoul National University, Seoul, Korea

1. Introduction

The accuracy performance of rotating spindle has been one of important key issues for the users and manufacturers of machine tools, and it has been widely acknowledged that there are 6 DOF (degree of freedom) error motions in the rotating spindle. The 6 DOF error motions are : two radial error motions, two tilt motions, one axial error motion, and one indexing error motions if required. Even though the 5 or 6 DOF spindle error motions are pretty well documented and procedured in many national and international standards, there have been needs or continued discussions for the performance characterisation for the spindle error motions, which can predict the real machining performance of machine tool spindles in more practical senses.

In this paper, a new method is proposed for characterizing the 3 dimensional performance of machine tool spindle, where two new terms of 3D error motions are introduced in addition to the existing 5 to 6 DOF spindle error motions: flatness error motion and cylindricity error motion. The flatness error motion of spindle can be calculated mathematically from the face motion of spindle in the rotating sensitive direction, which can predict the flatness tolerance of the machined. The cylindricity error motion also can be derived mathematically from the radial error motion in rotating sensitive direction along the axis of spindle movement, which can predict the cylindricity tolerance of the machined.

2. Spindle Error Motions

2.1 6 DOF spindle error motions

As mentioned in the introductory section, it has been widely acknowledged, e.g.[1], that a rotating spindle has 6 independant components, that is, degree of freedoms in error motions, and they are the radial error motions, tilt error motions, axial error motions, and the indexing error motion. A typical coordinate system for the spindle error motions is shown in fig.1, where the radial error motions, $X(\theta)$, $Y(\theta)$ are defined in the X, Y axis, respectively, and the axial error motion, $Z(\theta)$, in the Z axis. The rotary tilting motion can be defined in the X,Y axis, respectively, which are $\alpha(\theta)$,$\beta(\theta)$. The 6th component of spindle error motion is the indexing error motion of spindle, $\chi(\theta)$, which does virtually little or no effects on the machining accuracy of machine tool. The angle, θ, is the angle of rotation of spindle as it revolves. The radial error motions, $X(\theta)$,$Y(\theta)$, are generally defined from the combination of the pure radial error motions defined at the reference location and the tilting error motions, which are

$$X(\theta)=Xo(\theta)+L\beta(\theta) \quad (1)$$

$$Y(\theta)=Yo(\theta)-L\alpha(\theta) \quad (2)$$

where $Xo(\theta)$,$Yo(\theta)$ are the pure radial error motions in the X,Y directions, respectively, and L is the offset

distance between the two locations for the radial error motion observed.

2.2 3 dimensional spindle error motions proposed

In order to give more practical spindle performance explaining actual machining performance of machine tool spindles, two new error motions are proposed in this paper: cylindricity error motion and flatness error motion. When the rotating spindle is machining workpieces such as in drilling processes, the machining accuracy is greatly influenced especially by the radial error motions of spindle, and in this case, a third radial error motion, $R(\theta)$, can be defined in view of rotating sensitive direction[1], which is,

$$R(\theta)=X(\theta)\cos\theta+Y(\theta)\sin\theta \qquad (3)$$

where $R(\theta)$ simulates the actual radial error motion of spindle tool tip as it rotates.

As the practical machine tool spindle is going up and down with rotation, the concept of radial error motion in view of rotating sensitive direction can be expanded along the up and down spindle movement, which can be called as the cylindricity error motion. The cylindricity error motion, $C(\theta)$, can be derived mathematically by substituting eq(1),(2) into eq(3), that is,

$$\begin{aligned} C(\theta)&=(Xo(\theta)+L\beta(\theta))\cos\theta+(Yo(\theta)-L\alpha(\theta))\sin\theta \\ &=Xo(\theta)\cos\theta+Yo(\theta)\sin\theta+L(\beta(\theta)\cos\theta-\alpha(\theta)\sin\theta) \end{aligned} \qquad (4)$$

where the first two terms are the radial error motion in the rotating sensitive direction at the initial location, and the third and fourth terms indicate the variation of error motion along the cylindrical length, L. Eq(4) represents the error motion when the spindle machines cylindrical features, which can predict the cylindricity tolerance of machined cylinder when a radial fly cutter is equipped at the spindle.

For the better explanation on the practical performance of face machining of spindle, the flatness error motion can be introduced similarly.

When a spindle has the 5-6 DOF error motions, the accuracy of face machining is sensitively influenced by the axial error motion and the tilting error motions. When a face fly cutter is equipped at the distance r from the center of axis of rotation of spindle, the actual error motion of the cutter, $F(\theta)$, can be mathematically derived along the sensitive direction of face machining as the spindle rotates. That is,

$$\begin{aligned} F(\theta)&=Z(\theta)+\beta(\theta)r\sin\theta+\alpha(\theta)r\cos\theta \\ &=Z(\theta)+r(\beta(\theta)\sin\theta+\alpha(\theta)\cos\theta)) \end{aligned} \qquad (5)$$

where $Z(\theta)$ is the axial error motion of spindle, and $\alpha(\theta)$,$\beta(\theta)$ are the tilting error motions of spindle.

$F(\theta)$ in Eq(5) can be called as the flatness error motion of spindle, as eq(5) simulates the flatness tolerance of the machined surface when the face fly cutter is equipped at the sloindle. The first term in eq(5) indicates the axial error motion of spindle, and the next two terms are the variation of error motion along the distance from the

spindle center.

3. Spindle Error Measurement/Performance Evaluation System

In this paper, the system of spindle error measurement and performance evaluation system has been implemented. Fig. 1 shows the measurement setup of the spindle error measurement/performance evaluation system, where 5 cap sensors (LION Precision) and two master balls are arranged for the measurement of the 5 DOF spindle error motions. The signals from the gap sensors are conditioned and amplified to feed to the PC via a high frequency A/D interface board, which enables the spindle error measurement to be performed in real time environment even when the spindle is rotating at about few thousands rpm. The spindle error evaluation is performed fairly quick such that eccentricity removal, FFT analysis, etc. In order to give very precise measurement result, the roundness error of the master balls are also calibrated using the well known reversal technology, then the measurement results are compensated.

Not only the 5 DOF error motions, but the 3D error motions such as the cylindricity error motion and the flatness error motion are also evaluated in the PC environment.

4. Practical application and conclusion

The developed system has been practically applied to a ultra precision CNC lathe for the performance check of the developed system. Fig.2 shows the measurement results of the X radial error motion typically, while fig.3 shows the FFT spectrum of the X radial error motion measured. The flatness error motion of the spindle is also evaluated as in fig.4, where the 3 dimensional flatness error pattern is graphically illustrated, giving the flatness error motion of 2.33um.. The cylindricity error motion is also evaluated as in fig.5, where the 3 dimensional cylindricity error pattern is graphicaly shown. The cylindricity error motions has been found as 1.33um for the 100mm length of spindle movement.

Therefore a new method for characterisation for the 3D spindle error motions are presented and implemented for practical application, and conclusions are as follows.

(1)A new method of spindle characterisation method has been proposed, enabling the 3D error motions such as the cylindricity error motion and the flatness error motion.

(2)The spindle performance measurement/evaluation system has been implemented around gap sensors, master balls, A/D interface board, and the measurement/analysis software in PC environment. From the practical application to a ultra precision lathe, the performance and efficiency of the developed system have been demonstrated.

References

1.Axis of Rotation, Methods for Specifying and Testing, ANSI/ASME B83.4, 1985

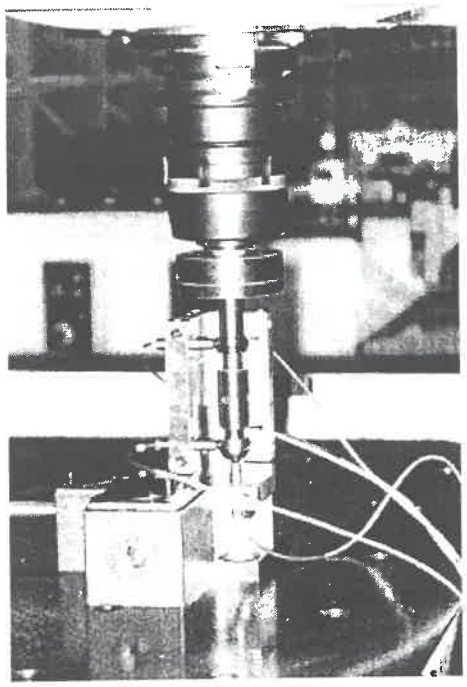

Fig.1: Spindle Measurement Setup

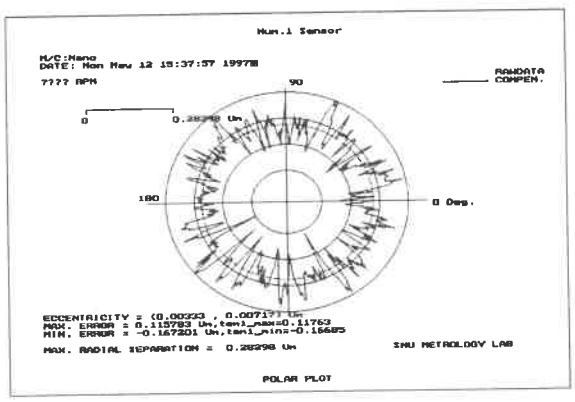

Fig.2 Measurement result of X radial error motion

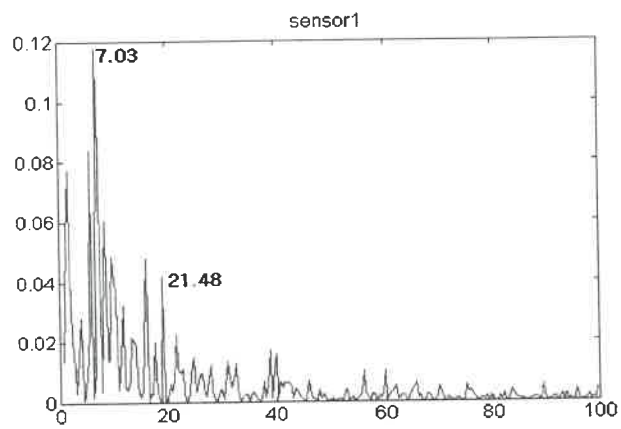

Fig.3 FFT spectrum analysis of X radial error motion

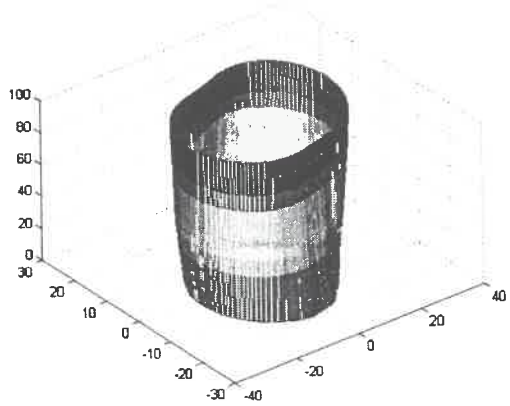

Fig.4 Flatness error motion of a precision lathe

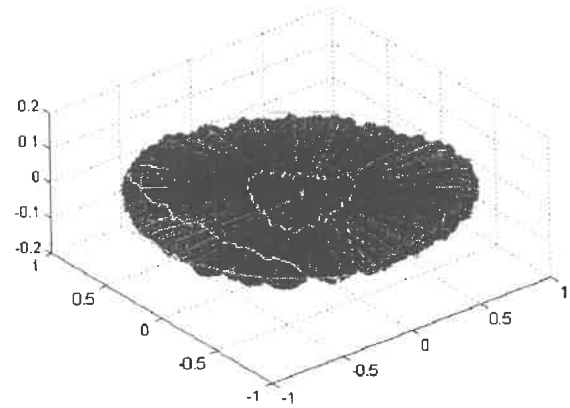

Fig.5 Cylindricity error motion of precision lathe

DYNAMIC ERROR CHARACTERIZATION OF A SCANNING COORDINATE MEASURING MACHINE

Paulo H. Pereira and Robert J. Hocken
Center for Precision Metrology
Department of Mechanical Engineering and Engineering Science
The University of North Carolina at Charlotte
9201 University City Blvd - Charlotte - NC - 28223 - USA

INTRODUCTION

As the competition for better positions in the market place stiffens, the pressure for more agile and efficient production methods increases. The inspection process is an important and often time-consuming portion of the fabrication of most manufactured goods. The expanding use of coordinate measuring machines because of their flexibility is an attempt to improve dimensional inspection productivity [1]. Specifically the ones with scanning capabilities that can achieve fast measurement speeds are good candidates for the task. However, they still cannot be used to the fullest because measurement accuracy degrades considerably with increasing speed.

With the central objective of improving the performance of a contact scanning coordinate measuring machine (CMM) a project was begun in 1997 at the Center for Precision Metrology - University of North Carolina at Charlotte. Partial results of this research work were previously reported [3,4,5]. This paper contains some further findings of the project.

EXPERIMENTAL PROCEDURE AND RESULTS

For the purpose of this work, dynamic errors are all those which happen or are heightened due to the use of the scanning mode of measurement on coordinate measuring machines capable of it. For the machine used in this study, such errors become more evident at speeds beyond 5 mm s^{-1} on open loop or known path scanning mode [3,4].

Although initial data pointed out the possibility that the analog probe head used by the test machine could be the biggest contributor to the dynamic errors of the measuring system during scanning [3], later results showed that there is a strong influence of the machine moving axes as well [4,5]. Because of that, an approach was devised to investigate these effects and, at the same time, to make it a generic kind of test that could be applied to different configurations of scanning capable coordinate measuring machines. The idea consists on the use of ring gages of different sizes measured on scanning mode at several speeds to provide data for developing a model to account for linear velocity and centripetal acceleration dependence of the observed errors.

In order to remove the ring gage errors from the analysis, the artifacts were measured using a roundness measuring machine (Mahr MFU-7) at several levels and the data were exported digitally for calculation of a Fourier series with fifty terms using procedures written in Matlab. This calculated profile was then removed from the ring gage results obtained with the

coordinate measuring machine. The errors of the roundness machine are very small when compared to the ring gage ones and are not being considered for this study.

The quasi-static errors of the coordinate measuring machine were also removed from the scanning output. The result from a Fourier analysis of a point-to-point measurement on the tested coordinate measuring machine minus the measured profile (Fourier calculated) of the roundness measurement was considered as the "quasi-static" CMM error profile. Some of the factors contributing to this class of errors are residual geometric errors (the machine is software compensated), thermal variations (the experiments were conducted in a controlled environment to minimize such effects), and fixturing [2]. As the point-to-point measurement mode is a quasi-static process, scanning errors should not be present.

The profile for the scanning or dynamic errors is then defined as the Fourier calculated result (with fifty terms) from the scanning trace minus the quasi-static and ring gage errors outlined above.

Three different diameters of ring gages were initially used, 25.4 mm, 112 mm and 164.98 mm. The scan speeds ranged from 5 to 50 mm s^{-1}. The ring gages were scanned with the same test speeds to investigate the impact of varying centripetal acceleration and later with the same acceleration to characterize the influence of scanning speed. The centripetal acceleration is the ratio of the square of the linear speed by the radius traveled by the center of the probe tip (which is different than the radius of the ring gage being scanned).

For all test runs data collection was extended 20° – 30° before and after the analyzed 360°. This was done to avoid transients common to the start and the end of the scanning traces. When unusual outliers were noticed the cause for them was fixed and the test repeated.

The linear acceleration remained unchanged during all the tests although it can vary from machine to machine and some manufacturers allow it to be freely adjusted by the user within

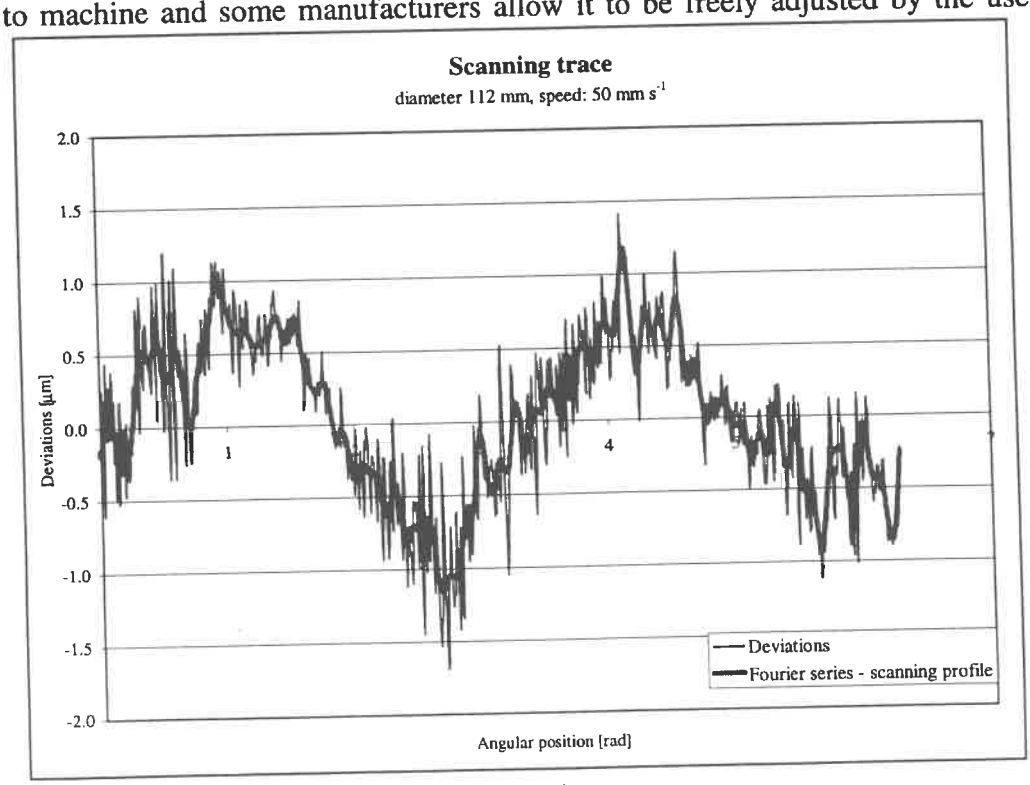

Figure 1 - Scanning trace

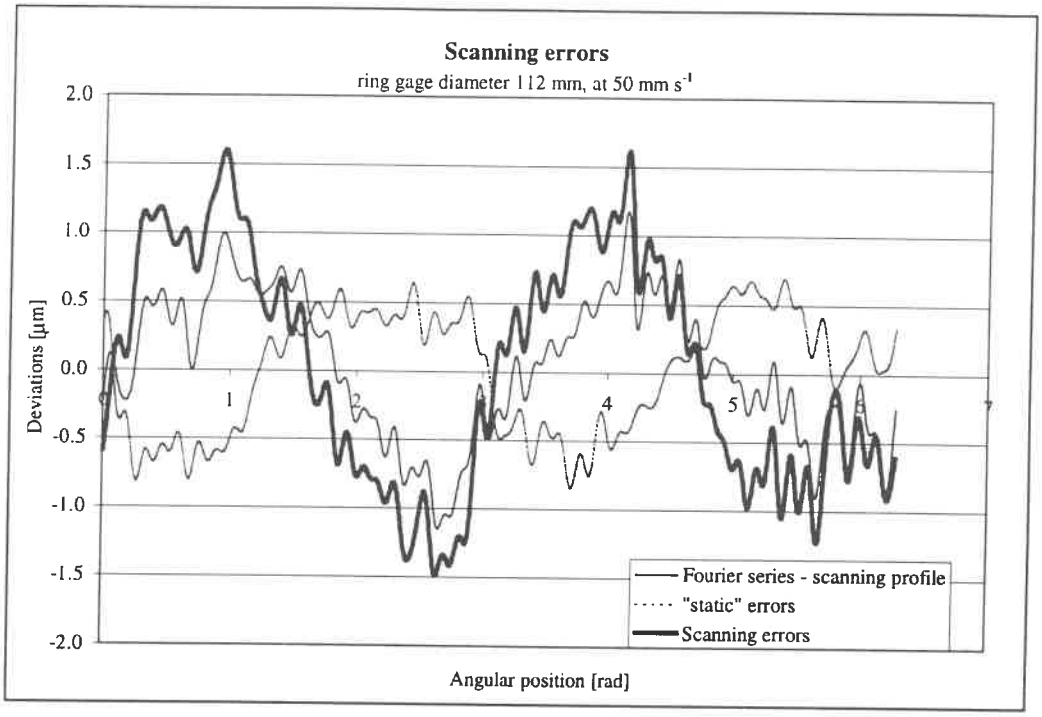

Figure 2 - Scanning errors

certain limits. This model does not make provisions for varying linear acceleration but it still can be applied to situations when a value other than the tested one is applied considering it is maintained constant. Normally, the default setting is the optimal maximum value the machine can still perform within specifications and should be the one chosen for the tests.

On the plot of Figure 1 there is a trace of a scanning measurement. Also, it shows the corresponding contour calculated by Fourier series with fifty terms. For this run, the ring gage used was one with nominal diameter of 112 mm and the scanning speed was 50 mm s^{-1} (the maximum available for this machine on open loop scanning mode). Figure 2 shows a plot with the same Fourier calculated profile plus the trace of the quasi-static errors and the difference between the two, which constitute the mentioned scanning errors.

The depicted example suggests that fewer than fifty terms could be used since the biggest contribution to the total error comes from lower order harmonics. If this trend is proven true after more data have been analyzed, the calculations can be made simpler to allow faster response even with a large number of data points.

Having collected data and performed the described analysis, the next step is to develop the model. This model has to include scanning speed and centripetal acceleration as input variables. It will be possible to estimate the errors for diameters and speeds other than the tested ones.

CONCLUSIONS

A procedure to create a model to compensate for the errors of a scanning coordinate measuring machine when measuring circular features is being described. Further tests and development still need to be carried out in order to fully validate the strategy. Also, the

applicability of such procedure to other features will be evaluated. Additionally, by performing such tests users can identify other scanning related problems particular to their machines that cannot be detected with standardized tests (eventually there will be tests in the proper standards specifically to address scanning performance of coordinate measuring machines).

The final output of this project will be a carefully outlined test procedure as to allow the use on practically any scanning coordinate measuring machine with little or no modifications. First, it will detail the data collection, then the analysis and finally the steps toward the elaboration of the compensation model will be explained.

ACKNOWLEDGMENTS

The Affiliates Program of the Center for Precision Metrology at The University of North Carolina at Charlotte is partially funding the work presented here. The first author is sponsored by the Brazilian Federal Agency CNPq - Conselho Nacional de Desenvolvimento Científico e Tecnológico (National Council for Scientific and Technological Development) under process number 200480/95-2. The NSF/IUCRC program for co-sponsoring the Center for Precision Metrology. Also, the authors would like to express their gratitude to Federal Products Co. for donating a number of ring gages necessary for the tests.

REFERENCES:

1. Bosch, J.A. *"Coordinate measuring machines and systems"*, Marcel Dekker, 1995.
2. Hocken, R.J. & Machine Tool Task Force. *"Machine tools accuracy.* Technology of Machine Tools, vol.5, Oct.1980.
3. Pereira, P.H., Hocken, R.J. & Muralidhar, A. *"Dynamic error characterization of a scanning probe CMM"*, in Proceedings of the 13th Annual Meeting, American Society for Precision Engineering, ASPE. St. Louis, MO - Oct.1998.
4. Pereira, P.H. & Hocken, R.J., *"Dynamic error investigation of a scanning coordinate measuring machine"*, Proceedings of the 8th Annual Industrial Engineering Research Conference. Phoenix, AZ – May.1999.
5. Pereira, P.H. & Hocken, R.J., *"Dynamic testing of a scanning coordinate measuring machine"*, Proceedings of the 1st International Conference and General Meeting of the European Society for Precision Engineering and Nanotechnology. Bremen, Germany – vol.2, p.312-315, Jun.1999.
6. Weekers, W.G. & Schellekens, PH.J. *"Compensation for dynamic errors of coordinate measuring machines"*, Measurement, Vol.20, No.9, 1997:197-209.

AN EXPERIMENTAL INVESTIGATION INTO SPINDLE ERROR MOTIONS UNDER LOAD

Aditya K. Sharma
The Boeing Company, Seattle, WA 98124
and
Steven R. Patterson
Center for Precision Metrology
University of North Carolina at Charlotte, Charlotte, NC 28223

Keywords: CNC vertical machining center, Loading device, Spindle error motions and Spindle error analyzer

Introduction

Current measurement methods, specified by ANSI/ASME B5.54-1993[1] and B89.3.4-1985[2] standards for spindle error motions, establish error motion characteristics with no load applied to the spindle bearings. It is possible that the application of load to the spindle bearings will result in different error motions, a different response to the error motions, or both.

In this study, a loading device [3], designed and built to apply loads to the spindle of a computer numerically controlled (CNC) machine, was used to study spindle error motions. Brief discussions of the results of spindle error motions under loaded and unloaded conditions and at various rpm's are included below.

The loading device is an external fixture that applies various axial loads to lower and upper bearings of a machine spindle. It allows traditional spindle testing with an artifact to study spindle error motions and the ability to perform the same tests under load while at speed. Further details of the loading device components and a discussion of axial forces due to cutting can be found in reference 3. A commercially available spindle error analyzer [4] (SEA) system with capacitance gauging techniques was used to measure error motions of the spindle.

Experimental Setup

The experimental setup of the loading device is shown in Figure 1 (SEA system not shown). When testing for spindle error motions under load, a thrust force of 140 lbs was applied to the spindle bearing system. An S-type load cell with a bridge resistance of 350 ohms was used to measure forces applied to the spindle.

All spindle error motions tests were conducted on a Monarch vertical machining center (VMC 45). The Monarch uses tapered roller bearings to support the spindle. Spindle bearing preload is controlled by a hydraulic integrated circuit and automatically reduced at high speeds. From 0-525 rpm, spindle bearing pressure is 400 psi, and from 525-1125 RPM, spindle bearing pressure is lowered to 100 psi.

Loaded and unloaded axial and radial error test runs were conducted at least 12 hours apart. Before starting each test battery, the spindle was operated for two hours to warm up its bearing system. After warm up, each run was conducted for 10-15 minutes at each rpm setting with approximately two minute intervals between test runs. All tests were conducted under stable ambient conditions with 128 data samples per revolution for 20 revolutions. In order to correlate data from a previous study, first test was conducted at 255 rpm.

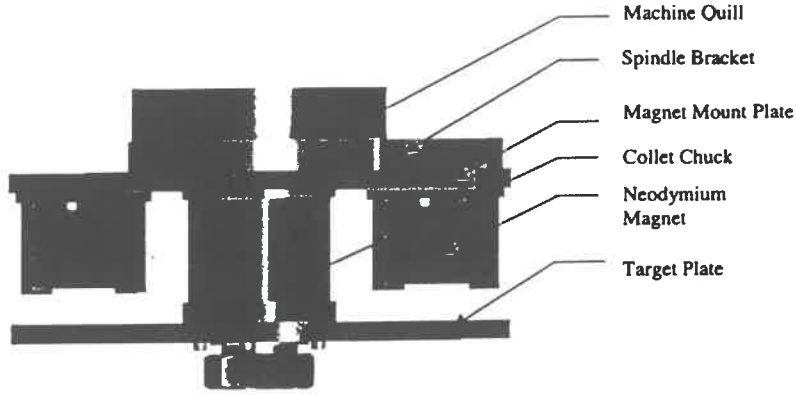

Figure 1: Loading Device Setup for Spindle Error Motion

Spindle Error Motions Under Loaded and Unloaded Conditions

Axial and radial error motions in a rotating sensitive direction were measured. For radial error motion tests, only asynchronous errors are analyzed and reported. Spindle error motions are defined in ANSI/ASME B89.3.4 – Axis of Rotation [2].

Axial error motion, rotating sensitive direction

In the SEA setup for axial error tests, the X-probe determines angular position while the Z-probe detects any in and out (axial) motion of the spindle during each rotation. Target eccentricity was minimized to avoid error in measurements.

Table 1 and Figures 2 (a) and (b) summarize results and show sample plots obtained with the loading device for spindle axial error motion under unloaded and loaded conditions.

Table 1: Axial error under loaded and unloaded conditions

Spindle rpm	Spindle preload (psi)	Axial error in microns at no load				Axial error in microns at 140 lbs of load		
		Run 1	Run 2	Run 3		Run 1	Run 2	Run 3
255	400	1.5	1.3	1.3		1.5	1.4	1.3
500	400	2.1	2.5	2.4		2.6	2.6	2.6
1000	200	1.3	1.3	1.4		1.7	2.0	1.9

At 255 rpm, the magnitudes of axial error remained same accept for some small variations under loaded and unloaded conditions of the spindle. For all six runs, a variation of 0.2 micron in axial error was noted. At 500 rpm, axial error increased by approximately one micron over similar

spindle conditions at 255 rpm. Furthermore, at 500 rpm under load, axial error is slightly higher and constant for all three test runs. Since the difference in axial error under load and no load is smaller than the variation within all measurements, it can not be considered significant in obtaining a correlation between spindle axial error motion at load and no load. Therefore, at 255 and 500 rpm, application of 140 lbs of thrust load did not affect spindle axial error motion.

At 1000 rpm, axial errors are smaller in magnitude compared to the other two test speeds. However, the amount of axial error increased under the application of the thrust load. It is possible that the magnitude of axial error is smaller at this rpm due to the change in preload to the spindle bearing system from 400 psi to 100 psi.

Radial error motion, rotating sensitive direction

In this setup, data is acquired from the X and Y probes positioned 90 degrees to each other. The probes measure X and Y change in position of the axis line of rotation and generate sine and cosine signals to produce a polar plot using the Tlusty method [4,5]. For all radial error measurement tests target eccentricity was maintained constant.

Table 2 and Figures 2 (a) and (b) summarize results and show sample plots obtained with the loading device for spindle radial error motion under unloaded and loaded conditions.

Table 2: Asynchronous error under loaded and unloaded conditions

Spindle rpm	Spindle preload (psi)	Asynchronous error in microns at no load				Asynchronous error in microns at 140 lbs of load		
		Run 1	Run 2	Run 3		Run 1	Run 2	Run 3
255	400	4.1	3.7	3.8		4.0	3.2	4.1
500	400	5.8	5.6	5.7		6.5	4.9	5.2
1000	200	7.0	7.3	5.9		5.1	5.5	5.7

At 255 and 500 rpm, it was noted that application of 140 lbs of axial load did not affect the asynchronous error motion of the spindle. However, at 1000 rpm, asynchronous error slightly decreased for all three runs under the application of thrust load to the spindle.

Conclusions and Future Work

A loading device designed and built in a previous study was utilized to further investigate spindle error motions under the application of thrust loads. Maximum load and spindle operating speeds were limited to 140 lbs and 1000 rpm.

For spindle error motions, axial and asynchronous error measurements were repeatable to within one-half micron. Due to this uncertainty, and the limited number of test runs, no direct correlation was established for spindle error motions under load and no load.

Future work will include tests conducted with the loading device on a machine that has different type of bearings and preload mechanism. Also, further analysis and tests will be done to separate machine structural motions from error motions of the spindle.

References

1. ANSI/ASME B5.54-1993, " Methods for Performance Evaluation of Computer Numerically Controlled Machining Centers," American Society of Mechanical Engineers, NY, 1992.
2. ANSI/ASME B89.3.4, "Axes of Rotation, Methods for Specifying and Testing" American Society of Mechanical Engineers, NY, 1985.
3. Sharma, A.K., "An Experimental Investigation into Thermal Spindle Growth Under Load", Masters Thesis, The University of North Carolina at Charlotte, 1997.
4. "Spindle Error Analyzer, Instructions Manual," Lion Precision, Inc., St. Paul, MN., 1996.
5. Tlusty, J. "System and methods of testing machine tools," Microtechnic, 13, 162-178, 1959.

Error Motion Plots

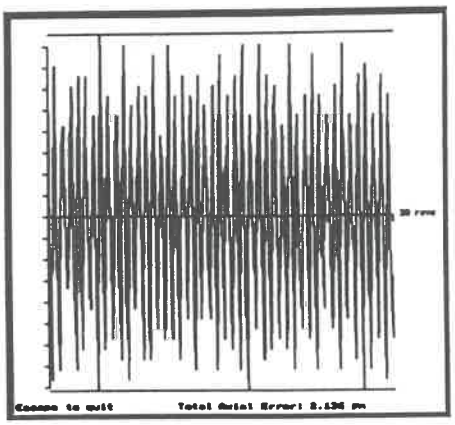

Figure 2(a):
Axial error motion at 500 rpm no load

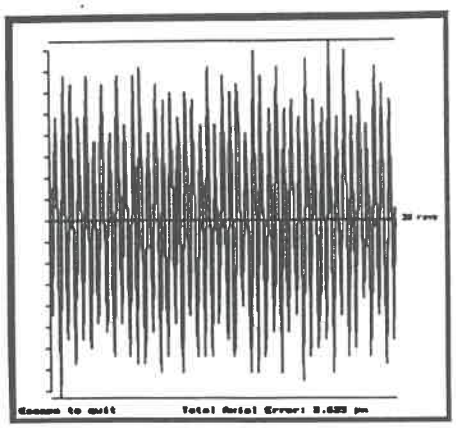

Figure 2(b):
Axial error motion at 500 rpm,140 lbs. thrust load

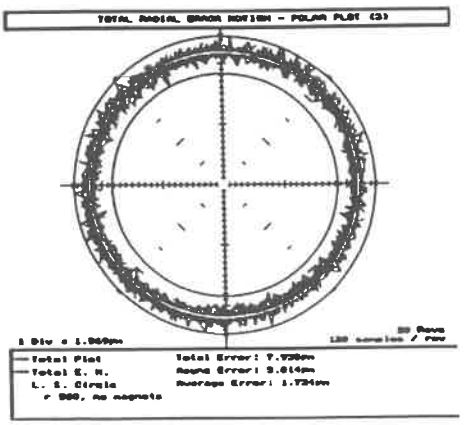

Figure 3(a):
Radial error motion at 500 rpm no load

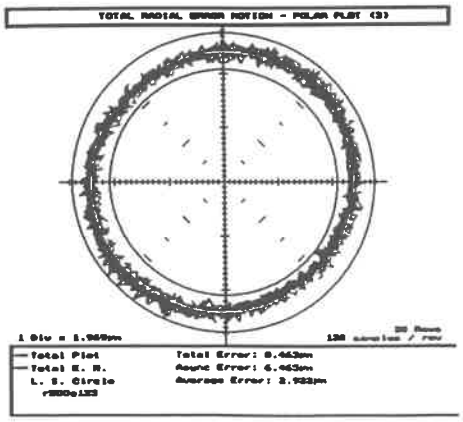

Figure 3(b):
Radial error motion at 500 rpm,140 lbs. thrust load

Study of Nano-tribology using Scanning Force Microscope

Tsunetaka Sumomogi, Toshiro Endo and Shinichi Matsuo
Faculty of Engineering, Hiroshima Kokusai Gakuin University
6-20-1 Nakano, Aki-ku, Hiroshima 739-0321, Japan

Introduction

The scanning force microscope (SFM) is a unique tool for nanometer-scale modification [1,2] and tribology [3]. When a tip scans on a sample surface in contact mode, there is not only a normal force but also a lateral force acting on the tip. Stick-slip motion with the periodicity of the lattice constant was detected between a tungsten tip and a mica surface. [4]. In ambient air, the presence of physisorbed or chemisorbed molecules could affect the nanotribological properties between the tip and the sample. The effects should be significant for high-resolution operation [2]. The influence of adsorbed water molecules and the capillary condensation on nanotribological phenomena has been characterized by means of SFM friction experiments on silicon wafers [5]. It was reported that friction and adhesive forces were affected by the relative humidity of ambient air, but the behavior of these forces in atomic scale imaging was not mentioned.

In the present experiment, the SFM is placed in an atmosphere control apparatus and the relative humidity around the tip and the sample is controlled at 30% or 70%. The lateral force images corresponding to atomic scale topography images are obtained on the cleaved surface of mica. The nanotribological effects of adsorbed water molecules and the capillary condensation of water is examined.

Experiment

The schematic of the main part of the SFM used for the present study is shown in Fig. 1. The lateral component F_L and the normal component F_N of the force acting on the tip are independently measured by twisting angle and bending inclination of the cantilever, respectively. We use a triangular microcantilever with ~25 nm tip-radius, which is made of Si_3N_4. Its spring constants of twisting and bending are 250 N/m and 0.58 N/m, respectively. The SFM unit is placed into a glove box connected to a precise air control apparatus and the atmosphere around the tip and the sample is controlled to a relative humidity (RH) of 30% or 70%, and a temperature of 30℃ [6].

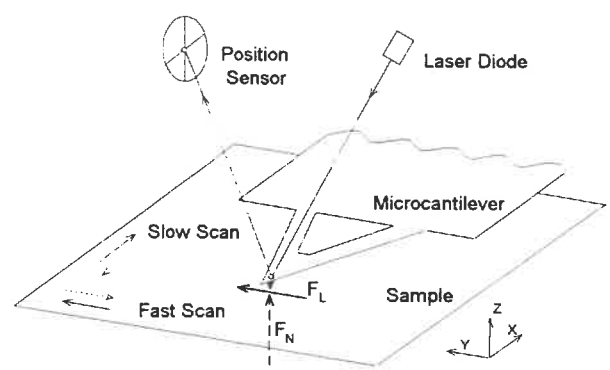

Fig. 1. Schematic of the main part of the SFM.

The normal force is 0-200 nN; here the zero force is defined as the force when the tip jumps up from the sample surface during retraction of the tip. With raster scanning of 5-10 nm width under the constant normal force, the topography image and the lateral force image are obtained simultaneously. The fast scan rate is 30 Hz or 60 Hz, so the scan speed is 0.6 μm/s or 1.2 μm/s when the scan width is 10 nm.

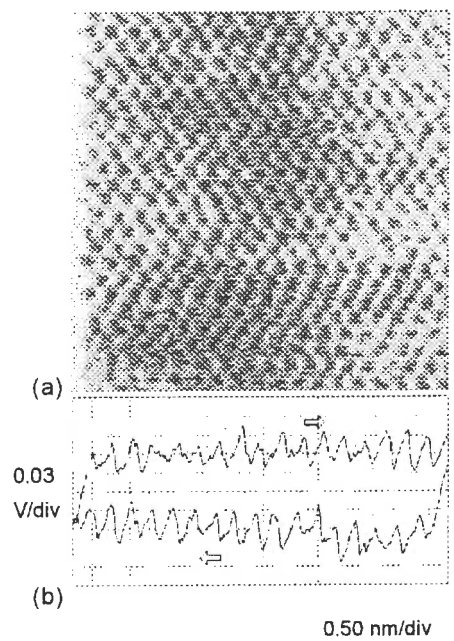

Fig. 2. An image and a lateral force signal profile for mica at 30% RH.

Results and discussion

Figure 2 shows an image and a signal profile of the lateral force for mica in 30% RH, with a normal force of 40 nN. The image indicates the periodicity of lattice structure at 0.52 ± 0.03 nm. The lattice constant and the symmetry of the image correspond to the mica (0001) face [4]. The lateral force signal profile indicates hysteresis according to the direction change of the lateral force in trace and retrace and, the occurrence of "stick-slip" processes due to spatially discrete adhesion and jumps with the lattice periodicity.

The amplitude of periodic change F_{LA} and the average value F_{LD} of the lateral force are evaluated from the lateral force signal profile, such as that shown in Fig. 2(b). Figure 3 shows F_{LA} and F_{LD} on lateral force signal profiles for mica in 30% RH as a function of normal load F_N. F_{LA} directly contributes to the contrast of the atomically resolved lateral force images. While F_{LA} is slightly dependent on F_N, F_{LD} is almost constant with the change of F_N.

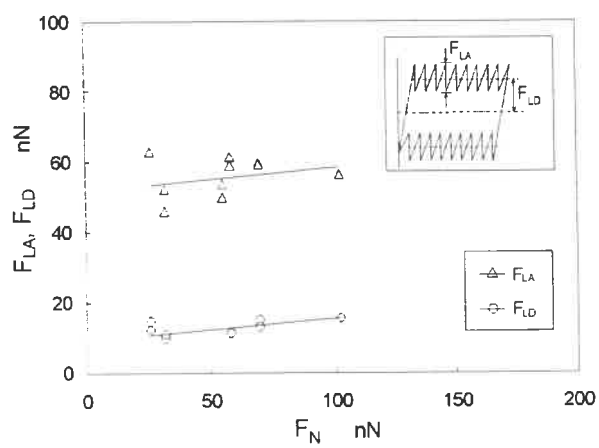

Fig. 3. F_{LA} and F_{LD} on lateral force signal profiles for mica at 30% RH as a function of F_N.

In order to compare the lateral force behaviors under 30% RH and 70% RH, F_{LA} on the lateral force signal profiles in these conditions is shown in fig. 4 as a function of F_N. The straight lines are obtained by a least-squares method. It is recognized that the atmosphere around the tip and the sample affects the dependence of the lateral force magnitude on the normal load. At low

relative humidity (30%), the lateral force magnitude in atomically resolved images is almost independent of the normal load. We can conclude that the adhesive force, independent of the normal force, is superior to the friction force, dependent on the normal force. At high relative humidity (70%), the lateral force magnitude is smaller than at 30% RH and exhibits a dependence on the normal load. We can conclude that the adhesive force is weaker than at 30% RH.

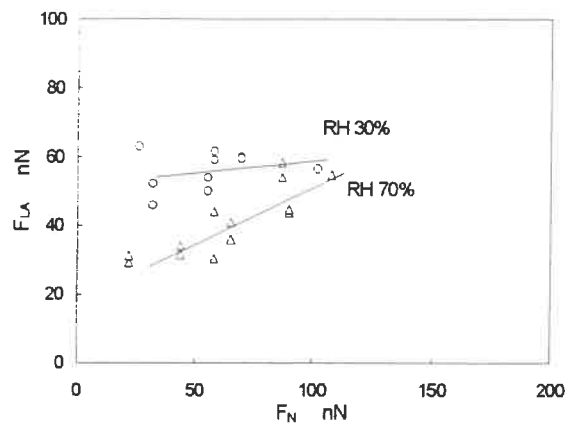

Fig. 4. F_{LA} on lateral force signal profiles for mica at 30% RH and 70% RH as a function of F_N.

The relative humidity of ambient air in this experiment, 30-70%, is high enough to cause water molecules and films to be adsorbed on mica surfaces [7]. Therefore, it is necessary to consider that the adhesive force due to the presence of the water in the tip-sample gap has a large influence upon the lateral force [8]. The adhesive force acting on the tip is considered to consist of the meniscus force and the interaction forces between the tip and the sample, where water is present in the gaps around the contacting asperities. We discuss the dependence of the adhesive force magnitude on the relative humidity of ambient air.

The adhesive force F_{ad} due to the meniscus between a spherically shaped tip and a flat surface is expressed as $F_{ad} \propto Rh\gamma/r \ (h << R)$, where R is the tip radius, h is the meniscus height, γ is the surface tension of water, and r is the radius of curvature of the meniscus [9]. Here, the effect of the vapor pressure on the meniscus radius is expressed with the Kelvin equation, $\ln(p/p_0) \propto 1/r$, where p_0 is the nominal vapor pressure, p is the observed vapor pressure, and r is negative for capillaries [10]. From the above considerations, it is conjectured that the absolute value of the meniscus radius increases, and accordingly the adhesive force due to meniscus decreases, with increasing relative humidity.

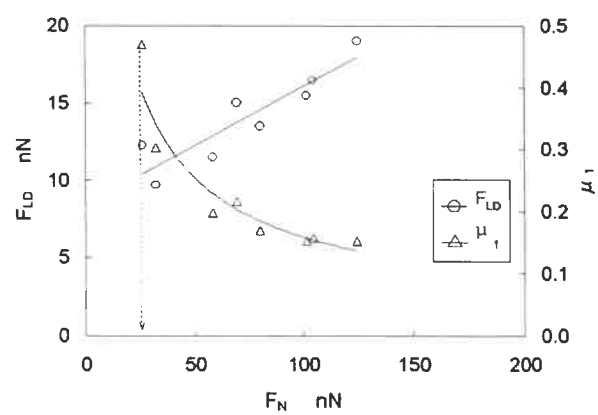

Fig. 5. F_{LD} and the apparent friction coefficient μ_1 for mica at 30% RH as a function of F_N.

We also consider the evaluation method of friction coefficient in order to clear the relationship between F_N and F_{LD}.

Since the lateral force signal profiles are looked as "stick-slip" process, the kinetic friction coefficient can be given by the magnitude of F_{LD}. The lateral force F_L is assumed to consist of the friction force due to the normal force F_N and the meniscus force F_{ad} due to the capillary condensation of water [5]. The friction force is the product of the friction coefficient μ_0 and F_N, the lateral force is expressed as $F_L = \mu_0 F_N + F_{ad}$. The apparent friction coefficient μ_1 is given by $\mu_1 = F_L / F_N = \mu_0 + F_{ad} / F_N$. The value of μ_1 becomes to be larger than μ_0 with decreasing F_N, because the meniscus force is superior to the friction force. In the present examination, we discuss in the sight of the apparent friction coefficient μ_1. Figure 5 shows F_{LD} and the apparent friction coefficient μ_1 for mica at 30% RH as a function of F_N. The value of μ_1 is considerably large in low F_N near to the adhesive force (F_{ad}=32nN) and becomes to be 0.1-0.2 in high F_N. It is obvious that the adhesive force due to adsorbed water molecules and the capillary condensation of water has a great influence upon the lateral force properties in low-load measurements.

Conclusion

In order to discuss the nanotribological effects of adsorbed water molecules and the capillary condensation of water, the lateral force images are examined quantitatively as a function of the normal load on the sample surface. The dependence of lateral force magnitude on the normal load is found to be affected by the atmosphere around the tip and the sample. The adhesive force due to the presence of water in the tip-sample gap has a large influence upon the lateral force properties in low-load measurements.

References

1. T. A. Jung, A. Moser, H. J. Hug, D. Brodbeck, R. Hofer, H. R. Hidber, and U. D. Schwarz, Ultramicroscopy **42-44**, 1446 (1992).
2. T. Sumomogi, T. Endo, K. Kuwahara, and R. Kaneko, J. Vac. Sci. Technol. **B13**, 1257 (1995).
3. R. Kaneko and E. Hamada, Wear **162-164**, 370 (1993).
4. R. Erlandsson, G.Hadziioannou, C. M. Mate, G. M. McClelland, and S. Chiang, J. Chem. Phys. **89**, 5190 (1988).
5. M. Binggeli and C.M. Mate, J. Vac. Sci. Technol. **B13**, 1312 (1995).
6. T. Sumomogi, K. Hieda, T. Endo, and K. Kuwahara, Appl. Phys. **A 66**, S299 (1998)
7. H. K. Chritenson, J. Colloid Interface Sci. **121**, 170 (1988).
8. D. A. Bonnell ed., Scanning Tunneling Microscopy and Spectroscopy (VCH Publishers, New York 1993), p.239.
9. J. N. Israelachvili, Intermolecular and Surface Forces, 2nd edn. (Academic Press, London 1985), p.330.
10. Y. Inoue, J. Jpn. Soc. Tribologgists *(in Japanese)* **36**, 296 (1991).

A Compact Industrial Distance Measuring Interferometer System

Mike Holmes, Les Deck, Bill Shull, Mark Samuels, Steve Altieri, Earl Ebert, Jim Soobitsky, Ron Gecewicz

Zygo Corporation
Laurel Brook Road, Middlefield, Connecticut, 06455-0448

Distance Measuring Interferometry (DMI) plays a key roll in the most demanding areas of precision engineering. Familiar applications include microlithography for integrated circuits, where the decreasing minimum feature size and manufacturing cost reductions provides the impetus for developing more accurate positioning stages. Machine tools circuit inspection systems that presently rely on encoders or glass scales are beginning to experience a similar demand for the higher accuracy. In many of these systems, the encoders and/or scales are the most significant contributors to measurement errors. There is consequently an open need for a DMI having greater accuracy and reliability than encoders but at a more accessible cost and size when compared to traditional heterodyne systems. We have therefore developed a new compact industrial DMI to assist in the transition from encoders to high-precision heterodyne interferometry. The new Zeeman laser based system has resolutions down to 10 nm and accommodates three axes of metrology at stage velocities up to 0.5 m/s.

Introduction

The authors listed represent the development team responsible for various parts of this project. This paper is organized as follows; it starts with a design overview and project goals, followed by some key calibration data, which demonstrates the performance capabilities of this new DMI and ends with a description of the error budgets and sub-systems.

Design Overview

Figure 1 shows a simple single axis DMI system consisting of the laser head, interferometer assembly, phase interpolator board, and a moving target mirror. The output from the laser head is two linearly polarized beams of light ($\lambda_{1,2}$=632.991 nm) which are separated in frequency by 3.65 ± 0.35 MHz. The polarization states are orthogonal to each other. The two components are separated in the interferometer. One component travels a constant path in the interferometer assembly while the other has a path length that is dependent upon the position of the target mirror. The two components rejoin inside the interferometer assembly, after traveling their separate paths, and are mixed and launched into a fiber optic cable. The other end of the fiber optic cable plugs into a fiber optic receiver that is mounted on the phase interpolator board. This optical signal will hereafter be referred to as the measurement signal. Exiting from the rear of the laser head is the optical phase reference signal, which is also directed to a fiber optic receiver on the phase measurement board via a fiber optic cable. This signal is hereafter referred to as the reference signal. As the target mirror moves in the indicated directions, the phase between the measurement and reference signals changes. The changing phase is converted to A-QUAD-B or UP/DOWN PULSES output data formats. The A-Quad-B output is comprised of two signals (for discussion purposes these will be referred to as S_0 and S_1) that are separated in phase by 90 degrees. The absolute phase angle of S_0, and corresponding absolute phase angle of S_1, is proportional to the displacement of the target mirror. By monitoring signals S_0 and S_1, changes in the position of the target mirror and the direction of motion can be determined. The up/down pulses output is simply two signals that pulse independently of each other but dependent on the target mirror motion. One pulse is generated for every least count of the phase measurement electronics. The phase interpolator board is configurable for least count resolutions of $\lambda/64$, $\lambda/32$, $\lambda/16$, and $\lambda/8$. The system was designed to support up to three measurement axes simultaneously with the measurement errors not to exceed 100 nm 3σ over any 24-hour period of time. This accuracy specification constrains the temperature excursions of the optical beam paths to ± 0.1 °C and the measurement range to 0.3048 m. We designed to a maximum output data rate of 16 MHz to accommodate a variety of third party servo controller boards. This data rate limits the velocity at the higher resolutions while the heterodyne frequency (3.65 MHz) limits it at the lower resolutions.

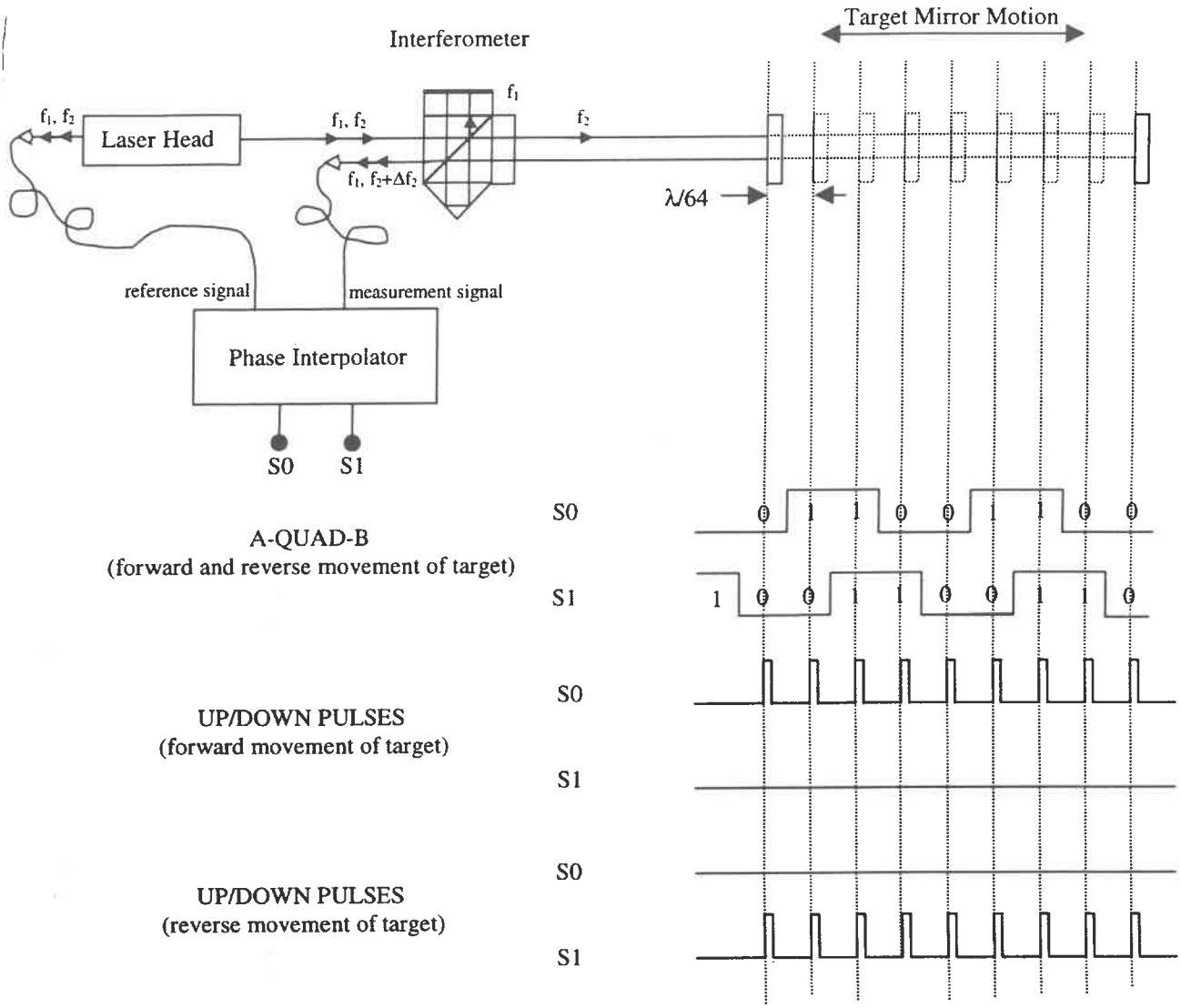

Figure 1 – typical distance measuring interferometer system

Performance

The performance of this DMI system was characterized in the labs of North Carolina's Center for Precision Metrology[1]. The new compact DMI was calibrated against the ZMI-2000 distance measuring interferometer system[2]. A common target mirror was mounted to the X-slide of a Leitz coordinate measuring machine which is located in the Center's temperature controlled metrology lab. The temperature is conveniently controlled to ± 0.1 °C. The two interferometers were aligned and measurements were taken throughout a 305 mm range of travel. This simultaneous linear displacement accuracy test then calibrates the newly developed compact DMI against the old proven DMI. The results of the test are shown in figure 2. Note that the new DMI more than meets the ± 100 nm accuracy specification.

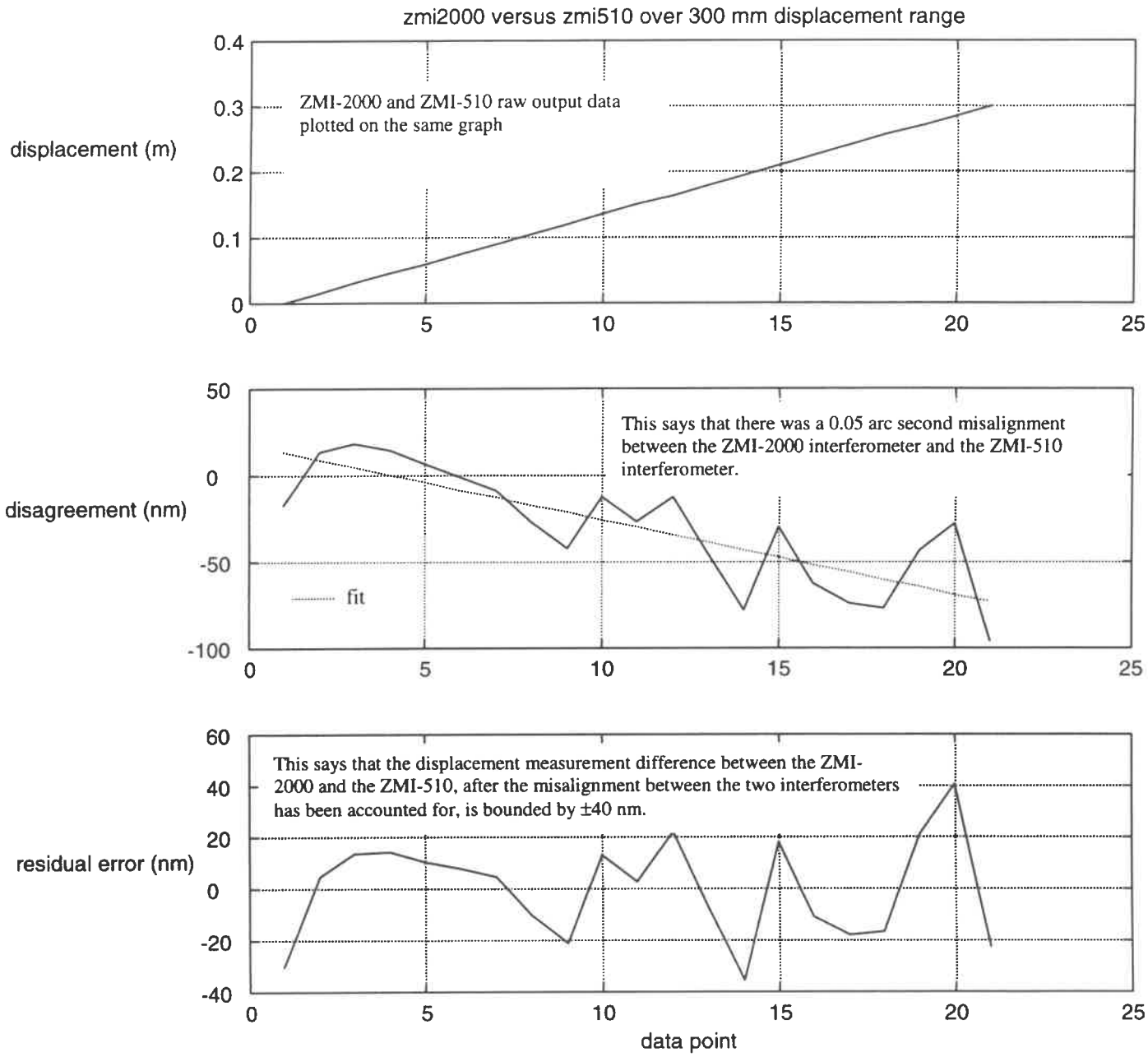

Figure 2 – system accuracy acceptance test data

Laser Head

The laser head is a single mode Zeeman split laser that samples light from the rear of the laser tube for stabilization. A low cost, but high performance optical frequency stabilization scheme was developed for the system. The results of this effort are shown in figure 3, which shows the frequency difference between the vertically polarized components of our new laser head and a frequency stable reference. Note that the frequency instability is less than 0.6 MHz (about 1.2 ppb) peak to peak over 2 hours. The DMI measurement error allotment to the laser head was about 12 nm. The minimum output optical power specification is 250 μW. The laser head dissipates about 6 Watts during normal operation. The laser head is 10.5 ″ x 2.5 ″ x 2.5 ″ and weighs about 2 ¼ pounds. The beam diameter is 4 mm to the $1/e^2$ points.

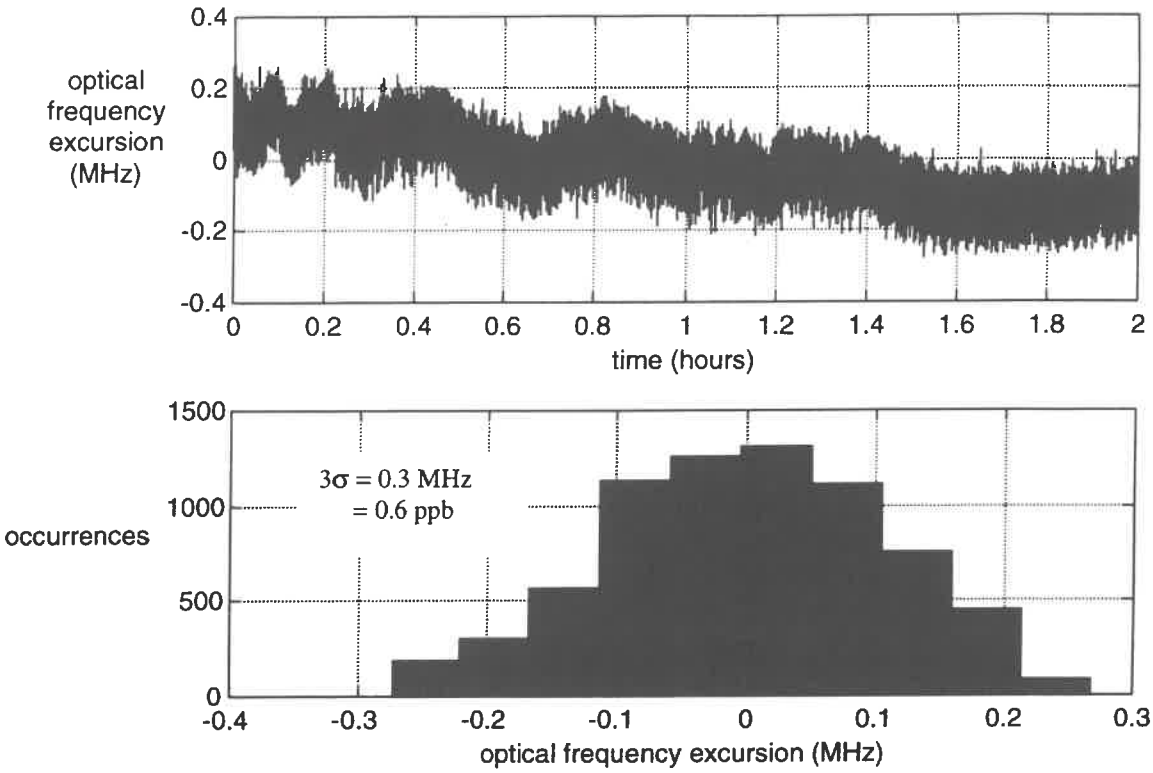

Figure 3 – laser head frequency instability data

Optics

An optical analysis was completed as part of the optical specification procedure. This analysis is based on Jones matrix models of the individual optical components that are assembled into the high-stability plane mirror interferometer configuration. The specifications for the individual components are plugged into the model and a simulation then predicts losses and measurement errors due to beam mixing. Errors due to wavefront distortion and target mirror rotation are also calculated. The analysis shows that if the components meet the specifications, that a 250 μW optical power source will deliver 3 μW to the phase interpolator's fiber optic receivers. It also predicts that the maximum interferometer related errors, not including thermally induced optical path length errors, is less than 20 nm. The temperature coefficient of the high-stability plane mirror interferometer is less than 10 nm/°C. The measurement error resulting from the optics is less than the allotment of 30 nm under the conditions specified in the design overview. All of the optics are miniature (i.e., ½ ″ polarization beam splitter cube).

Phase Interpolation Electronics Board

The phase interpolator board uses a digital algorithm to interpolate the phase between the measurement signals and the optical phase reference. Preliminary error analysis predicts that the most significant phase measurement error would stem from quantization error and shot noise in the photodiodes of the analog front end. Graphical representation of the two errors showed that quantization error would be the most significant error source at about 8.8 nm. Experiments carried out on the first electronic boards fabricated backup the preliminary analysis. The displacement measurement error resulting from the phase interpolation board is less than the allotment of 40 nm.

Acknowledgements

We would like to thank Dr. Robert Hocken, Jim Salsbury, and Paulo Pereira from UNC-Charlotte for their help in characterizing the new compact DMI system.

References

1) North Carolina Center for Precision Metrology, University of North Carolina at Charlotte, HWY 49 North, Charlotte, NC, 28223.
2) Zygo Corporation, Middlefield, CT, 06455.

Arbitrary N-Step Algorithm for Removal of Higher Order Test Optics Errors

Seung-Woo Kim, * Hyug-Gyo Rhee, Byung-Chang Kim
Korea Advanced Institute of Science and Technology
Department of Mechanical Engineering
Science Town, Taejon, 305-701
South Korea
*: Who is responsible for any correspondence.
Tel: ++82-42-869-3217; Fax: ++82-42-869-3210;E-mail: swk@kaist.ac.kr

1. INTRODUCTION

Optical testing suffers some inevitable systematic instrument errors caused by the fabrication imperfection and alignment inaccuracy of constituting optical components. When the required uncertainty in the measurement is of the same order as the instrument errors, self-calibration based upon principles of absolute test becomes important since no calibration standards with sufficiently quantified accuracy are usually available. Ever since the reversal principle of three-flat test was first known, a number of efforts have been made to extend the principle to the full-aperture test of lenses and mirrors [1,2]. One approach is adopting well-defined model functions such as the Zernike polynomials or Fourier series to approximate surface errors [3-6]. The use of model functions led to the N-step averaging method, which removes the instrument errors by averaging multiple wavefronts sampled by rotating the part to N equally spaced azimuthal positions about the optical axis [7-9]. In fact the part wavefront generated by rotation may be divided into three components; the rotationally variant (RV), angular harmonic (AH) of integer multiples of N, and rotationally invariant (RI) wavefronts [9]. The N-step averaging method successfully separates the RV wavefront from the instrument errors, but this is generally not the case for the AH and RI wavefronts except for some special situations [4].

Our intention in this paper is to improve the N-step averaging method with a particular attention of effective separation of the AH wavefront. In principle, the AH wavefront can be made insignificant in the N-step averaging method by increasing the number of part rotation. In practice, however, this requires a high precision in part rotation because higher order wavefront components are particularly sensitive to rotation errors. This problem could diminish with aids of an accurate azimuthal angle division device, but a more effective way would be modifying the current computational method as done in the 'arbitrary N-step algorithm' proposed in this paper. The new algorithm is not confined by the equal spacing requirement, permitting part rotations to be made at arbitrary azimuthal positions. This generalized algorithm eliminates calibration errors caused by rotation inaccuracy and also offers a great advantage of reducing the required number of part rotations drastically when higher order spatial frequency terms are of particular importance. The latter benefit is obtained by imposing a predetermined small amount of intentional offset in the azimuthal positions during part rotations.

2. N-STEP AVERAGING METHOD

The N-step averaging method starts with the basic assumption that the measured wavefront from interferometric optical testing is a superposition of two distinguishable contributions of

$$W = T + P \tag{1}$$

where T is the instrument error including the reference surface, while P is the part wavefront to be measured. To remove T from W, the part is rotated about the optical axis by some physical means while T remains stationary. For analysis, let W_j be the sampled wavefront of W when P is stationed at an azimuthal position of α_j with the subscript j indicating the rotation index ranging from 0 to N-1. It is assumed that $\alpha_0 = 0$ for convenience, and N is the total number of part rotations. Taking the Zernike polynomials, the part wavefront during rotation is expressed as

$$P_j(r,\theta) = P_0(r,\theta+\alpha_j) = \sum_{l,k} R_l^k(r)[c_{0,lk}\cos(k\theta+k\alpha_j) + \tilde{c}_{0,lk}\sin(k\theta+k\alpha_j)]$$
$$= \sum_{l,k} R_l^k(r)[c_{j,lk}\cos(k\theta) + \tilde{c}_{j,lk}\sin(k\theta)] \tag{2}$$

where $c_{j,lk} \equiv c_{0,lk}\cos(k\alpha_j) + \tilde{c}_{0,lk}\sin(k\alpha_j)$ and $\tilde{c}_{j,lk} \equiv \tilde{c}_{0,lk}\cos(k\alpha_j) - c_{0,lk}\sin(k\alpha_j)$. Parks [3] and Fritz [4] first suggested rigorous computational procedures to determine the coefficients $c_{0,lk}$ and $\tilde{c}_{0,lk}$ directly with only two wavefront measurements. This two-step algorithm is convenient to implement but invalid in case k equals 0 or integer multiples of $2\pi/\alpha_j$. This means that only the RV part wavefront is self-calibrated, excluding the RI and AH components.

Later Evans and Kestner [7] proposed the N-step averaging algorithm, which takes equally spaced part rotations around a revolution, i.e., $\alpha_j=2\pi j/(N-1)$. In this case, the Zernike coefficients yield two useful summing properties of

$$\sum_{j=0}^{N-1} c_{j,lk} = \sum_{j=0}^{N-1} \tilde{c}_{j,lk} = 0, \tag{3}$$

The part wavefront consequently cancels itself out if the measured wavefronts W_j are summed up, and this leads to the final form of the N-step averaging algorithm of

$$P_o = W_o - \frac{1}{N}\sum_{j=0}^{N-1} W_j. \tag{4}$$

In comparison with the previous two-step algorithm, this multiple N-step algorithm provides improvement in calibration accuracy with relatively simple arithmetic averaging. However, the problem that the RI and AH part wavefronts are not separated remains unsolved since the properties of Eq.(3) are not valid if k equals zero or integer multiples of N as in the previous algorithm.

3. ARBITRARY N-STEP ALGORITHM

The loss of the AH part wavefront may be minimized if the number of part rotation N is taken large enough. In practice, however, this requires a high precision in part rotation because higher order wavefront components are particularly sensitive to rotation errors. This problem could be coped with if an accurate device of azimuthal angle division is used. Nevertheless, a more effective way would be modifying the current computational method as in the 'arbitrary N-step algorithm' proposed hereafter. The new algorithm is not confined by the equal spacing requirement to permit part rotations to be made at arbitrary azimuthal positions. The key idea is to treat the rotated angles α_j as additional unknowns together with the coefficients $c_{0,lk}$ and $\tilde{c}_{0,lk}$, and adopt the least squares technique to determine the true values of the unknowns simultaneously. For this, P_0 is rearranged in a combined form of

$$P_0(r,\theta) \equiv \sum_k P_0{}^k(r,\theta) = \sum_k \{\sum_l^{L(k)} \xi_{0,l}^k Z_l^k(r,\theta)\} \tag{5}$$

where $Z_l^k(r,\theta) \equiv R_l^k(r)\begin{Bmatrix}\cos\\ \sin\end{Bmatrix}(k\theta)$ with $\xi_{0,l}^k$ being corresponding coefficients [11], and K is the maximum order up to which the Zernike polynomials to be identified. In addition, the wavefront difference $D_j(r,\theta)$ is newly defined as the subtraction of

$$D_j(r,\theta) = P_j(r,\theta) - P_0(r,\theta) \equiv \sum_{k=1}^{K} D_j^k(r,\theta) = \sum_{k=1}^{K}\{\sum_l^{L(k)} \Delta_{j,l}^k Z_l^k(r,\theta)\} \tag{6}$$

where $\Delta_{j,l}^k \equiv \xi_{0,l}^k[\cos(k\alpha_j) - 1] + \tilde{\xi}_{0,l}^k \sin(k\alpha_j)$

Now, when multiple measurements have been completed by rotation, let $\hat{D}_j^k(r,\theta)$ be the actually measured value of $D_j^k(r,\theta)$ with $\hat{\Delta}_{j,l}^k$ being the Zernike coefficients computed from $\hat{D}_j^k(r,\theta)$. Two cost functions to be minimized are then defined as

$$E_l^k = \sum_{j=0}^{N-1} \{\Delta_{j,l}^k - \hat{\Delta}_{j,l}^k\}^2 = \sum_{j=0}^{N-1} \left\{ \xi_{0,l}^k [\cos(k\alpha_j) - 1] + \tilde{\xi}_{0,l}^k \sin(k\alpha_j) - \hat{\Delta}_{j,l}^k \right\}^2 \quad \text{and} \tag{7}$$

$$E_j^k = \sum_{l}^{L(k)} \{\Delta_{j,l}^k - \hat{\Delta}_{j,l}^k\}^2 = \sum_{l}^{L(k)} \left\{ \xi_{0,l}^k [\cos(k\alpha_j) - 1] + \tilde{\xi}_{0,l}^k \sin(k\alpha_j) - \hat{\Delta}_{j,l}^k \right\}^2 . \tag{8}$$

According to the rules of least squares, the necessary conditions to minimize the above cost functions are given in the form of

$$\frac{\partial E_l^k}{\partial \xi_{0,l}^k} = \frac{\partial E_l^k}{\partial \tilde{\xi}_{0,l}^k} = \frac{\partial E_j^k}{\partial \cos(k\alpha_j)} = \frac{\partial E_j^k}{\partial \sin(k\alpha_j)} = 0 . \tag{9}$$

As described in detail in [11], the partial derivatives of Eq.(8) reduce to two linear algebraic matrix equations so that the true values of $\xi_{0,l}^k$, $\tilde{\xi}_{0,l}^k$, and α_j are obtained in an iterative way until 10^{-7} order convergence is achieved.

4. SIMULATION

The proposed arbitrary N-step algorithm has been tested to verify its advantages and usefulness through computer simulation. Figure 1 describes a case study in which the performances of the N-step averaging and AR-step (arbitrary N-step) algorithms are compared when there are significant amounts of azimuthal position errors in part rotations. Figure 1(a) illustrates the instrument error to be eliminated while the part wavefront is assumed perfectly flat. The number of steps was taken as 6 equally for both the algorithms and the maximum Zernike order of interest was K=5. In comparison, it can be seen that the AR-step algorithm is capable of effectively removing almost all the instrument error although part rotations are not accurately induced as intended. On the other hand, the N-step algorithm is limited in restoring the part wavefront especially around the circumference of the measured area..

(a) (b) (c)

Figure 1. Comparison of simulation results when true values of α_j are not equally spaced mistakenly with 0°, 61°, 121°, 179°, 241°, 299°. Original wavefront generated for simulation with all the Zernike coefficients being 0.1λ for k=1-5. (a) Fringe map of the original wavefront (P-V: 1.118μm and rms: 0.110λ). (b) The wavefront error extracted by the 6-step averaging technique (P-V: 0.017μm and rms: 0.001λ). (c) The wavefront error computed by the AR-step algorithm (P-V: 0.001μm and rms value: $3\times10^{-7}\lambda$).

Figure 2 describes another case in which higher order instrument errors are dominant in the range of k=6 to 8 as shown in (a). If the number of part rotation is taken as 6, the N-step algorithm fails to remove the 6th angular harmonic error components as illustrated in (b). On the other hand, the AR-algorithm suppress the higher order instrument errors with the same number of part rotations. Effective elimination of higher order errors are especially important when the surface irregularities of the part is to be examined accurately..

(a) (b) (c)

Figure 2 Suppression capabilities of high frequency components when α_j are intentionally taken as 0°, 61°, 121°, 179°, 241°, 299°. (a) Original wavefront generated for simulation with all the Zernike coefficients being 0.1λ for k=1-8 (P-V: 1.763μm and rms: 0.110λ). (b) The wavefront error extracted by the 6-step averaging technique (P-V: 0.409μm and rms: 0.001λ). (c) The wavefront error computed by the AR-step algorithm (P-V: 0.012μm and rms value: $2\times10^{-5}\lambda$).

5. CONCLUSIONS

Our intention in this paper is to improve the N-step averaging method with a particular attention of effective separation of the AH wavefront. The 'arbitrary N-step algorithm' proposed in this paper is not confined by the equal spacing requirement, permitting part rotations to be made at arbitrary azimuthal positions. This generalized algorithm eliminates calibration errors caused by rotation inaccuracy and also offers a great advantage of reducing the required number of part rotations drastically when higher order spatial frequency terms are of particular importance. The latter benefit is obtained by imposing a predetermined small amount of intentional offset in the azimuthal positions during part rotations.

REFERENCES

[1] J.E. Greivenkamp and J.H. Bruning, "Phase shifting interferometry," in *Optical Shop Testing*, 2nd ed., D. Malacara, ed., Wiley, New York, Chap.14 (1992).

[2] C. Evans, R. Hocken, and W. Estler, "Self-calibration: reversal, redundancy, error separation, and absolute testing," Annals of the CIRP **45**(2), 617(1996).

[3] R.E. Parks, "Removal of test optics errors," Proc. SPIE, **153**, 56(1978).

[4] B.S. Fritz, "Absolute calibration of an optical flat," Opt. Eng. **23**, 379(1984).

[5] C. Ai and J.C. Wyant, "Absolute testing of flats using even and odd functions," Appl. Opt. **32**, 4698(1993).

[6] V.Greco, R.Tronconi, C.D.Vecchio, M.Trivi, and G.Molesini, "Absolute measurement of planarity with Fritz's method: uncertainty evaluation," Appl. Opt. **38**(10), 2018(1999)

[7] C. Evans, R. Kestner, "Test optics error removal," Appl. Opt. **35**(7), 1015(1996).

[8] W.T. Estler, C.J. Evans, L.Z. Shao, "Uncertainty estimation for multi-position form error metrology," Prec. Eng. **21**(2/3), 72(1997)

[9] R.E.Parks, L.Shao, and C.J.Evans, "Pixel-based absolute topography test for three flats," Appl. Opt. **37**(25), 5951(1998).

[10] S.-W. Kim and H.-G. Rhee, "Self-calibration of high frequency test optics error by N-step rotation," Appl. Opt., to appear.

[11] D. Malacara and S.L. DeVore, "Interferogram evaluation and wavefront fitting," in *Optical Shop Testing*, 2nd ed., D. Malacara, ed., Wiley, New York, Chap.13 (1992).

Sensitivity Analysis of a Cylindrical Interferometer

P. Douglas Knight, Jr., Steve R. Patterson

Mechanical Engineering and Engineering Science Department
University of North Carolina at Charlotte
Charlotte, NC 28223

I. Introduction

A grazing incidence cylindrical interferometer for the measurement of cylindrical parts has been designed and manufactured by the Tropel Corporation.[1,2,3] During the measurement, the instrument interferometrically maps a cylindrical artifact onto a fringe annulus. Since the axial length of the cylinder is compressed into a smaller radial image distance, this leads to the question of what is the axial spatial frequency sensitivity of the instrument. To test the interferometer for axial instrument transfer function[4], cylindrical artifacts having azimuthally symmetric surface errors with a sinusoidal dependence on axial position were diamond-turned. The parts were measured with an upgraded Mahr MFU-7 and an early version of the Tropel CM25 cylindrical interferometer. Because of the lower resolution optical transfer function of this version of the instrument, it was a good platform to study instrument response. The measured waveform amplitudes from the interferometer were compared in frequency space to measurements from the mechanical roundness instrument.

II. Measurement Artifacts and Analysis

Three nominally 30-mm long brass parts were diamond turned using a Precitech Nanoform 350 diamond turning machine. Each artifact had a 1.0 um amplitude sinusoid turned along the part axis with a corresponding 15.0, 6.0 and 3.75 mm axial wavelength. An upgraded Mahr MFU-7 at the UNC Charlotte metrology lab measured straightness of each part. Twelve straightness measurements 30 degrees azimuthally apart were taken along a 20 mm axial trace starting 5 mm from the bottom of each artifact. Each trace consisted of 2000 data points and was taken with a 3 mm stylus tip and a stylus force of 3 grams. For each straightness trace, a Fourier transform of a centered measurement window equal in length to a integer multiple of waves was calculated. For each part, the results of the Fourier transform were averaged and the magnitudes of the spatial frequencies from 1 to 10 oscillations per window were calculated. The average of the twelve straightness traces along with the magnitude of the amplitude of each spatial frequency term is shown in Figures 1, 2 and 3. The dominant sinusoid amplitude of the 15 mm wavelength part was 0.87 um; for the 6 mm wavelength part, the dominant sinusoid amplitude was 0.99 um; and for the 3.75 mm wavelength part, the dominant sinusoid amplitude was 0.96 um. Based on a statistical evaluation of 12 data sets, the standard uncertainty of the dominant spatial frequency amplitude was 40 nm for the 15 mm wavelength part, 5 nm for the 6 mm wavelength part., and 15 nm for the 3.75 mm wavelength part. For the 15 mm wavelength part, the window length was equal to one period. This may have increased the magnitude of taper removal aliasing errors that contributed to a larger uncertainty. For the other parts the window was equal to three and four oscillations respectively and aliasing errors relating to taper removal would be reduced.

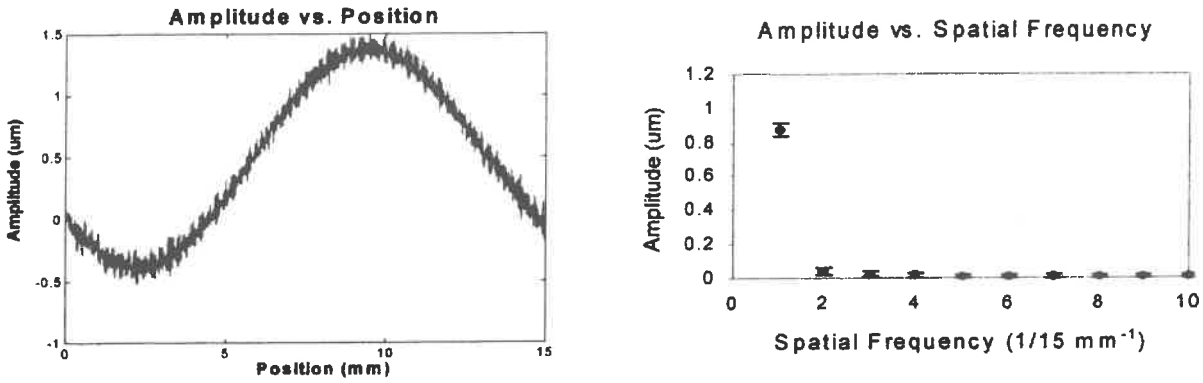

Figure 1: Average of 12 straightness traces of 15 mm window with taper removed taken by a Mahr MFU-7 for nominal 15 mm axial wavelength, 1.0 um amplitude artifact. Also, amplitude of each spatial frequency shown.

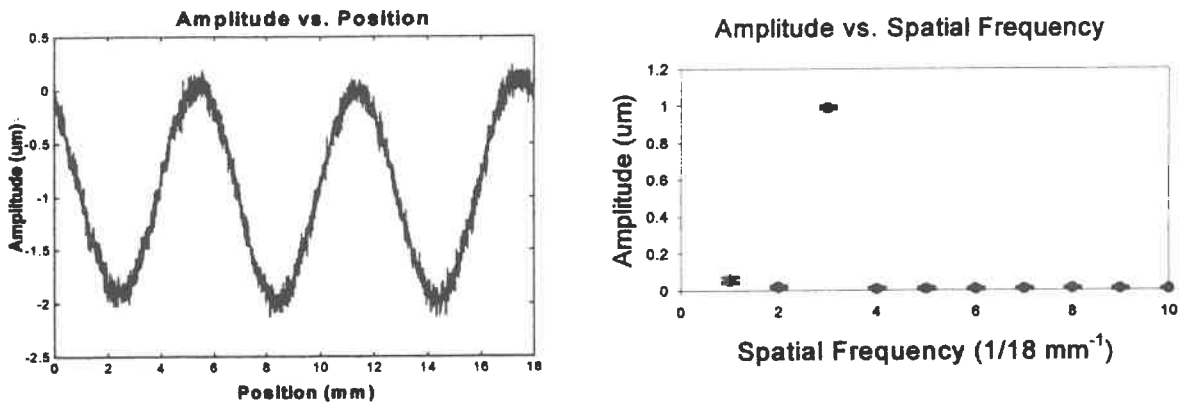

Figure 2: Average of 12 straightness traces of 18 mm window with taper removed taken by a Mahr MFU-7 for nominal 6 mm axial wavelength, 1 um amplitude artifact. Also, amplitude of each spatial frequency shown.

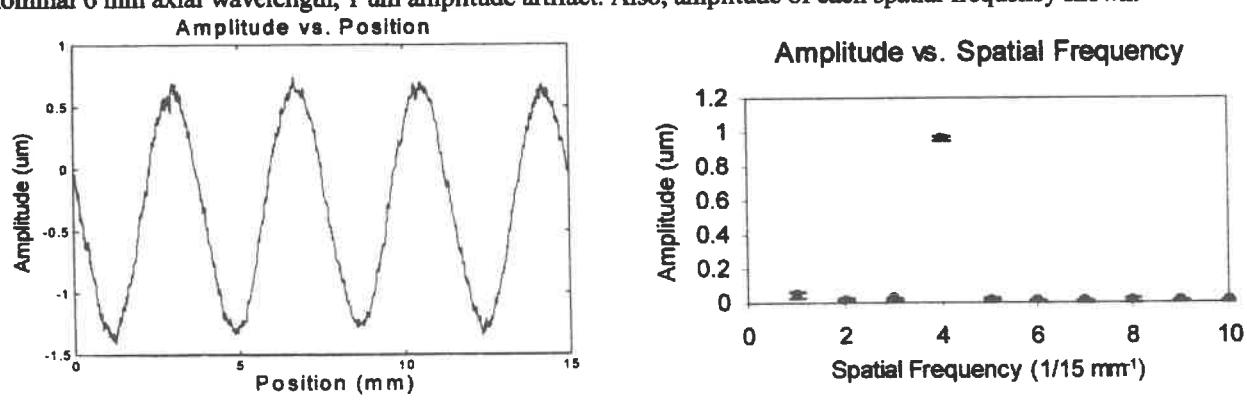

Figure 3: Average of 12 straightness traces of 15 mm window with taper removed taken by a Mahr MFU-7 for nominal 3.75 mm axial wavelength, 1 um amplitude artifact. Also, amplitude of each spatial frequency shown.

III. Optical Measurements and Analysis

Each axial sinusoid artifact was measured by the Tropel CM25 cylindrical interferometer with a shortest wavelength straightness cutoff filter of 0.8 mm. The measurement resulted in 256 straightness data sets evenly spaced around the artifact. For these parts, the straightness data sets were composed of 42 data points with a resolution of 1.58 pixels/mm. For the 15-mm and the

3.75 mm wavelength part, a 15.2-mm window that corresponded to 24 pixels of data was sampled from each straightness measurement. For the 6-mm wavelength part, a 18.2-mm window corresponding to 28 pixels of data was sampled from each straightness measurement. The measurement window for each part sampled the same axial length for both the mechanical and optical measurements. All straightness data sets for each window of straightness data and artifact were Fourier transformed and averaged. The straightness data sets with taper removed from the cylindrical interferometer data along with the amplitude of each spatial frequency term are shown in Figures 4, 5, and 6. The statistical uncertainty evaluation of the amplitude of each spatial frequency term was less than 2 nm. For the 15 mm wavelength part, the interferometer measured the part at the nominal part amplitude. As the wavelength of the axial sinusoid of nominally one micron amplitude decreased to 6 mm then to 3.75 mm, the magnitude of the response of the interferometer decreased. This may be a function of the interferometer reflecting light off the surface at grazing incidence shortening the axial profile causing larger slopes more difficult to resolve.[5]

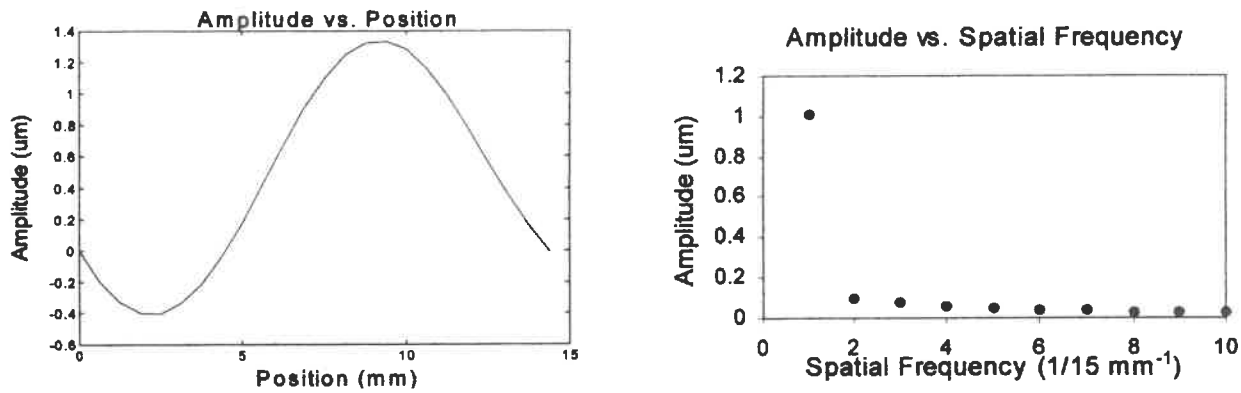

Figure 4: Average of 256 sets of axial data points of a 15 mm window from data taken by a Tropel CM25 cylindrical interferometer for nominal 15 mm axial wavelength, 1 um amplitude artifact. Also, Fourier transform of data shows amplitude of each spatial frequency.

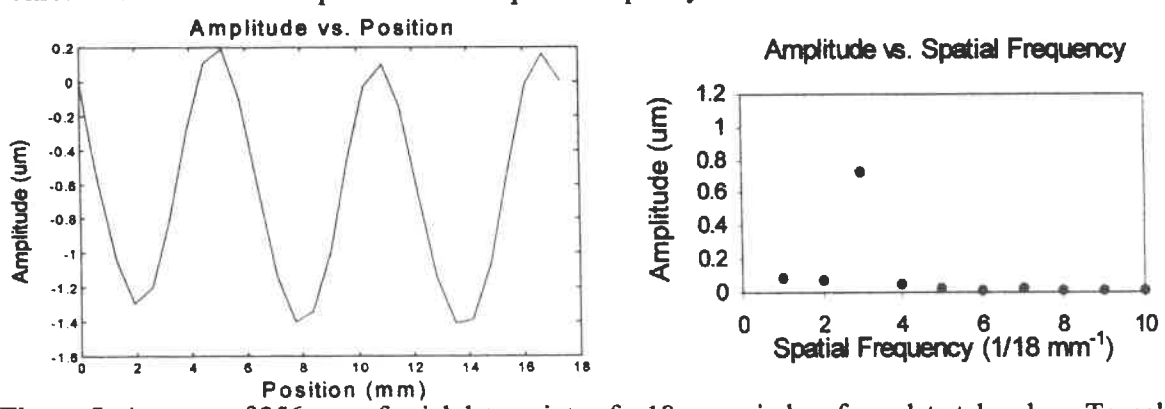

Figure 5: Average of 256 sets of axial data points of a 18 mm window from data taken by a Tropel CM25 cylindrical interferometer for nominal 6 mm axial wavelength, 1 um amplitude artifact. Also, Fourier transform of data shows amplitude of each spatial frequency.

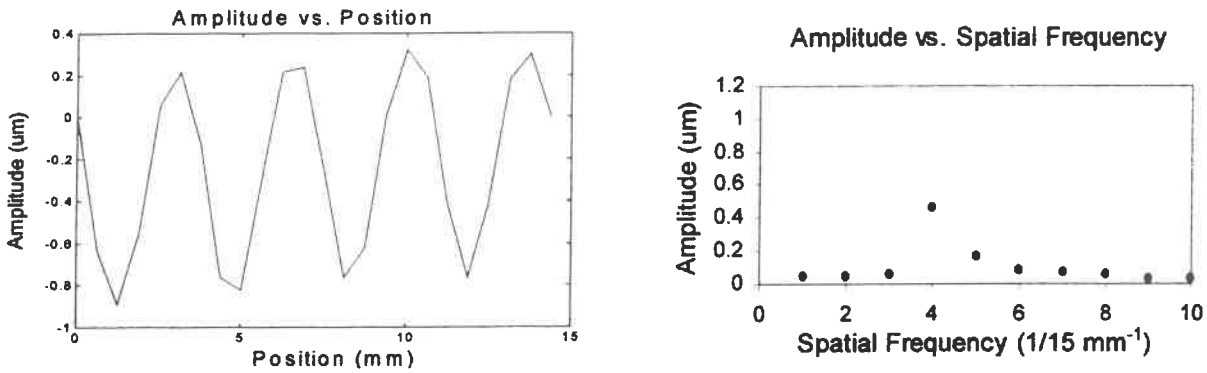

Figure 6: Average of 256 sets of axial data points of a 15 mm window from data taken by a Tropel CM25 cylindrical interferometer for nominal 3.75 mm axial wavelength, 1 um amplitude artifact. Also, Fourier transform of data shows amplitude of each spatial frequency.

IV. Conclusions

Three axially sinusoidal cylindrical artifacts of differing spatial wavelength and nominally similar amplitude were diamond turned and measured for axial straightness with both a mechanical and interferometric instrument. Based on the mechanical measurements, the sinusoid amplitude was nominally one micron for each artifact. At a one micron amplitude, as the spatial wavelength of the parts became shorter, the amplitude response of the cylindrical interferometer decreased. This effect appeared to be slope dependent, which would also make the response a function of both sinusoid amplitude and spatial frequency. This may be due to the interferometer reflecting light off the surface at grazing incidence shortening the axial profile, [5] the number of pixels in the axial direction sampling the artifact, or the optical modulation transfer function of the optical imaging system. Further work includes measuring the parts on the new, high-resolution version of the Tropel CM25 and investigating the response of the cylindrical interferometer as a function of artifact spatial slope.

V. References

1. Denes, L. and Salsbury, J., "Flatness, Parallelism and Other Novel Uses of Grazing-Incidence Interferometry in Precision Engineering," Proceedings of the ASPE, **11**, 20-23 (1995).

2. Knight, P.D. and Patterson, S.R., "Repeatability and Calibration of a Grazing Incidence Cylindrical Interferometer," Proceedings of the ASPE, **16**, 106-109 (1997).

3. Dresel, Thomas et al, "Grazing incidence interferometry applied to the measurement of cylindrical surfaces," *Opt. Eng.*, **34**, 3531-35 (1995).

4. J. W. Goodman, *Introduction to Fourier Optics*, Mc-Graw Hill, Inc., New York, NY (1968).

5. Harvey, James et al, "Transfer function characterization of grazing incidence optical systems," *Appl Opt.*, **27**(8), 1527-1533 (1988).

Non-contact Acousto Optic Scanning Laser Doppler Vibrometer

Ngoi.B.K.A., and Venkatakrishnan.K
Precision Engineering Strategic Research Programme
School of Mechanical and Production Engineering
Nanyang Technological University
Nanyang Avenue, Singapore 639798

Brief introduction

Laser vibration-measuring system has the advantage of being non-contact in measurement of vibration. Some application requires not only point vibration measurement but also surface vibration at several critical points by deflecting the beam at different angles by what is called the scanning technique. Current scanning technique which employs deflection mirror, can not achieve very high measurement accuracy and positioning accuracy because of the unavoidable vibration of the mechanically driven mirror. In this paper we design a novel scanning vibrometer using Acouso-optical deflector. It overcomes the limitation of conventional scanning vibrometer.

Scanning technique

In order to get parallel scanning beam, the AO Deflector is positioned such that its optical axis is at the focal length of the collimating lens CL1 and CL2. Moreover the collimated beam incident on the AO deflector at the Bragg's angle of the acoustic crystal.

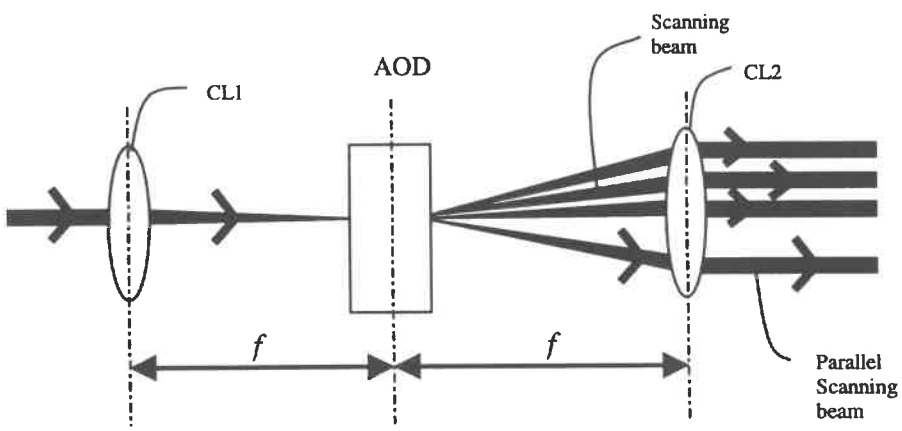

Fig.1 Optical system to generate parallel scan beams

Optical system design for a scanning heterodyne vibrometer

Referring to Fig.2, linearly polarised light from the laser source is modulated by an Acousto Optic Modulator (AOM). The Zero order beam from the AOM passes through a polarising beam splitter PBS1 where as the first order beam having a frequency shift with reference to the zero order beam(equal to the frequency of the acoustic wave in the AOM) is deflected by PBS1. The zero order beam acting as a measuring beam. It passes through a scanning system described as above.The parallel-scanning beam passes through the polarizing beam splitter PBS2 and the quarter wave plate WP1 to strike the target surface, whose dynamic characteristics are to be measured. The scanning beam thus reflected from the target surface, carrying the dynamic information is deflected by the PBS2 due to shift in the polarisation state by the WP1.

Similarly the 1st order beam from the AOM, which acts as the reference beam, is deflected by the PBS1 on to the deflecting mirror DM2. The Deflected beam has the optical path along the Collimating lens CL3, Acousto Optic Deflector AOD2 and collimating lens CL4 of the same configuration and purpose as the CL1, AOD1 and CL2 in the measuring beam path. The reference beam then strikes the reference surface via a quarter wave plate WP3. The polarising beam splitter PBS3 deflects the reflected beam where it is aligned with the measuring beam. The beam is focused by using an collimating lens CL5 and is made to interfere by the polariser P1. Also the 0th order beam from the AOD1 is made to interfere with the 0th order beam from the AOD2 by the polarising beam splitter PBS4 and the polariser P2. The photo detector 1 and photo detector 2 captures the interference signals.

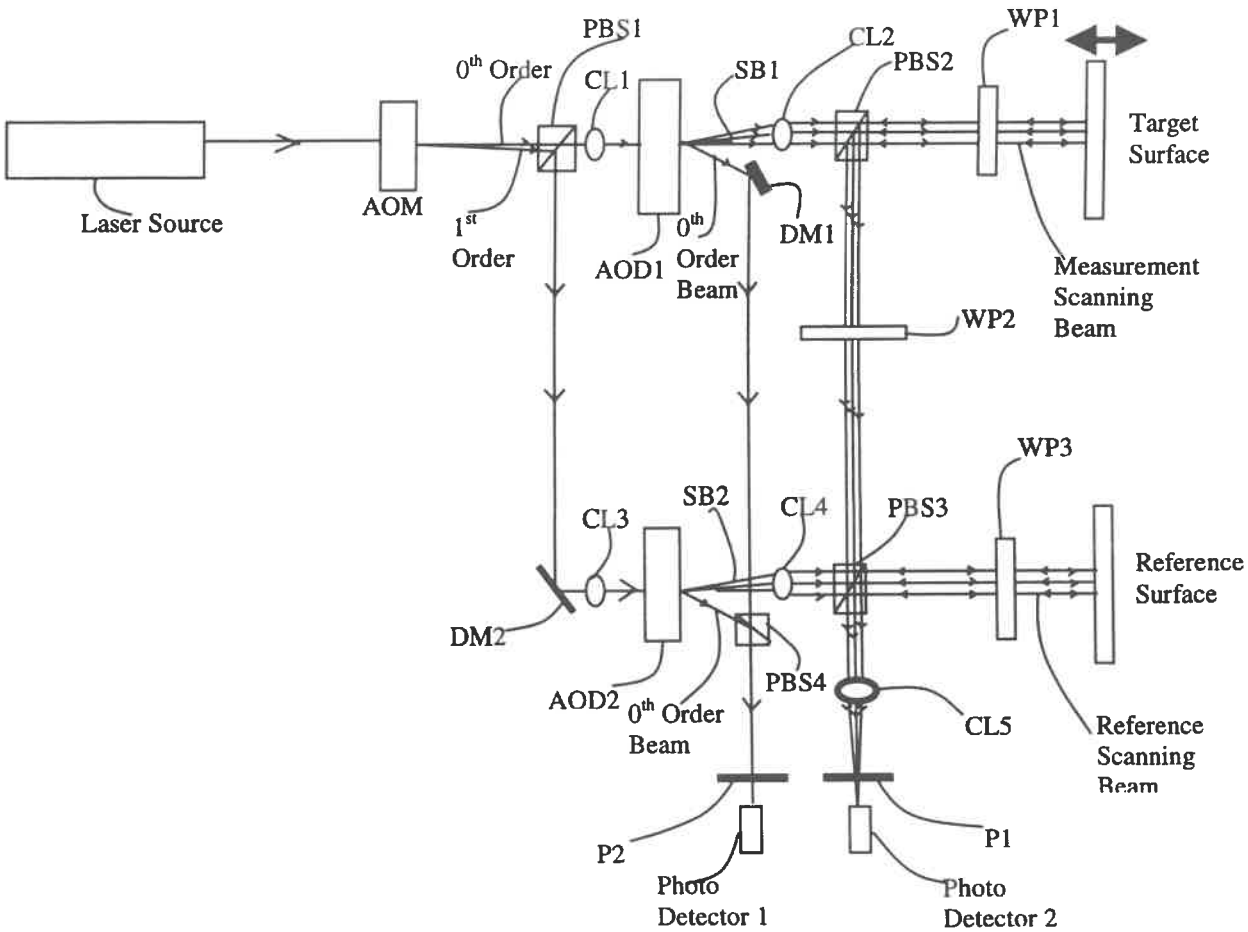

Fig.2 Optical Layout of the Scanning Heterodyne Vibrometer system

A common signal generator, whose signal is amplified by a common or independent power amplifier, drives the two Acousto Optic Deflector AOD1 and AOD2. The purpose of driving the two Acousto Optic Deflectors by a common drive is to obtain very precisely the same deflection angle for each of the input frequency. This is an essential factor for interfering the measuring and reference beam at each of the scan points automatically provided the beam was interfered at one of the scan points.

Interference mechanism of the measuring and the reference scanning beam:

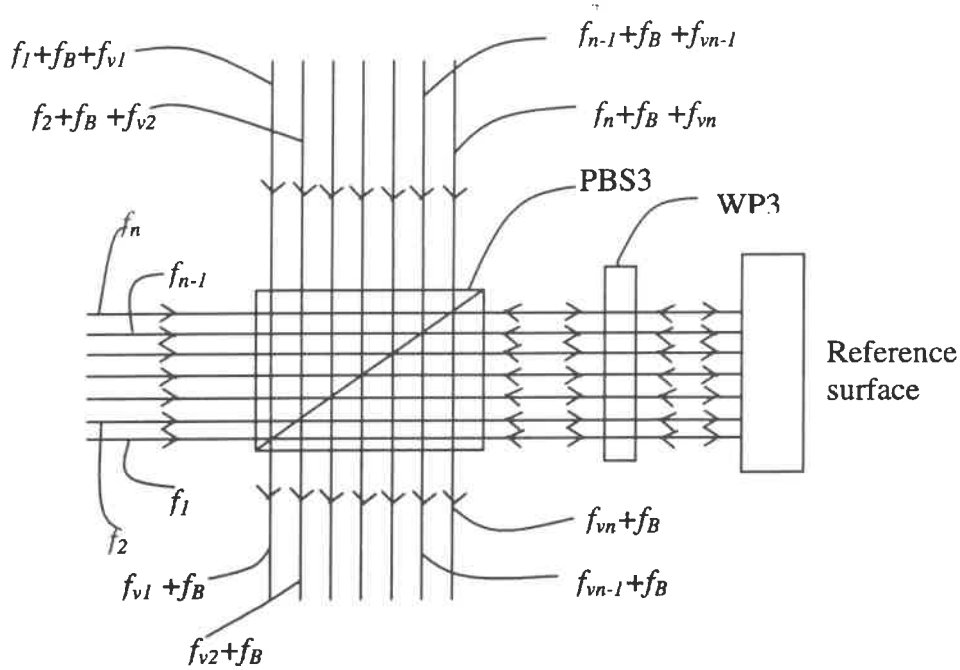

Fig. 3 Interference mechanism of the reference and measuring scanning beam

The Fig.(3) shows the interference phenomenon involved in this technique. The scanning first order laser beam from the Acousto Optic Deflector AOD1 has the minimum frequency shift of f_1 induced and the next higher level of frequency shift induced is f_2. Similarly the highest frequency shift induced is f_n and the highest but one frequency shift is f_{n-1}. All these frequency shifts are with reference to the frequency of the zero order beams. Same is the case with the Acousto Optic Deflector AOD2 since they are made of the same specification and driven by a common driving mechanism.

So the optical design is designed such that the measuring scanning beam from the AOD1 of frequency $f_1+f_B+f_{v1}$, $f_2+f_B+f_{v2}$,.....$f_{n-1}+f_B+f_{vn-1}$, $f_n+f_B+f_{vn}$ interferes with the reference scanning beam from the AOD2 of frequency f_1, f_2, ...f_{n-1}, f_n. Where f_B is the frequency shift induced due to the Acousto Optic Modulator. Hence the resultant frequency of the interference beam is given by $f_{v1}+f_B$, $f_{v2}+f_B$, ...$f_{vn-1}+f_B$, $f_{vn}+f_B$, where f_{v1}, f_{v2}, ...f_{vn-1}, f_{vn} are the frequency shift induced due to the vibration of the measuring surface at each of the corresponding scanning point. The photo detector 2 captures these interference signals. Also the zero order beam from the AOD 1 which has a frequency of f_o+f_B (where f_o is the frequency of the laser beam) interferes with the zero order beam from the AOD2 of frequency f_o. The photo detector 1 captures the resulting interference beam of frequency f_B. The photo detector 1 and photo detector 2 are connected to the reference and measuring port of the signal processor respectively.

Experiments

Experiment was carried out in a vibration isolation table using He-Ne laser (632.8nm) in a clean room environment. The beam was scanned on the surface of the rotating disk and the dynamic information (Run Out of disk) was recorded at various scan points.

The resultant displacement output of the signal processor is given by

$$d = \left(\frac{\phi_1}{2\pi} + N_1 \right) \frac{c}{2 f_0}$$

where d is the amplitude of vibration, ϕ_1 is the phase angle, N_1 is a integer, c is the velocity of light, f_0 is the frequency of the laser beam.
Fig. 4 shows the measured result.

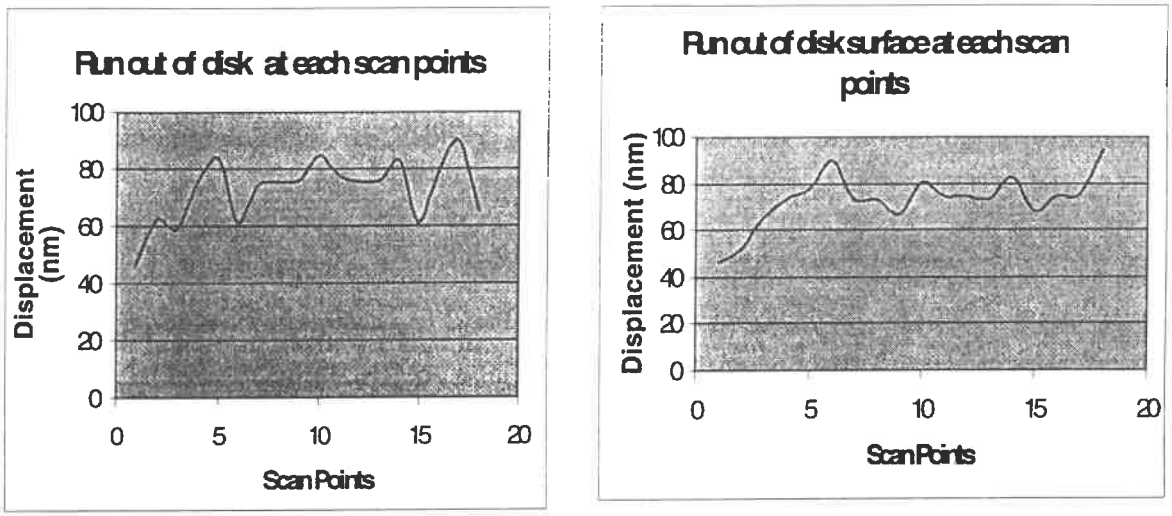

Fig.4 Run out of the disk at different scan point

Conclusion

Since the process applies Acousto optic Deflector, a non-mechanical means of scanning, for scanning the beam it has the following advantages

- High accuracy even when the beam is scanning at high speed.
- The number of resolvable points is about 68,000 point for each of the scanning axis, which is very difficult to be achieved by a mirror driven scanning means.
- It has a very high sweep rate.
- The Acousto Optic scanning mechanism has a very high positioning accuracy and repeatability.

The non-mechanical scanning method finds a wide application in optical storage, hard disk drive and also in MEMS application. The next challenge is the reduction in the spot size of the laser beam, which is limited by the divergence of the laser beam from the laser source.

Reference

1. Polytec Scanning Vibrometer Catalog
2. G.L.Rossi et.al " Dynamic characterization of a centrifugal compressor rotor by a laser scanning vibrometer", SPIE vol. 2686, 1996, pp290-293.
3. P.Castellini and C. Santolini, "Vibration measurement on blade of naval propeller rotating in water" SPIE vol. 2686, 1996, pp186-194.
4. Gianmarco Liotto and Charles Wang, " Vibration Measurement by Laser Doppler Displacement Meter" SPIE vol. 2686, 1996, pp337-343.Bb
5. Kanu G.Ashar, " Magnetic Disk Drive Technology", IEE Press, New York, 1997, pp276-298.

A LOW COHERENCE INTERFEROMETER FOR ABSOLUTE DISTANCE MEASUREMENT

Andrew D. Woodfin, Faramarz Farahi, Robert J. Hocken
University of North Carolina at Charlotte
9201 University City Blvd.
Charlotte, NC 28223

Introduction

Scanning white light interferometry (SWLI) has seen increasing applications in three-dimensional surface profiling as an alternative to conventional interference microscopy.[1,2] The established technique typically involves incrementally moving a microscope objective along its imaging axis and perpendicular to the surface under study. By incorporating an interferometric scheme (commonly a Michelson or Mirau configuration) within the objective, the axial scanning serves to monotonically vary the distance between the two optical paths. Conventional phase measuring methods are fundamentally limited to phase modulo 2π, unless phase-shifting techniques and accompanying phase unwrapping algorithms are employed; even then, abrupt large vertical scale surface features can confuse the signal interpretation. Under illumination by "white" light, however, the source's short coherence length affords a distinct optical path difference at which the interference contrast is maximum; thus the measurement range becomes effectively infinite, so long as the point of maximum interference contrast can be located and correlated with an axial position. The limitation here, however, is in the inability to isolate optical path differences arising solely from changes in displacement from those caused by other spurious contributions to optical phase changes. The contribution to displacement error from failure to consider the phase change on reflection from dissimilar interfaces can be on the order of at least 30 nm.[3]

The technique cursorily explained above is widely accepted and practiced, and several surface profiling devices are commercially available which exploit the unique properties of the low-coherence interferometric transfer function. Due to the necessary presence of bulk optical elements, coupled with the physical size of an incandescent source, current instruments are poorly suited to in situ inspection. Exceptions to these constraints exist, but only for particular applications which are still limited in scope by device size and geometry.

Our current work addresses the need for a compact, non-contact probe capable of in situ measurement and access to areas heretofore restricted by instrument size. The technique involves transmission of illumination to the sample via optical fiber, thus allowing for significant reduction in the size of the measurement head by physically separating it from the source. The work presented here outlines the instrument fundamentals preceding the development of a compact probe.

Utilizing a highly characterizable solid state light source with intermediate low coherence length, an interferometric technique has been developed to allow for unambiguous absolute distance measurement. A priori knowledge of the source characteristics allows for accurate distance determination with minimal required data density. Unlike broadband incandescent sources commonly employed in low coherence interferometry, as mentioned, the nature of the source employed here allows for a reduction in parasitic effects from dispersive reflecting

surfaces. The hallmarks of low coherence interferometry, namely long range capability and ability to discriminate non-displacement induced phase changes, are preserved.

This approach to compensating for phase change on reflection requires no a priori knowledge of the surface under study, a requirement in some commercially interferometric surface profilers that carries dubious reliability due to oxidation and variations in film depositions.[4] Further, our technique employs a relatively simple apparatus, both mechanically and computationally.

Principles of Operation

Under normal incidence, Fresnel's equations for the optical reflection coefficients at an interface reduce to

$$R_p = \frac{n-1}{n+1} \tag{1}$$

$$R_s = -\frac{n-1}{n+1} \tag{2}$$

where n is the quotient of the complex refractive indices of the reflecting and incident media, respectively, i.e., $n = n_2/n_1$. The subscripts s and p denote polarizations perpendicular and parallel to the plane of incidence, respectively.[5] At normal incidence, phase change on reflection is ignorant of polarization direction, so for simplicity it is given by

$$\phi = \arg(R_p)\,. \tag{3}$$

The general equation for the output of a low-coherence interferometer, assuming a relatively narrow linewidth with respect to the central wavelength, is

$$I = I_0[1 + V\,|\gamma_{11}(\Delta L)|\cos(k_0\Delta L + \phi)] \tag{4}$$

where V is the visibility function, ΔL is the optical path difference due to displacement, k_0 is the wavenumber corresponding to the central wavelength of the source, and ϕ is the phase change on reflection. The spectral characteristics of the light source determine the complex degree of coherence, $\gamma_{11}(\Delta L)$, which in this case is determined by a Gaussian spectral distribution, thus

$$\gamma_{11}(\Delta L) = \exp\left[\frac{|\Delta L|}{L_c}\right], \tag{5}$$

where L_c is the source coherence length.[6]

As the source used in our experiments has a relatively narrow linewidth (17 nm), dispersive effects on the interferometer output due to surface interfaces is minimized considerably when compared to dispersion suffered by illumination from a broadband incandescent source. In addition, the superluminescent diode spectral profile is highly characterizable as a true Gaussian distribution. As such, the interferometer output can be accurately represented by equation 4. By sampling the detected interference function under scanned translation of the reference mirror, the collected data can be fit to the expected output using conventional nonlinear curve fitting techniques.[7] From the resulting relevant parameters, namely ΔL and ϕ, we can extract the pure displacement between two successive measurements (difference in values of ΔL) while simultaneously determining the differing phase changes on reflection (ϕ).

Experimental Setup

A superluminescent diode from Superlum of Russia (model SLD-381-TO-SM) was chosen for illumination of the interferometer based on 3 considerations: a need for relatively broad spectral width (compared to a single mode laser), high luminous output (compared to a

conventional LED), and a desire for compactness. The source emits at 825 nm with a linewidth of 17 nm, corresponding to a coherence length L_c of about 40 μm.

Figure 1 provides a schematic representation of the optical system used for the experiments. The superluminescent diode is pigtailed to a length of single mode optical fiber, thus collimation optics are placed at the fiber endface prior to entering the interferometer. The standard Michelson configuration is modified with a movable mirror in each arm. The reference mirror is mounted to a machined flexure assembly, driven by a stack PZT element. The piezoelectric actuator is capable of 15 micrometer maximum range of travel. The flexure serves 2 purposes: to decouple spurious angular motion over the range of actuator travel from the actuator to the mirror, and also to amplify the net translation range of the actuator. The sample is mounted to a single axis translation stage to effect static path length changes in that arm of the interferometer, which can be measured using the proposed technique.

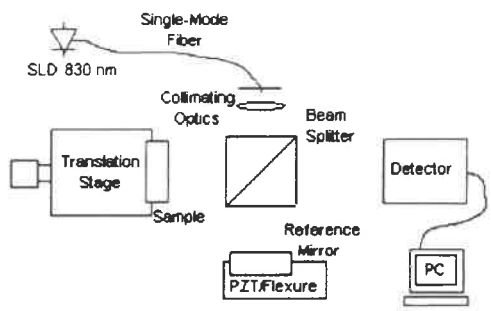

Figure 1 Experimental Setup

Experimental Results

The technique for measuring the distance between a reference mirror and a surface under study involves collecting the relevant coherence function data over a long enough range at two positions of the test surface. For a single target with homogeneous surface characteristics, the phase change on reflection becomes a moot point as it should be consistent between the two measurements. Comparing these two locations yields the change in position of the test surface. Figure 2 illustrates two scans superimposed, one for each position of a test mirror moved 20 micrometers between measurements. Note that the origin of the displacement scale is arbitrarily set to zero, as the absolute measurement is of the second position with respect to the first and not a comparison of either individual measurement with respect to an independent datum. The fitted parameters for the two interference functions yield, for the initial and final positions respectively,

$$\Delta L_1 = 41.20\ \mu\text{m and } \phi_1 = 0.384 \text{ rad} \quad (6)$$

$$\Delta L_2 = 61.21\ \mu\text{m and } \phi_2 = 0.384 \text{ rad} \quad (7)$$

The non-zero values for ϕ are most likely due to the contribution of phase change on reflection from the dielectric coating in the cube beamsplitter and the mismatch between the reference and sample mirror. The separation in ΔL values agrees with the translation stage displacement within less than 10 nanometers, which is due likely to limitations in verifying the stage position. Further experiments will validate the interferometric measurement against a more suitable means of displacement measurement.

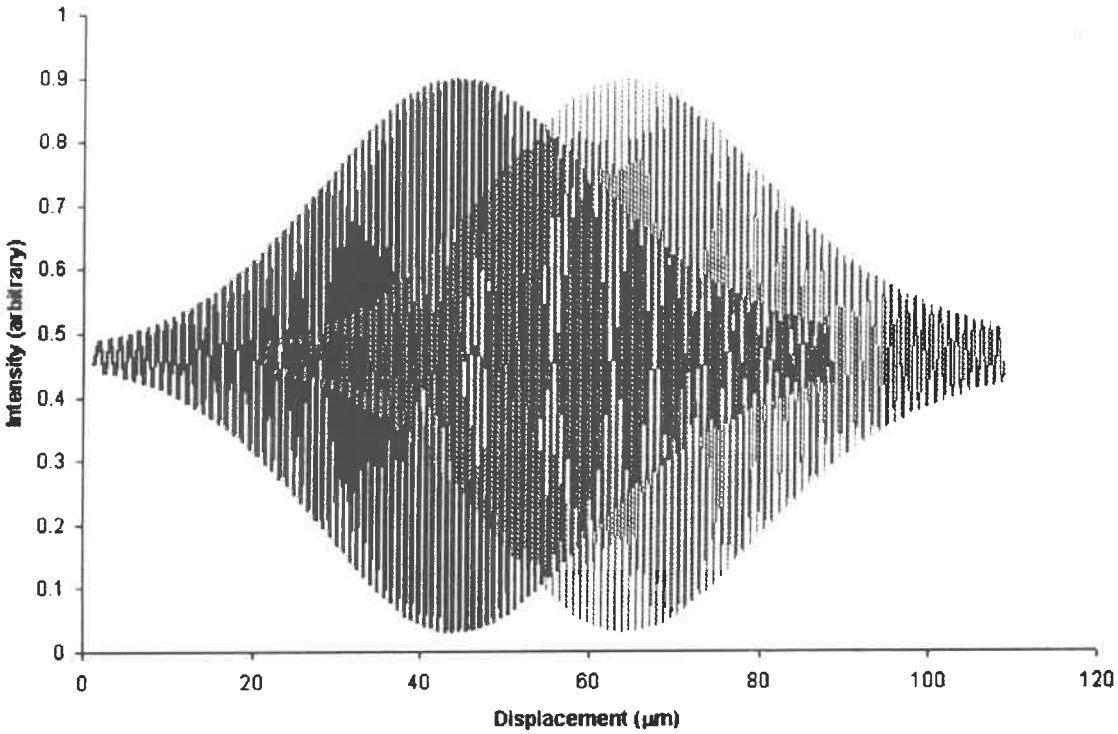

Figure 2 Interference functions for 2 positions of target surface

Acknowledgments

This work was supported by a grant from the National Science Foundation, as well as generous funding provided by the industrial affiliates of the University of North Carolina at Charlotte Center for Precision Metrology.

References

1. L. Deck and P. de Groot, "High-speed noncontact profiler based on scanning white-light interferometry," Appl. Opt., **33**, 7334-7338 (1994).
2. P. J. Caber, "Interferometric profiler for rough surfaces," Appl. Opt., **32**, pp.3438-3441, (1993).
3. J. F. Biegen, "Determination of the phase change on reflection from two-beam interference," Opt. Lett., 19, 1690-1692 (1995).
4. C. W. See, M. G. Somekh, and R. D. Holmes, "Scanning optical microellipsometer for pure surface profiling," Appl. Opt. **35**, 6663-6668 (1996).
5. M. Born and E. Wolf, *Principles of Optics*, 6th ed., (Cambridge Univ. Press, Oxford, UK, 1993), Chap. 1, pp. 40-41.
6. M. Born and E. Wolf, *Principles of Optics*, 6th ed., (Cambridge Univ. Press, Oxford, UK, 1993), Chap. 10, p. 506.
7. W. H. Press, S. A. Teukolsky, W. T. Vetterling, and B. P. Flannery, *Numerical Recipes in C*, (Cambridge Univ. Press, Oxford, UK, 1997), Chap. 15, pp. 683-687.

In-situ Absolute Calibration of Interference Microscopes

S. Zhang*, M. Kanai*, T. Aramaki, W. Gao* and S. Kiyono***
* : Tohoku University, Aoba-01 Sendai 980-8579, JAPAN
** : Nikon Corporation, Tokyo 140-8601, JAPAN

ABSTRACT

In the present study, a new in-situ absolute calibration method for an interference microscope is proposed, and a new calibration system is developed. This method can be used to determine not only the linearity error but also the mean sensitivity on the base of the wavelength. The calibration system combines a compact laser interferometer and the previously developed in-situ calibration system. The laser interferometer is used only to determine the necessary displacement shift quantity with an integer multiple of half wavelengths. Using this known displacement shift quantity, both the mean sensitivity and the linearity error of a microscope can be determined. The feasibility of the proposed method is demonstrated also with experimental results.

1. INTRODUCTION

Interference microscopes (microscopes) have long been used in quantitative characterization of surface structure. With recent phase detecting techniques, microscopes can achieve extremely high vertical resolution[1]. However, the accuracy of microscopes is affected by some inherent systematic errors[2]. In particular the linearity error (deviation from a linear calibration line) of the microscope output is much larger than the resolution level. In addition, because the characteristics of the linearity error are not stationary, but change with measurement circumstances, it is desirable to calibrate microscopes frequently in the circumstance where the microscope is working (in-situ calibration). However, an accurate calibration reference is necessary in the conventional comparison method, and it is difficult to get a reference with enough accuracy in practice. It is also much more difficult to carry out the in-situ calibration.

Authors have proposed an *in-situ* self-calibration method for a microscope[3]. However, the proposed method is based on the premise that the mean sensitivity (inclination of linear calibration line) of the microscope be given beforehand, therefore, only the linearity error can be determined.

In the present study, a new in-situ absolute calibration method for a microscope is proposed, and a calibration system is developed. This new method can be used to determine not only the linearity error but also the mean sensitivity on the base of the wavelength. The new system combines a compact laser interferometer and the previously developed in-situ calibration system[3]. The laser interferometer is used only to determine the necessary displacement shift quantity with an integer multiple of half wavelengths of the laser light source. Using this known displacement shift quantity, both the mean sensitivity and the linearity error of a microscope can be determined.

In the present report, the principle of the proposed in-situ absolute calibration for a microscope and its calibration system are introduced. A microscope[4] has been calibrated successfully to the limit of stability of this microscope which is determined from the signal-noise ratio.

2. ABSOLUTE CALIBRATION PRINCIPLE

Figure 1 shows a schematic diagram of the calibration target, which is a scanning white light interferometer microscope that employs a new spatial frequency domain analysis technique[1]. The test surface shown in Fig. 1 is scanned by moving the objective in the Z-direction using a PZT. Because the sampling position is decided by the scanning PZT, nonlinear motion of the PZT will greatly affect the linearity of the microscope. For example, although this microscope has a vertical resolution of 0.1 nm with a maximum vertical range of 100 μm, the assured accuracy is only 1.5% of the vertical range[4].

Assume the calibration curve of a microscope is described by the function f(z) that can generally be

expressed as the sum of a straight line having a slope of S_0 and the deviation function g(z) from the straight line[3]. The function f(z) is expressed as follows:

$$h = f(z) = S_0 \times z + g(z) \quad (1)$$

Here, S_0 and g(z) represent the mean sensitivity and the linearity error, respectively. Let the displacement output of the microscope at sampling position z_i be m_i, and that at position $z_i + \Delta z$ (Δz is the displacement shift quantity) be m_{i+}. If the inverse function of f(z) is given by :

$$h_i = m_i, \quad f^{-1}(h_i) = h_i / S_0 - b(h_i) \quad (i = 1, 2, \ldots, n) \quad (2)$$

where n is the sampling number and b(h) is the inverse function of g(z), the derivative of b(h) at the discrete i-th sampling point can be expressed by

$$b'(h_i) = 1/S_0 - \Delta z / \Delta m_i \quad (\Delta m_i = m_{i+} - m_i) \quad (3)$$

Here, the necessary displacement shift quantity Δz can be determined with an integer multiple of half wavelengths of the laser light source, S_0 can be calculated by

$$S_0 = \{ \sum \Delta m_i / \Delta z \} / n \quad (4)$$

and b(h) can be obtained by integrating $b'(h_i)$.

Figure 2 shows the experimental apparatus for calibrating the output curve of a microscope. The calibration system consists of a calibrated microscope, a compact laser interferometer which is used only to provide the necessary displacement shift quantity Δz with an integer multiple of half wavelengths, and an inclined flat surface as a test surface, which can give a continuous change in the input value z_i over the calibration range from z_1 to z_n, is used as specimen (see Fig. 4). The laser interferometer is fixed to the support stage of the microscope, and the inclined flat surface is fixed to the worktable center of the laser interferometer. The displacement of worktable, that is Δz, is moved by a tube PZT.

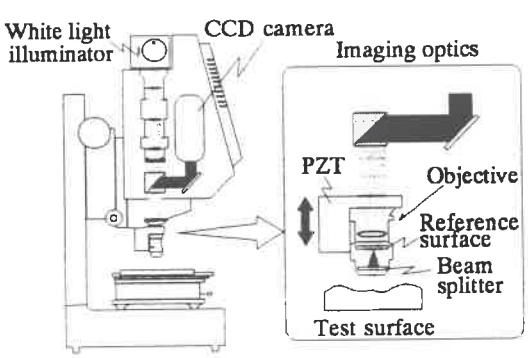

Fig. 1 Schematic of microscope

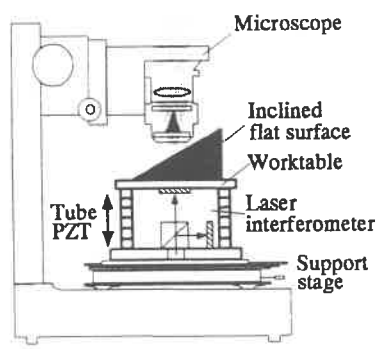

Fig. 2 Calibration system

Figure 3 shows the construction and optics system of the developed laser interferometer. The incident light from a laser light source system (LDS) is split into two beams by a cube beam splitter (BS) inside the tube PZT. One beam is reflected by moving mirror fixed on the bottom of the worktable, and the other beam is reflected by a fixed mirror. The two beams are then reflected back to the BS, producing an interference fringe, which is received by a 2-dividing photo-diode (2-PD) after passing through a bi-concave lens. When the worktable is moved by the tube PZT, the fringe moves according to the light distance change between the two reflected beams. The outputs at two points of phase difference π of the fringe are detected by the 2-PD. If x1 and x2 are the outputs of the 2-PD, and Y is the output of the laser interferometer, then Y is defined by the following equation:

$$Y = \frac{x1 - x2}{x1 + x2} \quad (5)$$

The differential detection method can be used to effectively eliminate intensity variations in the LDS of the laser interferometer. Furthermore, because the optical pitch difference between two interference beams be

as small as possible so that the stability of the fringes is good. However, wavelength variations of the LDS due to thermal drift cannot be eliminated by the differential detection method. Thus, in order to improve the stability of the wavelength and thereby achieve higher accuracy, a thermal controller was added to the LDS. The LDS shown in **Fig. 3(b)** consists of a laser diode (LD), a thermal sensor and a Peltier-element. The Peltier-element is used to regulate the detected temperature of the LD in order to suppress thermal drift in the LD. The output of the laser interferometer is a sinusoidal voltage signal of zero-line symmetry.

Figure 4 is a diagram of the signal processing system used to calibrate the microscope. The outputs of the calibrated microscope are detected and stored by the CCD camera shown in Fig. 1. The first, the calibration data m_i (i=1,2, ... ,n) of the output curve of the microscope are detected and stored. The second, the calibration data m_{i+} (i=1,2, ... ,n) corresponding to m_i are detected and stored after the tube PZT is moved by increasing offset voltage. The moved displacement quantity Δz of the tube PZT is an integer multiple of sinusoidal voltage signal period from the laser interferometer. This period is $\lambda/2$ (λ is the wavelength of the laser light source). This sinusoidal voltage signal is produced by the outputs of the 2-PD, which are converted by I-V converters and calculation circuits (addition, subtraction and division). In addition, in order to keep the Δz be constant during this period for detecting data m_{i+} and thereby achieve higher accuracy, a feedback control circuit shown in Fig. 4 was used after the tube PZT is moved. The proposed system provides an extremely simple mechanical structure, and is nor effected by the hysteresis and creep of the tube PZT.

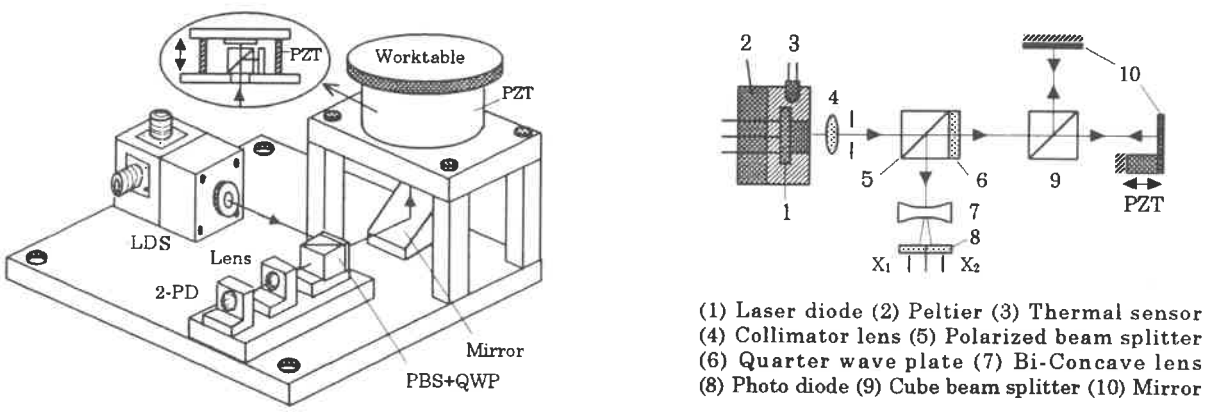

(a) Construction (b) Optics system

Fig. 3 Laser interferometer

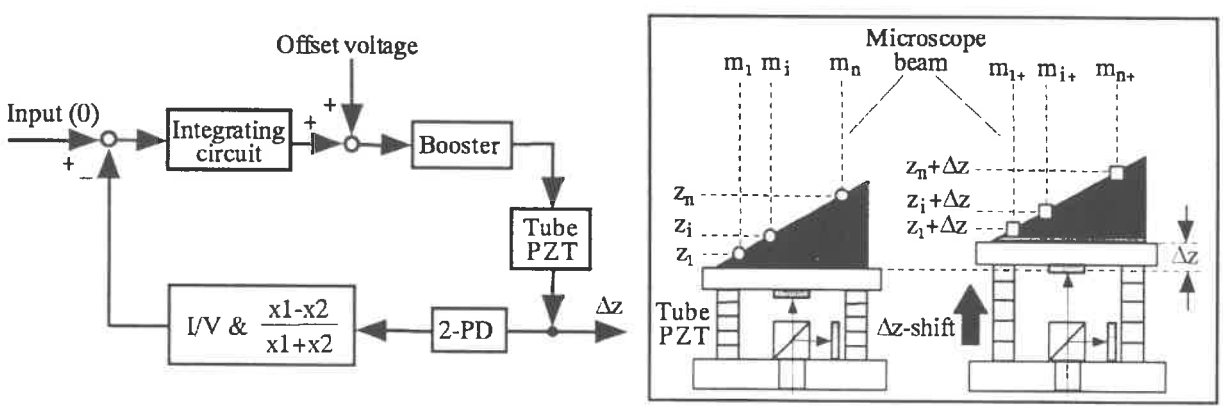

Fig. 4 Diagram of signal processing system

3. EXPERIMENTAL RESULTS

The nominal value of mean sensitivity of a calibrated microscope[4] as reported by the manufacturer is 1. The wavelength λ of the laser light is 784.73 nm as measured by an HP70950 optical spectrum analyzer. The necessary displacement shift quantity Δz for in-situ absolute calibration is $2 \times \lambda / 2$.

Figure 5 shows the mean sensitivities of the calibrated microscope. The abscissa represents the position of the specimen in the Z-direction, which is calculated from the output of the microscope. The dotted line is the nominal value, the other lines are the obtained value of three repeated calibrations, which are approximately 10% less than nominal value.

Figure 6 shows the linearity errors of three repeated calibrations of the calibrated microscope. The maximum linearity error was approximately 40 nm, which is approximately 0.2% of the calibration range of 20 μm. The maximum repeatability error of the three calibration results was approximately ± 2 nm, which is approximately $\pm 0.01\%$ of the calibration range of 20 μm.

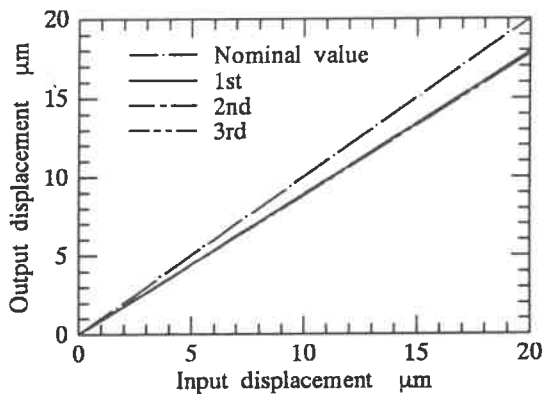

Fig. 5 Results of the mean sensitivity

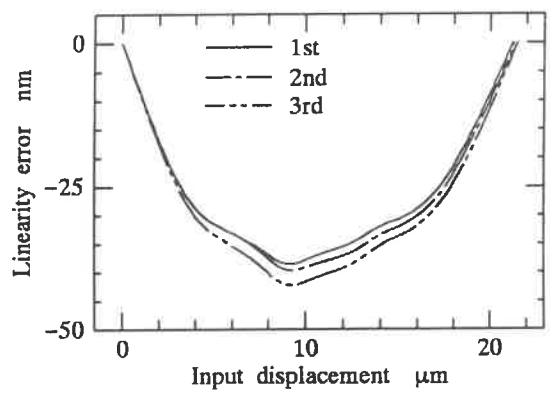

Fig. 6 Results of the linearity error

4. CONCLUSIONS

The results of the present research can be summarized as follows:

1) A new in-situ absolute calibration method is proposed for calibrating the output curve of an interference microscope. The effectiveness of the method was confirmed experimentally.
2) Accuracy of the method depends only on the stability of the calibrated microscope itself and that of the wavelength of the laser light source.
3) A microscope was calibrated successfully, and the maximum repeatability error of the calibration curve was approximately $\pm 0.01\%$ of the calibration range of the microscope.

ACKNOWLEGDGMENTS

This research was funded by the Grant-in-Aid for Scientific Research (A) of the Japanese Ministry of Education for the 1996, 1997 and for which the authors express their sincere appreciation.

REFERENCES

[1] P. Groot and L. Dech: Three-dimensional imaging by sub-Nyquist sampling of white-light interferograms, Optics Letters, **18** (17), 1462-1464 (1993).

[2] J. Schwider et al: Digital wave-front measuring interferometry: some systematic error sources, Appl. Opt., **22** (21), 3421-3432 (1983).

[3] Masays Kanai et al: Self-calibration of interferometer microscopes, Proceedings of ASPE 12th Annual Meeting, Norfolk, Virginia, (1997), pp.414-417.

[4] New View 100 Operation Manual OMP-0348K, Zygo Corporation.

A fully elastically guided 3-D CMM with a measuring volume of 1 cm^3

Albert Jansen, Nick Rosielle, Piet Schellekens
Precision Engineering section of the Mechanical Engineering Faculty
TUE, Eindhoven University of Technology

3D coordinate measuring machines (CMM's) have their accuracy related to the dimensions of the machine guides. For the particular task of measuring small objects, a small machine would do well. There are many reasons for building a suitably small CMM, scaling down is beneficial to reduce a number of errors in magnitude[1].
A concept which has fewer error terms was designed and built [2]. The aim for that machine was to reach 0.1 µm within 1 dm^3 to enable smaller products to be measured with better accuracy than is possible on 1 m^3 machines. In view of the "large" translation , x,y,z stroke of 100 mm, that machine [2] uses airbearings.
Theoretically the above line of thought could be extended further. The next machine on that line could be e.g. 1 cm^3 measuring volume with 0.01 µm accuracy.
Next a 1 mm^3 machine for 1nm? And then we reach scanning microscope work ranges and resolutions. AFM's use flexures for good mechanical performance at smaller dimensions.
Now if we return along the line and stop at the same milestones we see that the 1 cm^3 machine x,y,z travel of 10 mm, accuracy 0.01 µm could be built with flexures. Machines with much larger stroke than 10 mm need airbearings or more exotic things. Flexure design is bread and butter in Eindhoven since the early sixties so it was felt the 1 cm^3 all-flexure-bearing-machine design should see the light.

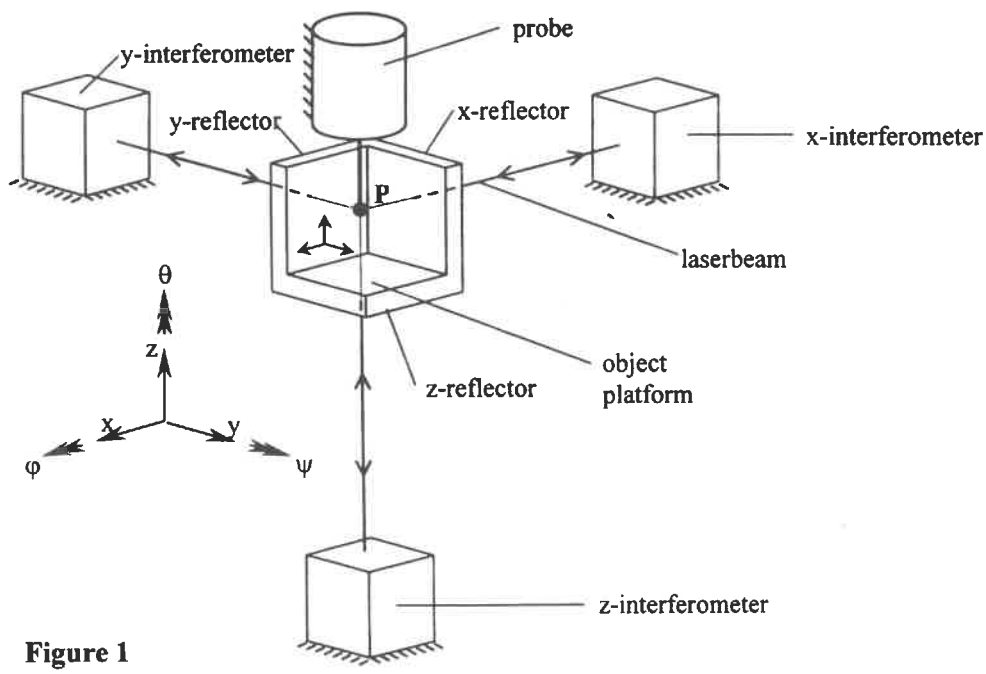

Figure 1

Concept building
After line-up of generated alternatives, the schematics of fig. 1 emerged, showing the probe fixed in space relative to x,y and z interferometer beams towards the probe for zero Abbe error x,y,z and the small (< 1 cm^3) object to be measured on the movable platform.

Various ways to hold and move the object platform were considered and finally fig. 2 emerged as the schematic version. The movable platform is represented by the central cube.
The x,y and z drive operate via pairs of parallel struts transferring axis motion for one axis whilst preventing rotation about another axis. The strut couplers are attached to parallel leafspring type drive units, capable of ± 5 mm movement which are equiped with linear motors.

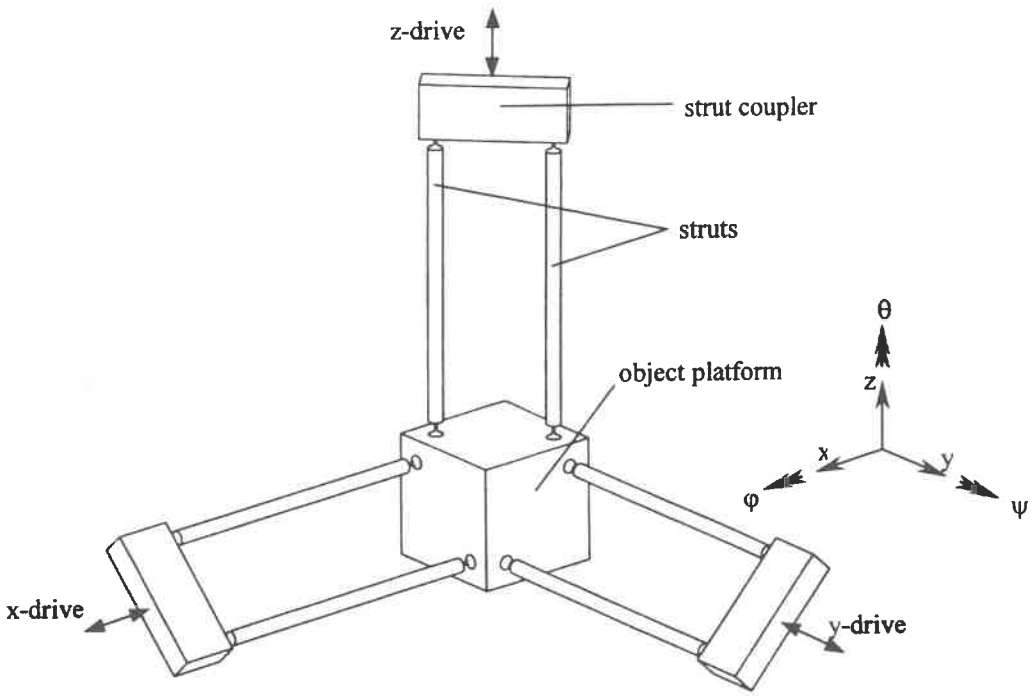

Figure 2

Fig 3 left top shows the central cube which moves x,y,z. It is conceived to consist of an aluminum body ABDE to which the aluminum strut pairs are attached. The central slab BDE-CFH is of zerodur and carries the reflectors for the x,y,z, laser interferometer system. This slab is attached in a statically determinate way to the aluminum corner ABDE i.e. on three hinged leafsprings, constraining 2 d.o.f. each. The cube corner CFGH is not used, the probe reaches in beyond G, the corner volume is for the object to be measured which is fixed to body BDE-CFH. Two struts from different pairs meet near a corner B,D,E of ABDE as shown in the lower left of figure 3. The measuring axes point to the probe tip (lower right of figure 3) in point P.
Measurement is directly to the platform. The platform carries the product to be measured and three laser interferometer reflectors on BEF, DEH and BCD. The interferometers are fixed at close range, to limit influence from variations of the refractive index of air. They are connected with a metrology frame of small thermal expansion to the also fixed (non moving) measuring stylus holder. The probe is conceived to be supported on a large size universal kinematic support via a probe-type specific adaptor. The laserinterferometers are held from the probe base in a statically determined mount also. Each interferometer head is placed close to the measuring object-carrying-platform (which carries the reflectors) between a pair of struts. Of course selection, design and calibration of a probe are challenges that have to be tackled. Calibration of the machine itself is much eased by the elimination of rotational errors.
Fig. 4 shows the lay-out which is symmetric with respect to gravity, provides platform access and fixed probe installation on top. There are no moving leads or hoses. The flexures were optimized e.g. the

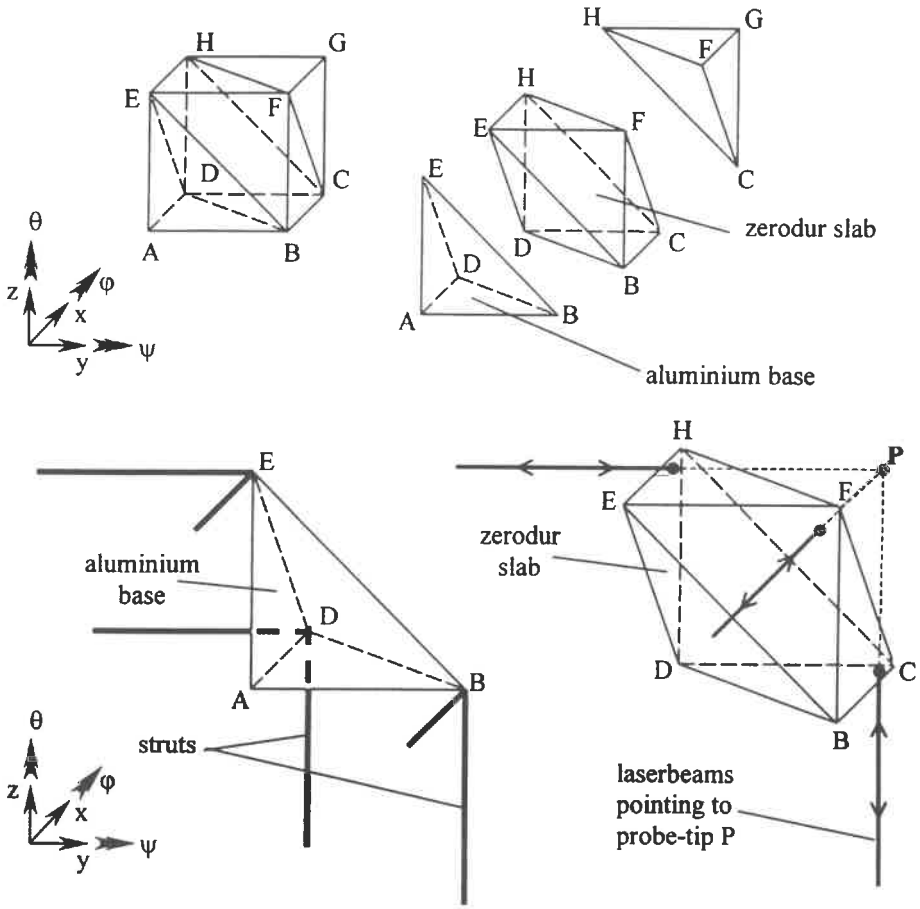

Figure 3

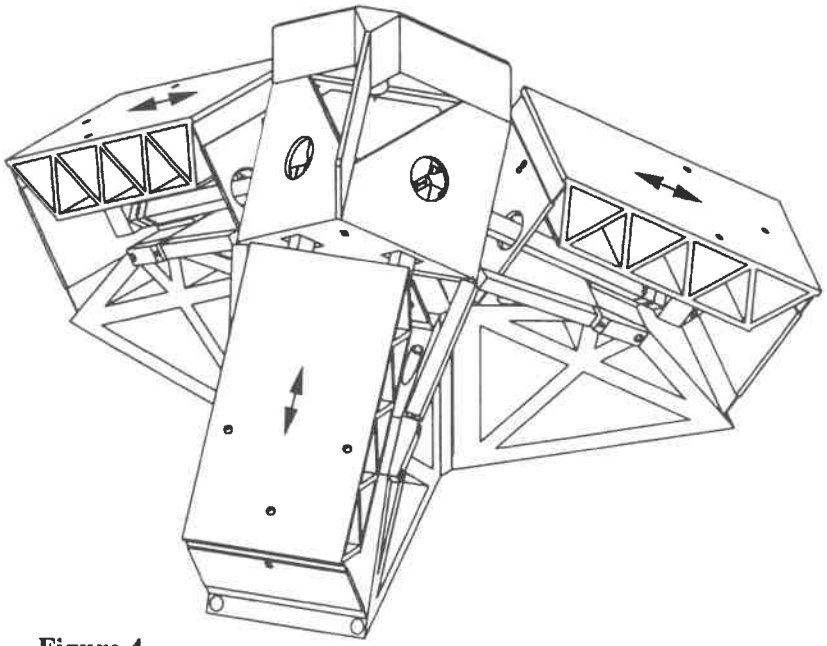

Figure 4

struts have a factor of 300.000 between axial and lateral stiffness and they have a lowest natural frequency well above 600 Hz. The parallellogram leafsprings are placed far apart (200 mm) to obtain high rotation stiffness at the base of the strut coupler. Strut centerlines are 65 mm apart.

Fig. 5 (plates removed for clarity) shows a side view of the probe position above the object platform with the reflectors, the interferometer optics, two out of six platform drive struts (moving) and two outof six probe support struts (non-moving).
The commercial lineair motor coil (non-moving) is mounted on the lower frame under each (moving) parallellogram to which the magnetic circuit is attached.

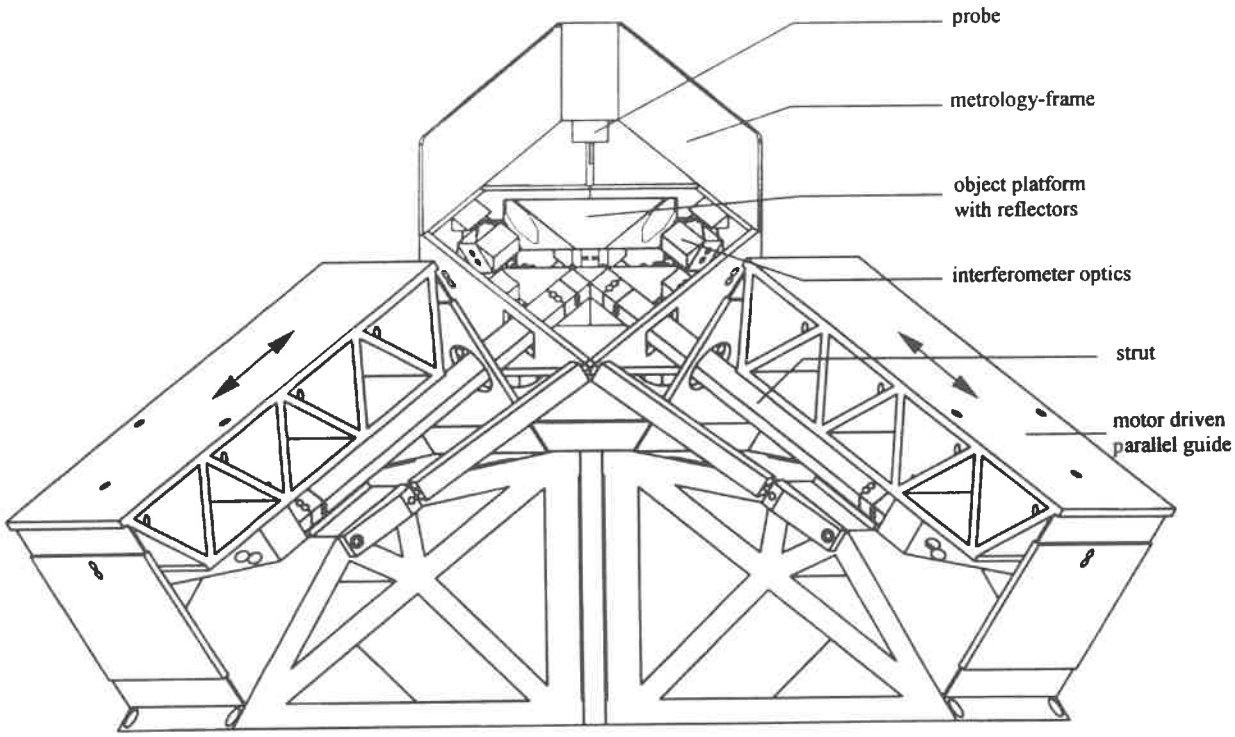

Figure 5

As the design progresses and various problems get solved the likelyhood of building such a machine is increasing steadily. The original design was based on commercial interferometers but the assembly of the interferometer head in terms of different materials and hence differences in thermal expansion as well as the lateral asymmetric mounting provided would prevent the use of a thermal centre on the optical axis.

Wire EDM
The sub-assemblies of the machine are using 2D wire EDM manufactured components to simplify the mechanics. This by reducing the number of component interfaces, and with that the associated amount of tolerance specification for the components on both sides of the interface and by reducing the number of alignment problems during fixation. They are rigidly connected by a 3D baseframe, with care to avoid contact hysteresis (thermal snapping).

[1] Precision Design, Schellekens et al. Keynote CIRP Annals 1998 volume 47/2 p557-586
[2] Design and Prototype-development of a High Precision 3D-Coordinate Measuring Machine, Thesis M. Vermeulen, TUE Eindhoven University of Technology, to be published september 28, 1999, ISBN ....

Sequential Determination of Kinematic Parameters in Assembled Parallel Kinematic Mechanisms

Bernhard Jokiel, Jr.
Sandia National Laboratories, Albuquerque, NM

John C. Ziegert
University of Florida Machine Tool Research Center, Gainesville, FL

1. Introduction

Over the last decade multi-axis machine tools and robots based on parallel kinematic mechanisms (PKMs) have been developed and marketed worldwide. Positional accuracy in these machines is controlled by accurate knowledge of the joint locations and distances between joint pairs (Figure 1.1). Since these machine tend to be rather large, the kinematic parameters are difficult to determine when these machines are in their fully assembled state. This work presents a method for determining the kinematic parameters of an assembled PKM where each kinematic parameter may be determined independently.

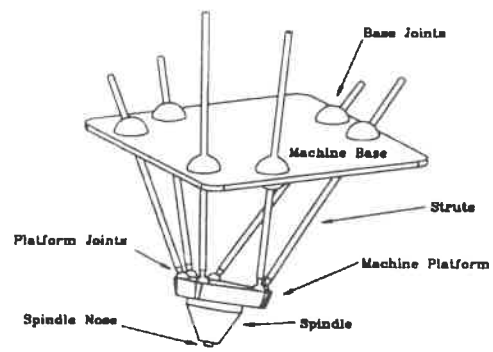

Figure 1.1: A 12-joint (6-6) Stewart platform six DOF device.

2. Sequential Determination Method

The proposed method has four parts: (1) locating a central reference frame, (2) identifying the joint center locations, (3) locating the spindle nose, and (4) determining the initial strut lengths.

2.1 Locating the Central Reference Frame (R)

Three gage points labelled r_1, r_2, and r_3 (usually some form of a kinematic mount) are secured at three corners of the worktable, creating a single fixed coordinate reference frame to which all future coordinate measurements collected in other floating reference frames will be transformed (Figure 2.1). Identifying the location of a chosen machine reference frame (M) may be performed at this time as well.

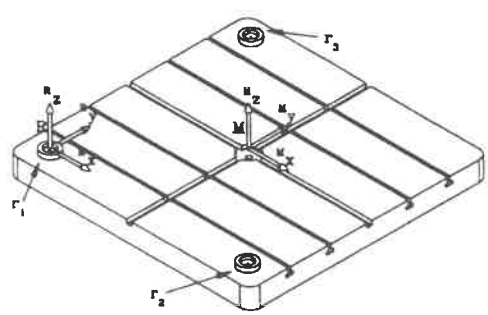

Figure 2.1: R and M reference frames.

2.2 Joint Center Location Identification

The platform is moved along an arbitrary predetermined path, while holding each strut in turn at an arbitrary fixed length. As the platform moves, the fixed-length strut rotates in its joints (Figures 2.2 and 2.3). Through measurement of the strut gage point coordinates and the corresponding platform poses, the locations of the base and platform joint centers may be determined by fitting

the transformed gage point coordinates to the equation of a sphere. Assuming the joints produce spherical motion, the center of the calculated best-fit sphere is the center of rotation of the joint in question. Performing this method once for each of the six struts, the coordinates for all 12 of the base and platform joint centers may be recovered.

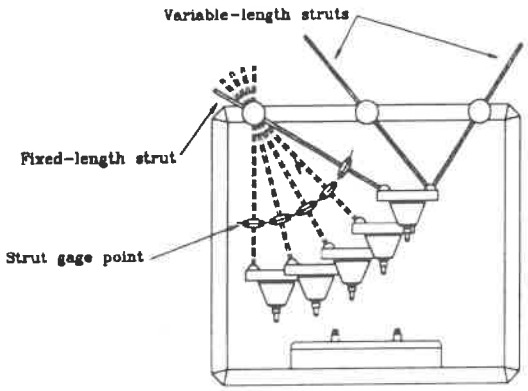

Figure 2.2: To an observer stationary relative to the M system, a point on the fixed length strut rotates about the base joint center.

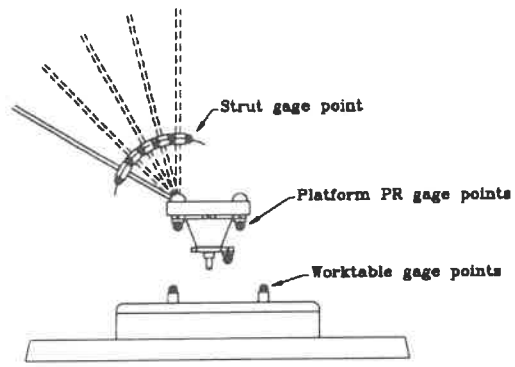

Figure 2.3: To an observer stationary relative to the PR system, a point on the fixed length strut rotates about the platform joint center.

2.3 Locating the Spindle Nose

A fixture holding a gage point attached to a tool holder mounted in the spindle is rotated slowly by hand. At approximately 30-40 different locations, the coordinates of the gage point are measured and fit to a skew circle (Figure 2.4). The unit normal vector of the best-fit plane is the unit orientation vector of the spindle relative to the PR system. The coordinates of the center of the circle projected along the positive direction of the normal vector by the offset distance are the coordinates of the center of the spindle nose.

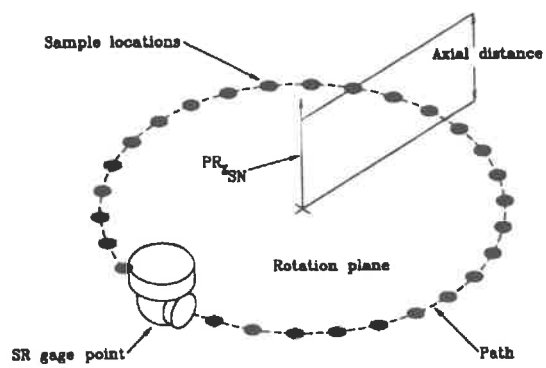

Figure 2.4: Spindle axis identification.

2.4 Determining the Initial Strut Lengths

The platform retracted to its home position. The coordinates of the PR gage points are measured. Knowing the locations of the base joints and the platform joints, the distances between the each of the six strut joint pairs are calculated. The platform is then moved from its home location, and the process is repeated. The initial strut reference length for each strut is taken to be the mean of the calculated strut lengths for each strut over all of the repetitions.

3. Uncertainty Analysis

The propagation of experimental data and machine positional uncertainties to the recovered kinematic parameters, and the propagation of the recovered parameter uncertainties to the tool tip were analyzed. The sequential determination method is dependent upon the accurate identifica-

tion of the joint locations. To determine the uncertainty in the joint positions, it is necessary to quantify the amount of uncertainty present in the length of the struts.

3.1 Error Budget

Factors which influence the length of the strut between the fixture and the base joint ("Base") are: joint motion sphericity, strut axial flexibility, thermal effects, strut length command mismatch, and the least count servo motion. Between the fixture and the platform joint ("Platform") are: joint motion sphericity, strut axial flexibility, and thermal effects. Four distinct scenarios were considered (Table 3.1): (1) is the best estimate of the uncertainty present in the real system; (2) assumes measurements are perfect; (3) assumes the machine is perfect; and (4) is a more optimistic version of #1.

Table 3.1: Scenario input uncertainties.

Scenario	Base (mm)	Platform (mm)	Measurement (mm)
1	0.016	0.015	0.025
2	0.016	0.015	0.000
3	0.000	0.000	0.025
4	0.010	0.010	0.013

3.2 Uncertainty in Kinematic Parameters

Propagation of strut length and measurement uncertainties to the recovered kinematic parameters was done by a Monte Carlo simulation. Each scenario was subjected to 10000 iterations. First, the reverse kinematic solver calculated the nominal strut lengths for the pose in each particular fixed-length strut toolpath given the set of nominal kinematic parameters. For each iteration, a small amount of uniformly distributed, random strut length uncertainty was added to the strut lengths. The new pose of the platform and gage point locations were calculated. Uniformly distributed, random measurement uncertainty was added to the gage point locations. Finally, the joint center locations and initial strut lengths were determined from the perturbed gage point locations. The mean and standard deviation of the sphericity and the center error distance (CED) were also calculated over all of the iterations for each scenario. Table 3.2 shows the results for strut 1, which are representative of the results for the other 5 struts.

Table 3.2: Joint center uncertainty.

	Scenario Number	Base Joint Mean (mm)	Base Joint σ (mm)	Platform Joint Mean (mm)	Platform Joint σ (mm)
Sphericity	1	0.045	0.008	0.064	0.014
	2	0.029	0.004	0.027	0.003
	3	0.033	0.006	0.057	0.013
	4	0.026	0.005	0.035	0.007
CED	1	0.067	0.044	0.098	0.064
	2	0.048	0.031	0.045	0.028
	3	0.050	0.032	0.086	0.057
	4	0.039	0.025	0.054	0.035

In a similar manner the propagation of the machine and measurement uncertainties to the initial strut lengths were calculated (Table 3.3).

Table 3.3: Uncertainty in the initial strut lengths.

Scenario	$\sigma_{Strut\ 1}$ (mm)	$\sigma_{Strut\ 2}$ (mm)	$\sigma_{Strut\ 3}$ (mm)	$\sigma_{Strut\ 4}$ (mm)	$\sigma_{Strut\ 5}$ (mm)	$\sigma_{Strut\ 6}$ (mm)
1	0.139	0.162	0.122	0.134	0.287	0.160
2	0.066	0.071	0.060	0.067	0.123	0.076
3	0.123	0.147	0.106	0.118	0.257	0.141
4	0.077	0.089	0.067	0.075	0.157	0.088

3.3 Uncertainty in Machine Motion

A Monte Carlo simulation was used to propagate the uncertainties in the calibration to the tool tip. First, path plans for six circular traces were developed (Table 3.4). Second, the inverse kinematics calculated the nominal poses of the mechanism for each path from the nominal parameters. Third, 1000 sets of parameters were selected from the 10000 previously simulated.

For each set, scenario and pose in each circular path, the error between the nominal and the recovered simulated parameters were calculated and projected on to the strut lines of action. Additional uniformly, randomly distributed strut length uncertainties were added. The forward kinematics determined the perturbed tool tip locations for each path. Using the perturbed tool tip locations the best-fit circle was calculated for each path.

Table 3.4: Locations of circular traces.

Circle Number	Nominal Circle Locations (mm) X	Y	Z	Radius
1	0	0	180	150
2	200	200	180	150
3	-200	200	180	150
4	-200	-200	180	150
5	200	-200	180	150
6	0	0	180	300

For each circular trace and uncertainty scenario, the mean and standard deviation of the X and Y circle center coordinates, radii and circularities were calculated over all of the iterations. Results for circle #1 for all four scenarios is shown in Table 3.5 and are representative of the other five traces.

Table 3.5: Circle #1 location uncertainty.

Scenario	$\overline{X}$ (mm)	σ_X (mm)	$\overline{Y}$ (mm)	σ_Y (mm)	$\overline{R}$ (mm)	σ_R (mm)	$\overline{Circ.}$ (mm)	σ_{Circ} (mm)
1	0.000	0.038	0.001	0.038	150.000	0.002	0.115	0.008
2	-0.001	0.018	0.000	0.018	150.000	0.001	0.115	0.008
3	0.001	0.033	-0.001	0.032	150.000	0.001	0.003	0.002
4	-0.001	0.021	0.000	0.021	150.000	0.001	0.074	0.005

4. Experimental Results

A total of three complete and independent trials were run of the proposed sequential determination method on a Hexel milling machine installed at Sandia National Laboratories. A SMX 4000 laser tracker was used to collect the spatial coordinate data for the kinematic parameter recovery. Fro brevity, the results for the kinematic parameters for each trial will not be listed here. However, interested readers are encouraged to contact the authors who will provide complete results.

Each of the three new kinematic parameter databases, as well as the original, were loaded into the machine controller. The machine was then commanded to follow the six circular traces listed in Table 3.4. The circular traces were measured using a Renishaw ball bar. Results appear in Table 4.1.

Table 4.1: Renishaw ball bar circular trace results.

Database	Circle Number	Radial Deviation Max µm	Min µm	Best-Fit Radius mm	Center Position X µm	Y µm
Original	1	32.2	-30.6	149.987	-7.2	-37.2
	2	27.5	-26.1	150.010	-32.6	-41.2
	3	61.1	-71.2	149.996	14.4	-21.1
	4	42.9	-37.1	149.965	-11.5	-5.5
	5	57.1	-56.2	149.987	-34.9	-21.1
	6	68.8	-61.3	299.996	1.0	-15.1
Trial 1	1	20.3	-20.1	149.978	-17.8	-39.9
	2	20.0	-27.1	149.990	-21.3	-25.9
	3	33.3	-40.5	149.986	3.7	-21.8
	4	45.5	-41.0	149.961	-18.1	-20.1
	5	46.5	-43.4	149.977	-10.9	-14.8
	6	41.3	-41.0	299.973	18.8	-9.5
Trial 2	1	24.6	-26.6	149.998	-36.9	-26.6
	2	36.5	-42.0	149.994	-50.9	-15.0
	3	46.6	-50.6	150.005	-5.0	-11.8
	4	35.8	-30.5	149.995	-6.5	4.8
	5	46.9	-35.9	149.994	-9.3	6.4
	6	59.0	-61.2	300.007	-8.7	-17.7
Trial 3	1	27.2	-31.6	149.996	13.8	-24.5
	2	22.6	-29.1	150.012	-14.4	-14.5
	3	19.5	-24.6	150.003	18.0	-16.6
	4	53.2	-63.3	149.982	-13.6	-23.2
	5	52.9	-56.9	150.003	-11.1	-0.9
	6	48.6	-56.5	300.022	18.1	-27.5

5. Conclusions

The theoretical and experimental evaluation of the proposed sequential determination method for identifying the kinematic parameters in fully assembled Stewart platform type PKMs appears to show that it is a viable technique.

Monte Carlo simulations show measurement uncertainty appears to have the greatest impact on the correct identification of the joint centers and the initial strut lengths. Uncertainties in the machine strut lengths does not appear to have as great of an effect on the recovered parameters.

The Renishaw ball bar circles used to evaluate the success of the calibration appear to show that the correct kinematic parameters were identified, although a great improvement in machine performance did not appear to have occurred. However, a rigorous application of the ASME B5.54 standard is warranted to decisively show improvements in positional accuracy.

References

[1] Jokiel, Jr. Bernhard. "Sequential Determination of Kinematic Parameters in Assembled Parallel Kinematic Mechanisms." Ph.D. Dissertation, University of Florida, 1999.

[2] Wang, Jian and Oren Masory. "On the Accuracy of a Stewart Platform - Part I The Effect of Manufacturing Tolerances." Proceedings IEEE International Conference on Robotics and Automation, Vol. 1, 1993. Los Alamitos, California: IEEE Computer Society Press, pages 114-120.

[3] Masory, Oren, Jian Wang, and Hanqi Zhuang. "On the Accuracy of a Stewart Platform - Part II Kinematic Calibration and Compensation." Proceedings IEEE International Conference on Robotics and Automation, Vol. 1, 1993. Los Alamitos, California: IEEE Computer Society Press, pages 725-731.

[4] Zhuang, Hanqi and Zvi S. Roth. "Method for Kinematic Calibration of Stewart Platforms." Journal of Robotic Systems, Vol. 10, No. 3, 1993. pages 391-405

[5] Zhuang, Hanqi. Lixin Liu and Oren Masory. "Autonomous Calibration of Hexapod Machine Tools." ASME Journal of Manufacturing Science and Technology, Vol 19, 1997. pages 202-211.

[6] Bourdet, P., C. Lartigue, and F. Leveaux. "Effects of Data Point Distribution and Mathematical Model on Finding the Best-Fit Sphere to Data." Precision Engineering. Vol. 15 No. 3, 1993. pages 150-157.

[7] Taylor, Barry N., Chris E. Kuyatt. "Guidelines for Evaluating and Expressing the Uncertainty of NIST Measurement Results." National Institute of Standards and Technology, NIST Technical Note 1297, 1994.

Experimental Study on Dynamic Accuracy Behavior of a High-speed CNC Machine Tool with Semi-closed and Fully-closed Feedback Control

Kazuo Yamazaki [1], Yasuhiro Kawahara [1], Jiancheng Liu [1],
Jan Braasch [2], Makoto Fujishima [3]
[1]: IMS-Mechatronics Laboratory, University of California, Davis, California
[2]: Johannes Heidenhain GmbH, Traunreut, Germany
[3]: Mori Seiki Co. Ltd., Nara, Japan

INTRODUCTION

The electromechanical feed drive system, with ball screw transmission elements, has a dynamic effect on the positioning accuracy of a CNC machine tool system, which is directly associated with the accuracy of a product machined. There are many error sources such as pitch error of the screw, backlash, elasticity, thermal deformation error, etc. If the errors are repeatable and constant, the compensation by software is possible in a position feedback control loop. As a matter of fact the current controllers are mostly using this quasi-static compensation technique. The thermal induced error in a ball screw feed drive system, however, is the most critical and also difficult to compensate since it behaves unpredictable and unrepeatable. In recent high-speed machine tool systems, compared to the conventional machine tool systems, more heat is generated between the screw and the nut during a high acceleration and deceleration motion, which results in dynamic and random behavior of the longitudinal thermal deformation of a ball-screw. Because of this dynamic behavior, the rotational angle readings of an encoder can not be used to precisely calculate the exact position of the worktable, thus leading to the position control accuracy deterioration of a CNC machine tool system. One solution for reducing the thermal expansion is to cool the screw system by water circulation in the hollow screw. But this methodology is difficult to maintain a reliable operation and costly compared to the conventional system. In recent years, some of high-speed machines, especially linear motor machines, are being equipped with a linear encoder system. But for a ball screw feed drive system, the effectiveness of linear encoder against the ball screw thermal deformation has not been well studied (1).

Therefore, the goal of this research is to investigate the positioning error behavior of the high-speed horizontal machining center with the ball screw and rotary encoder feedback, and to eventually build a high-speed horizontal machining center equipped with a switchable rotary and linear encoder motion control system. The main focus of the paper is on investigating the difference of motion control feedback behavior between a rotary encoder and a linear encoder feedback, and to discuss the effectiveness of the linear encoder based motion control. The experimental results measured by the rotary encoder from two types of high-speed machining centers are presented.

EXPERIMENTAL PROCEDURE

The system diagram for measuring the position of worktable is shown in Figure 1. Two horizontal machining centers were used in the experiments. The specifications are given in Table 1. A linear scale (VM182, Heidenhain) with a measurement range of 520mm was used for detecting the position of the spindle head. The data processing software (ACCOM Measurement Version 2.01) with Interface Card (VM121, Heidenhain) was installed in a computer. The experiments were designed and performed by following the standard procedures defined in ISO-230 (2). Figure 2 shows the parameters to define the traverse motion used to operating the machine tool. The parameters to define the motion are as follows:

- Target points (Test range): The distance between two target points defines the test range.
- Bi-directional measurement (Lead distance): Two additional distances adjacent to the both ends of test range defines the lead distance for getting rid of reversal error during the tests

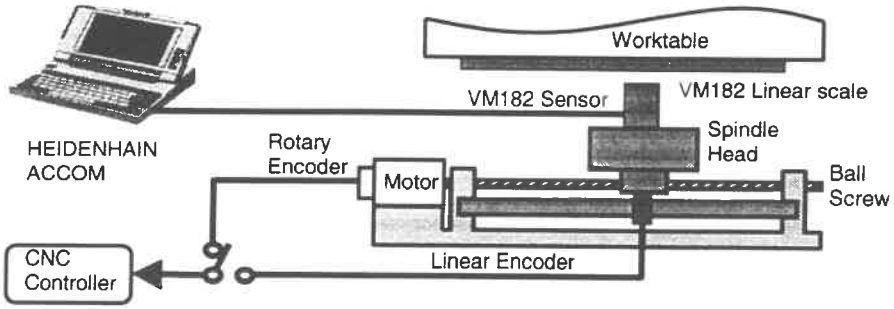

Figure 1. Measurement System Diagram

Table 1. Specification of Machine Tools

SPECIFICATIONS		MAKINO A55-A40	MORI SEIKI SH-
Travel	X-axis Stroke (mm)	560	840
	Y-axis Stroke (mm)	560	760
	Z-axis Stroke (mm)	560	840
Feedrate	Max Rapid Traverse Rate (mm/min)	24000	32000
Spindle	Max. Spindle Speed (mm^{-1})	12000	15000
	Spindle Bearing Inner Diameter (mm)	85	100
ATC	Type of Tool Shank	BT-40	HSK A100
	Tool Storage Capacity	40	60
APC	Number of Pallets	2	2
Motors	Feed Motors (X, Y, Z) (kW)	3.5, 3.5, 3.5	5.0, 7.3, 5.0
	Spindle Drive Motor (30min./continuous rating) (kW)	22 / 18.5	30 / 25

Table 2. Measurement Conditions

Machine Tool	MAKINO A55-A40	MORI SEIKI SH-630
Measurement System	HEIDENHAIN VM182 (Max. Measure Length 520mm)	HEIDENHAIN VM182 (Max. Measure Length 520mm)
Feedback Method	Rotary Encoder (YASKAWA)	Linear Encoder (HEIDENHAIN) and Rotary Encoder (FANUC)
Target Positions (Pisition A & B)	X axis: 15mm and 415mm away from machine home position Y axis: 20mm and 300mm away from machine home position	X axis: 300mm and 700mm away from machine home position Y axis: 20mm and 420mm away from machine home position
Dt: Distance between Target Positions	X axis: 400 mm Y axis: 280 mm	X axis: 400 mm Y axis: 400 mm
Dr: Distance between Target Position and Reversal Position	X axis: 15 mm Y axis: 19 mm	X axis: 20 mm Y axis: 20 mm
Traverse rate	Rapid Traverse rate (approximately 24000 mm/min)	1000, 5000, 10000, and 16000 mm/min
Dwell Time	3 sec.	3 sec.
Measurement Cycle (times / min.)	999 cycles / approximately 270 min.	up to 999 cycles / approximately 215 min.
Rest Time	At least 4 hours (240 min)	At least 4 hours (240 min)

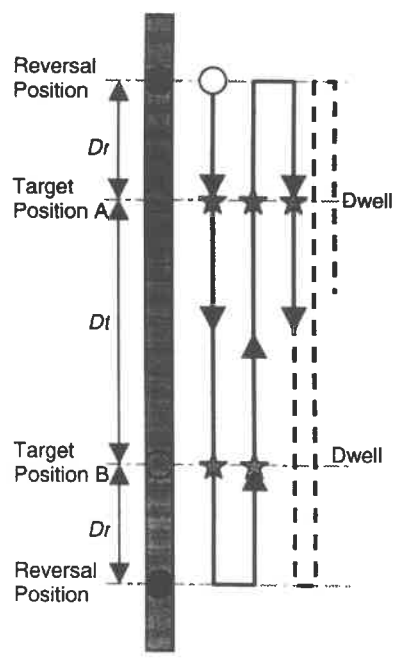

Figure 2. Motion Parameters

- Traverse Rate (Speed)
- Dwell time for holding the measurement point: A shorter dwell time may not be able to measure the point data because of the machine may not be stopping at the point completely (may have a vibration). A longer

dwell time may need to take a long time to get the thermal deformation error, because of the ball screw may be cool down during the dwell time.

- Measurement Cycles (Time): The ACCOM software, which is used in this test, can measure the data up to 999 cycles (single or bi-directional) for the linear motion test. The different traverse speed gives the different cycle time.
- Rest Time: During the rest time, machine tool will cool down.

MEASUREMENT RESULTS of THERMAL GROWTH

The measurement conditions in X and Y-axis direction for machine A55 is given in Table 2. The measured results are shown in Figure 3. From this figure, it is found that with the increase of the running time, the ball screw has a big thermal growth in both X and Y-axis. In the first two hours running, the thermal expansion increases rapidly. For example, the thermal growth reaches a value of 0.035mm for X and Y-axis. After that, the ball screw gradually expands. It was found that from these measurement results the thermal growth is remarkable. It can be deduced that there is a big difference between the position information reflected by the rotary encoder and the actual position measured directly by linear scale and therefore this will deteriorate the machined part accuracy. The machine SH-630 is different from the machine A55 in that SH-630 is equipped with both rotary encoder and linear scale position reading system. Figure 4 shows an example of measured results in the condition of feedrate of 16m/min (Y-axis direction). It is found that the linear encoder feedback has the small positioning error in comparison with the error by the rotary encoder feedback. Figure 5 show the change trends of the thermal growth in various motion conditions for SH-630 by the rotary encoder and linear scale feedback, respectively. The results show that with the increase of the feedrate, the positioning error increases and with the increase of the cycle number, the positioning

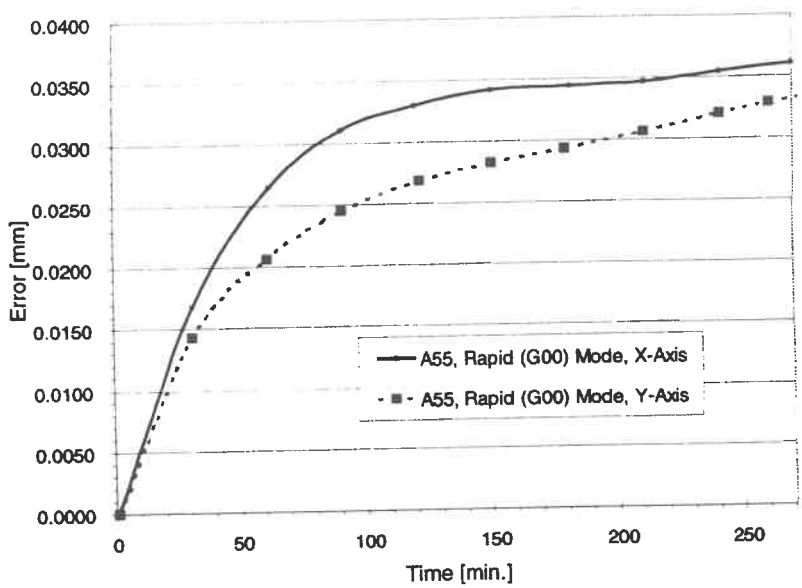

Figure 3 Positioning Error by Rotary Encoder Feedback (A55)

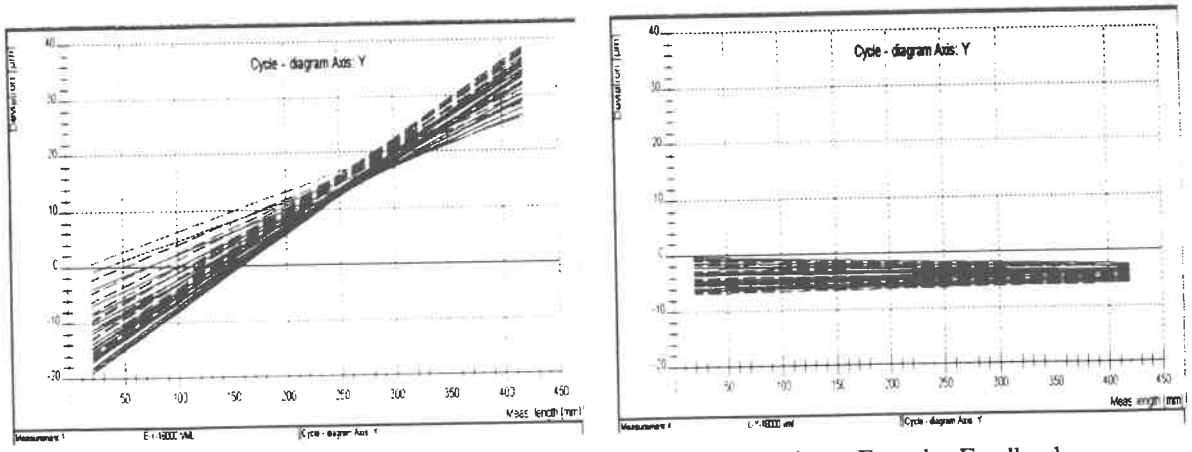

(a) Rotary Encoder Feedback (b) Linear Encoder Feedback

Figure 4. Measurement Results (SH-630, Y-Axis, Feedrate: 16 m/min)

error increases in the case of encoder feedback control. However, in the case of linear scale feedback case, the positioning error almost does not change either for an increase of cycle number or feedrate.

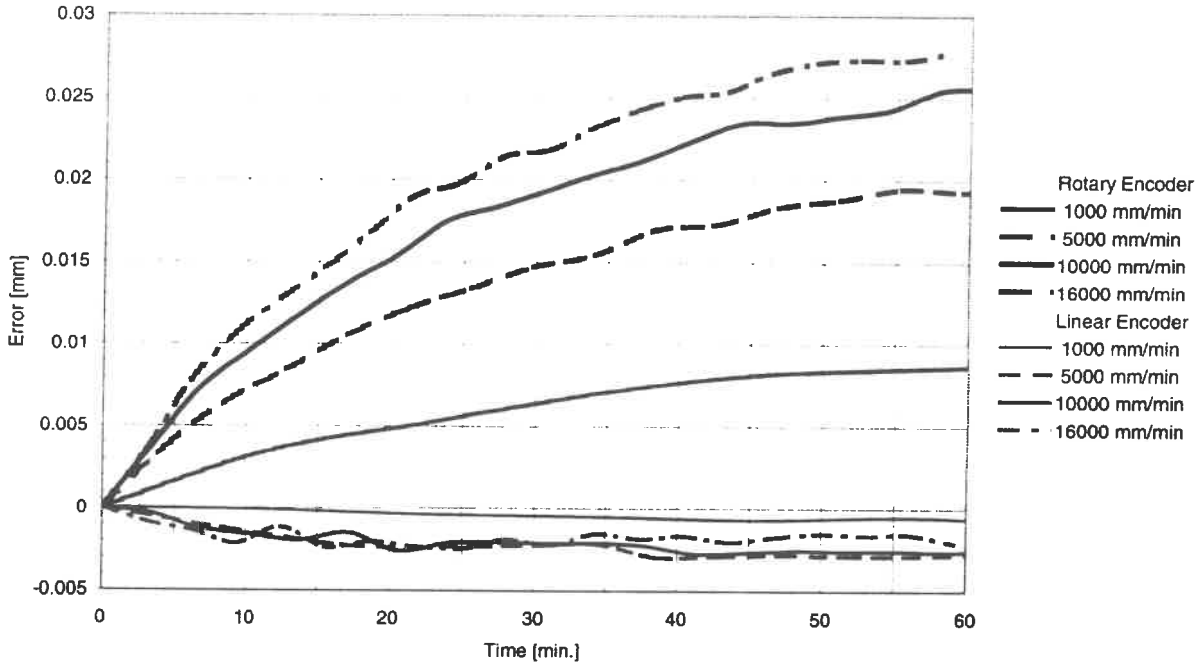

Figure 5. Positioning Error measured from Linear Encoder and Rotary Encoder Feedback in Y-axis (SH-630)

SUMMARY

The positioning performance using the rotary encoder and linear scale feedback system for the ball screw drive systems was investigated. When the rotary encoder feedback is used for relatively high speed repetitive traverse motion of the table, a thermal expansion of the ball screw causes positioning error in the magnitude of 0.04 mm when the machine running time is one to two hours in terms of the traverse speeds. In the case of linear scale feedback system, the thermal error can be dynamically monitored and the motion error of the worktable is greatly enhanced. In this research, the motion accuracy difference between the rotary encoder and the linear encoder control feedback was also examined in conjunction with the possible error causes including the measurement method of the errors. The next goal of this experimental study is to investigate the motion error due to the thermal growth in a circular motion.

REFERENCES

1. Braasch J., "Position Measurement on Machine Tools — By Linear Encoder or Ball screw and Rotary Encoder", Technical Article on the World Wide Web, HEIDEINHAIN (http://www.heidenhain.com)

2. ISO/TC 39/SC 2 - Draft International Standard ISO/DIS 230-3 "Test code for machine tools -Part 3: Determination of thermal effects"

NIF Optical Specifications and Means to Quantify Mounting Stresses

Paul R. Wilkins[1], P. Douglas Knight[2], R. E. English[1], Dave M. Aikens[1]

[1]Lawrence Livermore National Laboratory, Livermore, CA

[2]Department of Mechanical Engineering and Engineering Science
University of North Carolina at Charlotte, Charlotte, NC

1. Introduction

The National Ignition Facility (NIF) is a next generation inertial confinement laser which will utilize approximately 7,800 large, 0.5-meter square aperture laser optics within 192 separate laser beams that each focus upon a single target. Individual focal spots of each NIF laser beam must be of similar power and spot size for uniform illumination of the target while the encircled energy specification for coincident focused beams is 500 Terawatts within a 250 micron diameter spot. Eighty percent of the optical elements in the laser are flat polished surfaces used in either reflection or transmission. These surfaces require a unique set of wavefront specifications because of the extremely high fluences and nonlinear processes that dominate the laser wavefront evolution at these extreme power densities. The large number of optics in each laser beam encourages a statistical approach of specifying the finished optical surface as opposed to setting a traditional optical element specification of peak-to-valley deviation. Furthermore, the non-circular apertures used in NIF cannot be analyzed in terms of Zernike polynomials, so the NIF wavefront modeling group has chosen a spatial Fourier representation of the surface with separate specifications for certain spatial frequency bands.

2. NIF Optical Specifications

Figure 1 is a diagram of one of the 192 laser beams that constitute NIF. The

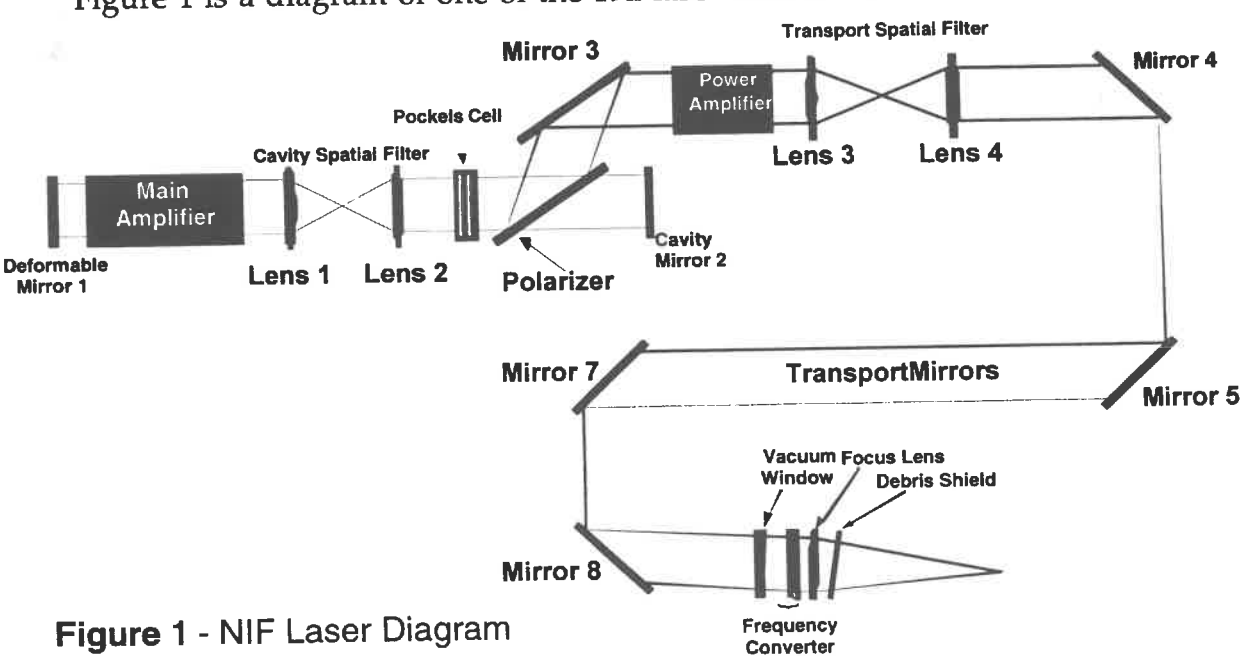

Figure 1 - NIF Laser Diagram

large-optics section of each NIF laser beam consists of a multi-pass, regenerative amplifier followed by a power amplifier, a spatial filter to clean the beam, transport mirrors, and a final optics assembly. The transport mirror section relays the beam to the target chamber at a specific angle and position where the final optical assembly, that mates to the chamber, will frequency double and triple the light while focussing the beam upon the target. The focusability requirement that has been placed upon the NIF requires an evolved optical specification that addresses all issues that increase spot size for various spatial frequency bands outlined in Table 1.

While diffraction theory dictates the minimum spot size for perfect optical surfaces, it is the wavefront root-mean-squared (RMS) gradient of all elements that provides the scaling of the spot size above the diffraction limit[1]. The distribution of gradients, which is typically a gaussian distribution, determines the basic focal spot characteristics of the laser. The energy distribution near a focal spot is dominated by the power spectral density function, which follows a fractal power-law distribution[2]. The energy falling on a spatial filter pinhole is determined by the integrated roughness within the PSD band, and the NIF PSD specification prevents pinhole plasma damage. In a high power laser system, small phase modulations in the beam at certain spatial frequencies create intensity modulations that under-go non-linear gain and steal power from the zero order mode[3]. The spatial frequencies of concern and the energy falling onto the spatial filter are covered by the PSD specifications. Surface roughness at high spatial frequencies causes scatter and energy loss to the beam. A specification for peak-to-valley is also assigned to limit the maximum surface deviation, but it is difficult to exceed the P-V without invalidating the RMS gradient specification.

Incorrect mounting of the NIF optical elements, such as transport mirrors, will change the local surface slope on a long spatial scale but will not affect the roughness or measured PSD. Based on the table below, only the PV and RMS Gradient specifications will suffer from incorrect mounting.

Table 1: NIF Optical Specifications vs. Spatial Period Bands

NIF Optical Specification	Spatial Period Band (Λ–mm)	Optical Specification	Affected by Mount Induced Stress	Mount Induced Figure Specification
MicroRoughness	$\Lambda < .12$ mm	Integ. $\sigma < 0.4$ nm	No	None
PSD II	2.5 mm $> \Lambda >$ .12 mm	Integ. $\sigma < 1.1$ nm	No	None
PSD I	33 mm $> \Lambda >$ 2.5 mm	Integ. $\sigma < 1.7$ nm	No	None
RMS Gradient	$\Lambda >$ 33 mm	Gradnt $< \lambda/75$/cm	Yes	Gradnt $< \lambda/75$/cm
Peak-to-Valley	All	P-V $< \lambda/3$	Yes	P-V $< \lambda/4$

3. Mounting Stress Effects on NIF Specifications

The mounting of transmission optics, such as windows and amplifier slabs generally does not affect the NIF optical specifications from a geometric optics

perspective. A slight bowing of a transmissive optic affects the transmitted wavefront as a second order effect in the same manner that a driver can easily see through a curved windshield. However, since the NIF laser uses linear polarized beams with polarization elements like Pockel cells and frequency conversion crystals, it is sensitive to polarization aberrations as a loss mechanism. Stress induced birefringence from mounting affects the polarization state of the transmitted beam and changes the linear polarization state. An imaging polarimeter optimized for low-retardance testing was developed to measure the very small residual stress induced birefringence from mounting. This retardance measurement technique is more sensitive that interferometry for mounting errors and the details of this testing are presented in a separate paper presented by one of the authors in the proceedings of this conference.

The NIF Transport mirrors are square in aperture and are supported from internally expanded lugs inside the mirror substrate. An improper support or torque of the optic by these mounting points and the optical surface can twist or bend into a shape that is a quadratic to first order. The primary effect of this type of mounting error is a change in the peak-to-valley specification and an increase in the RMS gradient of the surface. The focal spot then changes its aspect ratio and the power density across the focal spot is not uniform. The large number of transport mirrors, each at a unique angle and orientation, make traditional phase measuring interferometry difficult without a large custom structure that is prone to fringe vibration. It is proposed in this paper to use a slope measurement technique that can directly measure the surface gradient, or slope. This surface slope data can then be directly integrated into a surface profile for P-V departure.

4. Slope Measurement of Transport Mirrors

One of the earliest techniques for evaluating the quality of an optical surface is the Focault knife-edge test, a qualitative means to map the local slope of an optical surface along a particular axis[4]. The Focault knife-edge involves projecting a point source onto or through an optic and translating a one dimensional opaque edge across a returning convergent ray bundle that expands past focus and is imaged onto a detector array or film. Although the accuracy of this slope measurement technique is limited by principles of diffraction and the size of the point source, improvements including algorithms for peak detection and digital signal processing techniques can create a quantitative surface map of slope[5]. The typical mounting figure error anticipated with the NIF Transport Mirrors is anticipated to be quadratic to first order and exhibited as astigmatism. In the constructed prototype, the Focault opaque knife-edge is replaced with a phase-knife: a precise etched half-wave fused silica step that produces a sharp, narrow interference fringe. A single mode fiber provides an optimal point source that is converted into collimated light with an aspheric lens, reflected off of an optical surface under test and re-focused upon the phase knife. The location of the single fringe in the image of the optic surface as the phase-knife translates in the focal plane reveals the slope of the surface. The slope can then be numerically integrated into a surface profile map and fitted to astigmatism for quadratic departure, indicating mounting errors. The great

advantage of this system for a large integrated test station is sensitive to tilt only and is not interferometrically sensitive to the total optical path length of the beam.

As an example, the maximum tolerance for a poorly mounted NIF transport mirror is limited to a P-V departure of $\lambda/4$ from flatness, which gives a surface with an edge-to-edge surface slope deviation of 2.9 microradians. The prototype system for NIF evaluation would have a central fringe width of 1.8 microradians and a resolution around 10 nanoradians. More details on surface testing utilizing this phase-knife technique are provided in a separate paper presented by one of the authors included in the proceedings of this conference (Reference 5).

5. Acknowledgements

A review of the NIF optical specifications is presented along with some means of characterizing mount-induced stresses from reflective optical surfaces. A prototype means of measuring surface slope of incorrectly mounted optics using a scanning phase knife is outlined and initial data is presented. Additional data will be presented showing measurements of stress induced birefringence as a means of quantifying mounting stress in transmissive optics. This work has been performed in support of metrology testing of mounted optical components for the National Ignition Facility at the Lawrence Livermore National Laboratory. The authors appreciate the assistance of Janice Lawson, Dave Pigg, Bob Addis, Will House, and Mike McBurney for their roles in measurements and assistance concerning this work.

6. *References*

1. J. K. Lawson, J. M. Auerbach, R. E. English, Jr., M. A. Henesian, J. T. Hunt, R. A. Sacks, J. B. Trenholme, W. H. Williams, "NIF Optical Specifications – The Importance of the RMS Gradient," *Proc. SPIE* **3492**, pp. 336-343 (1998).
2. J.K. Lawson, D. M. Aikens, R. E. English, Jr., C. R. Wolfe, "Power spectral density specifications for high-power laser systems", *Specification, Production, and Testing of Optical Components and Systems, Proc. SPIE* **2775**,, pp. 345-356 (1996).
3. J.B. Trenholm,"1975 Laser Annual Report," *Lawrence Livermore National Laboratory*, ***UCRL-50021-75***, pp. 237-241 (1975).
4. D. E. Vandenberg, W. D. Humbel, and A. Wertheimer, "Quantitative Evaluation of optical surfaces by means of an improved Focault test approach," *Opt. Eng.*, **32**, 1951-1954 (1993).
5. P. R. Wilkins, P. D. Knight, D. C. Pigg, "A Scanning Phase-Knife Technique for Quantitative Surface Slope Measurements and Defect Identification," *Proc. ASPE Topical Meeting* (1999).
6. P. D. Knight, P. D. Wilkins, "Quantitative Stress-Induced Birefringence Measurements of Large Optics by a Prototype Imaging Polarimeter," *Proc. ASPE Topical Meeting* (1999).

This work was performed under the auspices of the U.S. Department of Energy by Lawrence Livermore National Laboratory under Contract No. W-7405-ENG-48.

UCRL-JC-133727-Abs

A PORTABLE GRAZING INCIDENCE INTERFEROMETER FOR MEASURING THE FLATNESS OF SLIDEWAYS AND SURFACE PLATES

Andrew W. Kulawiec, Paul G. Dewa, Richard S. Hordin, John H. Bruning
Tropel Corporation
60 O'Connor Road
Fairport, NY 14450

ABSTRACT

The flatness of machine slideways and surface plates is often critical to the precision of machined surfaces or the accuracy of measurements. Yet there are very few viable methods or techniques for measuring this important parameter. The most common methods use auto-collimators or electronic levels to measure angular deviations in the surface to arrive at an estimation of the flatness. These methods are time-consuming and result in a limited number of data points. The error motions of an assembled machine tool or metrology instrument can also be measured using conventional methods, but the contribution due to the slideway flatness is difficult to determine directly. A prototype grazing incidence interferometer capable of performing these measurements has been designed, built and tested at Tropel. Results of measurements of a variety of surfaces are given in order to illustrate the prototype instrument's capabilities. In particular, the results of measurements from a machine tool slideway and a granite surface plate are provided.

1. INTRODUCTION

For many years, grazing incidence interferometry has been used to accurately measure the flatness of precision machined surfaces.[1-2] Recently, the principle has been extended to measure the cylindricity and diameter of inside or outside diameter cylinders.[3-4] The principle of grazing incidence allows one to obtain high contrast interference fringes from relatively rough and diffuse surfaces. Furthermore, the large angle of incidence increases the fringe spacing, resulting in a much greater dynamic range than normal incidence interferometry. Finally, the application of digital phase measuring techniques allows one to greatly improve the accuracy and resolution of the measurement over visual evaluation of a fringe pattern. Until now, this method has been limited to measuring the flatness of individual components, up to about 200mm in diameter. In many cases, such as with machine slideways and surface plates, it is useful to know the flatness of a surface over an area which is only a part of a much larger structure. In these cases, it is necessary to bring the metrology instrument to the part, instead of the part to the metrology instrument.

2. DESIGN

The optical layout of the portable grazing incidence interferometer is given in Figure 1.

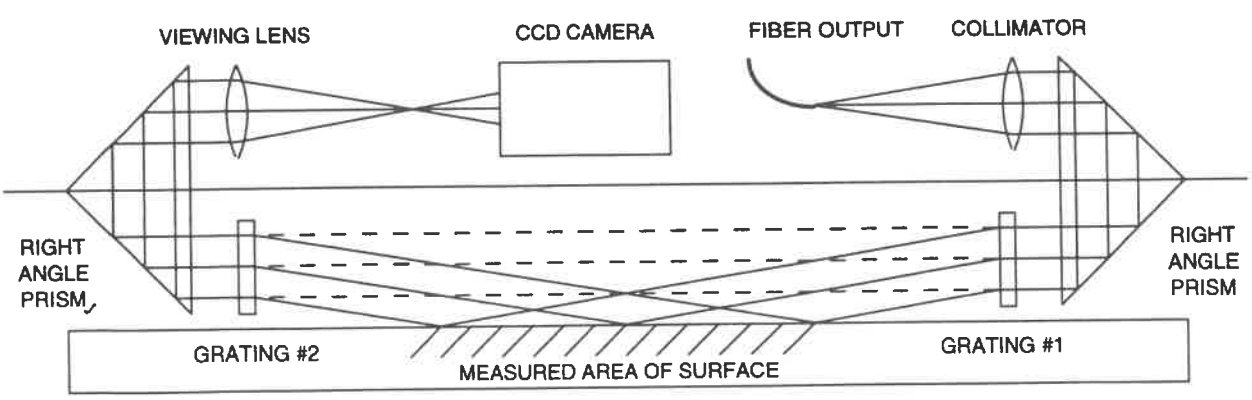

Figure 1. Optical layout of portable grazing incidence interferometer.

A fiber-coupled helium-neon laser is used as the source for the interferometer. This allows the heat from the laser to be located away from the interferometer. A 40mm diameter doublet lens produces a collimated wavefront which is directed to the first diffraction grating by a right angle prism. The interferometer uses two linear diffraction gratings to split and recombine the light into test and reference beams. The first order diffracted light from the first grating reflects off the surface at a grazing angle and serves as the test beam. The zero order diffracted light passes parallel to the surface and serves as the reference beam. The two beams are then recombined at the second grating. An interference pattern indicative of the surface height variations is imaged by the viewing lens and CCD camera. A linear translation of one of the gratings introduces a phase shift into the interferogram. Finally, a computer collects the phase shifted interferograms and calculates the surface flatness. Multiple measurements can be stitched together to measure the flatness of a much larger area.

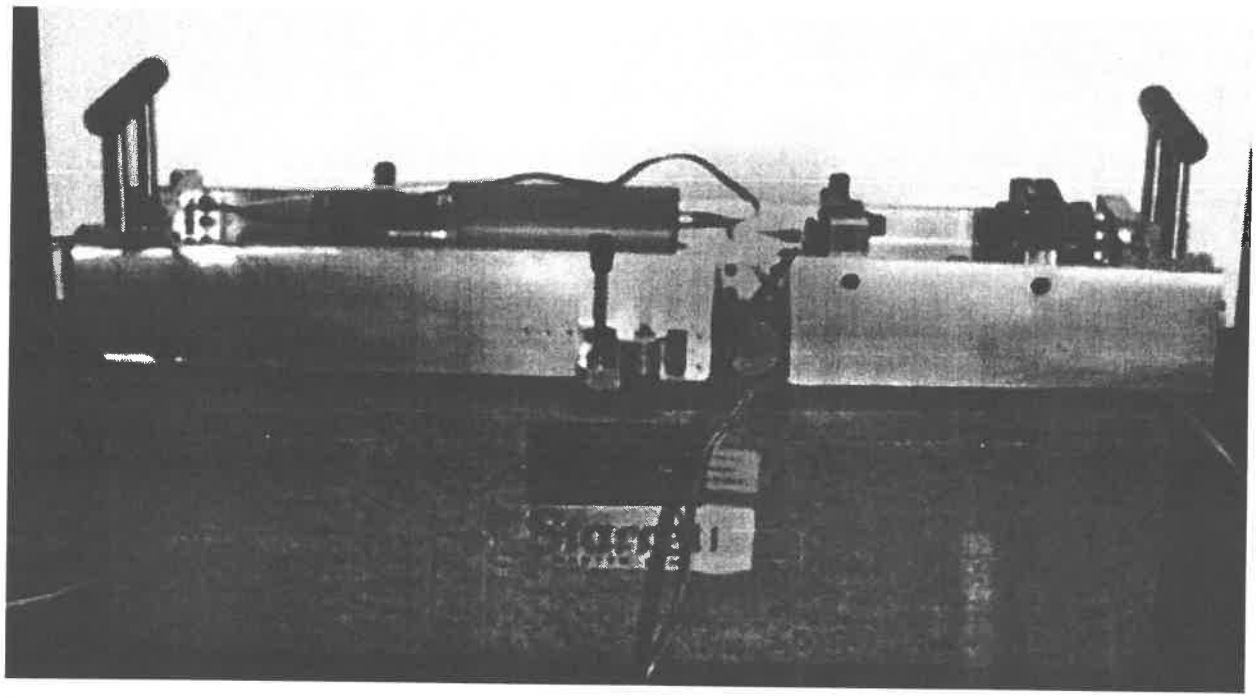

Figure 2. Photograph of portable grazing incidence interferometer measuring the flatness of a surface plate.

A photograph of the prototype interferometer is given in Figure 2. This prototype instrument measures an area approximately 1 inch wide by 15 inches long, and can easily be carried by hand to the surface to be measured. All of the optical components are mounted on an aluminum I-beam. The I-beam provides a stiff mounting structure while maintaining a low mass. The entire instrument weighs approximately 15 pounds. The source and viewing arms of the interferometer are located on the top half of the beam and the diffraction gratings are located on the bottom half. Three fine adjustment screws are located on the outside of the beam to permit fine alignment of the fringe pattern and repeatable placement of the instrument on the surface to be measured. Located next to each adjustment screw is an air dash-pot to reduce the likelihood of damage to the surface. The pitch of each diffraction grating is 10 microns, resulting in a fringe sensitivity of 5 microns per fringe. A translation of the first grating by 10 microns in a direction perpendicular to the grating lines results in a phase shift of one fringe. This motion is accomplished with a micro-stepping motor and an eccentric cam.

3. MEASUREMENTS

Figure 3 shows the results of a measurement of an 18" optical flat. This flat has been separately verified to have a figure error of less than 0.1 microns over the measured area. The top of the figure includes a photograph of the fringe pattern and an isometric view of the surface height map. The square image results from the geometric distortion caused by the grazing incidence angle. This distortion can be compensated for in software to display the measurement in the correct aspect ratio. The remaining plots in Figure 3 are contour and line profiles of the same measured area. The figure indicates a systematic interferometer error of less than 2 microns, including a periodic

error due to grating imperfections. This measurement is stored and used as a reference file to be subtracted from subsequent measurements.

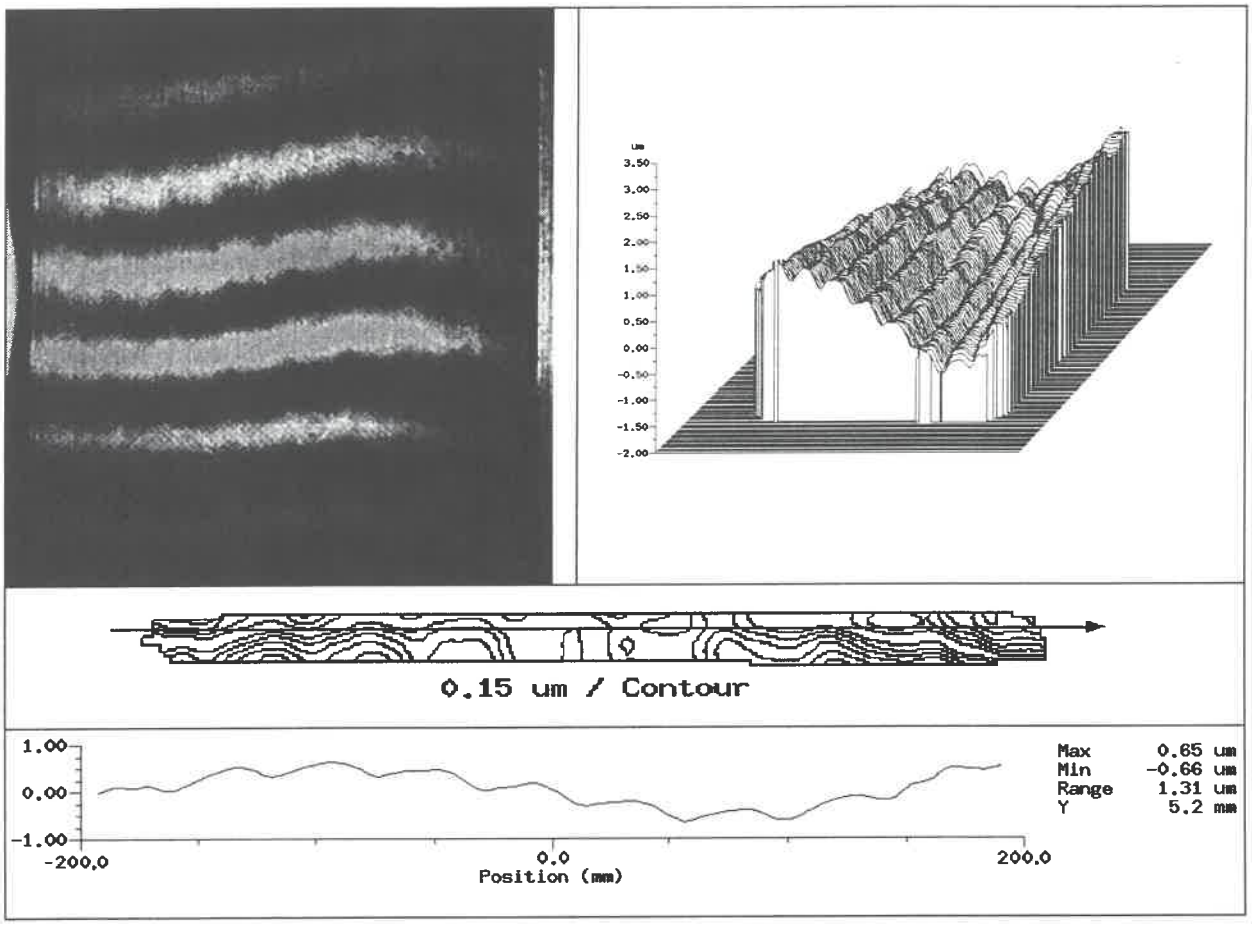

Figure 3. Measurement results from the 18" reference flat.

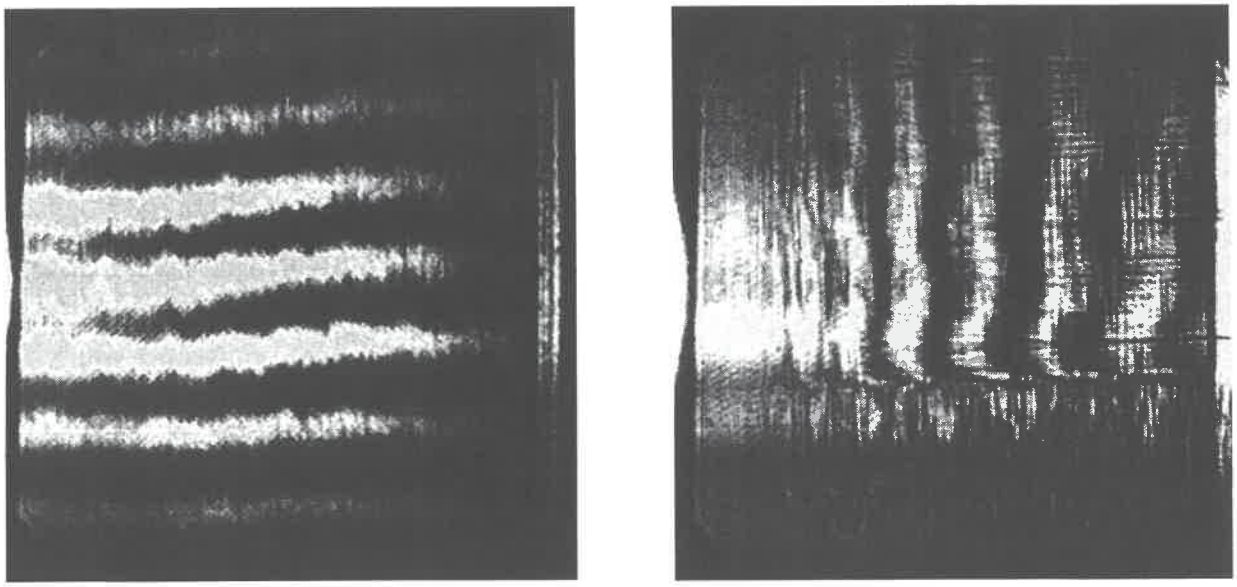

Figure 4. Fringe patterns obtained from a surface plate and a machine slideway.

The first fringe pattern in Figure 4 corresponds to the measurement of a granite surface plate. This fringe pattern does not appear significantly different than that of the reference flat. This indicates that there is little form error in this region of the surface plate. Figure 5 below shows the contour and line profile measurements from the surface plate after the reference file has been subtracted. The flatness in this region is measured to be less than 0.5 microns.

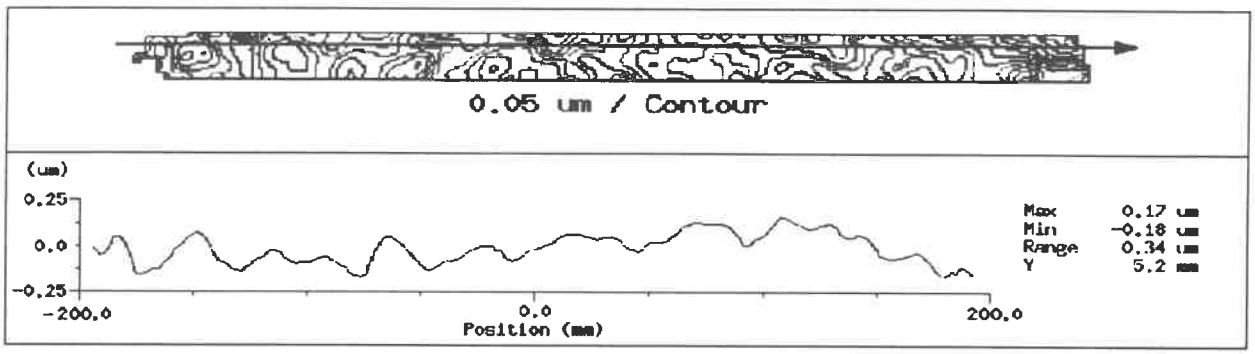

Figure 5. Measurement results from the granite surface plate.

The second fringe pattern in Figure 5 corresponds to the measurement of a machine tool slideway. The instrument has been placed over the edge of the slideway to illustrate the flatness along the edge. Higher order form variations are clearly evident in the fringe pattern. Figure 6 below shows the contour and line profile measurements of the slideway after the reference file has been subtracted. The flatness in this region is measured to be greater than 10 microns.

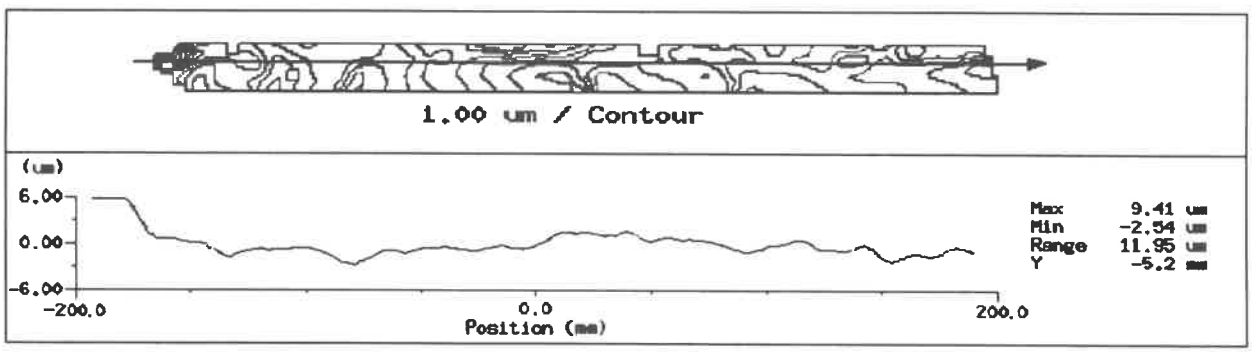

Figure 6. Measurement results from the machine slideway.

4. SUMMARY

In this paper, the design of a portable grazing incidence interferometer for flatness measurements of slideways and surface plates has been presented. The results of measurements of a variety of surfaces has been presented in order to illustrate the prototype instrument's capabilities. In particular, measurements of a machine tool slideway and a granite surface plate were demonstrated. Future work will include the stitching of multiple measurements together to measure the flatness of an entire surface plate and the comparison of this measurement with conventional methods.

5. REFERENCES

1. K.G.Birch, "Oblique incidence interferometry applied to non-optical surfaces," J.Phys. E., **6**, 1045-1048 (1973).
2. P.Hariharan, "Improved oblique-incidence interferometer," Opt. Eng. **14**, 257-258 (1974).
3. T.Dresel, J.Schwider, A.Wehrhahn and S.Babin, "Grazing incidence interferometry applied to the measurement of cylindrical surfaces," Opt. Eng. **34**, 3531-3535 (1995).
4. A.W. Kulawiec, J.F. Fleig and J.H. Bruning, "Interferometric measurements of absolute dimensions of cylindrical surfaces," 1997 Annual Meeting of the ASPE, Norfolk, VA, October 5-10, 1997.

FRINGE PROJECTION METHOD FOR MEASURING GEOMETRY AND WEAR OF CUTTING TOOL INSERTS

Albert Weckenmann*, Vasudevan P. Radhakrishnan**, Stefan Schmitz***

* Dept. Quality Management and Manufacturing Metrology, Univ. Erlangen-Nuremberg, Erlangen, Germany
** Manufacturing Eng. Section, Dept. of Mechanical Eng., Indian Inst. of Technology Madras Chennai, India
*** Robert Bosch GmbH, Bamberg, Germany

1 Introduction

Advanced metal cutting technologies like dry cutting, high speed machining and high precision machining have placed new demands on the used manufacturing resources. They, in comparison to those used in traditional metal cutting, must fulfil the high quality and reliability standards expected of them in their function and also from the economical side. This applies especially to the metal cutting tools, which have a significant influence on the quality of the workpieces. For a reliable and economically sound induction of these tools in the production line they must ensure a certain level of cutting performance and reliability through their shape, material and coating. In this context it is essential for the tool bits to ensure repeated positioning accuracy and quick clamping on the tool holder. Additionally they should closely adhere to a defined shape and cutting edge geometry to achieve high quality in production and should have high resistance to mechanical and thermal effects present in metal cutting. To ensure that only the functionally capable tool bits are used in the production line, their function related shape and wear characteristics are to be checked by the tool manufacturer as well as by the user. In tool insert production, the final tool bit as well as the green state part are checked for their shape. A wear monitoring procedure is also needed in the application of such tools.

2 Shape measurement approaches for tool inserts

The aim of shape measurement of new tool inserts is to determine the shape characteristics for example insert tip angle and nose radius, dimension and cutting edge radius (Fig. 1). For shape measurement of tool inserts mechanically probing measuring instruments, such as micrometer, dial gauge, indicating caliper, plug gauge, contour measuring instrument and optical measuring instruments, such as profile projector, tool maker's microscope, light-section microscope, tool presetting device are used so far.

For shape measurement with probing and optical 1D and 2D measuring instruments, the tool inserts are normally orientated manually for measurement, because an automation is hardly to realize and not flexible enough. The measured point scanning and selection for calculation the shape and wear characteristics of the tool inserts with two dimensional substitute geometry elements are also done manually by the operator. Because tool insert positioning, measured point scanning and selection are all manual, the results are largely dependent on the subjective judgment of the operator, which prevents precise, repeatable shape measurement. Another disadvantages is the long time for tool insert positioning, measuring and manual point selection. Moreover, 3D curved surfaces can only be inspected using optical coordinate measuring instruments if cuts are made which thus destroy the test specimen.

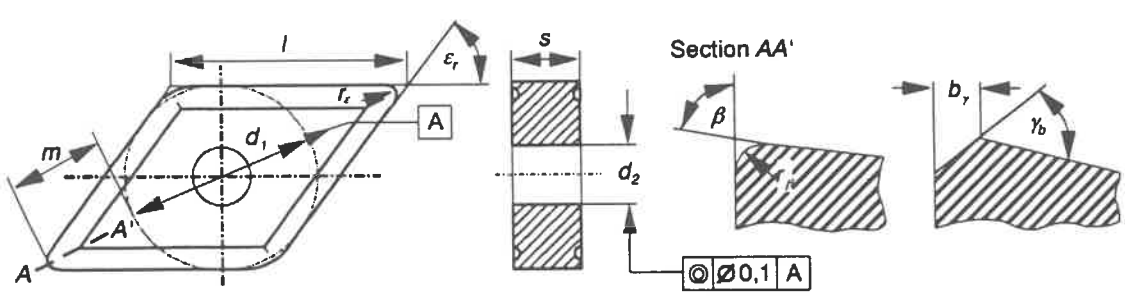

Fig. 1: Shape characteristics of a tool insert (1): r_ε nose radius, ε_r tip angle, β wedge angle, r_β cutting edge radius, b_γ width of chamfer, γ_b angle of chamfer, l insert length, m dimension, d_1 diameter of inscribed circle, d_2 diameter of clamping hole, s insert thickness

3 Optical 3D shape measurement of tool inserts with fringe projection system

In view of the above-mentioned drawbacks of the measuring instruments, an ideal measuring system distinguishes itself by a fast and operator independent measurements and the capability for automation. To be able to rule out the influence of positioning errors, a 3D measured point scanning is necessary to determine the orientation of the insert based on the 3D coordinates of the measured points. Compared with this requirements, the use of fringe projection systems is a promising approach for a repeatable 3D shape measurement. These systems enable a contactless measurement with high resolution, high density of measured points and a low measuring uncertainty. Other advantages are short measuring times, low sensitivity to the environment, great flexibility and universal applicability. The fringe projection systems are based on the principle of image triangulation. For 3D shape measurement, one or more sets of parallel light fringes are projected onto the object and are captured by the camera (Fig. 2).

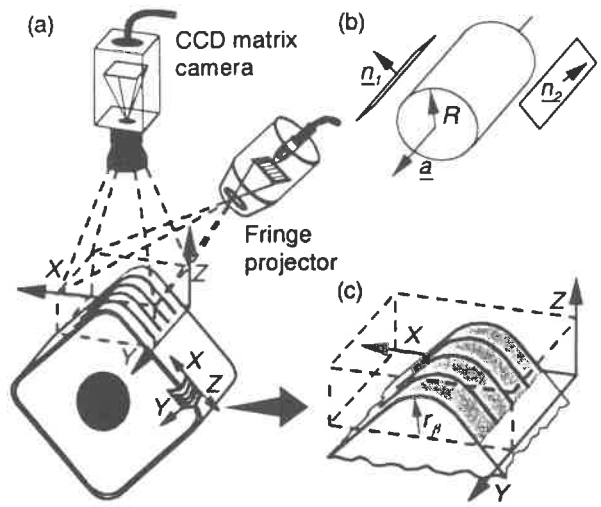

Fig. 2: (a) Cutting tool insert shape measurement using fringe projection system; (b) Substitute elements; (c) Section of the digitized cutting edge

3D shape measurement with fringe projection system

Using the fringe projection systems for assessment of the macroscopic shape parameters (tip angle, nose radius, dimension), only the part of the insert surface, necessary for determining the shape characteristics, is acquired optically and the 3D coordinates of the surface measured points are determined in a coordinate system defined by the instrument, i.e., the surface is digitized. To determine the dimension, various surface zones of the tool insert have to be digitized. For this purpose, the insert is kept on a rotary table and rotated within the fringe projection field and measured at defined positions. The individual sets of measurements are then transformed into a single higher level coordinate system for evaluation the dimension (Fig. 3). Regarding the measurement of inserts with a fringe projection system in (2), the described method enables an absolute determination of the shape characteristics of the inserts (3). In (2) the dimension and position of shape deviations of the chip breaker are checked by a comparison of the 3D measured points with the digitized surface of a master insert.

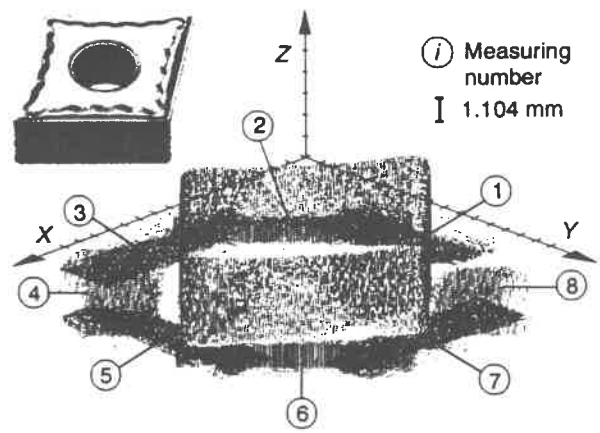

Fig. 3: Transformed 3D measured points from eight individual exposures taken on the presented insert kept on the rotary table

Pre-processing of the measured points

To calculate the shape characteristics dimension, cutting edge radius, nose radius and tip angle from the 3D measured points, it is necessary to substitute geometrically ideal form elements (cylinder, flat surface) for the digitized real tool inserts surface with shape deviations. From the substitute element parameters, the position, dimension and orientation of the observed insert segment can be determined. If determination of the shape characteristics is to be repeatable, it is necessary to assign the 3D measured points operator-independently,

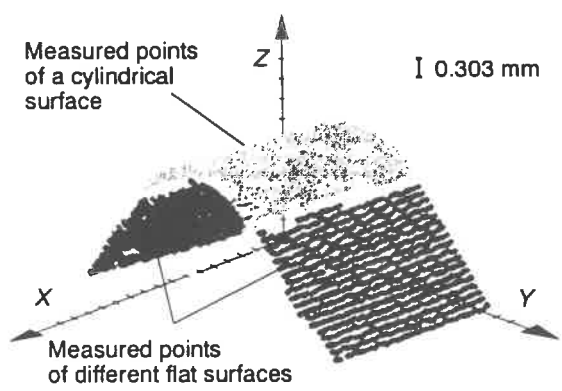

Fig. 4: Separated 3D measured points of a tool tip

i.e. automatically, to the flat and cylindrical substitute elements. Therefore a pre-processing software module was developed (3) to identify and separate the measured points belonging to the cylindrical and flat substitute elements from the 3D measured points. Fig. 4 shows the separated flat and cylindrical measured points of a tool tip.

Function oriented inspection of the tool insert shape

For function assessment of each shape feature of a tool insert, it is necessary to evaluate the 3D measured points in a functionally oriented way. For this purpose, the geometry and position parameters of the substitute elements are calculated using a fitting algorithm on the basis of the previously separated flat surface and cylinder measured points. Fitting according to the least square mean fit is only possible if the deviations of the measured values from the ideal geometry substitute element is caused by random errors. If the deviations of the measured values are caused by deviation of the actual shape of the object under test, approximation methods are required. In this case, approximation is performed by iteration subject to boundary conditions (approximation criteria), such as e.g. minimum circumscribed and maximum circumscribed conditions, that are defined in accordance with the inspection goals and functional needs of the object under test (4).

4 Tool wear and its monitoring

The aim of wear measurement is to acquire wear phenomena of used tool inserts and to calculate characteristic wear data for example flank or land wear, crater wear, from the measured points (Fig. 5). The measurements of wear are direct measurements on the tool by using tool maker's microscope, light section microscope, profile projector or surface profile measuring instruments. Direct measurement of the tool wear is often difficult in production, time consuming and the sculptured surfaces provided on the tool for cutting action and chip flow makes it even tougher. Crater wear monitoring by simple vision is not feasible as the depth parameters cannot be extracted using a single camera. The mechanism of tool wear is complex and depends on the cutting conditions, tool and workpiece material and machine tool characteristics. The simple wear characteristics, which could be measured conveniently, often do not give the total picture of the changes that have taken place on the cutting edge leading to inefficient cutting and bad surface finish. In this connection few methods for tool wear measurement and monitoring which could provide effective and reliable information on the state of wear of the tool are discussed.

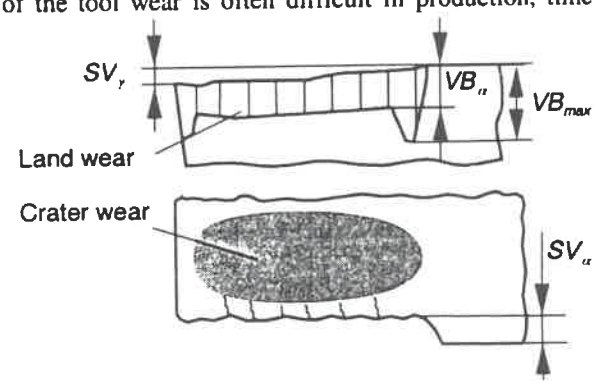

Fig. 5: Wear characteristics of a tool insert: *VB* width of land wear, *SV* cutting edge shift in direction of clearance (α) and of chip flow (γ)

Wear measurement with fringe projection microscope

The fringe projection microscope for measuring the cutting edge radius can also be used to measure worn cutting edges of tool inserts. Unlike with the tool microscope and 2D vision systems, with 3D measurement, precise orientation of the tool insert is no longer required, because the reference surfaces for characteristic calculation can also be determined from the 3D measured points. Fig. 6 shows the cutting edge of a used tool insert with wear.

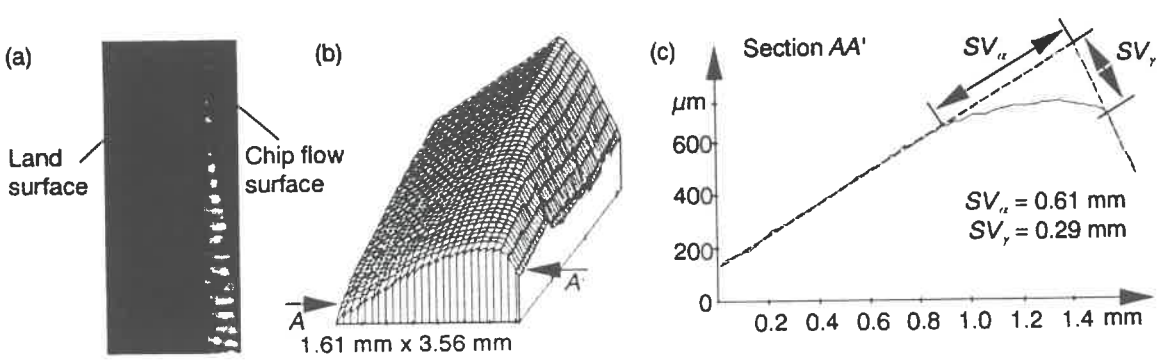

Fig. 6: Face and flank wear of a insert: (a) CCD camera picture with fringe pattern on the insert surface; (b) 3D measured points of the digitized part of the insert surface; (c) 2D profile from 3D measured points

Tool wear assessment by diffraction approach

Tool wear changes the cutting edge straightness and its relative position with reference to the tool geometry. Measurement of these features by conventional approaches is time consuming and requires relatively expensive facilities. This measurement can be done with a simple set up using laser diffraction (Fig. 7a). Here the tool is pressed against a template of the correct geometry so that the worn out edges form a gap. Through this gap the laser beam can be projected which will diffract (Fig. 7b). The pattern of diffraction captured by a CCD camera depends on the gap variations.

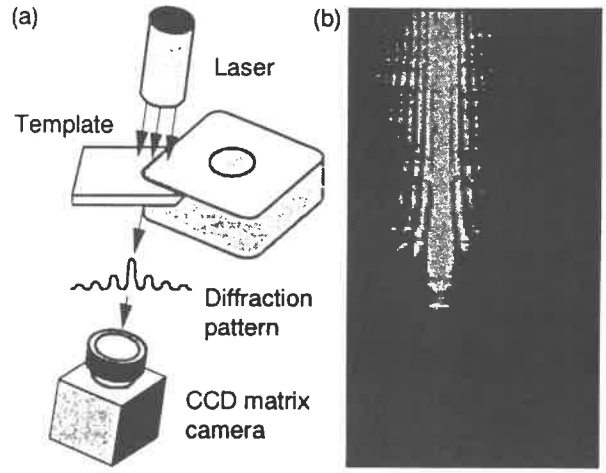

Fig. 7: (a) Measurement of tool wear by laser diffraction; (b) Diffraction pattern of a worn cutting tool

Wear land detection step for tool wear monitoring

Online tool wear monitoring techniques are based on the changes of the physical effects (cutting forces, vibration, acoustic emission) during the cutting process, due to tool wear (5,6). Detection methods using appropriate sensors have been developed to assess the tool condition based on these effects. However the detection of wear is not normally of consistent accuracy as the changes in the signal are gradual and are often mixed with noise. To avoid this difficulty, a tool having a wear detection feature, like a small step, provided on the flank could be used (Fig. 8). The step will contact the workpiece when the tool wear reaches the critical value and thereby changing the sensor signal in a significant manner.

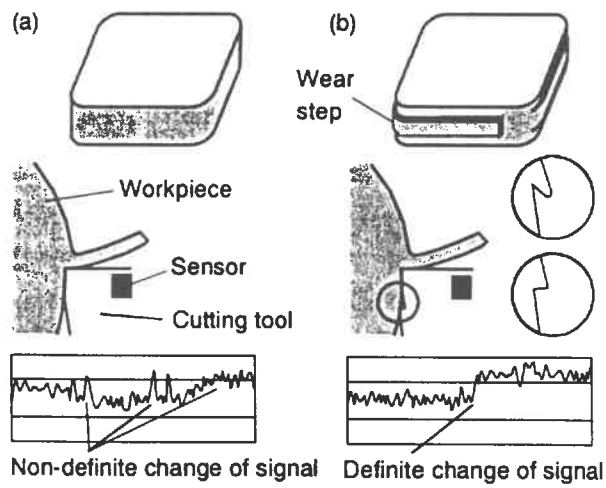

Fig. 8: Monitoring of a cutting tool (a) with and (b) without a land wear detection step

5 Conclusions

This paper dealt in detail on the possibilities of measuring and monitoring the geometry as well as wear of throw away cutting inserts. Application of fringe projection systems in an appropriate manner is of interest in this regard. Other methods suggested could provide reliable information on tool wear progression and a better understanding of the mechanism involved in tool wear. These include micro geometry changes on the cutting edge, characteristics of the worn surface at the micro level, introduction of an appropriate wear detection feature on the tool and diffraction based inspection of the full cutting edge wear.

6 References

(1) Norm DIN 4967 April 1987. Wendeschneidplatten aus Hartmetall mit Eckenrundung, mit Senkbohrung

(2) Leopold, J.: Process Monitoring of 3D - Cutting Inserts Using Optical Methods. In: Journal of Materials Processing Technology 61 (1996), pp. 34-38

(3) Schmitz, S.: Dreidimensionale Gestaltmessung von Wendeschneidplatten mit Streifenprojektion und Phasentriangulation. In: A. Weckenmann (Hrsg.): Berichte aus dem Lehrstuhl Qualitätsmanagement und Fertigungsmeßtechnik, Nr. 2 Erlangen, 1998. - Diss.

(4) Weckenmann, A.; Eitzert H.; Garmer, M.; Weber, H.: Functionally-oriented evaluation and sampling strategy in coordinate metrology. In: Precision Engineering 17 (1995), pp. 244-252

(5) Tönshoff, H.K., Wobker, H.G., Hartmann, M., Kilsmark, P.: The future of Machining. In: VDI Berichte Nr.1179, Überwachung von Zerspan- und Umformprozessen (1995), pp. 347-360

(6) Dornfeld, D.A.: Monitoring Technologies for Intelligent machining. In: VDI Berichte Nr.1179, Überwachung von Zerspan- und Umformprozessen (1995), pp. 71-90

Optical frequency stabilization of a compact heterodyne source for an industrial distance measuring interferometer system

Leslie L. Deck and Michael L. Holmes

Zygo Corporation, Laurel Brook Road, Middlefield, CT. 06455-0448

Introduction

Many optical metrology applications such as heterodyne interferometry and high resolution spectroscopy require a spectrally stable source. Despite advances in solid state laser technology, He-Ne lasers are still often chosen for these applications due to their spectral purity. Heterodyne interferometry applications are particularly aided by this and the relatively simple method of producing two orthogonal, frequency separated components via the Zeeman effect.

The ideal Zeeman He-Ne laser produces a beam consisting of two orthogonal, frequency shifted, circularly polarized beams. A traditional frequency stabilization technique for these lasers involves adjusting the laser cavity length in a feedback loop with the control signal derived from the intensity difference between these two beams.[1] A stabilization system based on this principle typically consists of a birefringent element to convert the polarization to linear and a polarization beam-splitter to separate and direct the two linear polarizations onto two detectors, which are differenced to create the control signal. From the standpoint of providing a stable source for heterodyne interferometry, this traditional approach is often adequate. However as laser production costs drop, the stabilization system becomes an increasingly large fraction of the total system cost. Furthermore, additional optical and electronic components are needed to establish the heterodyne reference, further increasing system cost and complexity.

We describe a simpler stabilization scheme that can be implemented when the two orthogonal frequency components possess elliptical rather than circular polarization.[2] Invariably, small stresses in the end mirrors of non-Brewster windowed HeNe lasers, due either to mounting or coating stresses, cause enough birefringence to produce an elliptical output beam. Indeed, careful control of the mirror mounting process during laser manufacture can repeatedly produce a particular beam ellipticity. Given elliptically polarized lasers with a particular ellipticity, the stabilization scheme described requires no optical components at all, just two detectors to measure the relative intensity of the two beams. The scheme further provides a variety of ways for producing the heterodyne reference signal required for heterodyne interferometry applications.

Method description

Consider a single mode HeNe laser whose beam is elliptically polarized with constant ellipticity e defined by $e = |E_{min}| / |E_{maj}|$, where E_{maj} and E_{min} are the complex electric field amplitudes of the major and minor axes of the polarization ellipse. This beam is incident onto a pair of detectors situated as shown in Figure 1. Detectors #1 and #2 are oriented at an angle of incidence θ_i to the incident beam with the detector planes parallel to each other. The detectors are standard silicon detectors without an anti-reflection coating. Under these circumstances, the bare silicon surface quickly grows a thin oxide layer 5 to 10nm deep. This SiO_2 layer provides good protection against water and other airborne contaminants but is thin enough to ignore when modeling the optical properties of the detector. Another nice bonus with this configuration is that optical feedback into the laser from scatter off of surfaces is virtually eliminated.

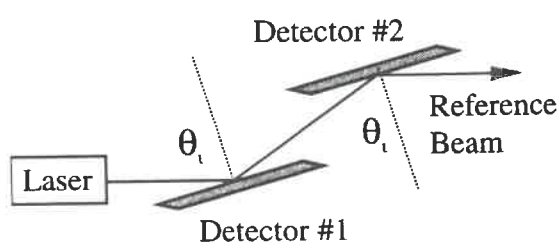

Figure 1: Detector geometry

The detector assembly is axially rotated so the S and P polarization states defined by the detector orientation relative to the beam are aligned with the major and minor axes of the polarization ellipse, so that the complex electric field components E_S and E_P satisfy $E_S = E_{\text{maj}}$ and $E_P = E_{\min}$. If the laser is now Zeeman split, the light exiting the laser is composed of two orthogonal, elliptically polarized beams at two slightly different optical frequencies determined by the Zeeman effect. Each beam has two complex electric field amplitudes E_S and E_P, which for beam #1 (with optical frequency ω_1) can be written as;

$$E_{1,S} = |E_{1,S}|\exp(i\omega_1 t), \quad E_{1,P} = e|E_{1,S}|\exp(i\omega_1 t + \varphi) \tag{1a}$$

while for beam #2 they are

$$E_{2,S} = e|E_{2,P}|\exp(i\omega_2 t - \varphi), \quad E_{2,P} = |E_{2,P}|\exp(i\omega_2 t) \tag{1b}$$

where we have used the definition for e and invoked orthogonality ($E_{1,S}E_{2,S}^* + E_{1,P}E_{2,P}^* = 0$). When the laser is stable, the two beams will have equal intensity so $|E_{1,S}| = |E_{2,P}|$ and $|E_{1,P}| = |E_{2,S}|$.

The instantaneous intensity seen by the first detector I_{D1} is given by the transmittance of the P and S polarization states of both beams,

$$I_{D1} = \left\{ \left| t_S(\theta_i,\theta_r)(E_{1,S} + E_{2,S}) \right|^2 + \left| t_P(\theta_i,\theta_r)(E_{1,P} + E_{2,P}) \right|^2 \right\}\eta \tag{2}$$

where $t_{P(S)}(\theta_i,\theta_r)$ and $r_{P(S)}(\theta_i,\theta_r)$ are the transmission and reflection amplitudes for the P(S) polarization states obtained from the Fresnel formula for a single boundary[3], θ_i and θ_r are the angles of incidence and refraction respectively at a detector boundary, $\eta = \dfrac{n_{Si}\cos(\theta_r)}{n_{air}\cos(\theta_i)}$ is required for energy conservation for the transmitted beam in the detector material and $n_{Si(air)}$ is the index of refraction for silicon(air). For clarity, we will omit the explicit dependence of the amplitudes on the angle of incidence and refraction in what follows.

The intensity seen by detector #1 modulates at the heterodyne beat frequency $\Omega = \omega_2 - \omega_1$ as can be confirmed by substitution of the complex field components Eq. 1. One obtains after some arithmetic;

$$I_{D1} = \eta E_1^2\left(|t_S|^2 + e^2|t_P|^2\right) + \eta E_2^2\left(e^2|t_S|^2 + |t_P|^2\right) + 2eE_1E_2\eta\left(|t_S|^2 + |t_P|^2\right)\cos(\Omega t - \varphi). \tag{3}$$

The 2nd detector observes the transmitted portion of the ray reflected from detector #1 and also modulates at the heterodyne frequency;

$$I_{D2} = \eta E_1^2\left(|t_S|^2|r_S|^2 + e^2|t_P|^2|r_P|^2\right) + \eta E_2^2\left(e^2|t_S|^2|r_S|^2 + |t_P|^2|r_P|^2\right) + \\ + 2eE_1E_2\eta\left(|t_S|^2|r_S|^2 + |t_P|^2|r_P|^2\right)\cos(\Omega t - \varphi). \tag{4}$$

The ideal control signal is $\mathrm{K}_{\text{ideal}} = \langle I_1\rangle - \langle I_2\rangle$, where $\langle I_{1,2}\rangle$ represents the time averaged intensity signal from the two orthogonal frequency shifted beams. As these individual beam intensities are not available, the following control signal is used,

$$\mathrm{K} = G\left(\langle I_{D1}\rangle - R\langle I_{D2}\rangle\right). \tag{5}$$

Where G is the electrical (trans-impedance) gain of detector #1 and R is the ratio of the gains of detector #2 to detector #1. For good closed loop performance, the average must be taken over a time interval short compared to the cavity length variations, but long compared to the heterodyne frequency. Using the time averaged portion of Eqs. 3 and 4, and the requirement that $\mathrm{K} = 0$ when the two beams have equal intensity, determines the necessary gain ratio R;

$$R = \frac{|t_S|^2 + |t_P|^2}{|t_S|^2|r_S|^2 + |t_P|^2|r_P|^2} \tag{6}$$

This gain ratio is dependent on the detector geometry and material, but independent of ellipticity. With this value for R, the control signal K measures the deviation of the two beams from equal intensity.

Control signal sensitivity

The sensitivity of the control signal to small changes of intensity in the neighborhood of the stability point can be easily obtained through differentiation in the linear approximation. We assume that for small changes ε in intensity, the two beams satisfy: $I_1(\varepsilon) = I - \varepsilon$ and $I_2(\varepsilon) = I + \varepsilon$. The sensitivity is then found to be

$$\frac{\partial \mathrm{K}}{\partial \varepsilon} = G\left(1 - e^2\right)\eta\left[\left(|t_P|^2 - |t_S|^2\right) - R\left(|t_P|^2|r_P|^2 - |t_S|^2|r_S|^2\right)\right]. \tag{7}$$

As expected, the sensitivity vanishes for circular polarization $(e = 1)$ and is maximized for linear polarization. Figure 2 shows the sensitivity, normalized by $G\left(1 - e^2\right)\eta$, as a function of the angle of incidence. The sensitivity peaks at a value of 2 which also corresponds to the peak sensitivity expected from the ideal control signal, but this only occurs at an angle of incidence equal to Brewsters angle for silicon;

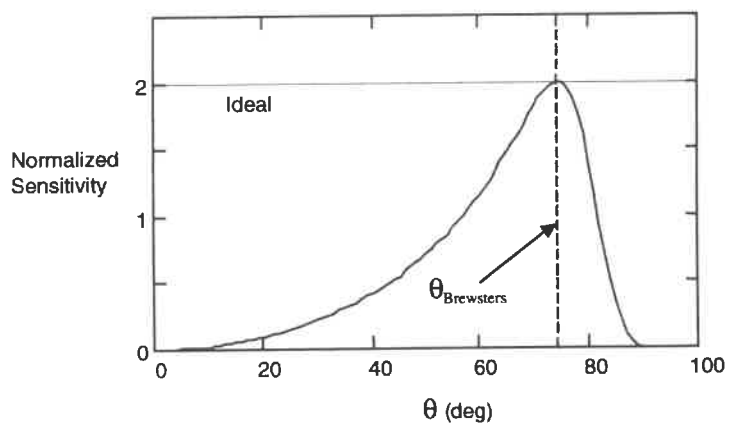

Figure 2: Control signal sensitivity as a function of detector angle.

$$\theta_B = \tan^{-1}\left(n_{Si}/n_{air}\right) \cong 74.5°.$$

This makes intuitive sense, in that at Brewsters angle, the p-polarization reflection amplitude is zero, thereby maximizing the effective separation of the s and p polarization components, which by design coincide with the principle axes of the polarization ellipse.

Heterodyne Reference

Heterodyne interferometry applications require a reference signal at the base heterodyne frequency to extract the Doppler shift from the test signal. Since both detectors see the heterodyne frequency, either one can be instrumented to receive this signal. From the formulas for the time dependent detector signals, Eqs. 3 and 4, the heterodyne signal contrast when the laser is stable with the two beams at equal intensity I works out to be $2e/\left(1 + e^2\right)$ for both detectors. This ellipticity dependence is opposite to that found in the control signal sensitivity, Eq. 7, which underscores a basic tradeoff in the stabilization system when used for heterodyne interferometry, one can improve stabilization only at the cost of reducing the heterodyne reference signal contrast.

For extremely high heterodyne frequencies, or in an electrically noisy environment, especially if the phase sensitive detection system is remote, it is difficult to transmit an electrical reference signal undistorted. Under these conditions an optical reference signal is preferred, which is available in the beam reflected from detector 2. The intensity of this beam is given by;

$$I_{\mathrm{REF}} = \left|r_S r_S \left(E_{1.S} + E_{2.S}\right)\right|^2 + \left|r_P r_P \left(E_{1.P} + E_{2.P}\right)\right|^2, \quad (8)$$

and has a heterodyne contrast identical to that seen by the detectors.

Experimental Verification

A small (~80mm cavity) single mode Zeeman split laser tube manufactured at our Zygo Laser Division facility (Longmont, CA) was stabilized using our method. Laser light emerged from both ends of the tube and the stabilization control assembly was located to intercept the 30μwatts leaking out the rear cavity mirror. The two frequency components were orthogonally elliptically polarized with an ellipticity $e = 0.54$. Four cylindrical permanent magnets surrounding the tube produced a split frequency of 3.6MHz. The two stabilization detectors were OSD100-0-COW large area uncoated silicon diodes from Centro Vision Inc. (Newbury Park, CA) and were both arranged at Brewsters angle and separately amplified before differenced to create the control signal. For this detector geometry and using a refractive index of 3.6-0.02i for silicon, the optimal gain ratio R is;

$$R = \frac{|t_S|^2 + |t_P|^2}{|t_S|^2 |r_S|^2} = 6.5. \quad (9)$$

The control signal was sent to a simple PI temperature controller, which controlled the current to a Minco (Minn. MN.) thin-film heating element attached to one end of the laser tube. When powered up, current to the heating element was set to maximum until the tube reached a predefined setpoint temperature, whereupon the feedback controller was engaged. The reference beam exiting the second detector was coupled into a 250μm core multimode fiber.

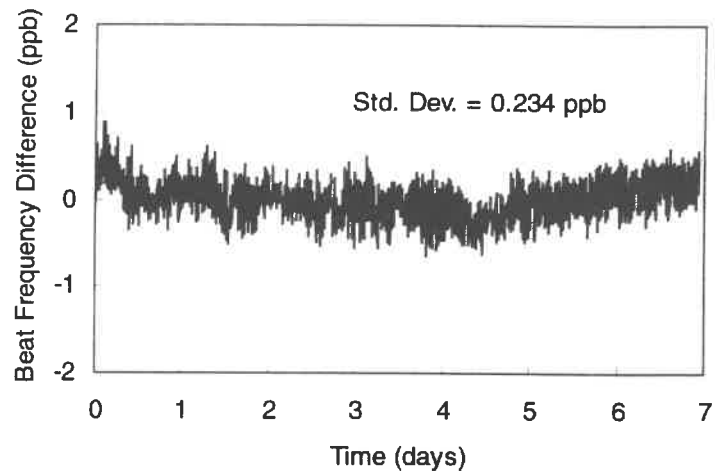

Figure 3: Laser frequency stability over 7 days.

The 350μwatts emanating from the front was used to monitor the laser stability by interfering it against a frequency standard and continuously monitoring the beat frequency. Figure 3 shows the beat frequency between the laser and the standard for 1 week starting from controller lock. The frequency stability measured 0.234 ppb (111 KHz) rms over the 7 day period.

Summary

We have shown that given a single mode, Zeeman split, elliptically polarized laser, only two detectors are required to generate an efficient frequency stabilization control signal. When coupled with a simple PI controller and a thermal transducer we have achieved optical frequency stabilization to better than 1 part per billion over 7 days. The detector geometry is compact, robust and inexpensive, and provides a number of convenient ways of generating a heterodyne reference signal, making the method useful for distance measuring interferometry applications.

References

[1] I. Tobias, M.L. Skolnick, R.A. Wallace, T.G. Polanyi, "Derivation of a frequency-sensitive signal from a gas laser in an axial magnetic field," Appl. Phys. Lett., **6**, 198-200 (1965)

[2] U.S. Patent pending.

[3] M. Born and E. Wolf, "Principles of Optics", 6th Ed., Pergamon Press (1989), Chap. 1.6.4

INFLUENCES ON SURFACE AND SUBSURFACE DURING ULTRASONIC ASSISTED GRINDING OF ADVANCED CERAMICS

Günter Spur, Eckart Uhlmann, Sven-Erik Holl, Nikolai Alexander Daus
Institute for Machine Tools and Factory Management
Technical University Berlin, Germany

Introduction

In ultrasonic assisted grinding, the kinematics of the conventional grinding process are superimposed with a high-frequency longitudinal motion of the tool or the workpiece. Like in ultrasonic lapping, the excitation is realized by an external voltage generator and a sonic transducer that works on the piezoelectric principle. The ultrasonic motion is characterized by a frequency of about 18-25 kHz and an amplitude of about 4 µm which, however, can be increased by up to 50 µm with the help of sonotrodes. Ultrasonic assisted grinding has a high potential for an economical machining of hard and brittle materials like glass or ceramics, particularly in the generation of complex contours. Adjusting the kinematic parameters also permits a purposeful micro-structuring of the workpiece surface and serves to avoid directional machining patterns normally observed in grinding.

Current investigations have shown that ultrasonic assistance leads to a fundamental change in the surface formation and wear mechanisms as compared to conventional grinding [Uhl98]. The thermal load is distinctly reduced, whereas the mechanical load increase due to the pulse-like grit engagement. It was noticed that this could reduce the grinding forces by at least 40%. At the same time, a very high surface quality and a low, almost stationary grinding wheel wear could be achieved.

The impact of ultrasonics on subsurface properties, however, is yet to be reported in the literature. To determine the subsurface damages caused by ultrasonics, experimental investigations on the bending strengths due to machining, residual stresses, and surface qualities, as well as grinding temperatures were carried out. This paper will show that ultrasonics do not cause a deterioration of the subsurface properties in comparison with conventional methods. Moreover, the generated compressive residual stresses are more favorable than during grinding without ultrasonic assistance.

Procedure variants and functional principle

In order to realize the different kinematics variants which show different positions of the active partners, tool and workpiece, in relation to each other, the ultrasonic vibration can be induced into the contact zone by the tool as well as by the workpiece. With reference to DIN 8589 T 11 the in **Figure 1** displayed kinematic modifications take place.

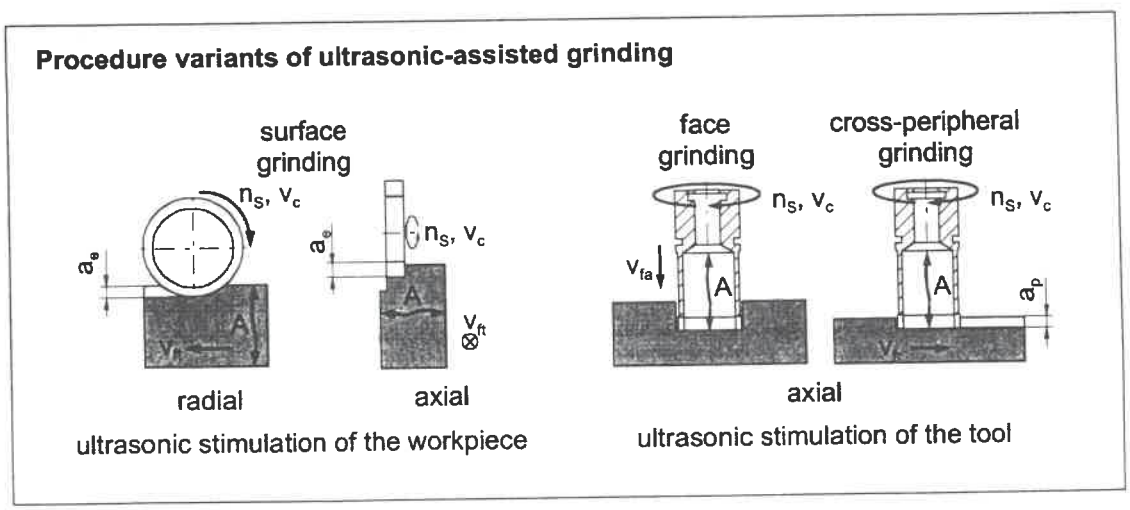

Figure 1: Procedure variants of ultrasonic assisted grinding [SpuH95]

The introduction of an additional motion component into the interacting zone leads to a change in the motional relations of diamond grit and workpiece surface. In **Figure 2** the changed kinematic conditions are displayed using surface grinding as an example. The introduction of an additional motion component in the interacting zone leads to a change in the motion ratios between the abrasive grain and the material surface.

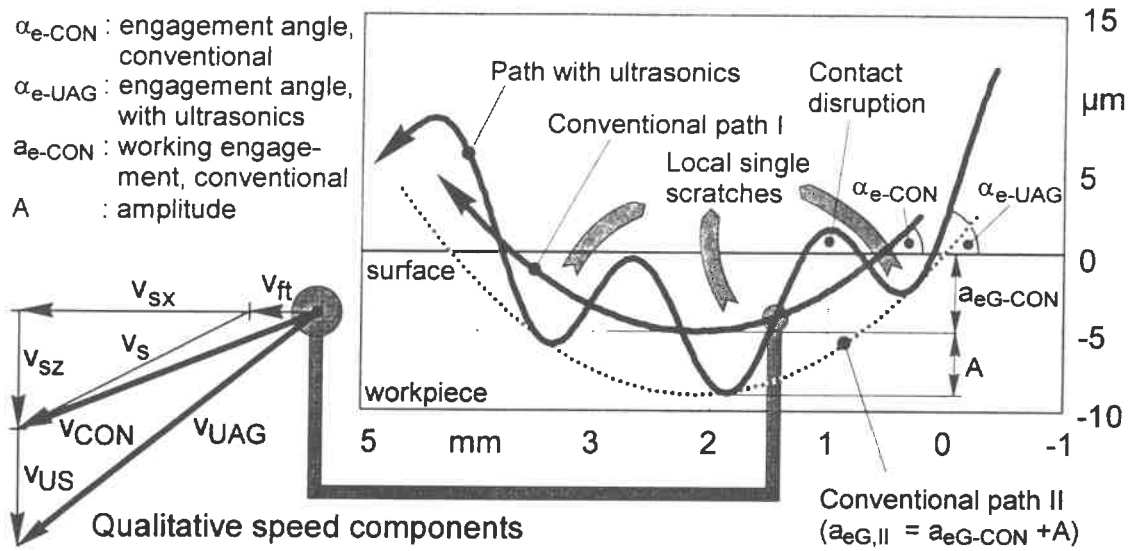

Figure 2: Calculated motion path of a cutting edge with radial ultrasonic stimulation of the workpiece in comparison with the conventional motion path

As a result of the ultrasonic motion there is a constant change of direction of the active speed and contact conditions, consequently the surface formation as well as the wear mechanisms change.

If the feed speed is ignored, the path of the grits during grinding without ultrasonic describes the segment of a circle. The grits penetrate into the material in relation to the conventional working engagement $a_{eG\text{-}CON}$ with a constant wheel speed v_s and a defined conventional angle of engagement $\alpha_{e\text{-}CON}$. The maximum depth of cut is reached at the lowest point of the curve. After leaving the surface, the grits have marked a trace of the length $l_{Rt\text{-}CON}$ [Uhl98].

Additional kinematic measures by means of longitudinal workpiece vibrations in radial direction cause significant deviations from the circuit described before. Depending on how many workpiece vibrations are realized per contact phase, a number of single scratches locally strung together with different depths and lengths of cut emerge instead of a circular engagement. The maximum depth of cut increases by the value of the amplitude A at nominally equal working engagements. Complete contact disruptions occur between the local single scratches. Due to the additional speed component in radial direction v_{US}, the grits hits the surface hereby at a larger angle of engagement with higher active speed v_{UAG}. Each local single scratch is characterized by distinctly shorter contact times and single lengths of scratch, as well as higher engagement depths [Uhl98].

Besides the described radial stimulation of an active partner, the ultrasonic vibration can also be generated axially to the tool axis during surface grinding. A complete disruption of contact between the tool and the workpiece, instead harmonious machining patterns are formed on the workpiece surface. Because of the kinematic conditions with a constant change of active direction, different contact paths are superimposed and the process forces are reduced as during radial ultrasonic stimulation. On the machined workpiece surface, homogenous surfaces with an improved tribological behavior are formed [Zap98]. **Figure 3** demonstrates the influence of the ultrasonic vibration on the structure of the machined surfaces. In the left part of Figure 3, locally lined up single scratches are noticeable, which de-

rive from the radial ultrasonic stimulation. The machining traces shown in the right part of Figure 3 are not disrupted, because the vibratory movement is superimposed here in axial direction.

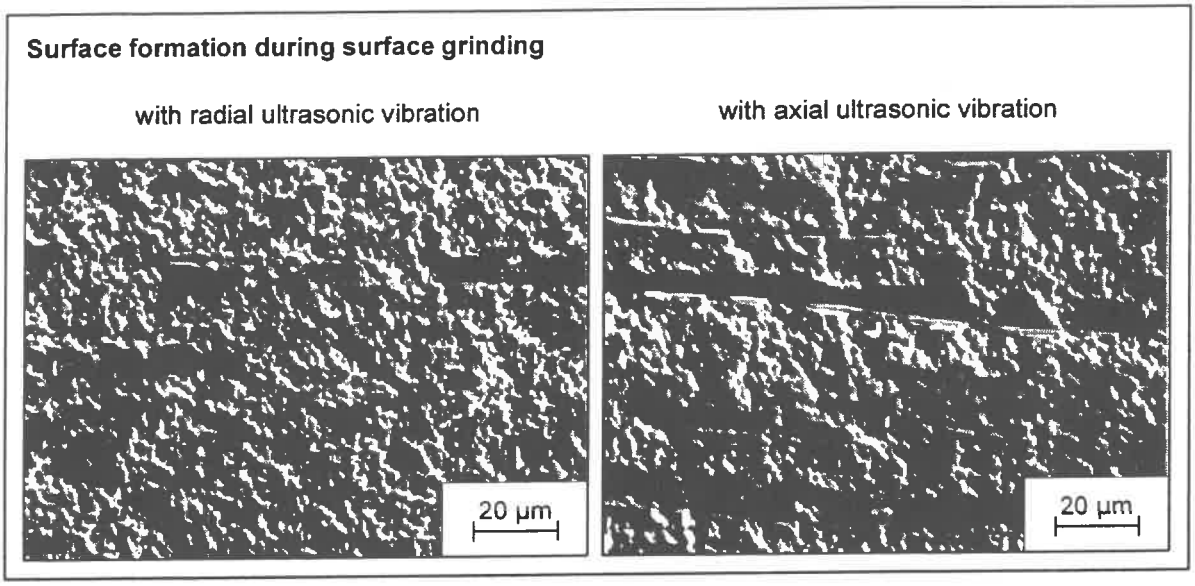

Figure 3: Surface formation during surface grinding with radial and axial ultrasonic vibration as shown in the example of Al_2O_3

Depending on the vibration frequency and the peripheral speed undulating machining patterns occur during each individual single contact, of which the layout is different than the one during conventional grinding.

Influence of ultrasonics on surface and sub-surface.

Increased mechanical load and reduced thermal load on both partners are a result of ultrasonic assistance. Due to a change of active principles during surface formation, a change of the wear behavior on the grinding tool occurs. Grit flattening on the diamonds are increasingly replaced by micro-splinterings. Contrary to conventional grinding, sharp single cutting edges are hereby generated. In the course of the process time, the amount of single cutting edges increases compared to conventional grinding. Hence the degressive increase of the process forces is significantly reduced and transmitted to a quasi-stationary force development. The respective wear mechanisms balance each other out, in a way that altogether an almost unchanged radial wear can be noted, compared to the conventional process.

Aside from the change in force behavior, a significant reduction of the grinding temperatures occurs in the contact zone. Due to the disruption of the tool-workpiece contact, the contact times of the individual diamond grits are shortened and thus the frictional effects between the active partners are reduced. Moreover, the introduction of the cooling lubricant and the transport of the material removal is improved. From the measurement of the marches of temperature using thermal elements in the sub-surface of the workpiece, a decrease in temperature of up to 30 % has been established during ultrasonic grinding. During the machining of silicon carbide for example, temperatures in the sub-surface decrease from 90 °C to 70 °C (**Figure 4**). The determined diminution of the sub-surface temperatures of the workpiece leads to the conclusion that the temperatures influencing the diamond grits also decrease.

In the course of further investigations at the IWF Berlin, the sub-surface characteristics after machining were compared. For the characterization, bending strengths and residual stress conditions are usually established. Additionally, the tool topography and the surface quality give information about fissures and strains that determine damages in the sub-surface area. The determination of the quality of the machining results is carried out by comparing the results with those of plan-parallel lapped workpieces.

Here it is important to clarify whether or not the ultrasonic superposition leads to intolerable damages on the component.

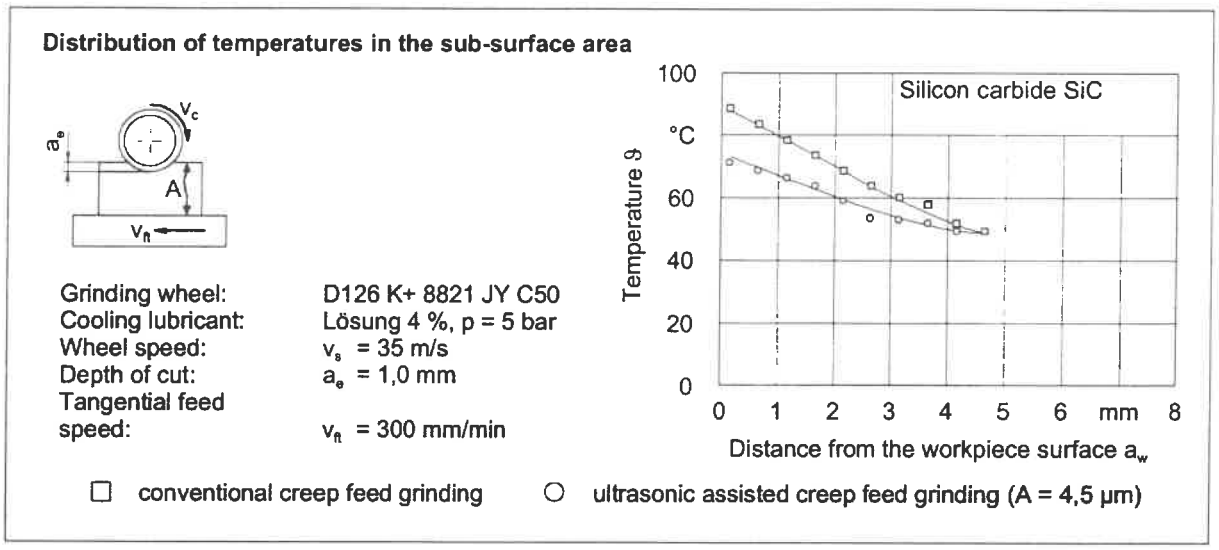

Figure 4: Distribution of temperatures in the sub-surface area of the workpiece during creep feed grinding of SiC with and without ultrasonic assistance

The bending strengths of ultrasonic assisted ground samples are lower than those measured during conventional grinding but higher than during lapping. It was also noted that greater compressive residual stresses in the sub-surface are a result of the ultrasonic assistance. During subjective observation of the surface structures with an SEM, slightly higher percentages of brittle fracture due to ultrasonics could be observed, which did not bring about a significant deterioration of the surface quality. For surface grinding with radial ultrasonic stimulation and cross-peripheral grinding with axial ultrasonic stimulation, critical sub-surface damages that hamper the application behavior can be excluded.

Conclusion

The superposition of grinding with an ultrasonic vibration causes a change of the process behavior. So far it had not been clarified to what extent the changes effect the process characteristics and the work result. Hence the influence of the superposition of the vibrations on the process forces and process temperatures as well as on the surface quality and the sub-surface characteristics were investigated. Distinctly reduced machining forces were measured. The thermal stresses decrease while the pulse-like alternating stress lead to higher mechanical load. The surface quality and the radial wear remain almost unchanged despite the significant changes of the surface formation and wear mechanisms. After the bending strength and residual stress investigations, critical sub-surface damages can be excluded.

References

[SpuH95] ***Spur, G.; Holl, S.-E.:*** Ultrasonic Assisted Grinding of Ceramics. International Conference on Precision Engineering '95, 2nd ICMT, 22.-24.11.1995, WCT Singapore.

[Uhl98] ***Uhlmann, E.:*** Surface Formation in Creep Feed Grinding Surface Formation in Creep Feed Grinding of Advanced Ceramics with and without Ultrasonic Assistance. Annals of the CIRP Vol. 47/1/1998, pp. 249 – 252.

[Zap98] ***Zapp, M.:*** Ultraschallunterstütztes Schleifen von Hochleistungskeramik – Ein Beitrag zur gezielten Beeinflussung der Eigenschaften von Bauteilen durch eine ganzheitliche Prozeßkettenbetrachtung. Dissertation Universität Kaiserslautern, 1998.

In-situ 3-D Observation of Active Grain Distribution on a Grinding Wheel and Introduction of Experimentally Evaluated Parameters to Grain Depth of Cut

Akira Kanai*, Fumio Inaba*, Atushi Tajima*, Masakazu Miyashita**
*Ashikaga Institute of Technology, 268 Omae, Ashikaga, Tochigi 326-8558, Japan
*Nanotec Associates, 1-13-5 Higashimotomachi, Kokubunji, Tokyo 185-0022, Japan

1. Introduction

Protrusion height distribution of active grains on a grinding wheel is one of the predominant parameters on grinding performance including surface roughness and surface integrity, because it dominates grain depth of cut. Especially for grinding of brittle materials, material removal mode in machining or ductile/brittle mode is decided by grain depth of cut. However there are few reports on protrusion height distribution of active grains, although there are many reports on only grain distribution not including the information on protrusion height. It is caused by two reasons. One is that the importance of protrusion height distribution had not been fully recognized until ductile mode grinding technology of brittle materials became a great target to be developed. Another is that the right measuring method of the distribution or an in-situ 3-D observation method of active grain distribution on a grinding machine has not existed. This paper describes the method of in-situ 3-D observation of active grain distribution and introduction of parameters derived from the observation to grain depth of cut.

2. Protrusion height distribution and grain depth of cut

Grain depth of cut was formulated geometrically by Malkin and others. The formula is as follows

$$d_g = 2a\frac{v_w}{v_s}\sqrt{\frac{d}{D_e}} \qquad (1)$$

d_g : grain depth of cut,
v_w : work-piece velocity, v_s : wheel velocity
D_e : equivalent wheel diameter d : wheel depth of cut
a : spacing between abrasive grains

This formula expresses the grain depth of cut done by the abrasive grain proceeded by a grain with the same protrusion height. This means that the formula is based on the imaginary grinding wheel with consecutive abrasive grains to be spaced in constant distance and same in protrusion height, and without both waviness on a wheel surface and run-out.

However, a real grinding wheel has waviness, run-out and protrusion height difference between a succeeding grain and a proceeding one. Considering these factors the formula is modified as follows.

$$d_g = 2a\frac{v_w}{v_s}\sqrt{\frac{d+w}{D_e}} + \delta \qquad (2)$$

w : run-out and/or wave amplitude of grinding wheel surface
δ : difference in protrusion height

This formula still gives only the grain depth of cut done by the succeeding abrasive grain of two adjoining grains. Furthermore, there is no criterion to give the value of spacing between active abrasive grains. To estimate the grain depth of cut generated by successive active abrasive grains on a periphery of a grinding wheel the protrusion height distribution of those successive active grains has to be taken into account. The peripheral envelope of the tops of successive active grains on a grinding wheel can be resolved into two components. One is the long component in wavelength to be equivalent to waviness. Another is the short one to be treated as the difference in protrusion height. The critical wavelength is six times the spacing between active abrasive grains[(1)]. The spacing is defined as a mean value of spacing between successive grains that exist in the specific random distribution of protrusion heights. The maximum grain depth of cut is estimated as follows. Here d_g, w and a are given the new definition, and Δh is newly defined.

$$d_g = 2a\frac{v_w}{v_s}\sqrt{\frac{d+w}{D_e}} + \Delta h \qquad (3)$$

d_g : maximum grain depth of cut,
w : maximum runout and/or wave amplitude of grinding wheel surface

a : mean value of spacing between successive cutting edges for Δh

Δh : protrusion height distribution of cutting grains

However, the spacing between the successive cutting grains, a, and the protrusion height distribution of grains, Δh, are to be evaluated experimentally. Since then, it is critically important how to observe the topography of abrasive grain tops.

3. In-situ 3-D observation of protrusion height distribution

For the estimation of the maximum grain depth of cut it is essential for observation of the topography of abrasive grain tops to be done on a grinding machine. If the observation is done outside the machine, the grinding wheel has to be trued and dressed after the wheel is mounted on the spindle again. The truing and dressing operations generate the entirely new distribution of protrusion height. This means that the observation system is required to be an 3-D observation system with high vertical and horizontal resolution and to function on a grinding machine. That system has two functions of both scanning a wheel surface on a grinding machine and detecting protrusion height of abrasive grains.

The possible constructions are listed in Table 1.

Table 1. Construction of in-situ 3-D observation system of protrusion height distribution

Functions	Methods
Detecting protrusion height	1. Stylus method 2. Non-contact method (optical probe)
Scanning a wheel surface	1. Scanning mechanism equipped for a observation system 2. Two axes positioning mechanism equipped for a grinding machine 3. Single axis driving mechanism equipped for a observation system plus single axis positioning mechanism equipped for a grinding machine

The in-situ 3-D observation system may be realized by coupling of these methods. A optical probe has advantage of no wear by probing a wheel surface, however disadvantage of low ability in probing a steep surface. Utilizing the positioning mechanism of a grinding machine for scanning is the best way to get the true topography of a grinding wheel surface, because protrusion height is observed from the reference of workpiece surface to be ground. However, it is worst in taking long time to scan. A scanning mechanism equipped for the observation system may be possible to be fast to scan because of small mass to be driven.

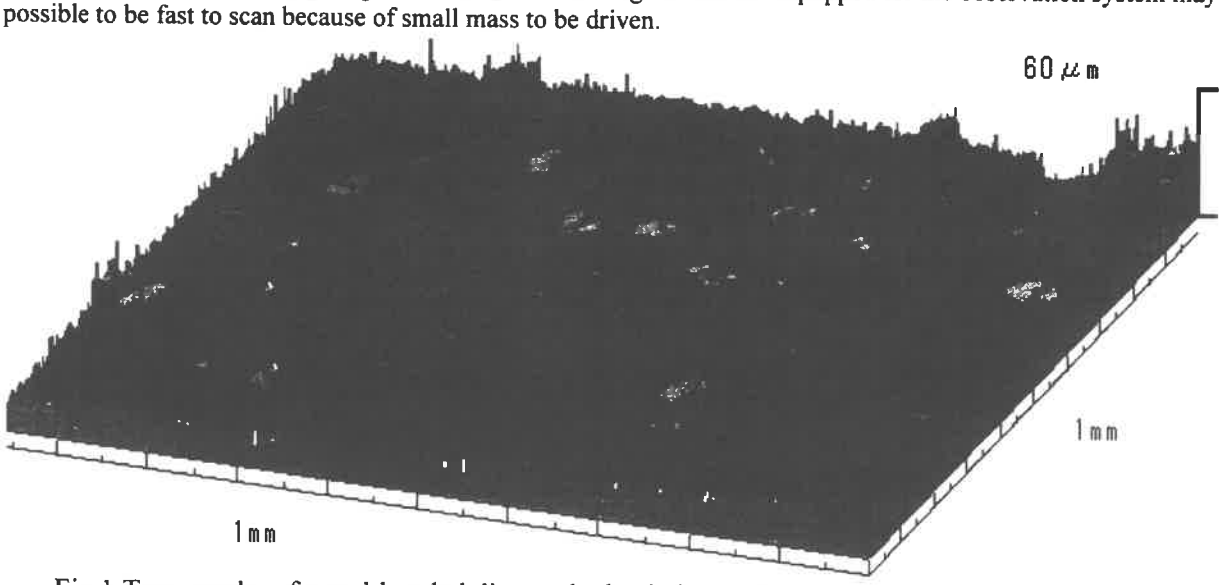

Fig.1 Topography of metal-bonded diamond wheel observed by optical system (grain size: #230)

In the present paper two combinations are tested. The first one was composed of an optical probe and 2-axes NC positioning system of a grinding machine with hydrostatic guideways. The optical probe has a beam of 2 μm in diameter, resolution of 0.1 μm and ability to probe surfaces inclined at less than 30 degree. The second one was the system equipped with a scanning mechanism. A 3-D surface profiler with a diamond stylus was utilized for 3-D

observation of protrusion height distribution of active grains on a grinding wheel. The surface profiler which has been recently developed is compact enough to be set on the workpiece table of a grinding machine. It has a stylus of 5 μm in radius, resolution of 6 nm and scanning area of 1 mm by 1 mm.

Figure 1 is an example of the topography observed by the optical system. The target wheel is a metal-bonded diamond wheel with grain size of #230 and concentration of 100. The observed area is 1 mm by 1 mm. The optical system generated incorrect data of steep surfaces at the edge of abrasive grains. This caused low vertical resolution. This defect may be able to be improved by any kind of filtering process.

Figure 2 is topography observed by the 3-D surface profiler. The target wheel is same as the optical system. The wheel surface in 1 mm by 1 mm was scanned in horizontal resolution of 2 μm for about 5 minutes. The topography of the grinding wheel is clearly captured. Both size and protrusion height of individual grains and spacing between them can be recognized clearly enough to study machning mechanism.

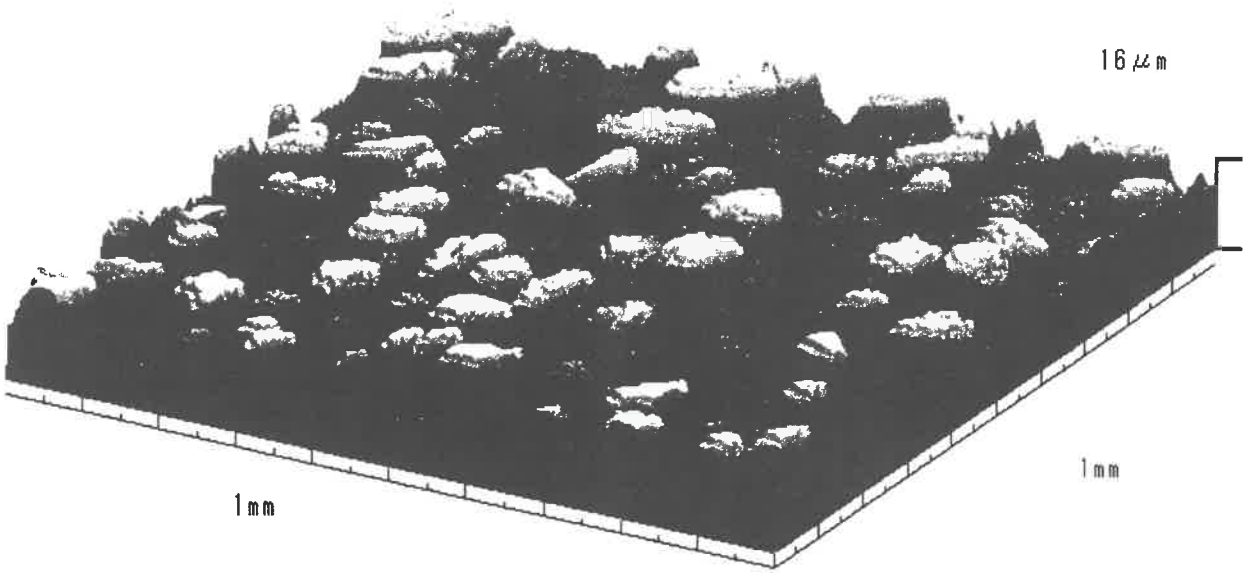

Fig.2 Topography of metal-bonded diamond wheel observed by 3-D surface profiler (grain size: #230)

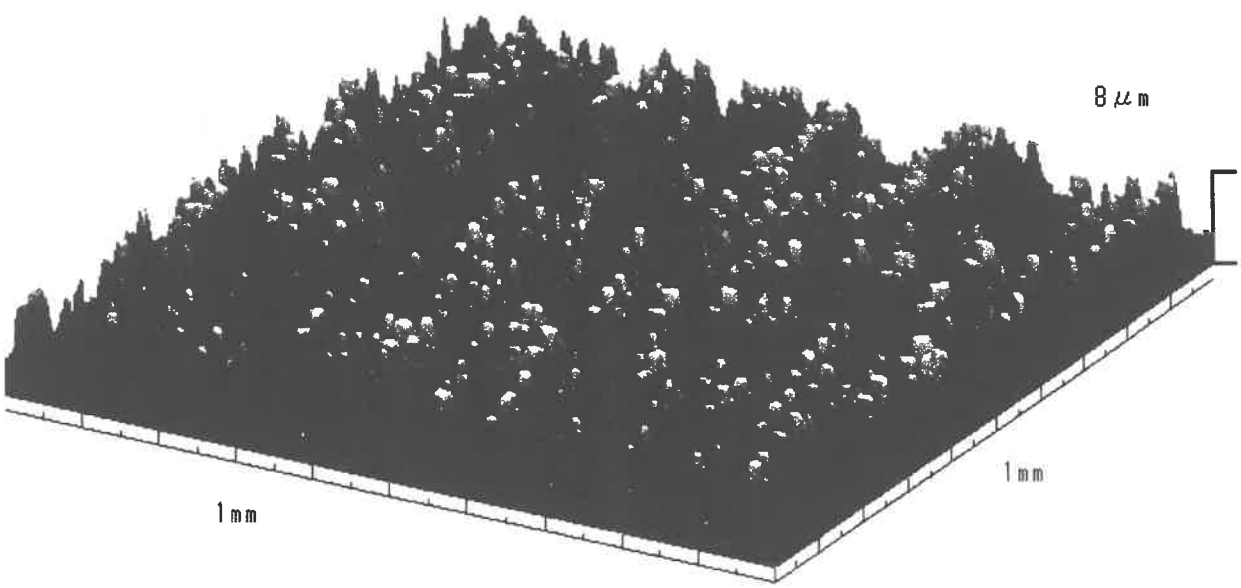

Fig.3 Topography of metal-bonded diamond wheel observed by 3-D surface profiler (grain size: #800)

4. Introduction of experimentally evaluated parameters to grain depth of cut

As mentioned above estimation of grain depth of cut requires introduction of experimentally evaluated parameters. These are a random distribution value of grain protrusion height and spacing between active grains derived from the distribution value. The topography data by in-situ 3-D observation can be analyzed to get those parameters.

Fig.3 is topography of a metal-bonded diamond wheel with grain size of #800 and concentration of 75. This was measured by the 3-D surface profiler. Individual grains of mean grain size of 20 μm in diameter can be recognized distinctly. For estimation of grain depth of cut the protrusion height of abrasive grains has to be evaluated from the highest top of grains, this means the closest cutting edge to a workpiece surface. Fig.4 shows the sliced surfaces of the topography shown in Fig.3 at a particular position downward from the highest top in the observed area. The slice level in Fig. 4 is 0.2 and 0.5 μm from the highest top. This kind of figure can be used to count the number of abrasive grains within the range from the highest top to the slice level, which corresponds to the random distribution of protrusion height of Δh. Fig.5 shows the number of active grains corresponding to Δh and from those number the spacing between active grains is derived. Fig.6 is a graph of the relationship between random distribution of protrusion height and spacing between grains. The spacing of six times the observed length is about 0.16 mm and Δh for this value of spacing is about 0.2 μm. Introducing these value, Δh of 0.2 μm and a of 0.16 mm to Equation 3 grain depth of cut in this case can be estimated to be about 0.2 μm.

Reference: (1) Kanai, A., Miyashita, M., Sato, M., Daito M., Proposal of High Productivity in Ductile Mode Grinding of Brittle Materials, Proc. of 1995 ASPE Annual Meeting

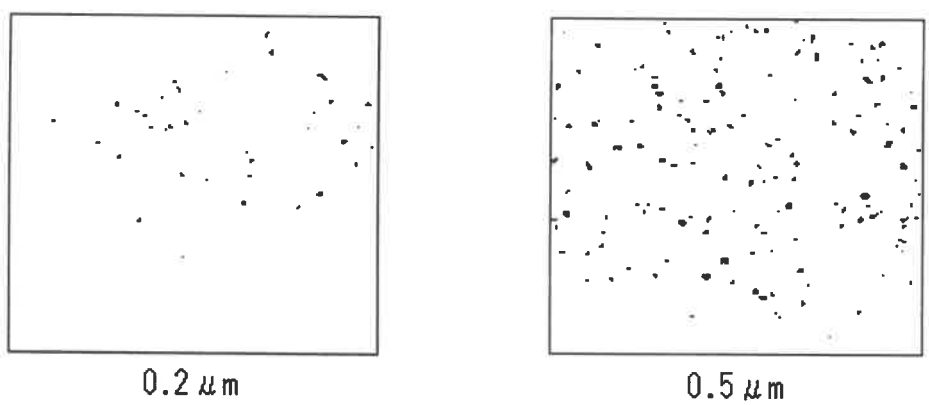

Fig.4 Grain distribution for slice level of 0.2 and 0.5 μm

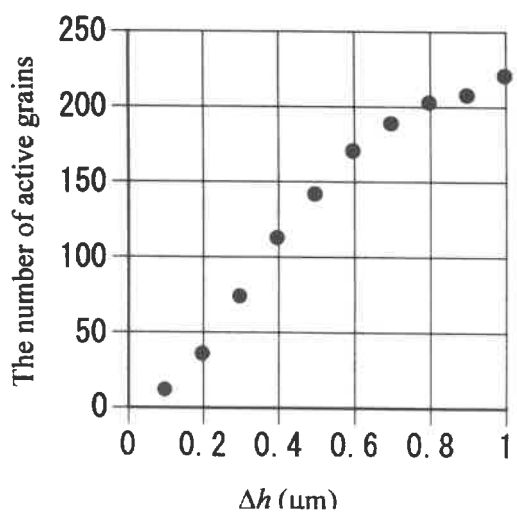

Fig.5 The number of active grain

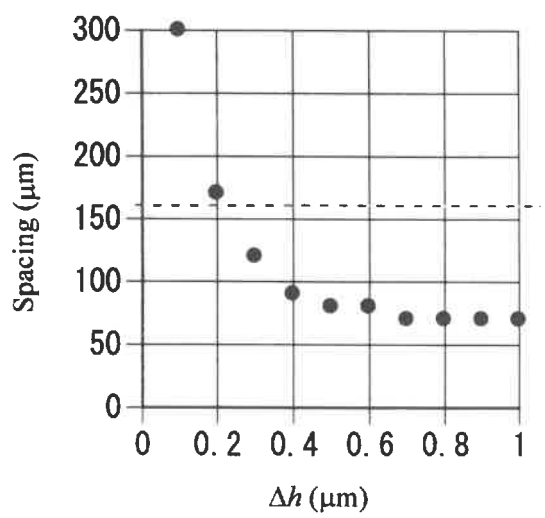

Fig.6 Spacing between active grains

Study on Vibration OD-Blade Slicing with Air-Mist Working Fluid for Environment

— Effect of Applied Vibration Amplitude on Slicing Characteristics —

Ken-ichi ISHIKAWA, Hitoshi SUWABE and Michio UNEDA
Kanazawa Institute of Technology
7-1 Ohgigaoka Nonoichi-machi Ishikawa 921-8501, Japan

1. Introduction

In recent years, development of the newly processing method that can improve the working and global environment has been demanded. The abrasive precision processing has been changing from the free abrasive slurry to the fixed abrasive grains. Furthermore, a few attempts to decrease the waste working fluid such as the cooling air grinding [1] have been reported.

According to this background, the authors tried to develop the newly OD-Blade slicing machining with air-mist working fluid and vibration as shown in **Figure 1**. The air-mist working fluid is mixed a minute quantity of the working fluid with the compressed air, and supplied to the machining point at high speed. The previous paper [2] addressed the high efficiency of OD-Blade slicing and to reduce a quantity of the working fluid. Concretely, this slicing method is one of the creep feed slicing such as the larger slicing depth. Therefore, it is difficult to supply the working fluid because of increasing of the contact-arc length as larger cutting depth. This method was made the experiments at the vibration conditions (in this case vertical detection) of the frequency of 20 Hz and the amplitude from 15μm to 45μm. This paper describes the effect of vibration amplitude, the wear characteristics of OD-Blade and the behavior of wafer accuracy under a series of experimental conditions as shown in **Table 1**.

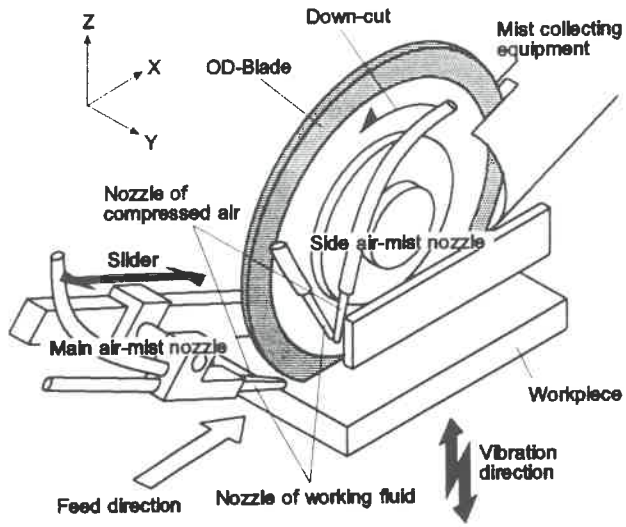

Fig.1 Model of the air-mist working fluid OD-Blade slicing with vibration

Table 1 Experimental conditions

OD-Blade, Diameter	D	ϕ125
Width of grain parts	T_g	1mm
Bond and grain		Metal-bond, SD#200
Blade peripheral speed	V_b	1963m/min
Slicing mode		Down-cut
Cutting depth	c	11.0mm
Feed rate	$\dot{X}$	40mm/min
Frequency	f	20Hz
Amplitude	a	15, 30, 45μm
Workpiece and size		Soda glass, 50 × 60 × 10mm
Working fluid		Water soluble coolant (50:1)
Flow of conventional nozzle	Q	3810g/min
Main air-mist nozzle		
Flow of working fluid	Q_m	20g/min
Pressure of compressed air	P_m	0.10MPa
Side air-mist nozzle		
Flow of working fluid	Q_s	10g/min
Pressure of compressed air	P_s	0.10MPa

2. Effect of vibration amplitude

Figure 2 shows behavior of the spindle motor current for 150 times slicing. The change of this motor current

shows a same tendency to the slicing load. Therefore, authors treated the spindle motor current instead of the slicing load. In case of this experiment, the total grinding amount is about 99,000mm^3 (1 time of slicing is about 660mm^3). In the non-vibration slicing with air-mist working fluid, not only the spindle motor current increases with increasing of the slicing number, but also a spark is sometimes occurred at the working point as the reason of less working fluid. The spindle current in vibration slicing, however, shows decrease and less variation rate than the current in non-vibration slicing, and shows almost no increasing under the conditions of the vibration amplitude: a = 30μm and 45μm.

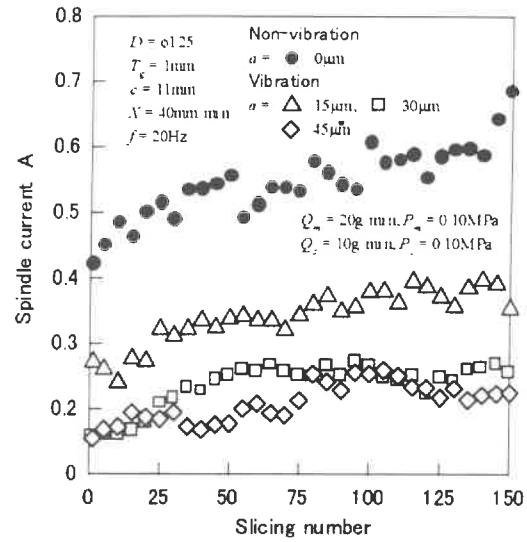

Fig.2 Behavior of spindle current for 150 times slicing

This decreasing and no increasing of the slicing force are occurred by an in/out flow effect of the working fluid that facilitates the inflow of the working fluid and the removing of the cutting debris. The photo observation of cutting area by a high speed camera is shown in **Figure 3**. This observation used the mechanical vibrator (vibration amplitude: a = 370μm)[3]. The results suggest that the in/outflow of the working fluid in vibration slicing is brought out during the separate time between OD-Blade and the workpiece in one vibration cycle. Therefore, the large amount of cutting debris are removed by vibration, thus slicing characteristics are improved. Furthermore, when the vibration is applied to the workpiece, it is clear that the effect becomes higher if the applied amplitude becomes large. The vibration effects for large amplitude show excellent slicing characteristics compared with the small amplitude.

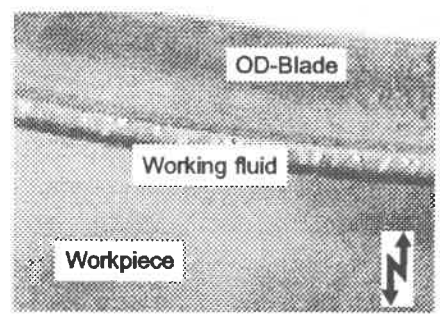

Fig.3 In/outflow effect of working fluid in vibration slicing observed by means of high speed camera

Figure 4 shows the scanning electron microscopy (SEM) micrographs of the diamond grains on the outer surface of OD-Blade after 150 times slicing. In the non-vibration slicing, the diamond grains have had the phenomenon of the glazing by attrition wear and the loading by the cutting debris. In the vibration slicing, a little glazing and loading are observed for the amplitude of 15μm. As shown in Figure 4-(c), less glazing and loading of the grains are observed for the amplitude of 30μm. Therefore, the spindle motor current in Figure 2 are able to maintain the constant value.

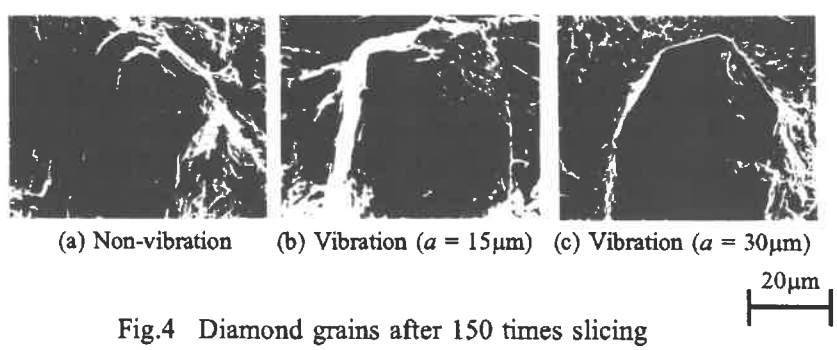

(a) Non-vibration (b) Vibration (a = 15μm) (c) Vibration (a = 30μm)

Fig.4 Diamond grains after 150 times slicing

Figure 5 shows the photo micrograph of grinding steak at the bottom surface after 150 times slicing. In case of the after dressing (as shown in Figure 5-(a)), the grinding steak is very clear along the grinding direction. In the non-vibration slicing, the grains have the glazing and the loading, thus the vividness is worsen compared with after dressing in Fig.5-(a). The vibration slicing has brought the in/outflow effect of working fluid and no

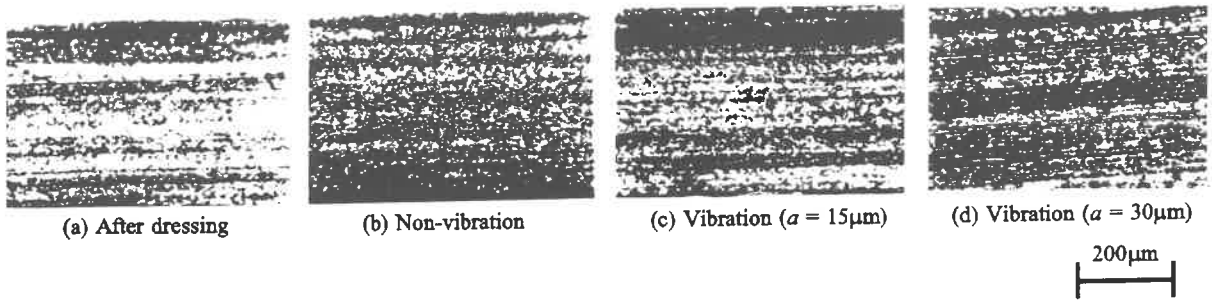

Fig.5 Grinding steaks after 150 times slicing

glazing of the grains, therefore, the grinding steak is clear even if 150 times slicing is finished. Furthermore, **Figure 6** shows the SEM micrographs of the bottom surface. In case of the non-vibration slicing, large melting parts are observed everywhere in bottom surface, because the working point has become a high temperature. As shown in Figure 6-(c), (d), the vibration slicing maintains clearly surface like after dressing.

Therefore, the vibration slicing with the air-mist working fluid is one of the excellent cutting system to realize the high slicing performance (in this case the slicing force and the longer life of the diamond grains). In other words, if the air-mist working fluid is used for environment, it is necessary to apply vibration to the workpiece.

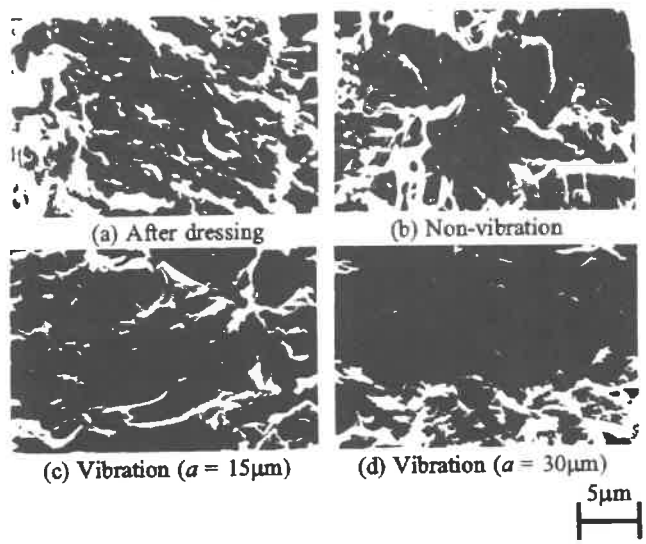

Fig.6 Bottom surfaces after 150 times slicing

3. Wear characteristics of OD-Blade

Figure 7 shows the behavior of the grinding ratio. The grinding ratio is the ratio of the grinding volume (mm^3) of the workpiece to the wear volume (mm^3) of OD-Blade. The blade size for two directions (in this case blade thick and blade diameter) are measured by a micrometer, and the wear volume of the blade is calculated. The grinding ratio in the vibration slicing with air-mist working fluid increases with increasing of the amplitude. This is the reason by the in/outflow effect of working fluid in one cycle of the vibration. Thus, the vibration slicing can restrain the wear of OD-Blade from the grinding temperature. Therefore, the vibration slicing decreases compared with the non-vibration slicing about the wear rate of grain parts when supplying an air-mist working fluid.

However, when the grinding ratios in case of the conventional working fluid and air-mist working fluid are compared, the grinding ratio with air-mist working fluid

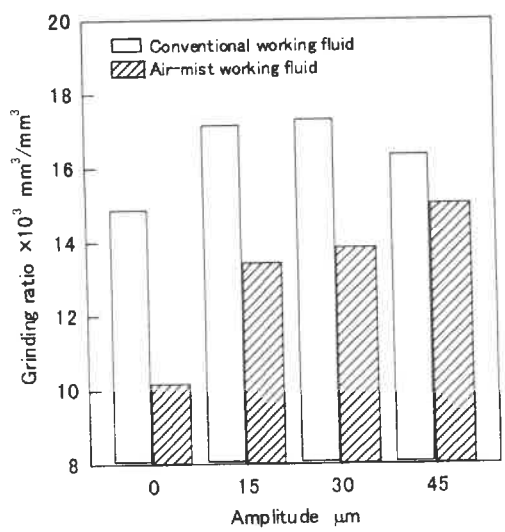

Fig.7 Relationship between grinding ratio and vibration amplitude

becomes less than the conventional method. Therefore, it is clear that the grinding ratio is not needed to make a problem by selecting the appropriate vibration conditions.

4. Slicing accuracy

Figure 8 shows wafer cross sectional wave form. In non-vibration slicing with the air-mist working fluid, the wafer waviness is worsen compared with the supplied conventional working fluid because of being unable to facilitate the inflow of the working fluid and the removing of cutting debris. However, the waviness of the vibration slicing is considerably improved compared with the non-vibration data.

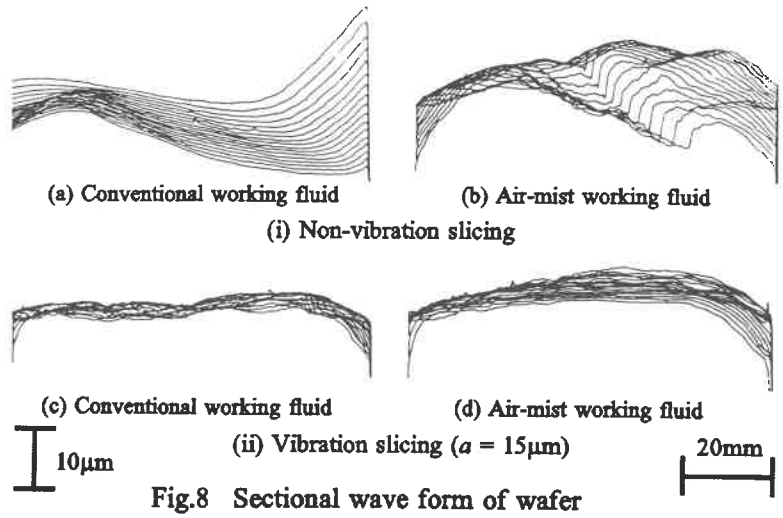

Fig.8 Sectional wave form of wafer

6. Conclusions

The vibration OD-Blade slicing with air-mist working fluid was investigated on the slicing characteristics. The following points have been noted:

1. Not only the slicing force is decreased by applied vibration, but also this decrease rate of slicing force is more effective when the large amplitude acts.
2. The vibration slicing can be continuously done over a long period with no dressing, even though an air-mist working fluid is supplied.
3. Wafer waviness for the slicing accuracy with an air-mist working fluid is worsen to be unable to facilitate the inflow of the working fluid and the removing of cutting debris in the non-vibration slicing case, however, the vibration slicing has brought the high accuracy regardless of the supply method of the working fluid.

Acknowledgments

The authors would like to express their sincere thanks to Osaka Diamond Ind. Co. Ltd. who provided us with many OD-Blade needed to carry out these experiments.

References

[1]Hiroyuki HONMA, Kazuhiko YOKOGAWA and Munehiko YOKOGAWA : Study on Environment Conscious CBN Cooling Air Grinding Technology, Journal of JSPE, 62, 11 (1996) 1638. (in Japanese)

[2]Ken-ichi ISHIKAWA, Hitoshi SUWABE and Michio UNEDA : Vibration Cutting Method of OD-Blade With Atomized Working Fluid, Proceedings of ASPE, (1998) 80.

[3]Ken-ichi ISHIKAWA, Hitoshi SUWABE and Michio UNEDA : Development of Vibration Cutting using OD-Blade, Proceedings of ASPE, (1996) 572.

Wear and Self-Dressing of Resin Bound Grinding Wheels

Michele H. Miller and Thrinath S. Kakumanu
Michigan Technological University, Houghton, MI

Introduction

The multiple cutters of a grinding wheel give grinding several advantages over single point cutting, especially for machining brittle work materials. While a single point tool will dull and require re-sharpening, a grinding wheel distributes wear over many cutters and is capable of replenishing itself. The grinding wheel strongly influences the process, and proper grinding wheel selection is critical to grinding performance [1-4].

For the fracture free grinding of brittle materials, resin bound diamond wheels tend to perform better than metal bound diamond wheels. Their greater compliance puts more grits in contact with the workpiece thus reducing chip size. In addition, their lower hardness causes faster wear thus maintaining a sharper wheel condition. Tang et al. observed two dominant wear mechanisms for resin bound wheels: grit pullout for blocky diamonds and grit fracture for friable diamonds [5].

The cutting process causes sharp abrasive grit edges to wear. As a cutting edge wears, the cutting force acting on the grit increases. When it becomes sufficiently high, the grit fractures or pulls out of the binder matrix. The self-dressing process, or the replenishment of sharp cutting edges, is a beneficial effect of wheel wear. Eventually the total force levels off as the wheel reaches an equilibrium condition. At this point the increase in grit forces is balanced by the reduction in force caused by a grit fracture or pullout. The grinding force and wheel wear rate associated with this equilibrium is critical to achieving high quality ground surfaces. There are two extremes. A wheel may wear so quickly that it does not efficiently remove work material. Or the wheel may become so dull that it can no longer remove work material. In between the two extremes is an optimum condition.

The self-dressing process depends on the wear rate of individual abrasives, on the threshold force for grit fracture or pullout, and the relationship between grinding force and grit shape. The purpose of this research is to develop a computer simulation that describes the self-dressing process and that can ultimately be used to aid in the selection of wheel parameters.

Computer Simulation

To improve our understanding of the wear and self-dressing processes, we developed a computer model that simulates the wear of the grinding wheel in plunge grinding. Figure 1 is a flow chart of the simulation algorithm. The program assumes that the grinding wheel consists of pyramidal shaped grits of uniform size. The wheel plunges into a workpiece that is represented by a two dimensional grid in the X-Z plane. During each grinding wheel revolution, the algorithm identifies the cutting grits as those whose path interferes with the workpiece surface grid. It calculates the chip area A_{chip} in the X-Z plane for each grit. It adjusts the Z values of affected grid points to reflect the position of the new work surface. It then calculates the cutting and thrust forces for each grit using the following equations:

$$F_{g,c} = pA_{chip} + \mu pA_{land}$$

$$F_{g,t} = pA_{land}$$

where p is the pressure exerted by the work material, μ is the friction coefficient, and A_{land} is the area of the grit's wear land. We set p equal to the material yield strength (estimated as hardness divided by three). The simulation also attempts to include the effect of chip loading. According to Younis et al., the force due to chip loading is proportional to the loading area [6]. The loading area should increase more slowly than the loading volume. As an approximation, we assumed the loading area to increase with the square root of the volume of work material removed by each grit. At the end of each revolution, the algorithm calculates the total tangential machining force as the sum of the chip formation grit forces (the $F_{g,c}$'s) and the chip load forces. (This total force is then multiplied by 12.5/289 because the workpieces used in the experiments were 12.5 mm long, and the wheel circumference was 289 mm.)

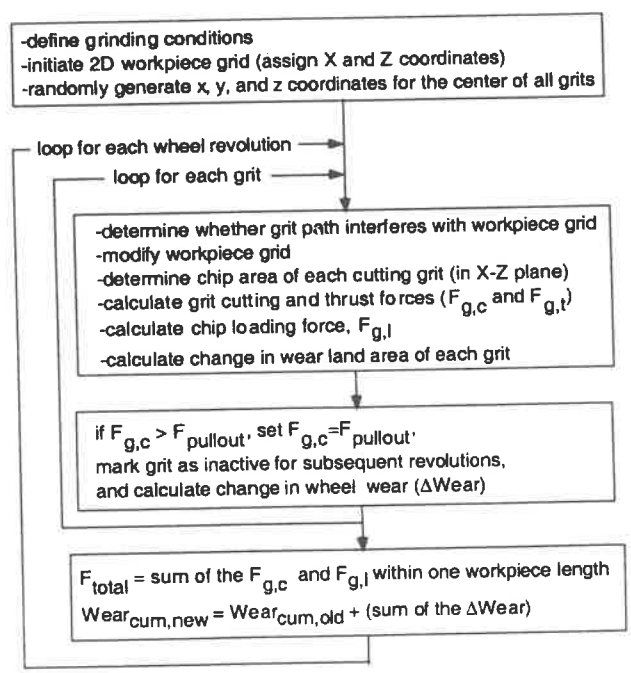

Figure 1: Flow chart of simulation algorithm

The wear land area for all the grits was initialized to a small non-zero value. The volume of wear of individual abrasive grains was assumed to be proportional to the thrust force multiplied by the sliding distance. The A_{land} for each grit then grows every time it cuts until the cutting force is sufficient to remove the grit from the binder (and from consideration in the program). This algorithm does not account for grit fracture. It assumes that grit pullout is the only mechanism for removing a dull cutting edge. The threshold force $F_{pullout}$ for pulling the grit out was a user input. As a starting point we estimated this force by multiplying half of a grit's surface area by the yield strength of a typical phenolic resin. A grit size of 6 μm and yield strength of 50 MPa, yields a force of about 0.002 N.

A series of simulations were performed to study the effect of infeed, work material, and binder strength on the cutting force and wheel wear. Table 1 outlines the conditions common to all the simulation trials. The pyramid angle of 30 degrees means that the cutting grits are assumed to have negative rake angles of –60 degrees.

Table 1: Simulation conditions

Grit pyramid angle	30 degrees
Range of initial wear land lengths	0.1 to 0.6 μm
Friction coefficient μ	0.2

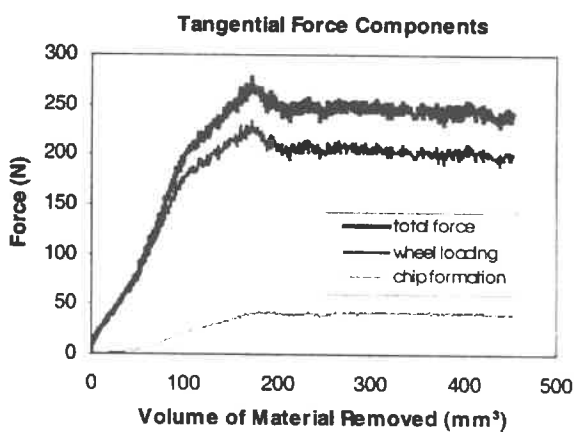

Figure 2: Force components for infeed = 40 nm, work yield strength = 4.7 GPa, and pullout force = 0.002 N

Figure 2 shows the output of one of the computer simulations. It shows the total tangential force as well as the chip formation and wheel loading force components (that add up to the total tangential force). It has been normalized to match the experimental result for this set of grinding conditions (see the 40 nm infeed curve in Figure 6). The wear rate of the diamond abrasives was selected to make the horizontal scale similar to that in the experiments. The workpiece strength of 4.7 GPa was chosen to approximate the strength of silicon carbide. The figure indicates that the equilibrium chip formation force is slightly less than 50 N. This is significantly less than the equilibrium force obtained in the experiments at these conditions. The proportionality constant relating work material removed to chip loading force was then selected to obtain a total force similar to the experimental result. The result in Figure 2 represents a baseline against which the other simulation results are compared.

Figure 3 shows the simulation prediction for wheel wear for the same conditions. This could also have been plotted in terms of change in wheel volume rather than thickness. Grits start to fall out after about 170 mm^3 of material removal. The wear rate indicated in the figure corresponds to a grinding ratio of 249.

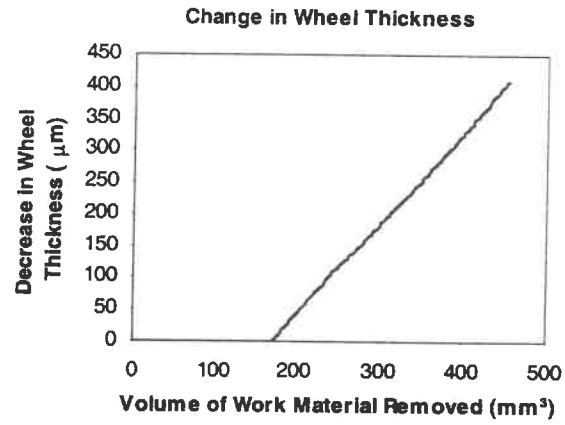

Figure 3: Simulated wheel wear

Experimental Setup

We conducted a series of experiments in which infeed, work material, and wheel composition were varied. The purpose was to measure the cutting force and determine the equilibrium force level and amount of time to reach equilibrium. Figure 4 shows the experimental setup. A cup wheel was mounted on an air bearing spindle. The workpiece was mounted to a 3-axis force transducer that in turn attached to a piezoelectric actuator. The actuator provided a fine infeed that plunged the workpiece into the grinding wheel.

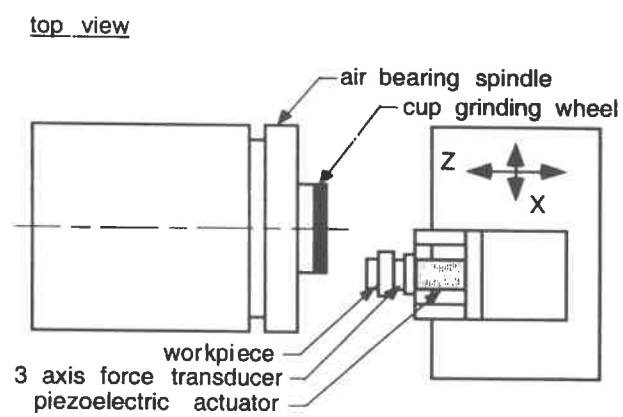

Figure 4: Schematic of experimental setup

Experiments were conducted with the conditions shown in Table 2. A fine diamond abrasive was chosen so that fracture

free grinding of silicon carbide and glass could be achieved. We characterized the hardness of the resin binders by performing micro-hardness tests using a 50 gram load. Despite the light load and attempts to indent in between abrasive grains, these hardness values are likely influenced by the presence of the diamond grains. The equipment we used to perform plunge grinding was limited to low cutting speeds. We conducted tests under five different combinations of infeed, work material, and wheel composition. Each test was performed twice to assure repeatability. (The results were quite repeatable. The results in the following section are an average of the two tests.)

Table 2: Conditions for plunge grinding experiments

Grinding wheel type	100 mm dia., 9.5 mm wide cup wheel with resin bond and diamond abrasive
Abrasive size	3000 mesh (6 μm avg. size)
Abr. vol. fraction	0.25
Wheel hardness	690 MPa (wheel 1) 630 MPa (wheel 2)
Coolant	Tap water
Workpiece materials	Reaction bonded silicon carbide (H=14 GPa) Pyrex glass (H=5 GPa)
Infeeds	10, 20, 40 nm/rev
Cutting speed	2.6 m/s

Before beginning a new experiment, the grinding wheel was dressed by plunging it into a glass workpiece coated with 3 μm diamond paste. During each plunge grinding experiment, the tangential force (y direction) was monitored. Because the actuator range was limited to 20 μm, one wear experiment consisted of multiple plunges (passes). After each 20 μm plunge, the actuator retracted, and we manually indexed the Z slide position toward the workpiece. Due to the long experiment time, forces were not collected continuously. Additionally, the force was periodic and synchronous with the wheel revolution. This was due to imperfect truing of the wheel and spindle error. To reduce the volume of data collected and to account for the periodic variation in force, we recorded the maximum force in a wheel revolution five times during each pass and then averaged the five readings. We ended each test shortly after the force leveled off, indicating an equilibrium.

Comparison of Results from Simulation and Experiment

Figures 5 and 6 show results from simulation and experiment, respectively, for three different infeeds. As expected, the equilibrium force increases with infeed in both the simulation and experiment. In the simulation, more work material must be removed before reaching equilibrium for a low infeed; the experimental results follow the opposite trend.

Figures 7 and 8 show simulation and experimental results, respectively, for two different workpiece materials: silicon carbide and Pyrex glass. Surprisingly, the simulation predicts that the weaker material achieves a higher equilibrium force and takes longer to reach it. In the simulation the weaker work material allows the grits to wear more before they pull out. As grits wear, more grits come into contact with the workpiece and contribute to the total force. The experimental results in Figure 8 follow the opposite trend. One of the reasons for the disparity between simulation and experiment may be a difference in chip accumulation for these two materials. We observed that the grinding wheel accumulated silicon carbide debris faster than glass debris. The simulation assumes the same rate of chip accumulation and the same rubbing force for both work materials.

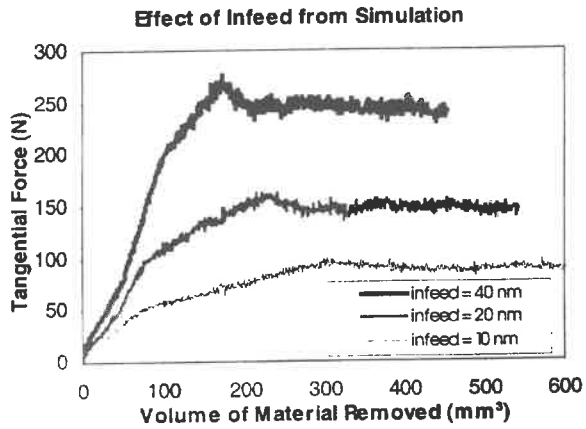

Figure 5: Effect of infeed on tangential force for work yield strength = 4.7 GPa and pullout force = 0.002 N

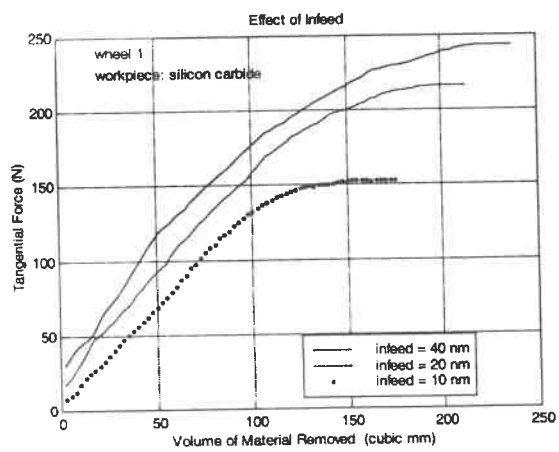

Figure 6: Effect of infeed on force (experimental data)

Figure 9 shows simulation results for three different abrasive pullout forces. (The pullout force depends on binder material, grit size, grit shape, etc.) As expected, the equilibrium force increases with pullout force. Experiments were conducted on silicon carbide with two wheels of different hardness. However, the results were not significantly different, and no meaningful conclusions could be drawn.

Grinding ratios (the volume of work material removed divided by the volume of wheel wear) were determined for the simulations. For the simulations in Figure 5, the grinding ratios ranged from 249 at 40 nm infeed to 539 at the 10 nm

infeed. Both in terms of lower wear and lower equilibrium force, the simulation indicates that the lower infeed rate is preferable. For the simulations in Figure 7, the grinding ratios were 249 for the SiC and 620 for the glass. For the simulations in Figure 9, the grinding ratios range from 249 for the highest pullout force down to 143 for the lowest pullout force. This means that the 0.0005 N pullout force wheel wears nearly twice as fast (249/143) as the 0.002 N wheel. In exchange for the faster wear, the equilibrium force for the 0.0005 N wheel is about 40% of that for the 0.002 N wheel.

Wear (and grinding ratios) were not measured experimentally, and the simulation values for grinding ratio seem rather high. Wear measurements would be helpful in estimating abrasive pullout force.

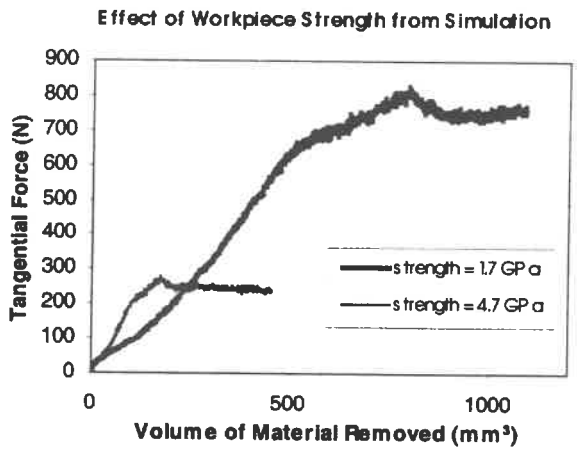

Figure 7: Effect of workpiece strength on tangential force for infeed = 40 nm and pullout force = 0.002 N

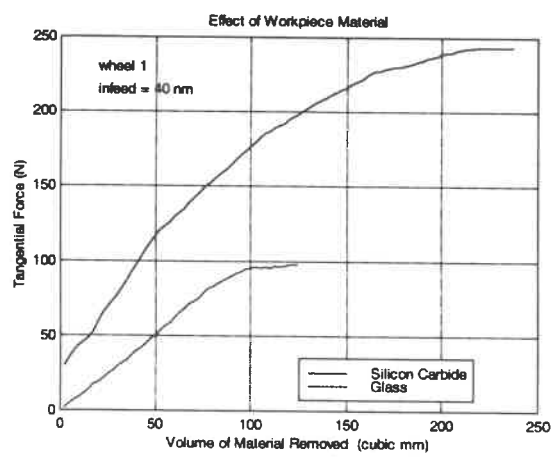

Figure 8: Effect of workpiece material on force evolution (experimental data)

Conclusions

The computer model described here adopted simple relationships for calculating grinding force based on chip area, wear land area, and wheel loading. It successfully replicated the force evolution that occurs during self-dressing: the tangential forces were low immediately after dressing and increased until reaching a steady-state condition. Infeed and work material had significant effects on the steady-state force level in both simulation and experiment. However, the simulation inadequately models the effect of workpiece material. Future work will attempt to improve the treatment of chip loading, as well as incorporate the effects of grit size and grit fracture. The ultimate goal is to use a simulation model to match wheel to workpiece and infeed. The proper choice of wheel parameters would produce a self-dressing condition at an equilibrium force level that corresponds to desired work surface quality.

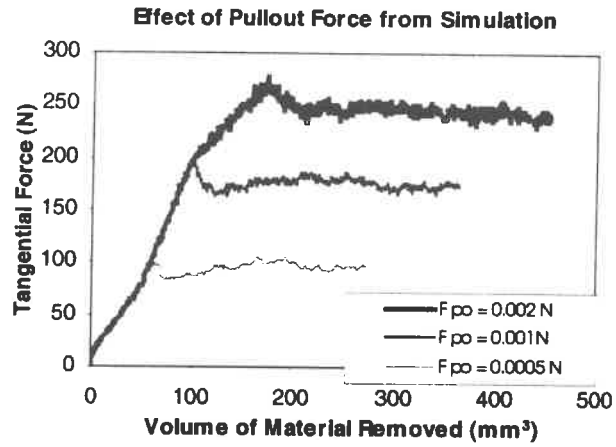

Figure 9: Effect of abrasive pullout force on tangential force for infeed = 40 nm and work yield strength = 4.7GPa

Acknowledgments

This research was supported in part by a Society of Manufacturing Engineers Research Initiation Award.

References

[1] Taylor, J. S., M. A. Piscotty, K. L. Blaedel and F. A. Gray, 1996, "Working with the Superabrasives Industry to Optimize Tooling for Grinding Brittle Materials," *Proc. of ASPE Spring Topical Meeting*, Annapolis, MD, Vol. 13, pp. 95-102.

[2] Subramanian, K. and R. P. Lindsay, 1992, "A Systems Approach for the Use of Vitrified Bonded Superabrasive Wheels for Precision Production Grinding," *J. of Eng. for Ind.*, Vol. 114, pp. 41-52.

[3] Ratterman, E. and R. Cassidy, 1992, "Abrasives," *Engineered Materials Handbook, Vol. 4: Ceramics and Glasses*, ASM International, pp. 329-335.

[4] Zhou, Y., M. Atwood, D. Golini, M. Smith, P. D. Funkenbusch, 1998, "Wear and self-sharpening of vitrified bond diamond wheels during sapphire grinding," *Wear*, Vol. 219, pp. 42-45.

[5] Tang, J., K. Syoji and D. Dornfeld, 1996, "Diamond Wheel Wear Sensing with Acoustic Emission," *Proc. of the ASPE Spring Topical Meeting*, Vol. 13, pp. 109-114.

[6] Younis, M., M. M. Sadek and T. El-Wardani, 1987, "A New Approach to Development of a Grinding Force Model," *Trans. of the ASME*, Vol. 109, pp. 306-313.

Fixed Abrasive Vertical Spindle™ process to generate mirror finishes on a variety of advanced ceramic components

Thomas Puthanangady and Marc Tricard
Norton Company, Worcester, MA

Introduction:
Some of the recent trends in the semiconductor industry have included decreasing size of device circuitry (smaller line widths), increasing device size and wafer diameter, while the storage industry on the other hand has seen increasing storage density, wafer size and decreasing device size. Such trends have meant tighter flatness requirements, finer surface finishes and better surface integrity. Traditional loose abrasive processes for ceramics have followed a familiar trend seen in Figure 1. As the quality of surface roughness improves there is an associated drop in productivity.

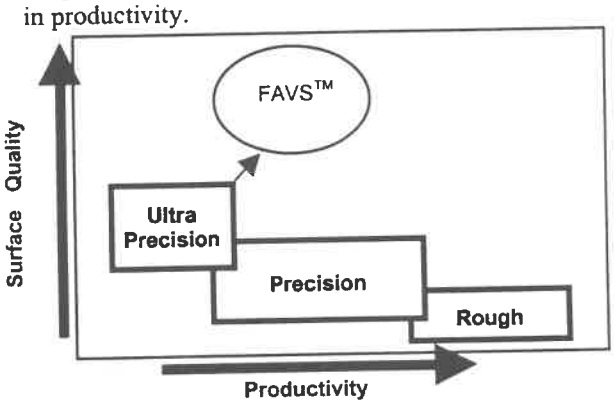

Figure 1. Objective of FAVS™

The FAVS™ approach however results in processes where high level of surface quality (mirror finishes) can be obtained without a loss of throughput.

Grinding Machine Features:
The FAVS™ process consists of a platform supporting two pairs of high precision air bearing grinding wheel and work chuck spindles. Grinding machines combine the benefits of ultra fine control on the infeed rate along with fine diamond abrasives to produce mirror finishes with minimal sub- surface damage.

FAVS™ Kinematics:
The most common configuration of the FAVS™ concept is shown in Figure 2. The middle of the

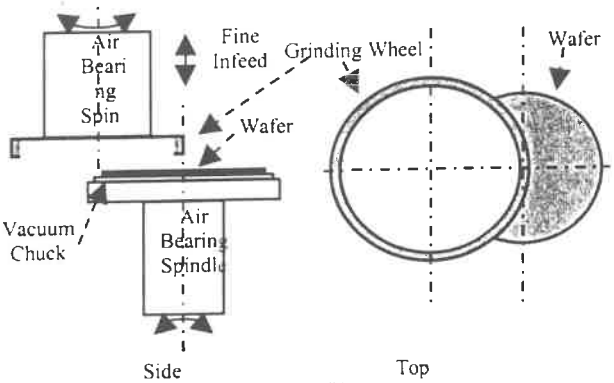

Figure 2. Schematic of FAVS™ process

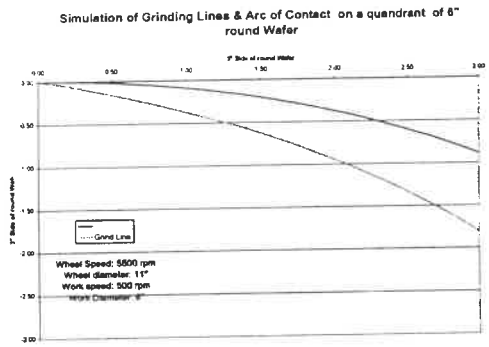

Figures 3-A&B: The simulated cutting path of a an idealized abrasive grain on the surface of a 6" wafer, shown above on a 3" quadrant at 5500 and 1100 rpm respectively.

grinding wheel abrasive rim typically grinds on the centerline of the work piece. The contact area between the wheel and the workpiece is defined by grinding wheel rim thickness, size of the part and the angles between the axis of the chuck and grinding wheel spindles. If the axes of rotation of the wheel and the part are parallel then the wheel makes contact on the part at both the entry and the exit of the grind.

The maximum cutting depth (undeformed chip thickness) taken by a single abrasive grain is shown here as 'h' [Reichenbach, G. S., et al]. The expression shown below was derived for straight surface grinding and is used here as an approximation. The parameter 'h' is useful in predicting the depth of cut taken by a single abrasive grain while travelling along a path shown above in Figure 3A&B. Using continuity analysis i.e. making a material balance between

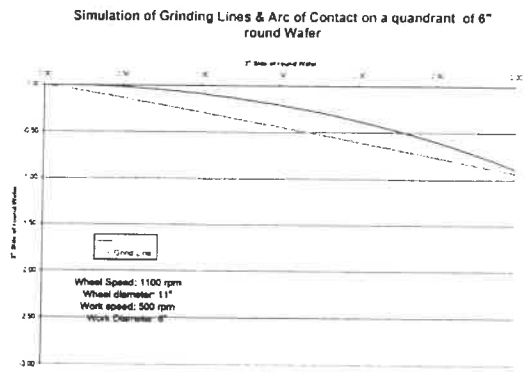

volume of chips produced at all the cutting points and bulk material removal, the following expression can be approximated for 'h'.

$$h \approx \sqrt{\left(\frac{V_w}{V_s}\right) \times \left(\frac{d}{D_e}\right)^{\frac{1}{2}} \times \left(\frac{1}{kC_g}\right)}$$

The C_g term denotes the number of grains in the grinding zone per unit area, while the 'k' term denotes geometry factors of the abrasive grain itself. The number of grains in the grinding zone per unit area increases exponentially with decrease in grain size. As a result, there is a significant decrease in chip thickness, as the abrasive grain size becomes smaller as one would find in ultra fine diamond wheels. [Subramanian,K., et al] have shown that by controlling the value of 'h', one can grind advanced ceramics in either ductile or brittle mode. Treating each interaction between the wheel and workpiece separately, controlling the chip thickness, abrasive grain size and the number of grains in the wheel C_g (coarse or fine grains), one can control the force per grain. As the grain size decreases the force per grain also decreases.

Unlike in loose abrasive lapping where the grain depth of cut is a probabilistic event, in grinding, the depth of cut is deterministically controlled by the work and wheel speeds and the down feed rate of the machine. In grinding the 'h' value can be lowered significantly by increasing wheel speed (V_s) while lowering 'h' in lapping typically means lowering abrasive grit size. In Figure 4 is shown an example of a "mirror finish" grinding on AlTiC material using the grinding parameters in Table –1, resulting in low chip thickness values.
The 15 Angstrom R_a finish shown in Figure 4 is a result of the low 'h' values that are obtainable in grinding. As can be seen from the expression for chip thickness, the ability to grind in either ductile or brittle mode is now controlled by the user. Conversely, one can use larger particle size abrasive grains and still grind with a low value of chip thickness 'h' by altering the machine operating parameters. This allows the user to optimize the process, potentially using a higher removal rate with a coarse wheel during roughing and a finer grit wheel for ductile grinding to get a fine surface roughness with minimal sub-surface damage.

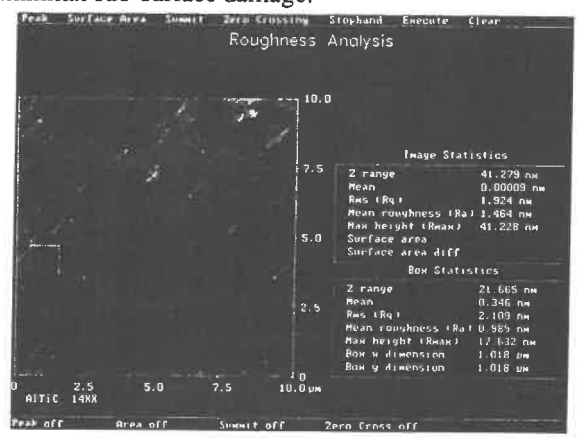

Figure 4. Atomic Force Microscope (AFM) of fine ground AlTiC material

Work Piece Dimensions:	4.5" square – 6" round – AlTiC
Wheel:	5 micron sized diamond
Wheel diameter:	11"
Wheel speed:	64 m/s
Work Speed:	500 rpm
Infeed rate:	0.1-0.3 μm/s
Coolant:	DI Water
Machine	Strasbaugh 7AF

Table 1. Grinding conditions used for ductile grinding in Figure 4

Comparison of lapping /polishing versus grinding:
Based on the expression for chip thickness it is possible to explain why grinding is able to achieve high quality surface finish with very low depth of damage typically observed only with lapping and polishing (Table 2 & 3). From the expression for chip thickness it can be shown for grinding that 'h' is inversely proportional to the product of cutting speed (≈wheel speed) and C_g the number of grains per unit area. Hence in grinding the chip thickness is proportional to (d_g/V_s), where d_g is the abrasive grain diameter and V_s is the abrasive speed. From empirical data (Figures 6&7) it may be observed that the

15 Angstrom R_a finish was obtained with a 5 μm diamond size grinding wheel. However a similar finish of 30 angstroms R_a was obtained with polishing with a 0.5 μm abrasive. This shows that for a given range of finish the grinding wheel can use a coarser abrasive allowing productivity improvements

Lapping / Polishing vs. Grinding		
GRINDING	***Operating Parameters***	**LAP /POLISH**
15	*Vw - Work speed [m/s]*	1
65	*Vs-Wheel Speed [m/s]*	1-2
5	*dg -Diameter of Grains [μm]*	0.5
low	*Cg -Grains /unit Area*	higher

Table 2. Comparison of attributes of Lapping / Polishing vs. Grinding.

Lapping / Polishing vs. Grinding		
LAP /POLISH	***ATTRIBUTE***	**GRINDING**
Loose / slurry	*abrasive*	Fixed / Wheel
Low	*Wheel Speed*	High
Batch	*Process*	Single /Multiple
Manual	*Load /Unload*	Cassette to Cassette
Excellent	*Finish*	Excellent
Environmental, issues	*Other*	Better on multiphase materials? Process simplification

Table 3. Comparison of Lapping /Polishing vs. Grinding attributes.

Machining Multi Phased Materials:
Unlike loose abrasive lapping and polishing, grinding is a deterministic process in which the machine infeed controls the actual removal from the material. However in loose abrasive lapping of multi-phase materials (Figure 5), the abrasive slurry – work interaction occurs mainly as a function of the hardness, toughness and wear resistance of the diamond abrasive in the slurry and the different phases in the work material.

In Figure 6, the effect of non-uniform material removal due to the random nature of interactions between abrasive grain and work material in loose abrasive polishing of AlTiC can be observed.

	Al_2O_3	TiC
Hardness [Gpa]	19	30
Toughness [MPa $m^{(1/2)}$]	3.5	4
Wear Resistance [$H^{(1/2)}$ K_1c]	12.3	15.5
Vol%	70	30

Table 4. Physical property measurements

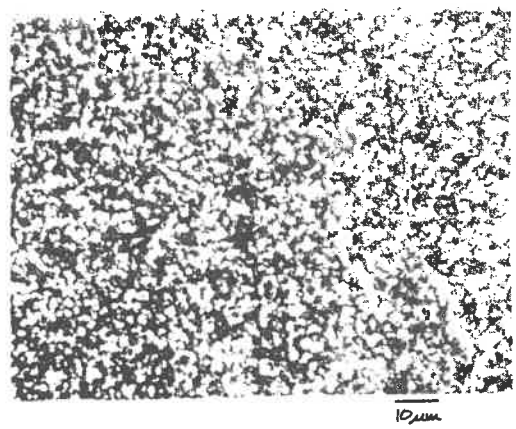

Figure 5. Micrograph of multiphase AlTiC material

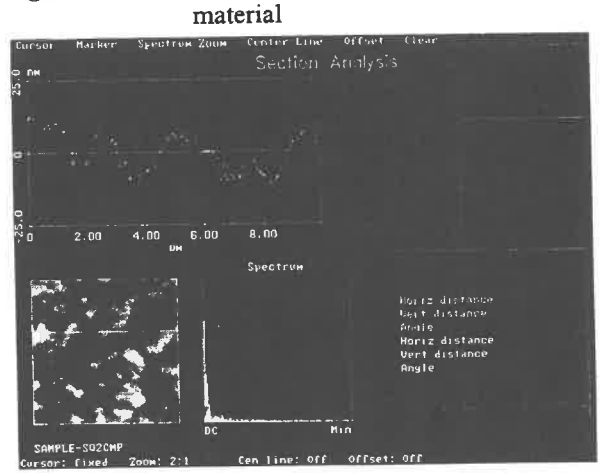

Figure 6. Atomic Force Measurements (AFM) of two phase AlTiC material after polishing (note recessed Al_2O_3 phase versus TiC phase).

The significant differences in hardness between the alumina (2100 knoop scale) and TiC (2800 knoop scale) phases translates into higher removal of the softer phase (here Al_2O_3). One

common problem that this phenomenon causes in the storage industry is termed pole tip recession. The local planarity on the surface of a read-write head has to be at the sub-micron level [Anna Mathai et al]. By contrast the AFM trace in Figure 7 shows much more uniformity in material removal as the wheel down feeds at a fixed rate showing no preferential treatment for either material.

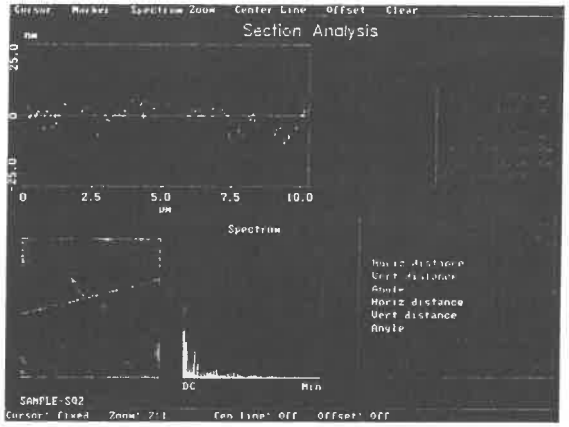

Figure 7. Atomic Force Measurements of AlTiC after grinding (note uniformity of material removal in both phases)

Total Thickness Variation and Shape:
Since the grinding process is deterministic, it is possible to control the thickness variation (TTV), flatness and shape to a higher degree using a combination of good stiffness and low grinding force. This combination allows one to grind ceramic components by imparting minimal pressure leaving the parts relatively stress free. The total thickness variation on 200 mm silicon wafers can for instance be reduced to less than 0.5 μm by keeping tight control on processing and ambient conditions.
The shape of the ceramic components can also be closely controlled to obtain convex, concave or flat surfaces as required. This is done by adjusting the angle of tilt between the work chuck and the grinding wheel spindles. In addition by controlling up or down grind along with spindle angles for rough and finish grind even hard to grind advanced ceramic materials can be ground flat even if only one side requires grinding.

Range of Materials:
The FAVS™ process has been tried on a variety of advanced ceramic materials. By controlling the chip thickness, even tough to grind materials like silicon carbide, sapphire, fully dense alumina or AlTiC can be thinned down using grinding at relatively high rates of removal. This ability is what allows the user to use the FAVS™ approach with a roughing and finishing wheel to often replace several rough lapping, finish lapping and polishing operations with one grinding machine. This leads to both increases in throughput and lowered manufacturing cost. Materials ground producing mirror finish with the FAVS™ approach range in hardness: from very soft (glass = 500 Knoop Scale) to very hard (TiC = 2800 Knoop), in fracture toughness: as low as 0.7 $MPa.m^{1/2}$ for glass; in strength: as high as 880 MPa for AlTiC and in thermal conductivity: as low as 2.7 W/m.K (Sapphire). It is expected that due to the kinematic advantages of the FAVS™ approach is likely to work on a wide variety of work materials.

What Lies ahead for FAVS™:
Different materials are being worked on currently to achieve surface roughness close to that obtained by loose abrasive lapping and / or polishing. The future goal is to achieve surface roughness as close to one Angstrom.

Acknowledgements:
The authors of this paper are indebted to Dr. Jeri Ikeda and Mr. Jason Wilson for their many contributions to this work.

Bibliography

1.Reichenbach, G. S.; Mayer, J. E.; Kalpakcioglu, S., and Shaw, M. C. The Role of Chip Thickness in Grinding. Transactions of the ASME. 1956 May:847-859.
2.Subramanian K., Ramanath S.,Tricard M., Mechanisms of Material removal in precision production grinding of ceramics; J. Mfg.Sc. &Eng. Nov '97. Vol. 119/509
3.Y Namba, R.Wada,K. Uno and A Tsuboi, K Okamura- Ultra Precision Surface grinder having glass ceramic spindle of zero thermal expansion, Annals of CIRP, Vol. 38/1/1989
4.Funkenbusch,PD, Zhou Yiyang, Takahashi, Toshio; Golini D.-Grinding of single crystal sapphire: workpiece roughness correlation's-Wear 218 (1998)1-7.
5.Tonshoff, HK; Lehnicke,S.-Subsurface damage reduction of ground silicon wafers, Prec. Eng. Nanotechnology, Proc., Vol. 6, May 31st -June 4th 1999, Bremen, Germany.
6.Mathai,A.,See,J.,Schneir,J,.Donnelly,J Measurement of pole tip recession in MR heads-Data Storage,Sept.1997.

Single Point Contributions to Free Abrasive Polishing

A E Gee and D F Williams

Cranfield University, School of Industrial & Manufacturing Science,
Cranfield, Bedford, MK43 0AL, UK. e-mail a.e.gee@cranfield.ac.uk

1. INTRODUCTION

Long experience (refs 1,2) has shown free abrasive hard and soft lapping to be capable of generating spherical and planar surfaces of high quality to sub-micrometre form specifications (an order or more better with effort) and nanometre finishes. 'Hogging' with an iron lap leaves surface damage of the order of tens of micrometres, much of which can be removed by finishing with a lap of pitch or elastic polymer. We observed that the geometrical values closely coincided with those obtained for respectively brittle and plastic material removal actions in single-point machining experiments, notably ruling on glass (with the diamond tool located by force, as pertains under a lap) and the paper correlates observations.

2. HARD LAP/WORKPIECE KINEMATICS

Empirically (ref 3, p50), it has been found that, for rapid form convergence through even material ablation over the work area, a lap is required to closely 'nest' with the workpiece over perhaps 70% or more of the surface. Interface shearing, required in at least two tangential motions, restricts the process intrinsically to planar, spherical and cylindrical surfaces. Radius differences in aspherics require smaller and/or flexible laps, sacrificing intrinsic form-averaging and requiring external measurement-based control; stressed blanks and adaptively controlled laps are possible approaches.

In minimal form, an abrasive grit particle might be a regular tetrahedron with 4 facets, 6 edges and 4 vertices, all at acute included angles. If breakage symmetrically truncates one vertex to another facet, this will generate 3 extra edges and 3 vertices (in place of the one removed) at obtuse angles. If it is envisaged that working abrasion removes 'sharp' vertices, the resulting polyhedra will be of mostly obtuse included angles, with perhaps the occasional acute or reflex angle.

Kinematic considerations (ref 4 pp585-590) applied to two rigid bodies in stable sliding contact require the number of degrees of freedom of motion of the one body with respect to the other, together with the number of points of contact (i.e. constraints), to sum to six. A rigid nominally spherical or planar lap therefore contacts a work-piece of corresponding form generally at three points, permitting three shearing degrees of freedom (N.B. cylindrical geometry requires four contact points, permitting two motions). With abrasive, 'point' contact will be through locally-proud grits. A single grit contacting one surface at three points can be stable whilst contacting the other surface at just one point. If it contacts one surface at two points and the other at one, it may roll about the axis defined by the first two. If it contacts each surface at only one point, roll will be defined by the shear vector. Roll permits interchange between contact conditions.

Subjected to a point force of 1N through an indenter, glasses crack to form 10μm scale conchoidal chips and corresponding surface damage (refs 5-8). If we apply a force of the order of N (due to weight plus preload) through the lap normal to the interface, either the workpiece or grit may yield,

causing the lap to bear down onto the next proudest grit in that region. If the work-piece cracks, the grit will most likely ingress substantially. Applying shear, the grit will experience torque about an axis parallel to the interface and rotate into fresh undamaged surface to extend the cracking/chipping process. If however a grit presents to the workpiece a facet at less than workpiece cracking pressure, then the grit may yield and the resulting smaller grits may settle below adjacent peaks in surface valleys and take little further part in abrasive action. This appears to be self-ordering to a scale of ~10μm defined by the geometry of brittle chip size (refs 9,10).

3. SOFT-LAP POLISHING: GRIT ACTIONS

The (10μm scale) roughness incurred with hard-lap hogging to form can be polished to about 1nm finish using a soft 'pitch' lap with a variety of abrasives and grit sizes of the order of 1μm. If such grits were to roll under the lap, the 10-100nm features of a 1μm chip would be likely to be reproduced by impression embossing in the glass in plastic mode. Such a process is not considered to contribute to achieving 1nm finish. Grit shear 'planing' suggested by Strong (ref 4 p32) might be expected to sustain polishing at the 1nm level and a conforming model for stable grit action has been proposed (ref 11).

Types of 'pitch' used in optical laps are variously obtained from tapping varieties of pine tree or as a by-product of oil or coal-tar production. Although relatively hard at room temperature, it is definitively a high viscosity liquid, which softens noticeably at temperatures above 60C. Its response to force in the manner of a viscous 'damper' will show low-pass temporal frequency filtering characteristics, yielding to slow effects such as sustained force on a grit particle but presenting near-rigid reaction to higher frequency effects like individual lap strokes.

When a pitch lap closes with a preformed workpiece, we may expect three proud grits to make initial kinematic contact and to start sinking into the pitch until a fourth grit makes contact and joins the process. This continues with the next proudest grit successively joining in to share the reaction force. Both the sink rate and individual grit loading reduce with increasing number of grits. The initial 'pressing' by optical glass-workers may be expected to align a large number of grits with the workpiece to support a combined lap-weight plus preload of 1kg or more.

Self-alignment can be seen in Figs 1(a) and (b), AFM micrographs of a pitch lap immediately following the finish-polishing of glass using a mixture of rouge and cerium oxide abrasive. The proudest grits have major exposed lateral dimensions of 3-6μm and peaks of perhaps 2μm diameter aligned about 1μm clear of the lap surface, (much in excess of the 1nm surface roughness obtained from the grit polishing action). The lap, of 50mm radius (r), had a matrix of facets separated by grooves (of perhaps 20% facet-pitch) so maximum contact area was approximately $A = \pi(0.8r)^2 = 0.64\pi(50 \times 10^{-3})^2 \sim 5 \times 10^{-3}\ m^2$ to sustain a load of 1kg. In all such measurements, over a 40μm square the number of aligned proud grits was 5±1. Taking 5 grits as typically sustaining the load over area $a = (40\mu m)^2 = 1.6 \times 10^{-9} m^2$, this grit/area density applied to the full lap area indicates the likely maximum total number of 'working' grits to be $5(A/a) \sim 5[5\times10^{-3}/1.6 \times 10^{-9}] \sim 1.6 \times 10^7$. With a load of 1kg, the force devolving to each grit is therefore ~ 60μg, well below the gram order critical values of brittle transition obtained using sub-micrometre radius tools (refs 9,10).

The action of a sinking grit is analogous to the falling sphere viscometer in which force $F = 6\pi\eta rv$ (where η is viscosity, r radius and v is sink-velocity) so larger dimension grits exert proportionally

larger force on the workpiece. Considering grits of different sizes but single polyhedral form, the area of the typical facet bearing on the surface will be proportional to the *square* of grit dimension and, since force is proportional to grit size, it follows that contact-pressure will be an *inverse* function of grit size. Moreover, should a grit tend to remain proud for any reason, it will bear a higher load and incur higher frictional heating so reducing the viscosity of adjacent pitch until the grit sinks to peer-level. Further, in shear, a grit facet which 'planes' the workpiece may be expected to experience tangential force proportional to its dimension and the viscous shear reaction force to be likewise proportional to dimension so 'working' grits would be dragged tangentially through the pitch at equal rates irrespective of size and so remain in the same relative position. These three autonomous mechanistic effects will tend to regulate even sharing of the lap-work by a large number of grits of not necessarily the same size, as has been observed (ref 12).

In other fields such as semiconductor wafer preparation, polymer elastic and/or fiber soft laps are employed with similar results but, unlike pitch, an elastic lap is not rate-sensitive. It will hold grits against a workpiece with a force determined by local deflection which is proportional to grit-dimension, coincidentally as in the pitch lap and so grits will likewise exert facet contact pressure on the workpiece as an inverse function of dimension. These very different underlying physical actions but coincidence of effect permit a variety of soft lap materials.

4. CONCLUSIONS

Whilst there remain issues of chemistry and fluid action, it is possible to analyse aspects of mechanical constraints on the actions of abrasive grits during polishing. This paper has considered how grits of micrometre dimension and protrusion from a soft pitch lap may yield surfaces in brittle glasses polished to roughness levels of the order of 1nm. It is shown experimentally that, under a pitch lap, abrasive particles maintain self-alignment and distribution so that the pressure exerted by any individual grit remains well below that leading to brittle cracking.

It is reasoned that an elastic polymer lap is mechanistically different but that, with respect to grits of different size, its action coincides with that of the viscous pitch lap.

5. REFERENCES

1. F. Twyman *Prism and Lens Making,* (2nd edn.) Hilger & Watts, London, 1952; republished Adam Hilger/IOP Publishing, Bristol, 1988.
2. D. F. Horne *Optical Production Technology,* Adam Hilger, London, 1972 (1st edn.); Adam Hilger, Bristol & Philadelphia PA 1981 (2nd edn.).
3. W. Zschommler *Feinoptik-Glasbearbeitung (Werkkunde fur den Feinoptiker)*, Carl Hanser Verlag, Munich/Vienna, Germany/Austria 1963; translated/published in English with additions by G K Sachdev and J Maxwell as *Precision Optical Glassworking,* Proc SPIE vol 472, SPIE, Bellingham, WA/Macmillan, Basingstoke, UK 1984.
4. J. Strong *Procedures in Experimental Physics,* Prentice Hall, Englewood Cliffs, NJ, 1938; (published in UK as *Modern Physical Laboratory Practise*, Macmillan, London)
5. B. R. Lawn and M. V. Swain "Microfracture beneath point indentation in brittle solids", J Mat Sci, vol.10, pp.113-122, 1975.
6. M. V. Swain and J. T. Hagan "Indentation plasticity and ensuing fracture of glass", J Phys D, vol 13, pp2201-2214, 1976.
7. K. E. Puttick, M. A. Shahid and M. M. Hosseini "Size effects in the abrasion of brittle materials" J Phys D, Vol. 13, pp2249-2262, 1980.

8. A. G. Atkins and Y.-W. Mai *Elastic and Plastic Fracture*. Ellis Horwood, Chichester, 1985.
9. K. E. Puttick, M. R. Rudman, K. J. Smith, A. Franks and K. Lindsey, "Single-point diamond machining of Glasses", Proc Roy Soc Lond A, vol. 426, pp19-30, 1989.
10. A. E. Gee, R. C. Spragg, K. E. Puttick and M. R. Rudman, "Single-point form finishing of glasses and other brittle materials", Proc SPIE, vol.1573, pp39-48, 1991.
11. A.E.Gee "Modelling the mechanics of free particulate abrasive polishing from the viewpoint of single-point processes" Proc SPIE Vol 2775, pp611-618, 1996
12. C.M.Lee and D J Bell "The effects of polishing particle size on the finish and sub-surface damage of glass" Proc ASPE vol 6 pp240-243 (ASPE Ann Mtg., Grenelefe, FLA) 1992

6. ACKNOWLEDGEMENTS

Commencement of this work resulted from discussion of ruling experiments on glass between AEG and Prof J Strong, U.Massachusetts, Amherst, MA. Further discussions are acknowledged with Mr E. Palmer of Hampton, Middx. who kindly prepared and made available a suitable lap and workpiece for post-polishing measurement. SPM measurements were undertaken by Mrs C Kimpton of Cranfield University.

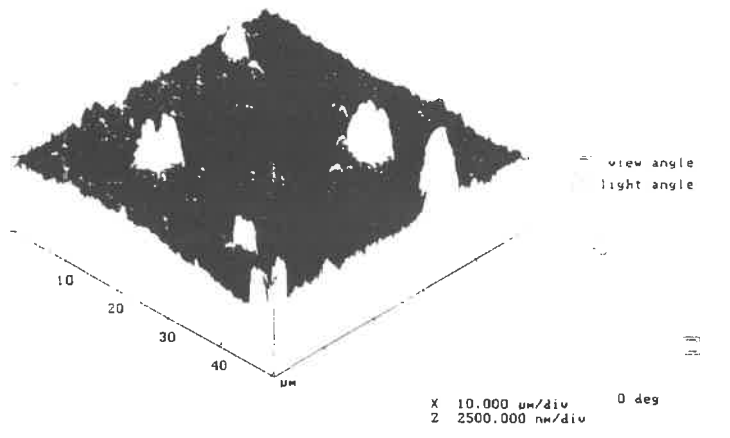

(a)

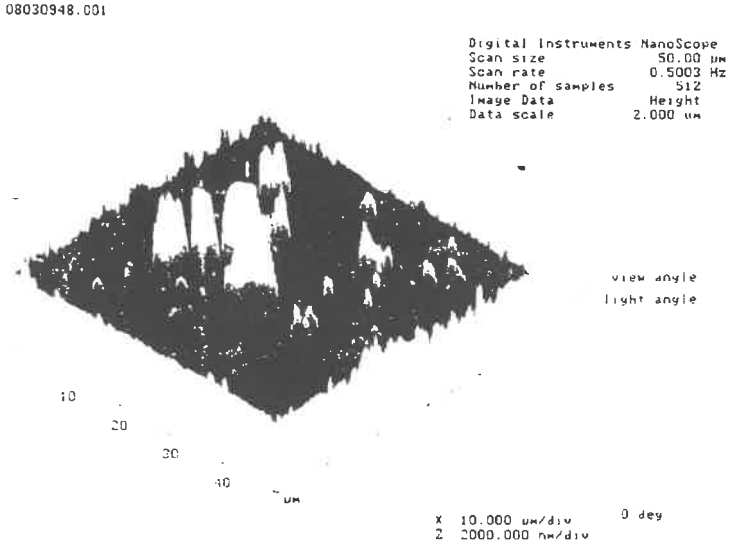

(b)

Fig 1 Scanning Force Micrographs of Grits in a Pitch Lap after Polishing Glass

NANO-ABRASION MACHINING OF BRITTLE MATERIALS

Osamu Horiuchi, Fumio Naruse and Junichi Ikeno
Toyohashi University of Technology, Toyohashi, Japan

1. INTRODUCTION

Recently great advances have been accomplished in ultraprecision machining, but it still remains difficult to obtain a form accuracy of a few nanometers by ultraprecision grinding of brittle materials. To improve the form accuracy, some corrective figuring is performed by local material removal cooperated with feedback of the form error map. The methods used for the local removal are polishing with a small polisher [1,2], elastic emission machining (EEM) [3], ion beam machining [4,5] and so on.

In this paper, a method of precision abrasion machining is proposed for the local removal and investigated are its fundamental characteristics and feasibility for corrective figuring of brittle materials.

2. NANO-ABRASION MACHINING

This method is similar with water jet abrasive machining or liquid honing. In water jet abrasive machining and liquid honing, generally, abrasive grits contained in water are ejected under a high pressure from a nozzle and collide on the surface of work materials at a high speed. Referring to the erosion tests by Sheldon and Finnie [6], if the collision energy is low and the collision angle is shallow, the abrasion rate may decrease down to a few nanometers per minute and ductile mode abrasion with surface roughness of a few nanometers may occur even for brittle work materials. Therefore this method is named "nano-abrasion machining". This method has a great advantage that the machining accuracy is almost independent of the machine accuracy because the working distance from the nozzle tip to the collision point is far enough. A warp of the workpiece induced by holding does not affect the machining accuracy therefore this method is suitable for repeating a post-process measurement and corrective figuring.

3. EXPERIMENTAL APPARATUS AND METHODS

Fig. 1 shows the schematic of experimental apparatus. In the machining chamber, the workpiece was mounted on a X-Y table controlled by a NC controller. The machining liquid composed of pure water and small amount of abrasive

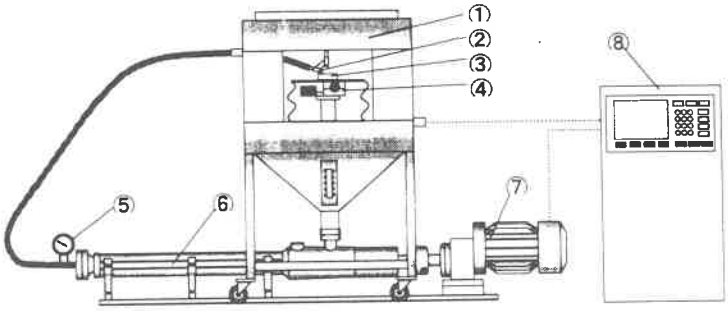

① Chamber ② Nozzle ③ Workpiece ④ X-Y table ⑤ Pressure gauge
⑥ Pump ⑦ Motor ⑧ NC controller

Fig.1 Experimental apparatus

grits was fed to a nozzle by a special screw pump under a high pressure.The nozzle made of ceramic was fixed inclining at a shallow angle to obtain ductile mode abrasion.

A series of fundamental experiments were performed without scanning of the nozzle against the workpiece. The work materials were optical glass of BK7 and Zerodur and single crystal silicon. The plane optical glasses were prepared by polishing with surface roughness 4nm Ry and the silicon wafer 2nm Ry. The machining liquid containing 1 % wt abrasive grains of white fused alumina (WA) was mainly used. The grain mesh sizes and mean diameters were #4000 (3.0μm), #8000 (1.2μm), #10000 (0.6μm) and #30000 (0.3μm). The diameter of nozzle was 1mm and the ejecting pressures were 2, 4 and 6 MPa, then the velocities of jet flow were 61, 91 and 106 m/s, respectively. The collision angle was fixed at 30° for a higher material removal rate, referring to the experimental results of air abrasive jet for plate glass [6]. The working distance was 20mm. The machining time was kept constant one hour. After the experiments, the machined surface was observed by an interferometer microscope to measure the depth profile and surface roughness.

4. EXPERIMENTAL RESULTS AND CONSIDERATIONS

Fig. 2 shows an example of removal spot observed by the interferometer microscope. The removal spot has an oval shape with approximately 3 x 6 mm in areal size and contour map is almost symmetric with respect to the center line of jet flow, as shown in Fig. (a) and (b). The longitudinal profile along the center line has an asymmetric V-shape as shown in Fig. (c) and the maximum depth was about 1.0μm. As shown in Fig. (d), the transverse profiles have two different shapes; parabolic and W-shape. The profile at a location before the deepest point is parabolic and after that it changes to W-shape whose central hill gradually increases the height. The W-shape profile is considered due to a local reduction of collision angle and velocity because a part of jet flow collided on the work surface and then the reflected flow interfered with the other part of jet flow. Fig. (e) and (f) show surface roughness measured at the deepest point where the roughness of prepared surface did not affect any longer. In this case, the surface roughness seems fine and uniform.

For different experiments, the removal spot had always an oval shape. The areal size increased with ejecting pressure and abrasive grain diameter, for example, it was approximately 7 x 14 mm for pressure 6 MPa and grain mesh size #4000. Moreover the contour map and profiles were basically similar to those shown in Fig. 2.

Fig. 3 shows the relationship of ejecting pressure versus maximum depth of removal spot for various experiments. The maximum depth which directly relates to the material removal rate increases together with the ejecting pressure. This result corresponds to the fact the material removal rate increases with collision energy and collision frequency. The working liquid contained a constant % wt of abrasive grains. Consequently, under an ejecting pressure, the product of collision energy and collision frequency is constant even for different grain sizes. The maximum depth for grain size #10000 is comparable or slightly smaller than that for #30000. However the maximum depth for #8000 is apparently greater and for #4000 is much greater than for #10000 or #30000. Therefore the maximum depth is not considered proportional to the above-mentioned product. There are small differences among the work materials; the maximum depth of Zerodur is slightly greater than that of single crystal silicon but smaller than BK7. All the maximum depth is greater than 0.1μm, therefore it is considered that the material removal rate of this method is high enough and applicable to corrective figuring.

Fig. 4 shows the relationship between ejecting pressure and surface roughness. The surface roughness slightly increases together with ejecting pressure except for grain size #4000. Generally the surface roughness is supposed to increase together with the grain diameter. However the differences of surface roughness are small for different grain sizes except #4000. There found small differences among the work materials, the surface roughness of Zerodur is

smaller than that of BK7 but larger than that of single crystal silicone. Optical surface roughness of 5-20nm Ry could be obtained with finer abrasive grains and under a lower ejecting pressure.

5. CONCLUSIONS

A method of precision abrasion machining was proposed for local removal of brittle materials and its fundamental characteristics and feasibility for corrective figuring were investigated. It has been ascertained by experiments that the obtained surface roughness and the material removal rate are sufficiently suitable for corrective figuring of brittle materials.

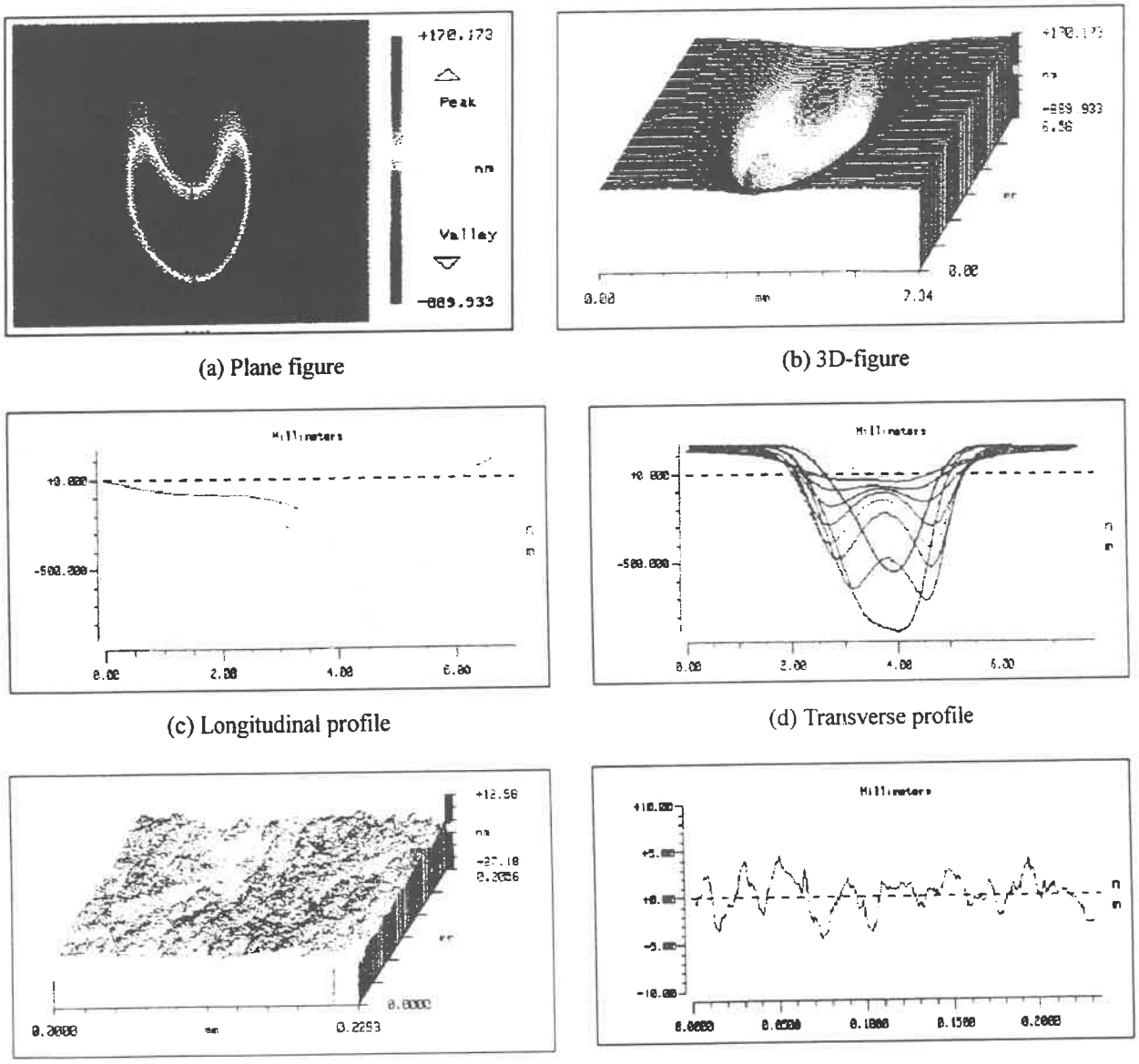

(a) Plane figure

(b) 3D-figure

(c) Longitudinal profile

(d) Transverse profile

(e) 3D-surface roughness at deepest point

(f) Surface roughness

Fig . 2 Example of removal spot on machined surface
Work : BK7, abrasives:WA30000, ejecting pressure:2MPa.

ACKNOWLEDGMENTS

This work was partially supported by the SRF of Japan Ministry of Education. We would like to express our sincere thanks to Nikon Corporation who gave us many workpieces. Great many thanks are also attributed to Mr. S. Itoh of Industrial Research Institute of Aichi Prefectural Government who supported us for measurements.

REFERENCES

[1] R. Aspden, R. McDonough and F.R. Nitchie, Appl. Opt., 11, 12 (1972) 2739.
[2] M. Ando, M. Negishi, M. Takimoto, A. Deguchi, N. Nakamura, M. Higomura and H. Yamamoto, SPIE, 1720 (1992) 22.
[3] Y. Mori, K. Yamauchi and K. Endo, Prec. Eng. 9 (1987) 123.
[4] S.R. Wilson, D.W. Reicher and J.R. McNeil, SPIE, 966 (1988) 74.
[5] M. Weiser, C. Kubler, K.H. Fiedler and K.F. Beckstette, Proc. 6th IPES, (1991) 209.
[6] G.L. Sheldon and I. Finnie, Trans. ASME, J. Eng. Ind., 88 (1966) 387.

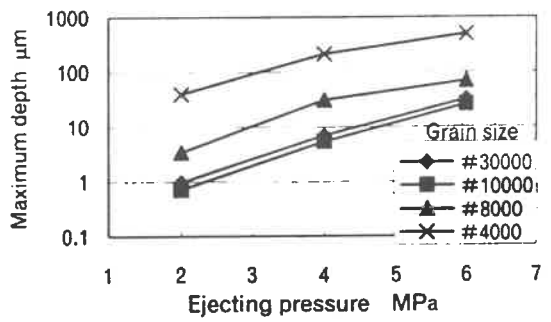

(a) BK7

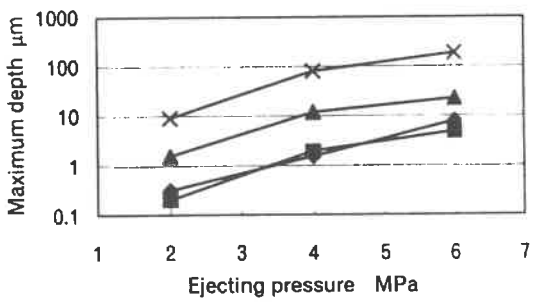

(b) Zerodur

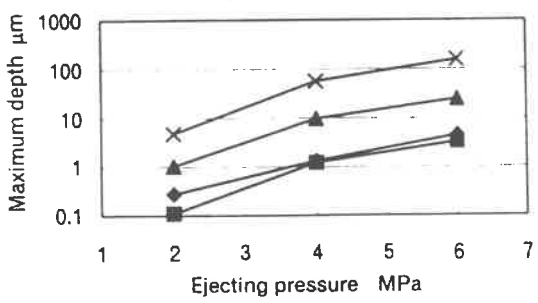

(c) Single crystal Si

Fig. 3 Relationship of ejecting pressure versus maximum depth.

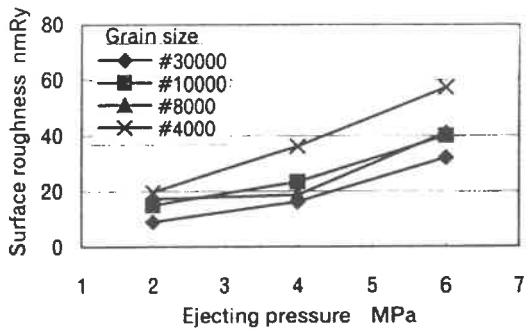

(a) BK7

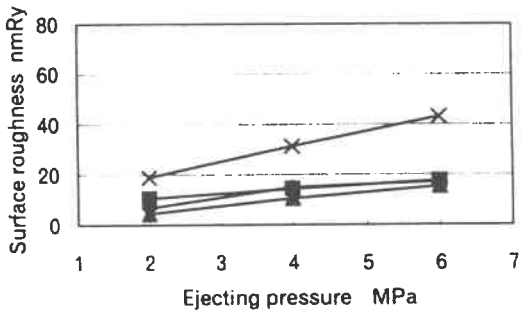

(b) Zerodur

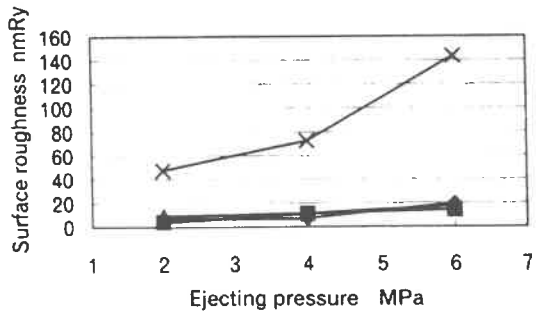

(c) Single crystal Si

Fig. 4 Relationship of ejecting pressure versus surface roughness.

Finishing of Optical Materials Using Fluid Jet Polishing

Oliver W. Fähnle[#]
FISBA-Optik
Rorschacherstrasse 268, CH-9016 St. Gallen, Switzerland
e-mail: oliver.faehnle@fisba.ch

Hedser van Brug
Delft University of Technology, Optics Research Group
Lorentzweg 1, NL-2628 CJ Delft, the Netherlands
e-mail: brug@optica.tn.tudelft.nl

Abstract

The characteristics of Fluid Jet Polishing (FJP), a newcomer in the field of optical fabrication, or more specifically optical finishing, are presented. Comments on the process possibilities are given, e.g. spot shape, process speed, and parameter dependencies. Preliminary results on a wide range of materials are discussed.

1 Introduction

The shaping and finishing of steep, concave sections of a-spheres, e.g. conformal optics, in brittle materials such as glass represent a challenge for optical fabrication research. Aspheres are usually finished applying sub-aperture-polishing methods moving a small polishing tool over the surface to be generated, requiring an accurate computer control. The applied finishing techniques can be e.g. CCP (computer controlled polishing) or MRF (MagnetoRheological finishing). Besides, using ion beams, the aspherical surface can be generated by shaping a previously finished spherical surface without increasing its surface roughness.

It is known to be possible to cut glass by the use of Abrasive Slurry Jets (ASJ) where a stream of premixed slurry is entrained and guided to the surface by the use of a nozzle. ASJ systems operate at pressures above 70 bar (typically several hundreds of bars).

It was our idea to employ an ASJ system at very low pressures to finish optical surfaces, and that it can then be used to reproduce the aqua planing effect as observed in bowl feed polishing. Bowl feed polishing is known for its very good results on flat surfaces. FJP is thus expected to be capable of bringing the results of bowl feed polishing to the production of steep aspherical surfaces.

This paper will first briefly discuss our experimental FJP system after which the experiments and their results will be highlighted. Finally the discussion will go into the possibilities of the presented method.

[#] The presented work was carried out while Oliver Fähnle was with DeCOS, Delft Center for Optical Surfaces, TNO Institute of Applied Physics, Delft, the Netherlands

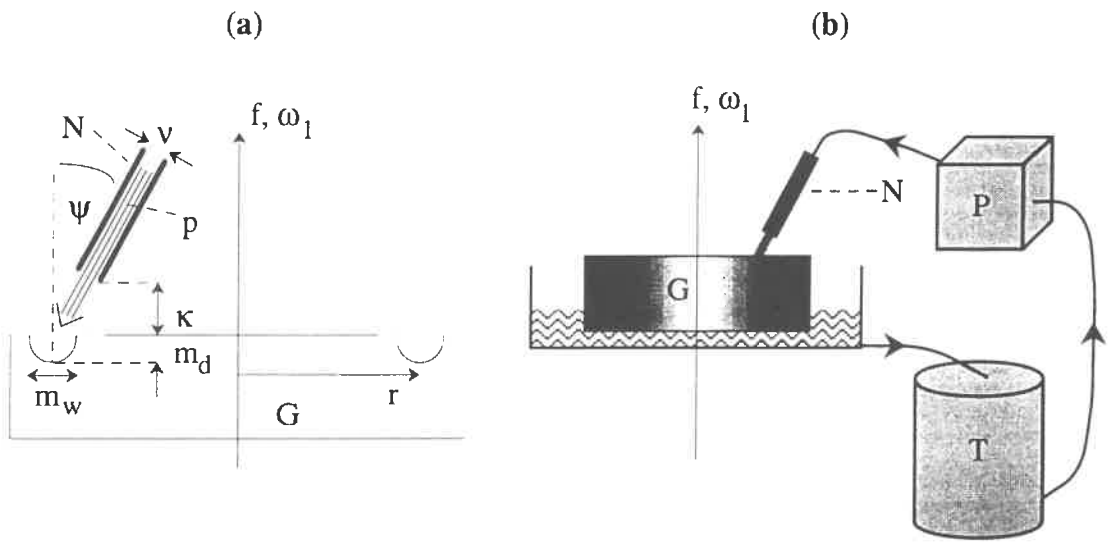

Figure 1 Schematic diagram of the experimental set-up used to demonstrate the finishing process of Fluid Jet Polishing (FJP). (a) Diagram showing the relative position of the nozzle N with respect to the work-piece G and defining the parameters. (b) Diagram of the closed loop set-up comprising the tank T containing the slurry, the pump P and the nozzle N that is positioned above a lapping machine.

2 Fluid Jet Polishing

The FJP process has already been described in literature[1,2,3] and will here only briefly be touched upon. A plastic tank T (see Fig. 1) is used to mix water and a grinding and/or polishing compound. This can be done either by mechanical stirring or by blowing air through the mixture. The water with the homogeneously mixed particles in it is referred to as the slurry. This slurry is pumped from the tank by means of a low-pressure pump P and guided through a nozzle N. Typically, the pressure values range from 0 up to 15 bar. The nozzle is positioned above the surface G being processed where the stand-off distance and the angle with respect to the surface normal can be chosen. After processing the surface, the slurry is collected and guided back to the tank for reuse.

The stand-off distance is typically in the order of some millimeters and the diameter of the cylindrical nozzle in the here described experiments was 0.84 mm. Other nozzles have also been utilized, cylindrical nozzles having other diameter as well as differently shaped nozzles. The closed loop design is found to work to our satisfaction. No degradation of the processing is observed, even after 20 hours of using the same slurry. The process is found to be independent of the stand-off distance (1 mm up to 10 cm) as long as no air is mixed within the slurry jet. The processing spot was found to be about 3 times the size of the nozzle diameter.

A typical concentration of the particle contents in the slurry is 5% to 10%. Used particles are Cerium Oxide (polishing compound) and #800 and #1200 Silicon Carbide (grinding compounds).

3 Results

We applied the FJP process to several different types of materials, i.e. glass, amorphous (BK7) as well as crystalline (silicon, ruby and sapphire), metals, and plastics. For all materials it was found that the surface shape could be altered, and that the roughness could be reduced. The material removal speed depends on the pressure within the FJP system and on the particles (concentration and type). Material removal of 1.5 μm in one hour was observed for polished sapphire while for softer materials, e.g. BK7 or aluminum, a removal as high as 40 μm or higher was found. These values were obtained with a pressure of 10 bar and an angle between the nozzle axis and the surface normal of 45 degrees.

To what extend the surface roughness could be reduced was found to depend on the initial surface roughness and on the surface hardness. For polished surfaces no surface degradation was observed due to the FJP processing. For ground surfaces it was found that the roughness could be improved by at least an order of magnitude in the case of BK7 and all of the metals. For the ground crystalline materials, sapphire and ruby, the improvement on the roughness was less significant, about 10 – 20%. The processing was performed with 10% #800 SiC particles in the case of the BK7 and the metal samples. For the crystalline samples the slurry contained 5% of #1200 SiC particles and 5% of cerium oxide.

4 Discussion

Although it was mentioned in the abstract that FJP is specifically suited for optical finishing, it has to be noted that it can also be applied for shaping purposes. As mentioned within Section 3, it is possible to shape a smooth, polished sample, without degrading its roughness. This makes FJP well suited for shape corrections after the surface has been finished and characterized.

Tentatively, we can explain the process of FJP as follows. The particles, present in the jet, are guided to the surface where the jet is redirected due to the collision with the surface. The particles, due to their higher density than water, are assumed to be forced to the outer-side of the fluid beam where they come in contact with the surface.

In our opinion, the interaction of the particles with the surface is dictated mainly by a few quantities, i.e. among others, the size and shape of the particles, the surface roughness and the surface hardness. For surfaces with a low hardness, e.g. plastics and some metals, the process is found to be ductile, while for high hardness materials, e.g. ruby and sapphire, the process will be brittle.

As soon as the surface roughness is smaller than several tens of nanometers, the material removal is always in a ductile manner. This is believed to be the case as soon as there are no chunks of material sticking out above the surface, which of course is the case for a polished surface. For these smooth surfaces, the particles in the fluid beam will no longer collide with protruding parts, and hence will only shear across the surface. Due to the shear force, material is removed in a ductile manner.

Experiments using different types of nozzle shapes have shown one the most powerful features of FJP. For cylindrical nozzles, i.e. nozzles with a circular cross section, the processing spot is found to be w-shaped for normal incidence operation, and to shift to a more u-shaped halo type of spot for increased angles between the nozzle and the surface normal. The ratio between spot size and the nozzle diameter was always found to be about three, independent of the stand-off distance, provided that no air was mixed into the fluid jet. By changing the nozzle cross-section, the processing spot can be altered. We started an investigation on the use of rectangularly shaped nozzles and found that these types of nozzle are promising candidates for fast finishing of larger areas, owing to their homogeneous operation.

Owing to the processing method, FJP can be used for the finishing and correcting of conformal optics. Steep concave parts of conformal mirrors are a challenge for the optical industry since the presently standard methods of polishing are not applicable in these areas. Since the tool in the case of FJP is only a small nozzle that can easily be reshaped if required, FJP can be used even in the case of steep concave surfaces.

5 Conclusions

We have discussed the fluid jet polishing process and pointed out what its capabilities are. It has been shown that it can be used for the finishing of optical surfaces, as well as for shaping. In general it can be stated that the roughness of a surface will not be degraded due to an FJP shaping process and in many cases it is found that the roughness even improves. It has been pointed out that FJP is one of the enabling technologies for the production of conformal optics.

References

[1] Oliver W. Fähnle, Hedser van Brug, and Hans J. Frankena, "Fluid Jet Polishing of Optical Surfaces". Applied Optics 37(28), pp. 6771 – 6773, 1998.

[2] Oliver W. Fähnle, Hedser van Brug, and Hans J. Frankena, "Kinetic finishing applying a low pressure abrasive slurry jet system", Trends in Optics and Photonics Series, Vol.24, 1999 (in press).

[3] Oliver W. Fähnle and Hedser van Brug, "Fluid Jet Polishing: removal process analysis", In Optical Systems Design and Production, Optical Fabrication and Testing, Ed. Roland Geyl, Europto/SPIE Vol.3739, Berlin 1999 (in press)

Overview of a 2nd Generation Large Aperture Deformable Mirror for the National Ignition Facility

S.E. Winters, T.J. Arnold, E.S. Bliss, M.J. Dailey, P.M. Danforth, J.A. Koch, R.A. Sacks, C.J. Stolz, W.T. Whistler, B.W. Woods and R.A. Zacharias

University of California, Lawrence Livermore National Laboratory
Livermore, California 94550

Abstract

A second generation large aperture prototype deformable mirror was designed, fabricated and tested at Lawrence Livermore National Laboratory (LLNL) for future application to the National Ignition Facility (NIF). Experimental results, collected while operating the deformable mirror in a laboratory environment demonstrate the value of a large aperture deformable mirror and that it can be predictably designed, built and operated as an alternative to making a "perfect" optical system.

1. Introduction

The National Ignition Facility (NIF), currently under construction by the Department of Energy at Lawrence Livermore National Laboratory, is a mega-Joule class laser and target irradiation facility for investigating the physics associated with stockpile stewardship and inertial confinement fusion (ICF). It is designed to produce 1.8 MJ of frequency-tripled radiation (351 nm) in 192 independently focusable beams, each with an amplifier system that has a square clear aperture of approximately 40 cm x 40 cm. These amplifiers have aberrations that contribute to the net wavefront and affect both conversion efficiency of the frequency converters and the size of the focus spot on the target.

We have built an adaptive optics system to address static aberrations in the main beam line and precorrect dynamic aberrations induced in the main power amplifiers so that NIF can meet requirements for its conversion efficiency and focus spot size. The adaptive optics system comprises a deformable mirror, Hartmann sensor, reference source and controller electronics.[1]

An adaptive optics system allows the overall laser system to be built using reasonable precision engineering tolerances, which helps to maintain costs, while still achieving its performance goals. Additionally, an adaptive optics system will allow for some steady-state system disturbances, such as optical mount settling, structural settling and thermal drift.

2. Design Requirements

Table 1.1 below overviews some of the key design requirements. Of the many design requirements, the residual surface error, flash lamp radiation and replaceable actuators combined to make the design extremely challenging. The residual surface error was established to minimize the amount of uncorrectable error added to the laser system by the adaptive optics system, without significantly increasing the manufacturing cost. The requirement for flash lamp radiation is due to the location of the deformable mirror, only 2 meters away from the laser amplifier where Xenon flash lamps can produce up to 10 J/cm^2 with a 200 μsec pulse length. Lastly, the replaceable actuators requirement was established due to the lifetime of approximately 30 years and the desire to maintain the adaptive optics system at LLNL.

Parameter	Requirement
General	
Number of Actuators	39
Actuator Configuration	Hexagonal
Actuator Spacing	68.4 mm
Actuator Type	PMN
Clear Aperture	365 mm x 365 mm
Actuators	Replaceable on site
Residual Surface Error (closed loop)	0.025 waves RMS
Surface Correction Range	>4 waves P-V >1 wave P-V for 4th order (@ 1.053)
Operating Environment	
Ambient Temperature	68°F+/-2°F
Relative Humidity	< 3%
Pressure	1 atm
Flash Lamp Radiation	10 J/cm^2
Mirror Bandwidth	
Open Loop (-3 dB)	>100 Hz

Table 1.1 NIF deformable mirror design requirements.

3. Design Description

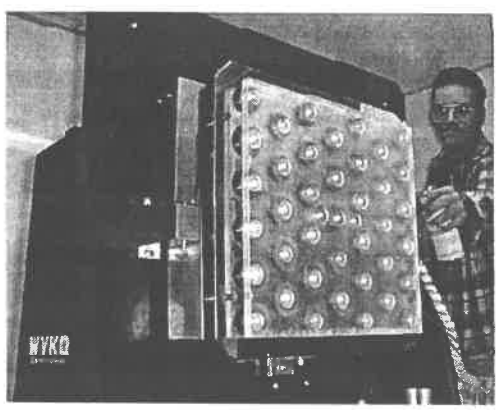

Figure 1.1 Large aperture 39 actuator deformable mirror.

As depicted in Figure 1.1, the large aperture prototype deformable mirror consists of a 390 mm x 390 mm x 15 mm faceplate with 39 cylindrical 20 mm diameter posts forming equilateral triangular subapertures. The faceplate and posts are machined from a continuous piece of BK-7 glass and then acid etched to minimize stress concentrations. After fabrication, the front side is coated with HfO_2/SiO_2 and then stress compensated with a SiO_2 back side coating. The circular posts are attached, through flexure plates, to electrostrictive actuators made from lead magnesium niobate (PMN). Each actuator has an unloaded stroke of approximately 15 μm at 150 volts and has approximately 5 percent

hysteresis. To protect epoxy used in connecting the posts to the flexures from the flash lamp energy, each circular post is coated with aluminum. The PMN actuator subassemblies are designed to be replaceable without removing the front faceplate. The actuator subassemblies are mechanically constrained in a 100 mm thick aluminum block. Electrical leads pass out of the aluminum block to a connector.

An important enhancement in this second generation design is the butt joint coupling used to attach the optical and mechanical subassemblies. Each components' 39 surfaces are precision lapped to better than 2 micrometers coplanar, as shown in Figure 1.3, prior to assembly.

Designing the prototype deformable mirror utilized both experimental and modeling capabilities at LLNL. Finite element models were developed for both stress estimation and surface deformation trade studies. Experimental facilities such as the flash lamp laboratory and mechanical measurement laboratory were utilized to test concepts before building the 39 actuator deformable mirror. Furthermore, experimental testing was completed at both the coating vendor and actuator vendor facilities.

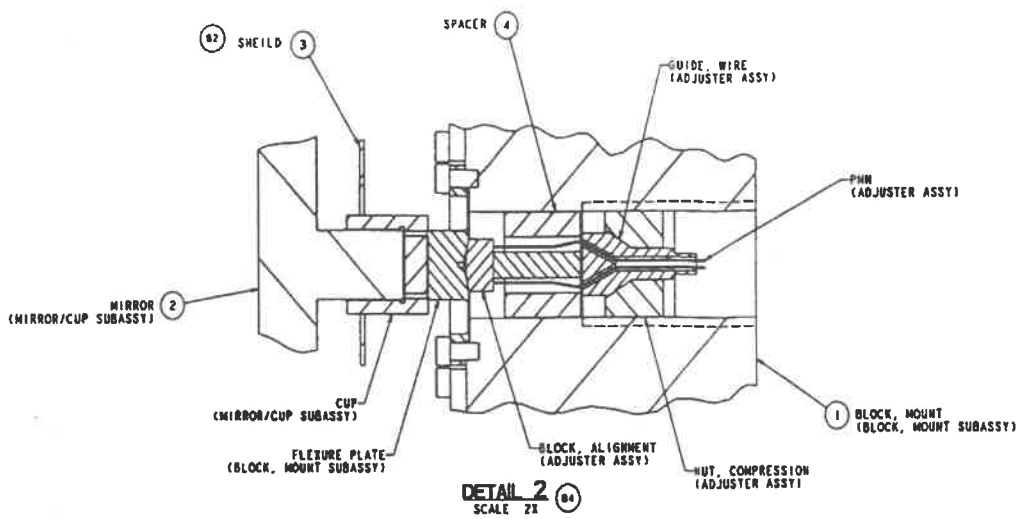

Figure 1.2 Detail of deformable mirror actuator/mirror connection.

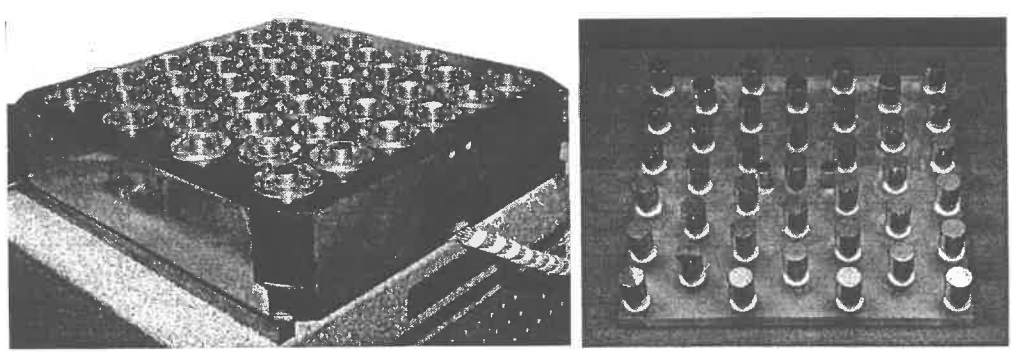

Figure 1.3 Precision lapping required to achieve residual error performance.

4. Laboratory Testing

Detailed testing utilized a 24" aperture Fizeau interferometer system, which was specially developed to characterize the performance of the NIF adaptive optics. This testing included closed loop operation using a NIF prototype electronic controller and a prototype Hartmann sensor. Additional tests included aberration correction and influence function measurements. These results matched the expected design objectives and when combined with other off-line test results gave confidence in the future successful development in NIF.[1] Figure 1.4 depicts the closed loop flat condition of 31 nanometers rms (λ=1.05 μm) and the surface response, or influence function, for the center actuator.

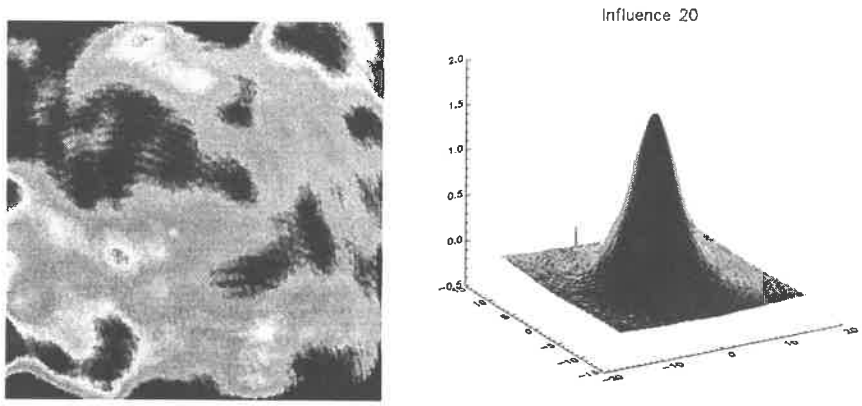

Figure 1.4 Surface figure for flat condition (31 nm rms) and center actuator (1.5 μm).

5. Conclusion

A large aperture prototype deformable mirror was designed, fabricated and tested at Lawrence Livermore National Laboratory (LLNL) for future application to the National Ignition Facility (NIF). Experimental results, collected while operating the deformable mirror in a laboratory environment, demonstrated the value of a large aperture deformable mirror. Benefits include requiring less actuator stoke, due to the double-pass configuration, and producing a smaller focal spot size in the spatial filter pinholes. Lastly, this work proved that a large aperture adaptive optic system can be predictably designed, built and operated as an alternative to making a "perfect" optical system.

6. Acknowledgments

This work was performed under the auspices of the U.S. Department of Energy by Lawrence Livermore National Laboratory under contract W-7405-Eng-48.

7. References

1. R.A. Zacharias, et al., "The National Ignition Facility Wavefront Control System," Solid State Laser for Application to Inertial Confinement Fusion Conference, Monterey, CA, Vol. 3492, July 1998.

NEW MICRO-ASSEMBLY TECHNIQUE OF THREE DIMENSIONAL MICRO-STRUCTURE BY YAG LASER BEAM

Daisuke Sawaki , Junichi Ikeno and Osamu Horiuchi
Toyohashi University of Technology , Toyohashi , Japan

1. Introduction

In recent years, the realization of micro-machine and micro-device with elements having various functions integrated becomes more and more necessary. If a new micro-machining technique which can manufacture material and shape at the same time is developed, the highly functional parts with less space can be expected. In this research, a new concept is considered by arranging the fine particles in three dimension according to the design of material and shape of the parts, and then sintering to strength the structure. However, to fulfill this task, the three dimension manipulation and micro-assembly technique of fine particles is indispensable. The laser trapping technique was suggested to manipulate fine particles in water with optical radiation pressure by Ashkin in 1970[1]. Since the manipulation is non-contact, the following advantages can be obtained: 1) Complex manipulation with high degree of freedom. 2) High speed manipulation without vibration. 3) Manipulation of multiple particles at the same time. On the other hand, the manipulation is considered difficult in the air because the surface tension is very big between the base plate and fine particles. However, considering the environment of micro-machining, the manipulation in the air is desirable to meet the requirements of high degree of freedom and stability. Hereby, this research proposed a new method on trapping the fine particles in the air and developed a new micro-machining technique by assembling three dimensional micro-structure from fine particles with laser beam.

2. Experiments on Trap of Fine Particles with Laser Beam

2.1 Trapping principle of fine particles with optical radiation pressure

The generation of optical radiation pressure can be explained by geometrical optics in case the optical wavelength is shorter than the diameter of fine particle to be trapped[2]. The generation of radiation pressure with an optical beam going through a fine particle is shown in **Figure 1**. When beam "a" goes into a fine particles, an optical radiation pressure "Fat" happens at the orthogonal direction of the interface. Then, when the beam goes out from the fine particle, the optical radiation pressure "Fa0" happens. The total force is "Fa". As for the beam "b", force "Fb" happens. The total force "F" of "Fa" and "Fb" is in the direction which always makes the center of fine particle according to the focal point of laser beam. Hence, the trapping of fine particles with laser light becomes possible. Shown in **Table 1**, the optical radiation pressure acting on silica fine particles caused by YAG laser light were calculated. Silica fine particles are transparent for YAG laser light, and laser light irritates from the upper of fine particles which are put on the optical axis. In case the position of focal point is from the upper part of fine particles to the lower part of particles, the calculation result is shown in **Figure 2**. Axis Z illustrates the position of focal point (Z=r/R, r means the distance between center of particle and

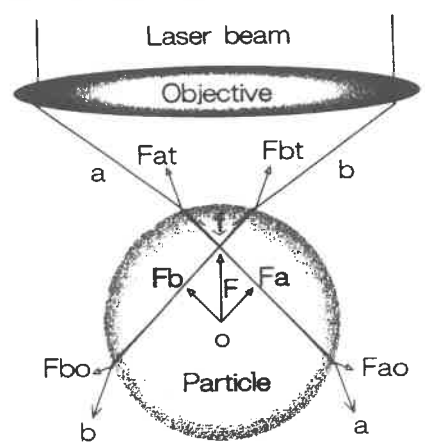

Fig.1 Qualitative view of particle trapping

focal point , R means the radius of particle), where +1.0 and -1.0 mean the top and bottom of fine particles respectively. Axis X shows the force acted on silica fine particles with the gravity force included. On this axis, the minus value means the force points downwards and the plus value means the force points upwards. When the output of laser is 14mW and focal point is on the upper part of fine particle, the total force from two directions offsets. When focal point is set at Z=0.75 with an output of 20mW, it is calculated that silica fine particles can be levitate into the air with optical radiation force.

Table 1 Conditions of calculation

YAG laser power	~20mW
Polarization	Circularly polarized light
Objective	N.A.=0.8
Particle	SiO_2(ϕ 8.0 μ m)
Refractive index	n=1.4
Enviroment	Air
Refractive index	n=1.0

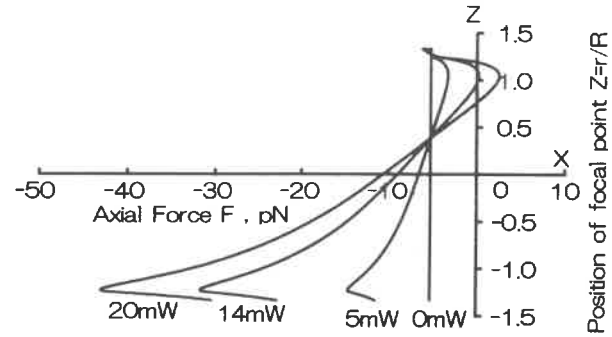

Fig.2 Relation between axial force and focal point

2.2 Experimental apparatus

The configuration of experimental system is illustrated in **Figure 3**, It is mainly consisted of three parts, laser oscillator, beam scanner and light accumulating part. The details of each are as follows:

1) Q-switched YAG laser (Lee Laser 818TQ, λ=1.06μm, maximum output 18W, beam Mode TEM_{00}) is applied in Laser oscillator.

2) Laser beam scanning part is constructed by two pieces of galvano mirror to realize horizontal laser scanning on X-Y surface which is orthogonal to optical axis. It is possible to scan the laser beam focal pointed by objective with high speed and at a resolution of 0.17μm.

3) Microscope is applied in the light accumulated part (Nikon X2-TI-EPI), YAG laser beam irradiates into the microscope, with the optical axis being the same as that of illumination. The bright field objective (CF IC EPI Plan × 50) is utilized. The aberration between visible light and YAG laser light has been removed through modification. The fine particles are observed in three-dimension space with CCD cameras arranged on the upper and side locations.

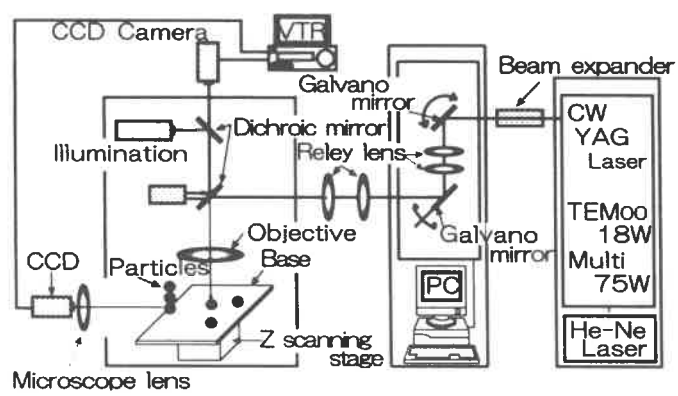

Fig3. Configuration of experimental system

2.3 Experiments on trap of fine particles

The trapping experiments were conducted in the air. The experimental results showed the output of laser must be more than 2W, which is 2 digits larger than that of calculation. It is supposed that the reason lies on the attractive force between the base plate and the fine particle caused by the moisture in the air. To overcome this force instantly, it is necessary to raise the peak output of laser light. Hereby the experiment was conducted by using Q-switch, whose condition is shown in **Table 2**. The focal point was set at the upper part of the fine particle. The experimental result showed that it is possible to trap a fine particle at a low output under 120mW. The trapped fine particle is shown in **Figure 4(a)**, the fine particle was trapped in three dimension for the first

time. And, when the focal point is set at the base plate, it can also be observed that the fine particle, shown in **Figure 4(b)**, was levitated about 1 μ m high. However, according to the optical radiation theory, the particle should be pushed onto the base plate when the focal point is set lower than the center of silica fine particle. Although the mechanism has not been clarified by now, this experiment confirmed the fine particles in the air can be manipulated by laser beam, which makes the assembly of micro-structure by laser beam possible.

Table 2 Experimental conditions

Laser power	120mW
Q-sw repetition rate	35kHz
Objective	N.A.=0.8
Particle	SiO_2(ϕ 8.5 μ m)
Refractive index	n=1.4
Enviroment	Air
Refractive index	n=1.0

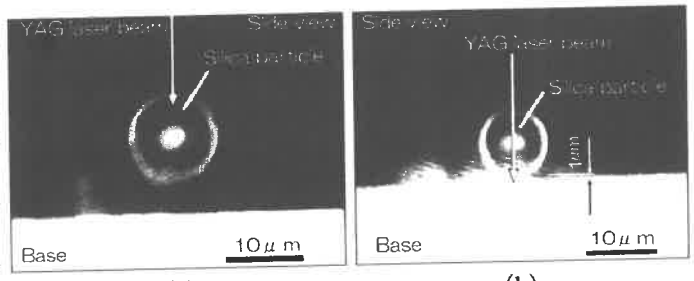

(a) (b)

Fig 4. Trapped silica particle in the air

3. Assembly of Three Dimensional Micro-Structure

3.1 Principle of assembly technique

The principle of assembly method is shown in **Figure 5**. Laser light is irradiated on a fine particle, shown in **Figure 5(a)**, to detach the fine particle from the base plate. Then Z stage is lowered to levitate fine particle to a certain assembly height in **Figure 5(b)**. **Figure 5(c)** shows that the fine particle is moved horizontally. Finally, in **Figure 5(d)**, the stage is raised to complete the assembly. According to this procedure, the assembly of three dimension micro-structure can be conducted.

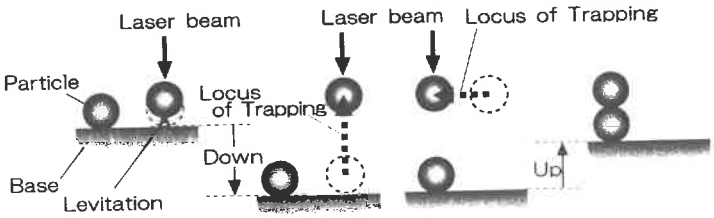

(a) (b) (c) (d)

Fig.5 Procedure of micro-assembly technique by laser trapping

3.2 Experiment of assembly in vertical direction

A series of consecutive photos of experiments are shown in **Figure 6(a)-(d)**. Silica fine particle (2) trapped in the air is shown in **Figure 6(a)**. In **Figure 6(b)**, the stage was lowered and particle (2) was transported to the position higher than particle(1) by vertical manipulation. **Figure 6(c)** illustrates the transportation of particle (2) to the top of (1) by horizontal manipulation. And finally, in **Figure 6(d)**, the stage was raised until two particles contacted. With the same procedure repeated, particle (3) and (4) were assembled in **Figure 6(e)**. Therefore a vertical assembly was completed.

3.3 Experiment of assembly in horizontal direction

If two fine particles adsorb each other by the surface tension force, the assembly in horizontal direction may be also possible. Hereby, the assembly experiments in horizontal direction were conducted, shown in **Figure 7(a)-(e)**. **Figure 7(a)** and **(b)** show particle (2) was assembled to the side of vertical assembled silica fine particle (1). Similarly, silica (3) was assembled. Furthermore, in **Figure 7(d)** and **(e)**, fine particle (4) was manipulated under (2) and (3). At this time, although part of the laser beam is disturbed by particle (2) and (3), manipulation still remains possible. Hence the more complex formation can be expected.

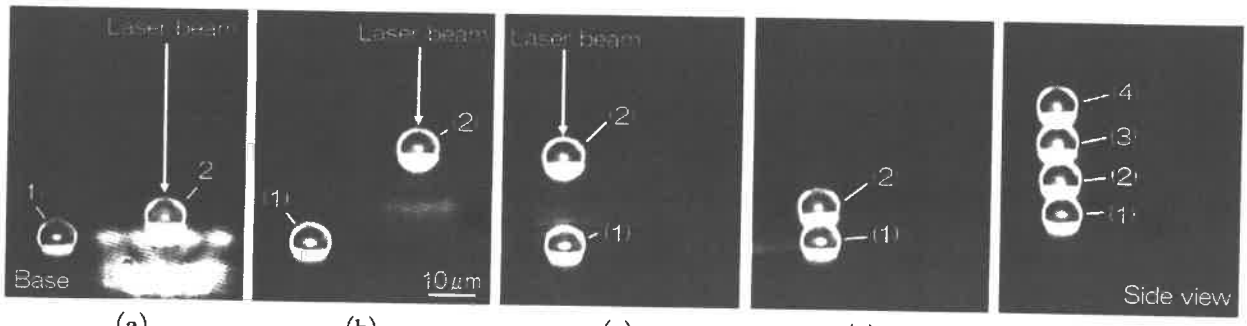

(a) (b) (c) (d) (e)

Fig.6 Silica particles assembled vertically

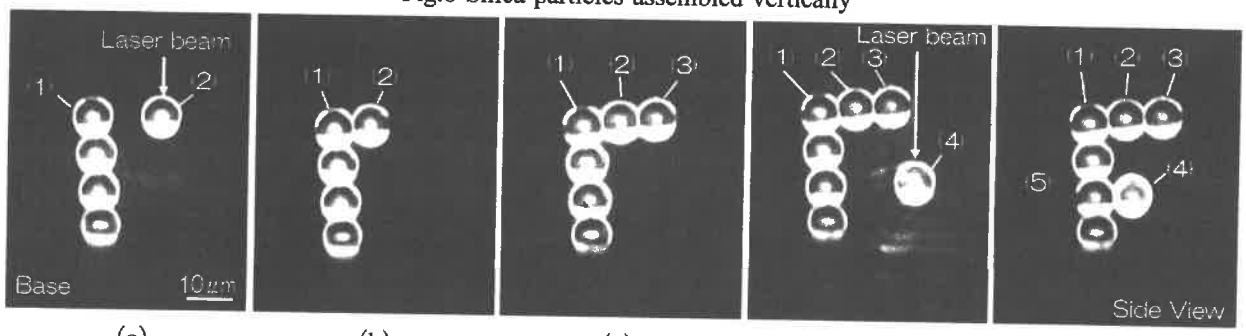

(a) (b) (c) (d) (e)

Fig.7 Silica particles assembled horizontally

3.4 Assembly of micro-structure in three dimension

After the basic assembly in vertical and horizontal directions was confirmed, the micro-structure in three dimension was conducted. Shown in **Figure 8**, the tetrahedron was assembled by 220 silica fine particles. Therefore, a three dimensional micro-structure was realized through the laser trapping technique developed in this research.

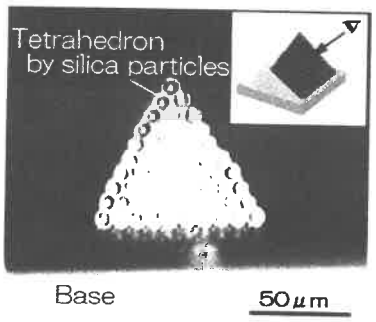

Fig.8 3-D micro-structure with a tetrahedron

4. Conclusions

The three dimensional manipulation technique of fine particles in the air and the assembly technique of micro-structure have been developed in this research. The following conclusions were obtained.

1) By using Q-switch, a fine particle can be easily trapped in the air, with an average of laser output under 120mW.

2) The fine particle was levitated 1μm high when the focal point of laser beam was set at the surface of base plate, lower than center of the particle. This phenomenon was difficult to be explained by the conventional theory.

3) The assembly of fine particles was supposed, and the assembly in vertical and horizontal direction succeeded in the experiments.

4) The assembly of three dimensional micro-structure is considered possible by using the technique developed in this paper.

-References-

1) A.Ashkin, Physical Review Letters, 24-4 (1970) ,156.
2) A.Ashkin, Biophysical Journal, Vol.16 (1992) ,569-582.

Nanoindentation by Using a Newly Developed Nanomachining Instrument

Wei Gao* , Robert Hocken**, John Patten**, John Lovingood**, and Don Lucca***

* Department of Mechatronics and Precision Engineering, Tohoku University, Sendai, JAPAN
** Center for Precision Metrology, The University of North Carolina at Charlotte, Charlotte NC
*** School of Mechanical and Aerospace Engineering, Oklahoma State University, Stillwater OK

INTRODUCTION

Single-point diamond turning (SPDT), which was originally developed for military use, has been improved to an ultra-precision machining technology for mass production of precision parts of ductile materials, such as computer hard disk substrates, print drums, polygon mirrors, etc. Recently, great efforts have being made to extend diamond turning to brittle materials such as germanium, silicon and even ceramics, and to push SPDT technology to a higher level of nanometer form accuracy and atomic surface finish. For this purpose, nanocutting experiments need to be carried out to understand the machining mechanism in the nanometer range[1].

A nanomachining instrument has been designed and built in the Center for Precision Metrology, The University of North Carolina at Charlotte[2]. This instrument, which is basically a single point diamond planer, was developed to perform two-dimensional nanocutting experiments especially on brittle materials. In this paper, we present some results of nanoindentation experiments using this nanomachining instrument.

DESCRIPTION OF THE INSTRUMENT

Figure 1 shows the schematic of the nanomachining instrument. A PZT tube scanner of 12.7 mm in diameter and 25.4 mm in length is employed to accomplish a maximum depth of cut of 4 μm with 0.1 nm resolution, and length of cut of more than 20 μm. The flexural stiffness and the axial stiffness of the PZT scanner are 6 x 10^6 N/m and 7 x 10^7 N/m , respectively. The sample is kinematically mounted on the PZT scanner, and the tool is held stationary during cutting. The infeed motion is monitored by a capacitance probe with a measurement range of 2 μm so that the nonlinearity and hysteresis of the PZT can be measured and compensated. There are two force sensors to measure thrust and cutting forces with a resolution of better than 0.2 mN. The stiffness of the structural loop is designed to be close to that of the PZT scanner. The cutting area is set to be very close to the top surface of the sample so that the machining process can be observed by optical microscopes and scanning electron microscopes.

EXPERIMENTAL SETUP FOR NANOINDENTATION

Nanoindentation experiments can be simply realized by replacing the cutting tool with a diamond

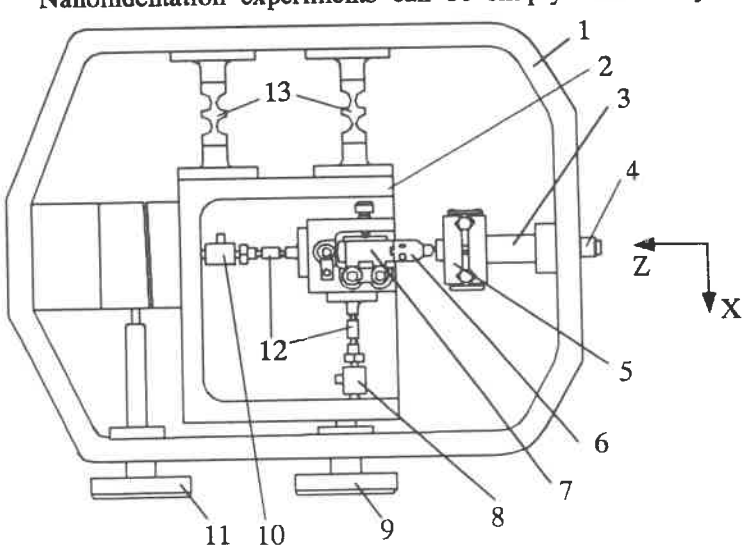

1: Main frame
2: Sub-frame
3: PZT
4: Capacitance probe
5: Sample holder
6: Tool shank and tool
7: Tool holder
8: Cutting force sensor
9: Y-directional fine positioning system
10: Thrust force sensor
11: Z-directional fine positioning system
12: Force decoupling flexures
13: Main flexures

Figure 1 Schematic of the nanomachining instrument

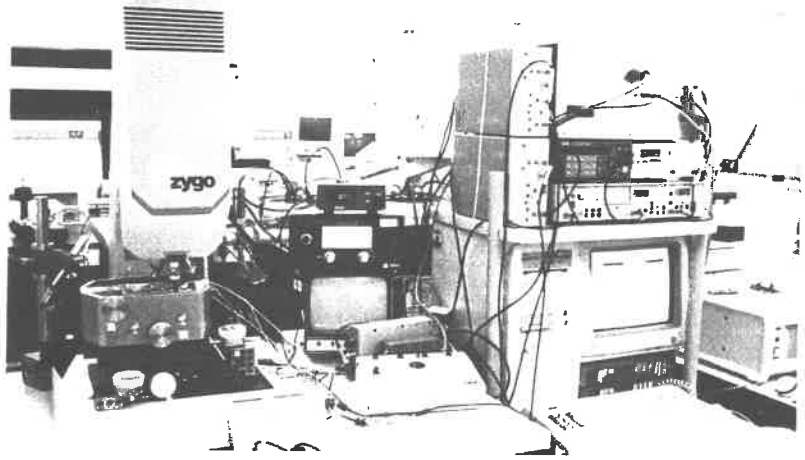

Figure 2 Photograph of the experimental setup for nanoindentation

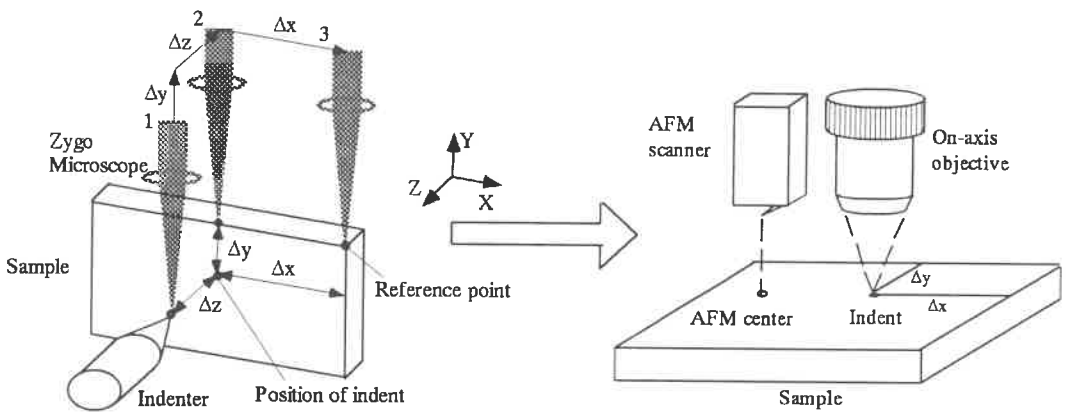

(a) Measuring the indent position on a Zygo (b) Imaging the indent on an AFM

Figure 3 Locating and imaging the indent

The load and the indentation depth can be measured by the thrust force sensor and the capacitance probe, respectively.

Figure 2 shows a photograph of the experimental setup for nanoindentaion. In nanoindentation experiments, it is desirable to know the position of the indent so that the indent can be easily imaged by an AFM. For this purpose, we mounted the instrument on a Zygo interference microscope. By using the high magnification optical microscope, we can clearly observe the tool-sample interface. As shown in Figure 3(a), the position of the indent on the sample can be measured precisely by respectively focusing the microscope on the indenter and a reference corner point on the top surface of the sample, and measuring the moving distances of the focal point. Once we obtain the coordinates Δx and Δy of the indent relative to the reference corner point, we can easily find the indent when it is imaged by an AFM. A PSI AutoProbe XL AFM system was used to image the indent. As can be seen in Figure 3(b), the PSI AFM provides an on-axis, high magnification view of the sample, making it easy to select an area of interest on the sample surface. After the on-axis view is focused on the indent based on the coordinates Δx and Δy, the system automatically moves the motor-driven sample stage so that the indent can be located in the AFM center, and can be imaged by the AFM.

MAKING TOOL-SAMPLE CONTACT

In nanoindentation experiments, it is important to establish sample-tool contact to nanometer accuracy. To make the tool-sample contact, we first manually move the tool toward the sample until the gap between the tool and the sample is within several microns by using the fine positioning system of the instrument with the visual feedback from the optical microscope. Then the sample is automatically moved closer to the tool by

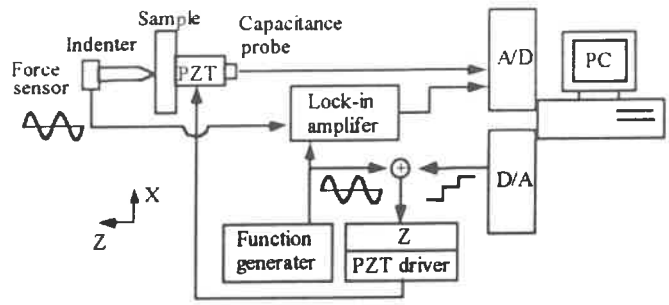

Figure 4 Diagram of making tool-sample contact

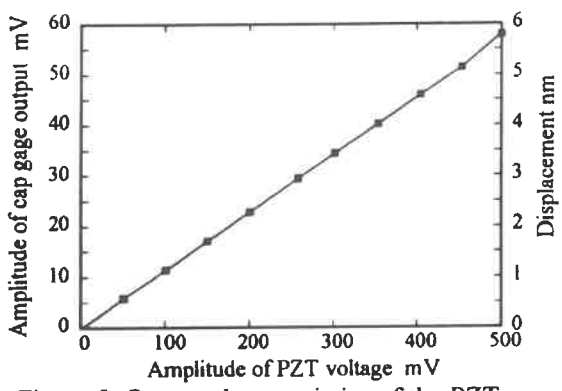

Figure 5 Output characteristics of the PZT

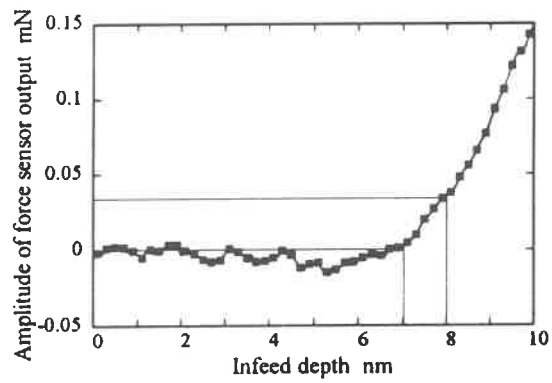

Figure 6 AC force output during making contact

using the PZT and small steps while monitoring the force sensor output. An increase of the force sensor output indicates the tool-sample contact, and the capacitance probe records the position of the PZT at the contact point.

The accuracy of establishing sample-tool contact is mainly determined by the sensitivity of the force sensor. Although the employed force sensor is quite sensitive, it is influenced by the system electronic noises and environmental mechanical vibrations. To improve the sensitivity of the force sensor, we convert the force to an AC signal. As can be seen in Figure 4, the sample is oscillated at a constant frequency by the PZT scanner when it is moved toward the tool. The output of the force sensor will correspond to the oscillation frequency of the sample once the sample comes in contact with the tool. The AC force sensor output is detected by a lock-in amplifier, which has the ability to detect and measure small AC signals down to a few nanovolts in the presence of noise.

In this case, the sample need to be oscillated at a stable amplitude of less than several nanometers. Figure 5 shows the characteristics of the PZT when being oscillated at small amplitude. The amplitude of the PZT displacement was measured by the capacitance probe. It can be seen that the output of PZT is stable in nanometer range.

Figure 6 shows the force sensor output during making tool-sample contact. The sample was oscillated at a frequency of 180Hz. It can be seen that the tool-sample contact can be made in nanometer accuracy.

INDENTATION EXPERIMENTS

Figure 7 shows the AFM image of indents on a silicon (111) surface. A diamond conical indenter with a radius of 5μm was used in the indentation experiments. Final depths are also shown in the figure. Figure 8 shows the load-displacement curve corresponding the number 2 indent in Figure 7. As can be seen in these figures, the developed instrument has the ability to perform depth-sensing nanoindentations.

Nanoindentations were also performed to evaluate the frame compliance (inverse of the frame stiffness) of the instrument. The frame compliance C_f can be expressed as [3]:

$$C_f = C_t - C_s = C_t - \frac{\sqrt{\pi}}{2E_r}\frac{1}{\sqrt{A}}$$

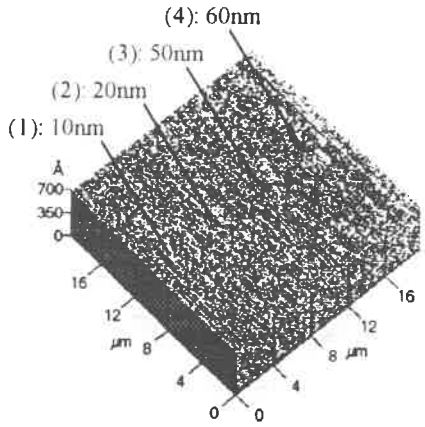

Figure 7 Indents on silicon

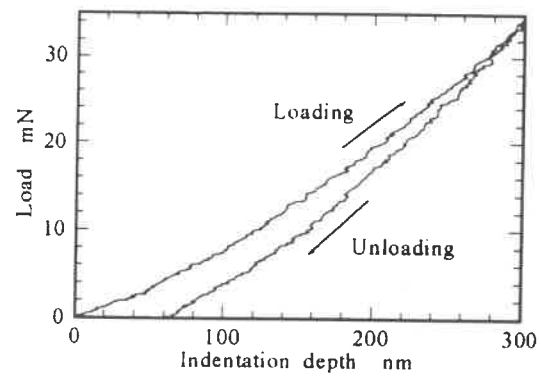

Figure 8 Indentation curve

Table 1 Measured frame compliance

NUM	C_t (nm/mN)	A (nm^2)	C_s (nm/mN)	$C_f=C_t-C_s$ (nm/mN)
1	7.874	2916432	7.454	0.420
2	5.291	6943482	4.831	0.460
3	4.237	11072425	3.826	0.411
4	4.149	12735762	3.567	0.582
5	4.082	11946209	3.683	0.399
Ave.				0.454

where C_t and C_s are the total measured compliance and sample compliance, respectively. E_r is the reduced modulus that is calculated from the elastic moduli and Poisson's ratios of the sample and indenter. A is the projected area of the indentation, which is measured by the AFM. Table1 shows the measured results. The frame compliance of the instrument was evaluated as 0.454nm/mN. Fused silica was used as the sample.

CONCLUSIONS

A newly developed nanomachining instrument has been used to perform nanoindentaion experiments. An experimental system has been constructed to make it easy to locate and image the indent. A technique has also been developed to make tool-sample contact with nanometer accuracy. Experimental results have shown that the developed instrument has the ability to perform depth-sensing nanoindentations. The frame stiffness of the instrument has also been evaluated from the indentation results.

ACKNOWDGEMENT

The authors would like to thank Dr. Stuart Smith for his valuable discussions. This work was financially supported in part by NSF and the Affiliates of Center for Precision Metrology. Wei Gao thanks the support from the Ministry of Education of Japan and the O.S.G. Science Foundation.

REFERENCES

[1] D. A. Lucca, et al: Effect of tool edge geometry on the nanometric cutting of Ge, CIRP, Vol.47/1/, (1998), pp. 475-478.

[2] R. Hocken, et al.: Design of second generation nanometric cutting instrument, Proc. of 1997 ASPE Meeting, pp. 386-389.

[3] W. C. Oliver and G. M. Pharr: An improved technique for determining hardness and elastic modulus using load and displacement sensing indentation experiments, J. Mater. Res., Vol. 7, No. 6, (1992), pp. 1564-1583.

A General Quantitative Method to Validate Instrument Calibration Techniques

Steven D. Phillips
National Institute of Standards and Technologies, Gaithersburg MD 20899

As international standards proliferate and laboratory accreditation programs become more common, there is increasing interest in the calibration of measuring instruments. For sophisticated instruments such as coordinate measuring machines (CMMs) or laser trackers, historically there has been little agreement on what constitutes a calibration of these instruments. Calibration services have often designed their own instrument assessment methods, which often differ widely among practitioners. Hence, a well-defined quantitative determination of whether a proposed assessment *method* of an instrument rises to the level of a calibration is clearly needed. A typical example is a claim that completing the performance evaluation described in the ASME B89.4.1 standard constitutes a CMM calibration. The standard itself, which was designed to promote commerce, carefully avoids the topic of CMM calibration. We will discuss some of the issues involved in an instrument calibration and how such a calibration claim might be assessed.

Recent thinking regarding the calibration concept might be summarized as stating that an instrument calibration specifies a well-defined measurand, a set of calibration conditions, and assesses all the reasonable error sources of the instrument that affect the accuracy of the measurement result. The accuracy is typically reported as an uncertainty statement that describes the dispersion of values about the measurement result that could reasonably be attributed to the measurand; sometimes the measurement bias is subsumed into the uncertainty statement and sometimes it is stated separately. Examining the previous "B89" CMM calibration claim, we see that the measurand is not identified. It is well known that the measurement of some features, e.g. partial arcs, are inherently less accurate than other features, hence the measurand must be identified and well specified. We will define the measurand of the proposed B89 calibration as the point-to-point length between any two points within the CMM workzone. Similarly, the conditions of the calibration are not defined; this would include specifying the probes, stylus configurations, environmental conditions and other factors that affect the CMM. For purposes of this example, we will adopt calibration conditions consisting of using a single probe and a simple straight stylus parallel to the ram axis, and ideal CMM environmental conditions (20 °C, negligible vibration etc.). More complex calibration conditions such as the use of multiple styli, stylus configurations that include a component perpendicular to the ram axis, or non-ideal environmental conditions would generally be included in an actual calibration but are omitted here for simplicity. Finally, we see that although a proposed error assessment method is described, i.e. as specified in the B89.4.1 standard, the construction of an uncertainty statement from the assessment results is absent. In this paper we will examine three different uncertainty statements and then explore how such statements might be validated.

While there are many different sources of CMM errors, in this paper we will only discuss those systematic errors associated with the CMM machine frame. For the calibration described above, the relevant B89 test procedures for these errors are the three linear displacement accuracy tests (LDAX, LDAY, LDAZ) and the volumetric performance test that yields the range of 20 ball bar measurements. We will construct different uncertainty statements using these test procedures and then attempt to validate the uncertainty statements based on computer simulation.

Conceptually, the validation procedure is based on a synthetic population of CMMs assumed to include any real CMM that a calibration service provider might encounter in actual practice. These CMMs are of different types, e.g. moving bridge or gantry, sizes, and most importantly, have different error characteristics. Some of these CMMs have large squareness errors, other have straightness errors, most have a mixture of many different parametric errors; some CMMs are in good working order and others have significant performance problems. The error behavior of each CMM is well defined, i.e. it has a specified set of parametric errors (in this paper we will consider only rigid body errors but this is easily

generalized), and the parametric error description of different CMMs is completely independent. Once a proposed calibration method is defined by specifying the measurand, calibration conditions, assessment method, and uncertainty statement construction, the proposed method can undergo validation. Consider selecting one CMM at random from the population of CMMs and performing the proposed assessment tests. Each aspect of the assessment test is computed just as it would occur in actual practice, e.g. for each LDA test, ten lengths are measured down the center of the workzone, parallel to the axis under consideration, and each of these 10 length errors is calculated. The results of the assessment tests are now available for the construction of the point-to-point length uncertainty statement (using a coverage factor of $k = 2$) applicable to future length measurements. To validate the uncertainty statement a length is generated between two randomly selected points in the CMM workzone. The details of this length (i.e. the start and end points) are available to the proposed uncertainty statement since the uncertainty may depend on details such as its the location, orientation and length. An uncertainty statement is produced and (since the complete error behavior of the CMM is known) the measurement error associated with this length can be calculated. If the error lies within the stated uncertainty then this is considered a success for *this particular length* measurement. Another length is randomly generated, an uncertainty statement produced, and the associated error is computed and compared with the uncertainty statement. This is repeated several hundred times so that a reasonable sample of all possible lengths in the workzone, i.e. the measurand, is produced. The percentage of uncertainty statements that are successful can now be computed. If at least 95 % of the cases are successful, i.e. their length errors lie within their associated uncertainty intervals, then the proposed calibration method is considered to have passed the validation test for *this particular CMM*. (The 95 % threshold is selected somewhat arbitrarily, see the discussion at the end of this paper.) Next, another CMM is drawn at random from the CMM population and the entire procedure repeated; note that this new CMM must undergo a new assessment as its error behavior is completely independent of the previous CMM. Once a few thousand CMMs have been selected from the CMM population and undergone the validation test, the percentage of CMMs that passed the test and the percentage of lengths that had their errors successfully contained within their uncertainty statements can be calculated. The validation test is outlined in Figure 1, and details of the verification test are briefly described in appendix I.

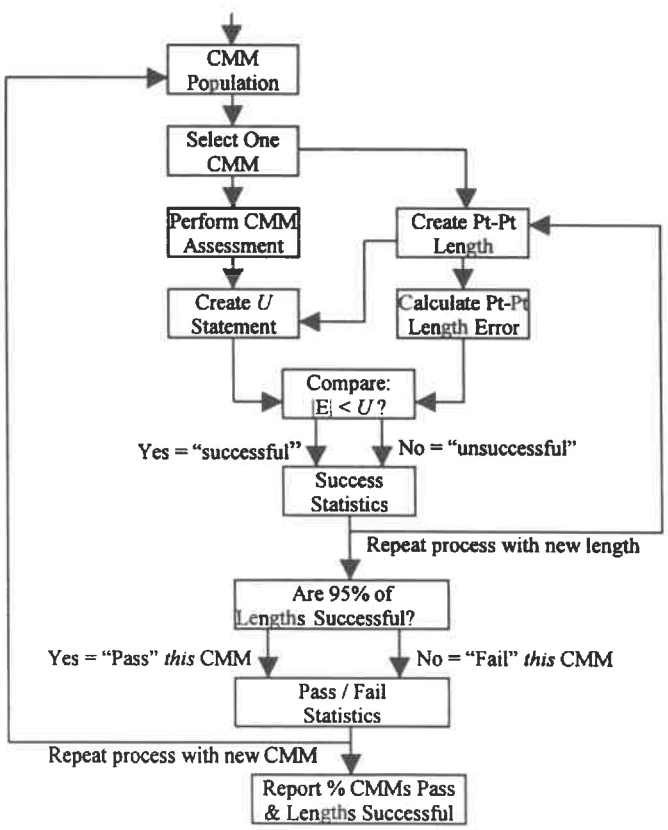

Figure 1:
An outline of the validation testing procedure.

Consider an uncertainty statement that proposes, for the calibration procedure previously defined, that any point-to-point length measurement within the workzone has an expanded uncertainty given by the root-sum-of-squares (RSS) of the three LDA values, i.e. $U = (LDAX^2 + LDAY^2 + LDAZ^2)^{1/2}$. Such an uncertainty statement seems inherently weak since the LDA tests are insensitive to many error sources, e.g. squareness. An interesting result of the simulation software is that this uncertainty statement passes 100 % of the (2,000) CMMs tested. It is relevant to note that the CMMs in the population have all the 21 parametric errors equally weighted, i.e. for a typical CMM all the parametric errors will be present at some level. This poses the question, "Does such an assessment method and associated uncertainty statement represent a valid calibration?" To address this issue we refer back to the definition of a calibration discussed earlier, and note that a calibration requires that all reasonable errors must be assessed by the procedure. Clearly the three squareness values are reasonable errors and subsequent simulation testing with the population of CMMs filtered to select those CMM with these parametric errors results in zero percentage of CMMs passing the validation test. Consequently, a proposed calibration procedure that involves an assessment involving only LDA tests fails to rise to the level of a calibration. This points out that the "reasonable errors" caveat requires that various sub-populations of CMMs, that display specific error behavior, be tested in addition to the general case of all errors being present. (A definitive statement about what constitutes "reasonable errors", and hence should or should not be tested in a validation program, is best left to standards committees.) Subsequent investigation of the RSS LDA method show that the technique passes 100 % of the CMMs having only scale errors, and 90 % of the CMMs having only angular motion errors (pitch, roll, and yaw on each axis); see Table 1. Hence the explanation of passing 100 % of the CMMs that have all error types present is a result of the over estimation afforded by examining the *range* of the errors (as specified by an LDA test value), together with the over estimation from the RSS summation (roughly a factor of 1.7) of the three LDA test results. Apparently these two over-estimations together compensate for the insensitivity to squareness and straightness errors for CMMs with equally weighted parametric errors.

Another possible uncertainty statement for point-to-point length measurements is given by the results of the volumetric performance test, i.e. the ball bar range (BBR) value. Since the volumetric performance test was designed to detect geometrical error in a CMM it is not surprising* that CMMs having only squareness errors or only angular errors pass the validation test at a level of 100 % and 99 % respectively. For CMMs having only scale errors, the validation test passes 93 % of the CMMs. The 7 % of the CMMs that failed, i.e. produced more than 5 % of the length errors outside of the uncertainty interval, typically have scale errors that are commonly biased, e.g. all positive; this common bias is undetectable using an uncalibrated ball bar. The results for the various sub-populations of CMMs examined are shown in Table 1, e.g. 98 % of those CMMs having only straightness parametric errors passed the validation test. This result involving straightness errors was an unexpectedly good showing considering that only half of the ball bar positions are sensitive to straightness errors and each position is only sensitive to the change in straightness between the two ball centers.

In light of the volumetric test's relative weakness with regard to parametric scale errors, we consider an alternative uncertainty statement that includes aspects of the LDA test since it is particularly strong on detecting scale errors. Instead of just adding the LDA and BBR results together we consider each point-to-point length in the testing program as a vector with a magnitude equal to its length and having components (L_X, L_Y, L_Z). We linearly "pro-rate" a portion of the appropriate LDA test result, e.g. LDAX (L_X/X_M), where X_M is the length of the X axis; similarly for the Y and Z cases. Finally we RSS these three terms together with the BBR value to create the expanded uncertainty statement; note that this

*For a CMM having only squareness errors, and a length extending between two extreme corners of the workzone, the length error may be relatively large. Apparently the fact the BBR value is a *range* of all the ball bar lengths, and that such extreme lengths occur infrequently, results in less than 5 % of the errors associated with randomly selected lengths lying outside an interval given by $\pm U = \pm$ BBR.

uncertainty statement depends on the length and orientation of the point-to-point length under consideration. As shown in Table 1, this significantly improves the passing percentage of CMMs having only scale errors.

Table 1. Three different Uncertainty Statements Tested Against Various CMM Populations

	RSS of LDAs		BBR		RSS of pro-rated LDAs & BBR	
CMM Population Description by Parametric Error Type	% Pass of CMMs,	% Success of all Lengths	% Pass of CMMs	% Success of all Lengths	% Pass of CMMs	% Success of all Lengths
Scale only	100	100	93	98.5	99	99.8
Straightness only	0	0	98	99.5	98	99.5
Angular only	90	98	99	99.5	99	99.7
Straightness & Angular	78	96	99	99.6	99	99.7
Squareness only	0	0	100	99.9	100	99.9
All Errors Present	100	99.9	98	99.5	99	99.8

(The % pass of CMMs, and the % success of all lengths are reproducible to 1 % and 0.5 % respectively.)

While we considered only three simple examples of uncertainty statements, all based on B89 test procedures, this validation methodology can be extended to any well-defined uncertainty statement and any assessment test procedure, including user concocted tests. Additionally the method can be applied to any system that can be mathematically modeled; we are currently developing this for laser tracker systems. In addition to being a useful tool in analyzing calibration procedures, this work raises several interesting questions. What are the "reasonable errors" of a measurement system? Since straightness errors and angular errors usually occur together and are kinematically related, should CMMs that only have straightness errors be considered "reasonable" errors? Similarly, on a mathematical level, what limitations should be placed on the functional forms of the parametric errors? Other interesting questions concern the application of uncertainty statements to the calibration process. For example, the standard interpretation of ($k = 2$) uncertainty statements implies that 5 % of the point-to-point length errors may lie outside their uncertainty intervals, however, due to the finite number of lengths tested per CMM, a 95 % success threshold may pass some "bad" CMMs and fail some "good" ones. Similarly, for any stated criteria for passing, what percentage of calibrated instruments are allowed to "fail" this criterion and still have the calibration *method* considered valid? For example, must each CMM population in Table 1 pass the validation test at the 100 % level? These and similar questions should keep standards committees debating for years.

Acknowledgments: This work was funded in part by the US Navy's CCG and the US Air Force's CCG program, and by NIST's computational metrology program.

Appendix I: Details of the CMM Population

In this paper we only consider CMM states that can be described by rigid body kinematics. Each state is composed of 18 functions and three scalar values. The functional form of the parametric error functions is created using low order polynomials and sinusoidal functions with random frequencies; an upper limit, typically of several cycles per axis, is imposed to maintain a plausible error form. Each term is given an independent random amplitude drawn from a uniform distribution in the interval (-1,+1). All terms of a particular parametric error, e.g. all terms in the functional form of X axis pitch, are multiplied by a prefactor which allows each parametric error to be given a relative weighting, including zero. Additionally, all 21 parametric errors are multiplied by another prefactor that controls the overall magnitude of the CMM errors. In our examples where all parametric errors are equally weighted, this means the prefactor for each parametric error is identical. However, for any one CMM state created, the various parametric errors can differ widely in their relative magnitudes due to the random nature of the amplitudes of each term in a parametric error expression. Hence the phrase "equally weighted" should be taken in a statistical sense.

PERFORMANCE EVALUATION FOR VISION COORDINATE MEASURING MACHINES

Chin-Chou Huang, X. David Zhang
Cummins Engine Company, Inc.
Fuel System Plant, M/C 41622
Columbus, IN 47201

INTRODUCTION

Non-contact vision (or video) type coordinate measuring machines (VCMM) have been used in the manufacturing industries for more than two decades. Common applications range from early efforts in two dimensional (2D) measurement of printed circuit boards to current three dimensional (3D) measurements of precision fuel system components. Despite the great growth in this market, very few attempts have been made to develop a method for VCMM's performance evaluation. The goal of this study is to investigate the correlation between error sources and measurement uncertainty and facilitate the development of a new VCMM evaluation methodology.

A common vision system in the VCMM includes a charge coupled device (CCD) camera, lens, and illumination lighting. With a vision system, images of a mechanical component are captured and then analyzed by image processing tools against inspection tolerances. For those features that can not be covered in a single field of view (FOV), the stage must move during the measurement. Therefore, the measurement uncertainty of a VCMM measurement will rely on the stage error, vision system error, image processing error, part surface/edge dullness, fixture error, sampling error, and environmental error. To evaluate a VCMM's performance, we will consider error sources unique to each measurement device: the stage, vision system, image processing and analysis. Though other error sources may be important in practical applications, they should be minimized to facilitate a standard evaluation technique.

In this study we intend to focus on the issues that will aid the users and purchasers when evaluating generalized claims regarding the VCMM's accuracy. Therefore, we evaluate the repeatability, optical focusing, reproducibility, and measurement bias, which are directly results from the stage error, vision system error, and image processing and analysis error. In addition we also investigate the sensitivity of the vision system to the geometric profiles of various measurants.

EXPERIMENTAL SETUP AND SAMPLING STRATEGY

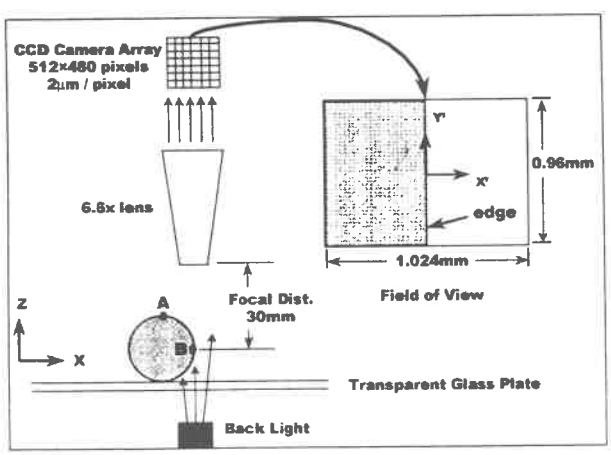

Figure 1 The optical parameters for the VCMM used in this study.

Environmental error and part form and surface finish error were minimized through the experimental design such as performing measurements in temperature controlled laboratory (20±0.25°C), vibration isolation floor, class 10,000 clean room, air circulation 300 cycles/hour, and using artifacts as the measurants. The VCMM used in this study has a work volume of 200×200×150mm in X, Y, and Z directions respectively. The VCMM optical parameters can be found in Figure 1. The stage travel speed is set at 200mm/sec, and glass scales with resolution of 0.5μm are attached on stage to provide stage travel reading. Only the backlight illumination system is used in this study, though there are other illumination types available. The backlight

illumination was chosen based on most VCMM manufacture's recommendation when measuring 3D artifacts as listed in Table 1.

The artifacts used in the performance evaluation are tabulated in Table 1. The gage pins are lying on the stage so that their diameters are calculated by measuring the distance between two edge lines. Sixty equally spaced points are taken along the circular edges. Thirty equally spaced points are taken along the linear edges.

Table 1 Artifacts used in this study

Geometry	Artifacts	Feature measured	Size (mm)	Certified uncertainty
	Gage bore	ID	2,11 25,40	0.125µm
	Gage sphere	OD	4,8 16,24	0.125µm
	Gage pin	OD	5,8 15, 25	0.125µm
	Gage block	Length	25,50 100	0.125µm
	Chromed scale	Length	25,50 75,10	0.25µm
	Chromed block	Length	13	0.25µm
	Chromed hole	ID	6.35	0.25µm

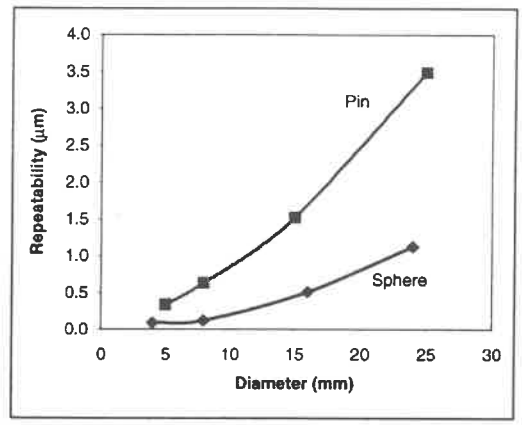

Figure 2 Measurement repeatability for gage pins and spheres by using the edge-focusing tool.

REPEATABILITY

Reference to ANSI/ASME B89.1.12M [1], this test is designed to check only the non-repeatable, i.e., random error at a particular position in the work zone. The definition for our repeatability test is two standards deviation (2σ) of the size variation determined by ten successive measurements under the same condition (same artifact, location, sampling, and fitting strategy.) The edge-focusing tool was used to determine the best contrast edge during each of the ten repeat measurements. All the artifacts listed in Table 1 are tested, and the results show that all the artifacts, except gage pins and spheres, have repeatability within 0.25µm. In the chromed artifacts the repeatability was within 0.16µm. For the pins and spheres, as shown in Figure 2, the bigger the diameter, the worse the repeatability. We will have further discussion of this phenomenon in next section.

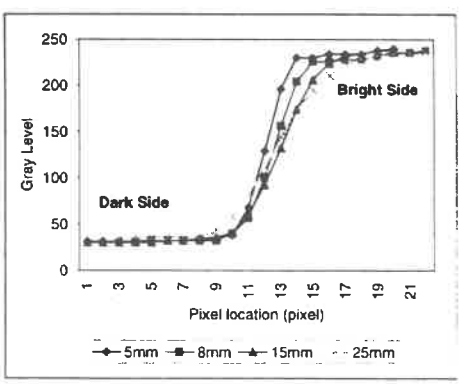

Figure 3 The gray level variation at the edge transition area for gage pins.

FOCUSING

Due to optical diffraction, it is observed that the smaller the diameter of the pin or sphere, the sharper and clearer the captured image edge. To illustrate the dullness of the image edge, the corresponding image gray level variation and gradient at the edge transition area are shown in Figures 3 and 4. Because of this dullness in the edge transition area for large diameter pin or sphere, the focusing-tool can not obtain a repeatable best contrast position. Consequently, we observed the greater repeatability deviation in larger diameter pins and spheres. Extraordinarily, better repeatability and accuracy are obtained by using the surface-focusing tool to obtain focused point on the top surface of the pin or sphere in the Z direction (point A shown in Figure 1), then replacing the edge-focus tool

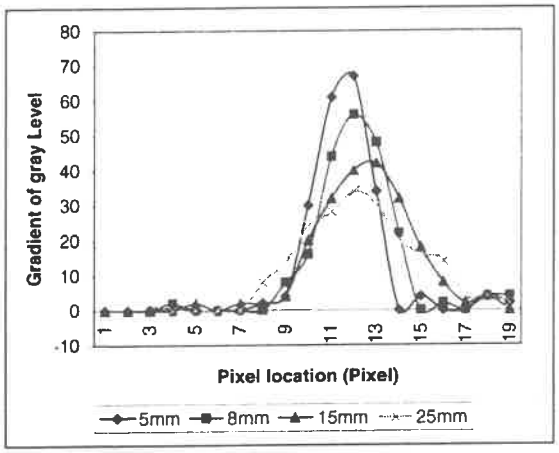

Figure 4 The gray level gradient at the edge transition area.

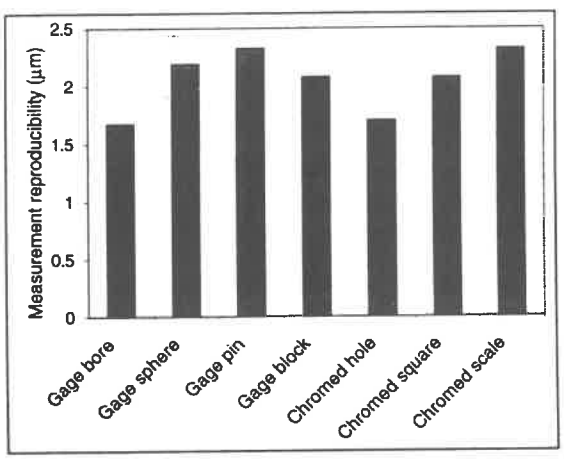

Figure 6 The measurement variation range in each geometric category between five different locations.

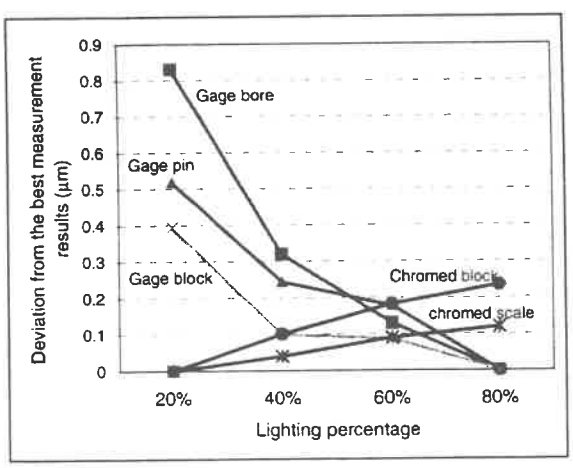

Figure 7 The measurement deviation from the best value illumination percentage.

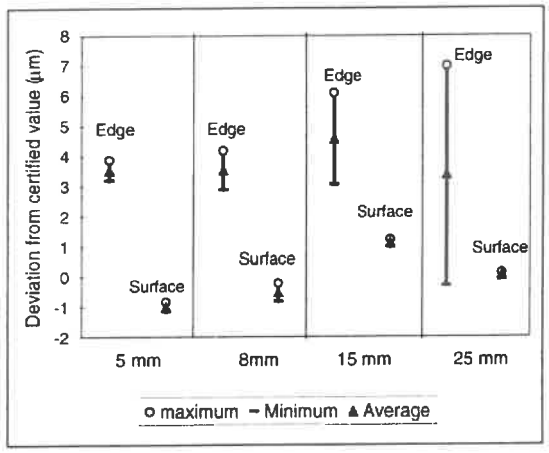

Figure 5 The measurement repeatability for gage pins by using different focusing tool.

by dropping a distance of the nominal radius of the pin in the Z direction (to point B in Figure 1). The improvements are shown in Figure 5. Using the same edge finding technique for pins and spheres in other working areas, the same level of measurement difference is observed.

REPRODUCIBILITY

In this test, we are trying to investigate the measurement variation between different working areas for the same artifact under the same testing conditions. According to the Germany VDI/VDE standard [2], the working area is divided into four quartered zones plus the central zone of the stage. To minimize the focusing error, the surface-focus tool was used in the gage pin and sphere tests. For the other artifacts, the edge-focus tool was adopted. In each of the test, the size is determined by the average of ten successive measurements. For the same artifact, comparing the five measurement values, the range of the deviation is the measurement reproducibility. In each geometric category, we selected the worst reproducibility value and plotted these in the Figure 6.

LIGHTING

The VCMM used in this test allows user to mechanically set the lighting power percentage to illuminate the measurants in a measurement procedure, such that the CCD camera can "see" the image of the measurants. In this study different values of lighting power percentage are used to investigate the lighting. Figure 7 only shows the light effect on bore (25mm), pin (15mm), block (100mm),

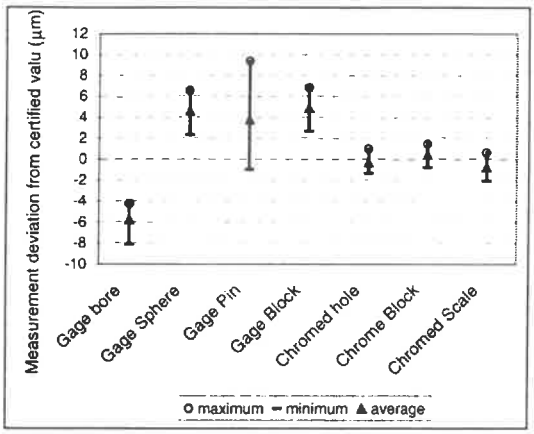

Figure 8 The measurement bias and variation range associated with different geometric artifacts.

and the chromed artifacts. However in the other 3D artifacts, the stronger light intensity still results better measurement accuracy. In contrast, for 2D chromed artifacts we observed the weaker light intensity produced better measurement results.

MEASUREMENT BIAS

In previous sections, we only compare the variation range but not include the variation from the certified value. Whenever the edge focus tool is used, comparing the measurement results with the certified values, no matter the geometry and size, significant systematic error is observed in the 3D components. Figure 8 shows the average measurement errors for different geometry artifacts. The associated deviation with the measurement bias are the effects from sizes, lighting, focusing repeatability, stage calibration, and the unidentified error factors.

CONCLUSION

It is found that the image focusing is a major factor of the measurement uncertainty for 3D components in our testing machine. By using the top focus (or surface focus) approach the experimenters obtained more accurate and repeatable results than using the edge focus approach. Experiments show that the illumination intensity is a relatively minor factor in the measurement uncertainty, compared to the focusing and stage errors. It also is observed that systematic errors of oversized and undersized occurred in the outer diameter and inner diameter measurements respectively. By knowing the correlation between the measurement uncertainty and error sources, one can design a procedure to assess the most critical error factors in the performance evaluation. Thus, a VCMM machine performance evaluation procedure can be established for initial purchasing acceptance and periodical performance assurance.

REFERENCE

1. ANSI/ASME B89.1.12M (1990), "Methods for Performance Evaluation of Coordinate Measuring Machines,"ASME, New York, NY, 1990.
2. German standard VDI/VDE 2617 Part 6, "Accuracy of Coordinate Measurement Machines, Coordinate Measuring Machines with Optical Probes-Basics."

Pixel Size Calibration of Video Probe Measuring Machines

James G. Salsbury
Center for Precision Metrology
University of North Carolina at Charlotte

Coordinate measuring machines (CMMs) equipped with video probing systems are becoming more and more popular for dimensional metrology in a variety of industries. The typical off-the-shelf machine being commonly implemented today utilizes a charge-coupled device (CCD) camera mounted to a two or three axis measuring machine frame. As with any type of measuring machine, there are calibration issues with the probing sensor. For a video probe measuring system, one of the key issues is the calibration of the actual magnification of the video system. This calibration process is usually referred to as the calibration of the pixel size, which is in reference to the use of a CCD camera with a particular array of pixels. The various magnification objectives (or zoom lens) will result in different amounts of the measured surface being mapped onto the pixel array. The pixel size calibration process is essentially the calibration of the video probe scale relative to a traceable length standard.

The most common method to calibrate the pixel size is to measure some type of artifact with calibrated features that fit completely inside the field of view of the video sensor for the particular magnification of interest. The ratio between the calibrated value of the feature and the number of measured pixels is used to calibrate the pixel size. Another less commonly used technique for pixel size calibration does not require an externally calibrated artifact but rather utilizes the scales of the measuring machine's own stage, i.e. a self-calibration technique.

In this paper the uncertainty of the process used to calibrate the pixel size is investigated. The effect of various types of calibration artifacts, such as chrome-on-glass circles, linewidths, and grid patterns are evaluated and contrasted. General equations are developed that allow the uncertainty of the pixel calibration process to be estimated for various types of machines and magnification levels. Experimental results are also presented.

Application and Assumptions

This paper is concerned with typical video probe measuring machines that are being implemented everyday in various industries. The application of these machines is to be considered general in nature. The calibration of the video probe is not considered to be specific to a particular measurement. If only a specific feature is to be measured with a machine of this class, then the calibration process should be developed to imitate the application in order to reduce the measurement uncertainty [1,2].

There are a large number of video probe CMM manufacturers; however, the vast majority of the machines, and the ones considered in this paper, fall into a class defined by a scale resolution of around 0.5 to 0.1 micrometers, a measuring field of view from 6 mm to 0.25 mm, and the use of a CCD camera with around 500-800 pixels linearly. These machines typically have a quoted accuracy in the neighborhood of 5 to 10 micrometers or less. Machine manufacturers handle the integration and calibration of the video probe in different manners. The analysis presented here will be kept general and will also only consider one axis for simplicity.

In estimating the measurement uncertainty, the approach of the ISO *Guide to the Expression of Uncertainty in Measurement* (GUM) [3] will be utilized. In this paper, a number of uncertainty sources will be considered negligible and others will be evaluated in specific manners based on convenience. The uncertainty of all the contributors will be estimated based on available data, experience, and knowledge, and will utilize the Type B evaluations allowed by the GUM. Specific uncertainty sources that will not be considered include distortion and illumination variation across the field of view and thermal effects.

Artifact Based Calibration

There are a variety of two-dimensional artifacts available that can be used for the pixel size calibration. The most common are chrome-on-glass where the features are circles, squares, grids, or lines. National labs such as NIST and PTB have programs for the calibration of some of these artifacts with uncertainties around 10 to 50 nm [1,4]. Various commercial calibration labs are also capable of calibrating these types of artifacts with uncertainties ranging from around 100 nm to 1 μm and up depending on capability and cost. When one of these types of artifacts is used

for the pixel size calibration, such as shown in Figures 1 and 2, the features to be measured need to be positioned completely inside the range, or the field of view, of the video probe sensor. With the initial pixel size set to some value, C_o, the feature is measured, and the calibrated value, L_c, is compared to the measured value L_m. The calibrated pixel size, C, is therefore defined by

$$C = C_0\left(\frac{L_c}{L_m}\right) \tag{1}$$

For the purposes of evaluating the uncertainty of the pixel size calibration, this equation is rewritten in terms of the number of measured pixels, N. Since $L_m = NC_o$, Eq. (1) can be reduced to

$$C = \frac{L}{N} \qquad \text{where L is used in place of } L_c. \tag{2}$$

In accordance to the GUM, the uncertainty of the pixel size, C, can be expressed as follows:

$$u_C^2 = \left(\frac{\partial C}{\partial L}\right)^2 u_L^2 + \left(\frac{\partial C}{\partial N}\right)^2 u_N^2 + 2\frac{\partial C}{\partial L}\frac{\partial C}{\partial N} u_L^2 u_N^2 \tag{3}$$

Since L and N are independent of each other, Eq. (3) reduces to the following, with the appropriate sensitivity coefficients also included:

$$u_C^2 = \frac{1}{N^2}\left[u_L^2 + \left(\frac{L}{N}\right)^2 u_N^2\right] \tag{4}$$

The uncertainty contributors, u_L and u_N, need to be estimated. Using a Type B evaluation, the uncertainty in the number of measured pixels, u_N, can be estimated for this class of machine using data and information from available literature [1,5,6,7,8]. Though there are a variety of error sources associated with using a video probe that might be included in the estimate of u_N, a detailed analysis of those sources is beyond the scope of this paper. Based on the available published data from the literature, the worst expected error is estimated to be 0.2 pixels. A Gaussian distribution for this uncertainty is assumed with the 95% limits being defined by +/- 0.2 pixels. This results in

$$u_N = 0.1 \quad \text{pixels} \tag{5}$$

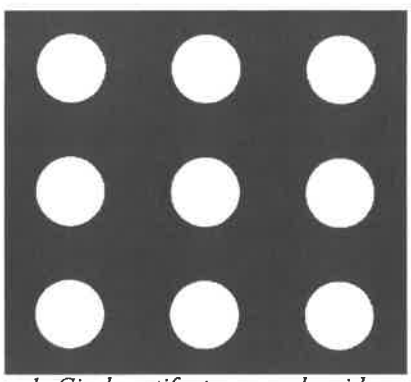

Figure 1: Circle artifact as seen by video probe.

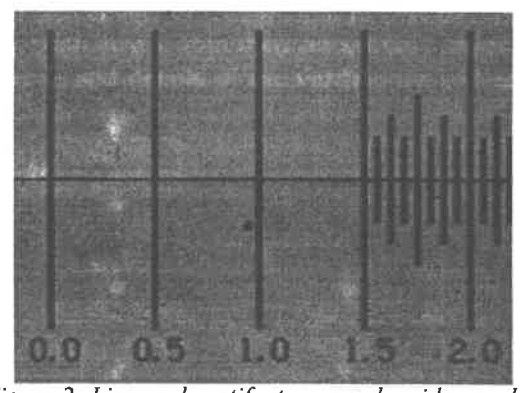

Figure 2: Line scale artifact as seen by video probe.

In this paper, two different types of artifacts are considered. The first type has the calibrated features being unidirectional in nature, such as distances between feature centers. The second has the calibrated features being bidirectional in nature, such as linewidths and circle diameters. Due to errors in edge finding, there is more uncertainty in the measurement of bidirectional features than unidirectional ones [1,5,6,7]. Since this bidirectional error will manifest itself in the measurement process as an increase or decrease in the size of the measured feature, the additional uncertainty due to using bidirectional features is combined into the uncertainty contributor u_L as

$$u_L^2 = u_a^2 + u_b^2 \tag{6}$$

where u_a is the estimated uncertainty of the calibrated value of the artifact and u_b is the additional uncertainty due to the use of a bidirectional artifact. Eq. (6) assumes independency with sensitivity coefficients of one. With a properly calibrated artifact, a Type B evaluation for the uncertainty estimate of u_a should be straightforward using the calibration certificate from the supplier. The estimate of u_b is more challenging; however, there are data available in the literature that can be used to make a Type B evaluation for this class of machine [5,6,7]. Based on the available data, plus additional data gathered on the machines under test, the maximum bidirectional error is estimated to be

approximately 0.35% of the field of view being used. For the purposes of this paper, the field of view is defined by a single number equal to the diameter, D, of the largest circle that can be circumscribed in the two-dimensional range of the video sensor when using a specific magnification. To estimate the standard uncertainty u_b, it is assumed that the bidirectional error follows a Gaussian distribution and that the maximum error defines the 95% limits of the distribution. The standard uncertainty can then be estimated by

$$u_b = \left(\frac{0.0035}{2}\right)D = 0.00175D \tag{7}$$

Eqs. (4) to (7) can be combined together to express the uncertainty of the artifact calibration approach, U_{AC}, using a coverage factor, k = 2, as

$$U_{AC} = \frac{2}{N}\left[u_a^2 + \left(\frac{0.1L}{N}\right)^2 + (0.00175\ D)^2\right]^{1/2} \tag{8}$$

where D is defined as equal to zero if the measured features are unidirectional in nature.

Self-Calibration Approach

An external artifact is not necessary to calibrate the pixel size. It is possible, instead, to calibrate the pixel size using the scales of the machine stage. This process simply requires a small measurable feature to be fixed to the stage and then moved across the field of view. The location of the small feature is measured in two positions along with the distance the machine stage is moved. This technique has been shown to be easily feasible on all video probe CMMs tested to date. The process is shown pictorially in Figures 3 and 4. In Fig. 3, the location of the small circular feature is measured along with the coordinates of the cross-hair shown. The stage is then moved and the location of the circular feature and cross-hair are again measured as shown in Figure 4. The difference between the two measurements of the cross-hair, L, which is independent of the video probe, determines the distance moved by the stage. The difference between the two measurements of the circular feature, δ, which is nominally zero, represents an amount of error that is the resultant of any error in the initial calibration of the pixel size. The self-calibration approach can be represented by the following:

$$C = C_0\left(\frac{L}{L-\delta}\right) \tag{9}$$

To estimate the uncertainty in the self-calibration of the pixel size, C, it is convenient to express δ in terms of the number of pixels, N, where $\delta = L - NC_o$. Eq. (9) can be shown to reduce to Eq. (2). Eqs. (2), (3), and (4) therefore apply to both the artifact and the self-calibration approaches, with the only difference being that L is defined as the length over which the self-calibration is done, instead of the length of the calibrated artifact feature.

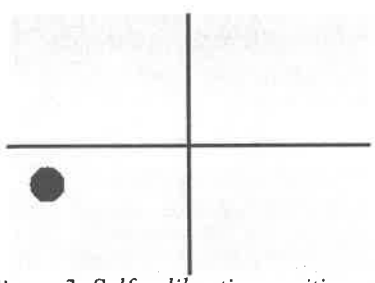

Figure 3: Self-calibration position one

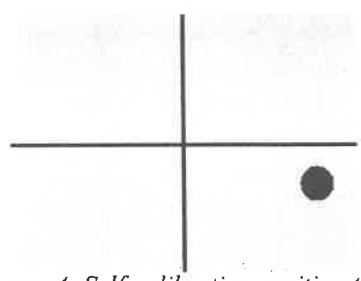

Figure 4: Self-calibration position two

As discussed previously for the artifact based approach, Eq. (5) also applies for the uncertainty of the pixel size, u_N, for the self-calibration approach. The uncertainty contributor, u_L, however, needs to be estimated. This is done by assuming that this uncertainty contributor can be estimated by two different uncertainty sources, u_{LDA}, the uncertainty due to linear displacement accuracy (or LDA) of the machine axis moved, and u_R, the uncertainty due to the apparent non-repeatability of the measuring system. Assuming that these contributors are independent with sensitivity coefficients equal to one, then u_L can be expressed as

$$u_L^2 = u_{LDA}^2 + u_R^2 \tag{10}$$

The uncertainty due to the apparent non-repeatability, u_R, is estimated with a Type B evaluation from machine specifications and from prior experience with the particular machines under test. In the context used here, u_R represents lack of repeatability in the machine stage and does not include effects of the video probe itself.

The estimation of the uncertainty due to the LDA is a bit more challenging. Well-accepted performance standards exist for calculating the LDA of measuring machines [9] and machine tools [10]. There are not, however, any generally accepted methodologies for reducing the LDA of a longer axis to generate uncertainty estimates over very short distances (where L<<full axis travel). A method is proposed here to estimate the maximum displacement error over a short distance by assuming some knowledge regarding the typical form of the error across the full travel of the axis. All the existing standards assume slowly spatially varying errors and have defaults for measurement points around every 25 mm or from 10% to 20% of the maximum traverse distance of the axes. From this information, the shortest likely wavelength of the displacement error, λ, is estimated; that assumption, along with an estimate of the maximum amplitude, A, is used to estimate the worse case displacement error over a much shorter distance, in particular, over the calibration length, L. The equation of the displacement error, δ, due to this shorter wavelength is defined by

$$\delta = A \sin\left(\frac{2\pi}{\lambda}\right) X \tag{11}$$

where X is the nominal motion of the machine axis. The maximum rate of change of this error is equal to the maximum slope of Eq. (11). Assuming that $L << \lambda$, then the error at the maximum slope is approximately linear over the distance L, and therefore the maximum error over the distance L can be approximated by the maximum slope multiplied by L. Assuming a triangular distribution for this uncertainty contributor with the higher and lower limits being equal to plus or minus the maximum error results in the following:

$$u_{LDA} = 2.5\left(\frac{AL}{\lambda}\right) \tag{12}$$

Eq.(12) is combined with Eqs. (10), (5), and (4) to express the uncertainty of the self-calibration approach. Applying a coverage factor, k =2, results in

$$U_{sc} = \frac{2}{N}\left[u_R^2 + \left(\frac{2.5AL}{\lambda}\right)^2 + \left(\frac{0.1L}{N}\right)^2\right]^{1/2} \tag{13}$$

Experimental Results

Experimental tests where done on a View Voyager and a Werth Inspector, two different video probe CMMs located in the Center for Precision Metrology at UNC Charlotte. The View has 0.1 μm scales and is a larger floor mounted machine; the Werth has 0.5 μm scales and is a smaller bench-top machine. Tests were done on both machines using the same 2X (D=3 mm, NA=0.055) and 20X (D=0.3 mm, NA=0.42) plan apochromat objectives from Mitutoyo. In reference to Eqs. (13) and (8), the estimates for the View machine are u_R = 200 nm and A = 2000 nm. For the Werth, the estimates are u_R = 300 nm and A = 3000 nm. For both machines, λ was estimated at 25 mm. The values for the remaining variables, u_a, N, and L, were determined from the specific artifact and sensor range used.

For each machine at each magnification, the pixel size was calibrated using three trials of six different methods, for a total of 72 different calibrations under various conditions. Of the six methods, two utilized unidirectional artifacts, two utilized bidirectional artifacts, and two utilized the self-calibration approach. The results for the Werth machine tests with the 20X objective are shown in Fig. 5. The pixel size deviation in the plot is determined by subtracting the pixel size of each calibration from the average of the three calibrations of the method with the lowest estimated uncertainty (trials 13-15 in this case). The plot shows both the calibration results and the estimated uncertainty. Trials 1-3 were done with an unidirectional circle artifact (see Fig. 1), trials 4-6 were done using the self-calibration technique, trials 7-9 and 10-12 were done with two different bidirectional circle diameter artifacts, trials 13-15 were done with a line scale calibrated at NIST (see Fig. 2), and trials 16-18 were done using the self-calibration technique using an average of nine independent trials.

To compare all 72 results with each other, the deviation of each was divided by its estimated uncertainty. These results are shown in Fig. 6. If the uncertainties were estimated well, then approximately 95% of the data would fall between ±1 in this plot. As can be seen in the plot, six points lie outside this band, which results in 91.7% of the points being inside. Three of the points are very near to being inside the band; if they are considered in, then the percentage increases to 95.8%. In addition, the standard deviation of the data shown in Fig. 6 is approximately equal to the ideal value of 0.5. Based on this limited sample size, the models used to estimate the measurement uncertainty seem to work well. In addition, the estimated uncertainties of the self-calibration techniques are less than the uncertainties of the calibrations with the bidirectional artifacts and are close in magnitude to the unidirectional tests.

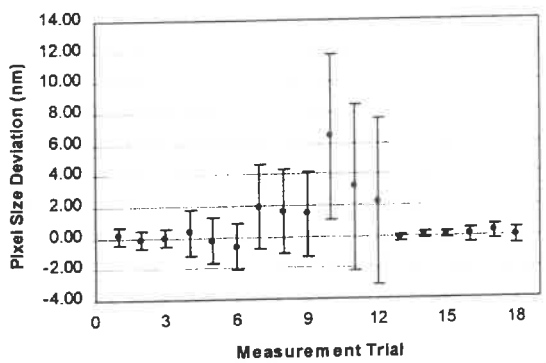

Figure 5: Werth 20X results and uncertainty

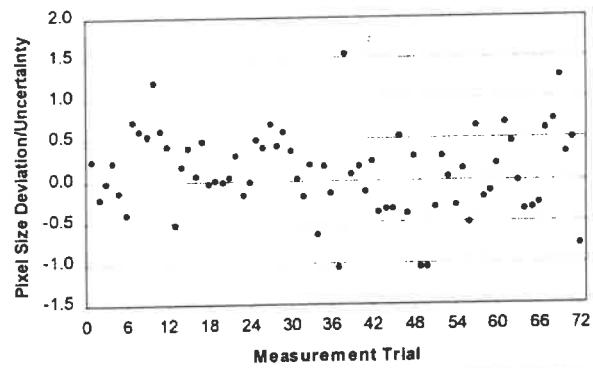

Figure 6: All results, expressed as (Deviation/Uncertainty)

These results indicate that the use of artifacts for pixel size calibration may be unnecessary except in cases where extremely high magnification and accuracy is needed or where the quality of the machine scale is poor. In this work, only the trials that were done with a NIST calibrated line scale, with a standard uncertainty of 10 nm, gave significant improvements over the self-calibration approach. For the class of machines considered in this work, extremely high magnification objectives are not common (rarely 50X or higher), and the machines will most likely have adequate scale accuracy for use with the self-calibration approach.

Acknowledgments

This work was made possible through the support of the National Science Foundation I/UCRC program and all the affiliate members of the Center for Precision Metrology at UNC Charlotte. In particular, the author would like to acknowledge the support of GSI-Lumonics (View Engineering). The author would also like to thank Scott Schmidt at Siecor Corporation and Art Whistler at Werth America for the use of artifacts that were critical to the experimental studies and Dr. Robert Hocken at UNC Charlotte for his review of this work.

References

1. Vezzetti, C., Varner, R. N., and Potzick, J. E., *Bright-Chromium Linewidth Standard, SRM 476, for Calibration of Optical Microscope Linewidth Measuring Systems*, NIST special publication 260-114, National Institute of Standards and Technology, Gaithersburg, MD, January 1991.
2. Hunsicker, R. J., Patten, J., Ledfort, A., Ferman, C., and Allen, M., "Automatic Vision Inspection and Measurement System for External Screw Threads," Journal of Manufacturing Systems, 13(5), 1994.
3. *Guide to the Expression of Uncertainty in Measurement*, International Organization for Standardization, Geneva, Switzerland, 1995.
4. Haβler-Grohne, W., and Bosse, H, "Characterization of the long-term reproducibility of 2D coordinate photomask calibration at the PTB", *Proceedings of the 1st International Conference of the European Society for Precision Engineering and Nanotechnology*, Bremen, 1999.
5. De Chiffre, L., and Hansen, H. N., "Metrological Limitations of Optical Probing Techniques for Dimensional Measurements," *Annals of CIRP*, 44(1), 1995.
6. Thakkar, H. H., *Characterization of Hybrid Coordinate Measuring Machines*, UNC Charlotte Master's Thesis, 1998.
7. Garces, A., Huser-Teuchert, D., Pfeifer, T., Scharsich, P., Torres-Leza, F., and Trapet, E., *Performance Test Procedures for Optical Coordinate Measuring Probes*, Report on contract no. 3319/1/0/159/89/8-BCR-D(30), European Communities, Brussels, 1993.
8. Kim, S., "Measurement Uncertainty Limit of a Video Probe in Coordinate Metrology," *Annals of CIRP*, 45(1), 1996.
9. ASME B89.4.1-1997, *Methods for Performance Evaluation of Coordinate Measuring Machines*, American Society of Mechanical Engineers, New York, NY, 1997.
10. ASME B5.54-1992 (R1998), *Methods for Performance Evaluation of Computer Numerically Controlled Machining Centers*, American Society of Mechanical Engineers, New York, NY, 1998.

Vector Touch Sensor Probe

Shane Woody and Stuart Smith
University of North Carolina at Charlotte, Precision Engineering, Charlotte NC

Introduction

Current contact sensors produce a single pulse or proportionate signal upon being contacted against a surface. The objective of the current sensor development is to determine the vector normal when the spherical tip of the probe is contacted with a solid surface. It is envisaged that this will be used in co-ordinate measuring machines and other applications requiring contact based information. A Vector Touch Sensor (VTS) has two unique features. Firstly, present touch trigger probes produce a single co-ordinate set per measurement and, therefore, require two points of contact to obtain an estimate of local slope. In contrast the VTS probe obtains position and slope from a single measurement thereby potentially doubling the Nyquist frequency. Subsequently, for scanning applications, there will be a potential doubling of the sampling speed for a given accuracy of profile reconstruction. Secondly, current touch trigger probes are limited in size. Consequently, metrological applications such as diesel injectors, MEMS and fiber optic technologies may be impractical. Contrary to market designs, VTS probes are not limited by geometrical scaling and thereby, may be adapted for the measurement of work-pieces with significantly smaller dimensions. The current sensor is fabricated with phase lock loop signal conditioning and piezo-electric ceramic (PZT) sensor/actuator pairs. This abstract presents a theoretical ideal for performance evaluation, a method for probe signal analysis, results from the characterization of three successive probe designs and shows a fourth generation probe.

Principal of operation/definitions

The principal of operation for VTS probes is based on the characteristic properties of both resonant frequencies and the associated phase response. Classically, output strains to input energy ratios are substantially higher at harmonic resonance and the phase response will lag by 180 degrees [1]. The rate of phase change with input frequency is determined by energy dissipation mechanisms. In general, the VTS resonating system is composed of a rigid rectangular metal bar with a ruby sphere attached to one end. Several pairs of piezo-electric elements (PZTs) are bonded on each side of the metallic bar. Functionally, PZTs will expand and contract when energized by an AC signal and vice versa. Hence, several PZTs function as actuators to the probe and additional PZTs detect the strains as they propagate through the rectangular body [2].

Consider a single lateral vibration about the axis of the metal bar while a constant force is applied about the VTS sphere. The magnitude of phase change will be greatest when the contact is co-linear to the vibrating axis and least along the orthogonal axis. Uniquely, this effect will be independent for each orthogonal, lateral vibration as long as the resonating frequencies are distinct. Thus, it might be expected that, at resonance, each lateral axis' phase response for a constant force load about the sphere varies harmonically with angle of contact, θ, figure 1. Additionally, phase response for the resonating longitundinal axis (z-axis) will also vary harmonically with angle β as shown in figure 2. In this case, phase response is greatest when the applied force is contacted on

top of the sphere or directly in line of the z-axis. Theoretically, phase response for the two lateral axes and single longitudinal axis will provide the necessary components to construct a three-dimensional phase sensitivity plot for any location about the probe's sphere, figure 2. Conceptually, each resonating axis can be characterized by two complete spheres based on the phase response at any location on the probe head due to a constant applied force load. Thus, the entire 3-D plot for all three resonating axes can be mapped by 6 nested spheres.

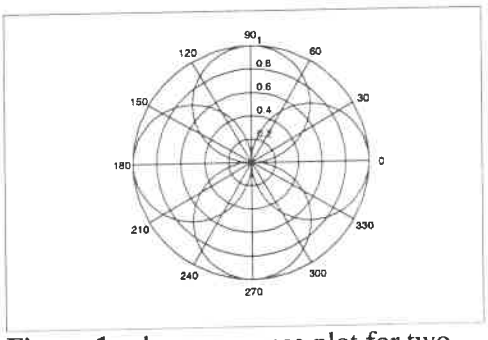

Figure 1: phase response plot for two orthogonal vibrations at constant applied force

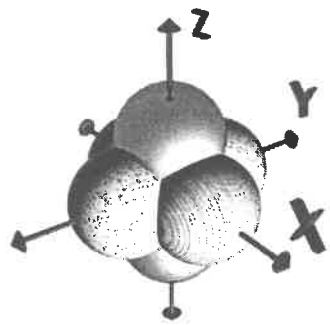

Figure 2: theoretical 3-d phase response for three resonating axes at constant applied force

Careful consideration is taken to precisely detect the output response due to added stiffness or damping upon contact with the probe head. In practice, two modes of measurement are possible. Firstly, mode I detection consists of exciting the probe at a harmonic frequency and tracking the magnitude of phase shift as contact force is added. Mode II utilizes phase locked loop (PLL) techniques and thereby, locks into a desired phase and measures the magnitude of frequency shift due to the added contact force [3].

Contact forces are measured using a simple notch flexure and capacitance gage, calibrated using dead weights with a resolution of 0.2 mN over a 300 mN range. The flexure is mounted to a single translation stage with a resolution of 1 nm and maximum displacement of 15 μm and the entire assembly is brought into contact with the probe sphere, figure 3. To provide contact forces at known locations on the probe sphere, the VTS probes are mounted to two stacked horizontal and vertical rotary tables. This provides two rotational degree of freedoms for the probe head. Also, LabView ™ is used to communicate through a DAQ card to control the force while simultaneously detecting phase response for each resonating axis, figure 4.

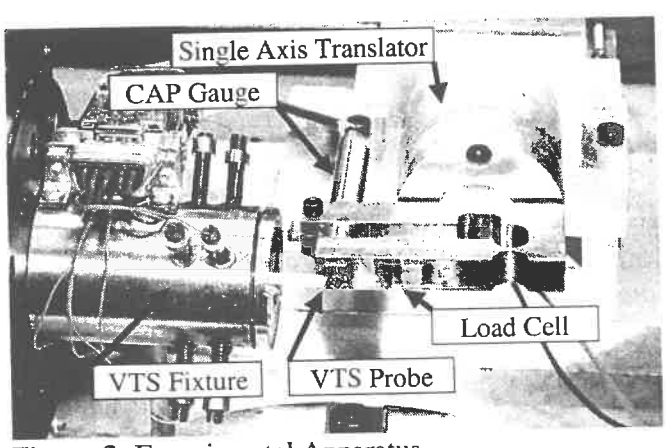

Figure 3: Experimental Apparatus

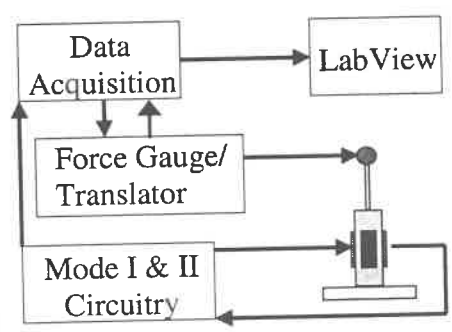

Figure 4: Experimental Procedure

Independently, each resonating axis provides a phase shift from which all three in combination may be analyzed to determine direction of applied force about the sphere. Each constructed phase response plot corresponding to figures 1 or 2 is only valid for a constant force. Therefore, a triggering force algorithm is needed evaluating the direction of applied force. Assuming the phase response for each axis varies harmonically with angle of contact as represented by figures 1 and 2, suitably scaled, the three phase responses may be combined to produce the root mean square (RMS) value. This RMS value will be the same at any location about the sphere for a specified applied normal force. In essence, during a scanning process, the three, combined phase responses will dependently provide the required triggering mechanism for instantaneous position of the probe and the direction of applied contact.

Probe development

As described above, triggering force on the entire sphere by way of RMS is only possible if all 6 spheres in figure 2 are of the same size. If this is not the case, scaling each phase response axis with respect to one another is a possible solution. However, this only applies if the two sensitivity spheres for each axis are the same. In an effort to achieve this, it has been necessary to undertake four generations of VTS probe design, see figure 5. Generations 1 and 2 have revealed that a pair of PZT actuator and sensors placed on opposite sides produce asymmetry in a single axis. Basically, the phase response, as in figure 1, is greater when a constant force is contacted on the sensor side and phase response slightly diminishes in comparison when contacted directly in line on the opposite, actuator side. Generations 3 and 4 address this by symmetrically placing PZT actuator/sensor pairs.

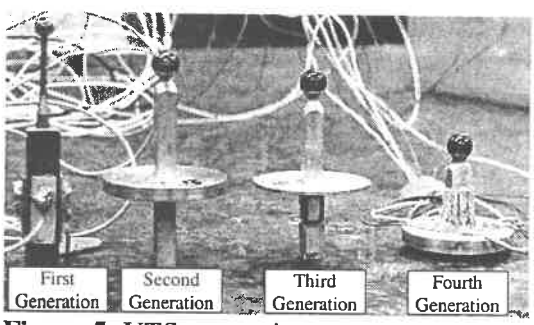

Figure 5: VTS generations

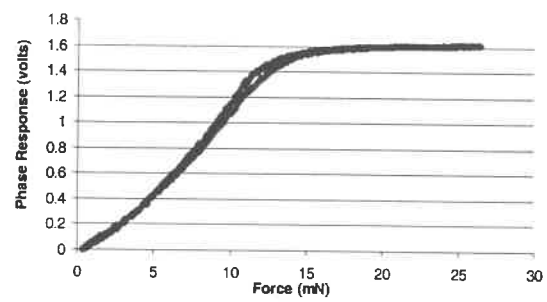

Figure 6: phase response for a longitudinal frequency Vs force load (contact point located at the top of the sphere or normal to the z-axis)

Additionally, generation 1 probes were threaded at the end of the bar and excited at first harmonic [3]. Experimentally, it was determined that threading caused non-repeatable phase response and resulted in a low Q value. Thus, a second-generation probe was designed with mountings located at node locations along the bar. This generated higher Q values but the phase response in each axis was not symmetrical. Thus, two non-systemically circular patterns were produced in each axis, see figure 7. The third generation attempted to combat the symmetry of phase response by bonding PZT sensors on all sides of the beam. In addition, actuators were also placed on each side in order to amplify the input energy. A total of 4 sensors and 4 actuators were placed around the third generation VTS probe (i.e. a sensor and actuator on each side of the beam). A comparison between the phase response of the second and third generation

probe 2 is presented in figures 7 and 8. From these figures it can be seen that the third generation partially improves the symmetry problem.

As discussed previously, mode I and II refer to locking into frequency and tracking phase response and locking into phase and tracking frequency respectively. Current probes may produce a linear phase response for loads of 1-10mN. However, at higher loads this tends to exhibit 'saturation', see figure 6. This is due to the sharpness of the phase change about the resonance. In practice, as stiffness is continuously added to the vibrating system the resonant frequency will increase with the monitored phase following the characteristic curve for a second order system. When the resonant frequency has shifted to a value far from the 'free' resonance, the phase shift will tend towards a constant. The advantage to phase locking circuitry, mode II, the change in natural frequency may be continuously measured over an arbitrarily wide load-range.

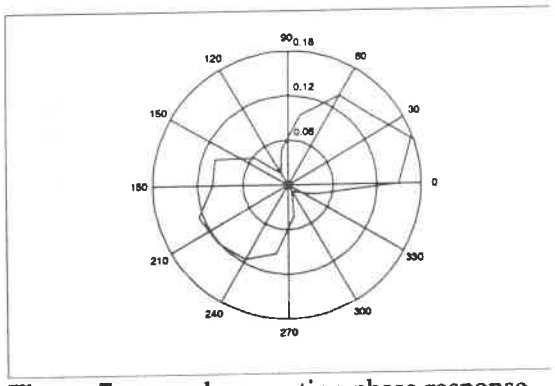

Figure 7: second generation phase response plot of a single axis

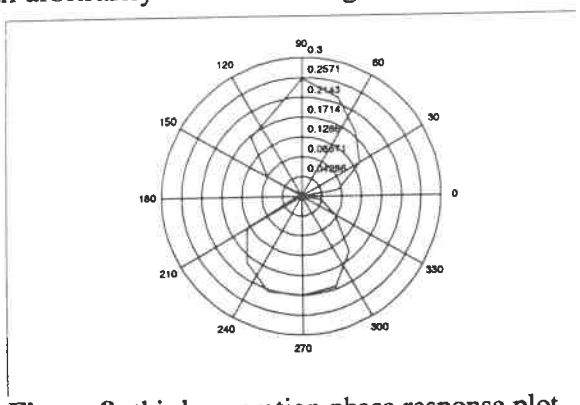

Figure 8: third generation phase response plot of a single axis

Current research aims to improve the phase response for a lighter force load while improving the symmetry of the phase response. Generation four is currently being assessed. As shown in figure 5, the generation four has an air gap separating the probe head and rigid base. The ceramics bridge the gap between the rigid base and the probe head. Initial results indicate a high sensitivity to contact force.

References

[1] Rayleigh, J.W.S., 1894, *The Theory of Sound*, Dover Publications, Inc. (1945).

[2] Vidic M., Harb S.M. and Smith S.T., 1998, Observations of contact measurements using a resonance based touch sensor, *Precision Engineering*, **22**(1), 19-36

[3] S.C. Woody and S.T. Smith, Vector Touch Sensor Probe, *Proc. of ASPE*, 1998, **18**, 471-474

Contour Mode Deterministic Microgrinding

Jeff Ruckman,* Ed Fess, Yi Li

Center for Optics Manufacturing – University of Rochester
240 E. River Rd, Rochester, NY 14623

ABSTRACT

The Center for Optics Manufacturing, along with its partners in the Consortium for the Deterministic Design, Manufacture and Assembly of Aspheric Optics, has recently completed (December, 1998) a three year, DARPA funded program to develop new manufacturing technology to produce axially symmetric, high departure aspheric optics. One result of the program was the development of a contour mode aspheric grinder and deterministic microgrinding process that repeatably produces aspheric optical surfaces in glass or IR materials with less than 1.0 wave p-v figure error, surface roughness of 100 Å rms, and less than 1 µm of sub-surface damage. Forty-millimeter diameter surfaces can be fabricated to these tolerances in less than 30 minutes from a rough blank. This paper will review the new machine and process manufacturing technologies that provide the capabilities outlined above. Details of the grinding process sequence are described. Results from grinding trials in a wide range of glass, crystalline and polycrystalline materials are reported. In addition, the results from demonstration parts fabricated for the Consortium partners in both glass and IR materials (FS, SLAM55, AMTIR, ZnSe, Silicon) will be shown.

Another DARPA funded consortia was formed to systematically identify and attack the manufacturing technology and cost drivers preventing the use of non-traditional optical shapes and materials in new capability optical sensors. The freeform grinding machine developed to meet these unique needs was recently completed and this paper reports on the machine design and the initial results from the grinder.

Keywords: deterministic microgrinding, glass grinding, contour grinding, aspheric and conformal optics fabrication

1. INTRODUCTION

1.1 Aspheric Optics

It is well known that aspheric lenses permit optical designs with fewer elements, resulting in decreased system weight, size, complexity, and cost, as well as increased transmissivity. For weapon and targeting systems, these benefits translate into military advantages, such as increased range or speed or improved target acquisition. However, the lack of a cost-effective manufacturing technology for the fabrication of glass aspheres has been a significant barrier preventing the widespread use of aspheres in precision, visible optical systems. Existing fabrication techniques are costly because of long cycle times, high costs for capital equipment and tooling, and a lack of deterministic finishing techniques.

As a result of these issues, the Defense Advanced Research Projects Agency (DARPA) funded a program to develop, demonstrate, and deploy a cost-effective precision asphere design, fabrication, and assembly capability within the optics industry. Under this program, the Center for Optics Manufacturing (COM) at the University of Rochester led a consortium that has successfully developed the *Nanotech™ 150AG*, a cost effective aspheric grinder that can deterministically microgrind aspheres in brittle materials. The resulting ground surfaces can then be deterministically polished using the magnetorheological finishing (MRF) technique also pioneered at COM and commercialized by QED Technologies. A key objective of our program was to demonstrate a prototype, automated process to microgrind and polish precision aspheres at 1/10th the cost of current volume production processes. The consortium members included: Byelocorp Scientific, Eastman Kodak, Lockheed-Martin, Moore Tool/Moore Nanotechnology Systems, Opkor, OptiPro Systems and Raytheon Systems.

1.2 Conformal Optics

All projections for future military systems indicate that the trend toward higher performance optical solutions will continue to accelerate. As next generation weapon systems evolve, military prime contractors are finding direct conflicts between requirements for optical sensors and the need for weapons systems to have low observability, aerodynamic improvements, and increased optical performance. Attempting to mitigate these conflicts using traditional optical shapes (spherical lenses, flat windows) results in unacceptable compromises that make the use of traditional optical shapes completely inadequate for many next generation systems. A new

* Email: jruc-com@LLe.rochester.edu; Telephone: 716-275-1093; Fax: 716-275-7225

class of optical shape is needed to meet these new requirements.

The new optical shapes are defined by the need to conform to the mechanical or aerodynamic requirements of the platform on which they reside. This class of optical shape has been named conformal optics. Conformal optical shapes include both axisymmetric and non-axisymmetric optical components and may have a combination of aspherical, spherical, cylindrical, conical, diffractive, plano, or ogive shapes. In some extreme cases, there may be no symmetry to the shape at all and these are called "freeform" shapes.

The combination of extreme accuracy requirements and difficult materials cause the optics required for next generation systems to be well beyond current fabrication capabilities – at any affordable cost. Another DARPA funded consortia was formed to systematically identify and attack the manufacturing technology and cost drivers preventing the use of non-traditional optical shapes and materials in new capability optical sensors. The grinding machine developed to meet these unique needs was recently completed and this paper reports on the machine design and the initial results from the grinder. In addition to COM, the consortia members included: Raytheon (several business units), Boeing, Rochester Photonics Corp., and the Optical Sciences Center, University of Arizona.

2. Asphere Grinding Machine Design and Results

2.1 Machine Design

The *Nanotech™ 150AG,* shown in Figure 1, is a high precision, cost-effective machine designed to grind rotationally symmetric aspheres with minimal mid-spatial frequency surface error. The grinder was designed and built by Moore Tool (Bridgeport, CT) under the direction of a COM-led Machine Technical Advisory Board. Moore Nanotechnology Systems, LLC (Keene, NH), an affiliate of Moore Tool Company was responsible for the final development of the aspheric grinder.

The *Nanotech™ 150AG* has two axes of linear motion mounted on a monolithic natural granite base. Both linear axes are fully constrained, oil hydrostatic, box way slides that use self-compensating bearing pads. There are two tool spindles, a ball bearing spindle for rough shaping operations (Parker Majestic) capable of speeds between 100 and 5,000 RPM and a choice of air bearing spindles for finish grinding operations (Westwind or Precision Instruments). The Westwind spindle is capable of speeds ranging between 5,000 and 40,000 RPM, the rough and finish grinding spindles are mounted to the

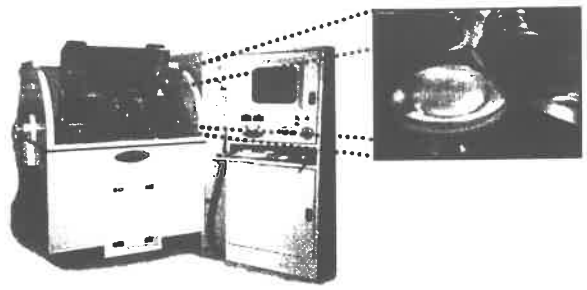

Figure 1: *The Nanotech™ 150AG*

X-axis, which traverses horizontally (350 mm travel). The work piece spindle (Precision Instruments) is also an air bearing design capable of speeds between 100 and 2,000 RPM. The work spindle is mounted to the vertical Z-axis (150 mm travel). The machine capacity allows for 150 mm diameter convex and concave components.

The *Nanotech™ 150AG* is controlled by an Aerotech PC-based NC control and has on-board instrumentation for dynamically measuring the effective grinding wheel diameter in order to compensate for wheel wear. In addition, an air bearing LVDT, mounted to the X-axis by the operator, can profile the ground optical surface before removing the part from the chuck. If necessary for extreme precision requirements, the data from the LVDT can be interfaced to a controller software routine to determine the tool path compensation needed for form error compensation.

2.2 Grinding Process

The standard grinding process developed for this machine is a two step sequence that uses a 10-20 μm diamond bronze bond tool for the roughing cut, and a 2-4 μm diamond resin bond tool for the finishing cut. Table 1 presents the typical process parameters used.

Table 1: Grinding tool specifications and process parameters

Tool	Bond	Manufacturer	Tool Speed (RPM)	Work Speed (RPM)	Feed rate (mm/min)	Depth of Cut (μm)
10/20	bronze	Scomac	7400	248	5	30
2/4	607c resin	Norton	12000	43	2	10†

† Depth of cut was taken in three passes of 5, 2.5, 2.5μm.

2.3 Contour Grinds of Spherical and Plano Surfaces

Several process development studies have been completed on a variety of materials. Because of the difficulties with metrology of large departure aspheres, the contour ground surfaces were either plano or spherical surfaces. Table 2 shows the p-v figure error and RMS roughness, averaged for several grinds in each material. All parts listed in Table 2

were 40-50 mm in diameter, 120 mm convex radius of curvature or plano. The contour grinding process consistently produces parts with figure error of 0.5 µm or less

Table 2: Figure and finish

Material	Average PV Figure error (µm)†	Average RMS roughness (Å)‡
Fused Silica	0.4	158
ZnSe	0.5	99
Silicon	0.4	79
Amtir	0.4	158

† Zygo GPI interferometer
‡ Zygo NewView 100, 20x mirau, areal roughness.

Most materials were ground to nearly final roughness specification, potentially eliminating the need for a polishing step. Measured subsurface damage was less than 1 µm for FS, the limit of the measuring technique. This correlates well with the p-v roughness measurement of 0.5 µm for this material.

In another study, the contour grinding process was used to grind 12 commonly used optical materials that represented a wide range of hardness and fracture toughness. The results demonstrate that the contour grind process is capable of producing parts to near-finished quality in a range of optical materials. Figure 2 shows the 12 materials included in the study and the results of the study.

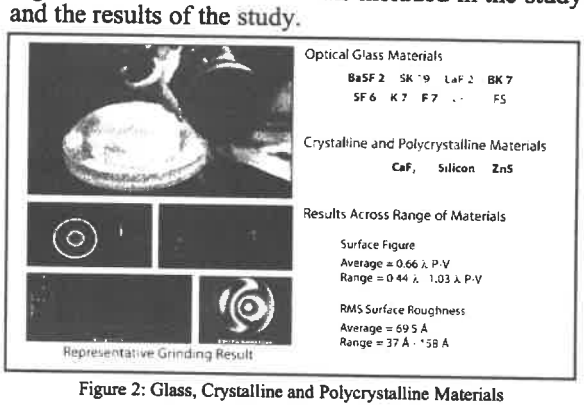

Figure 2: Glass, Crystalline and Polycrystalline Materials

The *Nanotech™ 150AG* was able to grind optical glasses to 50-100 Å rms surface finish and hold figure error to less than 1 µm. The crystalline and polycrystalline materials were ground to approximately 200 Å rms surface finish with figure error also less than 1 µm. Figure error was measured on the Zgyo GPI interferometer and surface roughness data was taken on the Zygo NewView 100. All values in the table are the average measurements of five parts for each material type.

2.4 Contour Grinds of Aspheres

Two aspheres were ground to demonstrate the machine's performance. The first asphere, a 58.5 mm diameter SLAM-55 optical glass from Ohara, had an aspheric departure of 120 µm from the best fit sphere. The same two tool process was used as described above, except that the tool used for the finish cut was a 10-20 µm resin tool (Norton 619c bond). Total grinding time was 25 minutes. Table 4 lists the final grinding results before polishing, and Figure 3 shows a plot of the figure error as measured by a Taylor Hobson Form Talysurf surface profilometer.

The second asphere, a 49.55 mm diameter zinc selenide optic, had an aspheric departure of 60 µm from the best fit sphere. The standard 2 tool process listed in Table 1 was used. The total grinding time was 49 minutes. This part had a longer grinding time because three finish cuts were taken using the 2-4 µm diamond wheel. Table 3 gives the final grinding results, and Figure 4 shows plots of the figure error.

Table 3: Aspheric results after grinding

Asphere	PV figure error (µm)†	RMS roughness (Å)‡
SLAM-55	0.6	2153
ZnSe	0.6	111

† Figure obtained from Form Talysurf surface profilometer
‡ Average of three places, Zygo NewView 100, 20x mirau

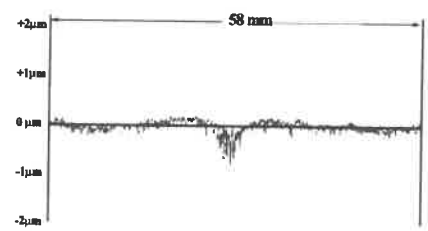

Figure 3: SLAM-55 Asphere Profile Error (unfiltered)

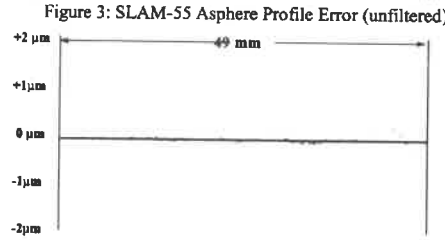

Figure 4: ZnSe Asphere Profile Error (unfiltered)

2. 5 Contour Grinding Surface Errors

In addition to the well understood low and mid spatial frequency surface errors caused by problems such as machine alignment, periodic screw or spindle asymmetry and thermal variations, we have identified several other sources of errors that are inherent to the contour grinding process. Understanding and controlling these errors is critical to achieving sub-micron figure accuracy. Separating these errors from each other and identifying each error with an understandable source was one of the most difficult engineering challenges required to achieve the results described above. The understanding of surface errors created in 2 axis contour grinding developed during the process development of this machine led to design features in the conformal machine. A complete discussion of these errors will be the topic of another paper. A listing of the error types identified to date is provided below.

Table 4: Summary of Contour Grinding Surface Error Types

LOW SPATIAL FREQUENCY OR FIGURE ERROR SOURCES	MIDDLE/HIGH SPATIAL FREQUENCY ERRORS
• Changes in volumetric removal	• Spiral marks
• Tool wear	• Annular rings
	• Chatter/ tool lobing

3. Conformal Grinding Machine Design and Results

3.1 Machine Design

The *Nanotech™ 500FG*, shown below, is designed to grind both axisymmetric and non-axisymmetric optical components and other shapes that may include a combination of aspherical, spherical, cylindrical, conical, diffractive, plano, or ogive shapes; or be freeform in materials ranging from optical glass and infrared materials, to non-ferrous metals, crystals, polymers and ceramics. The grinder was designed and built by Moore Nanotechnology Systems (Keene, NH) under the direction of a COM-led Machine Technical Advisory Board.

The computer numerically controlled, four-axis, ultra-precision machining system is capable of generating arbitrary conformal optical surface shapes within a 250 mm x 250 mm x 300 mm machining envelope. The machine has three linear motion axes and one rotary axis mounted on monolithic natural granite main base with natural granite risers to support the Z axis. All three linear axes use fully constrained, oil hydrostatic, box way slides. The horizontal work spindle is an air bearing design (Precision Instruments) capable of speeds between 100 - 2,000 RPM. The oil hydrostatic bearing grinding spindle (Moore Nanotechnology) is capable of speeds between 10,000 and 40,000 RPM. The grinding spindle is mounted horizontally on an air bearing rotary axis capable of a full 360 degrees of travel

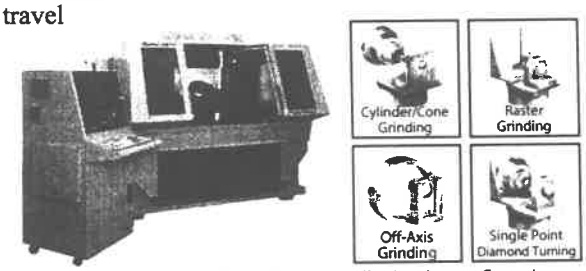

Figure 5: The *Nanotech™ 500FG* and grinding/turning configurations

In addition, an in-process, error compensation system using an air bearing LVDT can profile the ground optical surface before removing the part from the chuck. If necessary for extreme precision requirements, the data from the LVDT can be interfaced to a controller software routine to determine the tool path compensation needed for form error compensation.

3.2 Initial Acceptance Test Results

The conformal grinder recently completed acceptance testing trials at Moore Nanotechnology. The grinding process used was based on the knowledge gained from the experience with the asphere grinder. Table 5 shows the grinding tool specifications and process parameters.

Table 5: Grinding tool specifications and process parameters

Tool	Bond	Manufacturer	Tool Speed (RPM)	Work Speed (RPM)	Feed rate (mm/min)	Depth of Cut (μm)
2/4	607c resin	Norton	12000	43	2	10†

† Depth of cut was taken in three passes of 5, 2.5, 2.5μm.

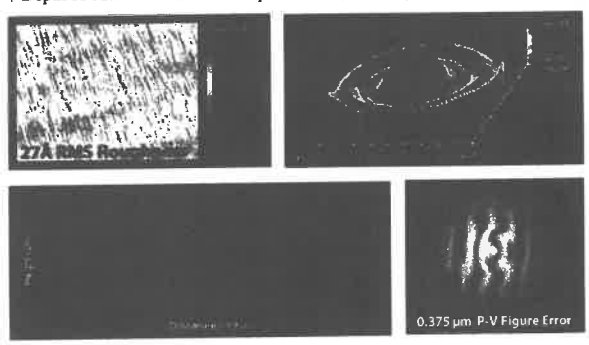

Figure 6: The initial results from the *Nanotech™ 500FG*; BaSF2 40 mm ϕ, 120mm radius sphere

SUMMARY

This paper reviewed recent work at the Center for Optics Manufacturing to develop a deterministic microgrinding capability for aspheric and conformal optical shapes. Average figure accuracy of 0.66 λ p-v was given for contour ground surfaces on a variety of materials for the *Nanotech™ 150AG* asphere grinder. Initial test results were shown for the *Nanotech™ 500FG* conformal optics grinder, indicating the ability to grind glass materials to under 0.5 λ p-v figure error.

ACKNOWLEDGEMENTS

The authors gratefully acknowledge the support of the Asphere and Conformal Machine Technical Advisory Boards – Robert Boucher, Lockheed Martin; Walter Czajkowski, Eastman Kodak Company; Richard Eichholtz, Raytheon Systems; Don Golini, QED Technologies; Robert Iacovazzi, Lockheed Martin; Harvey Pollicove, COM; John Schaefer, Raytheon Systems; John Vakiner, II-VI, Inc. In addition, the contributions of the grinding research team at COM, including Paul Funkenbusch, Sheryl Gracewski, John Lambropoulos, Dennis VanGee, and Jesse Van Ven Roy were invaluable to the success of these machines. The manuscript and graphics were prepared by Carolyn Pollicove. Support for this work is provided by the Defense Advanced Research Projects Agency (DARPA) and TACOM-ARDEC/U.S. Army Materiel Command.

COMPENSATION OF TOOL FORCES IN SMALL DIAMETER END MILLS

Thomas Dow, Edward Miller, Alexander Sohn and Kenneth Garrard
Precision Engineering Center, North Carolina State University
Thomas Wright
Eastman Kodak Co., Rochester, NY

ABSTRACT

Miniature solid carbide end mills are being used to produce small features in hard metal surfaces. These tools, in either straight or ball end configuration, can produce intricate shapes in very hard steel (H>55Rc), quickly and without grinding. However to reach into small features, the length of the tool becomes large enough (length/diameter ratio >5/1) to influence the dimensional tolerances of the machined part due to deflection of the tool. This deflection is a response of the tool to the machining forces that are in turn a function of the tool geometry, cutting condition, tool wear, lubrication, etc. This paper describes the magnitude of the cutting and thrust forces, the influence of tool wear, the stiffness of the tool and the errors in machined features as a result of the tool deflection.

INTRODUCTION

In past research programs, the Precision Engineering Center (PEC) has developed a model for predicting the forces on milling cutters in both the cutting and the radial direction. This model grew out more than a decade of involvement by the PEC with diamond turning and the need to predict tool force changes that accompany minor changes in the tool geometry due to wear. This model has been applied to the milling geometry and predicts cutting and thrust forces as well as changes in those forces associated with wear on the tool edge. For a small tool, the forces associated with cutting can produce a significant deflection of the tool and result in errors in the shape of the machined part. This is a particular problem for a ball end mill because cutting can take place at different points around the radius of the tool and therefore along directions with different stiffness. As a result, the shape of the part will be influenced. By developing compensation techniques for these errors, improved accuracy for machined parts are possible.

TOOL FORCES

PREDICTED FORCES

The tool force model provides a formula for calculating the cutting and thrust force developed during milling. The inputs to the model are the material properties (hardness, modulus), friction at the rake and flank faces of the tool, tool geometry (ball end radius), spindle speed, upfeed and cross feed, depth of cut and tilt angle of tool. The model can be written as:

$$F_c = \frac{HA_c}{3}\left(\frac{\cot\phi}{\sqrt{3}} + 1\right) + \mu_f A_f\left(0.62H\sqrt{\frac{43H}{E}}\right) \tag{1}$$

$$F_t = \mu\left[\frac{HA_c}{3}\left(\frac{\cot\phi}{\sqrt{3}} + 1\right)\right] + A_f\left(0.62H\sqrt{\frac{43H}{E}}\right) \tag{2}$$

where

A_c = cross section of the chip,
A_f = area of the tool flank face,
ϕ = shear angle in the workpiece,
μ = friction coefficient on rake face,
μ_f = friction coefficient on flank face,
H = hardness of the workpiece, and
E = modulus of the workpiece.

For the milling geometry, these forces rotate with the flank face of the tool. The predicted values can be converted to forces in the x,y, and z directions and then compared to measurements made with a stationary load cell.

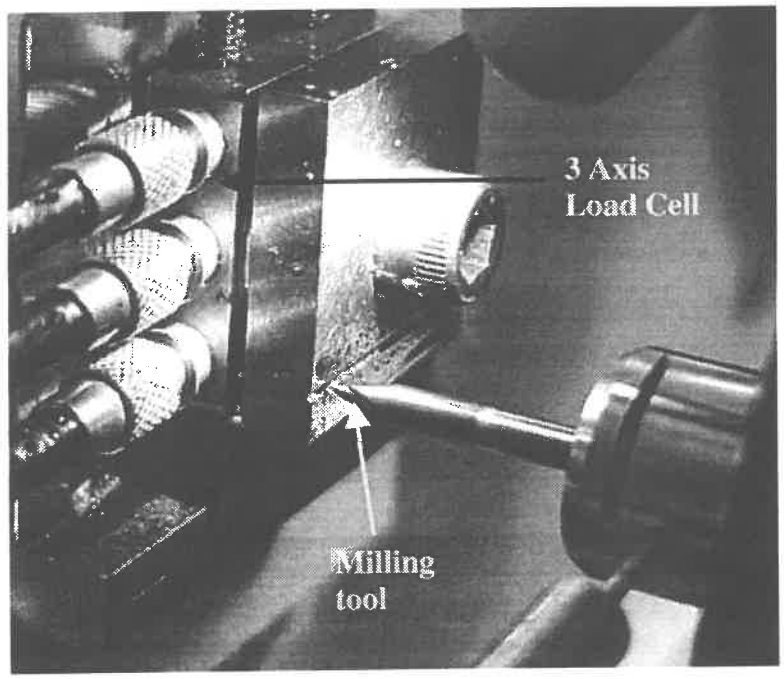

Measured Forces

The forces have been measured with a 3 axis piezoelectric load cell pictured at right. This load cell is mounted on the x axis of a diamond turning machine while a high speed spindle driving the milling tool is mounted on the z axis. The milling tool can be rotated at speeds up to 60,000 rpm and the axes can move at speeds up to 500 mm/min. The tool can be mounted such that it is normal to the workpiece or at an angle up to approximately 60°.

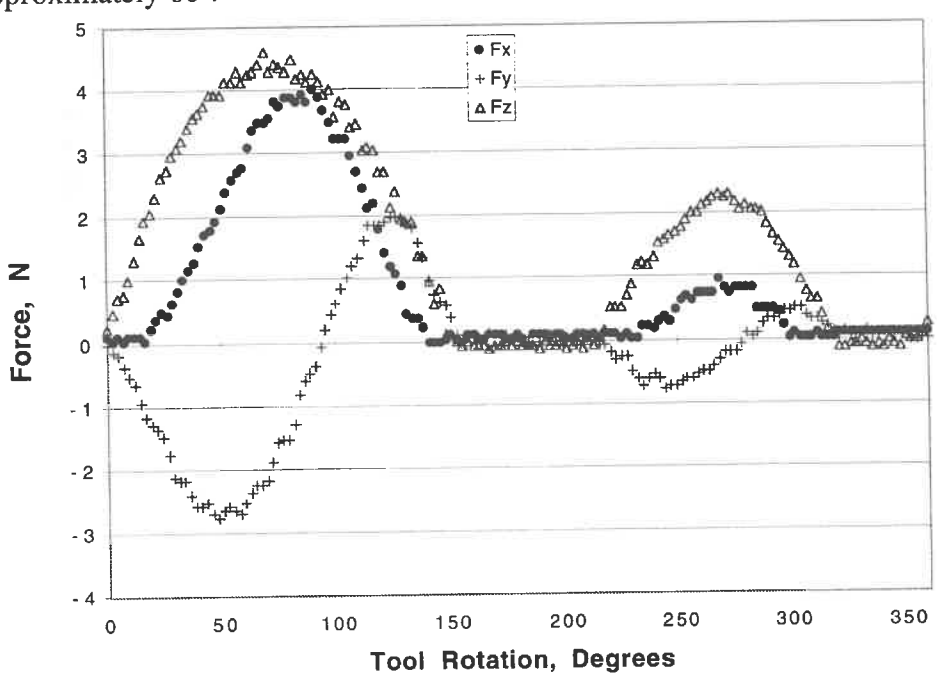

Figure 1. Measured tool forces cutting hard steel at 25 µm depth of cut, 19 µm/flute feed rate using an 0.8 mm diameter ball end mill at 20,000 rpm tilted 10° with respect to surface normal.

A sample of the output of the load cell is shown in Figure 1. This plot shows the average forces in the x, y and z directions for 3 consecutive rotations of the tool. Note that the forces for the first flute are significantly higher than for the second (approximately twice as large) as is the period of contact between the flute and the workpiece. The reason for this inequality in forces is likely the effect of tool runout; the magnitude of which is 10 μm for the high-speed spindle used. The z-component of the force in Figure 1 is dominated by the tool thrust force, Equation (2), because the tool is almost normal to the workpiece (10° of tilt). The x and y forces are influenced more by the cutting force, Equation (1), which rotates in the plane of the workpiece and changes from a force in the x direction to a force in the y direction for each 90° rotation of the tool.

TOOL STIFFNESS

The miniature milling tools are fabricated from tungsten carbide with a titanium aluminum nitride coating. The tools have a 3 mm shank which tapers down to the ball diameter (see the photograph above). The ball end can be at the end of the tapered section for the short tool or at the end of an extended section with a diameter equal to the ball. The long tool discussed later has an extended section of 5 mm. Typically a ball mill is used to fabricate free form surfaces and as a result the tool can be loaded axially, radially or both. The stiffness of the tool is quite a bit less in the radial direction than in the axial direction. Therefore, regions of the machined part that load the tool in the radial direction will cause significant tool deflection and the part dimensions will be different than expected.

The tool was modeled as a cantilever beam mounted in a spindle with finite axial and radial stiffness. Because it is made up of straight and tapered sections, the model is straightforward and a simple analytical calculation was made. However, the stiffness of the spindle is an unknown that must be measured. The measured and predicted stiffness are shown in the Table below. The predicted stiffness of the long tool is quite close to the measurements but the short tool stiffness is overpredicted because of unmodeled changes in the shape of the reduced section as a result of grinding the ball end mill geometry.

Tool Length (Stiffness direction)	Measured Stiffness, N/m	Calculated Stiffness Including Spindle Stiffness, N/m	Calculated Stiffness Neglecting Spindle Stiffness, N/m
Short (Radial)	406,203	557,000	971,000
Short (Axial)		845,000	300×10^6
Long (Radial)	198,533	208,000	250,000
Long (Axial)		840,000	60×10^6

TOOL DEFLECTION

DEFLECTION PREDICTION

With a force model and the stiffness of the tool measured, the deflection of the tool during machining can be predicted. Because the tool will be loaded in a variety of directions during a milling operation, the model of tool deflection must take into account the direction of the cutting

forces as well as their magnitude. Such a model has been created and used to predict deflections in several different experiments.

DEFLECTION MEASUREMENT

Variable Depth Groove One experiment used to corroborate the model is to mill a slot with a varing depth of cut using tools tilted at different angles with respect to the workpiece. In this way the influence of depth of cut and tool orientation can be evaluated quickly. The results on one set of experiments is shown in Figure 2. Figure 2(a) shows the measured and predicted deflections for a tool tilted at 25° to the surface normal and following a commanded slope beginning at 0 depth of cut and continuing to 75 µm after 20 mm of motion. The lower line is the predicted tool deflections for the feed and speeds of the experiment and the points represent the depth of cut measured on the part using a Form Talysurf at several locations along the line. The upper line is the desired path of the tool (0-75 µm slope) and the points are the result of the experiment where the theoretical compensation is applied to the cutter path. The data shows that the model does an excellent job of predicting the deflection as well as providing guidelines to produce the desired shape.

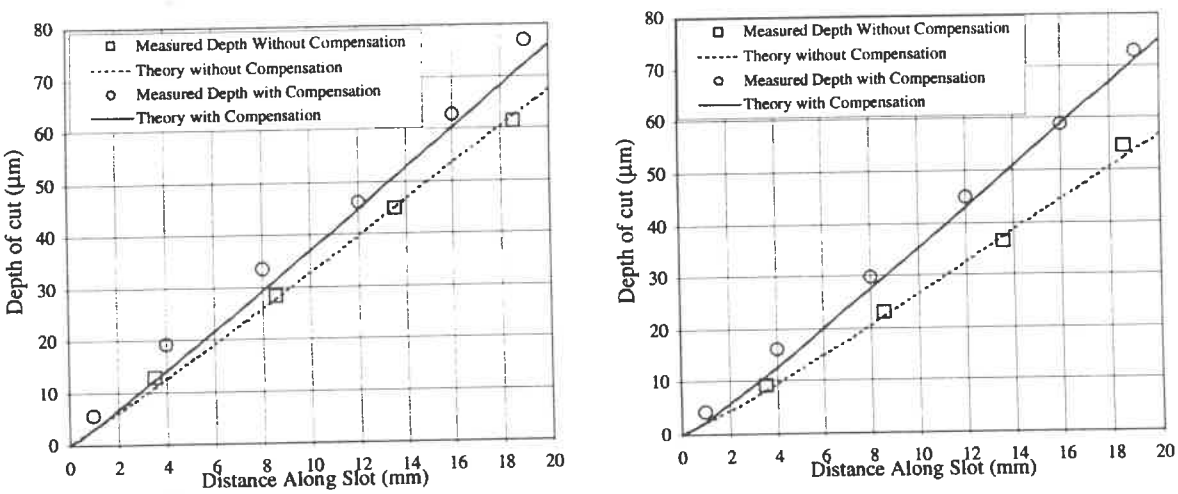

a) 25 degree tilt angle b) 50 degree tilt angle

Figure 2. Uncompensated and compensated tool deflections in hard tool steel machining a variable depth groove from 0-75 µm (feed rate = 10 µm/flute, speed = 20,000 rpm)

Figure 2(b) shows the results of similar experiments but with the tool tilted at 50° from the normal. In this case the forces are directed more in the radial direction (the direction of lower stiffness on the tool) and the uncompensated deflection is larger than the 25° case. The model provides an excellent fit both for the uncompensated deflections as well as target points to produce the desired slope.

DEFLECTION COMPENSATION

The process typically used to produce highly accurate parts is to machine the desired shape, measure the resulting shape and compensate the tool path to produce the desired shape. This is commonly applied to diamond turned optical parts but these geometries are much simpler than

the prismatic parts produced on a multi axis machining center. The proposed compensation technique is based on the shape of the part and the setup of the machine that influences the contact direction of the tool and workpiece at each point on the surface. Based on the model for force and tool deflection, the tool path can be modified to compensate for the deflection of the tool and produce a more accurate machined component on the first try.

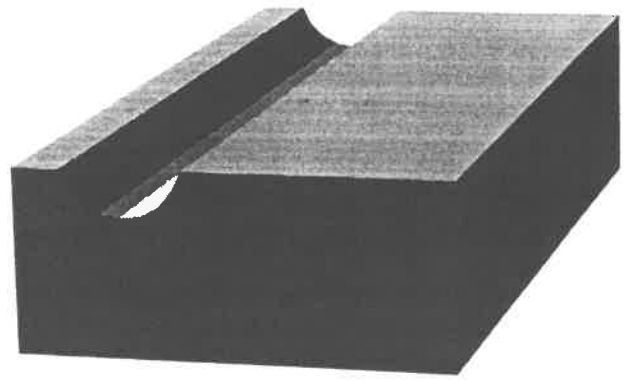

Figure 3. Geometry used for the compensation experiments

The geometry selected for the compensation experiments is shown in Figure 3. The particular feature of interest is the shape of a torus (with a radius of 8.4 mm, a width of 12 mm and a depth of 3 mm). The part was placed in the spindle of a DTM and rotated at low speed (<30 rpm). The specimen was first machined using a much stiffer poly-crystalline CBN tool that produces a reference shape within 1 μm of the desired radius. The part is then machined using the miniature end mill with a different up-feed and cross-feed rates and different depths of cut. The shape of the groove after the milling experiments was compared to the reference shape and the deflection of the tool was determined.

Other experiments were performed using a modified part program based on the stiffness of the tool and the angle of contact between the tool and the workpiece. This procedure is the same as described in Figure 2.. The compensation technique resulted in parts with significantly less shape error - the error was reduced by an order of magnitude to ±2 μm.

CONCLUSIONS

The forces generated during milling with a miniature tool are relatively small because of the limited size and strength of the tool edge. However, the tool deflection can be significant because of the low stiffness and long length of these tools. The model for tool force does an excellent job predicting the forces associated with cutting as well as the contribution from tool wear. The compensated tool path based on the forces and orientation of the tool with respect to the workpiece provides an avenue to produce the first part right.

REFERENCES

[1] Drescher, J.D., "Tool force, tool edge and surface finish relationships in diamond turning", Ph.D. Dissertation, NC State University, 1991.

[2] Arcona, C., "Tool force, chip formation and surface finish in diamond turning", Ph.D. Dissertation, NC State University, 1996.

[3] Minor, P.D., "Tool wear and tool forces in high speed milling of aluminum", MS Thesis, NC State University, 1998.

Deterministic Design of "Engineered Tool" (A New Diamond Tool)

T Tatsumi*, T.Ikeda*, K Imai**, H. Hashimoto**, T.Takeda***, S.Hamada***

*Komatsu Electronic Metals Co.,Ltd
**Kanagawa Institute of Technology, 1030 Shimo-ogino Atsugi-shi, Kanagawa,243-0292, Japan
Tel:81-46-291-3209, Fax:81-46-242-8735, e-mail:ken@me.kanagawa-it.ac.jp
***Sumitomo Heavy Industries, Ltd

1.Introduction

The present report demonstrates fly-cut experimental results for brittle materials cut using the Engineered Tool (a new diamond tool), and introduces the tool design of the Engineered Tool.

The reasons for developing the Engineered Tool and the experimental results for two kinds of Engineered Tool are obtained for fused silica and single-crystal Si as fundamental data in order to aid in the design of future Engineered Tool. The experimental results of shear (or ductile) mode grinding indicate two serious obstacles to the development of the Engineered Tool.

One obstacle is that the removal rate is limited by the wheel-to-workpiece contact area, which may cause heat generation. During the experiment, cracks caused by burning appeared on the ground surface, and shear mode grinding was impossible. The result indicated that a large contact area limits the induction of coolant and promotes high temperatures in the coolant zone where heat is generated. In some types of grinding geometry, a large contact area is difficult to avoid. Therefore, as suggested previously, an alternative is to excite the wheel at ultrasonic frequency, which also admits coolant between wheel and workpiece. The grinding force was found to be lower than that obtained with no vibration (conventional) grinding in shear mode [1]. Furthermore, exciting the wheel to induce a coolant in the contact zone was found to enable a two-fold increase in the removal rate.

The other obstacle is that the ground surface is scratched by various abrasive grits on the grinding wheel surface [2]. Therefore, it is very difficult to maintain a high-quality ground surface, because uniform grit size, form, density, and orientation are not possible when using the grinding wheel. Thus, the inadequacies of the grinding wheel clarified the need to develop a new diamond tool, which is called the Engineered Tool [3].

2. Engineered Tool

Engineered Tool has many small posts on a single crystal diamond surface (1,0,0). The diamond size is $2\times2\times1$ mm. In the example shown in *Fig.1*, the posts were precisely machined to be 15 μm apart using an excimer laser. Each post size is 5×5 μm square, having a height of 10 μm height as shown in *Fig.2*. This represents a very high density of active diamond of a constant and known spacing.

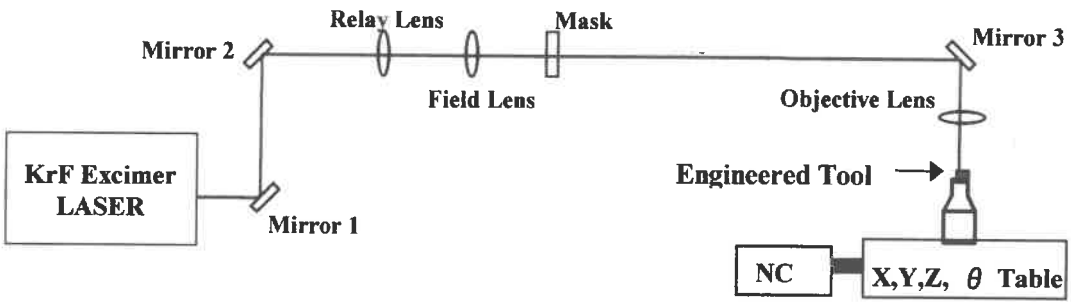

Fig.1 Manufacturing of ET using Excimer Laser

In addition, it is possible to align the diamond orientation can be aligned so as to provide uniform and minimal wear of the posts. The post size, form, and density of the Engineered Tool can be designed flexibly.

Clarification of the expected accuracy and the critical depth of cut of each material will allay a suitable tool to be designed for each material.

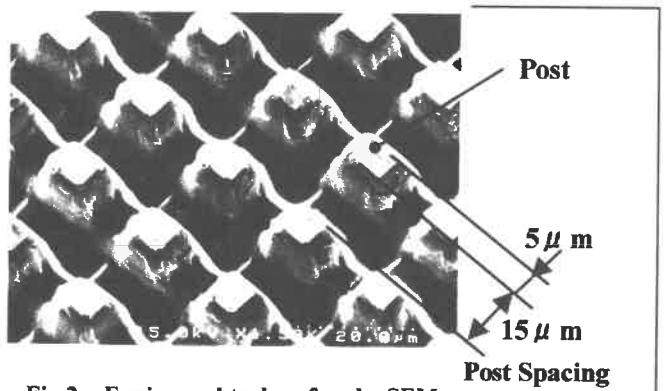

Fig.2 Engineered tool surface by SEM

3. Preparatory Experiment of Fly-Cut

A fly-cut experiment of single-crystal Si was performed using the Engineered Tool with ultrasonic vibration (*Fig.3*).

In this experiment, many individual cutting marks were examined using a laser microscope (*Fig.4, 5*) in order to measure the critical depth of cut. The critical depth of cut was found to be 0.21 μm.

In addition, the post patterns were found to have been precisely copied on the workpiece surfaces in shear (or ductile) mode [4].

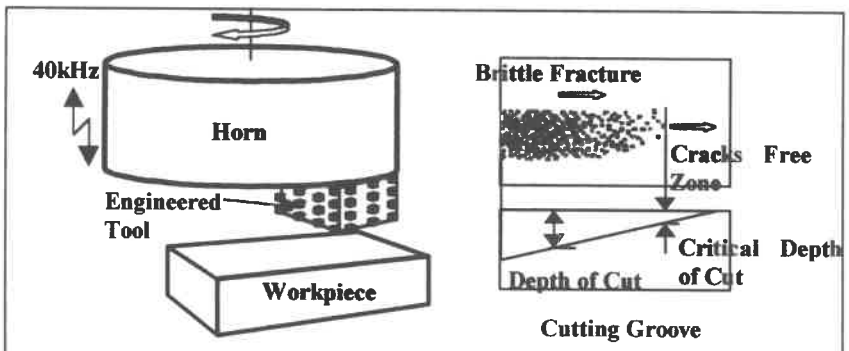

Fig.3 Schematic drawing Fly-cut experiment using Engineered

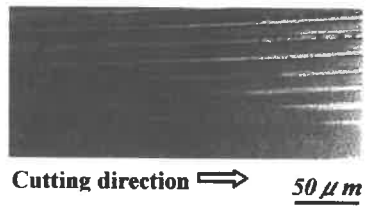

Fig.4 Photograph of cutting grooves using Engineered Tool

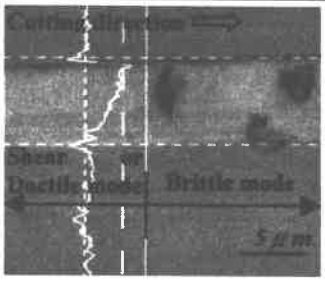

Fig.5 Transition boundary from shear (or ductile) mode to brittle

4. Deterministic Design of the Engineered Tool

Based on these results, design of the Engineered tool based on the expected accuracy and critical depth of cut, appears to be possible, because the successive active posts can be determined by distributed post patterns. The new design of the Engineered Tool is shown in *Fig.6*, in which [dt] is the total depth of cut, or n times [dc]. Furthermore, the rake angle of this tool can be determined by the critical depth of cut [dc] (*Fig.7*).

Therefore, the new Engineered Tool will enable the removal rate of a brittle material to be increased n times in shear (or ductile) mode.

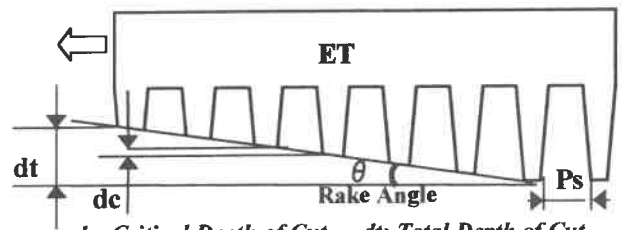

dc: Critical Depth of Cut *dt: Total Depth of Cut*
Ps: Post Spacing

Fig.6 Deterministic design of Engineered tool

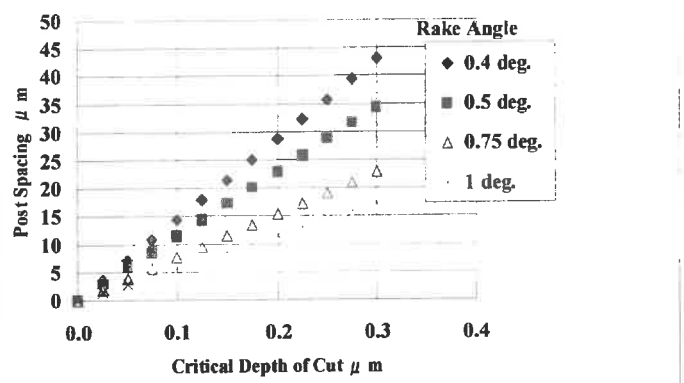

Fig.7 Post spacing versus critical depth of cut of the new Engineered tool

5. Fundamental Experiment of Fly-Cut using the New Engineered tool

The new Engineered tool was manufactured to the following specification rake angle; 0.4 degree, [dc]; ~0.1 μ m, [dt]; 8 μ m (*Fig.8*).

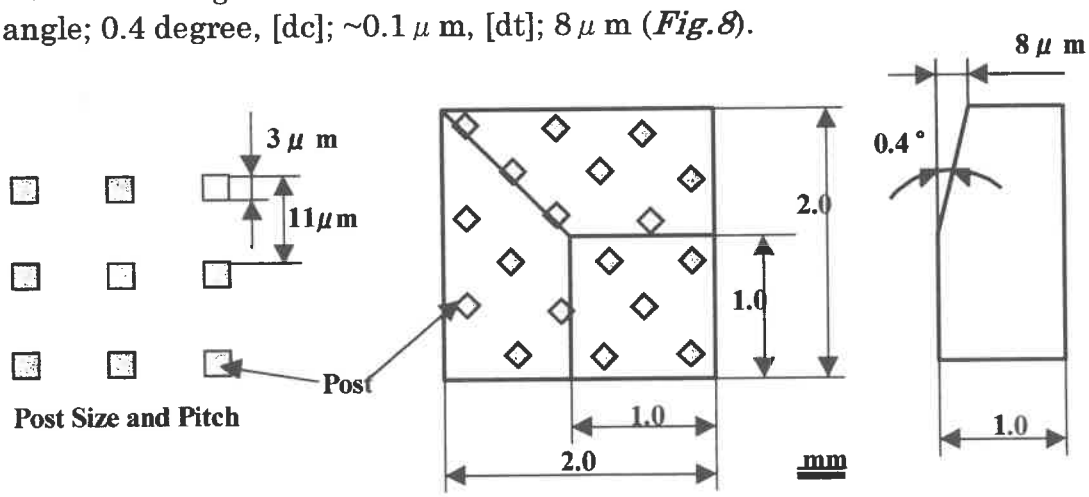

Fig.8 Schematic drawing of the new Engineered Tool

Using the new Engineered tool, single-crystal Si was cut in a fly-cut experiment. Then, a schematic drawing of the cutting mechanism is shown in *Fig.9*.

As a result, single-crystal Si was found to be machined in shear (or ductile) mode (*Fig.10*), at 6 μ m [dt], or about 30 times [dc].

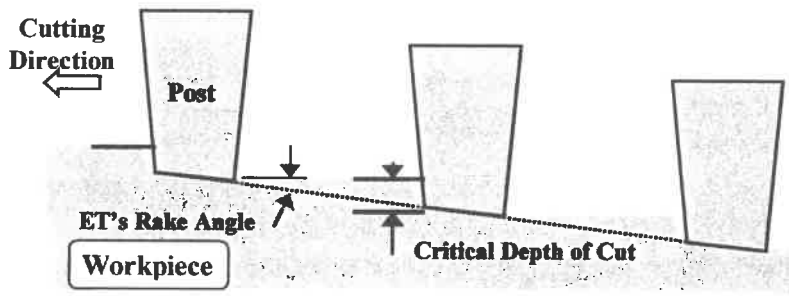

Fig.9 Schematic drawing of the cutting mechanism using the new Engineered Tool machining

Fig.10 Shear (or ductile) mode surface of the single-crystal Si using the new Engineered Tool

6.Conclusions

(1)The Engineered Tool can be designed based on the expected accuracy and critical depth of cut.

(2) A new Engineered tool was manufactured to have the following specifications rake angle; 0.4 degree, [dc]; ~0.1 μ m, [dt]; 8 μ m.

(3)Using the new Engineered tool, Single-crystal Si was found to be machined in shear (or ductile) mode until 6 μ m [dt], in this experiment.

These results indicate that the Engineered Tool is useful in high-precision machining of hard and brittle materials.

Reference

[1] Y.Yoshida, K.Imai, H.Hashimoto, et al.: An Application of 40 kHz Ultrasonic Vibration to Shear-mode Grinding of Silicon Wafers, 12th Annual Meeting of the ASPE, Norfolk, VA, pp.262-266, 1997.

[2] K.Imai and H.Hashimoto: Grinding Force Criteria in Shear-Mode Grinding, 13th Annual Meeting of the ASPE, St. Louis, Missouri, pp.136-139, 1998.

[3] H.Hashimoto, K.Imai, D.Dornfeld, and K.Blaedel: Speculation on Ultrasonic-Assisted Grinding with an Engineered Wheel, OSA Technical Digest Series Volume 12, Hawaii, OMB3-1, June, 1998.

[4] T.Tatsumi, J.Takeda, K.Imai, and H.Hashimoto: An Engineered Tool and Some Results of Fly-Cut Experiments, euspen, 1999.

An Empirical Survey on the Influence of Machining Parameters on Tool Wear in Diamond Turning of Large Single Crystal Silicon Optics

D. K. Born, C. Syn, P. Davis, M. Zimmermann, K. Blaedel, J. Carr, J. Haack
Lawrence Livermore National Laboratory, Livermore CA 94551
M. R. McClellan, Schafer Corp., Livermore CA 94550
W. A. Goodman, Schafer Corp., Calabasas CA 91302

1. INTRODUCTION

The research described in this paper is a continuation of the collaborative efforts by Lawrence Livermore National Laboratory (LLNL), Schafer Corporation and TRW to develop a process for single point diamond turning (SPDT) of large single crystal silicon (SCSi) optical substrates on the Large Optic Diamond Turning Machine (LODTM). The principal challenge to obtaining long track lengths in SCSi has been to identify a set of machining parameters which yield a process that provides both low and predictable tool wear. Identifying such a process for SCSi has proven to be a formidable task because multiple crystallographic orientations with a range of hardness values are encountered when machining conical and annular optical substrates. The LODTM cutting program can compensate for tool wear if it is predictable. However, if the tool wear is not predictable then the figured area of the optical substrate may have unacceptably high error that can not be removed by post-polishing. The emphasis of this survey was limited to elucidating the influence of cutting parameters on the tool wear. We present two preliminary models that can be used to predict tool wear over the parameter space investigated.

During the past two and one-half years a series of three evolutionary investigations were performed. The first investigation, the Parameter Assessment Study (PAS), was designed to survey fundamental machining parameters and assess their influence on tool wear [1]. The results of the PAS were used as a point-of-departure for designing the second investigation, the Parameter Selection Study (PSS). The goal of the PSS was to explore the trends identified in the PAS in more detail, to determine if the experimental results obtained in the PAS could be repeated on a different diamond turning machine (DTM), and to select a more optimal set of machining parameters that could be used in subsequent investigations such as the Fluid Down-Select Study (FDS). The goal of the FDS was to compare the performance of water, polyalkaline glycol (PAG) and HT200 as a cutting fluid for SCSi, and select a single baseline cutting fluid from this set for use in future SCSi SPDT efforts. Synopses of the experimental work and results of the PAS and PSS are now presented.

2. PARAMETER ASSESSMENT STUDY AND RESULTS

The cutting parameters surveyed during the PAS included depth of cut, surface velocity, feed rate, tool nose radius, rake angle and side rake angle, machined area and cutting fluid. The range of cutting parameters was selected to achieve material removal via the ductile mode [2-4]. Experimental design techniques were used to reduce the full factorial set of experiments to a reduced set of fourteen machining experiments, shown in Table 1 [1,5]. Multiple parameters were varied in each experiment, which allowed optimum statistical analysis of the data.

The PAS was performed on the LLNL DTM II, a precision lathe with a horizontal air bearing spindle and rolling element axes. Each experiment used a freshly sharpened diamond tool to cut a 25.4 mm wide track around an initially damage-free 143.5 mm diameter by 254 mm long (100) SCSi boule. Seven experimental tracks were cut prior to restoring the boule to a damage-free condition and completing the last 7 experiments.

Figure 1 shows the tool geometry used. The clearance angle was 7° for all tools. The tool nose profile was measured before and after each experiment by rotating an air bearing linear variable differential transformer (LVDT) probe around the nose of the tool. An example tool trace is shown in Figure 2. The x-axis shows the position along the tool radius in degrees while the y-axis shows the measured tool profile. The tool nose recession (wear) was calculated by taking the difference between the before and after tool nose profiles The wear pattern was observed using both optical and scanning electron microscopes. Figure 3 shows a SEM photograph of the tool wear. The rake face has developed a typical chip crater. Although the chip crater may eventually cause catastrophic failure of the tool, we are more concerned with the wear flat between the rake face and clearance face. This wear flat will produce unacceptable figure error in the part prior to tool failure.

The PAS was very successful in identifying machining parameter influences on tool wear. Since each parameter had a low and high value only simple, linear trends were made. Analysis of the Table 1 data indicated that low tool wear was attainable if: 1) the feed rate was high, 2) the depth of cut was low, 3) the cutting velocity was high, 4) the rake angle was negative, 5) the side rake angle was zero degrees and 6) the tool radius was large.

3. PARAMETER SELECTION STUDY AND RESULTS

The PSS was performed on the LLNL Phoenix DTM due to unavailability of DTM II. The Phoenix DTM, shown in Figure 4, is a precision lathe with a horizontal air bearing spindle and rolling element axes, and the same spindle design as the DTM II. The Phoenix DTM was outfitted with PAG compatible Tygon tubing prior to performing the experiments.

The PSS utilized the same experimental design techniques used in the PAS. Seven new experiments were designed and two PAS experiments (#1 and #2) were duplicated to confirm machine-to-machine repeatability. The new experiments explored the effects of increased feed rate, increased tool radius, increased negative rake angle, increased cutting area, decreased surface velocity, and eliminated side rake angle while retaining the same values for depth of cut. Again, freshly sharpened tools were used to cut the refurbished PAS SCSi boule. A single 25.4 mm wide track and three 50.8 mm wide tracks were cut prior to restoring the boule to a damage-free condition and completing the remaining experiments.

The experiments and results of the PSS are presented in Table 2. The duplicated PAS experiments showed that the SPDT of SCSi is repeatable over time and on different machines. A description of the tool wear models that were developed is required to discuss the influence of machining parameters on the tool wear. Two separate, yet similar, models were developed: the LLNL Tool Wear model is an extension of the Taylor Tool Life Equation, and the Goodman Tool Wear algorithm is an extension of the uncut chip thickness relationship.

4. MODEL DEVELOPMENT

The LLNL Tool Wear model departs from the expanded version of the Taylor Tool Life Equation that relates tool lifetime (T) to feed rate (f), depth of cut (doc), velocity (V) and a tool geometry constant (K) [6].

$$T = \frac{K}{V^{1/n} \quad f^{1/n_1} \quad doc^{1/n_2}} \qquad (1)$$

Equation (1) assumes that cutting speeds are high enough to ignore edge effects. Since this study uses relatively low speeds, the exponential relationship for velocity is not appropriate. Therefore, a quadratic expression that does not force tool wear to monotonically increase as velocity increases was used. The machine, machine operator and coolant delivery system differed in the PAS and PSS. Therefore, I_{f2} (for fluid #2) and I_{m1} (for DTM II) were introduced as binary parameters, having a value of unity if the condition of use was true, a value of zero if false. Tool wear as a function of tool rake angle was incorporated using a quadratic equation to define regions of high and low tool wear. Side rake angle was excluded from the model because data analysis showed little correlation with tool wear. Based on these premises, the LLNL Tool Wear Model is:

$$W = \left(a_1 V^2 + a_2 V\right) f^{a3} doc^{a4} \left(a_5 \alpha^2 + a_6 \alpha + a_7 I_{f2} + a_8 I_{m1} + 1\right) \qquad (2)$$

where I_{f2} is a unique constant for cutting fluid #2, I_{m1} is a unique constant for DTM II, and α is negative rake angle. The constants a_1-a_8 are determined from the experimental data. Equation (2) was fit to the experimental data in Tables 1 and 2 using a non-linear least squares algorithm. The tool wear data and model predictions are compared in Table 3. The results of the study show that: (1) tool radius, skew and area do not significantly affect the tool wear; (2) fluid #1 and fluid #3 affect tool wear in the same way, and fluid #2 minimizes the tool wear; (3) the best velocity within the range tested is 750 ft/min (maximum within the range tested) and the worst velocity is 389 ft/min; (4) the best feed rate is 250 μin/min (maximum within the range tested); (5) the best depth of cut is 40 μin (minimum within the range tested); and (6) the best rake angle is -30°. while the worst rake angle is -60°.

The Goodman Tool Wear algorithm, Equation (3), includes terms from the uncut chip relation, the tool radius (r), the machined area, rake angle (α), skew angle (β) and work energy. The constants x1-x7 were found using Schafer's proprietary non-linear optimization program to fit the data. Table 3 shows that the calculated tool wear

is in excellent agreement with the actual tool wear. Equation (3) favors a high negative rake angle, no skew and a large tool nose radius, but otherwise agrees with the LLNL Tool Wear Model predictions.

$$W = (x1)\,[(f)^{x2}\,(doc/r^2)^{x3}]\,(Area)^{x4}\,(1/\sin\alpha)^{x5}\,(\sin\beta)^{x6}\,(V)^{x7} \qquad (3)$$

Table 1. PAS Experimental Matrix and Resultant Tool Wear

Exp #.	*Surface Velocity (ft/min)*	*Feed Rate (μin/rev)*	*Depth of Cut (μin)*	*Tool Radius (in)*	*Rake Angle (degrees)*	*Side rake Angle (degrees)*	*Area (in^2)*	*Cutting Fluid**	*Tool Wear (μin)*
1	750	50	200	0.06	0	0	15.7	1	25.2
2	100	120	200	0.06	-40	0	15.7	1	6.8
3	100	120	40	0.03	0	40	15.7	1	19.5
4	750	50	40	0.06	0	40	15.7	1	12.7
5	100	50	40	0.03	-40	40	15.7	1	23.9
6	100	120	200	0.03	0	0	15.7	2	9.2
7	750	120	40	0.03	-40	0	15.7	2	2.6
8	100	50	40	0.03	0	40	15.7	2	30.5
9	750	120	200	0.06	0	40	15.7	2	5.5
10	100	50	200	0.06	-40	40	15.7	2	5.2
11	750	50	200	0.03	0	0	15.7	3	17.4
12	100	50	40	0.06	-40	0	15.7	3	20.3
13	100	120	40	0.06	0	40	15.7	3	16.9
14	750	120	200	0.03	-40	40	15.7	3	4.4

* Fluid 1=PAG; Fluid 2=PAG with water; Fluid 3=PAG with water and tri-potassium phosphate

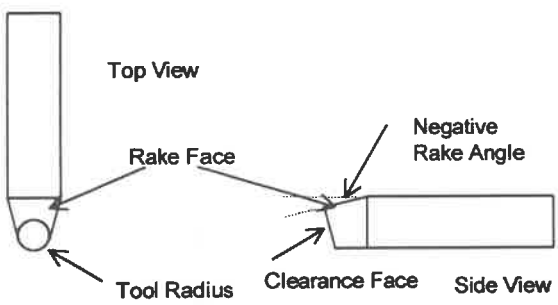

Figure 1. Tool Geometry

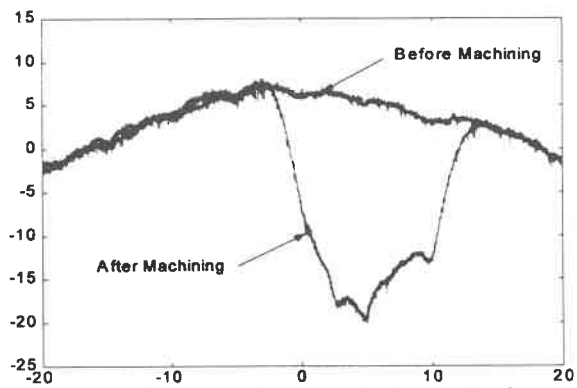

Figure 2. Example Tool Profile Scans

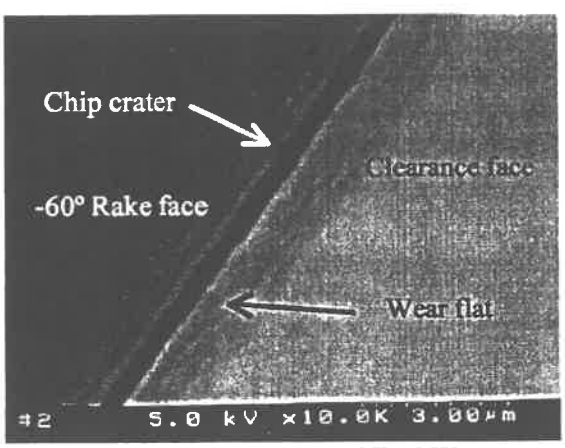

Figure 3. SEM Photograph of Tool Wear

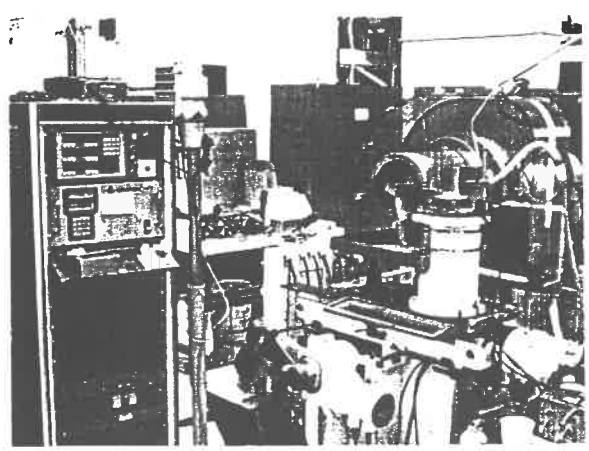

Figure 4. Phoenix DTM Used for PSS and FDS

Table 2. PSS Experimental Matrix and Resultant Tool Wear

Exp#.	*Velocity (ft/min)*	*Feed Rate (μin/rev)*	*DOC (μin)*	*Tool Radius (in)*	*Rake Angle (degrees)*	*Area (in^2)*	*Tool Wear (μin)*
Repeat of PAS #2	100	120	200	0.06	-40	15.7	7.0
1	100	50	200	0.06	-60	31.4	25.0
2	100	250	200	0.20	0	31.4	0.9
3	600	50	200	0.06	0	31.4	35.0
4	600	250	40	0.06	0	15.7	2.0
5	600	250	40	0.20	-60	31.4	2.75
6	100	250	200	0.20	0	31.4	1.0
7	**100**	**250**	**40**	**0.20**	**-60**	**31.4**	**5.0**
Repeat of PAS #1	750	50	200	0.06	0	15.7	31.0

PSS Experiment 7 Baselined for FDS Experiments

Table 3. Tool Wear Model Results

Experiment	Tool Wear (μin)	LLNL Model (μin)	Goodman Model (μin)
PAS #1	25.2	20.3	28.1
PAS #2	6.8	9.0	7.1
PAS #3	19.5	15.8	19.3
PAS #4	12.7	16.1	12.7
PAS #5	23.9	22.4	24.1
PAS #6	9.2	12.3	Not Modeled
PAS#7	2.6	0.36	Not Modeled
PAS #8	30.5	30.7	Not Modeled
PAS #9	5.5	4.0	Not Modeled
PAS #10	5.2	4.4	Not Modeled
PAS #11	17.4	20.3	Not Modeled
PAS #12	20.3	22.4	Not Modeled
PAS #13	16.9	15.8	Not Modeled
PAS #14	4.4	2.9	Not Modeled
Repeat of PAS #1	31.0	20.3	28.1
Repeat of PAS #2	7.0	9.0	7.1
PSS #1	25.0	25.1	24.8
PSS #2	0.9	2.65	1.83
PSS #3	35.0	34.5	35.1
PSS #4	2.0	3.3	1.33
PSS #5	2.75	3.8	0.13
PSS #6	1.0	2.7	1.83
PSS #7	5.0	2.4	0.25

1. C.K. Syn, D.A. Krulewich, P.J. Davis, M.R. McClellan, P.C. DuPuy, M.A. Wall, and K.L. Blaelel, "An Empirical Survey on the Influence of Machining Parameters in Diamond Turning of Large Single Crystal Silicon Optics", *ASPE Spring Topical Meeting on Silicon Machining Proceedings, 1998*, **17**, 44-49
2. P. N. Blake and R. O. Scattergood, "Ductile-regime machining of germanium and silicon", *Journal of the American Ceramic Society, 1990, 73 (4), 949-957.*
3. C. K.Syn, J. S. Taylor, R. R. Donaldson, and S. Shimada, *Proc. JSPE 1988 Spring Meeting, Kawasaki, Japan, pp. 781-782.*
4. W. S. Blackley and R. O. Scattergood, "Ductile-regime machining model for diamond turning of brittle materials", *Precision Engineering, 1991, 13 (2), 95-103.*
5. D.A. Krulewich, "Experimental design for single point diamond turning of silicon optics", *UCRL-ID-127385, (1996)*
6. E.J.A. Armarego and R.H. Brown, **The Machining of Metals**, Prentice-Hall, Inc., N.J. (1969)

Development of Ultra-Precision Double-Disk Grinding Machine for Silicon-wafer

Kazutoshi Hara, Sho Isobe, Hiroshi Nagata, Akio Iwase, Yoshiyuki Tomita
Sumitomo Heavy Industries, Ltd.
63-30 Yuuhigaoka, Hiratsuka-city, Kanagawa Pref.,254-0806, JAPAN
Akira Kanai
Ashikaga Institute of Technology
Masakazu Miyashita
Nano-Tec Associates

1. Introduction

Recently, ultra-precision grinding systems are remarkably expected for manufacturing super flat wafer in sub-micron order flatness, instead of conventional lapping and etching processes.[1] To respond to the demands, a double-disk grinding machine based on motion copying concept[2] is under development for 8" and 12" silicon-wafer process. This paper introduces the newly developed grinding system including the configuration, mechanical structure and control system, and also presents some experimental evaluations of system's performance.

2. Configuration of Ultra-precision Double-Disk Grinding System

Fig.1 shows a schematic configuration of the newly developed double-disk grinding machine. This machine has a horizontal double spindle-type configuration in line, consisting of a stationary spindle, a movable spindle mounted on the saddle, wafer support/drive unit, and 1.0m×2.0m granite base plate. Two spindles are located facing each other, and both sides of wafer are simultaneously ground via cup-type diamond grinding wheels mounted on these spindles.

Each of spindles has a stationary inner stator and outer rotor (Fig.2), levitated by hydrostatic bearing to obtain high stiffness, damping and rotational accuracy.[3] In order to effectuate the control of the attitude of the rotor, three thrust pads on each side of the stationary inner stator, and four radial pads on the circumference of the inner stator are equiped. Three capacitive transducers are located at the back of the thrust hydrostatic bearing to measure the spindle attitude. The grinding wheels of ϕ320mm are mounted on the spindles, and the temperature of hydraulic oil is controlled within ±0.1℃ accuracy. Each rotor is driven by a low vibration-type induction motor and seamless belt. The saddle, on which the movable spindle is located, is guided via a double-V linear slide mechanism with hydrostatic preloading unit, being driven by a force-operational hydraulic linear

actuator and a double nozzle-flapper type servo valve. A laser interferometer measurement system(HP 5518A USA) with the resolution of 2.5nm is used to obtain high-resolution position feedback signal for position servo control system. Its reflecting mirror is mounted on the side of the saddle near grinding point to minimize the wheel position measurement error based on the Abbe's principle. The wafer support/drive unit enables damage-free hold and rotation by employing opposed pad water hydrostatic bearing and friction drive mechanism using plastic rollers. Table 1 describes specifications of this machine.

3.Control System

A schematic block diagram of the control system is also shown in Fig.1. The machine control system consists of a host PC, saddle position control system, and the tilt control system for the two axis of the spindle. The saddle position control is achieved via the PID servo control system with the laser interferometer feedback, and that of the tilt motion of the two axis of the spindle by controlling the differential pressure of each thrust bearing pad using pressure control servo valves.

4. Experimental Evaluations

To realize the super-flat wafer grinding by the cup-type grinding wheels, the following machine performances are required.[4]

① High loop stiffness of machine.

② High positioning resolution in the order of 10nm.

Regarding this machine planned to use cup-type grinding wheel, we evaluated stiffness of spindle in the thrust direction, as a primary element to realize high loop stiffness. As a result the stiffness higher than 1,200 [N/μm] has been obtained as shown in Fig.3. The resultant value is significantly higher than that of the conventional rolling bearing.

Next we evaluated the saddle positioning capability. In the configuration of the machine the target mirror of the laser-interferometer is located near the grinding point, therefore the result of this evaluation is near equal as to the behavior of the movable spindle at the grinding point. Fig.4 shows the response to the 20nm stepwise motion command. The saddle feeding system realized 20nm positioning resolution without backlash and hysteresis. The evaluation of fundamental characteristics of the machine related with the grinding accuracy of wafers are in progress.

5.Conclusions

1) An ultra-precision double-disk grinding-machine for Si-wafer has been developed.

2) Some performance tests of its mechanical component have been carried out. The stiffness of

the spindle higher than 1,200 [N/μm] in the thrust direction has been achieved.
Moreover the 20nm positioning resolution exempt from backlash and hysteresis has been realized in response to the step motion commands.

References

(1)K.Abe, S.Okawa, Y.Koma, K.Arai, "Development of Ultraprecision Grinding Machine for Super-Large and Super-Flat Silicon Wafer";Proc. of 1998 ASPE Annual Meeting.
(2)J.Hisada, A.Kanai, M.Miyashita, "Experimental Analysis of Force-operated Feed Mechanism of Slide on Plain Bearing Guideways for Long Travel Range"; Proc. of 1994 ASPE Annual Meeting 267-270.
(3)J.Yoshioka, M.Miyashita, A.Kanai, M.Daito, F.Inaba,"Removable and High Stiffness Mount of Grinding Wheel Achieving Runout of 100nm";Proc. of 1989 ASPE Annual Meeting.
(4)K.Abe, N.Yasunaga, M.Miyashita, J.Yoshioka, M.Daito, "Ductile Mode Grinding for Silicon Wafer"; 1993 Proc. of The Society of Grinding Engineering, Japan, D02, 227.

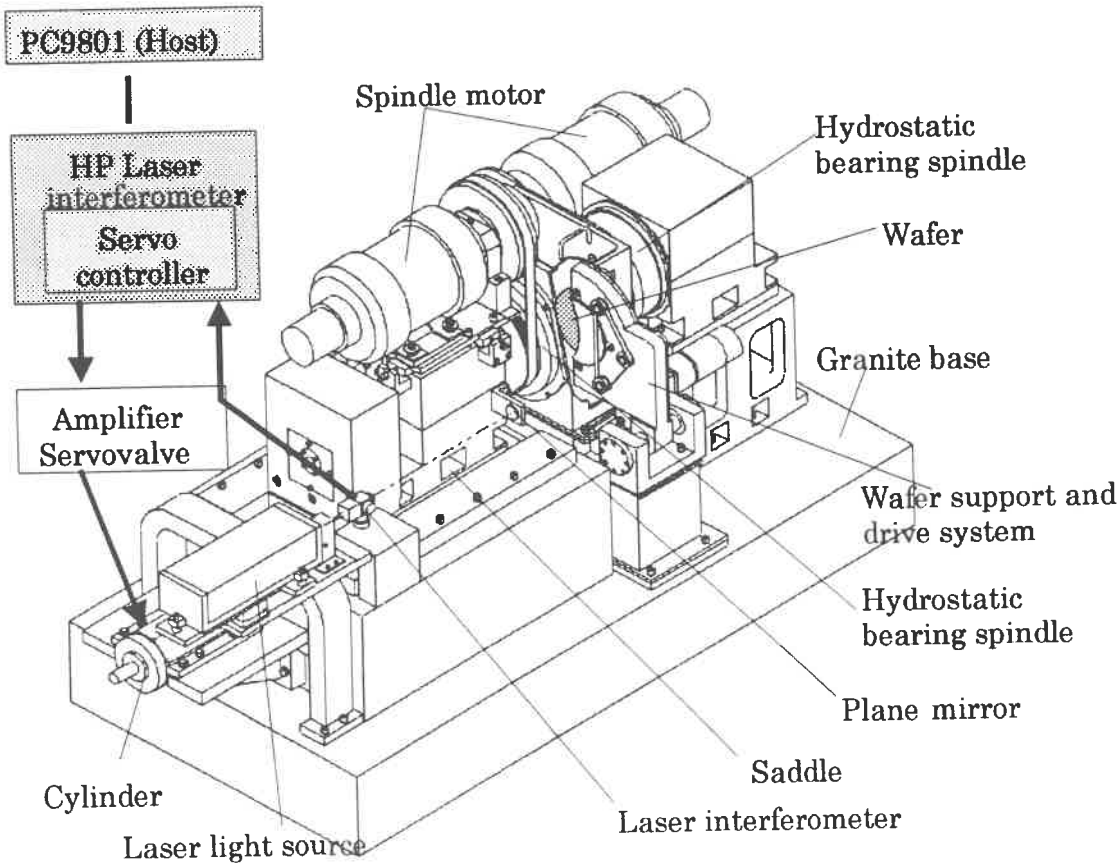

Fig.1 Configuration of Ultra-precision Double-Disk Grinding Machine

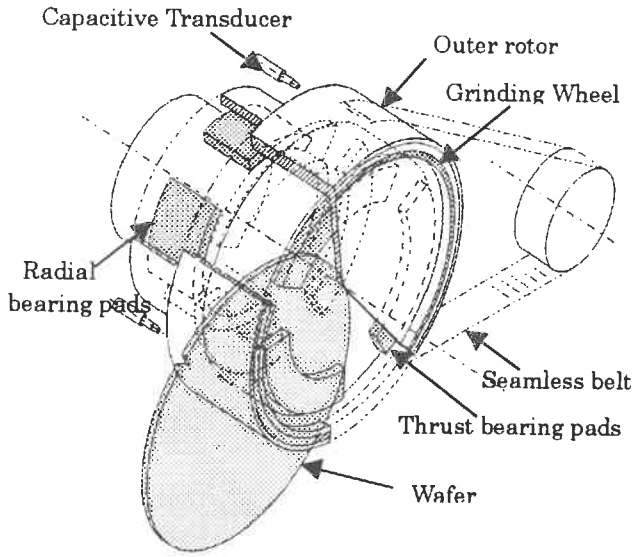

Fig.2 Spindle Structure

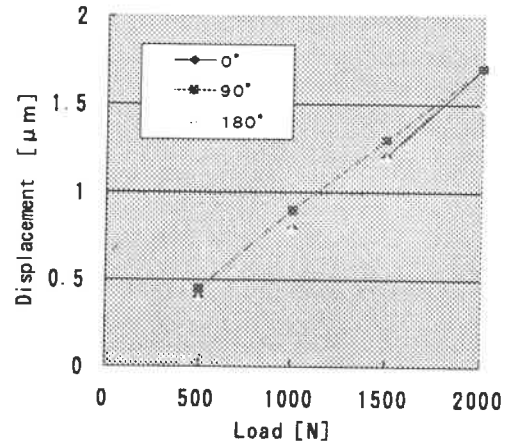

Fig.3 Result of Thrust Stiffness

Table1 Machine Specifications

	Machine specifications	Hydro-static spindle	
Configuration	Horizontal type double disk grinding system	Viscocity	10 cSt
Wafer size	200~300mm	Supplied pressure	2.94 MPa
Spindle	Hydrostatic bearing/Outer rotor	Rated speed	1910 rpm
Spindle motor	5.5kW/Belt drive	Thrust bearing	
Saddle	Stroke 100 mm／Velocity 20mm/min	Gap	30 mm
Drive of saddle	Operation by hydralic actuator	Pad configuration	3x2 pads
Position sensor	Laser interferometer(Resolution 2.5 nm)	Stiffness	1200 N／μm
Wafer support	Roller drive/Water-hydrostatic support	Radial bearing	
Dimension	1(W)×2(L)×1.3(H) m	Gap	30 μm
Weight	3.500 kg	Pad configuration	4pads

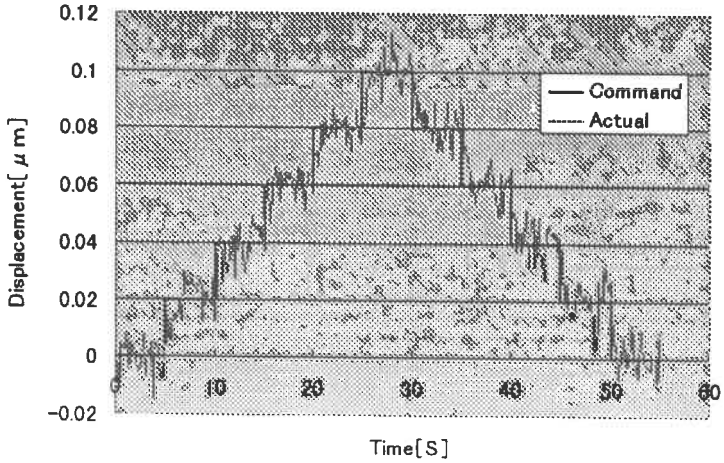

Fig.4 Response to Step Motion of 20nm

A Precise Track-following Control using a Single-stage Tracking Mechanism for Magneto-optical Disk Drives

Ichiro Watanabe, Takayuki Kawabe, Hiroki Kobayashi, and Jun-ichi Ichihara
Fujitsu Laboratories, Ltd., Kawasaki, Japan

Toru Ikeda and Shin-ichi Otsuka
Fujitsu Limited, Kawasaki, Japan

1. Introduction

The authors have developed a low-cost, high-performance *magneto-optical disk drive* whose track-following control was achieved using a novel *single-stage tracking mechanism*. Conventionally, the track following has been performed using the *dual-stage tracking mechanism*, which consists of a coarse positioner driven by a voice coil motor (*VCM*) and a fine lens actuator loaded on the positioner. The positioner and the actuator are simultaneously driven in the radial direction of the disk while following the track. The lens actuator is driven also in the direction of the optical axis of the lens for focusing control. Such a two-dimensional lens actuator has a complicated mechanism and increases the number of mechanical parts as shown in **Fig.1** (a).

In the newly developed *single-stage tracking mechanism* shown in **Fig.1** (b), the track following is performed only by a VCM-driven positioner, and the lens actuator only performs the focusing control. And slide bearings are employed for positioner suspension replacing ball bearings. Thus, the mechanism is drastically simplified and the cost is reduced. Moreover a shorter seek time is achievable because the simplified positioner has a smaller mass.

However, the Coulomb friction caused by the slide bearings of the positioner is a critical problem for achieving precise track following. In this paper, we propose a novel track-following control system with a learning controller which suppresses the influence of Coulomb friction and achieves precise track following.

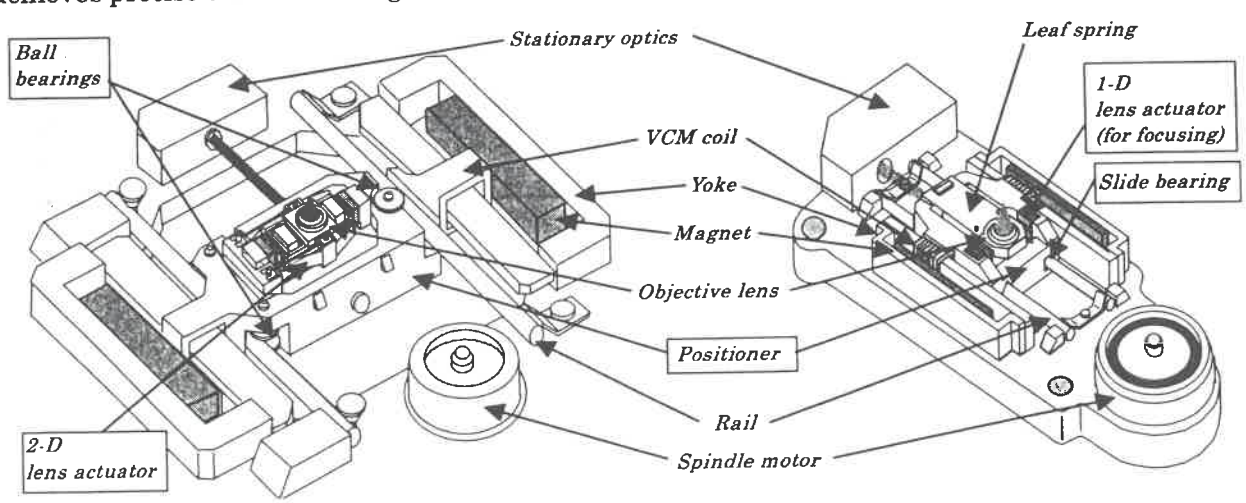

(a) Dual-stage tracking mechanism (conventional) (b) Single-stage tracking mechanism

Fig.1 Dual- and single-stage tracking mechanisms

2. An *ideal VCM current* signal to compensate for Coulomb friction disturbance

Fig.2 shows the Coulomb friction characteristic. The disturbance caused by the Coulomb friction is difficult to compensate for, because the Coulomb friction force rapidly changes its direction when the direction of the positioner motion changes. In the other words, the friction

disturbance includes high frequency components.

Fig.3 shows the relation, during track following under the influence of Coulomb friction, among the waveforms of the (a) positioner's acceleration to follow a sinusoidal track runout, (b) change of the friction disturbance, and (c) required VCM drive current. Waveforms for three disk rotations are displayed. The VCM current shown in (c) includes not only a signal to generate the positioner's acceleration shown in (a), but also a steep signal to cancel the friction disturbance shown in (b). Therefore this VCM current can achieve precise track following by compensating for the friction disturbance perfectly, and we call it an *ideal VCM current* in this paper. For the conventional feedback controller, it is impossible to generate this kind of current waveform including such steep changes because of the limitation of the control bandwidth. Since it is hard to increase the bandwidth because of the limitation of the positioner's mechanical resonance, large and steep tracking errors occur.

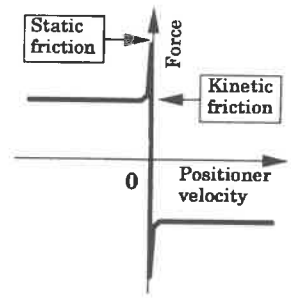

Fig.2 Coulomb friction

In order to solve this problem, we developed a learning controller, which generates and feeds an approximated signal of the *ideal VCM current* forward for precise tracking. As in Fig.3, the *ideal VCM current* is a kind of repetitive signal that almost has a time-invariant signal pattern synchronized to the rotation of the disk, and therefore, the controller can *learn* this signal.
(In Fig.3; Disk rotational frequency: 75 Hz (i.e. rotational period: 13.33 ms), radial runout of the track: 80 μmp-p, friction coefficient μ of slide bearing: 0.4 (for simplicity, the same coefficient is used for both static and kinetic friction), positioner's mass: 2.7 g, and positioner's acceleration coefficient: 99.5 m/s²/A, are assumed.)

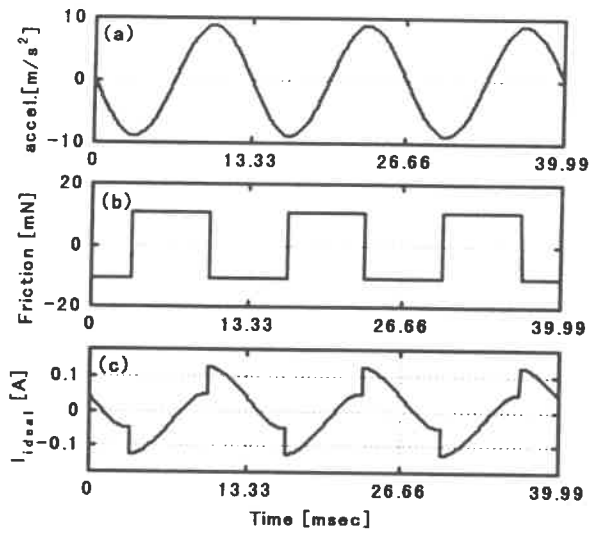

Fig.3 *Ideal VCM current* for precise tracking

3. Track-following controller with *ideal VCM current learning*

3.1 Structure of the track-following controller

Fig.4 shows the structure of the proposed track-following controller. I is the VCM current to drive the positioner. X, X_{RO}, and e denote the positioner's position, the target track's runout, and the tracking error (TE) respectively. The learning controller takes the output signal of the feedback controller I_{FB} as its input, and generates an approximated function I_{FF} of the *ideal VCM current*. The I_{FF} is added to I_{FB} as a feed-forward compensation signal.

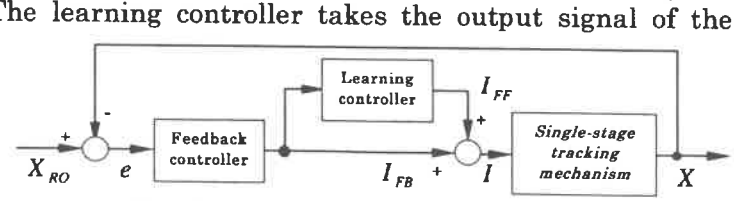

Fig.4 Track-following controller structure

3.2 Feedback controller

The feedback controller is implemented with an ordinary PID-like controller that consists of a series connection of a PI regulator, a 2nd-order phase-lead compensator, and a notch filter $G_{notch}(s)$ to eliminate the influence of mechanical resonance of the positioner existing from around 15 to 25 kHz.

$$G_{FB}(s) = \frac{I_{FB}}{e} = K_P \cdot (1 + \frac{K_I}{s}) \cdot \frac{(1+T_{Z1} \cdot s)(1+T_{Z2} \cdot s)}{(1+T_{P1} \cdot s)(1+T_{P2} \cdot s)} \cdot G_{notch}(s) \qquad (1)$$

Fig.5 shows the open loop frequency characteristics of the feedback control system. The actual controller was implemented on a fixed-point DSP. The sampling rate was 55 kHz. A control

bandwidth of 2.1 kHz was acheieved with a gain margin of 7 dB and a phase margin of 34 degrees.

3.3 Learning controller

Fig.6 shows the principle of the unknown function approximation. The bold solid line indicates an unknown *ideal VCM current* $I_{ideal}(t)$ to suppress the repetitive disturbance synchronized to the disk rotation. Time t in Fig.6 and the following eqs. (2) to (4) is the time synchronized to the disk rotation, and is reset to zero at a certain time in every rotation period (i.e. $0 \le t < T_L$, T_L: period of disk rotation).

Now we try to get an approximated function $\hat{I}_{ideal}(t)$ using a set of the heights of N rectangular functions, indexed from 0 to N- 1.

$$\hat{I}_{ideal}(t) = \hat{c}_i, \qquad (2)$$

where $i = floor(t/T)$, and T is the time width of each rectangular function (i.e. $T = T_L / N$, and $0 \le i < N-1$). $floor(x)$ is a function that rounds x to the nearest integer less than or equal to x.

The height $\hat{c}_i$ for each rectangular function is updated in real-time by a simple learning algorithm using the output of the feedback controller $I_{FB}(t)$ as the learning input.

$$\dot{\hat{c}}_i = \begin{cases} k \cdot I_{FB}(t) & if \quad iT \le t < (i+1)T \\ 0 & otherwise \end{cases} \qquad (3)$$

Where, k is a constant learning gain. This learning algorithm changes the height of each rectangular function in the direction that $I_{FB}(t)$ approaches toward zero.

Finally the learning controller outputs the feed-forward signal $I_{FF}(t)$ as follows.

$$I_{FF}(t) = \begin{cases} \hat{I}_{ideal}(t + \Delta t_{lead}) & if \ 0 \le t < (T_L - \Delta t_{lead}) \\ \hat{I}_{ideal}(t + \Delta t_{lead} - T_L) & if \ (T_L - \Delta t_{lead}) \le t < T_L \end{cases} \qquad (4)$$

Δt_{lead} is a constant time lead factor for stabilizing the learning convergence.

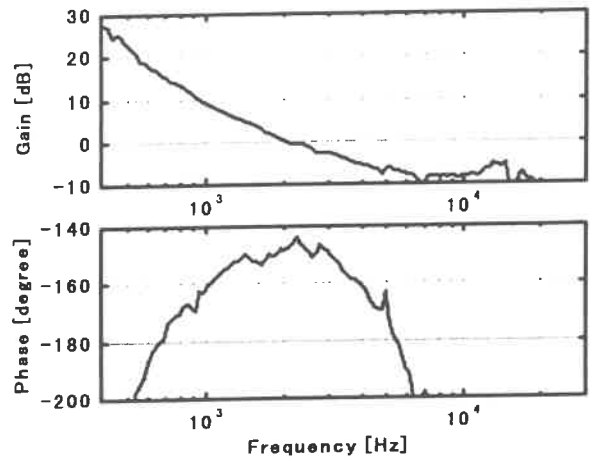

Fig.5 Open-loop characteristics of the system

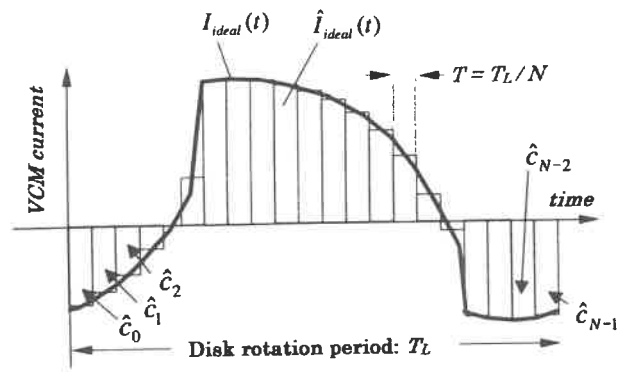

Fig.6 Reconstruction of unknown ideal VCM current

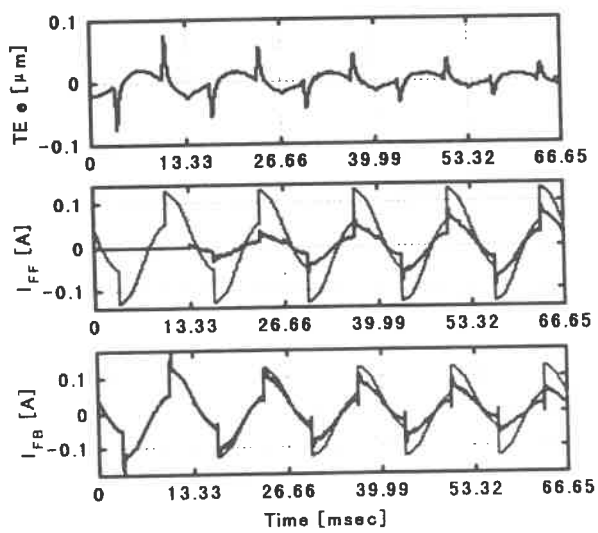

Fig.7 Learning simulation
- at the beginning -

4. Learning simulation

Fig.7 followed by Fig.8 shows the simulation result. A sinusoidal runout of 80 μmp-p at 75 Hz and a Coulomb friction of $\mu = 0.4$ were applied as disturbance. The characteristic of the feedback control system was set equivalent to that of Fig.5. For reference, the *ideal VCM current*, which was calculated using the applied disturbance in the

simulation, is indicated with gray lines in these figures. The learning law **eq.(3)** was started at 0 ms, and the feed-forward output by **eq.(4)** was started at 13.33 ms. Therefore during the first disk rotation until 13.33 ms, the positioner was driven by the feedback current I_{FB} only, and large tracking error (*TE*) *e* peaks occurred, when the friction direction changed. The *TE* caused by the sinusoidal runout was also conspicuous. After the second rotation, the *TE* was gradually reduced toward zero, as the learning progressed through one disk rotation after another. As shown in **Fig.8**, the learning output I_{FF} was precisely converging to the *ideal VCM current* and the *TE* became almost zero within 174 ms from the start of learning.

(Learning-related parameters in this simulation were set as follows; N = 128, T_L = 13.33 ms, T = 104 μs, Δt_{lead} = 109 μs, and k = 1852 /s.)

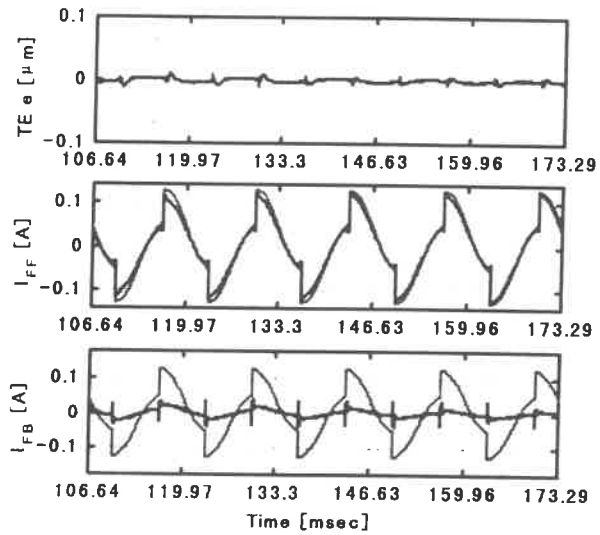

Fig.8 Learning simulation - almost conversing -

5. Experimental results

We also checked the efficiency of the proposed control system on a prototype drive using the *single-stage tracking mechanism* as shown in **Fig.1** (b). A 640MB MO disk having a track pitch of 1.1 μm and an actual radial track runout of 77 μmp-p, and rotating at 75 Hz was used. **Fig.9** shows the experimental results. The *TE* had large peaks before learning and was drastically reduced after learning. Since the learning gain was reduced because of a noise problem, time required for learning convergence was about 640 ms, longer than in the case of simulation. **Fig.10** shows the learning result I_{FF} recorded simultaneously with the *TE* data in **Fig.9** (b). It is obvious that the steep change caused by Coulomb friction is acquired by learning. We can estimate the friction coefficient μ at about 0.3 from this figure.

(Learning-related parameters in this experiment were set as follows; N = 91, T_L = 13.33 ms, T = 146 μs, Δt_{lead} = 109 μs, and k = 336 /s.)

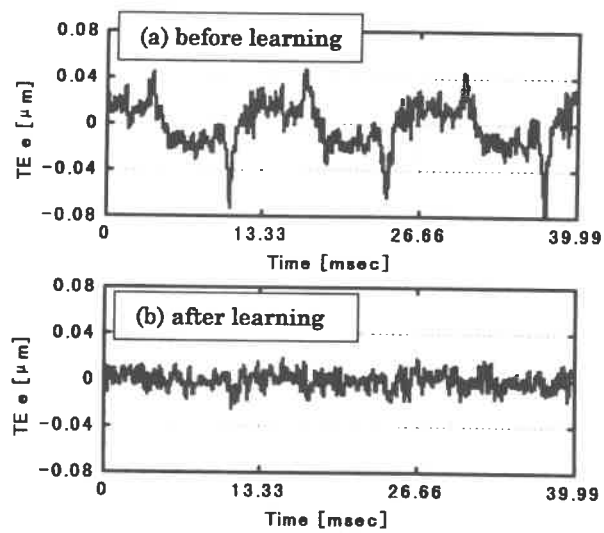

Fig.9 Experimental results

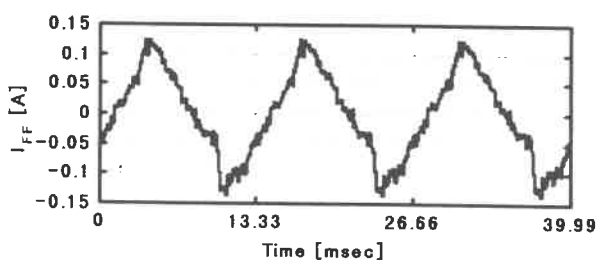

Fig.10 Learning result I_{FF} during Fig.9 (b)

6. Conclusion

We proposed a track-following controller with an *ideal VCM current learning controller* for achieving precise track following even under the Coulomb friction disturbance of the *single-stage tracking mechanism*.

The effect of the proposed controller was verified both by simulation and experiment.

The tracking error less than about 0.02 μm was confirmed under the Coulomb friction disturbance of μ = 0.3 using a MO disk rotating at 75 Hz with a radial track runout of 77 μmp-p. Also, a fast learning convergence of less than 640 ms was obtained.

Calibration and Control of a Rotary Fast Tool Servo

Stephen J. Ludwick, David A. Chargin, Joseph A. Calzaretta, David L. Trumper
Massachusetts Institute of Technology
Department of Mechanical Engineering
Cambridge, MA

Abstract

In this paper we present calibration and control methods developed for a diamond turning machine that includes a novel rotary fast tool servo. We have built a prototype turning machine specialized for the production of plastic spectacle lenses to test this concept. This machine can turn 100 mm diameter toric parts having surface asymmetries of up to 3 cm. The fast tool servo can track trajectories at frequencies of up to 500 Hz, and accelerations of 500 m/s^2. The calibration methods developed in this paper determine precise values for the arm length and encoder index locations. The control system consists of a conventional inner position control loop, feedforward filtering, and repetitive control. We present experimental results demonstrating the ability of the machine to turn a toric surface with tracking errors of less than 2 μm.

1 Introduction

A fast tool servo is a specialized axis on a lathe that allows the machine to turn asymmetric parts. Examples of these parts include cams, off-axis paraboloids, and ophthalmic lenses. Our focus in the present research is on the commercial production of plastic spectacle lenses. Traditional fast tool servos in the literature carry the cutting tool through an essentially linear path. However, a consequence of a linear design is that the bearings, actuator, and support structure all contribute equally to the mass that must be accelerated along with the cutting tool. The resulting reaction force applied to the base can excite structural resonances, and so counter-masses are often used in an attempt to contain this force [4].

The cutting tool in our rotary fast tool servo is carried at the end of an 8 cm arm that pivots about an axis of rotation. In this fashion, only the cutting tool at the end of the arm moves through the largest displacement. The bearings, actuator, and sensor, located closer to the axis of rotation, contribute less to the overall inertia. The benefits of this rotary configuration over a linear system include significantly reduced reaction forces, higher achievable accelerations (experimentally demonstrated at 500 m/s^2), lower cost, and more compact size. To further develop this concept we have built a prototype turning machine with a rotary fast tool servo, as shown in Figure 1. The mechanical design of the prototype machine has been documented in [1] and [2]. In this paper, we present calibration and control methods developed for it. A significant mechanical change to the machine design since the documented work has been the addition of a double-ended arm. The arm carries a polycrystalline diamond tool for roughing cuts on one end, and a single-crystal diamond tool at the other. It also contains an integrated flexure assembly for tool height adjustment within a 20 μm range. An advantage of the rotary-arm configuration is that the extra tool can be added for no increase in machine size, and only a small increase in inertia.

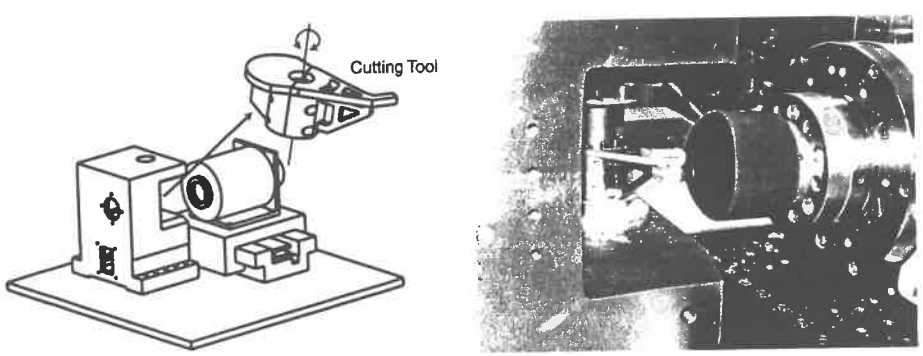

Figure 1: Drawing and photograph of the prototype turning machine using the rotary fast tool servo.

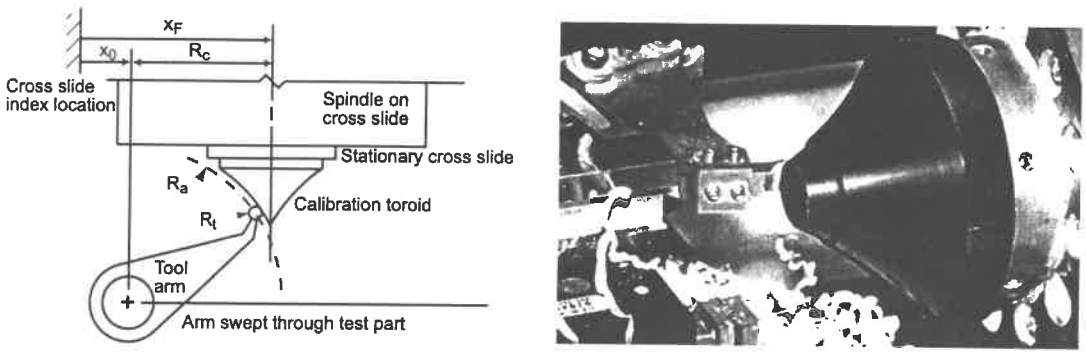

Figure 2: Diagram and photograph of the technique for determining arm length and cross-slide offset.

2 Calibration Techniques and On-Board Metrology

This section presents our latest calibration methods for determining more exact values of the tool arm length, and the location of the index pulses on the tool axis and cross slide encoders. A great asset in calibrating the machine as well as determining the lens error profile is our on-board metrology, which consists of a 0.1-μm resolution linear encoder mounted to the tool servo housing. This encoder measures part depth with a scanning probe of known radius R_p. By scanning the probe over the part, a surface profile is generated.

We developed a method which determines the tool arm length R_a and the cross-slide offset x_0, shown in Figure 2. After the tool is in place and the tool arm height is adjusted, we cut a test part with the cross-slide axis fixed at a known position x_F. This forms a toroidal surface obtained by revolving the arc of a circle about an axis. Once we cut this calibration toroid, we then use the probe to profile its surface. The gathered data is used to find the arc radius and distance R_c from the cusp to the arc center through a least-squares fit. The measured arc radius is equal to the sum of the tool arm length R_a and tool radius R_t, less the probe radius R_p. The cross slide offset x_0 is equal to the sum of R_c and x_F. This method allows us to determine these parameters to an accuracy on the order of one micron.

Figure 3 depicts the method for determining the tool arm offset angle, b_0. The machine cuts a series of flat lenses, and for each pass, we record the tool arm angle b_i. After each pass, we stop the spindle and measure the depth p_i with the probe. As seen from the figure,

$$R_a \sin(b_0 + b_i) = p_i - (R_t + p_0), \tag{1}$$

where p_0 is the depth of the tool axis in the frame of the indicator. The value of R_a is known from the preceding experiment. A least-squares fit to the data to determines the unknown parameters: the relatively unimportant $(R_t + p_0)$, and the tool arm offset angle b_0. This method allows us to determine the tool arm offset angle to within 0.01 mrad.

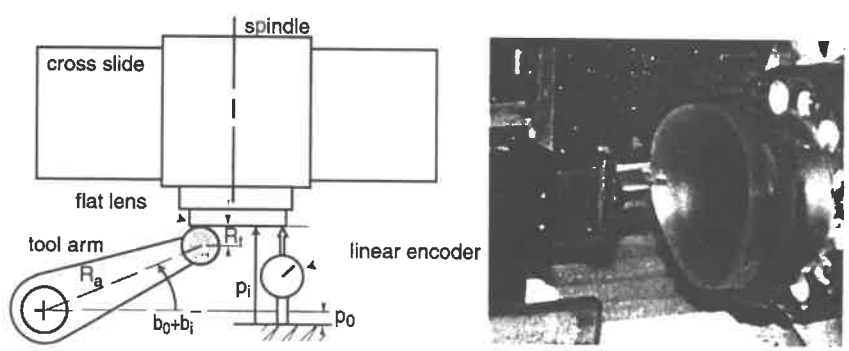

Figure 3: Procedure for calculating the tool offset angle.

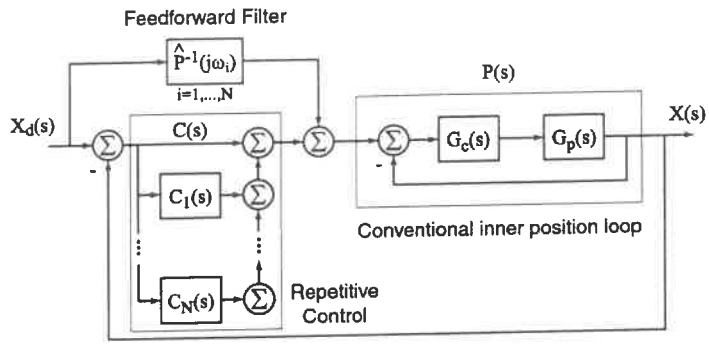

Figure 4: Overall control system design for the fast tool servo axis. The controller contains a conventional inner position loop, a feedforward filter that inverts the position loop response on a frequency-by-frequency basis, and a repetitive control algorithm to correct for modeling error and external disturbances.

3 Control System Design

The control system for the fast tool servo consists of three parts. The first is a position loop that achieves a closed-loop bandwidth of 230 Hz with conventional lead-lag compensation. The second part of the control system is a feedforward filter that pre-shifts the required tool trajectory by the measured frequency response of the position loop. This open-loop technique is sensitive to modeling errors and external disturbances (such as cutting loads). These are corrected for with a repetitive control algorithm which increases the dynamic stiffness of the axis at the multiples of the spindle frequency where the required trajectory and the disturbances are concentrated. Figure 4 shows a block diagram of the overall tool axis control system. All of the algorithms are implemented in discrete-time on a PC-based digital signal processor at a 10 kHz sampling frequency.

The required tool position is created in real-time from the the measured positions of the spindle and cross slide. Such a scheme exploits the high-bandwidth, high-acceleration capabilities of the fast tool servo to adjust for positioning errors in the other two axes. The software stores the coefficients of a Fourier Series representation of the toolpath, and thus the required trajectory consists entirely of a summation of sinusoids at integer multiples of the spindle rotational frequency. Representing the required tool position as z, the cross slide position as x, and the spindle angle as θ, we have that

$$z(x,\theta) = \sum_{n=0}^{N} a_n(x)\cos n\theta + b_n(x)\sin n\theta \tag{2}$$

The coefficients a and b are stored in the lookup table. Typically we require between 6 and 10 harmonics to capture to true shape to within sub-micron errors. We then use the measured frequency response of the position loop to pre-shift the tool trajectory on a frequency-by-frequency basis, thus approximately canceling the plant dynamics. Such a feedforward filter is very accurate at inverting the plant at particular frequencies, and is not affected by the presence of non-minimum phase zeroes. Feedforward filtering alone typically reduces our tracking errors to less than about 2%.

A repetitive control scheme further increases the tracking accuracy. This particular algorithm is based on work in adaptive feedforward cancellation by Messner and Bodson [3]. It contains a series of sinusoidal generators that produce the required control effort to drive the tracking error to zero. The concept is similar to using an integrator for achieving zero errors under constant inputs. This algorithm is equivalent to the linear system given by

$$C(s) = k\left(1 + \sum_{n=1}^{N} \frac{g_n s}{s^2 + n^2\omega_s^2}\right), \tag{3}$$

where ω_s represents the fundamental spindle frequency, and g_n is a constant gain. We are currently applying repetitive control to the first five even harmonics of the spindle frequency.

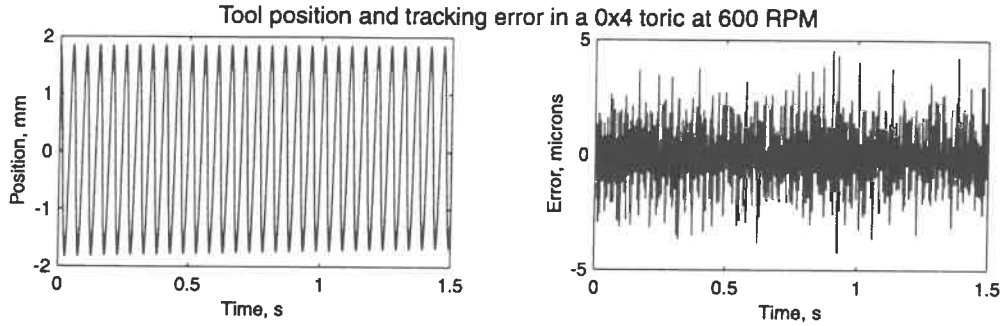

Figure 5: Tool servo tracking performance while turning a 0x4 toric surface in an optical plastic at 600 RPM. The left trace shows the position, and the right trace shows the tracking error.

4 Results

We are now concentrating on applying the calibration and control algorithms with the goal of turning plastic spectacle lenses with form accuracies of approximately one micron, and surface finishes of less than 200 nm R_q. It then becomes feasible that such lenses can be coated to optical clarity direclty, eliminating an existing time-consuming and inaccurate lapping and polishing process. We are near to such performance in the present prototype machine. Figure 5 shows the tracking performance of the fast tool servo system when turning a toric surface in CR39 (a common optical plastic) with the single-crystal tool. The trace was gathered at a cutting radius of about 30 mm and a spindle speed of 600 RPM. This lens surface is flat along one axis, and has a concave radius of 132.5 mm along the other. The resulting cylindrical surface is considered a very difficult prescription to cut by present standards. The residual tracking error has an rms value of 1.2 microns, and is concentrated at the 12th harmonic of the spindle frequency. The repetitive control algorithm can be expanded to attenuate this component of the error, but at present we are at the limits of processing capability on our DSP. We plan to upgrade it in the near future, and proceed with a second-generation machine design.

5 Acknowledgments

The authors would like to thank Prof. Robert Hocken from the University of North Carolina at Charlotte, and Mr. Jim Bryan, formerly of Lawrence Livermore National Laboratory, for their extensive help in developing the calibration procedures. We would also like to thank MicroE for their donation of an encoder system, the Moore Tool Company for their donation of a machine base, and Deka Research for performing the EDM work on the tool arm. Portions of this work form part of the Masters theses of David Ma and David Chargin, and the Doctoral thesis of Stephen Ludwick, all in the Mechanical Engineering department at M.I.T.

References

[1] Stephen J. Ludwick, David A. Chargin, Joseph A. Calzaretta, and David L. Trumper. Design of a rotary fast tool servo for ophthalmic lens fabrication. *Precision Engineering*, 1999. accepted for publication.

[2] Stephen J. Ludwick, David C. Ma, and David L. Trumper. A rotary arm based turning machine for ophthalmic lenses. In *Proceedings of the 13th Annual Meeting – The American Society for Precision Engineering*, volume 18, pages 53–56, 1998.

[3] William Messner and Marc Bodson. Design of adaptive feedforward algorithms using internal model equivalence. *International Journal of Adaptive Control and Signal Processing*, 9:199–212, 1995.

[4] M. Weck, H. Oezmeral, K. Kehlkopp, and T. Terwei. A long stroke fast-tool-servo with air bearings. In H. Kunzmann, editor, *Progress in Precision Engineering and Nanotechnology*, pages 393–396, 1997.

Quasi-Kinematic Couplings: A Low-Cost Method For Precision Coupling of Product Components and The Like In Manufacturing Processes

Martin L. Culpepper, Prof. Alexander H. Slocum
MIT Precision Engineering Research Group, Cambridge, MA

F. Zafar Shaikh
Ford Scientific Research Labs, Dearborn, MI

MOTIVATION

Traditionally, precision assemblies in high volume manufacturing have used pin-hole joints; however the evolution of more stringent design requirements has pushed the performance of this method to its practical performance limit of approximately five microns repeatability. Next generation designs (i.e. automotive engines and pump assemblies) require low-cost couplings which permit sealing between interfaces and deliver better than five micron repeatability. This presentation will introduce a fundamentally new type of kinematic coupling, the quasi-kinematic coupling, which costs less than most precision pinned joints, delivers sub-micron repeatability, and allows contact/sealing between mated components.

GEOMETRY

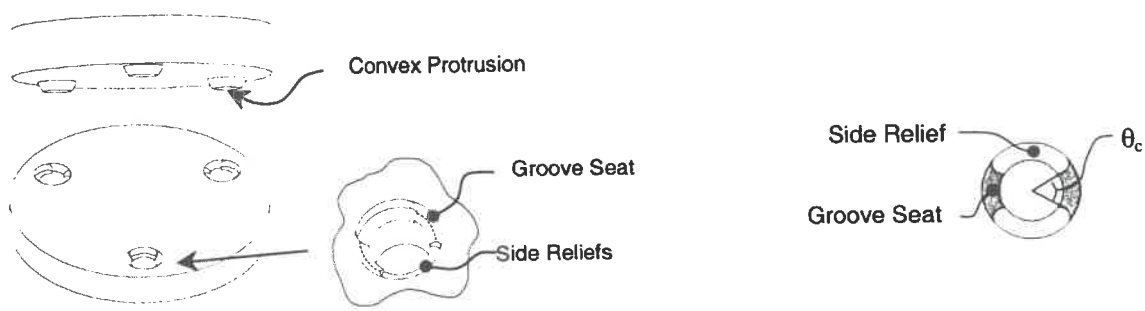

Figure 1 QKC With Detail of Conical Groove and Contact Angle θ_c

In general, Quasi-Kinematic Couplings (QKCs) are well-suited for high volume precision assembly, particularly where integral locating features and/or sealing contact are required. Quasi-kinematic couplings are similar to traditional Kinematic Couplings as they consist of three convex protrusions which mate with three corresponding grooves. However, QKC grooves and convex surfaces are formed as surfaces of revolutions (i.e. for instance a conical hole). Mating the kinematic elements results in six arced lines of contact (two at each groove-protrusion joint) not six points as in a kinematic

coupling. The result is a weakly over-constrained coupling whose behavior approaches that of a kinematic coupling as the groove seat contact angle (θc) decreases, thus the name quasi-kinematic.

FUNCTION

Due to friction and surface irregularities (surface finish affects (Slocum, 1992)), when the coupling is first mated the components will not occupy the most stable equilibrium. In force driven coupling proper seating can be induced by a preload that overcomes the contact friction and causes the spherical elements to brinell out surface irregularities at the contacts.

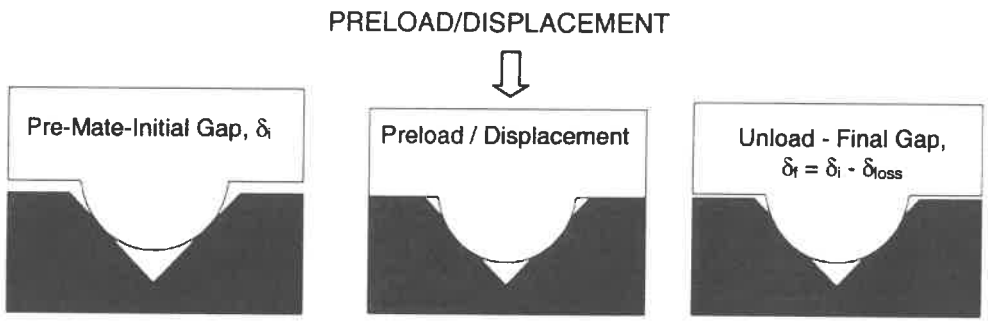

Figure 2 Mating Cycle of QKCs

When mating of opposed faces is desired (i.e. for sealing) one can design for displacement driven coupling. In this design, the compliance of the kinematic elements can be chosen such that a desired preload will brinell out surface irregularities and close the gap between components. On removal of the imposed displacement, all or part of the gap is restored through elastic recovery of the kinematic elements. This is necessary to maintain the quasi-kinematic nature of the joint for subsequent mates.

DESIGN

The design and analysis of Quasi-Kinematic Couplings is moderately complex and in some cases iterative, so preference in this abstract has been given to describing the coupling and its characteristics. A list of the basic components of the design and analysis are provided below. Thorough coverage will be given in the presentation.

-Listing Constraints and Functional Requirements

-Kinematics/Geometry of the Coupling Elements

-Continuum and Compliance Characteristics

-Error Motions

-Fatigue

-Performance Testing

MANUFACTURING

Method for Making QKC Grooves

Crowned Pegs

Figure 3 Examples of Inexpensive QKC Elements

Figure 3 shows inexpensive methods for making QKC grooves and convex members. Quasi-Kinematic Grooves seats can be made by machining cast-in reliefs with a form tool. In many cases, this allows the simultaneous machining of the groove surfaces and drilled holes. Crowned pegs or balls can be pressed into or otherwise attached to the components. If crowned pegs are used, their axisymmetric geometry makes them well suited for production on screw machines. When purchased in volume, these pegs can be attained for roughly the same cost as hollow dowels.

Tolerances on the location of QKC elements are less stringent than pinned joints because crowned pegs or spheres can easily fit into conical holes which are slightly misaligned; then force them to conform during the initial deformation (Culpepper 1999). Depending upon the application, the tolerance range for QKC element placement can be three times wider than pinned joints which are intolerant of pin-hole pattern misalignment.

PERFORMANCE / EXAMPLE

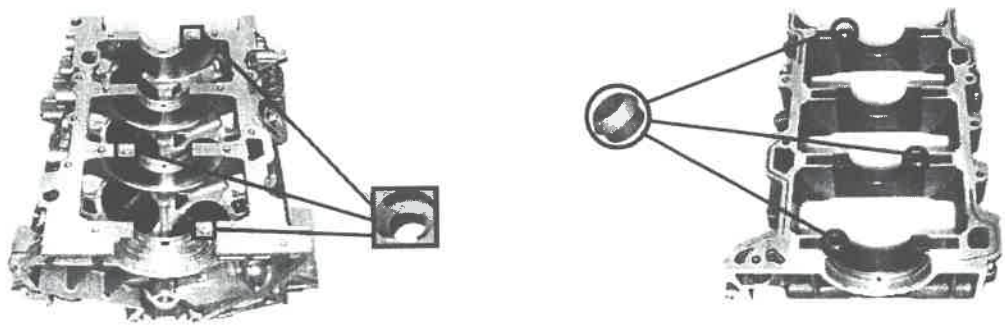

6 Cylinder Block: 3 Conical Grooves Coaxial With Threaded Bolt Holes

6 Cylinder Bedplate: 3 Spherical Shaped Pegs With Through Holes for Assembly Bolts

Figure 4 Engine Components With QKC Elements

The performance of QKCs will be demonstrated via a case study of an automotive engine assembly. Currently, two major components of the engine, the block and the bedplate (a monolithic part

containing the main bearing caps) are aligned via eight pinned joints. The two components are bolted together, then the crank bore is simultaneously machined into each component (a half bore in each.) Afterwards, the two components are disassembled, the main bearings and crank shaft are installed between them, and the block and bedplate are reassembled (Heck, 1997). Alignment of the two components before and after machining is critical as errors in the relocation of the half bore center lines can have negative affects on bearing performance (Shigley and Mischke, 1989). Maintaining the required 5 micron alignment (Vrsek, 1997) requires the elastic averaging effect of 8 pinned joints (Slocum, 1998). These joints require 16 precision holes, thus the design has high scrap/rework rates.

Tests on quasi-kinematic couplings in this applications have measured 0.6 microns linear repeatability and 3 micro-radians angular repeatability. As a result of this change, the number of precision features required for the engine coupling was reduced by 60% and coupling cost reduced by 40% (the new coupling costs less than a dollar.) In addition, since the coupling is capable of "forming out" initial misalignment between kinematic elements, feature size and feature placement tolerances are wider (+/- 0.10 mm) than those required by the pinned joints (+/- 0.04 mm.) Although the benefits to automotive engine manufacturing will be demonstrated, its use in other applications will be discussed.

KEY WORDS: Repeatability, Kinematic Coupling, Fixtures, Design For Manufacturing, Precision Alignment, Automotive Engines, Precision Assembly, Precision Manufacturing

REFERENCES

1. Heck, K., December 1997, Conversations with Kevin Heck, Manufacturing Engineer, Ford Engine Plant #2, Cleveland, OH.

2. Shigley, J. E., Mischke, C. R., 1989, "Mechanical Engineering Design," McGraw-Hill, Inc., New York, New York, pp 508 - 509

3. Slocum, A. H., 1992, "Precision Machine Design, " Prentice-Hall, Inc., Englewood Cliffs, New Jersey , pp. 401-412 and pp. 228-235.

4. Slocum, A. H., May 1998, Conversations with Prof. A. H. Slocum of MIT, Cambridge, MA.

5. Vrsek, Gary, December 1997, Conversations with Gary Vrsek, Powertrain Research Manager, Ford Scientific Laboratory, Dearborn, MI.

AFM VIBRATION ISOLATOR WITH HIGH PERFORMANCE USING EDDY CURRENT DAMPING

Gyung-Hoon Chung, Dae-Gab Gweon, Hoi-Won Chung, Jong-Yup Shim
SAMSUNG DISPLAY DEVICES CO. LTD.
575, Shin-Dong,, Paldal-Gu Suwon City
Kyungki-Do, Korea 442-391
(FAX)+82-0331-210-7967
(e-mail) letshee@sdd.samsung.co.kr

1. INTRODUCTION

This article describes the design of a vibration isolation system for AFM(Atomic Force Microscope)[1] to reduce the external mechanical oscillation down to a subatomic scale. The AFM senses forces between the tip and the sample. In order to measure the sample with orders of sub-nanometer resolution, the reduction of floor vibration effecting to AFM is required to this ultra-precision system firstly. Because no distance change between tip and sample is the important thing to AFM as shown in Fig. 1.

Damping force is based on the interaction of eddy currents and a magnetic field usually induced in a moving part. Recently eddy current damping is used in many areas. Especially it is powerful to this AFM vibration isolator which has no friction and coincides modeling with experimental results well. But the eddy current modeling is maintained at the qualitative level only. Therefore this article will show more precise analysis.

The vibration isolator constitutes of two metal plates suspended by coil spring and eddy current damper. It is designed symmetrically, so it can separate lateral mode and vertical mode. Also in order to reduce the leakage of magnetic flux greatly new concept of design is described calls 'closed loop eddy current damper'. And isolator is constructed by optimal design scheme.

The experimental results of the isolation performance are well explained by the analysis with figures. Thereby the progressive characteristics of eddy current damping

and vibration isolation are clarified.

2. THEORY OF VIBRATION ISOLATION FOR AFM

A. General consideration of vibration isolation

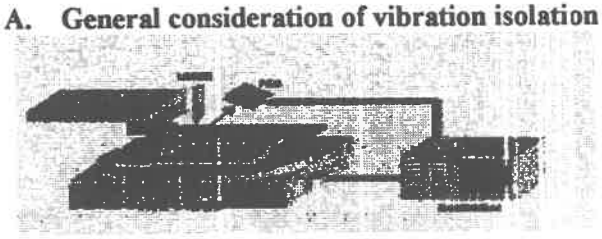

Fig. 1. AFM system

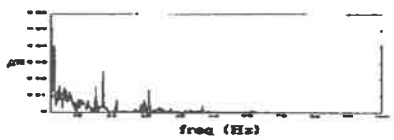

Fig. 2. Vibration amplitude on the floor

External vibrations coming along a building floor have wide varieties in their frequencies, amplitudes, and all of them change with time. Changes in displacement magnitude at the floor of the main building is shown in Fig. 2 as a function of mechanical oscillation frequency. The displacement magnitude reached the maximum of 40~50nm, which is far greater than an atomic scale. The level of the vibration amplitude to be achieved at the AFM is 1~10pm. Therefore vibration isolator is required in AFM.

B. The modeling of isolator and AFM

In order to simplify the principle of vibration isolation, we describe the isolator and the AFM assembly with two coupled oscillators having masses m_i, m_t and spring constants k_i, k_t without damping, as illustrated in Fig. 3. Equations of motion are given by

$$m_i x_i'' + (k_i + k_t)\, x_i = k_t x_t + k_i x_b \sin\omega t,$$

$$m_t x_t'' + k_t x_t = k_t x_i$$

where $x_b \sin\omega t$ is the displacement of the floor. The transfer function defined for the vibration isolator versus the floor $Z_i = 20\log(x_i/x_b)$ and that defined for the AFM assembly versus the vibration isolator $Z_t = 20\log[(x_t - x_i)/x_i]$ are curves I and II, respectively. The overall transfer function $Z = 20\log[(x_t - x_i)/x_b]$ is shown as

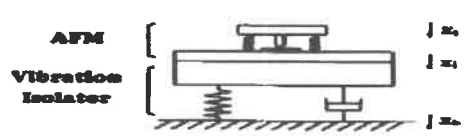

Fig. 3. The assembly of isolator and AFM

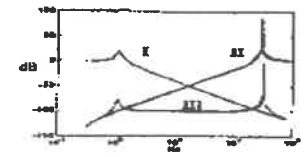

I : $Z_i = 20\log[x_i / x_b]$

II : $Z_t = 20\log[(x_t - x_i)/x_i]$

III : $Z = 20\log[(x_t - x_i)/x_b]$

Fig. 4. Transmissibility of the modeling

curve III in Fig. 4. The peaks at two natural frequencies are easily reduced by adding damping to the systems. [2]

In concluding, two important items should be noted. It is necessary to evaluate the floor vibration and design the vibration isolator being suitable for AFM in order to achieve the vibration amplitude of the AFM assembly down to pico-meter range. The overall isolation performance is improved by making the difference in the two natural frequencies larger and by making the slope of curve I above the natural frequency steeper.

3. DESIGN OF VIBRATION ISOLATION FOR AFM

A. Theory of eddy current damping force

Electromechanical braking is based on the interaction of eddy currents and a magnetic field, with the former usually induced in a moving part. The absolute value of the braking force F acting on the moving sheet is as follows[3].

$$F = \sigma\delta u B_z^2 4hb \frac{2}{\pi}\left\{\arctan\frac{h}{b} + \frac{1}{2}\left[\frac{h}{b}\ln\sqrt{1+(\frac{b}{h})^2} - \frac{b}{h}\ln\sqrt{1+(\frac{h}{b})^2}\right]\right\}$$

which has thickness δ, conductivity σ, velocity u,

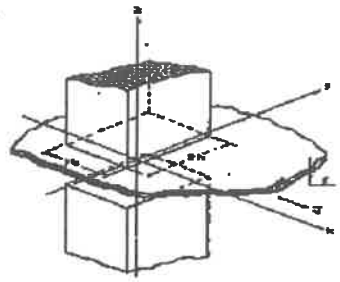

Fig. 5. The scheme of eddy current damping

magnetic flux density B_z, and b,h are the geometry of magnet as shown in Fig. 5.

B. Design Criteria of vibration isolator

Curve I in Fig. 4 shows the characteristics of the vibration isolation. Acquiring better effect of isolation by both making lower natural frequency of the curve I and steeper slope. The steeper slope means the lower damping. Regarding the simple first order system which has damping ratio ζ, mass m, and stiffness k. The undamped natural frequency ω_r is as follows

$$\omega_r = \omega_n \sqrt{1-2\zeta^2}$$

which $\omega_n=\sqrt{(k/m)}$. That means that two requirements of better isolation effect are in inverse proportion. Therefore we used an optimal design method, which is the design criteria of isolator for AFM.

4. EXPERIMENTAL RESULTS OF CONSTRUCTED ISOLATOR

A. System configuration

A schematic of the two-stage coil-spring suspension isolator for AFM is shown in Fig. 6. For minimize the leakage of magnetic flux from permanent magnet, the parts of damping are constructed as if closed loop type as shown in Fig. 6. Each end of the coil spring was terminated by a rubber ring in order to attenuate

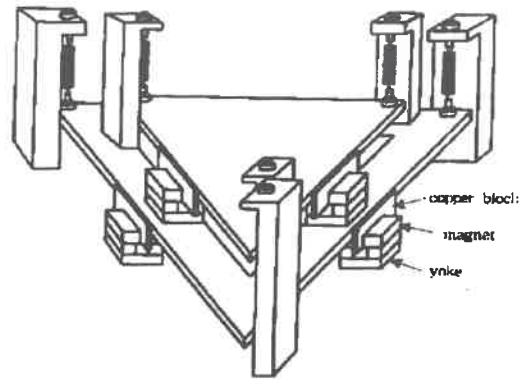

Fig. 6. Vibration isolator for AFM

the high frequency sound propagating along solid columns, plates, and coil springs. Eddy currents dampers consisting of copper blocks and permanent magnets also make the gravity center of the ends of the coil springs. The configuration prevents the translational motion along the gravity direction and the rotational motions around the gravity center. The triangle shape plate on which a AFM is placed enables easy access to wiring and simplifies the exchange procedure of samples and probing metal tips.

B. Effect of vibration isolation

The vibration amplitudes of the floor and on the isolator plate against frequencies are shown in Figs. 7(a) and 7(b) respectively. These show that the region of the above 5Hz frequencies is filtered by isolator.

C. Effect of vibration isolation in AFM and measured sample image

When AFM is placed on the vibration isolator, we regard the experimental results as shown in Fig. 4.. Curve I is the transmissibility of the isolator displacement amplitude versus floor. Curve II is the transmissibility of the tip-sample displacement change

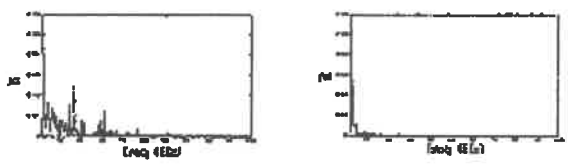

Fig. 7. (a) vibration of floor (b) vibration on the isolator

versus isolator And Curve III is the transmissibility of the tip-sample displacement change versus floor amplitude. In regarding curve III, isolation effect of the tip-sample displacement change against floor vibration is about -50dB. Therefore it attenuates the floor vibration isolation into the tip-sample displacement change about 10^{-3}order. For example, 3nm of floor vibration is attenuated 30pm in the tip-sample displacement change.

The measured sample results in the no vibration isolation and with vibration isolation respectively are shown in the Fig. 8. Thereby we can conclude that the performance of AFM with vibration isolator is very good . Also the AFM with vibration isolator has very high resolution and repeatability performance.

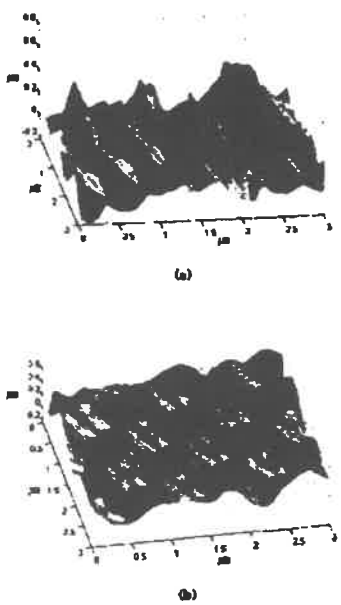

Fig. 8. AFM measurement (a)without (b)with the isolator

5. CONCLUSION

The technology of vibration isolation which suppresses the external perturbation down to a subatomic scale has been described. That is in making the natural frequency of the isolator lower and making the slope of isolator in the transmissibility steeper.

Surface atomic images were shown as an example of successful application of this vibration isolator with AFM.

ACKNOWLEDGMENTS

I would like to thank Dae-Gab Gweon, Hoi-Won Chung, and Jong-Yup Shim, for their helpful for discussions in performing the AFM experiments. And I sincerely thank Samsung Display Devices corporation.

REFERENCE

1. Binnig, G., Quate, C,F, & Gerber, Ch, 1986, "Atomic force microscope," *Physical Review Letters*, Vol. 56, pp.30~933.
2. M. Okano, K. Kajimura, S. Wakiyama, F. Sakai, 1987, "Vibration isolation for scanning tunneling microscopy", Journal of Vacuum Science Technology, A 5, PP. 3313~3320
3. D. Schiber, 1975, "Optimal Dimensions of Rectangular Electromagnet for Braking Purposes", *IEEE TRANSACTUIONS ON MAGNETS*, Vol. MAG-11, pp.948~952.

High-precision systems using modern high-energy permanent magnet materials

Harald Kube, Eberhard Kallenbach
Technical University of Ilmenau, Ilmenau, Germany

Beate Pawlowski, Joerg Toepfer
hitk e. V., Hermsdorf, Germany

ABSTRACT

To satisfy the demands of miniaturized high-precision systems new designs and new materials are necessary. Especially, the disadvantages of classical configurations like friction, hysteresis, and stick-slip effects have a great influence on miniaturized systems and will decrease the capacity of small drive systems. Therefore, new principles for driving and guidance are necessary. One possibility to guide small moving parts of high-precision drives is the usage of magnetic field forces. We developed such a magnetic guidance integrated in an electromagnetic drive. We use new high-energy rare earth magnet materials with a flat shape and a multi-pole striped magnetization. These magnetic layers are made of sintered or polymer-bonded neodymium iron boron. The layers are homogenous and will be magnetically structured by a capacitor discharge magnetization process. Layers of sintered NdFeB were prepared by machining of commercially available plates. New polymer-bonded materials have been developed, too. The main focus was the development of new material mixtures with better magnetic parameters and good molding capabilities. Different molding processes for the preparation of magnetic films with a thickness in the range from 20 µm to 1 mm as well as an improved subsequent magnetization process have been developed.
This paper discusses the development of such new polymer-bonded permanent magnetic materials, the molding processes to manufacture thin film and the magnetization process. The presented application of such magnetic films is multi-coordinate drive with a magnetically lifted and moved aluminum sheet.

THE HIGH-ENERGY PERMANENT-MAGNET MATERIALS

Introduction

Permanent magnetic materials and the corresponding magnetic parameters have undergone a dramatic evolution during the past decades. Especially the discovery of the NdFeB-family of permanent magnetic compounds in 1984 and the development of suitable industry-scale preparation routes for these rare-earth magnets have led to a widespread use of such magnets in many applications. The introduction of this new class of permanent magnets opened new horizons with respect to the miniaturization of magnet components. If one compares the evolution of the maximum energy product (BH)max achieved with NdFeB-materials clearly demonstrates the new dimension for miniaturization and volume reduction of magnetic-microactuators. Potential fields of application of the high-energy permanent magnets in micro-systems, especially in micro- actuators, require such miniaturization of the components with a simultaneously large mechanical driving power. Consequently, magnetic components are needed which are able to provide magnetic forces large enough to serve in actuator systems. Magnetic thin films of NdFeB prepared by sputtering [4] usually have a thickness of the film in the order of 1-20 microns. These films are not able to generate the needed induction on the surface or at a given distance from the surface of the film to be applied in micro- actuators. To successfully operate as permanent magnetic component in micro-drives NdFeB-films with a thickness of 50-1000 µm are necessary. Those magnets are commercially not available; conventional methods of NdFeB- magnet production either by the powder metallurgical route, by hot-forming of melt-spun powders or injection molding of polymer-bonded powders yield magnets with a thickness larger than 1 mm. Machining and grinding operations to obtain small magnets are not effective and very cost-intensive. Therefore methods for the preparation of magnetic thick films with a thickness of 50-1000 microns have to be developed. In this contribution we report on the preparation of such thick films using several techniques and the application of the films in integrated multi-coordinate drives [5], [6], [7], [11] with parallel kinematics.

Printed films

The magnetic material is mixed with binder to give a magnetic ink or paste. Films with a thickness between 20-100μm can be printed on different substrates (iron, ceramics, glass). After curing the epoxy the films exhibit the magnetic properties as shown below.

	NdFeB-films:	*Ferrit-films:*
B_R:	350-450 mT	60-100 mT
$_iH_C$:	300-700 kA/m	200 kA/m

Tape casted films

NdFeB powders, after wet milling, are dispersed in a special mixture of solvents and sequentially, this mixture is converted into a viscous casting slip through addition of binders and plasticizers. Shaping is realized by the doctor-blade method in a continuous casting machine with a stationary doctor-blade and a slowly moving casting surface. After removal of the solvent a flexible green tape is obtained. Annealing yields mechanically stable films of thickness between 100-1000 μm.

The remanent induction of the films ranges from 300 to 400 mT (depending on the volume loading of magnetic powder) while the coercivity varies between 300 - 700 kA/m (depending on grade of the magnetic powder used).

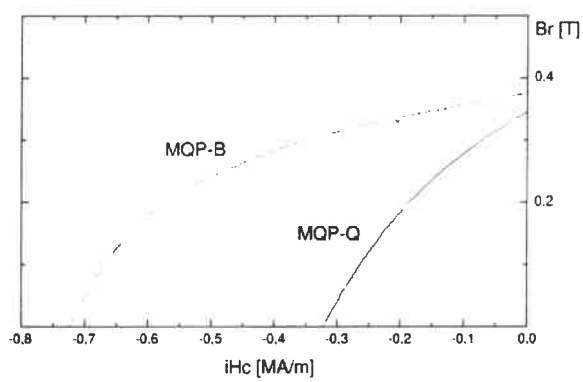

Figure 1: Demagnetization curve of tape casted films

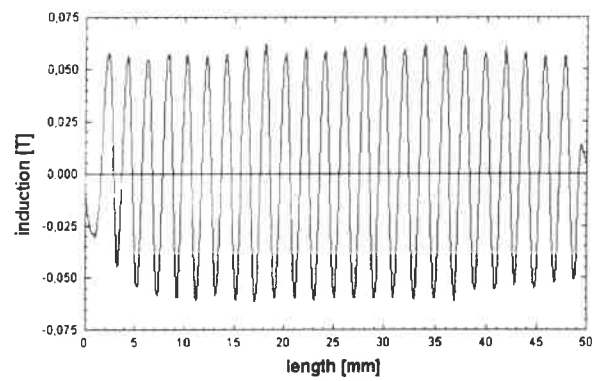

Figure 2: Typical curse of the surface-induction of tape casted films

Flexible foils

To prepare flexible magnetic foils NdFeB-powder (wet milled) is mixed (hot kneading, extrusion) with a polymer to form a composite material (compound). Subsequently the compound is transformed by calendering into a flexible foil with a thickness between 300-1000μm. The remanent induction of the foils 300 to 500mT are obtained with coercivities between 300-700kA/m.

Multi-pole magnetization

The films are magnetized with a multi-pole striped pattern with a pole distance of 2.0, 1.0 and 0.5 mm. A capacitor discharge magnetizer is used to produce a short current impulse. The magnetic film is placed on top of a copper wire wound fixture and the capacitor bank is discharged through the fixture. The obtained magnetic multi-pole pattern is measured by a Hall probe scanning the surface of the magnetic film.

APPLICATIONS

This kind of permanent magnetic film with a multi-pole striped pattern can be used for a widespread range of actuators like synchronous machines and hybrid stepper motors. Another possible kind of applications using permanent magnets with multi-pole striped pattern are linear drives [6], [7] and multi-coordinate drives as presented below.

Modeling of the magnetic field

To use this kind of permanent magnetic films for drives, we have to calculate the magnetic field generated by the film. The field strength depends on the material mixture and the maximum value of the magnetizing current. The

field distribution depends on the geometry of the magnetizing coil. The magnetic field around the film was calculated by using the FEA software MAXWELL 2D. To model the magnetization of the film, we used the Halbach magnet array structure [9] (Figure 3).

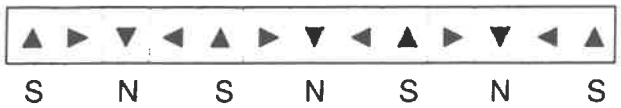

Figure 3: FEA model (Halbach magnet array)

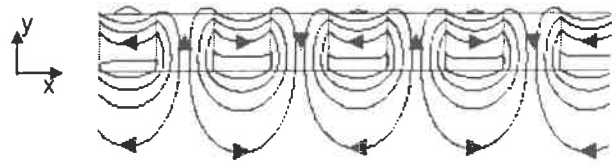

Figure 4: Magnetic field of the film

Figure 4 shows the simulated magnetic field. The field is concentrated below the film. In horizontal direction, the field strength changes sinusoidal. In vertical direction, the field strength amplitudes decreases with increasing distance from the skin of the film. Above the layer, there is nearly no magnetic field. The maximum induction of films with 2 mm wide magnetic stripes is about 0.12 T.

If a current carrying wire is arranged below the film, a force is exerted on the magnetic film depending on the current, the length of the wire and the position of the wire. Figure 5 shows the horizontal Force (F_x) and the vertical Force (F_z) at a current of 10 A.

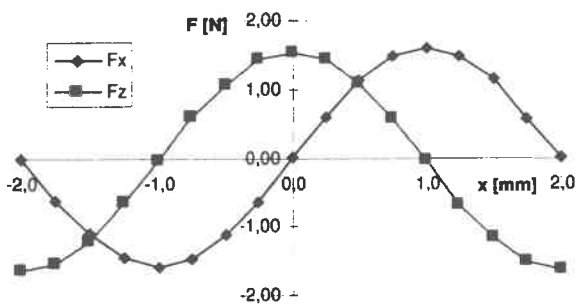

Figure 5: Force exerted on the film

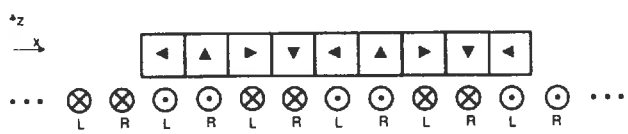

Figure 6: Drive design

To generate horizontal and vertical forces on the film at the same time, we arranged 2 wires multiple below the magnetic film (Figure 6). To distinguish between the wires, they are named with "L" and "R". The distance between these wire is equal to the half of the pole distance of the magnetic pattern. By applying currents to the wires, we can set up the forces in horizontal and vertical direction independently. The currents can be calculated by

$$I_R = K_x \sin\varphi + K_z \cos\varphi \tag{1}$$

$$I_R = K_x \cos\varphi - K_z \sin\varphi \,. \tag{2}$$

with $K_x = \dfrac{F_x}{B(z)l_w}$ and $K_z = \dfrac{F_z}{B(z)l_w}$.

Whereby, $B(z)$ is the maximum flux density at the distance z from the film skin. F_x and F_z are the forces in horizontal and vertical direction. The wire length is named as l_w.

Our drive uses four coupled actuators (Figure 7). Two of them work in x-direction and the other two actuators work in y-direction. All four actuators are used to lift the sheet. The actuators are coupled by mounting the four magnetic films below an aluminum sheet. To measure the position of this sheet, we use an optical incremental position measurement system, which can measure the position in x- and y-direction and the rotation around the z-axis. Four sensors between the actuators are used to measure the z-position of the sheet and the rotation around the x- and the y-axes. A PC with a data acquisition board is used to control the drive.

A special design criterion is the weight of the sheet because it is lifted by magnetic forces. If the weight of the sheet increases, the needed vertical force and the current through the wires also increases proportional, and the power losses and the heat dissipation of the drive coils increases quadratic.

This sheet can be lifted by some tenth millimeters, can be move in x- and y-direction by 50 mm and can be rotated by some degrees around all 3 axes.

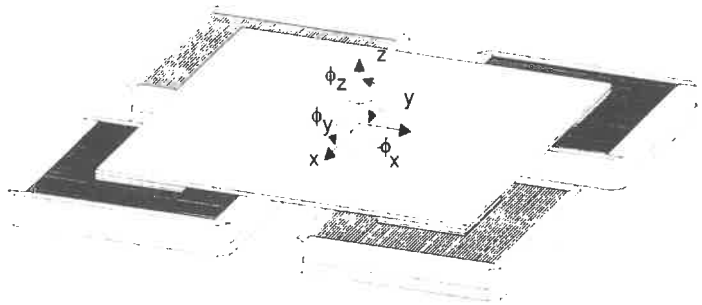

Figure 7: Multi-coordinate drive

CONCLUSIONS

This paper presents new polymer-bonded NdFeB permanent magnet materials which can be processed by film printing, calendring, and tape casting to manufacture films with a thickness of 50-1000 microns. The films are magnetized with a multi-pole striped pattern by the use of a capacitor discharge magnetizer. The pole distance of the magnetization can be 0.5, 1.0, or 2.0 mm. These films are used to design a electrodynamic multi-coordinate drive with a similar function principle to that one presented in [8] and [9]. The main advantages of our drive are the easier manufacturing of the magnetic film by batch processing and the shorter pole distance which leads to thinner permanent magnetic films. The short pole distance also gives the possibility to miniaturize these kind of drives, whereby the ratio between the generated forces and the mass of the lifted parts will become better.

LITERATURE

[1] B. Pawlowski, A. Rahmig, J. Töpfer "Preparation and Properties of NdFeB-Thick Films," Proceedings of the 15th Intern. Workshop on Rare-Earth Magnets and their Application, Dresden, pp. 1045-1050, August/September 1998

[2] B. Pawlowski, H. Beer, J. Töpfer "Preparation of Nd-Fe-B magnetic films by ceramic techniques," Key Engineering Materials, 132-136 (1997), pp. 1409-1411

[3] S. Yamashita et. al. "Anisotropic NdFeB Thin Film Magnets for Milli-Size-Motors," Journal of Appl. Physics 70 (1991) 10, pp. 6627-6630

[4] B. A. Kapitanow et. al.: "Sputtered Permanent NdFeB-Magnets," Journal of Magnetism and Magnetic Materials 127 (1993), pp. 297-298

[5] H. Beer „Schichtmagnete für Aktuatoren", F&M 105(1997) 1-2 S. 46 ff

[6] H. Kube, V. Zöppig, R. Hermann, A. Hoffmann, E. Kallenbach „Electromagnetic miniactuators and microactuators using thin magnetic layers," Smart Materials and Structures, Proceedings of the 4th European and 2nd MIMR Conference, Harrogate, UK, July 6-8, 1998

[7] H. Kube, E. Saffert, A. Hofmann, E. Kallenbach „Electrodynamic Linear Drive with Integrated Magnetic Bearing using Thin Magnetic Layers," Proceedings of the Fourth International Conference on Motion and Vibration Control (MoViC), August 25-28, 1998, Zurich, Switzerland

[8] D. L. Trumper, W. Kim, M. E. Williams "Design and Analysis Framework for Linear Permanent-Magnet Machines," IEEE Trans. on industrial Applications, vol. 32, 1996

[9] M. L. Holmes, R. J. Hocken, D. L. Trumper "A Long-Range Scanning Stage Design (The LORS-Project)," Proceedings ASPE 1997

[10] D. Enke, T. Frank, T. Gerlach „Mikropositionierantriebe für Lichtwellenleiter", Internationales wissenschaftliches Kolloquium Ilmenau, 1996, S. 164 ff

[11] E. Kallenbach, E. Saffert, Chr. Schäffel "Multi-coordinate Drive Systems - Opportunities and Limits," Proc. of the 3rd Heinz Nixdorf Symposium, Paderborn, Germany, 1999

[12] W. Kim, D. L. Trumper "Precision Control of Planar Levitator," ASPE 1998, Proc. pp. 606-609

Magnetic Levitation Scanning Stage for Extreme Ultraviolet Lithography

M.E.Williams[1], S.P.Tracy[2], P.Faill[1], P.Bischoff[2], J.Wronosky[3]

ABSTRACT

Previous papers have reported on the performance of a six degrees-of-freedom magnetic levitation (Mag-Lev) *step-and-repeat* photolithography stage[1][2][3]. This paper will describe the design of a *scanning* six degrees-of-freedom Mag-Lev stage for Extreme Ultraviolet Lithography (EUVL). This stage is significantly different from those previously described and has the potential to be the first use of Mag-Lev technology in a lithography tool. EUVL represents one of the most promising future lithography technologies and is expected to support pattern generation down to 30 nm. The EUVL development program is a joint venture funded by an Intel led consortium of semi-conductor manufacturers. An operational engineering test stand (ETS) is expected to be completed in 2001. The engineering test stand is a full field scanner that requires both a reticle stage and wafer stage scanning simultaneously. The Mag-Lev stage described in this paper is used in both capacities. During the design of this stage, two EUVL related technical difficulties had to be overcome. The first design difficulty is that EUVL is performed in a high vacuum. This limits available materials and the allowable power dissipation. The second difficulty was the stringent performance requirements on the scanning tracking error and jitter. Tracking error is the difference between the commanded and actual position during a constant velocity scan averaged over a moving 150msec window. Jitter is defined as the RMS position error averaged over the same moving window. The stage performance requirements for all six DOF are a tracking error of ±2.4 nm and jitter <8 nm. This paper describes a six DOF Mag-Lev wafer and reticle stage designed specifically to meet the EUVL performance, power dissipation, and vacuum requirements.

Stage Description

This section describes the Mag-Lev wafer and reticle stages as designed for the ETS EUV scanning lithography tool. The stages are functionally identical with minor differences in the mounting and the inclusion of a linear guide axis for the wafer stage.

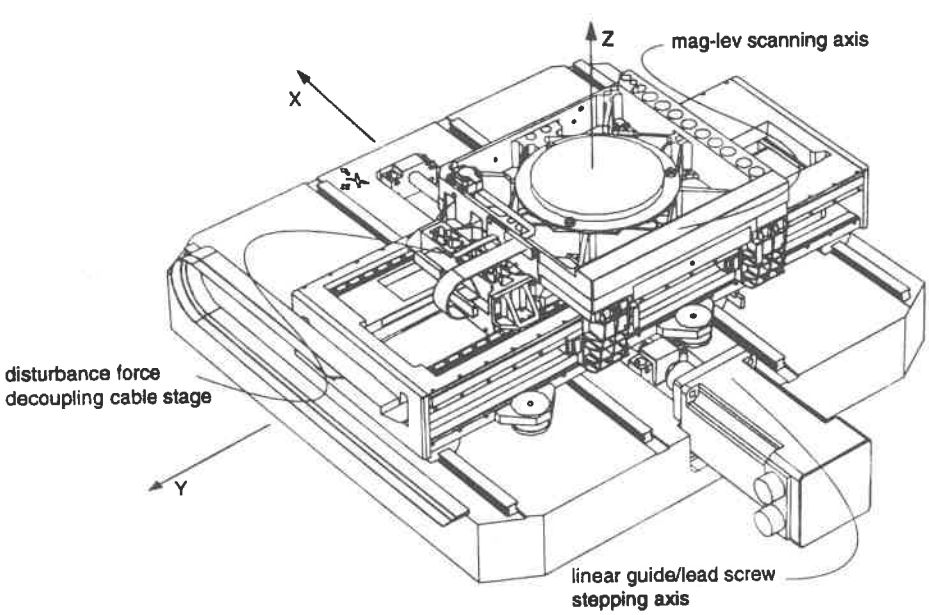

Figure 1 Mag-Lev scanning stage

Shown in Figure 1 is the wafer Mag-Lev/linear guide stage. The reticle stage is identical in geometry and layout without the stepping X axis and with minor changes made to the beam and mounting configuration. The Mag-Lev portion of the stage has a travel range of 500 μm in the *X* and *Z* directions, 225 mm in *Y* and 1 milliradian of θx, θy, θz rotation. The stepping axis has a travel range of 370 mm. The six degrees of freedom magnetic suspension scanning axis consists of ten variable-reluctance actuators and a single degree of freedom linear motor. The ten variable-reluctance actuators (five bi-polar pairs) control five degrees of freedom and the linear motor controls the long

[1]Equilibria, Inc., 496 Boston Road, Groton Ma, 01450, williams@eqlib.com
[2] Ultratech Stepper ,16 Jonspin Road, Wilmington Ma 01876
[3]Sandia National Laboratories, Albuquerque NM

travel scanning degree of freedom.

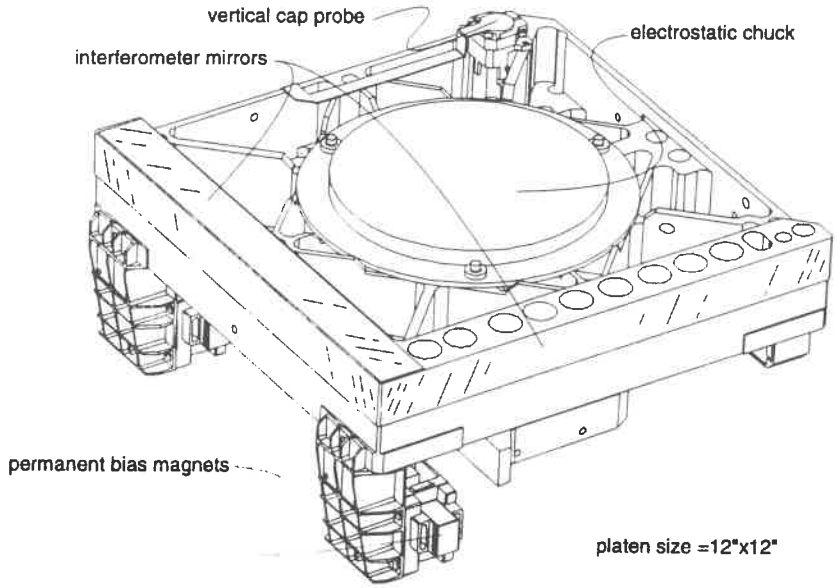

Figure 2 Mag-Lev scanning stage

Shown in Figure 2 and Figure 3 is the suspended wafer carrier portion of the stage and is henceforth referred to as the platen. The platen carries the variable-reluctance actuators and the magnet array of the linear motor. Shown in Figure 4 is a beam that contains the permeable targets that complete the magnetic circuit of the variable-reluctance actuators. The six vertical actuators are arranged in three bi-polar pairs at the vertices of a triangle (Figure 3) and provide kinematic control forces in three degrees of freedom (Z, θx, θy).

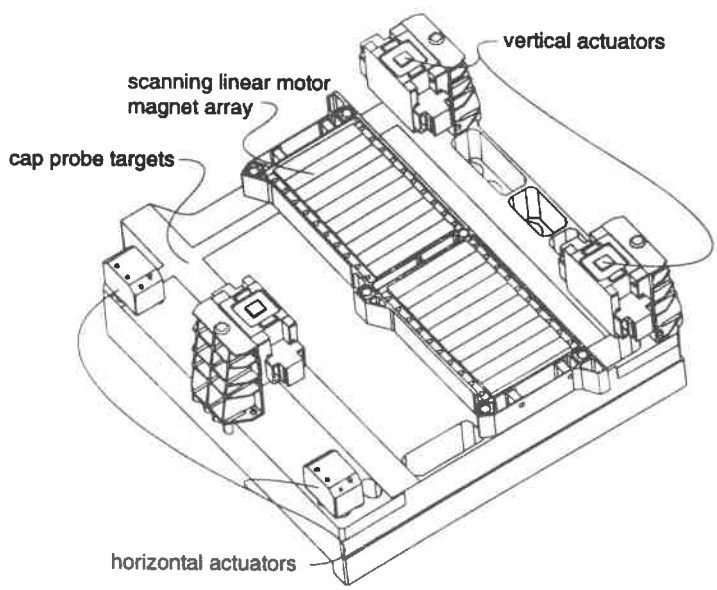

Figure 3 Mag-Lev platen underside

The vertical actuators are arranged such that platen center of gravity is coaxial with the vertical center of force of the three actuator pairs. As arranged, the actuators will each exert one third of the control effort and can be identically sized. Additionally, gravity off-setting permanent magnets attached to each of the actuator housings are identically sized and support an equal share of the gravitational load. The four horizontal actuators (Figure 3) are

arranged in two bi-polar pairs at the corners of the platen and provide X and θz control. The location of the horizontal actuators provides several benefits. First, it places the horizontal line of force close to the platen center of gravity which is located nearly at the bottom surface of the platen. This reduces the mechanical coupling between the X and θy degrees of freedom. Reduced coupling results in higher bandwidths and lower power dissipation due to the smaller required control effort. Second, it reduces the radius of gyration around the X and Y axes resulting in lower principal moments of inertia Ixx and Iyy. Lower moments of inertia also result in less control effort. With this configuration, the control forces applied to the body are completely kinematic.

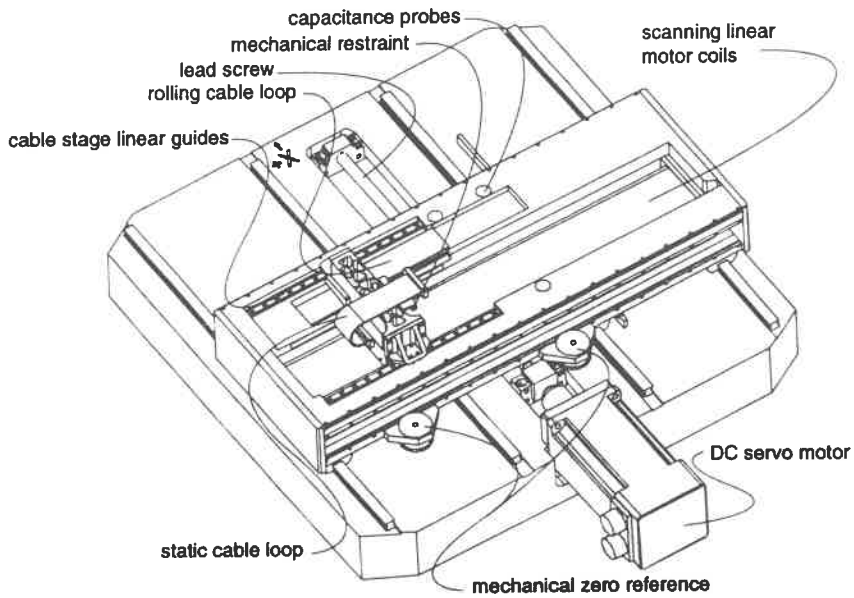

Figure 4 Mag-Lev support beam and stepping axis

Electric current to the variable-reluctance actuator coils is conducted through Kapton flex cables that have well defined single degree of freedom rolling paths. An advantage of stacking the X and Y axes is that the cable is only required to move in a single direction resulting in a repeatable and controllable motion. Since the variable-reluctance force is highly non-linear, five gap measuring capacitance gauges as seen in Figure 4 are located on the linear guide stage beam to provide force linearizing information.

Typical precision machine design techniques dictate that for best accuracy the force and metrology loops should be separate to prevent control forces from distorting the feedback measurement. This separation of loops is typically accomplished by kinematically mounting a separate mirror on the stage structure. This technique, if properly implemented, ensures that the forces seen by the mirror are kinematic and the mirror should remain dimensionally stable. In the EUVL stage implementation, the force and metrology loops are combined into a single monolithic structure. Despite being counter to conventional design practice, this geometry is acceptable due to the unique nature of the applied Mag-Lev control forces. Since Mag-Lev is non-contact, the platen is not rigidly constrained and the applied control forces as they are arranged are kinematic.

The platen consists of a Zerodur mirror with the active components (actuators, motor magnet array) mounted to it. The design intent is to reduce the suspended mass by using the mirror as a structural element. Both reduced mass and higher elastic modes will enable higher control bandwidths that reduce settling times and increase dynamic stiffness. In addition to avoiding over-constraining dynamic control forces, it is necessary to account for thermal and static distortions when attaching the individual parts to the mirror. For example, the linear motor magnet array is only rigidly attached at a single location. The remaining five attachment points are made through single degree of freedom flexures that are compliant in the radial direction of greatest thermal growth and very stiff in the perpendicular direction. This single degree of freedom flexure reduces the strain placed on the mirror by differential thermal growth between the mirror and magnet array. Also, thermal distortion of the mirror from actuator power dissipation is a concern. To reduce this power, the actuators are optimized for size and power and the total suspended mass of the stage is minimized. Through finite element simulations it was determined that the greatest thermal distortion in the mirror is six nanometers with the average distortion much less. Since the mirror is polished flat to approximately 30 nm, the thermal distortion is within practical limits.

To provide gravity offsetting DC bias force, permanent magnets are mounted on each side of the three actuator housings. As shown in Figures 2 and 3, these permanent magnets are located close to the location of the vertical control forces. This is done to retain the kinematic placement of the control and bias forces. The operating gap for the permanent magnets is designed to be approximately 1 cm. With a large magnet air gap the lifting force is insensitive to small changes in the platen vertical position thus reducing the potential for disturbance forces.

Included in the stage design is a cable stage that is designed to reduce the disturbance forces imparted on the scanning stage by rolling cables (Figure 4). The cable stage is actuated in the scanning direction by a permanent magnet linear motor which utilizes the Mag-Lev linear motor coils. The cable stage follows the Mag-Lev stage and is commutated similar to the scanning linear motor. The cable stage is coupled to the wafer stage through a very compliant static cable loop. During wafer stage motion, the relative position between the wafer stage and the cable stage should not change significantly and any disturbance force generated will be very low frequency and within the suspension control bandwidth. A rolling cable loop from the lower axis (Y) to the cable stage rolls under the cable stage in a channel parallel to the linear motor coils. The cable stage position is determined with an optical linear encoder. A capacitance probe located on the cable stage is used to determine the relative position between the cable stage and the wafer/reticle stage.

The long scanning axis (Y) position control is achieved with a Lorentz type planar linear motor. The motor is sized to dissipate no more than 1 watt during a 0.1g acceleration of a 10.5 kg mass. While the motor is sized for the required acceleration and power dissipation, it has the force capacity to accelerate the stage in excess of 1g. As stated, the magnet array of the motor is carried by the platen and the current conducting coils are carried by the beam as seen in Figure 4. In addition to providing Y control of the platen, the linear motor also controls the position of the cable stage. This means that two independent motions are controlled with the same linear motor coils. This is accomplished by maintaining individual current control of the coils of wire that are common to both the wafer stage and the cable stage. This is particularly useful in a vacuum where mechanical contact actuators (lead screws, belt drives, band drives, etc.) are undesirable. In addition to being a non-contact actuator, it packages well with the scanning stage and does not require any further in-the-vacuum hardware. As seen in Figure 4, the Mag-Lev stage is then transported in the off-axis direction (X) by a high stiffness well damped linear guide lead screw driven stage. It is not necessary for the lower stage to achieve maximum resolution since the Mag-Lev stage has a redundant degree of freedom in this direction which eliminates the positioning dependence on the bearing surface finish. In fact, the resolution limiting friction present in the linear guides should provide some very desirable coulomb damping. Linear guides also have high stiffness torsionally and laterally, which provides a very stable base for the Mag-Lev stage both in a step and repeat and a scanning mode of operation. The outer two parallel linear guide rails are used to position the stage and the inner two parallel linear guide rails are used for increased broad band damping of the elastic modes of the stage beam. A preloaded leadscrew is used to drive the linear guide stage. The leadscrew is chosen for the lower power dissipation provided by the mechanical advantage. Since the velocity requirements of this stage are low, the high speed and high acceleration advantages of a direct drive linear motor are not required. Also, by using a leadscrew the motor power is dissipated away from the stage.

Conclusions

The preceding text has described the design and construction of a high performance Mag-Lev scanning stage for use in a high vacuum. Current work being performed is focused on increasing stage control bandwidth and generating a linear motor mapping algorithm. Higher bandwidths and linear motor force correction maps are necessary to meet the EUVL tracking and jitter performance specifications.

This work, performed at Ultratech Stepper in collaboration with Sandia National Laboratories, is supported by the Extreme Ultraviolet Limited Liability Company (EUV LLC) and by the U. S. Department of Energy under contract DE-AC04-94AL85000.

Bibliography

[1] M.Williams, D.Trumper, "Six Degree of Freedom Magnetic Bearing Stage" ASPE Ninth Annual Meeting, Cincinnati, Ohio, 10/94

[2] M.Williams, D.Trumper, "Six Degree of Freedom Magnetic Bearing Stage for Photolithography", NASA 3rd International Symposium on Magnetic Suspension Technology, Tallahassee, Fla, 12/95

[3] M.Williams, P. Faill, et.al., ``Six Degree of Freedom Mag-Lev Stage Development", Proceedings of the SPIE Conference, March 1997, Vol. 3051.

An Invited Paper for ASPE 1999.

An Advance in Metrology & Manufacture - The Engineered Surface

By

K.J. Stout & L.Blunt

School of Engineering, University of Huddersfield, Huddersfield, HD1 3DH, UK.

Abstract

In recent years considerable progress has been made in the nature of manufacture and characterisation of surface finish in three dimensions. Recently in the latter field particular progress has been made in the development of protocols and parameters which can be used for international standardisation. These developments have embraced stylus devices, laser based optical systems and scanning probe methods. But the subjects of manufacture and surface characterisation as they have currently developed have much further to go if the process of surface characterisation is to impact on manufacturing process control. Engineers and researchers are beginning to realise that if the new tools available are to have a great impact on manufacturing industries, surface characterisation as a subject must be broadened to include measures of surface integrity and be related to the functional demands imposed on the surface in service. If these three factors are considered together, surface characterisation, surface integrity and function then a new and important subject is born, **Engineered Surfaces**.

This paper draws together the elements which go to create the subject the 'Engineered Surface' and in particular relate to surface integrity, surface topography and the bulk properties of the materials used to create the product. The paper presents a method by which this important subject can be developed to the benefit of the demands placed on the manufacturing industries in the early years of the new millennium.

A Philosophy of Manufacture.

In recent years considerable progress has been made in the characterisation of surface finish. This is essential since engineers, conscious of the importance that the surface character has on the functional performance of the component, have strived to improve their understanding. One factor

has become abundantly clear during the evaluation of three dimensional surface topography, although this is an important feature of the performance of a component or product, many other factors are also of equal importance. In recent studies, it has become recognised that the functional situation in which surfaces are employed should also be fundamentally investigated (ref. 1.)

What is it then that makes a functionally successful surface? It is a combination of the surface topography, the material selection which provides the underlying bulk properties of the selected material, the properties of the near surface layers, and the control of the manufacturing process by which the final surface is generated and as a consequence fine tune the properties of the surface layers produced.

Traditionally the majority of manufacturing processes (metal removal) which were specified for producing a wide variety of engineering components, defined the means of achieving the desired geometry through selection of the appropriate machining conditions. The nature of a typical machined surface and resultant sub surface layers normally consists of;-

- An oxide layer
- A plastically deformed layer
- A metallurgically affected layer
- The bulk material
- The topographic boundary between the workpiece and the environment

The surface that results has in many cases needs to be further modified by subsequent surface treatments (heat treatment, coatings, chemical treatment, mechanical treatment) to enable them to be more suited to the function for which they are intended. The purpose of this subsequent treatment, often referred to as surface engineering, is to modify the upper layers of the surface to impart specific properties such as wear resistance or fatigue resistance to improve functional suitability.

The importance and scope of this subject was demonstrated in an international survey of Surface Engineering, particularly directed to surface coatings, which was conducted at the University of Hull (UK), (ref. 2.). The findings of the report produced as a result of the survey indicated that in the UK alone the expenditure in this area would reach at least £5.5b by the year 2005. Clearly a large section of this expenditure would be related to re-engineering a variety of surfaces for function.

A third material modification process which must be added to the above group is component creation by forming. A technique where the material is physically deformed or moulded to create the desired shape and strength characteristics. These processes by their very nature invoke surface modifications which have an impact on their functional suitability.

Table 1 provides a typical list of processes, related to selected product precision which are created by either removal, addition or forming.

It is suggested that by the correct selection of the manufacturing process and the specific manufacturing conditions the expenditure which relates to post creation surface treatment might be largely eliminated by *'engineering the surface'* appropriately during the final stages of machining

or forming if the process parameters had been selected with understanding and care. Under such care it would be possible to create the surface features required of a surface rather that just to allow them to arise as a function of the process itself. Figure 1 presents typical features of an engineered surface.

SURFACE CREATION

Table 1 A surface is created by a combination of one or more formative processes

Creation / Material	Conventional ($10^{-3} - 10^{-4}$)m	Precision ($10^{-4} - 10^{-7}$)m	Nano-Processing ($10^{-7} - 10^{-10}$)m
Removal	Turning Milling Boring	Grinding Honing Lapping	Diamond Machining Etching Lithography
Addition	Painting Galvanising Plastic coating	Plating Mirroring Deposition	Plasma Atomic placement Vapour Deposition
Forming	Rolling Bending Forging	Extrusion Peening Moulding	Ultra Precision Moulding

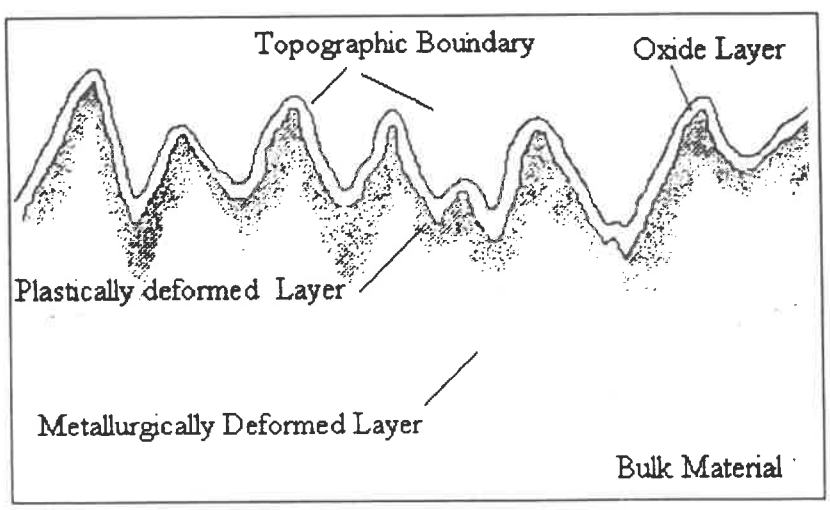

Fig. 1 The Features of an Engineered Surface

The Engineered Surface

The concept of 'engineered surfaces' implies that instead of creating a product using some form of machining, forming, casting or fabrication process, then modifying the surface produced to change its properties, a more analytical approach should be taken. This is usually undertaken in an attempt to improve functional performance. In fact it may be preferable and even cheaper in the long term, to begin to understand the consequences of the process of manufacture itself. This might be achieved by being able to carefully control the effects of the process or processes by which the component is produced to induce the desired physical properties of the surface layers. Control of the physical properties of the surface may be possible by specifying the final processing conditions which yield the desired surface topography and corresponding mechanical properties of the surface and sub-surface layers. Thus this better specification would result in a surface highly suited for its intended functional performance.

This philosophy is not completely new. Whitehouse (ref. 3.) showed that the current understanding of the surface generation of most machining processes was minimal, but in his paper he demonstrated that it was feasible to rationally examine the topography of a surface and consequently the physical properties of the surface, its integrity to begin to understand the consequences of any machining or fabrication process. He also showed that as engineering requirements become more precise and manufacturers are forced to bring down their manufacturing costs it is imperative to understand the implications that the selected manufacturing processes yield. He argued that in most well controlled past and present material processing the workpiece was defined by a small number of simple parameters and from these definitions the component was manufactured. For the current manufacturing situation, these steps are diagramatically shown in figure 2 below.

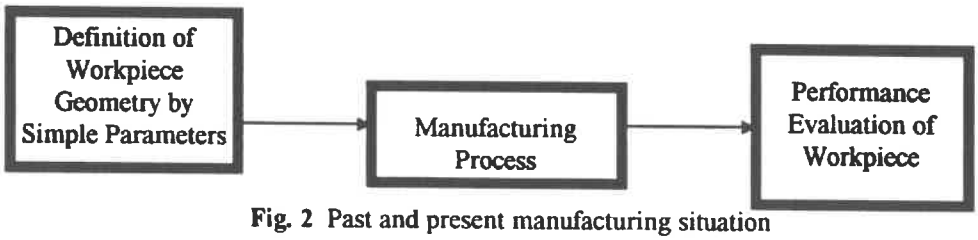

Fig. 2 Past and present manufacturing situation

A second and probably more scientific approach, is to develop a theoretical basis for the surface interaction and to explore that basis in relation to careful measurements of the component surface. Such a process has been suggested by Whitehouse (ref. 4.) in his definitive book on Surface Characterisation. Whitehouse suggested that in an 'enlightened future' the process of manufacture will require more comprehensive component specification; and as a consequence more complex workpiece geometry descriptions. This implies that the individual characteristics of the machine itself could all have a profound effect on the integrity of the surface produced.

As a consequence the process control parameters are likely in future to include specified limitations on tool wear, cutting speeds and feeds, tool dressing specifications accompanied by the selection and flow rate of the most appropriate coolant to be used during the cutting operation as well as the definition of parameters to be measured to ensure satisfactory compliance to specification. This will imply that a greater emphasis will need to be given to functional testing of components and

products in order for manufacture to conform to international quality standards as well as product reliability and both current and future liability legislation.

The approach suggested above relates to the need for a well organised programme of investigation into the factors which affect the functional behaviour of production surfaces. What is important in such an approach is that the data produced during such research is documented and made available to a wide range of interested users and manufacturers. In the twenty first century we can expect to see industry move to higher precision manufacture for much of its production. For example the expected growth in both ultra precision manufacture and nano technology (ref. 5.) and the growing requirement for smaller sizes, tolerances and improved compliance in precision products which will be demanded to meet the more stringent functional requirements of many products.

There will be two overwhelming requirements by these precision industries. These are accuracy of manufacture and the suitability of the components and products for its intended function. Such requirements will imply considerable investment by industry in the understanding of the machining processes and their consequence in the operation of a surface in service.

The Complex Inter-Relationships in an Engineered Surface.

Before we can make much progress in this broadly based subject - the 'engineered surface'. The complex inter-relationships which make up the engineered surface must be considered. They include;-

Bulk Material Properties - these have been carefully selected to provide the required component durability using the minimum of material and having the minimum weight. Much progress is currently being made in the automobile industry at the present time through laser welding of dissimilar metals and metals of various thickness. Further significant progress in design using modelling techniques such as FEA has enabled reduction in the bulk material. However these models only consider the bulk material properties and pay little attention to the subtle changes in surface properties induced by processing.

Surface Properties (either engineered or surface treated) - traditionally surface properties have been 'adjusted' by either thermal, chemical or mechanical treatments in order to impart some functional attribute. This, as indicated earlier has led to a large growth in surface modifying industries but by its very nature implies that the fabricated surface is not ideal for its intended application and to attain its functional properties further expensive processing is required.

Surface Interacting Conditions Their has been considerable activity in this broad area of engineering. For example there has been much progress in recent years in the improvement of lubricants. The greatest attention being paid to their wettability (their ability to wet and remain attached to the surface) and their design so that they remain effective as extremely thin films. This has been achieved by research into the effects of the inclusion of special additives to improve the tribological interaction. There has also been considerable improvements in surface prepared for both thermal conductivity, loading and electrical contact. Such applications require considerable attention to the creation of the shape of the surface to provide for large contact areas which either resist deformation (both elastic and plastic) or promote efficient electrical and thermal conductivity.

Surface Topography - currently a poorly understood subject in relation the functional use that surfaces are employed for. Depending upon the intended application, the required characteristics of the surface may need to differ. Currently progress is being made on characterisation methods but at this point in time they are more suited to the control of the manufacturing process. The progress which has been achieved is briefly outlined below. When these four areas are brought together a complete understanding of engineered surfaces is possible.

Surface Topographical Features and their effect on the Functional Performance of Surfaces.

Engineering surfaces can be divided into three groups based on their functionality, translational surfaces, static contact surfaces and non contacting surfaces. In addition to these three groups there is the category where surfaces are required to be specified comprehensively whose sole purpose is to create further topographies on secondary surfaces which then go into functional use.

Translational Surfaces are generally referred to a tribological surfaces and include bearings and slideways, surfaces experiencing friction, wear, galling or fretting. Clearly the amplitude of the roughness, its shape and the separation of the asperities and interconnecting valleys affect the interaction, the retention of the lubricant and affect the leakage of translational seals. The answer to operational performance is to identify the primary tribological interaction. Functional parameters such as valley volumes and valley interconnectability are of significance. A more comprehensive review, based on earlier work by Griffith (ref. 6.) in relation to static contact surfaces is presented in table 2 below. This figure (the first of four) indicates, as Griffith's suggested that there is evidence that the topography was indeed a contributory factor to operational performance. The way in which the information is presented illustrates the current degree of confidence in the correlation between surface finish and function.

TABLE 2 - TRANSLATIONAL SURFACES

Function	Heights	Distribution and Shape	Slopes and Curvature	Lengths and Peak Space	Lay	Surface Volume Parameters
Applications						
Bearings	●	●	◗	◗	●	●
Seals	●	●	●	◗	●	●
Sideways	●	●	◗	●	●	●
Mechanisms						
Friction	●	●	●	●	●	●
Wear	●	●	●	●	●	●
Galling	●	◗	●	O	O	●
Fretting	●	●	●	O	O	●

● Much Evidence ◗ Some Evidence O Little or Circumstantial Evidence

Static Contact involving joint stiffness, electrical or thermal contact, adhesion & bonding, fatigue, stress and fracture. This is a contact area related effect and therefore embraces both short wavelength and long wavelength effects. Under loading surface asperities deform both elastically and plastically. Clearly asperity heights, their shape and distribution, asperity slopes and curvatures are significant as is likely to be the peak spacing of asperities. The evidence of surface finish relationships in relation to function for the various types of static surface contact is presented in table 3 below. Much of this figure is again based on the work of Griffith (ref. 6.).

Clearly there may be more forms of description than have been so far defined and these will become apparent as further research is conducted, but the table below provides a useful starting point in the specification of surface parameters which will assist in developing an understanding of the consequences of surface topography on static contact surfaces.

TABLE 3 - STATIC CONTACT SURFACES

Function	Heights	Distribution and Shape	Slopes and Curvature	Lengths and Peak Space	Lay	Surface Volume Parameters
Functions						
Joint Stiffness	●	●	◗	◗	◗	◗
Contacts (elec/therm)	●	●	●	●	O	O
Adhesion & Bonding	●	●	◗	◗	◗	●
Mechanisms						
Fatigue	●	◗	O	O	●	●
Stress	●	O	◗	O	●	●
Fracture	●	O	O	O	●	●
Reflectivity	●		●	●	●	●

● Much Evidence ◗ Some Evidence O Little or Circumstantial Evidence

Non Contact surface, often related to finishings include plating, painting, polishing, reflectivity and hygiene. Functionally relevant parameters include asperity heights, slopes curvature and asperity separation. Highly reflective surfaces such as optical mirrors and precision lenses, characterisation and counting of 'digs' and 'blemishes' are significant. Non contact and magnetic data storage surfaces usually require optical assessment, often performed by optical techniques, or scanning probe microscopy so that surfaces are not damaged during assessment. The relationships between surface finish and function for non contacting surfaces is presented in table 4 below.

Although table 4 below is useful it is likely that further forms of parameter specification will be introduced as further development is undertaken. Clearly as precision manufacture further develops and the need for greater surface discrimination increases, particularly in the domain of optical surfaces, more specific descriptors may be necessary.

TABLE 4 - NON CONTACT SURFACES

Function	Heights	Distribution and Shape	Slopes and Curvature	Lengths and Peak Space	Lay	Surface Volume Parameters
Plating	●	◗	◗	◗	O	◗
Painting	●	◗	◗	◗	O	●
Polishing	●	◗	●	●	◗	◗
Reflectivity	●	O	●	●	●	◗
Hygiene	●	◗	◗	O	O	●
Corrosion	●	●	●	O	O	●

● Much Evidence ◗ Some Evidence O Little or Circumstantial Evidence

Shaped Surface Creation (which can be considered a hybrid of translational and static contact). These surfaces produce secondary functional surfaces and include the following processes, forming, drawing, extrusion and rolling. The parameters which are relevant to these surfaces include asperity heights, their shape and curvatures as well as their peak spacing. Complex relationship exist when one surface in effect produces a secondary surface. As a consequence it is not just the primary surface functional requirements which must be taken into account, in addition the desired functional attributes of the developed surface is also of significant importance. Evidence of the relationship between surface finish and function is presented in table 5.

TABLE 5 - SHAPED SURFACE CREATION

Function	Heights	Distribution and Shape	Slopes and Curvature	Lengths and Peak Space	Lay	Surface Volume Parameters
Forming	●	◗	◗	●	◗	●
Drawing	●	◗	◗	●	O	●
Extrusion	●	◗	◗	O	●	●
Rolling	●	●	◗	◗	●	●

● Much Evidence ◗ Some Evidence O Little or Circumstantial Evidence

Surface Mechanical Features which Affect the Functional Performance of Surfaces. (Surface Integrity).

Surface Hardness which will normally vary to some extent across the surface is partially responsible for the durability of the surface and its resistance to wear, plastic and elastic deformation. If two adjacent surfaces come into contact in a functional sense then their relative harnesses affect their ability to operate as pairs.

Residual Stresses;- These are induced during machining or other processing of the surface and can either be tensile or compressive in nature. Essentially residual stresses describe the stress state of the material lattice. Compressive residual stresses are highly desirable in that they suppress crack growth as the inter atomic stress acts to blunt any cracks. This enhances the wear and fatigue properties of the surface and improves stress corrosion resistance. Tensile residual stresses on the other hand tend to promote crack growth and are consequently deleterious to the material surface properties.

Plasticity index is a measure of a surface's ability to conform under loading. The complimentary effect is to assist the reduction of surface loading by spreading the load over an increased area. If there is substantial lubrication between the surface interface then little or no plastic or elastic deformation will occur as the lubricating fluid will integrate the loading by promoting a fluid pressure profile within the gap between the counter faces.

Sub-Surface Features which Affect the Functional Performance of Surfaces.

Sub-surface features which influence functional behaviour of a surface have also been suggested by Griffith (ref. 6.) and these include;-

Untempered martensite (UTM) - a state which is caused by thermally induced metallurgical transformations in steel and primarily induces tensile residual stress into the surface and sub-surface layers. The formation of untempered martensite has the effect of reducing fatigue life of materials increases the susceptibility to stress corrosion and cracking and reduces wear life. UTM is often induced by thermal energy resulting from high metal removal rates during machining.

Overtempered martensite (OTM) - is found beneath the UTM and is softer than the bulk material due to over tempering. The presence of OTM reduces the bulk material mechanical properties.

Plastic deformation of the surface layers which is usually identified by heavy plastically flowed layers which often appear featureless under the microscope and are termed 'white layers'. Such layers produce compressive residual stress in the surface which assist fatigue life, increase the resistance to corrosion cracking, improve wear properties and surface hardness and assist mechanical properties in general. Machining processes such as honing, light grinding, lapping and forming induce plastic deformation at surfaces and consequentially benefit material properties.

Some Examples of Engineered Surfaces.

Processes which have been commonly used and are related to the concept of "The Engineered Surface" whose key process constraint is controlled plastic deformation of the surface layers are described. Surprisingly these are not new processes. Many of them have been employed for almost a century to improve the integrity of the surface, but their specific understanding is limited and today they are mainly regarded as a 'black art' employed by skill workers and craftsmen who have learned to understand, in general how the process is to be employed and controlled.

Ballising. The process of driving a precision sphere through a machined hole or bore to improve the surface finish, to impart negative residual stresses into that surface to improve surface wear resistance and fatigue resistance. There are a number of

applications where such a process is invaluable in increasing, in particular, fatigue life and fatigue resistance, and many of these components are to be found in the aerospace industry and in automobile manufacture.

Barrel Finishing

This well established technique is used to improve the finish of a variety of ferrous, non ferrous and plastic components (ref. 7.). Parts slide or float in the medium used so fragile parts can be tumbled as well as heavier sections and the method can be used to improve surface finish without destroying the geometric surface and solid design specifications often required in high technology application. One application where the method is used to improve performance is in the manufacture of compressor blades for gas turbines. It is known that gas turbines, both aero and industrial, require turbo machinery components offering the highest possible efficiency (ref. 8.) and that gas turbines for mechanical drives require increasingly large power blocks and higher thermal efficiencies (ref. 9.). Sophisticated 3D CFD design methods are used to improve design performance and the advantages gained are matched with improvements in manufacturing tolerances. Similar gains are made from improved blade finish. Barrel finishing improves the 'as cast' surface from 63 μ inches to 20 μ inches.

Shot Peening

This is a further process where the surface properties, in particular the residual stress of the surface layers are modified by impinging the surface with particles, normally lead shot, at relatively high velocity. The kinetic energy imparted by the lead collisions with the surface induces plastic deformation which in turn induces negative residual stresses into upper surface layers, which improves the performance of the component.

Sheet Texturing

This is a relatively new process which has been introduced as part of the final rolling sequence for producing sheet steel and other sheet materials. A defined topography is deliberately imparted onto the finishing rolls which is then transferred to the sheet metal. This process has been introduced to create a defined roughness so that the sheet is able to contain lubricant in the valleys of the micro topography. This is done to reduce friction and avoid the risk of galling during for example, sheet forming. Such texturing can also improve the paintability of sheet materials and as a consequence it produces a surface which has visual improvement. Sheet texturing is conducted in one of two ways. Either EDT texturing or laser texturing of finishing rolls for sheet steel rolling and then transferring the topography to the sheet steel itself by rolling.

Honing

This is a widely used process which engineers the surface. In this machining process the surface is deliberately engineered to produced a stratified surface which retains lubricant to ensure a long service life. The process is particularly well developed in the automotive industry in the production of engine bores. More recently however a development of the process, the plateau honing process provides a surface which provides the characteristics of the run-in engine. Such conditions prevent early running failure and minimise engine emissions which is the subject of considerable international legislation. In recent times there has been the development of other forms of specialised surfaces by other more exotic processes to engineer engine bores. The objective of the new processes are to

create surfaces with greater consistency and which yield lower harmful engine emissions.

There are a number of other processes which fall into the category as those defined above. They all amount to processes which are introduced to deliberately "engineer the surface" to assist in improving the functional performance of the finished component through controlled plastic deformation. Engineering surfaces can be described as a technique which the surface is 'functionally finished' for the desired application.

Future Approach to the Engineered Surface.

For the Engineered Surface to become a broadly understood and scientific approach to surface production, much is needed to be known about the nature of material working and the physical effects that the finishing process has on the surface layers and near surface layers of the material. At present, although there is some understanding of the effects of the processes which work the surface as they are sized and shaped, there is little quantified information to aid the understanding. The modern surface specification and design philosophy is specified in figure 3.

There are two approaches;-

1. An experimental approach, whereby surfaces are produced under well defined machining or other finishing conditions and those surfaces are then subjected to functional tests, either in a well controlled programme on in 'real life' situations where there is sufficient control of the final product to obtain reliable feed back information. One such programme of this nature has been conducted at Chalmers University in collaboration with Volvo Cars (ref. 10.) with their Integrated Surface Modelling software for bores, gears and facia surfaces and Avesta Steel with their Surface Database (ref. 11.) aimed at specifying the production of stainless steel sheet finishes. Both of these systems use processing parameters, metrology information and functional testing to allow the optimal process parameters to be set for given functional outcomes. The approach is to determine an experimental rationale to explain the functional behaviour of the 'engineered surface'. This implies that the causes of the separate geometric components which are generated are identified. The topography provides, for example, the entire 'signature' of the machining operation within the surface asperities.

2. A second approach is to develop analytical models of the surface interactions during machining or fabrication, and through the results of these models, compare the predictions with the surfaces which have been produced. Such a model could take into account information on the influences of the machine tool itself, and this would include the effects of slideways, bearings and the machine stiffness on the resulting surface. Such inputs could contain direct information on the feed rate of the cutting tool, tool wear, coolant type and supply and other processing conditions. Such an analysis could embrace the effects of the material in-homogeneity itself. An illustration of a typical surface analysis and the way in which the signal can be interpreted is presented in figure 4.

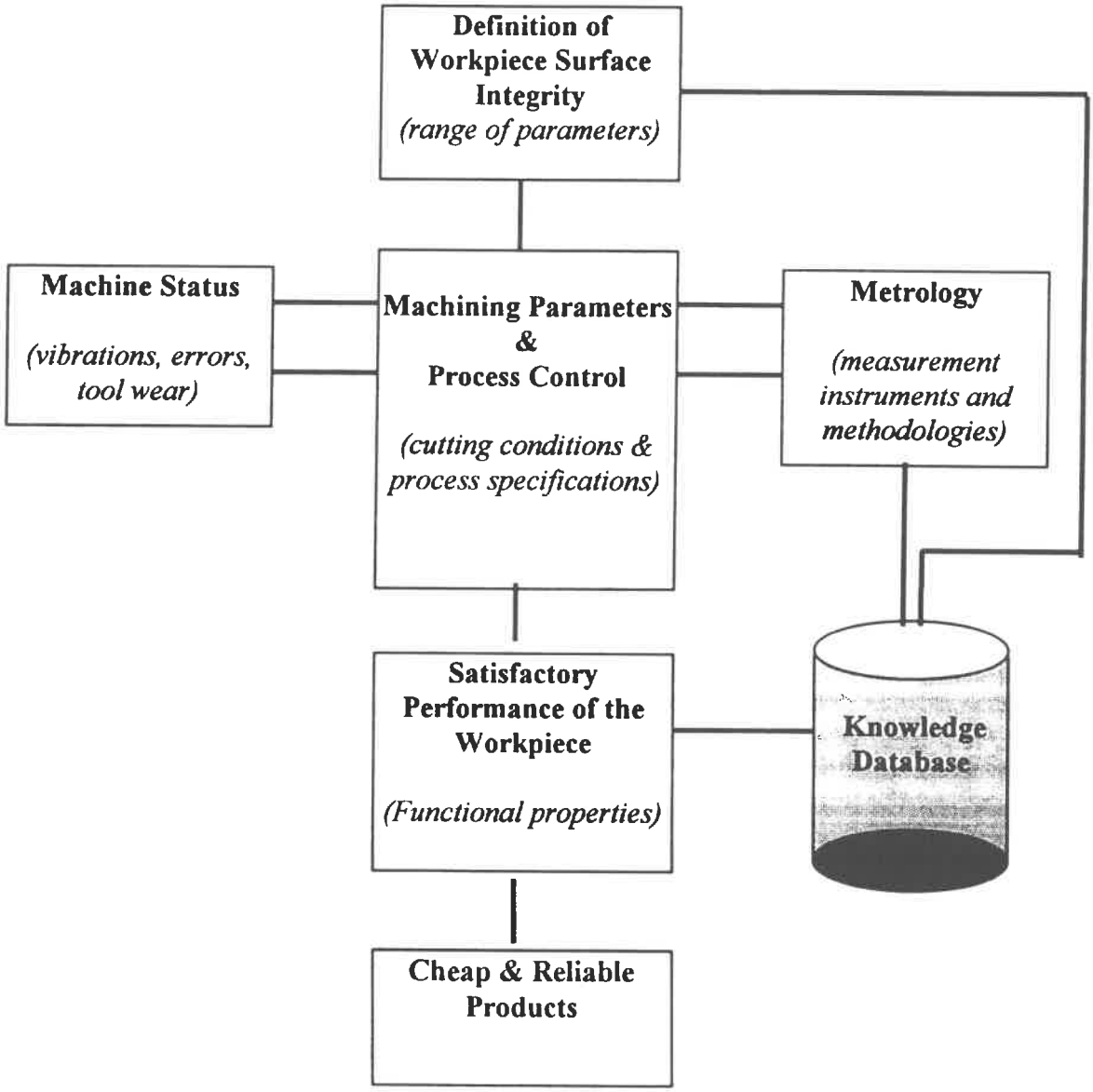

Figure 3 Modern surface specification and design philosophy

Comments.

There are a number of other processes which can be investigated to determine the surface conditioning as a result of the specific process used. If all or most of the parameters are investigated which relate to process, it would be possible to produce a comprehensive 'Atlas' of the surfaces produced in association with a range of processes. The development of a range of Atlases would enable the functional process control parameters to be accurately set, which would ensure that the produced topography and its consequential condition of the surface and near surface physical layers, is compatible to the intended function for the surface.

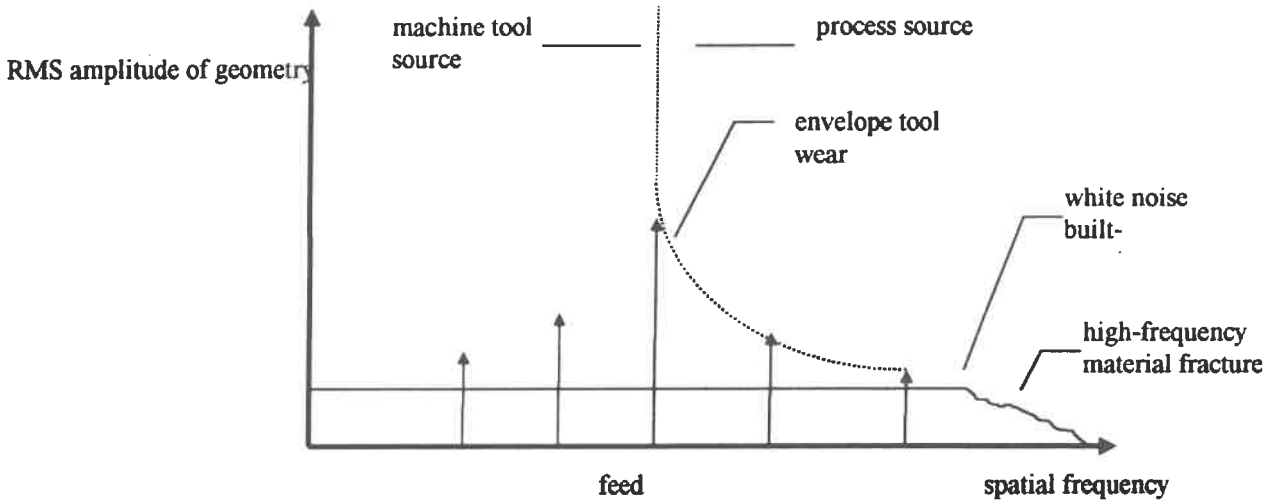

Fig. 4 Fingerprint of a single point cutting prcess. After Whitehouse (3)]

The industrial outcomes of 'engineering the surface' for its intended function include:- Increased product reliability and a reduction of the running-in time of tribological components. Reducing gas 'blow-by' in internal combustion engines to meet current and anticipated future legislation on gas and particle emissions from vehicle engines. The use of nanometre sized particles in the production of highly controlled porous materials, for example, to use for aerostatic bearing shells and high precision filters. The structuring of steel sheet and other metallic components for use in the automobile and other industries.

To support the proposals presented in this paper it is possible to state that there have been in recent times considerable developments in manufacturing processes. Also the development of new materials in recent years and the implications of surface topography combined with surface physics (the engineered surface) of these materials are particularly important in the following areas;-

a. increasing specification and use of multi-functional surfaces to reduce and hopefully running-in and increase both performance and service life of components and products.

b. The production of atomic scale finishes for use in the micro-circuit and micro-chip industries. This will imply energy beam processes and the use of atomic scale abrasives

c. The development of net shape fabrication processes in an effort to minimise post fabrication machining.

d. The need to develop more economical manufacturing methods. This will occur if the number of process in manufacture are reduced and the requirement to readjust the components after machining, shaping of fabrication is lessened.

Component Function Map

A way of characterising a component more comprehensively is through the creation of Component Function Maps, one of which is presented in figure 5 to illustrate the scope of the map. In the component function map many factors are interrelated, mode of function, the functional situation (either static, hybrid or dynamic application) and the scale of clearance or overlap required by the interaction with the mating part. In addition these inter relationships have been identified in terms of the functional application and the degree of precision required.

MODE	STATIC	FUNCTIONAL SITUATION HYBRID	DYNAMIC
Plastic	Energy Flow		Delamination
Interference	Locking	Electrical points	Dry wear
Elastic			Dry Friction
	Thermal/Electrical	*Contact*	
Fretting	Conductivity	Elasto Hydrodynamic Lubrication	Disk Drive Flying Heads
		Ultra Precision Air Bearings	Hip Joints
		Nano Separation	Running in
Pitting Scuffing	Flexures	Precision Rolling Elements	Dentist Drills
	Mechanical Seals	*Micro Separation*	Dynamic Seals
Running Clearance	Assembly Linkages	Hydrostatic Bearings	Rolling Element Bearing
	Plain Bearings	*Macro Separation*	Standard Bearings
Single Surface	Coatings	Cosmetics	Corrosion
	Paints		Fatigue

Fig. 5. Component Function Map

Concluding Comments.

It is these trends which will lead to more surfaces being *engineered* in the final processing of components to meet their long term functional requirements. It is believed that the recent interest in the 'engineered surface' has come to the forefront as greater demands for economy and functionality have been sought.

References.

Ref. 1. Blunt, L. Et. Al. "The Development of a Basis for 3D Surface Roughness Standards" First year progress report, Contract No. SMT CT98 - 2209, Collated and Prepared by the University of Huddersfield, UK.

Ref. 2. Matthews, A., Artley, R.J., Holiday, P. & Stevenson, P. "U.K. Engineering Coatings Industry in 2005." Report for the DTI, Published by the University of Hull, 1992.

Ref. 3. Whitehouse, D.J. "The Role of Surface Texture, Past, Present and Future." Seminar on Surface Metrology & Surface Analysis, D.T.I., Denmark, 20th September 1996.

Ref. 4. Whitehouse, D.J. "Handbook of Surface Metrology." Institute of Physics, ISBN 0-7503-0039-6, 1994.

Ref. 5. Stout, K.J. "A Review of nano-Technology" The Korean Journal of Precision Engineering, pp29-51, Vol. 14, No1, January 1997.

Ref. 6. Griffiths, B.J. "Surface Integrity, Functional Performance & Standards" Workshop on Engineered Surfaces, Cops la Sallette, France, June 1998.

Ref. 7. Wang, K.H., Blunt, L. & Stout, K.J. "The 3D Characterisation of the Surface Topography of the Ballising Process." 7th Int. Conf. on Metrology and Properties of Engineering Surfaces, Gotteborg, Sweden, 2-4th April 1997.

Ref. 8. Niebel, B.W., Draper, A.B. and Wysk, R. A. "Modern Manufacturing Process Engineering" McGraw Hill, pp530-532, 1989.

Ref. 9. Scrivener, C.T.J., Connolly, C.F., Cox, J.C. and Dailey, G.M. "Use of CFD in the design of modern multistage aero engine LP turbine design. C423/056 I. Mech. E. 1991.

KGM-plus - Device for Simultaneous Measurement in Six Degrees of Freedom on Machine Tool Trajectories

S. Weikert, Dr. W. Knapp
Inst. of Machine Tools and Mfg(IWF), Swiss Federal Institute of Technology (ETH), Zurich, Switzerland

Abstract:

The performance of linear axes is often tested on the basis of one set-up per one or two types of deviations from a NC path. With the application of multi-axes machining the contouring performance in more than two degrees of freedom is of interest.
The paper describes a measuring instrument to check the contouring performance of a machine tool in the six degrees of freedom. The three translations and the three rotations of the relative movement between tool side and workpiece side are measured simultaneously. Results of first measurements are presented and discussed.

Keywords:

Machine tool, Contouring performance, Measuring instrument

1 Introduction

The performance of a linear axis, i.e. positioning accuracy, straightness, roll, pitch, yaw, is generally measured on the basis of one set-up per one or two geometric deviations. For performance testing of rotary axes (or spindles) the simultaneous measurement of five degrees of freedom is common practice and this can be found already in existing standards [1] [2]. The simultaneous measurement of the five degrees of freedom of a spindle is helpful for the interpretation of the dynamic behaviour of the spindle.
For the contouring performance of linear axes of a machine tool the measurement of two translations in a plane are common, which is already described and summarised in standards [1] [3]. This is helpful for the interpretation of the deviations from a programmed path.
The simultaneous measurement of five to six degrees of freedom of a linear axis with a straightness standard is described in [4], a later development with laser-interferometers is described in [5]. These systems are mainly used for point-to-point measurements (static mode) parallel to a linear axis.

2 The system KGM+

The system KGM+ allows the simultaneous measurement of six degrees of freedom as a relative movement between the tool side and the workpiece side of a machine tool. The path to be checked has to be nominally in a plane. The plane is preferably situated parallel to a coordinate plane of the machine tool, i.e. in a XY-, YZ- or XZ-plane. Within the plane the path can be freely chosen, it might be linear, circular, a step, etc.

2.1 System-description

The system KGM+ [6] is based on a Heidenhain grid encoder [7] which is a two-dimensional linear scale. With one optical head the two translations in the plane of the grid plate, e.g. X and Y, are measured (Figure 1).
The combination with a second optical head gives the measurement of the rotation in the plane of the grid plate, e.g. C.
In the version used here, the grid plate itself is touched with three linear displacement transducers, i.e. the grid plate is taken as a plane master. The probes are incremental Heidenhain probes equipped with linear scales. By this, the signal processing is identical to the signal processing for the grid encoder.

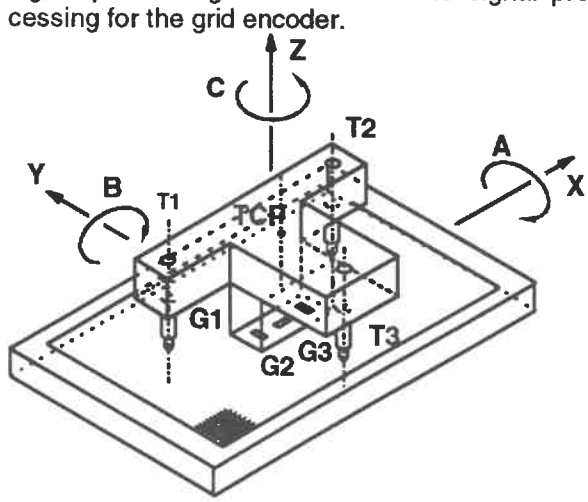

Figure 1: The KGM+ (enhanced cross grid measuring system; Gi..optical head (grid), Ti...linear displacement transducer, TCP.. Tool Centre Point.

Three linear displacement transducers measure the translation square to the grid plane, e.g. the Z-direction, and the two rotations around the axes in the grid plane, e.g. the rotations A and B.

The grid plate is mounted on the workpiece side, i.e. on the machine table. The two optical heads and the three probes are mounted in a fixture which is held in the blocked tool spindle.
The resolution of the grid encoder is 4 nm in its two directions, the resolution of the three linear displacement transducers is 20 nm. The resolution for the rotations depends on the distances between the optical heads and between the linear displacement transducers. In order to simplify the handling of the system, in this version the distances have been chosen as 90 mm and 60 mm, therefore the resolution for the rotation in the grid plate (rotation C) is 0,1µm/m (0,02 arcsec) and 0,5µm/m (0,1 arcsec) for rotations square to the grid plate (rotations A and B).
The area for contouring has a diameter of approximately 120 mm, the allowed travel square to the grid plate is ±0,5 mm. The system accuracy is about ±2 micrometer without applying any compensation. The accuracy for the rotations of this first system is in the order of ±25µm/m (±5 arcsec) for the rotations with no compensation. The maximum feed rate is above 24 m/min. The data, i.e. a set of 6 coordinates, can be read with a frequency of up to 5000 Hz.

3 Application

3.1 General

One application of the system is for testing the accuracy of the programmed paths in all six degrees of freedom at low feed rates. Here the accuracy of the system is of importance and this first version of the system would need some compensation.
Another application is testing the dynamic behaviour of NC drives, e.g. reversal test, test of uniformity of feed, and step-response-test for one axis, testing steps and circular test for two NC axes, as described in [8].
Another application we want to show in this paper, is the influence of the feed rate on the accuracy of a path. Here the deviations at a low feed rate are taken as a basis, and the changes that occur at higher feed rates are looked at. The simultaneous measurement of the six degrees of freedom gives the possibility to detect any cross-talk, i.e. that the movement of one machine axis introduces deviations in other axes or directions.

3.2 Measurements on a machining centre

The principal sequence of the machine axes of the horizontal machining centre under test is shown in Figure 2. The nominal path in the XY plane is a step where each of the single straight lines is 20 mm long. The programmed contouring feed rate is 5 m/min.

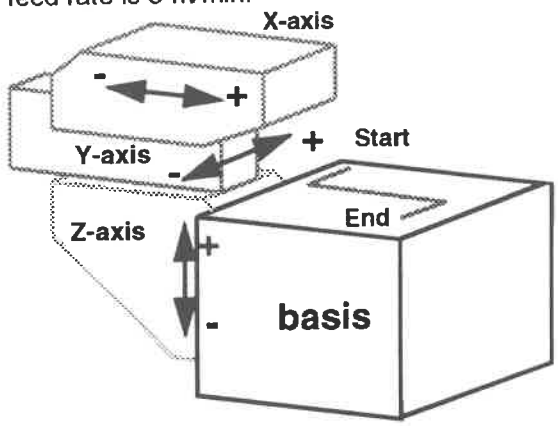

Figure 2: Axis configuration of machine tool

XY-deviations

Figure 3 shows the deviations in the XY-plane. The deviations from the straight lines are up to 52 micrometers due to axis cross-talk.

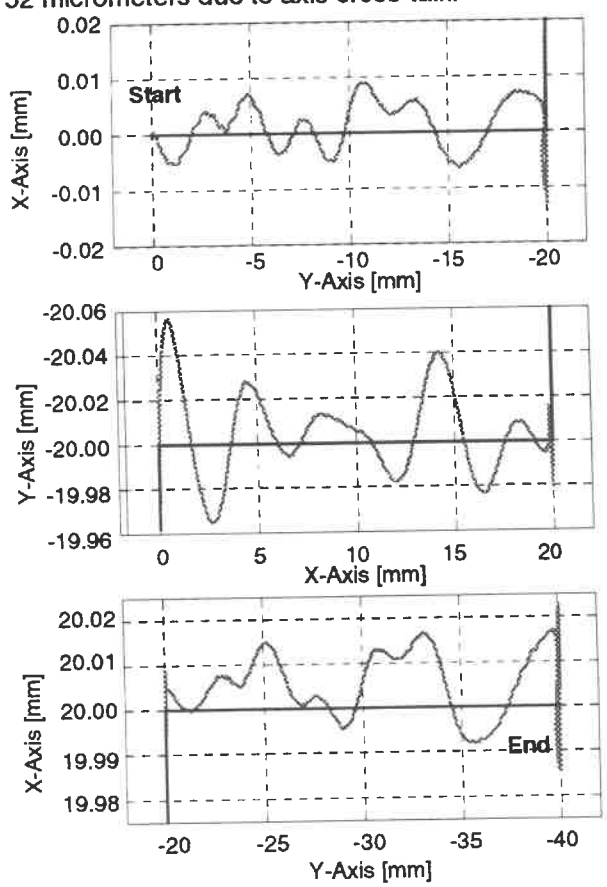

Figure 3: Deviations in X and Y along test path

Already at this velocity (5m/min), dynamic deviations exceed the static deviations by an order of magnitude.

Based on the X- and Y-coordinates which are shown in Figure 3, the velocity and the acceleration along the step can be evaluated (Figure 4 and 5). The velocity shows temporal variations which remain hidden, when being limited to X-Y-representation. A vibration can be observed during the X-axis movement, which can not be detected in Figure 3. The programmed feed rate of 5 m/min is reached with an overshoot of 15%.

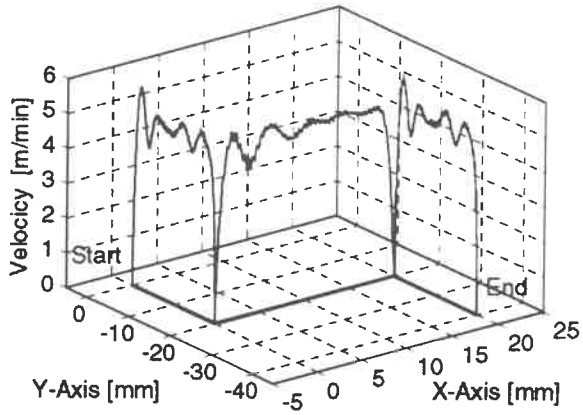

Figure 4: Measured velocity along the path

The acceleration time series (Figure 5) shows the drive-forces acting on the system during these movements. As will be shown later, deviations in Z, A and B have strong similarity with this acceleration curve. By this, acceleration-forces as primary cause for dynamic deviations is verified again.

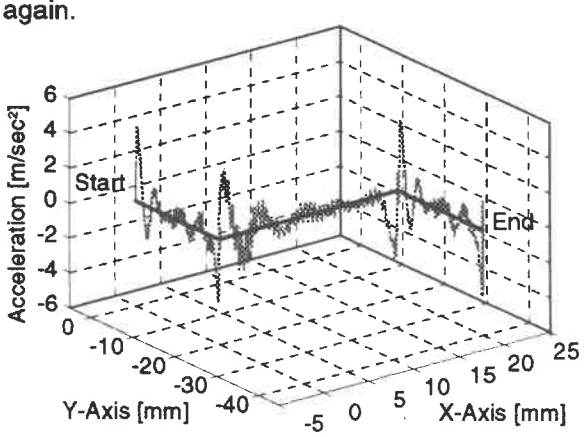

Figure 5: measured acceleration along the path

Vertical displacements

Looking at the vertical displacement, we recognize the effect of acceleration and deceleration of the X movement on vertical displacements. Y-movements show only minor effect on the Z coordinate. Deviations in Z-direction reach 41 µm (see Figure 6) which is the range that could be observed in the X-Y-plane. Whereas the deviations in X-Y-plane are also influenced by axis positioning, overshoot etc., these deviations in Z-direction are exclusively caused by axis cross-talk.

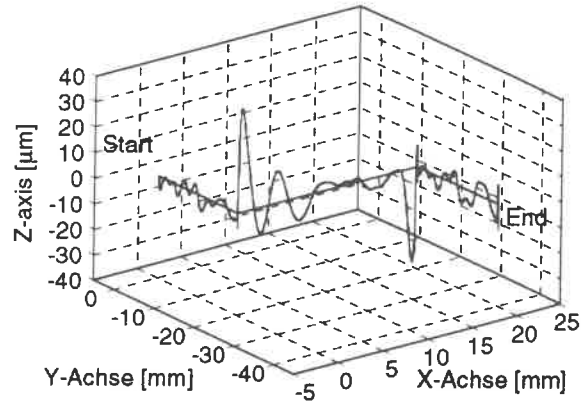

Figure 6: Measured Deviations in Z-direction

Roll, Pitch and Yaw

Looking at the rotation A – a rotation around axis X - we recognize the effect of deceleration of the X movement. The deviation (Figure 7) is up to 290 µm/m (58 arcsec). During Y-displacements, deviations show similarity to the acceleration values at these sections (see Figure 5).

When taking into account the axis configuration shown in Figure 2 and the movements that are to be carried-out here, the A-rotations are obviously resulting from acceleration- and deceleration forces in combination with the actual mass- and stiffness-configuration.

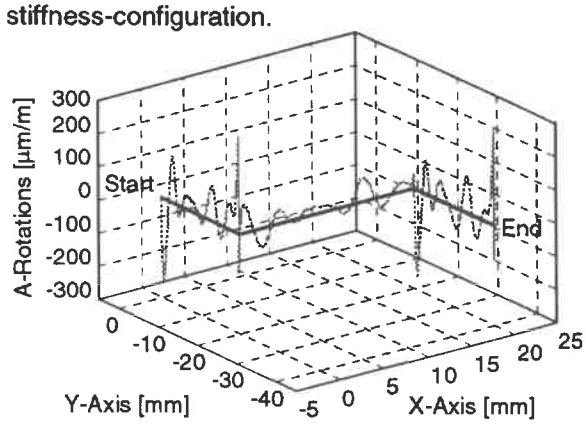

Figure 7: Deviations in A-direction

The B-Rotation – rotation around axis Y – (Figure 8) reaches -125µm/m (25 arcsec). In this case, the acceleration during the X-positioning shows similarity to the measured angular deviations. The vibration, that could be observed on the acceleration values can also be noticed.

The deviations are mainly caused by inertial forces due to accelerations as in the case of Z-, A- and B-deviations

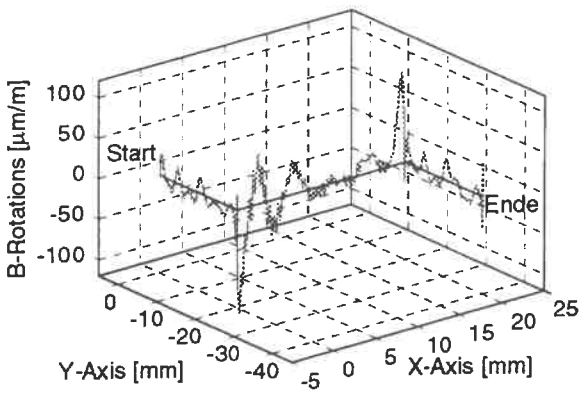

Figure 8: Deviations in B-direction

In contrast to the other rotatory components of motion the rotation in C – a rotation around axis Z - of up to 35µm/m (7 arcsec) has slight similarities to the acceleration values only during sections in parallel to the Y-axis. In this case, the offset between drive-force and the centre of inertia appears to be small in comparison with the other axes.

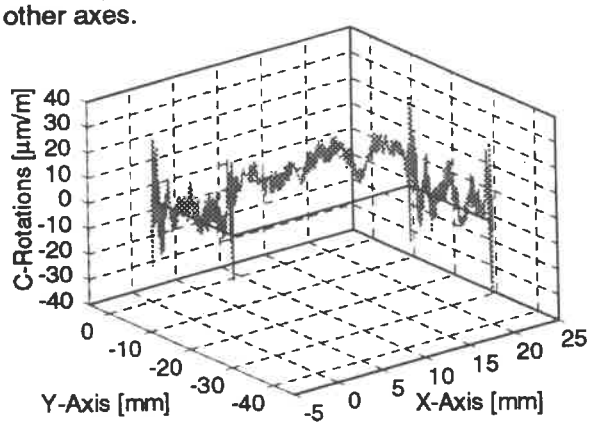

Figure 9: Deviations in C-direction

4 Outlook

Another application of the system will be a long version of KGM+ to be applied for testing linear axes. Here we want to verify the advantage of measuring all six degrees of freedom in one shot, especially at higher feed rates.

Another areas of further work are the improvement of the presentation of the results and the experimental verification of computer simulations to the path accuracy at higher feed rates on machine tools [9].

5 Summary

The system KGM+ for testing the six-dimensional contouring performance on NC paths in one plane is described in its design, resolution, accuracy and limitations.

The principal application for evaluation of the path accuracy of NC machine tools is presented. A practical application of testing the influence of acceleration forces on measurements carried-out on a vertical machining centre is shown.

The system and its application are still under development.

6 Acknowledgements

This project was supported by the Swiss Commission for the Promotion of Applied Research (KTI) and by the Swiss industrial partners Agie Ltd., Losone, DIXI SA, LeLocle, Heidenhain (CH) AG, Schwerzenbach, MIKRON SA Agno, MIKRON AG Nidau and RIGID Rorschacherberg.

7 References

[1] ANSI/ASME B5.54-1992, Methods for performance evaluation of computer numerically controlled machining centers.

[2] ISO/DIS 230-3, Test code for machine tools – Part 3: Evaluation of thermal effects, clause 5 Thermal distortions caused by rotating spindle.

[3] ISO 230-4:1996, Test code for machine tools – Part 4: Circular tests for numerically controlled machine tools.

[4] Treib, T., 1987, Error budgeting, Annals of the CIRP, 36/1:365-367.

[5] Huang, P.S., Li, Y., 1996, Laser measurement instrument for fast calibration of machine tools, ASPE-Proceedings Volume 14:644-647.

[6] Braasch, J., Kalimici, C., Weikert, S., 1997, Vorrichtung zur Erfassung der Position von zwei Körpern, Schweizerische Patentanmeldung Nr. 2279/97.

[7] Measuring systems for machine tool inspection and acceptance testing, February 1997, Dr. J. Heidenhain GmbH, Traunreut.

[8] Haas, F., 1994, Wie genau arbeitet Ihre CNC-Maschine? Die Dynamik im Brennpunkt, Technik Report 9A, September:27-31.

[9] Rehsteiner, F., Weikert, S., Rak, Z., 1998, Accuracy optimization of machine tools under acceleration loads for the demands of high-speed-machining, ASPE-Proceedings of the ASPE Annual Meeting, St. Louis, Mis., Oct, 25-30, 602-605.

Subsurface damage measurements as a tool for process monitoring

Robert-Jaap van der Bijl
Delft Centre for Optical Surfaces (DeCOS), TNO Institute of Applied Physics
P.O. Box 155, NL - 2600 AD Delft, The Netherlands
e-mail: bijl@optica.tn.tudelft.nl

Oliver W. Fähnle
FISBA-Optik
Rorschacherstrasse 268, CH - 9016 St. Gallen, Switzerland
e-mail: oliver.faehnle@fisba.ch

Hedser van Brug
Delft University of Technology, Optics Research Group
Lorentzweg 1, NL - 2628 CJ Delft, The Netherlands
e-mail: brug@optica.tn.tudelft.nl

Abstract

A new method is presented that is capable of measuring the surface quality, including subsurface damage, of optical surfaces. This method, called iTIRM, can easily be automated and used for process control and as an investigation tool for optical fabrication processes.

Keywords: Optical fabrication, subsurface damage, TIRM, process monitoring.

Introduction

During the fabrication of optical surfaces, subsurface damage (SSD) is generated in the workpiece. The nature and amount of SSD depends on the manufacturing method; brittle mode grinding induces radial cracks, with respect to the surface, in the workpiece, which can not be seen at the surface. The size of these cracks is related to the size of the grains used in the grinding process. These cracks impair the optical performance of the produced optical components and therefore, it is necessary to remove the SSD by a polishing process. Detection and measurement of SSD will thus be a helpful tool to improve optical fabrication.

Currently, the most common technique to measure SSD is dimpling[1], by which locally the depth of the SSD layer is measured in a destructive way. The method we present is based on a nondestructive inspection method, Total Internal Reflection Microscopy (TIRM)[2].

Within TIRM, a transparent optical component is tested using a laser beam that is incident from beneath the surface at an angle greater than the critical angle; the beam is thus totally reflected at the surface under test. Defects below or at the surface cause scattering, which can be detected with a microscope positioned above the surface. The distinction between scattering caused by defects on the surface (e.g. scratches, digs) and SSD (e.g. cracks) is obtained by comparing the measurement results using TIRM and Nomarski microscopy[3].

Measurement method

Within the framework of the presented method, we use a detector to measure the intensity of the specularly reflected beam and the method is therefore called iTIRM (intensity-detecting TIRM). Whenever the conventional TIRM method detects a defect by its scattering, the iTIRM method will detect a decrease in the intensity of the specularly reflected beam because of the requirement of energy conservation. Fig. 1 shows the measurement setup of the TIRM method with its detector at (A) and the iTIRM measurement setup with its detector at (B).

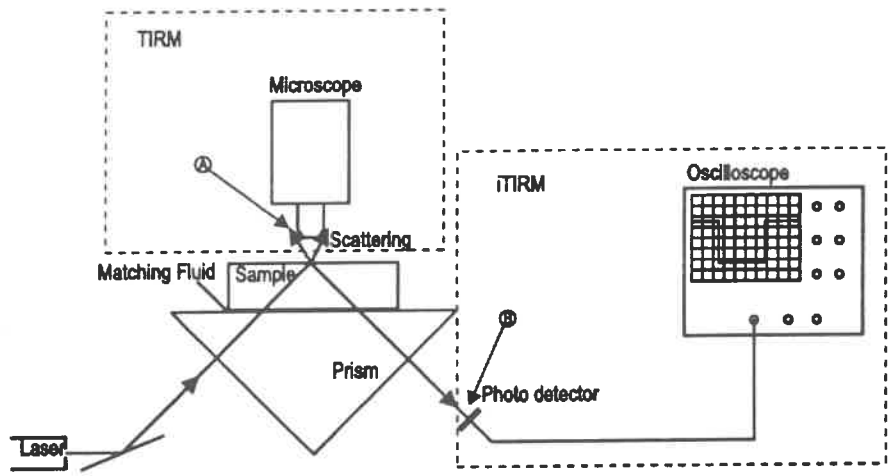

Fig. 1 TIRM and iTIRM measurement setup.

Application

The iTIRM method is, just as conventional TIRM, not only applicable to SSD measurements, but it can be used for measurement and detection of all kinds of surface defects. By scanning the laser spot (the point of total internal reflection) over the surface, the iTIRM method detects surface defects and SSD as a function of the xy-coordinates of the surface and determines its lateral size and depth. Focusing the laser beam on the surface will vary the resolution of the measurements. The energy density of a beam is maximal in its focus, hence a defect will induce more scattered light when it is in the focus of the laser beam. By shifting the focus of the beam perpendicularly to the surface, the depth of defects in the surface can be measured.

The iTIRM signal can be related to scratch/dig standards as well as it can be used as a tool for the characterisation of cracks and classification of different types of SSD (stress, cracks, etc). Unlike dimpling, iTIRM does not need surface preparation and is a quick and nondestructive tool for SSD investigation.

Comparison of an iTIRM signal from a sample surface with the signal from a well-polished surface generates a quantitative figure of the surface quality; this quality value consists of contributions from the roughness, scratches and digs, and SSD. Owing to its quantitative measurement possibility and because iTIRM does not need a detector above the fabricated surface, iTIRM can be used as an in-situ inspection technique to investigate and monitor fabrication processes of optical surfaces, while the precise positioning of the microscope above the beam spot in TIRM limits this possibility for TIRM. In the case of grinding, this can be used to optimise the different fabrication parameters, and to detect the transition between brittle and

ductile mode grinding. In the case of polishing, iTIRM can be used to detect when the desired surface smoothness is achieved and when all SSD is removed.

The iTIRM method is based on detecting variations in the specularly reflected intensity, a task that can easily be automated by connecting the intensity detector to a computer. The computer can compare the measurement signal with the signal value of the desired finishing state and automatically decide when the fabrication process should be stopped.

Experimental results

Several experiments have been carried out with the iTIRM measurement setup shown in Fig. 1. The spot of the laser beam was scanned over a sample that was partially polished and partially ground. The white parts in Fig. 2 and Fig. 3 represent the polished parts and the grey parts represent the ground parts. The thick black line indicates the path of the laser spot. The first experiment shows the difference in surface quality from the detected signal, Fig. 2. In the second experiment shown in Fig. 3, an additional polished area with gradually changing roughness from the centre to the edge was measured. The results show that iTIRM can measure a wide range of surface quality.

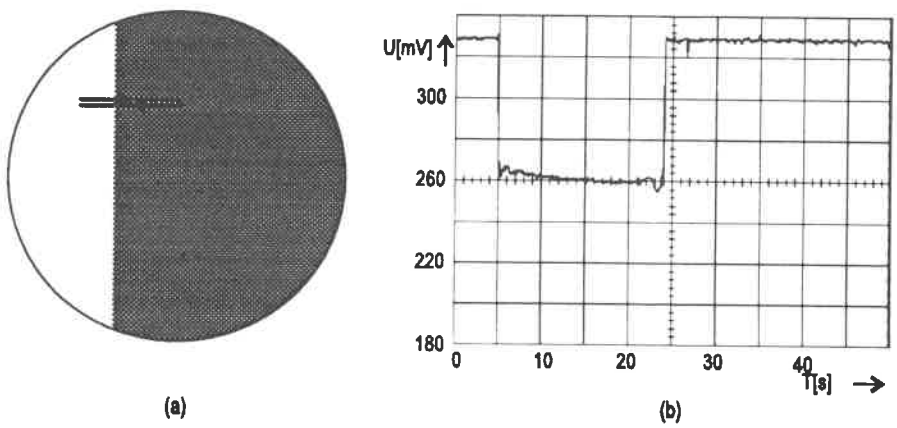

Fig. 2(a) Sample with polished (white) and ground (grey) parts and the laser spot path; (b) Output of intensity measurement.

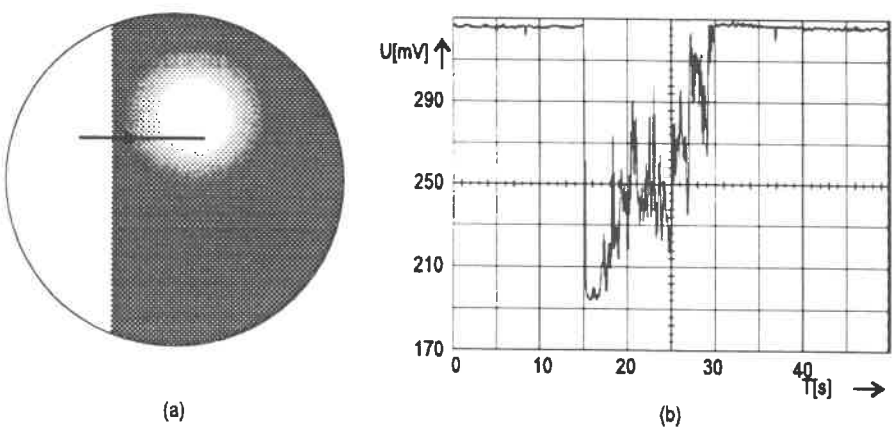

Fig. 3(a) Sample with polished (white) and ground (grey) parts and the laser spot path; (b) Output of intensity measurement.

In Fig. 4 the detection of a scratch is shown. Fig. 4(a) shows the result of a conventional TIRM measurement with a Nomarski microscope as detector, Fig. 4(b) shows the result of an iTIRM measurement when the laser spot is scanned across the scratch.

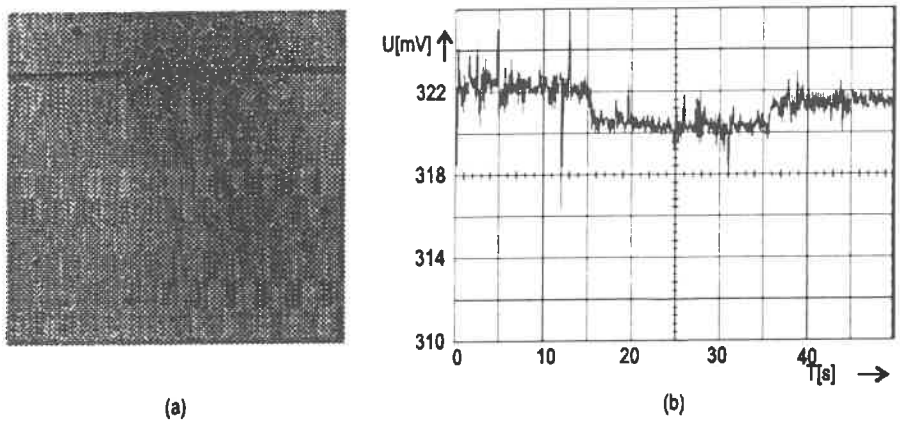

Fig. 4(a) Recording of scattering from a scratch by TIRM; (b) Output of intensity measurement using iTIRM with the laser spot scanning over the surface crossing the scratch.

Conclusions

iTIRM provides a nondestructive method to measure different kinds of defects that determine the quality of an optical surface and therefore the performance of an optical component. It enables the detection and quantification of: the roughness of a surface, scratches and digs on that surface, as well as SSD, this all in local areas of finished surfaces without special preparation of these surfaces. The iTIRM can also be used as an automated in-situ inspection method to monitor and investigate optical fabrication techniques. The presented iTIRM method is a helpful tool to diagnose optical components and their production.

References

[1] L. Dettmann, "Estimation of subsurface damage depth by dimpling", in *Science of Optical Finishing*, Vol. 9 of OSA 1990 Technical Digest Series (Optical Society of America, Washington, D.C., 1990), pp. 52-56.

[2] P. Temple, "Total Internal Reflection Microscopy: A Surface Inspection Technique," Appl. Opt. **20**, 2656-64 (1981).

[3] G. Nomarski, "Differential microinterferometer with polarized waves" J. Phys. Radium **16**, 9, (1955).

In-process measurement of wear of grinding wheel by hydrodynamic pressure

Katsushi FURUTANI *, Tomonao KATOH ** and Naotake MOHRI *
* Toyota Technological Institute
12-1, Hisakata 2-chome, Tempaku-ku, Nagoya 468-8511 Japan, e-mail: furutani@toyota-ti.ac.jp
** Toyota Technological Institute (NSK-Warner at present)

Key words: hydrodynamic pressure, wear, in-process measurement, repeatability

1. Introduction

Wet grinding is one of the major ways of high-precision machining. An error factor in grinding is wear of a grinding wheel. In order to reduce machining error, in-process measurement of grinding wheel wear is required. A number of methods for the in-process measurement of the wear of a grinding wheel have been studied:

(1) contact measurement with an AE sensor [1] for dry and wet grinding,

(2) noncontact measurement

a) with a triangular sensor [2] for dry grinding,

b) with an air micrometer [3] for dry grinding,

c) with an ultrasonic sensor [4] for wet grinding.

Grinding fluid usually causes difficulty in the wear measurement of the grinding wheel.

On the other hand, a grinding wheel drags grinding fluid into a small gap between a grinding wheel and a workpiece during wet grinding so that hydrodynamic pressure is generated in the gap [5]. Hence, the hydrodynamic pressure has been studied to investigate effects on machining accuracy in precision grinding or grinding performance [6].

In this paper, an in-process measurement method for the wear amount of a grinding wheel in wet condition is proposed. Grinding fluid is actively used to measure the wear in this method. The measurement principle is investigated by using a metallic disk for a trial. Then, accuracy in measurement of actual grinding wheels is discussed.

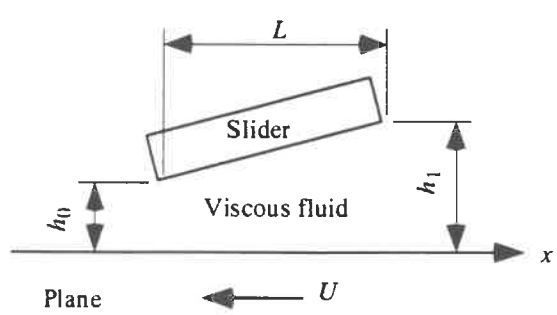

Fig. 1 Simplified model of slider and plane

2. Principle of measurement

A plane and a slider are arranged face to face with a small angle as shown in Fig. 1. The gap between the plane and the slider gradually narrows towards the moving direction of the plane. The gap is filled with viscous fluid. The plane moves in parallel with itself. Because the plane drags the viscous fluid into the gap, the hydrodynamic pressure is generated. Since the hydrodynamic pressure changes by the distance of the plane and the slider, the gap can be measured by measuring the hydrodynamic pressure.

Fig. 2 shows the measurement principle in the case of applying to a surface grinding process. A pressure sensor is set around a grinding wheel. Hydrodynamic pressure generated in the gap is measured with the pressure sensor. After we calibrate a relationship between the gap and the hydrodynamic pressure, the gap can be measured. Because the electromagnetic properties of the grinding wheel, a workpiece and grinding fluid do not affect the hydrodynamic pressure, the measurement process by this method becomes easier and more accurate than the measurement process with other noncontact sensors. Because the grinding fluid is actively used, other additional devices are not needed.

Suppose Fig. 1 to simplify a model of the system to

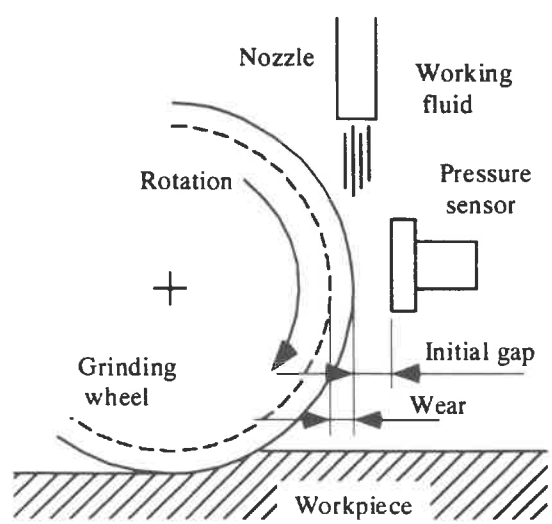

Fig. 2 Measurement principle

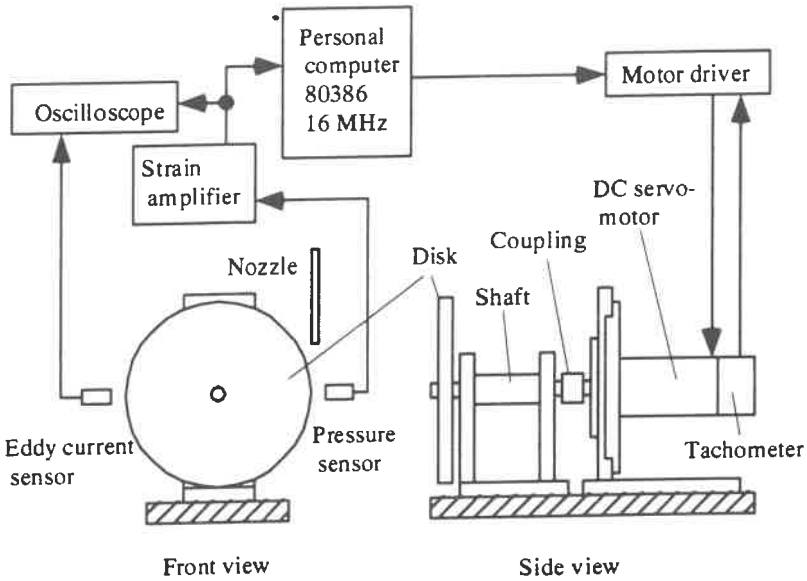

Fig. 3 Schematic view of experimental setup with disk

estimate the hydrodynamic pressure. The slider has infinite width.

Consider influence of a gap length on hydrodynamic pressure. By supposing that the grinding wheel with a radius R rotates at an angular velocity ω, variables are R and h_0, and Reynolds number is less than 1, change of the hydrodynamic pressure is given as a total differential form:

$$dp = \frac{3\mu\omega\alpha L}{2h_0(h_0+\alpha L)(2h_0+\alpha L)} \times \left\{ dR - \frac{5h_0^2 + 5\alpha L h_0 + \alpha^2 L^2}{2h_0(h_0+\alpha L)(2h_0+\alpha L)} dh_0 \right\} \quad (1)$$

where $h_1 = h_0 + \alpha L$, α indicates an inclination of the slider and μ is a coefficient of viscosity.

h_0 indicates a gap length between the wheel and a workpiece. When the grinding wheel wears, $dR = dh_0$ because a radius change of the grinding wheel causes a change of the gap length.

In actual use, h_0 becomes less than 100 μm so that the second term in the braces in Equation (1) is larger than the first term.

Therefore, the change of a gap length is equivalent to the radius change of the grinding wheel. In the following experiments, a gap length is changed to investigate hydrodynamic pressure in stead of changing the wheel radius.

3. Experiment by using metallic disk

3.1 Setup for basic experiments

Fig. 3 shows a setup for experiments with a disk. A device to rotate the disk is manufactured for the

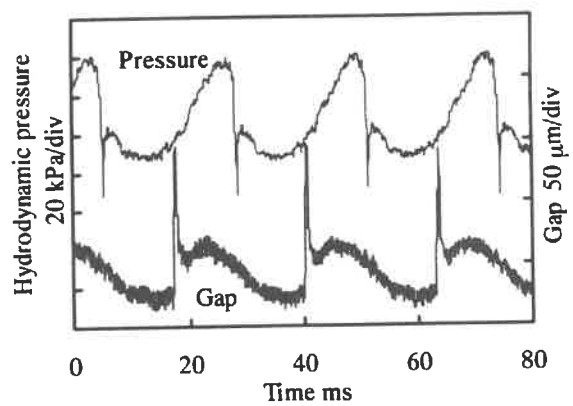

Fig. 4 Example of outputs of pressure sensor and displacement sensor

measurement of the hydrodynamic pressure. An aluminum disk is used instead of a grinding wheel to avoid roughness of the wheel periphery. Water is poured into the gap between the disk and a pressure sensor at 4 l/min. Hydrodynamic pressure is measured with the pressure sensor. The disk measures 200 mm in diameter and 10 mm in width. It is made by wire electric discharge machining. Both ends of the shaft are supported with ball bearings to reduce run out of a shaft. The device is driven with a DC servomotor with a tachometer. The pressure sensor is a diaphragm type with a diameter of 6 mm, a nominal maximum pressure of 0.098 Pa and a resonance frequency of 22 kHz. The output of the pressure sensor is detected with a strain amplifier with a frequency range from DC to 200 kHz.

The sensor is put at 1mm beneath the plate surface

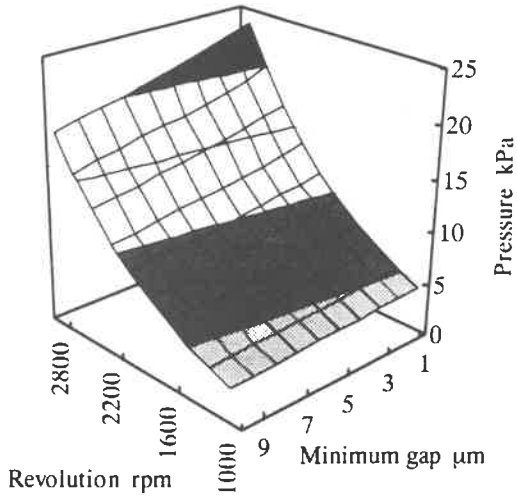

Fig. 5 Relationship between pressure, minimum gap and revolution

to prevent a crash of the disk with the pressure sensor. This plate is mounted on an xyz-stage to adjust a position of the sensor.

An eddy current displacement sensor with a sensitivity of 0.2 mm/V, a resolution of 0.4 μm and a frequency range of 18 kHz is used to compare a gap length with the output of the pressure sensor. The displacement sensor is symmetrically mounted on the opposite side with respect to the disk to the pressure sensor and both sensors are used simultaneously. A personal computer (80386, 16 MHz) is used to calculate average pressure and to set a reference revolution of the disk.

3.2 Generated hydrodynamic pressure

Hydrodynamic pressure is measured with the device. Fig. 4 shows an example of the hydrodynamic pressure and a gap length at a revolution of 2000 rpm and a minimum gap of 1 μm. A sensitivity of the pressure sensor including the strain amplifier is 1.02×10^{-4} V/Pa. The waveform of the output of the pressure sensor corresponds with that of the displacement sensor by shifting by a half cycle and turning upside down. An eccentricity of the disk and a groove with a width of 200 μm on the periphery of the disk cause waviness and projections of the waveforms, respectively.

Fig. 5 shows a relationship among average hydrodynamic pressure, minimum gap length and revolution of the disk. The minimum gap is changed from 1 to 10 μm. The revolution is changed from 1000 (10.5) to 2800 rpm (29.3 m/s). With the increase of the revolution or the decrease of the gap length, the hydrodynamic pressure becomes large. As the revolution is large, pressure is more sensitive to a gap length.

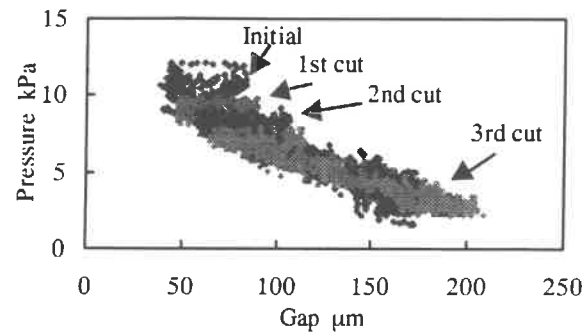

Fig. 6 Trajectory of pressure to gap

Table 1 Specifications of grinding wheels

	D#400	WA#46	WA#800
Outer diameter mm		305	
Inner diameter mm	127	127	76.2
Width mm	10	38	32
Grain	Diamond	White fused alumina	
Mesh size	400	46	800
Hardness		medium	
Bond	Resinoid	Vitrified	Shellac

3.3 Measurement of change of disk radius

The disk is actually worn to analyze influence of diameter change on the hydrodynamic pressure. Fig. 6 shows trajectories of the pressure versus the gap length. The disk is rotated at a peripheral speed of 29.3 m/s. The minimum gap is initially set to 40 μm. The disk is worn with a file three times. The change of the disk diameter and the pressure are measured after each wearing process. The measured pressure is disturbed because of turbulent flow of the water, low stiffness of the device and electric noise. Because these disturbances are often random, influence of them can be reduced by averaging. Each least square curve of the trajectories after the wearing process traces that of the initial trajectory.

4. Measurement of actual grinding wheels

4.1 Grinding machine used in experiments

Actual grinding wheels are measured on a surface grinding machine. Its wheel spindle rotates at 1800 rpm. The pressure sensor mounted on the xyz-stage is put on the table of the grinding machine. Grinding fluid is supplied at 25 l/min. Table 1 shows specifications of grinding wheels used in experiments. They have the same diameter of 305 mm to equalize peripheral speed. We define a Cartesian coordinate system where the x, y and z axes extend rightward, forward and upward, respectively.

4.2 Measurement of actual grinding wheel

Fig. 7 shows an example of a pressure distribution

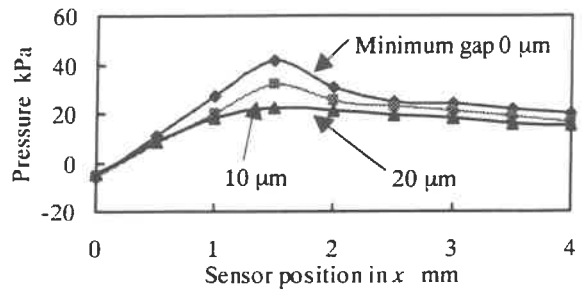

Fig. 7 Pressure distribution along x axis

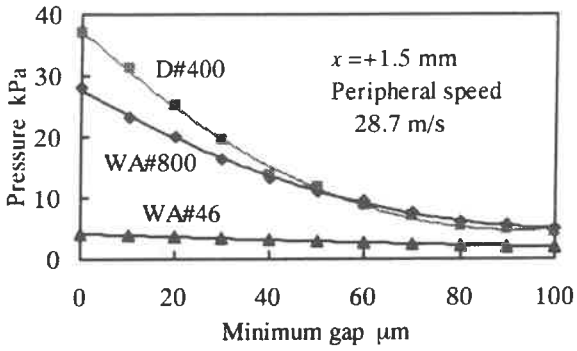

Fig. 8 Influence of mesh size

along the x-axis. Minimum gap is changed to 0, 10 and 20 μm. The hydrodynamic pressure becomes maximum at x = +1.5 mm. Hereafter, we measure the hydrodynamic pressure at x = +1.5 mm.

Fig. 8 shows a relationship between an average of a hydrodynamic pressure and a minimum gap length. The minimum gap length is changed from 0 to 100 μm. Grinding wheels are rotated at 28.7 m/s. The hydrodynamic pressure on actual grinding wheels changes in the same way as that on the disk. When a grain size is large or a bond has many pores, the average gap length becomes large so that the hydrodynamic pressure decreases.

Repeatability of the hydrodynamic pressure is investigated by using D#400 and WA#800. Fig. 9 shows a relationship between a hydrodynamic pressure and a minimum gap length, and a difference between the maximum and minimum pressure at each gap by using D#400. Results of 5 repetitive measurement are displayed in the figure. The maximum difference among measured pressure and an average pressures is equivalent to a gap error of 0.7 μm. Repeatability for WA#800 is almost the same as the repeatability for D#400.

5. Conclusions

An in-process measurement method for wear of a grinding wheel in wet condition is proposed in this

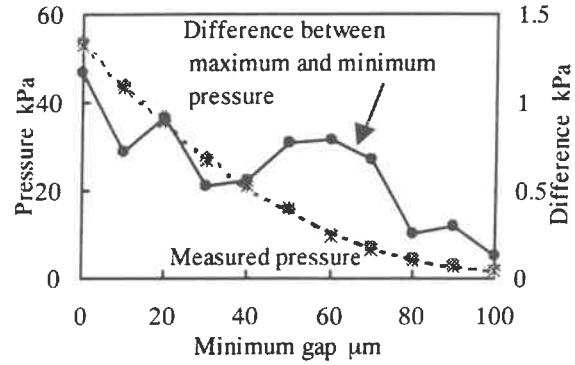

Fig. 9 Repeatability of measured pressure

paper. Conclusions can be drawn as follows:

(1) As a gap length increases, the hydrodynamic pressure is decreased.

(2) Repeatability of the hydrodynamic pressure is less than 1 %.

We will investigate influence of dressing, dulling or loading on the hydrodynamic pressure in actual grinding process.

Acknowledgement

We wish to thank Prof. Jiro Otsuka and Mr. Shigeomi Koshimizu of Shizuoka Institute of Science and Technology for their helpful advice, and Mr. Masaru Ohta and the staffs of the workshop of Toyota Technological Institute for their helpful cooperation. This study is financially supported by Suzuki Foundation and Foundation for Promotion of Advanced Automation Technology.

References

[1] W. P. Dong et al.: On-Line Measurement of Grinding wheel Wear Using Acoustic Emission, Proc. Annual Meeting of ASPE, Monterey, California, USA, pp. 566-571 (1996).

[2] E. Brinksmeier et al.: Monitoring of Grinding Wheel Wear, Ann. CIRP, 41, 1, pp. 373-376 (1992).

[3] H. J. Schreitmüller et al.: Pneumatisches Meßverfahren zur Ermittlung des Schleifscheibenverschleißes, Industrie-Anzeiger, 93, 68, 1733-1734 (1971).

[4] G. Spur et al.: Sensoren zur Erfassung von Prozesskenngrössen bei der Drehbearbeitung, Ann. CIRP, 24, 1, pp. 349-355 (1975).

[5] For example, R. D. Arnell et al.: Tribology - Principles and Design Applications, Macmillan Education, London, UK, pp. 163-165 (1991).

[6] M. Yokogawa et al.: Improving Grinding Performance of CBN Wheels by Dual-fluid Supply Method, Int. J. Japan Soc. Prec. Eng., 27, 1, pp. 11-16 (1993).

Authors Index

Ahn, J. H. 150
Ahn, J-Y. 233
Aikens, D. M. 466
Al-Regib, E. I. 200
Altieri, S. 429
Ament, C. 373
Aoyama, H. 257, 284
Aramaki, T. 449
Arnold, T. J. 513
Asakawa, K. 180
Ashida, A. 180
Bahowick, S. M. 309
Balon, S. A. P. 131
Bartel, D. S. 309
Bergstrom, T. S. 377
Bischoff, P. 583
Bittner, D. 253
Blaedel, K. 555
Bliss, E. S. 513
Blunt, L. A. 353, 381, 587
Bordatchev, E. V. 237
Born, D. K. 555
Braasch, J. 462
Brinksmeier, E. 163
Brown, C. A. 377
Bruning, J. H. 470
Bui, S. H. 337
Butler, D. L. 353, 381
Calzaretta, J. A. 567
Carlisle, B. . . . . *
Carr, J. 555
Chakravarthy, B. 265
Chandra, A. 119
Chang, J. J. 241
Chang, S-B. 241
Chargin, D. A. 567
Che, W-S. 175
Chen, J-S. 385
Chen, J-T. 333
Chen, Z. 276
Cherukuri, H. P. 265
Cho, I-H. 175
Cho, K-K. 154
Choi, D. K. 79
Choi, B. J. 196
Chou, B. C. S. 241
Chu, C. N. 79
Chung, G-H. 575
Chung, H-W. 575
Chung, S-C. 233, 249, 268
Chung, S-I. 154
Colburn, M. 196
Culpepper, M. L. 571
Cuttino, J. F. 212, 276
Dailey, M. J. 513
Danforth, P. M. 513
Danyluk, S. 139
Daus, N. A. 481
Davis, P. 555
Deck, L. L. 429, 477
Delbressine, F. L. M. 329
Devitt, A. J. . . . . *
Dewa, P. G. 470
Dow, T. A. 546
Dyer, S. W. 200
Ebert, E. 429
Edgeworth, R. M. 389
Endo, T. 425
Endoh, T. 357
English, R. E. 466
Evans, C. J. . . . . *
Fähnle, O. W. 509, 606
Faill, P. 583
Fang, F. Z. 62
Farahi, F. 445
Fawcett, H. E. 45
Fawcett, S. C. 45
Feng, Q. 313, 409
Ferreira, P. M. 401
Fess, E. 542
Fleddermann, C. 300
Fu, J. 393
Fu, Y. 192
Fujishima, M. 462
Fujishita, T. 288
Fukumoto, S. 37
Furutani, K. 159, 610
Gan, J. G. K. 296
Gao, W. 449, 521
Gao, Y. J. 317
Garrard, K. P. 546
Gatzen, H. H. 67, 83
Gecewicz, R. 429
Gee, A. E. 501
Gläbe, R. 163
Goch, G. 373
Goodman, W. A. 555
Gopalan, V. 337
Goto, T. 107
Graves, V. 245
Greene, P. 253
Grejda, R. D. 87, 405

*Extended abstract not available at press time.

Griffin, R. 365
Gweon, D-G. 280, 575
Haack, J. 555
Haga, H. 361
Haitjema, H. 329
Hale, L. . . . . *
Hamada, S. 551
Hanyu, H. 111
Hara, K. 559
Hara, S. 357
Hashimoto, H. 551
Haskew, T. 212
Hatamura, Y. 41
Heckele, M. 225
Herndon, B. 300
Hinnerichs, T. N. 272
Hiraki, Y. 127
Hirao, M. 95
Hirayama, H. 41
Hocken, R. J. 265, 393, 409, 417, 445, 521
Holl, S.-E. 481
Holmes, M. L. 429, 477
Honda, S. 229, 288
Honoki, T. 123
Hordin, R. S. 470
Horio, K. 135
Horiuchi, O. 505, 517
Horton, W. R. 309
Hosokawa, A. 99, 127
Hu, L-D. 333
Huang, C.-C. 529
Huang, H. 103
Huang, Y. 276
Hyohdoh, M. 135
Ichihara, J. 563
Iguchi, N. 95
Ikeda, T. 551, 563
Ikeno, J. 505, 517
Im, Y-G. 154
Imai, K. 551
Inaba, F. 485
Inada, A. 171
Ishii, T. 257
Ishikawa, K. 489
Ishikawa, Y. 216
Isobe, S. 559
Iwabe, H. 71
Iwase, A. 559
Izawa, M. 95
Janeczko, J. 365
Jansen, A. 453
Jensen, S. . . . . *
Jeong, D-S. 154
Jeong, H-D. 154, 175
Jiang, X. 381
Johnson, S. 196
Jokiel, Jr., B. 457
Jones, G. M. 67
Joseph, V. 184
Kaji, S. 107
Kakumanu, T. S. 493
Kallenbach, E. 579
Kanai, A. 485, 559
Kanai, M. 449
Kaneeda, T. 167
Kasai, T. 135
Kato, H. 111
Kato, S. 37, 204
Katoh, T. 610
Kawabe, T. 563
Kawahara, Y. 462
Kiani, S. 49
Kim, B-C. 433
Kim, S-C. 249
Kim, S-W. 433
Kiyono, S. 449
Knapp, B. R. 115
Knapp, W. 602
Knight, Jr., P. D. 341, 349, 437, 466
Kobayashi, H. 563
Koch, J. A. 513
Koyabu, K. 216
Kroll, J. J. 397
Kube, H. 579
Kulawiec, A. W. 470
Lamppa, K. 300
Lee, H-S. 361
Lee, I. H. 325
Lee, J. H. 280
Lee, M. C. 401
Leung, K. K. 208
Li, B. 261
Li, Y. 542
Liang, J. 313
Lim, H-S. 150
Lim, L. E. N. 317
Ling, Z. K. 75
Liu, J. 462
Locke, S. F. 57
Loh, B-G. 304
Lovingood, J. 521
Lu, G. 212
Lucca, D. A. 521
Ludwick, S. J. 567
Maeda, Y. 171
Malsbury, T. . . . . *
Marsh, E. R. 87, 115, 405
Martin, D. 405
Masuda, M. 71, 171
Matsui, S. 216

*Extended abstract not available at press time.

Matsumoto, K. 41
Matsuo, S. 425
Matsuzaki, J. 180
McClellan, M. R. 555
McCleskey, J. 300
Mehalso, R. M. 33
Miller, E. 546
Miller, J. A. 409
Miller, M. H. 119, 493
Mitchell, D. K. 45
Mitsuhashi, M. 221
Mitsui, K. 321
Miyaguchi, T. 71
Miyake, H. 159
Miyashita, M. 485, 559
Miyoshi, T. 345
Mohri, N. 159, 610
Montesanti, R. C. 57
Moon, D-M. 175
Moon, K. S. 75
Moronuki, N. 292
Morsbach, C. 67
Mu, Y. H. 296
Murashita, H. 257
Mutoh, A. 171
Nagashima, T. 361
Nagata, H. 559
Nair, P. K. 91
Nakamura, M. 107
Nakao, M. 41
Namba, Y. 369
Naruse, F. 505
Nayfeh, S. . . . . *
Ngoi, B. K. A. 296, 317, 369, 441
Nikumb, S. K. 237
Oh, H. R. 280
Ohira, F. 216
Ohno, K. 221
Ohno, M. 37, 204
Ohzeki, H. 257
Oishi, H. 180
Ono, T. 284
Ooi, T. 41
Ootani, K. 95
Otsubo, M. 41
Otsuka, S. 563
Pahk, H-J. 325, 413
Park, S. L. 280
Parker, D. H. 21
Patten, J. 521
Patterson, S. R. 397, 421, 437
Pawlowski, B. 579
Payne, J. M. 21
Peggs, G. N. . . . . *
Pereira, P. H. 417
Phillips, S. D. 525
Pigg, D. C. 349
Prakash, E. S. 184
Puthanangady, T. 497
Qu, W. 119
Radhakrishnan, V. P. 473
Raja, J. 337
Ramamoorthy, B. 91
Ramanan, V. 409
Reddy, K. H. P. 91
Rhee, H-G. 433
Ro, P. I. 304
Rorke, Jr., W. S. 25, 309
Rosielle, N. 453
Ruckman, J. 542
Ruprecht, R. 225
Ryu, S. H. 79
Sacks, R. A. 513
Sadashivappa, K. 184, 188
Saeki, M. 127
Sakai, K. 53
Sakamoto, S. 127
Sakata, M. 127
Sakuma, K. 99
Salsbury, J. G. 533
Samuels, M. 429
Saneto, A. 159
Sawaki, D. 517
Schaller, T. 225
Schellekens, P. H. J. 329, 453
Schinstock, D. 212
Schmitz, S. 473
Schmitz, T. L. 29
Schubert, K. 225
Seo, J. W. 280
Shaikh, F. Z. 571
Shan, L. 139
Shang, Z. 253
Sharma, A. K. 421
Sheridan, T. G. 309
Shigeno, T. 284
Shim, J-Y. 575
Shin, H-J. 413
Shintani, K. 111
Shirai, K. 345
Shirakata, S. 41
Shirakawa, M. 37, 204
Shirase, K. 95
Shirley, L. G. 15
Shull, B. 429
Siekmann, H. 83
Singaperumal, M. 184
Slocum, A. H. 49, 571
Smith, S. T. 538
Sohn, A. 546

*Extended abstract not available at press time.

Somashekhar, S. H. 188
Son, S-M. 150
Soobitsky, J. 429
Spur, G. 481
Sreenivasan, S. V. 196
Stolz, C. J. 513
Stout, K. J. 353, 381, 587
Subramanian, K. R. 337
Sumomogi, T. 107, 425
Suwabe, H. 489
Syn, C. 555
Syoji, K. 123
Tabata, M. 204
Tadokoro, S. 284
Tajbakhsh, H. . . . . *
Tajima, A. 485
Takahashi, S. 345
Takaya, Y. 345
Takeda, T. 551
Takeoka, E. 71
Takezawa, H. 159
Tan, B. H. 131
Tanaka, K. 123
Tatsumi, T. 551
Thompson, S. L. 57
Thorburn, B. 45
Tian, Q. 313
Toepfer, J. 579
Tomita, Y. 559
Tracy, S. P. 583
Tran, H. D. 272, 300
Tricard, M. 497
Trumper, D. L. 567
Uchiyama, K. 292
Ueda, T. 99
Uhlmann, E. 481
Une, A. 216
Uneda, M. 489
Utsumi, M. 167
Vallance, R. R. 49
van Brug, H. 509, 606
van der Bijl, R-J. M 606
van Dorp, B. W. J. J. A. 329
Venkatakrishnan, K. 441
Wada, T. 229
Wakabayashi, T. 361
Waki, Y. 171
Wang, B. 146
Wang, C. 365
Wang, X. D. 296
Watanabe, E. 167
Watanabe, I. 563
Webster, J. A. 353
Weckenmann, A. 473
Wegener, B. L. 71
Weikert, S. 602
Whistler, W. T. 513
Wilhelm, R. G. 265, 389
Wilkins, P. R. 341, 349, 466
Williams, D. F. 501
Williams, M. E. 583
Willson, C. G. 196
Winters, S. E. 513
Woodfin, A. D. 445
Woods, B. W. 513
Woody, S. C. 538
Wright, T. 546
Wronosky, J. 583
Yamaguchi, K. 53
Yamazaki, G. 127
Yamazaki, K. 462
Yan, Q. 123
Yanagi, K. 357
Yasui, H. 127
Yasui, T. 95
Yeo, S. H. 131
Yu, J. 369
Yuan, Z. J. 62
Zacharias, R. A. 513
Zhang, C. 146
Zhang, S. 449
Zhang, X. D. 146, 529
Zhang, Y. 192
Zhong, Z. W. 369
Zhou, M. 131
Zhu, Y-C. 333
Ziegert, J. C. 29, 457
Zimmermann, M. 555
Zou, W-Y. 333
Zou, Z-Q. 333

*Extended abstract not available at press time.